



Pertanika Journal of

**SCIENCE &
TECHNOLOGY**

JST

VOL. 33 (3) APR. 2025



PERTANIKA
JOURNALS

A scientific journal published by Universiti Putra Malaysia Press

PERTANIKA JOURNAL OF SCIENCE & TECHNOLOGY

About the Journal

Overview

Pertanika Journal of Science & Technology is an official journal of Universiti Putra Malaysia. It is an open-access online scientific journal. It publishes original scientific outputs. It neither accepts nor commissions third party content.

Recognised internationally as the leading peer-reviewed interdisciplinary journal devoted to the publication of original papers, it serves as a forum for practical approaches to improve quality on issues pertaining to science and engineering and its related fields.

Pertanika Journal of Science & Technology currently publishes 6 issues a year (*January, March, April, July, August, and October*). It is considered for publication of original articles as per its scope. The journal publishes in **English** and it is open for submission by authors from all over the world.

The journal is available world-wide.

Aims and scope

Pertanika Journal of Science & Technology aims to provide a forum for high quality research related to science and engineering research. Areas relevant to the scope of the journal include: bioinformatics, bioscience, biotechnology and bio-molecular sciences, chemistry, computer science, ecology, engineering, engineering design, environmental control and management, mathematics and statistics, medicine and health sciences, nanotechnology, physics, safety and emergency management, and related fields of study.

History

Pertanika Journal of Science & Technology was founded in 1993 and focuses on research in science and engineering and its related fields.

Vision

To publish a journal of international repute.

Mission

Our goal is to bring the highest quality research to the widest possible audience.

Quality

We aim for excellence, sustained by a responsible and professional approach to journal publishing. Submissions can expect to receive a decision within 90 days. The elapsed time from submission to publication for the articles averages 180 days. We are working towards decreasing the processing time with the help of our editors and the reviewers.

Abstracting and indexing of Pertanika

Pertanika Journal of Science & Technology is now over 32 years old; this accumulated knowledge and experience has resulted the journal being abstracted and indexed in SCOPUS (Elsevier), Journal Citation Reports (JCR-Clarivate), EBSCO, ASEAN CITATION INDEX, Microsoft Academic, Google Scholar, and MyCite.

Citing journal articles

The abbreviation for Pertanika Journal of Science & Technology is *Pertanika J. Sci. & Technol.*

Publication policy

Pertanika policy prohibits an author from submitting the same manuscript for concurrent consideration by two or more publications. It prohibits as well publication of any manuscript that has already been published either in whole or substantial part elsewhere. It also does not permit publication of manuscript that has been published in full in proceedings.

Code of Ethics

The *Pertanika* journals and Universiti Putra Malaysia take seriously the responsibility of all of its journal publications to reflect the highest in publication ethics. Thus, all journals and journal editors are expected to abide by the journal's codes of ethics. Refer to *Pertanika's Code of Ethics* for full details, or visit the journal's web link at http://www.pertanika.upm.edu.my/code_of_ethics.php

Originality

The author must ensure that when a manuscript is submitted to *Pertanika*, the manuscript must be an original work. The author should check the manuscript for any possible plagiarism using any program such as Turn-It-In or any other software before submitting the manuscripts to the *Pertanika* Editorial Office, Journal Division.

All submitted manuscripts must be in the journal's acceptable similarity index range:
 $\leq 20\%$ – **PASS**; $> 20\%$ – **REJECT**.

International Standard Serial Number (ISSN)

An ISSN is an 8-digit code used to identify periodicals such as journals of all kinds and on all media—print and electronic.

Pertanika Journal of Science & Technology: e-ISSN 2231-8526 (Online).

Lag time

A decision on acceptance or rejection of a manuscript is reached in 90 days (average). The elapsed time from submission to publication for the articles averages 180 days.

Authorship

Authors are not permitted to add or remove any names from the authorship provided at the time of initial submission without the consent of the journal's Chief Executive Editor.

Manuscript preparation

For manuscript preparation, authors may refer to *Pertanika*'s **INSTRUCTION TO AUTHORS**, available on the official website of *Pertanika*.

Editorial process

Authors who complete any submission are notified with an acknowledgement containing a manuscript ID on receipt of a manuscript, and upon the editorial decision regarding publication.

Pertanika follows a **double-blind peer-review** process. Manuscripts deemed suitable for publication are sent to reviewers. Authors are encouraged to suggest names of at least 3 potential reviewers at the time of submission of their manuscripts to *Pertanika*, but the editors will make the final selection and are not, however, bound by these suggestions.

Notification of the editorial decision is usually provided within 90 days from the receipt of manuscript. Publication of solicited manuscripts is not guaranteed. In most cases, manuscripts are accepted conditionally, pending an author's revision of the material.

The journal's peer review

In the peer-review process, 2 to 3 referees independently evaluate the scientific quality of the submitted manuscripts. At least 2 referee reports are required to help make a decision.

Peer reviewers are experts chosen by journal editors to provide written assessment of the **strengths** and **weaknesses** of written research, with the aim of improving the reporting of research and identifying the most appropriate and highest quality material for the journal.

Operating and review process

What happens to a manuscript once it is submitted to *Pertanika*? Typically, there are 7 steps to the editorial review process:

1. The journal's Chief Executive Editor and the Editor-in-Chief examine the paper to determine whether it is relevance to journal needs in terms of novelty, impact, design, procedure, language as well as presentation and allow it to proceed to the reviewing process. If not appropriate, the manuscript is rejected outright and the author is informed.
2. The Chief Executive Editor sends the article-identifying information having been removed, to 2 to 3 reviewers. They are specialists in the subject matter of the article. The Chief Executive Editor requests that they complete the review within 3 weeks.

Comments to authors are about the appropriateness and adequacy of the theoretical or conceptual framework, literature review, method, results and discussion, and conclusions. Reviewers often include suggestions for strengthening of the manuscript. Comments to the editor are in the nature of the significance of the work and its potential contribution to the research field.

3. The Editor-in-Chief examines the review reports and decides whether to accept or reject the manuscript, invite the authors to revise and resubmit the manuscript, or seek additional review reports. In rare instances, the manuscript is accepted with almost no revision. Almost without exception, reviewers' comments (to the authors) are forwarded to the authors. If a revision is indicated, the editor provides guidelines for attending to the reviewers' suggestions and perhaps additional advice about revising the manuscript.
4. The authors decide whether and how to address the reviewers' comments and criticisms and the editor's concerns. The authors return a revised version of the paper to the Chief Executive Editor along with specific information describing how they have addressed the concerns of the reviewers and the editor, usually in a tabular form. The authors may also submit a rebuttal if there is a need especially when the authors disagree with certain comments provided by reviewers.
5. The Chief Executive Editor sends the revised manuscript out for re-review. Typically, at least 1 of the original reviewers will be asked to examine the article.
6. When the reviewers have completed their work, the Editor-in-Chief examines their comments and decides whether the manuscript is ready to be published, needs another round of revisions, or should be rejected. If the decision is to accept, the Chief Executive Editor is notified.
7. The Chief Executive Editor reserves the final right to accept or reject any material for publication, if the processing of a particular manuscript is deemed not to be in compliance with the S.O.P. of *Pertanika*. An acceptance letter is sent to all the authors.

The editorial office ensures that the manuscript adheres to the correct style (in-text citations, the reference list, and tables are typical areas of concern, clarity, and grammar). The authors are asked to respond to any minor queries by the editorial office. Following these corrections, page proofs are mailed to the corresponding authors for their final approval. At this point, **only essential changes are accepted**. Finally, the manuscript appears in the pages of the journal and is posted on-line.

Pertanika Journal of
**SCIENCE
& TECHNOLOGY**

Vol. 33 (3) Apr. 2025



A scientific journal published by Universiti Putra Malaysia Press

UNIVERSITY PUBLICATIONS COMMITTEE

CHAIRMAN
Zamberi Sekawi

EDITOR-IN-CHIEF
Luqman Chuah Abdullah
Chemical Engineering

EDITORIAL STAFF

Journal Officers:
Ellyianur Puteri Zainal
Kanagamalar Silvarajoo
Siti Zuhaila Abd Wahid

Editorial Assistants:
Siti Juridah Mat Arip
Zulinaardawati Kamarudin

English Editor:
Norhanizah Ismail

PRODUCTION STAFF

Pre-press Officers:
Ku Ida Mastura Ku Baharom
Nur Farrah Dila Ismail

WEBMASTER

IT Officer:
Kiran Raj Kaneswaran

EDITORIAL OFFICE

JOURNAL DIVISION
Putra Science Park
1st Floor, IDEA Tower II
UPM-MTDC Technology Centre
Universiti Putra Malaysia
43400 Serdang, Selangor Malaysia.

General Enquiry
Tel. No: +603 9769 1622
E-mail:
executive_editor.pertanika@upm.edu.my
URL: <http://www.pertanika.upm.edu.my>

PUBLISHER

UPM Press
Universiti Putra Malaysia
43400 UPM, Serdang, Selangor, Malaysia.
Tel: +603 9769 8855
E-mail: dir.penerbit@upm.edu.my
URL: <http://penerbit.upm.edu.my>



ASSOCIATE EDITOR

2024-2026

Miss Laiha Mat Kiah
Security Services Sn: Digital Forensic, Steganography, Network Security, Information Security, Communication Protocols, Security Protocols
Universiti Malaysia, Malaysia

Saidur Rahman
Renewable Energy, Nanofluids, Energy Efficiency, Heat Transfer, Energy Policy
Sunway University, Malaysia

EDITORIAL BOARD

2024-2026

Abdul Latif Ahmad
Chemical Engineering
Universiti Sains Malaysia, Malaysia

Hsiu-Po Kuo
Chemical Engineering
National Taiwan University, Taiwan

Mohd. Ali Hassan
Bioprocess Engineering, Environmental Biotechnology
Universiti Putra Malaysia, Malaysia

Ahmad Zaharin Aris
Hydrochemistry, Environmental Chemistry, Environmental Forensics, Heavy Metals
Universiti Putra Malaysia, Malaysia

Ivan D. Rukhlenko
Nonlinear Optics, Silicon Photonics, Plasmonics and Nanotechnology
The University of Sydney, Australia

Nor Azah Yusof
Biosensors, Chemical Sensor, Functional Material
Universiti Putra Malaysia, Malaysia

Azlina Harun@Kamaruddin
Enzyme Technology, Fermentation Technology
Universiti Sains Malaysia, Malaysia

Lee Keat Teong
Energy Environment, Reaction Engineering, Waste Utilization, Renewable Energy
Universiti Sains Malaysia, Malaysia

Norbahiah Misran
Communication Engineering
Universiti Kebangsaan Malaysia, Malaysia

Bassim H. Hameed
Chemical Engineering: Reaction Engineering, Environmental Catalysis & Adsorption
Qatar University, Qatar

Mohamed Othman
Communication Technology and Network, Scientific Computing
Universiti Putra Malaysia, Malaysia

Roslan Abd-Shukor
Physics & Materials Physics, Superconducting Materials
Universiti Kebangsaan Malaysia, Malaysia

Biswajeet Pradhan
Digital image processing, Geographical Information System (GIS), Remote Sensing
University of Technology Sydney, Australia

Mohd Shukry Abdul Majid
Polymer Composites, Composite Pipes, Natural Fibre Composites, Biodegradable Composites, Bio-Composites
Universiti Malaysia Perlis, Malaysia

Sodeifan Gholamhossein
Supercritical technology, Optimization, nanoparticles, Polymer nanocomposites
University of Kashan, Iran

Ho Yuh-Shan
Water research, Chemical Engineering and Environmental Studies
Asia University, Taiwan

Mohd Zulkifly Abdullah
Fluid Mechanics, Heat Transfer, Computational Fluid Dynamics (CFD)
Universiti Sains Malaysia, Malaysia

Wing Keong Ng
Aquaculture, Aquatic Animal Nutrition, Aqua Feed Technology
Universiti Sains Malaysia, Malaysia

INTERNATIONAL ADVISORY BOARD

2024-2027

Hiroshi Uyama
Polymer Chemistry, Organic Compounds, Coating, Chemical Engineering
Osaka University, Japan

Mohini Sain
Material Science, Biocomposites, Biomaterials
University of Toronto, Canada

Mohamed Pourkashanian
Mechanical Engineering, Energy, CFD and Combustion Processes
Sheffield University, United Kingdom

Yulong Ding
Particle Science & Thermal Engineering
University of Birmingham, United Kingdom

ABSTRACTING AND INDEXING OF PERTANIKA JOURNALS

Pertanika Journal of Science & Technology is indexed in Journal Citation Reports (JCR-Clarivate), SCOPUS (Elsevier), EBSCO, ASEAN Citation Index, Microsoft Academic, Google Scholar and MyCite.

Pertanika Journal of Science & Technology
Vol. 33 (3) Apr. 2025

Contents

Foreword	i
<i>Luqman Chuah Abdullah</i>	
A Clustering-based Hybrid Approach for Analyzing High-grade Gliomas Using Radiomic Features	1105
<i>Sairam Vuppala Adithya, Navaneeth Bhaskar and Priyanka Tupe-Waghmare</i>	
A Transfer Function Modelling Using System Identification for Air-cooling Photovoltaic System	1119
<i>Rozita Mustafa, Mohd Amran Mohd Radzi, Azura Che Soh and Hashim Hizam</i>	
Growth Monitoring of Healthy and BSR-infected Oil Palm Seedlings Using Ground-based LiDAR	1137
<i>Nur Azuan Husin, Ray Clement Ridu, Normahnani Md Noh and Siti Khairunniza Bejo</i>	
<i>Review Article</i>	
Thermal and Mechanical Stability of Bismuth Doped Sn-Ag-Cu Lead-free Solder: A Comprehensive Review	1159
<i>Ong Jun Lin, Azmah Hanim Mohamed Ariff, Nuraini Abdul Aziz and Azizan As'arry</i>	
<i>Review Article</i>	
A Review on Experimental, Numerical, and Machine Learning-based Solar Energy Harvesting for Road Pavements Application	1185
<i>Muhammad Imran Najeed, Nurul Aqilah Razeman, Zarina Itam, Salmia Beddu, Nazirul Mubin Zahari, Mohd Zakwan Ramli, Mohd Hafiz Zawawi, Nur Liyana Mohd Kamal, Agusril Syamsir and Daud Mohamad</i>	
Examining the Impact of Battery Properties and Energy Storage Connectivity for Electric Vehicle Charging Performance	1209
<i>Muhammad Izzul Mawardi, Nik Hakimi Nik Ali, Muhamad Nabil Hidayat, Ezmin Abdullah, Muhammad Umair, Ahmad Sukri Ahmad and Muzakkir Mohammad Zainol</i>	

Review Article

- Thematic Trends on Data Quality Studies in Big Data Analytics: A Review 1231
Nazliah Chikon, Shuzlina Abdul-Rahman and Syaripah Ruzaini Syed Aris

- Numerical Study on the Effects of Wire bonding Looping Formation on 1257
Light-emitting Diode Encapsulation Process
Ahmad Amin Azmi Jaludin, Mohd Syakirin Rusdi, Mohd Sharizal Abdul Aziz and Mohammad Hafifi Hafiz Ishak

- Development of a Two-board Potentiostat for Square Wave Anodic 1273
Stripping Voltammetry: Prospects for Heavy Metal Monitoring
Siti Nur Hanisah Umar, Elmi Abu Bakar, Mohammad Nishat Akhtar, Noorfazreena Mohammad Kamaruddin and Naoki Uchiyama

- Design of a Two-layer SIW Power Divider with Slot Aperture Y-junction 1301
for Enhanced Narrowband Isolation
Gan Siang Tan, Siti Zuraidah Ibrahim, Mohd Nazri A Karim, Ping Jack Soh, Khuzairi Masrakin and Sugchai Tantivivat

- Phyto Constituents of *Ananas comosus* Leaf Extract Enhancing the 1321
Copper Nanoparticles Synthesis
Nur Diyana Zulpahmi, Wan Zuraida Wan Mohd Zain, Fazlena Hamzah, Nurul Wahida Ramli, Nur 'Amira Hamid, Irmaizatussyehdany Buniyamin, Wan Atikah Wan Hamidon and Siti Aisha Na'illa Che Musa

- Role of Brassinosteroid on Growth, Metabolic Contents and Wax Ester 1341
Fermentation in *Euglena* sp.
Deviko Mardiansah, Tia Erfianti, Khusnul Qonita Maghfiroh, Dedy Kurnianto, Ria Amelia, Brilian Ryan Sadewo and Eko Agus Suyono

- Comparative Evaluation of Python-based Heart Rate Variability Analysis 1367
Tools for Neonatal Sepsis Detection in Neonatal Intensive Care Units
Roshan David Jathanna, Dinesh Acharya Udupi, Faiza Iqbal, Krishnamoorthi Makkithaya and Leslie Edward Simon Lewis

Review Article

- Comprehensive Review on Sustainable Dam Infrastructure: Issues and 1387
Challenges, Factors Causing Dam Failure and Future Direction in a Globally Changing Climate
Nur Azwa Muhamad Bashar, Mohd Remy Rozainy Mohd Arif Zainol, Mohd Sharizal Abdul Aziz, Ahmad Zhafran Ahmad Mazlan, Mohd Hafiz Zawawi and Teh Sabariah Abd Manan

Assessment of the Bioavailability of Zinc (Zn), Lead (Pb), Nickel (Ni), and Cadmium (Cd) in the Sediments of the Sungai Buloh Estuaries, Selangor <i>Aqilah Mukhtar, Mohd Nazri M Yunus, Nur Amiera Kamarudin, Syaizwan Zahmir Zulkifli and Ahmad Ismail</i>	1413
Comparative Analysis of Ultrasonic Inspection Techniques for Corrosion Monitoring in Petrochemical Plants Using Analytic Hierarchy Process (AHP) <i>Jan Lean Tai, Mohamed Thariq Hameed Sultan and Farah Syazwani Shahar</i>	1439
<i>Review Article</i>	
Effectiveness of Using Augmented Reality-based Picture Exchange Communication System (PECS) in Improving Communication Skills of Autistic Students in Indonesian Language Subjects: Bibliometric Analysis <i>Munir, Dwi Novia Al Husaeni, Eka Fitrajaya Rahman and Rasim</i>	1459
Optimization and Analysis of Ultrasonic Wedge Bonding Parameters for Enhanced Bonding Performance in 21700 Cylindrical Lithium Battery Modules <i>Bin Luo, Mohamad Hanif Md Saad, Altaf Hossain Molla and Zambri Harun</i>	1483
Coastal Bris Wetland Hydrodynamics in Non-Monsoon and Monsoon Seasons at Mengabang Telipot Terengganu, Peninsular Malaysia <i>Syazuani Mohd Shariff, Edlic Sathiamurthy and Mohd Sofiyan Sulaiman</i>	1509
AI-driven Vision-based Pothole Detection for Improved Road Safety <i>Muhammad Aizat Rasee, Ung Ling Ling, Gloria Jennis Tan, Tan Chi Wee, Ron Buking, Norziana Yahya and Habibah Ismail</i>	1535
Investigation of Aged-related Metabolites in the Marine Polychaete (<i>Marphysa moribidii</i>) using ¹ H NMR Metabolomics and LC-MS/MS Analysis <i>Nurfarah Aini Mocktar, Mohamad Sofi Abu Hassan, Maulidiani Maulidiani, Wan Iryani Wan Ismail, Izwandy Idris, Farhanini Yusoff and Noor Aniza Harun</i>	1563
Energy Management Systems Development in Electric Vehicle Charging Stations Based on Multi-Source Inverters with Utilisation of Renewable Energy Sources <i>Iradiratu Diah Prahmana Karyatanti, Belly Yan Dewantara, Istiyo Winarno, Daeng Rahmatullah and Nuhman</i>	1595

Effect of Heat Treatment on the Properties of Perlis Dolomite Powder <i>Nur Hasnidah Ahmad Shukeri, Syed Nuzul Fadzli Syed Adam, Hasmaliza Mohamad, Heah Cheng Yong and Hamdan Yahya</i>	1613
Enhanced White Blood Cell and Platelet Segmentation: A Particle Swarm Optimization-based Chromaticity approach <i>Aiswarya Senthilvel, Krishnaveni Marimuthu and Subashini Parthasarathy</i>	1633
<i>Review Article</i>	
Weaving a Greener Tomorrow: A Mini Review of Bamboo Fiber, Textiles and Hand-woven Techniques for Sustainable Innovation <i>Marzie Hatef Jalil</i>	1661

Foreword

Welcome to the third issue of 2025 for the *Pertanika Journal of Science and Technology (PJST)*!

PJST is an open-access journal for studies in Science and Technology published by Universiti Putra Malaysia Press. It is independently owned and managed by the university for the benefit of the world-wide science community.

This issue contains 25 articles: six review articles; and the rest are regular articles. The authors of these articles come from different countries namely India, Indonesia, Japan, Malaysia and Thailand.

A regular article titled “AI-Driven Vision-Based Pothole Detection for Improved Road Safety” was written by Muhammad Aizat Rasee and co-researchers from Malaysia. Their research developed a pothole detection system using convolutional neural networks (CNN) and YOLO algorithms to improve road safety and infrastructure maintenance. The system, trained on 4,681 images, achieved a 92.85% accuracy rate, detecting potholes and providing real-time warnings to drivers. This enhances safety, reduces vehicle damage, and optimizes government spending on repairs. The project aligns with Malaysia’s sustainable development goals (SDG), particularly SDG 3 (Good Health and Well-being), SDG 9 (Industry, Innovation, and Infrastructure), and SDG 11 (Sustainable Cities and Communities). Detailed information on this study can be found on page 1535.

Nurfarah Aini Mocktar et al. from Universiti Malaysia Terengganu investigated the metabolite profiles of different age classes of *Marphysa moribidii*, a marine polychaete, using proton nuclear magnetic resonance (¹H NMR) and liquid chromatography-tandem mass spectrometry (LC-MS/MS). Thirty-five metabolites were identified via NMR, while LC-MS/MS detected 36, including amino acids, carbohydrates, fatty acids, and organic acids. The middle-aged class showed the highest concentration of metabolites, particularly amino and fatty acids, suggesting it was the ideal stage for harvesting. These metabolites may offer biological activities such as antioxidant, anti-inflammatory, and antibacterial properties. The findings highlight age-related metabolic variability and lay the groundwork for future studies on the genetic and biochemical mechanisms behind these changes, enhancing our understanding of *M. moribidii*’s physiology and ecology. Further details of the article are available on page 1563.

Another article that we wish to highlight is “Enhanced White Blood Cell and Platelet Segmentation: A Particle Swarm Optimization-based Chromaticity approach” by Aiswarya Senthilvel, Krishnaveni Marimuthu, and Subashini Parthasarathy from India. This study proposed a novel approach for accurately segmenting white blood cells (WBCs) and platelets in blood smear images to enhance the detection of sickle cell disease (SCD). By leveraging the RG chromaticity, the method

identifies regions with high pixel chromatic variance to differentiate WBCs and platelets from red blood cells (RBCs). Using particle swarm optimization (PSO), the optimal threshold values for segmentation were determined, achieving a high accuracy of 96.32%, a sensitivity of 96.97%, a precision of 96.96%, and an F-score of 97.46%. This approach improves upon traditional methods by considering chromaticity as a feature for segmentation, offering better precision than previous techniques. The method's future potential includes automating segmentation using convolutional neural networks (CNNs) to enhance diagnostic accuracy and efficiency in detecting conditions like leukemia. Comprehensive details about this study can be found on page 1633.

We anticipate that you will find the evidence presented in this issue to be intriguing, thought-provoking and useful in reaching new milestones in your own research. Please recommend the journal to your colleagues and students to make this endeavour meaningful.

All the papers published in this edition underwent Pertanika's stringent peer-review process involving a minimum of two reviewers comprising internal as well as external referees. This was to ensure that the quality of the papers justified the high ranking of the journal, which is renowned as a heavily-cited journal not only by authors and researchers in Malaysia but by those in other countries around the world as well.

We would also like to express our gratitude to all the contributors, namely the authors, reviewers and Editorial Board Members of PJST, who have made this issue possible.

PJST is currently accepting manuscripts for upcoming issues based on original qualitative or quantitative research that opens new areas of inquiry and investigation.

Editor-in-Chief

Luqman Chuah Abdullah

A Clustering-based Hybrid Approach for Analyzing High-grade Gliomas Using Radiomic Features

Sairam Vuppala Adithya¹, Navaneeth Bhaskar^{2*} and Priyanka Tupe-Waghmare¹

¹*Symbiosis Institute of Technology, Symbiosis International (Deemed University), 412115 Pune, India*

²*Department of Artificial Intelligence & Data Science, NMAM Institute of Technology, NITTE (Deemed to be University), Nitte - 574110, Karnataka, India*

ABSTRACT

Unlabeled data is a significant problem in healthcare and other fields that deal with huge datasets. Unsupervised learning has the potential to be an effective solution in this case. The use of unsupervised algorithms in disease diagnosis has not been widely explored. In this work, we have developed a clustering algorithm to analyze the gliomas using Magnetic Resonance Imaging (MRI) data. Glioma is a severe medical illness that necessitates an accurate and timely diagnosis to establish effective treatment options. We used Pyradiomics to extract radiomic characteristics from MRI scans, which were then fed into a number of clustering methods, with cluster fitness assessed using primary assessment metrics. The best clustering algorithm was used as the pre-processor and to train major classification algorithms. In this study, we examined the performance of three prominent clustering algorithms, with agglomerative clustering outperforming the others. We achieved 0.83 Silhouette Coefficient, 0.21 Davies-Bouldin Index, and 323.22 Calinski-Harabasz Index values using aggregative clustering using Pyradiomics features. The decision tree strategy outperformed all classification methods, achieving 99.54% accuracy when clustering was applied to preprocess the data before classification. The proposed work has considerable potential for faster and more accurate analysis of medical image problems, especially in gliomas.

Keywords: Classification Algorithms, clustering, gliomas, machine learning, magnetic resonance imaging, unsupervised learning

ARTICLE INFO

Article history:

Received: 10 February 2024

Accepted: 16 January 2025

Published: 26 March 2025

DOI: <https://doi.org/10.47836/pjst.33.3.01>

E-mail addresses:

sairam.v.mtech2023@sitpune.edu.in (Sairam Vuppala Adithya)

navbskr@gmail.com (Navaneeth Bhaskar)

priyanka.tupe@sitpune.edu.in (Priyanka Tupe-Waghmare)

* Corresponding author

INTRODUCTION

A glioma is a tumor that develops from glial cells, the central nervous system's support cells. Glioma is deemed dangerous for various reasons, including its nature and influence on the central nervous system. Gliomas are graded according to the criteria

specified by the World Health Organization (WHO). Grades 1 and 2 are considered low-grade gliomas, grade 3 is astrocytoma, and grade 4 is classified as glioblastoma (Chen et al., 2017). Grade 3 and grade 4 are classified as the aggressive category. A biopsy is the standard approach to diagnosing glioma. It is a surgical procedure that involves taking the sample from the affected area for pathological examination. Analysis using biopsy provides accurate results. However, it has certain drawbacks, such as proliferation, the need for mastery, time obligation, and the possibility of more cancer growth. Magnetic Resonance Imaging (MRI) is a non-invasive, non-surgical, quick imaging technology and a viable alternative for glioma analysis (Tupe-Waghmare et al., 2021).

The status of Isocitrate Dehydrogenase (IDH), the codeletion status of 1p19q, and the methylation status of O6-methylguanine-DNA-methyltransferase (MGMT) are the major molecular features for the diagnosis of gliomas. Monitoring the status of these biomarkers is important for evaluating the glioma profile and anticipating prognosis (Zheng et al., 2020). However, advanced techniques and medical procedures are required to analyze the status of these biomarkers using MRI images. An alternative diagnosis approach is to use data-driven decision-making using artificial intelligence. Artificial intelligence and machine learning algorithms are efficient and successful tools that assist physicians and support them in making decisions, boosting their confidence in making accurate diagnoses.

Unsupervised learning approaches are commonly used where data labeling is impossible or required. It is mainly applied to identify correlations in data. Labeling the data requires a high level of clinical skills in healthcare applications. Thus, it can be costly and time-consuming (Dike et al., 2018). Clustering is mainly adopted when a novel disease is most likely to happen with no prior medical records. Unlike supervised learning algorithms, where we train the model based on labeled data with already recorded values, unsupervised learning uses unlabeled data to identify unique patterns, relationships, or clusters. The unavailability of labeled data in clustering algorithms becomes a substantial barrier to evaluating the quality and validity of the clusters formed. Unsupervised clustering methods such as K-Means, Fuzzy clustering, Hierarchical clustering, and Kernel K-Means are commonly implemented; however, the model's efficiency is dependent on their ability to validate results (Govender & Sivakumar, 2020).

Naeem et al. (2023) have analyzed unsupervised learning techniques, including the Apriori algorithm, frequent pattern growth algorithm, k-means clustering, and principal component analysis. The clustering approaches are mainly categorized into two types: hierarchical clustering and partition clustering. The applications of unsupervised learning in domains such as machine vision, speech recognition, self-driving cars, and natural language processing have been highlighted in this review paper. Like machine learning approaches, unsupervised techniques do not require labeled data or manual feature selection, which causes flexibility and automation issues. Supervised learning techniques are used in most

healthcare research involving automated disease detection. Despite these, unsupervised learning techniques remain underexplored, especially in applications like disease prediction. In recent work, Mansour et al. (2021) developed an innovative unsupervised model called a variational autoencoder to predict COVID-19 cases. They trained and tested the model through several experiments, demonstrating its impressive performance, achieving high accuracy rates of 98.7% for binary classification and 99.2% for multi-class classification.

Bibi et al. (2022) have shown that unsupervised learning can be a good option for solving classification problems. Their research used concept-based and hierarchical clustering methods to analyze Twitter sentiments. The authors have combined popular hierarchical clustering techniques like single linkage, complete linkage, and average linkage in sequence. The authors have shown that unsupervised learning techniques, like supervised learning methods, can perform well. In a study by Zhang et al. (2023), hyperspectral imaging (HSI) and unsupervised classification techniques were used to identify normal and necrotic areas in small intestinal tissues. K-means and density peaks (DP) clustering algorithms were utilized to distinguish between these tissue types. Their results showed that the DP clustering algorithm attained an average clustering purity of 92.07%. They have concluded that HSI, along with DP clustering, can assist doctors in identifying normal and necrotic tissue in the small intestine.

Bhattacharjee et al. (2022) proposed unsupervised learning approaches to distinguish between benign and malignant stages of the prostate gland using images. Radiomic characteristics have been extracted from the entire slide image using important clustering techniques such as spectral clustering, agglomerative clustering, K-means, K-medoids, and the Gaussian mixed model (GMM). These methods were assessed using Silhouette and Rand scores. It was found that the best results were generated for the K-means algorithm. Song et al. (2023) used Chest X-rays to detect pneumonia. They used and analyzed unsupervised learning techniques for the detection. The X-ray pictures were transformed to grayscale and scaled to consistent dimensions. The radiometric characteristics were retrieved. Two algorithms were used for clustering, i.e., k-means clustering and spectral clustering. For spectral clustering, the Silhouette Coefficient, Davies-Bouldin Index, and Calinski-Harabasz Index values were 0.44, 1.025, and 311.5, respectively, while for k-means clustering, the values were 0, 8 and 0.28.

Unsupervised learning techniques study glioma analysis, focusing mainly on brain tumor segmentation (Bougacha et al., 2018). In many research studies, unsupervised learning techniques are used as part of their pipeline to segment the Region of Interest (RoI) and then supervised learning techniques are applied to improve the results. According to our current analysis, only a countable number of research have implemented unsupervised learning for preprocessing to cluster and identify subgroups in gliomas. The proposed research aims to provide a clustering technique for automatically detecting the status of

IDH biomarker index and grade of gliomas from MRI data. This is done by extracting radiomic features and using preprocessed data to improve the classification algorithm’s performance. This generic framework can cluster patients based on common features, which can be highly advantageous for disease analysis. A public glioma dataset is used to test and verify the proposed methodology. The proposed method can be applied to any medical imaging resource for disease analysis, including those without labels.

MATERIALS AND METHODS

Our work used the Cancer Genome Atlas (TCGA) dataset (Ganini et al., 2021). TCGA has genetic, clinical, and imaging data related to glioblastoma. MRI scans of patients, information on grades, and other biomarkers are present in the dataset. This study inspected 210 3D volumes of grades 3 and 4 with IDH mutation status using T1-weighted, Fluid-Attenuated Inversion Recovery (FLAIR), and T2-weighted modalities (Al-Saeed et al., 2009). Figure 1 portrays the workflow for the proposed method. Statistical features are reprocessed from the generated 3D volumes and used to create clustering algorithms. Trimming the image eliminates unwanted sections and emphasizes areas of interest. Here, several slices from the volume that do not contain gliomas have been deleted as we are interested mainly in gliomas. Based on this objective, the volumes were condensed and normalized to have voxel values ranging from 0 to 1. In our work, three main clustering algorithms: K-means clustering, agglomerative clustering, and Balanced Iterative Reducing and Clustering (BIRCH) (Wahyuningrum et al., 2021; Madan & Dana, 2016) are implemented. These models’ performance is evaluated by assessing various performance metric values.

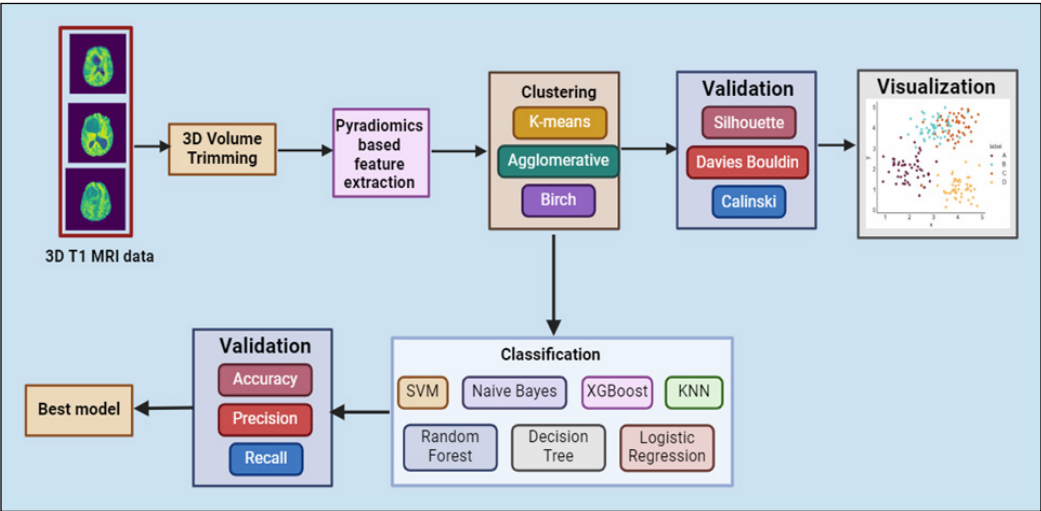


Figure 1. Workflow for the proposed approach

Feature Extraction and Reduction

The Pyradiomics module was used for automated feature extraction (Van Griethuysen et al., 2017). Pyradiomics is the Python package commonly used to extract features from images. The automated feature extractor tool automatically computes and extracts relevant statistical features from the data. This tool uses the image and the mask as input for feature extraction. The model has extracted 120 features from each medical image and mask data using statistics, shape, Gray Level Co-occurrence Matrix (GLCM), Gray Level Run Length Matrix (GLRLM), Gray Level Size Zone Matrix (GLSZM), Neighboring Gray Tone Difference Matrix (NGTDM), and Gray Level Dependence Matrix (GLDM).

The features extracted are First Order Statistics (19), Shape-2D (16), Shape-3D (10), GLCM (24), GLRLM (16), GLSZM (16), NGTDM (5), and GLDM (14). The generated dataset has 120 columns, which is extremely complex. Processing such a huge number of columns is time-consuming and can be expensive. This can result in postponed training of the clustering algorithms. This issue is addressed by using a suitable dimensionality reduction technique. Dimensionality reduction has to be performed before implementing the clustering algorithm. This work utilized the Principal Component Analysis (PCA) technique to minimize the dimensions (Jolliffe & Cadima, 2016). It is the best technique to deal with the challenges when a greater number of features are available per specimen.

Clustering Models

Three major clustering algorithms, K-means clustering, agglomerative clustering, and BIRCH, have been implemented and compared in our study. K-means is a well-known unsupervised clustering algorithm. It is the simplest technique, but it can handle complex data sets. Initially, centroids equivalent to a number of clusters are formed. Then, the distance between each data point and all the centroids is calculated. Next, the centroids are figured once again with the previously computed distance. This process is repeated until the centroids converge and remain constant (Wahyuningrum et al., 2021). Agglomerative clustering is a hierarchical and unsupervised learning method. A bottom-up approach is used in this process. Link distances are calculated based on the resemblance between two data points. Every data point is part of a single cluster, and the nearby points are combined using distance-based linkages. This method is repeated until all data points have been combined into a single cluster (Griffiths et al., 1984). BIRCH is another hierarchical clustering procedure. If the data set contains multiple features and is also huge, even then, this dynamic clustering method performs well. This method clusters data points using a height-balanced methodology and a feature tree (Madan & Dana, 2016).

Classification Models

We have used seven different machine-learning classification algorithms in this study. These include Support Vector Machine (SVM), Naive Bayes, KNN (K-Nearest Neighbor), Logistic Regression, Decision Tree, Random Forest, and Extreme Gradient Boosting (XGBoost) (Bhaskar, Bairagi et al., 2023). Logistic regression is a simple classification algorithm, and it is mainly used for binary classification problems. It uses the most common sigmoid activation function on the input data and classifies the output based on a certain limit.

Support Vector Machine is a commonly used machine learning technique as it is highly flexible. In Naive Bayes, the conditional probability of each attribute is examined separately using the Bayesian theorem principle. K-Nearest Neighbor is a learning approach that does not rely on labeled data, and it attempts to map a new data point to its nearest neighbor and perform the grouping accordingly. Decision trees and random forests are tree-based models. They make use of entropies and information gain to make predictions. XGBoost is another ensemble learning method that uses boosting to gain greater accuracy (Choudhary et al., 2022; Bhaskar, Tupe-Waghmare et al., 2023).

RESULTS AND DISCUSSION

The features extracted from the MRI images are converted to a CSV data file with a dimension of 70,128, with 128 features extracted from each of the 70 MRI volumes. We have performed clustering using the three unsupervised algorithms considered in this study. Three major performance parameters, the Silhouette Coefficient, Davies-Bouldin Index, and Calinski-Harabasz Index values (Ashari et al., 2023), were used to evaluate the performance of these models. The Silhouette Coefficient is calculated using the following Equation 1:

$$S(i) = (b(i) - a(i)) / \max\{a(i), b(i)\} \quad [1]$$

where $S(i)$ is the Silhouette Coefficient for data point i , $a(i)$ represents the intra-cluster distance, and $b(i)$ represents the inter-cluster distance.

Davies-Bouldin matrix index is used to measure the cluster fitness. This method can be used to assess the suitability of various data divisions. The goal is to bring this index as near to zero as possible. The following Equation 2 represents the formula for the Davies-Bouldin index:

$$DB = (1 / k) * \sum(i = 1 \text{ to } k) \max(R(ij)), \text{ where } i \neq j \quad [2]$$

Where k is the number of clusters, and $R(ij)$ is the measure of dissimilarity between cluster i and cluster j .

The Calinski-Harabasz Index is theoretically determined as the inter-cluster and intra-cluster dispersion ratio. A higher value for this index indicates that the observations within each cluster are dense and well-separated (Aik et al., 2023). Calinski-Harabasz Index value can be determined with the following Equation 3:

$$CH = (B / (k - 1)) / (W / (n - k))$$

[3]

Where B is the variation between clusters, k is the number of clusters, W is the variance inside the clusters, and n is the total number of data points.

Table 1 displays the results of various clustering algorithms, both with and without PCA feature reduction. The Agglomerative clustering algorithm outperformed all other algorithms in our analysis, producing the highest Silhouette Coefficient and Calinski-Harabasz Index scores and the lowest Davies-Bouldin Index scores. PCA has significantly enhanced the performance of unsupervised algorithms, with scores increasing almost double when compared to algorithms trained on the same dataset without PCA. Figure 2 shows scatterplot representations of K-means and BIRCH clustering techniques with and without PCA. The scatterplots produced show the separation of clusters generated by various clustering approaches. Each point on the plot represents a data point, and the values of the features define its location. The scatter plot generated for the agglomerative clustering algorithm is shown in Figure 3. The plot clearly distinguishes between categories, indicating that the clustering method effectively groups comparable data points.

The dendrogram diagram of the agglomerative clustering showing the hierarchical relationships between different entities is depicted in Figure 4. Entities refer to the individual data points clustered by the agglomerative clustering technique. Each branch of the dendrogram symbolizes the merging or splitting of clusters, and the length of the branches reflects the clusters' dissimilarity or distance. The dendrogram illustrates the graphical depiction of the clustering results that allow for a better understanding of the links between distinct data points or clusters.

Table 1
Performance metrics obtained for different models compared in this study

Clustering Algorithm	Feature Reduction	Silhouette Coefficient	Davies-Bouldin Index	Calinski-Harabasz Index
K-means	No	0.399	1.21	78.06
	PCA	0.529	0.70	300.9
Agglomerative	No	0.77	0.37	69.5
	PCA	0.83	0.21	323.22
BIRCH	No	0.242	1.51	70.2
	PCA	0.55	0.64	265.05

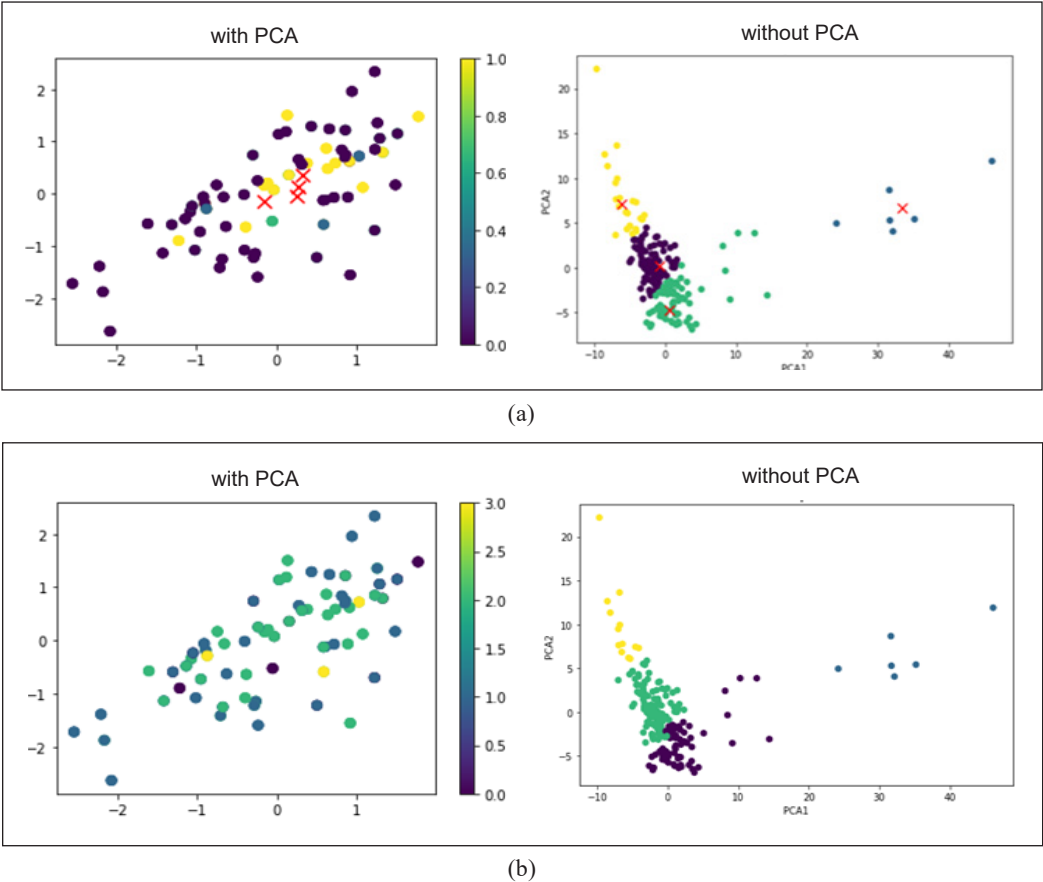


Figure 2. Scatterplot representations (a) K-Means clustering with and without PCA (b) BIRCH clustering with and without PCA

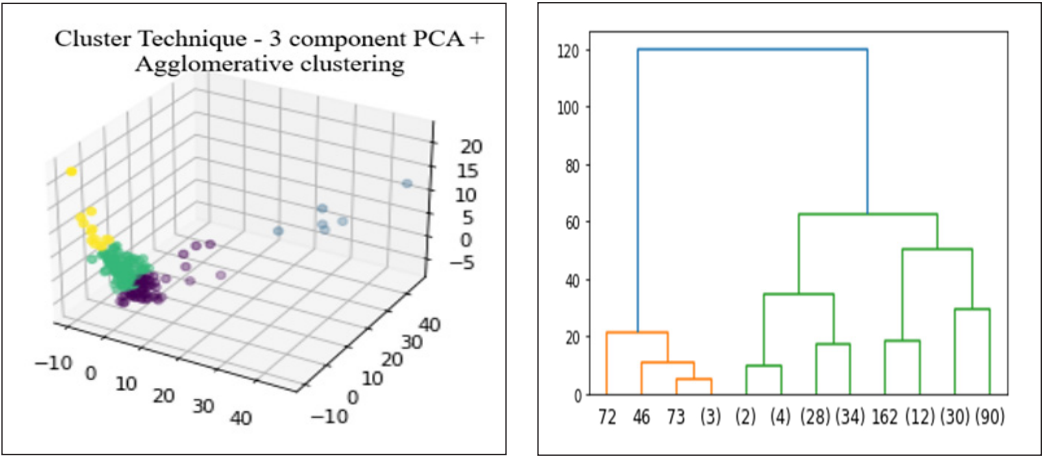


Figure 3. Scatterplot representations for agglomerative clustering with PCA

Figure 4. The dendrogram diagram for the agglomerative clustering algorithm

Clusters are produced more effectively using PCA. In high-dimensional spaces, the distance between points can become meaningless, and data points can be sparsely distributed. PCA decreases dimensionality by focusing on the most relevant features, resulting in more meaningful distances and clearly defined clusters. As seen in Figure 3, all clustering algorithms struggled to discriminate between the green and dark blue color groups. These clusters potentially correspond to data points from the G3 mutant and G4 wild classes, which have been clinically shown to be significantly related. Additional clustering approaches can help provide a more complete picture of the data’s intrinsic structures. Combining results from different clustering algorithms using ensemble approaches may improve overall clustering performance. Integrating autoencoders into the process can also help to increase feature learning.

Out of the three clustering approaches examined in this study, agglomerative clustering produced the best results and was thus selected as the pre-processor. The labels acquired from agglomerative clustering are used to train classification algorithms. We measured the primary performance parameters to evaluate the models’ performance. Table 2 shows the supervised classification algorithms’ accuracy, precision, and recall values on the training and testing sets after applying the clustering technique. Figure 5 shows a visual comparison of the validation accuracy of the training models.

It is apparent that using agglomerative clustering as a preprocessing step improves the performance of classification systems. We observed an average improvement of nearly 3 percentage points in accuracy after incorporating agglomerative clustering as a preprocessing step. By structuring data into meaningful clusters before training, we observed accuracy, precision, and recall metrics improvements across various classification algorithms. This approach optimizes model training and facilitates better pattern recognition and predictive accuracy in complex datasets. The SVM and Naive Bayes models achieved less than 90% validation accuracies, while the other models produced more than 90% validation accuracies. The validation accuracy of 99% was achieved for the decision tree

Table 2
Performance evaluation of machine learning techniques with clustering

Models	Training Data			Validation		
	Accuracy	Precision	Recall	Accuracy	Precision	Recall
SVM	80.6	93.75	81.11	76.19	92.64	82.14
Naive Bayes	92.72	88.57	96.06	83.33	71.38	90.47
KNN	97.57	98.78	92.23	95.23	97.17	97.17
XGBoost	100	100	100	95.23	97.17	97.17
Logistic Regression	100	100	100	97.61	98.33	98.95
Decision Tree	100	100	100	99.54	99.33	99.33
Random Forest	100	100	100	99.34	99.12	99.12

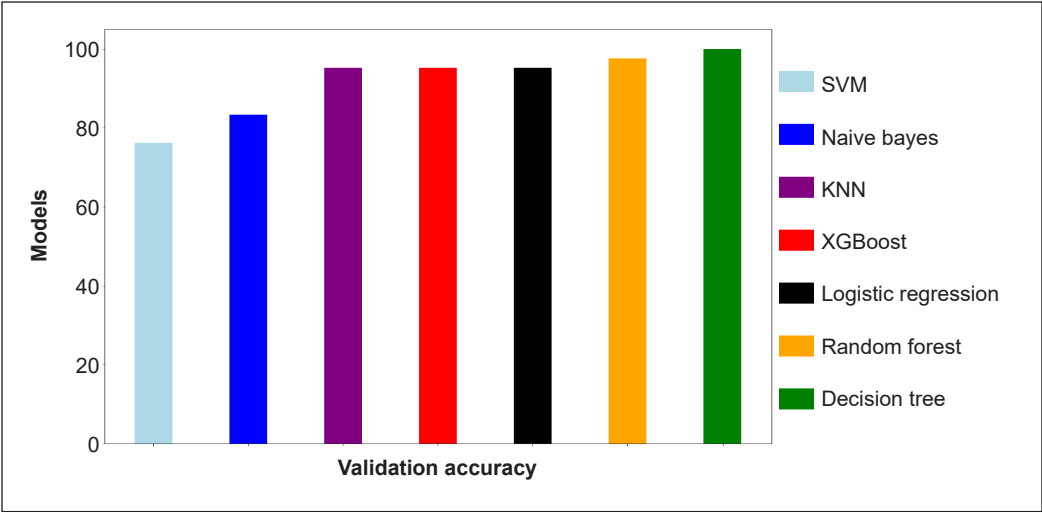


Figure 5. Comparison of the validation accuracy of the training models with clustering

and random forest. In addition, the precision and recall scores are very high, which justifies that the models were properly trained. The models have not shown signs of overfitting, with just a negligible variation in training and testing performance. The clustering approach grouped the grade and IDH based on similarities, which may have assisted the machine learning models in better training, thus enhancing the performance. Furthermore, reducing the dimensions using PCA before clustering also improved the performance of all three techniques, with a 7% increase in silhouette coefficient and a 16% decrease in the Davies-Bouldin score.

It is clearly noted that machine learning algorithms trained on clustered datasets consistently performed better than those on datasets without clusters in terms of accuracy, precision, and recall. Models like XGBoost, decision tree, and random forest exhibited momentous overfitting on the unclustered dataset, which was eased when clustering was applied. These implementations have supported the fact that, by integrating clustering techniques in the preprocessing phase, the performance of the machine learning algorithms is significantly uplifted in identifying grade and mutation status. This method not only decreases the need for extensive dataset labeling but also streamlines the process of anomaly detection in medical imaging applications. By integrating dimensionality reduction techniques, we aim to increase efficiency by not compromising performance, making this method a better choice for handling large, unlabeled datasets in healthcare applications.

The unsupervised learning method proposed in this paper can significantly support clinical practitioners, reducing the time and cost associated with diagnosing oncology patients. This technique requires minimum labeling and thus allows clinicians to process

and analyze large datasets of medical images effortlessly. Applying clustering techniques to new patient data enables automatic annotation, which can then train supervised classifiers for detecting abnormalities in new cases. Incorporating dimensionality reduction techniques further improves algorithm efficiency and speed without reducing the performance. Overall, this approach provides a powerful, time-saving solution for handling unlabeled data, streamlining diagnostic workflows, and aiding in treatment planning in oncology.

CONCLUSION

In this paper, we have used statistical feature extraction techniques and classification algorithms. Clustering of MRI images for glioma analysis using unsupervised algorithms is presented. Accuracy and reliability are ensured by evaluating the results. The performance of classification algorithms is significantly improved by using the proposed framework. These machine learning algorithms have yielded results comparable to deep learning techniques, with the advantage of lower computational costs. The agglomerative clustering algorithm outperformed all other algorithms in our analysis, with the highest Silhouette Coefficient and Calinski-Harabasz Index scores and the lowest Davies-Bouldin Index scores. The decision tree-based model outperformed all classification approaches in the testing set, achieving an accuracy of 99.54% when clustering was used as a preprocessing step. The results show that the proposed system may be used for quick and accurate glioma analysis without requiring computationally intensive hardware.

ACKNOWLEDGEMENT

We thank NMAM Institute of Technology, NITTE (Deemed to be University), Karnataka, India, and Symbiosis Institute of Technology, Symbiosis International (Deemed University), Pune, India, for their support and facilities in conducting this research.

REFERENCES

- Aik, L. E., Choon, T. W., & Abu, M. S. (2023). K-means algorithm based on flower pollination algorithm and Calinski-Harabasz Index. In *Journal of Physics: Conference Series* (Vol. 2643, No. 1, p. 012019). IOP Publishing. <https://doi.org/10.1088/1742-6596/2643/1/012019>
- Al-Saeed, O., Ismail, M., Athyal, R. P., Rudwan, M., & Khafajee, S. (2009). T1-weighted fluid-attenuated inversion recovery and T1-weighted fast spin-echo contrast-enhanced imaging: A comparison in 20 patients with brain lesions. *Journal of Medical Imaging and Radiation Oncology*, 53(4), 366-372. <https://doi.org/10.1111/j.1754-9485.2009.02093.x>
- Ashari, I. F., Nugroho, E. D., Baraku, R., Yanda, I. N., & Liwardana, R. (2023). Analysis of Elbow, Silhouette, Davies-Bouldin, Calinski-Harabasz, and Rand-Index evaluation on K-means algorithm for classifying flood-affected areas in Jakarta. *Journal of Applied Informatics and Computing*, 7(1), 95-103. <https://doi.org/10.30871/jaic.v7i1.4947>

- Bhaskar, N., Bairagi, V., Boonchieng, E., & Munot, M. V. (2023). Automated detection of diabetes from exhaled human breath using deep hybrid architecture. *IEEE Access*, 11, 51712-51722. <https://doi.org/10.1109/ACCESS.2023.3278278>
- Bhaskar, N., Tupe-Waghmare, P., Nikam, S. S., & Khedkar, R. (2023). Computer-aided automated detection of kidney disease using supervised learning technique. *International Journal of Electrical and Computer Engineering (IJECE)*, 13(5), 5932-5941. <https://doi.org/10.11591/ijece.v13i5.pp5932-5941>
- Bhattacharjee, S., Hwang, Y. B., Sumon, R. I., Rahman, H., Hyeon, D. W., Moon, D., Carole, K. S., Kim, H. C., & Choi, H. K. (2022). Cluster analysis: Unsupervised classification for identifying benign and malignant tumors on whole slide image of prostate cancer. In *2022 IEEE 5th International Conference on Image Processing Applications and Systems (IPAS)* (pp. 1-5). IEEE Publishing. <https://doi.org/10.1109/IPAS55744.2022.10052952>
- Bibi, M., Abbasi, W. A., Aziz, W., Khalil, S., Uddin, M., Iwendi, C., & Gadekallu, T. R. (2022). A novel unsupervised ensemble framework using concept-based linguistic methods and machine learning for twitter sentiment analysis. *Pattern Recognition Letters*, 158, 80-86. <https://doi.org/10.1016/j.patrec.2022.04.004>
- Bougacha, A., Boughariou, J., Slima, M. B., Hamida, A. B., Mahfoudh, K. B., Kammoun, O., & Mhiri, C. (2018). Comparative study of supervised and unsupervised classification methods: Application to automatic MRI glioma brain tumors segmentation. In *2018 4th International Conference on Advanced Technologies for Signal and Image Processing (ATSIP)* (pp. 1-5). IEEE Publishing. <https://doi.org/10.1109/ATSIP.2018.8364463>
- Chen, R., Smith-Cohn, M., Cohen, A. L., & Colman, H. (2017). Glioma subclassifications and their clinical significance. *Neurotherapeutics*, 14, 284-297. <https://doi.org/10.1007/s13311-017-0519-x>
- Choudhary, S., Kumar, A., & Choudhary, S. (2022). Prediction and comparison of diabetes with logistic regression, Naïve Bayes, random forest, and support vector machine. In *International Conference on Innovations in Computer Science and Engineering* (pp. 273-283). Springer. https://doi.org/10.1007/978-981-19-7455-7_20
- Dike, H. U., Zhou, Y., Deveerasetty, K. K., & Wu, Q. (2018). Unsupervised learning based on artificial neural network: A review. In *2018 IEEE International Conference on Cyborg and Bionic Systems (CBS)* (pp. 322-327). IEEE Publishing. <https://doi.org/10.1109/CBS.2018.8612259>
- Ganini, C., Amelio, I., Bertolo, R., Bove, P., Buonomo, O. C., Candi, E., Cipriani, C., Daniele, N. D., Juhl, H., Mauriello, A., Marani, C., Marshall, J., Melino, S., Marchetti, P., Montanaro, M., Natale, M. E., Novelli, F., Palmieri, G., Piacentini, M., ... & Melino, G. (2021). Global mapping of cancers: The cancer genome atlas and beyond. *Molecular Oncology*, 15(11), 2823-2840. <https://doi.org/10.1002/1878-0261.13056>
- Govender, P., & Sivakumar, V. (2020). Application of k-means and hierarchical clustering techniques for analysis of air pollution: A review (1980–2019). *Atmospheric Pollution Research*, 11(1), 40-56. <https://doi.org/10.1016/j.apr.2019.09.009>
- Griffiths, A., Robinson, L. A., & Willett, P. (1984). Hierarchic agglomerative clustering methods for automatic document classification. *Journal of Documentation*, 40(3), 175-205. <https://doi.org/10.1108/eb026764>

- Jolliffe, I. T., & Cadima, J. (2016). Principal component analysis: A review and recent developments. *Philosophical transactions of the royal society A: Mathematical, Physical and Engineering Sciences*, 374(2065), Article 20150202. <https://doi.org/10.1098/rsta.2015.0202>
- Madan, S., & Dana, K. J. (2016). Modified balanced iterative reducing and clustering using hierarchies (m-BIRCH) for visual clustering. *Pattern Analysis and Applications*, 19, 1023-1040. <https://doi.org/10.1007/s10044-015-0472-4>
- Mansour, R. F., Escorcia-Gutierrez, J., Gamarra, M., Gupta, D., Castillo, O., & Kumar, S. (2021). Unsupervised deep learning based variational autoencoder model for COVID-19 diagnosis and classification. *Pattern Recognition Letters*, 151, 267-274. <https://doi.org/10.1016/j.patrec.2021.08.018>
- Naeem, S., Ali, A., Anam, S., & Ahmed, M. M. (2023). An unsupervised machine learning algorithm: Comprehensive review. *International Journal of Computing and Digital Systems*, 13(1), 911-921. <http://dx.doi.org/10.12785/ijcds/130172>
- Song, J., Gu, Y., & Kumar, E. (2023). Chest disease image classification based on spectral clustering algorithm. *Research Reports on Computer Science*, 2(1), 77-90. <https://doi.org/10.37256/rrcs.2120232742>
- Tupe-Waghmare, P., Malpure, P., Kotecha, K., Beniwal, M., Santosh, V., Saini, J., & Ingahalikar, M. (2021). Comprehensive genomic subtyping of glioma using semi-supervised multi-task deep learning on multimodal MRI. *IEEE Access*, 9, 167900-167910. <https://doi.org/10.1109/ACCESS.2021.3136293>
- Van Griethuysen, J. J., Fedorov, A., Parmar, C., Hosny, A., Aucoin, N., Narayan, V., Beets-Tan, R. G. H., Fillion-Robin, J. C., Pieper, S., & Aerts, H. J. (2017). Computational radiomics system to decode the radiographic phenotype. *Cancer Research*, 77(21), e104-e107. <https://doi.org/10.1158/0008-5472.CAN-17-0339>
- Wahyuningrum, T., Khomsah, S., Suyanto, S., Meliana, S., Yunanto, P. E., & Al Maki, W. F. (2021). Improving clustering method performance using K-means, mini batch K-means, BIRCH and spectral. In *2021 4th International Seminar on Research of Information Technology and Intelligent Systems (ISRITI)* (pp. 206-210). IEEE Publishing. <https://doi.org/10.1109/ISRITI54043.2021.9702823>
- Zhang, L., Huang, D., Chen, X., Zhu, L., Xie, Z., Chen, X., Cui, G., Zhou, Y., Huang, G., & Shi, W. (2023). Discrimination between normal and necrotic small intestinal tissue using hyperspectral imaging and unsupervised classification. *Journal of Biophotonics*, 16(7), Article 202300020. <https://doi.org/10.1002/jbio.202300020>
- Zheng, L., Zhang, M., Hou, J., Gong, J., Nie, L., Chen, X., Zhou, Q., & Chen, N. (2020). High-grade gliomas with isocitrate dehydrogenase wild-type and 1p/19q codeleted: A typical molecular phenotype and current challenges in molecular diagnosis. *Neuropathology*, 40(6), 599-605. <https://doi.org/10.1111/neup.12672>

A Transfer Function Modelling Using System Identification for Air-cooling Photovoltaic System

Rozita Mustafa^{1,2,3}, Mohd Amran Mohd Radzi^{1,2*}, Azura Che Soh¹ and Hashim Hizam^{1,2}

¹Department of Electrical and Electronic Engineering, Faculty of Engineering, Universiti Putra Malaysia, 43400 UPM, Serdang, Selangor, Malaysia

²Advanced Lightning, Power and Energy Research (ALPER) Centre, Universiti Putra Malaysia, 43400 UPM, Serdang, Selangor, Malaysia

³Electrical and Electronics Department, German Malaysian Institute, Jalan Ilmiah, Taman Universiti, 43000 Kajang, Selangor, Malaysia

ABSTRACT

Mathematical modelling is essential in comprehending, optimising, and administering air-cooling photovoltaic (PV) systems by considering factors like temperature, irradiance, and module characteristics. Mathematical modelling allows for informed decision-making, optimisation, and risk management in designing, operating, and maintaining air-cooling PV systems. This study creates mathematical models to identify an air-cooling PV system and anticipate the PV module's output performance based on the solar irradiance received. The air-cooling PV system is modelled using the system identification toolbox, which relies on experiment data. The modelling process utilises a black-box approach, eliminating the necessity for internal parameter knowledge. The transfer function estimation method was selected as the best non-linear model due to its superior fit percentage. Prior to the installation of the air-cooling system, the data-driven analysis produced

a continuous-time transfer function with an accuracy of 90% for the PV module model, whereas the air-cooling PV system model obtained an accuracy of 94.3%. The validity of the acquired models was assessed using Simulink by employing multiple levels of PSH. The model exhibits a failure rate of less than 10% in predicting inequality. The validation results for the PV module model were 90.1% and 90.8% for high, moderate, and low PSH, respectively. Similarly, the air-cooling PV system model got validation results of 91.7%, 93.2%, and 91.5%, while the mean output

ARTICLE INFO

Article history:

Received: 10 May 2024

Accepted: 16 January 2025

Published: 26 March 2025

DOI: <https://doi.org/10.47836/pjst.33.3.02>

E-mail addresses:

rozitamustafa@gmi.edu.my (Rozita Mustafa)

amranmr@upm.edu.my (Mohd Amran Mohd Radzi)

azuracs@upm.edu.my (Azura Che Soh)

hhizam@upm.edu.my (Hashim Hizam)

* Corresponding author

voltage increased by 10.8%, 17.5%, and 15.3%. Consequently, a continuous-time transfer function model is created, which will be utilised for developing and tuning controllers in future research.

Keywords: Air-cooling PV system model, mathematical model, modelling, system identification, transfer function model

INTRODUCTION

Cooling is required for a photovoltaic (PV) module because it can substantially boost the PV output performance. Without proper cooling, a substantial quantity of energy is lost as heat, as only 13-15% of solar radiation is converted into electricity (Mattei et al., 2006). Solar irradiance and operation temperature of the PV module (T_{cell}) were found to be impediments to reaching larger PV system outputs (Mustafa et al., 2023). A PV module's power output and electrical efficiency are determined by its T_{cell} and temperature coefficient (Dubey et al., 2013; Popovici et al., 2016). For each degree over 25°C, there is an average reduction in efficiency of around 0.45% (Haidar et al., 2018). The output voltage of the PV module can be calculated using Equation 1:

$$V_{pv_x} = V_{x_stc} \times \left[1 + \left(\frac{\gamma_{V_x}}{100} \right) (T_{cell} - 25^\circ C) \right] \quad [1]$$

where V_{pv_x} is the voltage for the PV module at x condition, V_{x_stc} is the voltage for x condition at Standard Test Condition (Volt), and γ_{V_x} is the temperature coefficient for the voltage at x condition.

There are two categories of cooling methods for PV modules: active cooling, which involves energy consumption, and passive cooling, which utilises conduction or natural convection to remove heat. Wind cooling can improve the performance of PV modules, but passive cooling is inefficient due to the limitations of natural heat transfer (Mustafa et al., 2024). Despite the fact that water cooling is more effective, air cooling is preferred due to its minimal construction and operating costs. PV module efficiency was better by 6.2% as a result of the cooling experiment (Erol et al., 2021). In addition to lowering the T_{cell} continuous cooling also increases the power of the PV module by 20% compared to the non-cooled one (Luboń et al., 2020). Cooling PV module is a key strategy for enhancing the efficiency of their output performance.

Mathematical models serve as the foundation for most analytical techniques used in engineering. These models can be derived by a theoretical method that relies on fundamental physical rules or through an experimental approach based on system measurements (Assani et al., 2022; Cheng & Lu, 2022). Generating models based on empirical data is commonly referred to as system identification (SI) (Bhuvaneswari, 2012) and numerical modelling can be enhanced with the use of an additional experimental-based approach (Al Hadad et al., 2018). An identification experiment aims to ascertain the dynamic properties of a certain

process. One of the benefits of using models is that the step test employ is comprehensive, making it simple and cost-effective to apply. Step testing is often conducted on a system once the process has been identified or stabilised. Mathematics modelling is a systematic procedure that involves acquiring, structuring, processing, and identifying mathematical models derived from raw data from real-world systems. Modelling process control is of utmost significance since an effective control system is contingent upon the presence of a well-constructed model that precisely depicts the dynamics of the process (Tawerghi et al., 2021).

Modelling photovoltaic systems is challenging due to their non-linear characteristics, particularly when integrated with cooling structures (Adak et al., 2022). Several studies have previously focused on mathematical models for PV modules, but none of them have specifically addressed air-cooling PV systems. An air-cooling PV system requires a mathematical model to facilitate engineering analyses involving PV modules and air-cooling systems (Adak et al., 2021). Mathematical modelling plays an important role in optimising the efficiency of air-cooling PV systems, both in terms of PV module performance and the effectiveness of the air-cooling mechanism. Algorithms for air-cooling PV systems provide notable advantages by enabling cost reduction through the simulation and evaluation of the cooling system prior to its physical implementation. For existing air-cooling PV systems, having a data-based model is essential. The quality of a model is contingent upon the calibre of the input data, which is acquired through experimental methodologies. Therefore, the experiment must be conducted according to the appropriate standard procedures, and all factors that might impact the outcome must be considered to ensure the accuracy of the data. This model enables the analysis of the system's impact and facilitates research on enhancing the performance of the air-cooling system and PV module under different irradiance levels without the need for additional devices, resulting in a cost reduction. This air-cooling PV system model allows for accurate prediction of the performance of PV modules and the air-cooling PV system without the need for conducting experiments.

Therefore, the aim of this paper is to develop mathematical models using real data experiments to predict the output voltage of the PV module and prove that the recommended air-cooling PV system successfully increased its output performance. One of the greatest challenges in this study was to make sure the obtained models were appropriate and met the high, medium and low levels of solar irradiance in a day according to the solar irradiance and expected output PV based on the mathematical relationship. This study uses black-box methods for non-linear systems to investigate a data-based model for PV module output and air-cooling PV systems. Different black-box model structures are used for precise models. Data collection for this study involves solar irradiance, T_{cell} output voltage, and PV module power.

System Identification

SI is the process of creating mathematical representations of dynamic systems using statistical techniques applied to collected data. The process of designing experiments to effectively collect data from the system to develop models and lower model complexity was part of the study of SI. In the process of SI, a mathematical model is constructed to represent a dynamic system by utilising a collection of measured stimulus and response samples. The present focus lies on the identification of parameters and attributes of dynamic systems through the utilisation of specialised identification methods (Valousek & Jalovecky, 2021). SI uses measured input and output data to construct a precise model to create a mathematical representation of the system (Schoukens et al., 2012). Input and output vectors are used to define these systems, but the majority of physical systems are non-linear, making their models difficult to linearise analytically (Dorf & Bishop, 2010). Constructing models that meet analytical criteria may require non-linear engineering models. The mathematical model accurately determines the effects and reactions on the constructed model (Tuhta, 2021).

The process of SI involves several key components, including experiment design, experiment implementation, data pre-processing, model structure selection, model fitting to data, and model validation, as shown in Figure 1 (Šajić et al., 2022). These components are essential for effectively identifying and understanding the various aspects of a given system. Continuous time transfer functions (TF) can be used to describe physical models more generally. In MATLAB, the SI toolbox is a series of procedures used to identify and analyse different system components, including their structure, properties, and measured data from the time domain (Ljung, 2012). It also simplifies SI using experimental data. The SI tool incorporates the transfer function (TF) models or process models’ functionalities, which facilitate the use of distinct identification approaches. A dynamical mathematical model is a mathematical representation that explains the behaviour of a system or process dynamic, which can occur in either the time

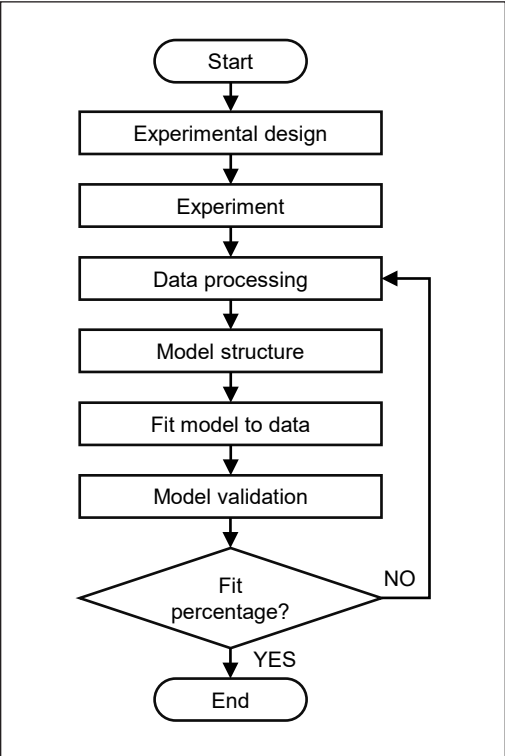


Figure 1. Cycle for system identification

or frequency domain (Åström & Eykhoff, 1971). The programme offers a dependable and near-accurate model structure. The proposed model underwent testing and simulation to demonstrate its effectiveness and reliability. This approach can also be used to estimate the model of an air-cooling PV system. Various modelling techniques, such as intelligent, linear, and non-linear models, can be applied.

METHODOLOGY

This study used the SI toolbox in MATLAB as an approach for the data-based model development. The research in this study includes the collecting and processing of all essential data, the selection and creation of the model structure, the estimate of model parameters, and the validation of the model. An experiment at an existing PV system in a tropical region, Kajang, Selangor, Malaysia, provided the data. All collected data was divided into training and testing sets. SI process and collected data were utilised in a black box for transfer function model development with different time delays and orders. Various models are investigated to determine the best structure yielding satisfactory accuracy based on the fit percentage. The selected model was tested using high, medium and low levels of solar irradiance generated data in a day from the experiment for optimisation, evaluation and validation for the most optimal model.

Data Collection and Pre-processing

A PV system was chosen at the German Malaysian Institute in Kajang, Selangor, Malaysia. The system consists of two 3kW PV sub-arrays of poly-crystalline PVs. Each sub-arrays grid-connected PV system utilised 12 pieces of 250 W poly-crystalline PV modules, installed by one string with 12 modules per string. An air-cooling system prototype was installed on a 250 W module of the PV system. Only one module was tested in the experiments. The irradiance metre was strategically placed near the PV module area to ensure the accuracy of the measured irradiance for analysis. A digital temperature sensor was attached to the back of the PV module to monitor temperature fluctuations on the T_{cell} . An energy meter was connected to the PV module to record voltage and current measurements. Small boxes are added to both ends of the cross-flow fan to elevate it away from the heated surface of the roof, as shown in Figure 2. This is done to guarantee that the temperature of the fan is not impacted by the surface temperature of

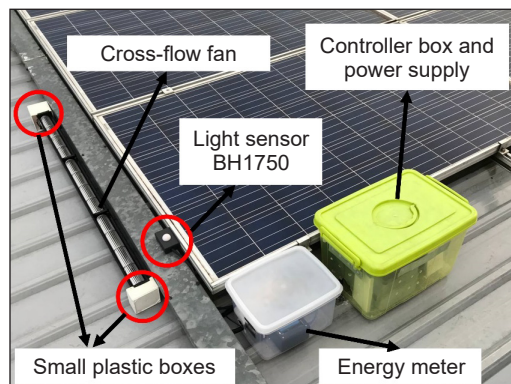


Figure 2. The placement of the fan, irradiance meter, energy meter, and controller box in the PV system

the roof and, therefore, the wind created by the fan is not affected by the roof’s temperature. The experiment was conducted at the site for 12 consecutive hours, from 7.00 a.m. to 7.00 p.m., for several days before and after the installation of an air-cooling system. All data for solar irradiance, T_{cell} and electrical parameters data are trended at 3-second i ntervals.

The output voltage of the PV module, $V_{pv_{exp}}$, T_{cell} , and solar irradiance were measured and recorded during the experiment before and after applying the cooling system. Estimating the current output of a PV module or array under real-world operating circumstances is critical. This is because irradiance and temperature are instantaneous factors that directly influence the PV module’s output. The concept of expected instantaneous output, where how much output of PV module per peak sun factor (PSF) at 1000 Wm^2 , was implemented in this study using Equation 2 (Mustafa et al., 2024):

$$PSF = \frac{G_{array_plane}}{1000\text{ Wm}^2} \tag{2}$$

where G_{array_plane} is solar irradiance in array plane (Wm^2).

The expected output voltage for the PV module at the maximum power point, $V_{pv_{roc}}$, corresponding to the T_{cell} , can be calculated from Equation 1. Technically, peak sun hour (PSH) is the number of hours in a day with an irradiance intensity of 1000 Wm^2 . An estimation of solar irradiance magnitude using total solar irradiance (TSI) was used in order to differentiate between levels of solar irradiance received (Egorova et al., 2018; Seleznyov et al., 2011). Total PSH in a day was used as TSI to classify the level of solar irradiance received per day. Solar irradiation levels are classified as high when the number of PSH exceeds 5.5, moderate when the range is between 3.5 and 5.4, and low when the level is below 3.5. Figure 3 shows a graph for the high, moderate and low levels of PSH used in this study to develop the desired models.

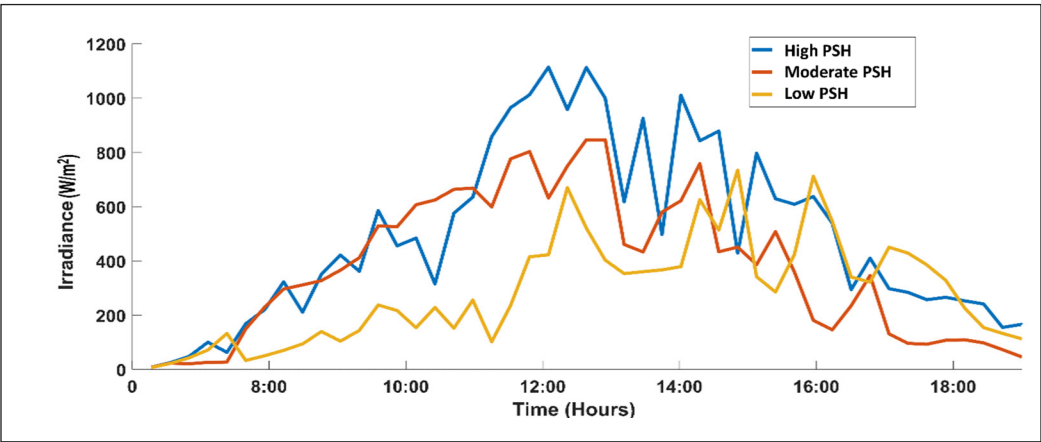


Figure 3. High, moderate and low PSH received in a day

T_{cell} and V_{pvexp} data were used to develop a data-based model using SI. These models will then be used as model-based control for further work on controller design and investigation to improve the efficiency of the proposed air-cooling system. This air-cooling PV system model refers to a PV module using an air-cooling system. PV module output and air-cooling PV system model was developed using SI. The strategies of SI might use all acquired data as input and output data or solely the output data. As shown in Figure 4, the PV module model input is T_{cell} while the model output was the output voltage of PV before applying an air-cooling system. This output voltage of PV data will be an input to the air-cooling PV system model, while the output voltage after applying the cooling system data will be the output for the air-cooling PV system model. During the development of the data-based model, the following assumptions were considered.

- (i) Due to the tiny airspace between the PV module and the roof and the restriction of natural heat transmission, the wind does not affect the T_{cell} .
- (ii) Solar irradiance and T_{cell} were evaluated in this study as the determining factor for PV module output.

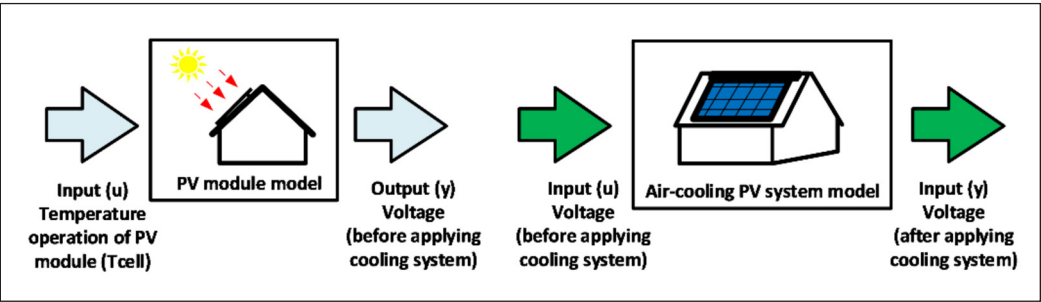


Figure 4. Input and output for PV module and air-cooling PV system model

Model Estimation and Optimisation

The developed models rely significantly on data. The available data set allowed us to evaluate a non-linear model of a PV module’s output in the context of solar irradiance, voltage and T_{cell} . Experimentation on the PV module before and after installation of the air-cooling PV system provides the data used for the model estimate. For every 3 seconds from 7.00 a.m. to 7.00 p.m., 14 400 data points were sampled at the German Malaysian Institute. Prior to testing, the analysis of input and output signal processing is conducted, and the TF of the system is determined using MATLAB’s SI Toolbox. Parametric models are employed to identify, wherein a mathematical model is derived from empirical data (Rachad et al., 2014; Sumalatha & Rao, 2016). It is imperative for the model to possess the ability to quantify the output of the system. In order to optimise the transfer function estimation system and achieve precise output (Donjaroennon et al., 2021) of the photovoltaic (PV)

module, it is imperative to design the Pole and Zero of the system in a manner that maximises the fit of the graph. Various models were found with the aim of determining the most optimum solution. The transfer function was employed in these structures to establish the most effective model, whereby the order of the polynomial functions of the numerator $Nu_i(s)$ and denominator $De_j(s)$ was manipulated (Equation 3).

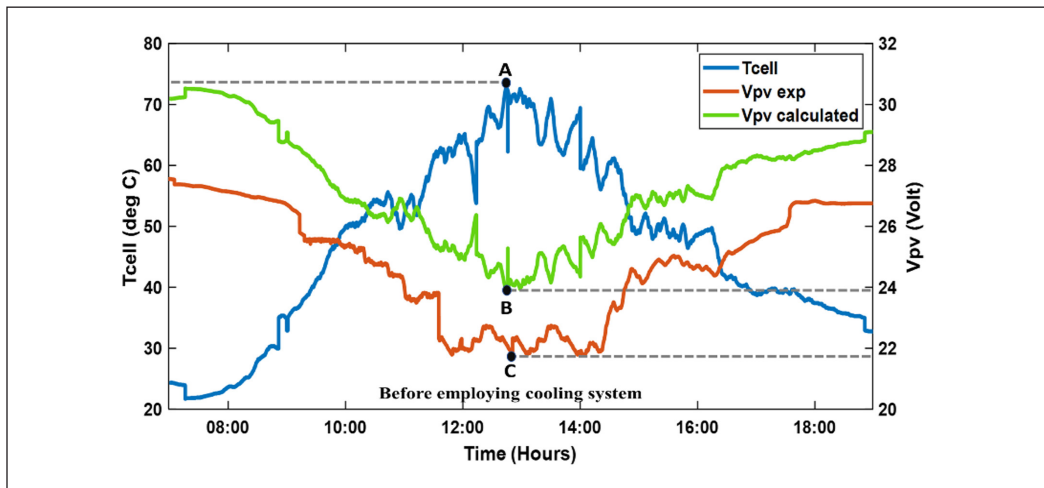
$$G(S) = \frac{Nu_i(s)}{De_j(s)} \quad [3]$$

The identification procedure entails iteratively choosing model structures, identifying the optimal model inside the structure, and assessing the features of this model to determine their adequacy. The models that demonstrated the highest performance were chosen for validation based on the assessment measure employed. After successfully completing the model validation procedure, the model's acceptability may be determined by comparing the output of the measurement with the model's simulation output, which leads to the creation of the model's outcome curve. The acquired models were utilised in Simulink to verify their performance under varying levels of irradiance, including high, moderate, and low levels.

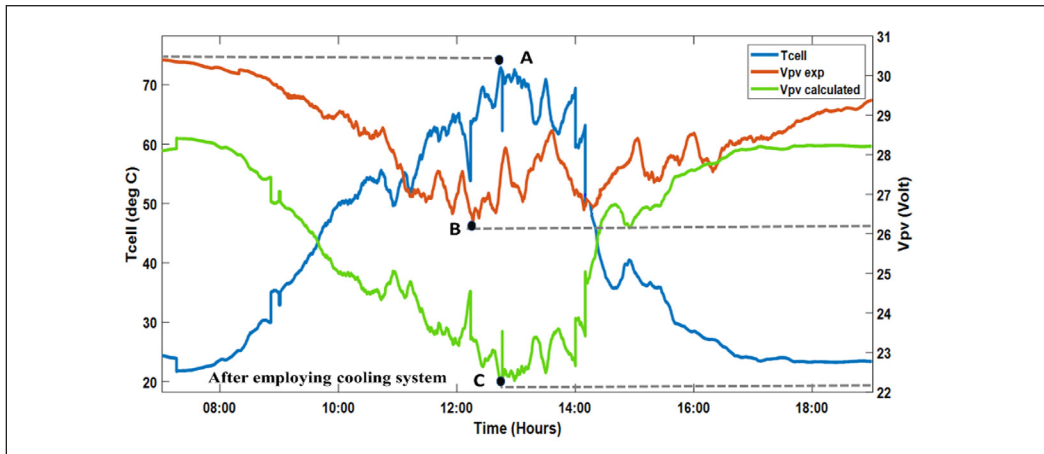
RESULTS AND DISCUSSION

Figure 5(a) depicts the graph for V_{pv_exp} that was influenced by T_{cell} , compared to the calculated data, $V_{pv_calculated}$, before installing the air-cooling PV system. The highest T_{cell} (point A) was 74.3°C. It is essential to ensure that the backside of the PV module is cooled to reduce the T_{cell} . An initial rise in irradiance led to an increase in the V_{pv_exp} and T_{cell} . However, based on the experimental data depicted in the graph, the V_{pv_exp} started to lower due to the rising temperature and irradiance. The increase in T_{cell} resulted in a significant decrease in V_{pv_exp} compared to $V_{mp_calculated}$ before implementing an air-cooling system. The lowest $V_{pv_calculated}$ (point B) was 23.9 V, while the lowest V_{pv_exp} (point C) was 21.8 V. The measured value of V_{pv_exp} remains lower than the calculated value of $V_{pv_calculated}$. After 3.00 p.m. both V_{pv_exp} and $V_{pv_calculated}$ exhibit an upward trend, whereas T_{cell} experiences a decline. This is caused by a decrease in irradiance at this particular time. Consequently, the decline in T_{cell} no longer results in a rise in V_{pv_exp} and $V_{pv_calculated}$ at this juncture as a result of the diminishing irradiance. Figure 5(b) depicts the graph after employing an air-cooling system. As the irradiance increased, an increase in T_{cell} led to a decrease in both V_{pv_exp} and $V_{pv_calculated}$, with V_{pv_exp} remaining higher than the calculated value. The lowest V_{pv_exp} (point B) was 26.2 V, while the lowest $V_{pv_calculated}$ (point C) was 22.2 V. Figure 5 satisfies Equation 1, which states that the voltage will decrease when the T_{cell} exceeds the standard test condition (STC) temperature, 25°C. This happened because of the thermal effect on the PV module due to the negative value of the temperature coefficient for voltage and power, γ .

The input and output signals for the PV module model are shown in Figure 6. The input is the value of T_{cell} , and the output is the output voltage of the PV module. For the air-cooling PV system model, the input and output signals are shown in Figure 7. The input is the output voltage of the PV module without the air-cooling system, $V_{pv_{exp_uncool}}$, while the output signal is the output voltage of the PV module with the air-cooling system, $V_{pv_{exp_cool}}$. The model was constructed using the PV module's output voltage at maximum power point, corresponding to the current irradiance. The data was separated into two sections for model estimation. The initial section of data is used to determine the system's model, while the other part is used to validate the model. SI toolbox in MATLAB was utilised to perform all estimation processes.



(a)



(b)

Figure 5. Experimental and calculated values (a) before and (b) after employing an air-cooling PV system based on the corresponding T_{cell} for the respective testing day

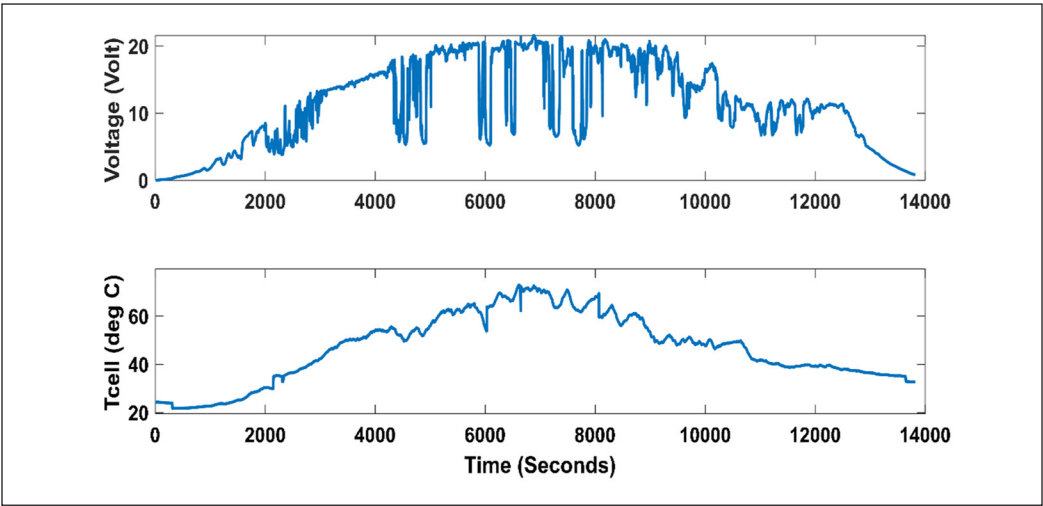


Figure 6. Input and output signals in system identification toolbox MATLAB for PV module model development

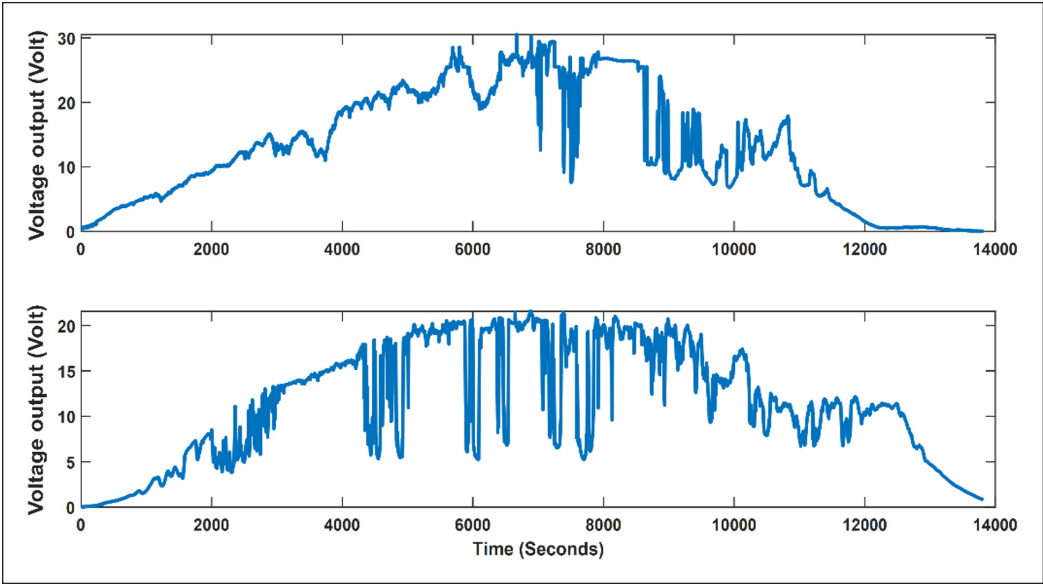


Figure 7. Input and output signals in system identification toolbox Matlab for air-cooling PV system model development

Validation

As a general rule, models can be accepted when the percentage of fit is at least 90%. Figures 8 and 9 depict the output model curve from which the TF model polynomials may be derived. The output models' curves reveal that the percentage of fit is 90% for the PV module model and 94.3% for the air-cooling PV system model. Figure 8 demonstrates

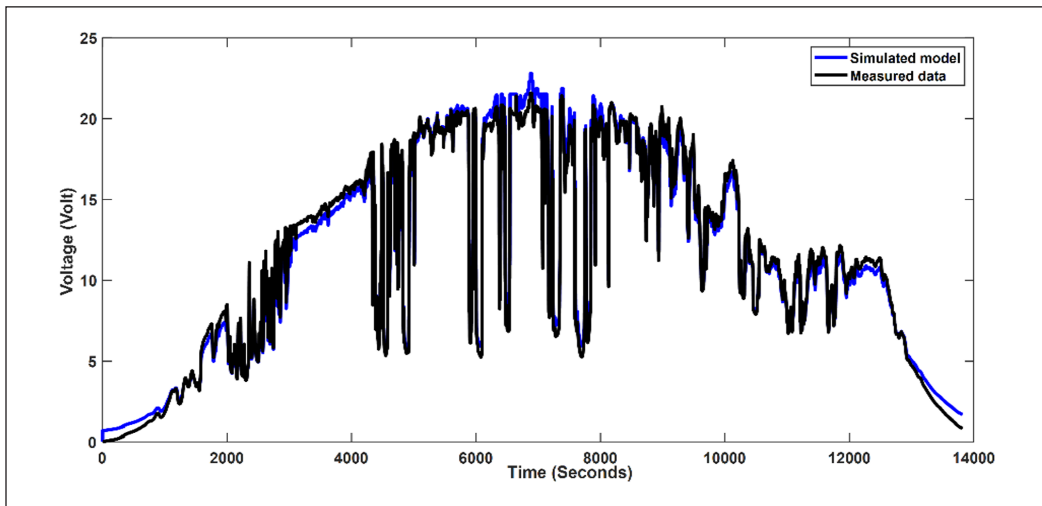


Figure 8. Estimated PV module model in *German Malaysian Institute*

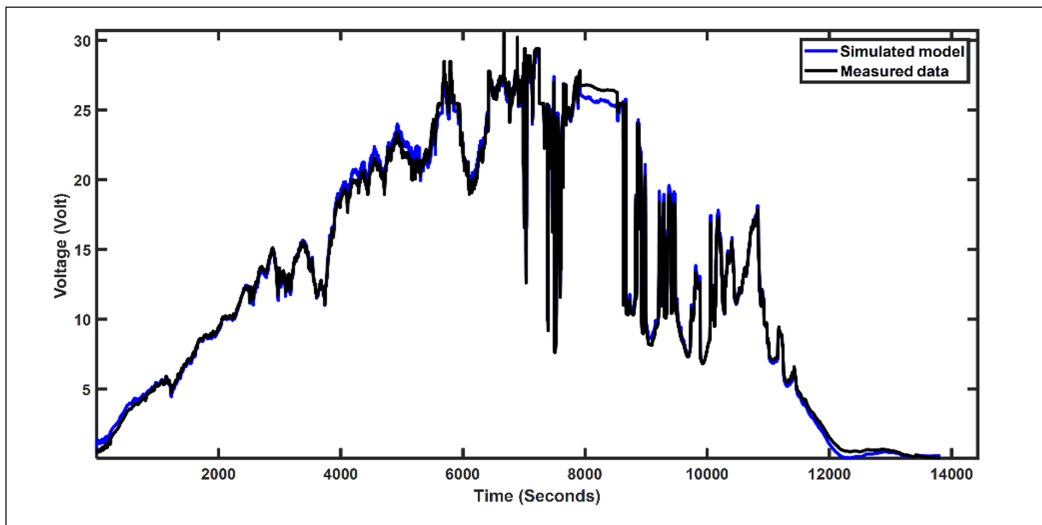


Figure 9. Estimated air-cooling PV system model in *German Malaysian Institute*

the output voltage for the PV module before implementing an air-cooling system, while Figure 9 demonstrates the output voltage for the PV module after implementing an air-cooling system.

The Simulink model of the air-cooling PV system is designed to represent parameter changes over time-based on solar irradiation. The model was developed as a transfer function, which is performed in the continuous-time domain, as stated in Equation 4.

$$G(S) = \frac{728.1s^2 + 0.121s + 0.0003856}{s^3 + 563.7s^2 + 0.09345s + 0.0002981} \quad [4]$$

The transfer function model $G(s)$ contains three poles and two zeros. It accurately represents the data from the German Malaysian Institute's system, with a fit of up to 94.3%. The transfer function associated with the third-order differential equation yields a linear model. Additionally, the controllability and observability of the developed mathematical models were evaluated. The Bode plot in Figure 10 displays the frequency response of the model. The pole and zero were plotted for each model and observed to narrow down the model. An optimal model will exhibit stability when all its poles and zeros are located within the unit circle. A model is considered the best when all its poles and zeros are located within the unit circle, indicating stability.

Figure 11 illustrates that each zero and pole is inside the unit circle. This is referred to as a minimal phase model. This model specifically focuses on the principles of causality and stability. It is intended to be utilised for in-depth research and to establish a relationship between both input and output variables. The model used to estimate the output of a PV module with an air-cooling system is noteworthy for its linearity and description by a transfer function. Additionally, it relates to a third-order differential equation. The model guaranteed stability, allowing for further examination of its controllability and observability aspects.

These mathematical models were used to achieve the highest output of the PV module when receiving solar irradiance by decreasing the influence of T_{cell} . A model estimate of solar irradiance and voltage was performed using a generic SI approach, including data analysis, model structure selection, parameter estimation, and model validation (Ljung, 2012). Data evaluation is done to acquire decent data. The model structure is selected to ascertain the desired model for generation. It may take linear, non-linear, or intelligent model form. Validation serves the objective of comparing the predicted output of the model with

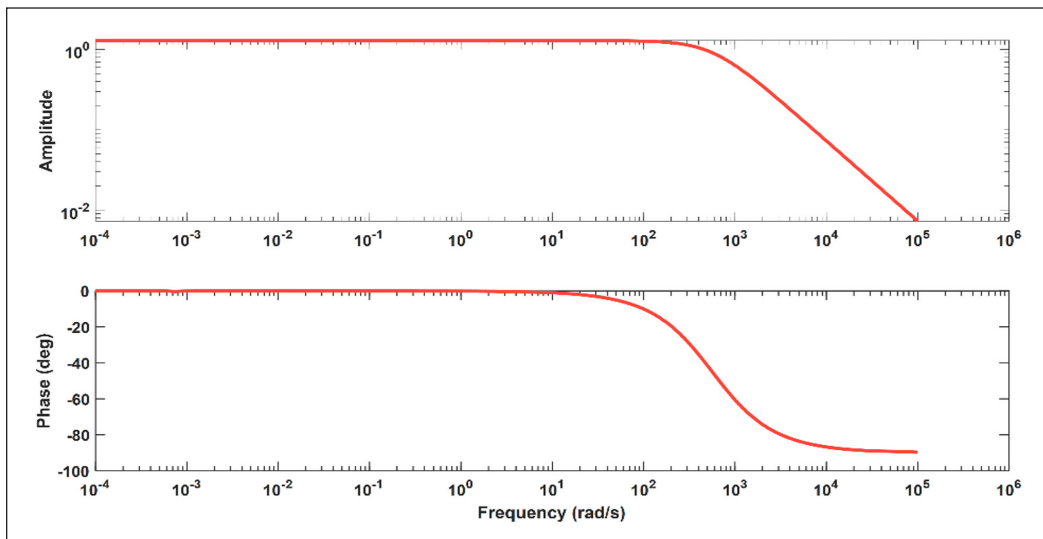


Figure 10. Frequency response for the air-cooling PV system development

the observed outcome of the experiments. It might be deemed acceptable if the model validation satisfies the required percentage of fit and other criteria (Ljung, 2012). In contrast to traditional approaches, this identification technique exhibits enhanced speed and accuracy. The highest percentage of fit was utilised to determine its selection and ascertain the transfer function that most accurately reflects the accuracy of the estimation output model with respect to the input data. It is necessary to compare the accuracy of the selected transfer function computation with the input data provided by MATLAB. Furthermore, MATLAB

can generate graphical representations such as output response, impulse response, and Bode diagrams based on the transfer function. In Simulink implementation, the models obtained were used to observe the output performance of the PV module before and after implementing the proposed air-cooling system using different levels of solar irradiance data. This step is very important to ensure that the developed models are compatible with multiple levels of solar irradiance. Figure 12 shows the simulation block diagram in Simulink used for air-cooling PV system observation.

The simulated data for multiple levels of PSH obtained from the model was then compared to measured data. Table 1 shows the percentage achieved for the validation models. From Table 1, the percentage of validation for high, moderate and low are above 90%. This means that the developed models are capable of anticipating a voltage output almost as accurately as the value when the experiment was carried out. The model's failure rate in predicting inequality is less than 10%. The results shown in Table 1 demonstrate the generated models' effectiveness in handling different PSH levels.

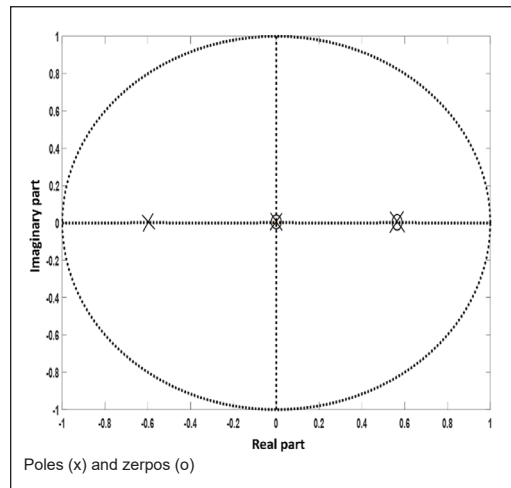


Figure 11. Pole zero plot for the air-cooling PV system model

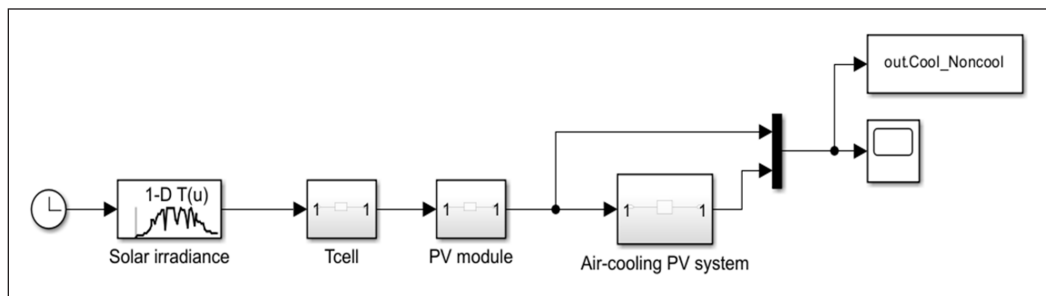


Figure 12. Simulation block diagram for air-cooling PV system

Strong evidence that the air-cooling PV system successfully boosted the output performance of the PV module was found when the output voltage after implementing the air-cooling PV system, V_{pvexp_cool} , was higher than before implementing the cooling system, V_{pvexp_uncool} . Using different levels of solar irradiance to represent multiple levels of PSH as an input to the model-based

control developed, Figure 10 shows the output voltage, V_{pvexp} , before and after applying the air-cooling PV system for high, moderate and low PSH. The results from Figure 13 indicate a 10.8% gain in mean output voltage after implementing the proposed air-cooling PV system for high PSH, 17.5% for moderate PSH and 15.3% for low PSH.

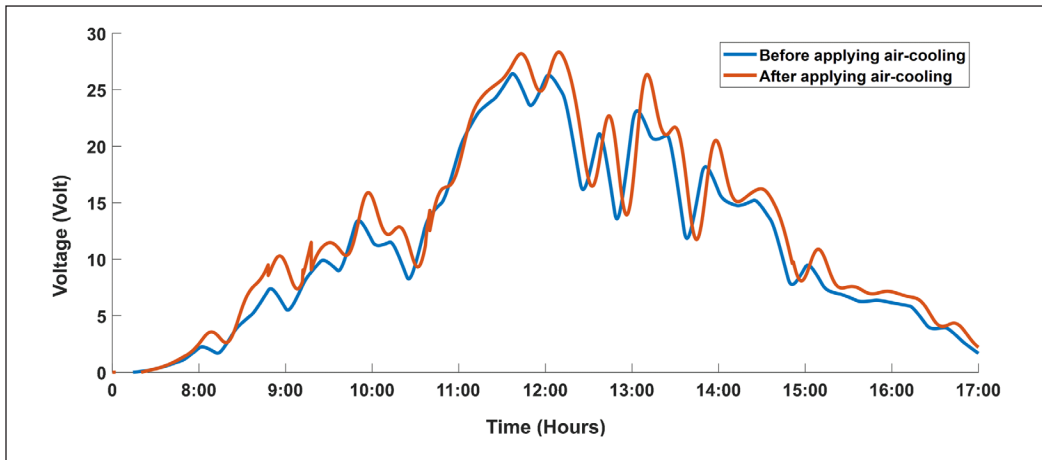
Since the PV module has the largest T_{cell} , it has the lowest percentage increase in output voltage under high solar irradiance. While it is probable that the fan in the cooling system has reached its maximum rotational speed, further time is required to decrease T_{cell} because, at the same time, the higher solar irradiance can keep T_{cell} high. Hence, while the PV module experiences a significant amount of solar irradiance at any one moment, the prolonged time of solar irradiance receipt also contributes to the time to decrease the T_{cell} . In moderate solar irradiance, the T_{cell} exhibits a lower magnitude compared to high solar irradiance. PV modules that receive moderate solar irradiance have a shorter time of high solar irradiance acceptance, resulting in a quicker temperature reduction compared to modules that receive high solar irradiance. This phenomenon results in a greater magnitude of voltage production compared to both high and low solar irradiance levels. While the T_{cell} experiences a decrease when exposed to low solar irradiance, the percentage output voltage rise is rather small compared to the moderate solar irradiance it receives. Despite the low temperature, it is important to acknowledge that a decrease in solar irradiation will result in a corresponding decrease in output voltage. The receipt of ample sun irradiance values in cold temperatures is highly advantageous for PV modules. This demonstrates the indispensability and significance of cooling in the restoration of the PV performance module, and the suggested air-cooling system is capable of effectively managing this task. The simulation results above demonstrate that the generated models effectively adjust to various amounts of solar irradiation, indicating their potential for further research.

CONCLUSION

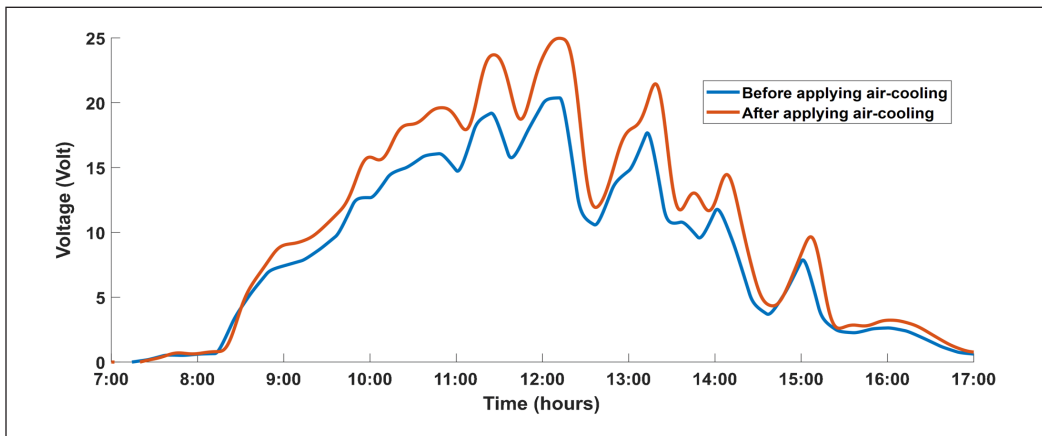
Before and after installing an air-cooling PV system, solar irradiance, T_{cell} and voltage output were measured to determine the actual PV output, V_{pvexp} . Before installation of the proposed air-cooling PV system, the higher T_{cell} will cause the voltage and power output

Table 1
Percentage of validation simulated model to measured data under high, moderate and low levels of solar irradiance

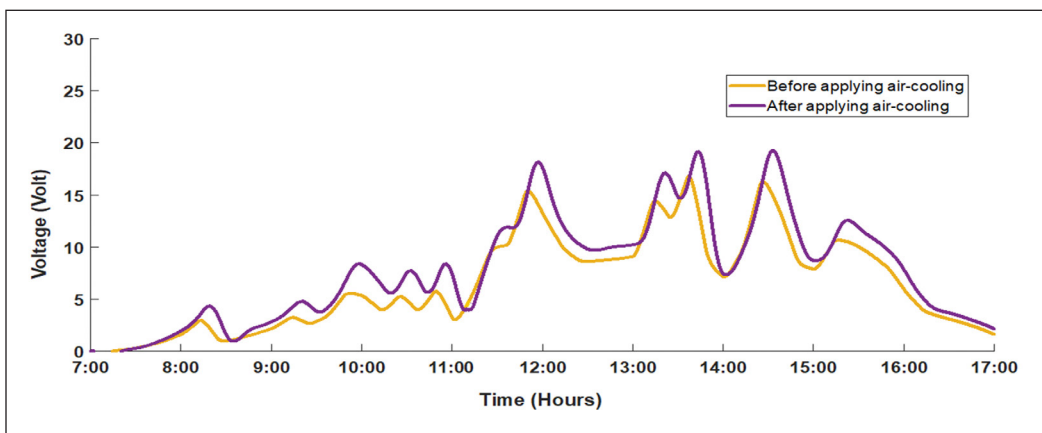
Model	High PSH	Moderate PSH	Low PSH
PV module	90.1%	92.4%	90.8%
air-cooling PV system	91.7%	93.2%	91.5%



(a)



(b)



(c)

Figure 13. The output voltage of the PV module before and after applying an air-cooling system using the SI model for (a) high-level irradiance, (b) moderate-level irradiance, and (c) low-level irradiance

of the *PV* system to decrease. The air-cooling *PV* system used to cool down the T_{cell} subsequently enhanced the output performance of the *PV* module. This paper develops and stimulates a data-driven mathematical model for *PV* modules and air-cooling *PV* systems. The experiment was conducted continuously for a duration of 12 hours, which is the longest period of uninterrupted data collection compared to prior studies. The data was taken at 3-second intervals, resulting in a total of twelve thousand data points, which is the highest number compared to the prior study. The use of extensive data in the development of a more precise model for air-cooling photovoltaic systems is a unique aspect of this work. A mathematical model has been constructed to optimise the performance of a *PV* module and air-cooling *PV* system under varying levels of solar irradiance. The lack of development in the prior air-cooling *PV* system model necessitated the development of this new model, which is a significant innovation in this study. The developed models could be utilised in future research endeavours aimed at enhancing the efficiency of the *PV* module and the proposed air-cooling *PV* system. The analysis shows that the TF model provides the greatest fit. The percentage of fitness for the *PV* module model is 90%, while it is 94.3% for the air-cooling *PV* system model. The simulation findings indicate minimal disparities in the average output voltage between the model system and the actual data across all levels of solar irradiation, with each discrepancy being less than 10%. The *PV* module model demonstrated validation values of 90.1%, 92.4% and 90.8% for high, moderate, and low PSH, respectively. The validation results for the air-cooling *PV* system model were 91.7%, 93.2%, and 91.5%. The output mean voltage exhibits a progressive increase, reaching 10.8% higher under conditions of high PSH, 17.5% higher under conditions of moderate PSH, and 15.3% higher under conditions of low PSH. Upon careful analysis of the data received from the validation of the models, as well as the findings from the simulation, it can be concluded that the produced model-based control has been effectively developed and may be utilised in future research, particularly in the field of controller design, to ensure optimal performance of the proposed cooling system.

ACKNOWLEDGEMENTS

The authors would like to acknowledge the Ministry of Higher Education for financial support via research grant GP-IPB/2020/9688702. Also, a special thanks to Advanced Lightning Power Energy Research (ALPER), Universiti Putra Malaysia, and the German Malaysian Institute for providing lab and equipment and an award to the project's primary author.

REFERENCES

- Adak, S., Cangi, H., Eid, B., & Yilmaz, A. S. (2021). Developed analytical expression for current harmonic distortion of the *PV* system's inverter in relation to the solar irradiance and temperature. *Electrical Engineering*, 103(1), 697–704. <https://doi.org/10.1007/s00202-020-01110-7>

- Adak, S., Cangi, H., Yilmaz, A. S., & Arifoglu, U. (2022). Development software program for extraction of photovoltaic cell equivalent circuit model parameters based on the Newton–Raphson method. *Journal of Computational Electronics*, 22(1), 413–422. <https://doi.org/10.1007/s10825-022-01969-8>
- Al Hadad, W., Maillet, D., & Jannot, Y. (2018). Experimental transfer functions identification: Thermal impedance and transmittance in a channel heated by an upstream unsteady volumetric heat source. *International Journal of Heat and Mass Transfer*, 116, 931–939. <https://doi.org/10.1016/j.ijheatmasstransfer.2017.09.079>
- Assani, N., Matic, P., & Kezic, D. (2022). Flow control process identification using Matlab’s system identification toolbox. In *2022 8th International Conference on Control, Decision and Information Technologies (CoDIT)* (pp. 1228–1232). IEEE Publishing. <https://doi.org/10.1109/CoDIT55151.2022.9803906>
- Åström, K. J., & Eykhoff, P. (1971). System identification - A survey. *Automatica*, 7(2), 123–162. [https://doi.org/10.1016/0005-1098\(71\)90059-8](https://doi.org/10.1016/0005-1098(71)90059-8)
- Bhuvaneswari, N. (2012). System identification and modeling for interacting and non-interacting tank systems using intelligent techniques. *International Journal of Information Sciences and Techniques*, 2(5), 23–37. <https://doi.org/10.5121/ijist.2012.2503>
- Cheng, Z., & Lu, Z. (2022). System response modeling of HMCVT for tractors and the comparative research on system identification methods. *Computers and Electronics in Agriculture*, 202, Article 107386. <https://doi.org/10.1016/j.compag.2022.107386>
- Donjaroennon, N., Nuchkum, S., & Leeton, U. (2021). Mathematical model construction of DC motor by closed-loop system Identification technique using Matlab/Simulink. In *2021 9th International Electrical Engineering Congress (IEECON)* (pp. 289–292). IEEE Publishing. <https://doi.org/10.1109/IEECON51072.2021.9440305>
- Dorf, R., & Bishop, R. (2010). *Modern control systems* (12th ed.). Prentice-Hall Int.
- Dubey, S., Sarvaiya, J. N., & Seshadri, B. (2013). Temperature dependent photovoltaic (PV) efficiency and its effect on PV production in the world - A review. *Energy Procedia*, 33, 311–321. <https://doi.org/10.1016/j.egypro.2013.05.072>
- Egorova, T., Schmutz, W., Rozanov, E., Shapiro, A. I., Usoskin, I., Beer, J., Tagirov, R. V., & Peter, T. (2018). Revised historical solar irradiance forcing. *Astronomy & Astrophysics*, 615, Article A85. <https://doi.org/10.1051/0004-6361/201731199>
- Erol, H., Mahmut, U., & Kesilmiş, Z. (2021). Water cooled PV panel efficiency in Osmaniye environment. *International Advanced Researches and Engineering Journal*, 5(1), 008–013. <https://doi.org/10.35860/iarej.787168>
- Haidar, Z. A., Orfi, J., & Kanesamkandi, Z. (2018). Experimental investigation of evaporative cooling for enhancing photovoltaic panels efficiency. *Results in Physics*, 11, 690–697. <https://doi.org/10.1016/j.rinp.2018.10.016>
- Ljung, L. (2012). *System Identification Toolbox™ User’s Guide* (5th ed.). The MathWorks Inc.
- Luboń, W., Pełka, G., Janowski, M., Pająk, L., Stefaniuk, M., Kotyza, J., & Reczek, P. (2020). Assessing the impact of water cooling on PV modules efficiency. *Energies*, 13(10), Article 2414. <https://doi.org/10.3390/en13102414>

- Mattei, M., Notton, G., Cristofari, C., Muselli, M., & Poggi, P. (2006). Calculation of the polycrystalline PV module temperature using a simple method of energy balance. *Renewable Energy*, 31(4), 553–567. <https://doi.org/10.1016/j.renene.2005.03.010>
- Mustafa, R., Radzi, M. A. M., Hizam, H., & Soh, A. C. (2024). An innovative air-cooling system for efficiency improvement of retrofitted rooftop photovoltaic module using cross-flow fan. *International Journal of Renewable Energy Development*, 13(2), 223–234. <https://doi.org/10.61435/ijred.2024.60068>
- Mustafa, R., Radzi, M. A. M., Hizam, H., & Soh, A. C. (2023). Solar insolation and PV module temperature impact on the actual grid connected solar photovoltaic system in German Malaysian Institute. In *IOP Conference Series: Earth and Environmental Science* (Vol. 1261, No. 1, p. 012001). IOP Publishing. <https://doi.org/10.1088/1755-1315/1261/1/012001>
- Popovici, C. G., Hudişteanu, S. V., Mateescu, T. D., & Cherecheş, N. C. (2016). Efficiency improvement of photovoltaic panels by using air cooled heat sinks. *Energy Procedia*, 85, 425–432. <https://doi.org/10.1016/j.egypro.2015.12.223>
- Rachad, S., Fouraiji, H., & Bensassi, B. (2014). Modeling a production system by parametric identification approach. In *2014 Second World Conference on Complex Systems (WCCS)* (pp. 402–406). IEEE Publishing. <https://doi.org/10.1109/ICoCS.2014.7060882>
- Šajić, J. L., Langthaler, S., Schröttner, J., & Baumgartner, C. (2022). System identification and mathematical modeling of the pandemic spread COVID-19 in Serbia. *IFAC-PapersOnLine*, 55(4), 19–24. <https://doi.org/10.1016/j.ifacol.2022.06.003>
- Schoukens, J., Pintelon, R., & Rolain, Y. (2012). *Mastering system identification in 100 exercises*. John Wiley & Sons.
- Selezniov, A. D., Solanki, S. K., & Krivova, N. A. (2011). Modelling solar irradiance variability on time scales from minutes to months. *Astronomy & Astrophysics*, 532, Article A108. <https://doi.org/10.1051/0004-6361/200811138>
- Sumalatha, A., & Rao, A. B. (2016). Novel method of system identification. In *2016 International Conference on Electrical, Electronics, and Optimization Techniques (ICEEOT)* (pp. 2323–2328). IEEE Publishing. <https://doi.org/10.1109/ICEEOT.2016.7755109>
- Tawerghi, O., Arebi, Y., & Alnkeeb, A. (2021). Modeling a third order noninteracting liquid level tank system empirically and theoretically. In *2021 IEEE 1st International Maghreb Meeting of the Conference on Sciences and Techniques of Automatic Control and Computer Engineering MI-STA* (pp. 198–203). IEEE Publishing. <https://doi.org/10.1109/MI-STA52233.2021.9464379>
- Tuhta, S. (2021). Using deep learning on system identification of the retaining wall model. *EURAS Journal of Engineering and Applied Sciences*, 2(2), 79–95. https://doi.org/10.17932/EJEAS.2021.024/ejeas_v02i2002
- Valousek, L., & Jalovecky, R. (2021). Use of the MATLAB® System Identification Toolbox® for the creation of specialized software for parameters identification. In *2021 International Conference on Military Technologies (ICMT)* (pp. 1–5). IEEE Publishing. <https://doi.org/10.1109/ICMT52455.2021.9502786>

Growth Monitoring of Healthy and BSR-infected Oil Palm Seedlings Using Ground-based LiDAR

Nur Azuan Husin^{1,2*}, Ray Clement Ridu², Normahnani Md Noh³ and Siti Khairunniza Bejo^{1,2,4}

¹Smart Farming Technology Research Centre, Universiti Putra Malaysia, 43400 UPM, Serdang, Selangor, Malaysia

²Department of Biological and Agricultural Engineering, Faculty of Engineering, Universiti Putra Malaysia 43400 UPM, Serdang, Selangor, Malaysia

³Sime Darby Plantation R&D Centre, KM 10, Jalan Banting-Kelanang, 42700, Banting, Selangor, Malaysia

⁴Institute of Plantation Studies, Universiti Putra Malaysia, 43400 UPM, Serdang, Selangor, Malaysia

ABSTRACT

The most threatening disease to the oil palm is Basal Stem Rot (BSR) disease caused by *Ganoderma boninense*. Besides matured oil palm trees, palm seedlings are susceptible to BSR disease. Therefore, it is crucial to detect the symptoms of the disease at an early stage so that the infected plants can be treated immediately. This study focuses on growth monitoring to differentiate between the infected (INF) seedlings and non-infected (NONF) seedlings by using ground-based LiDAR. This study used one hundred INF seedlings and 20 NONF seedlings, where the NONF seedlings acted as a control. The parameters measured using LiDAR were the height, stem diameter, and point density of the seedlings, which were measured four times every two-week intervals. The results showed significant differences in mean height and mean stem diameter between INF and NONF seedlings. Results from the LiDAR measurements were consistent with the manual measurements, with more than 86% correlations. In temporal measurements, the mean stem diameter for NONF seedlings consistently increased over the six weeks, while for INF seedlings, it was inconsistent throughout the time. Furthermore, in the last three measurements, the mean point density of NONF seedlings was higher than that of INF seedlings, which indicated better growth of non-infected seedlings than infected seedlings.

ARTICLE INFO

Article history:

Received: 29 May 2024

Accepted: 04 November 2024

Published: 26 March 2025

DOI: <https://doi.org/10.47836/pjst.33.3.03>

E-mail addresses:

nurazuan@upm.edu.my (Nur Azuan Husin)

rayclement98@gmail.com (Ray Clement Ridu)

normahnani.md.noh@simeдарby-plantation.com (Normahnani Md Noh)

skbejo@upm.edu.my (Siti Khairunniza Bejo)

* Corresponding author

Keywords: *Ganoderma boninense*, height, infected oil palms, point clouds, stem diameter

INTRODUCTION

Elaeis guineensis, or oil palm, is widely planted throughout Southeast Asia, where Malaysia is the world's second-largest producer of palm oil. The planted area

reached 5.67 million hectares in 2022, with most of the area in Sabah and Sarawak encompassing 3.13 hectares (Parveez et al., 2022). Over the last 30 years, the annual exports have been increasing steadily, thus making palm oil and palm-based products among the top 10 exports in the country. Oil palm is the most beneficial vegetable oil plant, which can be harvested for more than 25 years (Yap et al., 2021). In other oil-producing crops such as soybean and rapeseed, the output-to-input energy is 3:1, whereas the oil palm output-to-input energy ratio is higher, 9:1 (Farraji et al., 2021).

The most threatening disease to the oil palm is the Basal Stem Rot (BSR) disease caused by *Ganoderma boninense* (*G. boninense*). The disease could cause a reduction of fresh fruit bunch (FFB) yield up to 4.3 tonnes per hectare (Husin et al., 2020a). An estimated RM2.2 billion in economic losses are incurred annually by Malaysia due to the fact that diseased trees are present in approximately 60% of plantation areas (Bharudin et al., 2022). Over the last 30 years, the annual exports have been increasing steadily, thus making palm oil and palm-based products among the top 10 exports in the country. The disease can affect mature trees and oil palm seedlings, with the latter group experiencing earlier and more severe symptoms (Azmi et al., 2020). The symptoms of a *G. boninense* infection resemble those of water stress and nutrient deprivation because *G. boninense* generates enzymes that have the potential to break down cellulose, lignin layers, woody tissues, and xylem, significantly disrupting the flow of nutrients and water to the upper portion of the palm. There are no notable symptoms that the unaided eye may observe, so it is challenging to identify BSR signs in its early phases (Khairunniza-Bejo et al., 2021).

When oil palm seedlings are infected with *G. boninense*, the first noticeable symptom is the appearance of fruiting bodies at the bole part. The fronds then exhibit mottling or partial leaf yellowing, and when more than 50% of the stem base has been internally destroyed, necrosis occurs. However, the fruiting body may or may not appear prior to the development of foliar symptoms, making visual identification difficult and commonly overlooked. In severe situations, the incapacity to complete photosynthesis may result in reduced development, particularly in girth, height and frond count (Zevgolisi et al., 2022). However, because a fungal mass can emerge before or after leaf withering, it can be difficult to see with the unaided eye and frequently goes unnoticed. Infection with *G. boninense* can also be found in the longitudinal sectioning and roots of the infected bole, even in the absence of visible symptoms (Azmi et al., 2021). A dark discolouration and white mycelium poking through the root epidermis are typically seen in the longitudinal section, which indicates an upward infection progression within the seedling. However, because it is a labour-intensive procedure that can destroy trees, bole and root detection is not practicable in large-scale plantations. In typical nursery practice, a human-performed manual census is utilised to track the course of the disease in relation to different treatments. A human examination mostly depends on the disease's outward manifestations. This approach is prone to inaccuracy because of little experience, arbitrary assessments, and situations with no symptoms.

Some researchers have used laboratory methods for *Ganoderma* BSR disease detection. Madihah et al. (2014) developed immunoassay-based detection methods for *G. boninense* detection using Enzyme-linked immunosorbent assay (ELISA), which uses both monoclonal and polyclonal antibodies. Meanwhile, Akul et al. (2018) used Loop-mediated isothermal amplification (LAMP), which consists of two outer and two inner primer sets of the target DNA, to specifically identify the manganese superoxide gene (MnSOD) of *G. boninense* for the BSR disease detection in oil palm. Madihah et al. (2018) also used the LAMP method, where only the bug1A primer combination, out of eight sets of LAMP primers, which could differentiate between other actinomycetes/basidiomycetes fungus and *Ganoderma* non-pathogenic strains and pathogenic strains (*G. boninense*). In addition, Hilmi et al. (2022) used the Polymerase chain reaction (PCR) method created using a primer based on the ribosomal DNA internal transcribed spacer (ITS) region to identify a pathogenic *Ganoderma* species. The laboratory-based methods are reliable for early detection of the disease, but the cost is high, the procedure is complex and time-consuming, and some are unsuitable for outdoor conditions (Azuan et al., 2019).

Remote sensing technology is a method that is reliable, fast, and suitable for outdoor activity. Laser scanning or LiDAR (Light Detection and Ranging) is one of the popular remote sensing techniques. A laser scanner uses high-speed laser technology to acquire millions of laser points to generate a three-dimensional (3D) set of data in space known as point clouds in a significantly short time. 3D laser scanners have the potential to distinguish information about plant biomass or plant architecture. Single plant organs can be determined automatically, and the volume of information can be determined, which has been shown to have a high correlation to the actual measurement (Buja et al., 2021). The benefits of LiDAR-based systems over passive ones - which are limited by variations in light, atmospheric conditions, viewing angle, and canopy structure - include enhanced data-gathering flexibility, a high degree of automation, and the ability to deliver data at a rapid pace. The application of machine learning techniques for spatially and temporally distributed big data, along with a multi-sensor systems approach that focuses on conventional optimal estimation, can lead to increased accuracy in plant disease detection (Husin et al., 2022). One such technique is the fusion of LiDAR with existing electro-optical sensors. These electro-optical sensors provide novel ways to predict and respond to plant disease when used on a range of platforms, including satellites, ground-based robotic vehicles, handheld devices, and aerial vehicles. LiDAR technology can be used in oil palm fields due to the benefits of obtaining detailed three-dimensional (3D) data without physical contact with the scanned object.

Crop health monitoring is increasingly using remote sensors, which provide plant disease detection and quantification at many evaluation levels in a non-destructive, spatialised manner. The advancement of sensor technology has helped the development of new precision agricultural techniques. Emerging methodologies for acquiring phenotypic

features through LIDAR shape profiling have been established, with the major metrics being the height and leaf area density (Fahey et al., 2020). Similarly, as part of a high-throughput characterisation platform, LIDAR shape profiling is used to assess the canopy and above-ground biomass. The information could be used to analyse physiological growth and detect different substances in plants for ecological applications such as disease detection. The analysis of the use of LiDAR in phenotyping is still in its infancy, but the depth and variety of information provided by LIDAR in a short amount of time at a low cost, particularly in relation to plant structure, is advantageous. Metric measurements of trees were obtained using the laser scanning method, where various tree characteristics were extracted, i.e., diameters at breast height and tree height (Cabo et al., 2018; Liu et al., 2018), crown diameter, crown area, height and tree volume (Wagers et al., 2021), crown base height, crown diameter and crown volume (Hillman et al., 2021) and diameter, stem curve and height measurements, crown width (Pitkänen et al., 2021) with high correlations and accuracies. Therefore, the applications of laser scanners for metric measurements were proven for accurate metric measurements aimed at growth monitoring and could be used for disease detection. For example, a Terrestrial Laser Scanner (TLS) was used by several researchers (Azuan et al., 2019; Husin et al., 2020a) to study the physical characteristics of mature oil palm trees on a plantation. Several parameters such as crown size, oil palm frond's number, the gap between the oil palm fronds (measured in degree), number of unopened new fronds (also known as spears), perimeter and area of the trunk were used to detect and determine the level of BSR disease infection (Husin et al., 2020b; Husin et al., 2020c). These parameters were measured in different levels of infections, thus using statistical analysis, detection models, and machine learning integration. Early detection of BSR disease was done, and infected and non-infected oil palm trees were discriminated successfully.

Temporal data on palm seedling oil is important for monitoring the conditions of the seedlings and for offering disease-related data that can help clarify the course and dissemination of the disease (Husin et al., 2022). Meanwhile, the compilation and analysis of temporal data can be used to diagnose the disease early in advance of a potential diagnostic outbreak (Santoso et al., 2011; Azahar et al., 2011). Therefore, the objectives of this study were to measure the changes in oil palm seedlings due to infection of BSR disease using temporal data and to differentiate between healthy and BSR-infected oil palm seedlings using point cloud images taken by ground-based LiDAR sensors, also known as Terrestrial Laser Scanner (TLS). It is hypothesised that enzymes produced by *G. boninense* fungus have impaired the xylem and phloem tissues, which are essential for storing and moving water and carbohydrates in plants. Infected seedlings may endure significantly low carbohydrate intakes and severe water deficiencies that restrict the plant's ability to perform regular photosynthesis. These would inhibit tree growth and affect the physiological conditions of the seedlings, such as the diameter of the stem, the plant's height, and total

point density, which can be measured. The study could be used to differentiate between infected and uninfected oil palm seedlings towards an early detection approach and management control of the disease (Husin et al., 2021).

MATERIALS AND METHODS

Study Area

The study was conducted in an oil palm greenhouse nursery located at Sime Darby Plantation Banting, Selangor, Malaysia (2°48'08.6" N, 101°27'33.0" E). The greenhouse was utilised to cultivate all seedlings, maintaining regulated humidity and temperature levels, where the area was 16 m length × 6 m width × 2 m height. The roof and the wall were made from transparent UV plastic, and black netting was used to cover them. UV plastic was used to prevent the seedlings from getting excess water from the rain and harmful UV light, while black netting was used to reduce heat from the sun. There was a control system that could automatically adjust the amount of water and fertilisers applied to all the seedlings; therefore, all the seedlings could be monitored. The temperature of the greenhouse was averaged at 27°C, and the humidity was about 90%. The seedlings used for this study were Tenera hybrids, and the seedlings were eight months old. One hundred BSR-infected seedlings (INF) were inoculated with *G. boninense* inoculum (Naidu et al., 2018) by attaching a colonised *G. boninense* rubberwood block to the roots of the seedlings for five months, and only 20 healthy seedlings (NONF) were used as a control.

The arrangement of seedlings in the greenhouse was as follows: five lines of infected seedlings and one line for non-infected seedlings, each consisting of 20 seedlings at a distance of 0.5 m apart from each other. Six water tanks were placed in the middle of the greenhouse to supply water through a drip irrigation system, where the seedlings received approximately 1.0 L/polybag/day. They were fertilised with 50 g nitrogen (N), phosphorus (P) and potassium (K) solid fertiliser according to plantation practice. Biosafety guidelines were followed by implementing the Integrated Ganoderma Management (IGM) system by all the personnel and researchers working in the nursery facilities. The infected and non-infected plants were placed without barriers according to plantation practices. The infection process that occurs after root contact with an infection source has been proven by years of extensive investigation, both in the lab and the field (Rees et al., 2009). In the early stages of the disease, spores were not involved, while both the infection process and bracket formation on young, infected palms did not contribute to the same (Sanderson, 2005).

For data gathering, the scanner was positioned atop a surveying tripod at a height of approximately one metre. The area was scanned from eight scan points to capture the 3D image of the seedlings (Figure 1). Six high-reflective sphere references were arranged at a specific point that could be detected from all scan points. The function of the sphere

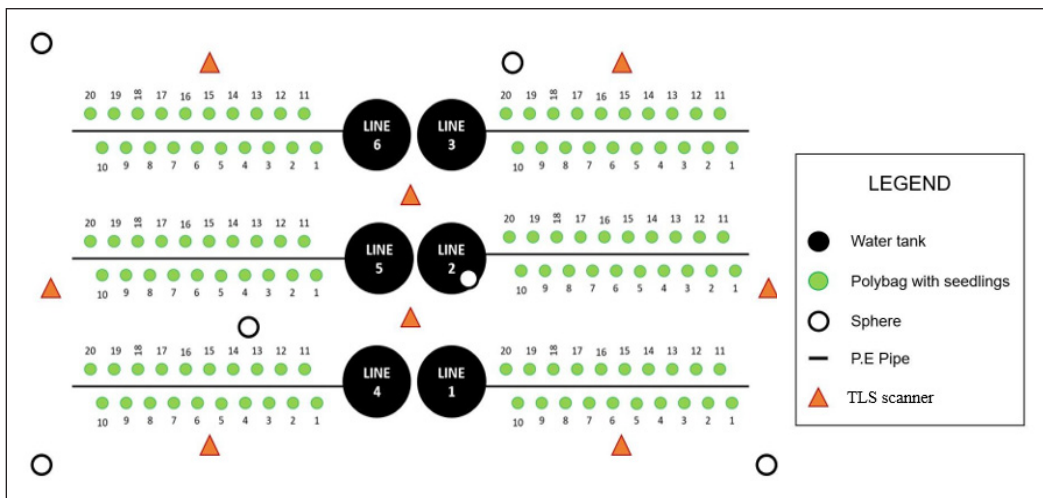


Figure 1. Setup of data acquisition

was to transform the multiple different views of images into the same coordinate frame. Despite the position of the scan, the geometry of the spheres was noticeable, and it was easily used to merge the scan files in case it could not detect the scan locations (Bornaz & Rinaudo, 2004). The data acquisitions were taken every two weeks.

Point Cloud Processing Using SCENE Software

The laser scans were recorded on a removable SD memory card that was subsequently transferred for further analysis using SCENE software (version 6.2, FARO Technologies, Inc.). SCENE is FARO's processing software for point clouds, where the main steps involved in post-processing are filtering, registration, and extraction of the area of interest (AOI). The "registration" step was completed to match the multiple scan positions and synchronise the laser point data to create a cluster of point clouds. Before filtering, the scan points usually contain noise caused by reflections on water in the polybags and the presence of small particles in the air. Thus, the desired scan points could be corrected, and noise could be removed from the scans by using a filter. The scan point clouds were created first, and then a "clipping box" was used to isolate the AOI from the environment. This enabled "slicing" the point cloud and "clipping" (separate) specific areas as needed to display or hide certain points of the 3D point cloud.

Stem Diameter and Height Measurements

The stem diameter was measured in the SCENE software, where parts of the seedlings were zoomed, and a "measure points" tool was used to obtain the cross-section image of the stem seedlings. The stem diameter was measured at the middle section of the stem,

which was about 2 cm from the base or soil level. Meanwhile, the height of the seedlings was measured from the tip of the plant to the base or soil level and was obtained using CloudCompare software (Cloud Compare [GPL software] v2.9 Omnia). The steps were to save the .pts file from the SCENE point cloud data, import it into the CloudCompare software, and save the file as a .bin file. The format .bin was used because it was smaller and more compatible with the CloudCompare software. Next, the image was converted into a scalar field image in Z coordinates. After that, outliers and unwanted objects, i.e., water tanks and poles, were removed through the segmentation process using a “segment” tool and a “cross-section” tool. The top polybags, which were about 40 cm in height, were set as a reference for the ground level to measure the height of the oil palm seedlings. The height was considered from the top of the soil, where all the seedlings had almost the same planting depth. The oil palm seedlings’ point cloud images that were processed in the CloudCompare software are displayed in Figure 2.

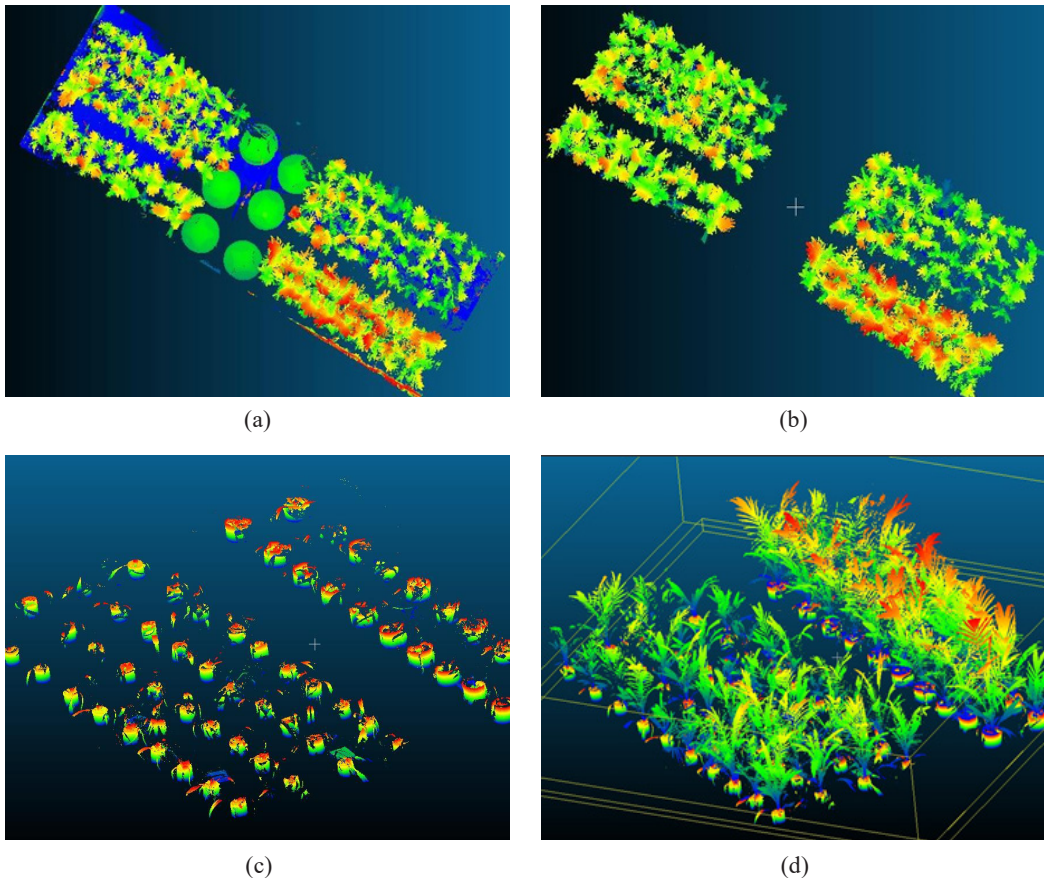


Figure 2. Steps of point cloud processing: (a) Conversion to scalar image; (b) Removal of unwanted objects; (c) Polybags separation; and (d) Metric measurements

Measurements of Point Density

The plant density, which consists of point cloud data, was calculated using the volume density features in the CloudCompare software (Girardeau-Montaut, 2016). LiDAR sensor measured the reflected pulses; therefore, a scanned object with a larger area and volume would reflect higher pulses. A similar approach was used, where a segmentation process was undertaken to remove all the outliers and unnecessary captured objects such as polybags, poles, pipelines and water tanks. After that, the geometric features tool was selected, and then the volume density was ticked to obtain the point density of the NONF and INF oil palm seedlings. The tool's main function was to estimate the volume density captured by TLS by counting each point in the point cloud.

Manual Measurement of the Seedlings

The physical properties of the seedlings were manually measured to compare and validate the results from TLS scans. A flexible steel measuring tape was used to measure the maximum height, which was determined from the soil surface in the polybag to the tip of the seedlings. Then, the stem diameter of the seedlings was measured by using a stainless steel vernier calliper. Similar to the point clouds measurement, the stem diameter was measured at a height of 2 cm from the base or soil level (Figure 3). Both measurements, height and stem diameter, were repeated three times and averaged. In total, four temporal measurements were taken, and the interval between the measurements was two weeks.

Statistical Analysis

A t-test was used to check and observe the significant difference in mean height and mean stem diameter between the eight-month INF and NONF oil palm seedlings. In addition, a

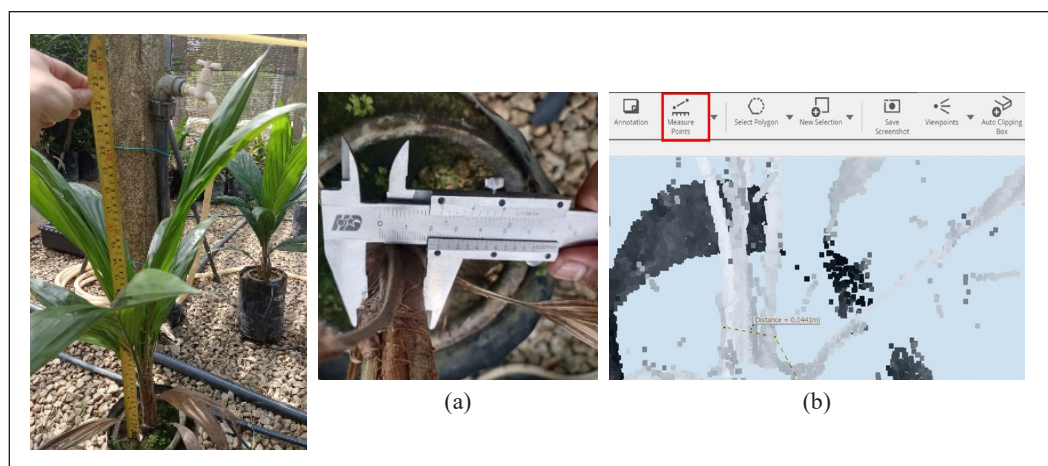


Figure 3. Measurements of oil palm seedlings: (a) manual; and (b) LiDAR point cloud measurements

Tukey HSD test was conducted to determine significant differences in the temporal changes between the measurements. Each statistical analysis was run using the JMP statistical software package (SAS Institute, Cary, USA). The α value was set to 0.05 confidence level. Furthermore, a correlation analysis was performed using Microsoft Excel (Microsoft, Redmond, WA) to observe the association between the manual measurement and TLS measurement. The closer the R^2 value to 1.0, the higher the correlation of the measurements. Figure 4 shows the steps of the method used in this study.

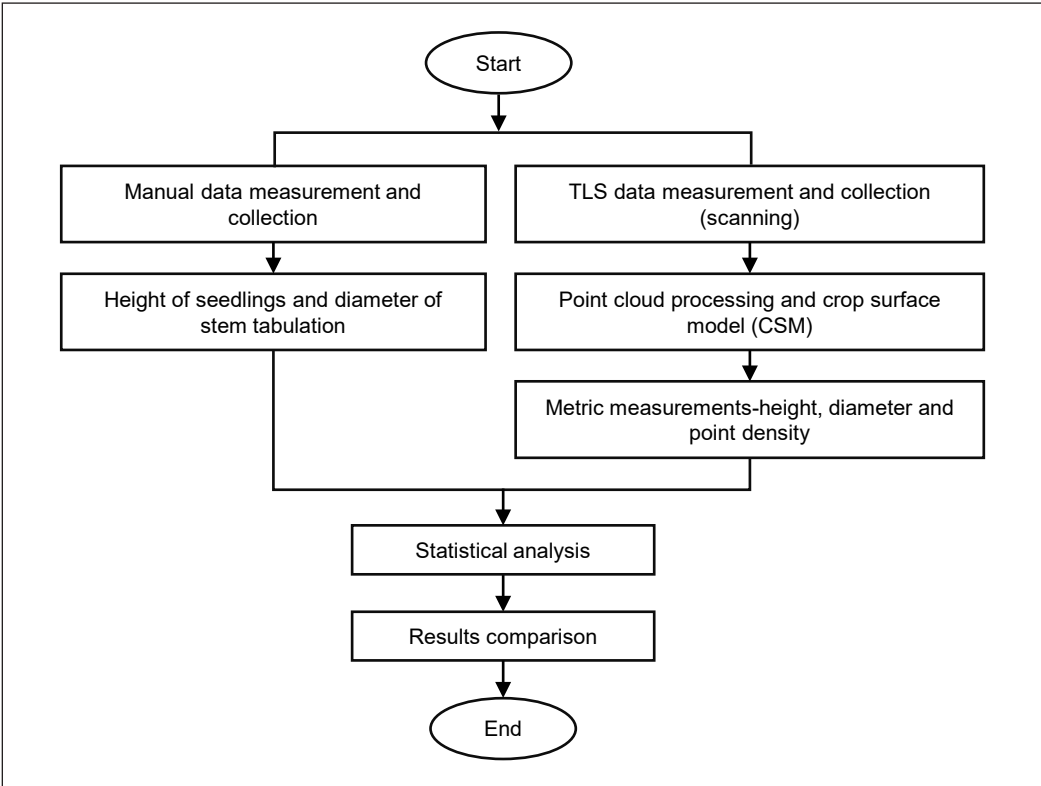


Figure 4. Flowchart of the method

RESULTS AND DISCUSSION

Analysis of Height and Stem Diameter

Figure 5 shows that the mean height of NONF and INF seedlings showed a continuous increment from the first measurement to the fourth measurement with R^2 values, 0.97 for the NONF seedlings and 0.98 for the INF seedlings. The mean height of the NONF seedlings increased with an average difference of $0.154\text{ m} \pm 0.05\text{ cm}$, while the mean height of the INF seedlings increased with an average difference of $0.139\text{ m} \pm 0.05\text{ cm}$ over the six weeks of TLS measurements in the nursery. Tukey HSD test showed significant differences between

all measurement times except the first and second measurements of the NONF seedlings (Table 1). The NONF seedlings had the highest and the lowest difference, which was from the second to the third measurement ($0.22\text{ m} \pm 0.05\text{ cm}$) and from the first to the second measurement ($0.073\text{ m} \pm 0.05\text{ cm}$), respectively. In all measurements, the mean height of NONF seedlings was significantly higher compared to INF seedlings at a 0.05 confidence level with all p-values less than 0.0001. The results show that the growth of NONF seedlings was better than the INF seedlings. NONF seedlings have a well-developed root system that can efficiently absorb water and nutrients from the soil. These nutrients are essential

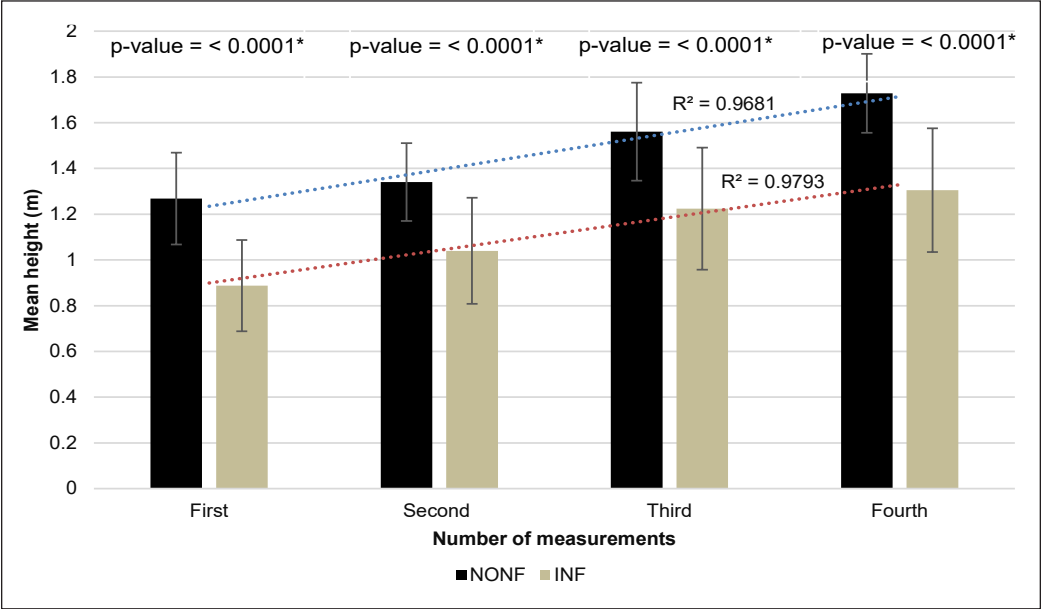


Figure 5. Mean height (\pm standard deviation) of the NONF and INF seedlings
Note. * significant at 5% level

Table 1
Tukey HSD test of temporal measurements for mean height and mean stem diameter

Type of Seedlings	Comparison of Measurements	Mean height		Mean stem diameter	
		Difference (m \pm 0.05cm)	p-value	Difference (mm \pm 0.01 mm)	p-value
NONF	First and second	0.073	0.6126	2.487	0.2914
	Second and third	0.220	0.0026*	2.487	0.0835
	Third and fourth	0.168	0.0334*	4.092	0.5893
INF	First and second	0.152	0.0011*	0.018	1.000
	Second and third	0.184	<0.0001*	5.314	<0.0001*
	Third and fourth	0.081	0.0303*	6.887	<0.0001*

Note. * significant at 5% level

for growth, photosynthesis, and plant vigour. Meanwhile, the fungus *G.boninense* causes root rot (Figure 6), severely impairing the seedling's ability to absorb water and nutrients. This leads to nutrient deficiencies, which stunts growth and weakens the seedlings (Surendran et al., 2017). This means that BSR disease significantly affects the growth of oil palm seedlings. The results from Table 1 show that the height parameter is a better indicator for the temporal measurements, where all seedlings showed significant differences between the measurements except for the first and second measurements in NONF seedlings.

The mean stem diameter of NONF seedlings in Figure 7 showed an increasing trend from the first measurement to the fourth measurement with R^2 values of 0.69. The growth of the mean stem diameter of the NONF seedlings continuously increased with an average difference of $2.375 \text{ m} \pm 0.01 \text{ mm}$. In contrast, the INF seedlings



Figure 6. Root and stem bole damage to oil palm seedlings due to BSR

showed a relatively slower growth rate with a mean diameter difference of $4.073 \text{ m} \pm 0.01 \text{ mm}$ over the six weeks of TLS measurements in the nursery. Even though the increase in stem diameter from the first to the second measurement and from the second to the third measurement were not significant, the trend showed an increase in healthy growth seedlings (Table 1). There was a slight decrease in the mean stem diameter from the third to the fourth measurement ($1.517 \pm 0.01 \text{ mm}$). The reduction in the mean diameter of the NONF seedlings between the third measurement and the fourth measurement might be due to the growth phase transition, where the seedlings might have transitioned from a rapid growth phase to a maintenance or stress response phase, where energy and resources were redirected to support other parts of the plant or to cope with environmental challenges, leading to temporary reductions in stem diameter (Huijser & Schmid, 2011). Meanwhile, the mean stem diameter of the INF seedlings was inconsistent with an R^2 value of 0.0005. It decreased from the first measurement to the second measurement ($0.018 \pm 0.01 \text{ mm}$), then increased at the third measurement ($5.314 \pm 0.01 \text{ mm}$) before drastically decreasing for the fourth measurement ($6.887 \pm 0.01 \text{ mm}$). The inconsistency of stem diameter might be due to the plant stress responses, where the response of the seedlings to *G.boninense* infection can fluctuate, with periods of higher stress leading to reduced growth and periods of recovery or compensatory growth (Shoresh et al., 2010). This could cause the stem diameter to increase at one point (as seen in the third measurement) and then decrease again as the infection progresses or as the seedlings exhaust their resources. In addition, the activation of defence mechanisms such as lignification (thickening of cell walls) or the

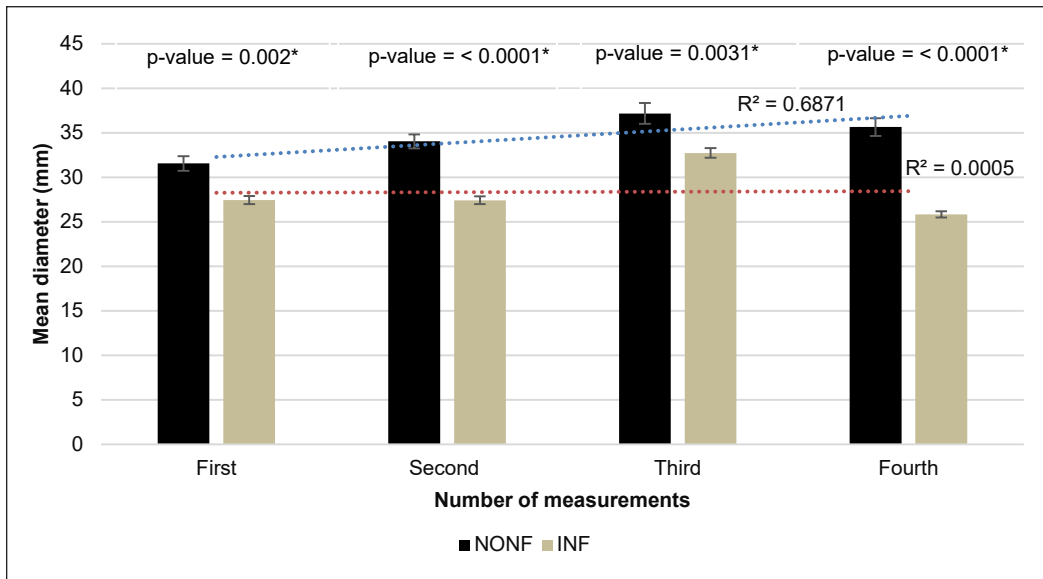


Figure 7. Mean diameter (\pm standard deviation) of the NONF and INF seedlings
 Note. * significant at 5% level

production of antifungal compounds by INF seedlings might temporarily affect growth rates, leading to inconsistent stem diameters (Faizah et al., 2022). The mean stem diameter of NONF seedlings was significantly larger than INF seedlings in all measurements at 0.05 confidence level with a p-value for the first measurement of 0.002, the second and fourth measurements were less than 0.0001, and the third measurement was 0.0031.

Analysis of Point Density

Figure 8 shows the average point density of the NONF and INF oil palm seedlings. The point density can be considered as the volume or surface area representation of the seedlings (Hosoi & Omasa, 2009). The first measurement of the point cloud was excluded due to an error in the NONF seedlings. The NONF seedlings presented higher point density from the second measurement to the fourth measurement compared to INF seedlings. It shows that NONF seedlings had normal and healthier growth compared to the stunted growth of INF seedlings. The point density for the NONF seedlings decreases from the second to the fourth measurement, with an average difference of point density of about 51 million points. Meanwhile, the point density of the INF seedlings increases from the second to third measurement and then decreases from the third to fourth measurement. The average difference in point density from the second to fourth measurement was about 23 million points. Growing plants often develop more complex surface structures with varied textures and angles. This increased roughness can scatter the LiDAR pulses more diffusely, reducing the number of pulses that return directly to the sensor and decreasing the point density

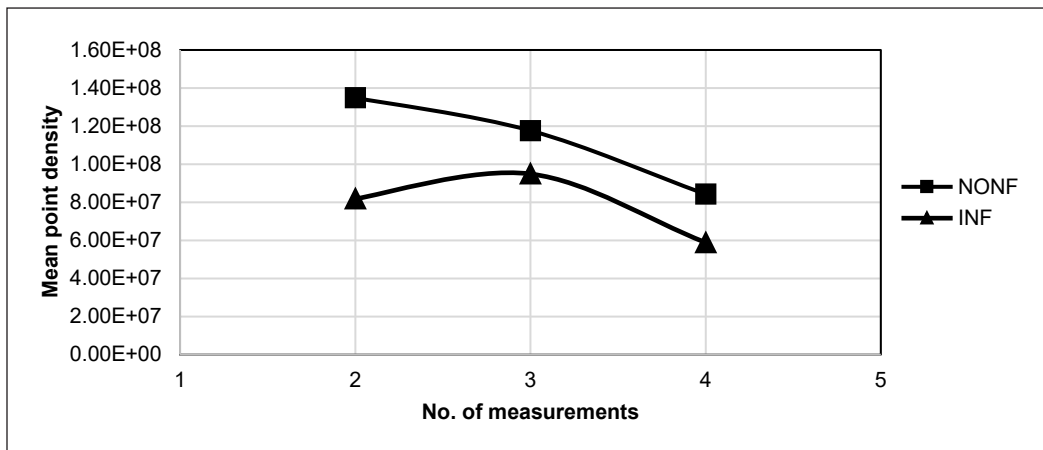


Figure 8. Point density of NONF seedlings and INF seedlings

(Rosette et al., 2012). Meanwhile, as the plant grows and the leaf orientation becomes more varied, some leaves may become angled in such a way that they reflect less laser energy back to the sensor, reducing point density (Gregorio & Llorens, 2021).

The differences in results between the NONF and INF seedlings were not likely because of fertiliser due to the same amount of fertiliser used for both types of seedlings. Two examples of infection modes are roots that came into contact with nearby infected palms and airborne basidiospores. The basidiospores of *G.boninnense* initiate root damage by germinating on the part of oil palm seedlings and invading root tissues with hyphae and secreting enzymes that degrade the root structure (Bharudin et al., 2022). It was noted that contaminated soil tissues rather than airborne spores were the cause of the disease spreading to healthy roots so widely (Sanderson, 2005). The NONF seedlings maintained optimal chlorophyll content, which allowed for efficient photosynthesis, which was needed for growth and development. However, the INF seedlings showed chlorosis, which diminishes the plant's ability to perform photosynthesis and leads to less energy for growth. It was also stated that the effects of the BSR disease infection could be seen on the seedlings at four and seven months after planting, which affected the development and growth of the oil palm seedlings (Faizah et al., 2022). In addition, using eye and manual inspection, the colour and condition of the leaves in some INF seedlings turned from green to yellow and then necrotic and wilted. Also, fungal whitish fruiting bodies like the mushroom structure were seen around the base of the stem or in the soil near the roots.

Correlation Analysis

The correlation analysis for the TLS and manual methods showed a strong relationship in every measurement, with an average of R^2 equal to 0.95 for the height (Figure 9) and an average of R^2 equal to 0.93 for the stem diameter (Figure 10). The range value of R^2

from the first until the fourth readings of the height was between 0.9272 and 0.9646, while the stem diameter was between 0.8601 and 0.9810. The highest correlation was at the second measurement of stem diameter with R^2 equal to 0.981, and the lowest correlation was at the third measurement of stem diameter with R^2 equal to 0.8601. LiDAR technology is known for its high accuracy and precision in measuring dimensions. This accuracy translates into measurements that have a very high correlation with the manual method. Unlike manual measurements, which can vary depending on the person performing the measurement, LiDAR provides consistent results. The high correlation values showed that ground-based LiDAR, like TLS, was a reliable tool to measure the diameter and height of the seedlings. It was stated by Johnson and Liscio (2015) that the height determination of an object by using TLS was duplicable and accurate on a static object. Moreover, Maas et al. (2008) found that TLS was able to present good and accurate stem geometry data and was efficient for plants. Lumme et al. (2008) also mentioned that TLS was useful equipment for growth height estimation and could be used as a precision farming tool in agriculture. Instead of collecting data manually, TLS may be used for metric measurements since correlation analysis showed satisfactory outcomes. However, based on this study, more scan points are needed to obtain a clearer image of

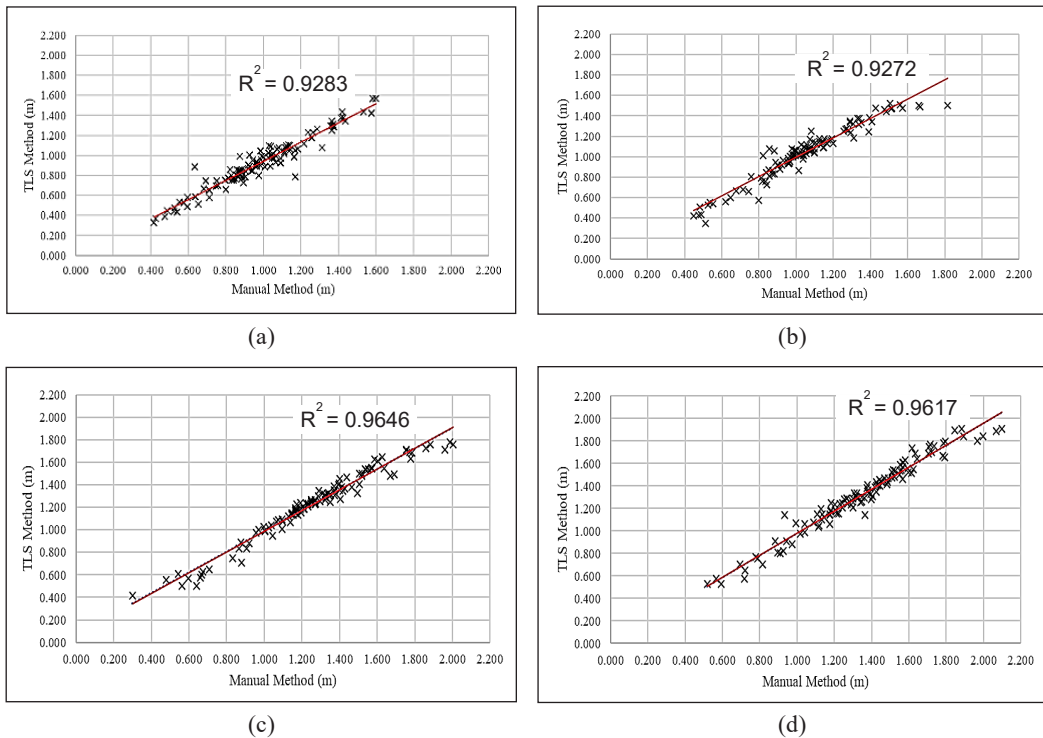


Figure 9. Correlation analysis of height: (a) First measurement; (b) Second measurement; (c) Third measurement; and (d) Fourth measurement

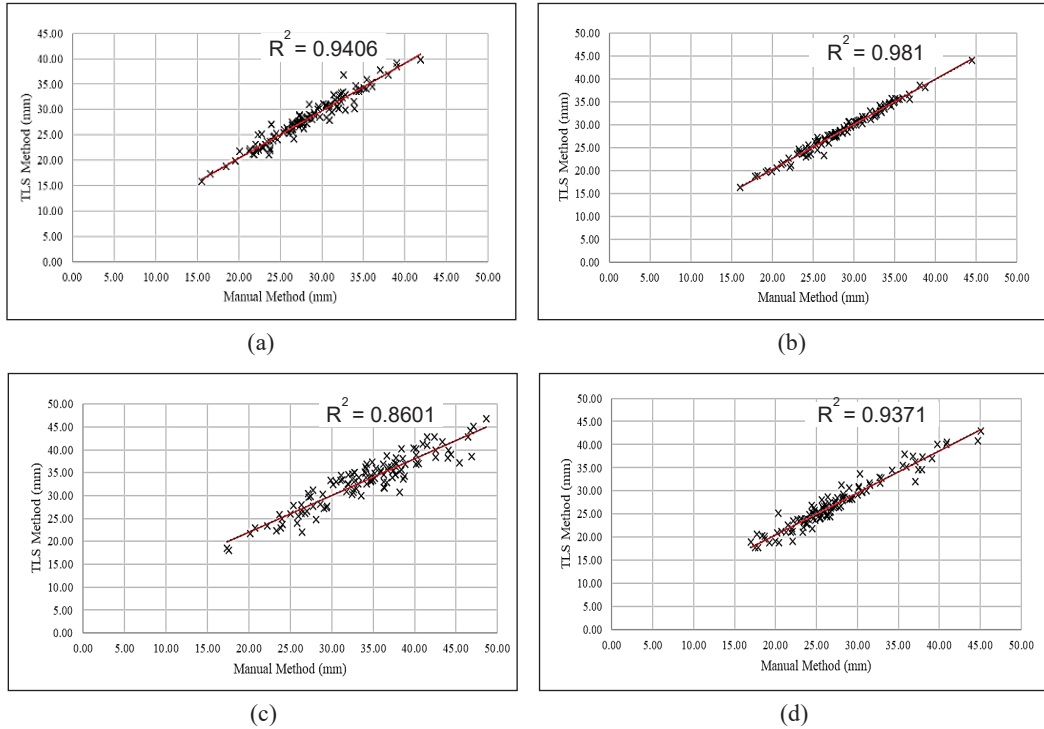


Figure 10. Correlation analysis of stem diameter: (a) First measurement; (b) Second measurement; (c) Third measurement; and (d) Fourth measurement

the stem cross-section. Overall, the high correlations (R^2 values) suggest that LiDAR is a reliable method that can produce results closely matching those obtained through manual measurements. The factors mentioned contribute to the strong relationship observed between the two measurement methods.

The metric features developed utilising point cloud data for BSR disease detection were height, stem diameter, and point density. The parameters or metric features could be utilised to distinguish between oil palm seedlings that are not infected with BSR and seedlings that are BSR-infected. This was the first in-depth analysis of oil palm seedlings in the nursery employing TLS to distinguish the changes brought by BSR disease. For the early diagnosis, management, and control of the disease, this cutting-edge image processing method using the physical characteristics of the oil palm seedlings was crucial. With the aid of pre-and post-processing facilities, it was also practical for in-situ applications. To achieve precision agricultural objectives, TLS offers information at the plant level. A sensing system utilising innovative algorithms and on-site technology may be able to deliver more accurate data to create a current health database for oil palm seedlings in nurseries.

Further research into the features of the oil palm seedlings could be undertaken for semi-auto calculation. Three characteristics - height, stem diameter, and point density

- could serve as the basis of the application. In this study, LiDAR showed a significant potential for BSR detection in oil palm seedlings, with accuracies of around 90%. Future health monitoring with LiDAR holds great promise, especially when coupled with chlorophyll data. For the classification of BSR diseases, further research may be done to establish a standard range based on the height, diameter, and point density of NONF and INF seedlings. Further research towards a model for BSR detection that includes height, diameter, and point density is possible. It has the potential to build complex models that take into consideration the leaf orientation, laser returns, and percentage of occlusion in oil palm seedlings.

The high-density LiDAR data is a useful tool for foliar and metric measurements. Although much effort needs to be made before realising this, these and other preliminary data may imply it. A 3D view of the seedlings could be used, and the view can be rotated to check the overlapping fronds between the seedlings. Additionally, by physically weighing the seedlings, the point density of the oil palm seedlings may be compared with their biomass. The outcomes further demonstrated the accuracy and dependability of TLS measurements. Despite its promise, the biggest disadvantage of the suggested method was the procedure of extracting the data, as some parameters required to be calculated manually. In the future, a deep learning technique might be used to automate the feature extraction process. The plantation manager could examine the condition of the seedlings in real time and create an alert system utilising an online platform. More research should be done to analyse oil palm seedlings with various levels of infection severity. Future research should give greater thought to adapting the data for a general approach to detecting *Ganoderma* disease because there are many potential methods to improve the procedures for usefulness and operation in plantation nurseries. To distinguish between oil palm seedlings that are not infected by BSR and BSR-infected seedlings, this study gives fundamental findings about the usage of static LiDAR.

The results of this work demonstrate the potential of TLS for precise 3D measurements of oil palm seedlings. It offers low-cost, high degree of information and is accurate, non-destructive, and high-precision measurements (Stovall et al., 2018). TLS allows for repeatable views and imaging from various angles and just comes at a one-time initial equipment cost. The benefits of the terrestrial laser scanner include its small size, portability, lightweight, and wide scanning range. For remote sensing, TLS sensors would be more economical and cost-effective. Both professionals and amateurs could easily manage it (Liang et al., 2016). This is the initial thorough investigation of the physical characteristics of oil palm seedlings utilising TLS for BSR disease. Additionally, it is a non-destructive measurement because it eliminates the need for human measurement, which might break and spoil the seedlings. Manual observation is time-consuming, individualised for each worker, and potentially exhausting. Continuous monitoring of each seedling is required

for naked-eye observation, which is time-consuming. Another concern is the lack of personnel in the plantation sector. The novel discovery of this study has the potential to close a knowledge gap in the field of laser scanning research and be an eye-opener for the community in this area.

TLS is regarded as an easy-to-use technology for information collection. Thus, since it is independent of the individual tasks of the workers, the process of scouting seedlings can be completed more quickly and effectively. Additionally, the use of a portable laser scanner may give greater flexibility and precision in terms of visuals and dimensions. Furthermore, LiDAR data may be crucial because it allows for the investigation and potential expansion of the model correlations between metric measurements and the level of BSR infection across a larger area. The progress and growth of laser scanning technology, which consistently enhances data quality, scanning speeds, and spatial coverage and offers a variety of platform types, bodes well for the proposed method in this study, even though it necessitates a processing procedure.

The initial setup costs for a ground-based laser scanner are around RM300,000, including the accessories, software and training for a single operator. Additional costs for calibration, software updates, and possible repairs are about RM 15,000. The advantages of ground-based LiDAR are less personnel needed; a single operator can handle the scanner with minimal assistance, saving labour costs and rapidly scanning large areas, reducing field time and field operation. The accuracy of the sensor is also extremely high, and the quality of the data is comprehensive, allowing for repeated analysis and additional measurements without returning to the field. Meanwhile, the manual vegetative measurements are around RM144,000 annually for four personnel. Manual measurements are arduous, and the fieldwork might take several hours to days, depending on the area size and the number of measurements. The data is usually recorded manually and entered in spreadsheets or databases, which can be time-consuming. The initial investment for a laser scanner is substantial, but the operational costs can be lower in the long run due to reduced labour and time efficiency and high-accuracy measurements.

Future research may examine the differences between BSR-infected oil palm seedlings and other symptoms of abiotic stresses such as drought. Fast and on-site diagnosis of plant diseases and long-term monitoring of plant health conditions are now possible, especially in situations with limited resources, thanks to portable imaging technologies (such as smartphones). By exchanging and transmitting data almost in real-time, the recent development of field-portable sensor equipment, such as smartphone devices or plant wearables, opens up promising new opportunities for the in-situ investigation of pathogens in the field (Li et al., 2020). Today's smartphones come with LiDAR sensors, making it possible to create mobile applications for identifying and categorising BSR illnesses using deep-learning object identification models.

CONCLUSION

In conclusion, the analysis demonstrates that the growth and development of oil palm seedlings are significantly impacted by Basal Stem Rot (BSR) disease, as evidenced by the differences in height, stem diameter, and point density between non-infected (NONF) and infected (INF) oil palm seedlings. The NONF seedlings consistently showed superior growth, indicating that healthy root systems are crucial for nutrient uptake and overall plant vigour. In contrast, the INF seedlings exhibited stunted growth due to the damaging effects of the *G. boninense* fungus, which impairs the roots' ability to absorb nutrients and water, leading to nutrient deficiencies and weakened seedlings. The use of ground-based LiDAR, specifically the Terrestrial Laser Scanner (TLS) technology, proved to be a reliable and precise method for monitoring the physical characteristics of oil palm seedlings. The high correlation between TLS and manual measurements highlights the potential of TLS as a non-destructive, accurate, and efficient tool for early detection and management of BSR disease in oil palm nurseries. Future research should focus on enhancing the TLS-based model by incorporating additional parameters like chlorophyll data and exploring the use of deep learning techniques for automated feature extraction. The findings from this study pave the way for more advanced and cost-effective approaches to disease management in agriculture, highlighting the value of integrating modern sensing technologies with traditional plantation practices.

ACKNOWLEDGEMENT

This research was funded by Universiti Putra Malaysia (UPM) under research project code GP-IPM/2021/9697200.

REFERENCES

- Akul, Y., Kumar, V., & Chong, K. P. (2018). Designing primers for loop-mediated isothermal amplification (LAMP) for detection of *Ganoderma boninense*. *Bulgarian Journal of Agricultural Science*, 24(5), 854-859.
- Azahar, T. M., Mustapha, J. C., Mazliham, S., & Boursier, P. (2011). Temporal analysis of basal stem rot disease in oil palm plantations: An analysis on peat soil. *International Journal of Engineering & Technology*, 11(3), 96-101.
- Azmi, A. N. N., Bejo, S. K., Jahari, M., Muharam, F. M., Yule, I., & Husin, N. A. (2020). Early detection of *Ganoderma boninense* in oil palm seedlings using support vector machines. *Remote Sensing*, 12(23), Article 3920. <https://doi.org/10.3390/rs12233920>
- Azmi, A. N. N., Khairunniza-Bejo, S., Jahari, M., Muharram, F. M., & Yule, I. (2021). Identification of a suitable machine learning model for detection of asymptomatic *Ganoderma boninense* infection in oil palm seedlings using hyperspectral data. *Applied Sciences*, 11(24), Article 11798. <https://doi.org/10.3390/app112411798>

- Azuan, N. H., Khairunniza-Bejo, S., Abdullah, A. F., Kassim, M. S. M., & Ahmad, D. (2019). Analysis of changes in oil palm canopy architecture from basal stem rot using terrestrial laser scanner. *Plant Disease*, 103(12), 3218-3225. <https://doi.org/10.1094/PDIS-10-18-1721-RE>
- Bharudin, I., Wahab, A. F. F. A., Samad, M. A. A., Yie, N. X., Zairun, M. A., Bakar, F. D. A., & Murad, A. M. A. (2022). Review update on the life cycle, plant-microbe interaction, genomics, detection and control strategies of the oil palm pathogen *Ganoderma boninense*. *Biology*, 11(2), Article 251. <https://doi.org/10.3390/biology11020251>
- Bornaz, L., & Rinaudo, F. (2004). Terrestrial laser scanner data processing. *XXth ISPRS Congress Istanbul*, 123(123006), 1-4.
- Buja, I., Sabella, E., Monteduro, A. G., Chiriaco, M. S., De Bellis, L., Luvisi, A., & Maruccio, G. (2021). Advances in plant disease detection and monitoring: From traditional assays to in-field diagnostics. *Sensors*, 21(6), Article 2129. <https://doi.org/10.3390/s21062129>
- Cabo, C., Ordóñez, C., López-Sánchez, C. A., & Armesto, J. (2018). Automatic dendrometry: Tree detection, tree height and diameter estimation using terrestrial laser scanning. *International Journal of Applied Earth Observation and Geoinformation*, 69, 164-174.
- Fahey, T., Pham, H., Gardi, A., Sabatini, R., Stefanelli, D., Goodwin, I., & Lamb, D. W. (2020). Active and passive electro-optical sensors for health assessment in food crops. *Sensors*, 21(1), Article 171. <https://doi.org/10.3390/s21010171>
- Faizah, R., Putranto, R. A., Raharti, V. R., Supena, N., Sukma, D., Budiani, A., Wening, S., & Sudarsono, S. (2022). Defense response changes in roots of oil palm (*Elaeis guineensis* Jacq.) seedlings after internal symptoms of *Ganoderma boninense* Pat. infection. *BMC Plant Biology*, 22(1), Article 139. <https://doi.org/10.1186/s12870-022-03493-0>
- Farraji, H., Dahlan, I., & Eslamian, S. (2021). Water recycling from palm oil mill effluent. In S. Eslamian (Ed.), *Handbook of Water Harvesting and Conservation: Basic Concepts and Fundamentals* (pp. 307-320). John Wiley & Sons. <https://doi.org/10.1002/9781119478911.ch20>
- Girardeau-Montaut, D. (2016). *CloudCompare - Point Cloud Processing Workshop*. EDF R&D Telecom ParisTech. https://www.eurosdri.net/sites/default/files/images/inline/04-cloudcompare_pcp_2019_public.pdf
- Gregorio, E., & Llorens, J. (2021). Sensing crop geometry and structure. In R. Kerry & A. Escolà (Eds.), *Sensing Approaches for Precision Agriculture* (pp. 59-92). Springer. https://doi.org/10.1007/978-3-030-78431-7_3
- Hillman, S., Wallace, L., Reinke, K., & Jones, S. (2021). A comparison between TLS and UAS LiDAR to represent eucalypt crown fuel characteristics. *ISPRS Journal of Photogrammetry and Remote Sensing*, 181, 295-307. <https://doi.org/10.1016/j.isprsjprs.2021.09.008>
- Hilmi, N. H. Z., Idris, A. S., Maizatul-Suriza, M., Madihah, A. Z., & Nur-Rashyeda, R. (2022). Molecular PCR assays for detection of *Ganoderma* pathogenic to oil palm in Malaysia. *Malaysian Applied Biology*, 51(1), 171-182. <https://doi.org/10.55230/mabjournal.v5i1l.2201>
- Hosoi, F., & Omasa, K. (2009). Estimating vertical plant area density profile and growth parameters of a wheat canopy at different growth stages using three-dimensional portable lidar imaging.

- ISPRS Journal of Photogrammetry and Remote Sensing*, 64(2), 151-158. <https://doi.org/10.1016/j.isprsjprs.2008.09.003>
- Huijser, P., & Schmid, M. (2011). The control of developmental phase transitions in plants. *Development*, 138(19), 4117-4129. <https://doi.org/10.1242/dev.063511>
- Husin, N. A., Bejo, S. K., Abdullah, A. F., Kassim, M. S., & Ahmad, D. (2021). Relationship of oil palm crown features extracted using terrestrial laser scanning for basal stem rot disease classification. *Basrah Journal of Agricultural Sciences*, 34, 1-10. <https://doi.org/10.37077/25200860.2021.34.sp1.1>
- Husin, N. A., Khairunniza-Bejo, S., Abdullah, A. F., Kassim, M. S., Ahmad, D., & Aziz, M. H. (2020a). Classification of basal stem rot disease in oil palm plantations using terrestrial laser scanning data and machine learning. *Agronomy*, 10(11), Article 1624. <https://doi.org/10.3390/agronomy10111624>
- Husin, N. A., Khairunniza-Bejo, S., Abdullah, A. F., Kassim, M. S., Ahmad, D., & Azmi, A. N. (2020b). Application of ground-based LiDAR for analysing oil palm canopy properties on the occurrence of basal stem rot (BSR) disease. *Scientific Reports*, 10(1), Article 6464. <https://doi.org/10.1038/s41598-020-62275-6>
- Husin, N. A., Khairunniza-Bejo, S., Abdullah, A. F., Kassim, M. S., & Ahmad, D. (2022). Multi-temporal analysis of terrestrial laser scanning data to detect basal stem rot in oil palm trees. *Precision Agriculture*, 23(1), 101-126. <https://doi.org/10.1007/s11119-021-09829-4>
- Husin, N. A., Khairunniza-Bejo, S., Abdullah, A. F., Kassim, M. S. M., & Ahmad, D. (2020c). Study of the oil palm crown characteristics associated with Basal Stem Rot (BSR) disease using stratification method of point cloud data. *Computers and Electronics in Agriculture*, 178, Article 105810. <https://doi.org/10.1016/j.compag.2020.105810>
- Johnson, M., & Liscio, E. (2015). Suspect height estimation using the Faro Focus3D laser scanner. *Journal of Forensic Sciences*, 60(6), 1582-1588. <https://doi.org/10.1111/1556-4029.12829>
- Khairunniza-Bejo, S., Shahibullah, M. S., Azmi, A. N. N., & Jahari, M. (2021). Non-destructive detection of asymptomatic *Ganoderma boninense* infection of oil palm seedlings using NIR-hyperspectral data and support vector machine. *Applied Sciences*, 11(22), Article 10878. <https://doi.org/10.3390/app112210878>
- Li, Z., Yu, T., Paul, R., Fan, J., Yang, Y., & Wei, Q. (2020). Agricultural nanodiagnostics for plant diseases: Recent advances and challenges. *Nanoscale Advances*, 2(8), 3083-3094. <https://doi.org/10.1039/C9NA00724E>
- Liang, X., Kankare, V., Hyypä, J., Wang, Y., Kukko, A., Haggrén, H., Yu, X., Kaartinen, H., Jaakkola, A., Guan, F., Holopainen, M., & Vastaranta, M. (2016). Terrestrial laser scanning in forest inventories. *ISPRS Journal of Photogrammetry and Remote Sensing*, 115, 63-77. <https://doi.org/10.1016/j.isprsjprs.2016.01.006>
- Liu, G., Wang, J., Dong, P., Chen, Y., & Liu, Z. (2018). Estimating individual tree height and diameter at breast height (DBH) from terrestrial laser scanning (TLS) data at plot level. *Forests*, 9(7), Article 398. <https://doi.org/10.3390/f9070398>
- Lumme, J., Karjalainen, M., Kaartinen, H., Kukko, A., Hyypä, J., Hyypä, H., Jaakkola, A., & Kleemola, J. (2008). Terrestrial laser scanning of agricultural crops. *The International Archives of the Photogrammetry, Remote Sensing and Spatial Information Sciences*, 37, 563-566.

- Maas, H. G., Bienert, A., Scheller, S., & Keane, E. (2008). Automatic forest inventory parameter determination from terrestrial laser scanner data. *International Journal of Remote Sensing*, 29(5), 1579-1593. <https://doi.org/10.1080/01431160701736406>
- Madiah, A. Z., Idris, A. S., & Rafidah, A. R. (2014). Polyclonal antibodies of *Ganoderma boninense* isolated from Malaysian oil palm for detection of basal stem rot disease. *African Journal of Biotechnology*, 13(34), 3455-3463. <https://doi.org/10.5897/AJB2013.13604>
- Madiah, A. Z., Maizatul-Suriza, M., Idris, A. S., Bakar, M. F. A., Kamaruddin, S., Bharudin, I., Bakar, F. D. A., & Murad, A. M. A. (2018). Comparison of DNA extraction and detection of *Ganoderma*, causal of basal stem rot disease in oil palm using loop-mediated isothermal amplification. *Malaysian Applied Biology*, 47(5), 119-127.
- Naidu, Y., Siddiqui, Y., Rafii, M. Y., Saud, H. M., & Idris, A. S. (2018). Inoculation of oil palm seedlings in Malaysia with white-rot hymenomycetes: Assessment of pathogenicity and vegetative growth. *Crop Protection*, 110, 146-154. <https://doi.org/10.1016/j.cropro.2018.02.018>
- Parveez, G. K. A., Kamil, N. N., Zawawi, N. Z., Ong-Abdullah, M., Rasuddin, R., Loh, S. K., Selvaduray, K. R., Hoong, S. S., & Idris, Z. (2022). Oil palm economic performance in Malaysia and R&D progress in 2021. *Journal of Oil Palm Research*, 34(2), 185-218. <https://doi.org/10.21894/jopr.2022.0036>
- Pitkänen, T. P., Raunonen, P., Liang, X., Lehtomäki, M., & Kangas, A. (2021). Improving TLS-based stem volume estimates by field measurements. *Computers and Electronics in Agriculture*, 180, Article 105882. <https://doi.org/10.1016/j.compag.2020.105882>
- Rees, R. W., Flood, J., Hasan, Y., Potter, U., & Cooper, R. M. (2009). Basal stem rot of oil palm (*Elaeis guineensis*); Mode of root infection and lower stem invasion by *Ganoderma boninense*. *Plant Pathology*, 58(5), 982-989. <https://doi.org/10.1111/j.1365-3059.2009.02100.x>
- Rosette, J., Suárez, J., Nelson, R., Los, S., Cook, B., & North, P. (2012). Lidar remote sensing for biomass assessment. *Remote Sensing of Biomass—Principles and Applications*, 24, 3-27. <https://doi.org/10.5772/17479>
- Sanderson, F. R. (2005). An insight into spore dispersal of *Ganoderma boninense* on oil palm. *Mycopathologia*, 159(1), 139-141. <https://doi.org/10.1007/s11046-004-4436-2>
- Santoso, H., Gunawan, T., Jatmiko, R. H., Darmosarkoro, W., & Minasny, B. (2011). Mapping and identifying basal stem rot disease in oil palms in North Sumatra with QuickBird imagery. *Precision Agriculture*, 12(2), 233-248. <https://doi.org/10.1007/s11119-010-9172-7>
- Shoresh, M., Harman, G. E., & Mastouri, F. (2010). Induced systemic resistance and plant responses to fungal biocontrol agents. *Annual Review of Phytopathology*, 48(1), 21-43. <https://doi.org/10.1146/annurev-phyto-073009-114450>
- Stovall, A. E., Anderson-Teixeira, K. J., & Shugart, H. H. (2018). Assessing terrestrial laser scanning for developing non-destructive biomass allometry. *Forest Ecology and Management*, 427, 217-229. <https://doi.org/10.1016/j.foreco.2018.06.004>
- Surendran, A., Siddiqui, Y., Saud, H. M., & Manickam, N. S. A. A. S. (2017). The antagonistic effect of phenolic compounds on ligninolytic and cellulolytic enzymes of *Ganoderma boninense*, causing basal stem rot

in oil palm. *International Journal of Agriculture & Biology*, 19, 1437-1446. <https://doi.org/10.17957/IJAB/15.0439>

Wagers, S., Castilla, G., Filiatrault, M., & Sanchez-Azofeifa, G. A. (2021). Using TLS-measured tree attributes to estimate aboveground biomass in small black spruce trees. *Forests*, 12(11), Article 1521. <https://doi.org/10.3390/f12111521>

Yap, P., Rosdin, R., Abdul-Rahman, A. A. A., Omar, A. T., Mohamed, M. N., & Rahami, M. S. (2021). Malaysian sustainable palm oil (MSPO) certification progress for independent smallholders in Malaysia. In *IOP Conference Series: Earth and Environmental Science* (Vol. 736, No. 1, p. 012071). IOP Publishing. <https://doi.org/10.1088/1755-1315/736/1/012071>

Zevgolis, Y. G., Alsamail, M. Z., Akriotis, T., Dimitrakopoulos, P. G., & Troumbis, A. Y. (2022). Detecting, quantifying, and mapping urban trees' structural defects using infrared thermography: Implications for tree risk assessment and management. *Urban Forestry & Urban Greening*, 75, Article 127691. <https://doi.org/10.1016/j.ufug.2022.127691>

Review Article

Thermal and Mechanical Stability of Bismuth Doped Sn-Ag-Cu Lead-free Solder: A Comprehensive Review

Ong Jun Lin^{1*}, Azmah Hanim Mohamed Ariff^{1,2}, Nuraini Abdul Aziz¹ and Azizan As'array¹

¹Department of Mechanical and Manufacturing Engineering, Faculty of Engineering, Universiti Putra Malaysia, 43400 UPM, Serdang, Selangor; Malaysia

²Advanced Engineering Materials and Composites, Faculty of Engineering, Universiti Putra Malaysia, 43400 UPM, Serdang, Selangor; Malaysia

ABSTRACT

Expansion in technology urges for better advancement, thus resulting in miniaturization of electronic products with rising concern for the reliability of electronic packaging material. Lead-free solder, being one of the most prominent alternatives in the electronic packaging industry, is constantly exposed to harsh conditions, which are especially exacerbated with smaller solder joints and a closer pitch. Hence, with the effort of attaining a more reliable solder alloy, research has been intensively executed to overcome the hurdle of maximizing the potential of SAC solders. The scope of the review thus focuses on identifying the aptitude of bismuth-doped SAC solders by analyzing their microstructure evolution in isothermal aging while understanding their thermal and mechanical stability in different fatigue tests. In the earlier days, Bismuth was found to realize a better melting point when interacting with the tin matrix due to its unique solid solution-strengthening mechanism. Bismuth-doped solders can also induce a more robust solder joint with smaller IMC particles and a thinner interfacial layer that enables significant improvement in fatigue resistance compared to traditional SAC alloys. Therefore, the review concludes that bismuth-doped SAC solder tends to

outshine the conventional alternative as well as offering immense advancement in thermal and mechanical properties, portraying them as a potential alternative for the assembly of high-reliability electronic products, especially in industries with extreme conditions such as aviation, automotive, and military.

Keywords: Aging, bismuth, mechanical cycling, micro-alloying, reliability, SAC, thermal cycling

ARTICLE INFO

Article history:

Received: 19 June 2024

Accepted: 07 January 2025

Published: 26 March 2025

DOI: <https://doi.org/10.47836/pjst.33.3.04>

E-mail addresses:

gs68057@student.upm.edu.my (Ong Jun Lin)

azmah@upm.edu.my (Azmah Hanim Mohamed Ariff)

nuraini@upm.edu.my (Nuraini Abdul Aziz)

zizan@upm.edu.my (Azizan As'array)

* Corresponding author

INTRODUCTION

Soldering is a process similar to welding, where two metals are joined together with the aid of a filler material. In the case of the soldering process, a solder such as tin-lead (Sn-Pb) is utilized (Darwish et al., 2000). According to historical records, soldering has been one of the most commonly practiced metal and artifact fabrication techniques since even thousands of years ago, during the Chinese dynasties. In the early 2000s, Sn-Pb solders were widely used in either first- or second-level interconnects for printed circuit boards (PCBs) in the manufacturing of electronic products due to their superior reliability, performance, and quality in actual service. Despite being one of the most economically friendly approaches, it exhibits optimum physical and mechanical properties due to the presence of lead (Pb). However, the increased concern for environmental issues and global health has led to a restriction on lead usage in electronic products due to its adverse effects on both environmental and human health since July 1, 2006. The mandatory prohibition of lead then begins to be enforced globally, first by the legislation and restrictions imposed by the European Union (EU) under the Restriction of Hazardous Substances (RoHS) Directive (Kanlayasiri & Sukpimai, 2016).

Hence, the shift in global trends and views on the soldering industry then fostered the development of lead-free solders as a replacement for Sn-Pb solders, which encouraged researchers to cultivate the potential of lead-free solders with ideal reliability and properties to be utilized in electronic applications in various industries. Lead-free solders can be classified into two categories depending on the number of elements involved in making up the composition of a solder system, typically with tin (Sn) as the primary matrix. In general, lead-free solders include either binary or ternary compounds depending on the number of alloying elements through mechanical alloying (Abtew & Selvaduray, 2000). Incorporating lead-free solders into high-reliability applications requires a thorough understanding and evaluation of a solder's properties, ranging from the melting point, wetting ability, and mechanical properties, to ensure a product's stability in real-world operation. Furthermore, the presence of Ag content in SAC solders tends to deteriorate a solder's resistance to mechanical stress due to the formation of unique IMC compounds such as Ag_3Sn .

Although it was proven that the atom-pinning effect of Ag_3Sn provides additional strength by inhibiting cracks, IMC compounds such as Ag_3Sn and Cu_6Sn_5 composites are prone to agglomerating when exposed to heat, which embrittles a solder under elevated working conditions (Bhavan et al., 2024). Therefore, it is crucial to seek improvement in the said solder to further enhance its credibility and better integrate it with modern applications, especially in industries with extreme operating conditions, such as the automotive, aviation, and military sectors. In some literature, increasing Ag content within ternary SAC alloy was deemed to be beneficial, as proven by Coyle et al. (2015), who achieved a better thermal fatigue property with SAC405 solder in comparison to its other peers with lower

Ag composition. Despite the possibility of coalescing and coarsening the Ag₃Sn atom in a solder space when exposed to heat, higher Ag content, in turn, incurs a greater cost on manufacturing and production.

Although one may say that the obstacle can be easily overcome by utilizing a ternary SAC solder with lower Ag content, reducing the Ag content compromises the solder's thermal fatigue resistance, which deviates from the initial motive. Therefore, to attain a better consequence without compromising either the thermal-mechanical or the drop impact strength of a SAC solder, some of the literature has been actively researching the possibility of introducing a fourth element into the solder matrix, such as indium (In) (Ren et al., 2023), gallium (Ga) (Zhang et al., 2023), bismuth (Bi) (Tarman et al., 2024), or even nanomaterials such as carbon nanotubes (CNT) (Dele-Afolabi et al., 2019) and graphene nanosheets (GNS). Li et al. (2021), for instance, reviewed the mechanical performance and properties of various lead-free solders when they interact with different elements ranging from metal particles to transition elements, with the primary objective of understanding and predicting the performance of the solder among modern PCBs. Bismuth, or Bi, in particular, was deemed to be exceptional thanks to its unique effect when coming into contact with the Sn atom. Differing from elements such as Ag, Bi tends to strengthen a Sn-based solder through its unique solid-solution strengthening mechanism that embeds itself into the molten Sn matrix during reflowing (Liu et al., 2024). The attribute, therefore, further pins down the movement of atoms and affects the growth kinetics of both the IMC compound and the IMC layer, which dictates the mechanical strength of a solder under isothermal aging.

In recent studies, researchers have focused on studying different micro- and nanoparticles and their potential in SAC solders. However, only a handful of suggested materials are viable for the current market with both advantages in cost and performance. Being one of the cheaper candidates, such as Bi, gains a great deal of interest, especially when it was discovered to enhance a solder's melting temperature. Therefore, to understand better the benefits of Bi in lead-free solders, the present study aims to study the effects of Bi addition on microstructure, isothermal aging, as well as thermal and mechanical stability of a SAC-Bi alloy, which is deemed to be essential, especially in the case of continuous miniaturization of technology that demands solder material with ideal resistance towards thermal and mechanical stresses.

MICROSTRUCTURE

Hodúlová et al. (2018) stated that a conventional SAC solder may consist of a network of dendritic structures made up of Sn dendrites encompassed by a eutectic region with Sn atoms and IMC compounds, as shown in Figure 1. Apart from the Sn solder matrix, a solder also comprises an IMC layer that occupies the interface between the pad and solder

to provide robust joint strength. An IMC composite is typically formed from the interaction of elements from both the pad and within the solder matrix that migrate to form composites such as Cu_6Sn_5 or Ag_3Sn compounds. IMC particles may also occupy the space between dendrites to form a network that exhibits extra strength and stability toward the structural integrity of an SAC product. Since Ag_3Sn holds a significant role in refining the grain of the Sn matrix due to its immense presence in the eutectic region of a solder matrix, it helps in defining the thermal dependability of an SAC solder. Ag_3Sn atoms serve as the pinning factor that regulates the movement of dislocation but tend to deteriorate with detrimental aging, especially during high-temperature operating conditions. Therefore, to refine the grain morphology and increase the solder's resistance to thermal-related testing, dopants such as Bi are often utilized to improve structural integrity and reliability.

Similar to other micro- or nano-constituents, Bi helps in refining the grain structure of a SAC solder, which enhances its mechanical integrity and properties. Unlike the particle-strengthening mechanism, the inert Bi element is highly solid-soluble in Sn, as evidenced by Mahdavi et al. (2015). Hence, Bi does not react with other constituents in an SAC

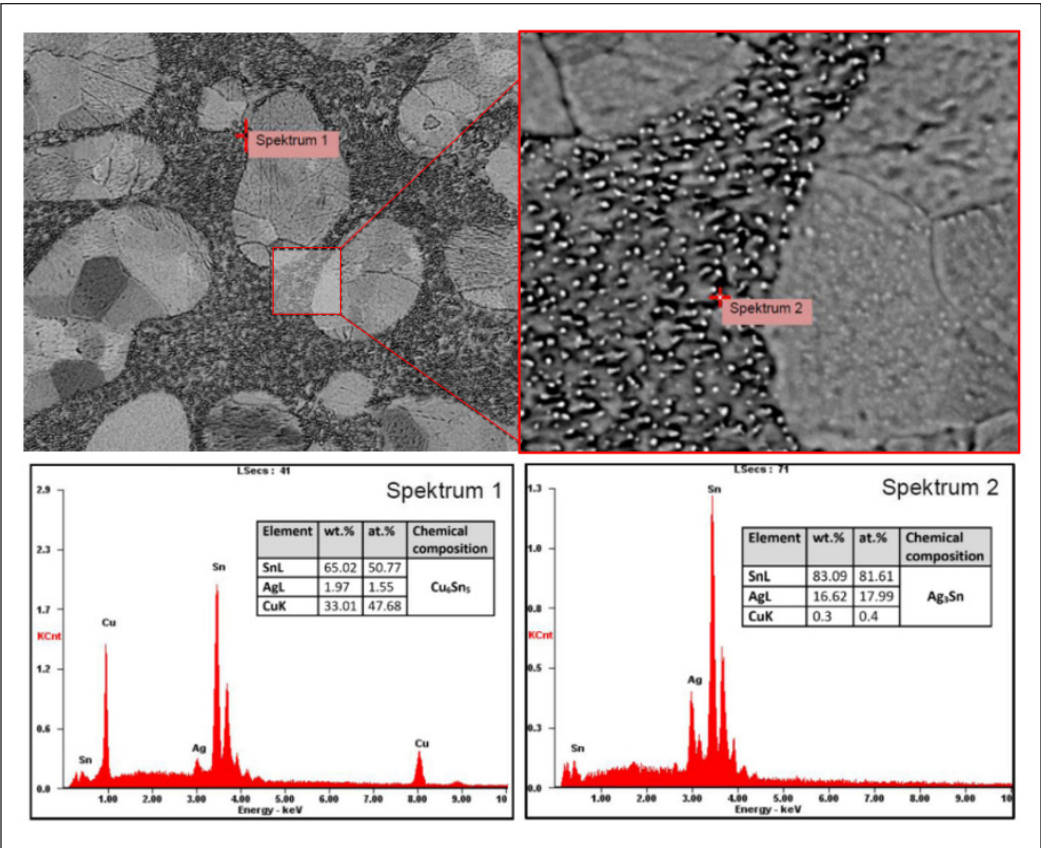


Figure 1. SEM Image and EDX analysis of SAC305 solder (Hodúlová et al., 2018)

solder matrix that could form a secondary composite, such as Ag_3Sn . From morphology, Bi atoms are capable of refining a solder's grain size and distributing the IMC compound within the eutectic region evenly. The effect increases with increasing Bi content, as Ali et al. (2024) demonstrated. Refinement of a solder's grain structure greatly relies on the size of the reinforcement material that helps in reconstructing the lattice structure of a solid solder whilst obstructing the movement of both particles and dislocations, as evidenced by Yang et al. (2022). The phenomenon identically occurs in the case of Bi atoms. A compositional analysis was carried out and validated the fact that SAC157 solder with a Bi composition of 0.5 and 5.0 wt.% displays a slight difference in particle distribution with the IMC compound, which is more uniformly spreads within the solder matrix in the case of higher Bi content (Figure 2). The result concurs with Gao et al. (2023), who observed a left shift in the XRD plot with increasing Bi content that was inferred to be a diminishment in grain size followed by a disturbance in the orderly management of the lattice structure (Figure 3).

The phenomenon results from the distortion of the crystal lattice of the Sn structure by the Bi atom, which also generates internal stress that hinders dislocation motion. A

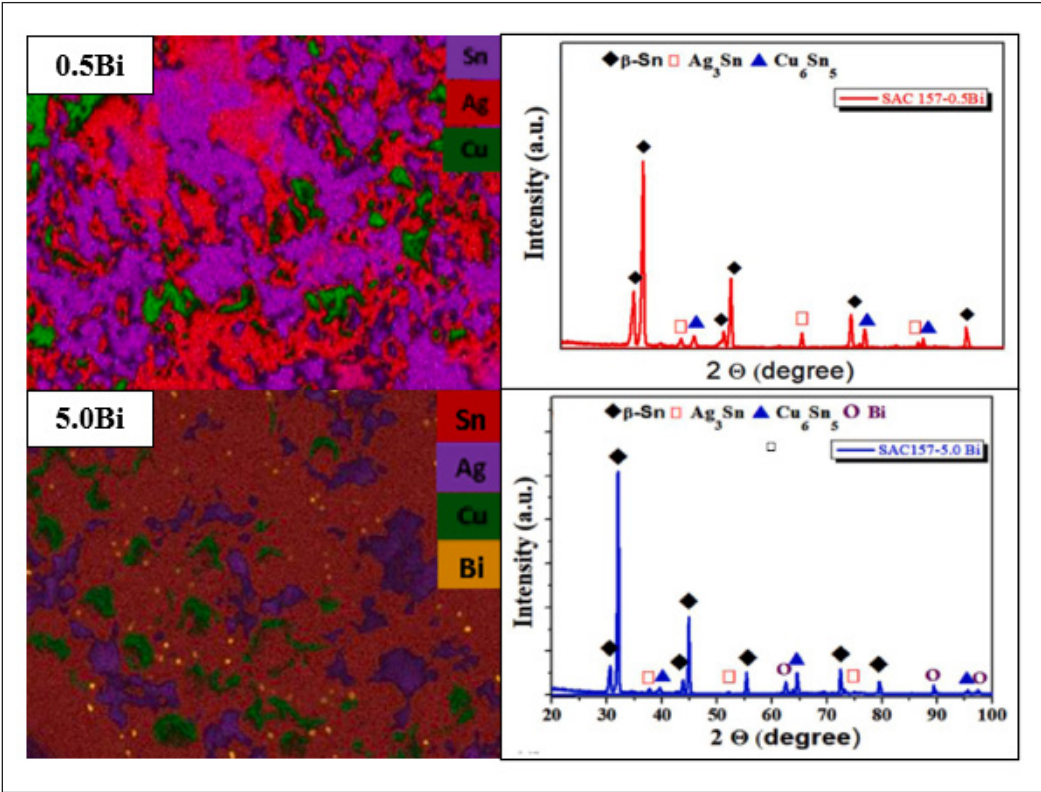


Figure 2. EMPA mapping and XRD analysis of SAC157 solder with 0.5 and 5.0 wt.% Bi (Ali et al., 2024)

smaller movement of atoms cuts down the interaction between different constituents, eventually diminishing the volume fraction of IMC compounds within the eutectic region of a solder matrix. A more homogeneous structure can then be attained within an SAC solder with a more uniformly distributed IMC compound along the grain boundary of the Sn dendrite and eutectic region. A homogeneous solder structure ensures mechanical stress is more well distributed, which prevents the formation of a single stress concentration point that negatively affects the mechanical strength of a solder alloy, which conceivably induces cracks when exposed to thermomechanical and mechanical stress. The noticeable enhancement was proven by Yang et al. (2022) through the enhancement of SAC105 alloy using various materials, including antimony (Sb), bismuth (Bi), and titanium (Ti), which portray a reduction in grain size that accompanies an improvement in mechanical tensile strength.

Interestingly, white spots, which were deduced to be Bi-rich phases, were found to separate and reside on the surface of the Sn dendritic structure in the case of Wu et al. (2019). The exceptional solid solubility of Bi allows Bi to freely diffuse along the grain boundaries of the β -Sn dendrite; thus, when the content exceeds a certain limit, phase separation occurs, and white Bi particles may then resurface above the Sn matrix of the SAC solder. The threshold limit typically falls at a range of 3 to 7 wt.%. The XRD graph presented further verifies the threshold limit of Bi in SAC alloy to be at a range not exceeding 4 wt.%. The theoretical understanding explains the peak of Bi content detected when a Bi content of 5 wt.% was incorporated into the SAC157 alloy. By studying the Sn-Bi phase diagram, the solid solubility limit of Bi in Sn elements typically increases with increasing temperature, which thus explains the ability of Bi to enhance the mechanical integrity of an Sn-based alloy when exposed to high-temperature aging.

The reaction between the Sn atom and other constituents, such as Cu and Ag, also brings about the formation of the IMC layer that exists at the interface between the metal pad and a solder bulk. Depending on the metal element, the IMC layer normally consists of a thermal unstable Cu_6Sn_5 that is most likely to degenerate to form a brittle Cu_3Sn layer that affects the reliability and structural integrity of a solder alloy. Cu_3Sn can either be formed from the dissolution of Cu_6Sn_5 or from the interfacial solid-state diffusion of Cu

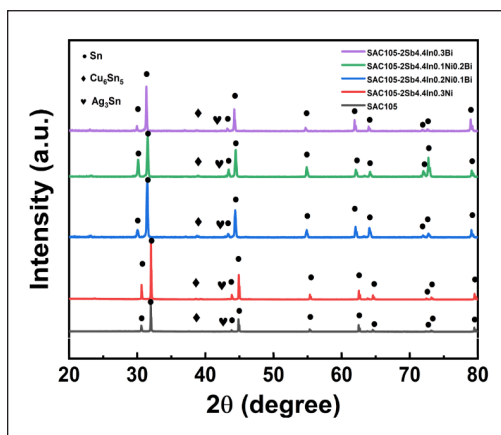


Figure 3. Compositional XRD Analysis for SAC105 solder with different reinforcement materials where a left shift in the plot was noticed as a result of distortion in the crystal lattice structure of the Sn matrix (Gao et al., 2023)

and Sn that reacts and remains at the solder-to-pad interface region. During aging, Cu_3Sn starts to grow and embrittles the entire solder alloy. Opposing what was expected, Bi does not play a significant role in inhibiting the growth of Cu-based IMC layer during as-cast conditions such as other elements, including Sb (Miao et al., 2024) or nickel (Ni) that directly participate and control the atomic diffusion of Cu and Sn during the solidification process.

For instance, Ni atoms interact with free IMC composites to form an alternative Cu-based composite that acts as the barrier in regulating the diffusion of both Cu and Sn atoms. The idea was proved from the SEM image presented by Sivakumar et al. (2021), where the thickness of SAC-Bi Ni solder does not vary much from a pure SAC405 alloy during as-reflowed conditions. This occurrence results from the characteristic of the Bi element, which is insoluble in other constituents besides the Sn atom. Despite that, knowing that Bi is highly soluble in the Sn matrix, the presence of Bi leads to the formation of a finer grain structure with a more finely dispersed IMC compound. This behavior thus slows down the diffusivity of the Sn atom, which reduces the growth rate of the IMC layer due to its pinning effect similar to those of Ag_3Sn particles. Apart from noticing an improvement in fatigue resistance for the case of Bi-doped solder, Jian, Hamasha, Alahmer, Wei et al. (2023) also noticed a betterment in IMC layer condition to grow more uniformly compared to a pure SAC solder despite achieving an increased thickness in Cu_6Sn_5 layer. The ability of Ag present in a SAC solder, along with the addition of Bi element, further inhibits the movement of particles and dislocations, which regulates the aging effect when exposed to elevated temperature.

During aging, Ag_3Sn plates start to coalesce and coarsen, thus losing their pinning effect, which reduces the hardness of a Sn-based solder. The presence of Bi atom, in turn, solid solution hardens the solder matrix, thus increasing the hardness of a SAC solder with preliminary aging. Although the Bi atom may seem trivial in the participation of regulating IMC layer thickness, it shines tremendously in high-temperature working conditions due to its distinctive feature.

ISOTHERMAL AGING

Isothermal aging is a process in which solders are exposed to temperatures higher than their real-life operating temperature for an extensive period to understand the tested solder's mechanical and microstructural behavior, which helps identify its durability, reliability, and stability. The interaction between the solder and substrate results in the formation of a thin IMC layer near the interface, which provides additional strength to the solder structure in an as-reflowed condition, especially with the presence of Cu_6Sn_5 , which serves as a key factor in the improvement of lead-free solder systems (Ramli et al., 2022). However, with prolonged aging, Cu_6Sn_5 compounds are prone to dissolution, thus resulting in the formation

of their weaker counterparts, known as Cu_3Sn , that are naturally brittle in strength (Dele-Afolabi et al., 2019). Hence, various researchers have sought different ways to understand the growth kinetics of the IMC layer in lead-free solders to counteract the detrimental effect of a thick IMC layer, primarily through the utilization of dopants. Bismuth, for instance, not only proved to be beneficial in decreasing the melting point of solder but was found to be highly stable under high-temperature exposure due to its exceptional pinning effect.

In accordance with Zhong et al. (2022), although reflowed solder for pure and Bi-doped SAC solder attained identical IMC layer thickness and composition, elements such as In and Bi are potential candidates that have the capability of substituting Sn in IMC to form an alternative compound given as $\text{Cu}_3(\text{Sn}, \text{In})$ or $\text{Cu}_3(\text{Sn}, \text{Bi})$, respectively. The observation can be inferred as the competency of Bi in not only hindering the movement of dislocations and IMC particles, which diminishes the Ostwald Ripening effect but also acting as a protective barrier similar to those nickel-contained IMC compounds that assist in limiting the diffusion rate of Cu atoms from either the solder matrix or the metal substrate. Apart from that, Sn-Bi lead-free solder bumps are also often utilized along with SAC solder paste to form composite solders that provide additional fortification, which was discerned to show positive results at different reflow temperatures (Shen et al., 2019). The result was proved by Zhang et al. (2024), who investigated the fracture behavior of the SAC305/Sn-Bi solder composite in the presence and absence of Co particles and the influence of different surface finishes. In the early 2000s, the improvement was found to be achieved along with the implementation of 1% Bi in SAC305 solder, especially in inhibiting the formation of thick IMC layers during isothermal aging, as demonstrated by Rizvi et al. (2006).

Bi comes along with high solid solubility and a solid strengthening mechanism; the growth rate of IMC thickness in the case of SAC-1Bi was much slower and in a linear manner when compared with pure SAC305 solder, which was further proven by other researchers who not only discovered the exceptional aging ability but also reported the embrittlement of SAC solder with high Bi content that subsequently affects the fatigue life of the as-reflowed solder (Kanchanomai et al., 2002; Li & Shi, 2006; Zhao et al., 2009). On the other hand, Ramli et al. (2022) reviewed the performance of different elements when added to a SAC solder matrix. They found that, apart from the great reliability of indium addition, the incorporation of 3 wt.% Bi, along with 0.05 wt.% erbium, helps in refining the thickness of the IMC layer during isothermal aging. As aforementioned, the formation of a brittle Cu_3Sn layer near the interface of a bare copper pad on the package or substrate side can be bestowed on the contribution of copper atoms from either the metal pad itself or from the dissolution of Cu_6Sn_5 compounds that react partially with Sn atoms to form their brittle Cu_3Sn form (Dele-Afolabi et al., 2020). Correspondingly, Sivakumar et al. (2021) were able to present results that concur with the statement despite achieving a thicker Cu_6Sn_5 IMC layer for the case of SAC-Bi, Ni solder ball, the Cu_3Sn layer was

much thinner in the said solder compared to pure SAC405 samples due to the fact of a higher migration rate of Cu in SAC405 during thermal aging.

Apart from its marvelous ability in controlling the growth of the IMC layer, bismuth was also found to be capable of regulating the coarsening effect of IMC particles that reside within the eutectic region. For instance, Ali et al. (2021) investigated the microstructure behavior of as-cast and thermally aged solder with bismuth compositions ranging from 1 wt.% to 3 wt.%. In the case of SAC-3Bi solder, the grain boundaries were found to be less scattered with a more refined Sn grain structure even under aging temperatures of 100°C and 200°C, which indicates the aptitude of bismuth particles in the movement of dislocation and IMC particles. Wu et al. (2021) studied the effect of different bismuth content and aging temperature on the IMC particle diameter. They found that apart from increasing particle diameter with increasing aging temperature due to an increase in diffusion rate and Ostwald ripening effect, the normalized particle diameter size of SAC-3Bi was the smallest in all cases, as shown in Figure 4. The author explained that the amount of bismuth that resides within the eutectic region of an SAC305 solder decreases as it gradually propagates toward the direction of the dendritic structure with increasing aging time. Initially, three different structures with distinct colors, including grey tin dendrites, black IMCs, and white bismuth, were observed in an as-reflowed bismuth-doped SAC305 solder bulk structure. However, with increasing aging periods, larger brittle IMC particles, particularly Ag_3Sn compounds, start to form at the expense of their smaller forms, which are portrayed as depicted in Figure 5.

Bismuth was thus deemed to be extremely beneficial in the SAC solder system, partially due to its non-reactivity with other constituents but also due to its high solid solubility in molten tin upon heating, which helps in anchoring the movement of dislocations and IMC compounds and encourages the formation of solder with comparatively better strength and structural integrity. Similar work was carried out by Ahmed et al. (2016), and it was discovered that by assimilating merely 2.4 wt.% of bismuth into SAC105 solder, the solder achieved improved performance in stress-strain behavior with higher resistance towards aging compared to the pure condition. Both authors were able to achieve a lower degree of Ostwald ripening effect along with the presence of bismuth, which verifies the pinning ability of bismuth atoms comparable to Ag_3Sn particles. All in all, the performance of SAC-Bi solder in isothermal aging proves its suitability and potential in high-temperature applications.

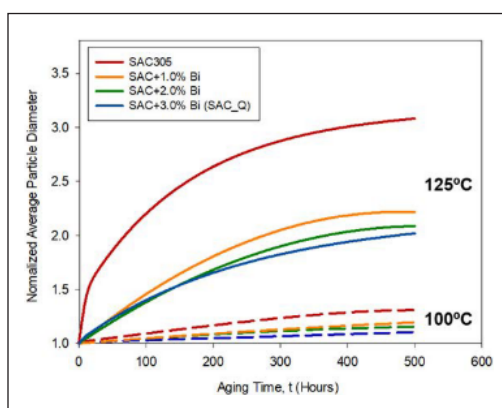


Figure 4. The normalized particle diameter of IMC particles at various conditions (Wu et al., 2021)

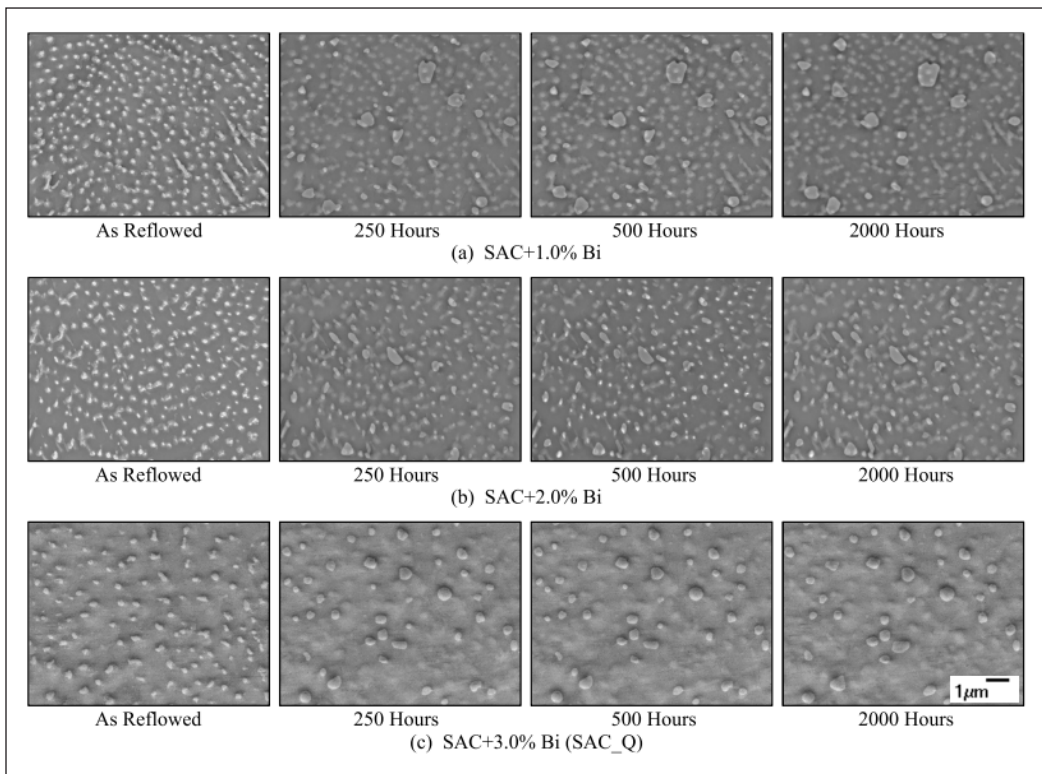


Figure 5. Microstructural evolution of SAC405 solders with different bismuth content after aging for 2000 hours at 125°C (Wu et al., 2021)

THERMAL CYCLING

Thermal cycling, as the name implies, is the fluctuation of heat a material is exposed to in its working environment. In the case of lead-free solders, thermal fatigue is often viewed as the most damaging factor that causes a connected solder joint to lose its structural integrity and electrical connectivity. Moreover, under exposure to either constant heat or thermal fluctuations, SAC solders tend to exhibit features that affect the reliability of an electronic device. The presence of an IMC layer or IMC precipitates within the solder matrix adversely affects morphology when exposed to heat, which explains the reason for lead-free solders with low ductility and creep resistance in operating conditions with high temperatures (Depiver et al., 2021). During thermal fatigue, the repeating changes in temperature cause iterating expansion and contraction of the mounted device and PCB at a different rate due to a dissimilar coefficient of thermal expansion (CTE).

Therefore, along with the miniaturization of technology and increasing solder density, understanding thermal cycling in terms of the solder's microstructural and mechanical behavior is extremely crucial in improving an electronic product's reliability and sustainability in different environments and circumstances. To understand the behavior and

prevent malfunctioning of developed boards, industrial manufacturers typically carry out reliability testing prior to product delivery. Reliability testing is the process in which the assembled boards are given a series of harsh trials to ensure that they are able to handle various working situations without failing. Correspondingly, for thermal cycling reliability testing, second-level assembled boards are exposed to extreme temperature fluctuations, typically within the -40°C to 125°C range, with a holding time of 10 to 15 minutes at each extremity and a ramping rate commonly below $10^{\circ}\text{C}/\text{min}$ in accordance with the IPC9701 standard (Romdhane et al., 2022). However, Hokka et al. (2013) explained that the characteristic life of a lead-free solder may somehow differ depending on not only the constituents but also the cycle parameters. The author thus concluded that the most appropriate parameters should be selected based on the industries and applications involved. Nevertheless, lead-free solders were proven to creep and deform when exposed to intense conditions, which causes cracks to initiate and propagate along the misoriented grains resulting from prior recovery and recrystallization phases. Therefore, doping was viewed as a viable approach to fostering a solder with durable and reliable joint strength to improve its microstructural behavior and reduce the coarsening of second-phase particles.

From the context of microstructural behavior, Libot et al. (2018) investigated the thermal fatigue behavior of a SAC305 solder by understanding its microstructural changes. Thermal fatigue-induced creep in a lead-free solder typically follows a sequential process starting from recovery and recrystallization before an intergranular crack is observed. In general, thermal cycling generates thermal stresses that excite the movement of particles such as Ag_3Sn and dislocations, which is often known as the recovery phase. The movement of dislocations disrupts the arrangement of grains and introduces grain boundaries with misoriented angles, causing the grain angle to increase. The grain continues to grow to a higher angle as the thermal stress accumulates, resulting in the commencement of the recrystallization phase. Continuous expansion and contraction of PCB and module thus employ thermomechanical stress on the solder, which causes cracks to propagate along the designated path created by the recrystallized grains. In modern technology, SAC305 has proven to achieve a good performance that even surpassed the traditional Sn-Pb solders in terms of thermal cycling reliability (Arfaei et al., 2015). Despite being one of the environmentally friendly candidates, the SAC solder displays better thermal creep fatigue resistance than the traditional Sn-Pb alternative due to its stable microstructure and the presence of Ag and Cu elements.

As previously mentioned, Ag_3Sn and Cu_6Sn_5 IMC composites are two common particles that can be detected in a SAC solder matrix, whereas the IMC composites of Sn-Pb alloy rely on the type of adjacent metal that a solder is attached to and typically comprise only of Cu_6Sn_5 . Although the Ag-based solder is prone to coalesce and coarsens with heat, Ag_3Sn does serve as a good pinning factor that assists in resisting thermal-induced failure.

However, Ag_3Sn may eventually agglomerate and even pin it to the misoriented grain boundaries, which encourages the nucleation of new grains that exacerbates the thermal cycling defect. This encourages the discovery of third-generation alloys such as Innolot to be utilized in industries with harsh environments and necessitates zero failure during service. The adaptation of Innolot opens the chapter for the potential of Bi in elevated temperatures and to delve deeper into its possibility in large temperature ranges.

From the morphology, it was observed that Bi is highly solid-soluble in molten Sn, which enhanced the mechanical and microstructural properties of an SAC alloy during solidification. For instance, the Sn-58Bi alloy was able to attain an exceptionally low melting temperature thanks to the distinctive capability of Bi. The positive benefits of Bi also improve the thermal fatigue performance of a Sn-based alloy, as Tian et al. (2022) demonstrated by investigating the interaction between SAC305 nanoparticles in the Sn-58Bi alloy. Furthermore, by looking into SAC-Bi, Innolot (SAC407 with 0.15 wt.% Ni, 1.40 wt.% Sb, and 3.00 wt.% Bi addition), SAC-In, SAC-305, and SAC-Mn solders, the bismuth-containing SAC-Bi and Innolot solders were found to achieve a better characteristic life at above 3,000 cycles for all cases when compared with their relative peers (Akkara et al., 2022). Similar to other thermally related testing, Bi serves an identical purpose as Ag_3Sn particles that help impede the movement of grains, particles, and dislocations, slowing down the thermal cycling-induced alterations. Bi elements behave similarly to Sb and Ni, which embed themselves in the Sn matrix, and solid-solution strengthens a Sn-based solder.

This phenomenon thus explains the increase in characteristic life or longevity of bi-doped solder when compared to a conventional SAC alloy. It is essential to investigate the microstructural changes that the Bi element causes to a pure SAC alloy to evaluate the thermal fatigue performance of an SAC solder. Fundamentally, the Ag_3Sn precipitates define the performance of a solder's thermal fatigue resistance (Belhadi, Wei, Vyas et al., 2022). From the SEM images of as-cast solder, Ag and Sn interact to form a large network that holds the Sn dendrites in place while pinning the movement of dislocations. With subsequent thermal cycling, the Ag_3Sn precipitates begin to coarsen in both pure and bi-doped BGA but were found to be more severe in the case of pure SAC and Sn-Pb solder. The presence of Bi atoms improved the microstructure integrity of the entire solder bulk, which reduces the Ostwald-Ripening effect of Ag_3Sn particles that contribute to the formation of recrystallized grains. The growth kinetics of the IMC layer were also enhanced in the bi-doped SAC alloy case, especially under additional reinforcement material, including Sb and Ni elements, which regulate the diffusivity of Cu and Sn atoms.

Since the IMC layer acts as the localized stress area that triggers the formation of microcracks, a thinner Cu_3Sn layer, in the case of SAC-Bi alloy, also discouraged cracks from propagating and thus increased a solder's working life. The betterment of a solder's

lifespan can also correlate to an improvement in mechanical strength under thermal cycling reliability testing, which simulates a real-life working condition that a solder may be exposed to. When exposed to thermal-induced stress for an extensive period, solder tends to soften and eventually crack due to a deterioration in mechanical strength. Bi-doped SAC solder, on the other hand, helps enhance the microstructural integrity of a solder and improve the mechanical strength of an SAC solder from a long-term perspective. For instance, Hassan et al. (2020) discovered that the mechanical strength of a SAC405 solder can be greatly improved with the incorporation of merely 3 wt.% Bi. The mechanical degradation of SAC-3Bi under various thermal cycling conditions was found to decrease more steadily than a pure SAC solder. Material is bound to degrade when exposed to different forms of stress due to the accumulation of stress that results in microstructural changes within the material matrix.

Despite having a steady drop in elastic modulus for the case of SAC-3Bi, an abrupt fall was observed in the case of SAC405 alloy, thus concurring with the positive effect of Bi in regulating thermal cyclic failure whilst maintaining a considerably optimal mechanical strength in spite of long-term thermal cycling. In real-life circumstances, it is common for solders to be exposed to both thermal stresses and mechanical loads, such as in the case simulated by Belhadi, Wei, Qasimeh et al. (2022). Due to the benefits of Bi in the Sn matrix, the tested SAC-3Bi solder was able to achieve betterment in resistance towards not only thermal cycling but also creep-induced deformation. Similar to the effect of Ag in resisting thermal cycling, Bi greatly reduces the creep extension of solder due to its solid solution and precipitate hardening mechanism. Interestingly, increasing Ag content also assists in the formation of more refined networks of grain with smaller interparticle spaces, thus reducing the chances of grain boundary sliding caused by either thermal cycling or creep deformation.

Nevertheless, a considerable addition of Ag is essential to diminish the Ostwald Ripening effect of the primary Ag_3Sn precipitates, potentially aggravating thermal-induced failure. The phenomenon was proven by Liu et al. (2024) by improving the fatigue life of SCN-Bi solder compared to Ag-rich SAC-Bi alloy. However, the presence of foreign atoms such as Bi, Ge, and Co further refines the morphology of the involved solder, which not only improves the solder's thermal fatigue life but enhances its hardness and mechanical strength. Furthermore, it was observed that SAC-Bi actually outperformed SAC solder in a more severe thermal cycling condition with a larger temperature range but instead portrays a weaker behavior in shorter temperature extremes, as shown in the life prediction of the solder in Figure 6 (Delhaise et al., 2020). Stacking fault energy (SFE) generally indicates the energy required for dislocation to climb and glide. Higher SFE indicates that a material has a narrower stacking fault and allows dislocation to slide between atoms more easily than lower SFE, typically observed in alloy systems such as SAC-Bi.

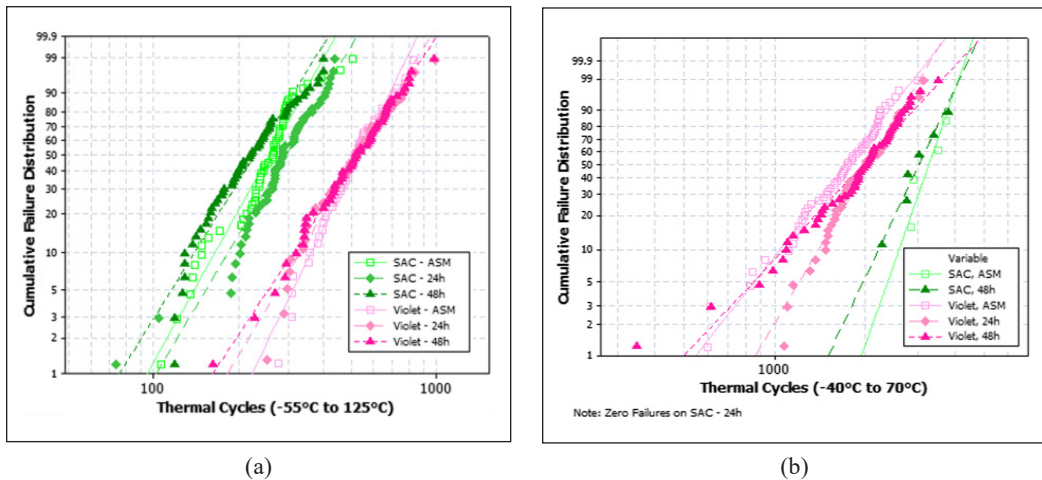


Figure 6. The Weibull plot shows that the characteristic life of SAC405-6Bi ('Violet') was higher in the case of (a) high-temperature cycling and lower in the case of (b) low-temperature cycling (Delhaise et al., 2020)

As previously mentioned, thermal cycling causes strain accumulation, which triggers systems to release the accumulated damage in any possible way, either through recovery (dislocation movement) or recrystallization (grain restructure). In the scenario with higher ΔT , a larger strain causes both systems to spend less time in the plastic region; thus, the recrystallization phase occurs relatively sooner. However, in the case of smaller ΔT , the SAC solder with lower SFE spends a longer time in the recovery phase due to its ductile property, whereas SAC-Bi, despite achieving better strength, tends to recrystallize sooner due to wider stacking faults that hinder dislocation movement. Therefore, in spite of aging being a detrimental process, preliminary aging at a moderate level positively enhanced the thermal fatigue life of a doped system, such as the case of SAC-Bi solder. Comparatively to clarification by Cai et al. (2021), homogeneous Sn-Bi structure actually exceeds the longevity of SAC/Sn-Bi composite during thermal cycling tests that regulate the nucleation of grain that causes cracks to propagate in an undesirable manner.

Therefore, this further signifies the importance of achieving ideal homogeneity (Swanson & Anselm, 2023). From the presented morphology, as shown in Figure 7, the solder typically encounters failure at the solder's neck. An intergranular fracture that propagates along the recrystallized grain may often be observed and typically focuses on the area close to the package or substrate side. Table 1 summarizes the achievement of Bi in solder reliability of various types of SAC solder. Clearly, from the highlighted studies, Bi serves as an excellent reinforcement material due to its essential solid-solution strengthening mechanism, which contributes to its exceptional solid-solubility in Sn, which especially outshines the pure solder alternative in extreme temperature conditions that cater to industries operating in harsh environments.

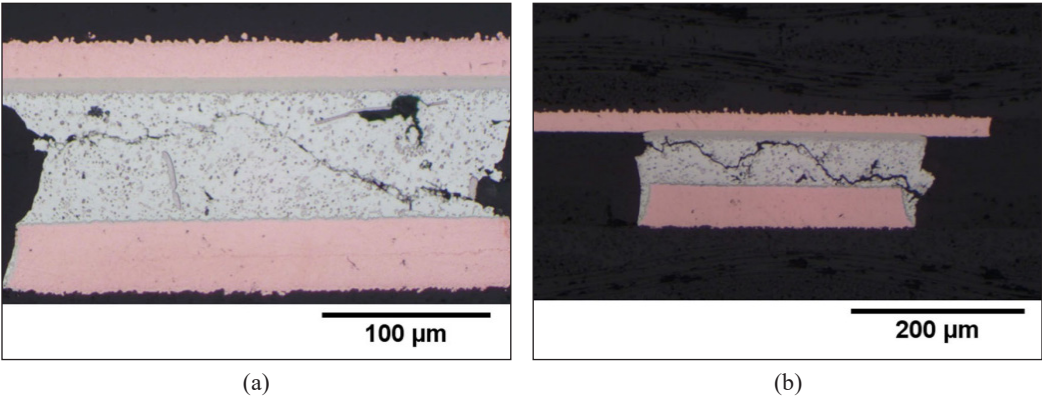


Figure 7. Solder morphology of both (a) SAC305 and (b) Violet under temperature cycling of -40°C to 70°C, with the latter showing a larger factor of recrystallization (Delhaise et al., 2020)

Table 1
The effect of Bi dopants in conventional Sn-based solder

Solder	Findings	Reference
SAC-Bi SCN-Bi	SCN-Bi solder was able to display astonishingly high characteristic life despite the absence of Ag. This phenomenon clarifies that despite Ag being beneficial in enhancing fatigue life, a high amount of incorporation encourages Ag ₃ Sn coarsening, which reduces the significance of its positive effect in LFS.	Liu et al., 2024
SAC-2Bi	Bi helps lower the acceleration factor (AF) of the SAC solder in thermal cycling, thus implicating the ability of the solder to resist fatigue life degradation in extreme loading conditions.	Jeon et al., 2023
SAC-3Bi	Doping of elements including Bi, Sb, In, and Ni greatly enhances the fatigue life of a SAC solder, which even surpasses the traditional Sn-Pb in thermal cycling.	Belhadi, Wei, Vyas et al., 2022
Innolot SAC-3Bi	ENIG surface finishing provides the best result due to the presence of Ni atoms. Conversely, when elements such as Ni, Sb, and Bi were added to a pure SAC solder, the solder was strengthened as a solid solution, which increased its fatigue life.	Akkara et al., 2022
SAC405 (1 – 4% Bi)	A lower failure rate indicating a better characteristic life was attained for SAC405 added with 3 to 4 wt.% of Bi. Similar to Bi, a small addition of Sb further enhanced the reliability of the solder, especially in high-temperature cycling.	Zou et al., 2021
Sn-Bi	Homogeneous Sn-Bi solder displays better fatigue life compared to SAC solder and mixed SAC/Sn-Bi solder.	Cai et al., 2021
SAC205 -6Bi	Bi addition enhances the performance of SAC solder in thermal cycling with a larger range between -40°C to 125°C but is weaker when compared to SAC305 at a smaller range between -40°C to 70°C.	Delhaise et al., 2020
SAC405-3Bi	The material property degradation of SAC-Bi solder was much steadier compared to pure SAC solder at various conditions, including thermal cycling, thermal shock, and isothermal aging, which indicates the capability of Bi to enhance a solder’s thermal fatigue life.	Hasan et al., 2020

MECHANICAL CYCLING

Thermal cycling has been playing a significant role in identifying the reliability of solder joints in the second level of interconnects for an electronic assembly. However, similar to aging, thermal cycling lacks efficiency due to its extensive testing period. With the fact that thermal cycling is a well-established testing practice with restricted standards, acceleration of the said method can only be achieved by either increasing the temperature swing or shortening the cycle time by augmenting the ramp rate, which potentially changes the failure mode of a tested solder and questions the credibility of the obtained results for the life prediction of a solder's lifespan. According to Graver et al. (2009), a thermal cycling test with a temperature range between 0°C and 100°C requires around half a year for the tested lead-free solder-jointed board to exhibit failure. To enhance efficiency, the author proposed the idea of utilizing mechanical cycling as a four-point bending test. This practice is often common in industry to create an environment that a solder structure may experience, which helps understand a solder's behavior holistically.

For instance, testing approaches such as mechanical vibration are occasionally designed to be carried out along with thermal cycling. By doing so, board manufacturers and reliability engineers were able to identify the weaknesses of a designed product more easily, thus enabling subsequent improvements. Through coherent testing of mechanical vibration and thermal cycling, Borgesen et al. (2019) were able to concur with the idea by clarifying that the behavior of SAC and Sn-Bi solders may differ from thermal cycling tests. Introducing an additional type of stress further exacerbates the damage intensity that accumulates within the solder matrix, which results in different microstructural and mechanical behavior. Consequently, different approaches have also been actively researched by correlating the aging effect with mechanical simulated thermal strain by cycling with tests that exert flexural stress (Vandevelde et al., 2017; Wang et al., 2009; Wang et al., 2020), tensile stress (Maruf et al., 2024), and shear stress (Hoque et al., 2021; Su et al., 2020). Different from conventional thermal cycling tests, isothermal mechanical cycling tests can be carried out either with thermal and mechanical stress introduced simultaneously or through the utilization of preliminary aged solder. However, the absence of thermal-induced strain results in a lower degree of grain, and IMC coarsening triggers the recovery and recrystallization stage in a thermal cycling test, thus removing the adverse effect that causes microstructure instability within a solder bulk. The occurrence causes the failure mode to be slightly different during isothermal mechanical testing in spite of essentially achieving an analogously identical fracture mode that cracks in the form of an intergranular crack along the IMC layer within the interface region.

SAC solder, as aforementioned, is often doped with dissimilar-size particles to enhance its mechanical and thermal properties. Similar to thermal-related testing, SAC-Bi was presumed to outperform a pure SAC alloy in a mechanical cycling test. Unlike the inverse

relationship of Ag content with the mechanical stability of a solder in a lead-free solder, the presence of Bi solution strengthens the overall mechanical properties of an SAC (El-Daly et al., 2015). Higher Bi content typically helps in fortifying the mechanical strength of an SAC solder, as demonstrated by Belhadi et al. (2019) when investigating solders including SAC305, SAC-3Bi, and SAC-6Bi. At the as-reflowed condition, an increment of Bi content provides additional support to the ductile solder through the means of a solid-solution strengthening mechanism. Bi plays an essential role in enhancing the thermal and mechanical stability of a solder by mitigating the detrimental effect attributable to dislocation movement. The betterment in shear strength was achieved in the case of SAC-6Bi in unaged conditions. However, it regularly deteriorated with an increasing aging period that eventually outshined the SAC-3Bi solder in severe aging circumstances. Since aging encourages agglomeration of particles, the excess number of Bi atoms acting as the solute of the entire system tends to coalesce and coarsen when the solvent atoms (Sn matrix) are fully occupied and redundant.

Coagulation of the Bi atom causes its brittle nature to dominate and thus embrittles the SAC system at higher aging hours, even though a low strain rate was utilized during the testing of SAC-6Bi solder with a preliminary aging of 1000 hours. From Figure 8, increasing stress amplitude generally leads to a lower characteristic life of both pure and bi-doped SAC solders. Comparatively, the Bi element was again proven to mitigate the adverse effect of aging and help attain a solder with enhanced strength and lower ductility. Furthermore, Bi refines the solder grain, elevating the mechanical stability of a SAC solder. This was proven by Al Athamneh and Hamasha (2020), where despite both solders failing at the approximately identical cyclic range, the bi-doped solder was able to withstand a higher stress amplitude thanks to its improvement in fatigue resistance. Furthermore, Jian, Hamasha, Alahmer, Hamasha et al. (2023) demonstrated that SAC-Bi generally displays a betterment in fatigue resistance, especially when cycled within moderate and high-stress conditions. The presence of Ag and Bi atoms refines the Sn grain size and increases the phase boundaries of a solder morphology. Both the Ag_3Sn particles that formed from the interaction of Ag and Sn atoms, as well as the Bi-rich phases that surround the eutectic region of a solder matrix, further obstruct the movement of dislocation, which adversely catalyzes the softening of a metal alloy.

Both the boundaries and formed composites act as a robust barrier that mitigates the chances of crack initiation that results from the formation of defects such as grain boundaries, voids, and other surface defects. The phenomenon explains the achievement of SAC-3.3Bi in achieving a higher characteristic life when compared with Sn-Cu-Bi solder during shear cycling in various aging conditions in spite of utilizing a higher Bi content. Fundamentally, Kaimkuriya et al. (2024) highlighted where harder materials tend to be more susceptible to plastic deformation, which thus results in lower fatigue life. Material

with higher strength is typically associated with lower ductility, such as what was observed in the case of SAC-Bi solders. The presence of Bi atoms strengthens the structure of the soft, ductile SAC solder by means of a solid solution strengthening mechanism. Bi atom alters the atomic structure, which causes a material to induce less plastic deformation work per cycle. The material accumulates damage over time during fatigue cycling by absorbing and dissipating energy. Higher plastic deformation work per cycle results in microstructural changes that benefit crack initiation and propagation, which signifies a lower fatigue life within a solder material with higher ductility.

Figure 9 records the comparison in the hysteresis loop (left) and average work per cycle (right) among various solder alloys during shear cycling. A larger hysteric loop of SAC solder with 0.08 wt.% of Bi element denotes that the solder alloy experiences a larger plastic deformation work during the cyclic test. On the other hand, Su et al. (2020) again

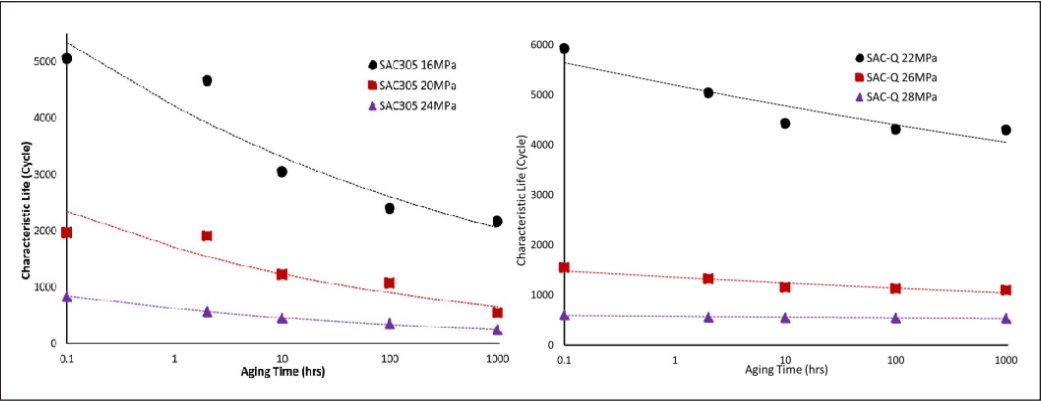


Figure 8. Comparison in characteristic life of SAC305 and SAC-3.3Bi at various stress amplitudes and aging time (Al Athamneh & Hamasha, 2020)

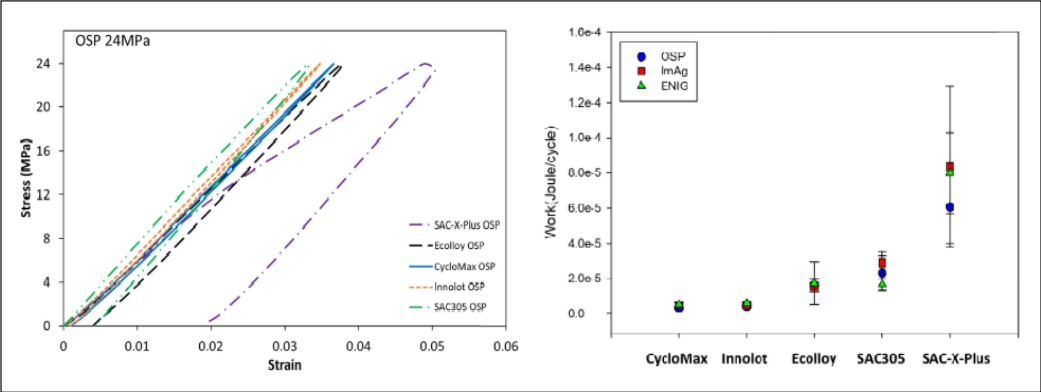


Figure 9. Comparison in hysteresis loop and average plastic deformation work per cycle for various alloys with different surface finishes (Su et al., 2020)

proved that a strong and brittle alloy can be achieved with lower average plastic work per cycle when an adequate addition of Bi particles at a range of 2 to 3 wt.% was added to a pure SAC system. Apart from that, to understand and correlate the difference in tensile properties between pure and bismuth-doped SAC solder, Ahmed et al. (2016) utilized a six-axis load cell testing machine to identify the stress-strain behavior of SAC105 and SAC105-Bi solder when placed within a thermal chamber with different temperature ranges between 25°C and 125°C. Thanks to the capability of Bi to resist aging, the SAC-Bi alloy achieved an improvement in mechanical stability, making it optimal to be incorporated in low-Ag content solder. By utilizing an adequate amount of Bi to replace Ag in low-Ag alloys, the coarsening effect of IMC composites can be diminished, which alleviates aging-related degradation while augmenting its fatigue resistance towards both mechanical and thermal stresses.

Moreover, Haq et al. (2022) and their respective peers were able to study the effect of mechanically cycled SAC405 solder with bismuth compositions of 1 wt.%, 2 wt.%, and 3 wt.%. However, a lower fatigue life was attained for the case of SAC-3Bi due to the embrittlement of Bi when integrated with the SAC solder matrix. The phenomenon concurs with the idea that an appropriate amount of Bi is required, and further research is needed to cultivate a solder structure with excellent strength and reliability whilst minimal sacrifice on ductility that adversely causes cracks to initiate and propagate when exposed to stresses in real-world situations.

CONCLUSION

Lead-free solders have been gaining great attention among industrial experts due to their exceptional sustainability and reliability, along with their ability to achieve greener technology that benefits both the environment and human health, making them a good candidate for competing with traditional Sn-Pb solders. Taking the renowned SAC solder as an example, despite its great achievement in nurturing strong and robust joints for electrical connection of devices to PCBs at the second interconnect assembly level, its relatively high melting temperature of approximately 217°C to 220°C has led to several complications, including complex IMC as well as difficulty in the design and consolidation of electronic packages. Hence, the doping of third-party alloys, for instance, bismuth, is often considered to not only achieve a breakthrough in mechanical strength but also primarily to attain a more ideal melting temperature that is compatible with both the glass transition temperature and the decomposition temperature of the PCB and to-be mounted device, respectively.

However, because of its brittle nature, the ductility of the aforementioned system tends to deteriorate eventually, which serves as the main reason for promoting a soldering system with weak reliability in response to thermal and mechanical stresses. Due to the

high solid solubility of bismuth in tin solvent when exposed to heat, the bismuth atom tends to reside within the dendritic structure. It restricts the movement of dislocations as well as particles that potentially contribute to particle coarsening with prolonged heating, which ultimately leads to thermal fatigue fracture, which thus explains its exceptional performance in aging. Nonetheless, in the future, work should be focused on understanding a bismuth-enhanced lead-free solder system in thermal cycling and mechanical cycling reliability to understand the behavior of bismuth when reacting with a tin-based solder matrix such as the SAC system, thus assisting in cultivating the potential of bismuth in real-life industries and preventing unprecedented situations from happening in the future due to immature results.

ACKNOWLEDGEMENT

The authors wish to express their gratitude for the support and opportunities provided by the Faculty of Engineering at Universiti Putra Malaysia. Special thanks to Micron Memory Malaysia Sdn. Bhd. for their funding through Research Grant (6300426-10801).

REFERENCE

- Abtew, M., & Selvaduray, G. (2000). Lead-free solders in microelectronics. *Materials Science and Engineering*, 27, 95–141.
- Ahmed, S., Basit, M., Suhling, J. C., & Lall, P. (2016). Effects of aging on SAC-Bi solder materials. In *2016 15th IEEE Intersociety Conference on Thermal and Thermomechanical Phenomena in Electronic Systems (ITherm)* (pp. 746-754). IEEE Publishing. <https://doi.org/10.1109/ITHERM.2016.7517621>
- Akkara, F. J., Hamasha, S., Alahmer, A., Evans, J., Belhadi, M. E. A., & Wei, X. (2022). The effect of micro-alloying and surface finishes on the thermal cycling reliability of doped SAC solder alloys. *Materials*, 15(19), Article 6759. <https://doi.org/10.3390/ma15196759>
- Al Athamneh, R., & Hamasha, S. (2020). Fatigue behavior of SAC-Bi and SAC305 solder joints with aging. *IEEE Transactions on Components, Packaging and Manufacturing Technology*, 10(4), 611–620. <https://doi.org/10.1109/TCPMT.2019.2949719>
- Ali, H. E., El-Taher, A. M., & Algarni, H. (2024). Influence of bismuth addition on the physical and mechanical properties of low silver/lead-free Sn-Ag-Cu solder. *Materials Today Communications*, 39, Article 109113. <https://doi.org/10.1016/j.mtcomm.2024.109113>
- Ali, U., Khan, H., Aamir, M., Giasin, K., Habib, N., & Owais Awan, M. (2021). Analysis of microstructure and mechanical properties of bismuth-doped SAC305 lead-free solder alloy at high temperature. *Metals*, 11(7), Article 1077. <https://doi.org/10.3390/met11071077>
- Arfaei, B., Mutuku, F., Coyle, R., Cotts, E., & Wilcox, J. (2015, May). Failure mechanism and microstructural evolution of Pb-free solder alloys in thermal cycling tests: Effect of solder composition and Sn grain morphology. In *2015 IEEE 65th Electronic Components and Technology Conference (ECTC)* (pp. 118-126). IEEE Publishing. <https://doi.org/10.1109/ECTC.2015.7159580>

- Belhadi, M. E. A., Wei, X., Qasaimeh, Q., Vyas, P., Zhao, R., Hmasha, E., Ali, D., Suhling, J., Hamasha, S., Lall, P., Ali, H., & Prorok, B. C. (2022). Indentation creep properties evolution of lead-free solder joints subjected to thermal cycling. In *2022 21st IEEE Intersociety Conference on Thermal and Thermomechanical Phenomena in Electronic Systems (iTherm)* (pp. 1-8). IEEE Publishing. <https://doi.org/10.1109/iTherm54085.2022.9899582>
- Belhadi, M. E. A., Wei, X., Vyas, P., Zhao, R., Hamasha, S., Ali, H., Suhling, J., Lall, P., & Prorok, B. C. (2022). Reliability and IMC layer evolution of homogenous lead-free solder joints during thermal cycling. In *IPC APEX 2022 Technical Conference Proceedings* (pp. 1–14). ResearchGate. <https://www.researchgate.net/publication/364722213>
- Belhadi, M. E. A., Wentlent, L., Al Athamneh, R., & Hamasha, S. (2019). Mechanical properties of SAC-Bi solder alloys with aging. In *Proceedings of SMTA International* (pp. 431–438). ResearchGate. <https://www.researchgate.net/publication/337439000>
- Bhavan, J. S., Pazhani, A., Amer, M., Patel, N., & Unnikrishnan, T. G. (2024). Microstructural evolution and phase transformation on Sn–Ag solder alloys under high-temperature conditions focusing on Ag₃Sn phase. *Advanced Engineering Materials*, 26(13), Article 2400660. <https://doi.org/10.1002/adem.202400660>
- Borgesen, P., Wentlent, L., Alghoul, T., Sivasubramony, R., Yadav, M., Thekkut, S., Cuevas, J. L. T., & Greene, C. (2019). A mechanistic model of damage evolution in lead free solder joints under combinations of vibration and thermal cycling with varying amplitudes. *Microelectronics Reliability*, 95, 65–73. <https://doi.org/10.1016/j.microrel.2019.02.001>
- Cai, C., Xu, J., Wang, H., & Park, S. B. (2021). A comparative study of thermal fatigue life of eutectic Sn-Bi, hybrid Sn-Bi/SAC and SAC solder alloy BGAs. *Microelectronics Reliability*, 119, Article 114065. <https://doi.org/10.1016/j.microrel.2021.114065>
- Coyle, R. J., Sweatman, K., & Arfaci, B. (2015). Thermal fatigue evaluation of Pb-free solder joints: Results, lessons learned, and future trends. *JOM*, 67(10), 2394–2415. <https://doi.org/10.1007/s11837-015-1595-1>
- Darwish, S. M., Al-Habdan, S., & Al-Tamimi, A. (2000). A knowledge-base for electronics soldering. *Journal of Materials Processing Technology*, 97(1–3), 1–9.
- Dele-Afolabi, T. T., Hanim, M. A. A., Ojo-Kupoluyi, O. J., & Calin, R. (2019). Impact of different isothermal aging conditions on the IMC layer growth and shear strength of MWCNT-reinforced Sn–5Sb solder composites on Cu substrate. *Journal of Alloys and Compounds*, 808, Article 151714. <https://doi.org/10.1016/j.jallcom.2019.151714>
- Dele-Afolabi, T. T., Hanim, M. A. A., Calin, R., & Ilyas, R. A. (2020). Microstructure evolution and hardness of MWCNT-reinforced Sn-5Sb/Cu composite solder joints under different thermal aging conditions. *Microelectronics Reliability*, 110, Article 113681. <https://doi.org/10.1016/j.microrel.2020.113681>
- Delhaise, A. M., Snugovsky, P., Kennedy, J., Hillman, D., Matijevic, I., Meschter, S., Adams, D., Kammer, M., Romansky, M., Juarez, J., Straznický, I., Snugovsky, L., Wilcoxon, R., & Perovic, D. D. (2020). Thermal preconditioning and restoration of bismuth-containing, lead-free solder alloys. *Journal of Electronic Materials*, 49(1), 116–127. <https://doi.org/10.1007/s11664-019-07666-w>

- Depiver, J. A., Mallik, S., & Harmanto, D. (2021). Solder joint failures under thermo-mechanical loading conditions - A review. In *Advances in Materials and Processing Technologies* (Vol. 7, Issue 1, pp. 1–26). Taylor and Francis Ltd. <https://doi.org/10.1080/2374068X.2020.1751514>
- El-Daly, A. A., El-Taher, A. M., & Gouda, S. (2015). Novel Bi-containing Sn-1.5Ag-0.7Cu lead-free solder alloy with further enhanced thermal property and strength for mobile products. *Materials and Design*, 65, 796–805. <https://doi.org/10.1016/j.matdes.2014.10.006>
- Gao, Y., Bian, X., Qiu, X., Jia, Y., Yi, J., & Wang, G. (2023). Investigation of microstructure and mechanical properties of SAC105 solders with Sb, In, Ni, and Bi additions. *Materials*, 16(11), Article 4059. <https://doi.org/10.3390/ma16114059>
- Graver C. C. C., Yu, C. K., Tina, S., Cherie, C., & Jeffrey, L. (2009). The correlation investigation between cyclic bending and thermal cycling testing in CSP package on board. In *2009 4th International Microsystems, Packaging, Assembly and Circuits Technology Conference* (pp. 510-513). IEEE Publishing. <https://doi.org/10.1109/IMPACT.2009.5382231>
- Haq, M. A., Hoque, M. A., Suhling, J. C., & Lall, P. (2022). Mechanical behavior and microstructure evolution in SAC+Bi lead free solders subjected to mechanical cycling. In *2022 21st IEEE Intersociety Conference on Thermal and Thermomechanical Phenomena in Electronic Systems (iTherm)* (pp. 1-8). IEEE Publishing. <https://doi.org/10.1109/iTherm54085.2022.9899538>
- Hasan, S. K., Fahim, A., Suhling, J. C., & Lall, P. (2020). Mechanical behavior evolution of SAC+ Bi lead free solder exposed to thermal cycling. In *2020 19th IEEE Intersociety Conference on Thermal and Thermomechanical Phenomena in Electronic Systems (iTherm)* (pp. 1180-1190). IEEE Publishing. <https://doi.org/10.1109/iTherm45881.2020.9190579>
- Hodúlová, E., Li, H., Šimeková, B., & Kovaříková, I. (2018). Structural analysis of SAC solder with Bi addition. *Welding in the World*, 62(6), 1311–1322. <https://doi.org/10.1007/s40194-018-0629-z>
- Hokka, J., Mattila, T. T., Xu, H., & Paulasto-Kröckel, M. (2013). Thermal cycling reliability of Sn-Ag-Cu solder interconnections - PART 2: Failure mechanisms. *Journal of Electronic Materials*, 42(6), 963–972. <https://doi.org/10.1007/s11664-013-2475-5>
- Hoque, M. A., Haq, M. A., Suhling, J. C., & Lall, P. (2021). Mechanical behavior and microstructure evolution in lead free solders subjected to mechanical cycling at elevated temperatures. In *2021 IEEE 71st Electronic Components and Technology Conference (ECTC)* (pp. 2340-2347). IEEE Publishing. <https://doi.org/10.1109/ECTC32696.2021.00366>
- Jeon, C., Choi, Y., Jeong, H., Seo, K., Rhew, K., Bae, J., & Hwang, Y. (2023). Investigation of acceleration factors for SnAgCu-Bi solder Joints under various temperature cycling test conditions. In *2023 IEEE 73rd Electronic Components and Technology Conference (ECTC)* (pp. 846-851). IEEE Publishing. <https://doi.org/10.1109/ECTC51909.2023.00146>
- Jian, M., Hamasha, S., Alahmer, A., Hamasha, M., Wei, X., Belhadi, M. E. A., & Hamasha, K. (2023). Analysis and modeling of aged SAC-Bi solder joints subjected to varying stress cycling conditions. *Materials*, 16(2), Article 0750. <https://doi.org/10.3390/ma16020750>
- Jian, M., Hamasha, S., Alahmer, A., Wei, X., Belhadi, M. E. A., Alakayleh, A., & Tahat, S. (2023). Shear fatigue analysis of SAC-Bi solder joint exposed to varying stress cycling conditions. *IEEE Transactions*

- on Components, Packaging and Manufacturing Technology, 13(2), 274–283. <https://doi.org/10.1109/TCPMT.2023.3240367>
- Kaimkuriya, A., Sethuraman, B., & Gupta, M. (2024). Effect of physical parameters on fatigue life of materials and alloys: A critical review. *Technologies*, 12(7), Article 100. <https://doi.org/10.3390/technologies12070100>
- Kanchanomai, C., Miyashita, Y., & Mutoh, Y. (2002). Low-cycle fatigue behavior of Sn-Ag, Sn-Ag-Cu, and Sn-Ag-Cu-Bi lead-free solders. *Journal of Electronic Materials*, 31, 456–465.
- Kanlayasiri, K., & Sukpimai, K. (2016). Effects of indium on the intermetallic layer between low-Ag SAC0307-xIn lead-free solders and Cu substrate. *Journal of Alloys and Compounds*, 668, 169–175. <https://doi.org/10.1016/j.jallcom.2016.01.231>
- Li, G. Y., & Shi, X. Q. (2006). Science press effects of bismuth on growth of intermetallic compounds in Sn-Ag-Cu Pb-free solder joints. *Transactions of Nonferrous Metals Society of China*, 16, s739-s743. [https://doi.org/10.1016/S1003-6326\(06\)60292-6](https://doi.org/10.1016/S1003-6326(06)60292-6)
- Li, M. L., Zhang, L., Jiang, N., Zhang, L., & Zhong, S. J. (2021). Materials modification of the lead-free solders incorporated with micro/nano-sized particles: A review. *Materials & Design*, 197, Article 109224. <https://doi.org/10.1016/j.matdes.2020.109224>
- Libot, J. B., Alexis, J., Dalverny, O., Arnaud, L., Milesi, P., & Dulondel, F. (2018). Microstructural evolutions of Sn-3.0Ag-0.5Cu solder joints during thermal cycling. *Microelectronics Reliability*, 83, 64–76. <https://doi.org/10.1016/j.microrel.2018.02.009>
- Liu, V., Zou, Y. S., Chen, Y. Y., Chang, W. L., Foo, X. Q., Chen, Y. J., Chen, C. M., Chung, M. H., & Gan, C. L. (2024). Solder joint reliability performance study and shear characterization of low-Ag SAC lead-free solders for handheld application. *Materials Science in Semiconductor Processing*, 179, Article 108489. <https://doi.org/10.1016/j.mssp.2024.108489>
- Mahdavi, M. H., Sabri, M. F. M., Shnawah, D. A., Said, S. M., Badruddin, I. A., & Rozali, S. (2015). The effect of iron and bismuth addition on the microstructural, mechanical, and thermal properties of Sn-1Ag-0.5Cu solder alloy. *Microelectronics Reliability*, 55(9–10), 1886–1890. <https://doi.org/10.1016/j.microrel.2015.06.134>
- Maruf, M. A., Mazumder, G. R., Chakraborty, S., Suhling, J. C., & Lall, P. (2024). Effects of combined isothermal aging and mechanical cycling exposures on the mechanical behavior of lead-free solder alloys. In *2024 23rd IEEE Intersociety Conference on Thermal and Thermomechanical Phenomena in Electronic Systems (ITherm)* (pp. 1-8). IEEE Publishing. <https://doi.org/10.1109/ITherm55375.2024.10709399>
- Miao, Y., Dong, T., Li, C., Yang, J., Lu, Q., Xu, Z., Zhang, X., Peng, J., & Yi, J. (2024). Effects of Sb on the properties and interfacial evolution of SAC305-2Bi-xSb/Cu solder joints. *Journal of Materials Research and Technology*, 30, 9494–9502. <https://doi.org/10.1016/j.jmrt.2024.06.023>
- Ramli, M. I. I., Salleh, M. A. A. M., Abdullah, M. M. A. B., Zaimi, N. S. M., Sandu, A. V., Vizureanu, P., Rylski, A., & Amli, S. F. M. (2022). Formation and growth of intermetallic compounds in lead-free solder joints: A review. *Materials*, 15(4), Article 1451. <https://doi.org/10.3390/ma15041451>

- Ren X. L., Wang, Y. P., Lai, Y. Q., Shi, S. Y., Liu, X. Y., Zou, L. J., & Zhao, N. (2023). Effects of in addition on microstructure and properties of SAC305 solder. *Transactions of Nonferrous Metals Society of China (English Edition)*, 33(11), 3427–3438. [https://doi.org/10.1016/S1003-6326\(23\)66344-7](https://doi.org/10.1016/S1003-6326(23)66344-7)
- Rizvi, M. J., Chan, Y. C., Bailey, C., Lu, H., & Islam, M. N. (2006). Effect of adding 1 wt% Bi into the Sn-2.8Ag-0.5Cu solder alloy on the intermetallic formations with Cu-substrate during soldering and isothermal aging. *Journal of Alloys and Compounds*, 407(1–2), 208–214. <https://doi.org/10.1016/j.jallcom.2005.06.050>
- Romdhane, E. B., Roumanille, P., Guedon-Gracia, A., Pin, S., Nguyen, P., & Fremont, H. (2022). QFN (Quad Flat No-lead) SAC solder joints under thermal cycling: Identification of two failure mechanisms. In *2022 IEEE 72nd Electronic Components and Technology Conference (ECTC)* (pp. 716-722). IEEE Publishing. <https://doi.org/10.1109/ECTC51906.2022.00120>
- Shen, Y. A., Zhou, S., Li, J., Yang, C. H., Huang, S., Lin, S. K., & Nishikawa, H. (2019). Sn-3.0Ag-0.5Cu/Sn-58Bi composite solder joint assembled using a low-temperature reflow process for PoP technology. *Materials and Design*, 183, Article 108144. <https://doi.org/10.1016/j.matdes.2019.108144>
- Sivakumar, P., O'Donnell, K., & Cho, J. (2021). Effects of bismuth and nickel on the microstructure evolution of Sn-Ag-Cu (SAC)-based solders. *Materials Today Communications*, 26, Article 101787. <https://doi.org/10.1016/j.mtcomm.2020.101787>
- Su, S., Jian, M., & Hamasha, S. (2020). Effects of surface finish on the shear fatigue of SAC-based solder alloys. *IEEE Transactions on Components, Packaging and Manufacturing Technology*, 10(3), 457–466. <https://doi.org/10.1109/TCPMT.2019.2942806>
- Swanson, T. J., & Anselm, M. K. (2023). Properties of mixing SAC solder alloys with bismuth-containing solder alloys for a low reflow temperature process. *Journal of Surface Mount Technology*, 36(3), 25-34. <https://doi.org/10.37665/smt.v36i3.6>
- Tarman, W., Alahmer, A., Bolanos, S., Pouya, S., Alakayleh, A., El Amine Belhadi, M., & Hamasha, S. (2024). Evaluating shear properties of individual solder joints in ball grid arrays: The impact of silver (Ag) and bismuth (Bi) content. In *2024 23rd IEEE Intersociety Conference on Thermal and Thermomechanical Phenomena in Electronic Systems (ITherm)* (pp. 1-8). IEEE Publishing. <https://doi.org/10.1109/ITherm55375.2024.10709615>
- Tian, R., Wang, C., Huang, Y., & Guo, X. (2022). Effects of nanoparticle addition on the reliability of Sn-based Pb-free solder joints under various conditions: A review. *Nano*, 18(01), Article 2330001. <https://doi.org/10.1142/S1793292023300013>
- Vandeveld, B., Vanhee, F., Pissort, D., Degrendele, L., De Baets, J., Allaert, B., Lauwaert, R., Zanon, F., Labie, R., & Willems, G. (2017). Four-point bending cycling: The alternative for thermal cycling solder fatigue testing of electronic components. *Microelectronics Reliability*, 74, 131–135. <https://doi.org/10.1016/j.microrel.2017.04.008>
- Wang, J., Ye, Y., Zhao, J., Liu, S., Tu, Y., Li, S., & Song, Z. (2009). Assessment of LF solder joint reliability by four point cyclic bending. In *2009 International Conference on Electronic Packaging Technology & High Density Packaging* (pp. 572-576). IEEE Publishing. <https://doi.org/10.1109/ICEPT.2009.5270686>

- Wang, W., Chen, Z., Wang, S., & Long, X. (2020). Mechanics-based acceleration for estimating thermal fatigue life of electronic packaging structure. *Microelectronics Reliability*, 107, Article 113616. <https://doi.org/10.1016/j.microrel.2020.113616>
- Wu, J., Ahmed, S., Suhling, J. C., & Lall, P. (2019). Investigation of aging induced microstructural changes in doped SAC+ X solders. In *2019 18th IEEE Intersociety Conference on Thermal and Thermomechanical Phenomena in Electronic Systems (ITherm)* (pp. 405-415). IEEE Publishing. <https://doi.org/10.1109/ITherm.2019.8756501>
- Wu, J., Hassan, K. M. R., Alam, M. S., Suhling, J. C., & Lall, P. (2021). Investigation and comparison of aging effects in SAC+Bi solders exposed to high temperatures. In *2020 IEEE 70th Electronic Components and Technology Conference (ECTC)* (pp. 492-503). IEEE Publishing. <https://doi.org/10.1109/ITherm51669.2021.9503187>
- Yang, T., Chen, Y., You, K., Dong, Z., Jia, Y., Wang, G., Peng, J., Cai, S., Luo, X., Liu, C., & Wang, J. (2022). Effect of Bi, Sb, and Ti on microstructure and mechanical properties of SAC105 alloys. *Materials*, 15(14), Article 4727. <https://doi.org/10.3390/ma15144727>
- Zhang, H., Ma, Z., Yang, S., Fan, M., & Cheng, X. (2023). Microstructure and mechanical properties of Sn-xGa alloys and solder joints. *Journal of Materials Research and Technology*, 26, 3830–3839. <https://doi.org/10.1016/j.jmrt.2023.08.151>
- Zhang, S., Qiu, Q., Ding, T., Long, W., Zhong, S., Paik, K. W., He, P., & Zhang, S. (2024). Investigation of isothermal aged Sn-3Ag-0.5Cu/Sn58Bi-Co hybrid solder joints on ENIG and ENEPIG substrate with various mechanical performances. *Materials Today Communications*, 39, Article 108609. <https://doi.org/10.1016/j.mtcomm.2024.108609>
- Zhao, J., Cheng, C. qian, Qi, L., & Chi, C. yu. (2009). Kinetics of intermetallic compound layers and shear strength in Bi-bearing SnAgCu/Cu soldering couples. *Journal of Alloys and Compounds*, 473(1–2), 382–388. <https://doi.org/10.1016/j.jallcom.2008.05.082>
- Zhong, S. J., Zhang, L., Li, M. L., Long, W. M., & Wang, F. J. (2022). Development of lead-free interconnection materials in electronic industry during the past decades: Structure and properties. *Materials and Design*, 215, 110439. <https://doi.org/10.1016/j.matdes.2022.110439>
- Zou, Y. S., Chung, M. H., Gan, C. L., Hsu, Y. T., & Takiar, H. (2021). Effects of Sb and Bi addition on IMC morphology and reliability of Pb-free solder/Cu-OSP. In *2021 IEEE 23rd Electronics Packaging Technology Conference (EPTC)* (pp. 419-422). IEEE Publishing. <https://doi.org/10.1109/EPTC53413.2021.9663897>

Review Article

A Review on Experimental, Numerical, and Machine Learning-based Solar Energy Harvesting for Road Pavements Application

**Muhammad Imran Najeeb¹, Nurul Aqilah Razeman², Zarina Itam^{3,4*},
Salmia Beddu⁴, Nazirul Mubin Zahari⁴, Mohd Zakwan Ramli⁴,
Mohd Hafiz Zawawi⁴, Nur Liyana Mohd Kamal⁴, Agusril Syamsir^{3,4}
and Daud Mohamad⁴**

¹*Department of Engineering Education, Faculty of Engineering and Built Environment, Universiti Kebangsaan Malaysia, 43600 Bangi, Selangor, Malaysia*

²*College of Graduate School, Universiti Tenaga Nasional, Jalan IKRAM - UNITEN, 43000 Kajang, Selangor, Malaysia*

³*Institute of Energy Infrastructure, College of Engineering, Universiti Tenaga Nasional, Jalan IKRAM - UNITEN, 43000 Kajang, Selangor, Malaysia*

⁴*Civil Engineering Department, College of Engineering, Universiti Tenaga Nasional, Jalan IKRAM - UNITEN, 43000 Kajang, Selangor, Malaysia*

ABSTRACT

Revolutionizing solar energy utilization through solar pavement technology offers a path to sustainable infrastructure and reduced greenhouse emissions. This review article synthesizes findings from experimental, numerical and machine learning-based studies to optimize solar energy harvesting in pavement applications. The experimental and numerical analyses focus on achieving optimal thermal efficiency and maximizing the outlet pipe's temperature in Pavement Solar Collectors (PSC) through

detailed parametric studies. Machine learning tools are then employed to further enhance PSC performance by integrating additional input parameters, varied PSC designs, and diverse environmental conditions. Key insights from this review indicate that integrating machine learning into PSC design significantly broadens the scope and efficiency of these technologies, positioning solar pavement as a viable approach to reducing greenhouse gas emissions. Future works from this technology include looking into a multi-functional renewable energy system that produces hydrogen powered by solar power.

ARTICLE INFO

Article history:

Received: 15 July 2024

Accepted: 24 December 2024

Published: 26 March 2025

DOI: <https://doi.org/10.47836/pjst.33.3.05>

E-mail addresses:

imran.najeeb@ukm.edu.my (Muhammad Imran Najeeb)

aqilahrazeman@gmail.com (Nurul Aqilah Razeman)

izarina@uniten.edu.my (Zarina Itam)

salmia@uniten.edu.my (Salmia Beddu)

nazirul@uniten.edu.my (Nazirul Mubin Zahari)

zakwan@uniten.edu.my (Mohd Zakwan Ramli)

mhafiz@uniten.edu.my (Mohd Hafiz Zawawi)

yana_kamal@uniten.edu.my (Nur Liyana Mohd Kamal)

agusril@uniten.edu.my (Agusril Syamsir)

daud@uniten.edu.my (Daud Mohamad)

* Corresponding author

Additionally, the adaptability of these developed models suggests potential applications in solar collectors for roof tiles, building walls, and related energy-efficient systems.

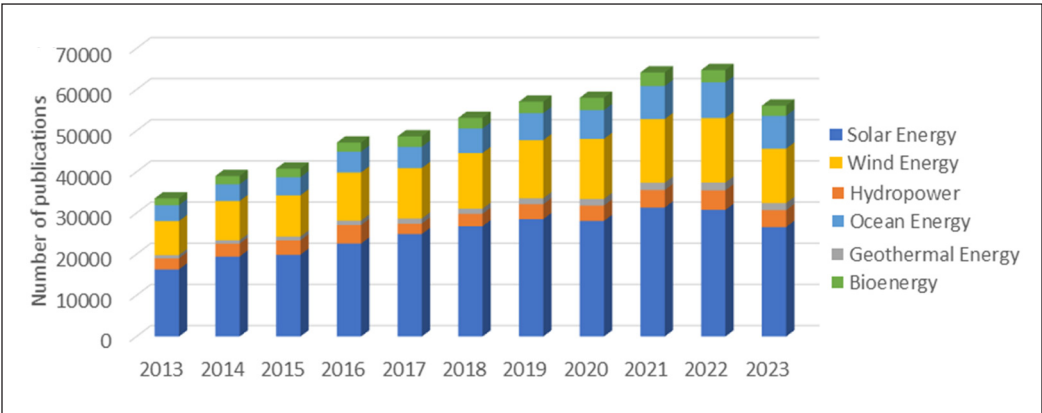
Keywords: Asphalt, heat exchange, machine learning, solar energy, solar pavement collector

INTRODUCTION

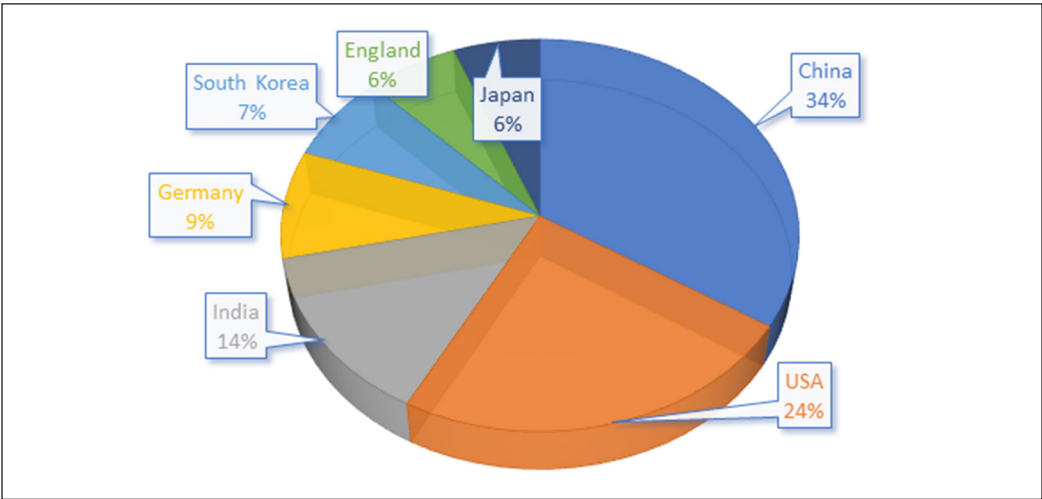
Over the past hundred years, the world has heavily relied on oil and fossil fuels to generate power. This source of energy is not renewable, and the by-products produced from power generation, such as greenhouse gases, cause the average temperature to rise (Yoro & Daramola, 2020). This indirectly contributes to global warming by increasing carbon dioxide emissions, causing detrimental effects on the environment, such as disrupting the existing ecosystem, rising ocean temperatures, increasing sea water levels, and many more (Bhan et al., 2020). The surge in the global population and the relentless march of globalization are contributing to an escalating demand for energy and heightened consumption levels. As a result, the world's reliance on non-renewable energy sources leads to the rapid depletion of fossil fuel reserves. Primc et al. (2021) identified several key issues associated with non-renewable dependencies, such as the complexity of power lines management, lack of local substations, and outdated monitoring technologies, leading to increased electricity costs. Hence, identifying viable renewable energy sources is essential to meet energy demand while preserving natural resources. Desired features of alternative renewable energy sources include those that are naturally replenished, such as solar, hydropower, wind, geothermal, bioenergy, and ocean energy (Owusu & Asumadu-Sarkodie, 2016).

Renewable resources have gained popularity as effective energy source substitutes to overcome power shortages, halt continuous environmental degradation, and meet future global energy demands (Esposito & Romagnoli, 2023). Extensive studies conducted on renewable energy as an alternative energy source show promising potential in the future compared to fossil energy, driven by the United Nations Sustainable Development Goal (SDG 7) for affordable and clean energy. As depicted in Figure 1(a), pertinent literature was gathered from the Web of Science Master Journal List utilizing specific keywords that include “solar energy,” “hydropower,” “wind energy,” “geothermal energy,” “bioenergy,” and “ocean energy.” Subsequently, the refine tab was applied for the last ten years. Solar energy is among the renewable resources that have emerged as a leading sector with considerable global research and development. Notably, the top-performing countries in solar energy research are also pioneering advanced solar technologies, as Figure 1(b) highlights.

The introduction of solar energy technology has significant future market potential due to its cleanliness and abundant availability (Hayat et al., 2019). There were two ways of generating solar electricity: solar-photovoltaic (PV) cells and concentrating solar power



(a)



(b)

Figure 1. (a) Studies on renewable energy field; and (b) Top seven countries leading in research and development in renewable energy field for the past decade

(CSP) technologies. Recent developments in solar PV cell technology show improvements in terms of efficiency, up to 34.1%, shown by multi-junction (MJ) photovoltaic cells. A diverse array of companies has embraced solar energy technologies as an alternative energy source. Besides, the technology is now available at reasonable prices. The energy generated from this source was used for heating, cooling, and outdoor and indoor lighting, as CSP uses linear cavity receivers, which minimize the heat escape (Kalidasan et al., 2023). Several factors affected the receivers' thermal performance, such as the cavity geometry, thermal emissivity, fluid temperature, and wind direction (Garg & Saini, 2018). Besides, studies have been conducted to utilize solar energy in drying technologies for food preservation, known as solar dryers. The solar dryers' performance was enhanced by integrating with

phase change materials (PCMs) and other heat storage systems to improve drying kinetics and efficiency (Tyagi et al., 2024). Moreover, the PCMs can also be used to enhance thermal energy storage in diverse solar thermal systems, emphasizing low, medium, and high-temperature applications (Kalidasan et al., 2020).

Another method to attain sustainable development using renewable energy sources is by utilizing surface solar radiation. Surface solar radiation is the amount of sunlight energy reaching the Earth’s surface, which influences the surrounding environment, including solar power production. Yang et al. (2018) concluded that the thermodynamic and dynamic state of the Earth’s atmospheric systems are important signals that reflect climate change. Researchers globally have studied solar radiation variations and other factors affecting it using observed data. Since solar radiation is gaining importance as an energy source on the Earth’s surface, research on utilizing solar radiation as a renewable energy source is essential. The optimal approach for tapping into solar energy and radiation without constructing additional infrastructure, such as solar farms, involves integrating solar technologies into existing structures, like road pavements. For instance, Saudi Arabia recorded over 73,000 km of paved roads in 2019, illustrating the vast potential this region holds for future opportunities since they had a high average mean surface temperature recorded between 16°C and 33°C yearly (Statista, 2021; The World Bank Group, 2021). A typical road pavement solar collector typically includes pipes with a circulating liquid within the pipes, as shown in Figure 2.

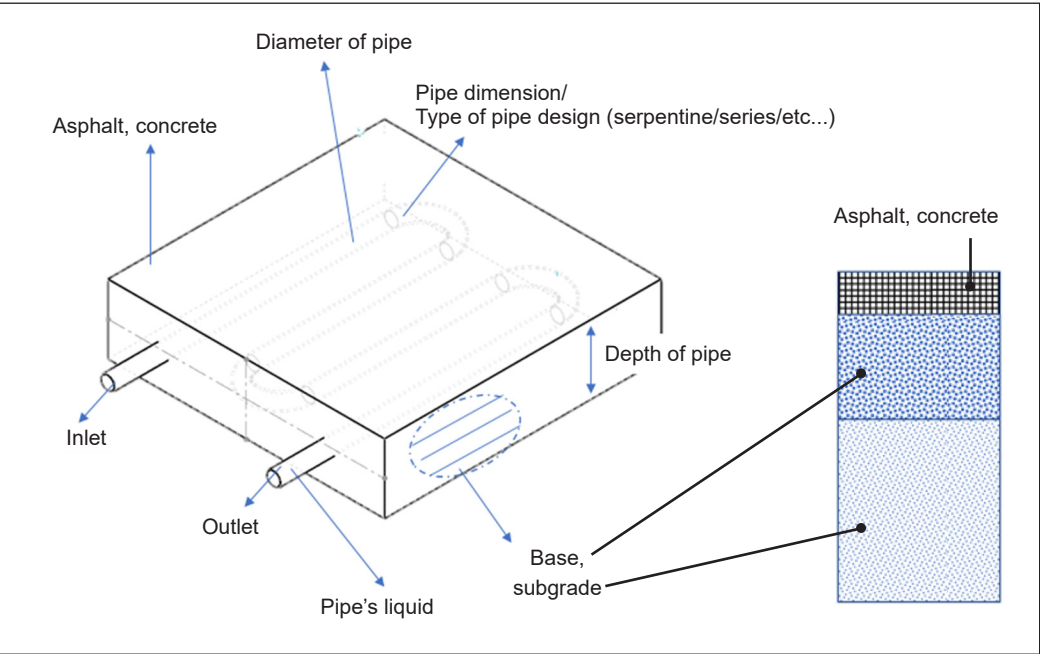


Figure 2. A general view of pavement solar collector components

This review is significant as it consolidates the latest breakthroughs in solar pavement technology, emphasizing the role of experimental, numerical, and machine-learning methodologies in enhancing efficiency and application. This research offers a comprehensive evaluation of solar pavement technology, integrating diverse techniques, in contrast to other studies focusing on isolated features like thermal efficiency or specific material performance. This paper identifies significant improvements in experimental discoveries, design optimizations, and machine learning applications that have not been thoroughly explored in a single review previously. This review is innovative due to its comprehensive approach, examining existing limits and upcoming prospects to improve solar energy capture in pavement applications. This contribution aims to give researchers and industry practitioners a strategic framework, emphasizing possible effects on urban energy systems, sustainable infrastructure, and environmental advantages, including reductions in greenhouse gas emissions. Furthermore, the results are anticipated to broaden the domain of solar pavement research, providing a basis for additional investigations and applications in diverse structures, including roof tiles and building walls, beyond conventional pavement settings.

SOLAR ENERGY HARVESTING PRINCIPLE AND ITS APPLICATIONS

Solar energy transforms a significant amount of radiant energy into heat, which is then harnessed for various applications. This approach is one of the most widely employed methods for harnessing solar energy. It has reached an advanced stage of industrialization, is characterized by its simplicity of implementation, and holds the greatest promise to eventually supplant conventional strategies and technologies reliant on fossil fuels. Gong et al. (2019) studied the approach of solar energy conversion for electricity or thermal power generation by utilizing photovoltaics or photothermal transduction agents (PTAs). Research on both inorganic and organic hybrid perovskites showed notable enhancements in photovoltaic efficiency as well as device stability.

The solar technology category depends on the methods employed for capturing, converting, and distributing solar energy, primarily falling into two distinct categories: passive solar and active solar energy systems (Kabir et al., 2018). The thermoelectric effect of active solar technology is an actual occurrence that turns a temperature differential into voltage via a thermocouple. One fundamental phenomenon underlying this effect is the Seebeck Effect, which occurs when an electric voltage is generated across two different conductive materials due to a temperature gradient. For instance, thermoelectric generators utilize the Seebeck Effect to convert waste heat into electricity, commonly found in power plants (Gonçalves et al., 2020). The Seebeck Effect occurs when two types of semiconductors, P-type and N-type, are chemically combined, forming a p-n junction and generating electromotive force (Kim et al., 2017). Carriers (conductors and semiconductors), along with passive and active

materials, move in response to a temperature gradient to complete the transformation from solar thermal to electrical energy (Kabir et al., 2018).

Moving on to renewable energy perspectives, solar energy enables the direct conversion of solar energy to electricity with rapid and easy grid connection despite the restricted power generation. During the day, photovoltaics provide renewable energy to the grid. Additionally, the power generated during the day can be stored in batteries or supercapacitors and later used to meet a portion of the electrical demand at night (Carrasco et al., 2006).

The benefits of solar energy in the new energy system include diverse sources, no pollution, and abundant energy (Ferreira et al., 2020). Additional studies confirm that solar energy technologies have been proven to reduce carbon emissions, which were previously sourced from fossil fuels for electricity. This allows for the powering of signage and lighting in remote areas, resulting in improved safety for road users. Solar radiation absorbs significant heat from the pavement, allowing for its collection. A study developed a cutting-edge thermoelectric generator system capable of transforming the heat differential between the road surface and the soil underneath into electrical energy and producing 29 milliwatts of electrical energy on average (Johnsson & Adl-Zarrabi, 2020).

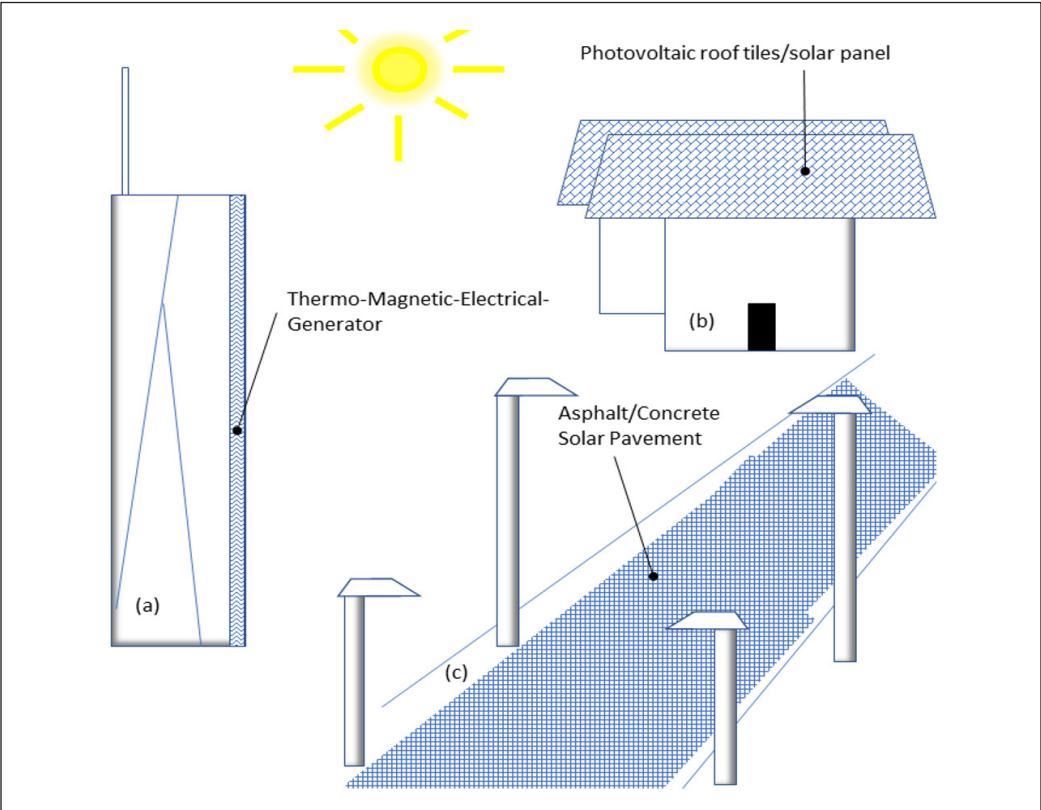


Figure 3. Renewable energy system: (a) Wall building; (b) roof; and (c) road pavement

Interest has shifted toward the integration of photovoltaic cell technology into civil-building structures such as roof tiles, walls, and road pavement, as shown in Figure 3. However, the conversion efficiency of photovoltaic cells is temperature-dependent, where high temperatures can cause a reduction in efficiency. Alim et al. (2020) found that to regulate the temperature of the solar cells, it is essential to integrate them with phase change material (PCM) into the mortar roof tiles. For this integration, the tile was added with a concentration of 3% by weight of PCM, which shows 4.1% more electrical output compared to without PCM filler. The PCM properties were able to absorb and release thermal energy efficiently.

A study on an Indian smart city concept by Saha and Frøyen (2021) shows that the main part of a smart city is the need to continuously produce and supply electricity to sustain the city, as they heavily rely on technologies powered by electricity. Therefore, it is important to utilize each part and area of the city to harness solar energy. Several cities have achieved success in becoming a national benchmark for large-scale adoption of solar energy in their cities. For example, Diu Smart City in India and Trondheim in Norway utilize renewable solar energy during the daytime, setting a benchmark for other local cities to follow and implement the technology. Another solar application capable of transforming sunlight on wall surfaces into heat energy is the installation of a thermo-magnetic-electrical-generator (TMEG) on building surfaces. The TMEG units are fixed between two wall layers with varying temperatures (hot and cold walls). This is made possible through the use of Gadolinium (Gd) as the ferromagnetic material due to its convenient Curie point, allowing it to move in a space between two zones with varying temperatures (Homadi et al., 2020).

Next are the solar collectors for asphalt or concrete pavement applications. Pipes containing water or other fluids were incorporated beneath the pavement layers, functioning to accumulate heat, which would later be harvested for energy (Todd, 2011). Kehagia et al. (2019) outlined two different types of solar pavements: thermal collectors and electrical collectors. These were examples of sophisticated structures that can contribute to long-term road infrastructure sustainability. Incorporating innovative technology into asphalt pavements has demonstrated the viability of harnessing solar energy. Solar pavement collectors (PSC) are used to fulfill the urban environment's thermal and electrical demands. The thermal collection process starts with the accumulation of heat from the sun. This warmth is captured by the water running through the network of pipes buried in the lane's surface layer, enabling continuous heat collection on hot summer days and supplying on-site renewable energy. Heat moves from a hotter location to a cooler side, either from the pavement to the water in the piping system or the other way around. These help regulate the pavement temperature during the summer and winter (Kehagia et al., 2019). For instance, a Dutch company, Ooms Avenhorn Holding, used PSC technology to gather solar energy from asphalt roadways during the summer and use it during the winter to

warm the apartment buildings and Dutch Air Force runways. Furthermore, implementing road energy systems can quickly cool hot roads during the summer and prevent rapid deterioration (Xu et al., 2021).

The design of PSCs was observed to offer ample opportunities for upgrades aimed at enhancing their efficiency, such as modifying the albedo, fluid flow rate, and pipe spacing (Johnsson & Adl-Zarrabi, 2020). Guldentops et al. (2016) conducted research that evaluated the effect of the integrated pipe's design on the PSC's thermodynamics and efficiency using experiments and numerical analysis. The pipe design and configuration influence the thermal efficiency up to 70% (Guldentops et al., 2016). On the other hand, the performance of the PSC is affected by its region of usage. For example, an urban street canyon equipped with a PSC system shows, on average, 36.08% more thermal collection with a 27.11% surface temperature reduction compared to the PSC application in a rural area (Nasir et al., 2015). The PSC systems are suitable for sustainable city projects since they serve as a dual-function system that reduces the ground surface temperature and is a tool for harnessing heat energy. van Bijsterveld et al. (2001) conducted a thermal analysis using a finite element module for materials science and structural engineering (FEMMASSE), a finite element program. The input data were collected from a site test located in the northern Netherlands that employed polyethylene tubes on the main road to regulate the pavement temperature. The developed finite element modeling shows there were high stresses and strains forming around the tubes (van Bijsterveld et al., 2001). With this discovery, it is also important to note the effect of the structure of the PSC system in the long run due to the heat exchange process, which could impact the integrity of the road structure. Dezfooli et al. (2017) found that when using solar pavements as a renewable energy producer to generate voltage compared to solar panels, solar pavements have the capacity to enhance the rutting performance for transportation applications. The components used in the assembly of the solar pavement include rubber tubes, steel pipes, and serpentine copper. Researchers evaluated the design of these pavements based on energy supply, surface safety movements, and structural performance. The suitable efficiency of solar pavements was also measured based on structural resistance and skid resistance.

Solar pavement technology must demonstrate to future users that it makes economic sense to change their current installations or integrate them into new installations or retrofits. The method considered by Ryms et al. (2017) was to replace the asphalt or concrete pavement with an electronic layer structure comprising a multi-layer system between the base solar collectors and the wearing courses. The wearing course will be translucent, allowing sunlight to reach through the collection sheet. The sun powers the electrical core, enabling it to flash signals and produce energy for motorists to replace signs and markings. Beddu et al. (2016) studied the use of hot surface energy in electricity production and the concurrent reduction in pavement temperature during the season. Researchers tested the

heat exchange rate and temperature effect through measurement and modeling (Beddu et al., 2016). The thermally transmitted fluid has a direct effect on peak power output, and thermoelectric modules resist it. According to the authors, the surrounding weather and fluid temperature mostly affect the efficiency of heat transfer.

According to the literature, research on solar collector technologies has predominantly focused on analyzing the thermal characteristics of road pavement compared to roof tiles and wall buildings. This underscores the pressing need for sustainable development, emphasizing the pivotal role of promoting solar energy as a renewable source for future energy needs.

THE PAVEMENT SOLAR COLLECTOR

Solar radiation exposure, pavement materials, and innovative design create an ideal environment for harnessing solar energy on a large scale. Xu et al. (2021) proposed replacing regular roadways with photovoltaic solar panels, known as “Solar Roadways”. Asphalt pavement solar heat collectors have been proven to be highly effective in practical applications worldwide. In real-life applications, a few parameters need to be taken into account to evaluate the heat harnessing efficiency, such as the slope gradient, slope exposure, and orientation of the streets and open spaces (Finn et al., 2021). Therefore, various simplifications are necessary for performing heat transfer simulations due to the complex structure of solar panel pavement conversion (Vinod et al., 2018). On top of that, the solar panel pavement is a multi-layered structure composed of homogeneous and isotropic layers. Sunlight absorbed by the solar panel that is not converted to electricity is considered to be converted to heat. Dust and any other discharged substances on the photovoltaic pavement surface that have an effect on the solar panel’s absorptivity would be overlooked due to their minor influence. Meanwhile, because the sides of a solar panel are so tiny in comparison to the top and bottom faces, the energy lost via the sides is ignored (Ma et al., 2019). Figure 3 illustrates the thickness layers of asphalt/concrete (AC) pavements. The life cycle assessment (LCA) showed the utilization of solar pavements for long-term environmental benefits, even though the economic cost was higher than conventional concrete and asphalt pavements (Hu et al., 2023). Hence, a few parameters need to be considered for the pavement solar collectors’ efficiency.

DESIGN AND MATERIAL CONSIDERATIONS FOR PIPES IN PSC SYSTEMS

Asphalt pavements absorb a large quantity of thermal energy from solar radiation throughout the day. The Pavement Solar Collectors (PSC) represent a method of harvesting solar energy and converting it to thermal energy. Zaim et al. (2020) found that PSCs comprise a series of metal or non-metal pipes (like copper, rubber, stainless steel, and polyethylene pipes)

buried in paving slabs. A moving fluid inside the PSCs collects heat from the hot pavements (Zaim et al., 2020). There were several pipe designs being studied, including serpentine, series, ladder configuration, balanced-ladder configuration, and parallel.

Pipe Design

An experiment conducted by Zaim et al. (2020) placed a steel pipe at a depth of 300 mm below the top surface of the PSC. Stainless steel pipes in a series configuration filled with water were placed at the center of the PSC (Zaim et al., 2020). The pipe’s internal diameter is 15.8 mm, and the pipes were arranged consistently with roughly 110 mm center-to-center spacing. The experiments were conducted in Bam, Iran, and monitored through both the summer and winter seasons. The experimental setup determined the peak output temperature, the temperature disparity, and the pressure loss of the pipes. Results show that the experimental design parameters have a considerable impact on the PSC’s characteristics and functionality. Furthermore, the authors developed and evaluated four pipe configurations using simulation analysis under the same conditions as mentioned above to determine the effect of pipe arrangement on PSC performances. Four distinct pipe configurations were explored, each with general and specific technological characteristics. These configurations were categorized based on the fluid flow pattern within the PSC. The illustration of the pipe configurations is presented in Figure 4. The result shows that the serpentine configuration resulted in a greater distance covered by the flowing water than the other three configurations. Experimental results also show that the fluid flow rate is constant along the circulation route for the serpentine configuration, while the intake fluid flow is segmented into several channels for the other configurations.

The intake and outlet temperatures are the other critical components affecting a pavement solar collector’s performance. The serpentine pipe configuration shows greater temperature differences compared to the other configurations. Zaim et al. (2020) further discussed that the water traveling distances and the temperature differences obtained in the balanced-ladder (d) and parallel (b) arrangements are close to each

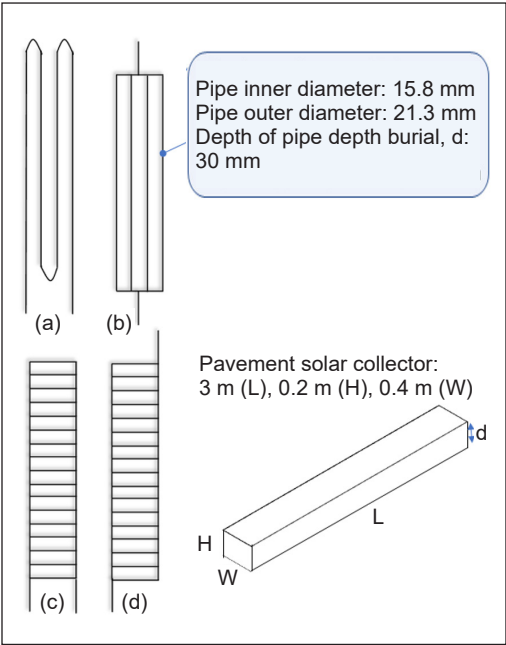


Figure 4. Pipe dimension and configuration: (a) Serpentine; (b) parallel; (c) ladder; and (d) balanced ladder

other. As for the ladder configuration (c), the circulating water goes just the shortest distance within the pipe, showing that it is not a good configuration as it does not cover all the pavement areas.

In different studies, Zhou, Pei, Hughes et al. (2021) recommended separating the asphalt slab into two sections: side A (the water inlet) and side B (the water outlet). Thermocouples (K-type) monitored the temperature at three pavement depths: top, middle, and bottom. The results show that the heat on pipes has a substantial effect on the mechanical response, thermal reaction, and coupling response of the pavement structure. The heat pipe's surrounding structure, particularly at the bending zone, is the weakest part of the total pavement structure. The serpentine heat pipe greatly reduced the maximum bottom tensile stress. It is reasonable to conclude that the heat pipe can help prevent cracking in asphalt pavements. On the other hand, the idea of the pavement-integrated photovoltaic thermal system (PIPVT) is based on the building-integrated photovoltaic thermal system (BIPVT), which combines the study of PV pavement and thermal energy harvesting pavement. This integral aids in the recovery of the solar cells from severe solar heating and reduces the operating temperature of the solar cells (Zhou, Pei, Nasir et al., 2021).

Besides the shape of the pipe, the pavement materials themselves influence the heat exchange efficiency between the pavement and the pipe. A study showed that using conductive asphalt improved the solar extraction energy from the pavement to the pipe. A study shows that using conductive material, conductive hot-mix asphalt (limestone aggregates + silica sand + slag filler in place of limestone filler + 4% steel wool fibers) improved 20.94% thermal efficacy compared to normal hot-mix asphalt (all aggregates comprised limestone) (Abbas & Alhamdo, 2024).

Although the study of the pipe design provides robust data, more investigation is needed to examine how the various layouts affect pavement maintenance and longevity over a long period. Furthermore, the tribology effects on the PSC system and lifetime should be considered to guarantee its feasibility from various points of view.

Polyethylene Pipes

Polyethylene pipes in the upper layers of the pavement circulate fluid in a pavement solar collector (PSC). The pavement surface heats due to heat absorption from solar radiation, which is then transferred to the circulating fluid. Research conducted by Johnsson and Adl-Zarrabi (2020) found that modifying the albedo, fluid flow rate, and pipe spacing has an impact on the PSC's performance. The authors discovered that by adjusting the albedo and flow rate of the fluid, efficiency increased to 49%. However, when pipes are positioned closely, they present extra limitations. It is important to avoid excessively small bending radii for pipes to prevent damage. Additionally, if multiple pipes are placed in the pavement, the pavement's load-bearing capability will be affected. In general, a deeper position

and closer spacing between pipes result in a greater amount of generated electricity. The harvested energy has been measured at 245 kWh/m², boasting a solar efficiency of 42%.

Rubber and Copper Pipe

Apart from the polyethylene material, copper and rubber pipe were also used for investigation at the maximum outlet temperature. A study on serpentine copper and rubber pipes by Ahmad et al. (2018) proved that sustainable energy production by utilizing pavement surfaces as heat collectors is feasible. Henceforth, the calculation of solar efficiency under the paved surface using the finite element approach is needed. Serpentine, copper, and rubber pipes were employed in asphalt pavement. ANSYS software was used to prepare a model of asphalt pavement with dimensions of 300 mm x 500 mm. The asphalt surface is embedded with 40-mm-diameter serpentine copper and rubber pipes. Solar heat is gathered at 50-, 100-, and 150-mm depths in asphalt pavement. Coordinates are generated to locate the fluid flow in the pipes at the inlet and outlet. The meshing process of the two regions has been established, where one represents the link between pipes and asphalt pavement, and the second is between pipes and fluid flow in pipes. The results show that the maximum outlet temperature for rubber pipes was less than 12.63% compared to copper pipe at a 50-mm depth. Besides ANSYS, transient system simulation software (TRNSYS) has also been used to investigate the PSC efficiency of using a copper serpentine pipe through the evaluation of the temperature differential between the input and output of the pipe (Al-Manea et al., 2022). Table 1 summarizes the pavement and pipe material.

Table 1
Summary of pavements and pipe material for specific environmental conditions and practical application

Material	Properties	Practical application
Conductive asphalt	High thermal conductivity; durable under various temperature	Regions with high-temperature fluctuations (e.g., hot summers and cold winters)
Polyethylene (PE)	High corrosion resistance, impact and pressure	Suitable for air with high water pressure
Copper	Good thermal conductivity, corrosion resistance, easy to joints	Ideal for humid environment
Rubber	High flexibility, thermal insulation, and abrasion resistance.	High traffic zone

TYPES OF PIPE’S LIQUID AND ITS EFFICIENCY

Fluid flows through pipes to store heat energy. The rate of fluid flow has an effect on the amount of energy gathered. According to Johnsson and Adl-Zarrabi’s (2020) research, increasing the fluid flow rate decreases the average fluid temperature, thereby improving heat transfer. If the flow rate is exceedingly low, the Pavement Solar Collector (PSC) will perform

inefficiently because of the small temperature difference between the fluids and the pavement layer. An increased fluid flow rate decreases the mean pavement temperature (Johnsson & Adl-Zarrabi, 2020). Therefore, the study revealed that increasing the fluid flow rate from 0.02 L/s to 0.17 L/s resulted in a rise in captured energy from 140 kWh/m² to 280 kWh/m².

Besides the fluid flow rate, the physical and thermal properties of the fluid, including density, specific heat capacity, and thermal conductivity, were important in investigating their influences on heat transfer in the PSC system. Additionally, compressibility and viscosity are important properties of a fluid from the standpoint of fluid mechanics (Nakayama, 2018).

Water

Water is a common fluid that is accessible, low-cost, and used in solar-collecting pipes. Cycled water in pipe systems collects heat energy and carries the extracted energy out of pavement solar collectors (Zaim et al., 2020). Therefore, an accurate calculation of the circulating water temperature is critical for analyzing the PSC's performance. Water was pumped at a constant rate and ejected at atmospheric pressure. Many distinct kinds of velocity initial conditions are employed at the pipe set's inlet and outlet portions, including intake velocity and outflow. As a result, the temperature of the water that has been stored within the storage tank began to rise in direct proportion to the flow rate of the returning water. The collector discharges water from the storage tank's bottom side to reduce heat dissipation. Based on research, the temperature records from the data logger and thermocouples revealed a notable difference between the initial and final temperatures at various slab depths and sides.

On the other hand, Zhou, Pei, Hughes et al. (2021) found that after 60 minutes of adding water to the asphalt slab, the surface temperature dropped from 80.6°C to 71.9°C. This also suggests that the heat pipe's circulating water has lowered the asphalt's surface temperature by 10.8%, which, by increasing the flow rate of the water, the efficiency of the pipes (Zhou, Pei, Hughes et al., 2021). However, Nasir et al. (2015) highlighted that increasing the flow rate of water does not reduce the pavement temperature significantly. Additionally, a comparable study discovered that changing the pipe's depth to 25 mm from 125 mm reduced the pavement temperature by 30%. Research has discovered that altering the temperature of the inlet water has the highest impact on the PSC system efficiency compared to the other parameters, such as water flow rate, solar radiation, and sun heat, as shown by a sensitivity analysis (Ahmadi et al., 2020).

Coolant (A Cooling Fluid)

The Pavement Integrated Photovoltaic Thermal System (PIPVT) absorbs solar energy and converts it to electricity. It also harvests some of the absorbed heat as thermal energy

using coolant circulated beneath the solar cells through serpentine copper pipes. The system increases solar energy utilization efficiency and can concurrently meet the power and thermal energy needs of households along the path.

Ethylene Glycol

Talib et al. (2017) conducted field tests on solar pavement under actual atmospheric conditions. The test consisted of asphalt pavement, an exchanger with a heat tube filled with ethylene glycol, solar heat, thermocouples, and data logging systems. The test set-up included empty steel pipes and steel pipes filled with ethylene glycol. At a depth of 150mm, ethylene glycol collected the highest amount of heat at 51.2°C. Over three days, the pipe temperature increased by 71% at a depth of 50mm, 78% at 100mm, and 62% at 150mm when using ethylene glycol. In comparison to a pipe without ethylene glycol, the impact of ethylene glycol was more apparent, and the pipe could hold additional heat.

Recommendation

Based on the findings, the optimum pipe design for pavement solar collectors is to have a pipe depth of around 50mm, pipe spacing of roughly 110mm and a fluid flow rate of 0.17L/s. The additional recommendation is to have a serpentine pipe configuration and conductive asphalt for pavement material. Table 2 shows the justification for the optimum configuration for the solar pavement collector.

Table 2
Summary of optimal pavement solar collector

Parameter	Optimal value	Justification
Pipe depth	50 mm	Balances heat absorption with pavement structural integrity
Pipe spacing	110 mm center-to-center	Ensure efficient heat collection and consistent flow distribution
Flow rate	0.17L/s	Improve energy efficiency
Pipe configuration	Serpentine	Optimal temperature difference and fluid flow reduce pavement cracking
Pavement material	Conductive asphalt	Improve thermal flow across the pavement

MACHINE LEARNING-BASED (ML)

The emergence of machine learning (ML) brings huge add-ons through more detailed parametric studies, especially for experimental and numerical modeling, to save time and high computational costs. There were many ML algorithms available either as open source or by subscription. ML includes gated recurrent units (GRU), artificial neural networks (ANN), Bayesian structural time series modules (BSTS), autoencoder networks,

feedforward neural networks (FFNN), long short-term memory (LSTM), convolutional neural networks (CNN), bidirectional long short-term memory (Bi-LSTM), Bayesian neural network module (BNN), least squares support vector machines (LSSVM), and adaptive neuro-fuzzy inference system (ANFIS) as shown in Figure 5 (Milad et al., 2021).

A study using ANN expanded the parametric studies by inputting the asphalt solar collector (ASC) system parameters, which were the thermal conductivity and surface absorptivity of asphalt, inlet water temperature, the water flow rate, solar irradiance, and time of day in the cold and warm months of November and August, investigating the outlet water temperature. The temperature difference between inlet and outlet water is 24 °C, with 45% thermal efficiency in August. Meanwhile, the temperature difference in November is 14 °C, with 35% thermal efficiency (Masoumi et al., 2020). Besides conducting parametric studies, the ANN model is also used in prediction investigations. In a study using an ANN

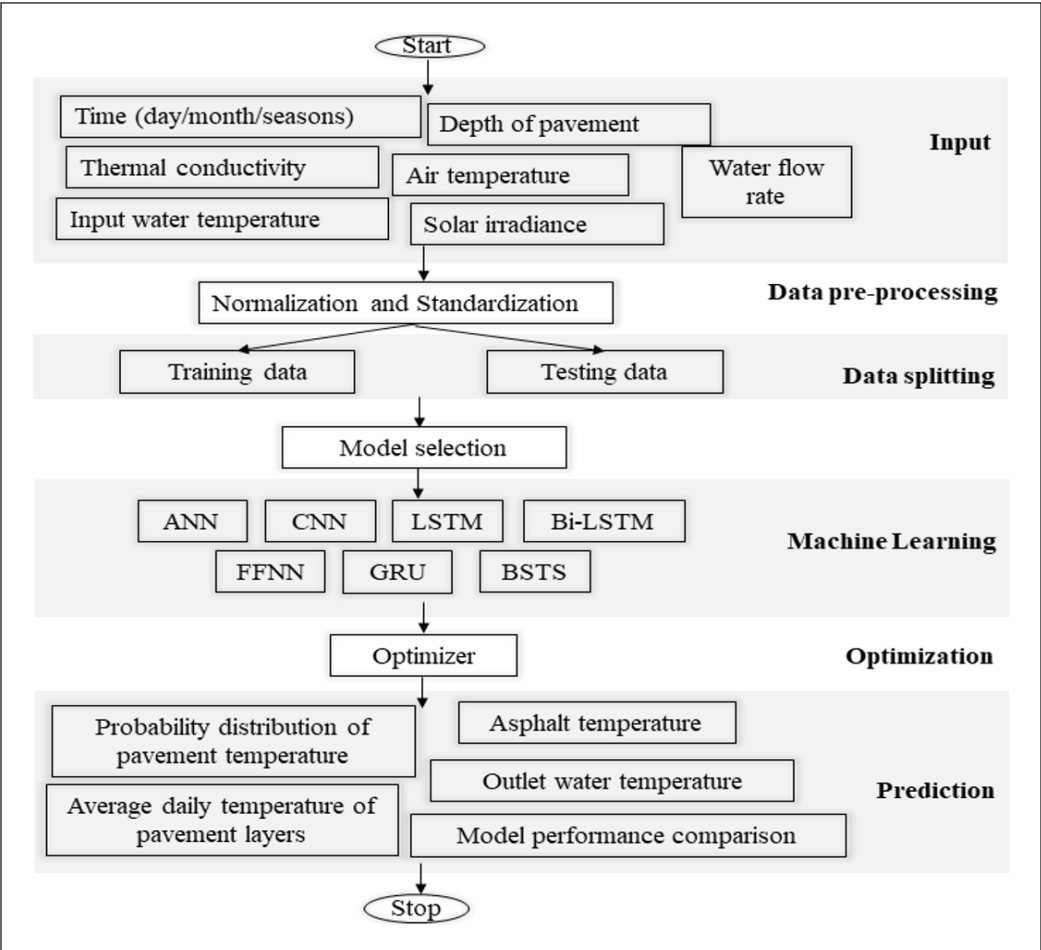


Figure 5. Machine learning model flowchart summary from literature

algorithm to predict the ASC layer temperature, The determination of the ASC layer under the influence of temperature is important for understanding its structural capacity due to its viscoelastic behavior (Nojumi et al., 2022). Therefore, prediction accuracy is required based on the input parameters (Abo-Hashema, 2013).

Another study used three different machine learning models to create a prediction model for ASC temperature using the autoencoder networks FFNN and LSTM. The algorithms show that the applied machine learning achieved accurate predictions, where the temperature was recorded between 2.80°C and 0.51°C for the mean absolute error (MAE). The autoencoder network model demonstrates the highest accuracy in predicting asphalt temperatures, followed by the FFNN and LSTM models. These studies also demonstrated that having additional input parameters such as wind speed and relative humidity enhanced the machine learning models significantly (Ghalandari, Shi et al., 2023). Besides predicting the asphalt pavement temperature, ML can also be used to predict the pavement's base and subgrade layer temperatures. A study developed a new ML approach using air temperature and number of days to predict the average daily temperature at the base and subgrade layers (Huang et al., 2023). Researchers used air temperature and pavement depth (0, 2, 5.5, and 7 cm) data for asphalt across different seasons (winter, summer, spring, and autumn) from the entire Gaza Strip between March 2012 and February 2013. The parameters were used as input in four types of ML, which were CNN, LSTM, Bi-LSTM, and GRU, to predict asphalt pavement temperature (APT) based on the input parameters (air temperature, depth, and seasons). The result of Bi-LSTM shows a robust APT prediction system and fine-tunes the training parameters (Milad et al., 2021).

The ML approach is also used to assist in decision-making for road maintenance during the winter season. Since the thermal environment is complex in winter conditions, the prediction result for the pavement temperature should be a probability distribution instead of a single value. The author developed two different ML models in this case: BSTS and BNN. The BNN module shows a significant relationship between the two factors of slippery index and pavement surface condition and pavement surface temperature at 0°C. On the other hand, the BSTS algorithm consists of four sections: the local linear trend, seasonal component, regression component, and uncertainty of pavement surface temperature. The regression component shows a significant importance section for the BSTS module compared to the rest of the sections (Li et al., 2022). In the latest work, the author developed a hybrid model of finite element modeling with a machine learning algorithm to reduce the computational time required to conduct a parametric study. The studies examine the relationships between the pipe depth, temperature inlet, and length of the pipe to assess their impact on the thermal responses of the PSC. The findings reveal that, among the investigated inputs, the length of the pipe exerts the most significant impact on the outcomes. The research predicts that, over the course of a year, the heat

energy capacity can reach an impressive 1.17 GJ/m² with less than 2% error (Ghalandari, Hernando et al., 2023). On the other hand, a study excluded pipe design and only assessed these four parameters (water inlet temperature, water flow rate, solar radiation, and sun heat) using ANN, ANFIS, and LSSVM machine learning models for parametric studies. The result shows that the LSSVM had the best approach and predictability compared to the rest of the investigated ML because the modeling had less deviation compared to the experimental data (Ahmadi et al., 2020).

Therefore, ML algorithms significantly enhance experimental and numerical modeling by reducing computational costs and time through parametric studies. Besides that, ML helps the design engineer predict thermal performance and optimize systems in complex environments.

FUTURE DIRECTIONS

Future studies should focus on addressing the current dearth of comprehensive studies integrating machine learning into PSC research, particularly ones that encompass all essential inputs, such as pavement surface, sub-layers, the material composition of the pavement surface and sub-layers, pipe material, pipe design, pipe depth, airspeed on the pavement surface at various heights, pipe design and thickness, type of liquid, and the liquid's flow rate. In addition, researchers need to assess the mechanical properties and behavior of PSC subjected to a range of temperatures and moisture. There were studies by Curiosity Lab in Georgia and New York where they embedded solar panels and smart city sensors into paving to generate electricity to power electric car charging ports. These pilot projects are expected to expand to prove that this technology is reliable and able to support the growth of electric vehicles (Skip, 2020).

Apart from converting solar to electrical energy, recent studies show a growing trend in solar harness technologies like the photovoltaic cells being used for hydrogen production (solar to hydrogen). Since the current energy production is insufficient, researchers are seeking alternative eco-friendly energy at a lower cost. A study shows that the level cost of energy (LCOE) of using solar to hydrogen system brings less than \$2/kWh at the optimal conditions, with PV output reaching 100W while reducing carbon emission by up to 13% (Shboul et al., 2024). Further, a study hybrid on the spiral fluid solar photovoltaic thermal collector (SPVTC) with small-scale Hoffman's electrocatalytic hydrogen production cell (EHPC) improves the electrical power and hydrogen productivity of PV and EHPC by investigating the cooling fluid (water and air) at different flow rates. The results show an improvement in hydrogen daily production from 3.07 kg_{H2}/d to 3.24–4.41 kg_{H2}/d, while the electricity productivity increased from 69.45 kWh/d to 92.45 kWh/d–74.77 kWh/d. Economic analysis shows that the optimized system of PV-EHPC results in lower hydrogen production costs by 7.04% to 32.10% (El-Hadary et al., 2023). On the other

hand, the performance of PVTC-EHP for hydrogen production can be predicted by using artificial intelligence modeling consisting of vector functional links and mayfly optimizers. The modeling helps the author enhance its prediction accuracy and optimize the system performance, resulting in more reliable and validated results (Elaziz et al., 2021). This system also contributes to the sustainable development goals by promoting green energy solutions.

Utilizing the technology for hydrogen production adds beneficial value in terms of economic, environmental and social perspectives to the current solar energy harnessing technology.

CHALLENGES AND LIMITATION

The implementation of pavement solar collectors (PSC) and other solar energy systems presents several challenges and limitations that need to be addressed for successful adoption. Three points of view needed to be looked into: structural integrity, heat transfer efficiency, and economic feasibility. The PSC system for road pavement faces challenges in managing heavy traffic, affecting the pavement's load-bearing capacity. Additionally, the high costs associated with installing solar energy harnessing systems and ongoing maintenance present significant limitations, especially during the initial stages. Effective implementation requires specific locations and substantial subsidies or incentives to accelerate the adoption of these technologies. Given their expense, it is essential to enhance the efficiency of current solar energy systems to maximize energy capture within a limited area.

CONCLUSION

Researchers across engineering fields have widely investigated solar energy harvesting technology for a sustainable future. The implementation of Pavement Solar Collectors (PSC) systems in big cities leads to clean energy harvesting, improving pavement service life, and mitigating the urban heat island (UHI) effect. Based on the literature on PSC systems, the following main conclusion can be drawn:

1. The PSC system transforms a considerable amount of radiant energy from solar energy into heat and utilizes it. This approach is among the most widely used and implemented techniques for renewable energy sources, as it has industrialized to the furthest degree. It is possible to implement the studied system, and it has significant potential to emerge as a prominent energy source, further reducing reliance on fossil fuels. Solar collector pavement technology uses photovoltaics or photothermal transduction agents (PTAs) for solar energy conversion, enabling electricity or thermal power generation.
2. Compared to the other parameters investigated, the length of the pipe and inlet water temperature most influence the temperature outlet of the PSC system. In addition, the

serpentine pipe design at 50 mm in depth produced the highest outlet temperature, showing that this configuration had the most effective heat absorption from the pavement surface to the buried pipe. However, it's crucial to balance thermal efficiency with structural integrity, as pipes placed too close to the surface can compromise the pavement's load-bearing capacity.

3. Future work on this technology was seen to develop an efficient multi-functional renewable energy system, which is hydrogen production powered by solar power. The integration of electrolytic hydrogen production cells (EHP) with the photovoltaic (PV) system showcases a sustainable method of generating hydrogen, a green energy to meet the world's energy demand.

ACKNOWLEDGMENTS

The authors convey their gratitude to the Ministry of Higher Education Malaysia for the generous sponsorship of the research under the FRGS research grant FRGS/1/2020/TK0/UNITEN/02/18. This research was funded by the Dato' Low Tuck Kwong International Grant (20238002DLTK), the Higher Institution Centre of Excellence (HICoE), Ministry of Higher Education (MOHE), Malaysia under the project code 2024001HICOE as referenced in JPT(BPKI)1000/016/018/34(5), and the BOLD Refresh Postdoctoral Fellowships under Grant J510050002-IC-6 BOLDREFRESH2023-Centre of Excellence. Special thanks to the IRMC of Universiti Tenaga Nasional for the full cooperation given to make this project achievable.

REFERENCES

- Abbas, F. A., & Alhamdo, M. H. (2024). Experimental and numerical analysis of an asphalt solar collector with a conductive asphalt mixture. *Energy Reports*, 11, 327–341. <https://doi.org/10.1016/j.egy.2023.11.065>
- Abo-Hashema, M. A. (2013). Modeling pavement temperature prediction using artificial neural networks. *Airfield and Highway Pavement* 2013, 490–505. <https://doi.org/10.1061/9780784413005.039>
- Ahmad, M., Itam, Z., Beddu, S., Alanimi, F. B. I., & Soanathan, S. A. P. (2018). A determination of solar heat collection in serpentine copper and rubber pipe embedded in asphalt pavement using finite element method. *Journal of Engineering and Applied Sciences*, 13(1), 181–189. <https://doi.org/10.3923/jeasci.2018.181.189>
- Ahmadi, M. H., Baghban, A., Sadeghzadeh, M., Zamen, M., Mosavi, A., Shamshirband, S., Kumar, R., & Mohammadi-Khanaposhtani, M. (2020). Evaluation of electrical efficiency of photovoltaic thermal solar collector. *Engineering Applications of Computational Fluid Mechanics*, 14(1), 545–565. <https://doi.org/10.1080/19942060.2020.1734094>
- Al-Manea, A., Al-Rbaihat, R., Kadhim, H. T., Alahmer, A., Yusaf, T., & Egab, K. (2022). Experimental and numerical study to develop TRNSYS model for an active flat plate solar collector with an internally serpentine tube receiver. *International Journal of Thermofluids*, 15, Article 100189. <https://doi.org/10.1016/j.ijft.2022.100189>

- Alim, M. A., Tao, Z., Abden, M. J., Rahman, A., & Samali, B. (2020). Improving performance of solar roof tiles by incorporating phase change material. *Solar Energy*, 207, 1308–1320. <https://doi.org/10.1016/j.solener.2020.07.053>
- Beddu, S., Talib, S. H. A., & Itam, Z. (2016). The potential of heat collection from solar radiation in asphalt solar collectors in Malaysia. In *IOP Conference Series: Earth and Environmental Science* (Vol. 32, No. 1, p. 012045). IOP Publishing. <https://doi.org/10.1088/1755-1315/32/1/012045>
- Bhan, C., Verma, L., & Singh, J. (2020). Alternative fuels for sustainable development. In *Environmental Concerns and Sustainable Development* (pp. 317–331). Springer. https://doi.org/10.1007/978-981-13-5889-0_16
- Carrasco, J. M., Franquelo, L. G., Bialasiewicz, J. T., Galvan, E., PortilloGuisado, R. C., Prats, M. A. M., Leon, J. I., & Moreno-Alfonso, N. (2006). Power-electronic systems for the grid integration of renewable energy sources: A survey. *IEEE Transactions on Industrial Electronics*, 53(4), 1002–1016. <https://doi.org/10.1109/TIE.2006.878356>
- Dezfooli, A. S., Nejad, F. M., Zakeri, H., & Kazemifard, S. (2017). Solar pavement: A new emerging technology. *Solar Energy*, 149, 272–284. <https://doi.org/10.1016/j.solener.2017.04.016>
- Elaziz, M. A., Senthilraja, S., Zayed, M. E., Els Sheikh, A. H., Mostafa, R. R., & Lu, S. (2021). A new random vector functional link integrated with mayfly optimization algorithm for performance prediction of solar photovoltaic thermal collector combined with electrolytic hydrogen production system. *Applied Thermal Engineering*, 193, Article 117055. <https://doi.org/10.1016/j.applthermaleng.2021.117055>
- El-Hadary, M. I., Senthilraja, S., & Zayed, M. E. (2023). A hybrid system coupling spiral type solar photovoltaic thermal collector and electrocatalytic hydrogen production cell: Experimental investigation and numerical modeling. *Process Safety and Environmental Protection*, 170, 1101–1120. <https://doi.org/10.1016/j.psep.2022.12.079>
- Esposito, L., & Romagnoli, G. (2023). Overview of policy and market dynamics for the deployment of renewable energy sources in Italy: Current status and future prospects. *Heliyon*, 9(7), Article e17406. <https://doi.org/10.1016/j.heliyon.2023.e17406>
- Ferreira, A. C., Silva, J., Teixeira, S., Teixeira, J. C., & Nebra, S. A. (2020). Assessment of the stirling engine performance comparing two renewable energy sources: Solar energy and biomass. *Renewable Energy*, 154, 581–597. <https://doi.org/10.1016/j.renene.2020.03.020>
- Finn, J., Leitte, A., Fabisch, M., & Henninger, S. (2021). Analysing the efficiency of solar roads within settlement areas in Germany. *Urban Climate*, 38, Article 100894. <https://doi.org/10.1016/j.uclim.2021.100894>
- Garg, A., & Saini, R. P. (2018). Study on design of cavity receiver of concentrating solar power plants - A review. In L. Chandra & A. Dixit (Eds.), *Concentrated Solar Thermal Energy Technologies: Recent Trends and Applications* (pp. 69–77). Springer. https://doi.org/10.1007/978-981-10-4576-9_7
- Ghalandari, T., Hernando, D., Hasheminejad, N., Moenielal, M., & Vuye, C. (2023). Lessons learnt from thermo-mechanical feasibility assessment of pavement solar collectors using a FE-ANN approach. *Case Studies in Construction Materials*, 19, Article e02582. <https://doi.org/10.1016/j.cscm.2023.e02582>
- Ghalandari, T., Shi, L., Sadeghi-Khanegah, F., Van den bergh, W., & Vuye, C. (2023). Utilizing artificial neural networks to predict the asphalt pavement profile temperature in western Europe. *Case Studies in Construction Materials*, 18, Article e02130. <https://doi.org/10.1016/j.cscm.2023.e02130>

- Gonçalves, W. D. G., Caspers, C., Dupont, J., & Migowski, P. (2020). Ionic liquids for thermoelectrochemical energy generation. *Current Opinion in Green and Sustainable Chemistry*, 26, Article 100404. <https://doi.org/10.1016/j.cogsc.2020.100404>
- Gong, J., Li, C., & Wasielewski, M. R. (2019). Advances in solar energy conversion. *Chemical Society Reviews*, 48(7), 1862–1864. <https://doi.org/10.1039/C9CS90020A>
- Guldentops, G., Nejad, A. M., Vuye, C., Van den bergh, W., & Rahbar, N. (2016). Performance of a pavement solar energy collector: Model development and validation. *Applied Energy*, 163, 180–189. <https://doi.org/10.1016/j.apenergy.2015.11.010>
- Hayat, M. B., Ali, D., Monyake, K. C., Alagha, L., & Ahmed, N. (2019). Solar energy - A look into power generation, challenges, and a solar-powered future. *International Journal of Energy Research*, 43(3), 1049–1067. <https://doi.org/10.1002/er.4252>
- Homadi, A., Hall, T., & Whitman, L. (2020). Using solar energy to generate power through a solar wall. *Journal of King Saud University - Engineering Sciences*, 32(7), 470–477. <https://doi.org/10.1016/j.jksues.2020.03.003>
- Hu, H., Vizzari, D., Zha, X., & Mantalovas, K. (2023). A comparison of solar and conventional pavements via life cycle assessment. *Transportation Research Part D: Transport and Environment*, 119, Article 103750. <https://doi.org/10.1016/j.trd.2023.103750>
- Huang, Y., Molavi Nojumi, M., Hashemian, L., & Bayat, A. (2023). Evaluation of a machine learning approach for temperature prediction in pavement base and subgrade layers in Alberta, Canada. *Journal of Transportation Engineering, Part B: Pavements*, 149(1), Article 04022076. <https://doi.org/10.1061/JPEODX.PVENG-1010>
- Johnsson, J., & Adl-Zarrabi, B. (2020). A numerical and experimental study of a pavement solar collector for the northern hemisphere. *Applied Energy*, 260, Article 114286. <https://doi.org/10.1016/j.apenergy.2019.114286>
- Kabir, E., Kumar, P., Kumar, S., Adelodun, A. A., & Kim, K. H. (2018). Solar energy: Potential and future prospects. *Renewable and Sustainable Energy Reviews*, 82, 894–900. <https://doi.org/10.1016/j.rser.2017.09.094>
- Kalidasan, B., Hassan, M. A., Pandey, A. K., & Chinnasamy, S. (2023). Linear cavity solar receivers: A review. *Applied Thermal Engineering*, 221, Article 119815. <https://doi.org/10.1016/j.applthermaleng.2022.119815>
- Kalidasan, B., Pandey, A. K., Shahabuddin, S., Samykano, M. M. T., & Saidur, R. (2020). Phase change materials integrated solar thermal energy systems: Global trends and current practices in experimental approaches. *Journal of Energy Storage*, 27, Article 101118. <https://doi.org/10.1016/j.est.2019.101118>
- Kehagia, F., Mirabella, S., & Psomopoulos, C. S. (2019). Solar pavement: A new source of energy. In *Bituminous Mixtures and Pavements VII* (pp. 441–447). CRC Press. <https://doi.org/10.1201/9781351063265-61>
- Kim, J., Lee, S. T., Yang, S., & Lee, J. (2017). Implementation of thermal-energy-harvesting technology on pavement. *Journal of Testing and Evaluation*, 45(2), Article 20140396. <https://doi.org/10.1520/JTE20140396>
- Li, Y., Chen, J., Dan, H., & Wang, H. (2022). Probability prediction of pavement surface low temperature in winter based on bayesian structural time series and neural network. *Cold Regions Science and Technology*, 194, Article 103434. <https://doi.org/10.1016/j.coldregions.2021.103434>

- Ma, T., Yang, H., Gu, W., Li, Z., & Yan, S. (2019). Development of walkable photovoltaic floor tiles used for pavement. *Energy Conversion and Management*, 183, 764–771. <https://doi.org/10.1016/j.enconman.2019.01.035>
- Masoumi, A. P., Tajalli-Ardekani, E., & Golneshan, A. A. (2020). Investigation on performance of an asphalt solar collector: CFD analysis, experimental validation and neural network modeling. *Solar Energy*, 207, 703–719. <https://doi.org/10.1016/j.solener.2020.06.045>
- Milad, A., Adwan, I., Majeed, S. A., Yusoff, N. I. M., Al-Ansari, N., & Yaseen, Z. M. (2021). Emerging technologies of deep learning models development for pavement temperature prediction. *IEEE Access*, 9, 23840–23849. <https://doi.org/10.1109/ACCESS.2021.3056568>
- Nojumi, M. M., Huang, Y., Hashemian, L., & Bayat, A. (2022). Application of machine learning for temperature prediction in a test road in Alberta. *International Journal of Pavement Research and Technology*, 15(2), 303–319. <https://doi.org/10.1007/s42947-021-00023-3>
- Nakayama, Y. (2018). Chapter 6 - Flow of viscous fluid. In Y. Nakayama (Ed.), *Introduction to Fluid Mechanics (2nd ed.)* (pp. 99–133). Butterworth-Heinemann. <https://doi.org/10.1016/B978-0-08-102437-9.00006-1>
- Nasir, D. S. N. M., Hughes, B. R., & Calautit, J. K. (2015). A study of the impact of building geometry on the thermal performance of road pavement solar collectors. *Energy*, 93, 2614–2630. <https://doi.org/10.1016/j.energy.2015.09.128>
- Owusu, P. A., & Asumadu-Sarkodie, S. (2016). A review of renewable energy sources, sustainability issues and climate change mitigation. *Cogent Engineering*, 3(1), Article 1167990. <https://doi.org/10.1080/23311916.2016.1167990>
- Princ, K., Dominko, M., & Slabe-Erker, R. (2021). 30 years of energy and fuel poverty research: A retrospective analysis and future trends. *Journal of Cleaner Production*, 301, Article 127003. <https://doi.org/10.1016/j.jclepro.2021.127003>
- Ryms, M., Denda, H., & Jaskuła, P. (2017). Thermal stabilization and permanent deformation resistance of LWA/PCM-modified asphalt road surfaces. *Construction and Building Materials*, 142, 328–341. <https://doi.org/10.1016/j.conbuildmat.2017.03.050>
- Saha, K., & Frøyen, Y. (2021). An automated approach to facilitate rooftop solar PV installation in smart cities: A comparative study between Bhopal, India and Trondheim, Norway. In P. Sharma (Ed.), *Geospatial Technology and Smart Cities: ICT, Geoscience Modeling, GIS and Remote Sensing* (pp. 75–92). Springer. https://doi.org/10.1007/978-3-030-71945-6_5
- Statista. (2021). *Length of Completed Main Paved Roads in Saudi Arabia from 2010 to 2019*. <https://www.statista.com/statistics/628720/saudi-arabia-total-length-of-main-paved-roads-completed/#statisticContainer>
- Shboul, B., Zayed, M. E., Tariq, R., Ashraf, W. M., Odat, A. S., Rehman, S., Abdelrazik, A. S., & Krzywanski, J. (2024). New hybrid photovoltaic-fuel cell system for green hydrogen and power production: Performance optimization assisted with Gaussian process regression method. *International Journal of Hydrogen Energy*, 59, 1214–1229. <https://doi.org/10.1016/j.ijhydene.2024.02.087>
- Skip, D. (2020). *High-Tech Roads Are Powering Electric Cars, Sensors and More*. Government Technology. <https://www.govtech.com/fs/high-tech-roads-are-powering-electric-cars-sensors-and-more.html>

- Talib, S. H. A., Hashim, S. I. N. S., Beddu, S., Maidin, A. F., & Abustan, M. S. (2017). Heat lump in different pavement layer using ethylene glycol as a solar heat collector. In *MATEC Web of Conferences* (Vol. 87, p. 01015). EDP Sciences. <https://doi.org/10.1051/mateconf/20178701015>
- The World Bank Group. (2021). *Climatology*. <https://climateknowledgeportal.worldbank.org/country/saudi-arabia/climate-data-historical>
- Todd, D. A. (2011). *Asphalt Pavement Solar Collectors: The Future is Now*. Buildipedia. <http://buildipedia.com/aec-pros/engineering-news/asphalt-pavement-solar-collectors-the-future-is-now?print=1&tmpl=component>
- Tyagi, V. V., Pathak, S. K., Chopra, K., Saxena, A., Kalidasan B., Dwivedi, A., Goel, V., Sharma, R. K., Agrawal, R., Kandil, A. A., Awad, M. M., Kothari, R., & Pandey, A. K. (2024). Sustainable growth of solar drying technologies: Advancing the use of thermal energy storage for domestic and industrial applications. *Journal of Energy Storage*, 99, Article 113320. <https://doi.org/10.1016/j.est.2024.113320>
- van Bijsterveld, W. T., Houben, L. J. M., Scarpas, A., & Molenaar, A. A. A. (2001). Using pavement as solar collector: Effect on pavement temperature and structural response. *Transportation Research Record: Journal of the Transportation Research Board*, 1778(1), 140–148. <https://doi.org/10.3141/1778-17>
- Vinod, Kumar, R., & Singh, S. K. (2018). Solar photovoltaic modeling and simulation: As a renewable energy solution. *Energy Reports*, 4, 701–712. <https://doi.org/10.1016/j.egy.2018.09.008>
- Xu, L., Wang, J., Xiao, F., El-Badawy, S., & Awed, A. (2021). Potential strategies to mitigate the heat island impacts of highway pavement on megacities with considerations of energy uses. *Applied Energy*, 281, Article 116077. <https://doi.org/10.1016/j.apenergy.2020.116077>
- Yang, L., Jiang, J., Liu, T., Li, Y., Zhou, Y., & Gao, X. (2018). Projections of future changes in solar radiation in China based on CMIP5 climate models. *Global Energy Interconnection*, 1(4), 452–459. <https://doi.org/10.14171/j.2096-5117.gei.2018.04.005>
- Yoro, K. O., & Daramola, M. O. (2020). CO₂ emission sources, greenhouse gases, and the global warming effect. In *Advances in Carbon Capture* (pp. 3–28). Elsevier. <https://doi.org/10.1016/B978-0-12-819657-1.00001-3>
- Zaim, E. H., Farzan, H., & Ameri, M. (2020). Assessment of pipe configurations on heat dynamics and performance of pavement solar collectors: An experimental and numerical study. *Sustainable Energy Technologies and Assessments*, 37, Article 100635. <https://doi.org/10.1016/j.seta.2020.100635>
- Zhou, B., Pei, J., Nasir, D. M., & Zhang, J. (2021). A review on solar pavement and photovoltaic/thermal (PV/T) system. *Transportation Research Part D: Transport and Environment*, 93, Article 102753. <https://doi.org/10.1016/j.trd.2021.102753>
- Zhou, B., Pei, J., Hughes, B. R., Nasir, D. S. N. M., Vital, B., Pantua, C. A. J., Calautit, J., & Zhang, J. (2021). Structural response analysis of road pavement solar collector (RPSC) with serpentine heat pipes under validated temperature field. *Construction and Building Materials*, 268, Article 121110. <https://doi.org/10.1016/j.conbuildmat.2020.121110>

Examining the Impact of Battery Properties and Energy Storage Connectivity for Electric Vehicle Charging Performance

**Muhammad Izzul Mawardi¹, Nik Hakimi Nik Ali^{1,2*},
Muhamad Nabil Hidayat^{1,2}, Ezmin Abdullah^{1,2}, Muhammad Umair^{1,2},
Ahmad Sukri Ahmad³ and Muzakkir Mohammad Zainol⁴**

¹*School of Electrical Engineering, College of Engineering, Universiti Teknologi MARA, 40450 Shah Alam, Selangor, Malaysia*

²*Battery Energy Storage Technology Laboratory (BEST), College of Engineering, Universiti Teknologi MARA, 40450 Shah Alam, Selangor, Malaysia*

³*Petronas Research Sdn Bhd, Bangi Government, and Private Training Centre Area, 43000 Bandar Baru Bangi, Selangor, Malaysia*

⁴*School of Chemical Engineering, College of Engineering, Universiti Teknologi MARA, 40450 Shah Alam, Selangor, Malaysia*

ABSTRACT

Carbon emissions from fossil fuels significantly contribute to global warming. To mitigate these emissions, Electric Vehicles (EVs) and renewable energy stored in Energy Storage Systems (ESS) have been introduced to achieve net-zero carbon emissions. Various types of batteries, including Lithium-Ion (Li-Ion), Lead Acid (Pb-Acid), and Nickel Cadmium (NiCd), are used in EVs and ESS to meet the increasing demand. This article examines the effect of different battery profiles on the performance of batteries in ESS. The paper presents a simulation study of an EV charging system using MATLAB, incorporating a 600 V ESS battery with a 100 Ah capacity and an EV battery rated at 400 V and 50 Ah. The study explores the charging and discharging performance of Li-Ion, Pb-Acid,

and NiCd batteries and investigates the impact of different battery connection arrangements and aging factors on battery performance. According to the findings, the state of charge (SOC), voltage, and current significantly influence battery charging and discharging performance. The results suggest that Li-Ion batteries with series-parallel connections outperform others, maintaining approximately 49.93% SOC with a minimal 0.07% drop after 10 seconds. Furthermore, aging batteries show a faster SOC decline, with Li-Ion batteries demonstrating the most stable performance across metrics. The

ARTICLE INFO

Article history:

Received: 31 July 2024

Accepted: 16 January 2025

Published: 26 March 2025

DOI: <https://doi.org/10.47836/pjst.33.3.06>

E-mail addresses:

Muhammadizzulizz972@gmail.com (Muhammad Izzul Mawardi)

hakimialik@uitm.edu.my (Nik Hakimi Nik Ali)

mnabil@uitm.edu.my (Muhamad Nabil Hidayat)

ezmin@uitm.edu.my (Ezmin Abdullah)

drumair@uitm.edu.my (Muhammad Umair)

ahmadsukri.ahmad@petronas.com (Ahmad Sukri Ahmad)

muzakkir@uitm.edu.my (Muzakkir Mohammad Zainol)

*Corresponding author

research highlights that series-parallel Li-Ion configurations best support EV charging applications due to their efficiency and durability.

Keywords: Battery properties, electric vehicle, energy storage system

INTRODUCTION

Vehicles powered by gasoline play a significant role in emitting carbon, adversely impacting the environment. In 2015, such vehicles were responsible for 40% of the world's carbon dioxide emissions, projected to double by 2050 (Al-Hanahi et al., 2022; Jeon et al., 2021). Carbon emissions significantly contribute to global warming and climate change, resulting in extreme weather events. To achieve zero carbon emissions, electric vehicles (EVs) present a viable alternative to reduce the number of gasoline-fueled vehicles on the road (Umair et al., 2024; Said et al., 2015; Said, 2021; Said & Elloumi, 2022). EVs can operate with the same potential as gasoline-fueled vehicles while benefiting the environment by producing no carbon emissions. EVs and energy storage systems (ESS) rely on batteries for power by utilizing various types of batteries such as Lithium-Ion (Li-Ion), Lead-Acid (Pb-Acid), and Nickel-Cadmium (NiCd). However, several battery parameters must be considered when designing and modeling ESS and EVs. The parameters used to assess battery performance in ESS and EVs include state of charge (SOC), depth of discharge (DOD), state of discharge (SOD), battery efficiency, temperature, and degradation (Rosewater et al., 2019; Schommer et al., 2024). It is important to select the appropriate battery type to optimize system performance.

One major issue is the lack of an adequate model to analyze EV charging performance, which hinders the development of public charging infrastructure (Alghamdi et al., 2020; Arfeen et al., 2010). To increase the widespread use of EVs, a robust charging performance infrastructure must be established to support the growing demand (Al-Hanahi et al., 2022; Samadani et al., 2012). Different battery types affect the performance of ESS and EVs due to their unique characteristics. Each battery type exhibits varying performance and efficiency in charging and discharging, necessitating in-depth analysis and simulation to understand these differences (Gong et al., 2015). Li-Ion batteries exhibit higher energy density, longer cycle life, and lower self-discharge rates than Pb-Acid batteries (Miao et al., 2019; Talele et al., 2024; Bais et al., 2024; Jiang et al., 2024). Li-Ion batteries also have a relatively flat discharge voltage curve, offer stable output over a wide SOC range, and are lightweight (Hannan et al., 2018; Tran et al., 2021). While less expensive, Pb-Acid batteries are considered safer and have a flatter discharge voltage curve, making them suitable for cost-sensitive applications. NiCd batteries, known for their temperature tolerance and reliability, fall between Pb-Acid and Li-Ion batteries in terms of energy density and weight. NiCd batteries can tolerate overcharging and deep discharging better but may be

susceptible to memory effects. The choice of battery technology in ESS and EVs depends on cost, cycle life, weight, safety, and specific application requirements.

The connection arrangement of the battery, whether in series, parallel or a combination series-parallel, also significantly influences battery charging and discharging performance (Gong et al., 2015). Additionally, charging and discharging can cause battery degradation, reducing cycle life and capacity due to the heat generated during these processes. This highlights the need for a comprehensive exploration of EV charging performance, considering battery connection arrangements and aging profiles (Timilsina et al., 2023; Lehtola & Zahedi, 2021). The connection arrangement of batteries in an ESS profoundly influences charging and discharging dynamics, whether in series, parallel, or combination configurations (Cho et al., 2019). In series connections, batteries are linked end-to-end, increasing the total voltage while maintaining the same overall capacity. In parallel connections, where batteries are connected with corresponding terminals, the total voltage is maintained while the overall capacity is improved.

The series-parallel combination allows for achieving specific voltage, capacity, and current requirements. During charging, series and parallel configurations impact current and voltage distribution. The arrangement determines the overall voltage and current handling capabilities during discharging. Careful consideration of these connections is essential, including balancing individual batteries to prevent over-charging, over-discharging, and uneven current distribution. This ultimately influences the performance and lifespan of the ESS and EV (Cho et al., 2019). The aging factor in battery systems refers to the gradual degradation of a battery's performance over time, influenced by cycle life, calendar life, temperature, DOD, and charging practices (Li et al., 2023). This aging process significantly affects the SOC and SOD of the battery. As the battery ages, its capacity diminishes, reducing the achievable SOC during charging and the available energy during discharge. Additionally, changes in voltage characteristics and increased internal resistance further complicate accurate SOC estimation (Kumar et al., 2023; Said, 2021).

The primary objective of this study is to develop and design a model for an ESS charging system using MATLAB. The study also aims to simulate and analyze the effect of three different battery types, Li-Ion, Pb-Acid, and NiCd, on charging and discharging performance. The research focuses on analyzing EV charging performance as influenced by the type of battery, connection arrangement, and aging factor of ESS. This study is particularly important due to the increasing demand for efficient and sustainable ESS in EVs. As EV adoption continues to grow, understanding the variation of battery performance and longevity is critical for optimizing charging systems. Previous research has primarily focused on individual aspects of battery performance or specific battery types without considering a holistic approach that simultaneously encompasses different battery chemistries, their arrangement, and aging effects.

Contribution

The novelty of this paper lies in its comprehensive approach to studying the interplay between various battery types and configurations within an ESS charging system through a bidirectional DC-DC (BDC) converter to charge EV batteries. By employing MATLAB for simulation, the research provides detailed insights into how each variable affects overall performance. This study addresses a significant research gap by integrating multiple factors that influence EV charging efficiency and battery life, which have often been studied in isolation. The findings from this research contribute new knowledge to the literature, offering a more complete understanding of ESS dynamics with battery types, connections arrangement, and aging factors study and paving the way for advancements in EV technology and sustainable transportation solutions.

METHODOLOGY

Overall System

Figure 1 shows a complete layout diagram of the proposed AC-DC EV Charging Station with ESS integration. As per Nissan Leaf EV specifications, a 400 V with 40 kW power for each EV is considered for the charging station (Sundararajan & Iqbal, 2021). In this paper, ESS will help balance the supply and demand of energy for EV chargers using a bidirectional DC-DC converter. The system simulation is performed using MATLAB. Still, this study only focused on one type of mode, which is discharging ESS to EV Battery

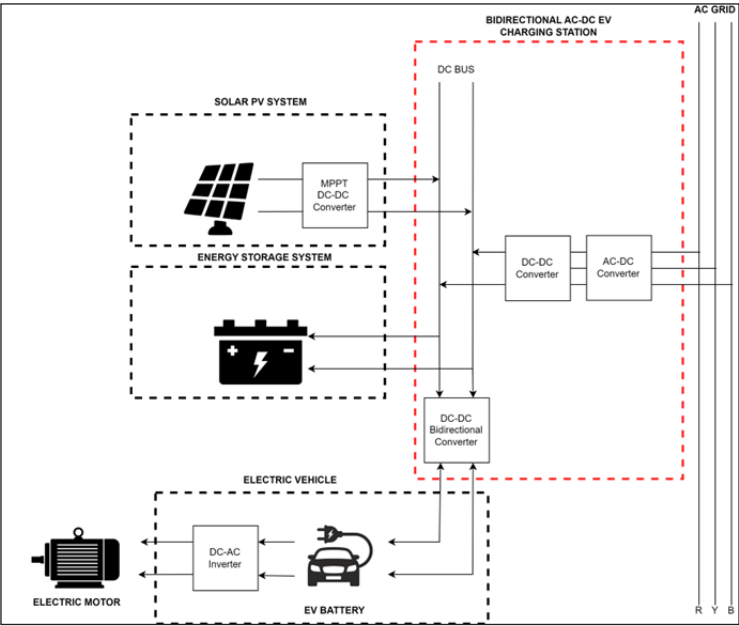


Figure 1. Layout diagram of proposed AC-DC EV Charging Station with ESS integration

Integration, because this mode is crucial for optimizing the efficiency and reliability of EV charging stations. By focusing on discharging, the study aims to ensure that the energy stored in the ESS can be effectively and efficiently transferred to the EV batteries, a common and essential operation in practical scenarios. The ESS battery type was Li-Ion, Pb-Acid, or NiCd. The ESS was connected to a bidirectional converter connecting to the EV battery to allow bidirectional charging and discharging to operate in two directions.

Flowchart of System

The flowchart shows the data collection based on established standards in the simulation process. Parameters were defined, and the circuit design was developed accordingly. Subsequently, system testing was conducted to validate the design. A decision point was introduced to address potential errors. If an error was detected, the flowchart directed the process to troubleshooting steps. In the absence of errors, the simulation proceeded with different cases. Three cases are defined in this study: Case 1, Case 2, and Case 3.

Case 1 utilized Li-Ion, Pb-Acid, and NiCd with identical battery parameters but varying discharging characteristics based on their specific chemistry and discharge curves. Every type of battery will produce its battery properties.

Case 2 involved testing different connection arrangements of batteries. Series, parallel, and series-parallel connections were tested in the simulation, using six batteries connected in series and another set of six batteries connected in parallel. A combination connection arrangement with twelve batteries connected in a series-parallel configuration was included.

Case 3 explored the aging factor of the batteries. The performance of aged batteries was compared with non-aged batteries for a comprehensive assessment of performance changes over time.

Finally, the simulation concluded with an in-depth analysis of the results. This structured approach facilitated a systematic and comprehensive simulation process, allowing for efficient troubleshooting and the exploration of various scenarios in the simulation environment. The flowchart is shown in Figure 2.

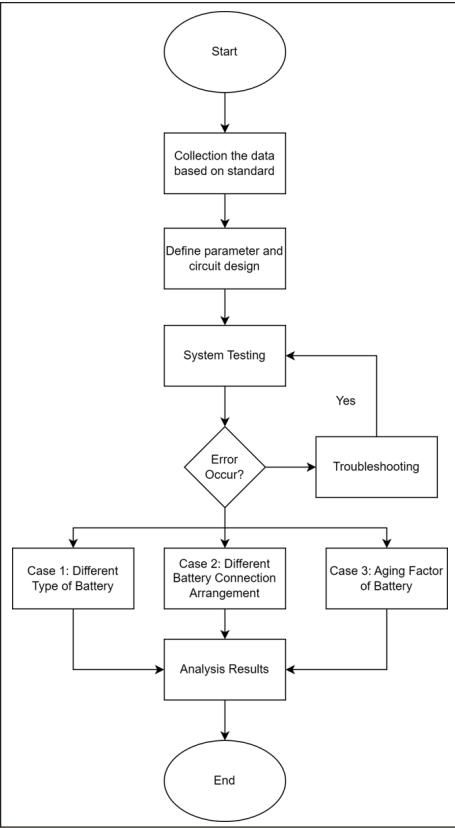


Figure 2. Flowchart of system

System Parameters

Table 1 represents the battery parameters of ESS and EV. A battery model was developed with three types of batteries: Li-Ion, Pb-Acid, and NiCd, to integrate with the ESS, while the EV only uses the Li-Ion type. The model ESS consists of one battery bank with 600 V 100 Ah while the EV battery 400 V 50 Ah is connected in series. The battery model includes parameters such as types of battery, rated capacity, nominal voltage, initial SOC, rated power, and connection. SOC indicates the current charge level of a battery as a percentage of its total capacity. In simple terms, SOC represents how much energy is currently stored in the battery relative to its full capacity (Singh et al., 2023). SOC expression is shown in Equation 1. In battery configuration, there are two processes which are charging and discharging. The expression of charging and discharging expression is shown in Equations 2 and 3.

Table 1
Battery parameters of ESS and EV

Performance Characteristics	Energy Storage System (ESS) Battery	Electric Vehicle (EV) Battery
Types of Battery	Lead acid, Lithium-ion, and Nickel Cadmium	Lithium-ion
Rated Capacity (Ah)	100	50
Nominal Voltage (V)	600	400
Initial State of Charge (%)	50	50
Rated Power (kWh)	60	20
Connection	series, parallel, series-parallel	series
Aging effect	Aging effect (50 cycles) Without the Aging effect (zero cycle)	Not applicable

$$\text{SOC (\%)} = \frac{\text{Capacity Remaining(Ah)}}{\text{Total Capacity (Ah)}}$$

[1]

$$\text{Charging Time (In Hours)} = \frac{\text{Battery Capacity (Ah)}}{\text{Charging Current (A)}}$$

[2]

$$\text{Discharging Time (In Hours)} = \frac{\text{Battery Capacity (Ah)}}{\text{Drawing Current (A)}}$$

[3]

Converter Circuit and Battery Connection

Figure 3 shows the ESS battery model with an integrating buck-boost BDC to charge the EV battery. The theoretical equation for the buck-boost bidirectional converter is presented below:

The equations describe the relationship between input and output power. Equation 4 shows that input power (P_{in}) is the product of input voltage (V_{in}) and input current (I_{in}). Equation 5 defines output power (P_{out}) as the product of output voltage (V_{out}) and output current (I_{out}). Equation 6 expresses output power in terms of output voltage squared divided (V_{out}^2) by load resistance (R).

$$P_{in} = V_{in} I_{in} \quad [4]$$

$$P_{out} = V_{out} I_{out} \quad [5]$$

$$P_{out} = \frac{V_{out}^2}{R} \quad [6]$$

Equation 7 defines the duty cycle (D) of a converter as the ratio of the absolute value of the output voltage $|V_{out}|$ to the sum of the input voltage (V_{in}) and the absolute output voltage. The duty cycle determines the proportion of time the switch is on during each cycle, affecting the overall voltage regulation and power transfer efficiency of the converter.

$$D = \frac{|V_{out}|}{V_{in} + |V_{out}|} \quad [7]$$

Equation 8 represents the inductor current (I_L) in a converter, calculated as the product of the input voltage V_{in} and the duty cycle D , divided by the resistance R and the square $(1 - D)$. This equation helps determine the current flowing through the inductor, which is critical for analyzing the converter's operation and performance, particularly in managing energy storage and power delivery.

$$I_L = \frac{V_i D}{R(1 - D)^2} \quad [8]$$

Equations 9 and 10 describe the maximum (I_{max}) and minimum inductor currents (I_{min}) in a converter, where (V_{in}) is the input voltage, (D) in duty cycle, (R) is the load resistance, (T) is switching time, and (L) is inductor.

$$I_{max} = \frac{V_{in} D}{R(1-D)^2} + \frac{V_{in} DT}{2L} \quad [9]$$

$$I_{min} = \frac{V_{in} D}{R(1-D)^2} - \frac{V_{in} DT}{2L} \quad [10]$$

Equation 11 calculates the minimum inductance (L_{min}) necessary for proper operation of a converter, given $(\frac{(1-D)^2 R}{2f_s})$ where (D) is the duty cycle, (R) is the resistance, and (f_s) is the switching frequency. This equation helps ensure that the inductor is sized correctly to maintain circuit stability and minimize current ripple.

$$L_{min} = \frac{(1-D)^2 R}{2f_s} \quad [11]$$

Equation 12 calculates the capacitance (C) needed in a converter circuit, given by $(\frac{D}{Rr f_s})$ where (D) is the duty cycle, (R) is the load resistance, (r) is a ripple voltage, and (f_s) is the switching frequency. This equation helps determine the appropriate capacitor value to ensure stable voltage regulation and minimize voltage ripple in the circuit.

$$C = \frac{D}{Rr f_s} \quad [12]$$

However, this simulation focuses only on the battery part of ESS by considering different battery types, connections, and aging factors. The Li-Ion batteries are connected in three ways: series connection, parallel connection, and series-parallel connection, as shown in Figures 4, 5, and 6. The voltage input to the ESS is set at 600 V. The function of the buck-boost bidirectional converter is to adjust the directional flow of charging and discharging with the current stability to the EV battery from ESS by using the proportional-integral (PI) Controller algorithm. The connection arrangement of the battery was compared between series, parallel, and series-parallel configurations. Finally, the battery aging factor was applied to compare with a non-aging battery only for Li-Ion battery in MATLAB because Li-Ion batteries exhibit more complex degradation mechanisms compared to Pb-Acid and NiCd batteries and limitations on MATLAB block. In this simulation, the battery is cycled 50 times to show the effect of aging and compare it with a battery with a zero life cycle. A new battery means zero life cycle. A new battery that has not undergone any charge or discharge cycles. This battery is used as a baseline to compare the effects

of aging. A battery that has been cycled 50 times to simulate aging. This battery is used to study the impact of 50 charge or discharge cycles on its performance. All these factors were observed and analyzed, including the battery's SOC, voltage, and current performance (Singh et al., 2023).

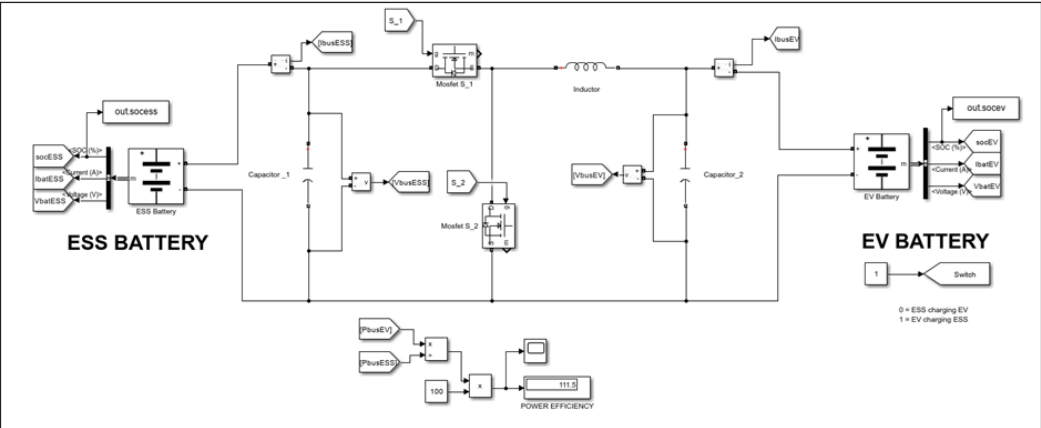


Figure 3. The circuit design for different types of batteries and the aging factor of ESS and EV

In a series connection, the batteries are connected end-to-end, positive to negative, to increase the overall voltage while keeping the same capacity (Gong et al., 2015). The expressions for total voltage and total capacity are shown in Equations 13 and 14.

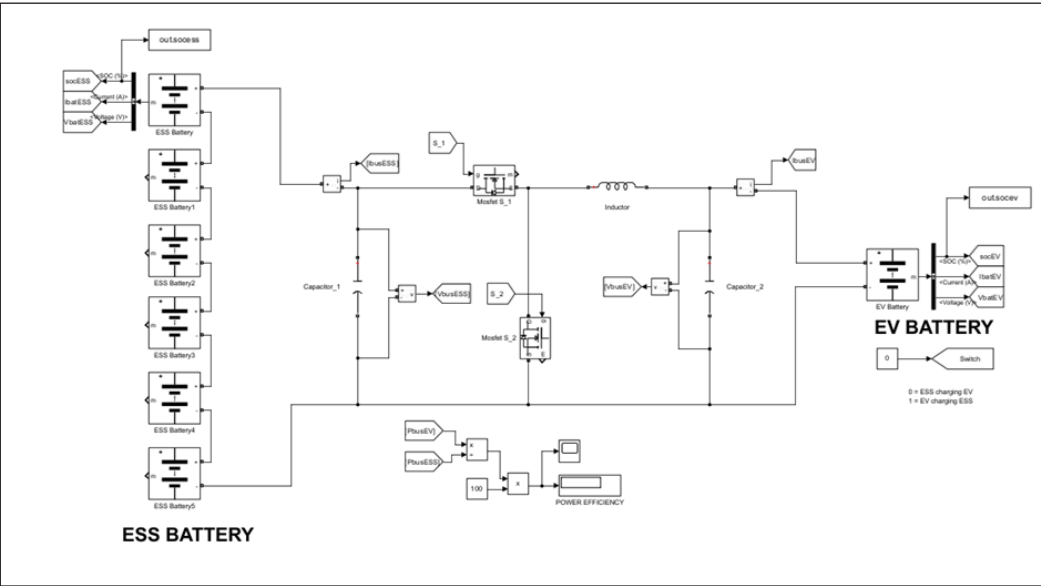


Figure 4. The circuit design of the system for series connection battery

$$\text{Voltage}_{\text{total}} = V_1 + V_2 + V_3 + V_n \tag{13}$$

$$\text{Capacity}_{\text{total}} = \text{Capacity}_1 = \text{Capacity}_2 = \text{Capacity}_3 = \text{Capacity}_n \tag{14}$$

In a parallel connection, the batteries are connected positive to positive and negative to negative to increase the overall capacity while keeping the voltage the same (Gong et al., 2015). The expression of total voltage and total capacity is shown in Equations 15 and 16.

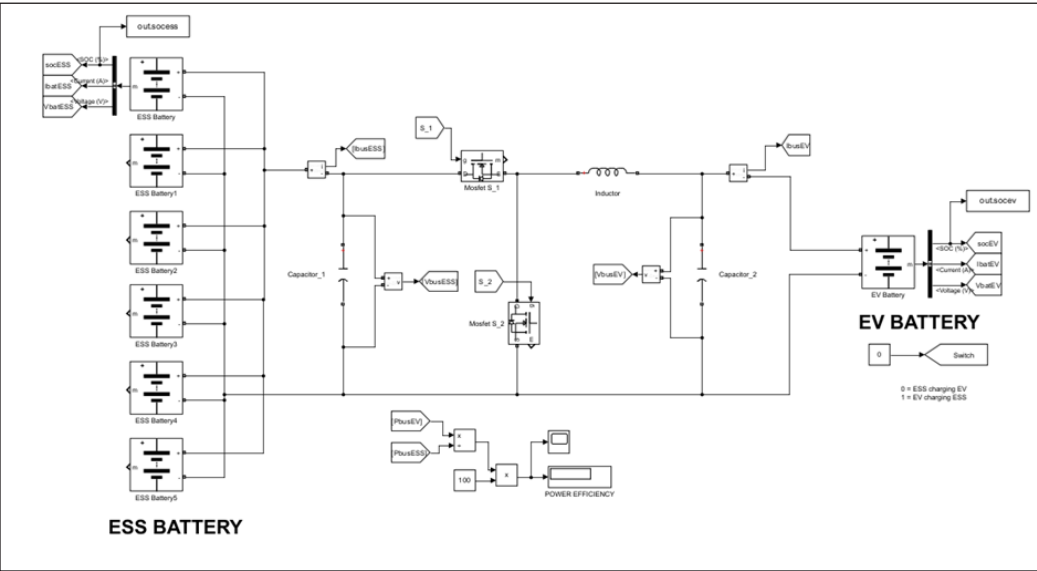


Figure 5. The circuit design of the system for parallel connection battery

$$V_{\text{total}} = V_1 = V_2 = V_3 = V_n \tag{15}$$

$$\text{Capacity}_{\text{total}} = \text{Capacity}_1 + \text{Capacity}_2 + \text{Capacity}_3 + \text{Capacity}_n \tag{16}$$

In a series-parallel connection, the batteries are connected, with some in series and others in parallel. In the series portion, batteries are connected positive to negative, increasing the overall voltage while keeping the same capacity. In the parallel portion, batteries are connected positive to positive and negative to negative, increasing the overall capacity while maintaining the same voltage (Gong et al., 2015). The expressions for total voltage and total capacity are shown in Equations 17 and 18. where n_s is the number of batteries in a series, V is the voltage of a single battery, and n_p is the number of parallel groups, and C is the capacity of a single battery.

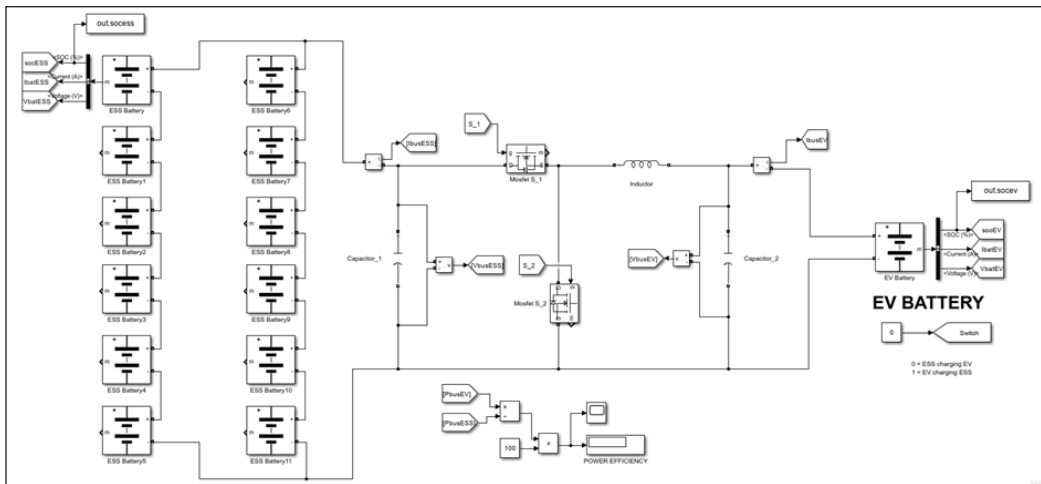


Figure 6. The circuit design of the system for series-parallel connection battery

$$V_{\text{total}} = n_s \times V \quad [17]$$

$$\text{Capacity}_{\text{total}} = n_p \times C \quad [18]$$

PI Controller Algorithm

Figures 7 and 8 present the charging and discharging control algorithms for the buck-boost bidirectional converter to integrate ESS into EV operation. A proportional-integral (PI)-based Pulse width Modulation (PWM) generator is implemented for controlling the bidirectional battery charger circuit using a buck-boost converter with constant-current (CC) 100 A and constant-voltage (CV) 400 V for the EV battery. The comparator compares the reference current and actual current, the output of the comparator generator error signal. The EV battery charges while the ESS battery discharges simultaneously during the buck operation. The converter's input voltage is the DC-link voltage V_{batESS} generated by the ESS battery, and the output of the converter is the battery voltage V_{batEV} . The control algorithm in Figure 7 regulates the charging process by controlling the two IGBT switches (S_1 and S_2). Initially, the DC-link voltage V_{batESS} energizes both the inductor and the EV battery. Once the inductor is fully energized, the battery is charged solely by the energy stored in the inductor. The algorithm compares the measured V_{batEV} with the desired EV battery voltage. The PI voltage controller then minimizes and eliminates the errors to ensure they are equal until the EV battery reaches 100% SOC.

In the boost operation, the control algorithm in Figure 8 regulates the discharging of the EV battery and the charging of the ESS battery simultaneously. The converter's input voltage is the DC-link voltage V_{batEV} generated by the EV battery, and the output of the converter is the battery voltage V_{batESS} . The control algorithm manages the discharging

process by controlling the two MOSFET switches (S_1 and S_2). Initially, the DC-link voltage V_{batEV} energizes the inductor and the ESS battery. Once the inductor is fully energized, the ESS battery is charged solely by the energy stored in the inductor. The algorithm compares the measured V_{batESS} with the desired ESS battery voltage. Figure 9 shows the operation switch of the BDC to change between two modes: Buck mode (charging the EV by discharging the ESS) and Boost mode (discharging the EV by charging the ESS). After the mode operation is selected, the battery current reference I_{bat_ref} sends a signal to the PI current controller, as shown in Figure 10, to control the PWM of the two MOSFETs.

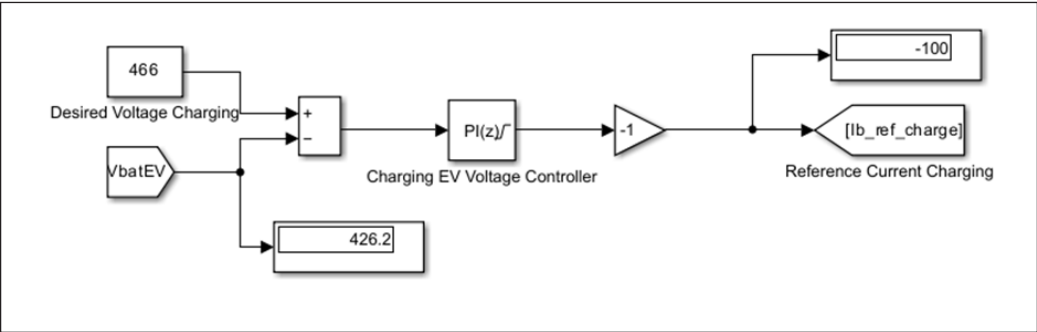


Figure 7. Reference current for charging EV operation

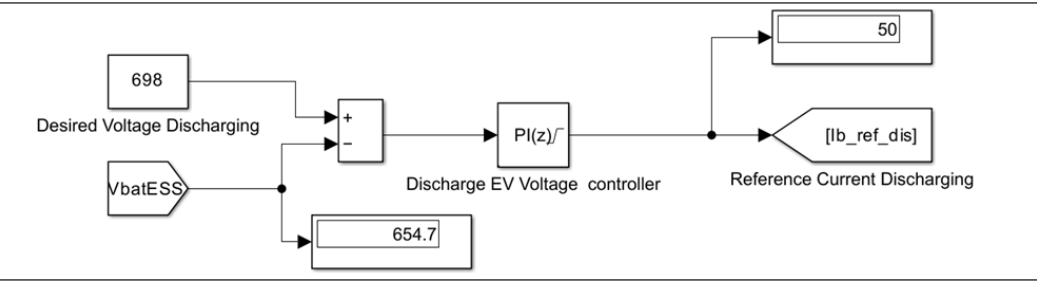


Figure 8. Reference current for discharging EV operation

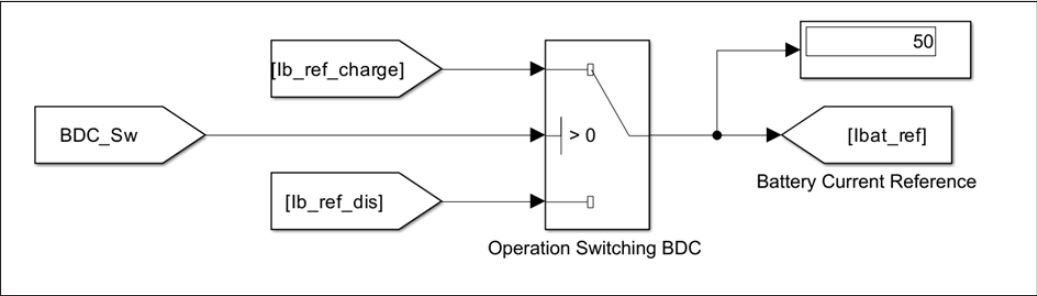


Figure 9. Operation switching of BDC

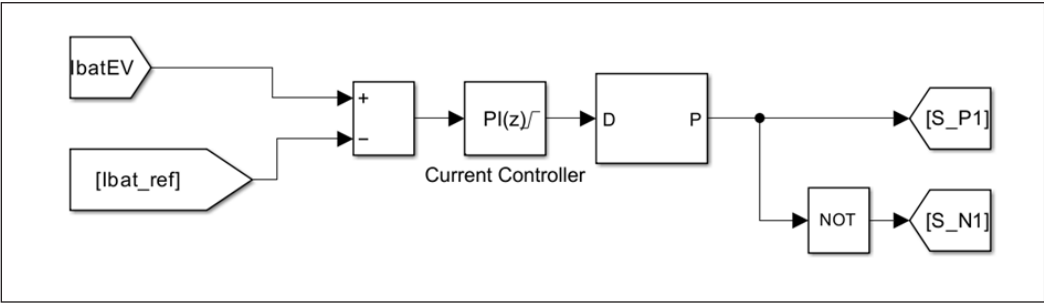
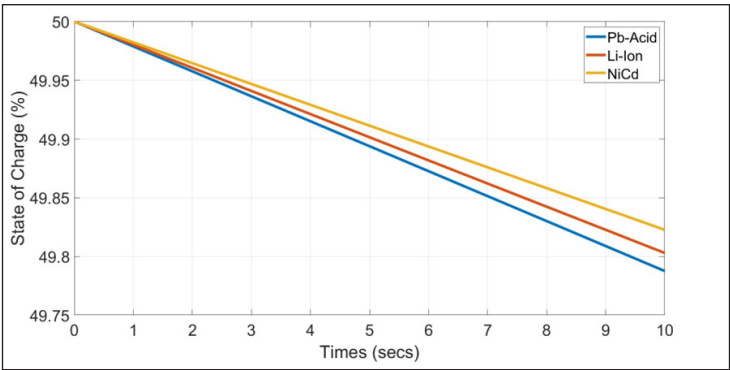


Figure 10. PI Controller used for PWM (Pulse Width Modulation) control

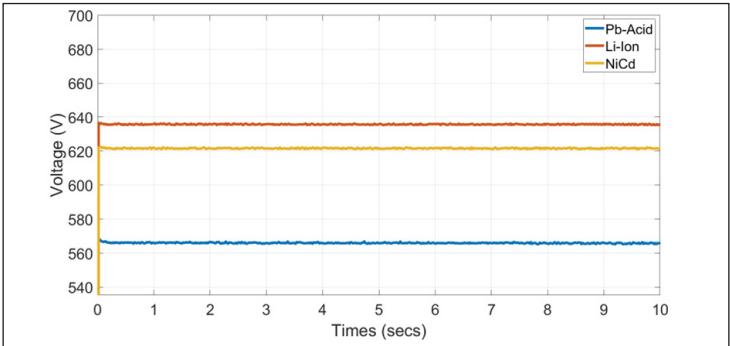
SIMULATION RESULTS

Case 1 – Battery Types

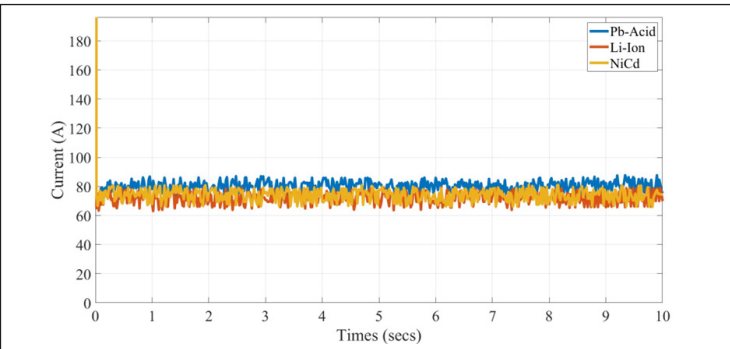
Figure 11 illustrates the SOC, voltage, and current of three different types of batteries: Pb-Acid, Li-Ion, and NiCd over time. All three batteries show a decrease in SOC, as expected during discharge. The Pb-Acid battery (blue line) has the steepest slope, indicating the fastest discharge rate. In contrast, the Li-Ion battery (red line) has a moderate slope, showing a slower discharge rate compared to Pb-Acid but faster than NiCd. The NiCd battery (yellow line) has the least steep slope, indicating the slowest discharge rate. Initially, time, $t=0$, all three batteries start with a SOC of 50%. By $t=10$, the SOC of the Pb-Acid battery drops to about 49.75%, the Li-Ion battery to around 49.8%, and the NiCd battery maintains the highest SOC at about 49.85%. It is observed that the SOC of Pb-Acid, Li-Ion, and NiCd dropped by 0.5%, 0.4%, and 0.3% in 10 seconds, respectively. The Li-Ion battery has the highest nominal voltage at around 640 V, followed by NiCd at approximately 620 V and Pb-Acid at about 560 V, showing minimal fluctuations over time. It was found that the nominal voltage of Li-Ion was around 14.29% higher than the nominal voltage of Pb-Acid batteries for a defined period $t=10$. The current readings reveal that Pb-Acid delivers a higher and more stable current, around 80 A, indicating a more constant load, while the Li-Ion and NiCd batteries, both around 75 A, show more fluctuations, reflecting dynamic responses to load changes. This trend highlights that Pb-Acid batteries, with higher internal resistance and lower efficiency, discharge more quickly. In contrast, Li-Ion batteries, with higher energy density and better efficiency, discharge more slowly. Despite having lower energy density than Li-Ion, NiCd batteries are robust and have a lower self-discharge rate, resulting in the slowest SOC decrease among the three types. Overall, the observed current and voltage levels align with the characteristics of these battery types, with Pb-Acid typically providing higher discharge currents compared to Li-Ion and NiCd.



(a)



(b)

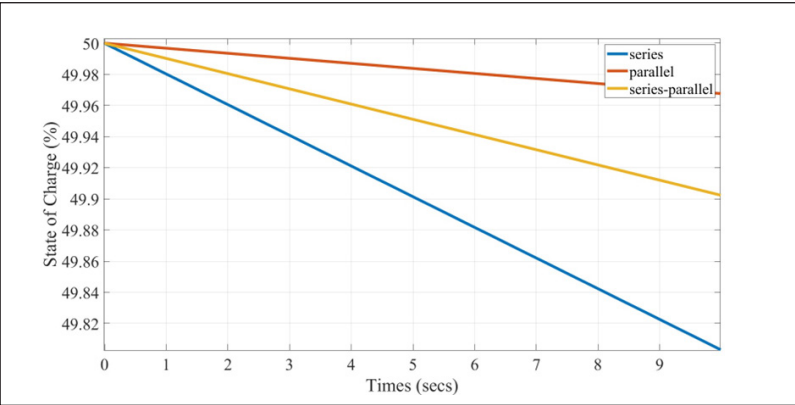


(c)

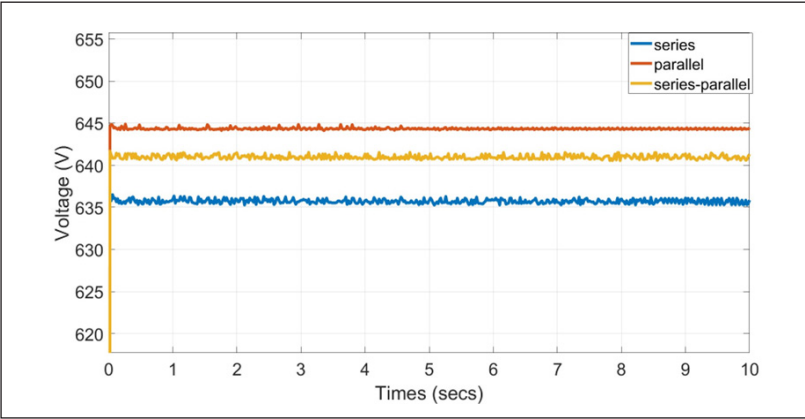
Figure 11. Result of battery Li-Ion, Pb-Acid, NiCD (a) SOC, (b) Voltage, (c) Current of different types of battery

Case 2 – Different Connection Arrangement of Battery

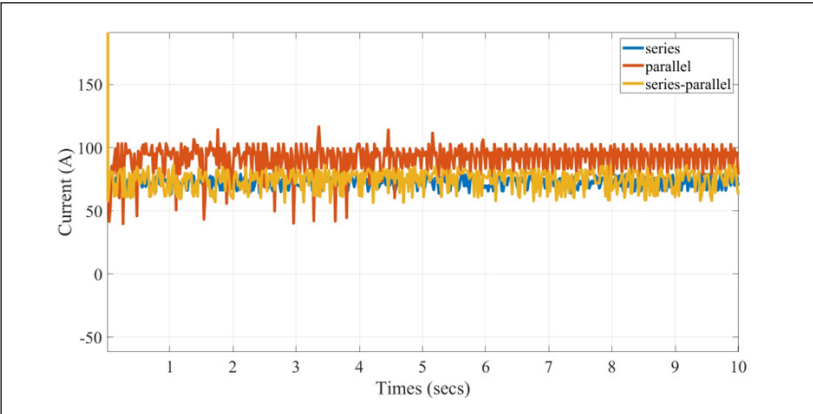
Figure 12 illustrates the SOC voltage and current for three battery configurations, series, parallel, and series-parallel, over time using a Li-Ion battery. All configurations show a decrease in SOC during discharge, with the series configuration (blue line) exhibiting the



(a)



(b)



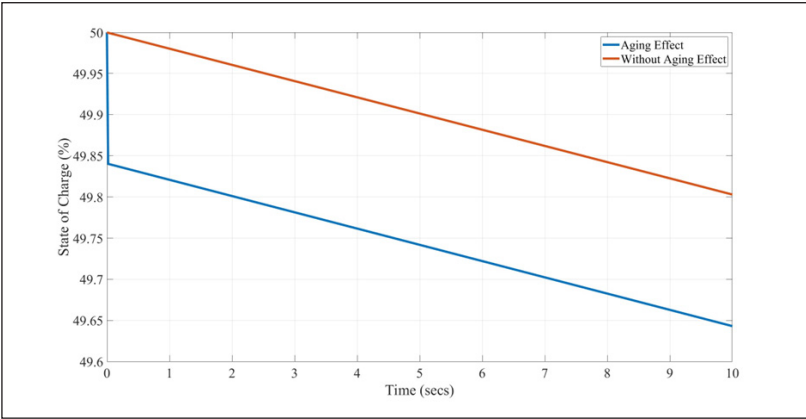
(c)

Figure 12. Result of battery connection (a) SOC, (b) Voltage, (c) Current of different battery arrangement

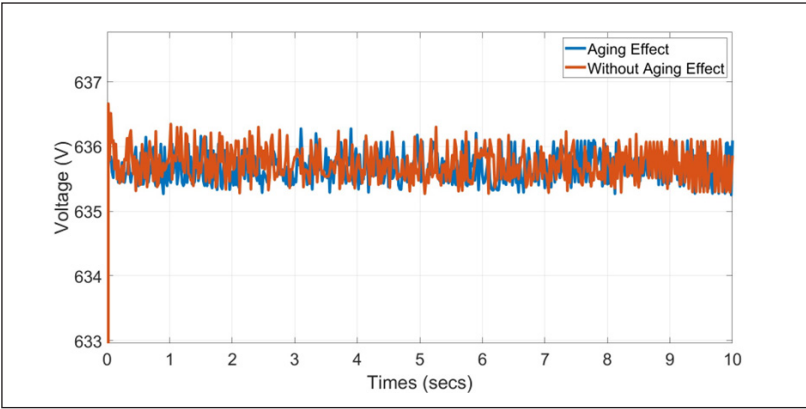
steepest slope, indicating the fastest discharge rate, dropping from 50% to about 49.82% by $t=10$ seconds. The parallel configuration (red line) shows a moderate discharge rate, decreasing to around 49.96%, while the series-parallel configuration (yellow line) maintains about 49.93% SOC, indicating the slowest discharge rate. Initially, all configurations start with a SOC of approximately 50%. As time progresses, the series configuration consumes energy more rapidly, while the series-parallel configuration retains charge most efficiently, making it suitable for applications requiring prolonged energy availability. The battery's SOC for series, parallel and series-parallel configurations dropped by 0.18%, 0.04%, and 0.07%, respectively. Voltage stability is observed across all configurations, with the parallel configuration having the highest nominal voltage, averaging around 645 V, followed by series-parallel at approximately 640 V and series at about 635 V. Minimal voltage fluctuations suggest reliable performance under load. Current fluctuations indicate varying load conditions, with the parallel configuration showing the highest and most variable current, averaging around 100 A, the series-parallel configuration averaging about 85 A with moderate fluctuations, and the series configuration having the lowest and most stable current, averaging around 70 A, indicating consistent performance under load. Overall, the series-parallel configuration demonstrates the best balance of discharge rate, voltage stability, and current consistency, making it ideal for applications requiring steady and prolonged energy output.

Case 3 – Battery Aging Factor

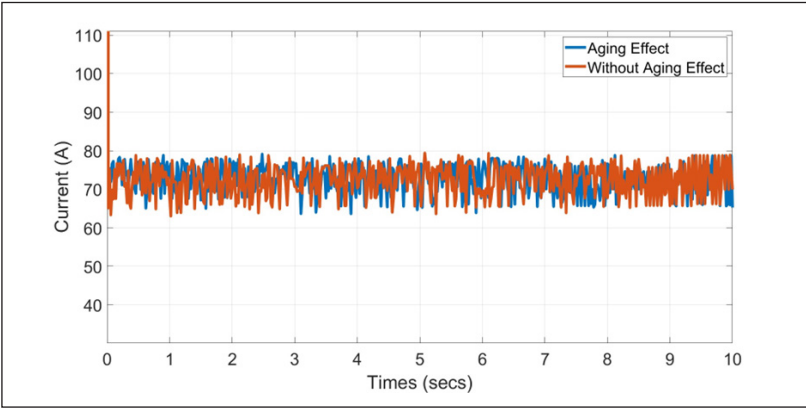
Figure 13 shows the SOC over time with and without the aging effect only for Li-Ion because the batteries exhibit more complex degradation mechanisms compared to Pb-Acid and NiCd batteries. Both lines decrease over time, as expected during battery discharge. The line with the aging effect (blue) has a steeper slope, indicating a faster discharge rate. In comparison, the line without the aging effect (orange) has a gentler slope, showing slower discharge and better efficiency. At the start ($t=0$), both configurations begin with a SOC of approximately 50%. By time $t=10$, the SOC with aging decreases to about 49.6%, whereas it remains higher at around 49.85% without aging. It was found that the SOC of a battery without aging decreased by 0.15% after 10 seconds, but the SOC of an aged battery decreased by 0.4%. This illustrates that the battery, without aging, retains its charge better, reflecting optimal performance. The graph highlights that aging leads to a faster SOC decline, emphasizing the importance of managing battery health. Additionally, the voltage with aging is slightly lower and exhibits moderate fluctuations, indicating increased internal resistance, while without aging, the voltage remains higher and more stable. The current with aging is lower overall and fluctuates slightly, whereas, without aging, the current is higher and more stable, reflecting better battery health and consistent current delivery under load. Overall, the battery without aging shows more stable performance across all metrics.



(a)



(b)



(c)

Figure 13. The result of the comparison of aging batteries and non-aging batteries is (a) SOC, (b) Voltage, and (c) Current for the aging factor of the battery

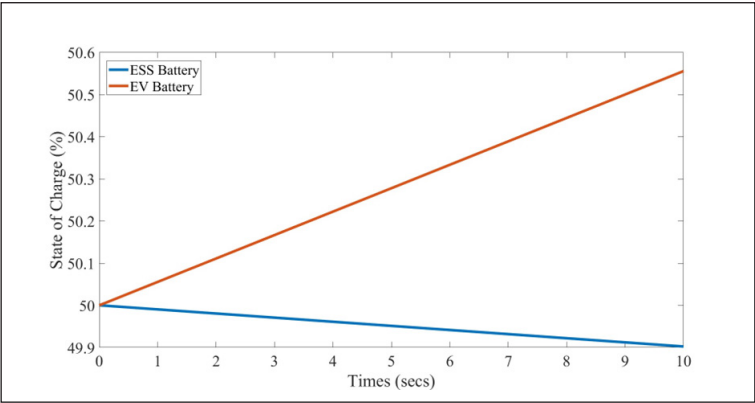
DISCUSSION

The study examines the performance of different battery types and configurations in various scenarios. Pb-Acid batteries discharge the fastest due to higher internal resistance, while Li-Ion batteries offer moderate discharge rates with better efficiency and energy density. NiCd batteries exhibit the slowest discharge, benefiting from robustness and low self-discharge rates. In terms of connection arrangements, the series configuration discharges rapidly, the parallel configuration maintains high voltage with variable current, and the series-parallel configuration provides a balance of efficient energy retention, stable voltage, and consistent current. Regarding the effects of aging, batteries without aging retain charge better, maintain more stable voltage and current, and underscore the importance of battery health management. Overall, Li-Ion batteries in a series-parallel configuration are ideal for ESS applications to charge EV batteries, offering a balance of efficiency, stability, and adaptability to varying load conditions. Figure 14 illustrates the charging of EVs by discharging ESS using selected battery properties and connections. The SOC graph shows the EV battery's charge increasing from 50% to approximately 50.6% by $t=10$ seconds, indicating efficient charging, while the ESS battery's SOC decreases slightly from 50% to about 49.9%, reflecting its role as the energy source. The voltage graph indicates that the ESS battery maintains a stable voltage of around 600 V, while the EV battery holds a steady voltage of about 450 V, suggesting consistent performance.

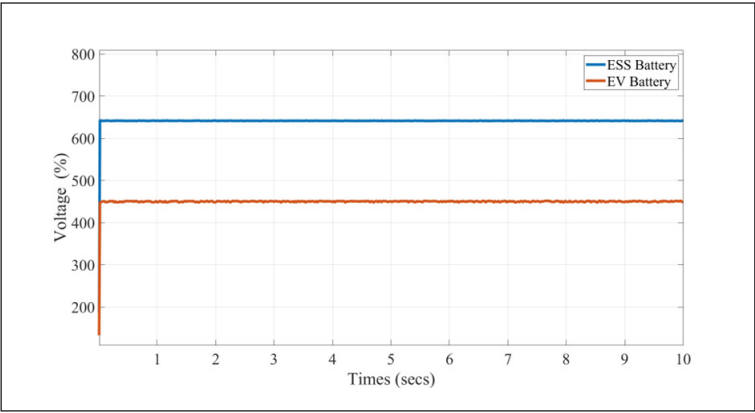
The current graph shows that the EV battery has a higher average current, around 100 A, with more fluctuations. In contrast, the ESS battery maintains a lower average current, around 75 A, with less variability. This demonstrates effective energy transfer, with the ESS supplying steady energy while the EV battery charges efficiently, highlighting the system's reliability and effectiveness. From Equations 2 and 3 charging and discharging, the EV battery can receive a current of 100 A, fully charging from 0% to 100% SOC in approximately 30 minutes. Meanwhile, the ESS will fully discharge its 100 Ah capacity with a discharging current of 75 A in about 1 hour and 33 minutes. This demonstrates that the ESS, with a constant current controlled by a PI controller to minimize losses, can act as a backup supply, supporting nearly three complete charges of the EV battery with good efficiency.

CONCLUSION

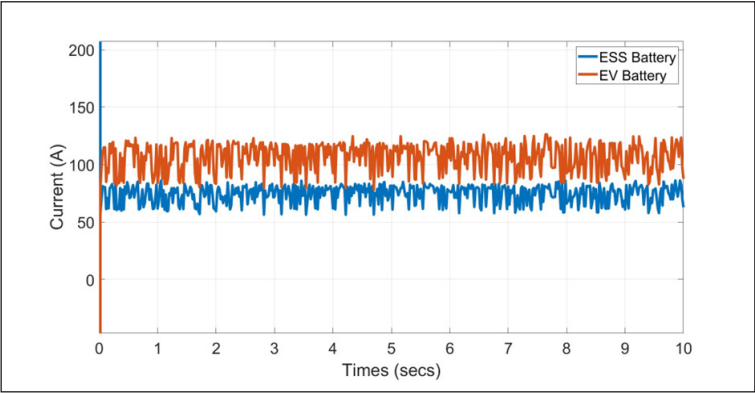
The simulation study successfully developed an EV charging system model using MATLAB. The analysis showed that Li-Ion batteries are most suitable for ESS due to their high energy density and stable voltage profile. The study also found that series-parallel battery connections enhance performance by 0.07%, offering balanced load distribution and improved maintenance. Additionally, the impact of battery aging was highlighted, emphasizing the need for effective battery management. As a result of the selected Li-Ion



(a)



(b)



(c)

Figure 14. Graph of Charging EV by discharging ESS (a) SOC, (b) Voltage, (c) Current for best battery properties and connection arrangement

battery with no aging factor and series-parallel connection, the EV battery can receive a current of 100 A, fully charging from 0% to 100% SOC in approximately 30 minutes. Meanwhile, the ESS will fully discharge its 100 Ah capacity with a discharging current of 75 A in about 1 hour and 33 minutes. This demonstrates that the ESS, with a constant current controlled by a PI controller to minimize losses, can act as a backup supply, supporting nearly three complete charges of the EV battery with good efficiency. This research provides valuable insights into the automotive and renewable energy sectors, promoting more efficient and sustainable energy solutions. Future work should focus on advancements in battery technology and management systems to further optimize ESS and EV performance.

ACKNOWLEDGMENTS

The authors sincerely thank the individuals and organizations contributing to this research project. First, the authors would like to thank Petronas Research Sdn. Bhd. for their support. The authors also thank the CHAdEMO Association for their continuous technical support. Finally, the authors would like to thank the College of Engineering, Universiti Teknologi MARA, for the excellent facility provided for the research, administrative support, and technical assistance.

REFERENCES

- Alghamdi, T. G., Said, D., & Mouftah, H. T. (2020). Decentralized game-theoretic approach for D-EVSE based on renewable energy in smart cities. In *ICC 2020-2020 IEEE International Conference on Communications (ICC)* (pp. 1-6). IEEE Publishing. <https://doi.org/10.1109/ICC40277.2020.9148718>
- Al-Hanahi, B., Ahmad, I., Habibi, D., Pradhan, P., & Masoum, M. A. S. (2022). An optimal charging solution for commercial electric vehicles. *IEEE Access*, 10, 46162–46175. <https://doi.org/10.1109/ACCESS.2022.3171048>
- Arfeen, Z. A., Khairuddin, A. B., Munir, A., Azam, M. K., Faisal, M., & Arif, M. S. B. (2020). En route of electric vehicles with the vehicle to grid technique in distribution networks: Status and technological review. *Energy Storage*, 2(2), Article e115. <https://doi.org/10.1002/est2.115>
- Bais, A., Subhedar, D., & Panchal, S. (2024). Experimental investigations of a novel phase change material and nano-enhanced phase change material based passive battery thermal management system for Li-ion battery discharged at a high C rate. *Journal of Energy Storage*, 103, Article 114395. <https://doi.org/10.1016/j.est.2024.114395>
- Cho, I., Lee, P. Y., & Kim, J. (2019). Analysis of the effect of the variable charging current control method on cycle life of li-ion batteries. *Energies*, 12(15), Article 3023. <https://doi.org/10.3390/en12153023>
- Gong, X., Xiong, R., & Mi, C. C. (2015). Study of the characteristics of battery packs in electric vehicles with parallel-connected lithium-ion battery cells. *IEEE Transactions on Industry Applications*, 51(2), 1872–1879. <https://doi.org/10.1109/TIA.2014.2345951>

- Hannan, M. A., Hoque, M. M., Hussain, A., Yusof, Y., & Ker, P. J. (2018). State-of-the-art and energy management system of lithium-ion batteries in electric vehicle applications: Issues and recommendations. *IEEE Access*, 6, 19362–19378. <https://doi.org/10.1109/ACCESS.2018.2817655>
- Jeon, S. U., Park, J. W., Kang, B. K., & Lee, H. J. (2021). Study on battery charging strategy of electric vehicles considering battery capacity. *IEEE Access*, 9, 89757–89767. <https://doi.org/10.1109/ACCESS.2021.3090763>
- Jiang, Q., Zhang, Y., Liu, Y., Xu, R., Zhu, J., & Wang, J. (2024). Structural optimization of serpentine channel water-cooled plate for lithium-ion battery modules based on multi-objective Bayesian optimization algorithm. *Journal of Energy Storage*, 91, Article 112136. <https://doi.org/10.1016/j.est.2024.112136>
- Kumar, R. R., Bharatiraja, C., Udhayakumar, K., Devakirubakaran, S., Sekar, K. S., & Mihet-Popa, L. (2023). Advances in batteries, battery modeling, battery management system, battery thermal management, SOC, SOH, and charge/discharge characteristics in EV applications. *IEEE Access*, 11, 105761–105809. <https://doi.org/10.1109/ACCESS.2023.3318121>
- Lehtola, T. A., & Zahedi, A. (2021). Electric vehicle battery cell cycle aging in vehicle to grid operations: A review. *IEEE Journal of Emerging and Selected Topics in Power Electronics*, 9(1), 423–437. <https://doi.org/10.1109/JESTPE.2019.2959276>
- Li, S., Zhao, P., Gu, C., Li, J., Huo, D., & Cheng, S. (2023). Aging mitigation for battery energy storage system in electric vehicles. *IEEE Transactions on Smart Grid*, 14(3), 2152–2163. <https://doi.org/10.1109/TSG.2022.3210041>
- Miao, Y., Hynan, P., Von Jouanne, A., & Yokochi, A. (2019). Current li-ion battery technologies in electric vehicles and opportunities for advancements. *Energies*, 12(6), 1–20. <https://doi.org/10.3390/en12061074>
- Rosewater, D. M., Copp, D. A., Nguyen, T. A., Byrne, R. H., & Santoso, S. (2019). Battery energy storage models for optimal control. *IEEE Access*, 7, 178357–178391. <https://doi.org/10.1109/ACCESS.2019.2957698>
- Said, D. (2021). Intelligent photovoltaic power forecasting methods for a sustainable electricity market of smart micro-grid. *IEEE Communications Magazine*, 59(7), 122–128. <https://doi.org/10.1109/MCOM.001.2001140>
- Said, D., & Elloumi, M. (2022). A new false data injection detection protocol based machine learning for P2P energy transaction between CEVs. In *2022 IEEE International Conference on Electrical Sciences and Technologies in Maghreb (CISTEM)* (Vol. 4, pp. 1–5). IEEE Publishing. <https://doi.org/10.1109/CISTEM55808.2022.10044067>
- Said, D., Cherkaoui S., & Khoukhi, L. (2015). Guidance model for EV charging service. In *2015 IEEE International Conference on Communications (ICC)* (pp. 5765–5770). IEEE Publishing. <https://doi.org/10.1109/ICC.2015.7249241>
- Samadani, E., Panchal, S., & Mastali, M. (2012). *Battery Life Cycle Management for Plug-In Hybrid Electric Vehicle (Phevs) and Electric Vehicles (Evs)*. [Transport Canada Report]. University of Waterloo.
- Schommer, A., Sciortino, D. D., Morrey, D., & Collier, G. (2024). Experimental investigation of power available in lithium-ion batteries. *Journal of Power Sources*, 618, Article 235168. <https://doi.org/10.1016/j.jpowsour.2024.235168>

- Singh, A., Pal, K., & Vishwakarma, C. B. (2023). State of charge estimation techniques of Li-ion battery of electric vehicles. *E-Prime - Advances in Electrical Engineering, Electronics and Energy*, 6, Article 100328. <https://doi.org/10.1016/j.prime.2023.100328>
- Sundararajan, R. S., & Iqbal, M. T. (2021). Dynamic modelling of a solar energy system with vehicle to home and vehicle to grid option for newfoundland conditions. *European Journal of Electrical Engineering and Computer Science*, 5(3), 45-52. <https://doi.org/10.24018/ejece.2021.5.3.329>
- Talele, V., Morali, U., Khaboshan, H. N., Patil, M. S., Panchal, S., Fraser, R., & Fowler, M. (2024). Improving battery safety by utilizing composite phase change material to delay the occurrence of thermal runaway event. *International Communications in Heat and Mass Transfer*, 155, Article 107527. <https://doi.org/10.1016/j.icheatmasstransfer.2024.107527>
- Timilsina, L., Badr, P. R., Hoang, P. H., Ozkan, G., Papari, B., & Edrington, C. S. (2023). Battery degradation in electric and hybrid electric vehicles: A survey study. *IEEE Access*, 11, 42431–42462. <https://doi.org/10.1109/ACCESS.2023.3271287>
- Tran, M. K., DaCosta, A., Mevawalla, A., Panchal, S., & Fowler, M. (2021). Comparative study of equivalent circuit models performance in four common lithium-ion batteries: LFP, NMC, LMO, NCA. *Batteries*, 7(3), Article 51. <https://doi.org/10.3390/batteries7030051>
- Umair, M., Hidayat, N. M., Ahmad, A. S., Ali, N. H. N., Mawardi, M. I. M., & Abdullah, E. (2024). A renewable approach to electric vehicle charging through solar energy storage. *PLoS ONE*, 19(2), Article e0297376. <https://doi.org/10.1371/journal.pone.0297376>

Review Article

Thematic Trends on Data Quality Studies in Big Data Analytics: A Review

Nazliah Chikon, Shuzlina Abdul-Rahman* and Syaripah Ruzaini Syed Aris

College of Computing, Informatics and Mathematics, Universiti Teknologi MARA, 40000 Shah Alam, Selangor, Malaysia

ABSTRACT

Data quality has become a critical issue in research and practice in the era of exponential data generation and increasing reliance on big data analytics (BDA) across industries. This study conducts a thematic analysis of literature published between 2020 and 2024 to examine the prevailing trends, challenges, and advancements in data quality studies within the domain of BDA. Guided by the systematic thematic review methodology, the research analysed 34 peer-reviewed studies identified from SCOPUS and Web of Science (WoS) databases, using qualitative data analysis tools such as ATLAS.ti. The findings reveal five major themes: Ontology and Data Quality Frameworks, Big Data Analytics in Various Industries, Machine Learning and AI Integration, Governance and Data Stewardship, and Tools and Techniques for Data Analysis. These themes highlight a shift towards interdisciplinary approaches, integrating advanced technologies like Artificial Intelligence (AI) and the Internet of Things (IoT) to address data quality issues. Limitations include potential selection bias from database restrictions and the exclusion of subscription-based journals, which may limit the generalisability of the findings. The study contributes to the theory by providing a comprehensive synthesis of data quality trends and their implications across various sectors. Methodologically, it demonstrates the utility of thematic analysis for consolidating diverse research. Practically, the insights inform data practitioners and policymakers on governance and technological strategies for

ensuring data integrity. This review is original in its systematic exploration of thematic trends in data quality, offering a valuable roadmap for future research and addressing the critical intersection of data quality and BDA.

ARTICLE INFO

Article history:

Received: 12 August 2024

Accepted: 07 February 2025

Published: 26 March 2025

DOI: <https://doi.org/10.47836/pjst.33.3.07>

E-mail addresses:

nazliah.uitm@gmail.com (Nazliah Chikon)

shuzlina@uitm.edu.my (Shuzlina Abdul Rahman)

ruzaini@uitm.edu.my (Syaripah Ruzaini Syed Aris)

*Corresponding author

Keywords: Artificial intelligence, big data analytics, data analytics, data quality, governance

INTRODUCTION

In an era characterised by an exponential increase in data generation and computational capabilities, the role of data quality within Big Data Analytics (BDA) has become paramount. As various sectors, including shipping, facilities management, and healthcare, increasingly rely on big data to drive decision-making and operational efficiency, the integrity and reliability of this factor cannot be overstated. Barba-González et al. (2024) emphasised that data quality should be the cornerstone of Artificial Intelligence (AI) initiatives from the onset, where measurement and evaluation of data quality are crucial to determining its usability for specific tasks. This perspective is crucial as industries adopt digital transformations, venturing into domains like Shipping 4.0, where BDA serves as a disruptive force enhancing operational energy efficiency (Bui & Perera, 2021).

Moreover, integrating BDA with technologies such as the Internet of Things (IoT) is recognised as a strategic investment by firms aiming to differentiate themselves in competitive markets (Côte-Real et al., 2020). This integration also highlights the importance of data quality from sensor input in leveraging business value from BDA investments. The quality of sensor data is crucial in BDA, as errors like missing values, outliers, and drift can lead to incorrect decisions. Teh et al. (2020) provide a comprehensive review of sensor data quality issues and solutions, highlighting the importance of addressing these errors to ensure accurate insights.

The multifaceted impact of data quality is also evident in its role in enhancing machine learning (ML) readiness for large-scale datasets (Hart et al., 2022) and in driving data-driven decision-making in marketing (Johnson et al., 2021). Medeiros et al. (2021) identify the increasing necessity for organisations to establish robust data quality policies and processes as regulatory demands grow and the scope of database analyses broadens across various business areas. As industries evolve, expectations from big data also shift, demanding not only the collection and storage of vast amounts of data but also ensuring that this data is of high quality to generate accurate and actionable insights. Therefore, it will be interesting to see the trends and patterns that emerge in research integrating data quality in BDA in the literature and the direction of future research. The purpose of this article is to conduct a thematic analysis of discussions on data quality in the domain of BDA that have been published between 2020 and 2024.

METHODS

This section describes the methodology used in this thematic review. The term "thematic review" and the use of ATLAS.ti as a tool to conduct thematic review were introduced by Zairul (2020; 2021), Zairul et al. (2023), and Zairul and Zaremohzzabieh (2023). Clarke and Braun (2013) defined thematic analysis as a systematic process of identifying patterns and developing themes from a meticulous reading of the subject matter's contents (Zairul,

2021). The study employs Thematic Review FlowZ (TreZ), which is protected by copyright under the registration number CRLY2023W02032 (Zairul, 2023). The method is employed because the study's methodology adheres to the thematic analysis procedure for conducting literature reviews. Figure 1 illustrates the thematic review flow in TreZ.

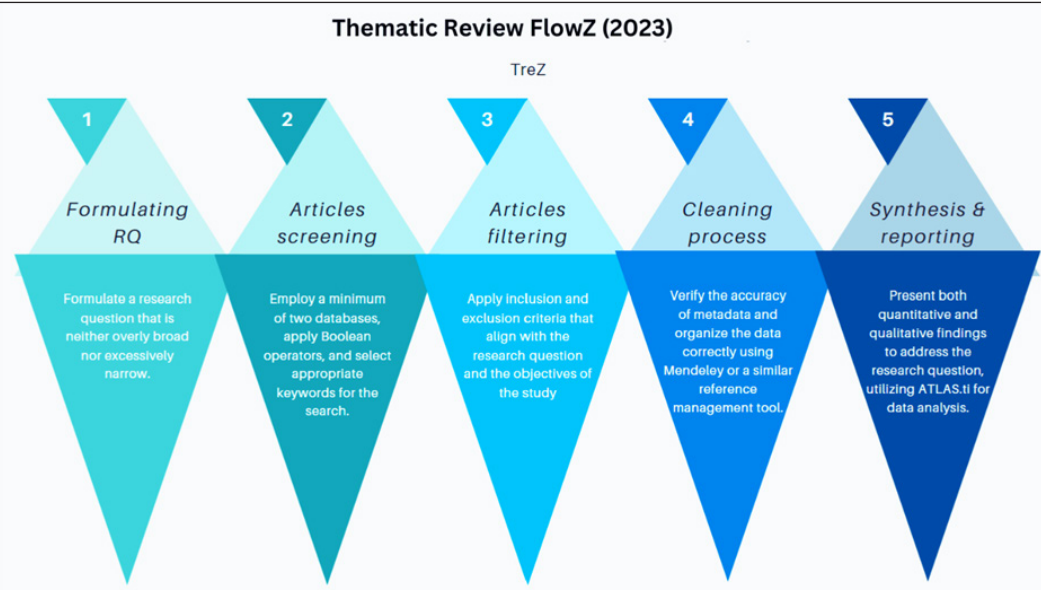


Figure 1. Thematic Review FlowZ (TreZ) (Zairul, 2023)

The TreZ outlines a systematic approach for conducting thematic literature reviews. The process begins with formulating a research question, defining the study's scope and focus, and ensuring the research is manageable and the conclusions are meaningful. The process followed with article screening using a minimum of two databases, Boolean operators and appropriate keywords for the search. Subsequently, articles are filtered using inclusion and exclusion criteria that are aligned with the research question and objective of the study. The fourth step involves a thorough double-checking of the metadata of the article and organising the data using reference management software like Mendeley. The final step is data extraction, where a thematic analysis is conducted using tools like ATLAS.ti to analyse the data and develop themes based on discussions of the subject matter in the selected articles (Figure 2). This methodology provides a structured framework for executing an exhaustive and effective literature review.

The next step involves identifying patterns and constructing themes to comprehend the trends related to data quality studies in BDA, as discussed in the literature from 2020 to 2024. To ensure a comprehensive and relevant analysis, the selection of literature for this review was guided by specific criteria: (1) the publication date range from 2020

(LIMIT-TO (PUBSTAGE, "final"))). This search strategy yielded 28 articles, indicating a substantial body of recent literature. Conversely, the search in WoS was smaller, using the same keywords across all fields without specific field restrictions, and focused only on open-access articles in English. This approach yielded 27 results. The difference in the number of articles retrieved from each database is primarily due to their varying coverage and focus and distinct indexing policies. Table 1 shows the search strings used, resulting in the initial search, which guarantees a thorough selection of studies aiming to encompass a broad spectrum of relevant literature.

Table 1
Search strings from Scopus and WoS

Source	Keywords	Results
SCOPUS	TITLE-ABS-KEY ("data quality" AND "big data analytics") AND PUBYEAR > 2019 AND PUBYEAR < 2025 AND (LIMIT-TO (DOCTYPE, "ar")) AND (LIMIT-TO (SRCTYPE, "j")) AND (LIMIT-TO (LANGUAGE, "English")) AND (LIMIT-TO (PUBSTAGE, "final")) AND (LIMIT-TO (OA, "all"))).	28 results
Web of Science (WoS)	"data quality" AND "big data analytics" (Topic) and Open Access and 2024 or 2023 or 2022 or 2021 or 2020 (Publication Years) and Article (Document Types) and English (Languages).	27 results

Upon merging the search results from both databases, we proceeded to identify and remove duplicate entries to maintain the uniqueness of each record in subsequent analyses. A total of 15 duplicates were identified and excluded from the dataset. The consolidated list of records then underwent rigorous screening based on predefined inclusion and exclusion criteria. These criteria were meticulously developed to align closely with the research question and objective of this study: (1) the record must be related to the objective of this study, and (2) the record must provide empirical findings. Six records were excluded during this phase as they did not meet the necessary criteria, ensuring that only the most pertinent studies were retained.

After this thorough screening process, 34 studies were selected for inclusion in this thematic review (TreZ). These studies collectively met all specified eligibility requirements and are expected to provide substantial insights pertinent to the research question. The systematic approach to selecting relevant papers highlights the diligence required to conduct a thorough review. This selection process ensures the inclusion of relevant data and minimises biases, contributing significantly to the reliability of the review's conclusions. This report serves as a foundational component of this review paper, providing clarity and transparency about the methods used in study selection, which is critical for replicability and trust in the findings presented. This process is illustrated in Figure 3.

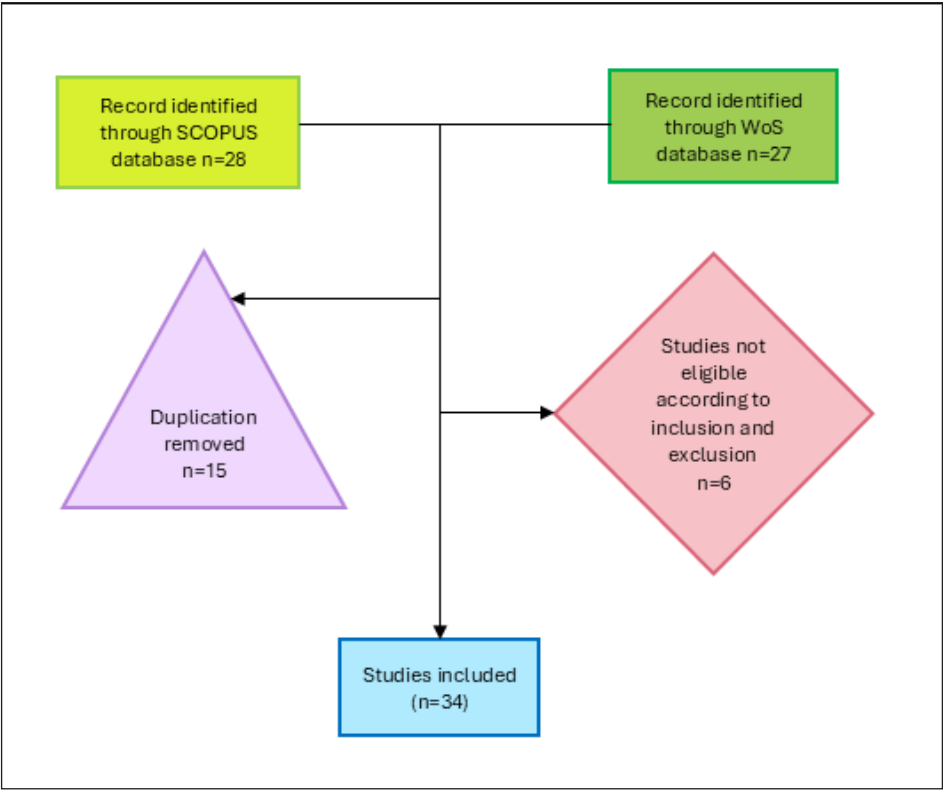


Figure 3. Selection process of studies in TreZ (Zairul, 2023)

RESULTS AND DISCUSSIONS

Following the meticulous methodology described in the previous section, 34 records were collected and analysed to identify the main themes and emerging patterns, which will help answer the research question. This analysis used ATLAS.ti, a qualitative data analysis tool that helps organise and interpret data systematically. Important results of the thematic review are summarised in this section. Both the quantitative and qualitative findings will be discussed next.

Quantitative Finding

Year of publications, industrial background, research location, and focal concept were used to analyse the study trends, which somewhat mirror the patterns of the data quality studies in the BDA domain to some extent. The number of relevant articles published gradually increased from 2020 to 2021 and reached a significant peak in 2022, as shown in Figure 4, but fell in 2023 before having a slight increase in 2024, indicating a continued interest in the study. Additionally, the trend of publications is illustrated in Figure 5.

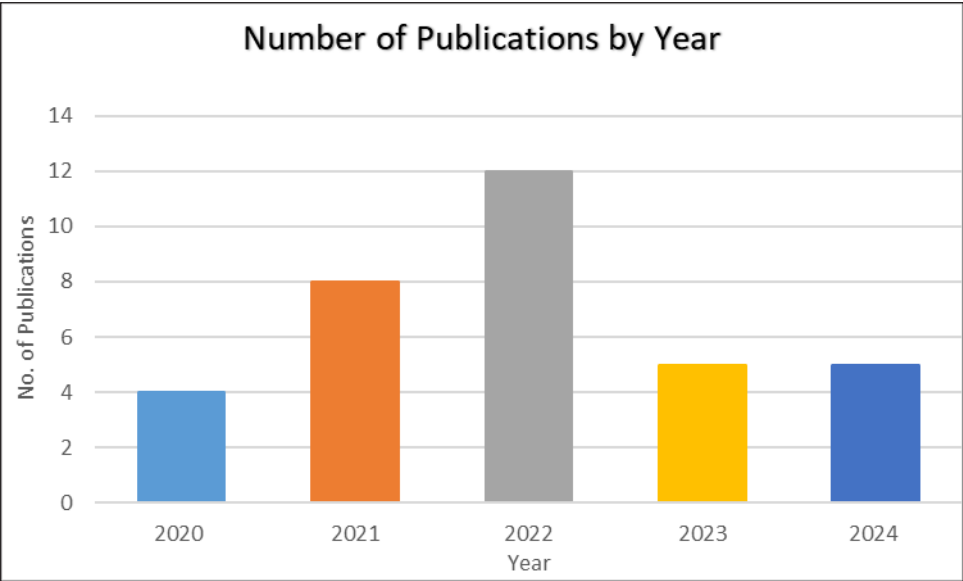


Figure 4. Paper breakdown by year of publication

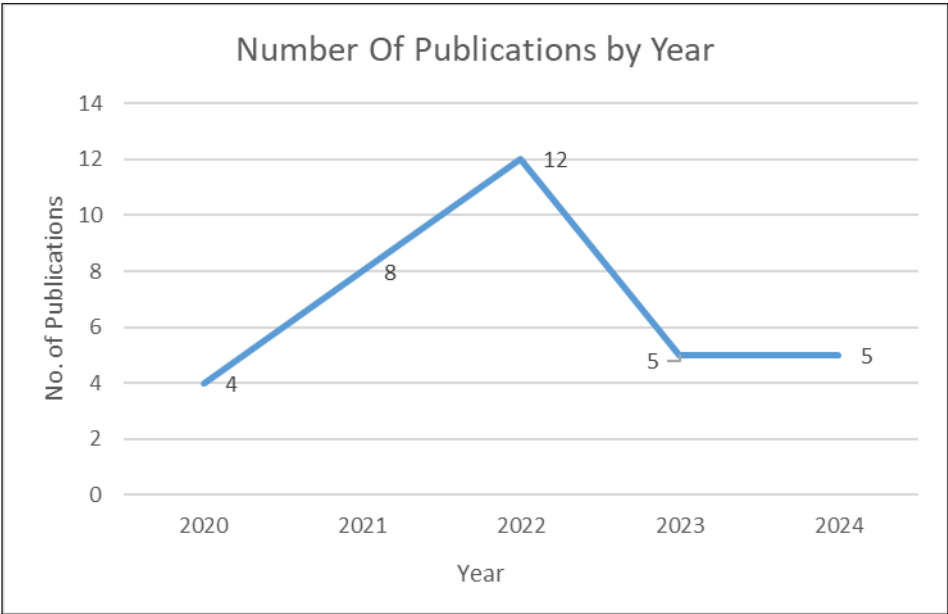


Figure 5. Publication trends from 2020 until 2024

The geographical dispersion reflects the global interest in BDA and disparities in research output that may correlate with different countries' economic, educational, and technological capacities. Figure 6 depicts the geographical distribution of articles published

across various countries from 2020 to 2024. In terms of publications, the topic of data quality in BDA is highly popular in developed countries, particularly in the United States of America (US) and the United Kingdom (UK), highlighting its significant role as a key player in the global research arena, especially within technology-driven sectors.

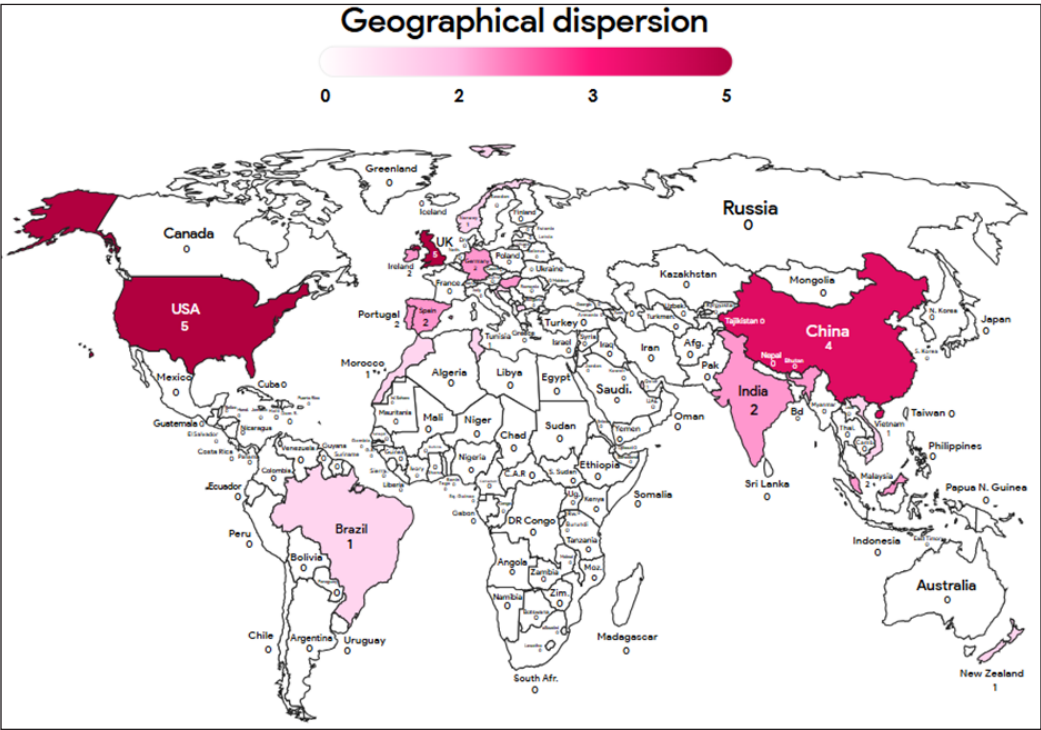


Figure 6. Geographical dispersion of articles published

The US and UK emerge as the frontrunners with the highest number of five publications. Most of the discussion is on data analytics and machine learning. (Hart et al., 2022), marketing insights for decision-making (Johnson et al., 2021), quality of Volunteer-contributed Geographic Data (VGI) (Zhang, 2022), use of BDA in purchasing and supply management (Patrucco et al., 2023), and factors of BDA success in various industries (Chen et al., 2022). The UK discussion, on the other hand, centres on the challenges of BDA implementation in the Facilities Management industry (Konanahalli et al., 2022), governance considerations of BDA in food consumer science (Timotijevic et al., 2022), AI in supply-chain decision-making (Hao & Demir, 2024), role-based access control using AI in Agriculture 4.0 (Spanaki et al., 2021), and aligning BDA capabilities (BDAC) and business models (BM) in small and medium-sized enterprises (SMEs) (Song et al., 2022). China was ranked third in terms of article numbers and had many technical developments in BDA, which include integration of Morris design with AI and BDA to enhance network

performance and user experience (F. Song, 2024), detection of environmental violators using a big data approach (Chang et al., 2021), data pricing and utility evaluation in big data trading market (Chen et al., 2023), and determinants of BDA adoption in decision-making, specifically in New Zealand, China, and Vietnam (Yu et al., 2022). This latest study is consistent with the former perspective on data quality, organisational support, and technology readiness (Chen et al., 2022; Konanahalli et al., 2022; Timotijevic et al., 2022). The rest of the nations having publications on the topic are Germany (2), Hungary (2), India (2), Ireland (2), Malaysia (2), Portugal (2), Spain (2), Brazil (1), Croatia (1), Macedonia (1), Morocco (1), New Zealand (1), Norway (1), Qatar (1), Tunisia (1) and Vietnam (1).

Next, the study identified the themes and concerns of shortlisted articles. Five themes, namely T1 (Ontology and Data Quality Frameworks), T2 (Big Data Analytics in Various Industries), T3 (Machine Learning and AI Integration), T4 (Governance and Data Steward), and T5 (Tools and Techniques for Data Analysis) were specifically identified from the articles examined following the study's focus topic, as shown in Table 2. Figure 7 illustrates themes discussed in the literature. Each theme plays a distinct role in propelling the field of BDA forward, showcasing an equitable emphasis on a wide array of aspects.

The consistent importance attributed to "Tools and Techniques for Data Analysis" and "Machine Learning and AI Integration" highlights their foundational significance. At the same time, the enduring relevance of "Ontology and Data Quality Frameworks", "Big Data Analytics in Various Industries", and "Governance and Data Stewardship" emphasises their crucial contributions to the discipline. This equilibrium approach guarantees a thorough and resilient advancement in BDA, tackling diverse challenges and seizing opportunities to foster innovative and efficient solutions.

Figure 2 depicts the word cloud derived from collecting all 34 articles focusing on data quality within the domain of BDA from 2020 to 2024. It displays significant themes and core concepts relevant to scholarly investigations during this timeframe. The word cloud is generated using ATLAS.ti, utilising frequency-based weighting to highlight terms that appear frequently across numerous articles, resulting in their larger size in the word cloud. The prevalence of terms like "data", "quality", "analytics", "big", and "management" emphasise their fundamental significance within the discipline. These terms highlight the importance of upholding high standards and dependability of data, emphasising managerial procedures to sustain and enhance data quality. Keywords such as "information", "business", "decision", and "performance" indicate the considerable influence of data quality on organisational decision-making and overall performance. At the same time, terms like "research", "systems", "processing", and "technologies" suggest a combination of theoretical underpinnings and practical methodologies in the field.

In addition to that, operational terms like "implementation", "analysis", "models", "ai", and "tools" suggest the utilisation of analytical techniques and technological tools

to ensure the integrity of data. The terms "value", "adoption", and "impact" emphasise the broader consequences and advantages of implementing data quality protocols within organisations and industries. Furthermore, terms like "governance", "capability", and "innovation" propose a strategic viewpoint, highlighting the significance of governance structures and innovative strategies. Consequently, the word cloud portrays the intricate nature of data quality research in the domain of BDA, emphasising their strategic relevance and immediate influence on business and organisational outcomes.

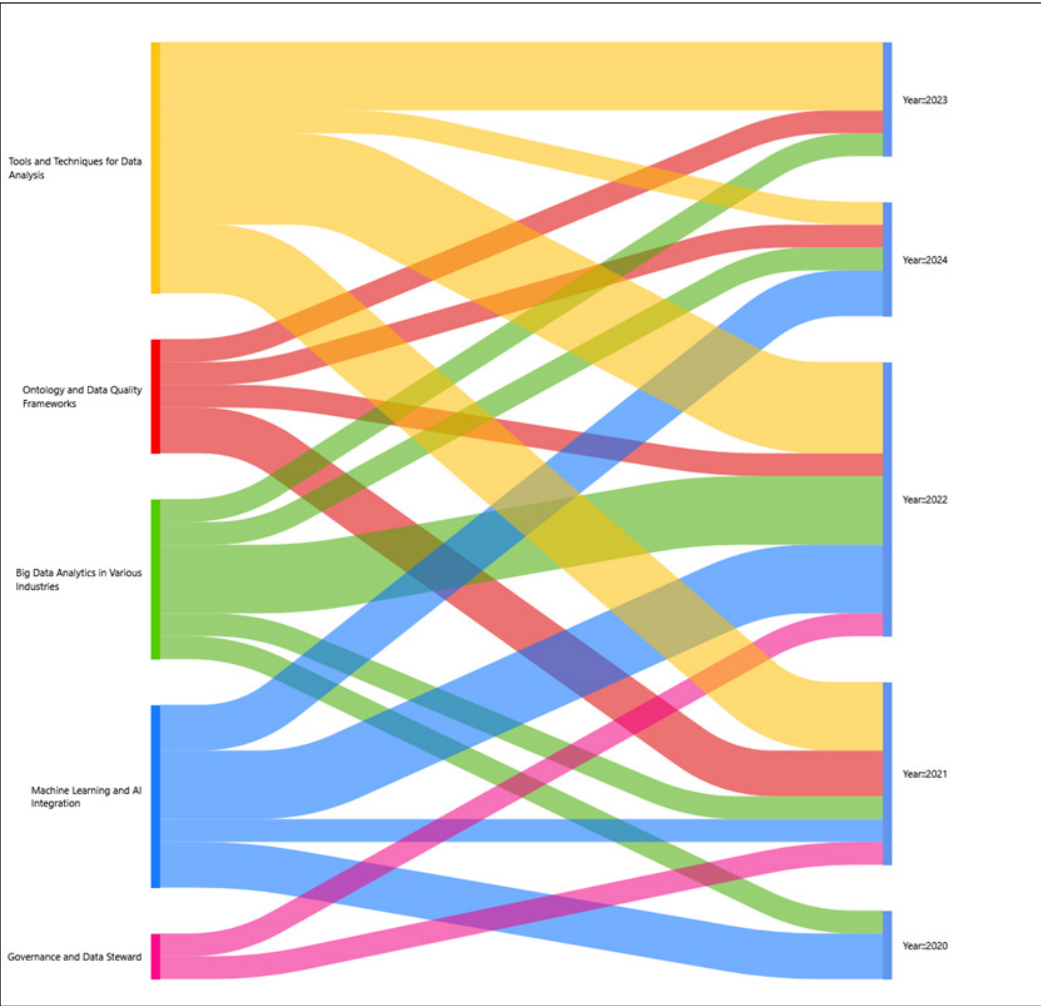


Figure 7. Themes discussed in the literature

Table 2
Tabulation of authors vs theme

	Theme 1: Ontology and Data Quality Frameworks	Theme 2: Big Data Analytics in Various Industries	Theme 3: Machine Learning and AI Integration	Theme 4: Governance and Data Steward	Theme 5: Tools and Techniques for Data Analysis
Barba-González et al. (2024)	/	-	-	-	-
Bui & Perera (2021)	-	-	-	-	/
Côrte-Real et al. (2020)	-	-	-	-	/
Hart et al. (2022)	/	-	-	-	-
Johnson et al. (2021)	-	/	-	-	-
Konanahalli et al. (2022)	-	/	-	-	-
Medeiros et al. (2021)	-	-	-	/	-
Radhakrishnan et al. (2022)	-	-	/	-	-
Song (2024)	-	-	/	-	-
Šprem et al. (2024)	-	-	-	-	/
Szukits & Móricz (2023)	-	-	-	-	/
Timotijevic et al. (2022)	-	-	-	/	-
Widad et al. (2023)	/	-	-	-	-
Wurster et al. (2024)	-	/	-	-	-
Yahia et al. (2021)	-	-	-	-	/
Yu et al. (2022)	-	-	-	-	/
Chen et al. (2023)	-	-	-	-	/
Al-Madhrahí et al. (2022)	-	-	-	-	/
Stach et al. (2022)	-	-	-	-	/
Lavalle et al. (2020)	-	-	/	-	-
Shidaganti & Prakash (2021)	/	-	-	-	-
(Shahi, 2023)	-	-	-	-	/
Zhang (2022)	-	-	-	-	/
Wook et al. (2021)	-	-	/	-	-
Phan & Tran (2022)	/	-	-	-	-
Jha et al. (2020)	-	-	/	-	-
Chang et al. (2021)	-	-	-	-	/
Savoska & Ristevski (2020)	-	/	-	-	-
Hao & Demir (2024)	-	-	-	/	-
Patrucco et al. (2023)	-	/	-	-	-
Spanaki et al. (2021)	/	-	-	-	-
Chen et al. (2022)	-	/	-	-	-
Rana et al. (2022)	-	-	/	-	-
Song et al. (2022)	-	/	-	-	-

Qualitative Finding

This thematic review paper studied publications and coded the data quality patterns in BDA. However, it did not address the future direction of BDA implementation. The initial codes were recorded, combined, and categorised in several rounds. Codes that were occasionally used and could not be categorised into any topic were removed since this study concerned aspects extensively discussed and investigated by researchers. Results from quantitative investigations that were not statistically significant were also removed. Furthermore, generic sociodemographic characteristics were not considered because they may not be universally applicable to all circumstances.

The first round of coding produced 12 initial codes, and the first stage was to become acquainted with the data. The first stage was to complete a thorough review of all the gathered articles and find relevant codes to develop the possible themes. BDA issues, BDA capabilities, data quality, data management, techniques and tools were among the phrases that prompted the creation of the initial subject. The next phase was generating, reviewing, and defining the final themes. A few rounds of discussions were held to refine these themes, resolving differences through consensus. This step ensured that the themes were consistent and accurately represented the data. Next, the themes were compared with findings from previous studies to confirm their relevance and alignment with existing research in the field. To ensure reliability, multiple researchers independently reviewed the themes. Finally, five major themes were identified, focusing on different aspects of data quality in BDA. The themes highlight diverse approaches and dimensions researchers cover, from data quality management, theoretical frameworks, and practical applications to technical advancements. Each theme contributes uniquely to advancing the understanding of data quality in BDA to ensure a balanced and comprehensive review of the study by addressing theoretical, applied, and technical dimensions.

Figure 8 systematically categorises significant themes that emerged from the analysis of 34 articles in the research area from 2020 to 2024. Theme 1, "Ontology and Data Quality Frameworks," focuses on developing standardised data definitions and the assurance of data integrity across various applications, underlining the need for robust frameworks to support data reliability. Theme 2, "Big Data Analytics in Various Industries," explores the widespread application of BDA across different sectors, indicating customised adaptations to meet specific industry challenges and foster innovation. A central query about the trends in data quality within this period intersects with Theme 3, "Machine Learning and AI Integration," which suggests incorporating advanced algorithms to enhance data analytics processes. Themes 4 and 5, "Governance and Data Steward" and "Tools and Techniques for Data Analysis," address the regulatory frameworks and practical tools necessary for effective data management and analysis. This diagram provides a structured framework for understanding the current and emerging trends in BDA, particularly focusing on enhancing data quality and integrating machine learning and AI.

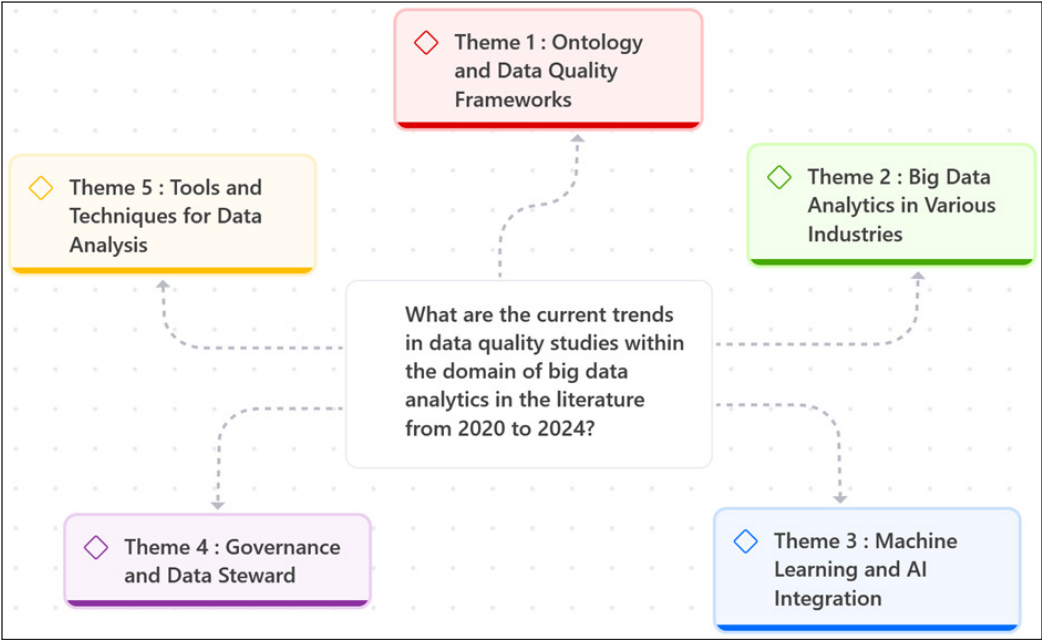


Figure 8. Overall network to answer research question

Theme 1: Ontology and Data Quality Frameworks

Figure 9 for "Theme 1: Ontology and Data Quality Frameworks" presents five articles, each contributing uniquely to data quality frameworks through ontology-based approaches. These articles collectively offer insights and methodologies applicable across various industries, emphasising the critical role of data quality in BDA. Spanaki et al. (2021) address the agricultural sector by proposing a framework for role-based data access control, emphasising the need for secure and efficient data management in environments where data sharing is crucial. In contrast, Phan and Tran (2022) focus on the banking sector, arguing that the complexities and regulatory demands of banking require a tailored approach to data quality management through BDA to improve operational efficiency and decision-

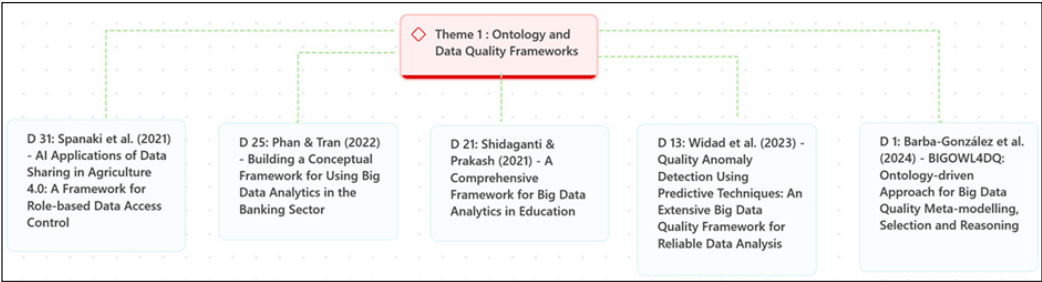


Figure 9. Theme 1: Ontology and Data Quality Frameworks

making. Shidaganti and Prakash (2021) take a different sectoral approach, presenting a framework for the educational sector that highlights the necessity of high data quality for effective educational analytics and the unique challenges in educational data management.

Widad et al. (2023) offer a broader perspective by introducing a framework for anomaly detection using predictive techniques applicable across various industries to maintain high data quality standards through advanced analytics. Barba-González et al. (2024) further broaden the scope with an ontology-driven approach, BIGOWL4DQ, for big data quality meta-modelling, selection, and reasoning; these studies argue that sophisticated ontology-based frameworks are essential for enhancing data integration and interoperability across diverse data environments. Together, these studies highlight the varied approaches and sector-specific needs in developing robust data quality frameworks, underscoring the importance of tailored and advanced methodologies to ensure high data quality standards in BDA.

Theme 2: Big Data Analytics in Various Industries

Figure 10 for "Theme 2: Big Data Analytics in Various Industries" presents articles exploring the diverse applications and implications of BDA across different sectors. Patrucco et al. (2023) emphasise the importance of absorptive capacity in strategic purchasing and supply chain management, arguing that the ability to absorb and utilise big data can significantly enhance decision-making processes. In contrast, using an exploratory factor analysis approach, Konanahalli et al. (2022) identify the drivers and challenges of implementing big data within the UK facilities management sector. This study suggests that while big data holds potential, its implementation faces numerous hurdles, including organisational and attitudinal barriers. Chen et al. (2022) delve deeper into these barriers, highlighting data, attitudinal, and organisational determinants that affect adopting BDA systems. The findings of Chen et al. (2022) align with those of Konanahalli et al. (2022), reinforcing that successful implementation requires addressing these fundamental issues. Meanwhile, Wurster et al. (2024) examine the impact of big data on the healthcare sector, focusing on implementing electronic medical records in a German hospital. Wurster argues that big data can improve documentation completeness and healthcare delivery, a perspective that contrasts with the more cautious views of Chen et al. (2022) and Konanahalli et al. (2022), who emphasise the challenges over the benefits.

Savoska and Ristevski (2020) discuss the pharmaceutical industry, advocating for adopting big data concepts to improve operational efficiencies and innovation. This perspective adds to Patrucco et al.'s (2023) arguments for strategic advantages in supply chain management. Both studies demonstrate how big data can transform business operations. Song et al. (2022) further support this view by demonstrating how SMEs leveraged BDA capabilities to maintain competitive performance during COVID-19. Song

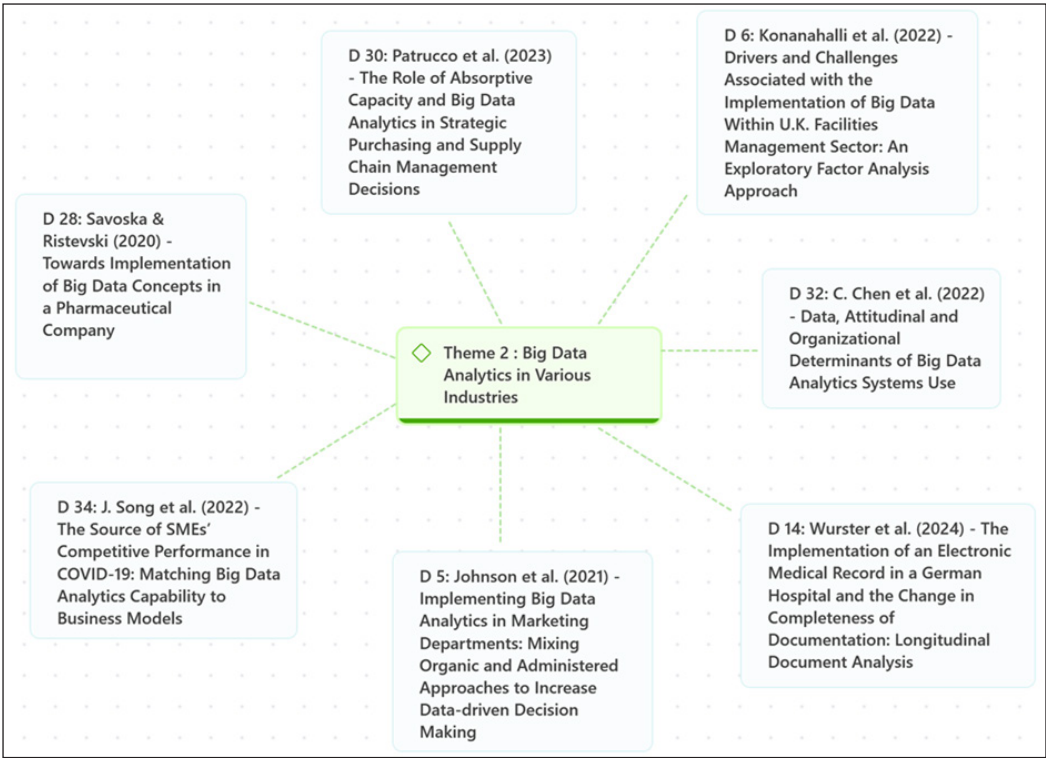


Figure 10. Theme 2: Big Data Analytics in Various Industries

et al.'s (2022) study highlight the adaptability and resilience that big data can provide to businesses, which resonates with the optimistic outlook of Savoska and Ristevski (2020). Johnson et al. (2021) explore the integration of BDA in the marketing sector, proposing a mix of organic and administered approaches to enhance data-driven decision-making. This approach highlights the need for flexibility and innovation in implementing big data solutions, echoing the broader themes of adaptability and strategic advantage found in Patrucco et al.'s (2023) and Song et al.'s (2022) studies. Although BDA offers significant benefits across various industries, its successful implementation requires overcoming substantial organisational, attitudinal, and data-related challenges. The contrasting perspectives and sector-specific insights emphasise the need for tailored strategies to harness the full potential of BDA.

Theme 3: Machine Learning and AI Integration

Several authors explore the integration of machine learning (ML) and AI across different sectors, highlighting the benefits and challenges of such implementations (Figure 11). Jha et al. (2020) emphasise the importance of developing BDA capabilities within supply chains, arguing that ML and AI can enhance efficiency and responsiveness. This perspective aligns

with Hart et al. (2022), who apply ML to large-scale synchrophasor datasets, demonstrating the need to evaluate the "machine learning-readiness" of data to ensure effective power grid management. Contrasting these optimistic views, Rana et al. (2022) explore the dark side of AI in business analytics, highlighting potential operational inefficiencies and competitiveness issues that can arise from AI integration. Rana et al.'s (2022) findings serve as a cautionary tale, suggesting that while AI has substantial potential, it also carries risks that need careful management. This argument is supported by Hao and Demir (2024), who propose an environmental, social, and governance (ESG) framework for AI in supply chain decision-making, emphasising the need for responsible AI integration that considers broader societal impacts.

Wook et al. (2021) take a more technical approach, exploring big data's traits and quality dimensions necessary for successful ML and AI applications. By using partial least squares structural equation modelling, they highlight the critical role of high-quality data in achieving effective AI outcomes. This technical focus is echoed by Lavalle et al. (2020), who advocate using visualisation techniques in smart cities to enhance sustainability through big data captured by IoT devices. Their work illustrates how ML and AI can be leveraged to improve urban efficiency and sustainability. Song (2024) offers another dimension by incorporating Morris' design thoughts for AI and big data to optimise wireless communication networks in China. This study highlights the technological advancements

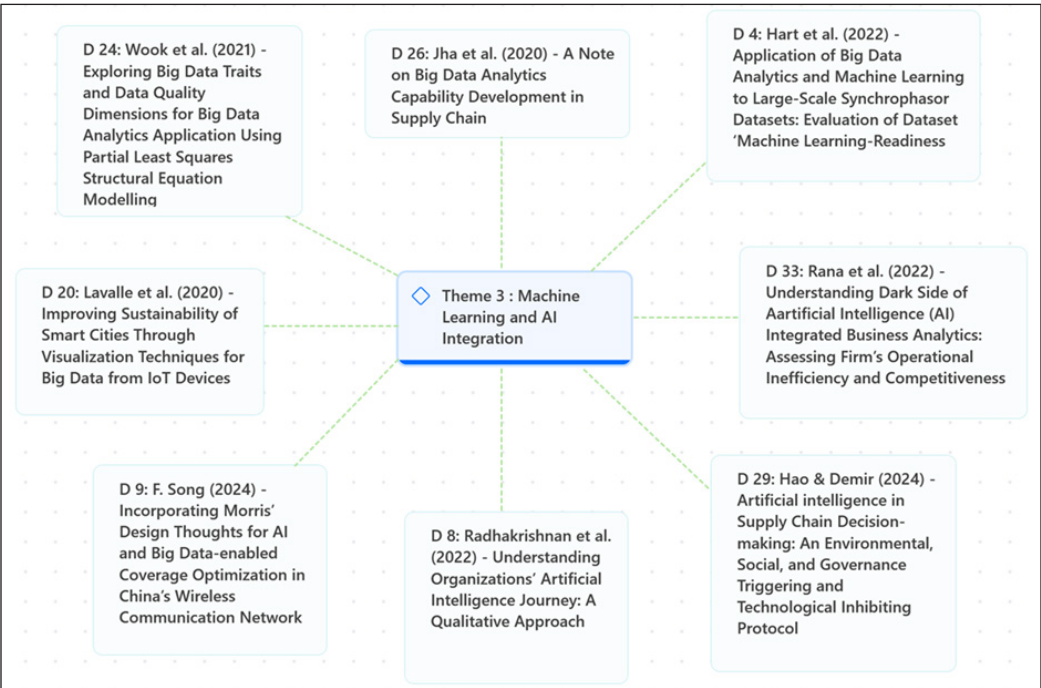


Figure 11. Theme 3: Machine Learning and AI Integration

that ML and AI can drive, showcasing their potential to optimise complex systems. Meanwhile, Radhakrishnan et al. (2022) provide a qualitative approach to understanding the AI journey of organisations, offering insights into the practical challenges and strategies for AI adoption. Radhakrishnan et al.'s (2022) work complements the technical and sector-specific studies by focusing on AI integration's human and organisational aspects. ML and AI integration has potential benefits and significant challenges and can drive efficiency, sustainability, and technological optimisation. However, successful implementation requires careful consideration of data quality, potential risks, and responsible governance. This balanced perspective emphasises the need for tailored, context-specific strategies to fully harness the potential of ML and AI in BDA.

Theme 4: Governance and Data Steward

The theme of "Governance and Data Steward" within BDA is explored through two scholarly works that illustrate the critical impact of governance in different contexts: sector-specific and corporate (Figure 12). Timotijevic et al. (2022) focus on implementing governance within the food and nutrition sector, highlighting how specialised governance frameworks are necessary to ensure data integrity and reliability, particularly when data accuracy directly impacts public health. This approach highlights the protective and regulatory dimensions of governance tailored to meet stringent sector-specific challenges. In contrast, Medeiros et al. (2021) discuss the strategic role of data stewardship in corporate performance management, advocating that effective governance is pivotal for managing data and harnessing it to drive corporate strategies and enhance operational efficiencies. This perspective positions data stewardship as a transformative tool for achieving competitive advantages in the business field. These contrasting viewpoints emphasise the versatility of governance roles: On one hand, Timotijevic et al. (2022) present a protective stance focused on compliance and safety; on the other hand, Medeiros et al. (2021) highlight the

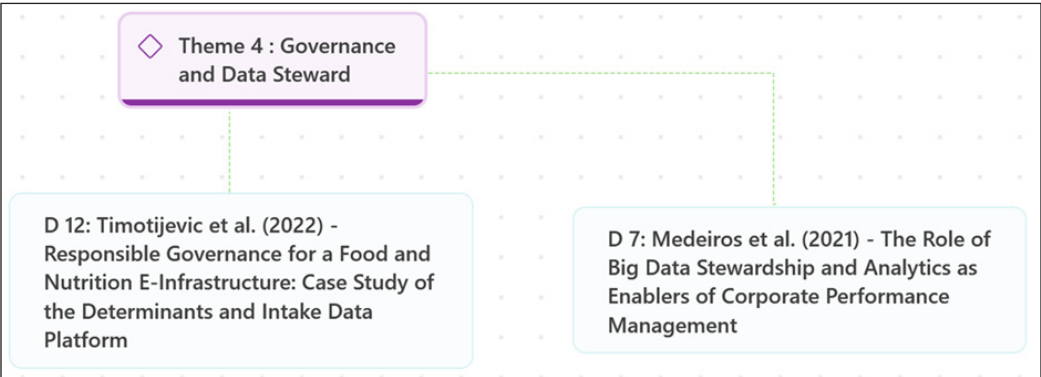


Figure 12. Theme 4: Governance and Data Steward

potential of governance to catalyse business insights and success. Despite an adaptable governance strategy that aligns with specific organisational goals and sector requirements, data integrity and ethical management principles have varying applications and impacts depending on the context.

Theme 5: Tools and Techniques for Data Analysis

The “Tools and Techniques for Data Analysis” theme reveals diverse approaches and insights across various studies (Figure 13). The works of Bui & Perera (2021) and Corte-Real et al. (2020) highlight the integration of IoT with BDA to address domain-specific challenges. While Bui & Perera (2021) focus on monitoring ship performance under unique operational conditions, Corte-Real et al. (2020) examine IoT and big data use within European and American firms. These studies suggest a preference for combining IoT-generated data with advanced analytics, as this synergy provides actionable insights tailored to the operational context. Similarly, Šprem et al. (2024) and Yahia et al. (2021) delve into developing tools and frameworks for handling large-scale data processes. Šprem et al. (2024) focus on creating web applications to streamline data ingestion and processing,

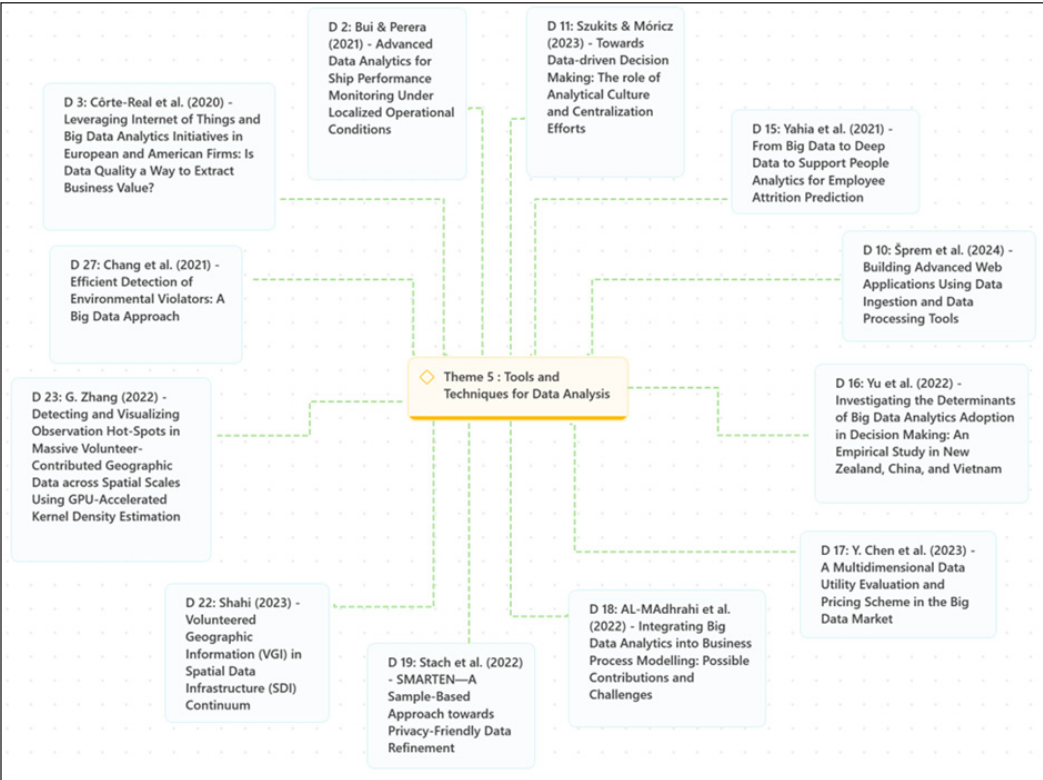


Figure 13. Theme 5: Tools and Techniques for Data Analysis

while Yahia et al. (2021) leverage advanced big data techniques, such as ML, to predict employee attrition. Both studies demonstrate a trend toward creating specialised tools that simplify data handling and enhance business decision-making capabilities.

Chen et al. (2023) and Yu et al. (2022) extend this focus by analysing economic and decision-making implications. Chen et al. (2023) evaluate pricing schemes in the big data marketplace, while Yu et al. (2022) investigate the factors influencing big data adoption in decision-making within organisations across New Zealand, China, and Vietnam. Their findings reveal an emerging emphasis on understanding the economic impact of data analysis tools and their effectiveness in supporting organisational strategies. Environmental and spatial data applications are explored in studies like Chang et al. (2021), Zhang (2022), and Shahi (2023). Chang et al. (2021) address detecting environmental violations using big data, while Zhang (2022) presents GPU-accelerated methods to visualise geographic data at scale. Shahi (2023) investigates volunteered geographic information (VGI) in spatial data infrastructures. These studies illustrate a preference for leveraging domain-specific tools, such as geographic visualisation and environmental monitoring platforms, to address unique analytical challenges.

Stach et al. (2022) and Al-Madhrabi et al. (2022) tackle privacy and ethical considerations. Stach et al. (2022) introduce the SMARTE approach for privacy-focused data refinement, and Al-Madhrabi et al. (2022) explore the integration of analytics into business process modelling. These contributions highlight the growing concern for ethical practices and the necessity of embedding privacy-preserving measures in analytics frameworks. Finally, Szukits and Móricz (2023) examine the organisational culture around data-driven decision-making. The study emphasises the role of analytical centralisation in fostering effective data usage, reflecting a broader pattern where organisations are increasingly investing in cultural shifts to embrace data-centric approaches.

Across these studies, certain patterns emerge, such as the reliance on domain-specific tools and a growing emphasis on integrating advanced techniques like machine learning and GPU acceleration. There is also a noticeable focus on the ethical and economic aspects of data analysis tools, highlighting evolving priorities in the field. By considering these patterns, businesses and researchers can align their strategies with proven practices and adopt tools that meet their specific analytical needs.

LIMITATION OF THE STUDY

This study offers valuable insights into trends in data quality within the BDA domain. However, several limitations exist that may affect the generalizability and interpretation of the findings. These limitations are particularly related to database selection bias, dependence on open-access literature, and geographical dispersion of research.

First, the search strategy employed in this study focused on two databases, SCOPUS and WoS, both known for their coverage of high-quality, peer-reviewed research. However, selection bias arises from excluding other databases, such as IEEE Xplore or Google Scholar, which may include additional relevant studies. By limiting the scope to these databases, the study may have missed significant contributions from disciplines or regions underrepresented in SCOPUS and WoS. For instance, emerging economies advancing in BDA may publish relevant works in local or regional journals not indexed in these databases. Additionally, reliance on open-access publications may introduce potential publication bias. Open-access studies do not always represent the broader scientific discourse, as they often exclude works published in subscription-based journals, which may offer valuable and diverse perspectives. This limitation may restrict the comprehensiveness of the findings and the generalizability of the conclusions drawn.

Second, the geographical distribution of research articles highlights disparities in research productivity, with significant contributions from the US, UK and China. Conversely, regions in developed countries such as Canada, Australia, and Russia are underrepresented in the findings despite their potential contributions to BDA. This uneven representation may reflect systemic biases in publication practices or limitations in the search methodology. Future studies could explore alternative sources or collaborate with researchers from underrepresented regions to achieve a more balanced geographical representation.

Finally, while the study identifies critical themes, such as ontology frameworks, machine learning integration, and governance in BDA, the focus remains on theoretical and methodological discussions. The absence of extensive real-world applications limits the contextual relevance of the findings. Addressing practical challenges, particularly from the perspective of BDA implementation in diverse sectors, could provide a more comprehensive understanding of how data quality issues affect decision-making and outcomes.

DISCUSSION AND RECOMMENDATION

Artificial intelligence (AI) has emerged as a pivotal tool in addressing the long-standing data quality issue in BDA. The literature consistently highlights the criticality of data quality in ensuring accurate, reliable, and actionable insights from large datasets. High-quality data enhances the value of BDA, while poor-quality data compromises decision-making and operational efficiency. AI offers a range of capabilities that can directly address data quality issues. Machine learning algorithms can identify patterns and anomalies in data, flagging inconsistencies and potential errors. For example, predictive models have been employed to detect quality anomalies, as highlighted by Widad et al. (2023). Similarly, ontology-driven approaches, such as BIGOWL4DQ proposed by Barba-González et al. (2024), facilitate data integration and interoperability, addressing structural and semantic

inconsistencies. These approaches highlight the potential of AI to enhance data accuracy and reliability across various sectors.

AI's ability to learn and adapt also allows for dynamic quality monitoring. AI-powered tools can continuously audit datasets to ensure compliance with quality standards. For instance, role-based access frameworks discussed by Spanaki et al. (2021) integrate AI to manage data securely, ensuring that only high-quality and relevant data is accessed and utilised. Moreover, AI-driven natural language processing (NLP) and automation reduce the manual effort required for data cleaning and preparation, making the process more efficient and less error-prone.

Despite its potential, AI-integrated BDA faces several challenges. Data governance frameworks, essential for managing and maintaining data quality, often lag behind technological advancements. Many frameworks fail to adequately address the complexities of real-time data processing and multi-source data integration. Moreover, ethical concerns such as data privacy, algorithmic bias, and implications of poor data quality on decision-making remain significant barriers. Data privacy is a critical concern in BDA, especially with the increasing use of personal and sensitive information. AI models often require large volumes of data for training, which may lead to privacy violations if data is inadequately anonymised or secured. Studies like Timotijevic et al. (2022) highlight the need for stringent governance mechanisms to protect sensitive data, particularly in sectors like healthcare and food safety. Bias in AI models is another pressing issue. If training datasets are skewed or incomplete, AI algorithms may perpetuate existing biases, leading to unfair or inaccurate outcomes. Rana et al. (2022) emphasise how biases in business analytics can exacerbate operational inefficiencies and competitiveness issues. Furthermore, poor data quality, manifesting as missing, inaccurate, or outdated data, can severely compromise decision-making. For instance, decision-support systems relying on flawed data may produce misleading insights, ultimately affecting organisational performance and trust in AI systems.

Integrating governance frameworks with AI and BDA offers a pathway to mitigate these challenges. Effective governance ensures data is managed responsibly, ethically, and aligned with regulatory standards. AI can be harnessed within these frameworks to automate compliance monitoring, flag governance breaches, and ensure adherence to ethical norms. For example, Hao and Demir (2024) propose an ESG framework for AI-driven supply chain decision-making, which balances technological efficiency with environmental and social considerations. Such frameworks can also address the dual challenges of privacy and security by embedding robust encryption and access control mechanisms. By incorporating AI, governance frameworks can become adaptive and responsive, dynamically evolving with emerging challenges in the data ecosystem. Governance frameworks can also play a crucial role in mitigating bias. Combined with explainable AI models, transparent governance structures can ensure accountability and fairness. For instance, Wook et al.

(2021) highlight the importance of data quality dimensions in achieving unbiased AI outcomes. By integrating governance mechanisms with AI, organisations can foster ethical decision-making processes while leveraging the full potential of BDA.

The future of data quality in BDA is intertwined with advancements in emerging technologies such as blockchain, edge computing, and quantum computing. These technologies offer transformative potential to address current limitations and shape the future trajectory of the field. Blockchain technology provides a decentralised and immutable ledger for data storage and sharing, ensuring transparency and traceability. Blockchain can enhance data quality by preventing tampering and maintaining an auditable record of data modifications. This technology is particularly valuable in sectors where data integrity is paramount, such as healthcare and finance. Future studies could explore the integration of blockchain with AI to create secure and transparent data ecosystems. Edge computing shifts data processing closer to the source, reducing latency and improving the quality of real-time analytics. This approach is especially relevant for IoT applications, where timely insights are critical. By enabling localised data processing, edge computing minimises the risk of data degradation during transmission. Researchers could investigate how edge computing can be combined with AI to enhance the accuracy and timeliness of data analytics in distributed environments. Quantum computing, though still in its nascent stages, holds promise for solving complex optimisation problems and processing vast datasets with unparalleled speed. Future research could examine how quantum algorithms might be applied to data quality challenges, particularly in handling large-scale unstructured data.

In addition to these technologies, there is a growing need for frameworks prioritising ethical considerations in AI and BDA. The development of explainable AI (XAI) models, which provide transparent reasoning for algorithmic decisions, can build trust and accountability. Studies could also focus on developing international data quality and governance standards, ensuring consistency across borders and industries.

CONTRIBUTIONS AND BENEFITS OF STUDY

The contributions of this study are manifold, offering a comprehensive analysis of present trends in data quality studies within the BDA field from 2020 to 2024. This review emphasises the multidimensional nature of data quality issues and their broad applicability across different sectors. The study reveals significant trends, such as the maximum number of publications recorded in 2022, emphasising how important data quality is for using big data for various applications. The geographical dispersion of research output, particularly the prominence of the United States and the United Kingdom, reflects the global interest and its correlation with the economic, educational, and technological capacities of different countries.

The study's thematic review classifies publications into five themes: Ontology and Data Quality Frameworks, Big Data Analytics in Various Industries, Machine Learning and AI Integration, Governance and Data Stewardship, and Tools and Techniques for Data Analysis. This method efficiently synthesises much information, which makes it easier to identify gaps, new trends, and areas that require more research. In addition to highlighting the fundamental importance of tools and methods for data analysis and the fusion of AI and machine learning, this organised framework also highlights the vital function that strong data quality frameworks and governance structures play. The study shows how big data technology may be flexible and transformational in various fields by looking at industry-specific applications, such as marketing, supply chain management, and healthcare. This comprehensive overview not only guides future research but also informs best practices in BDA implementation, capturing the complexity and dynamic nature of this field.

ACKNOWLEDGEMENTS

The authors express their sincere gratitude to the College of Computing, Informatics, and Mathematics, the Institute of Postgraduate Studies (IPSiS), and the Research Management Centre, Universiti Teknologi MARA, Shah Alam, Selangor, Malaysia, for providing the infrastructure and facilities for this research and supporting the publication of this paper.

REFERENCES

- Al-Madhrahi, Z., Singh, D., & Yadegaridehkordi, E. (2022). Integrating big data analytics into business process modelling: Possible contributions and challenges. *International Journal of Advanced Computer Science and Applications*, 13(6), 461–468. <https://doi.org/10.14569/IJACSA.2022.0130657>
- Barba-González, C., Caballero, I., Varela-Vaca, Á. J., Cruz-Lemus, J. A., Gómez-López, M. T., & Navas-Delgado, I. (2024). BIGOWL4DQ: Ontology-driven approach for big data quality meta-modelling, selection and reasoning. *Information and Software Technology*, 167, Article 107378. <https://doi.org/10.1016/j.infsof.2023.107378>
- Bui, K. Q., & Perera, L. P. (2021). Advanced data analytics for ship performance monitoring under localized operational conditions. *Ocean Engineering*, 235, Article 109392. <https://doi.org/10.1016/j.oceaneng.2021.109392>
- Chang, X., Huang, Y., Li, M., Bo, X., & Kumar, S. (2021). Efficient detection of environmental violators: A big data approach. *Production and Operations Management*, 30(5), 1246–1270. <https://doi.org/10.1111/poms.13272>
- Chen, C., Choi, H. S., & Ractham, P. (2022). Data, attitudinal and organizational determinants of big data analytics systems use. *Cogent Business & Management*, 9(1), Article 2043535. <https://doi.org/10.1080/23311975.2022.2043535>
- Chen, Y., Bai, R., Wu, Y., Li, T., & Zhou, H. (2023). A multidimensional data utility evaluation and pricing scheme in the big data market. *Wireless Communications and Mobile Computing*, 2023(1), Article 6217495. <https://doi.org/10.1155/2023/6217495>

- Clarke, V., & Braun, V. (2013). Teaching thematic analysis: Overcoming challenges and developing strategies for effective learning. *The Psychologist*, 26(2), 120–123.
- Côrte-Real, N., Ruivo, P., & Oliveira, T. (2020). Leveraging internet of things and big data analytics initiatives in European and American firms: Is data quality a way to extract business value? *Information & Management*, 57, Article 103141. <https://doi.org/10.1016/j.im.2019.01.003>
- Hao, X., & Demir, E. (2024). Artificial intelligence in supply chain decision-making: an environmental, social, and governance triggering and technological inhibiting protocol. *Journal of Modelling in Management*, 19(2), 605–629. <https://doi.org/10.1108/JM2-01-2023-0009>
- Hart, P., He, L., Wang, T., Kumar, V. S., Aggour, K., Subramanian, A., & Yan, W. (2022). Application of big data analytics and machine learning to large-scale synchrophasor datasets: Evaluation of dataset ‘Machine Learning-Readiness’. *IEEE Open Access Journal of Power and Energy*, 9, 386–397. <https://doi.org/10.1109/OAJPE.2022.3197553>
- Jha, A. K., Agi, M. A. N. N., & Ngai, E. W. T. T. (2020). A note on big data analytics capability development in supply chain. *Decision Support Systems*, 138(2020), Article 113382. <https://doi.org/10.1016/j.dss.2020.113382>
- Johnson, D. S., Sihi, D., & Muzellec, L. (2021). Implementing big data analytics in marketing departments: Mixing organic and administered approaches to increase data-driven decision making. *Informatics*, 8(4), Article 66. <https://doi.org/10.3390/informatics8040066>
- Konanahalli, A., Marinelli, M., & Oyedele, L. (2022). Drivers and challenges associated with the implementation of big data within U.K. facilities management sector: An exploratory factor analysis approach. *IEEE Transactions on Engineering Management*, 69(4), 916–929. <https://doi.org/10.1109/TEM.2019.2959914>
- Lavalle, A., Teruel, M. A., Maté, A., & Trujillo, J. (2020). Improving sustainability of smart cities through visualization techniques for big data from IoT devices. *Sustainability*, 12(14), Article 5595. <https://doi.org/10.3390/su12145595>
- Medeiros, M. M., MaçAda, A. C. G., & Hoppen, N. (2021). The role of big data stewardship and analytics as enablers of corporate performance management. *Revista de Administracao Mackenzie*, 22(6), Article eRAMD210063. <https://doi.org/10.1590/1678-6971/eRAMD210063>
- Patrucco, A. S., Marzi, G., & Trabucchi, D. (2023). The role of absorptive capacity and big data analytics in strategic purchasing and supply chain management decisions. *Technovation*, 126(2023), Article 102814. <https://doi.org/10.1016/j.technovation.2023.102814>
- Phan, D. T., & Tran, L. Q. T. (2022). Building a conceptual framework for using big data analytics in the banking sector. *Intellectual Economics*, 16(1), 5–23. <https://doi.org/10.13165/IE-22-16-1-01>
- Radhakrishnan, J., Gupta, S., & Prashar, S. (2022). Understanding organizations’ artificial intelligence journey: A qualitative approach. *Pacific Asia Journal of the Association for Information Systems*, 14(6), 43–77. <https://doi.org/10.17705/1pais.14602>
- Rana, N. P., Chatterjee, S., Dwivedi, Y. K., & Akter, S. (2022). Understanding dark side of artificial intelligence (AI) integrated business analytics: assessing firm’s operational inefficiency and competitiveness. *European Journal of Information Systems*, 31(3), 364–387. <https://doi.org/10.1080/0960085X.2021.1955628>

- Savoska, S., & Ristevski, B. (2020). Towards implementation of big data concepts in a pharmaceutical company. *Open Computer Science*, 10(1), 343–356. <https://doi.org/10.1515/comp-2020-0201>
- Shahi, K. (2023). Volunteered Geographic Information (VGI) in Spatial Data Infrastructure (SDI) continuum. *EAI Endorsed Transactions on Internet of Things*, 9(1), Article e3. <https://doi.org/10.4108/eetiot.v9i1.2979>
- Shidaganti, G., & Prakash, S. (2021). A comprehensive framework for big data analytics in education. *International Journal of Advanced Computer Science and Applications*, 12(9), 218–227. <https://doi.org/10.14569/IJACSA.2021.0120926>
- Song, F. (2024). Incorporating Morris’ design thoughts for AI and big data-enabled coverage optimization in China’s wireless communication network. *Journal of Information Systems Engineering and Management*, 9(1), Article 23622. <https://doi.org/10.55267/iadt.07.14076>
- Song, J., Xia, S., Vrontis, D., Sukumar, A., Liao, B., Li, Q., Tian, K., & Yao, N. (2022). The source of SMEs’ competitive performance in COVID-19: Matching big data analytics capability to business models. *Information Systems Frontiers*, 24, 1167–1187. <https://doi.org/10.1007/s10796-022-10287-0>
- Spanaki, K., Karafilis, E., & Despoudi, S. (2021). AI applications of data sharing in agriculture 4.0: A framework for role-based data access control. *International Journal of Information Management*, 59, Article 102350. <https://doi.org/10.1016/j.ijinfomgt.2021.102350>
- Šprem, Š., Tomažin, N., Matečič, J., & Horvat, M. (2024). Building advanced web applications using data ingestion and data processing tools. *Electronics*, 13(4), Article 0709. <https://doi.org/10.3390/electronics13040709>
- Stach, C., Behringer, M., Bräcker, J., Gritti, C., & Mitschang, B. (2022). SMARTEN - A sample-based approach towards privacy-friendly data refinement. *Journal of Cybersecurity and Privacy*, 2(3), 606–628. <https://doi.org/10.3390/jcp2030031>
- Szukits, Á., & Móricz, P. (2023). Towards data-driven decision making: The role of analytical culture and centralization efforts. *Review of Managerial Science*, 18(10), 2849–2887. <https://doi.org/10.1007/s11846-023-00694-1>
- Teh, H. Y., Kempa-Liehr, A. W., & Wang, K. I. K. (2020). Sensor data quality: A systematic review. *Journal of Big Data*, 7(1), 1–49. <https://doi.org/10.1186/s40537-020-0285-1>
- Timotijevic, L., Carr, I., De La Cueva, J., Eftimov, T., Hodgkins, C. E., Seljak, B. K., Mikkelsen, B. E., Selnes, T., Van’t Veer, P., & Zimmermann, K. (2022). Responsible governance for a food and nutrition e-infrastructure: Case study of the determinants and intake data platform. *Frontiers in Nutrition*, 8, Article 795802. <https://doi.org/10.3389/fnut.2021.795802>
- Widad, E., Saida, E., & Gahi, Y. (2023). Quality anomaly detection using predictive techniques: An extensive big data quality framework for reliable data analysis. *IEEE Access*, 11, 103306–103318. <https://doi.org/10.1109/ACCESS.2023.3317354>
- Wook, M., Hasbullah, N. A., Zainudin, N. M., Jabar, Z. Z. A., Ramli, S., Razali, N. A. M., & Yusop, N. M. (2021). Exploring big data traits and data quality dimensions for big data analytics application using partial least squares structural equation modelling. *Journal of Big Data*, 8(1), 1–15. <https://doi.org/10.1186/s40537-021-00439-5>

- Wurster, F., Beckmann, M., Cecon-Stabel, N., Dittmer, K., Jes Hansen, T., Jaschke, J., Köberlein-Neu, J., Okumu, M. R., Rusniok, C., Pfaff, H., & Karbach, U. (2024). The implementation of an electronic medical record in a German Hospital and the change in completeness of documentation: Longitudinal document analysis. *JMIR Medical Informatics*, 12(1), Article e47761. <https://doi.org/10.2196/47761>
- Yahia, N. B., Hlel, J., & Colomo-Palacios, R. (2021). From big data to deep data to support people analytics for employee attrition prediction. *IEEE Access*, 9, 60447–60458. <https://doi.org/10.1109/ACCESS.2021.3074559>
- Yu, J., Taskin, N., Nguyen, C. P., Li, J., & Pauleen, D. J. (2022). Investigating the determinants of big data analytics adoption in decision making: An empirical study in New Zealand, China, and Vietnam. *Pacific Asia Journal of the Association for Information Systems*, 14(4), 62–99. <https://doi.org/10.17705/1pais.14403>
- Zairul, M. (2020). A thematic review on student-centered learning in the studio education. *Journal of Critical Reviews*, 7(2), 504–511. <https://doi.org/10.31838/jcr.07.02.95>
- Zairul, M. (2021). A thematic review on Industrialised Building System (IBS) publications from 2015-2019: Analysis of patterns and trends for future studies of IBS in Malaysia. *Pertanika Journal of Social Sciences and Humanities*, 29(1), 635–652. <https://doi.org/10.47836/PJSSH.29.1.35>
- Zairul, M. (2023). *Thematic Review template (Patent No. CRLY2023W02032)*. Controller of Copyright.
- Zairul, M., Azli, M., & Azlan, A. (2023). Defying tradition or maintaining the status quo? Moving towards a new hybrid architecture studio education to support blended learning post-COVID-19. *Archnet-IJAR: International Journal of Architectural Research*, 17(3), 554–573. <https://doi.org/10.1108/ARCH-11-2022-0251>
- Zairul, M., & Zaremohzzabieh, Z. (2023). Thematic trends in Industry 4.0 Revolution potential towards sustainability in the construction industry. *Sustainability*, 15, Article 7720. <https://doi.org/10.3390/su15097720>
- Zhang, G. (2022). Detecting and visualizing observation hot-spots in massive volunteer-contributed geographic data across spatial scales using GPU-accelerated kernel density estimation. *ISPRS International Journal of Geo-Information*, 11(1), Article 55. <https://doi.org/10.3390/ijgi11010055>

Numerical Study on the Effects of Wire bonding Looping formation on Light-emitting Diode Encapsulation Process

Ahmad Amin Azmi Jaludin¹, Mohd Syakirin Rusdi², Mohd Sharizal Abdul Aziz² and Mohammad Hafifi Hafiz Ishak^{1*}

¹*School of Aerospace Engineering, Universiti Sains Malaysia, Engineering Campus, 14300 Nibong Tebal, Seberang Perai Selatan, Penang, Malaysia*

²*School of Mechanical Engineering, Universiti Sains Malaysia, Engineering Campus, 14300 Nibong Tebal, Seberang Perai Selatan, Penang, Malaysia*

ABSTRACT

This study focused on evaluating the effects of different wire-bonding looping formations on key mechanical properties during the encapsulation process of light-emitting diodes (LEDs). The specific properties investigated included total maximum deformation, maximum equivalent elastic strain, and maximum von Mises stress, which are critical to ensuring LEDs' structural integrity and performance under encapsulation. The encapsulation process was simulated using advanced computational methods, including Volume of Fluid (VOF), Fluid-Structure Interaction (FSI), and system coupling techniques within the ANSYS software environment. The simulations were designed to mimic the behavior of epoxy molding compound (EMC) as it interacts with various wire configurations over time, providing insights into the dynamic responses of the LED structures. These simulation results were rigorously validated against experimental data to ensure accuracy and reliability. Among the wire configurations tested, the Type 2 wire demonstrated high compatibility with the EMC, exhibiting the highest maximum strain and stress values. Conversely, the square-loop (type 3) configuration emerged as the most optimal, offering the lowest levels of total deformation, strain,

and stress, thereby indicating superior overall performance. The comparative analysis ranked the wire configurations in the following order of performance with the EMC: Type 2, type 1, and type 3. These findings provide valuable insights for optimizing wire configurations in LED encapsulation processes, potentially leading to improved durability and reliability of LED devices.

ARTICLE INFO

Article history:

Received: 22 August 2024

Accepted: 16 January 2025

Published: 26 March 2025

DOI: <https://doi.org/10.47836/pjst.33.3.08>

E-mail addresses:

aminazmi.jaludin@student.usm.my (Ahmad Amin Azmi Jaludin)

syakirin@usm.my (Mohd Syakirin Rusdi)

msharizal@usm.my (Mohd Sharizal Abdul Aziz)

mhafifihafiz@usm.my (Mohammad Hafifi Hafiz Ishak)

*Corresponding author

Keywords: Encapsulation process, fluid-structure interaction, LED, wire configuration

INTRODUCTION

LEDs are solid-state lighting (SSL) that transform power into light. LEDs are monochromatic due to the semiconductor's energy bandgap. There are various LED light varieties on the market. Common LED light types are hole-type, SMD-type, bi-color, RGB-type, and HP-LED. LEDs can replace incandescent and halogen bulbs due to their energy efficiency, low cost, extended lifespan, environmental friendliness, and portability (Hamidnia et al., 2018). LED chip packaging protects the connected wire and chip from flaws through LED encapsulation. Encapsulation and lens formation affect LED chip light extraction (Roslan et al., 2020). Silicone and epoxy resins are the principal LED encapsulating mediums. Epoxy resins are popular due to their inexpensive cost, adhesive strength, and dielectric constant. Silicone resins have outstanding thermal and optical properties, a long lifespan, and a wide working temperature range (Alim et al., 2021). The encapsulant fills the LED package cavity and encloses the bonding wires because materials have various CTEs and thermos-mechanical stress affecting LED failure (Packwood et al., 2018). Wire bonding provides communication and power between chips and substrates in LED packages. Semiconductor packaging uses gold wire bonding to connect the substrate and chip. Gold wire offers consistent chemical characteristics, good weldability, and high ductility (Tian et al., 2019). Bonding wires during LED operation help dissipate heat. Wire-bonding technologies have a limited material selection and risk bond surface defects and wear (Alim et al., 2021). LEDs use semiconductors to convert electrical energy into visible, Ultraviolet, or Infrared light (Koutchma, 2019). The region where active electrons and holes are injected is referred to as the p-n junction (Alim et al., 2020; Ünal et al., 2022).

The active layer of an LED chip captures all the electron-hole pairs and turns the output energy into optical power in the ideal circumstance. Nevertheless, some electrical energy is transformed into heat energy in the actual condition. The electrons and holes enter the active zone and combine radiatively or non-radiatively when an LED turns on. The goal of employing LED is to produce photons by radiative recombination. Meanwhile, non-radiative recombination generates heat at the active layer, and Joule heating at the interconnects and diode's series electrical resistance (Hamidnia et al., 2018). The creation of the new LED that combined the three fundamental colors to generate white light and other color temperatures made LED technology suitable for indoor illumination (Montoya et al., 2017). For LED equipment exceeding 10W, Chip-on-Board (COB) packaging is the method of choice. This technology attaches LED chips to their substrates, boosting LED performance over single-chip packaging. LED packaging is easier to make, cheaper, and smaller than normal packaging. Different levels of electrical packaging exist. The semiconductor is level zero, and its connections and encapsulation are level one. Second-level packaging connects the microelectronic package to the printed circuit board (PCB). Both single-chip and multi-chip packaging are available for two-dimensional microelectronic devices.

Encapsulated single-chip packages are lead frame and substrate. Lead-frame packages are surface-mounted or through-hole mounted to the PCB. Through-hole technology in the 1960s required package leads to be inserted into plated circuit board through-holes. Place the leads and wave solder the electrical connection. Pin-grid array (PGA), dual in-line package (DIP) and Single in-line package (SIP) are the most popular through-hole packages. Surface-mounted packages include Small-outline package (SOP), Plastic-leaded chip carrier (PLCC), Quad-flat-pack (QFP), and Ball-grid array (BGA). These packages for discrete implantation on printed wiring boards have components on both sides of the circuit board. Ball grip package (BGA), chip scale package (CSP), chip-on-board (COB), and flip chip (FC) are substrate single-chip packaged (Arriola et al., 2023).

Electronic devices commonly use T-pack LED chips, the original LED chip. However, they are weak and emit a limited amount of light. Most UV LEDs are SMD, which are attached to a printed circuit board and contain one or more chips in ceramic packaging. Chip-on-board (COB) LEDs with appropriate equipment are installed onto the circuit board (Koutchma, 2019). Despite its enormous heat dissipation area, the widely used SMD LED light has poor optical efficiency. Many COB (Chip on board) LED lamps have improved optical efficiency, but thermal issues remain, especially in applications over 100W (Moon et al., 2017). Encapsulating the LED prevented deterioration because biological molecules are susceptible to environmental factors. Various thicknesses of Al_2O_3 films were produced using atomic layer deposition at 85°C to attain optimal development (Mahmood et al., 2022). Continuous oxygen and moisture exposure degrades LEDs quickly. The main causes of OLED degradation are interface delamination, organic material crystallization, electrode oxidation, and layer physical and chemical changes. The hygrothermal aging test was performed in a humidity chamber at 85°C and 85% RH using commercially encapsulated LEDs. At high temperatures, trapped moisture became a gas, and the gas expansion pressure weakened the cathode-polymer layer adhesion, causing bubble defects on the cathode's surface. Defects destroyed the aluminum film and caused the device to fail (Azrain et al., 2019).

EMC flow behavior in molds affected electronic package operation and reliability, making it important to examine. Transfer molding speed injection and stacking affected EMC flow and void formation during encapsulation. A multi-flip chip package molded underfill (MUF) was numerically investigated using ANSYS Fluent's Castro Macosko model. Shear rate and velocity profiles in the free passage and flip chip region are negatively linked to EMC viscosity (Azmi et al., 2018). Epoxy resin's bonding strength and material properties can vary with temperature. When the temperature rises, the epoxy resin of elastic modulus falls. The viscosity of epoxy and dispensed volume both had an impact on the quality of the LED package. The adhesive viscosity can be accurately estimated using the viscosity model, and the appropriate jetting temperature can be determined (Shan

& Chen, 2018). Package warpage was the main issue in packaging innovation. Surface mount technology (SMT) issues include mounting errors during chip attachment and poor solder connections between the package and PCB. The thermal properties of the epoxy molding compound (EMC), including its coefficient of thermal expansion (CTE) curing, shrinkage (CS), and viscoelastic behavior, influence the warpage. EMC viscoelasticity was measured using a three-point bending stress relaxation test. Dielectric and Fibre Bragg grating (FBG) sensors assessed EMC internal strain and recovery. EMC aluminum bi-layer strip warpage was determined via FEM simulation, which resulting EMC cure shrinkage, which is important in forecasting semiconductor warpage (Baek et al., 2022). Additionally, the encapsulant reduced the LED's brightness and color emission efficiency. Excess epoxy pressured gold wire bonding and affected the PCB-gold wire interface. Insufficient epoxy caused poor LED light output.

This research investigates how gold wire configurations influence fluid behavior and mechanical properties during LED encapsulation. Advanced simulation techniques such as Volume of Fluid (VOF) and Fluid-Structure Interaction (FSI) are employed, and the results are validated through comparison with experimental data. By exploring the effects of wire configurations, this work advances LED technology and offers valuable insights for innovative design and manufacturing approaches that enhance the durability, efficiency, and performance of LED products across various applications.

METHODOLOGY

Physical Model and Computational Domain

The geometry model of the LED package, featuring three different wire bonding looping formations: Type 1, Type 2 and Type 3, was created using SolidWorks and then imported into ANSYS. These wire configurations were selected due to their widespread use in the industry, each providing distinct mechanical and thermal performance characteristics. The needle tip's inner diameter is 1 mm, while the domain has a height of 4 mm and a diameter of 3 mm. The gold wire used has a diameter of 0.03 mm. The syringe and domain are considered fluid bodies, whereas the gold wires and substrates are treated as solid bodies. Figure 1 illustrates the geometry model of the Type 1 wire configuration. An isometric and front view of all three wire configurations connecting the LED chip to the substrate is depicted in Figure 2. System Coupling was employed to simulate and analyze the interaction between the epoxy material and the wires. This setup allows Fluent to address fluid dynamics while Static Structural handles wire deflection and stress analysis. During the simulation, data from the Fluent and Static Structural simulations are transferred to System Coupling, with force data moving from Fluent to Static Structural and displacement data sent from Static Structural to Fluent.

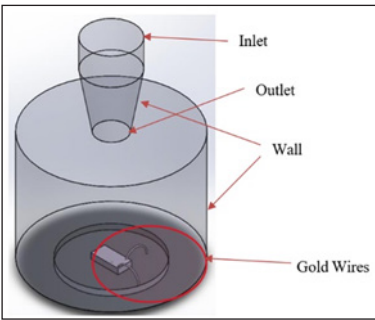


Figure 1. LED Encapsulation process geometry model

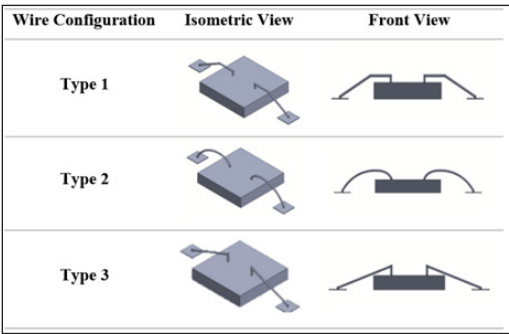


Figure 2. Isometric view and Front view of the three different types of wire configuration

The fluid domain meshes in Figure 3(a) are polyhedral and 0.10mm in size. The fluid domain has 126511 elements and 151428 nodes. Figure 3(b) shows poly-hexacore solid body meshes with 0.01mm element size. The solid body has 3366 components and 16356 nodes. In the simulation, the Volume of Fluid (VOF) is used to measure the interface between two fluids with different properties, such as air and water (Garoosi & Mahdi, 2022). The interface is where one fluid’s volume fraction goes from zero to one and the other from one to zero.

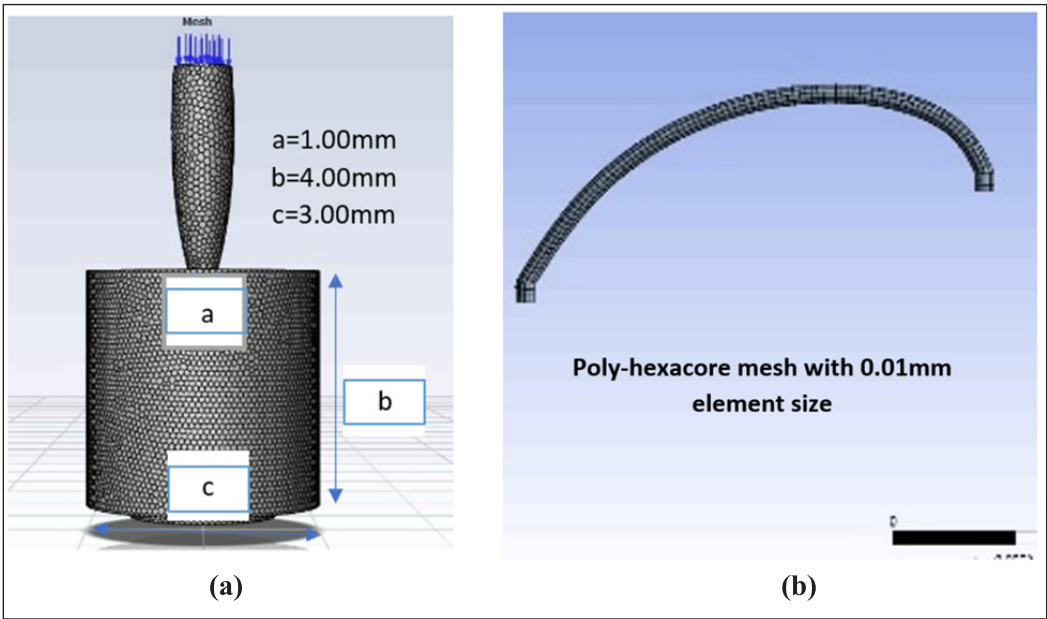


Figure 3. Mesh generation (a) fluid domain, (b) solid domain

The Laminar model was used as the viscous model. A user-defined function (UDF) was employed in the simulation to mimic the encapsulant injection motion flow process where the motion is initially important but later becomes stationary. After the setup, the data generated from the Fluent and Static Structural simulations is transferred to the System Coupling. In the system coupling, the force data is transferred from Fluent to Static Structure, while the displacement data is transferred from Static Structural to Fluent. The real-time analysis of FSI simulation is shown in Figure 4.

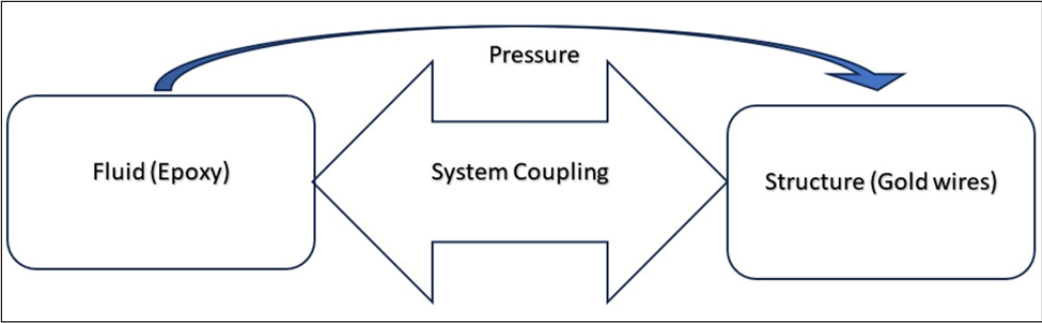


Figure 4. Concept of fluid-structure interaction analysis between epoxy and gold wires

The output analysis from the static structural simulation includes maximum total deformation, equivalent elastic strain and von Mises stress. The maximum total deformation, defined as the largest overall displacement experienced at any point within the structure, was analyzed to assess the structural response under load. The equivalent elastic strain is a scalar quantity derived from the strain tensor, representing the intensity of elastic deformation in a material. It provides a simplified measure to compare different strain states on a unified scale, helping identify areas of significant elastic deformation. Von Mises stress is a widely used criterion to determine whether a material will yield or fail under complex loading conditions. It provides a scalar value that combines the effects of different stress components acting in three dimensions, which offers a single measure to evaluate the material response.

Material Properties and Boundary Conditions

In the simulation setup, boundary conditions and material properties for the gold wire were obtained from previous studies (Roslan et al., 2020) and the ANSYS database, as presented in Tables 1 and 2. Figure 5 displays the boundary conditions for the fluid domain and the fixed boundary for the solid model. The top surface of the needle is defined as the inlet, with the needle body and domain acting as walls. The fixed boundary is located at the wire's end in the structural analysis. The simulation uses an inlet velocity of 2 m/s and an

injection time of 3 seconds. The epoxy molding compound in the analysis has a viscosity of 0.448 kg/ms, a constant density of 1800 kg/m³, and a surface tension of 0.005 N/m.

Table 1
Material Properties of gold wire

Gold Wire	Unit	Properties
Density	kg/m ³	193300
Young’s Modulus	Pa	7.85 x 10 ¹⁰
Tensile Yield Strength	Pa	1.84 x 10 ⁸
Tensile Ultimate Strength	Pa	1.99 x 10 ⁸
Poisson’s Ratio	-	0.42
Diameter	mm	0.03

Table 2
Boundary condition for the simulation

Boundary Condition	Unit	Detail
Needle Diameter, a	mm	1.00
Distance of Needle to Base, b	mm	3.00
Base Diameter, c	mm	3.00
Inlet Speed	m/s	2.00
Injection time	s	0.3

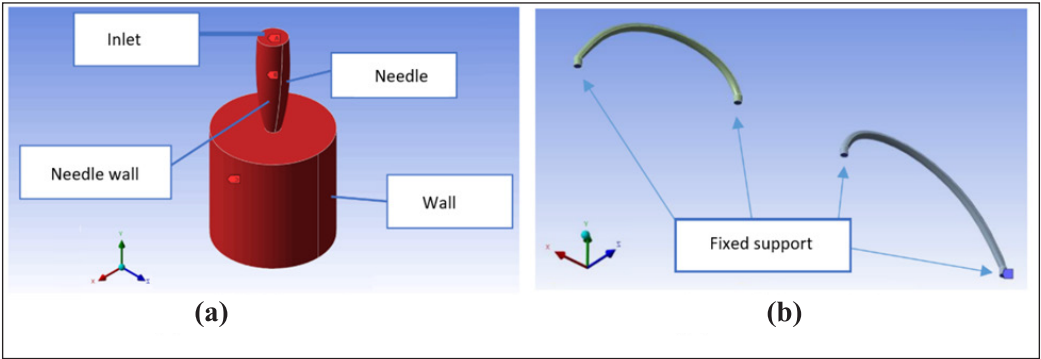


Figure 5. Boundary conditions of (a) fluid domain and (b) solid model

Grid-independent Test

The grid-independent test ran the same simulation with multiple grid sizes or mesh refinement levels to determine the minimum mesh refinement required for an accurate solution in the simulation (Lee et al., 2020). The model used is Type 2 with 0.03mm gold wire. Five levels of refinements, which are Mesh-1 (0.10 mm), Mesh-2 (0.15 mm), Mesh-3 (0.20 mm), Mesh-4 (0.25 mm), and Mesh-5 (0.30 mm), have been analyzed to determine the optimal mesh element size for the simulation study. Figure 6 illustrates the grid-independent test for different mesh element sizes against the Von Mises Stress using the Type 2 configuration with 0.03mm gold wire. In this study, Mesh-2 with an element size of 0.15 mm was chosen for all simulations as it showed optimal results in terms of result and computing time.

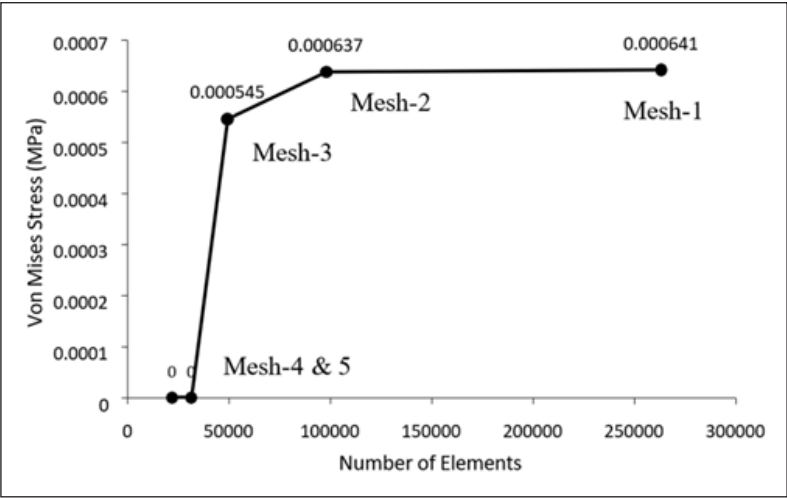


Figure 6. Grid independent test (Von Mises stress curve for different mesh counts)

Experiment Setup

The encapsulation process plays a crucial role in protecting the LED components from environmental factors and ensuring optimal performance. Simulation techniques have been widely used to model the LED encapsulation process; however, experimental validation is essential to verify the accuracy of simulation results. In this study, an experiment is conducted to validate the LED encapsulation process using digital image analysis. The experimental setup included a micrometer, syringe, light source, laboratory stand, microscope, and monitor, all configured to achieve standardized results with minimal error, as illustrated in Figure 7. The distance between the needle tip and the substrate was controlled using a knob. The encapsulant used in the tests consists of two parts. Part A contains epoxy ($C_{21}H_{25}ClO_5$), while part B serves as the hardener (Alicyclic anhydrides). Part-A and Part-B are mixed in equal volume percentages before being used as an encapsulant.

Three methods were employed to determine the average drop volume. First, twenty drops were collected in a pre-tared beaker, and the average droplet volume was calculated. Microscopic images were taken, and the droplet volume was manually calculated using image processing software called “Open Drop.” Epoxy droplets were dispensed from 3.240 mm above the substrate. All experiments were conducted at room temperature before curing. The epoxy was then cured at 120°C for 1 hour, inspected, and the curing process continued at 125 °C for an additional 2 hours. The optimal epoxy coverage area was identified after curing using the open-source software “Image-J. In order to analyze the epoxy dispensing further, the epoxy-covered area was measured and compared with the simulation, as shown in Figure 8. The average area covered was compared between simulation and experimental

results, as shown in Table 3. The result indicated that the simulation epoxy-covered area is calculated as 55.36 mm², while the experimental volume is measured at 52.45 mm², resulting in a percentage difference of 5.55%. This comparison results verified that the simulation configuration accurately predicts the epoxy encapsulation process.

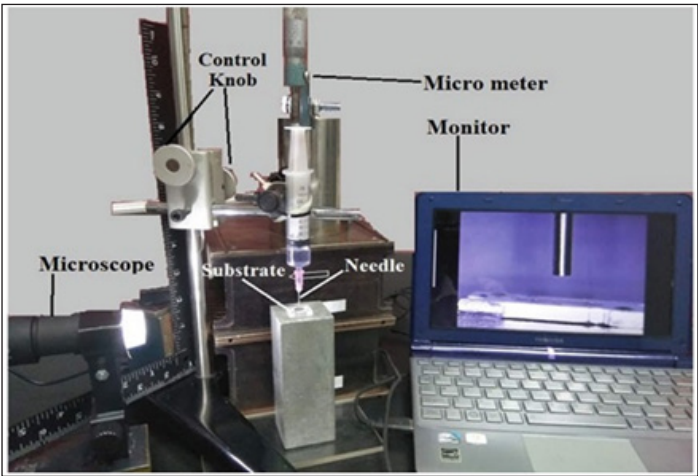


Figure 7. Experimental setup for dispensing the epoxy

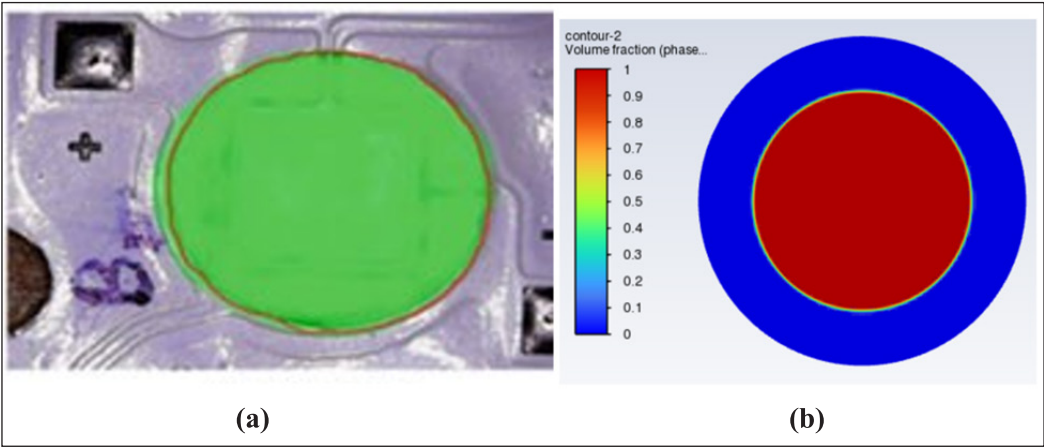


Figure 8. Covered area measurement by (a) Image-J software and (b) Ansys simulation

Table 3
Comparison of simulation and experimental results

	Experiment	Simulation
Covered Area (mm ²)	52.45	55.36
Percentage Difference	-	5.55%

RESULTS AND DISCUSSION

Effect of Gold Wire Configuration on Maximum Total Deformation

Wire deformation plays a critical role in the reliability of LED assemblies, as misalignment or improper seating of wire bonds can lead to interconnection failures between the LED chip and the substrate. Such failures can disrupt power and signal transmission, compromising LED functionality. Moreover, deformation-induced stresses may degrade the encapsulation material, increasing the risk of cracking or delamination and exposing the LED chip and bonding wires to environmental threats such as moisture and contaminants (Quispe-Aguilar et al., 2023). The maximum total deformation is defined as the largest displacement experienced within the structure to assess the resilience of different wire configurations under load. The stress might cause the encapsulant to crack or delaminate, thereby reducing its ability to protect the LED chip and bonding wires from external elements like moisture and contaminants.

Figure 9 presents a comparison of the maximum total deformation, δ , for the gold wire layouts with EMC at a viscosity of 0.448 kg/ms. These differences in deformation can be attributed to the structural characteristics and geometry of each wire design. Type 2 configurations exhibit the largest total deformation at 9.878×10^{-6} mm due to its complex loop structure, which is more susceptible to significant deformations when subjected to external forces or pressure during encapsulation. Following that, the Type 1 configurations rank second in total deformation at 7.843×10^{-6} mm due to their simpler design compared

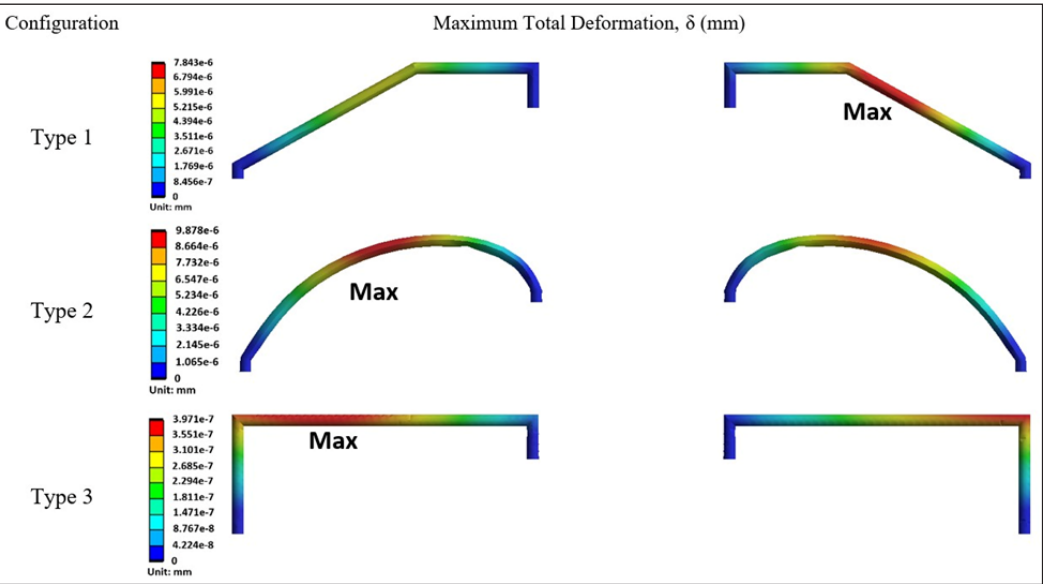


Figure 9. The maximum total deformation of the three types of wire configurations highlights the impact of geometry on deformation behavior

to the Type 2. While it has fewer bends and curves, it still experiences notable deformation due to the inherent flexibility of the wire material. This can be attributed to its specific shape and orientation, which may increase stress concentrations and deformation under applied loads. This can lead to increased stress concentrations in certain regions, consistent with observations in encapsulated interconnects, where encapsulant properties and wire orientation play critical roles in stress distribution (Van Keymeulen et al., 2014).

Lastly, the type 3 wire exhibits the lowest maximum total deformation at 3.971×10^{-7} mm due to the triangular shape influencing its deformation characteristics, balancing structural rigidity and flexibility. The stability and balance of the Type 3 configuration results in a more consistent spread of mechanical stresses throughout the wire. This geometric feature gives the Type 3 configuration an advantage in enduring the forces and pressures encountered during encapsulation, making it more resilient than other configurations. These findings complement prior studies demonstrating that encapsulation geometry can significantly influence deformation behavior, with optimized designs like triangular layouts exhibiting improved durability and mechanical performance (Mosallaei et al., 2018). Furthermore, studies on wire sweep during semiconductor encapsulation highlight the impact of encapsulant viscosity and wire geometry on deformation patterns, reinforcing the importance of shape in mitigating deformation (Han & Wang, 1995). Overall, these findings corroborate existing research on the deformation behaviors of various wire geometries under encapsulation and provide a quantitative comparison of deformation magnitudes. The results emphasize the critical role of wire design in optimizing mechanical performance and minimizing stress concentrations, offering valuable insights for improving encapsulated wire layouts in practical applications.

Effect of Gold Wire Configuration on Maximum Equivalent Elastic Strain

Equivalent elastic strain quantifies the deformation or stretching of the wire material when subjected to external forces during the LED encapsulation process. This strain is essential for evaluating the mechanical strength and reliability of wire connections within an LED device. Figure 10 compares the three wire arrangements based on their largest equivalent elastic strain. The type 2 configuration exhibits the highest equivalent elastic strain at 4.234×10^{-6} . The type 1 configuration demonstrates a maximum equivalent elastic strain of 3.871×10^{-6} . The type 3 configuration has the lowest equivalent elastic strain at 2.113×10^{-7} . As previously noted, the geometric features of the type 3 configuration enhance its structural integrity, providing greater resistance to deformation and strain, which leads to superior elastic behavior compared to other wire configurations. The 90-degree angles in the square shape likely contribute to the wire's increased rigidity, preventing excessive stretching or bending. This structural integrity enables the square-loop wire to retain its shape and resist deformation, resulting in lower elastic strain values, as supported by Wu

and Huang (2011), who found that stronger configurations reduce deformation and strain levels in LED assemblies. They emphasized that structural design significantly impacts mechanical stability, with simpler and well-balanced configurations more resistant to stress and deformation. Additionally, Packwood et al. (2018) examined the effects of varying encapsulant media on wire bond stress under thermal cycling, revealing that stress distribution and deformation levels are highly dependent on material and geometric choices. Their findings underscore the importance of tailoring wire configurations to achieve mechanical stability during encapsulation.

The results confirm trends observed in previous studies and contribute new insights into the impact of specific geometric features, such as the triangular shape in the Type 3 configuration, on strain minimization. This work emphasizes the critical role of wire geometry in ensuring the mechanical reliability of LED assemblies and bridging a gap in understanding how design optimizations translate into practical performance improvements.

Effect of Gold Wire Configuration on Maximum von Mises Stress

Von Mises stress represents the equivalent stress at a specific point in a material derived from individual stress components. Monitoring Von Mises stress allows for structural integrity of gold wires to be assessed during encapsulation. High von Mises stress values may reveal areas where the wire is vulnerable to deformation or failure. Thus, understanding von Mises stress in gold wires during LED encapsulation is crucial for gaining insights into the wire's mechanical behavior. Figure 11 compares three-wire configurations in terms of their maximum von Mises stress. The type 2 configuration wire exhibits a maximum von Mises stress of 0.3042 MPa. The type 1 configuration shows a maximum von Mises stress of 0.2811 MPa. Lastly, the type 3 configuration displays a maximum von Mises stress of 0.001547 MPa. Hooke's Law states that stress is directly proportional to strain, a relationship clearly demonstrated in the type 3 configuration, which shows the lowest elastic strain (Figure 10) and the lowest von Mises stress. The higher von Mises stress observed in other wire configurations reflects higher strain levels, thereby increasing the likelihood of mechanical failure. Conversely, lower stress in certain configurations indicates that these wire shapes are more effective at resisting applied forces, helping to maintain structural integrity. The simulation results confirmed that Type 3 wires exhibit the lowest total deformation, equivalent elastic strain, and von Mises stress. This outcome underscores the significant impact of the gold wire's geometrical characteristics on its mechanical properties.

The findings of this study underscore the superior mechanical and stress performance of the Type 2 and Type 3 configurations during the transfer molding process, advancing the understanding of encapsulation mechanics in electronic devices. Notably, the observation that the Type 2 configuration exhibited the highest equivalent elastic strain and von Mises stress aligns with findings by Tian et al. (2019), who reported reduced signal transmission

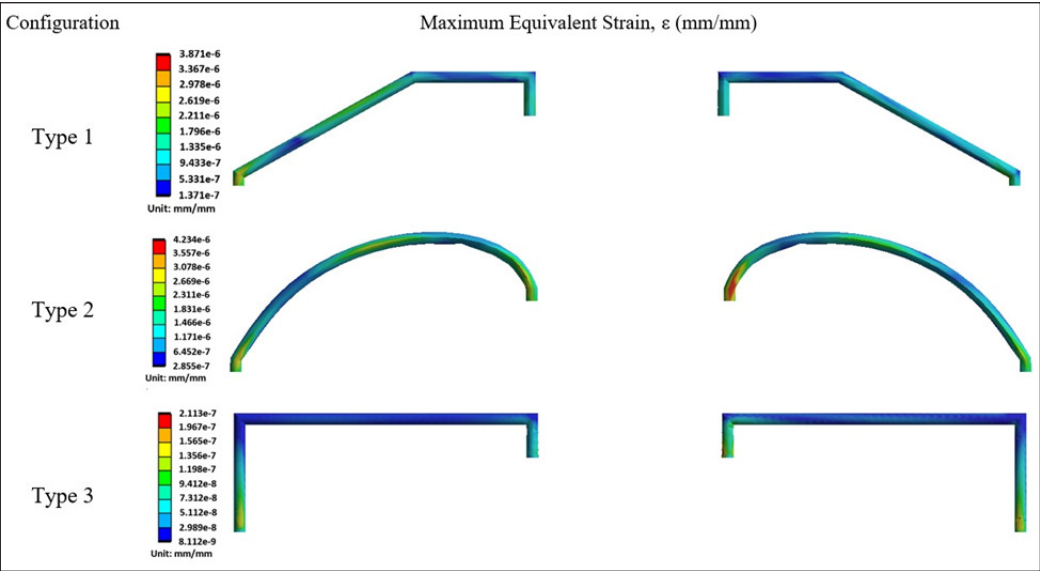


Figure 10. The maximum equivalent strain of the three types of wire configurations highlights the impact of geometry on strain behavior

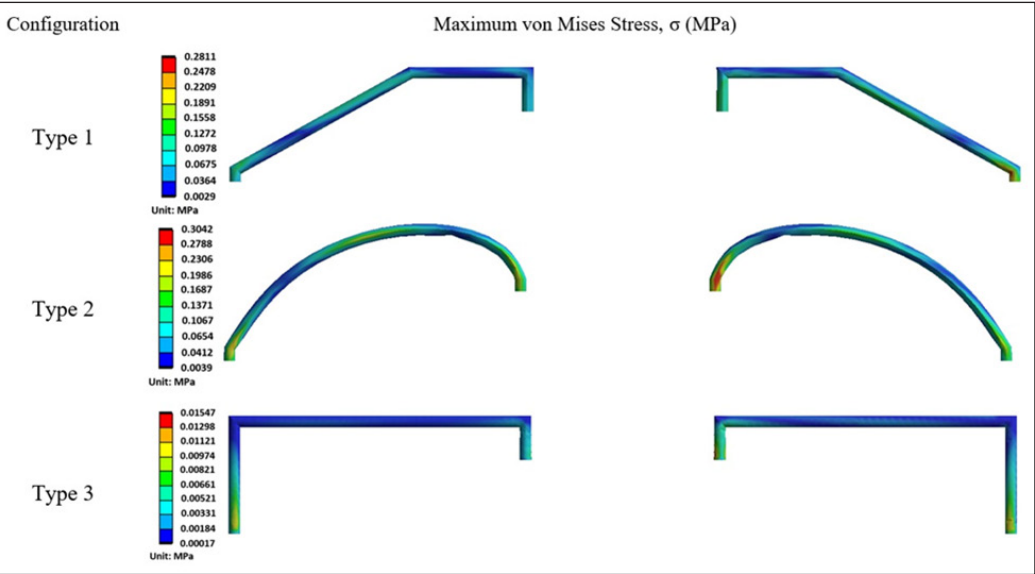


Figure 11. The maximum von Mises stress of the three types of wire configurations highlights the impact of geometry on stress behavior

quality (34.32%) in the Type 2 configuration compared to the Type 1 configuration (36.69%) under similar conditions. This suggests that while Type 2 configurations endure higher stress levels, they may trade off performance in electrical signal integrity.

Furthermore, the results indicate that the Type 3 configuration demonstrates superior resilience with the lowest maximum total deformation, equivalent elastic strain, and von Mises stress. This aligns with the findings of Choube and Sambhe (2020), who found that square cross-section springs outperformed rectangular cross-sections in stress scenarios. This correlation directly supports the effectiveness of the square-loop Type 3 configuration in mitigating mechanical and thermal stresses encountered during LED encapsulation processes. These comparisons illustrate how the present study builds on prior research by reinforcing the significance of wire geometry in stress distribution and encapsulation efficiency. Specifically, it confirms the advantages of the Type 3 configuration in mechanical performance and its potential for improved reliability under operational stresses.

CONCLUSION

This study focussed on investigating the impact of wire bonding looping formation on the LED encapsulation process. This numerical study used a fluid with a viscosity of 0.448 kg/ms aligned with experiments using EMC with the same viscosity. Both simulation and experimental data indicated that The comparison results verified that the simulation configuration accurately predicted the epoxy encapsulation process with a 5.55% volume difference, confirming the accuracy of the simulation configuration.

Three gold wire designs were evaluated with EMC at 0.448 kg/ms viscosity for deformation, equivalent elastic strain and maximum von Mises stress. The type 2 wire demonstrated good compatibility with EMC during LED encapsulation, exhibiting the highest deformation, equivalent elastic strain and von Mises stress among the three designs. The Type 1 wire showed better performance than the Type 2 wires in terms of maximum total deformation, equivalent elastic strain, and von Mises stress. However, the Type 3 wire emerged as the optimal gold wire topology for LED encapsulation due to its low maximum total deformation, equivalent elastic strain, and von Mises stress, highlighting its efficacy in LED encapsulation processes.

ACKNOWLEDGEMENTS

This work was supported by the Ministry of Higher Education (MoHE) Malaysia for the Fundamental Research Grant Scheme with Project Code: FRGS/1/2022/TK10/USM/03/11

REFERENCES

- Alim, M. A., Abdullah, M. Z., Aziz, M. S. A., & Kamarudin, R. (2021). Die attachment, wire bonding, and encapsulation process in LED packaging: A review. *Sensors and Actuators A: Physical*, 329, Article 112817. <https://doi.org/10.1016/j.sna.2021.112817>
- Alim, M. A., Abdullah, M. Z., Aziz, M. S. A., Kamarudin, R., Irawan, A. P., & Siahaan, E. (2020). Experimental study on luminous intensity of white LEDs of different configurations. *IOP Conference Series: Materials Science and Engineering*, 1007(1), Article 012145. <https://doi.org/10.1088/1757-899X/1007/1/012145>

- Arriola, E. R., Ubando, A. T., Gonzaga, J. A., & Lee, C. C. (2023). Wafer-level chip-scale package lead-free solder fatigue: A critical review. *Engineering Failure Analysis*, 144, Article 106986. <https://doi.org/10.1016/j.engfailanal.2022.106986>
- Azmi, M. A., Abdullah, M. K., Abdullah, M. Z., Ariff, Z. M., Ismail, M. A., & Aziz, M. S. A. (2018). Flow behavior analysis of EMC in molded underfill (MUF) encapsulation for multi flip-chip package. *Journal of Physics: Conference Series*, 1082(1), Article 012015. <https://doi.org/10.1088/1742-6596/1082/1/012015>
- Azrain, M. M., Omar, G., Mansor, M. R., Fadzullah, S. H. S. M., & Lim, L. M. (2019). Failure mechanism of organic light emitting diodes (OLEDs) induced by hygrothermal effect. *Optical Materials*, 91, 85–92. <https://doi.org/10.1016/j.optmat.2019.03.003>
- Baek, J. H., Park, D. W., Oh, G. H., Kawk, D. O., Park, S. S., & Kim, H. S. (2022). Effect of cure shrinkage of epoxy molding compound on warpage behavior of semiconductor package. *Materials Science in Semiconductor Processing*, 148, Article 106758. <https://doi.org/10.1016/j.mssp.2022.106758>
- Choube, A. M., & Sambhe, R. U. (2020). Stress analysis of square and rectangular cross section helical spring. *International Journal of Scientific Research in Science, Engineering and Technology*, 7(1), 1–6.
- Garoosi, F., & Mahdi, T. F. (2022). Numerical simulation of three-fluid Rayleigh-Taylor instability using an enhanced Volume-Of-Fluid (VOF) model: New benchmark solutions. *Computers & Fluids*, 245, Article 105591. <https://doi.org/10.1016/j.compfluid.2022.105591>
- Hamidnia, M., Luo, Y., & Wang, X. D. (2018). Application of micro/nano technology for thermal management of high power LED packaging – A review. *Applied Thermal Engineering*, 145, 637–651. <https://doi.org/10.1016/j.applthermaleng.2018.09.078>
- Han, S., & Wang, K. K. (1995). A study on wire sweep in encapsulation of semiconductor chips using simulated experiments. *Journal of Electronic Packaging*, 117, 178–184. <https://doi.org/10.1115/1.2792089>
- Koutchma, T. (2019). Technology of LED light sources and systems from visible to UV range. In *Ultraviolet LED Technology for Food Applications* (pp. 25–33). Elsevier. <https://doi.org/10.1016/B978-0-12-817794-5.00002-9>
- Lee, M., Park, G., Park, C., & Kim, C. (2020). Improvement of grid independence test for computational fluid dynamics model of building based on grid resolution. *Advances in Civil Engineering*, 2020(1), Article 8827936. <https://doi.org/10.1155/2020/8827936>
- Mahmood, S., Kant, C., Raj, A., Lin, H. C., & Katiyar, M. (2022). Evaluation of encapsulation strategies for solution-processed flexible organic light-emitting diodes. *Materials Chemistry and Physics*, 292, Article 126808. <https://doi.org/10.1016/j.matchemphys.2022.126808>
- Montoya, F. G., Peña-García, A., Juaidi, A., & Manzano-Agugliaro, F. (2017). Indoor lighting techniques: An overview of evolution and new trends for energy saving. *Energy and Buildings*, 140, 50–60. <https://doi.org/10.1016/j.enbuild.2017.01.028>
- Moon, S. H., Park, Y. W., & Yang, H. M. (2017). A single unit cooling fins aluminum flat heat pipe for 100 W socket type COB LED lamp. *Applied Thermal Engineering*, 126, 1164–1169. <https://doi.org/10.1016/j.applthermaleng.2016.11.077>

- Mosallaci, M., Jokinen, J., Kanerva, M., & Mäntysalo, M. (2018). The effect of encapsulation geometry on the performance of stretchable interconnects. *Micromachines*, 9(12), Article 645. <https://doi.org/10.3390/mi9120645>
- Packwood, M., Li, D., Mumby-Croft, P., & Dai, X. (2018). Thermal simulation into the effect of varying encapsulant media on wire bond stress under temperature cycling. In *2018 19th International Conference on Electronic Packaging Technology (ICEPT)* (pp. 152–155). IEEE Publishing. <https://doi.org/10.1109/ICEPT.2018.8480816>
- Quispe-Aguilar, M., Aparco, R., Otero, C., Huamán, M., & Huamán-Romani, Y. (2023). A probabilistic Bayesian machine learning framework for comprehensive characterization of bond wires in IGBT modules under thermomechanical loadings. *Journal of Electronic Materials*, 53(1), 123–134. <https://doi.org/10.1007/s11664-023-10868-y>
- Roslan, H., Aziz, M. S. A., Abdullah, M. Z., Kamarudin, R., Ishak, M. H. H., Ismail, F., & Irawan, A. P. (2020). Analysis of LED wire bonding during encapsulation process. *IOP Conference Series: Materials Science and Engineering*, 1007(1), Article 012173. <https://doi.org/10.1088/1757-899X/1007/1/012173>
- Shan, X., & Chen, Y. (2018). Experimental and modeling study on viscosity of encapsulant for electronic packaging. *Microelectronics Reliability*, 80, 42–46. <https://doi.org/10.1016/j.microrel.2017.11.011>
- Tian, W., Cui, H., & Yu, W. (2019). Analysis and experimental test of electrical characteristics on bonding wire. *Electronics*, 8(3), Article 365. <https://doi.org/10.3390/electronics8030365>
- Ünal, D., Varol, S. F., Brault, J., Chenot, S., Al Khalfioui, M., & Merdan, Z. (2022). Improved performance of near UV-blue n-ZnO/p-GaN heterostructure LED with an AlN electron blocking layer. *Microelectronic Engineering*, 262, Article 111830. <https://doi.org/10.1016/j.mee.2022.111830>
- Van Keymeulen, B., Gonzalez, M., Bossuyt, F., De Baets, J., & Vanfleteren, J. (2014). Mechanical analysis of encapsulated metal interconnects under transversal load. In *2014 15th International Conference on Thermal, Mechanical and Mult-Physics Simulation and Experiments in Microelectronics and Microsystems (EuroSimE)* (pp. 1-8). IEEE Publishing. <https://doi.org/10.1109/EuroSimE.2014.6813842>
- Wu, F. T., & Huang, Q. L. (2011). A precise model of LED lighting and its application in uniform illumination system. *Optoelectronics Letters*, 7(5), 334-336. <https://doi.org/10.1007/s11801-011-1031-x>

Development of a Two-board Potentiostat for Square Wave Anodic Stripping Voltammetry: Prospects for Heavy Metal Monitoring

Siti Nur Hanisah Umar^{1*}, Elmi Abu Bakar², Mohammad Nishat Akhtar², Noorfazreena Mohammad Kamaruddin² and Naoki Uchiyama³

¹*School of Mechanical Engineering, Engineering Campus, Universiti Sains Malaysia, Nibong Tebal, 14300, Malaysia*

²*School of Aerospace Engineering, Engineering Campus, Universiti Sains Malaysia, Nibong Tebal, 14300, Malaysia*

³*Department of Mechanical Engineering, Toyohashi University of Technology, Tenpaku Cho, Hibarigaoka, Toyohashi-shi, Aichi, Japan*

ABSTRACT

Heavy metals such as cadmium, lead, arsenic, mercury, and chromium are harmful to human health, even in a trace amount. Despite existing guidelines and regulations for handling these toxic substances, mortality cases among wild animals due to heavy metal poisoning continue to occur. To effectively investigate the sources of heavy metal contaminants in the environment, it is essential to establish real-time monitoring systems across affected areas. This paper presents the design and development of a potentiostat device (HMstat) with the capability to perform a square wave anodic stripping voltammetry (SWASV). The HMstat was realized using a two-board type potentiostat design, incorporating through-hole technology for the analog component and the myRIO platform for the digital component. Performance evaluations indicated that the HMstat is capable of performing the SWASV method. The results demonstrated that the HMstat achieved an accuracy of 99.014%, remained within the tolerance range of components used and surpassed the existing solution.

ARTICLE INFO

Article history:

Received: 31 August 2024

Accepted: 16 January 2025

Published: 26 March 2025

DOI: <https://doi.org/10.47836/pjst.33.3.09>

E-mail addresses:

snhanisah@usm.my (Siti Nur Hanisah Umar)

meelmi@usm.my (Elmi Abu Bakar)

nishat@usm.my (Mohammad Nishat Akhtar)

fazreena@usm.my (Noorfazreena Mohammad Kamaruddin)

uchiyama@tut.jp (Naoki Uchiyama)

*Corresponding author

Keywords: Heavy metal, potentiostat, square wave anodic stripping voltammetry

INTRODUCTION

Heavy metals such as cadmium, lead, arsenic, mercury, and chromium are toxic even in small amounts. They pose significant risks to human health and the environment

due to their toxicity and ability to accumulate in living organisms. Environmental contamination by heavy metals is predominantly due to anthropogenic activities. These metals possess specific properties that make them suitable for various industrial applications, including metal finishing, electrical and electronics, textiles, food processing, chemicals, palm oil, rubber, wood, and iron and steel manufacturing (IARC, 2012).

Despite increased awareness and regulations surrounding the use of heavy metals in Malaysia, cases of heavy metal poisoning continue to occur. For instance, in recent cases in Sabah, Malaysia, three Borneo pygmy elephants were reported to have died from heavy metal poisoning, with high levels of cadmium found in their livers and kidneys. However, the source of the heavy metal remains unknown (Vanar, 2021). To effectively investigate the sources of heavy metal contaminants in the environment, it is essential to establish real-time monitoring programs that evaluate water quality and agricultural practices across affected areas, highlighting the need for on-site monitoring techniques.

Traditionally, spectrometric techniques have been used to detect heavy metals in the environment. Various instruments have been developed for this purpose, including spectrometric techniques such as inductively coupled plasma mass spectrometry (ICP-MS), inductively coupled plasma atomic emission spectrometry (ICP-AES), inductively coupled plasma-optical emission spectrometry (ICP-OES), flame atomic absorption spectrometry (F-AAS), and graphite furnace atomic absorption spectrometry (GF-AAS). These instruments are highly sensitive and selective and have been used to detect cadmium levels in water (Ahmed et al., 2020; Zanuri et al., 2020), air (Azid et al., 2018; Mohamed et al., 2014), soil (Chaudhary et al., 2020; Kusin et al., 2018), fish (Ishak et al., 2020; Poong et al., 2020), tobacco (Janaydeh et al., 2019), and human blood (Zulkifli et al., 2019).

However, these spectrometric instruments are expensive, have complex operational procedures, and require skilled and trained personnel. Additionally, these instruments are laboratory-based, bulky, and unsuitable for in-situ application, making samples susceptible to contamination during storage and transportation from site to laboratory, potentially leading to inaccurate results (Fakude et al., 2020; Lu et al., 2018). To avoid contamination, the in-situ monitoring of heavy metals is necessary. Electrochemical techniques are well-suited for in-situ monitoring due to their rapid analysis, ease of use, and adaptability for integration into compact circuits, making them ideal for portable and in-situ applications (Bansod et al., 2017; Lu et al., 2018; Lv et al., 2017).

The commercial electrochemical instruments, which the potentiostats can be purchased as bench-top instruments that offer a broad operating potential range, user-friendly software for data interface and display, and a wide range of specialized applications, including characterization of batteries, fuel cells, biosensors, corrosion, environmental monitoring, and the electrochemical synthesis of materials (Irving et al., 2021). However, in practice, only a few of the built-in features are frequently used. This often makes

commercial potentiostats overly complex and overpriced, particularly when only simple electroanalytical applications are required (Tichter et al., 2023). Additionally, the bulky size of bench-top potentiostats limits their application in laboratory environments.

In contrast, hand-held potentiostats, such as the EmStat4S from PalmSens and the DropStat from Metrohm, offer portability, making them suitable for in-situ applications. However, commercial potentiostats are typically distributed as “black boxes,” making it impossible to reprogram and modify the devices (often for warranty reasons) to accommodate measurement routines beyond the standard functions (Dryden & Wheeler, 2015; Tichter et al., 2023).

Nowadays, several designs of self-built potentiostat have been reported for heavy metal ion detection (Adams et al., 2019; Cordova-Huaman et al., 2021; Nemiroski et al., 2014; Rowe et al., 2011; Umar et al., 2021; Umar, Bakar et al., 2020; Umar, Akhtar et al., 2020; Wu et al., 2017). Most designs implement a single board type with surface-mounted integrated circuits, which can be manufactured in small sizes regardless of the component complexity. These designs typically feature 12-bit or higher input/output resolution, sufficient for performing square wave anodic stripping voltammetry method (SWASV), a widely used technique for rapid analysis of heavy metals ions (Bansod et al., 2017; Borrill et al., 2019). However, they require skilled personnel and sophisticated tools for fabrication and component assembly, creating hindrances for researchers who wish to undertake in-house fabrication and modification.

An alternative approach is the two-board type potentiostat, where the digital (signal controller) and the analog components are designed on separate boards (Li et al., 2018; Meloni, 2016; Umar et al., 2018). This type of potentiostat implements an off-the-shelf board as the digital component and a custom-fabricated daughterboard with through-hole technology for the analog component. This design allows in-house self-fabrication and modification, regardless of the researcher's background, even with limited fabrication skills and equipment. One of the self-built potentiostat developments is an Arduino-based potentiostat fabricated using simple through-hole electronic components capable of performing simple electrochemical experiments. However, the Arduino-based potentiostat requires external Analog-to-Digital Converter (ADC) and Digital-to-Analog Converter (DAC) components, making the design more complicated. Moreover, the Arduino-based potentiostat has limitations in operating high-frequency electrochemical methods such as SWASV (Li et al., 2018; Meloni, 2016; Umar et al., 2018).

Thus, the main aim of this study is to design and develop a potentiostat device (HMstat) capable of performing SWASV. This study provides a detailed description of the development of the HMstat and evaluates its ability to execute the SWASV method using cell replication. The testing is limited to imitation scenarios. Although it does not involve real heavy metal samples, the HMstat is intended for future applications in heavy metal detection.

METHODOLOGY

Design of HMstat

The proposed device, HMstat, is designed using a two-board approach. The design comprises three components (Figure 1): the analog component, known as the potentiostat read-out circuit component (PRCC); the digital component, referred to as the control signal component (CSC); and the graphical user interface (GUI).

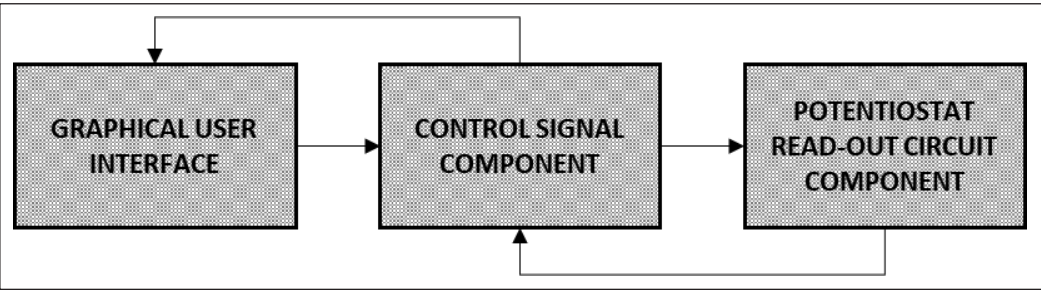


Figure 1. General overview of components of HMstat

Potentiostat Read-out Circuit Component PRCC

The PRCC is designed by implementing through-hole technology. This technology facilitates the fabrication and modification process of the PRCC regardless of researchers' backgrounds, even with limited skills and tools. The PRCC comprises two primary components: the potential control part (PCP) and the current measurement part (CMP).

Potential Control Part

The PCP's role is to regulate the interfacial potential at the working electrode (WE) concerning the reference electrode (RE) through the counter electrode (CE) in the electrochemical cell. The PCP is structured into two stages, utilizing distinct operational amplifier configurations, as illustrated in Figure 2. The first stage is the summing amplifier (OA_{SUM}), and the second is the voltage follower (OA_{FOL}), which is positioned in the negative feedback loop of OA_{SUM} . OA_{FOL} functions to limit any potential current flow through the RE and serves as a unity gain buffer. The potential at the WE is controlled by applying a voltage signal, V_{ap} , to the negative input of OA_{SUM} . As V_{ap} deviates from the fixed potential of RE, the output of OA_{SUM} adjusts to direct current flow between the CE and WE, thereby equalizing the positive and negative inputs of OA_{SUM} .

Current Measurement Part

The second component of PRCC is the CMP, which consists of a single-stage trans-impedance amplifier (OA_{TIA}), as depicted in Figure 2. The purpose of the CMP is to measure

the current passing through the electrochemical cell between the CE and WE, which corresponds to the varying potential output from OA_{SUM} . This current is quantified as a voltage drop across the feedback resistor (R_{gain}) of OA_{TIA} . The output of OA_{TIA} is further amplified before being recorded.

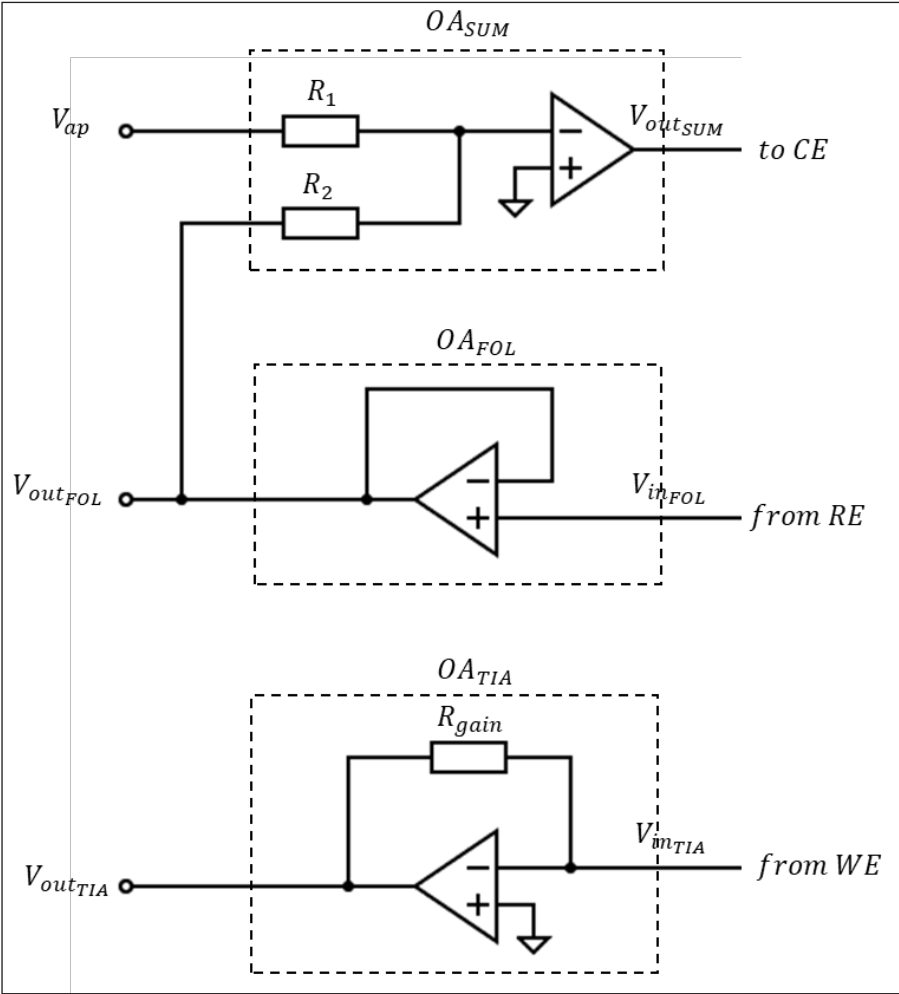


Figure 2. Block diagram of potential control part and current measurement part in potentiostat read-out circuit component

Control Signal Component

The CSC for HMstat was developed using the myRIO platform as the digital core. Under this platform, the signal generation/acquisition and dedicated Graphical User Interface (GUI) was developed to allow for real-time signal monitoring. Several attributes of the myRIO platform render it well-suited to serve as the CSC for HMstat. Notably, it

comes equipped with a built-in 12-bit DAC and ADC, offering analog output and input functionality that can be effectively utilized in both polar directions. This capability is accessible through the miniSystem port (MSP C) (Figure 3), which includes:

- Power Outputs: +5 V, +15 V, and -15 V power outputs.
- Analog Input Channels: Two differential analog input channels (AI0+/AI0- and AI1+/AI1-). It can be used to measure signals up to ± 10 V.
- Analog Output Channels: Two single-ended analog output channels (AO0 and AO1). It can be used to generate signals up to ± 10 V.
- General-Purpose Digital Lines: Eight general-purpose digital lines, capable of 3.3 V output and 3.3 V or 5 V compatible input (DIO0 to DIO7).
- Reference Grounds: DGND serves as a reference for digital lines and +5 V power output, while AGND serves as a reference for analog input and output, as well as +15V and -15V power outputs.

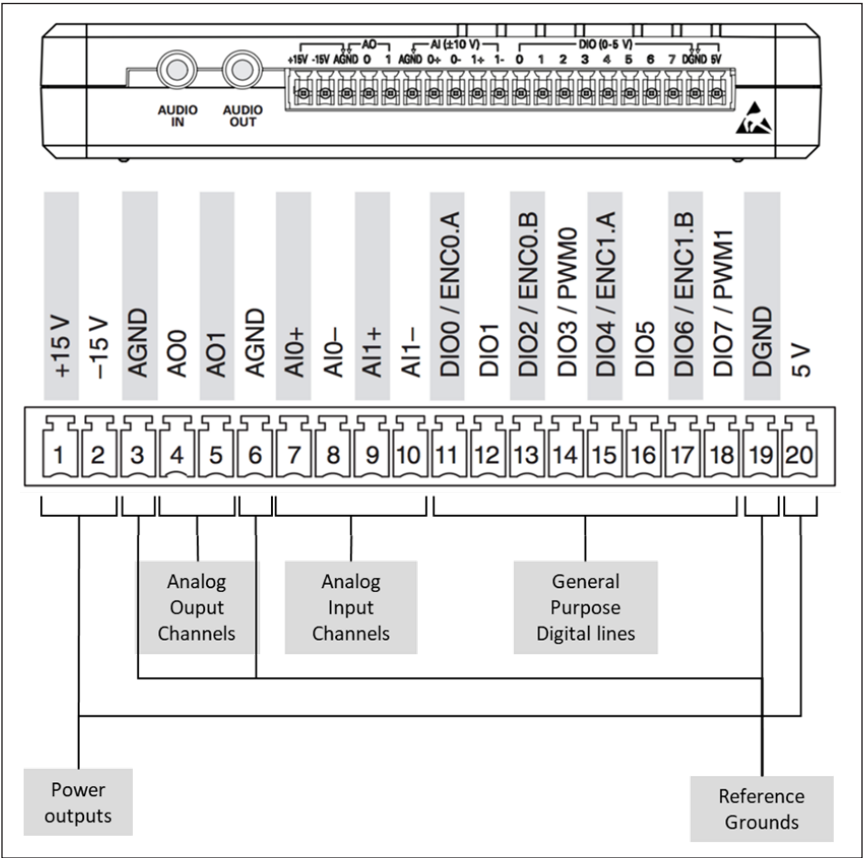


Figure 3. Input-output of CSC

Signal Generation and Process

Signal generation, acquisition, and processing are designed and executed within the CSC using the LABVIEW graphical programming environment. Figure 4 depicts the basic structure of the LABVIEW program. It comprises six main components: loops, signal blocks, an analog output block, an analog input block, data collection blocks, a measurement file block, and waveform charts blocks.

The loops used include the while loop, case structure loop, for loop, and control loop. The analog output block writes the value or passes the generated signal to the analog output channel of AO0 (analog output 0). The analog input block reads value or acquires signal from the two analog input channels, AI0 and AI1 (analog input 0 and analog input 1). The data collection blocks collect signals at each time step of the signal writes (generates) and reads (acquires) and return them as collected signal values along with time data. The measurement file block stores the data collected by the data collection block and stores it in Microsoft Excel files (.xlsx). The waveform chart blocks display the generated and acquired signal, enabling real-time monitoring by the user.

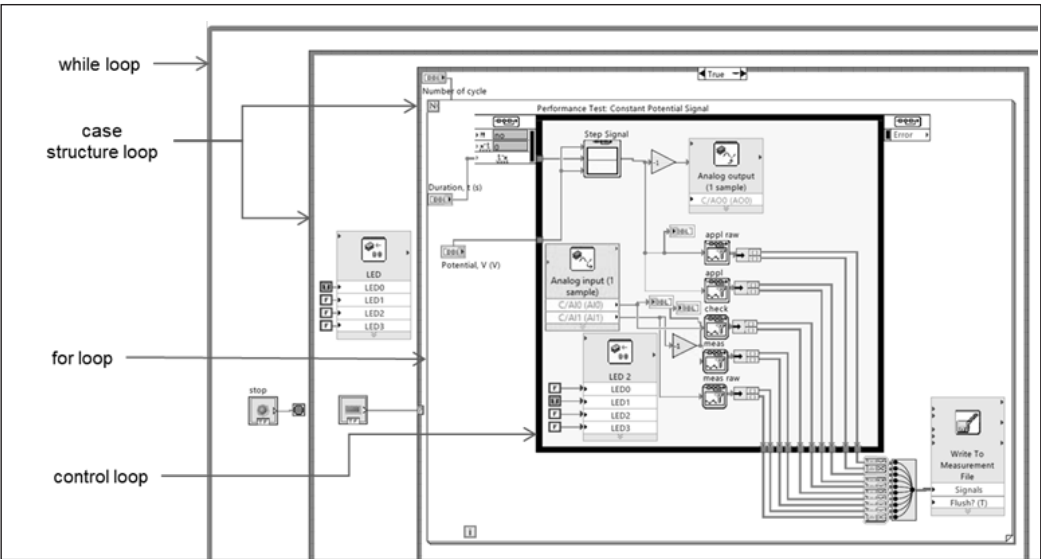


Figure 4. LABVIEW graphical program

The signal block is used to generate the desired potential signals. For HMstat to perform the SWASV method, three signals are designed: constant, ramp, and square wave voltammetry (SWV). These three signals are the core elements used in the SWASV method. Constant and SWV signals are the core elements used in the SWASV method, while the ramp signal is a constituent of cyclic voltammetry (CV), performed prior to measurement as a surface treatment for the electrode, particularly the screen-printed electrode. This process

aims to achieve a proper baseline and a stable response during heavy metal detection or measurement (Bernalte et al., 2020).

Generation of Constant Signal

The basic parameters for generating the constant signal are the desired constant potential and the duration of the applied constant potential. The constant signal is generated using a step signal block (Figure 5). This block requires three input parameters: the initial, final, and step time. The initial and the final values are set to the desired constant potential, and the step time determines the duration for which the constant potential is applied.

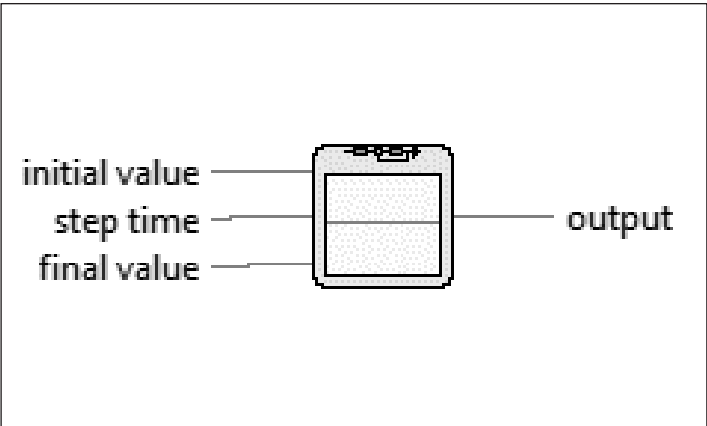


Figure 5. Step signal block

Generation of the Ramp Signal

The key parameters for generating the ramp signal are the initial and final potential, along with the scan rate. The ramp signal is generated using a ramp signal block (Figure 6), which requires three input parameters: the initial output, the start time, and the slope of the ramp signal. The initial output corresponds to the initial potential of the ramp signal, the start time is set to 0 for all measurements, and the slope is determined by the scan rate.

Generation of SWV Signal

SWV signal combines a square wave and staircase signal. The main parameters in SWV are the initial and final potential, the modulation amplitude, the step amplitude, and the frequency of the SWV signal. The SWV signal is generated using a combination of the ramp signal block (Figure 6), the discrete signal block [Figure 7(a)], and the pulse signal block [Figure 7(b)]. The ramp signal block is first discretized using the discrete signal block to form a staircase signal, which is then superimposed with the square wave signal generated

using the pulse signal block. The input parameters for the ramp signal block include the initial potential as the initial output, the start time of 0, and the slope as a product of the step amplitude and the frequency of the SWV signal.

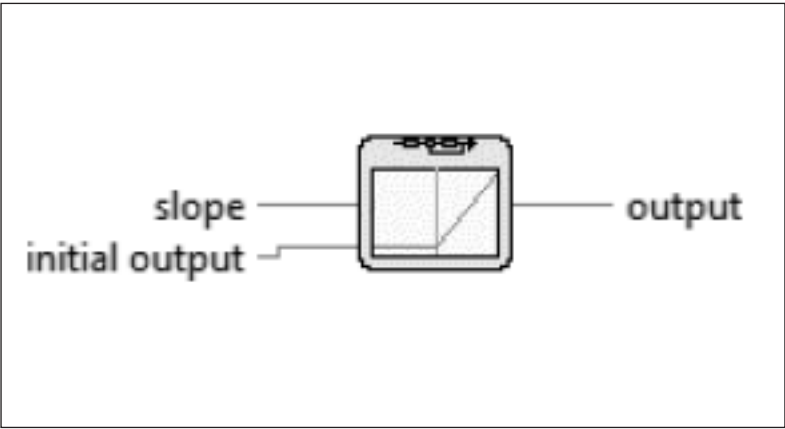


Figure 6. Ramp signal block

The input parameters for the discrete signal block are the sample period and the sample skew. The sample period is set as 1/frequency of the SWV signal, and the skew is set to 0. The pulse signal block requires five input parameters: the start time, amplitude, offset, duty cycle, and period. The start time is set to 0, the amplitude is half of the modulation amplitude, the offset is negative half of the modulation amplitude, the duty cycle is 50%, and the period is 1/frequency.

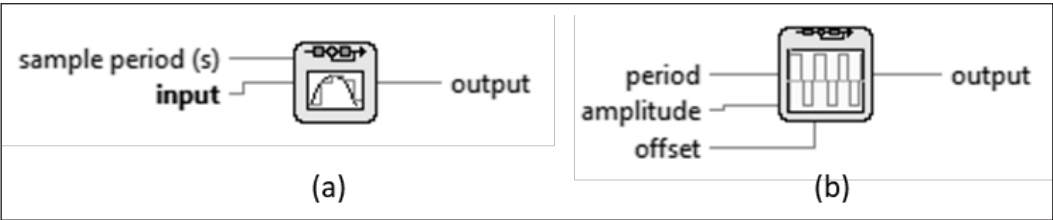


Figure 7. Discrete signal block and pulse signal block

User Interface

A graphic user interface (GUI) allows the user to control the test parameters and provides real-time monitoring for both signal generation and acquisition. The GUI is designed and developed using the LABVIEW program. The three basic signals, constant, ramp and SWV, are integrated into the GUI under the ‘Cell Replication Bench Test’ tab (Figure 8).

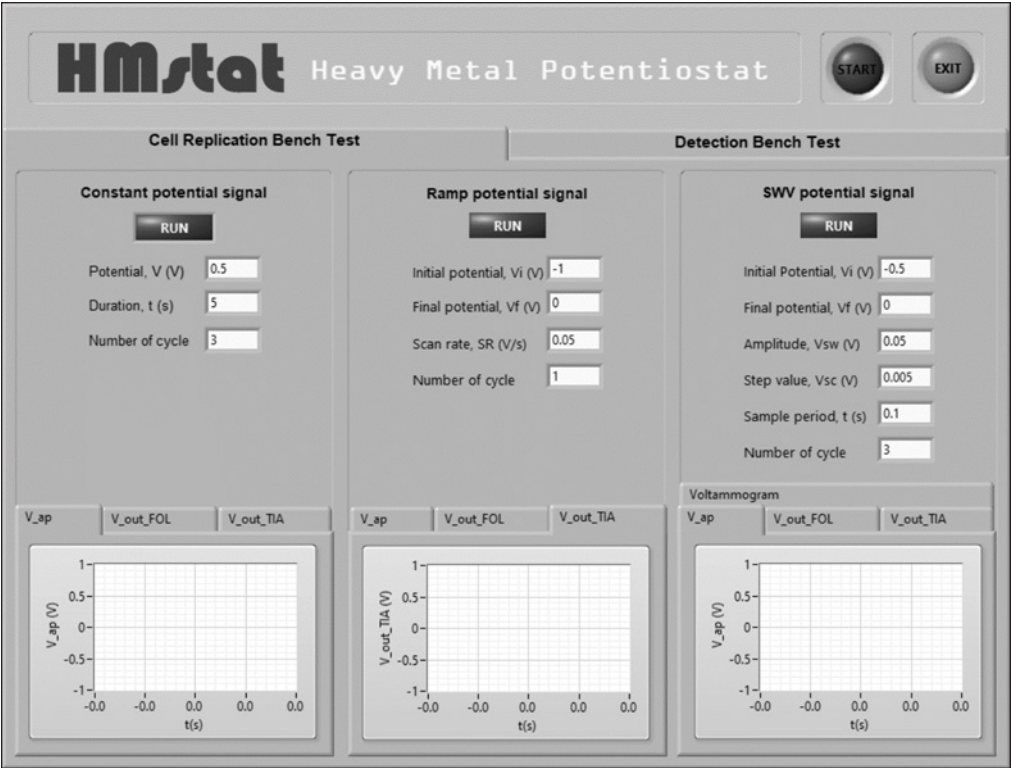


Figure 8. Graphical user interface developed for real-time performance monitoring

Fabrication of HMstat

This section describes the electronic components used to fabricate and assemble the HMstat's PRCC. Table 1 lists all required electronic components for building the PRCC. Initially, the electronic components were assembled on a breadboard to assess their functionality. Once confirmed, they were permanently soldered onto a stripboard.

A single-sided stripboard is used, as shown in Figure 9. The size of the stripboard is 13 × 16 [Figure 10(a)]. The stripboard is cut into the desired size using a circuit board cutter. The thin copper lanes are broken at the appropriate locations using a drill bit. The locations of the broken copper lanes are shown in Figure 10(b). The placement of electronic components, such as the operational amplifier (LM324N), resistors (R1 and R2), and terminal blocks (2-PMSTB and 3-PMSTB1,2,3), is illustrated in Figure 10(c). The placement of wires is shown in Figure 10(d). The feedback resistor, R_{gain} , is connected to PRCC through a 2-pin male screw terminal block (2-PMSTB) to allow for flexibility in operating the current range [Figure 10(e)]. The R_{gain} value can be replaced with a larger or smaller resistance value for a smaller or larger current range.

Table 1
Bill of materials (1 MYR = 0.2127 EUR = 0.2218 USD)

Designator	Component	Unit	Cost per unit -currency	Total cost - currency	Source of materials	Material type
R ₁ ,R ₂	Resistor 10kΩ	2	0.5 MYR	1.0 MYR	Shopee	Metal
R _{gain}	Resistor 499kΩ	1	0.5 MY	0.5 MYR	Shopee	Metal
R _{WE/RE}	Resistor 100kΩ	1	0.5 MYR	0.5 MYR	Shopee	Metal
LM324N	IC Quad Op-Amp LM324N	1	2.0 MYR	2.0 MYR	Shopee	Other
LM324N	IC Quad Op-Amp LM324 socket	1	0.4 MYR	0.4 MYR	Shopee	Other
Wire	Jumper wire	20	0.2 MYR	4.0 MYR	Shopee	Metal/ Polymer
Stripboard	Single-sided stripboard	1	2.0 MYR	2.0 MYR	Shopee	Other
3-PMSTB	3-pin Male Screw terminal block	3	1.0 MYR	3.0 MYR	Shopee	Other
2-PMSTB	2-pin Male Screw terminal block	1	1.0 MYR	1.0 MYR	Shopee	Other
CSC	myRIO	1	3984.0 MYR	3984.0 MYR	Element14	Other
Cell replication	Prototype breadboard	1	25.0 MYR	25.0 MYR	Element14	Other

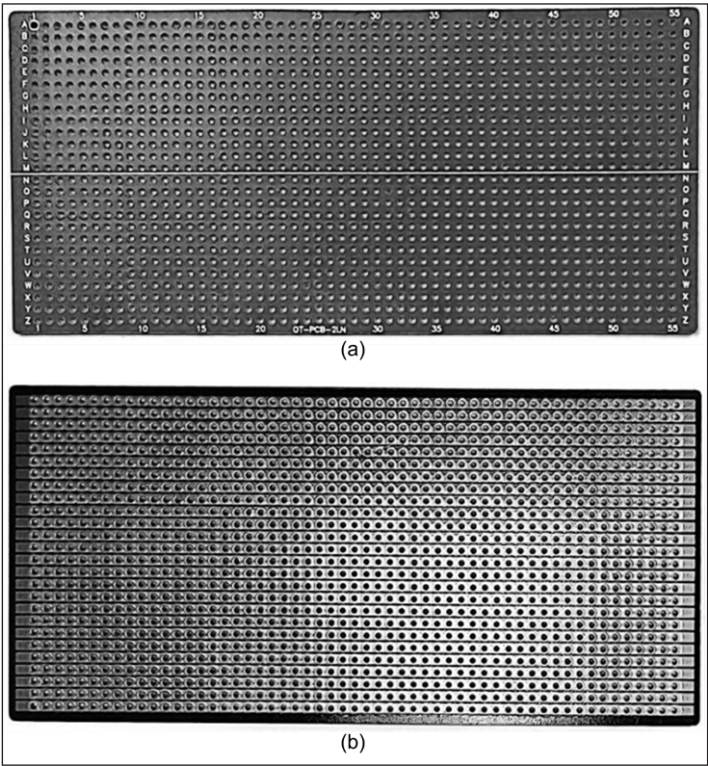


Figure 9. (a) Stripboard front (no copper strip) and (b) stripboard rear (with copper strip)

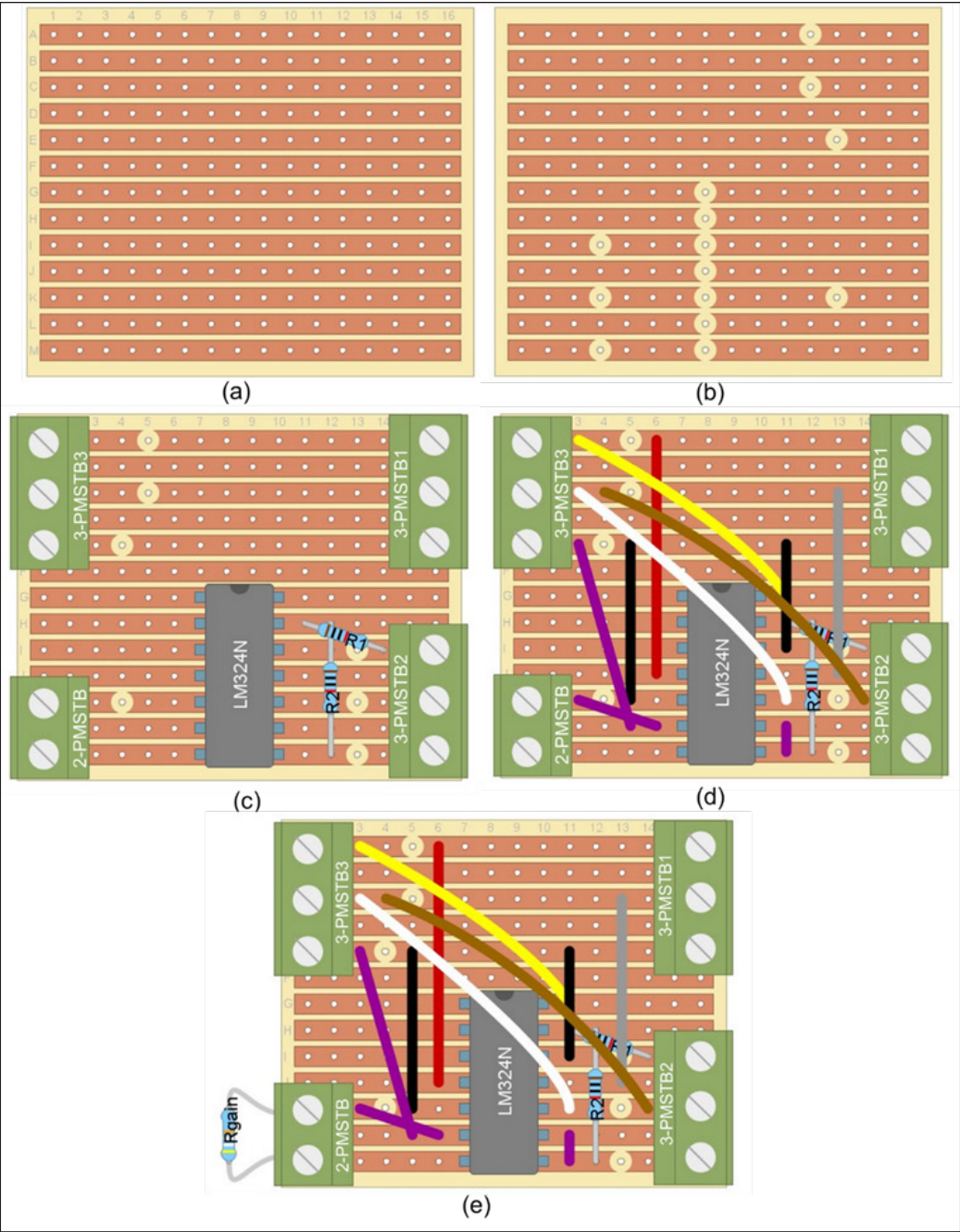


Figure 10. (a) Stripboard cutout dimension of 16 × 13 (front). (b) Breakage points (rear). (c) Placement of electronic component on stripboard (LM324N, R1 and R2, 3-PMSTB1,2,3, and 2-PMSTB2). (d) Placement of wires. (e) Placement of R_{gain}

The connection between the PRCC and CSC is illustrated in Figure 11. Six interconnections between CSC and PRCC are involved. The CSC provides dual-polarity power outputs of +15V and -15V to the LM324N operational amplifier, with AGND serving as the reference point for these power outputs. Additionally, the voltage signal, denoted as V_{ap} , generated by the CSC, is transmitted to the PRCC via the analog output (AO0). The CSC, in turn, receives two distinct signals from the PRCC through two differential analog inputs (AI0+ and AI1+). The signals obtained from AI0+ and AI1+ correspond to the output signals from the OA_{FOL} , V_{outFOL} and, OA_{TIA} , V_{outTIA} of the PRCC, respectively. A summary of the connections is provided in Table 2.

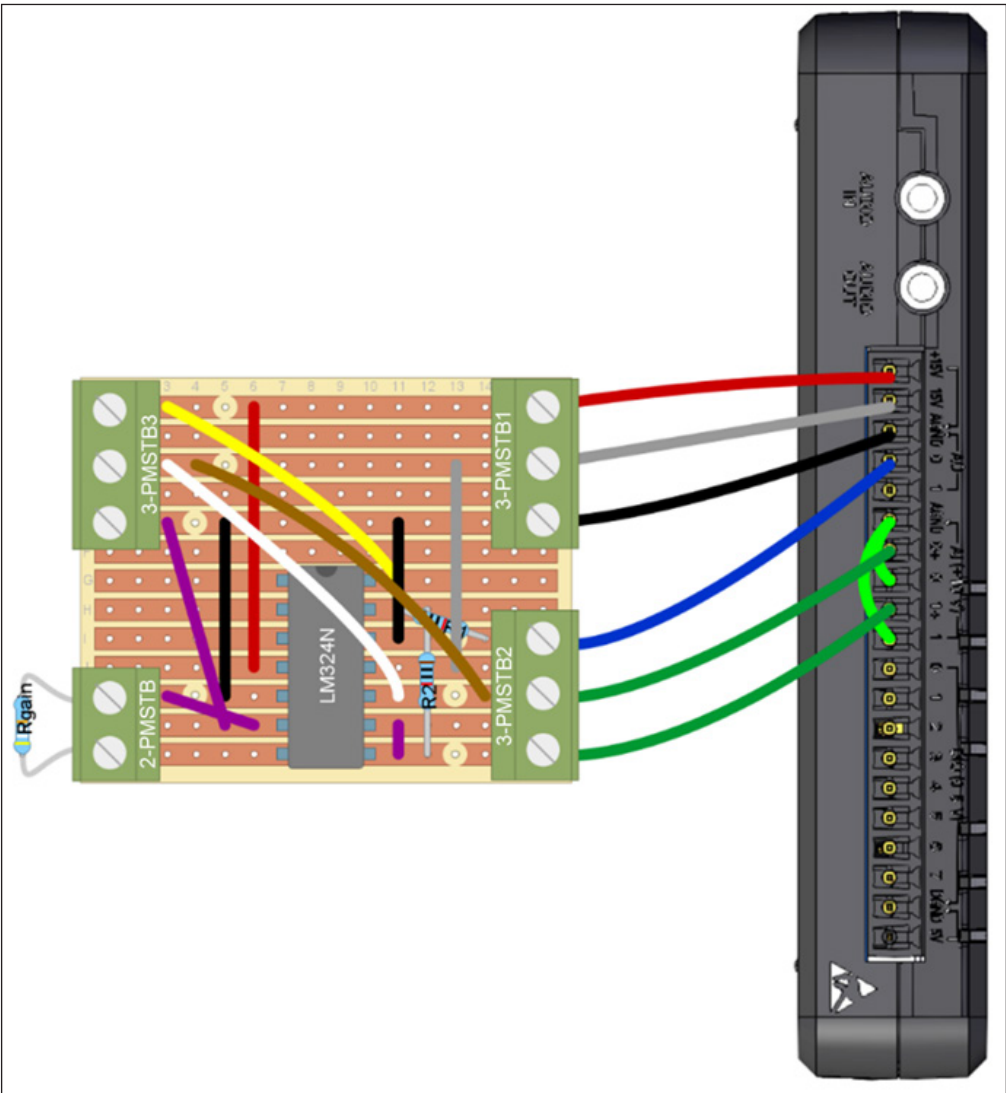


Figure 11. Connection of PRCC to CSC

Table 2
Summary connection between CSC and PRCC

PRCC			CSC		Wire colour
Description	Symbol	Terminal block	Description	Symbol	
Positive supply of LM324N operational amplifier	+V	3-PMSTB1_1	Positive power output	+15V	—
Negative supply of LM324N operational amplifier	-V	3-PMSTB1_2	Negative power output	-15V	—
Inverting input of summing amplifier (LM324N 4)	V_{inSUM}	3-PMSTB2_1	Analog output 0	AO0	—
Output of voltage follower (LM324N 3)	V_{outFOL}	3-PMSTB2_2	Analog input	AI0+	—
Output of transimpedance amplifier (LM324N 3)	V_{outTIA}	3-PMSTB2_3	Analog input	AI1+	—
Positive input of summing amplifier (LM324N 2)	-	3-PMSTB1_3	Ground	AGND	—
The positive input of transimpedance amplifier (LM324N 3)	-	3-PMSTB1_3	Ground	AGND	—

RESULTS AND DISCUSSION

This section describes the assessment of the HMstat in terms of device functionality and accuracy. The performance of the HMstat is evaluated using a cell replication bench test. This test employs a single resistance between RE (V_{inFOL}) and WE (V_{inTIA}), representing the primary electrochemical cell. This test uses a resistance value ($R_{RE/WE}$) of $100\text{ k}\Omega \pm 5\%$.

Device Functionality

The HMstat is first linked to the cell replication of $R_{RE/WE}$, as illustrated in Figure 12. To interface the cell replication with the HMstat, the output of OA_{SUM} and the positive input of OA_{FOL} are connected to one terminal of $R_{RE/WE}$, while the other terminal of $R_{RE/WE}$ is connected to the negative input of OA_{TIA} [Figure 12(a)]. As illustrated in the circuit layout [Figure 12(b)] and the prototype [Figure 12(c)], the 3-pin male screw terminal block 3 (3-PMSTB3) served as the interconnection between cell replication and the HMstat.

The HMstat is powered using an external power supply cable and connected to the personal computer via a USB cable. The real-time monitoring GUI is launched (Figure 8). Pressing the green start button activates the GUI, as indicated by the illumination of LED0 on the myRIO platform. Under the “Cell Replication Bench Test” tab, the parameters of the signal testing are set.

For constant V_{ap} signal, 11 different constant signals (-0.5V, -0.4V, -0.3 V, -0.2 V, 0V, 0.1 V, 0.2 V, 0.3 V, 0.4 V, and 0.5 V) are applied for a duration of 20 seconds. The ramp

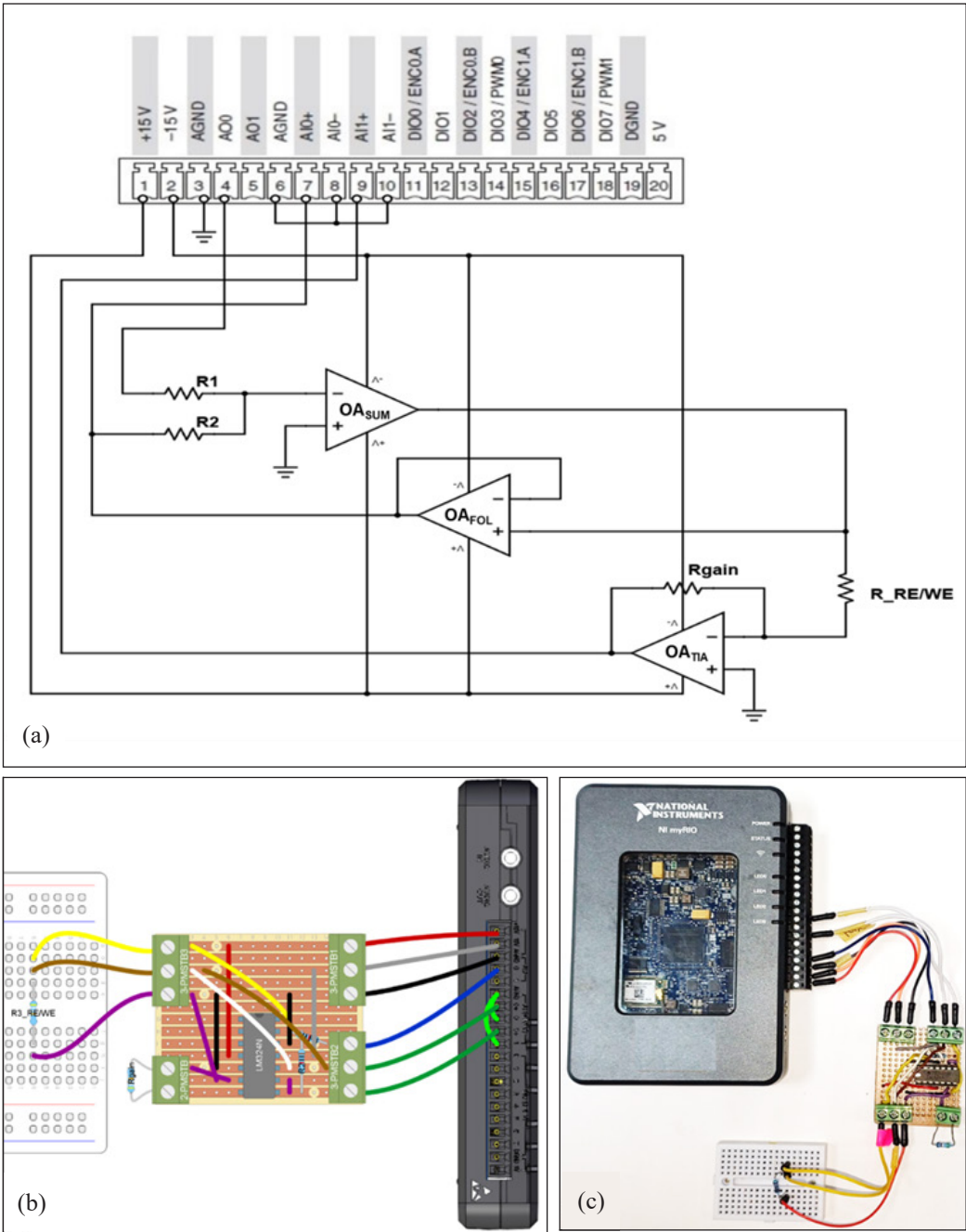


Figure 12. (a) The circuit diagram, (b) circuit layout, and (c) prototype of HMstat connected to cell replication

V_{ap} signal sweeps from an initial potential of -0.5 V to +0.5 V with a scan rate of 0.05 V/s. The SWV V_{ap} signal is scanned from an initial potential of -0.5 V to 0 V, with a modulation amplitude of 0.05 V, a step amplitude of 0.005 V, and a frequency of 10 Hz. Each signal is applied for a single cycle.

The measurement starts when the Run button is clicked. During the measurement, real-time signal generation and acquisition were monitored on the graph panel, as illustrated in Figure 13. The measurement can be stopped at any time by pressing the EXIT button. Upon completion, the stored data is available in .xlsx format for further manipulation and analysis.

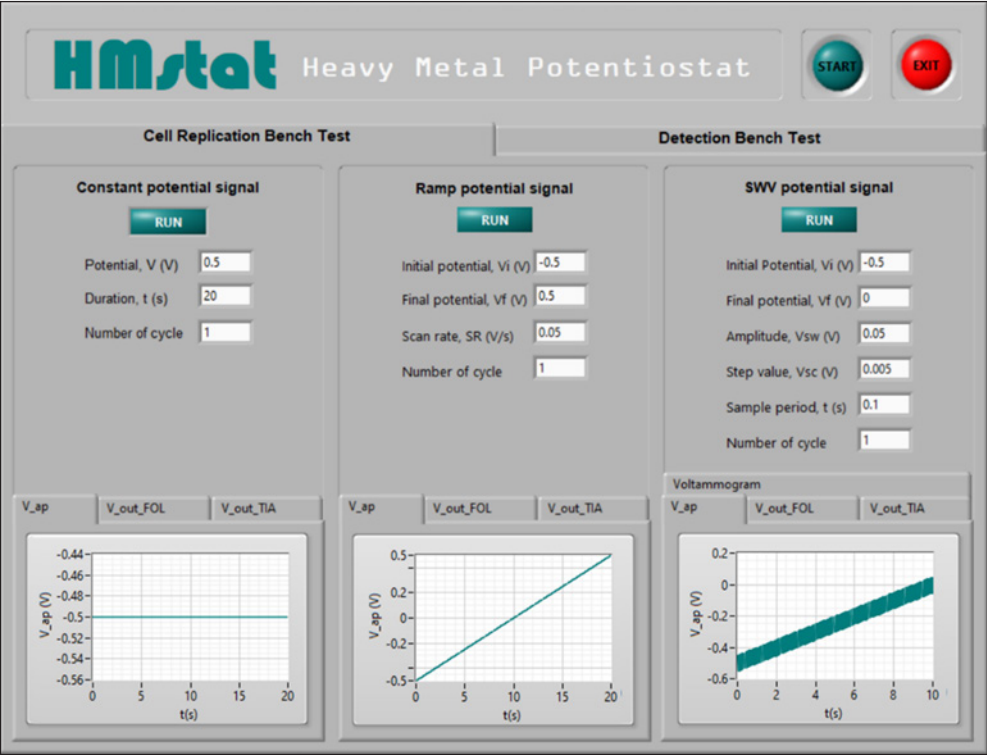


Figure 13. Real-time monitoring of signal generation and acquisition

The response of the HMstat is obtained through the output of PCP and CMP. The output results of PCP are acquired as $V_{out_{FOL}}$ from the PRCC, accessed through AI0+ of the CSC. The output results of CMP are acquired as $V_{out_{TIA}}$ from the PRCC, accessed through AI1+ of the CSC. The formulation of the output from PCP and CMP is derived based on Kirchhoff's law and Ohm's law. Ideally, the current flow into the input terminal of the operational amplifier is zero. Thus, the measured voltage applied to the WE, $V_{out_{FOL}}$

is expressed in terms of the applied voltage signal, V_{ap} , as given in Equation 1. Given that $R_1 = R_2 = 10\text{ k}\Omega$, the magnitude of $V_{out_{FOL}}$ is expected to be equal to V_{ap} .

$$V_{out_{FOL}} = -\frac{R_2}{R_1}V_{ap} \quad [1]$$

The output results of PCP under constant, ramp, and SWV V_{ap} signals are shown in Figures 14(a)-(c). In Figure 14(a), 11 constant V_{ap} signals ranging from -0.5 V to 0.5 V are applied to PCP. The results demonstrate that the magnitude of $V_{out_{FOL}}$ signals is consistent with the magnitude of V_{ap} signals, aligned with Equation 1, as $R_1 = R_2$, thus $V_{out_{FOL}} = V_{ap}$. In Figure 14(b), the result of the ramp V_{ap} signal sweeping from -0.5 V to 0.5 V is shown, with $V_{out_{FOL}}$ increasing in accordance with V_{ap} . The results shown in Figure 14(c) demonstrate that the PCP is capable of operating under the SWV V_{ap} signal. However, slight deviations and fluctuations were observed. The deviation was particularly evident in the responses to the constant V_{ap} signals, while noise was present in the results for both constant and ramp V_{ap} signals.

The ideal current measurement can be expressed as shown in Equation 2. The experimental current measurement of HMstat is obtained as a voltage drop across the feedback resistor, R_{gain} as $V_{out_{TIA}}$. The formulation is shown in Equation 3. Combining Equations 2 and 3, the expression for $V_{out_{TIA}}$ in terms of V_{ap} is given in Equation 4. Since $R_{gain} = 499\text{ k}\Omega$ and $R_{RE/WE} = 100\text{ k}\Omega$, thus, $V_{out_{TIA}} = 4.99V_{ap}$.

$$I_{WE/RE} = \frac{V_{ap}}{R_{RE/WE}} \quad [2]$$

$$I_{WE/RE} = \frac{V_{out_{TIA}}}{R_{gain}} \quad [3]$$

$$\frac{V_{ap}}{R_{RE/WE}} = \frac{V_{out_{TIA}}}{R_{gain}} \quad [4]$$

In Figures 15(a) – (c), the output results of CMP under constants, ramp, and SWV V_{ap} signals are shown. Figure 15(a) demonstrates the response of CMP to 11 constant V_{ap} signals ranging from -0.5 V to 0.5 V. The results indicate that the $V_{out_{TIA}}$ signals are approximately five times the V_{ap} signals, consistent with Equation 4 as $R_{gain} = 499\text{ k}\Omega$ and $R_{RE/WE} = 100\text{ k}\Omega$; thus, $V_{out_{TIA}} = 4.99V_{ap}$. The response of CMP under ramp V_{ap} signals [Figure 15(b)] also aligns with Equation 4, with $V_{out_{TIA}}$ signals increasing with V_{ap} signals. The CMP is also capable of operating under SWV V_{ap} signals, with results following the applied signal. Similar to the result observed for the PCP, deviations and noise were also present in each CMP result.

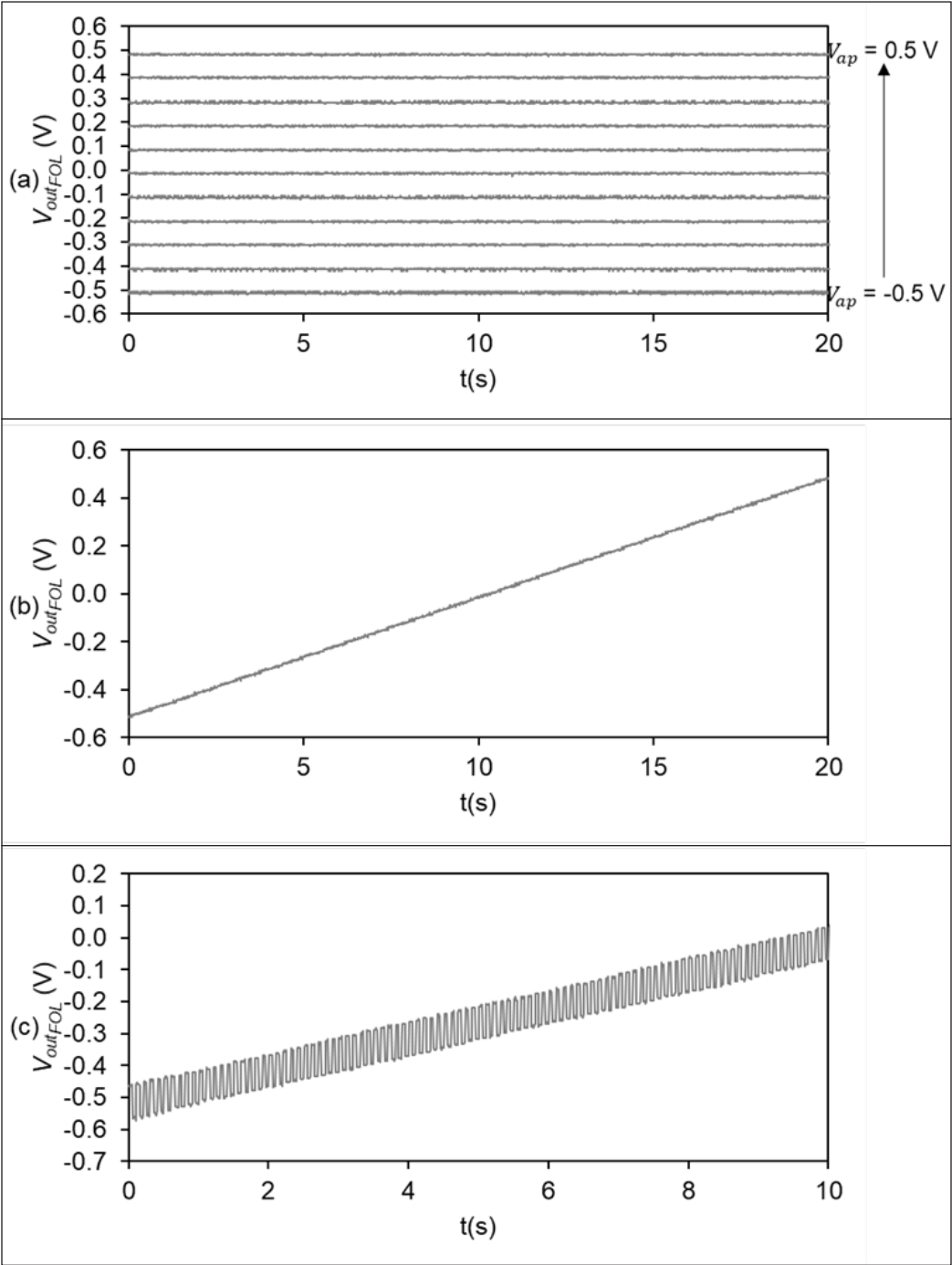


Figure 14. The output of PCP under (a) constant, (b) ramp, and (c) SWV V_{ap} signals, respectively

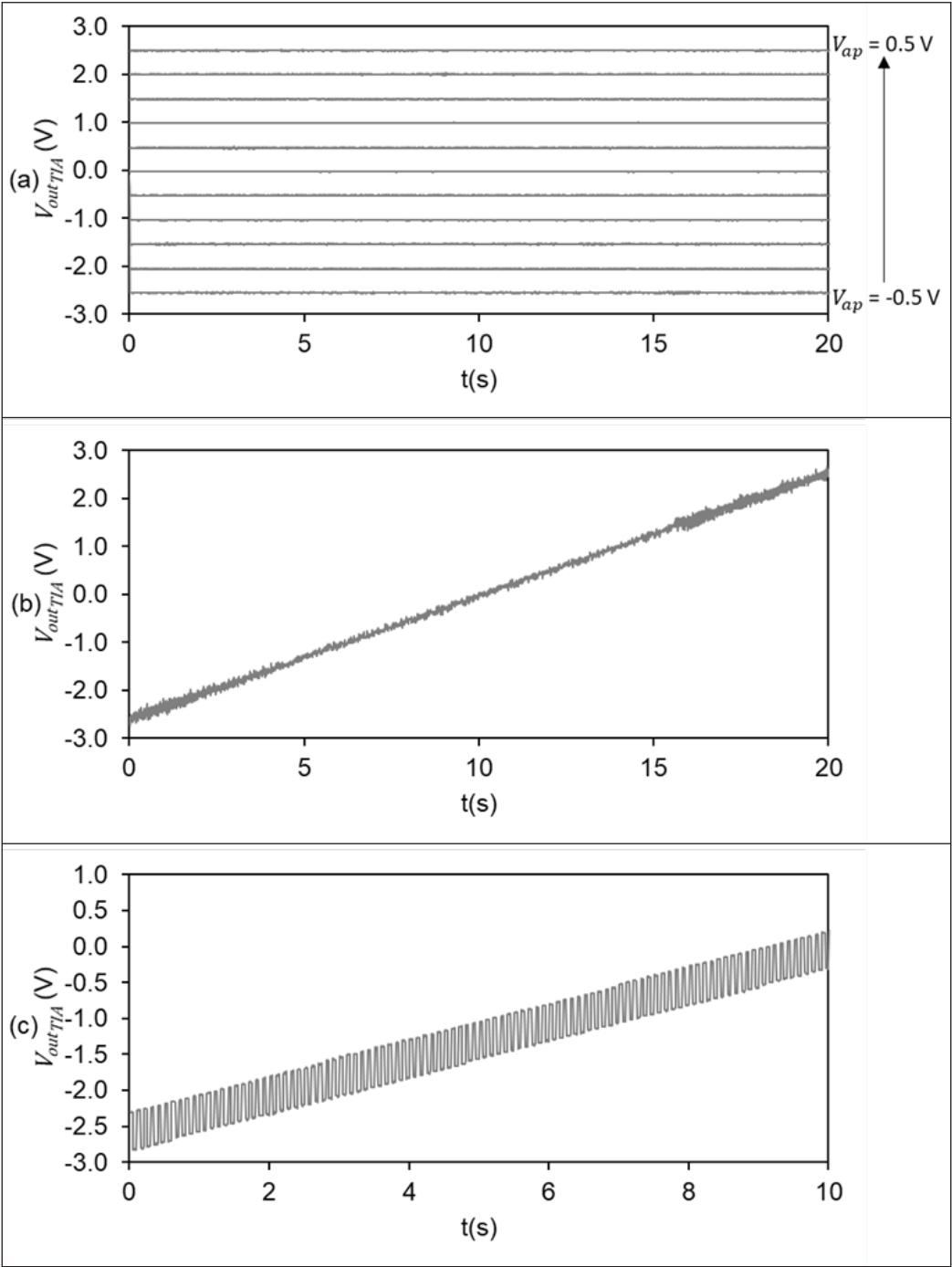


Figure 15. The output of CMP under (a) constant, (b) ramp, and (c) SWV V_{ap} signals, respectively

Accuracy Performance

The accuracy of the HMstat is assessed by plotting the voltammogram shown in Figure 16. The dashed line represents the best-fit line through the data. The R^2 value indicates the correlation coefficient of the best-fit line, where a value of 1 signifies that the data point lies perfectly on the straight line. The equation of the straight line $y = 10.0996x + 0.0901$ can be expressed in the form $y = mx + b$, where m represents the slope of the best-fit line and can be calculated as $1/R_{RE/WE}$. From this equation, $R_{RE/WE}$ is calculated to be 99.014 k Ω . Since the $R_{RE/WE}$ used in this study is 100 k $\Omega \pm 5\%$, the accuracy of the HMstat is calculated to be 99.014%. This measured value falls within the precision rating of the resistor used, which is 95 k Ω to 105 k Ω .

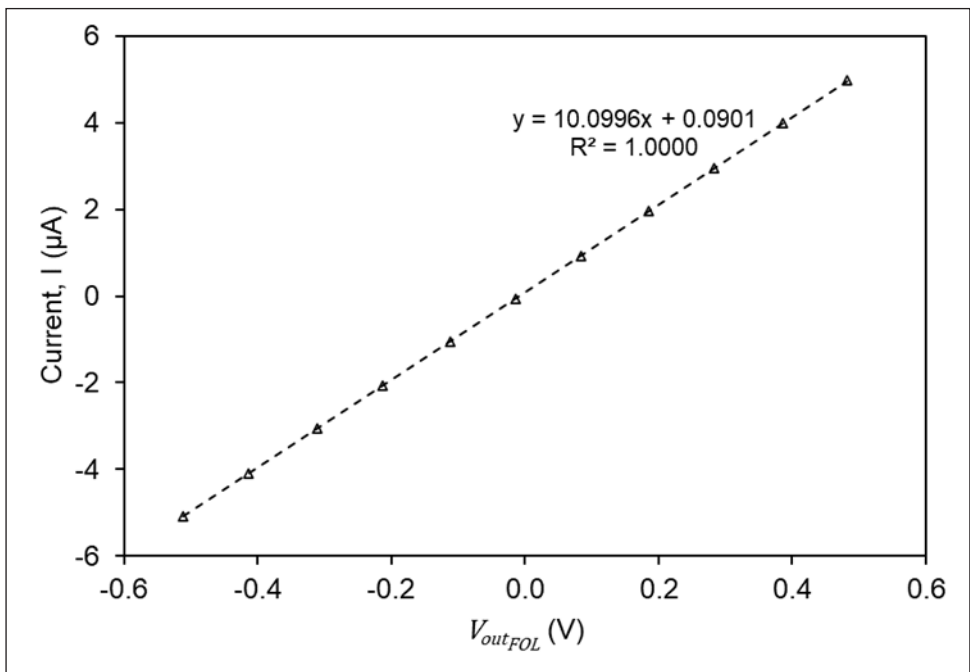


Figure 16. Voltammogram under a variety of constant V_{ap} signal

Comparison to an Existing Solution

The HMstat is compared to an existing solution, which is the Arduino-based potentiostat (Li et al., 2018; Meloni, 2016; Umar et al., 2018). The details of the design and development of the Arduino-based potentiostat are referred to in Umar et al. (2018). For comparison, the parameters of the V_{ap} signals were adapted to those used in the Arduino-based potentiostat. The ramp V_{ap} signal sweeps from an initial potential of -1 V to +1 V with a scan rate of 0.05 V/s. The SWV V_{ap} signal is scanned with an initial potential of -1 V to 0 V, with

modulation and step amplitude of 0.05 V and a frequency of 10 Hz. The R_{gain} and $R_{RE/WE}$ values used in the test were 1 k Ω .

The results are normalized into the current measurement, $1/R_{RE/WE}$ calculated using Equation 3. Figures 17(a) and (b) show the response of HMstat and Arduino-based potentiostat under ramp and SWV V_{ap} signals, respectively. For the ramp V_{ap} signal, both the HMstat and Arduino-based potentiostat exhibit similar increasing patterns in current response, although significant offset and higher noise are observed in the Arduino-based potentiostat's results. The results indicate that both devices can operate under a ramp V_{ap} signal. Existing studies support the result of Arduino-based potentiostat (Cordova-Huaman et al., 2021; Li et al., 2018; Meloni, 2016) that demonstrate its to perform CV and LSV (part of ramp V_{ap} signal).

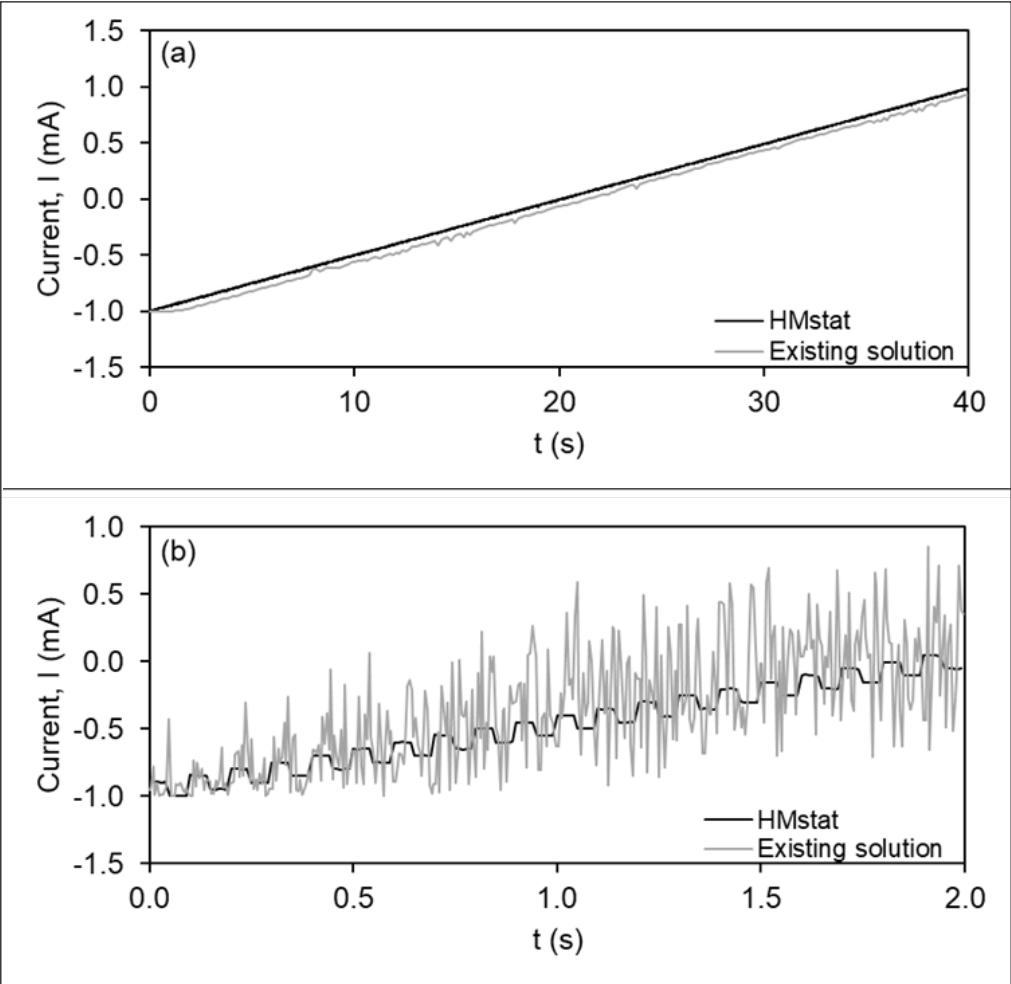


Figure 17. Response of HMstat and the existing solution under the ramp and SWV V_{ap} signal

The results under SWV V_{ap} signals show that the Arduino-based potentiostat produces higher current noise than HMstat [Figure 17(b)]. This is attributed to the Arduino's 8-bit PWM DAC resolution, which is insufficient for performing the SWV V_{ap} signal. In contrast, the HMstat uses a built-in 12-bit DAC resolution, adequate for SWV V_{ap} signals. Consequently, the HMstat demonstrates superior performance in handling SWV V_{ap} signal compared to Arduino-based potentiostat.

CONCLUSION

The design and development of the HMstat have been successfully achieved by employing a two-board potentiostat system. This system comprises the analog component, known as the potentiostat read-out circuit component (PRCC), and the digital component, which is the control signal component (CSC). The implementation of through-hole technology for the PRCC has facilitated the fabrication process, allowing for in-house fabrication and modification, irrespective of the researcher's background. Additionally, the use of the myRIO platform for the CSC has simplified and reduced the stages in the PRCC from the previous design (Umar et al., 2018) to just three stages. This reduction is due to the myRIO platform's built-in 12-bit DAC and ADC, dual polarity analog inputs and outputs, and supply power capabilities. The real-time signals generated and acquired are accessible for monitoring through a GUI developed on the LabVIEW platform.

The capability of HMstat was evaluated through both static and dynamic V_{ap} signals. The HMstat demonstrated its ability to operate under constant, ramp, and SWV V_{ap} signals, indicating its suitability for performing the SWASV method, as the V_{ap} signals are essential components of SWASV. The accuracy of the HMstat was found to be 99.014%, which is within the tolerance range of the components used (5%). Comparative performance verification between HMstat and an existing Arduino-based potentiostat has shown that the HMstat is superior in handling both ramp and SWV V_{ap} signals. The results confirm that the HMstat outperforms the existing solution, demonstrating its enhanced capability and accuracy.

Overall, the specifications of the HMstat are comparable to that of a commercial hand-held potentiostat, as shown in Table 3. The EmStat4S by DropSens comes in two versions: low range and high range. The low range operates within a potential range of ± 3 V and a maximum measurable current of ± 30 mA. In contrast, the high range operates within ± 6 V and a maximum measurable current of ± 200 mA. It is capable of performing various voltammetric, amperometric, galvanostatic, and pulse techniques. The DropStat by Metrohm offers a narrower potential range of ± 2 V and a maximum measurable current of ± 0.2 mA, and it supports some amperometric and voltammetric techniques. Meanwhile, the DropStat Plus provides a wider potential range of ± 4 V and a maximum measurable current of ± 40 mA, and it is capable of operating amperometric, galvanostatic

and voltammetric techniques. The HMstat offers the widest potential range up to ± 10 V. Although its maximum current range is limited to ± 0.1 mA, this limit can be adjusted by modifying the feedback gain, R_{gain} , depending on the application. The HMstat is capable of performing techniques used for heavy metal detection, including CV, SWV, and SWASV.

Table 3
Specification of potentiostat

Name	Potential range	Maximum measurable current	Available technique	Device page on the company's website
EmStat4S	± 3 V or ± 6 V	± 30 mA or ± 200 mA	Voltammetric: LSV, CV; Amperometric: CA, ZRA, CC, MA, PAD; Galvanostatic: LSP, CP, MP, OCP; Pulsed technique: DPV, SWV, NPV	https://www.palmsens.com/product/emstat4s/?utm_source=google_ads&utm_medium=cpc&utm_campaign=landen&gad_source=1&gclid=CjwKCAiApY-7BhBjEiwAQMrrERongQ-vwLg-0rgdg0tTt193PyKo3HvoDaphB CcuoWxAtfLTjGpk6hoCLJ0QAvD_BwE
DropStat	± 2 V	± 0.2 mA	Amperometric: AD; Voltammetric: LSV, CV, SWV, DPV	https://metrohm-dropsens.com/products/instruments/electrochemical-instruments/electrochemical-reader-dropstat/
DropStat Plus	± 4 V	± 40 mA	Amperometric: AD; Voltammetric: LSV, CV, SWV, DPV; Galvanostatic: OCP	https://metrohm-dropsens.com/products/instruments/electrochemical-instruments/standalone-electrochemical-reader-customized-for-your-final-application/
HMstat	± 10 V	± 0.1 mA	CV, and SWV, and SWASV	-

Chronoamperometric (CA), Zero Resistance Amperometry (ZRA), Chronocoulometry (CC), MultiStep Amperometry (MA), Pulsed Amperometric Detection (PAD), Linear Sweep Potentiometry (LSP), Chronopotentiometry (CP), MultiStep Potentiometry (MP), Open Circuit Potentiometry (OCP), Differential Pulse Voltammetry (DPV), Normal Pulse Voltammetry (NPV)

For further progress, the HMstat should be assessed for detecting heavy metal ions in solution by coupling it with an electrode sensor. To enable in-situ detection, a compact electrode sensor is preferred to meet the intended purpose. A screen-printed electrode sensor is a suitable choice, as it integrates three essential electrodes on the same surface. The pictorial representation of the HMstat coupled with the screen-printed electrode is shown in Figure 18. A small sample solution containing heavy metal ions will be dropped onto the surface of the electrode sensor.

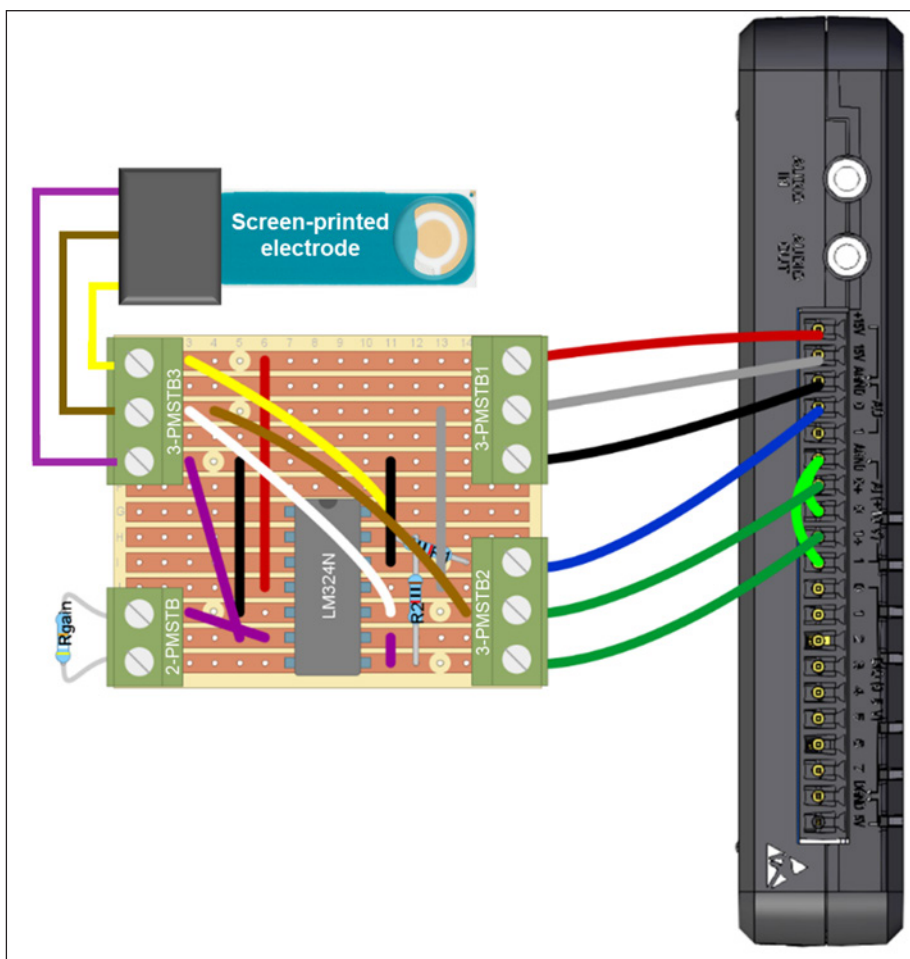


Figure 18. Setup for heavy metal detection using HMstat and screen-printed electrode

ACKNOWLEDGEMENT

Special thanks to Universiti Sains Malaysia for financial assistance through Short Term Grant (R501-LR-RND002-0000000556-0000).

REFERENCES

- Adams, S., Doeven, E. H., Quayle, K., & Kouzani, A. (2019). MiniStat: Development and evaluation of a mini-potentiostat for electrochemical measurements. *IEEE Access*, 7, 31903–31912. <https://doi.org/10.1109/ACCESS.2019.2902575>
- Ahmed, M. F., Mokhtar, M., Alam, L., Mohamed, C. A. R., & Ta, G. C. (2020). Investigating the status of cadmium, chromium and lead in the drinking water supply chain to ensure drinking water quality in Malaysia. *Water*, 12(10), 1–26. <https://doi.org/10.3390/w12102653>

- Azid, A., Noor, S., Amin, S. M., Khalit, S. I., Ismail, S., Samsudin, M. S., Yusof, K. M. K. K., Latiffah, N., Rani, A., Amran, M. A., Yunus, K., Shakir, A., & Saudi, M. (2018). Determination of selected heavy metals in airborne particles in industrial area: A baseline study. *Malaysian Journal of Fundamental and Applied Sciences*, 14(2), 251–256.
- Bansod, B. K., Kumar, T., Thakur, R., Rana, S., & Singh, I. (2017). A review on various electrochemical techniques for heavy metal ions detection with different sensing platforms. *Biosensors and Bioelectronics*, 94, 443–455. <https://doi.org/10.1016/j.bios.2017.03.031>
- Bernalte, E., Arévalo, S., Pérez-Taborda, J., Wenk, J., Estrela, P., Avila, A., & Di Lorenzo, M. (2020). Rapid and on-site simultaneous electrochemical detection of copper, lead and mercury in the Amazon river. *Sensors and Actuators, B: Chemical*, 307, Article 127620. <https://doi.org/10.1016/j.snb.2019.127620>
- Borrill, A. J., Reily, N. E., & Macpherson, J. V. (2019). Addressing the practicalities of anodic stripping voltammetry for heavy metal detection: A tutorial review. *Analyst*, 144(23), 6834–6849. <https://doi.org/10.1039/c9an01437c>
- Chaudhary, S., Sagar, S., Lal, M., Tomar, A., Kumar, V., & Kumar, M. (2020). Partitioning of heavy metals in different environmental and biotic components in the coastal waters of the Straits of Malacca, Peninsular Malaysia. *Journal of Environment Biology*, 41, 812–820.
- Cordova-Huaman, A. V., Jauja-Ccana, V. R., & La Rosa-Toro, A. (2021). Low-cost smartphone-controlled potentiostat based on Arduino for teaching electrochemistry fundamentals and applications. *Heliyon*, 7(2), Article e06259. <https://doi.org/10.1016/j.heliyon.2021.e06259>
- Dryden, M. D. M. M., & Wheeler, A. R. (2015). DStat: A versatile, open-source potentiostat for electroanalysis and integration. *PLOS ONE*, 10(10), 1–17. <https://doi.org/10.1371/journal.pone.0140349>
- Fakude, C. T., Arotiba, O. A., & Mabuba, N. (2020). Electrochemical aptasensing of cadmium (II) on a carbon black-gold nano-platform. *Journal of Electroanalytical Chemistry*, 858, Article 113796. <https://doi.org/10.1016/j.jelechem.2019.113796>
- IARC. (2012). Cadmium and cadmium compounds. In *Arsenic, Metals, Fibres and Dusts* (pp. 121–145). International Agency for Research on Cancer.
- Irving, P., Cecil, R., & Yates, M. Z. (2021). MYSTAT: A compact potentiostat/galvanostat for general electrochemistry measurements. *HardwareX*, 9, Article e00163. <https://doi.org/10.1016/j.ohx.2020.e00163>
- Ishak, A. R., Zuhdi, M. S. M., & Aziz, M. Y. (2020). Determination of lead and cadmium in tilapia fish (*Oreochromis niloticus*) from selected areas in Kuala Lumpur. *The Egyptian Journal of Aquatic Research*, 46(3), 221–225. <https://doi.org/10.1016/j.ejar.2020.06.001>
- Janaydeh, M., Ismail, A., Zulkifli, S. Z., & Omar, H. (2019). Toxic heavy metal (Pb and Cd) content in tobacco cigarette brands in Selangor state, Peninsular Malaysia. *Environmental Monitoring and Assessment*, 191, Article 8. <https://doi.org/10.1007/s10661-019-7755-y>
- Kusin, F. M., Azani, N. N. M., Syed Hasan, S. N. M., & Sulong, N. A. (2018). Distribution of heavy metals and metalloid in surface sediments of heavily-mined area for bauxite ore in Pengerang, Malaysia and associated risk assessment. *Catena*, 165, 454–464. <https://doi.org/10.1016/j.catena.2018.02.029>

- Li, Y. C., Melenbrink, E. L., Cordonier, G. J., Boggs, C., Khan, A., Isaac, M. K., Nkhonjera, L. K., Bahati, D., Billinge, S. J., Haile, S. M., Kreuter, R. A., Crable, R. M., & Mallouk, T. E. (2018). An easily fabricated low-cost potentiostat coupled with user-friendly software for introducing students to electrochemical reactions and electroanalytical techniques [Product-review]. *Journal of Chemical Education*, 95(9), 1658–1661. <https://doi.org/10.1021/acs.jchemed.8b00340>
- Lu, Y., Liang, X., Niyungeko, C., Zhou, J., Xu, J., & Tian, G. (2018). A review of the identification and detection of heavy metal ions in the environment by voltammetry. *Talanta*, 178(2018), 324–338. <https://doi.org/10.1016/j.talanta.2017.08.033>
- Lv, Z. L., Qi, G. M., Jiang, T. J., Guo, Z., Yu, D. Y., Liu, J. H., & Huang, X. J. (2017). A simplified electrochemical instrument equipped with automated flow-injection system and network communication technology for remote online monitoring of heavy metal ions. *Journal of Electroanalytical Chemistry*, 791(2017), 49–55. <https://doi.org/10.1016/j.jelechem.2017.03.012>
- Meloni, G. N. (2016). Building a microcontroller based potentiostat: A inexpensive and versatile platform for teaching electrochemistry and instrumentation. *Journal of Chemical Education*, 93(7), 1320–1322. <https://doi.org/10.1021/acs.jchemed.5b00961>
- Mohamed, R. M. S. R., Aziz, F. H. C., & Kassim, A. H. M. (2014). An assessment of selected heavy metal concentrations (Pb, Cu, Cr, Cd, Ni, Zn) in university campus located in industrial area. *ARP Journal of Engineering and Applied Sciences*, 9(12), 2724–2730.
- Nemiroski, A., Christodouleas, D. C., Hennek, J. W., Kumar, A. A., Maxwell, E. J., Fernandez-Abedul, M. T., Whitesides, G. M., & Paper, S. I. of K. (2014). Universal mobile electrochemical detector designed for use in resource-limited applications. *Proceedings of the National Academy of Sciences*, 111(33), 11984–11989. <https://doi.org/10.1073/pnas.1405679111>
- Poong, J. H., Tee, L. S., Tan, E., Yip, T. H., Ramli, M. H., Hassan, A. R. A., Ali, A., Meng-Hsien, C., Wah, J. L. C., & Chuan, O. M. (2020). Level of heavy metals in bamboo sharks (*Chiloscyllium* sp.) in Straits of Malacca, Malaysia. *Malaysian Journal of Analytical Sciences*, 24(4), 546–557.
- Rowe, A. A., Bonham, A. J., White, R. J., Zimmer, M. P., Yadgar, R. J., Hobza, T. M., Honea, J. W., Ben-Yaacov, I., & Plaxco, K. W. (2011). CheapStat: An open-source, “do-it-yourself” potentiostat for analytical and educational applications. *PLoS ONE*, 6(9), Article e23783. <https://doi.org/10.1371/journal.pone.0023783>
- Tichter, T., Gernhard, M., & Vesborg, P. C. K. (2023). PolArStat: An Arduino based potentiostat for low-power electrochemical applications. *Electrochimica Acta*, 469, Article 143119. <https://doi.org/10.1016/j.electacta.2023.143119>
- Umar, S. N. H., Bakar, E. A., Kamaruddin, N. M., & Uchiyama, N. (2020). A prototype development and evaluation of electrochemical device for heavy metal measurement. In *Proceedings of International Conference of Aerospace and Mechanical Engineering 2019* (pp. 117-125). Springer. https://doi.org/10.1007/978-981-15-4756-0_11
- Umar, S. N. H., Akhtar, M. N., Bakar, E. A., Kamaruddin, N. M., & Othman, A. R. (2020). Development of heavy metal potentiostat for batik industry. *Applied Sciences*, 10(21), Article 7804. <https://doi.org/10.3390/app10217804>

- Umar, S. N. H., Bakar, E. A., Kamaruddin, N. M., & Uchiyama, N. (2018). A low cost potentiostat device for monitoring aqueous solution. *MATEC Web of Conferences*, 217(04001), Article 8. <https://doi.org/10.1051/mateconf/201821704001>
- Umar, S. N. H., Bakar, E. A., Kamaruddin, N. M., Uchiyama, N., & Akhtar, M. N. (2021). Performance of heavy metal potentiostat for batik industry. In *Intelligent Manufacturing and Mechatronics: Proceedings of SympoSIMM 2020* (pp. 885-894). Springer. https://doi.org/10.1007/978-981-16-0866-7_77
- Vanar, M. (2021, October 12). Cadmium found in elephant carcasses. *The Star Online*. <https://www.thestar.com.my/news/nation/2021/10/12/cadmium-found-in-elephant-carcasses>
- Wu, P., Vazquez, G., Mikstas, N., Krishnan, S., & Kim, U. (2017). Aquasift: A low-cost, hand-held potentiostat for point-of-use electrochemical detection of contaminants in drinking water. In *2017 IEEE Global Humanitarian Technology Conference (GHTC)* (pp. 1-4). IEEE Publishing. <https://doi.org/10.1109/GHTC.2017.8239306>
- Zanuri, N. B. M., Abdullah, M. B., Darif, N. A. M., Nilamani, N., & Hwai, A. T. S. (2020). Case study of marine pollution in Teluk Bahang, Penang, Malaysia. In *IOP Conference Series: Earth and Environmental Science* (Vol. 414, No. 1, p. 012032). IOP Publishing. <https://doi.org/10.1088/1755-1315/414/1/012032>
- Zulkifli, H. M., Elias, S. M., Aris, A. Z., Bakar, S. A., & Noor, F. A. M. (2019). Seafood consumption and blood cadmium level of respondents along the coastal area of Melaka, Malaysia. *Malaysian Journal of Medicine and Health Sciences*, 15(SP4), 68–75.

Design of a Two-layer SIW Power Divider with Slot Aperture Y-Junction for Enhanced Narrowband Isolation

Gan Siang Tan¹, Siti Zuraidah Ibrahim^{1,2*}, Mohd Nazri A Karim¹, Ping Jack Soh³, Khuzairi Masrakin⁴ and Sugchai Tantivivat⁵

¹Faculty of Electronic Engineering & Technology, Universiti Malaysia Perlis, 02600 Arau, Perlis, Malaysia

²Centre of Excellence for Advanced Communication Engineering, Universiti Malaysia Perlis, 02600 Arau, Perlis, Malaysia

³Faculty of Information Technology & Electrical Engineering, University of Oulu, 90570 Finland

⁴Department of Electrical & Electronic Engineering, School of Electrical Engineering & Artificial Intelligence, Xiamen Universiti Malaysia, 43900 Sepang, Selangor, Malaysia

⁵Department of Electrical Education, Faculty of Industrial Education and Technology, Rajamangala University of Technology Srivijaya, 90000 Songkhla, Thailand

ABSTRACT

This study presents a 3 dB power divider based on a two-layer Substrate Integrated Waveguide (SIW) structure designed to achieve high isolation and optimal return loss at both output ports while maintaining low insertion loss. The initial configuration uses a conventional Y-junction SIW power divider, which demonstrates limited isolation between output ports. A rectangular slot was incorporated at the Y-junction, significantly enhancing isolation. Although this adjustment

introduced some insertion loss, a second substrate layer with a copper patch was added above the slot, effectively minimizing insertion loss and preserving strong isolation without the need for an isolation resistor. The resistor-free design simplifies fabrication and improves reliability by avoiding components that may fail under high power conditions. Due to fabrication constraints, the power divider is optimized for performance at two center frequencies, 12 GHz and 24 GHz, with prototyping focused on 12 GHz. Simulated and measured results at 12 GHz are in close agreement, confirming measured isolation performance with at least 10 dB of isolation over a fractional bandwidth of 9.9%. While this narrowband design may not suit all applications, it offers high precision for systems

ARTICLE INFO

Article history:

Received: 14 September 2024

Accepted: 05 February 2025

Published: 26 March 2025

DOI: <https://doi.org/10.47836/pjst.33.3.10>

E-mail addresses:

tgschumi@hotmail.com (Gan Siang Tan)

sitizuraidah@unimap.edu.my (Siti Zuraidah Ibrahim)

nazrikarim@unimap.edu.my (Mohd Nazri A Karim)

Pingjack.Soh@oulu.fi (Ping Jack Soh)

khuzairi.masrakin@xmu.edu.my (Khuzairi Masrakin)

sugchai.t@rmuts.ac.th (Sugchai Tantivivat)

*Corresponding author

that require strict frequency isolation, making it especially advantageous for targeted narrowband applications where isolation and reliability are critical.

Keywords: 3 dB power divider, bi-layered substrate, slot aperture, substrate integrated waveguide

INTRODUCTION

In microwave systems, power dividers play a crucial role by enabling the division of signals into predetermined sub-paths. Depending on the specific application, these divisions can occur with equal or varying power levels. Historically, traditional waveguide structures were commonly employed to perform this function due to their ability to handle high-frequency signals efficiently. However, these conventional waveguides had significant drawbacks. They were often large and required complex and costly manufacturing processes, which made them impractical for widespread use, particularly in mass production environments where compactness and cost-effectiveness are key considerations. Power dividers have been widely implemented in various subsystems such as antenna feeding networks, interferometers, and other critical components that are integral to microwave systems.

In more recent years, microstrip-based power dividers have become increasingly preferred in many applications. This shift is primarily due to the planar structure of microstrip technology, which offers excellent compatibility with modern printed circuit board (PCB) designs. Microstrip-based designs also allow for easier integration into electronic devices, which often need to be both compact and lightweight to meet industry standards for portability and efficiency. The T-junction power divider, for example, is one of the most popular types of microstrip-based power dividers. Its appeal lies in its simple design and relatively straightforward manufacturing process. Despite these advantages, the T-junction power divider has some inherent limitations. Specifically, it is typically narrowband in nature, as it is challenging to match the impedance at the output ports, which often results in poor return loss and limited isolation performance (Chen et al., 2010; He et al., 2013).

An alternative structure known as the Wilkinson power divider has been developed to address the shortcomings of the T-junction design. This design offers several advantages, including improved isolation between the output ports and a broader operational bandwidth. Furthermore, the Wilkinson power divider is relatively compact, making it well-suited for applications requiring space-efficient components (Kao et al., 2012; Feng et al., 2017). It achieves these benefits by utilizing isolation resistors, crucial in enhancing isolation performance. Additionally, its compact form factor allows it to be integrated into modern microwave systems where space is at a premium (Peng et al., 2013).

A relatively new method for implementing Wilkinson power dividers is using Substrate Integrated Waveguides (SIW). SIW technology combines the high-power handling

capabilities of traditional waveguides with the low-loss characteristics of microstrip circuits, making it an ideal solution for modern high-frequency applications. One of the significant advantages of SIW is its ability to maintain the performance characteristics of conventional waveguides while offering the compactness and ease of integration associated with planar structures (Duraismy et al., 2022). Over the last decade, SIW technology has been widely adopted in designing various microwave components, such as tunable filters, amplifiers, couplers, and filters (Shen et al., 2021).

Further advancements in this field have focused on improving isolation performance in SIW-based Wilkinson power dividers. A notable development is the Half-Mode SIW (HMSIW) Wilkinson power divider. The HMSIW design reduces the overall size of the power divider while maintaining its performance characteristics. However, this design still relies on the use of isolation resistors, which, although improving isolation, can introduce unwanted cross-coupling effects and radiation losses due to the discontinuities in the structure (Smith & Abhari, 2009; Kim et al., 2010). These limitations have led to further exploration of alternative approaches, one of which involves the construction of ring-based power dividers within the SIW structure. This design aims to mitigate the disadvantages associated with the HMSIW structure by compensating for the losses introduced by isolation resistors (Djerafi et al., 2013; Djerafi et al., 2014; Moulay & Djerafi, 2018).

Narrowband power dividers are particularly useful in applications that benefit from precise signal isolation over specific frequency bands. For instance, phased array and beam-steering systems often rely on narrowband power dividers to achieve focused frequency isolation, ensuring stability and minimal interference within targeted operating ranges. These designs provide effective isolation within a specified band, making them well-suited for applications that do not require broad frequency isolation but benefit from precise control within a limited range (Zarghami & Hayati, 2022).

This study introduces a novel SIW power divider that improves isolation but eliminates the need for isolation resistors using a two-layer structure. The design starts with a conventional Y-junction SIW power divider and incorporates a rectangular slot aperture at the junction on the lower layer to direct signal propagation forward, enhancing isolation performance. To address the increased insertion loss caused by the slot, a second substrate layer with a precisely aligned copper patch is added, enabling improved isolation while controlling insertion loss. This resistor-free configuration simplifies the fabrication process and enhances durability, making it well-suited for applications that require reliable isolation without added component complexity.

The proposed power divider is demonstrated at two frequency bands centered at 12 GHz and 24 GHz, targeting applications that require focused isolation within specific narrow frequency ranges. This work suggests that the proposed resistor-free, dual-layer SIW power divider provides a practical, high-performance solution for compact microwave systems where isolation, compactness, and ease of integration are critical.

METHODOLOGY

This study explores the design of an SIW power divider operating at two center frequencies, 12 GHz and 24 GHz. The design process begins with a conventional Y-junction SIW power divider, as illustrated in Figure 1.

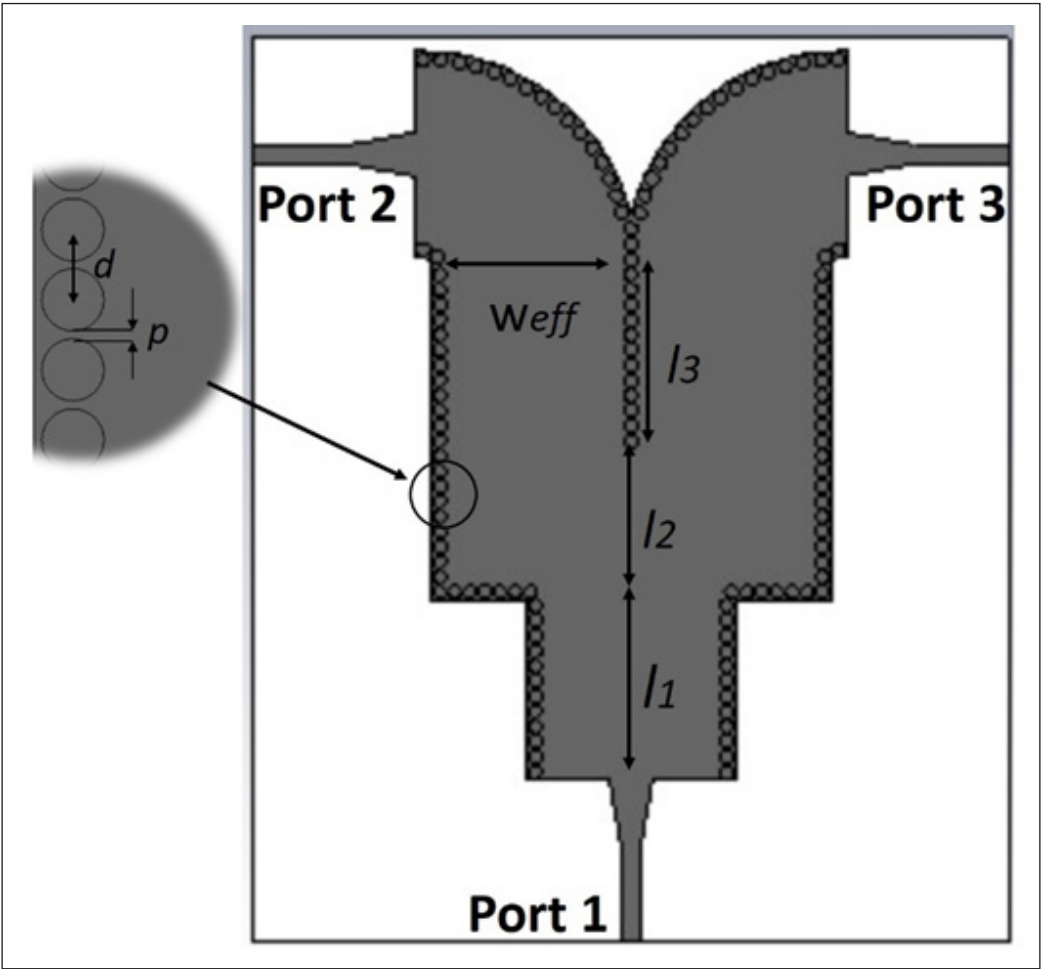


Figure 1. Topology of the conventional Y-junction SIW power divider

This conventional design was previously introduced in a 24 GHz SIW power splitter developed for six-port short-range radar-based sensors (Tan et al., 2016). In that study, the design used a basic Y-junction layout focused on simulations, with output ports positioned side by side. Practical considerations for physical measurements, such as SMA connector placement, were not included, as the design was intended only for simulation purposes.

The current study introduces a bending SIW structure at both output ports to address these limitations. This modification repositions the output ports on opposite sides of the

divider, allowing for easier connection to SMA connectors for practical measurements. This configuration enhances accessibility and supports physical prototyping and testing without altering the fundamental Y-junction layout.

Several critical parameters influence the design and performance of the SIW structure, including the effective width (W_{eff}), the diameter of the via holes (d), and the separation between via holes (p). Additionally, the lengths of sections within the Y-junction, designated as l_1 , l_2 and l_3 , are essential in tuning the design to the desired frequencies. Among these, the length l_2 is particularly significant, as it directly influences the operating frequency, targeted at 12 GHz and 24 GHz.

The dimensions of the via holes and their spacing are designed to meet specific criteria to ensure efficient wave propagation and prevent unwanted modes. According to Xu and Wu (2005), the ratio of via-hole separation to cutoff wavelength (p/λ_c) should be less than 0.25. Additionally, the diameter (d) must be smaller than the spacing (p), with the following condition satisfied (Equation 1).

$$d < p < 2d \quad [1]$$

These constraints ensure that the structure supports the desired TE_{m0} modes, particularly the dominant TE_{10} mode, which is essential for stability at both targeted frequencies (Cassivi et al., 2002).

Empirical formulas based on established research are used to estimate initial values for these critical parameters (Cassivi et al., 2002; Deslandes & Wu, 2006). The cutoff frequency for the TE_{10} mode is determined by using Equation 2:

$$f_{c(TE10)} = \frac{c}{2\sqrt{\epsilon_r}} \cdot \left(W - \frac{d^2}{0.95 \times p} \right)^{-1} \quad [2]$$

Where c is the speed of light, ϵ_r is the relative permittivity of the substrate, W is the width of the SIW, d is the diameter of the via holes, and p is the separation between via holes. This formula is crucial in aligning the cutoff frequencies with the target operating frequencies of 12 GHz and 24 GHz.

The effective width of the SIW (W_{eff}) is calculated using Equation 3:

$$W_{eff} = W - \frac{d^2}{0.95 \times p} \quad [3]$$

This effective width influences the waveguide's propagation characteristics, affecting the distribution of electromagnetic fields within the SIW structure.

Figure 2 shows the proposed power divider design, which introduces a rectangular slot aperture at the Y-junction of the conventional SIW structure to enhance isolation by

disrupting the electric field distribution. This slot, along with a rectangular metallic patch positioned directly above it, effectively reduces coupling between output ports, thereby improving isolation. The key parameters of this slot include its position (S_p), width (S_w) and length (S_l), which are optimized to achieve maximum isolation performance.

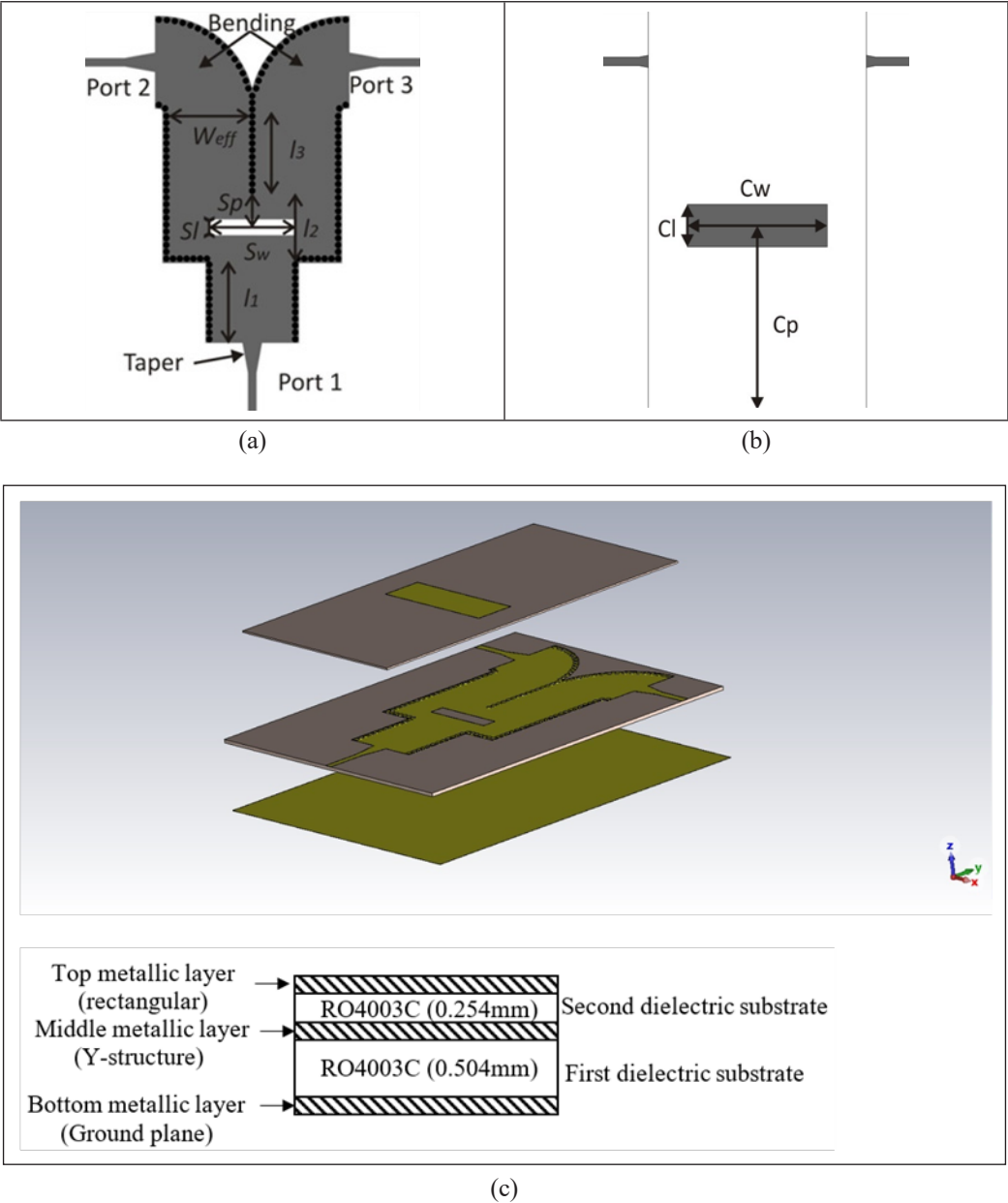


Figure 2. Configuration of the proposed SIW power divider (a) front view of the proposed Y-structure with slot aperture (b) front view (with two layers) (c) exploded view

However, the addition of the slot can result in increased insertion loss. A thin dielectric substrate layer with a rectangular metallic patch is placed directly above the slot to counter this. This patch, precisely aligned over the slot, reflects the signal into the structure, thereby minimizing insertion loss while preserving the improved isolation. The parameters of this top rectangular metallic patch, such as its position (C_p), width (C_w), and length (C_l), are carefully optimized to align with the slot, ensuring effective signal reflection and low insertion loss.

The modified structure combines the optimized slot aperture and the patch-covered layer to achieve a balance of high isolation and low insertion loss. It is suitable for high-frequency applications that demand effective power division and robust isolation. The careful alignment of slot and patch parameters enables the structure to address isolation and insertion loss, providing a practical and efficient solution for high-performance microwave systems.

The proposed power divider is designed using the RO4003C substrate, chosen for its low-loss dielectric properties, which are ideal for high-frequency applications. The bottom layer has a standard thickness of 0.508 mm to provide robust support for the waveguide. The top layer, designed with the same RO4003C substrate but a thinner profile of 0.254 mm, is used to improve insertion loss, reduce overall bulk, and enhance the electromagnetic performance of the power divider by minimizing signal loss.

The designs are validated at two frequency ranges, 12 GHz and 24 GHz, using CST Microwave Studio, a commercially available electromagnetic simulation software, to demonstrate the effectiveness of the proposed structure. After optimizing the designs at these center frequencies, the final dimensions of each design are provided in Table 1.

Table 1
Dimensions of conventional and proposed SIW power divider

Parameter	Description	Conventional (single layer)	Proposed (two-layer)	Conventional (single layer)	Proposed (two-layer)
f	Centre Frequency (GHz)	12	12	24	24
W_{eff}	Effective width of the Substrate Integrated Waveguide (mm)	10.6	10.6	4.5	4.5
l_1	Length of various sections of the Y-junction(mm)	10.6	10.6	4.4	4.4
l_2	Length of various sections of the Y-junction(mm)	9.3	9.3	3.4	3.4
l_3	Length of various sections of the Y-junction(mm)	10.7	10.7	4.4	4.4
d	Diameter of the via holes(mm)	0.8	0.8	0.5	0.5

Table 1 (continue)

Parameter	Description	Conventional (single layer)	Proposed (two-layer)	Conventional (single layer)	Proposed (two-layer)
p	Pitch (separation) between the via holes(mm)	0.9	0.9	0.6	0.6
C_l	Length of the top metallic layer(mm)	Not available	5.9	Not available	2.7
C_w	Width of the top metallic layer(mm)	Not available	20.2	Not available	8.5
C_p	Position of the top metallic layer(mm)	Not available	21.7	Not available	10.15
S_l	Length of the rectangular slot on the middle metallic layer(mm)	Not available	2.1	Not available	0.6
S_w	Width of the rectangular slot on the middle metallic layer(mm)	Not available	11.4	Not available	5.5
S_p	Position of the rectangular slot on the middle metallic layer(mm)	Not available	3.4	Not available	1.9

RESULTS AND DISCUSSION

Initial simulations at 12 GHz and 24 GHz were conducted to examine the electric field (E-field) distribution and to assess the effect of the two-layer design versus a single-layer configuration. Figure 3 shows the E-field distribution at 12 GHz and 24 GHz, illustrating the critical role of the rectangular slot and top substrate layer in achieving improved isolation and reducing insertion loss.

In the single-layer SIW configuration, signal propagation from port 1 to port 2 is less isolated, with noticeable energy leakage to port 3 due to the Y-junction structure. However, in the two-layer SIW power divider, the rectangular slot acts as an aperture that guides signal propagation outward through the slot, while the top substrate layer minimizes signal loss. When the slot is on top of the SIW, controlled radiation occurs, as the electric current is directed along the slot, resulting in a specific current distribution around it. This current distribution is influenced by the position of the slot (denoted by S_p), which affects the amount of radiated power and, subsequently, the device's overall isolation and transmission characteristics.

The structure within the l_2 section of the power divider can be approximated as a series impedance. In this configuration, adding a top metallic layer over the slot establishes a resonant condition, ensuring that the device's impedance is primarily resistive with minimal reactive contribution. By reducing reactive impedance, this design promotes efficient signal propagation and achieves the desired isolation between output ports.

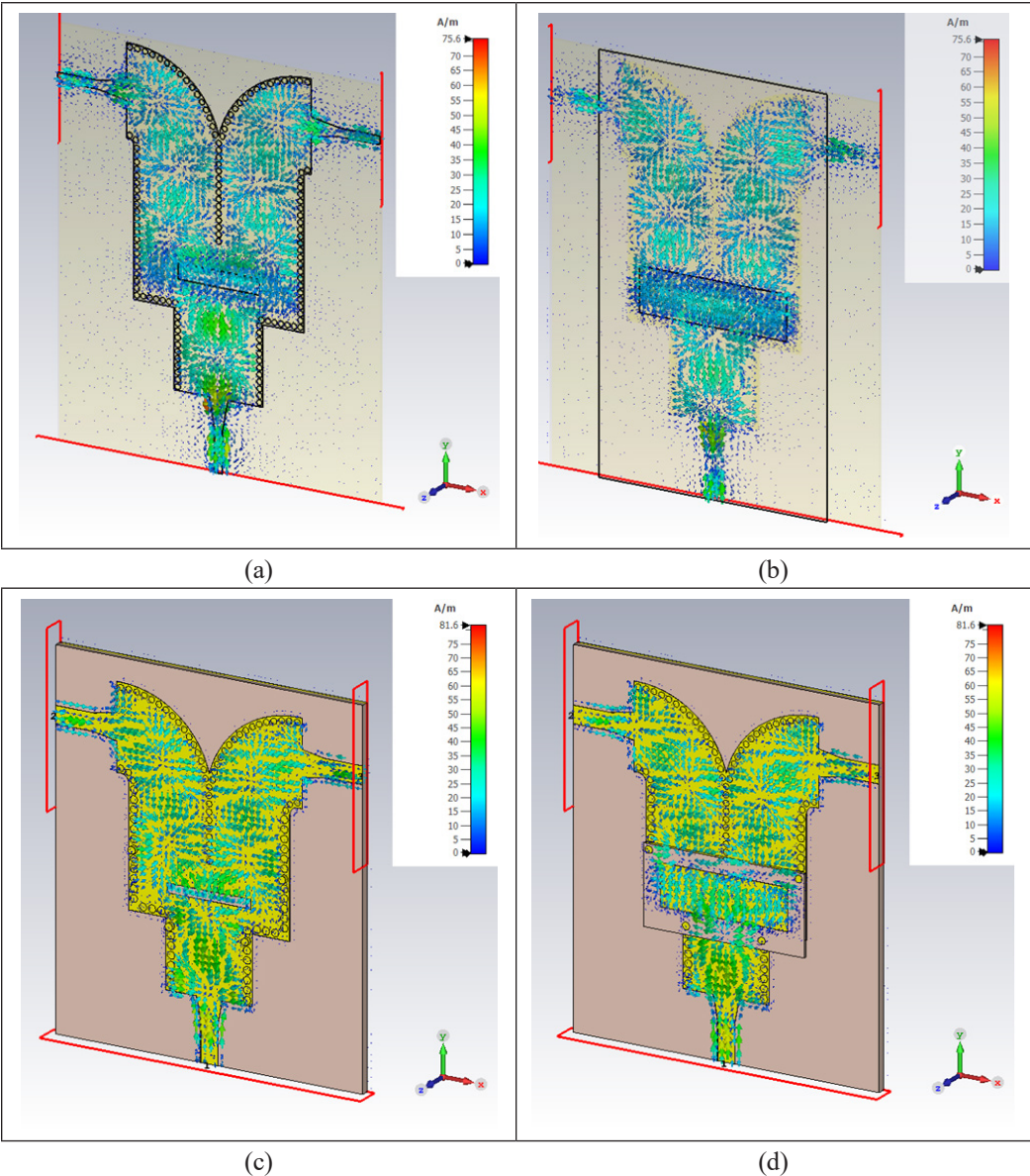


Figure 3. E-field distribution for (a) 12 GHz (single), (b) 12 GHz (dual), (c) 24 GHz (single), and (d) 24 GHz (dual)

The coordinated interaction between the slot, top substrate layer, and metallic components effectively isolates the SIW power divider. This design ensures minimal signal loss while maintaining high isolation levels, even with minor fabrication imperfections, making the SIW power divider a reliable solution for high-frequency applications.

The single-layer and dual-layer SIW power dividers were simulated at two frequency ranges around 12 GHz and 24 GHz to evaluate their performance. For the 12 GHz range, simulations were conducted from 9.5 GHz to 13 GHz, while for the 24 GHz range, simulations covered 22 GHz to 26 GHz. The simulation results for the 12 GHz range are presented in Figure 4, while those for the 24 GHz range are shown in Figure 5. The simulation results for both single-layer and dual-layer designs are summarized in Table 2.

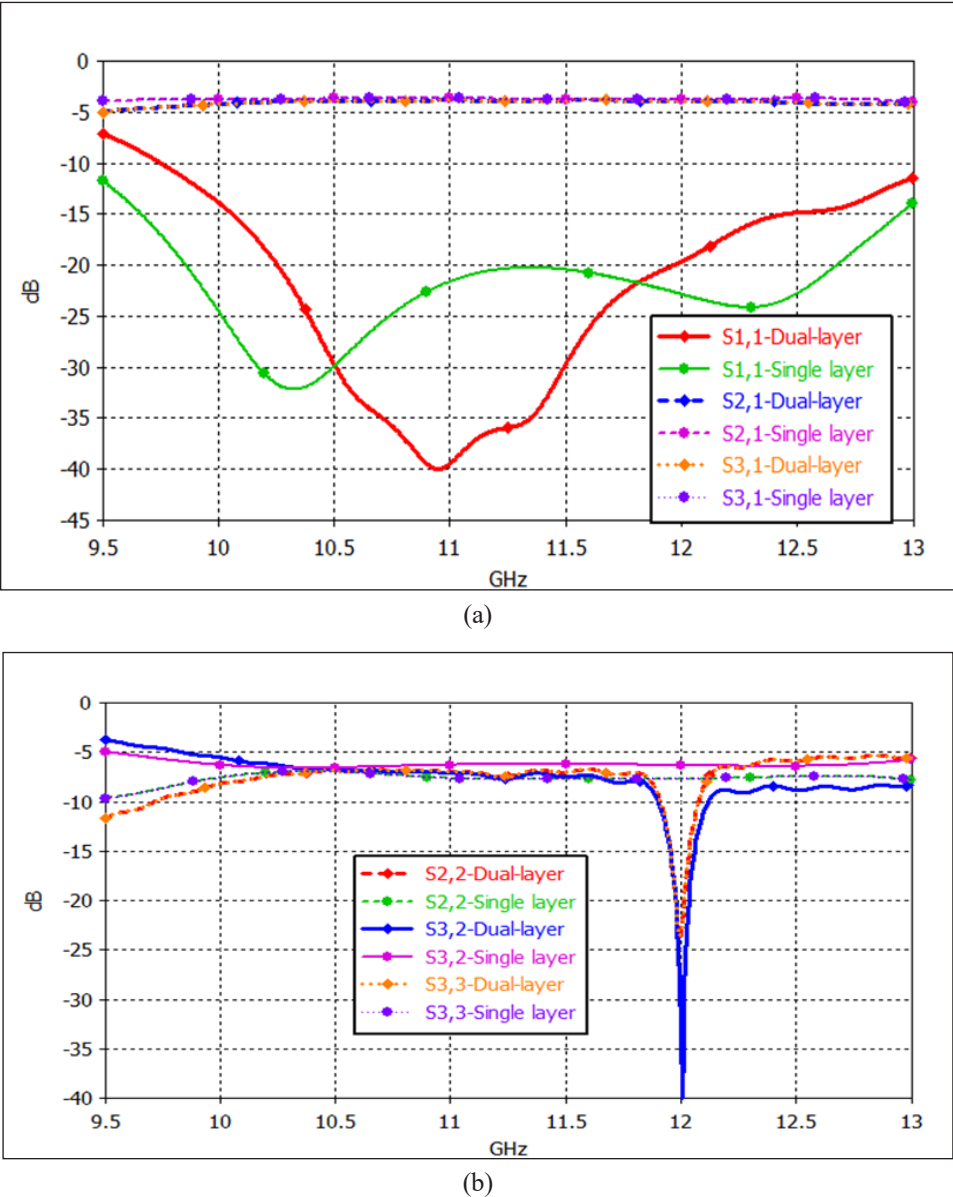
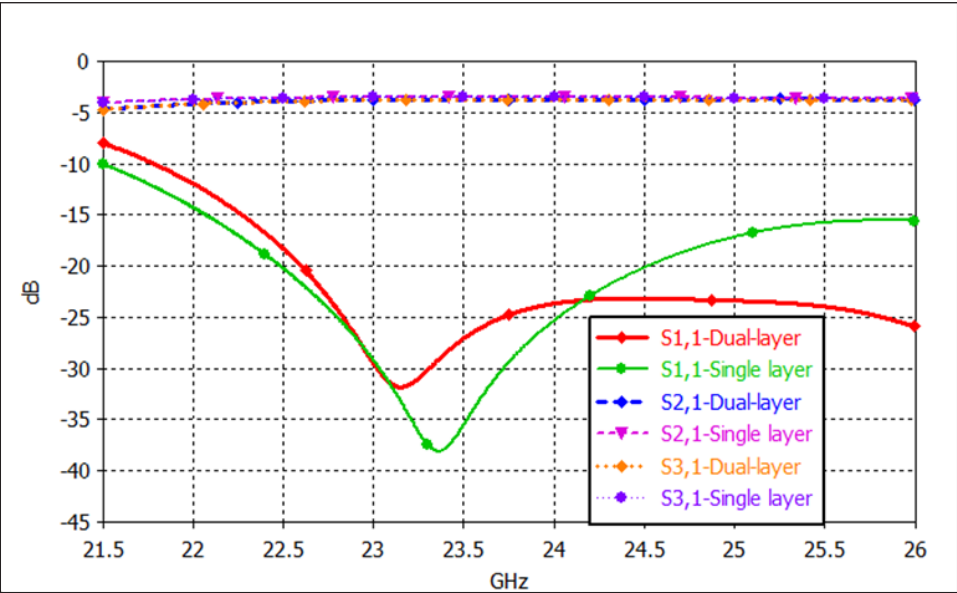
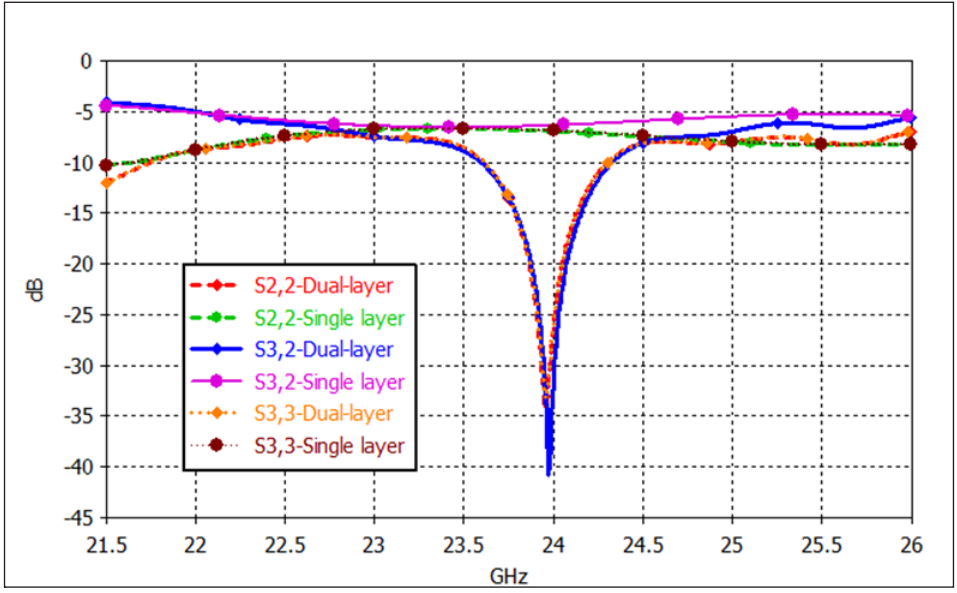


Figure 4. Simulation of S-parameters for single-layer and dual-layer SIW power dividers at 12 GHz: (a) S11, S21, and S31, (b) S22, S33, and S32



(a)



(b)

Figure 5. Simulation of S-parameters for single-layer and dual-layer SIW power dividers at 24 GHz: (a) S11, S21, and S31, (b) S22, S33, and S32

The results indicate that single-layer SIW power dividers offer a wider bandwidth but lower isolation compared to dual-layer designs. The dual-layer SIW power dividers demonstrate superior isolation performance for both the 12 GHz and 24 GHz ranges,

with maximum isolation levels of 40 dB, confirming the effectiveness of the dual-layer configuration in enhancing isolation. Additionally, the fractional bandwidth isolation at 24 GHz is better compared to 12 GHz, further highlighting the enhanced isolation capabilities at higher frequencies.

The return loss for both output ports also improves with the dual-layer design, showing a performance trend similar to isolation. This similarity arises because the introduction of a slot enhances impedance matching, reducing reflections at the output ports. The insertion loss is almost similar between the dual-layer and single-layer configurations, confirming the effectiveness of the top-layer substrate with a rectangular patch in minimizing radiation loss caused by the slot on the bottom layer.

Table 2
Simulation results of single-layer and dual-layer SIW power dividers

SIW Power Divider	10 dB isolation fractional bandwidth (GHz)	Maximum Isolation (dB)	Insertion Loss (dB)
Single-Layer at 12 GHz	NA	7	3.6 ± 0.5
Single Layer at 24 GHz	NA	5.7	3.5 ± 0.5
Dual-Layer at 12 GHz	2.90%	40	3.8 ± 0.5
Dual-Layer at 24 GHz	3.75%	40	3.7 ± 0.5

Only the 12 GHz design of the proposed SIW power divider was fabricated and tested. Figure 6 shows the fabricated device, demonstrating its layered structure.

In this design, the top layer is glued to the bottom layer, securing the two substrate layers together and ensuring structural integrity for optimal performance. Performance measurements were conducted using an Agilent E8362B vector network analyzer to

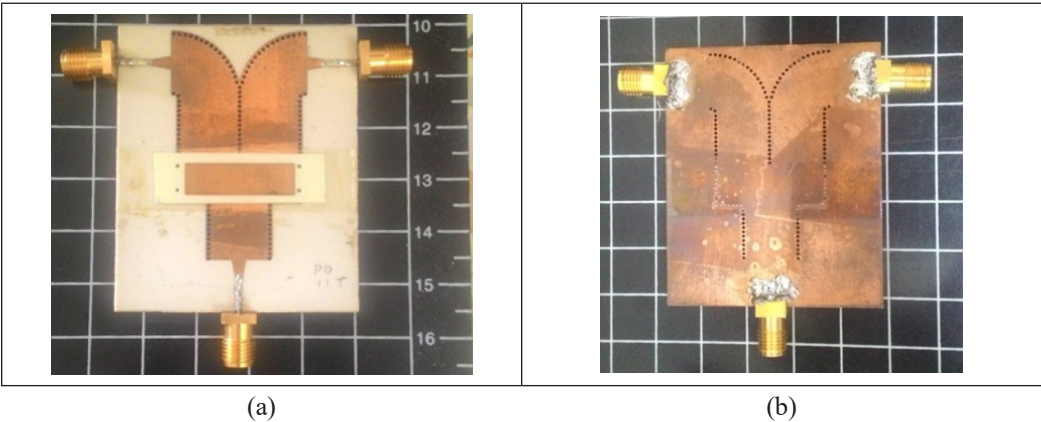


Figure 6. Photo of fabricated SIW power divider (a) top view (b) bottom view

evaluate the high-frequency characteristics, and the measured results were compared to simulation data in Figure 7 to validate the design.

Measured transmission values for S_{21} and S_{31} were around 4.3 ± 0.9 dB across 10.5 GHz to 13 GHz, closely matching the simulation results and confirming effective power division between output ports. Return loss measurements indicated better than 10 dB from 9.8 GHz to 13 GHz, showing minimal reflection at the input port and confirming efficient power transmission through the device. Isolation measurements revealed that isolation between output ports exceeded 10 dB within the range of 11.8 GHz to 12.3 GHz, ensuring minimal interference between ports and supporting the device's effectiveness in signal separation.

However, during the testing, it was noted that the operational frequency of both output ports was shifted towards lower frequencies compared to the simulation results. This shift can likely be attributed to fabrication errors, such as misalignment between the two substrate layers during assembly. Additionally, variations in the dimensions of the fabricated device may have introduced discrepancies between the simulation and the actual measured performance. Misalignment between the layers could alter the electromagnetic field distribution, leading to changes in the resonant behavior of the structure and, consequently, shifting the operational frequency.

In this work, a parametric study is conducted to investigate the sensitivity of key design parameters and their influence on the isolation performance of the structure. This analysis aims to identify critical dimensions that affect the isolation characteristics, providing insight into potential tuning and optimization strategies. The parametric study helps refine the design and explains the discrepancies observed between the measured and simulated results. Variations in fabrication, such as layer misalignment or dimensional inaccuracies, can lead to shifts in the isolation frequency and performance. By systematically exploring these factors, the study highlights how small deviations in key parameters can account for the observed differences, contributing to a deeper understanding of the design's behavior and enhancing the accuracy of future prototypes.

The investigation is performed to study the effects of the slot sizes and locations (S_p , S_l , and S_w) by observing their isolation performance at the 12 GHz band. For this purpose, the parameters of the copper layer on the top substrate, namely C_w , C_l and C_p are fixed at 20.2 mm, 5.9 mm and 21.5 mm, respectively. Firstly, parameters S_p and S_l are fixed at 2.8 mm and 2.1 mm, respectively, when a parametric study of S_w is performed. As depicted in Figure 8(a), the increment of S_w slightly shifts the isolation towards a lower frequency, with increased isolation levels. Meanwhile, parameters S_p and S_w are set at 2.8 mm and 11.4 mm, respectively, when S_l is studied. The increment in S_l , as shown in Figure 8(b), was also found to be slightly affecting the frequency of the peak isolation band, which shifted to 12 GHz due to the increase of the energy flow out of the slot, resulting in the increase in the isolation.

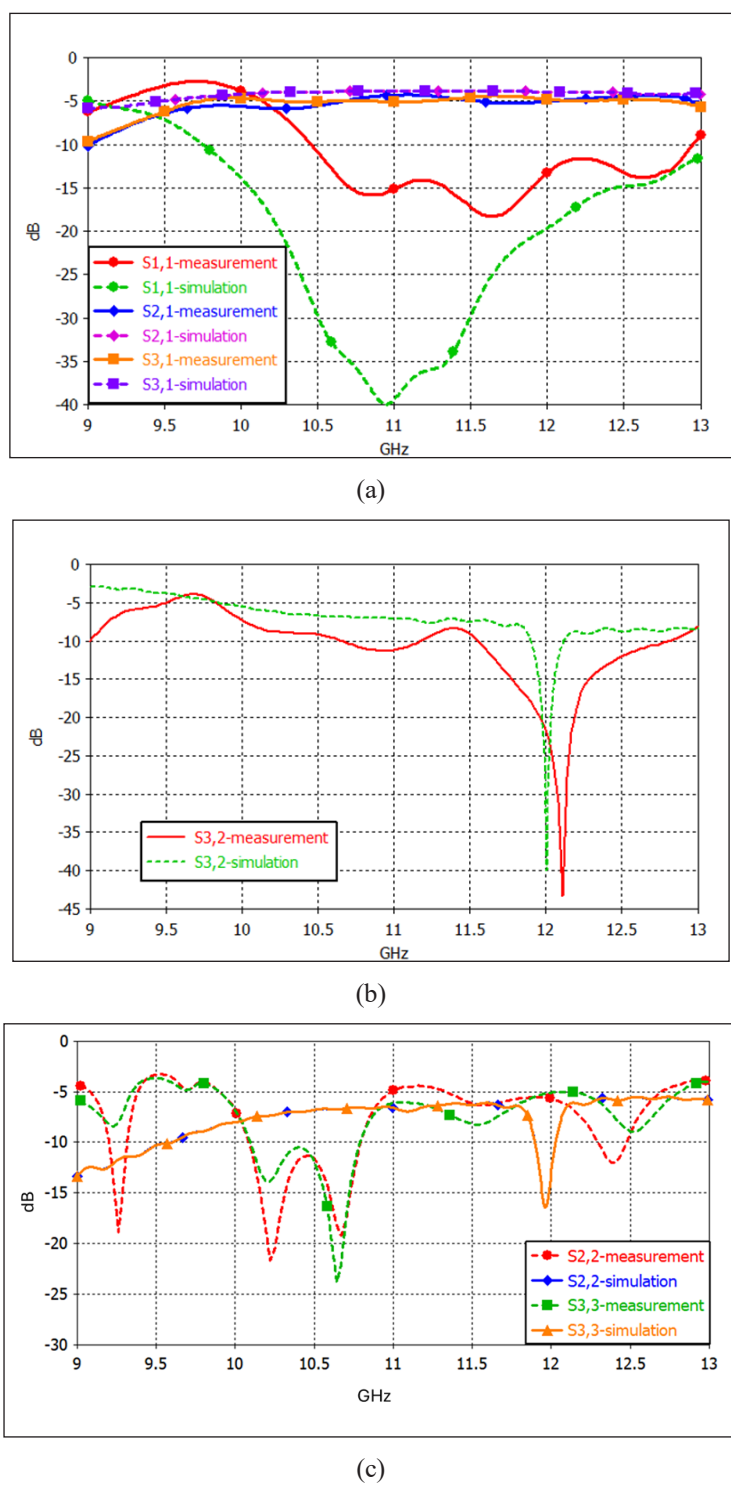


Figure 7. Comparison between simulation and measurement results (a) S_{11} , S_{21} and S_{31} (b) S_{32} , and (c) S_{22} , S_{33}

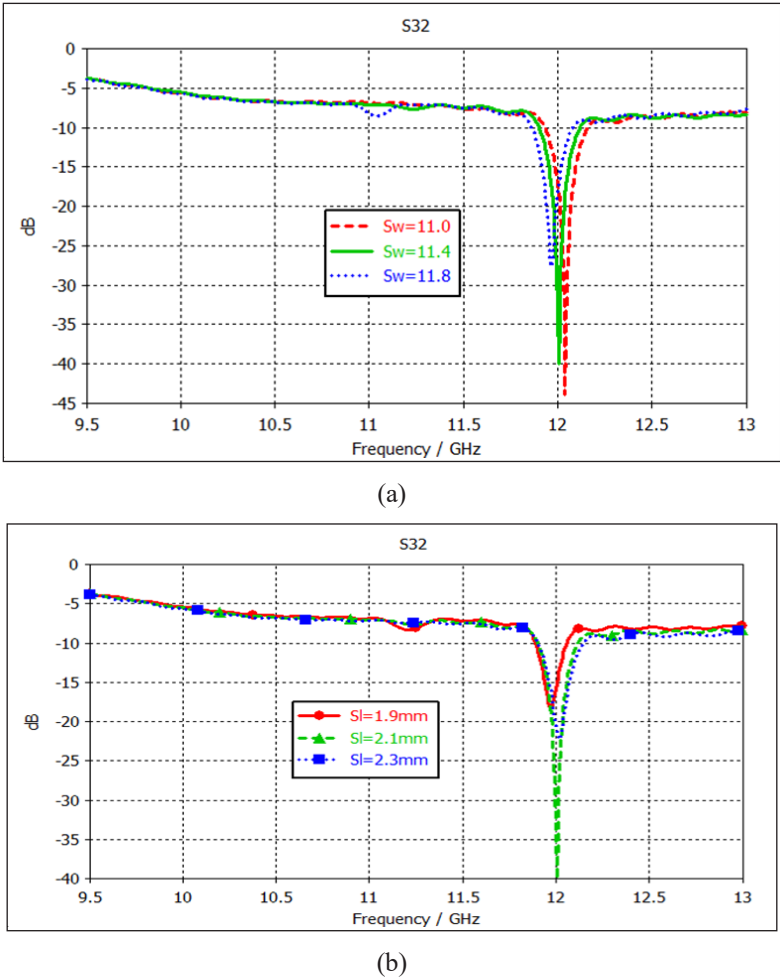


Figure 8. Simulations results of S_{22} (a) slot width, S_w and (b) slot length, S_l

Next, the dimensions of the copper layer are then studied in terms of isolation performance using parameters C_p , C_l and C_w . Parameters C_p and C_l are set at 21.7 mm and 5.9 mm, respectively, while a parametric study is performed on C_w . The increase of C_w shifts the isolation towards the lower frequency, with an isolation peak of 31 dB at $C_w = 20$ mm, due to the reduction of the resonant frequency of the top layer, as shown in Figure 9(a). Meanwhile, another parameter study is conducted to investigate the effects of C_l when parameters C_p and C_w are fixed at 21.7 mm and 20.2 mm, respectively. The simulation results shown in Figure 9(b) indicated that the increase in C_l shifted the isolation towards the lower frequencies, besides improved isolation performance due to the reduction of the resonant frequency of the top layer and increase of the energy capacity. Therefore, C_w is increased first to obtain the target frequency, followed by the optimization of C_l for the best isolation.

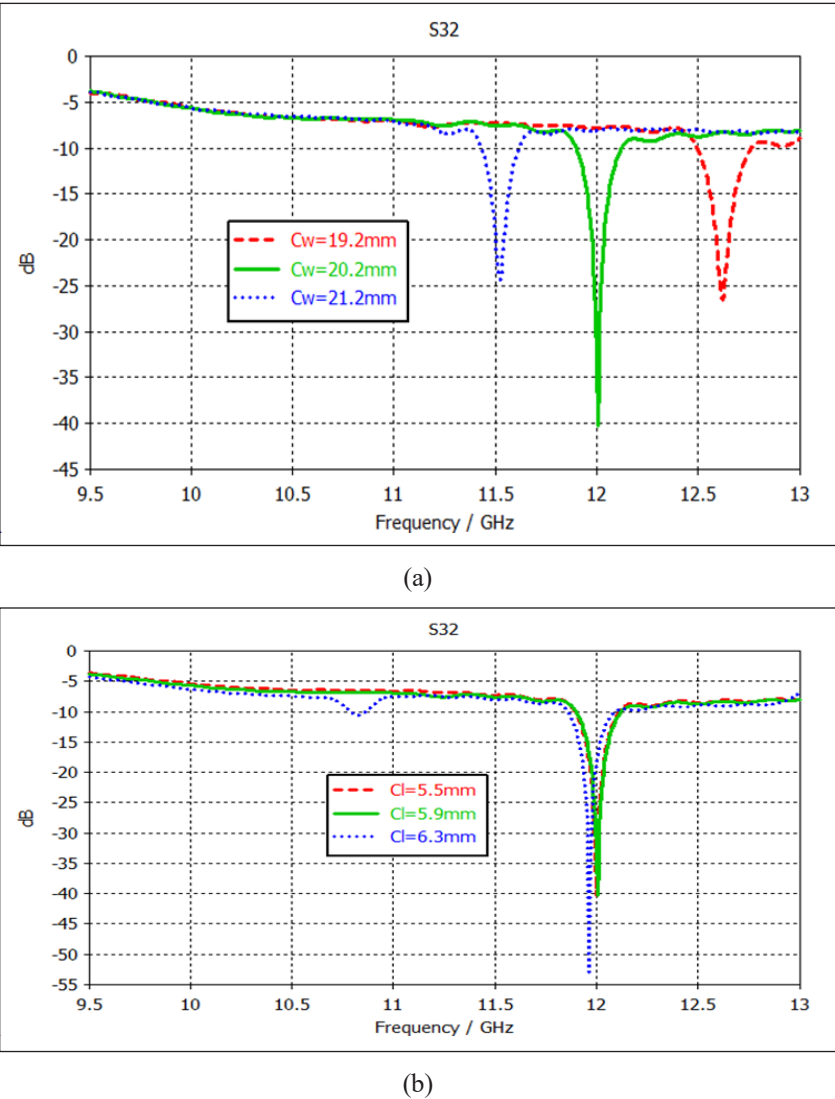


Figure 9. Parametric study of the proposed SIW power divider with (a) different copper widths, C_w and (b) different copper lengths, C_l

Table 3 compares this work and previous SIW Wilkinson power dividers. The proposed bi-layered power divider with a slot, as highlighted in Table 3, achieves the highest peak isolation of 43 dB, with a 10 dB isolation fractional bandwidth of 9.91%, suitable for practical applications. The insertion loss (4.2 ± 0.5 dB) and phase imbalance (5°) are comparable to other methods. At the same time, the top-layer substrate with a rectangular patch effectively minimizes radiation loss caused by the slot on the bottom layer. The design's simplicity, achieved by eliminating resistors, enhances its robustness and makes it efficient for high-frequency applications. However, it is important to acknowledge that

Table 3
Comparison between the proposed SIW power divider and other works

Reference	Technique	Peak Isolation (dB)	Peak Frequency (GHz)	10 dB isolation fractional bandwidth (%)	Insertion loss (dB)	Phase Imbalance	Resistor
(Kim et al., 2010)	Wilkinson HMSIW	19	14.5	10.82	4 ± 0.5	3.3°	1
(Djerafi et al., 2013)	Ring Wilkinson SIW	26	9.85	27.41	3.25 ± 0.5	3.3°	3
(Moulay & Djerafi, 2018)	Wilkinson with fixed width SIW line	24	10	27.13	3.3 ± 0.2	1°	8
(Yang et al., 2016)	Wilkinson HMSIW with DGS	15.3	9	39.02	4.1 ± 0.5	5.1°	1
(Yang et al., 2021)	Integrated substrate gap waveguide (ISGW)	15	26	43.38	3.53 ± 0.5	0.2°	1
(Liu et al., 2021)	Filtering power divider (FPD) on SIW	39	6.1	13.5	3.1 ± 0.2	2.3°	1
(Chi et al., 2020)	SIW filtering power divider (FPD)	20	28.2	3.54	3 ± 0.5	3.2°	2
(Yazdamanah et al., 2016)	SIW	20	4.9	4.08	4.55 ± 0.5	NA	1
(Nguyen et al., 2024)	Ku-band SIW power divider with coupled resonators	19.7	14.12	5.3	4.6	1°	None
(Huang et al., 2017)	SIW power combiner/divider with absorbing material	15	16	36	4.5 ± 0.5	±2.2°	None
(Nguyen et al., 2021)	Air-filled SIW with surface-mounted absorber	15	33.5	38.8	3.59 ± 0.51	3.71°	None
Proposed	Bi-layered with slot	43	12.1	9.91	4.2 ± 0.5	5	None

recent works, such as Nguyen et al. (2021, 2024), have demonstrated resistor-free designs with high isolation and wider fractional bandwidths. These advancements highlight ongoing efforts to optimize SIW power dividers by enhancing isolation while maintaining broad bandwidth.

CONCLUSION

In conclusion, a SIW power divider with enhanced isolation has been successfully designed at 12 GHz and 24 GHz, demonstrating the versatility of the proposed technique. Conventional SIW power dividers often face challenges in achieving high isolation and low loss without relying on lumped components, which can increase complexity and introduce additional losses. The proposed design incorporates a slot and an additional substrate layer, eliminating the need for lumped components while improving performance. The 12 GHz design was fabricated and measured, achieving good agreement with simulations. The results showed transmission values of approximately 4.2 dB, return loss better than 10 dB, and isolation exceeding 10 dB in the targeted frequency range. These results confirm the effectiveness of the proposed design for microwave systems requiring high isolation and low loss, highlighting its potential for applications in modern communication and radar technologies.

ACKNOWLEDGEMENT

This research is fully supported by an FRGS grant under grant number FRGS/1/2019/STG02/UNIMAP/02/5. The authors fully acknowledged the Ministry of Higher Education (MOHE) and Universiti Malaysia Perlis (UniMAP) for the approved fund, which makes this important research viable and effective.

REFERENCES

- Cassivi, Y., Perregrini, L., Arcioni, P., Bressan, M., Wu, K., & Conciauro, G. (2002). Dispersion characteristics of substrate integrated rectangular waveguide. *IEEE Microwave and Wireless Components Letters*, 12(9), 333–335. <https://doi.org/10.1109/LMWC.2002.803188>
- Chen, K., Yan, B., & Xu, R. (2010). A novel W-band ultra-wideband substrate integrated waveguide (SIW) T-junction power divider. In *2010 International Symposium on Signals, Systems and Electronics* (Vol. 1, pp. 1-3). IEEE Publishing. <https://doi.org/10.1109/issse.2010.5638214>
- Chi, P. L., Chen, Y. M., & Yang, T. (2020). Single-layer dual-band balanced substrate- integrated waveguide filtering power divider for 5G millimeter-wave applications. *IEEE Microwave and Wireless Components Letters*, 30(6), 585–588. <https://doi.org/10.1109/LMWC.2020.2987170>
- Deslandes, D., & Wu, K. (2006). Accurate modeling, wave mechanisms, and design considerations of a substrate integrated waveguide. *IEEE Transactions on Microwave Theory and Techniques*, 54(6), 2516–2526. <https://doi.org/10.1109/TMTT.2006.875807>

- Djerafi, T., Hammou, D., Tatu, S., & Wu, K. (2013). Bi-layered substrate integrated waveguide Wilkinson power divider/combiner. In *2013 IEEE MTT-S International Microwave Symposium Digest (MTT)* (pp. 1-3). IEEE Publishing. <https://doi.org/10.1109/MWSYM.2013.6697556>
- Djerafi, T., Hammou, D., Wu, K., & Tatu, S. O. (2014). Ring-shaped substrate integrated waveguide Wilkinson power dividers/combiners. *IEEE Transactions on Components, Packaging and Manufacturing Technology*, 4(9), 1461–1469. <https://doi.org/10.1109/TCPMT.2014.2342156>
- Duraisamy, T., Kamakshy, S., Sholampettai Subramanian, K., Barik, R. K., & Cheng, Q. S. (2022). Design and implementation of compact tri- and quad-band SIW power divider using modified circular complementary split-ring resonators. *International Journal of Microwave and Wireless Technologies*, 14(10), 1241–1249. <https://doi.org/10.1017/S1759078721001720>
- Feng, W., Hong, M., Xun, M., & Che, W. (2017). A novel wideband balanced-to-unbalanced power divider using symmetrical transmission lines. *IEEE Microwave and Wireless Components Letters*, 27(4), 338–340. <https://doi.org/10.1109/LMWC.2017.2678403>
- He, Z., Cai, J., Shao, Z., Li, X., & Huang, Y. (2013). A novel power divider integrated with SIW and DGS technology. *Progress In Electromagnetics Research*, 143, 223–242. <https://doi.org/10.2528/PIER13022005>
- Huang, Y. M., Jiang, W., Jin, H., Zhou, Y., Leng, S., Wang, G., & Wu, K. (2017). Substrate-integrated waveguide power combiner/divider incorporating absorbing material. *IEEE Microwave and Wireless Components Letters*, 27(10), 885–887. <https://doi.org/10.1109/LMWC.2017.2744699>
- Kao, J. C., Tsai, Z. M., Lin, K. Y., & Wang, H. (2012). A modified wilkinson power divider with isolation bandwidth improvement. *IEEE Transactions on Microwave Theory and Techniques*, 60(9), 2768–2780. <https://doi.org/10.1109/TMTT.2012.2206402>
- Kim, K., Byun, J., & Lee, H. Y. (2010). Substrate integrated waveguide Wilkinson power divider with improved isolation performance. *Progress In Electromagnetics Research Letters*, 19, 41–48. <https://doi.org/10.2528/pier110082407>
- Liu, B. G., Lyu, Y. P., Zhu, L., & Cheng, C. H. (2021). Compact square substrate integrated waveguide filtering power divider with wideband isolation. *IEEE Microwave and Wireless Components Letters*, 31(2), 109–112. <https://doi.org/10.1109/LMWC.2020.3042332>
- Moulay, A., & Djerafi, T. (2018). Wilkinson power divider with fixed width substrate-integrated waveguide line and a distributed isolation resistance. *IEEE Microwave and Wireless Components Letters*, 28(2), 114–116. <https://doi.org/10.1109/LMWC.2018.2790706>
- Nguyen, N. H., Ghiotto, A., Martin, T., Vilmot, A., Wu, K., & Vuong, T. P. (2021). Fabrication-tolerant broadband air-filled SIW isolated power dividers/combiners. *IEEE Transactions on Microwave Theory and Techniques*, 69(1), 603–615. <https://doi.org/10.1109/TMTT.2020.3036127>
- Nguyen, N. N. T., Nguyen, T. H., Luong, D. M., Van, T. M., Nguyen, T. L., & Tran, T. T. H. (2024). A Ku-band SIW power divider with high isolation using coupled resonators. In *2024 9th International Conference on Integrated Circuits, Design, and Verification (ICDVI)* (pp. 239–244). IEEE Publishing. <https://doi.org/10.1109/ICDVI61346.2024.10617110>
- Peng, H., Yang, Z., Liu, Y., Yang, T., & Tan, K. (2013). An Improved UWB Non-Coplanar Power Divider. *Progress In Electromagnetics Research*, 143, 223–242. <https://doi.org/10.2528/PIER13011003>

- Shen, W., Ling, X. B., Zou, W. J., Huang, S., & Chen, K. (2021). A tri-section substrate integrated waveguide filtering power divider with a wide stopband. *Journal of Electromagnetic Wave and Applications*, 36(4), 479–487. <https://doi.org/10.1080/09205071.2021.1972843>
- Smith, N. A., & Abhari, R. (2009). Compact substrate integrated waveguide Wilkinson power dividers. In *2009 IEEE Antennas and Propagation Society International Symposium* (pp. 1-4). IEEE Publishing. <https://doi.org/10.1109/APS.2009.5171656>
- Tan, G. S., Ibrahim, S. Z., & Razalli, M. S. (2016). 24GHz substrate integrated waveguide power splitter for six-port short-range radar-based sensor. In *2016 IEEE Asia-Pacific Conference on Applied Electromagnetics (APACE)* (pp. 113-116). IEEE Publishing. <https://doi.org/10.1109/APACE.2016.7915865>
- Xu, F., & Wu, K. (2005). Guided-wave and leakage characteristics of substrate integrated waveguide. *IEEE Transactions on Microwave Theory and Techniques*, 53(1), 66–72. <https://doi.org/10.1109/TMTT.2004.839303>
- Yang, M. X., Shen, D., Zhang, X., & Yuan, H. (2021). Multilayer slot coupling ultra-wideband power divider based on integrated substrate gap waveguide. In *2021 13th Global Symposium on Millimeter-Waves & Terahertz (GSMM)* (pp. 1-3). IEEE Publishing. <https://doi.org/10.1109/GSMM53250.2021.9511961>
- Yang, Z., Chen, W., Lin, H., Yang, T., & Jin, H. (2016). A novel SIW power divider with good out-of-band rejection and isolation. *EICE Electronics Express*, 13(8), Article 20160160. <https://doi.org/10.1587/elel.13.20160160>
- Yazdanpanah, I., Afrooz, K., & Moznebi, A. (2016). High Q power divider/combiner with high output isolation using substrate integrated waveguide technology. *Journal of Communication Engineering*, 5(2), 106–115. <https://doi.org/10.22070/jce.2017.1764.1009>
- Zarghami, S., & Hayati, M. (2022). Narrow-band power dividers with wide-range tunable power-dividing ratio. *Scientific Reports*, 12, Article 17351. <https://doi.org/10.1038/s41598-022-22178-0>

Phyto Constituents of *Ananas comosus* Leaf Extract Enhancing the Copper Nanoparticles Synthesis

Nur Diyana Zulpahmi¹, Wan Zuraida Wan Mohd Zain^{1,2}, Fazlena Hamzah², Nurul Wahida Ramli¹, Nur 'Amira Hamid¹, Irmaizatussyehdany Buniyamin³, Wan Atikah Wan Hamidon⁴ and Siti Aisha Na'illa Che Musa^{1*}

¹Faculty of Plantation and Agrotechnology, Universiti Teknologi MARA, Cawangan Melaka, Kampus Jasin, 77300 Merlimau, Melaka, Malaysia

²Biocatalyst and Biobased Material Technology Research Group, School of Chemical Engineering, College of Engineering, Universiti Teknologi MARA, 40450 Shah Alam, Malaysia

³NANO-SciTech Laboratory, Centre for Functional Materials and Nanotechnology (FMN), Institute of Science, Universiti Teknologi MARA (UiTM), 40450 Shah Alam Selangor, Malaysia

⁴Product Development & Biotechnology Division, Malaysian Pineapple Industry Board, Wisma Nenas, No. 5, Jalan Padi Mahsuri Bandar Baru UDA, 81200 Johor Bahru, Johor, Malaysia

ABSTRACT

Ananas comosus leaf is one of the agricultural wastes that has resulted in environmental pollution. Recently, this waste has been explored for its potential in synthesising environmentally friendly metallic nanoparticles. *Ananas comosus* leaf extract has been proposed as a viable and economical option for reducing, capping, and stabilising agents in synthesising copper nanoparticles. This study used *Ananas comosus* leaf extract and copper sulphate as precursor materials to produce copper nanoparticles in the green synthesis process. The results show that the absorption spectra in the UV-visible range exhibit a peak absorption value at a wavelength of 238 nm. Fourier Transform Infrared analysis revealed the presence of bioactive compounds in the *Ananas comosus* leaf extract,

which are responsible for reducing Cu²⁺ ions to Cu⁰ nanoparticles. The Field Emission Scanning Electron Microscope analysis indicated that the copper nanoparticles have a face-centred cubic crystal structure, which is significant for innovative nanoparticle applications. The average particle size was determined to be 56.71 nm. X-ray diffraction analysis revealed peaks at 43.46°, 50.57°, and 74.23°, corresponding to the (111), (200), and (220) lattice planes, respectively, confirming the structural properties of the synthesised nanoparticles. Energy Dispersive X-ray examination found that the

ARTICLE INFO

Article history:

Received: 15 May 2024

Accepted: 07 January 2025

Published: 04 April 2025

DOI: <https://doi.org/10.47836/pjst.33.3.11>

E-mail addresses:

nurdiyana9830@gmail.com (Nur Diyana Zulpahmi)

wanzuraida@uitm.edu.my (Wan Zuraida Wan Mohd Zain)

fazlena@uitm.edu.my (Fazlena Hamzah)

nurulwahida87@uitm.edu.my (Nurul Wahida Ramli)

nuramira87@uitm.edu.my (Nur 'Amira Hamid)

syehdany@uitm.edu.my (Irmaizatussyehdany Buniyamin)

wanatikah@mpib.gov.my (Wan Atikah Wan Hamidon)

nailla@uitm.edu.my (Siti Aisha Na'illa Che Musa)

*Corresponding author

synthesised copper nanoparticles are primarily composed of copper, accounting for 95.24% of the total composition. The phytochemicals in the extract have been effectively utilised in the green synthesis of copper nanoparticles, demonstrating potential applications in medicine and agriculture.

Keywords: *Ananas comosus*, copper nanoparticles, Energy Dispersive X-ray, Field Emission Scanning Electron Microscope, Fourier Transform Infrared, green synthesis, UV-visible, X-ray diffraction

INTRODUCTION

Ananas comosus is a botanical species characterised by its tropical origins and fruit, suitable for human consumption (Ali et al., 2020). The MD2 variety of *Ananas comosus* is widely cultivated in Malaysia due to its significant popularity in global markets (Ramli, 2020). The annual global harvest of *Ananas comosus* fruit for consumption and use in the food and beverage sectors amounts to around 30 million tonnes, which also generates a significant quantity of *Ananas comosus* waste (van Tran et al., 2023). The primary waste components of *Ananas comosus* consist of the crown, peel, stem, and core (Zulpahmi et al., 2023). Agricultural industries worldwide generate substantial quantities of biomass residues, posing environmental challenges. These waste materials frequently end up in landfills, where a significant portion is converted into greenhouse gases and methane (van Tran et al., 2023).

Therefore, biotechnological and adaptable methodologies can ensure the sustainable use of by-products derived from *Ananas comosus* (Fouda-Mbanga & Tywabi-Ngeva, 2022). This is primarily due to the abundant presence of phytochemicals, antioxidants, biofuels, and phenolic compounds (Sarangi et al., 2022). According to Vijayaram et al. (2023), green synthesis tools are considered more appropriate for developing nanoparticles within the 1 to 100 nm size range. Green synthesis methods are increasingly replacing physical and chemical processes as they utilise natural and eco-friendly substances (Ying et al., 2022). Particle size affects various features and functions (Buniyamin et al., 2022). Metal nanoparticles can be synthesised in the presence of green materials and under appropriate conditions (Vijayaram et al., 2023). In previous studies, several metallic nanoparticles have been synthesised using plant extracts.

For instance, zinc oxide nanoparticles (ZnO NPs) have been synthesised using the unripe fruit extract of *Aegle marmelos* (Am-ZnO NPs), the leaf extract of *Lawsonia inermis*, whereas iron oxide nanoparticles have been produced with the assistance of *Tamarindus indica* fruit extract (Senthamarai & Malaikozhundan, 2022; Vinothini et al., 2023; Malaikozhundan et al., 2024). The current status of bio-assisted synthesis primarily encompasses various interconnected factors, including the composition and concentration of the biological reducing agent, the starting concentration of precursor salts, the stirring speed, the reaction duration, the pH level, temperature, and exposure to light. These factors

influence the properties of the synthesised nanoparticles. Therefore, optimising a biological methodology is a comprehensive undertaking that requires a substantial investment of time and resources (Crisan et al., 2022). Among various metal nanoparticles, copper stands out from others, such as gold, silver, and zinc, due to its larger surface area, cost-effective production, and notable antibacterial and antioxidant properties (Malaikozhundan, Krishnamoorthi et al., 2022). Copper nanoparticles have received significant attention from the public (Crisan et al., 2022). They include distinctive characteristics that render them highly relevant in many domains, including their utilisation as antioxidants, anticancer agents, antibacterial agents, nanosensors, nanocatalysts, and materials with exceptional strength (Alahdal et al., 2023). These nanoparticles' production has been achieved by reducing aqueous copper ions using various plant extracts (Hano & Abbasi, 2022). The wide range of accessible oxidation states of copper (Cu^0 , Cu^+ , Cu^{2+} , and Cu^{3+}) allows for diverse reactions and promotes reactivity in copper-based materials.

This reactivity can occur through both one- and two-electron pathways (Alahdal et al., 2023). Several protective compounds have been recommended to mitigate the process of oxidation (Alahdal et al., 2023). Capping agents play a crucial and diverse role in the synthesis of nanoparticles. Plant extracts contain a wide range of compounds, including amines, amides, alkaloids, flavonoids, phenols, terpenoids, proteins, and pigments (Thatyana et al., 2023). Previous studies have also shown the presence of various phytochemical compounds in different parts of *Ananas comosus*, as portrayed in Table 1. The bioactive compounds used as reducing and capping agents during nanomaterial synthesis were identified to assess the rate of the mechanism, surface morphology, and size of the nanoparticle, along with its stability (Buniyamin, Halim et al., 2023). Therefore, using plant extracts presents a viable approach for efficiently forming metallic nanoparticles through environmentally friendly methodologies (Alahdal et al., 2023).

The use of plants as reducing agents in the synthesis of nanoparticles effectively eliminates harmful toxic substances (Malaikozhundan, Lakshmi et al., 2022). The secondary metabolites derived from plants contribute to the stability of nanoparticles, prevent agglomeration, and facilitate control over their shape and size (Sidhu et al., 2022). Additionally, biomolecules present during the synthesis step can prevent particle agglomeration, resulting in dispersed nanoparticles and a high surface area-to-volume ratio (Buniyamin, Mahmood et al., 2023).

To the best of our knowledge, previous research has concentrated on copper nanoparticles derived from fresh aqueous extracts of *Ananas comosus* fruit and peel (Ranjitham et al., 2015; Mitra et al., 2024), neglecting other parts of *Ananas comosus*. Therefore, this study aims to focus on the novelty of the *Ananas comosus* leaf by utilising it for the synthesis of copper nanoparticles that enhance environmental sustainability and renewability due to its abundance compared to the fruit, which is predominantly utilised in

the food and beverage industry. This effort facilitates the exploration of new opportunities for significant impact, applications, or future additional research. These findings help Malaysia enhance its scientific research in nanotechnology while addressing the issue of excessive waste generated from the *Ananas comosus*.

Table 1
Phytochemical compound of Ananas comosus

Plant Part	Chemical Compounds	References
Fruits	Alkaloids: Phenolamine, piperidine, plumerane, pyridine, pyrrole, quinoline Flavonoids: Flavonols, flavonones, flavones, flavonoid carbonoside, flavanols Lipids: Free fatty acids, glycerol ester, lysophosphatidylcholine, sphingolipids Amino acids and derivatives, proteins Lignans and coumarins Nucleotides and derivatives Organic Acids: Acetic acid, citric acid, oxalic acid, malic acid Phenolic Acids: Chlorogenic acid, gallic acid, gentisic acid, syringic acid, vanillin, ferulic acid, sinapic acid, isoferulic acid, o-coumaric acid polyphenols: gallic acid, catechin, epicatechin, ferulic acid saponins, tannins, steroids, terpenoids, napthoquinone, inulin, phenols Bromelain, other compounds: 1-hexanol, nonanal	Chen et al., 2023; Rahman et al., 2020; Hikal et al., 2021; Spanier et al., 1998; Gao et al., 2022; Salome et al., 2011
Stem	Flavonoids, alkaloids, saponins, tannins, phytosterol, carbohydrates, bromelain, proteins	Febrianti et al., 2016; Rahman et al., 2020
Peel	Protein, alkaloids, tannins, flavonoids, steroids, saponins, terpenoids, inulin, glycosides, phenolic compounds, polyphenols, anthraquinones, coumarins, triterpenes, sterols, oxalate, phytate, quinine, carbohydrate, bromelain	Rahman et al., 2020
Crown	Bromelain, protein: Ribulose biphosphate carboxylate, peroxidase, acid, alkaline phosphatase, nuclease, α -amylase Polyphenols: Ferulic acid, syringic acid	Rahman et al., 2020 Hikal et al., 2021
Pulp	Esters: Methyl hexanoate, Ethyl hexanoate, Methyl 3-(methylthio) propanoate, Methyl octanoate, Ethyl deanoate Aromatic compounds: A-terpineol, nonanal, decanal	Teai et al., 2001
Shell	Phenolic compounds: Myricetin, salicylic acid, tannic acid, trans-cinnamic acid, p-coumaric acid	Hikal et al., 2021
Core	Ascorbic acid, phenolic acids: Ferulic acid, syringic acid	Hikal et al., 2021
Leaves	Flavonoids, terpenoids, phytosterol, amino acids, phenols, tannins, carbohydrates, glycosides, proteins, alkaloids, saponins, triterpenoids, steroids, citric acids, bromelain Phenolic compounds: Caffeic acid, chlorogenic acid, p-coumaric acid	Rahman et al., 2020; Hikal et al., 2021 Ma et al., 2007

MATERIALS AND METHOD

Oven (Brand: Memmert/UF260), soil crusher with sieve (Brand: Retsch) to grind the dried chopped leaf, copper (II) sulphate (Brand: Sigma Germany) as the precursor salt, Whatman No. 1 filter paper (Brand: Cytiva) to filter the extract, glass Petri dish to dry the mixture of copper nanoparticle solution, universal bottle to store the dried copper nanoparticles, high-speed refrigerated centrifuge (Brand: Hitachi) and centrifuge tubes to centrifuge the *Ananas comosus* leaf extract and colloidal solution of copper nanoparticles, UV-Visible Diffuse Reflectance Spectroscopy (DRS) to measure the optical properties of copper nanoparticles (Model: Cary 5000 Varian, using a PbSmart detector and controlled by Cary WinUV software), X-ray diffraction (XRD) operated using the PANalytical X'pert PRO XRD model with CuK α radiation ($\lambda=1.17545$ Å) at ca. $2\theta = 5^\circ\text{--}90^\circ$ with 45 kV and a scan speed of $0.417782^\circ/\text{sec}$ at 40 mA, with a 2 degree/min setting, Fourier Transform Infrared (FTIR) Spectrophotometer measured using the Perkin Elmer Spectrum 400 within the region 400 to 4000 cm^{-1} by the Attenuated Total Reflectance (ATR) technique, Field Emission Scanning Electron Microscope (FESEM) (Brand: Thermo Scientific Apreo 2) and Energy Dispersive X-ray (EDX) microanalysis (Brand: Thermo Scientific Apreo 2) to analyse the structure, shape, and characteristics of synthesised copper nanoparticles, and OriginPro 2024 (Graphing and Analysis) software for plotting graphs of results obtained.

Preparation of Leaf Extract

The preparation of *Ananas comosus* leaf extracts was conducted with minor modifications and the inclusion of an additional method. The *Ananas comosus* leaf, obtained from a plantation owned by the Malaysian Pineapple Industrial Board (MPIB) located in Chin Chin, Melaka, Malaysia, was subjected to a washing process, followed by chopping and subsequent drying at a temperature of 60°C (Hamdiani & Shih, 2021). The dried leaf was ground into a fine powder. The leaf extract was prepared by combining 20 g of powdered leaf with 200 mL of distilled water in a 250 mL conical flask. The mixture was then boiled and stirred constantly using a magnetic stirrer on a hot plate set at 80°C for 30 minutes (Olajire & Mohammed, 2019). After boiling, the mixture was cooled and subsequently centrifuged at 15,000 revolutions per minute (rpm) to separate and eliminate sediment. The filtrate was then subjected to three rounds of filtration using Whatman No. 1 filter paper to enhance clarity (Hassanein et al., 2018). The sample was stored at 4°C in a Schott bottle for subsequent use in synthesising copper nanoparticles (Hamdiani & Shih, 2021).

Phytochemical Screening of *Ananas comosus* Leaf Extract

The extract was used for phytochemical analysis following established frameworks, with minor modifications to the quantities of chemicals and extract used. The qualitative tests for secondary metabolites were conducted as follows in Table 2.

Table 2
Chemical tests for various compounds in Ananas comosus leaf extract

Test	Procedure	Indication of Presence	References
Flavonoid	Add leaf extract to 1.5 mL of diluted NaOH.	Yellow precipitate formation	Hassan et al., 2020
Phenols	Mix 2 mL of leaf extract with a small amount of 10% aqueous ferric chloride.	Blue or green colour	Rajkumar et al., 2022
Tannins	Add ferric chloride to 2 mL of leaf extract.	Black or brownish-blue colour	Rajkumar et al., 2022
Saponins	Mix 1 mL of leaf extract with 5 mL of water and shake rapidly.	Formation of significant lather	Hassan et al., 2020
Steroids	Add 1 mL of leaf extract to 1 mL of glacial acetic acid, 1 mL of acetic anhydride, and 2 drops of concentrated H ₂ SO ₄ .	Colour change from red to bluish-green	Godlewska et al., 2022
Alkaloids	Mix 1 mL of leaf extract with Dragendorff's reagent.	Orange colour	Godlewska et al., 2022
Quinones	Mix 1 mL of leaf extract with 1 mL of concentrated H ₂ SO ₄ .	Red colour	María et al., 2018
Terpenoids	Mix 5 mL of leaf extract with 2 mL of chloroform, then add 3 mL of concentrated H ₂ SO ₄ .	The reddish-brown colour at the interface	Dubale et al., 2023
Carbohydrates	Mix 5 mL of Benedict reagent with leaf extract, boil for 2 minutes, then cool.	Red precipitate	Pooja et al., 2022

Synthesis of Copper Nanoparticles Using *Ananas comosus* Leaf Extract

The method used was based on recent research by Ranjitham et al. (2015) with minor modifications. Copper nanoparticles were synthesised by dissolving 1.6 g of copper (II) sulphate in 500 mL of distilled water to generate a stock solution (0.02 g/mL) with a blue colouration. Subsequently, 200 mL of prepared *Ananas comosus* leaf extract was introduced into the aqueous solution of copper sulphate. The reaction mixture was subjected to vigorous agitation using a water bath shaker, and the colour changes of the colloidal solution were used as evidence of the presence of synthesised copper nanoparticles. The mixture then underwent a separation process using centrifugation, followed by two rounds of rinsing with distilled water until the filtrate achieved purity. The copper nanoparticles were subsequently dried at a temperature of 60°C for 24 hours, resulting in powdered copper nanoparticles. The specimen was kept for subsequent characterisation analysis using UV-visible diffuse Reflectance Spectroscopy (DRS), X-ray Diffraction (XRD), Energy Dispersive X-ray Spectroscopy (EDX), Fourier Transform Infrared Spectroscopy (FTIR), and Field Emission Scanning Electron Microscopy (FESEM). The parameters for

this research were fixed as outlined below. At the end of the investigation, all results with graphs and peaks were plotted using OriginPro 2024 (Graphing and Analysis) software. The parameters listed in Table 3 were based on the optimal results obtained in the prior study by Ranjitham et al. (2015).

Table 3
Experimental parameters for the synthesis of copper nanoparticles using Ananas comosus leaf extract

Parameter	Details
Composition	1:4 volume ratio of copper sulphate aqueous solution to <i>Ananas comosus</i> leaf extract used for synthesising copper nanoparticles.
Temperature	Synthesis was conducted at 80°C in a water bath.
Time Interval	The formation of a colloidal solution of synthesised copper nanoparticles was recorded at 60 minutes.

RESULTS AND DISCUSSION

Phytochemical Screening of *Ananas comosus* Leaf Extract

The findings of the phytochemical analysis of the aqueous extract derived from *Ananas comosus* are presented in Table 4. The results demonstrate the presence of secondary metabolites, including phenol, tannin, saponin, steroid, alkaloid, quinone, anthraquinone, terpenoid, carbohydrates, coumarin, and flavanone. Positive (+) and negative (-) marks are used to denote the presence and absence of specific phytochemical elements, respectively. Phenolic compounds are significant as phytoconstituents due to their inherent capacity to act as reducing agents in redox reactions (Amini & Akbari, 2019). They can be categorised into distinct groups, including coumarins and quinones (Gan et al., 2019).

Secondary metabolites derived from plants, such as steroids, saponins, tannins, terpenoids, polyols, alkaloids, flavonoids, and phenolics, exhibit robust detoxifying, reducing, and stabilising properties (Sidhu et al., 2022). Previous studies have also demonstrated that carbohydrates in plant extracts stabilise and reduce agents during nanoparticle formation (Rani et al., 2023). This assertion is supported by prior scholarly

Table 4
Phytochemical screening of Ananas comosus leaf extract

Phytochemicals	Phenol	Tannin	Saponin	Steroid	Alkaloid	Quinone	Terpenoid	Carbohydrates	Coumarin	Flavanone
Results (+/-)	+	+	+	-	+	-	+	+	+	+
	-	-	-	+	-	+	-	-	-	-

investigations, which have shown the use of phenolic acids derived from plants in the green synthesis of nanoparticles. Nanoparticle synthesis involves the use of reducing agents and stabilisers, which play dual roles in the process (Amini & Akbari, 2019). Therefore, this qualitative screening aids in identifying the phytochemical compounds present in the extract of *Ananas comosus* leaf.

Visual Observation of Synthesised Copper Nanoparticles Using *Ananas comosus* Leaf Extract

The formation of copper nanoparticles was detected through a discernible alteration in the colour of the reaction mixture. Initially, the copper sulphate solution exhibited a pale blue colour. When the leaf extract of *A. paniculata* was added, the copper sulphate solution underwent a colour transformation from light blue to green, eventually turning a dark greenish-brown colour due to the synthesis of copper nanoparticles (Rajeshkumar et al., 2021). This study demonstrated that the blue aqueous copper sulphate solution changed to dark greenish-brown and eventually dark brown upon the introduction of *Ananas comosus* leaf extract into the aqueous solution of copper sulphate, given the heat and time required for synthesising copper nanoparticles, a pink precipitate formed at the base of the conical flask by the end of the synthesis process. The initial observation in this study was the presence of a pink precipitate consisting of colloidal copper nanoparticles. Previous investigations have shown that colloidal copper solutions' pink to violet colour is directly associated with the observed copper surface plasmon band (Bárta et al., 2010). Subsequently, this precipitate was dried in an oven, forming black powdered copper nanoparticles. The powdered nanoparticles were then subjected to characterisation analysis using spectroscopy, microscopy, and diffraction techniques.

UV-visible Spectrophotometry

A diffuse reflectance analysis was conducted to obtain the spectral data of reflection performance. As a result, the energy band gaps of the nanoparticles could be detected (Buniyamin et al., 2022). The investigation focused on copper nanoparticles synthesised using *Ananas comosus* leaf extract, with the analysis performed using UV-visible Diffuse Reflectance Spectroscopy (DRS). The black powdered copper nanoparticles were evaluated based on their reflectance activity, as measured by UV-visible diffuse reflectance (UV-visible DRS). The synthesised copper nanoparticles exhibited surface plasmon resonance (SPR) spectra with absorption peaks ranging from 200 to 800 nm. The presence of copper nanoparticles was verified by observing a distinct peak at 238 nm using a UV-visible diffuse reflectance (UV-visible DRS) spectrophotometer. The data were plotted using OriginPro 2024 (Graphing and Analysis) software, as depicted in Figure 1. A prominent peak in absorbance was detected, attributed to the ionisation of phenolic groups found

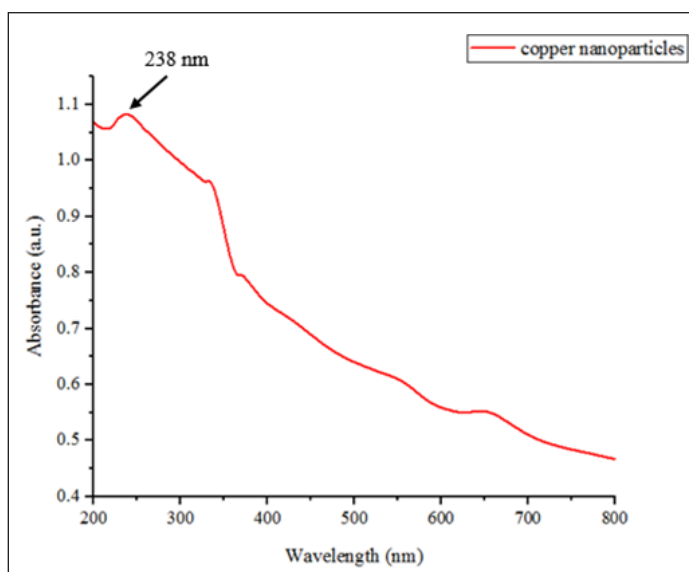


Figure 1. The UV-visible diffuse Reflectance Spectroscopy (DRS) of synthesised copper nanoparticles using *Ananas comosus* leaf extract

within the plant extract. Copper nanoparticles typically demonstrate a distinct surface plasmon resonance peak within the wavelength range of 560–570 nm (Mohamed, 2020). The observed variations in reduction, capping, and stabilising processes can be attributed to the diverse properties of the plant extracts utilised. It may also be caused by using different types of UV-visible spectrophotometers. UV-visible spectroscopy is commonly associated with absorption spectroscopy, measured through transmission. On the other hand, DRS specifically refers to diffuse reflection spectroscopy. Typically, the former is employed for solutions or thin films, whereas DRS is increasingly utilised. Spectroscopy is a commonly employed, fundamental method of spectrophotometry used to analyse powders and surfaces and requires minimal sample preparation (Morozzi et al., 2021).

X-ray Diffraction Analysis (XRD)

X-ray diffraction (XRD) is a non-destructive technique used to analyse the chemical composition and crystallographic structure of dried synthesised copper nanoparticles, regardless of whether they exhibit an amorphous or crystalline nature. Figure 2 depicts the analysis conducted on the synthesised copper nanoparticles. The pattern shows peaks at 2θ values of 43.46° , 50.57° , and 74.23° , which correspond to the lattice planes (111), (200), and (220), respectively. All observed peaks correspond to the face-centred cubic (FCC) crystal structure and show satisfactory agreement with the standard Joint Committee on Powder Diffraction Standards (JCPDS) No. 04-0836 reference. The observed peak positions align with documented findings related to metallic copper, and no additional peaks associated

with impurities were observed in the sample according to the JCPDS (Tsilo et al., 2023). Therefore, the synthesised copper nanoparticles exhibit a high level of purity.

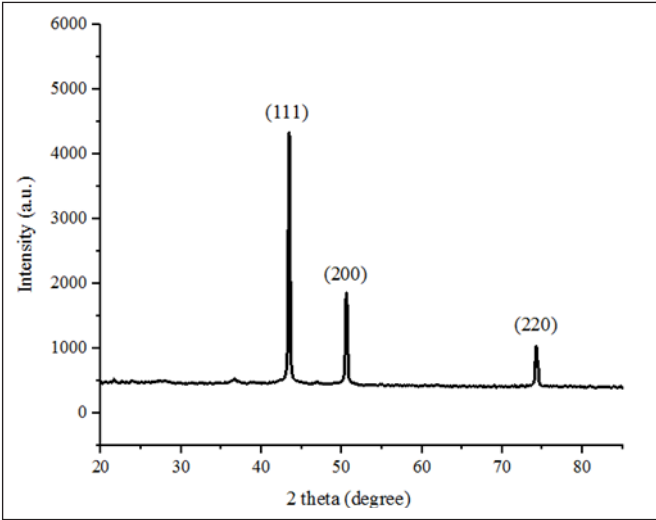


Figure 2. The X-ray diffraction analysis (XRD) of synthesised copper nanoparticles using *Ananas comosus* leaf extract

Energy Dispersive X-ray (EDX)

The Energy Dispersive X-ray (EDX) technique can perform qualitative and quantitative investigations of the elemental composition that could potentially contribute to the production of nanoparticles. Based on Table 5, using energy-dispersive X-ray analysis facilitated the identification of the composition of synthesised copper nanoparticles, which consisted of 95.24% pure copper, 4.08% carbon, and 0.68% oxygen, as determined by weight percentage. The study further revealed that the synthesised copper nanoparticles consisted of 79.68% pure copper, 18.07% carbon, and 2.25% oxygen, as determined by atomic percentage. Copper served as a prominent constituent element within the copper nanoparticles, demonstrating a correlation between the copper content and the overall percentage of copper present in these nanoparticles. The Energy Dispersive X-ray analysis depicted in Figure 3(a) shows the EDX pattern obtained from copper nanoparticles synthesised using *Ananas comosus* leaf extract, revealing a significant concentration of copper. This research suggests that the copper particles obtained exhibit high purity. The utilisation of Energy Dispersive X-ray microanalysis facilitates the acquisition of morphological data pertaining to the synthesised copper

Table 5
The weight and atomic percentage of element presence in the synthesised copper nanoparticles

Result	Copper	Carbon	Oxygen
Mass Norm. (%)	95.24	4.08	0.68
Atom (%)	79.68	18.07	2.25

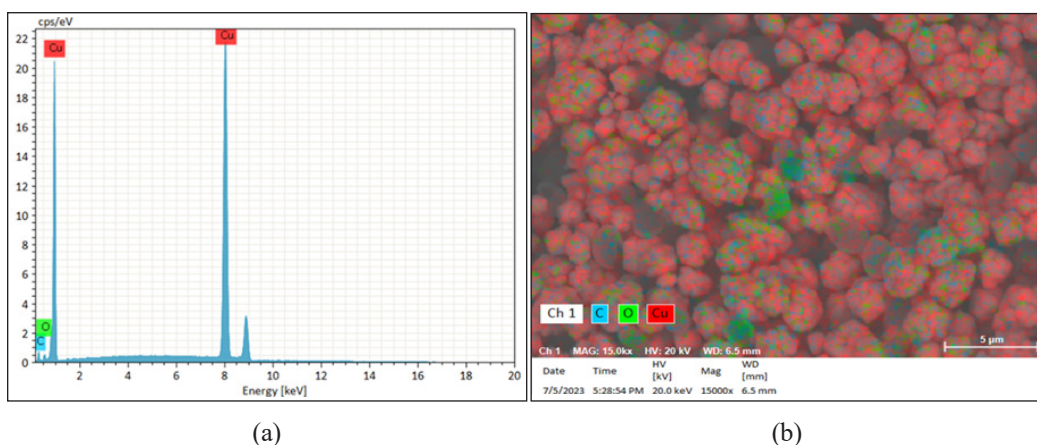


Figure 3. (a) The Energy Dispersive X-ray (EDX) of synthesised copper nanoparticles using *Ananas comosus* leaf extract (b) The portrayed composition of elements present in the synthesised copper nanoparticles using *Ananas comosus* leaf extract

nanoparticles. Based on the data presented in Figure 3(b), it can be observed that the *Ananas comosus* leaf extract, containing copper (Cu), carbon (C), and oxygen (O) elements, plays a significant role in the formation of face-centred cubic copper nanoparticles. Face-centred structures are known to have a higher degree of space efficiency. The observed red colouration of the copper nanoparticles can be attributed to the densely packed arrangement of copper atoms, which contributes to their enhanced stability. The blue colour refers to the carbon elements, while the green indicates the presence of oxygen elements. The colours were used to differentiate the presence of elements in the synthesised copper nanoparticles. Prior studies have indicated that the face-centred cubic structure is a crucial factor in the exploration of innovative nanoscale structures (Cheedarala & Song, 2020). It has been shown that the structure of copper nanoparticles was capped and stabilised by the carbon and oxygen present in minute quantities, which originate from the extract of *Ananas comosus* leaf. The resulting strong structure, as depicted in Figure 3(b), can be attributed to the capping and stabilising mechanism. Therefore, this study has demonstrated the efficacy of phytochemical constituents derived from *Ananas comosus* leaf extract in synthesising copper nanoparticles. X-ray diffraction (XRD) analysis validated the successful formation of a face-centred cubic (FCC) crystalline structure. The diffraction patterns revealed distinct peaks that correspond to the FCC lattice planes, confirming the presence of this structural configuration.

Fourier Transform Infrared Spectroscopy (FTIR)

Fourier Transform Infrared (FTIR) analysis was conducted to investigate the impact of capping or reducing agents and to demonstrate the characteristics of different functional

groups within the plant extract responsible for the synthesis of copper nanoparticles through the reduction of copper. The FTIR study covered the spectral region of 400–4000 cm^{-1} , as depicted in Figures 4(a) and 4(b). Figure 4(a) displays the FTIR spectra of *Ananas comosus* leaf extract, revealing a prominent peak at 3347 cm^{-1} . This spectral feature is attributed to the O-H stretching motion of an alcohol molecule. The observed peaks at 2998, 1378, and 1325 cm^{-1} correspond to the absorption of C-O single bonds. The presence of absorption bands in 1723 and 1649 cm^{-1} suggests C=O carbonyl and C=C stretching vibrations, respectively, likely due to the cyclic aromatic ring. The carboxylic acid functional group shows characteristics of both alcohols and ketones, encompassing the O-H bond characteristic of alcohols and the C=O carbonyl bond typical of ketones.

Hence, carboxylic acids exhibit a pronounced spectral band from 2800 cm^{-1} to 3500 cm^{-1} corresponding to the O-H bond stretching in alcohols. Secondary amines display a singular N-H bond, observed at 3343 cm^{-1} , resulting in a solitary peak. The amide functional group includes both the N-H amine bond and the C=O carbonyl bond, presenting a prominent and moderately wide absorption band in the 3100 cm^{-1} to 3500 cm^{-1} range, corresponding to the N-H amine bond stretching. The observed peaks indicate the presence of functional groups commonly found in the principal chemicals of the *Ananas comosus* leaf extract. The synthesised copper nanoparticles displayed several distinctive peaks in the *Ananas comosus* leaf extract, as shown in Figure 4(b), with modest variations in peak positions and intensities.

FTIR analysis can also be used quantitatively to determine the concentration of certain functional groups, provided that the underlying chemistry is understood and standard reference materials are available. Figure 4(b) illustrates the correlation between the transmittance of the synthesised copper nanoparticles and the absorption of infrared light. When a sample absorbs a significant portion of incident light, transmission through the sample is nearly non-existent. The synthesised copper nanoparticles exhibit a high level of absorbance and a correspondingly low level of transmission. The sample concentration may also influence the intensity of absorption bands in an IR spectrum. According to the Beer-Lambert equation, absorbance is directly proportional to both the concentration of the absorbing substance in the solution and the length of the light path (Bhanvase & Barai, 2021).

The results showed that the composition of the synthesised copper nanoparticles retained the organic constituents derived from the *Ananas comosus* leaf extract. The observed peaks in the nanoparticles suggest functional groups from organic compounds such as flavonoids, alkaloids, and terpenoids encapsulated them. Past research has shown that most flavonoids possess a C6-C3-C6 structure with two benzene rings (A and B) linked by a heterocyclic pyrone ring (C) containing oxygen (Dias et al., 2021). Flavonoid classification is based on specific chemical groups. For instance, flavanols are characterised by a hydroxyl group at

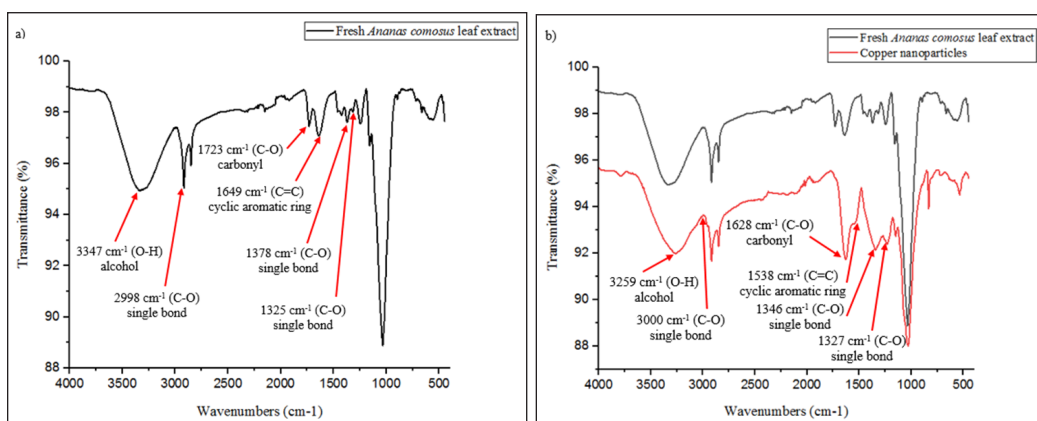


Figure 4. (a) The Fourier Transform Infrared Spectroscopy (FTIR) analysis of fresh *Ananas comosus* leaf extract (b) The Fourier Transform Infrared Spectroscopy (FTIR) analysis of fresh *Ananas comosus* leaf extract and synthesised copper nanoparticles

the 3-position, while flavanones have a C2–C3 double bond, confirming the presence of flavonoid compounds in the synthesised copper nanoparticles (Kumar & Pandey, 2013). Additionally, terpenoids, which are derived from terpenes and include oxygen atoms, likely derive their oxygen from the carbonyl group of the fresh *Ananas comosus* leaf extract, connected to the cyclic aromatic ring of the terpenoid (Adefegha et al., 2022). Alkaloids, chemicals typically containing one or more nitrogen atoms in a heterocyclic ring structure (amine functional group), are also present (Lamponi, 2021). This research confirmed that amines in the fresh *Ananas comosus* leaf extract exhibit a singular N-H bond at 3343 cm⁻¹. Thus, the study indicates that the surface of the copper nanoparticles was effectively covered and stabilised by these organic molecules during synthesis, suggesting the nanoparticles' non-oxidative and highly pure nature.

Field Emission Scanning Electron Microscopy (FESEM)

Figure 5 depicts the synthesised copper nanoparticles' morphological characteristics and structural configuration. The images were obtained using Field Emission Scanning Electron Microscopy (FESEM) with magnifications ranging from the smallest to the largest. The synthesised copper nanoparticles exhibited a tendency to form a disordered agglomeration. The dispersion of the copper nanoparticles is characterised by a loose structure, which leads to agglomeration due to adhesion. Only a limited number of agglomerations occurred, resulting in non-uniform copper nanoparticles. The copper nanoparticles synthesised in this study exhibited strong aggregation due to the dense packing of pure copper atoms. Figure 5 demonstrates that the shape of copper nanoparticles is irregular, while Figure 6 shows that the predominant diameters of the synthesised copper nanoparticles are 51.91

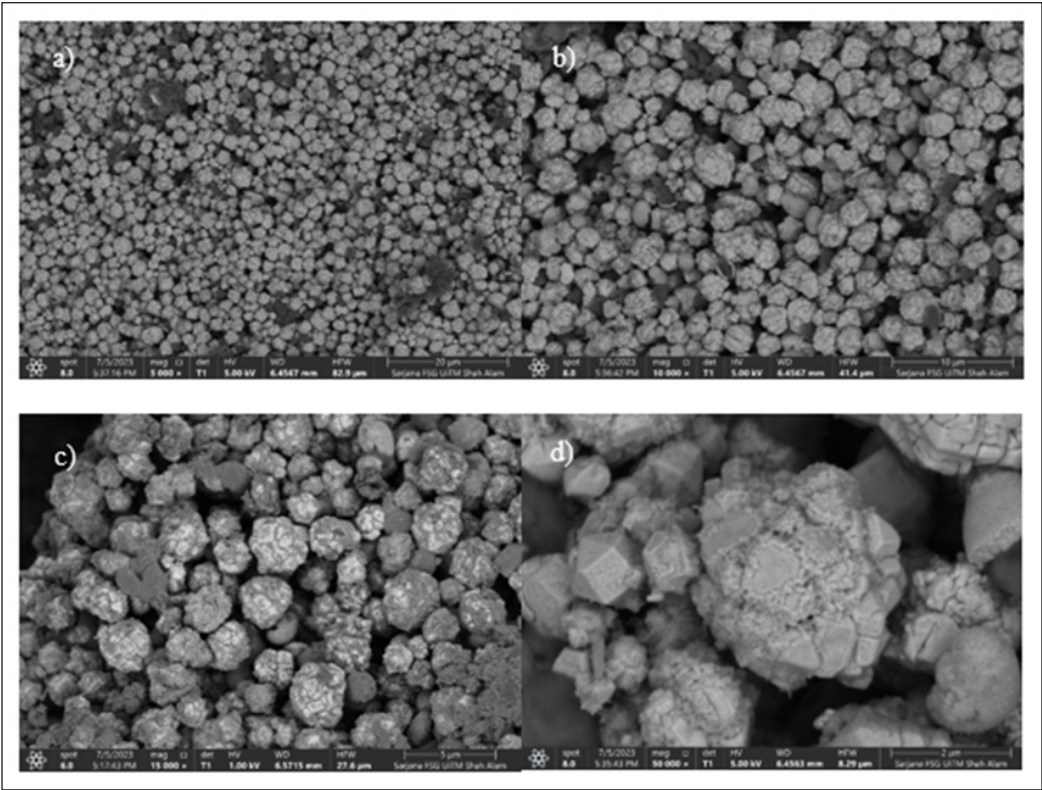


Figure 5. The morphological surface structure of synthesised copper nanoparticles using *Ananas comosus* leaf extract using (a) 1000×, (b) 10000×, (c) 15000×, and (d) 50000× magnification of Field Emission Scanning Electron Microscopy (FESEM)

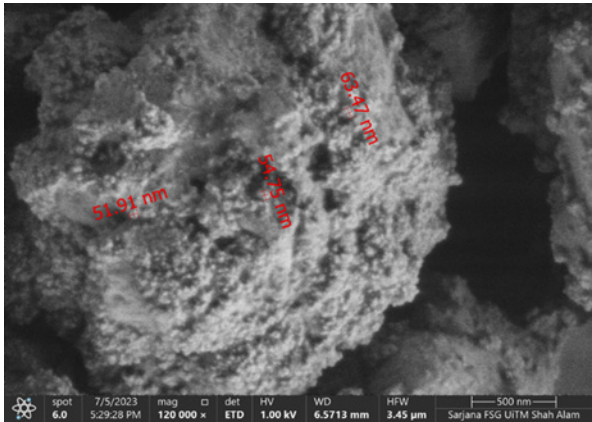


Figure 6. The average size of synthesised copper nanoparticles using *Ananas comosus* leaf extract under 120000 x magnification of Field Emission Scanning Electron Microscopy (FESEM)

nm, 54.75 nm, and 63.47 nm. The average size of the synthesised copper nanoparticles was 56.71 nm. Determining the shape and average size of synthesised nanoparticles allows for the assessment of their specifications and effectiveness in various applications, such as medicinal, antibacterial, antifungal, magnetic, and electrical effects. The findings of this experiment indicate that the structure of the copper nanoparticles remains stable and consistent with the specified size of the nanoparticles.

CONCLUSION

In the current study, *Ananas comosus* leaf extract was successfully used to synthesise copper nanoparticles through the processes of reduction, capping, and stabilisation by the secondary metabolites present in the extract. The existence of functional groups from secondary metabolites such as flavonoids, alkaloids, and terpenoids derived from the extract facilitated the synthesis process. The synthesised copper nanoparticles succeeded in terms of their crystallographic, optical, and surface morphological properties. Since the synthesis of copper nanoparticles only involves raw materials from *Ananas comosus* leaf and a small amount of copper sulfate, the production cost is very affordable, especially for smallholders. In the future, implementing technological improvements aimed at enhancing the safety of nanoparticles created through green synthesis could potentially boost the development of agricultural economics, particularly in applications such as plant pathogen treatments and microbiology.

ACKNOWLEDGMENTS

The authors thank the Ministry of Higher Education, Malaysia (MOHE) for funding this work under the Fundamental Research Grant Scheme, FRGS/1/2022/STG01/UITM/03/2. The authors also acknowledge the Malaysian Pineapple Industry Board (MPIB) as industrial collaborators for this research.

REFERENCES

- Adefegha, S. A., Oboh, G., & Oluokun, O. O. (2022). Chapter 11 - food bioactives: The food image behind the curtain of health promotion and prevention against several degenerative diseases. *Studies in Natural Products Chemistry*, 72, 391–421. <https://doi.org/https://doi.org/10.1016/B978-0-12-823944-5.00012-0>
- Alahdal, F. A. M., Qashqoosh, M. T. A., Manea, Y. K., Mohammed, R. K. A., & Naqvi, S. (2023). Green synthesis and characterization of copper nanoparticles using *Phragmanthera austroarabica* extract and their biological/environmental applications. *Sustainable Materials and Technologies*, 35, Article e00540. <https://doi.org/https://doi.org/10.1016/j.susmat.2022.e00540>
- Ali, M. M., Hashim, N., Aziz, S. A., & Lasekan, O. O. (2020). Pineapple (*Ananas comosus*): A comprehensive review of nutritional values, volatile compounds, health benefits, and potential food products. *Food Research International*, 137, Article 109675. <https://doi.org/10.1016/j.foodres.2020.109675>

- Amini, S. M., & Akbari, A. (2019). Metal nanoparticles synthesis through natural phenolic acids. *IET Nanobiotechnology*, 13(8), 771–777. <https://doi.org/10.1049/iet-nbt.2018.5386>
- Bárta, J., Pospíšil, M., & Čuba, V. (2010). Photo and radiation-induced preparation of nanocrystalline copper and cuprous oxide catalysts. *Journal of Radioanalytical and Nuclear Chemistry*, 286, 611–618. <https://doi.org/10.1007/s10967-010-0748-5>
- Bhanvase, B., & Barai, D. (2021). Stability of nanofluids. In *Nanofluids for Heat and Mass Transfer: Fundamentals, Sustainable Manufacturing and Applications* (pp. 69–97). Academic Press. <https://doi.org/10.1016/B978-0-12-821955-3.00009-1>
- Buniyamin, I., Akhir, R. M., Asli, N. A., Khusaimi, Z., Malek, M. F., & Mahmood, M. R. (2022). Nanotechnology applications in biomedical systems. *Current Nanomaterials*, 7(3), 167–180. <https://doi.org/10.2174/2405461507666220301121135>
- Buniyamin, I., Eswar, K. A., Asli, N. A., Halim, M. F. A., Khusaimi, Z., & Mahmood, M. R. (2023). Bio-synthesized tin oxide nanoparticles (SnO₂ NPs) as a photocatalyst model. *Malaysia Journal of Invention and Innovation*, 2(3), 1-5.
- Buniyamin, I., Halim, M. F. A., Eswar, K. A., Jalani, K. J., Kadir, S. A. I. A. S. A., Mohammad, M., Idorus, M. Y., Asli, N. A., Mahmood, M. R., & Khusaimi, Z. (2023). Natural biomolecules in leaf and fruit extracts mediate the biosynthesis of SnO₂ nanoparticles: A mini review. *International Journal of Pharmaceuticals, Nutraceuticals and Cosmetic Science*, 6(2), 24–40. <https://doi.org/10.24191/IJPNaCS.v6i2.03>
- Buniyamin, I., Mahmood, M. R., & Khusaimi, Z. (2023). Utilization of tin oxide nanoparticles synthesized through plant-mediated methods and their application in photocatalysis: A brief review. *International Journal of Chemical and Biochemical Sciences*, 24(7), 116-123.
- Cheedarala, R. K., & Song, J. (2020). Face-centred cubic CuO nanocrystals for enhanced pool-boiling critical heat flux and higher thermal conductivities. *International Journal of Heat and Mass Transfer*, 162, Article 120391. <https://doi.org/10.1016/j.ijheatmasstransfer.2020.120391>
- Chen, J., Yao, Y., Zeng, H., & Zhang, X. (2023). Integrated metabolome and transcriptome analysis reveals a potential mechanism for water accumulation mediated translucency in pineapple (*Ananas comosus* (L.) Merr.) fruit. *International Journal of Molecular Sciences*, 24(8), Article 7199. <https://doi.org/10.3390/ijms24087199>
- Crisan, M. C., Teodora, M., & Lucian, M. (2022). Copper nanoparticles: Synthesis and characterization, physiology, toxicity and antimicrobial applications. *Applied Sciences*, 12(1), Article 141. <https://doi.org/10.3390/app12010141>
- Dias, M. C., Pinto, D. C. G. A., & Silva, A. M. S. (2021). Plant flavonoids: Chemical characteristics and biological activity. *Molecules*, 26(17), Article 5377. <https://doi.org/10.3390/molecules26175377>
- Dubale, S., Kebebe, D., Zeynudin, A., Abdissa, N., & Suleman, S. (2023). Phytochemical screening and antimicrobial activity evaluation of selected medicinal plants in Ethiopia. *Journal of Experimental Pharmacology*, 15, 51–62. <https://doi.org/10.2147/JEP.S379805>
- Febrianti, S., Cevanti, T., & Sumekar, H. (2016). The secondary metabolites screening and the effectiveness (*Ananas comosus* (L.) Merr of the queen pineapple stems in decreasing the number of *Enterococcus faecalis*'s colonies. *DENTA*, 10, Article 89. <https://doi.org/10.30649/denta.v10i1.41>

- Fouda-Mbanga, B. G., & Tywabi-Ngeva, Z. (2022). Application of pineapple waste to the removal of toxic contaminants: A review. *Toxics*, 10(10), Article 561. <https://doi.org/10.3390/toxics10100561>
- Gan, R. Y., Chan, C. L., Yang, Q. Q., Li, H. B., Zhang, D., Ge, Y. Y., Gunaratne, A., Ge, J., & Corke, H. (2019). 9 - Bioactive compounds and beneficial functions of sprouted grains. In *Sprouted Grains* (pp. 191-246). AACC International Press. <https://doi.org/https://doi.org/10.1016/B978-0-12-811525-1.00009-9>
- Gao, Y., Yao, Y., Chen, X., Wu, J., Wu, Q., Liu, S., Guo, A., & Zhang, X. (2022). Metabolomic and transcriptomic analyses reveal the mechanism of sweet-acidic taste formation during pineapple fruit development. *Frontiers in Plant Science*, 13, Article 971506. <https://doi.org/10.3389/fpls.2022.971506>
- Godlewska, K., Pacyga, P., Szumny, A., Szymczycha-Madeja, A., Welna, M., & Michalak, I. (2022). Methods for rapid screening of biologically active compounds present in plant-based extracts. *Molecules*, 27(20), Article 7094. <https://doi.org/10.3390/molecules27207094>
- Hamdiani, S., & Shih, Y. F. (2021). A green method for synthesis of silver-nanoparticles-diatomite (AgNPs-D) composite from pineapple (*Ananas comosus*) leaf extract. *Indonesian Journal of Chemistry*, 21, Article 740. <https://doi.org/10.22146/ijc.63573>
- Hano, C., & Abbasi, B. H. (2022). Plant-based green synthesis of nanoparticles: Production, characterization and applications. *Biomolecules*, 12(1), Article 31. <https://doi.org/10.3390/biom12010031>
- Hassan, A., Akmal, Z., & Khan, N. (2020). The phytochemical screening and antioxidants potential of *Schoenoplectus triqueter* L. Palla. *Journal of Chemistry*, 2020, Article 3865139. <https://doi.org/10.1155/2020/3865139>
- Hassanien, R., Husein, D., & Al-Hakkani, M. (2018). Biosynthesis of copper nanoparticles using aqueous *Tilia* extract: Antimicrobial and anticancer activities. *Heliyon*, 4, Article e01077. <https://doi.org/10.1016/j.heliyon.2018.e01077>
- Hikal, W., Mahmoud, A., Said-Al Ahl, H., Bratovcic, A., Tkachenko, K., Kacaniova, M., & Rodriguez, R. M. (2021). Pineapple (*Ananas comosus* L. Merr.), waste streams, characterisation and valorisation: An overview. *Open Journal of Ecology*, 11, Article 9039. <https://doi.org/10.4236/oje.2021.119039>
- Kumar, S., & Pandey, A. K. (2013). Chemistry and biological activities of flavonoids: An overview. *The Scientific World Journal*, 2013, Article 162750. <https://doi.org/10.1155/2013/162750>
- Lamponi, S. (2021). The importance of structural and functional analysis of extracts in plants. *Plants*, 10(6), Article 1225. <https://doi.org/10.3390/plants10061225>
- Ma, C., Xiao, S., Li, Z., Wang, W., & Du, L. (2007). Characterization of active phenolic components in the ethanolic extract of *Ananas comosus* L. leaf using high-performance liquid chromatography with diode array detection and tandem mass spectrometry. *Journal of Chromatography A*, 1165(1), 39–44. <https://doi.org/https://doi.org/10.1016/j.chroma.2007.07.060>
- Malaikozhundan, B., Krishnamoorthi, R., Vinodhini, J., Nambi, K. S. N., & Palanisamy, S. (2022). Multifunctional iron oxide nanoparticles using *Carica* papaya fruit extract as antibacterial, antioxidant and photocatalytic agent to remove industrial dyes. *Inorganic Chemistry Communications*, 144, Article 109843. <https://doi.org/https://doi.org/10.1016/j.inoche.2022.109843>
- Malaikozhundan, B., Lakshmi, V. N., & Krishnamoorthi, R. (2022). Copper oxide nanoparticles using *Mentha spicata* leaf as antibacterial, antibiofilm, free radical scavenging agent and efficient photocatalyst to degrade

- methylene blue dyes. *Materials Today Communications*, 33, Article 104348. <https://doi.org/https://doi.org/10.1016/j.mtcomm.2022.104348>
- Malaikozhundan, B., Mohandoss, S., Krishnamoorthi, R., Bharathi, P. V., Palanisamy, S., & Vinodhini, J. (2024). Enhanced bactericidal, antibiofilm and antioxidative response of Lawsonia inermis leaf extract synthesised ZnO NPs loaded with commercial antibiotic. *Bioprocess and Biosystems Engineering*, 47(8), 1241–1257. <https://doi.org/10.1007/s00449-024-03000-9>
- María, R., Shirley, M., Xavier, C., Jaime, S., David, V., Rosa, S., & Jodie, D. (2018). Preliminary phytochemical screening, total phenolic content and antibacterial activity of thirteen native species from Guayas province Ecuador. *Journal of King Saud University Science*, 30(4), 500–505. <https://doi.org/https://doi.org/10.1016/j.jksus.2017.03.009>
- Mitra, S., Dua, T. K., Easmin, S., Sarkar, S., Roy, A. P., Sahu, R., Nandi, G., Haydar, M. S., Roy, S., & Paul, P. (2024). Green synthesis of copper nanoparticles by using pineapple peel waste: in vitro characterizations and antibacterial potential. *Bioprocess and Biosystems Engineering*, 47(8), 1151–1161. <https://doi.org/10.1007/s00449-024-02982-w>
- Mohamed, E. A. (2020). Green synthesis of copper & copper oxide nanoparticles using the extract of seedless dates. *Heliyon*, 6(1), Article e03123. <https://doi.org/https://doi.org/10.1016/j.heliyon.2019.e03123>
- Morozzi, P., Ballarin, B., Arcozzi, S., Brattich, E., Lucarelli, F., Nava, S., Gómez-Cascales, P. J., Orza, J. A. G., & Tositti, L. (2021). Ultraviolet–visible diffuse reflectance spectroscopy (UV–Vis DRS), a rapid and non-destructive analytical tool for the identification of Saharan dust events in particulate matter filters. *Atmospheric Environment*, 252, Article 118297. <https://doi.org/https://doi.org/10.1016/j.atmosenv.2021.118297>
- Olajire, A. A., & Mohammed, A. A. (2019). Green synthesis of palladium nanoparticles using *Ananas comosus* leaf extract for solid-phase photocatalytic degradation of low density polyethylene film. *Journal of Environmental Chemical Engineering*, 7(4), Article 103270. <https://doi.org/https://doi.org/10.1016/j.jece.2019.103270>
- Pooja, S., Sonali, M., Charmi, P., Dhumi, S., Rathod, Z., & Meenu, S. (2022). A Review on Qualitative and Quantitative Analysis of Carbohydrates Extracted from Bacteria. *Acta Scientific Microbiology*, 5, 60–68.
- Rahman, I. A., Camalxaman, N., Rambely, A. S., Haron, N., & Mohamed, E. (2020). *Ananas comosus* (L.) Merr: A mini review of its therapeutic properties *Health Scope*, 3(2), 54–59.
- Rajeshkumar, S., Vanaja, M., & Kalirajan, A. (2021). Degradation of toxic dye using phytomediated copper nanoparticles and its free-radical scavenging potential and antimicrobial activity against environmental pathogens. *Bioinorganic Chemistry and Applications*, 2021, Article 1222908. <https://doi.org/10.1155/2021/1222908>
- Rajkumar, G., Panambara, P., & Sanmugarajah, V. (2022). Comparative analysis of qualitative and quantitative phytochemical evaluation of selected leaf of medicinal plants in Jaffna, Sri Lanka. *Borneo Journal of Pharmacy*, 5, 93–103. <https://doi.org/10.33084/bjop.v5i2.3091>
- Ramli, A. N. M. (2020, October 14). Pineapple waste commercialisation. *UMPSA News*. <https://news.umpsa.edu.my/experts/pineapple-waste-commercialisation>

- Rani, N., Singh, P., Kumar, S., Kumar, P., Bhankar, V., & Kumar, K. (2023). Plant-mediated synthesis of nanoparticles and their applications: A review. *Materials Research Bulletin*, 163, Article 112233. <https://doi.org/https://doi.org/10.1016/j.materresbull.2023.112233>
- Ranjitham, A., Ranjani, G., & Caroling, G. (2015). Biosynthesis, characterization, antimicrobial activity of copper nanoparticles using fresh aqueous *Ananas comosus* L. (Pineapple) extract. *International Journal of PharmTech Research*, 8, 750–769.
- Salome, Y. S. E., Kouakou, H. T., Kouakou, L. K., Kouadio, J., Patrice, K., & Mérillon, J. M. (2011). Phenolic profiles of pineapple fruits (*Ananas comosus* L. Merrill) influence of the origin of suckers. *Australian Journal of Basic and Applied Sciences*, 5, 1372–1378.
- Sarangi, P., Thangjam, A., Singh, N., Shadangi, K., Srivastava, R., Singh, A., Chandel, A., Pareek, N., & Vivekanand, V. (2022). Sustainable utilization of pineapple wastes for production of bioenergy, biochemicals and value-added products: A review. *Bioresource Technology*, 351, Article 127085. <https://doi.org/10.1016/j.biortech.2022.127085>
- Senthamarai, M. D., & Malaikozhundan, B. (2022). Synergistic action of zinc oxide nanoparticle using the unripe fruit extract of *Aegle marmelos* (L.) - Antibacterial, antibiofilm, radical scavenging and ecotoxicological effects. *Materials Today Communications*, 30, Article 103228. <https://doi.org/https://doi.org/10.1016/j.mtcomm.2022.103228>
- Sidhu, A., Verma, N., & Kaushal, P. (2022). Role of biogenic capping agents in the synthesis of metallic nanoparticles and evaluation of their therapeutic potential. *Frontiers in Nanotechnology*, 3, Article 801620. <https://doi.org/10.3389/finano.2021.801620>
- Spanier, A. M., Flores, M., James, C., Lasater, J., Lloyd, S., & Miller, J. A. (1998). Fresh-cut pineapple (*Ananas* sp.) flavor. Effect of storage. In E. T. Contis, C. T. Ho, C. J. Mussinan, T. H. Parliment, F. Shahidi, & A. M. Spanier (Eds.), *Developments in Food Science* (Vol. 40, pp. 331–343). Elsevier. [https://doi.org/https://doi.org/10.1016/S0167-4501\(98\)80057-5](https://doi.org/https://doi.org/10.1016/S0167-4501(98)80057-5)
- Teai, T., Claude-Lafontaine, A., Schippa, C., & Cozzolino, F. (2001). Volatile compounds in fresh pulp of pineapple (*Ananas comosus* [L.] Merr.) from French Polynesia. *The Journal of Essential Oil Research*, 13, 314–318. <https://doi.org/10.1080/10412905.2001.9712222>
- Thatyana, M., Dube, N. P., Kemboi, D., Manicum, A. L. E., Mokgalaka-Fleischmann, N. S., & Tembu, J. V. (2023). Advances in phytonanotechnology: A plant-mediated green synthesis of metal nanoparticles using *Phyllanthus* plant extracts and their antimicrobial and anticancer applications. *Nanomaterials*, 13(19), Article 2616. <https://doi.org/10.3390/nano13192616>
- Tsilo, P. H., Basson, A. K., Ntombela, Z. G., Dlamini, N. G., & Pullabhotla, R. V. S. R. (2023). Biosynthesis and characterization of copper nanoparticles using a bioflocculant produced by a yeast *Pichia kudriavzevii* isolated from Kombucha Tea Scoby. *Applied Nano*, 4(3), 226–239. <https://doi.org/10.3390/applnano4030013>
- van Tran, T., Nguyen, D. T. C., Nguyen, T. T. T., Nguyen, D. H., Alhassan, M., Jalil, A. A., Nabgan, W., & Lee, T. (2023). A critical review on pineapple (*Ananas comosus*) wastes for water treatment, challenges and future prospects towards circular economy. *Science of the Total Environment*, 856, Article 158817. <https://doi.org/https://doi.org/10.1016/j.scitotenv.2022.158817>

- Vijayaram, S., Razafindralambo, H., Sun, Y. Z., Vasantharaj, S., Ghafarifarsani, H., Hoseinifar, S. H., & Raeeszadeh, M. (2023). Applications of green synthesised metal nanoparticles: A review. *Biological Trace Element Research*, 202(1), 360-386. <https://doi.org/10.1007/s12011-023-03645-9>
- Vinothini, P., Malaikozhundan, B., Krishnamoorthi, R., Dayana Senthamarai, M., & Shanthi, D. (2023). Potential inhibition of biofilm forming bacteria and fungi and DPPH free radicals using Tamarindus indica fruit extract assisted iron oxide nanoparticle. *Inorganic Chemistry Communications*, 156, Article 111206. <https://doi.org/https://doi.org/10.1016/j.inoche.2023.111206>
- Ying, S., Guan, Z., Ofoegbu, P. C., Clubb, P., Rico, C., He, F., & Hong, J. (2022). Green synthesis of nanoparticles: Current developments and limitations. *Environmental Technology & Innovation*, 26, Article 102336. <https://doi.org/https://doi.org/10.1016/j.eti.2022.102336>
- Zulpahmi, N. D., Musa, A. N. C., Zain, W. Z. W. M., Hamid, A., Ramli, N. W., Hamzah, F., & Buniyamin, I. (2023). Green synthesis of copper nanoparticles using *Ananas comosus* waste and their antimicrobial activity: A review. *International Journal of Chemical and Biochemical Sciences*, 24(7), 1-9. www.iscientific.org/Journal.html

Role of Brassinosteroid on Growth, Metabolic Contents and Wax Ester Fermentation in *Euglena* sp.

Deviko Mardiyansah¹, Tia Erfianti¹, Khusnul Qonita Maghfiroh¹,
Dedy Kurnianto^{1,2}, Ria Amelia¹, Brilian Ryan Sadewo^{3,4} and Eko Agus Suyono^{1,4*}

¹Faculty of Biology, Universitas Gadjah Mada, Yogyakarta 55281, Indonesia

²Research Center for Food Technology and Processing, National Research and Innovation Agency (BRIN), Yogyakarta 55861, Indonesia

³Department of Chemical Engineering, Faculty of Engineering, Universitas Gadjah Mada, Yogyakarta, 55284, Indonesia

⁴Center of Excellence for Microalgae Biorefinery, Universitas Gadjah Mada, Sleman 55281, Yogyakarta, Indonesia

ABSTRACT

Euglena is one of the alternative natural resources for medicine, food, and energy, and it is important to develop its metabolic contents to fulfill human demands. Improvement of metabolic content in *Euglena* was conducted in several ways, such as by adding the phytohormone. Brassinolide is one of the phytohormones and is well-known for its ability to stimulate and protect the plant from stressful environments. The application of brassinolide is still lacking. In addition, previous studies have never applied this phytohormone to *Euglena* sp. cultures. This research aimed to analyze the effect of brassinolide on the growth, metabolic content and wax fermentation in *Euglena* sp. The growth rate was measured during cultivation, and the metabolic content was analyzed at the late exponential phase before entering the fermentation process. Gas Chromatography-Mass Spectrometry (GC-

MS) was carried out to reveal the wax ester content after the fermentation process. The result showed that brassinolide significantly increased the growth rate and metabolic content at lower concentrations, while high concentration tends to inhibit the effect. The high metabolite content, including carbohydrate, lipid, protein, and paramylon, was 0.47 ± 0.02 g/L, 0.20 ± 0.01 g/L, $15.91 \pm 1.21 \times 10^{-3}$ g/L, and $145 \pm 0.10 \times 10^{-3}$ g/L, respectively. Interestingly, wax esters at lower brassinolide concentrations showed contrasting results compared to the control treatment. These findings provide information

ARTICLE INFO

Article history:

Received: 20 June 2024

Accepted: 16 January 2025

Published: 04 April 2025

DOI: <https://doi.org/10.47836/pjst.33.3.12>

E-mail addresses:

devikomardiyansah@mail.ugm.ac.id (Deviko Mardiyansah)

tiaerfianti@mail.ugm.ac.id (Tia Erfianti)

khusnulqonitamaghfiroh@mail.ugm.ac.id (Khusnul Qonita Maghfiroh)

dedy.kurnianto@mail.ugm.ac.id (Dedy Kurnianto)

ria.amelia@mail.ugm.ac.id (Ria Amelia)

brilian.ryan.s@mail.ugm.ac.id (Brilian Ryan Sadewo)

eko_suyono@mail.ugm.ac.id (Eko Agus Suyono)

*Corresponding author

about the effect of brassinolide in *Euglena* sp., and advanced research is needed to reveal the mechanism of brassinolide in *Euglena* sp.

Keywords: Brassinolide, *Euglena* sp., fermentation, metabolite

INTRODUCTION

The exponential growth of the human population has led to a significant reduction in natural resources such as food, fuel, and medicine. This overconsumption and associated land deforestation and greenhouse gas emissions have directly contributed to global climate change (Maja & Ayano, 2021). The urgency of this issue is underscored by the fact that we need to explore and develop alternative natural resources that align with the Sustainable Development Goals (SDGs) set by the United Nations for 2030.

Microalgae, particularly *Euglena*, stands out as a promising candidate for future alternative natural resources. *Euglena* is easily found in fresh and brackish water (rich in organic matter), consists of single cells, and exhibits rapid growth (Borowitzka, 2018). *Euglena's* ability to thrive is not only under photoautotroph conditions, where it uses light as a proton source for photosynthesis and energy production but also under heterotrophic conditions (Leander et al., 2017). This unique adaptability makes *Euglena* a fascinating subject for further exploration. Additionally, *Euglena's* metabolic content is diverse, encompassing protein, lipids, pigments, paramylon, wax ester, and more (Kottumparambil et al., 2019).

The metabolic content of *Euglena* holds immense promise for human life. For instance, the protein in *Euglena gracillis* can be harnessed as dietary protein (Gissbl et al., 2019). Conversely, paramylon and wax ester produced by *Euglena* are of particular interest. Paramylon in *Euglena* has numerous benefits; for example, in medicine, paramylon extracted from *E. gracillis* has shown an anticancer effect on *A4gnt* mice by reducing the gene expression of gastric dysplasia (Lida et al., 2021). Moreover, the conversion of paramylon to wax ester through fermentation could produce biofuel rich in 28 carbon chains (Inui et al., 2017). The diverse range of beneficial metabolites obtained from *Euglena* underscores the need for further research and improvement in its metabolic content, given its potential to support almost all aspects of human life.

Significant improvements in the metabolic content of various microalgae species have been demonstrated in previous studies. For instance, the protein content of *Chlorella vulgaris* was found to increase by up to 296% (Bajguz, 2000). Similarly, improvements in monosaccharide, chlorophyll a+b, and photosynthesis rate were 330%, 329%, and 298%, respectively, in *Scenedesmus quadricauda* (Bajguz & Czerpak, 1998). Moreover, *S. quadricauda* also demonstrated a significant enhancement, with the lipid and carotenoid content reaching 107.43 mg/g and over 140 ng/cell, respectively. These improvements were all observed under the addition of Brassinosteroids (BRs).

Brassinosteroids, which are steroidal hormones similar in structure to steroids in animals and insects (Divi & Krishna, 2009), have been widely used in plants as growth stimulators and stress protectants by regulating and enhancing the photosynthesis process (Liu et al., 2023) and regulating the stress defense mechanism both enzymatic and non-enzymatic (Vardhini & Anjum, 2015). For instance, adding brassinolide (BL), an active type of BRs, enhanced fruit yields of over 175 tons/ha in peaky pears (Atteya et al., 2022). Brassinolide also regulates the phenolic content and produces unsaturated fatty acids for cell membrane integrity in banana fruit under chilling injury (Zhang et al., 2022). Given these beneficial effects in plants, the potential application of BRs, particularly BL, in microalgae such as *Euglena* is worth exploring.

The role of BL in plants has demonstrated significant effects and is commonly used to enhance productivity under normal or stressful environments. However, its application in microalgae is relatively unexplored. As mentioned earlier, we have observed the application of BL in some microalgae species, such as *Chlorella*, which has been extensively studied. In this research, we delve into the potential of BL in *Euglena* sp. cultivation, inspired by the positive effects observed in other microalgae and the potential impact of BL on *Euglena* sp. We focus on the growth rate and metabolic production after and before fermentation. As we mentioned before, the metabolites and pigments produced by *Euglena* had a wide beneficial scope, including energy, food, and medicine. Thus, analyzing those parameters becomes our focus. Moreover, we have conducted growth kinetic modeling and cell morphology distribution in this study.

MATERIALS AND METHODS

Culture Condition

The culture of *Euglena* sp. was obtained from the Biotechnology Laboratory, Faculty of Biology Universitas Gadjah Mada, isolated from Dieng plateau, Indonesia, which was isolated from the result of research by Maghfiroh et al. (2023). The culture grew on Cramer and Myers (CM) medium at 5 liters volume, 2 liters of *Euglena* stock (OD₆₅₀: 0.370) and 3 liters of the medium for nine days or reached the late-log phase that was determined from preliminary results (unpublished data). Brassinolide was added in the early cultivation of *Euglena* sp. The aeration of culture was 4.25 LPM, containing 15% CO₂ (0.75 LPM), and the light was 3.600 lux with a white LED lamp (CRI index 80) for 24 h (Mardiyansah, 2023). The pH culture during the cultivation process was controlled and adjusted to 3.50 by adding 1N KOH or 1N H₂SO₄—however, the temperature was adjusted to 24°C. After reaching the late-log phase, the culture was fermented by changing the culture condition to dark hypoxia for three days to generate wax fermentation. The dark condition was conducted by placing the culture in a dark place and wrapping it with three layers of aluminum foil. The hypoxia condition was performed by turning off the aeration during fermentation (low oxygen level).

Growth Rate Analysis

The growth rate of *Euglena* sp. under BL treatment was analyzed by observing the cell density and growth kinetic modeling. Cell density was monitored daily by taking 2 mL of culture sample and was read by spectrophotometer UV-Vis (Genesys 150 Thermo, USA) at 680 nm (Suzuki et al., 2015). The cell growth kinetic model was performed using Logistics and Gompertz. The logistic model will calculate using Equations 1 and 2 (Phukoetphim et al., 2017; Nurafifah et al., 2023).

$$\frac{dx}{dt} = \mu_{max} \left(1 - \frac{x}{\mu_{max}}\right) x \quad [1]$$

$$x = \left(\frac{x_0 \cdot \exp(\mu_{max} \cdot t)}{1 - \left(\frac{x_0}{x_{max}}\right)(1 - \exp(\mu_{max} \cdot t))} \right) \quad [2]$$

Where $\frac{dx}{dt}$ is growth rate, X is cell density, X_0 is initial cell, X_{max} is maximum cell density, and μ_{max} is maximum of specific growth rate.

The Gompertz model is calculated by using Equations 3 and 4 (Phukoetphim et al., 2017; Nurafifah et al., 2023).

$$x = x_0 + [X_{max} \cdot \exp[-\exp\left(\frac{r_m \cdot \exp \exp(1)}{x_{max}}\right)(t_L - t) + 1]] \quad [3]$$

$$R^2 = \left(1 - \frac{SSR}{SST}\right) \quad [4]$$

Where r_m is maximum cell production, t_L is lag time, SSR is a sum of square residual, and SST is the total sum square.

Biomass Measurement

The biomass was measured and conducted by vacuum filtration every three days after fermentation (twelfth day). About 20 mL of sample (V) was poured into a vacuum filtered with filter paper (GF/C Whatman filter paper 47 mm, China), which had been weighed before (W1). The filtered biomass dried for 90 min at 100°C (OV-65 B-ONE, China). The dried biomass was weighed at an analytical balance (GR-200 AND, Japan) (W2). The biomass content was measured by using Equation 5 (Morais et al., 2021).

$$\text{Biomass (g/L)} = \frac{W2 - W1}{V} \quad [5]$$

Cell Morphology Distribution

Cell morphology distribution was observed on the ninth day following Kim et al. (2022) with several modifications. Cell morphology was observed under an Inverted Microscope (BDS400 DRAWELL, China). Cells fixed with 1% Lugol solution. The ratio of cell and fixative was 1:1, given directly to avoid movement from the cell during the fixation process. The 100 cells in each sample were measured with Optilab Viewer v4 (Miconos, Indonesia). Cell shape was justified by comparing the aspect ratio (AR). Cells were categorized as spherical when AR was under 1.5, spindle when AR was between 1.5 and 5, and elongated when AR was more than 5 (Jeon et al., 2019).

Primary Metabolite Analysis

Primary metabolite was measured on the ninth day of cultivation. The pellet was collected from a centrifugation process ($1327 \times g$; 10 min) (Ultra 8s LW Scientific, USA) of 10 mL culture used for primary metabolite determination, consisting of carbohydrates, lipids, and proteins. The Bradford method was used to determine the protein level (Bradford, 1976). The pellet was extracted by adding 1 mL of 10% sodium dodecyl sulfate (SDS) and continued with incubation at 95°C for 5 min and 4°C for 5 min, respectively. The sample took about 8 µL into 96 well-plates, followed by the addition of 200 µL Bradford reagent. After that, the absorbance read at 595 nm wavelength using an ELISA reader (ELx800 BioTek, USA). The protein standard curve used bovine serum albumin (BSA). The blank solution consisted of 10% SDS and Bradford reagent.

The carbohydrate content was determined using the phenol-sulphuric acid method (Dubois et al., 1956; Suyono et al., 2016). The pellet was added by 1:5 of 5% phenol and H₂SO₄. The sample was incubated for 30 min at room temperature and homogenized before reading the absorbance at 490 nm wavelength using a UV-Vis spectrophotometer (Genesys 150 Thermo, USA). The carbohydrate standard was glucose. The blank solution was composed of 5% phenol and H₂SO₄.

The lipid was analyzed using the Bligh-Dyer method (Bligh & Dyer, 1959). The pellet was added with 1 mL of methanol and 1 mL of chloroform. The sample was mixed using a vortex until homogenized. Afterward, about 1 mL of chloroform and 1 mL of distilled water (Water One-ONEMED, Indonesia) were added and remixed. The sample was centrifuged at $1327 \times g$ for 10 min and continued removing the polar solution. The non-polar solution was poured into a petri dish, which weighed before (M1). The lipid was incubated overnight at 33°C (OV-65 B-ONE, China) until the solvent perfectly evaporated and continued with measuring the petri dish (M2) using an analytical balance (GR-200 AND, Japan). The lipid content was obtained by reducing the weight of M2 and M1 divided by volume (V).

Pigment Analysis

The pigment was analyzed by following Pruvost et al. (2011) on the ninth day of cultivation. Ten mL of the sample was centrifuged (Ultra 8s LW Scientific, USA) at $1327 \times g$ for 10 min. The supernatant was discarded, and the pellet was added with 2 mL of methanol. After that, the sample was homogenized by vortexing until well-mixed. The homogenate was incubated overnight at 4°C in a dark condition by covering it with aluminum foil. The sample was centrifuged ($1327 \times g$; 10 min), and the supernatant read at 665, 662, and 480 nm at spectrophotometer UV-Vis (Genesys 150 Thermo, USA). The absorbance of the supernatant was converted by using Equations 6, 7 and 8 to determine the pigment content.

$$\text{Chlorophyll a } (\mu\text{g/L}) = -8.0962 \times \lambda_{652} + 16.5169 \times \lambda_{665} \quad [6]$$

$$\text{Chlorophyll b } (\mu\text{g/L}) = 27.4405 \times \lambda_{652} - 12.1688 \times \lambda_{665} \quad [7]$$

$$\text{Carotenoid Total } (\mu\text{g/L}) = 4 \times \lambda_{480} \quad [8]$$

Paramylon Analysis

According to Kim et al. (2020), Paramylon was analyzed with several modifications on the ninth day and after fermentation (twelfth day). The pellet from 20 mL of sample was collected through centrifugation ($1327 \times g$; 10 min) (Ultra 8s LW Scientific, USA) and added with 3 mL of 1% SDS. The sample was incubated at 95°C for 30 min using a water bath (WNB-22 Memmert, Germany), then centrifuged ($1327 \times g$; 10 min) to discard the supernatant. The sample was washed twice using distilled water (Water One-ONEMED, Indonesia). About 2 mL of 0.5N NaOH was added into the pellet and homogenized by vortexing. Paramylon was determined by taking 500 μL of aliquots and analyzed using the phenol-sulphuric acid (Dubois et al., 1956). The standard curve was made with D-glucose.

Productivity Measurement

The productivity of biomass, primary metabolite, pigment, and paramylon was calculated using Equation 9.

$$\text{Productivity (g/L/day)} = \frac{\Delta C}{\Delta T} \quad [9]$$

Where: ΔC is the difference in concentration between day-n and day-0, and ΔT is the time period.

Gas Chromatography-Mass Spectrometry (GC-MS) Analysis

GC analysis was used to determine the organic compounds after fermentation, following Padermshoke et al. (2016) with several modifications. The pellet, harvested on the twelfth day, was collected from 2L culture centrifugation (Universal 320R Hettich, Germany) for 4 min, $2468 \times g$, 4°C , added with 100 μL pyridine followed by sonication (JPS-10A Digital Pro+, China) to dissolve the organic compound. About 1 μL chlorotrimethylsilane and 99 μL N, O-Bis(trimethylsilyl) were added and continued with sonification. The extract was dried for 30 min at 37°C using an oven and resuspended with 1 mL n-hexane as a solvent. After filtration, the dissolved extract was injected into GC-MS (QP2010 Shimadzu, Japan). The GC condition fixed: DB one capillary column ($30 \text{ m} \times 0.25 \text{ mm I.D.}$ and $0.25 \mu\text{m}$); column temperature: 10°C ; Injection temperature: 290°C ; Programed temperature: early temperature was 70°C (held for 5 min) until end temperature 285°C in addition 6°C per min (held for 20 min); interface temperature: 270°C ; split ratio was 1:0; pressure 108.1 kPa; helium gas was used as carrier gas. The database library on GC-MS (NIST II library Version) was used to identify detected organic compounds. The quantification of each compound was based on the percentage area of each GC-MS peak.

Statistical Data Analysis

The data was technically collected and analyzed with ANOVA One way (p-value: 0.05) continued with Duncan's multiple range test (DMRT). Microsoft Excel v.2013 (Microsoft Inc., USA), IBM SPSS Statistic v.26 (IBM, USA) and Origin Pro Student Version v.2023b (Origin Lab, USA) were used to perform and analyze the data. The data showed in means followed by standard deviation.

RESULTS

Growth and Biomass of *Euglena* sp.

In this research, the growth and biomass of *Euglena* sp. are positively affected by the presence of BL during the cultivation process. Figure 1a illustrates the growth curve of *Euglena* sp. under BL treatment at nine days of cultivation. The growth of *Euglena* sp. fluctuated, but 0.05 mg/L BL showed the highest cell density over other treatments after day sixth cultivation. In contrast, 0.10 and 1.50 mg/L BL treatments performed lower cell density than the control treatment. Moreover, a similar result was found in the biomass of *Euglena* sp. (Figure 1b). Before the seventh day of cultivation, the biomass of *Euglena* sp. under BL addition showed identical results among all BL treatments and became different from the seventh until the ninth day of cultivation ($p < 0.05$). The 0.05 mg/L BL showed the highest biomass and productivity for about $0.60 \pm 0.01 \text{ g/L}$ and $58.30 \pm 1.47 \text{ g/L/day}$, respectively.

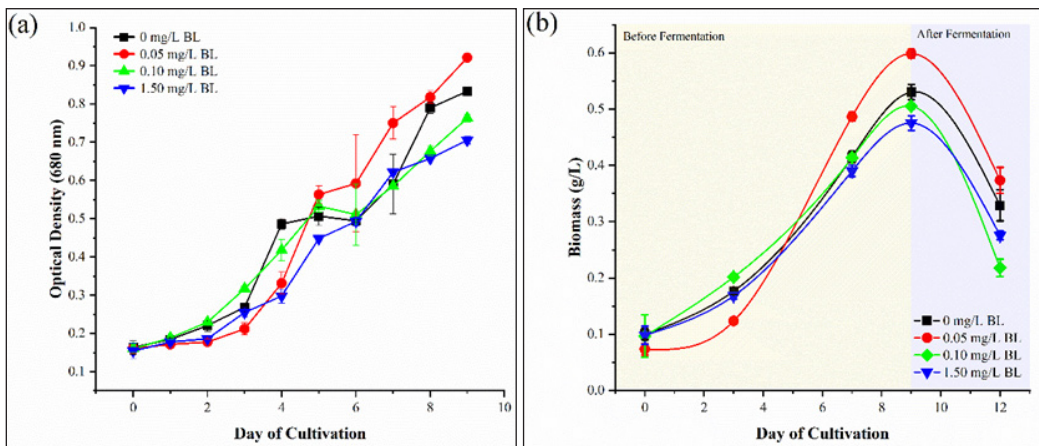


Figure 1. Growth curve (a) and biomass (b) of *Euglena* sp. under BL treatment. Error bars represent standard deviation (n=3)

The precision of our Gompertz and Logistic models in predicting *Euglena* sp.'s growth under BL treatment is noteworthy. Figure 2 illustrates the Gompertz model, with 0.05

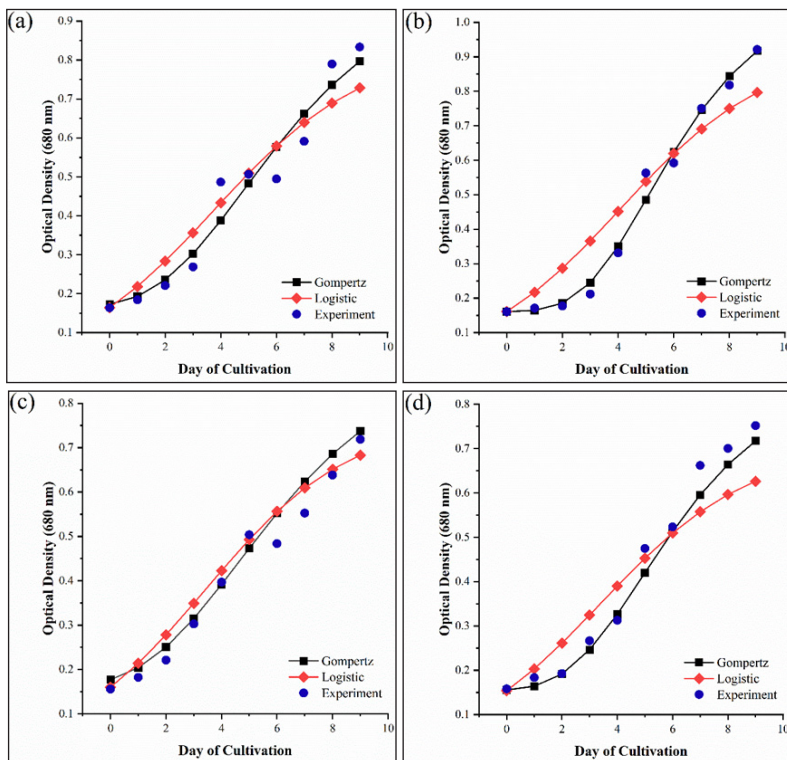


Figure 2. Growth kinetic modeling of *Euglena* sp. under BL treatment: 0 mg/L BL (a), 0.05 mg/L BL (b), 0.10 mg/L BL (c), and 1.50 mg/L BL (d), respectively

mg/L BL showing the highest r_m (0.14) and t_L (2.70). All BL treatments demonstrated an impressive R^2 (Table 1). The Logistic model, on the other hand, showed that 0.10 mg/L BL had the best μ_{max} . While the R^2 of the Logistic model was lower than the Gompertz model, it still scored above 0.900 in all models, instilling confidence in the accuracy of our predictions.

Table 1
The growth parameter of Gompertz and Logistic model in *Euglena sp.* under BL treatment

BL Concentration (mg/L)	Gompertz Model			Logistic Model	
	r_m	t_L	R^2	μ_{max}	R^2
0	0.10	1.68	0.947	0.37	0.912
0.05	0.14	2.70	0.988	0.38	0.901
0.10	0.08	1.16	0.977	0.39	0.961
1.50	0.10	2.21	0.992	0.37	0.916

Morphology Distribution of *Euglena sp.*

Morphology distribution of *Euglena sp.* under BL treatment was different on day 0 (early), day 9 (late exponential), and after fermentation. On day 0 cultivation, the cell morphology distribution was dominated by spindle shape. This condition changed at the end of cultivation, with cell morphology dominated by elongated shape in all BL treatments. After the culture condition changed to dark hypoxia, the observation of cell morphology distribution showed that the shape domination changed into spherical and spindle shapes. The most spherical shape was found in 0.05 mg/L BL and 0.10 mg/L BL treatments, while the spherical shape showed in 0 mg/L BL and 1.50 mg/L BL treatments (Figure 3).

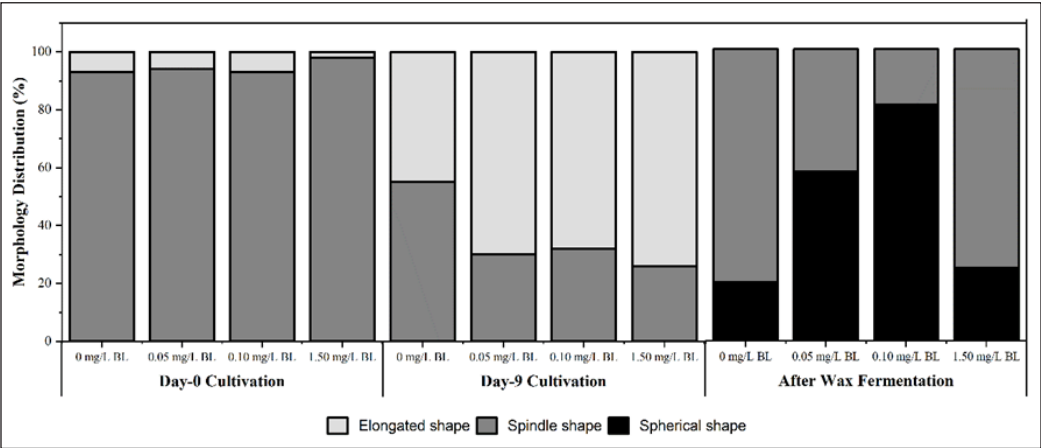


Figure 3. Morphology distribution of *Euglena sp.* under BL treatment on 0 days, 9 days, and after fermentation (12 days)

Primary Metabolites Content of *Euglena* sp.

Brassinolide in *Euglena* sp.'s culture affected the primary metabolite, as seen in Figure 4. Protein content showed a significant improvement at 0.05 mg/L BL up to $15.92 \pm 1.20 \times 10^{-3}$ g/L ($p < 0.05$). This condition was contrasted with 0.10 mg/L BL and 1.50 mg/L BL treatments where the protein content amount was lower than 0 mg/L BL. Besides BL enhancing the protein, the lipid under BL treatment significantly improved ($p < 0.05$). The high lipid content performed in 0.05 mg/L BL treatment was about 0.20 ± 0.01 g/L, but insignificant result with 0.10 mg/L BL based form Duncan test. The positive effect of BL addition also showed in carbohydrate content ($p < 0.05$). The 0.05 mg/L BL gave the highest carbohydrate content compared to other treatments. The carbohydrate content at 0.05 mg/L BL reached 0.47 ± 0.03 g/L. Based on Figure 4c, the lowest carbohydrate level performed at 0.10 mg/L BL, while the 0 and 1.50 mg/L BL showed insignificant results. According to Table 2, the productivity of primary metabolites was performed in high quantities at 0.05 mg/L BL treatment.

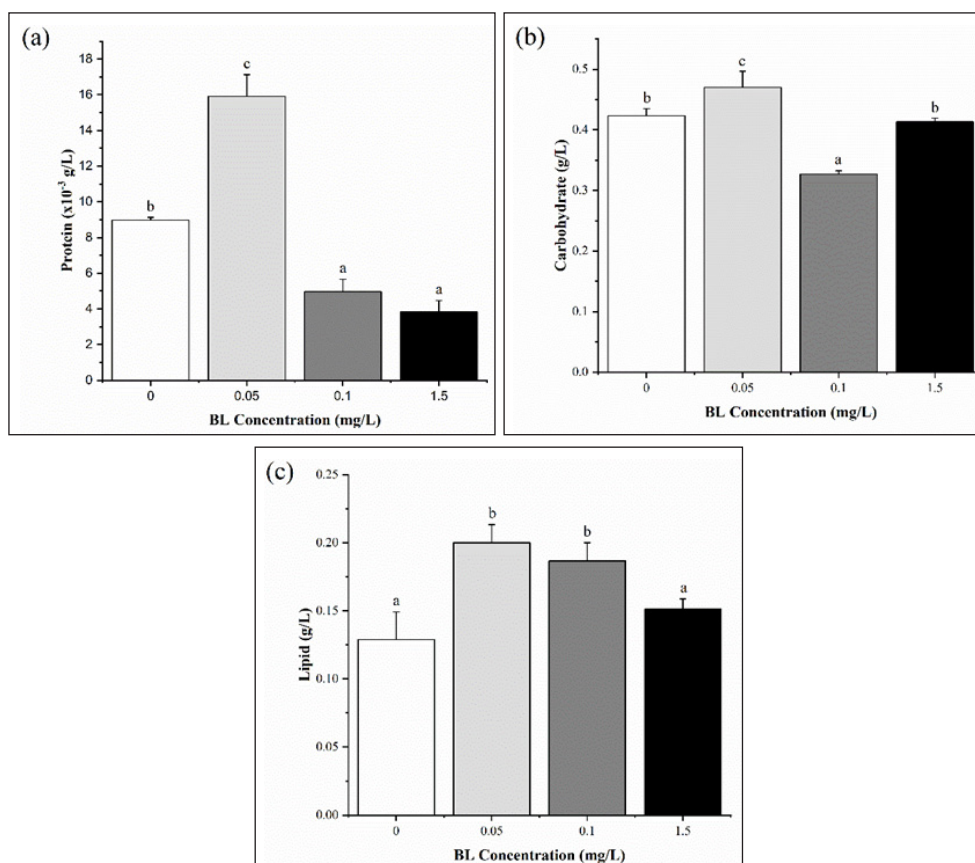


Figure 4. Primary metabolites content of *Euglena* sp. under BL treatment at ninth-day cultivation: protein content (a), carbohydrate content (b), and lipid content (c), respectively. The lowercase letter shows the significant differences based on Duncan's Test ($p < 0.05$). Error bars represent standard deviation ($n=3$)

Table 2

The productivity of biomass, primary metabolites, pigment, and paramylon in *Euglena sp.* under BL treatment

Productivity ($\times 10^{-3}$ g/L/day)	BL Concentrations (mg/L)			
	0	0.05	0.10	1.50
Biomass	47.80 \pm 1.67 ^b	58.30 \pm 1.47 ^c	45.40 \pm 4.66 ^{ab}	41.90 \pm 3.06 ^a
Primary metabolites				
Carbohydrate	40.70 \pm 0.58 ^b	46.30 \pm 2.89 ^c	31.70 \pm 0.58 ^a	40.00 \pm 1.00 ^b
Lipid	9.00 \pm 0.00 ^a	15.00 \pm 0.00 ^{bc}	12.70 \pm 2.52 ^{bc}	11.00 \pm 1.70 ^{ab}
Protein	0.82 \pm 0.01 ^b	1.58 \pm 0.14 ^a	0.34 \pm 0.05 ^c	0.28 \pm 0.07 ^a
Pigment				
Chlorophyll a	0.23 \pm 0.03 ^a	0.23 \pm 0.02 ^a	0.26 \pm 0.01 ^{ab}	0.29 \pm 0.02 ^b
Chlorophyll b	0.46 \pm 0.01 ^{ab}	0.59 \pm 0.01 ^c	0.48 \pm 0.02 ^b	0.43 \pm 0.04 ^a
Carotenoid Total	0.14 \pm 0.01 ^a	0.17 \pm 0.01 ^b	0.15 \pm 0.01 ^{ab}	0.14 \pm 0.01 ^a
Paramylon	10.70 \pm 1.41 ^b	13.80 \pm 0.12 ^c	6.40 \pm 1.76 ^a	7.50 \pm 1.01 ^a

Notes. The data is shown in the means followed by the standard deviation (n=3). The lowercase in the same row showed significant differences based on Duncan's Test ($p < 0.05$)

Pigment Content on *Euglena sp.*

The pigment content at the end of cultivation revealed a significant effect ($p < 0.05$) in BL treatments (Table 3). The 1.50 mg/L BL gave the highest chlorophyll a for about 4.14 ± 0.10 $\mu\text{g/mL}$, while the highest chlorophyll b and carotenoid total found in 0.05 mg/L BL, 5.43 ± 0.07 $\mu\text{g/mL}$ and 1.83 ± 0.03 $\mu\text{g/mL}$, respectively. In addition, 0.05 mg/L BL exhibited a high amount of chlorophyll a+b but decreased the chlorophyll a/b. The chlorophyll a and b productivity significantly increased in 1.50 mg/L BL and 0.05 mg/L BL, respectively.

Table 3

Pigment content on *Euglena sp.* under BL treatment on the ninth day of cultivation

BL Concentration (mg/L)	Chl a ($\mu\text{g/mL}$)	Chl b ($\mu\text{g/mL}$)	Car. Total ($\mu\text{g/mL}$)	Chl a+b ($\mu\text{g/mL}$)	Chl a/b	Car./Chl a+b
0	4.00 \pm 0.01 ^b	4.37 \pm 0.02 ^b	1.70 \pm 0.03 ^b	8.73 \pm 0.03 ^b	0.92 \pm 0.00 ^b	0.20 \pm 0.00 ^b
0.05	3.73 \pm 0.03 ^a	5.43 \pm 0.07 ^c	1.83 \pm 0.03 ^c	9.16 \pm 0.05 ^c	0.69 \pm 0.01 ^a	0.20 \pm 0.00 ^b
0.10	4.02 \pm 0.06 ^b	4.36 \pm 0.23 ^b	1.70 \pm 0.04 ^b	8.38 \pm 0.17 ^b	0.92 \pm 0.06 ^b	0.20 \pm 0.00 ^b
1.50	4.14 \pm 0.10 ^c	3.86 \pm 0.36 ^a	1.54 \pm 0.08 ^a	7.99 \pm 0.27 ^a	1.08 \pm 0.12 ^c	0.19 \pm 0.00 ^a

Notes. The data shows in means followed by standard deviation (n=3). The lowercase in the same column showed significant differences based on Duncan's Test ($p < 0.05$)

Paramylon Content of *Euglena sp.*

Paramylon content of *Euglena sp.* under the presence of BL showed a significant effect ($p < 0.05$) (Figure 5). The concentration of BL at 0.05 mg/L gave the great result of paramylon

production at the end of cultivation, accounting for $145 \pm 1.04 \times 10^{-3}$ g/L. In contrast, the high BL concentration performed the lowest concentration of paramylon, where 0.01 mg/L BL and 1.50 mg/L BL were $92.7 \pm 7.97 \times 10^{-3}$ g/L and $55.3 \pm 2.80 \times 10^{-3}$ g/L, respectively. On the other hand, 0.05 mg/L BL showed the highest paramylon productivity than other BL treatments (Table 2). The depletion of paramylon occurred after the fermentation process, which was conducted for three days at dark-hypoxia conditions. All paramylon contents were depleted, and the highest depletion of paramylon was found at 0.05 mg/L BL. Due to the highest production and depletion of paramylon found at 0.05 mg/L BL, this treatment was chosen to determine the organic compound by GC-MS. Besides that, the 0 mg/L BL was used as a control treatment to compare with the selected treatment. Therefore, this treatment continued for further analysis through GC-MS.

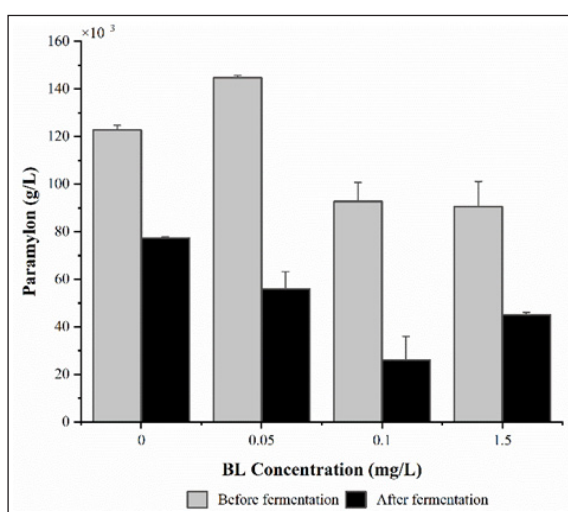


Figure 5. Paramylon content in *Euglena* sp. is under BL treatment on the ninth and twelfth days of cultivation. Error bars represent the standard deviation (n=3)

Wax Ester of *Euglena* sp.

The untargeted GC-MS results revealed the presence of 14 and 15 organic chemical compounds at 0 and 0.05 mg/L BL treatment, respectively. Among these, we detected the presence of a unique organic compound, which we assumed to be a wax ester, in both treatments after 40 min reading at GC-MS (Figure 6). The wax ester content at 0 mg/L BL remained higher than 0.05 mg/L BL treatment. We classified the wax ester species from carbon chain numbers 26 to 36 (Table 4). The wax ester concentration was dominated by carbon chain numbers 26 (lauryl myristate), 28 (myristyl myristate), and 30 (cetyl myristate), while the other wax ester species were present in low concentrations. Interestingly, at 0.05 mg/L BL, we found a menthol compound in higher concentration than a wax ester, namely $C_{10}H_{20}O$ or neomenthol, for about 18.75 ± 1.15 %.

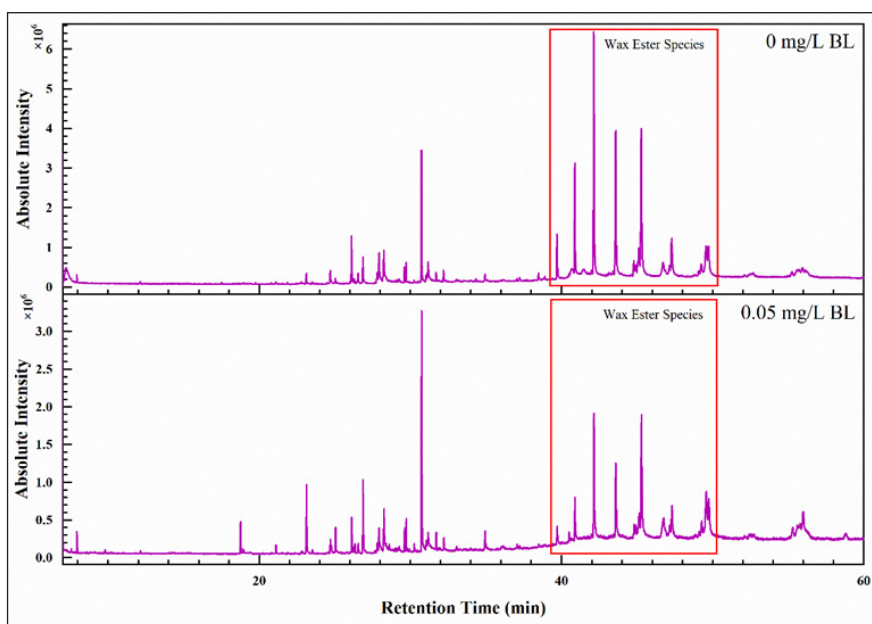


Figure 6. TIC graph from GC-MS analyses the most significant treatment in *Euglena* sp. after fermentation (twelfth day)

Table 4

Wax ester species of Euglena sp. under BL treatment after wax fermentation (twelfth day)

0 mg/L BL				
Ret. Time (min)	Similarity Index	Name	Formula	Relative Abundance (%±SD)
42.137	87	Myristyl myristate	C ₂₈ H ₅₆ O ₂	24.74±1.54
43.579	89	Lauryl myristate	C ₂₆ H ₅₂ O ₂	16.97±1.48
45.276	87	Cetyl myristate	C ₃₀ H ₆₀ O ₂	19.76±0.89
47.289	88	Lauryl palmitate	C ₂₈ H ₅₆ O ₂	5.34±0.04
49.721	89	Stearyl stearate	C ₃₆ H ₇₂ O ₂	3.59±2.08
0.05 mg/L BL				
Ret. Time (min)	Similarity Index	Name	Formula	Relative Abundance (%±SD)
30.746	89	(1S, 2S, 5R)-(+)-Neomenthol	C ₁₀ H ₂₀ O	18.75±1.15
42.146	89	Myristyl myristate	C ₂₈ H ₅₆ O ₂	13.67±1.17
43.590	88	Lauryl myristate	C ₂₆ H ₅₂ O ₂	8.80±0.49
45.289	87	Cetyl myristate	C ₃₀ H ₆₀ O ₂	15.76±0.49
47.308	88	Stearyl stearate	C ₃₆ H ₇₂ O ₂	4.01±0.02
49.740	88	Cetyl palmitate	C ₃₂ H ₆₄ O ₂	4.92±0.24

Notes. The data is shown in the means followed by the standard deviation (n=2)

DISCUSSION

Growth and Biomass of *Euglena* sp.

In this study, we presented the effect of BL on improving the growth rate and metabolic content in *Euglena* sp., where the lowest concentration gave the best result (0.05 mg/L BL) at the end of cultivation. Bajguz and Czerpak (1998) reported that a lower concentration of BRs gave insignificant results, while a higher concentration gave inhibition effects. Brassinolide affected the growth rate of *Euglena* sp. by increasing the cell number; this result was indicated by cell density. The promotion of cell numbers depends on the cell division process. Brassinolide addition promotes cell division by up-regulating the *CyD3*, a cyclin-dependent kinase (CDK) family, which has a role in the division of eukaryotic cells (Hu et al., 2000). Bajguz and Czerpak (1998) and Kozlova et al. (2017) demonstrated a similar result in improving cell numbers by adding BL. According to this result, adding BL could promote *Euglena* sp.'s growth rate. However, the difference between 0 mg/L BL and 0.05 mg/L BL was slightly different and less than the given impact of other phytohormones in *Euglena* sp., such as indole-3-acetic acid (IAA), which greatly enhanced the growth rate of *Euglena* sp. (Hakim et al., 2023). The life cycle of *Euglena* was varying. Patil et al. (2024) showed that on the tenth day of cultivation, the culture of *Euglena* entered the stationary phase. A similar result was shown in research by Erfianti et al. (2024) that the tenth day of *Euglena* cultivation undergoes the stationary phase. Moreover, Jung et al. (2021) exhibited *Euglena*'s earlier late exponential phase, which was the seventh day of cultivation. It was indicated that the life cycle of *Euglena* was varying, and in this research, the presence of BL could not change the life cycle of *Euglena* but enhance the cell division during the cultivation process.

The cell biomass increased during the cultivation process. Cell biomass production is affected by the presence of BL through photosynthesis. BL could promote the photosynthesis process by affecting the pigment, photosynthesis rate, and fixation of CO₂. Singh et al. (2016) showed that the high photosynthesis rate resulted in a high accumulation of biomass. As a result of the high photosynthesis rate, the product of photosynthesis remains high and supports the cell development marked by the cell biomass. The cell biomass was positively correlated with the cell concentration (Lim et al., 2022). This was similar to this research, showing the improvement of cell concentration followed by the cell biomass.

The growth kinetic modeling was carried out to illustrate the suitable growth model for *Euglena* sp. under BL treatment. Gompertz and Logistic models, which are commonly used to demonstrate the growth kinetic model in microorganisms, especially in microalgae (Erfianti et al., 2023; Naser et al., 2023; Širić et al., 2023), were employed in this study. The R² value obtained from both models described how appropriate those models represented the data (Ajala & Alexander, 2020). For instance, the growth kinetic model of *C. vulgaris* performed extensively with an R² value of more than 0.98 in the Gompertz and Logistic

model (Kothari et al., 2023). According to the R^2 value, the Gompertz model is more appropriate to demonstrate *Euglena sp.*'s growth rate under BL treatment. Gompertz's model showed the r_m value, which corresponds to biomass production. Moreover, the t_L value also extensively describes the lag phase based on the cell density; for instance, in 0.05 mg/L, BL has the highest value of t_L , which means the time needed by the cell to continuously in log phase, and this result was appropriate with a growth curve that shows the time of lag phase is longer than other treatments.

Morphology Distribution of *Euglena sp.*

Cell elongation was one effect resulting from the presence of BL through the BL mechanism signaling process (Yang et al., 2011). Mumtaz et al. (2022) revealed that the absence of BL in tomato *abs 1 mutant* generated the smaller fruit size, which means the presence of BL was needed to avoid the dwarfism in tomato plants that caused the smaller fruit size. The role of BL in promoting cell elongation was also presented in Yayao (gourd cultivar) seeds grown at salt-stress conditions (Liu et al., 2023). In addition, the same result of BL in promoting cell elongation was shown in the sesame cultivar (Nasser & Sarhan, 2023). Besides BL promoting cell elongation through regular mechanisms described by Muller and Munne-Bosch (2021), BL could encourage the elongation of cells by interacting with some hormones. Improvement of *D18/GAox-2* gene transcription exhibited under the presence of BL (Tong et al., 2014). The *D18/GAox-2* gene was a family gene in gibberellic acid (GA_3), which has a role in the elongation of plant cells. The mechanism of how BL promotes cell elongation has not been well-observed. However, the mechanism of BL promoting cell elongation in plants illustrated how BL works. BL probably promoted cell elongation in *Euglena* by interacting with the GA_3 , which could promote cell elongation in plant cells (Figure 3). Thus, it indicates that BL could promote cell elongation in *Euglena sp.*

Primary Metabolites Content of *Euglena sp.*

The primary metabolites had similar results to previous studies that revealed a significant improvement in primary metabolites. Research by Bajguz and Czerpak (1998) demonstrated the improvement of monosaccharides in *C. vulgaris*. As a result of the photosynthesis process, carbohydrates play crucial roles in cell activity in the case of energy supply. In photosynthesis, BL had a positive effect in light and dark cycles. The depletion of some carbohydrates resulted in the photosynthesis process, which would be converted into lipids, which is affected by some factors. A stressful environment could trigger lipid accumulation, for instance, lightning and CO_2 stress, nutrient modification, cultivation process, and chemical addition (Song et al., 2022). Moreover, Huang et al. (2022) reported that adding a phytohormone combination (GA_3 , IAA, and BL) with turbulence intensity improved lipid content in *S. quadricauda*. Improvement in lipid content under BL was also found

at *S. quadricauda*, both at BL and epi-brassinolid (EBL) addition (Kozlova et al., 2017). Additionally, Pokotylo et al. (2014) and Liu et al. (2018) showed improved lipid content under BL treatment in a stressful environment.

Adding BL induced the related genes from *Euglena* sp. as a response to BL and affected the improvement of transcription and translation in *Euglena* sp. The presence of BL was verified to enhance the genetic material, DNA and RNA in *C. vulgaris*, improving protein level by up to 296% (Bajguz, 2000). In addition, a similar result was also performed in *Wolffia arrhiza*, showing that protein levels were elevated by about 25% (Chmur & Bajguz, 2021). Moreover, free amino acids and soluble protein improvement were performed under BL treatment on *Pinnela ternate* (Guo et al., 2022), showing that BL could affect protein levels.

All the primary metabolites, including carbohydrates, lipids, and proteins, were significantly enhanced under the presence of BL. This result was similar to cell growth and cell biomass, which significantly improved. In this result, BL is enhanced in photosynthesis, resulting in a high accumulation of glucose that will break down into some metabolites, such as lipids. In addition, the protein content is elevated by cell response, DNA and RNA under BL. Further analysis of the effect of BL in the photosynthesis process completely describes pigment content.

Pigment Content on *Euglena* sp.

Brassinolide's role in regulating chlorophyll synthesis, a process it tends to suppress, has significant implications. Tachibana et al. (2022) demonstrated this, reporting that the BRASSINOZOLE insensitive mutant 1 in Arabidopsis exhibited a light-green leaf color. Intriguingly, the Arabidopsis BRASSINOLIDE insensitive mutant 1 showed a dark green leaf morphology and high chlorophyll content (Zhang et al., 2021). Even in the presence of BL, chlorophyll biosynthesis was suppressed, but BL could also promote chlorophyll biosynthesis by interacting with certain phytohormones. The addition of exogenous BL was found to induce GA₃ synthesis (Peres et al., 2019). Furthermore, the mutation in tomato *abs 1* led to a lower expression of *GA20ox1*, GA₃ gene, and chlorophyll genes (Mumtaz et al., 2020). The role of GA₃ in improving chlorophyll content was found to have a significant effect (Khandaker et al., 2015; Iftikhar et al., 2019). Additionally, BL was found to interact with cytokinin (CK), further enhancing chlorophyll content (Bajguz & Potrowska-Niczyporuk, 2014; Peres et al., 2019).

The addition of BL did not improve pigment content but improved photosystem II (PSII) efficiency and CO₂ assimilation. PSII efficiency increased after the addition of BL, even in normal and stressful conditions, and enhanced net photosynthesis (Yuan et al., 2012; Ma & Guo, 2014; Lima & Lobato, 2017; Zhao et al., 2019; Liu et al., 2022; Sun et al., 2022; Liu et al., 2023). The high chlorophyll b content indicated the stress condition

and caused the lower ratio of chlorophyll a/b (Yuan et al., 2012). Overexpression of chlorophyllide an oxygenase (CAO) affected the reduction of chlorophyll a because the chlorophyll a converted into chlorophyll b, causing the depletion of chlorophyll a/b ratio but enlarging the antenna size (Tanaka et al., 2014). Furthermore, photosynthetically effective radiation (PAR) had a crucial role in the ratio of chlorophyll a/b (Kume et al., 2018). In a similar study, Amelia et al. (2023) found that light shade adaptation to light intensity exhibited lower chlorophyll a, supporting our findings. Following this research, adding a lower concentration of BL probably promotes *Euglena* sp. to respond in cell adaptation to light by regulating the CAO activity and improving the PSII efficiency. Because of this, net photosynthesis increased and was marked by high biomass accumulation (Yuan et al., 2012). Moreover, the accumulation of primary metabolites was high under lower BL treatment, affecting photosynthesis. At the same time, high photosynthesis activity will produce more glucose than used to, for example, lipid biosynthesis (Li et al., 2020).

Assimilation of CO₂ was assumed to improve the chlorophyll content by an unknown mechanism - BL addition has proven to enhance CO₂ assimilation (Yuan et al., 2012; Bajguz & Potrowska-Niczyporuk, 2014). Xia et al. (2009) showed the improvement of six genes related to carbon fixation by the addition of EBL and improved the maximum Rubisco carboxylation rate (V_{cmax}) and maximum RuBP regeneration rate (J_{max}). A similar result was presented on maize seedlings added by EBL that up-regulates eight genes that worked on the dark cycle of photosynthesis (Gao et al., 2021). The great Rubisco activity illustrated that the CO₂ absorption elevated and produced glucose as the main product of the dark cycle. Consequently, carbohydrate content in this research reached a significant result at 0.05 mg/L BL treatment. A similar result was shown in *W. arrhiza*, where monosaccharides were elevated under BL addition (Chmur & Bajguz, 2021).

Paramylon Content of *Euglena* sp.

Paramylon, the energy storage from *Euglena* sp., is formed in granules composed of β -1,3-glucan (Zakryś et al., 2017), catalyzed by paramylon synthase (β -1,3-glucan synthase or callose synthase) from uridin diphosphate (UDP) (Marechal & Goldemberg, 1964; Yoshida et al., 2016). Production of paramylon reached the highest content at the late exponential phase, remained constant, and tended to decrease while entering the stationary and death phases (Kim et al., 2019). Thus, the analysis of paramylons is conducted at the late exponential phase, which is the ninth day before the wax fermentation process and at the twelfth day after the wax fermentation process. The addition of phytohormones into *Euglena* culture has been found to play a crucial role in increasing the production of paramylon. This intriguing phenomenon was observed in a study by Kim et al. (2019), where the production of IAA by bacteria significantly enhanced paramylon production. Furthermore, this study also revealed that BL promotes the production of paramylon under low concentrations. As

mentioned earlier, a lower concentration of BL significantly increased the protein content. This may correlate with paramylon production in *Euglena* sp. by regulating gene-coded protein (enzyme) that works in the biosynthesis of paramylon.

Wax Ester of *Euglena* sp.

Fermentation was conducted to produce wax ester through a mechanism described by Inui et al. (2017). After the fermentation process, the depletion of biomass and paramylon content occurred in all treatments. This result was similar to Jung et al. (2021) in that the depletion of both parameters occurred after fermentation and increased in fatty acid, rich in 14 carbon chains (myristic acid), which is useful for biofuel. Moreover, Padermshoke et al. (2016) and Ogawa et al. (2022) showed the domination of 28 carbon chains (myristyl myristate) after wax fermentation. According to this result, the wax ester on BL treatment showed lower wax ester content than the control treatment.

On the other hand, the presence of neomenthol (a cyclic monoterpene) in BL treatment remained high. This is significant as terpenoids are synthesized through the mevalonate acid (MEV) pathway and methylerythritol phosphate (MEP) pathway (Harrewijin et al., 2000; Kang & Lee, 2016). The formation of monoterpenoids and their subsequent conversion into neomenthol, as described by Croteau et al. (2005), is a key process. Chizzola et al. (2004) demonstrated the presence of a menthol derivative after fermenting the *Thuja orientalis* into a rusteic system. Moreover, BL plays a pivotal role in the stress environment response by regulating the stress defense mechanism, whether enzymatic or non-enzymatic (Vardhini & Anjum, 2015). Dark hypoxia, a stress condition, may induce the stress defense mechanism in *Euglena* sp. The presence of BL probably affected *Euglena* by stimulating the stress defense mechanism. The change in cell morphology, particularly the drastic shift to a spherical shape at 0.05 mg/L BL compared to 0 mg/L BL after fermentation, may be correlated with this result. Consequently, the lower wax ester content on BL treatment was likely due to neomenthol, which uses the same substrate as wax ester during the fermentation process as a stress defense mechanism generated by the presence of BL under dark hypoxia conditions.

CONCLUSION

Adding BL has a positive effect on *Euglena* sp., especially in terms of growth rate, primary metabolite, and pigment content. The positive result was shown at lower BL concentration, whether high concentration tends to give a contrast result. Moreover, BL also promoted cell elongation on *Euglena* sp. After wax fermentation, the BL treatment showed a contrasting result, which produced lower wax ester content. This improvement made BL one of the chemical stimulators that enhance the productivity of *Euglena* sp. as a candidate for alternative natural resources. Research about the effect of BL in *Euglena* sp.

remained rare and has yet to be studied. As a result, advanced research on the BL mechanism affecting *Euglena* sp.'s growth rate and metabolic content is still needed to give more precise information.

ACKNOWLEDGEMENTS

The authors thank Universitas Gadjah Mada, especially the Biotechnology Laboratory-Faculty of Biology, who provided all the facilities that supported this research. This manuscript is part of the first author's thesis.

REFERENCES

- Ajala, S. O., & Alexander, M. L. (2020). Assessment of *Chlorella vulgaris*, *Scenedesmus obliquus*, and *Oocystis minuta* for removal of sulfate, nitrate, and phosphate in wastewater. *International Journal of Energy and Environmental Engineering*, 11, 311-326 <https://doi.org/10.1007/s40095-019-00333-0>
- Amelia, R., Akmal, W. R., & Suyono, E. A. (2023). Enhancement of astaxanthin content in mixed culture of *Dunaliella* sp. and *Azospirillum* sp. under light intensity treatment. *Jurnal Ilmiah Perikanan dan Kelautan*, 15(2), 430-437. <https://doi.org/10.20473/jipk.v15i2.38596>
- Atteya, A. K. G., El-Serafy, R., El-Zaabalawy, K. M., Elhakem, A., & Genaidy, E. A. E. (2022). Brassinolide maximized the fruit and oil yield, induced the secondary metabolites, and stimulated linoleic acid synthesis of *Opuntia ficus-indica* oil. *Horticulturae*, 8(5), 452-467. <https://doi.org/10.3390/horticulturae8050452>
- Bajguz, A. (2000). Effect of brassinosteroids on nucleic acids and protein content in cultured cells of *Chlorella vulgaris*. *Plant Physiology and Biochemistry*, 38(3), 209-215. [https://doi.org/10.1016/S0981-9428\(00\)00733-6](https://doi.org/10.1016/S0981-9428(00)00733-6)
- Bajguz, A., & Czerpak, R. (1998). Physiological and biochemical role of brassinosteroids and their structure-activity relationship in the green alga *Chlorella vulgaris* Beijerinck (Chlorophyceae). *Journal of Plant and Growth Regulation*, 17, 131-139. <https://doi.org/10.1007/PL00007026>
- Bajguz, A., & Piotrowska-Niczyporuk, A. (2014). Interactive effect of brassinosteroids and cytokinins on growth, chlorophyll, monosaccharide and protein content in the green alga *Chlorella vulgaris* (Trebouxioophyceae). *Plant Physiology and Biochemistry*, 80, 176-183. <https://doi.org/10.1016/j.plaphy.2014.04.009>
- Bligh, E. G., & Dyer, W. J. (1959). A rapid method of total lipid extraction and purification. *Canadian Journal of Biochemistry and Physiology*, 37(8), 911-917. <https://doi.org/10.1139/o59-099>
- Borowitzka, M. A. (2018). Biology of microalgae. In I. A. Levine (Ed.), *Microalgae in Health and Disease Prevention* (pp. 23-72). Academic Press. <https://doi.org/10.1016/B978-0-12-811405-6.00003-7>
- Bradford, M. M. (1976). A rapid and sensitive method for the quantitation of microgram quantities of protein utilizing the principle of protein-dye binding. *Analytical Biochemistry*, 72(1-2), 248-254. [https://doi.org/10.1016/0003-2697\(76\)90527-3](https://doi.org/10.1016/0003-2697(76)90527-3)
- Chizzola, R., Hochsteiner, W., & Hajek, S. (2004). GC analysis of essential oils in the rumen fluid after incubation of *Thuja orientalis* twigs in the Rusitec system. *Research in Veterinary Science*, 76(1), 77-82. <https://doi.org/10.1016/j.rvsc.2003.07.001>

- Chmur, M., & Bajguz, A. (2021). Brassinolid enhances the level of brassinosteroids, protein, pigments, and monosaccharides in *Wolffia arrhiza* treated with brassinazole. *Plants*, 10(7), 1311-1328. <https://doi.org/10.3390/plants10071311>
- Croteau, R. B., Davis, E. M., Ringe, K. L., & Wildung, M. R., 2005. (–)-Menthol biosynthesis and molecular genetics. *Naturwissenschaften*, 92(12), 562-577. <https://doi.org/10.1007/s00114-005-0055-0>
- Divi, U. K., & Krishna, P. (2009). Brassinosteroid: A biotechnological target for enhancing crop yield and stress tolerance. *New Biotechnology*, 26(3-4), 131-136. <https://doi.org/10.1016/j.nbt.2009.07.006>
- Dubois, M., Gilles, K. A., Hamilton, J. K., Rabers, P. A., & Smith, F. (1956). Colorimetric method for determination of sugars and related substances. *Analytical Chemistry*, 28(3), 350-356. <https://doi.org/10.1021/ac60111a017>
- Erfianti, T., Daryono, B. S., Budiman, A., & Suyono, E. A. (2024). Growth and metabolite enhancement of acidophile *Euglena* sp. isolated from Indonesia under different photoperiod cycles. *Jurnal Ilmiah Perikanan dan Kelautan*, 16(1), 15–30. <http://doi.org/10.20473/jipk.v16i1.46193>
- Erfianti, T., Maghfiroh, K. Q., Amelia, R., Kurnianto, D., Sadewo, B. R., Marno, S., Devi, I., Dewayanto, N., Budiman, A., & Suyono, E. A. (2023). Nitrogen sources affect the growth of local strain *Euglena* sp. isolated from Dieng Peatland, Central Java, Indonesia, and their potential as bio-avtur. In *IOP Conference Series: Earth and Environmental Science* (Vol. 1151, No. 1, p. 012059). IOP Publishing. <https://doi.org/10.1088/1755-1315/1151/1/012059>
- Gao, Y., Jiang, T., Xiang, Y., He, X., Zhang, Z., Wen, S., & Zhang, J. (2021). Epi-brassinolide positively affects chlorophyll content and dark-reaction enzymes of maize seedlings. *Phyton-International Journal of experimental Botany*, 90(5), 1465-1476. <https://doi.org/10.32604/phyton.2021.014811>
- Gissibl, A., Sun, A., Care, A., Nevalainen, H., & Sunna, A. (2019). Bioproducts from *Euglena gracilis*: Synthesis and applications. *Frontiers in Bioengineering and Biotechnology*, 7, Article 108. <https://doi.org/10.3389/fbioe.2019.00108>
- Guo, C., Shen, Y., Li, M., Chen, Y., Xu, X., Chu, J., & Yao, X. (2022). Principal component analysis to assess the changes of yield and quality of two *Pinellia ternata* cultivars after brassinolide treatments. *Journal of Plant Growth Regulation*, 41, 2185-2197. <https://doi.org/10.1007/s00344-021-10434-y>
- Hakim, W. H. A., Erfianti, T., Dhiaurahman, A. N., Maghfiroh, K. M., Amelia, R., Nurafifah, I., Kurnianto, D., Siswanti, D. U., Suyono, E. A., Marno, S., & Devi, I. (2023). The effect of IAA (Indole-3-Acetic Acid) on growth, lipid, protein, carbohydrate, and pigment content in *Euglena* sp. *Malaysian Journal of Fundamental and Applied Science*, 19, 513-524. <https://doi.org/10.11113/mjfas.v19n4.2884>
- Harrewijin, P., van Oosten, A. M., & Piron, P. G. M. (2000). Production of terpenes and terpenoids. In P. Harrewijin, A. M. van Oosten, & P. G. M. Piron (Eds.), *Natural Terpenoids as Messengers* (pp. 11-57). Springer. https://doi.org/10.1007/978-94-010-0767-2_2
- Hu, Y., Bao, F., & Li, J. (2000). Promotive effect of brassinosteroids on cell division involves a distinct CycD3-induction pathway in *Arabidopsis*. *The Plant Journal*, 24(5), 693-701. <https://doi.org/10.1046/j.1365-313x.2000.00915.x>
- Huang, H., Zhong, S., Wen, S., Luo, C., & Long, T. (2022). Improving the efficiency of wastewater treatment and microalgae production of biofuels. *Resources Conservation and Recycling*, 178, Article 106094. <https://doi.org/10.1016/j.resconrec.2021.106094>

- Iftikhar, A., Ali, S., Yasmeen, T., Arif, M. S., Zubair, M., Rizwan, M., Alhaithloul, H. A. S., Alayafi, A. A. M., & Soliman, M. H. (2019). Effect of giberellic acid on growth, photosynthesis and antioxidant defense system of wheat under zinc oxide nonparticle stress. *Environmental Pollution*, 254(Part B), Article 113109. <https://doi.org/10.1016/j.envpol.2019.113109>
- Inui, H., Ishikawa, T., & Tamoi, M. (2017). Wax ester fermentation and its application for biofuel production. In S. Schwartzbach, & S. Shigeoka (Eds.), *Euglena: Biochemistry, Cell and Molecular Biology. Advances in Experimental Medicine and Biology* 979 (pp. 269-283). Springer. https://doi.org/10.1007/978-3-319-54910-1_13
- Jeon, M. S., Oh, J. J., Kim, J. Y., Han, S. I., Sim, S. J., & Choi, Y. E. (2019). Enhancement of growth and paramylon production of *Euglena gracilis* by co-cultivation with *Pseudoalteromonas* sp. MEBiC 03485. *Bioresource Technology*, 288, Article 121513. <https://doi.org/10.1016/j.biortech.2019.121513>
- Jung, J. M., Kim, J. Y., Jung, S., Choi, Y. E., & Kwon, E. E. (2021). Quantitative study on lipid productivity of *Euglena gracilis* and its biodiesel production according to the cultivation conditions. *Journal of Cleaner Production*, 291, Article 125218. <https://doi.org/10.1016/j.jclepro.2020.125218>
- Kang, A., & Lee, T. S. (2016). Secondary metabolism for isoprenoid-based biofuels. In C. A. Eckert & C. T. Trinh (Eds.), *Biotechnology for Biofuel Production and Optimization* (pp. 35-71). Elsevier. <https://doi.org/10.1016/B978-0-444-63475-7.00002-9>
- Khandaker, M. M., Majrashi, A., & Boyee, A. N. (2015). The influence of giberelic acid on the chlorophyll fluorescence, protein content and PAL activity of wax apple (*Syzygium samarangense* var. jambu madu) fruits. *Australian Journal of Crop Science*, 9, 1221-1227.
- Kim, J. Y., Oh, J. J., Jeon, M. S., Kim, G. H., & Choi, Y. E. (2019). Improvement of *Euglena gracilis* paramylon production through a cocultivation strategy with the indole-3-acetic acid-producing bacterium *Vibrio natrigens*. *Applied and Environmental Microbiology*, 85, Article e01548-19. <https://doi.org/10.1128/AEM.01548-19>
- Kim, S., Lee, D., Lim, D., Lim, S., Park, S., Kang, C., Yu, J., & Lee, T. (2020). Paramylon production from heterotrophic cultivation of *Euglena gracilis* in two different industrial byproducts: Corn steep liquor and brewer's spent grain. *Algal Research*, 47, Article 101826. <https://doi.org/10.1016/j.algal.2020.101826>
- Kim, S., Lim, D., Lee, D., Yu, J., & Lee, T. (2022). Valorization of corn steep liquor for efficient paramylon production using *Euglena gracilis*: The impact of precultivation and light-dark cycle. *Algal Research*, 61, Article 102587. <https://doi.org/10.1016/j.algal.2021.102587>
- Kothari, R., Azam, R., Singh, H. M., Kumar, P., Kumar, V., Singh, R. P., & Tyagi, V. V. (2023). Nutrients sequestration from slaughterhouse wastewater with kinetic model studies using *C. vulgaris* for lipid production and reduction in freshwater footprint: A synergistic approach. *Waste and Biomass Valorization*, 15, 1807-1818. <https://doi.org/10.1007/s12649-023-02226-0>
- Kottuparambil, S., Thankamoy, R. L., & Agusti, S. (2019). *Euglena* as a potential natural source of value-added metabolites. A review. *Algal Research*, 37, 154-159. <https://doi.org/10.1016/j.algal.2018.11.024>
- Kozlova, T. A., Hardy, B. P., Krishna, P., & Levin, D. B. (2017). Effect of phytohormones on growth and accumulation of pigments and fatty acids in the microalgae *Scenedesmus quadricauda*. *Algal Research*, 27, 325-334. <https://doi.org/10.1016/j.algal.2017.09.020>

- Kume, A., Akitsu, T., & Nasahara, K. N. (2018). Why is chlorophyll b only used in light-harvesting system? *Journal of Plant Research*, 131, 961-972. <https://doi.org/10.1007/s10265-018-1052-7>
- Leander, B. S., Lax, G., Karnkowska, A., & Simpson, A. G. B. (2017). Euglenida. In J. M. Archibald, A. G. B. Simpson & C. H. Slamovits (Eds.), *Handbook of the Protists* (pp. 1-12). Springer. https://doi.org/10.1007/978-3-319-28149-0_13
- Li, P., Sun, X., Sun X., Tang, J., Turaib, A., Wang, X., Cheng, Z., Deng, L., & Zhang, Y. (2020). Response of lipid productivity to photosynthesis of *Chlorella vulgaris* under various nutrient stress modes. *Journal of Renewable Sustainable Energy*, 12, Article 056102. <https://doi.org/10.1063/1.5144539>
- Lida, M., Desamero, M. J., Yasuda, K., Nakashima, A., Suzuki, K., Chambers, J. K., Uchida, K., Ogawa, R., Hachimura, S., Nakayama, J., Kyuwa, S., Miura, K., Kakuta, S., & Hirayama, K. (2021). Effects of orally administered *Euglena gracilis* and its reserve polysaccharide, paramylon, on gastric dysplasia in A4gnt knockout mice. *Scientific Reports*, 11, Article 13640. <https://doi.org/10.1038/s41598-021-92013-5>
- Lim, Y., A., Khong, N., M., H., Priyawardana, S., D., Ooi, K., R., Ilankoon, I., M., S., K., Chong, N., M., & Foo, S. C. (2022). Distinctive correlations between cell concentration and cell size to microalgae biomass under increasing carbon dioxide. *Biosurce technology*, 347, 1-6. <https://doi.org/10.1016/j.biortech.2022.126733>
- Lima, J. V., & Lobato, A. K. S. (2017). Brassinosteroids improve photosystem II efficiency, gas exchange, antioxidant enzymes and growth of cowpea plants exposed to water deficit. *Physiology and Molecular Biology of Plants*, 23(1), 59-72. <https://doi.org/10.1007/s12298-016-0410-y>
- Liu, C., Feng, B., Zhou, Y., Liu, C., & Gong, X. (2022). Exogenous brassinosterpids increases tolerance to shading by altering stress responses in mung bean (*Vigna radiate* L.). *Photosynthesis Research*, 151, 279-294. <https://doi.org/10.1007/s11120-021-00887-3>
- Liu, F., Yang, J., Mu, H., Li, X., Zhang, X., Wen, Y., & Zhang, X. (2023). Effects of brassinolide on growth, photosynthesis rate and antioxidant enzyme activity of ornamental ground under salt stress. *Russian Journal of Plant Physiology*, 70(6), Article 137. <https://doi.org/10.1134/S1021443722603202>
- Liu, J., Qiu, W., & Xia, D. (2018). Brassinosteroid improves lipid productivity and stress tolerance of *Chlorella* cells induced by high temperature. *Journal of Applied Phycology*, 30, 253-260. <https://doi.org/10.1007/s10811-017-1223-2>
- Ma, Y. H., & Guo, S. R. (2014). 24-epibrassinolide improves cucumber photosynthesis under hypoxia by increasing CO₂ assimilation and photosystem II efficiency. *Photosynthetica*, 52, 96-104. <https://doi.org/10.1007/s11099-014-0010-4>
- Maghfiroh, K. M., Erfianti, T., NurAfifah, I., Amelia, R., Kurnianto, D., Sadewo, B. R., Maggandari, R., Aji, B. R., Budiman, A., & Suyono, E. A. (2023). The effect of photoperiodism on nutritional potency of *Euglena* sp. Inonesian strains. *Malaysian Journal of Nutrition*, 29(3), 453-466. <https://doi.org/10.31246/mjn-2023-0004>
- Maja, M., & Ayano, S. F. (2021). The impact of population growth on natural resources and farmers' capacity to adapt to climate change in low-income countries. *Earth System and Environment*, 5, 271-283. <https://doi.org/10.1007/s41748-021-00209-6>
- Mardiyansah, D. (2023). *Pengaruh penambahan brasinolid terhadap pertumbuhan dan kandungan metabolit pada Euglena sp.* [The effect of brasinolide on growth and metabolite compound in *Euglena* sp.] [Unpublished Master dissertation]. Universitas Gadjah Mada.

- Marechal, L. R., & Goldemberg, S. H. (1964). Uridine diphosphate glucose- β -1,3-glucan β -3-glucosyltransferase from *Euglena gracilis*. *Journal of Biological Chemistry*, 239(10), 3163-3167. [https://doi.org/10.1016/S0021-9258\(18\)97699-4](https://doi.org/10.1016/S0021-9258(18)97699-4)
- Morais, K. C. C., Conceição, D., Vargas, J. V. C., Mitchell, D. A., Mariano, A. B., Ordonez, J. C., Galli-Terasawa, L. V., & Kava, V. M. (2021). Enhanced microalgae biomass and lipid output for increased biodiesel productivity. *Renewable Energy*, 163, 138-145. <https://doi.org/10.1016/j.renene.2020.08.082>
- Muller, M., & Munne-Bosch, S. (2021). Hormonal impact on photosynthesis and photoprotection in plants. *Plant Physiology*, 185(4), 1500-1522. <https://doi.org/10.1093/plphys/kiaa119>
- Mumtaz, M. A., Li, F., Zhang, X., Tao, J., Ge, P., Wang, Y., Wang, Y., Gai, W., Dong, H., & Zhang, Y. (2022). Altered brassinolide sensitivity1 regulates fruit size in association with phytohormones modulation in tomato. *Horticulturae*, 8(11), Article 1008. <https://doi.org/10.3390/horticulturae8111008>
- Mumtaz, M. A., Munir, S., Liu, G., Chen, W., Wang, Y., Yu, H., Mahmood, S., Ahiakpa, J. K., Tamim, S. A., & Zhang, Y. (2020). Altered brassinolide sensitivity1 transcriptionally inhibits chlorophyll synthesis and photosynthesis capacity in tomato. *Plant Growth Regulation*, 92, 417-426. <https://doi.org/10.1007/s10725-020-00650-z>
- Naser, A. S., Asiandu, A. P., Sadewo, B. R., Tsurayya, N., Putra, A. S., Kurniawan, K. I. A., & Suyono, E. A. (2023). The effect of salinity and tofu wastewater on the growth kinetics, biomass, and primary metabolites in *Euglena* sp. *Journal of Applied Biology and Biotechnology*, 11(6), 124-132. <https://doi.org/10.7324/JABB.2023.114931>
- Nasser, S. E. D. M., & Sarhan, I. A. (2023). Effect of spraying with brassinolide on yield and its components of sesame cultivars. In *IOP Conference Series: Earth and Environmental Science* (Vol. 1213, No. 1, p. 012028). IOP Publishing. <https://doi.org/10.1088/1755-1315/1213/1/012028>
- Nuraffiah, I., Hardianto, M. A., Erfianti, T., Amelia, R., Maghfiroh, K. Q., Kurnianto, D., Siswanti, D. U., Sadewo, B. R., Egistha, R. A., & Suyono, E. A. (2023). The effect of acidic pH on growth kinetics, biomass productivity, and primary metabolite contents of *Euglena* sp. *Makara Journal of Science*, 27(2), 97-105. <https://doi.org/10.7454/mss.v27i2.1506>
- Ogawa, T., Nakamoto, M., Tanaka, Y., Sato, K., Okazawa, A., Kanaya, S., & Ohta, D. (2022). Exploration and characterization of chemical stimulators to maximize the wax ester production by *Euglena gracilis*. *Journal of Bioscience and Bioengineering*, 133(3), 243-249. <https://doi.org/10.1016/j.jbiosc.2021.12.005>
- Padermshoke, A., Ogawa, T., Nishio, K., Nakazawa, M., Nakamoto, M., Okazawa, A., Kanaya, S., Arita, M., & Ohta, D. (2016). Critical involvement of environmental carbon dioxide fixation to drive wax ester fermentation in *Euglena*. *PLoS One*, 11(9), Article e0162827. <https://doi.org/10.1371/journal.pone.0162827>
- Patil, S., V., Koli, S., H., Mohite, B., V., Salunkhe, N., S., & Patil, A., S. (2024). Isolation and cultivation of *Euglena*. In N. Amaran, & K. A. Chandarana (Eds.), *Practical Handbook on Soil Protists* (pp. 195-200). Springer. https://doi.org/10.1007/978-1-0716-3750-0_33
- Peres, A. L. G. L., Soares, J. S., Tavares, R. G., Righetto, G., Zullo, M. A. T., Mandava, B., & Menossi, M. (2019). Brassinosteroids, the sixth class of phytohormones: A molecular view from the discovery to hormonal interactions in plant development and stress adaptation. *International Journal of Molecular Science*, 20(2), Article 331. <https://doi.org/10.3390/ijms20020331>

- Phukoetphim, N., Salakkam, A., Laopaiboon, P., & Laopaiboon, L. (2017). Kinetic models for batch ethanol production from sweet sorghum juice under normal and high gravity fermentations: Logistic and modified Gompertz models. *Journal of Biotechnology*, 243, 69-75. <https://doi.org/10.1016/j.jbiotec.2016.12.012>
- Pokotylo, I. V., Kretynin, S. V., Khripach, V. A., Ruelland, E., Blume, Y. B., & Kravets, V. S. (2014). Influence of 24-epibrassinolide on lipid signalling and metabolism in *Brassica napus*. *Plant Growth Regulation*, 73, 9-17. <https://doi.org/10.1007/s10725-013-9863-y>
- Pruvost, J., Vooren, G. V., Gouic, B. L., Couzinet-Mossion, A., & Legrand, J. (2011). Systematic investigation of biomass and lipid productivity by microalgae in photobioreactors for biodiesel application. *Bioresource Technology*, 102(1), 150-158. <https://doi.org/10.1016/j.biortech.2010.06.153>
- Singh, S., Angadi, S. V., St. Hilaire, R., Grover, K., & VanLeeuwen, D. M. (2016). Spring safflower performance under growth stage based irrigation in the southern high plains. *Crop Science*, 56(4), 1878-1889. <https://doi.org/10.2135/cropsci2015.08.0481>
- Širić, I., Abou-Fayssal, S., Adelodun, B., Mioč, B., Andabaka, Ž., Bachheti, A., Goala, M., Kumar, P., AL-Huqail, A. A., Taher, M. A., & Eid, E. M. (2023). Sustainable use of CO₂ and wastewater from mushroom farm for *Chlorella vulgaris* cultivation: Experimental and kinetic studies on algal growth and pollutant removal. *Horticulturae*, 9(3), Article 308. <https://doi.org/10.3390/horticulturae9030308>
- Song, X., Liu, B. F., Kong, R., Ren, N. Q., & Ren, H. Y. (2022). Overview on stress-induced strategies for enhanced microalgae lipid production: Application, mechanisms and challenges. *Resources Conservation and Recycling*, 183, Article 106355. <https://doi.org/10.1016/j.resconrec.2022.106355>
- Sun, S., Yao, X., Liu, X., Qiao, Z., Liu, Y., Li, X., & Jiang, X. (2022). Brassinolide can improve drought tolerance of maize seedlings under drought stress: By inducing the photosynthetic performance, antioxidant capacity and *ZmMYB* gene expression of maize seedlings. *Journal of Soil Science and Plant Nutrition*, 22, 2092-2104. <https://doi.org/10.1007/s42729-022-00796-x>
- Suyono, E. A., Nopitasari, S., Zusron, M., Khoirunnisa, P., Islami, D. A., & Prabeswara, C. B. (2016). Effect of silica on carbohydrate content of mixed culture *Phaeodactylum* sp. and *Chlorella* sp. *Bioscience Biotechnology Research Asia*, 13(1), 109-114. <http://dx.doi.org/10.13005/bbra/2011>
- Suzuki, K., Mitra, S., Iwata, O., Ishikawa, T., Kato, S., & Yamada, K. (2015). Selection and characterization of *Euglena anabaena* var. minor as a new candidate *Euglena* species for industrial application. *Bioscience Biotechnology and Biochemistry*, 79(10), 1730-1736. <https://doi.org/10.1080/09168451.2015.1045828>
- Tachibana, R., Yamagami, A., Miyagi, S., Nakazawa-Miklasevica, M., Matsui, M., Sakuta, M., Tanaka, R., Asami, T., & Nakano, T. (2022). *BRZ-INSENSITIVE-PALE GREEN 1* is encoded by chlorophyll biosynthesis enzyme gene that functions in the downstream of brassinosteroid signaling. *Bioscience Biotechnology and Biochemistry*, 86(8), 1041-1048. <https://doi.org/10.1093/bbb/zbac071>
- Tanaka, R., Koshino, Y., Sawa, S., Ishiguro, S., Okada, K., & Tanaka, A. (2014). Overexpression of chlorophyllide a oxygenase (CAO) enlarges the antenna size of photosystem II in *Arabidopsis thaliana*. *The Plant Journal*, 26(4), 365-373. <https://doi.org/10.1046/j.1365-3113.2001.2641034.x>
- Tong, H., Xiao, Y., Liu, D., Gao, S., Liu, L., Yin, Y., Jin, Y., Qian, Q., & Chu, C., (2014). Brassinosteroid regulates cell elongation by modulating gibberellin metabolism in rice. *The Plant Cell*, 26(11), 4376-4393. <https://doi.org/10.1105/tpc.114.132092>

- Vardhini, B. V., & Anjum, N. A. (2015). Brassinosteroids make plant life easier under abiotic stresses mainly by modulating major components of antioxidant defense system. *Frontiers in Environment Science*, 2(67), 1-16. <https://doi.org/10.3389/fenvs.2014.00067>
- Xia, X. J., Huang, L. F., Zhou, Y. H., Mao, W. H., Shi, K., Wu, J. X., Asami, T., Chen, Z., & Yu, J. Q. (2009). Brassinosteroids promote photosynthesis and growth by enhancing activation of Rubisco and expression of photosynthetic genes in *Cucumis sativus*. *Planta*, 230(6), 1185-1196. <https://doi.org/10.1007/s00425-009-1016-1>
- Yang, C. J., Zhang, C., Lu, Y. N., Jin, J. Q., & Wang, X. L. (2011). The mechanisms of brassinosteroids' action: From signal transduction to plant development. *Molecular Plant*, 4(4), 588-600. <https://doi.org/10.1093/mp/ssr020>
- Yoshida, Y., Tomiyama, T., Maruta, T., Tomita, M., Ishikawa, T., & Arakawa, K. (2016). De novo assembly and comparative transcriptome analysis of *Euglena gracilis* in response to anaerobic conditions. *BMC Genomics*, 17, Article 182. <https://doi.org/10.1186/s12864-016-2540-6>
- Yuan, L., Shu, S., Sun, J., Guo, S., & Tezuka, T. (2012). Effects on 24-epibrassinolide on the photosynthetic characteristic antioxidant system, and chloroplast ultrastructure in *Cucumis sativus* L. under Ca(NO₃)₂ stress. *Photosynthesis Research*, 112(3), 205-214. <https://doi.org/10.1007/s11120-012-9774-1>
- Zakryś, B., Milanowski, R., & Karnkowska, A. (2017). Evolutionary origin of *Euglena*. In S. Schwartzbach & S. Shigeoka (Eds.), *Euglena: Biochemistry, Cell and Molecular Biology. Advances in Experimental Medicine and Biology* 979 (pp.3-17). Springer. https://doi.org/10.1007/978-3-319-54910-1_1
- Zhang, D., Tan, W., Yang, F., Han, Q., Deng, X., Guo, H., Liu, B., Yin, Y., & Lin, H. (2021). A BIN2-GLK1 signaling module integrates brassinosteroid and light signaling to repress chloroplast development in the dark. *Developmental Cell*, 56(3), 310-324. <https://doi.org/10.1016/j.devcel.2020.12.001>
- Zhang, L., Cao, X., Wang, Z., Zhang, Z., Li, J., Wang, Q., & Xu, X. (2022). Brassinolide alleviated chilling injury of banana fruit by regulating unsaturated fatty acid and phenolic compound. *Scientia Horticulturae*, 297, Article 110922. <https://doi.org/10.1016/j.scienta.2022.110922>
- Zhao, M., Yuan, L., Wang, J., Xie, S., Zheng, Y., Nie, L., Hou, S. J., Chen, G., & Wang, C. (2019). Transcriptome analysis reveals a positive effect of brassinosteroids on the photosynthetic capacity of wucai under low temperature. *BMC Genomics*, 20, Article 810. <https://doi.org/10.1186/s12864-019-6191-2>

Comparative Evaluation of Python-based Heart Rate Variability Analysis Tools for Neonatal Sepsis Detection in Neonatal Intensive Care Units

Roshan David Jathanna¹, Dinesh Acharya Udupi^{1*}, Faiza Iqbal², Krishnamoorthi Makkithaya¹ and Leslie Edward Simon Lewis²

¹Department of Computer Science and Engineering, Manipal Institute of Technology, Manipal Academy of Higher Education, Manipal, 576104, Karnataka, India

²Department of Pediatrics, Kasturba Medical College, Manipal Academy of Higher Education, Manipal, 576104, Karnataka, India

ABSTRACT

Neonatal sepsis is a severe systemic infection occurring within the first month of life and remains a significant cause of morbidity and mortality worldwide, particularly in low- and middle-income (LMICs). Despite advancements in medical care, challenges such as limited healthcare access and inadequate diagnostic capabilities persist. This study explores the impact of real-time data analytics on managing neonatal sepsis, highlighting its potential to enhance early detection, diagnosis, and treatment outcomes in neonatal intensive care units (NICUs) in LMICs. This study provides an architecture for continuously monitoring neonates using cardiopulmonary monitors and applying real-time analysis to identify sepsis onset. Data from eight infants were collected and analyzed, with each ECG signal recorded at 500 Hz, generating 36 to 126 million samples per channel. The study compared four Python packages for Heart Rate Variability (HRV) computation (NeuroKit2, HRV, HeartPy, Systole) based on features, computational efficiency, and ease of use. NeuroKit2 provided the most features but had the highest computational load, while Systole and HeartPy offered a balance of functionality and efficiency. The findings underscore the potential of real-time data analytics in improving neonatal sepsis management. Early diagnostic testing and advanced monitoring technologies can significantly enhance neonatal outcomes, particularly in resource-limited settings.

These technological advancements align with Sustainable Development Goal Target 3.2 and underscore the need for continued research, policy support, and collaborative efforts to reduce neonatal mortality globally.

Keywords: Low- and middle-income countries, neonatal intensive care unit, neonatal mortality, neonatal sepsis, real-time data analytics, sustainable development goal 3.2

ARTICLE INFO

Article history:

Received: 22 June 2024

Accepted: 07 January 2025

Published: 04 April 2025

DOI: <https://doi.org/10.47836/pjst.33.3.13>

E-mail addresses:

roshan.jathanna@manipal.edu (Roshan David Jathanna)

dinesh.acharya@manipal.edu (Dinesh Acharya Udupi)

faizaifra@yahoo.in (Faiza Iqbal)

k.moorthi@manipal.edu (Krishnamoorthi Makkithaya)

leslie.lewis@manipal.edu (Leslie Edward Simon Lewis)

*Corresponding author

INTRODUCTION

Neonate refers to a baby who is younger than four weeks old. Neonatal sepsis, characterized by systemic infection occurring within the first month of life, remains a critical healthcare challenge globally, particularly in low- and middle-income countries (LMICs). Despite advancements in medical care, neonatal sepsis continues to be a leading cause of morbidity and mortality among newborns. According to the World Health Organization (WHO, 2024) report, out of the 5 million deaths that occurred in the year 2022 in children under the age of five years globally, 2.3 million are neonates. In India, a significant proportion of child deaths under the age of five occur within the initial four weeks after birth. The Sustainable Development Goal (SDG) target 3.2 aims to reduce newborn mortality to 12 per 1,000 live births by 2030 (WHO, 2024). Neonatal Intensive Care Units (NICUs) specialize in providing care for sick or premature neonates, with medical practitioners at NICUs having saved countless lives of neonates born ill or prematurely. The management of neonatal sepsis in these settings is often hindered by a myriad of factors, including limited access to healthcare facilities, shortages of skilled healthcare providers, inadequate diagnostic capabilities, and challenges in accessing and affording lifesaving interventions. However, diagnosing neonatal infection can be challenging due to the subtle clinical features and the underdeveloped immune system of newborns. Therefore, maintaining a high index of suspicion for neonatal diseases and conducting early diagnostic testing, even without apparent clinical signs, is crucial.

A newborn's immune system overreacting to an infection can result in neonatal sepsis, a potentially fatal illness that causes systemic inflammation and septic shock. This inflammatory reaction may impair the blood supply to essential organs, depriving them of the nutrition and oxygen that they require, which may result in organ failure and even death. After preterm birth and birth asphyxia, neonatal sepsis ranks third among the leading causes of newborn mortality and continues to pose a severe risk (WHO, 2024). In LMICs, where healthcare systems are often strained, and resources are limited, the management of neonatal sepsis presents unique challenges. Early identification and prompt treatment are essential for improving outcomes, yet many healthcare facilities in LMICs lack the necessary tools and infrastructure to facilitate timely diagnosis and intervention. In LMICs, where healthcare systems are often strained and resources are limited, the management of neonatal sepsis presents unique challenges (Procianoy & Silveira, 2020). Early identification and prompt treatment are essential for improving outcomes, yet many healthcare facilities in LMICs lack the tools and infrastructure to facilitate timely diagnosis and intervention. However, amidst these challenges, recent advancements in healthcare technology, particularly in the realm of data analytics, offer promising opportunities to revolutionize the management of neonatal sepsis in LMICs (Bohanon et al., 2015; Fairchild et al., 2013; Jathanna et al., 2023; Khazaei et al., 2015; McGregor et al., 2012; Mithal et al., 2016; Moorman et al., 2011; Quinten et al., 2017; Wee et al., 2020).

Clinical Risk Index for Babies (CRIB) II is a scoring system used to predict mortality risk in very low birth weight infants, combining birth weight, gestational age, and other clinical factors obtained during the first 12 hours of admission to the NICU (Parry et al., 2003). Moorman et al. (2011) studied 3003 VLBW neonates in 9 NICU. The neonates were divided into two groups. The heart rate characteristics (HRC) of only one group were displayed to the clinicians. It was observed that the mortality rate reduced from 10.2% to 8.1% in the group whose HRC was displayed. This study indicates the importance of HRC in the NICU. SNAPPE-II (Score for Neonatal Acute Physiology with Perinatal Extension-II) is used to determine the severity of disease and identify the risk of fatality in neonates admitted to NICU. The score estimates the health state of the neonate by considering both perinatal and physiological parameters. Neonates with higher SNAPPE-II scores are susceptible to sepsis due to their compromised health condition (Harsha, 2015).

Fairchild et al. (2013) developed a monitor that analyses ECG and HRC for patterns to predict sepsis at an early stage. The algorithm calculates the heart rate observations (HeRO) score using standard duration on heartbeat interval, sample asymmetry and entropy. Sample asymmetry measures the skewing of heart rate, and sample entropy measures the irregularity of heart rate. The algorithm uses logistic regression to predict the probability of sepsis in the next 24 hours. HeRO score is calculated instantaneously but displayed hourly on the monitor. The proposed system requires investing in separate hardware devices. Further, clinical decision support could be improved by using other clinical factors. Iqbal et al. (2024) used machine learning (ML) models to predict culture-positive sepsis (CPS) and clinical sepsis (CNS) in neonates using a dataset of 90 essential variables. The study concluded that Random Forest (RF) and Bagging algorithms outperformed in predicting CPS and CNS, with RF achieving an accuracy of 98.4% and ROC of 0.994. Tachycardia, bradycardia, and the presence of a central line catheter were identified as predictors of CPS.

Khazaei et al. (2015) designed and developed an Artemis framework to acquire and store physiological and clinical data for real-time analytics and visual representation. The authors use cloud services to collect and integrate data from various healthcare services. Data from various patients and devices can be concurrently streamed and analyzed using temporal analysis. The system uses variables that decide the length of stay, such as features of gestation age and probabilities of condition onset. The system has been deployed in McMaster Children's Hospital, Canada and is being used by researchers to work on various infections in neonates, including sepsis. However, the proposed system requires devices that capture physiological data to output their data for collection through an Ethernet and/or serial port. Even if the current setup has devices that can output data through required ports, the hospitals may not be willing to allow external devices to connect to the existing devices. The other limitation is that the proposed framework uses proprietary software.

Mansoor et al. (2019) proposed a Modified Sick Neonatal Score (MSNS) tailored for resource-limited settings through a study conducted in India involving 585 neonates. It

assesses disease severity at admission and shows statistically significant score differences between surviving and deceased neonates, with a cutoff score of ≤ 10 being highly predictive of mortality. This suggests that MSNS is a viable tool for evaluating neonatal disease severity in settings lacking advanced diagnostics, potentially guiding early interventions and referrals to higher-tier care facilities. Shirwaikar et al. (2015) used supervised ML techniques for the diagnosis of neonatal diseases. They found that the ensemble technique has better predictive power than the Support Vector Machine (SVM), decision trees, and neural networks.

Lipton et al. (2016) used RNN with long short-term memory (LSTM) to identify patterns in a multivariate time series of observations obtained from the intensive care unit (ICU). For the study, an anonymized clinical time series extracted from the EHR system at Children's Hospital, LA, of 10,401 NICU visits. They trained a model to classify 128 diagnoses given 13 frequently but irregularly sampled clinical measurements. The 13 variables were diastolic and systolic blood pressure, peripheral capillary refill rate, end-tidal CO₂, fraction of inspired O₂, glasgow coma scale, blood glucose, heart rate, pH, respiratory rate, blood oxygen saturation, body temperature, and urine output. Episodes vary in length from 12 hours to several months. Their results indicate that LSTM RNNs, especially with target replication, can successfully classify diagnoses of critical care patients given clinical time series data.

Mithal et al. (2016) proposed an algorithm called RALIS that uses physiological parameters to detect sepsis in neonates approximately 2.5 days prior to the blood tests. The algorithm uses heart rate, respiratory rate, body temperature and weight, desaturations ($< 85\%$) and bradycardias (< 100 beats per minute) to arrive at a score between 0 to 10. Any score above 5 for 6 hours was considered critical. The algorithm could correctly identify sepsis in 28 out of 34 cases of proven sepsis. The limitation of RALIS is that it falsely identified one out of four neonates to have sepsis, which is a critical concern as it results in the overuse of antibiotics. Iqbal et al. (2023) developed an ML model to predict the mortality of neonates using non-invasive vital sign data, as well as maternal and neonatal attributes using the WEKA tool. The study reviewed 388 neonates diagnosed with neonatal sepsis over five-years. The mortality rate was 39.6% ($n = 154$). The study used the "OneR attribute evaluation" method for feature selection, which identified several significant attributes, including birth weight, gestational age, and mode of delivery. The model performed well using the Logistic Regression algorithm, with an accuracy of 88.4% and a ROC of 0.906.

Joshi et al. (2020). Researchers combined features derived from Heart Rate Variability (HRV), breathing patterns, and estimated infant movement in preterm infants to improve the accuracy of sepsis prediction compared to using a single measure. This suggests that monitoring changes like abnormal heart rate patterns, irregular breathing, and decreased movement, all captured through readily available physiological data, could be a valuable tool for the early detection of sepsis in newborns.

Leon et al. (2021) explored the use of HRV analysis with visibility graphs to predict LOS in premature infants. Researchers compared HRV data from infants who developed LOS (receiving antibiotics) to a control group. ML analysis incorporating visibility graph features achieved an accuracy of 87.7% (AUROC) in predicting LOS as early as 42 hours before antibiotics, suggesting its potential as a non-invasive tool for early detection and improved outcomes. However, further research with larger studies is needed to confirm these findings. Rao et al. (2024) presented a systematic literature review of predictive analytics methods for early diagnosis of neonatal sepsis, highlighting their potential to improve healthcare management. The study reviews 16 studies between 2014 and 2024, including prospective and retrospective data, and utilizing various predictive modeling techniques, such as ML and Deep Learning (DL). The study concluded that ML algorithms have high effectiveness in predicting neonatal sepsis and have the potential to improve the early diagnosis of neonatal sepsis.

McAdams et al. (2022) have used a classification stacking model to predict four main neonatal diseases: sepsis, birth asphyxia, necrotizing enterocolitis (NEC), and respiratory distress syndrome, which together account for 75% of neonatal deaths. The dataset was collected from Asella Comprehensive Hospital between 2018 and 2021. Comparisons were made with three other ML models (Xtreme Gradient Boosting, Random Forest, and SVM), and the developed stacking model demonstrated superior performance. The findings suggest that ML can significantly contribute to early detection and accurate diagnosis of neonatal diseases, particularly in resource-limited healthcare facilities. Zeigler et al. (2023) explored the efficacy of the HeRO score and neonatal sequential organ failure assessment (nSOFA) in predicting sepsis and mortality among very low birth weight infants. From 2011 to 2019 data, the study reveals that the HeRO score can serve as an early alert for late-onset sepsis, while the nSOFA score, especially when assessed 12 hours after a blood culture, accurately predicts mortality. This suggests that leveraging both HeRO and nSOFA scores could significantly improve clinical outcomes for these infants.

A heart rate that is complicated and continually changing indicates good health. Various algorithms have been proposed to calculate the HRV from raw ECG signals. Time domain indices use variance in time intervals between consecutive heartbeats to quantify the HRV. The frequency domain uses power distribution among four bands to compute HRV. The non-linear domain appropriately describes the unpredictability of a time series (Chiera et al., 2020; Wee et al., 2020). HRV has become an easy-to-capture and dependable marker for the early identification of many diseases and abnormalities in neonates, including sepsis. Despite its promising clinical applications, HRV remains underutilized in the NICU (Chiera et al., 2020). This gap between research and practice can be attributed to a confluence of factors, impacting the implementation of this potentially valuable tool for monitoring and managing the delicate health of premature and sick neonates:

- **Lack of Standardized Protocols:** Variations in electrode placement, recording duration, signal processing techniques, and chosen analysis parameters significantly impact HRV measurements, making data interpretation and comparisons across studies and clinical settings challenging. Establishing reliable clinical benchmarks and translating research findings into practice necessitates the development of consensus guidelines encompassing best practices for data acquisition, analysis, and reporting (Latremouille et al., 2021).
- **Lack of Normative Data:** A limited amount of normative data is available for HRV parameters in neonates, particularly for preterm and sick infants. This makes it challenging to establish reference ranges and interpret HRV values accurately (Chiera et al., 2020; Kurul et al., 2022).
- **Dynamic HRV Patterns in Early Life:** A newborn's nervous system is still developing, especially an autonomic nervous system that controls heart rate. This ongoing maturation process causes rapid shifts in HRV patterns during the first few weeks and months. Because HRV is constantly changing, interpreting individual results and setting reference ranges becomes trickier in this early stage (Chiera et al., 2020; Patural et al., 2022).
- **Influence of external factors:** HRV assessment in neonates can be influenced by various external factors, such as sleep-wake cycles, feeding patterns, and environmental stimuli like loud noises or uncomfortable temperatures. Controlling these factors can be challenging, leading to potential confounding effects on HRV measurements (Chiera et al., 2020; Statello et al., 2021).
- **Practical Implementation Challenges:** The specialized equipment, software, personnel training, data storage, and management systems required for accurate HRV measurement and analysis can be expensive, particularly for NICU units with limited resources (Arslantas & Ozdemir, 2020; McGregor et al., 2012; Moorman et al., 2011; Ranjit & Kisson, 2021; Statello et al., 2021).

Real-time data analytics, powered by advances in digital health platforms, electronic health records (EHRs), and mobile health technologies, enable healthcare providers to collect, analyze, and act upon clinical data in real time. By leveraging these technologies, healthcare providers can rapidly identify and respond to cases of neonatal sepsis, improve diagnostic accuracy, optimize treatment strategies, and ultimately reduce newborn morbidity and mortality rates. This paper aims to explore the transformative impact of real-time data analytics on neonatal sepsis management, shedding light on its potential to revolutionize healthcare delivery and outcomes for newborns in LMICs and beyond. Based on the literature review, it is evident that there is a need for a real-time data capture,

storage, and processing system in NICU that uses the existing setup and does not require a huge investment in proprietary software or hardware.

MATERIALS AND METHODS

Study Setting

This study was conducted at the NICU of Kasturba Hospital, Manipal, Karnataka, India. Ethical approval was obtained from the Institutional Ethics Committee (IEC: 350/2018) of Kasturba Hospital. Each infant admitted to the NICU at Kasturba Hospital underwent continuous monitoring using a Philips Intellivue MP 20/30 cardiopulmonary monitor. This monitoring device employs electrodes attached to the infant to measure vital parameters, including heart activity, blood oxygen saturation (O₂ sat), blood pressure, and respiratory rate. The cardiopulmonary monitors from various beds were interconnected to a central monitoring system (M3140 Low Acuity Information Center, CPQ0A80 HP RP5700 Business System), facilitating simultaneous data display from different beds, as depicted in Figure 1. To ensure patient confidentiality, the collected data were de-identified in accordance with the Health Insurance Portability and Accountability Act (HIPAA) guidelines before integration into the newly proposed NICU database. Adhering to the safe harbor method outlined in the HIPAA Privacy Rule guidelines, specific identifiers that could potentially reveal an individual’s identity, such as names, addresses, dates of birth,

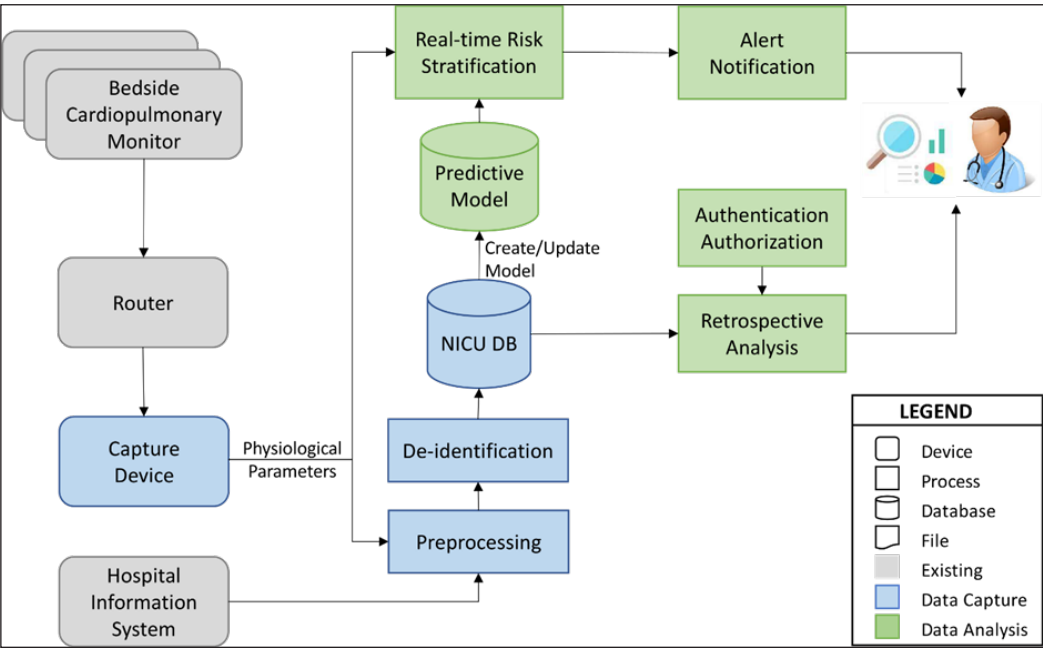


Figure 1. Overall architecture

admission dates, contact information, and unique identifiers, were removed or de-identified from the dataset. This meticulous de-identification process effectively mitigated the risk of unintentional disclosure of protected health information, safeguarding patient privacy and ensuring compliance with HIPAA regulations (Moore & Frye, 2019).

Data Capture and Decoding

Cardiopulmonary monitors from various beds connect to the central monitoring system through an ethernet switch using the LAN interface. The capture device will replace the central monitoring system. The capture device is a Windows 10 PC with a capture service, upload service, and an influxdb time-series database, as shown in Figure 2.

The capture service is a Windows service written in C# programming language that communicates with monitors and processes and stores data in the influxdb database. The Windows service extends VSCaptureMP (Karippacheril & Ho, 2013), a high-fidelity datalogging software platform. The monitors communicate using the Universal Datagram Protocol/Internet Protocol (UDP/IP). All the monitors periodically broadcasted the

connection indication messages with device information through the UDP port 24005 until a central monitoring system established a logical connection. The connection indication message also contains a UDP port (default is 24105) that the protocol will use for further communication. The capture device will receive this connection indication message and respond with the association request, as shown in Figure 3. The monitor responds with an association response indicating whether the association was successful. In the case of a successful association, the monitor sends a medical device system (MDS) message to create an event with system information and configuration. After successful association, the capture device sends poll data requests for numeric and wave data. The monitor responds with the requested data. The association release request is sent from the capture device whenever the association needs to be closed.

The capture device decodes the data received using the steps shown in Figure 4. The data received are first validated to ensure that they only contain hexadecimal characters.

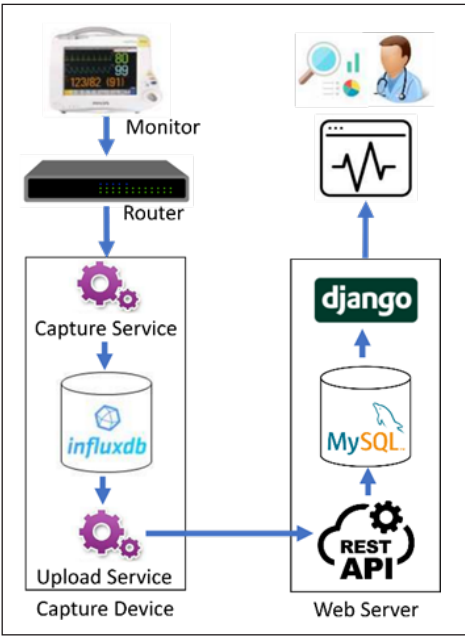


Figure 2. Data capture

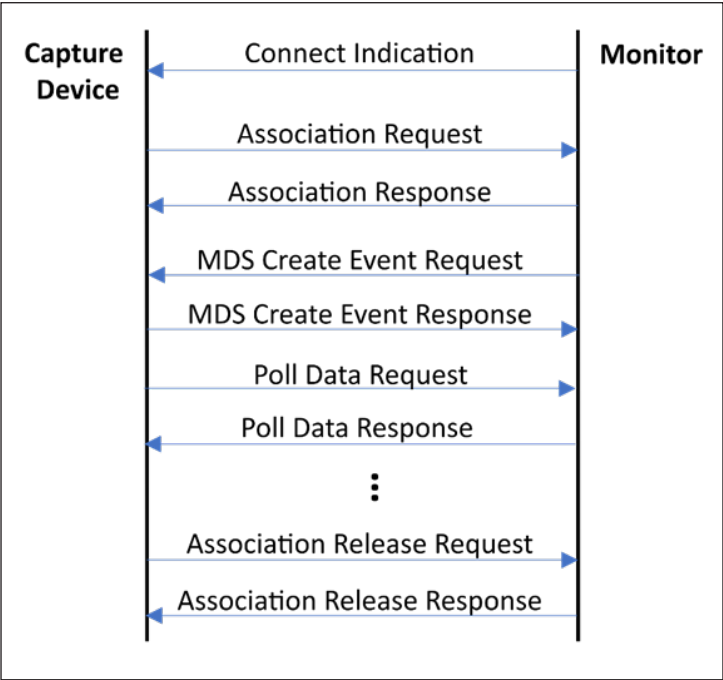


Figure 3. Protocol dialog between philips intellivue monitor and capture device

Once validated, the data is converted to an 8-bit unsigned integer. The session_id is present in the first two bytes, and if it has a fixed value of 0xE100, then the packet contains data export commands. The frame length is at the 6th and 7th bytes. The remote operation (RO) and the command types start at the 4th and 10th bytes, respectively. The packet contains physiological data if the RO type is 1 or 2 and the command type is 0. The following 14 bytes are skipped, and the rest of the packet is traversed to find either physiological numeric or wave keys. There are 932 and 47 physiological numeric and wave keys, respectively (Philips, 2015). The developed software only captures and displays the values of the physiological keys mentioned in Table 1, which are essential for detecting sepsis. The data includes the measurement state, the unit code and the value. The capture device creates a JSON object with physiological parameter values and sends it to the web server using representational state transfer (ReST) API calls. The web server receives the data and stores it in the database. For real-time monitoring, the web server features a web page designed to display the data in real time. Using JavaScript's setTimeout function, the web page periodically initiates ReST API calls to the server for continuous updates of current values. Moreover, incorporating the requestAnimationFrame method signals the browser to prepare for an animation update prior to the next repaint, optimizing the user's visual experience.

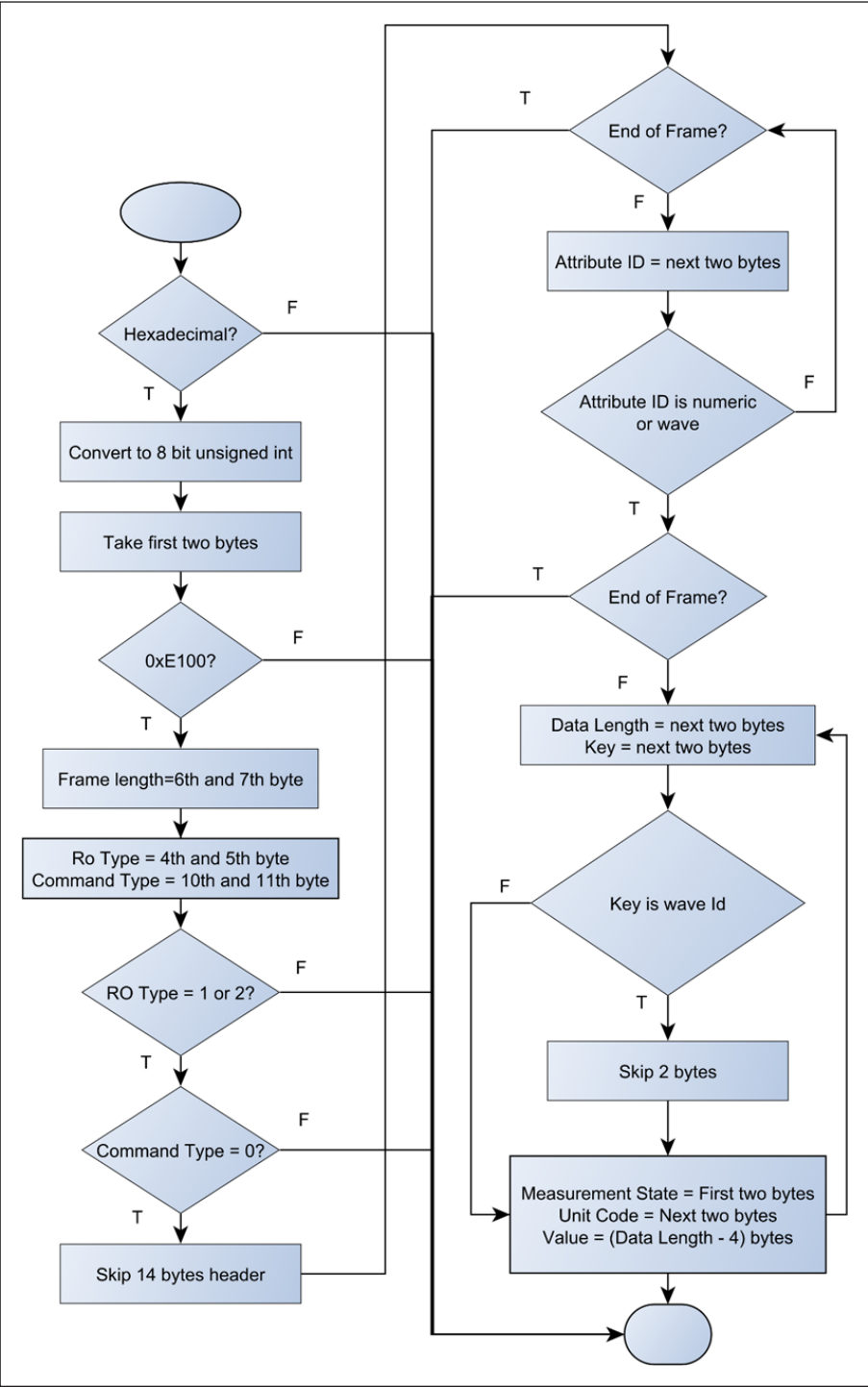


Figure 4. Data decoding

The upload service is a Windows service written in the C# programming language to periodically retrieve data from the influxdb database and upload it to the web server using the representational state transfer (ReST) API calls. The ReST API uses the Django framework and saves the physiological data in the MySQL database.

Table 1
Physiological ID with units

Physiological Id	Description	Units
0X4BB8	Arterial Oxygen Saturation (SpO ₂)	Percentage
0X4822	Pulse rate	Beats per minute
0X4182	Heart rate	Beats per minute
0X500A	Respiration rate	Respiration per minute
0x0102	ECG Lead II	Milli-volt

Data Mapping

Other necessary information on neonates, such as maternal data, radiographic findings, and laboratory data from the current hospital information system, is pre-processed, de-identified, and mapped to bedside data before being integrated into the NICU database. A website with two web pages was developed to ease the mapping. The first webpage shows the list of bedside monitors from which data were not received for 30 minutes, indicating that the baby on the bed may have changed. A waiting time of 30 minutes is proposed to rule out device errors.

The mapping is performed by clicking the ‘map’ button, which opens the web page shown in Figure 5. Details such as the reason for not receiving data and the new patient ID must be entered. The reason for not receiving data can be a device error, a shift because of

Mapping Details for Bed 10 (192.168.2.12)

Old Baby Details

IP Address:	192.168.2.12
Stopped DateTime:	02-03-2024 14:30
Patient No:	1233323
Reason for not Recieving Data*:	Device Error

New Baby Details

IP Address:	192.168.2.12
Start DateTime:	02-03-2024 15:30
New Patient No*:	
<div>SAVECANCEL</div>	

Figure 5. Webpage to map bed to baby

sepsis, a shift to another bed or discharge from the NICU. The stakeholders can view real-time physiological data of all neonates using the responsive website, which was developed using the Django framework. Historical physiological data and various neonatal scores of the selected neonates are displayed after they click the cell for a particular bed.

The major challenge in storing data from monitors in the NICU is the generation of high-frequency ECG data for each neonate. The ECG data can be stored as they are or can be compressed (Jha & Kolekar, 2022). In this study, ECG data were stored without compression. We compared and evaluated four popular Python packages used for computing HRVs from ECG signals, such as Neurokit2 (Makowski et al., 2021), HRV (Bartels & Peçanha, 2020), HeartPy (van Gent et al., 2019) and Systole (Legrand & Allen, 2022). The comparison focused on assessing the performance, dependencies, memory consumption, and ease of use of packages. The goal was to provide insights into the strengths and limitations of each package, enabling researchers and developers to make informed choices when selecting the appropriate tool for their HRV analysis needs.

Real-time Risk Stratification

The physiological data from the capturing device is analyzed in real time using predictive models to detect the onset of complications. Neonates will be scored using various scoring schemes, such as CRIB II (Parry et al., 2003), SIRS (Poggi et al., 2023), SNAPPE-II (Harsha, 2015), MSNS (Mansoor et al., 2019) and nSOFA (Berka et al., 2022). If the score crosses the permissible limit, appropriate stakeholders will be notified through an alert notification system.

Authentication and Authorization

All the data in the NICU database can only be accessed with proper credentials. Authentication determines whether a user can access the data. The authorization will control what part of the information the user can access.

Retrospective Analysis

Researchers can use the data collected in the NICU database for retrospective analysis with proper consent from Kasturba Hospital's ethical committee. With the committee's approval, credentials with appropriate permission will be created.

RESULTS AND DISCUSSION

Data from eight infants depicted in Table 2 was collected using a single-channel electrocardiogram (ECG) signal from a 3-lead ECG setup on bedside patient monitors (Gee et al., 2017; Goldberger et al., 2000). Each ECG signal was recorded at a sampling rate

of 500 Hz, resulting in 500 data points per second. The recording durations ranged from approximately 20 to 70 hours per infant, resulting in a data volume of 36 million to 126 million samples per channel. A 10-minute segment of each ECG recording (600 seconds) was extracted, resulting in 300,000 data points per baby used for HRV computation. The study assessed computational efficiency by measuring the average time taken and the average number of function calls during the HRV calculation process on the 10-minute data samples.

Table 2
Summary of dataset

Subject	Weight (kg)	Postconceptional Age (weeks)
Infant 1	1.76	30.71
Infant 2	1.71	30.71
Infant 3	0.84	30.14
Infant 4	1.14	30.14
Infant 5	1.11	30.14
Infant 6	2.10	32.43
Infant 7	1.23	30.57
Infant 8	1.90	34.29

The computational efficiency of various Python packages for HRV calculation was evaluated by comparing the number of features each package offers, as illustrated in Figure 6(a). NeuroKit2 stands out with the highest number of features, offering a total of 89 features. This extensive functionality makes it a comprehensive tool for HRV analysis but may also contribute to longer processing times and higher computational demands. In contrast, the HRV package offers the fewest features, with only 7, suggesting that it may be suitable for simpler HRV analysis tasks where computational efficiency is prioritized over the range of available features. HeartPy provides a moderate number of features, with 23 indicating that it can deliver efficient performance while still offering a reasonable range of HRV analysis capabilities. Similarly, Systole provides 32 features, balancing computational efficiency and the breadth of HRV analysis functionalities.

Further analysis of the packages included the number of function calls and primitive calls, as shown in Figures 6(b) and 6(c). NeuroKit2 again showed the highest computational load, with 5,952,381 function calls and 5,754,083 primitive calls. The HRV package showed significantly fewer function calls at 2,400,222 and 2,400,218 primitive calls. HeartPy demonstrated much lower values, with 60,740 function calls and 60,651 primitive calls, reflecting its more efficient performance. Systole also showed superior computational efficiency, with 35,208 function calls and 34,803 primitive calls.

NeuroKit2 is the most popular package, with 862 stars, reflecting its extensive community support and usage. HeartPy follows with 689 stars, indicating significant

popularity. The HRV package has 160 stars, and Systole has 55 stars, showing relatively lower popularity, as depicted in Figure 6(d). The number of required packages for each tool varies, with NeuroKit2 requiring the most dependencies (862), HeartPy (689), HRV (160), and Systole (55), as seen in Figure 6(e). This indicates the complexity and potential setup effort needed for each package. The time taken for HRV computation was also measured, with NeuroKit2 taking the longest at 4.94 seconds. The HRV package took 2.28 seconds, HeartPy took 0.8 seconds, and Systole was the fastest, taking only 0.6 seconds as seen in Figure 6(f). This highlights the differences in computational efficiency among the packages, with Systole and HeartPy being the most efficient, followed by HRV. Then, NeuroKit2 is the least efficient in terms of time taken. In summary, NeuroKit2, despite its comprehensive functionality and popularity, requires a significant number of dependencies, potentially complicating its setup and use. HeartPy and Systole offer a balance of popularity and manageable dependency requirements, making them more accessible. The HRV package, while less popular, has the least number of dependencies, simplifying its installation and use. This evaluation helps in selecting the most suitable Python package for HRV calculation based on the specific needs and constraints of the study.

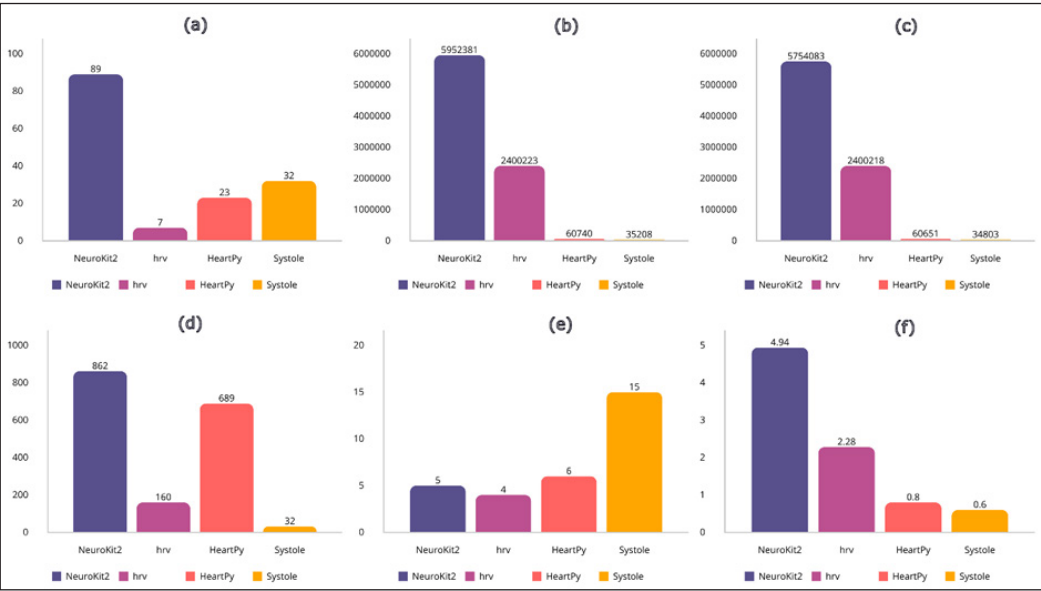


Figure 6. Comparison of various python packages (a) Number of features (b) Function calls (c) Primitive calls (d) Stars in GitHub (e) Required packages (f) Time Taken (in milliseconds)

CONCLUSION

Based on the findings of this study, neonatal mortality, mainly due to conditions such as neonatal sepsis, remains a significant global health challenge. As we navigate through

the complexities of neonatal care, particularly in the context of India, where a substantial proportion of child deaths under five occur within the first month of life, the indispensable role of NICUs and advanced technological interventions comes to the forefront. In conclusion, this study sheds light on the critical challenges faced in reducing neonatal mortality and highlights promising pathways forged by technological and clinical advancements. Integrating real-time data analysis, predictive modeling, and comprehensive physiological monitoring presents hope for enhancing neonatal outcomes, particularly in LMICs. These innovations must be embraced and scaled up as we move forward, paving the way for a future where neonatal mortality is significantly reduced. In alignment with Sustainable Development Goal target 3.2, which aims to end preventable deaths of newborns and children under five years. Through collaborative efforts, continued research, and policy support, we can ensure that the most vulnerable populations receive the care and protection they need during the most critical phase of life.

Limitations of the Study

The primary limitation of this study lies in the inconsistency across the NICU infrastructures, which can affect the adaptability of systems in other settings. Variability in monitoring equipment, regulatory requirements, and IT resources across regions could also impede seamless integration, especially in under-resourced NICUs. Furthermore, the storage of high-frequency, uncompressed ECG data demands substantial computational and storage resources, limiting scalability. Reliance on specific hardware (e.g., Philips monitors) and software configurations also constrains generalizability, potentially requiring additional compatibility adjustments for broader implementation.

Future Directions and Recommendations

Future work could enhance the predictive accuracy of the system by adding various clinical parameters, such as maternal health data and laboratory biomarkers, to allow personalized risk assessments. Exploring other data compression techniques can also improve storage and affirm efficiency in data-intensive settings. Further research could evaluate emerging HRV analysis tools and ML methods for anomaly detection, broadening analytical capabilities. Finally, multi-site validation studies would help standardize protocols across diverse NICUs, facilitating larger-scale adoption and improving generalizability.

ACKNOWLEDGEMENTS

The authors would like to thank Kasturba Hospital for granting the ethical clearance necessary for this study.

REFERENCES

- Arslantas, M. K., & Ozdemir, H. (2020). Sepsis management in resource-limited settings. *Anesthesia & Analgesia*, 130(2), Article e37. <https://doi.org/10.1213/ANE.00000000000004536>
- Bartels, R., & Peçanha, T. (2020). HRV: A pythonic package for heart rate variability analysis. *Journal of Open Source Software*, 5(51), Article 1867. <https://doi.org/10.21105/joss.01867>
- Berka, I., Korček, P., Janota, J., & Straňák, Z. (2022). Neonatal sequential organ failure assessment (nSOFA) score within 72 hours after birth reliably predicts mortality and serious morbidity in very preterm infants. *Diagnostics*, 12(6), Article 1342. <https://doi.org/10.3390/diagnostics12061342>
- Bohanon, F. J., Mrazek, A. A., Shabana, M. T., Mims, S., Radhakrishnan, G. L., Kramer, G. C., & Radhakrishnan, R. S. (2015). Heart rate variability analysis is more sensitive at identifying neonatal sepsis than conventional vital signs. *The American Journal of Surgery*, 210(4), 661–667. <https://doi.org/10.1016/j.amjsurg.2015.06.002>
- Chiera, M., Cerritelli, F., Casini, A., Barsotti, N., Boschiero, D., Cavigioli, F., Corti, C. G., & Manzotti, A. (2020). Heart rate variability in the perinatal period: A critical and conceptual review. *Frontiers in Neuroscience*, 14, 1–23. <https://doi.org/10.3389/fnins.2020.561186>
- Fairchild, K. D., Schelonka, R. L., Kaufman, D. A., Carlo, W. A., Kattwinkel, J., Porcelli, P. J., Navarrete, C. T., Bancalari, E., Aschner, J. L., Walker, M. W., Perez, J. A., Palmer, C., Lake, D. E., O’Shea, T. M., & Moorman, J. R. (2013). Septicemia mortality reduction in neonates in a heart rate characteristics monitoring trial. *Pediatric Research*, 74(5), 570–575. <https://doi.org/10.1038/pr.2013.136>
- Gee, A. H., Barbieri, R., Paydarfar, D., & Indic, P. (2017). Predicting bradycardia in preterm infants using point process analysis of heart rate. *IEEE Transactions on Biomedical Engineering*, 64(9), 2300–2308. <https://doi.org/10.1109/TBME.2016.2632746>
- Goldberger, A. L., Amaral, L. A. N., Glass, L., Hausdorff, J. M., Ivanov, P. Ch., Mark, R. G., Mietus, J. E., Moody, G. B., Peng, C. K., & Stanley, H. E. (2000). PhysioBank, PhysioToolkit, and PhysioNet: Components of a new research resource for complex physiologic signals. *Circulation*, 101(23), e215–e220. <https://doi.org/10.1161/01.CIR.101.23.e215>
- Harsha, S. S. (2015). SNAPPE-II (score for neonatal acute physiology with perinatal extension-II) in predicting mortality and morbidity in NICU. *Journal of Clinical and Diagnostic Research*, 9(10), SC10–SC12. <https://doi.org/10.7860/JCDR/2015/14848.6677>
- Iqbal, F., Chandra, P., Khan, A. A., Lewis, L. E. S., Acharya, D., Vandana, K. E., Jayashree, P., & Shenoy, P. A. (2023). Prediction of mortality among neonates with sepsis in the neonatal intensive care unit: A machine learning approach: Prediction of Mortality in neonates. *Clinical Epidemiology and Global Health*, 24, Article 101414. <https://doi.org/10.1016/j.cegh.2023.101414>
- Iqbal, F., Chandra, P., Lewis, L. E. S., Acharya, D., Purkayastha, J., Shenoy, P. A., & Patil, A. K. (2024). Application of artificial intelligence to predict the sepsis in neonates admitted in neonatal intensive care unit. *Journal of Neonatal Nursing*, 30(2), 141–147. <https://doi.org/10.1016/j.jnn.2023.07.016>
- Jathanna, R. D., Acharya, D., Lewis, L. E. S., & Makkithaya, K. (2023). Early detection of late onset neonatal sepsis using machine learning algorithms. *Engineered Science*, 26, Article 976. <https://doi.org/10.30919/es976>

- Jha, C. K., & Kolekar, M. H. (2022). Electrocardiogram data compression techniques for cardiac healthcare systems: A methodological review. *IRBM*, 43(3), 217–228. <https://doi.org/10.1016/j.irbm.2021.06.007>
- Joshi, R., Kommers, D., Oosterwijk, L., Feijs, L., van Pul, C., & Andriessen, P. (2020). Predicting neonatal sepsis using features of heart rate variability, respiratory characteristics, and ECG-derived estimates of infant motion. *IEEE Journal of Biomedical and Health Informatics*, 24(3), 681–692. <https://doi.org/10.1109/JBHI.2019.2927463>
- Karippacheril, J., & Ho, T. (2013). Data acquisition from S/5 GE Datex anesthesia monitor using VSCapture: An open source.NET/Mono tool. *Journal of Anaesthesiology Clinical Pharmacology*, 29(3), 423–424. <https://doi.org/10.4103/0970-9185.117096>
- Khazaei, H., Mench-Bressan, N., McGregor, C., & Pugh, J. E. (2015). Health informatics for neonatal intensive care units: An analytical modeling perspective. *IEEE Journal of Translational Engineering in Health and Medicine*, 3, 1–9. <https://doi.org/10.1109/JTEHM.2015.2485268>
- Kurul, Ş., van Ackeren, N., Goos, T. G., Ramakers, C. R. B., Been, J. V., Kornelisse, R. F., Reiss, I. K. M., Simons, S. H. P., & Taal, H. R. (2022). Introducing heart rate variability monitoring combined with biomarker screening into a level IV NICU: A prospective implementation study. *European Journal of Pediatrics*, 181(9), 3331–3338. <https://doi.org/10.1007/s00431-022-04534-4>
- Latremouille, S., Lam, J., Shalish, W., & Sant’Anna, G. (2021). Neonatal heart rate variability: A contemporary scoping review of analysis methods and clinical applications. *BMJ Open*, 11(12), 1–18. <https://doi.org/10.1136/bmjopen-2021-055209>
- Legrand, N., & Allen, M. (2022). Systole: A python package for cardiac signal synchrony and analysis. *Journal of Open Source Software*, 7(69), Article 3832. <https://doi.org/10.21105/joss.03832>
- Leon, C., Carrault, G., Pladys, P., & Beuchee, A. (2021). Early detection of late onset sepsis in premature infants using visibility graph analysis of heart rate variability. *IEEE Journal of Biomedical and Health Informatics*, 25(4), 1006–1017. <https://doi.org/10.1109/JBHI.2020.3021662>
- Lipton, Z. C., Kale, D. C., Elkan, C., & Wetzel, R. (2016). *Learning to Diagnose with LSTM Recurrent Neural Networks*. ArXiv Preprint. <https://doi.org/10.48550/arXiv.1511.03677>
- Makowski, D., Pham, T., Lau, Z. J., Brammer, J. C., Lespinasse, F., Pham, H., Schölzel, C., & Chen, S. H. A. (2021). NeuroKit2: A python toolbox for neurophysiological signal processing. *Behavior Research Methods*, 53(4), 1689–1696. <https://doi.org/10.3758/s13428-020-01516-y>
- Mansoor, K. P., Ravikiran, S. R., Kulkarni, V., Baliga, K., Rao, S., Bhat, K. G., Baliga, B. S., & Kamath, N. (2019). Modified sick neonatal score (MSNS): A novel neonatal disease severity scoring system for resource-limited settings. *Critical Care Research and Practice*, 2019, 1–6. <https://doi.org/10.1155/2019/9059073>
- McAdams, R. M., Kaur, R., Sun, Y., Bindra, H., Cho, S. J., & Singh, H. (2022). Predicting clinical outcomes using artificial intelligence and machine learning in neonatal intensive care units: A systematic review. *Journal of Perinatology*, 42(12), 1561–1575. <https://doi.org/10.1038/s41372-022-01392-8>
- McGregor, C., Catley, C., & James, A. (2012). Variability analysis with analytics applied to physiological data streams from the neonatal intensive care unit. In *2012 25th IEEE International Symposium on Computer-Based Medical Systems (CBMS)* (pp. 1-5). IEEE Publishing. <https://doi.org/10.1109/CBMS.2012.6266385>

- Mithal, L. B., Yogev, R., Palac, H., Gur, I., & Mestan, K. K. (2016). Computerized vital signs analysis and late onset infections in extremely low gestational age infants. *Journal of Perinatal Medicine*, 44(5), 491-497. <https://doi.org/10.1515/jpm-2015-0362>
- Moore, W., & Frye, S. (2019). Review of HIPAA, part 1: History, protected health information, and privacy and security rules. *Journal of Nuclear Medicine Technology*, 47(4), 269–272. <https://doi.org/10.2967/jnmt.119.227819>
- Moorman, J. R., Carlo, W. A., Kattwinkel, J., Schelonka, R. L., Porcelli, P. J., Navarrete, C. T., Bancalari, E., Aschner, J. L., Walker, M. W., Perez, J. A., Palmer, C., Stukenborg, G. J., Lake, D. E., & O'Shea, T. M. (2011). Mortality reduction by heart rate characteristic monitoring in very low birth weight neonates: A randomized trial. *Journal of Pediatrics*, 159(6), 900–906. <https://doi.org/10.1016/j.jpeds.2011.06.044>
- Parry, G., Tucker, J., & Tarnow-Mordi, W. (2003). CRIB II: An update of the clinical risk index for babies score. *The Lancet*, 361(9371), 1789–1791. [https://doi.org/10.1016/S0140-6736\(03\)13397-1](https://doi.org/10.1016/S0140-6736(03)13397-1)
- Patural, H., Franco, P., Pichot, V., & Giraud, A. (2022). Heart rate variability analysis to evaluate autonomic nervous system maturation in neonates: An expert opinion. *Frontiers in Pediatrics*, 10, Article 860145. <https://doi.org/10.3389/fped.2022.860145>
- Philips. (2015). *Data Export Interface Programming Guide - Intellivue Patient Monitor & Avalon Fetal Monitor*. <http://incenter.medical.philips.com/doclib/GetDoc.aspx?func=ll&objId=11407611&objAction=Open&AppLibId=1.DAD>
- Poggi, C., Ciarcià, M., Miselli, F., & Dani, C. (2023). Prognostic accuracy of Neonatal SOFA score versus SIRS criteria in preterm infants with late-onset sepsis. *European Journal of Pediatrics*, 182(10), 4731–4739. <https://doi.org/10.1007/s00431-023-05143-5>
- Procianoy, R. S., & Silveira, R. C. (2020). The challenges of neonatal sepsis management. *Jornal de Pediatria*, 96, 80–86. <https://doi.org/10.1016/j.jpeds.2019.10.004>
- Quinten, V. M., van Meurs, M., Renes, M. H., Ligtenberg, J. J. M., & ter Maaten, J. C. (2017). Protocol of the sepsivit study: A prospective observational study to determine whether continuous heart rate variability measurement during the first 48 hours of hospitalisation provides an early warning for deterioration in patients presenting with infection or sepsis to the emergency department of a Dutch academic teaching hospital. *BMJ Open*, 7(11), Article e018259. <https://doi.org/10.1136/bmjopen-2017-018259>
- Ranjit, S., & Kissoon, N. (2021). Challenges and solutions in translating sepsis guidelines into practice in resource-limited settings. *Translational Pediatrics*, 10(10), 2646–2665. <https://doi.org/10.21037/tp-20-310>
- Rao, K. V. K. L. N., Dadabada, P. K., & Jaipuria, S. (2024). A systematic literature review of predictive analytics methods for early diagnosis of neonatal sepsis. *Discover Public Health*, 21, Article 96. <https://doi.org/10.1186/s12982-024-00219-5>
- Shirwaikar, R. D., Acharya, U. D., Makkithaya, K., Surulivelr, M., & Lewis, L. E. S. (2015). Machine learning techniques for neonatal apnea prediction. *Journal of Artificial Intelligence*, 9(1–3), 33–38. <https://doi.org/10.3923/jai.2016.33.38>
- Statello, R., Carnevali, L., Sgoifo, A., Miragoli, M., & Pisani, F. (2021). Heart rate variability in neonatal seizures: Investigation and implications for management. *Neurophysiologie Clinique*, 51(6), 483–492. <https://doi.org/10.1016/j.neucli.2021.10.002>

- van Gent, P., Farah, H., van Nes, N., & van Arem, B. (2019). HeartPy: A novel heart rate algorithm for the analysis of noisy signals. *Transportation Research Part F: Traffic Psychology and Behaviour*, 66, 368–378. <https://doi.org/10.1016/j.trf.2019.09.015>
- Wee, B. Y. H., Lee, J. H., Mok, Y. H., & Chong, S. L. (2020). A narrative review of heart rate and variability in sepsis. *Annals of Translational Medicine*, 8(12), 768–768. <https://doi.org/10.21037/atm-20-148>
- WHO. (2024). *End preventable deaths of newborns and children under 5 years of age*. World Health Organization. https://www.who.int/data/gho/data/themes/topics/sdg-target-3_2-newborn-and-child-mortality
- Zeigler, A. C., Ainsworth, J. E., Fairchild, K. D., Wynn, J. L., & Sullivan, B. A. (2023). Sepsis and mortality prediction in very low birth weight infants: Analysis of HeRO and nSOFA. *American journal of perinatology*, 40(04), 407-414. <https://doi.org/10.1055/s-0041-1728829>

Review Article

Comprehensive Review on Sustainable Dam Infrastructure: Issues and Challenges, Factors Causing Dam Failure and Future Direction in a Globally Changing Climate

**Nur Azwa Muhamad Bashar^{1,2}, Mohd Remy Rozainy Mohd Arif Zainol^{1,3*},
Mohd Sharizal Abdul Aziz⁴, Ahmad Zhafran Ahmad Mazlan⁴,
Mohd Hafiz Zawawi⁵ and Teh Sabariah Abd Manan^{1,6}**

¹*School of Civil Engineering, Engineering Campus, Universiti Sains Malaysia, Seberang Perai Selatan, 14300 Nibong Tebal, Pulau Pinang, Malaysia*

²*Civil Engineering Studies, College of Engineering, Universiti Teknologi MARA, Pulau Pinang Branch, Permatang Pauh Campus, 13500, Pulau Pinang, Malaysia*

³*River Engineering and Urban Drainage Research Centre (REDAC), Engineering Campus, Universiti Sains Malaysia, Seberang Perai Selatan, 14300 Nibong Tebal, Pulau Pinang, Malaysia*

⁴*School of Mechanical Engineering, Engineering Campus, Universiti Sains Malaysia, Universiti Sains Malaysia, Seberang Perai Selatan, 14300 Nibong Tebal, Pulau Pinang, Malaysia*

⁵*Department of Civil Engineering, College of Engineering, Universiti Tenaga Nasional, 43000, Kajang, Selangor Darul Ehsan, Malaysia*

⁶*Institute of Tropical Biodiversity and Sustainable Development, Universiti Malaysia Terengganu, 21030, Kuala Nerus, Terengganu, Darul Iman, Malaysia*

ABSTRACT

A dam is a hydraulic structure built to achieve the Sustainable Development Goals (SDGs) and provide a safe and reliable water supply in a world where climate change is severe. This article provides a comprehensive review of the sustainability aspects of dams in terms of current issues and challenges in dam safety and factors causing dam failure based on the selected case studies. In

addition, the selected dam safety guidelines are compared and addressed with the studied issues, challenges and factors leading to dam failure, as these two elements represent an integrated relationship. Future directions are identified to highlight high-risk scenarios and fascinating research areas for dam sustainability. The issues and challenges identified are mainly related to climate change impacts and operations. This study offers a wealth of benefits, such as the identification of factors leading to a failure

ARTICLE INFO

Article history:

Received: 01 August 2024

Accepted: 23 January 2025

Published: 04 April 2025

DOI: <https://doi.org/10.47836/pjst.33.3.14>

E-mail addresses:

nurazwa.bashar@student.usm.my; nurazwa.bashar@uitm.edu.my

(Nur Azwa Muhamad Bashar)

ceremy@usm.my (Mohd Remy Rozainy Mohd Arif Zainol)

msharizal@usm.my (Mohd Sharizal Abdul Aziz)

zhafran@usm.my (Ahmad Zhafran Ahmad Mazlan)

Mhafiz@uniten.edu.my (Mohd Hafiz Zawawi)

tehsabariah@gmail.com (Teh Sabariah Abd Manan)

*Corresponding author

(hydrological impacts, geotechnical condition, geological characteristics and ageing of the structure), improvements in decision-making (shortened time scale) and important fundamental research (fluid-structure interactions) for the modification of emergency plans and the development of early warning systems. In addition, the current study could provide a solid reference for accurate formulation and amendment of design standards, selection of reliable dam construction methods based on the factors of previous dam failures, and appropriate dam safety measures (monitoring and emergency response). In a nutshell, dam safety evaluation is crucial for the sustainability of dams, for accurate engineering decisions on regular maintenance measures and for protection against dam failures.

Keywords: Climate change, dam failure, dam safety, dam sustainability, failure factor

INTRODUCTION

The dam provides an alternative to clean hydropower for a continuous energy supply from an emission-free source, water. Dam infrastructures also serve as a solution to global water scarcity, severe droughts and flood mitigation. However, the constant stress of global climate change has significant disadvantages for these megastructures, particularly limited water storage capacity and structural ageing (Concha et al., 2023; Fluixá-Sanmartín et al., 2018; Islam et al., 2024; Lazin et al., 2023; Liu et al., 2022; Ma et al., 2024; Milly et al., 2002; Mortey et al., 2019; Sun et al., 2022). Climate change has caused hydro-geo-meteorological disasters such as earthquakes and extreme rainfall patterns (leading to flooding and flash floods) (Al-Fugara et al., 2023; Alcocer-Yamanaka et al., 2020; Hasan, 2015; Lee et al., 2022; Wieland, 2016), as well as seasonal flooding and landslides triggered by debris flows (Bocchiola & Rosso, 2014; Carneiro et al., 2022; Chang et al., 2022; Hirabayashi et al., 2013; Hu & Huang, 2017; Lee et al., 2022; Milly et al., 2002; Saber et al., 2022). Soil erosion has led to a sedimentation problem in the downstream section of the dam (Bai et al., 2020; Kondolf & Yi, 2022; Saber et al., 2022). Therefore, a holistic integration of sustainable dam management, monitoring and surveillance approaches is equally important. The adverse effects of climate change are manageable. Continuous inspection, monitoring, and data analysis over a certain period guarantee the long-term viability of the infrastructure and provide a control plan for the early prevention of structural damage, which is crucial as part of the technical measures (Yavaşoğlu et al., 2018). This initiative is in line with the United Nations Sustainable Development Goals (SDGs): No. 6 (Clean Water and Sanitation) and No. 13 (Climate Action) (Jensen, 2022; SPANCOLD, 2017).

The safety of dams has been an important issue for operators, engineers and policymakers around the world for several years, as it can harm socio-economic aspects. The sustainability of dams, especially the structural aspect, is crucial for the smooth operation of dams, operational safety, adequate maintenance and suggestions for short and long-term emergency planning (Wieland, 2016). Safety has been an issue in the construction

of dams for almost half a century; for example several high-profile dam failures, such as the collapse of the 230-metre-high Oroville Dam in 2017 (France et al., 2018; Stelloh et al., 2017; White et al., 2019) and the concrete slab spillway-2 of the Toddbrook Dam in England during the flood in August 2019 (Heidarzadeh & Feizi, 2022). Another dam failure event is the collapse of the Niedów earth fill dam due to extreme rainfall and flooding in 2010 (Kostecki & Banasiak, 2021; Kostecki & Rędownicz, 2014). Several deficiencies were identified in the reported incidents: insufficient design capacity, substandard material, environmental aspects, hydraulic impact and geotechnical failure of the dam. Consequently, the development of future dams (design and construction) and renovation works should prioritise the amendment of design standards, real-time monitoring, on-site inspection and maintenance to meet current and future conditions.

The spillway was built primarily to channel and control the flow of water from the reservoir into the downstream and lower reaches (Chanson, 1994). This structure should be operated efficiently to ensure its stability and minimise the impact of dam overtopping (Gu et al., 2017). Proper design of the spillway is, therefore, crucial to guarantee the functionality of the structure throughout its operational life (Kocaer & Yazar, 2020). Conventionally, the spillway was designed based on the PMF (Probable Maximum Flood) criteria and the meteorological and hydrological conditions of the site. The flow over the spillway has a higher velocity and high kinetic energy, namely turbulence. Therefore, a sedimentation basin was provided at the end of the spillway to minimise this turbulent effect and avoid erosion and sedimentation problems in the downstream part of the dam. The design of the sedimentation basin depends on the hydraulic jump characteristics and the underwater depth (Peterka, 1984).

This article aims to shed light on the overall concept of sustainability for hydraulic structures and water supply conservation under changing climatic conditions. Furthermore, the trending and rising issues of climate change uncertainties, ageing infrastructure, especially high dams, dams without any real-time monitoring system, requirement on the revised design guidelines and rising concern on the environmental standards challenge the sustainability, safety and security of the dam sustainability. This study aims to conduct a comprehensive review of the published and current literature related to dam sustainability, particularly dam safety and security. The specific objectives of this study are (1) to identify the key issues and challenges which may jeopardise the dam sustainability, (2) to evaluate the factors causing dam failure based on the analysed key issues and challenges and (3) To evaluate the adequacy of selected established dam safety guidelines on addressing the climate change based on reviewed issues and challenges as well as factors causing dam failure. It provides a comprehensive overview of dam safety by highlighting the causes of threats and challenges to dam safety through selected case studies. Additionally, it is a good reference source for stakeholders (authorities, policymakers, planners,

technical experts, designers and consultants) in the decision-making process for selecting appropriate measures, constructing new dams and/or rehabilitating damaged or ageing dam infrastructure.

MATERIAL AND METHODS

This study aims to provide a comprehensive study: a systematic review of recent research on dam safety aspects of supporting dam sustainability under climate change uncertainties. This study emphasises the current dam safety aspect, including dam safety guidelines, the issues and challenges of dam safety and dam failure mechanisms based on the existing monitoring effort, which compromises the structural integrity of the dam. This study preferred to apply the reporting style based on the systematic reviews and meta-analyses (PRISMA) method (Moher et al., 2009). The chosen method is reliable and feasible as it covers the appropriate approach for disaster management (Shaffril et al., 2021). This study intends to delve into the following specific questions: What factors affect the safety, particularly dam safety issues, and what are the challenges that can jeopardise the sustainability of dams? Are there specific factors causing dam failure based on the issues and challenges analysed? Are the available dam safety guidelines adequate to address the safety issues caused by climate change? What is the current approach and future direction to promote dam sustainability?

Identification

The systematic review comprises four key stages in the selection of appropriate articles to be considered in this study. The first stage started with choosing a recent researchable study title based on the current issue in the disaster management field. The process followed at the second stage with the selection and decision of the appropriate keywords using an authorised medium such as act, regulation, guidelines, independent expert report, previous research, database suggestion (e.g. SCOPUS), thesauruses.com, encyclopaedias, and dictionaries. Several applicable electronic databases, such as official government websites and the Web of Science (WOS), were used for the search process after the final decision on the main keywords and associated keywords (similar to the main keywords) at the third stage. In the fourth stage, the search process was conducted based on the decided keywords based on the designed search string.

Searching Strategy

This study used two searching techniques (systematic and manual searching) and numerous electronic databases to ensure a rigorous search process and data validity. The explored electronic databases used were the Official Regulated Body or Government Website (Federal

Emergency Management Agency, International Commission on Large Dams, Department of Irrigation and Drainage Malaysia, United States Society on Dams, The British Dam Society, New South Wales Government, India Government, WOS, SCOPUS, ScienceDirect, Taylor and Francis, Emerald, Springer, American Society of Civil Engineers (ASCE). The search process was conducted in three stages: January 2024 (first searching process), August 2024 (Subsequent searching process), and October 2024 (based on the suggestion for this study). The main keywords such as *climate change*, *dam failure*, *dam safety*, *dam sustainability* and *failure factor* were searched in the electronic databases based on the proposed title and the research question developed. Several additional keywords similar to the main keywords in the second stage were identified, including *climate uncertainty*, *climate risks*, *catastrophic failure*, *dam failure*, *dam safety guidelines*, *dam security*, *earthquake*, *extreme weather*, *flood*, *flooding*, *hydraulic structure*, *spillway*, and *structural integrity*. The single and combinations of these keywords were processed using several search functions, for example, field code function (TITLE-ABS-KEY and TS) and Boolean operators ('AND' or 'OR') in two databases: WOS and SCOPUS. Manual searching: Handpicking was used in databases other than WOS and SCOPUS (Shaffril et al., 2021).

Screening

The screening process involves the selection of the related paper based on criteria such as type of material, year of publication, language and scope of the paper. In this study, the chosen materials were safety guidelines, research-based, systematic review, literature review, and scoping review, published in English between 2014 and 2024. Additionally, the scope of the selected paper should be aligned with the identified main and associated keywords. Additionally, in WOS, the consideration of search criteria is followed in specific editions: Science Citation Index Expanded (SCI-EXPANDED), Conference Proceedings Citation Index-Science (CPCI-S), and Emerging Sources Citation Index (ESCI). A total of 4968 potential materials were identified from the listed databases based on the two applied methods and the first on-site database screening process.

Eligibility Criteria

Several eligibility criteria were determined in this study to ensure the study is specific and aligned with the title and objectives. Criteria such as the scope of the paper, including the title and research content, are compulsory to ensure the clarity, quality and consideration of exclusion criteria (as mentioned in the screening stage) for the current study.

Data Abstraction and Analysis

Several extensive assessment approaches followed carefully based on PRISMA guidelines were considered repetitively for the screening, analysis, and synthesised processes to ensure the validity and exclusiveness of the current study (Moher et al., 2009). Notably, the selected papers should align with the scope of the current study. Figure 1 illustrates the comprehensive process of paper selection for the current study. A total of 1098 papers (including dam safety guidelines) were selected and compiled in the Endnote. Subsequently, 1080 papers were eliminated due to being outside the scope and inaccessible and ended up with 18 papers (including dam safety guidelines) that were considered eligible for the critical review.

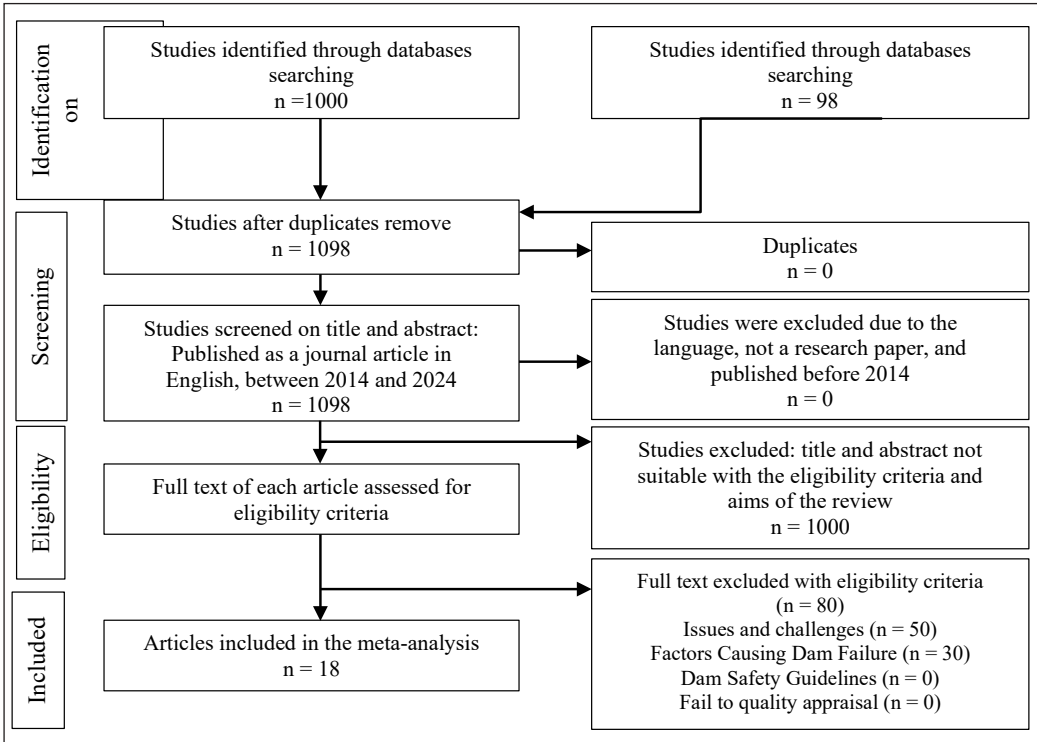


Figure 1. PRISMA flow diagram of dam sustainability: issues and challenges on dam safety, factors leading to dam failure and current approaches to promoting the sustainability of dams

RESULT AND DISCUSSION

Identification of reliable dam safety issues and challenges is critical to supporting dam sustainability and keeping it in line with the SDGs. The issues and challenges are related to the mechanism of dam failure, as the key factors have been identified based on the published and reported case studies. The combination of issues and challenges and the

factors causing dam failure were combined to provide an extensive explanation of the focus area. In addition, the guidelines published by the authorised organisation are considered important and appropriate in addressing the issues and challenges related to the mechanism of dam failure. These contexts may provide a future direction for the fascinating research in this area by highlighting the limitations and gaps in the reviewed literature.

ISSUES AND CHALLENGES OF DAM SAFETY

The safety of dams is an important element in ensuring the sustainability of critical infrastructure. Therefore, rigorous measures are required to preserve the infrastructure and ensure the continuous operation of the system. Diverse research has been conducted on non-structural and structural measures to support the sustainability of dams. However, the criteria for dam sustainability should be linked to the root cause, namely the issues and challenges. Identifying issues and challenges can reveal the scope of the main problem and the associated factors causing the dam failure and lead to an appropriate technical decision-making process.

The identified factors that potentially jeopardise sustainable dams can be divided into environmental, structural integrity, structural design and operational, management and maintenance factors as summarised in Table 1 (Balmforth, 2020; France et al., 2018; Goodling et al., 2018; Heidarzadeh & Feizi, 2022; Hollins et al., 2018; Hughes, 2020; Koskinas et al., 2019; Kostecki & Rędowicz, 2014; Patra et al., 2024; Vahedifard et al., 2017; White et al., 2019; Xiao et al., 2022; Xie et al., 2022; Yang et al., 2024). The environmental factor, namely climate change (CC), which is closely related to the rising hydrological stress, is known to be the most important among the others (Heidarzadeh & Feizi, 2022). The hydrological factors, such as extreme precipitation and flooding, lead to runoff fluctuations and the failure of structures, especially ageing and deteriorated dams (Heidarzadeh & Feizi, 2022; Hollins et al., 2018; Koskinas et al., 2019). In addition, soil erosion and sedimentation occur downstream due to the high flow velocity during floods (Heidarzadeh & Feizi, 2022). These factors jeopardise the safety and sustainability of the dams. Therefore, the triangular relationship between the concept of dam sustainability and the exact relationship between the SDGs and dam sustainability is emphasised. The increasing trend of hydrological factors leading to dam failures is alarming, as this has enormous implications for the entire system, such as socio-economic and ecological aspects.

FACTORS CAUSING DAM FAILURE

The factors of dam failure can be viewed from different angles and analysed according to geometric characteristics (type of dam, height of dam, size of dam), hydro-meteorological characteristics (climatic conditions: persistent rainfall, natural hazards, earthquakes, infiltration of seepage water: internal erosion), geotechnical characteristics (type of rock,

type of soil), structural characteristics (ageing) and type of failure mode (cascade failure, partial failure and total failure). These factors of dam failure are derived from the issues and challenges in dam safety, as in Table 1. Hydro-meteorological and geotechnical characteristics have a significant influence on the factors and mechanisms of dam failure. Controlling these factors is a challenge due to the severe effects of climate change. However, the exacerbated impacts can be minimised with appropriate controlled measures, and intervention can be made. This approach can reduce the devastating effects on the safety of dams in the short or long term. Therefore, a holistic methodological framework for dealing with the factors of dam failure is required for failure control right from the planning stage. Consequently, this factor deeply contributed to analysing and managing the dam failure mechanism.

The condition of the construction site and the behaviour of the structure should be recorded with real-time monitoring instruments, and possible malfunctions should be eliminated to ensure the highest safety of the dam. Based on the collected or historical data, prediction models can be proposed for early failure prediction, e.g., dam failure simulation. However, careful data management (up-to-date data, error-free data, accurate processing medium) is essential to avoid incorrect predictions of events and types of failure modes. In this way, a dam failure can be predicted at an early stage, an early warning system can be developed, and a warning message can be reliably disseminated. Catastrophic events could be controlled, and the massive losses associated with a dam failure could be minimised. Socio-economic losses and environmental impacts are also minimised.

Climate Change, Hydrological and Hydraulic Factors

The current and future effects of climate change are devastating worldwide. Climate change can drive and contribute to changes in hydrological patterns, e.g. from low to high rainfall (extreme) within a short period. For example, extreme precipitation patterns and capacities change the hydraulic flow patterns in surface reservoirs (reservoirs) and rivers, e.g., turbulent and high-velocity flows.

The 29-metre-high Sardoba Dam in Uzbekistan was supposed to hold 922 million cubic metres of water. Unfortunately, the dam burst on 1 May 2020 after several days of extreme rainfall and strong winds. The incidents began with the breach of the western embankment wall of the Sardoba Dam due to the effects of uncontrolled water loading. The Niedów Dam collapsed due to extreme rainfall and the 100-year flood (Kostecki & Banasiak, 2021). The gate was under maintenance and was closed during the catastrophic event. Therefore, the upper banks were flooded with massive amounts of water, which had an impact on the roads and other facilities.

The Toddbrook Dam partially collapsed, mainly at the auxiliary spillway, because floodwaters flowed uncontrollably through the spillway at a high velocity of 15 m/s due

to rainfall and flooding (Heidarzadeh & Feizi, 2022). In the case of the spillway problem at Oroville Dam, Lake Oroville released water over the main spillway a few days before the incident to prepare for an additional inflow of 1550 m³/s (Koskinas et al., 2019). The discharge was released due to the rise in water levels in Lake Oroville as a result of the effects of the prolonged and extreme rainfall (White et al., 2019).

To summarise, most of these incidents are due to the effects of global climate change caused by human intervention. Therefore, protecting the global climate is essential to preserving and prolonging the sustainability of dams. In the case of a new project, a thorough environmental impact assessment and cost-benefit analysis should be considered to understand the post-construction impacts on the existing system in the vicinity of the proposed project.

Geological and Geotechnical Conditions

A site investigation from a geological and geotechnical point of perspective is important to ensure the rock identification and soil stability of the selected site, especially for hydraulic engineering projects. The factors identified are important for the selection of the correct foundation size, the reinforcement works for soil strengthening and the settlement value over the years. Therefore, a special assessment is carried out before, during, and after construction to avoid any disadvantages to the structure. The physical assessment was compiled together with the robust equipment (i.e. satellite and radar data) for the site inspection and simulation work to determine and predict the difference between the two factors.

Three data sets from Google Earth, namely ICESat-2 data (satellite-based medium), Sentinel-1 SAR data (multi-geometry) and optical images from Sentinel-2 satellites, were used together with global precipitation measurements (GPM) to determine factor-induced damage for the Sardoba Dam in Uzbekistan. The observed images and the collected analyses identified internal erosion as the main cause of failure (Xiao et al., 2022). Other studies showed that the breached section of the Sardoba Dam in Uzbekistan had a settlement difference of about 4.7 cm. Secondary consolidation contributes to post-construction deformations. In addition, the differential settlement and water loads lead to structural transverse cracks in the dam. The recent study relied on hybrid methods: hazard framework, dam-related hazard investigation (RSDHI) and numerical modelling (Xie et al., 2022).

Several landslides occurred at Toddbrook, with the critical area being on the upstream slope of the dam. Long-term systemic design and construction issues, including poor site investigation and foundation stability (poor bedrock condition), have been identified as a possible partial failure factor of the 49-year-old Oroville Spillway (Koskinas et al., 2019). Rapid water runoff triggered landslides and erosion during prolonged heavy rainfall (Heidarzadeh & Feizi, 2022; Koskinas et al., 2019; Martin et al., 2024).

Overall, a proper site investigation and evaluation is required to understand the geographical condition of the site. This is crucial for proper site selection to avoid future incidents. Once the work is completed, the selected project site should be compared with other similar project sites in the vicinity and a critical technical assessment should be carried out by a certified person (geotechnical engineer/geologist). In addition, appropriate numerical simulation and assessment tools are required, which will have a major impact on the project and allow precautions to be taken if the project decides to proceed with construction work.

Inadequate Design Capacity, Design Flaws, Ageing and Structural Failure

Structural design has proven to be an important criterion for the functionality, safety and sustainability of infrastructures. With the help of numerical simulations, malfunctions can now be recognised early. However, the effects of climate change, hydrological influences and hydraulic factors are rarely predicted. Therefore, the dynamic properties of the structure are most strongly influenced by the changing static and dynamic loads.

In the case of the Niedów Dam, the foundation of the Niedów Dam was eroded by a catastrophic flood. The concrete crown had broken and was washed away terribly quickly into the downstream section (Kostecki & Rędownicz, 2014). The breach damaged the concrete slab first, followed by the abutments and the retaining wall. These structures could not withstand the increased flow and water pressure upstream. The shorter event caused a massive flood wave in the downstream section (Kostecki & Banasiak, 2021).

Hybrid methods (field studies, desk studies and numerical modelling) and cascade models focusing on the failure mechanism of the Toddbrook Dam were investigated (Heidarzadeh & Feizi, 2022). The capacity of the auxiliary spillway was unable to withstand the unprecedented extreme rainfall, resulting in overtopping and failure of the structure. The slabs on the surface of the spillway were breached by the combined effects of physical problems and internal forces (dense vegetation), water injection between the slab spacing and uplift pressure within the slabs. The lightweight, thin slab section (15.0 cm) was designed and constructed with limited steel reinforcement and poor joints between slab sections (without water bars and in vertical joints). Therefore, the supported slabs shrank and moved due to the uplift pressure within the slab section. In addition, the eroded foundation is affected by the high flow velocity and water injection into the slab and foundation.

Furthermore, no sedimentation basin was constructed to control the scour problem caused by the water transfer upstream and across the spillway. Another independent checker (Balmforth, 2020) came to the same conclusion as (Hughes, 2020) that the failure was due to design problems (thin concrete slabs and no internal pipework system for water flow to the spillway) and poor maintenance (insufficient sealant between the joints with the

concrete slabs, severe cracking in the concrete slabs and dam crest, and dense vegetation between the slab joints). In another case, the formation of a large hole on the surface of the concrete spillway at Oroville Dam was noted due to the intermittent pattern of flowing water (Hollins et al., 2018; Koskinas et al., 2019). Theoretically, the continuous inflow into Lake Oroville exceeds the minimum flood control elevation, resulting in frequent overflows. This situation limits repair time and eliminates the need for remedial measures. As a result, the increased flood water flows continuously over the main spillway and the unclosed weir. The flowing water then moves dramatically over the collapsed concrete partition wall to the slope and experiences soil erosion. The additional spillway (without a closed weir) was built to absorb the overflow from the main spillway and has never been tested on actual events (Koskinas et al., 2019).

Poor Maintenance and Operation

Excellent and smooth management of spillway maintenance is required to ensure the optimal operating condition of the hydraulic infrastructure. Therefore, an appropriate time base (weekly inspection or case-by-case inspection of the changes in discharge and built infrastructure elements) is required to avoid shock incidents. Toddbrook has experienced two spillway incidents, the first in 1964 and the most recent during the 2019 flood (Hughes, 2020). The capacity of the main spillway was supplemented by an additional spillway that could be used for overflow or maintenance purposes. Unfortunately, the constructed auxiliary spillway also failed due to poor monitoring and maintenance, resulting in a dense cover of vegetation on the surface of the concrete spillway (Balmforth, 2020; Heidarzadeh & Feizi, 2022; Hughes, 2020). The frightening incident at the highest dam in the USA, the Oroville Dam (235 m), was taken seriously, especially the emergency measures and the management and maintenance of the spillway. The presence of a hole on the surface of the spillway remained undetected. However, the water flowing over the spillway showed a rare pattern during the incident (Hollins et al., 2018; Koskinas et al., 2019).

Seepage and Drain Failure

A reliable and robust pipework and drainage system is essential for the smooth operation of the spillway. However, this system is not easily visible during physical inspection. The removal of the slabs on the surface of the spillway during the Oroville incident shows internal erosion due to seepage and failure of the internal drainage (Hollins et al., 2018; Koskinas et al., 2019). This poses a high risk to the dam and can lead to its catastrophic failure.

Table 1
Safety issues and challenges in dam engineering

Category/ Issue(s)	Challenge(s)	Parameter(s)/ Variable(s)	Quantitative Data	Qualitative Data	Method	Dam and Country (size and type)	Researcher
Environmental Factor	Hydrological stress	Precipitation Water speed Reservoir volume	Rainfall rate Velocity (15 m/s) Volume (1.29 million m ³)	Flooding frequency Maximum capacity of reservoir	Physical Inspection (on-site evaluation)	Toddbrook Dam, England, United Kingdom	(Balmforth, 2020; Heidarzadeh & Feizi, 2022; Hughes, 2020)
Structural Integrity factor	Hydrological stress	Material degradation Concrete cracking Damaged foundation	Level of degradation (severe)	Ageing Infrastructure	Mixed method (qualitative analysis and quantitative modelling, namely cascading risk analysis model)	(24-m high and zoned earth-fill dam with a clay core)	
Design factor	Flaws in spillway-2 design	Concrete slab	Concrete slabs design (15-m thickness without any reinforcement)	Inadequate concrete design			
Structural Design factor	Flaws in spillway-2 design	Spillway profile	Designed slope (based on the downstream slope of the embankment – 2H:1V)	Inadequate spillway profile			
Design factor	No stilling basin for sediment collection	Erosion Sedimentation	Level of degradation (severe scouring) Sedimentation rate (severe sediment deposition)	Old dam built in 1840			
Operational Factor	Maintenance frequency and cost of repair	Maintenance frequency	Regular maintenance (based on the	Inadequate maintenance (growth of vegetation and trees)			

Table 1 (continue)

Category/ Issue(s)	Challenge(s)	Parameter(s)/ Variable(s)	Quantitative Data		Qualitative Data	Method	Dam and Country (size and type)	Researcher
Environmental Factor	Hydrological stress Seismic stress	Precipitation	Annual rainfall	Gradually rainfall	pattern	Case Study	Oroville Dam, United States (235-m high and zoned earth-fill embankment structure)	(Goodling et al., 2018; Koskinas et al., 2019; White et al., 2019)
		Flood volume	Winter Storm	Flooding frequency		(using		
		Water speed	5392 m ³ /s	Maximum capacity	resilience	framework)		
Structural Integrity Factor	Hydrological stress	Reservoir volume	Velocity (15 m/s)	of reservoir			Oroville Dam, United States (235-m high and zoned earth-fill embankment structure)	(France et al., 2018; Goodling et al., 2018; Hollins et al., 2018; Koskinas et al., 2019; Vahedifard et al., 2017)
		Type of flow	Volume (59.6 million m ³)	Turbulent flow				
			Level of degradation (severe)	Ageing Infrastructure		Physical Inspection (on-site evaluation)		
Management and operational Factors	Hydrological stress Severe main spillway damage Untested auxiliary spillway	Material degradation	Not related	The capability of the main spillway and untested auxiliary spillway		Case Study (using resilience framework)	Oroville Dam, United States (235-m high and zoned earth-fill embankment structure)	Koskinas et al., 2019; Vahedifard et al., 2017)
		Concrete cracking Damaged spillway surface						
Environmental Factor	Hydrological stress Spillway foundation Seepage problem	Decision-making					Oroville Dam, United States (235-m high and zoned earth-fill embankment structure)	Koskinas et al., 2019; Vahedifard et al., 2017)
		Spillway material	Level of degradation (severe)	Ageing Infrastructure Internal deterioration		Combination of methods (field investigations, failure analysis, and numerical modelling)		
Structural Design factor	Flaws in floor slab design Flaws in drain design	Invert slabs	Inadequate drains capacity				Oroville Dam, United States (235-m high and zoned earth-fill embankment structure)	Koskinas et al., 2019; Vahedifard et al., 2017)
		Slab dimension Drain dimension and capacity Pressure	Drain capacity (small) Level of water pressure (high)					

Table 1 (continue)

Category/ Issue(s)	Challenge(s)	Parameter(s)/ Variable(s)	Quantitative Data	Qualitative Data	Method	Dam and Country (size and type)	Researcher
Environmental Factor	Hydrological stress	Precipitation Reservoir volume	Rainfall rate (Heavy rainfall) Volume (922 million m ³)	Flooding frequency Maximum capacity of reservoir	Earth observation techniques Satellite- based monitoring tools	Sardoba Dam, Uzbekistan (32-m high and U-shaped earthen dam)	(Xiao et al., 2022; Xie et al., 2022)
Environmental Factor	Geotechnical stress	Soil settlement	Local differential settlement (~4.7 cm) Maximum settlement at North Bank (~270 mm)	Settlement frequency	Remote sensing-based Multi- platform approach		
Structural Integrity Factor	Hydrological stress Structural stress	Transverse structural crack	Deformation	Breaching frequency			
Environmental Factor	Hydrological stress	Precipitation Water level Reservoir volume	Rainfall rate Water level height (fluctuation) Volume capacity (18.5 billion m ³)	Flooding frequency Maximum capacity of reservoir	Multi-source satellite data analysis	Kakhovka Dam, Ukraine (30-m tall and Earth-fill embankment with gravity sections)	(Yang et al., 2024)
Maintenance and Operational Factors	Maintenance frequency Mode of operation (protocol) Military conflict	Maintenance frequency	Restricted Maintenance capacity	Restricted areas and conflicting conditions cause potential maintenance delays and late notification of structural deterioration.	Meteorological reanalysis Dam design criteria assessment		

Table 1 (continue)

Category/ Issue(s)	Challenge(s)	Parameter(s)/ Variable(s)	Quantitative Data		Qualitative Data	Method	Dam and Country (size and type)	Researcher
Environmental Factor	Hydrological Stress Seismic Vulnerability	Discharge data Seismic data Volume rate	Discharge capacity (16,500 m ³ /s)		Flooding frequency	Parametric analysis	Koyna Dam, Maharashtra, India (103-m tall and Concrete Gravity Dam)	(Patra et al., 2024)
			Seismic rate of Koyna (magnitude ~6.5) Volume capacity (2,780 million m ³)		Seismic prone area	2D structural modelling techniques		
Design Factor	Design Limitations (Older Dam) Variability in Material and Structural Parameters (Older Dam)	Seismic data	Not measured		The seismic factor is not included in the design			
Environmental Factor	Hydrological Stress Seismic Vulnerability	Discharge data Seismic data Volume rate	Discharge capacity (5,700 m ³ /s)		Flooding frequency	Parametric analysis	Pine Flat Dam, California, United States (122-m tall and Concrete Gravity Dam)	(Patra et al., 2024)
			Seismic rate of Pine Flat (not reported) Volume capacity (1,000 million m ³)		Seismic prone area	2D structural modelling techniques		
Design Factor	Design limitations (Older Dam) Variability in material and structural parameters (Older Dam)	Seismic data	Not measured		The seismic factor is not included in the design	Concrete damage plasticity model		

Table 1 (continue)

Category/ Issue(s)	Challenge(s)	Parameter(s)/ Variable(s)	Quantitative Data	Qualitative Data	Method	Dam and Country (size and type)	Researcher
Environmental Factor	Hydrological stress	Precipitation Water level Reservoir volume	Rainfall rate Water level height (fluctuation) Volume capacity (18.5 billion m ³)	High-intensity rainfall Flooding frequency Maximum capacity of reservoir Flooding frequency	Hydrodynamic modelling Observational analysis (Collection of Empirical Data) Impact Analysis	Niedow Dam, Poland (17-m height and Concrete Gravity Dam)	(Kostecki & Rędownicz, 2014)
Management factor	Flood management and extreme weather (insufficient technical guidelines) Lack of emergency preparedness	Not measured	Not measured				
Design factor	Structural design limitation (Older Dam)	Structural failure risk Erosion resistance Hydraulic capacity	Lack of new reinforcement size and quantity Erosion rate Flow rate	Structural risk (deterioration) Overflow capacity and not designed to cater to extreme event			

THE ESTABLISHED DAM SAFETY GUIDELINES

The International Commission on Large Dams (ICOLD) is an international non-governmental organisation and was founded with the participation of members from various regions (Europe, Asia, America, Africa, and Oceania) such as the United States Society on Dams (USSD), the British Dam Society (BDS), the Australian National Committee on Large Dams (ANCOLD), and the Malaysian National Committee on Large Dams (MyCOLD). ICOLD has provided general standards and guidelines for the construction of dams and safety guidelines, a valid global database on large dams built, and documentation on dams registered worldwide, including a database on dam failures (data on dam failures and technical reports on dam failures from participating members).

The ICOLD guidelines are comprehensive in a global context but do not address the specific guidelines for participating countries. Participating countries should develop their guidelines based on the main organisation (e.g., MyCOLD) in the participating country or provide internal and extended specific guidelines based on the primary guidelines, which can be adapted to the state or specific organisation. Table 2 shows the global dam safety guidelines and associated parameters for evaluation. Based on the listed guidelines, MyDAMS and Queensland are said to be essential in consideration of climate changes compared to Federal Emergency Management Agency (FEMA) with a specific focus on climate-specific assessment parameters (extreme rainfall and seasonal droughts, which can exacerbate dam strain and potential failure risks) (DRDMW, 2024; FEMA, 2023; Government of Malaysia et al., 2017). Hence, the improvement of FEMA in terms of long-term climate change adaptation is essential to provide a robust framework for dam safety. Another comparison is in terms of incorporating artificial intelligence (AI) in monitoring dam safety. Currently, the MyDAMS is a good digital data collection with an extensive data collection system. However, this guideline has flaws in the framework, such as immediate risk response and coordinated safety protocols. This also applies to the New South Wales (NSW) and Queensland frameworks, where considering AI is vital to provide a robust framework that can be applied as a real-time monitoring system. This improvement is associated with the context of FEMA, which considers the emergency preparedness model to support dam sustainability (DRDMW, 2024; FEMA, 2023; NSW Government, 2021; Government of Malaysia et al., 2017). The guidelines issued by the Central Water Commission on the safety of dams are limited to basic climatic considerations. Therefore, these guidelines should follow other enhanced guidelines.

Table 2
Global dam safety guidelines

Guideline Source	Name of safety guideline	Guideline level	Specific area	Limitations/Gaps	Climate change considerations	Suggestion for Improvement	Reference
MyCOLD	Malaysia Dam Safety Management Guidelines (Mydams)	National	Digital Monitoring	Lack of comprehensive guidelines Risk management is obsolete and not properly addressed	Minimal climate change aspect	Expanding digital monitoring to include the aspect of climate resilience	(Government of Malaysia, 2017)
Federal Emergency Management Agency	Federal Guidelines for Dam Safety	National	Flood Risk Management	Limited focus on the structural aspect	Limited to the flood risk aspect	Integrating proactive flood and structural risk frameworks	(FEMA, 2023)
Central Water Commission, India	Guidelines for Safety Inspection of Dams	National	Routine Inspection Framework	Digital integration of data is limited Lack of quantitative risk aspect	Basic climate consideration	The development of resilience frameworks	(Central Water Commission, 2018)
New South Wales	Dams Safety NSW Guideline Dam safety management system	State/ Regional	Regular Safety Inspections	The emergency aspect is limited Focus on regular inspection	Minimal climate change aspect	Promoting real-time monitoring and a practical flexibility approach	(NSW Government, 2021)
Queensland	Dam Safety Management Guideline	State/ Regional	Risk Assessment and Monitoring	Reactive rather than predictive	Moderate climate considerations	The development of tools to predict extreme climate impacts should follow the ICOLD	(DRDMW, 2024)

FUTURE DIRECTION OF THE RESEARCH WORK

The advantages, constraints, best practices and gaps have been identified and discussed. Therefore, several future research studies can be conducted to address various non-structural measures.

Comprehensive Guidelines for Disaster Preparedness

The current draft of the guidelines should consider disaster risk reduction parameters such as the climate change index, two- and three-dimensional flows, and real-type flows (turbulent) as additional criteria in the disaster risk reduction guidelines. Therefore, after a thorough discussion with the industry and the scientific community (policymakers, engineers and researchers), the published guidelines will be revised to include these parameters. In addition, the prepared guidelines should be carefully reviewed in several stages by a competent person (a professional engineer) and verified by the government authority and the international or national engineering society. The phased approach is crucial to cover the fundamentals and the technical aspects. In addition, major revisions, such as the current extreme indicator and sedimentation accumulation, require new guidelines for designing and managing the specific case study. Therefore, the problem raised can be applied to designing new dams and improving old or ageing dams. This is consistent with the rising issues and challenges as well as the dam failure mechanism aspect related to climate change issues (hydrological factor) (Heidarzadeh & Feizi, 2022; Hollins et al., 2018; Koskinas et al., 2019; Kostecki & Rędowicz, 2014).

Development of a Holistic Framework for Dam Safety Risk and Sustainability Through the Integration of Cycle Approaches with Climate Change Classification

The inclusion of the cause-effect relationship is crucial to ensure a higher level of dam safety and to harmonise the sustainability of dams with climate change. Therefore, stakeholders (policymakers, dam operators, engineers, evaluators, researchers and the public) should play a crucial role in the development of this framework. The framework should consider the fundamental issues and integrate the problem with the associated non-technical or technical solution). The proposed measures should be adapted to climate change, and the remediation criteria should be defined and categorised according to the severity index. Furthermore, it should be based on other proven examples or case studies, critically reviewed, discussed and presented to stakeholders to gather opinions and feedback. In this way, a specific document with technical content can be created. The prepared framework can be included in the national agenda and used as a national practice to improve dam management and operation. The holistic approach is possible since the current dam safety guidelines for the selected country and region are not standardised and focus on the general aspect rather than specific as listed in the issues and challenges, as well as a directed failure mechanism,

which is mostly majored by hydrological stress (climate change impact)(Heidarzadeh & Feizi, 2022; Koskinas et al., 2019; Government of Malaysia et al., 2017).

Development, Implementation and Improvement of the Emergency Response and Action Plan Together with the Robust Flood Mitigation Plan

Extreme climatic conditions can alter rainfall patterns and flooding conditions. Therefore, a further study to amend the emergency plan based on the current state of flood defence integration is essential to consider downstream impacts during a flood event (FEMA, 2023; Kostecki & Rędownicz, 2014).

Hydrological Study and Simulation of Dam Failures Considering Climate Change, a Relationship Study (Climate Change-structural Failure), a Real-time Monitoring Tool (Early Warning System) for the Classification of Dam Failure Events, and Preparation of a Flood Mapping (Downstream)

The current forecast for the hydrological study should take into account the parameters of climate change. The input data must be error-free, and problems with missing or outdated data should be avoided. In this case, new inflow and outflow data for the capacity of reservoirs, dams (intake, spillway, stilling basin) and runoff patterns should be taken into account. The current capacity of the dam infrastructure should be evaluated and addressed as a limitation. The inundation map should be created, and the dam failure event should be classified according to the hazard index. In this way, future predictions can be made for the worst event, and an early warning system can be set up for those affected (Heidarzadeh & Feizi, 2022; Kostecki & Rędownicz, 2014).

Socio-economic and Environmental Risk Assessment in the Context of Climate Change

Climate change may affect water storage capacity and mapping downstream. Therefore, a study to integrate socio-economic and environmental linkages is essential due to the impacts that are currently being investigated. The development of models based on a mixed approach (quantitative and qualitative approach) is required to minimise loss of life, loss of property and severe environmental damage (Heidarzadeh & Feizi, 2022). Advanced tools such as satellite and radar-based measurements to identify the most affected areas (Xiao et al., 2022; Xie et al., 2022; Yang et al., 2024). Therefore, an early intervention programme can be predicted.

Vulnerability Assessment of Critical Infrastructure Under Climate Change Impact, Especially Areas Prone to Flooding and Seismic Activities

A dam is a critical infrastructure known as an important source of water supply, flood control and hydropower development. For structured management, smooth operation, and

planning of new dams, it is therefore crucial to assess the current state of this infrastructure in terms of the severity of climate change. New dams should be designed to withstand the worst-case scenario of climate change throughout their operational life. An economical and sustainable approach can be proposed for the construction of a new dam without compromising quality. In addition, consideration of areas prone to natural hazards such as floods and earthquakes is recommended to ensure that the critical aspect is taken into account to support the sustainability of dams, especially for new dams. A range of data on the frequency of rainfall and flooding and the prediction of extreme events is essential along with seismic data to support the current and future dam sustainability (Koskinas et al., 2019; Patra et al., 2024; Vahedifard et al., 2017; White et al., 2019).

CONCLUSION

This comprehensive study on dam safety and sustainability applies a systematic review approach to the field of dam safety and sustainability, which makes an important contribution to understanding the challenges, factors causing dam failure, and associated guidelines for dam safety. Interestingly, the environmental factor of climate change seems to be the main factor for the change in hydrological parameters, such as extreme flooding within a short precipitation period. This main factor has been identified as a stress tensor for catastrophic failure of a dam due to deterioration of structural integrity. Another important issue is the structural design factors that deal with the inadequate sizing of structures with the current capacity, such as spillways. In addition, ageing and old dams are highly susceptible to failure due to unprotected environmental criteria such as seismic activity, especially in vulnerable areas. The combination of hydrological (flooding) and seismic loading should be critically considered due to the cyclic or continuous dynamic loading of the dam structure. The concrete and earth fill dams are vulnerable to this source due to the risk to structural integrity, especially the ageing, old, and high dams. The dam safety guidelines issued by selected authorities contain a variety of criteria relevant to the management and operation of dams.

However, most of the published guidelines are limited to specific criteria, such as flood protection and digital data collection tools that cover only a small part of the impacts of climate change (normal hydrological data). To address this problem, robust guidelines with a comprehensive framework are crucial to closing the gaps. In addition, the holistic integration of globally harmonised guidelines suitable for all countries is feasible to ensure the impacts of climate change, especially extreme events and other parameters such as seismic activity, erosion and sedimentation due to the increasing number of natural hazards and to provide an adequate solution during the decision-making process. In addition, the proposed framework should align with the ICOLD Technical Guidelines (to ensure an update of technical information).

In addition, the integration of methods (parametric study, physical experiment, and numerical model simulation) in the assessment and prediction work is proposed to support the conventional measurement, i.e., a physical inspection, and provide a more robust and reliable measurement to avoid misinterpretation of the problems and allow faster identification and prediction of dam failures. The improvement of the structural aspects can thus be carried out before the actual construction of the dam, as the costs are very high due to the specialised and extensive infrastructure. By integrating these elements, the sustainability aspect of dams can be promoted and established. Future work can provide an extension of the hybrid dam safety assessment method (experimental and numerical simulations) that includes structural integrity assessment and fluid-structure interaction study, focusing on the extreme event and dynamic loading (turbulent flow).

ACKNOWLEDGEMENTS

The first author gratefully acknowledges the Ministry of Higher Education Malaysia (MOHE) and Universiti Teknologi MARA (UiTM) for the fully funded PhD scholarship under Skim Latihan Akademik Bumiputera (SLAB) and the School of Civil Engineering, Universiti Sains Malaysia (USM) for the continuous training, guidance, motivation, support, and opportunity provided through the Train to Publish (T2P) programme.

REFERENCES

- Al-Fugara, A. K., Mabdeh, A. N., Alayyash, S., & Khasawneh, A. (2023). Hydrological and hydrodynamic modeling for flash flood and embankment dam break scenario: Hazard mapping of extreme storm events. *Sustainability*, 15(3), Article 1758. <https://doi.org/10.3390/su15031758>
- Alcocer-Yamanaka, V. H., Murillo-Fernández, R., Federman, D. K., Elizalde, M., & Aparicio, J. (2020). Effects of the September 2017 earthquakes on Mexican dams. *Journal of Performance of Constructed Facilities*, 34(4), Article 04020043. [https://doi.org/10.1061/\(asce\)cf.1943-5509.0001417](https://doi.org/10.1061/(asce)cf.1943-5509.0001417)
- Bai, L., Wang, N., Jiao, J., Chen, Y., Tang, B., Wang, H., Chen, Y., Yan, X., & Wang, Z. (2020). Soil erosion and sediment interception by check dams in a watershed for an extreme rainstorm on the Loess Plateau, China. *International Journal of Sediment Research*, 35(4), 408-416. <https://doi.org/https://doi.org/10.1016/j.ijsrc.2020.03.005>
- Balmforth, D. (2020). *Toddbrook Reservoir Independent Review Report*. https://assets.publishing.service.gov.uk/government/uploads/system/uploads/attachment_data/file/872769/toddbrook-reservoir-independent-review-reporta.pdf
- Bocchiola, D., & Rosso, R. (2014). Safety of Italian dams in the face of flood hazard. *Advances in water resources*, 71, 23-31. <https://doi.org/10.1016/j.advwatres.2014.05.006>
- Carneiro, B. L. D. S., Filho, F. D. A. D. S., Carvalho, T. M. N., & Raulino, J. B. S. (2022). Hydrological risk of dam failure under climate change. *Brazilian Journal of Water Resources*, 27, 1-10. <https://doi.org/10.1590/2318-0331.272220220017>

- Central Water Commission. (2018). *Guidelines for Safety Inspection of Dams* (CDSO_GUD_DS_07_v1.). Ministry of Water Resources, River Development & Ganga Rejuvenation, Government of India. https://damsafety.cwc.gov.in/ecm-includes/PDFs/Guidelines_for_Safety_Inspection_of_Dams.pdf
- Chang, M., Luo, C., Wu, B., & Xiang, L. (2022). Catastrophe process of outburst debris flow triggered by the landslide dam failure. *Journal of Hydrology*, 609, Article 127729. <https://doi.org/https://doi.org/10.1016/j.jhydrol.2022.127729>
- Chanson, H. (1994). *Hydraulic design of stepped cascades, channels, weirs and spillways*. Pergamon.
- Concha, L. P., Lall, U., & Hariri-Ardebili, M. A. (2023). Needs for portfolio risk assessment of aging dams in the United States. *Journal of Water Resources Planning and Management*, 149(3), Article 04022083. <https://doi.org/10.1061/jwrmd5.wreng-5673>
- DRDMW. (2024). *Dam Safety Management Guideline*. Department of Regional Development, Manufacturing and Water, Queensland Government. https://www.resources.qld.gov.au/__data/assets/pdf_file/0007/78838/dam-safety-management.pdf
- FEMA. (2023). *Federal Guidelines for Dam Safety* (FEMA P-93). Federal Emergency Management Agency. [https://damtoolbox.org/wiki/Federal_Guidelines_for_Dam_Safety_\(FEMA_P-93\)](https://damtoolbox.org/wiki/Federal_Guidelines_for_Dam_Safety_(FEMA_P-93))
- Fluixá-Sanmartín, J., Altarejos-García, L., Morales-Torres, A., & Escuder-Bueno, I. (2018). Review article: Climate change impacts on dam safety. *Natural Hazards and Earth System Sciences*, 18(9), 2471-2488. <https://doi.org/10.5194/nhess-18-2471-2018>
- France, J. W., Dickson, P. A., Falvey, H. T., Rigbey, S. J., & Trojanowski, J. (2018). *Independent Forensic Team Report Oroville Dam Spillway Incident*. <https://damsafety.org/sites/default/files/files/Independent%20Forensic%20Team%20Report%20Final%20001-05-18.pdf>
- Goodling, P. J., Lekic, V., & Prestegard, K. (2018). Seismic signature of turbulence during the 2017 Oroville Dam spillway erosion crisis. *Earth Surface Dynamics*, 6(2), 351-367. <https://doi.org/10.5194/esurf-6-351-2018>
- Government of Malaysia. (2017). *Malaysia Dam Safety Manamegement Guidelines (MyDAMS)*. Drainage and Irrigation Department, Kuala Lumpur, Malaysia. [https://www.water.gov.my/jps/resources/PDF/MyDAMS_2017_\(Free_Copy\).pdf](https://www.water.gov.my/jps/resources/PDF/MyDAMS_2017_(Free_Copy).pdf)
- Gu, S., Ren, L., Wang, X., Xie, H., Huang, Y., Wei, J., & Shao, S. (2017). SPHysics simulation of experimental spillway hydraulics. *Water*, 9(12), Article 973. <https://doi.org/10.3390/w9120973>
- Hasan, T. (2015). Earthquakes and dams. In M. Abbas (Ed.), *Earthquake Engineering* (pp. 189-202). IntechOpen. <https://doi.org/10.5772/59372>
- Heidarzadeh, M., & Feizi, S. (2022). A cascading risk model for the failure of the concrete spillway of the Toddbrook dam, England during the August 2019 flooding. *International Journal of Disaster Risk Reduction*, 80, Article 103214. <https://doi.org/https://doi.org/10.1016/j.ijdr.2022.103214>
- Hirabayashi, Y., Mahendran, R., Koirala, S., Konoshima, L., Yamazaki, D., Watanabe, S., Kim, H., & Kanae, S. (2013). Global flood risk under climate change. *Nature Climate Change*, 3(9), 816-821. <https://doi.org/10.1038/nclimate1911>

- Hollins, L., Eisenberg, D., & Seager, T. (2018). Risk and resilience at the Oroville dam. *Infrastructures*, 3(4), Article 49. <https://doi.org/10.3390/infrastructures3040049>
- Hu, T., & Huang, R. Q. (2017). A catastrophic debris flow in the Wenchuan earthquake area, July 2013: Characteristics, formation, and risk reduction. *Journal of Mountain Science*, 14(1), 15-30. <https://doi.org/10.1007/s11629-016-3965-8>
- Hughes, A. (2020). *Report on the Nature and Root Cause of the Toddbrook Reservoir Auxiliary Spillway Failure on 1st August 2019*. <https://canalrivertrust.org.uk/refresh/media/thumbnail/41505-report-on-toddbrook-reservoir-by-dy-andrew-hughes.pdf>
- Islam, M. R., Fereshtehpour, M., Najafi, M. R., Khaliq, M. N., Khan, A. A., Sushama, L., Nguyen, V. T. V., Elshorbagy, A., Roy, R., Wilson, A., Perdikaris, J., Masud, M. B., & Khan, M. S. (2024). Climate-resilience of dams and levees in Canada: A review. *Discover Applied Sciences*, 6(4), Article 174. <https://doi.org/10.1007/s42452-024-05814-4>
- Jensen, L. (2022). *The Sustainable Development Goals Report 2022*. <https://unstats.un.org/sdgs/report/2022/>
- Kocaer, Ö., & Yazar, A. (2020). Experimental and numerical investigation of flow over ogee spillway. *Water Resources Management*, 34(13), 3949-3965. <https://doi.org/10.1007/s11269-020-02558-9>
- Kondolf, M., & Yi, J. (2022). Dam renovation to prolong reservoir life and mitigate dam impacts. *Water*, 14(9), Article 1464. <https://doi.org/10.3390/w14091464>
- Koskinas, A., Tegos, A., Tsira, P., Dimitriadis, P., Iliopoulou, T., Papanicolaou, P., Koutsoyiannis, D., & Williamson, T. (2019). Insights into the Oroville dam 2017 spillway incident. *Geosciences*, 9(1), Article 37. <https://doi.org/10.3390/geosciences9010037>
- Kostecki, S., & Banasiak, R. (2021). The catastrophe of the Niedów Dam - The causes of the dam's breach, its development, and consequences. *Water*, 13(22), Article 3254. <https://doi.org/10.3390/w13223254>
- Kostecki, S., & Rędownicz, W. (2014). The washout mechanism of the Niedów dam and its impact on the parameters of the flood wave. *Procedia Engineering*, 91, 292-297. <https://doi.org/https://doi.org/10.1016/j.proeng.2014.12.062>
- Lazin, R., Shen, X., Moges, S., & Anagnostou, E. (2023). The role of renaissance dam in reducing hydrological extremes in the upper Blue Nile Basin: Current and future climate scenarios. *Journal of Hydrology*, 616, Article 128753. <https://doi.org/https://doi.org/10.1016/j.jhydrol.2022.128753>
- Lee, T., Seong, K., Lee, S. O., & Yoo, H. J. (2022). Safety first? Lessons from the Hapecheon dam flood in 2020. *Sustainability*, 14(5), Article 2975. <https://doi.org/10.3390/su14052975>
- Liu, B., Fan, Y., Xue, B., Wang, T., & Chao, Q. (2022). Feature extraction and classification of climate change risks: A bibliometric analysis. *Environmental Monitoring and Assessment*, 194(7), Article 495. <https://doi.org/10.1007/s10661-022-10074-z>
- Ma, J. H., Yoo, C., Yun, T. S., & Jung, D. (2024). Dilemma of a small dam with large basin area under climate change condition. *Computers and Concrete*, 33(5), 559-572. <https://doi.org/10.12989/cac.2024.33.5.559>
- Martin, H. K., Edmonds, D. A., Yanites, B. J., & Niemi, N. A. (2024). Quantifying landscape change following catastrophic dam failures in Edenville and Sanford, Michigan, USA. *Earth Surface Processes and Landforms*, 49(9), 2767-2778. <https://doi.org/10.1002/esp.5855>

- Milly, P. C. D., Wetherald, R. T., Dunne, K. A., & Delworth, T. L. (2002). Increasing risk of great floods in a changing climate. *Nature*, 415(6871), 514-517. <https://doi.org/10.1038/415514a>
- Moher, D., Liberati, A., Tetzlaff, J., & Altman, D. G. (2009). Preferred reporting items for systematic reviews and meta-analyses: The PRISMA statement. *PLoS Medicine*, 6(7), Article e1000097. <https://doi.org/10.1371/journal.pmed.1000097>
- Mortey, E. M., Kouassi, K. L., Diedhiou, A., Anquetin, S., Genoud, M., Hingray, B., & Kouame, D. G. M. (2019). Sustainable hydroelectric dam management in the context of climate change: Case of the Taabo dam in Côte D'Ivoire, West Africa. *Sustainability*, 11(18), Article 4846. <https://doi.org/10.3390/su11184846>
- NSW Government. (2021). *Dams Safety NSW Guideline Dam safety management system*. NSW Department of Planning, Industry and Environment. https://www.damsafety.nsw.gov.au/__data/assets/pdf_file/0011/488378/Dam-safety-management-system-guideline-March-2021.pdf
- Patra, B. K., Segura, R. L., & Bagchi, A. (2024). Modeling variability in seismic analysis of concrete gravity dams: A parametric analysis of Koyna and Pine flat dams. *Infrastructures*, 9(1), Article 10. <https://doi.org/10.3390/infrastructures9010010>
- Peterka, A. J. (1984). *Hydraulic Design of Stilling Basins and Energy Dissipators*. Department of the Interior, Bureau of Reclamation.
- Saber, M., Kantoush, S. A., Sumi, T., Ogiso, Y., Alharrasi, T., Koshiba, T., Abdel-Fattah, M., Al-Maktoumi, A., Abdalla, O. A., Takemon, Y., Nohara, D., Kobayashi, S., Almamari, M., Al Hooti, K., Al Barwani, A., Almamari, H., Ellithy, D., Holzbecher, E., & Hadidi, A. (2022). Integrated study of flash floods in Wadi Basins considering sedimentation and climate change: An international collaboration project. In *Wadi Flash Floods: Challenges and Advanced Approaches for Disaster Risk Reduction* (pp. 401-422). Springer. https://doi.org/10.1007/978-981-16-2904-4_15
- Shaffril, H., Samah, A. A., & Kamarudin, S. (2021). Speaking of the devil: A systematic literature review on community preparedness for earthquakes. *Natural hazards*, 108(3), 2393-2419. <https://doi.org/10.1007/s11069-021-04797-4>
- SPANCOLD. (2017). *Dams and The Sustainable Development Goals*. https://www.spancold.org/wp-content/uploads/2019/03/181220_DAMS-AND-SDGs.-Technical-Working-Document.pdf
- Stelloh, T., Blankstein, A., Silva, D., & Abdelkader, R. (2017, February 13). Oroville dam spillway failure: Nearly 190,000 ordered to evacuate. *NBC News Digital*. <https://www.nbcnews.com/news/us-news/potentially-catastrophic-tens-thousands-evacuated-amid-dam-spillway-failure-n720051>
- Sun, M. C., Sakai, K., Chen, A. Y., & Hsu, Y. T. (2022). Location problems of vertical evacuation structures for dam-failure floods: Considering shelter-in-place and horizontal evacuation. *International Journal of Disaster Risk Reduction*, 77, Article 103044. <https://doi.org/https://doi.org/10.1016/j.ijdr.2022.103044>
- Vahedifard, F., AghaKouchak, A., Ragno, E., Shahrokhbadi, S., & Mallakpour, I. (2017). Lessons from the Oroville dam. *Science*, 355(6330), 1139-1140. <https://doi.org/10.1126/science.aan0171>
- White, A. B., Moore, B. J., Gottas, D. J., & Neiman, P. J. (2019). Winter storm conditions leading to excessive runoff above California's Oroville dam during January and February 2017. *Bulletin of the American Meteorological Society*, 100(1), 55-70. <https://doi.org/10.1175/bams-d-18-0091.1>

- Wieland, M. (2016). Safety aspects of sustainable storage dams and earthquake safety of existing dams. *Engineering*, 2(3), 325-331. <https://doi.org/https://doi.org/10.1016/J.ENG.2016.03.011>
- Xiao, R., Jiang, M., Li, Z., & He, X. (2022). New insights into the 2020 Sardoba dam failure in Uzbekistan from Earth observation. *International Journal of Applied Earth Observation and Geoinformation*, 107, Article 102705. <https://doi.org/https://doi.org/10.1016/j.jag.2022.102705>
- Xie, L., Xu, W., Ding, X., Bürgmann, R., Giri, S., & Liu, X. (2022). A multi-platform, open-source, and quantitative remote sensing framework for dam-related hazard investigation: Insights into the 2020 Sardoba dam collapse. *International Journal of Applied Earth Observation and Geoinformation*, 111, Article 102849. <https://doi.org/https://doi.org/10.1016/j.jag.2022.102849>
- Yang, Q., Shen, X., He, K., Zhang, Q., Helfrich, S., Straka, W., Kelldorfer, J. M., & Anagnostou, E. N. (2024). Pre-failure operational anomalies of the Kakhovka dam revealed by satellite data. *Communications Earth & Environment*, 5(1), Article 230. <https://doi.org/10.1038/s43247-024-01397-5>
- Yavaşoğlu, H. H., Kalkan, Y., Tiryakioğlu, İ., Yigit, C. O., Özbey, V., Alkan, M. N., Bilgi, S., & Alkan, R. M. (2018). Monitoring the deformation and strain analysis on the Ataturk dam, Turkey. *Geomatics, Natural Hazards and Risk*, 9(1), 94-107. <https://doi.org/10.1080/19475705.2017.1411400>

Assessment of the Bioavailability of Zinc (Zn), Lead (Pb), Nickel (Ni), and Cadmium (Cd) in the Sediments of the Sungai Buloh Estuaries, Selangor

Aqilah Mukhtar^{1*}, Mohd Nazri M. Yunus², Nur Amiera Kamarudin^{2,3}, Syaizwan Zahmir Zulkifli² and Ahmad Ismail²

¹Department of Earth Sciences and Environment, Faculty of Science and Technology, Universiti Kebangsaan Malaysia, 43600 Bangi, Selangor, Malaysia

²Department of Biology, Faculty of Science, Universiti Putra Malaysia, 43400 UPM, Serdang, Selangor, Malaysia

³International Institute of Aquaculture and Aquatic Sciences, Lot 960, Jalan Kemang 6, 71050 Port Dickson, Negeri Sembilan, Malaysia

ABSTRACT

A study was conducted on sediment samples from Kuala Sungai Buloh, located within the cockle cultivation area of Selangor. The research focused on assessing the presence of selected heavy metals, including zinc (Zn), lead (Pb), nickel (Ni), and cadmium (Cd). The total concentration of heavy metals within the sediment matrix was determined through aqua regia digestion. Meanwhile, the speciation of these metals was identified using sequential extraction technique (SET). The mean concentrations of Zn, Pb, Ni, and Cd were 130.41 ± 25.61 , 29.22 ± 7.81 , 13.08 ± 4.96 , and 0.166 ± 0.074 $\mu\text{g/g}$, respectively ($p < 0.05$). The fractionation distribution of Zn, Pb, and Ni followed the trend [residual] > [oxidisable-organic] > [acid-reducible] > [exchangeable]. For Cd, the trend was [residual] > [acid-reducible] > [oxidisable-organic] > [exchangeable]. Based on the geoaccumulation index (I_{geo}) assessment, sediments from Kuala Sungai Buloh were categorised

as unpolluted to moderately contaminated at selected sampling points for Zn and Pb. The Contamination Factor (CF) suggested moderate contamination levels for Zn and Pb and low contamination levels for Ni and Cd. Additionally, the Pollution Load Index (PLI) classified the area as non-polluted since all values were less than 1. These heavy metals in the river and estuaries of Sungai Buloh are attributed to natural processes, as well as moderate industrial, agricultural, and domestic activities. Understanding heavy metals is crucial for assessing ecotoxic effects in aquatic

ARTICLE INFO

Article history:

Received: 16 August 2024

Accepted: 16 January 2025

Published: 04 April 2025

DOI: <https://doi.org/10.47836/pjst.33.3.15>

E-mail addresses:

aqilamukhtar@ukm.edu.my (Aqilah Mukhtar)
mohdnazriyunus96@gmail.com (Mohd Nazri M. Yunus)
nuramiera2510@gmail.com (Nur Amiera Kamarudin)
eazwan@gmail.com (Syaizwan Zahmir Zulkifli)
ismailmt56@yahoo.com.my (Ahmad Ismail)

* Corresponding author

environments. This knowledge is crucial for safeguarding ecosystems and advancing Sustainable Development Goal 14 (SDG14), emphasising the conservation of life below water.

Keywords: Contamination, heavy metal, sediments, sequential extraction technique, sustainability

INTRODUCTION

Heavy metal pollution is a major global issue, especially in aquatic ecosystems, due to its harmful effects on both the environment and human health. Heavy metals originate from two primary sources: natural phenomena and human activities. Natural processes such as rock weathering, soil erosion, and volcanic activity contribute to the occurrence of heavy metals in the environment. However, human activities significantly exacerbate heavy metal pollution through mining, industrial processes, improper disposal of industrial waste, urban runoff, sewage disposal and more. Heavy metals released into the environment can dissolve in water or accumulate in sediments. Heavy metals often settle into the lower layers of water bodies, making them more prevalent in sediments than in the water column (Bhuyan et al., 2023). As a result, pollutants such as heavy metals tend to accumulate in sediments (Aydin et al., 2023). Sediments are crucial in transporting heavy metals and often act as key reservoirs for these pollutants. In addition, geographical variation also plays a significant role in influencing heavy metals in sediments. A previous study conducted along the west coast of Peninsular Malaysia reported that the concentrations of heavy metals in surface sediments ranged from 66 to 443 $\mu\text{g/g}$ for Zn, 2 to 54 $\mu\text{g/g}$ for Pb, 11 to 30 $\mu\text{g/g}$ for Ni, and 0.5 to 1.7 $\mu\text{g/g}$ for Cd (Buhari, 2020). These findings suggest that higher concentrations of heavy metals were primarily associated with sampling sites in close proximity to anthropogenic sources, such as domestic discharges, industrial activities, shipping operations, and other pollution inputs.

Heavy metals are not biodegradable. Once they enter the aquatic ecosystem, they can spread throughout the water body, accumulate in sediments, or be absorbed by aquatic organisms (Frémion et al., 2016). Metals that settle in sediments are associated with bioaccumulation processes. When pollutants accumulate, they contaminate the food chain and cause significant ecotoxic stress on both humans and aquatic organisms (Okereafor et al., 2020; Wang et al., 2022). Exposure to heavy metals can lead to their buildup in human bones and fat tissue, resulting in nutritional deficiencies and a weakened immune system (Aziz et al., 2023). Additionally, certain heavy metals, such as cadmium and lead, have been associated with intrauterine growth retardation (Zinia et al., 2023). Therefore, assessing the health of aquatic ecosystems is crucial for managing pollution caused by human activities.

Most studies concentrate on the total metal content in sediment, which does not adequately address the metal's mobility, bioavailability, and toxicity (Abollino et al., 2011; Swati & Hait, 2017; Abubakar et al., 2018). Thus, evaluating the speciation of heavy metals is crucial for understanding their potential mobility and bioavailability, as

the bioavailable fraction, despite being small, plays a significant role in determining the overall metal content and its environmental impact (Swati & Hait, 2017; Abubakar et al., 2018). Heavy metal speciation can be determined using various techniques such as Sequential Extraction Techniques (SET) (Khan et al., 2020; Awad et al., 2021; Golui et al., 2021), Laser-Induced Breakdown Spectroscopy (LIBS) (Yoon et al., 2021; De Moraes et al., 2022), Diffusive Gradients in Thin Films (DGT) (Yuan et al., 2020; Gu, 2021; Liang et al., 2023; Liu et al., 2023), and X-ray Absorption Spectroscopy (XAS) (Ye et al., 2022). Among these methods, SET is the most widely used due to its affordability, simplicity, and ability to provide insights into metal bioavailability, mobility, and environmental risks, which are critical for monitoring efforts.

The sequential extraction technique involves multiple steps using various chemical reagents and conditions (Domingues & e Silva, 1990). The SET procedure comprises four fractions: exchangeable, acid-reducible, oxidisable-organic, and residual. This technique differentiates between lithogenic metals and those of natural origin, offering insights into the main binding sites, the intensity of metal interactions with particulates, and the phase associations of trace elements in sediments. Understanding these aspects is crucial for deciphering the mobilisation of heavy metals and the potential risks they pose. In addition to these analytical approaches, alternative methods have also been explored to address heavy metal contamination. Phytoremediation using specific plants, such as water hyacinth (*Eichhornia crassipes*), lettuce (*Pistia stratiotes*), and duckweed (*Lemna minor*), offers a sustainable solution for mitigating heavy metal contamination (Ali et al., 2020). Phytoremediation not only addresses the contamination but also enhances the ecological health of the affected areas. Integrating such methods with sediment analysis and treatment strategies could enhance the overall effectiveness of pollution management.

Kuala Sungai Buloh has been the site of a cockle farming project initiated by the Department of Fisheries Malaysia (DOFM) since 2008. However, human activities along the Sungai Buloh River have released various pollutants, including heavy metals from industrial, boating activities, and agricultural and domestic sources. Cockle farming can be significantly influenced by sediment contamination as cockles are benthic organisms that inhabit and feed in close association with the sediment. Blood cockles and filter feeders are particularly susceptible to accumulating heavy metals and other pollutants. These contaminants can be absorbed through dissolved metals passing through their gills or ingested with food particles during dietary intake (Rainbow, 2018). Bivalves are known to bioaccumulate heavy metals in their tissues, which can lead to toxic effects such as reduced metabolic activity and impaired physiological functions (Pavón et al., 2022). The bioaccumulation in blood cockles is closely linked to their feeding behaviour and environmental conditions, making them valuable bioindicators of heavy metal pollution in aquatic ecosystems. Sediment contamination also impacts the broader ecosystem by altering habitat quality, disrupting benthic community balance, and interfering with nutrient cycling.

Therefore, this study aims to i) assess the levels of selected heavy metals, including Zn, Pb, Ni, and Cd, in the sediment of Kuala Sungai Buloh from vertical profile, ii) measure the heavy metal speciation on the surface sediment, and iii) evaluate the contamination of these heavy metals using pollution indices, such as the Index of Geoaccumulation (I_{geo}), Contamination Factor (CF), and Pollution Load Index (PLI). By integrating vertical profiling, surface sediment speciation, and pollution indices, this study comprehensively assesses the spatial distribution and environmental risks of heavy metals. The findings will contribute valuable data for monitoring pollutants released into the environment, enhancing understanding of heavy metal interactions in marine ecosystems. This is essential for protecting marine environments from harmful impacts and supports Sustainable Development Goal 14 (SDG 14), which focuses on conserving and sustainably using the oceans, seas, and marine resources.

MATERIAL AND METHOD

Study Area

The study was conducted in Kuala Sungai Buloh, Selangor (3.255880°N, 101.303401°E), located on the west coast of Peninsular Malaysia. Manufacturing industries and using fertilisers and pesticides in agricultural activities, fisheries, tourism, and domestic activities significantly contribute to metal loading in Sungai Buloh. Seven sampling stations (A, B, C, D, E, F, and G) were selected for this study (Figure 1).

Sampling

Throughout the sampling process, in-situ parameters, including temperature, salinity, dissolved oxygen (DO), and pH, were recorded using a YSI meter Model 556 MPS at a depth of approximately one meter from surface water.

Sediment collection involved the use of a 1-meter-long PVC tube with caps at each sampling point. The PVC tube was inserted until it reached the bottom sediment layer, then capped and removed. The sediment inside the PVC tube was removed using another PVC tube equipped with a piston mechanism. Subsequently, the sediments were sectioned using a plastic knife into layers of approximately 3 cm thickness from the sediment surface. A study by Mohamed et al. (2008) in Sabak Bernam, near the current study, reported that the sedimentation rate is an average of 0.2 cm/year; thus, each 3 cm section of sediment describes 15 years of sediment load. Each sediment sample was labelled with the sampling plot and its specific depth level and then placed into polyethene bags.

Sediment samples were immediately placed in an icebox for transport to the Ecology Laboratory, Department of Biology, Universiti Putra Malaysia. Upon arrival, they were frozen at -10°C to preserve them until further analysis.



Figure 1. Sampling points of sediment in Sungai Buloh estuaries, Selangor

Preparation of Samples

The sediment samples underwent thawing at room temperature for a minimum of 6 hours. The samples were then dried in an oven at 80°C for 72 hours or until a constant dry weight was achieved. After drying, the samples were ground using a mortar and pestle to obtain a fine powder. The powdered samples were then sieved through a 63 µm stainless steel sieve to ensure a consistent particle size. The prepared samples were kept in sealed plastic bags with labels to prevent contamination prior to further laboratory procedures, such as aqua regia and sequential extraction techniques.

Experimental Analysis

Total Heavy Metals in Sediment by Aqua Regia Method

The total metal content in the sediment was determined through aqua regia digestion (Ismail & Ramli, 1997; Zulkifli et al., 2010). Digestion was performed on sediment samples categorised by plot and depth level. A sample weighing approximately 1.0 g was placed in a digestion tube. A 10 mL of a mixed acid solution, prepared in a 4:1 ratio of concentrated

nitric acid (HNO_3 , 65%, AnalaR grade, R&M Chemicals) to perchloric acid (HClO_4 , 70%, AnalaR grade, R&M Chemicals), was added to the sample. The digestion tubes were then placed in a digestion block and heated to ensure complete digestion of the samples. The temperature was initially set to 40°C for the first hour, followed by an increase to 140°C for the next three hours. Once digestion was finished, the tubes were allowed to cool to room temperature. The volume was adjusted to 40 ml by adding double-distilled water, and the samples were subsequently filtered using Whatman® No. 1 filter paper (12.5 cm diameter and 11 μm pore size). The filtered samples were analysed using an Atomic Absorption Spectrophotometer (AAS) (Perkin-Elmer Model AAnalyst 800). The limit of detection (LOD) for Zn, Pb, Ni and Cd were 0.01 $\mu\text{g/g}$, 0.02 $\mu\text{g/g}$, 0.05 $\mu\text{g/g}$, and 0.001 $\mu\text{g/g}$, respectively.

Speciation of Heavy Metal in Sediment using Sequential Extraction Technique (SET)

Surface sediment from each sampling point was analysed for heavy metal speciation using the sequential extraction technique (SET), which was adapted from the methods of Badri and Aston (1983), Naji et al. (2010) and Abubakar et al. (2018).

A 10 g sediment sample was added to a conical flask to determine the exchangeable fraction. About 15 ml of 1.0 M ammonium acetate ($\text{NH}_4\text{CH}_3\text{COO}$) solution was then introduced, adjusted to pH 7.0. The mixture was subjected to continuous shaking at 100 rpm for 3 hours at room temperature. Subsequently, the mixture was filtered using Whatman filter paper, and the obtained supernatant was immediately analysed.

For the acid-reducible fraction, the residue from the first fraction was mixed with 50 ml of 0.25M hydroxylammonium chloride ($\text{NH}_2\text{OH}\cdot\text{HCl}$), acidified to pH 2.0 with hydrochloric acid (HCl), and shaken for another 3 hours at 100 rpm at room temperature.

The residue from the preceding step was transferred to a conical flask to determine the oxidisable organic fraction. This residue was oxidised by adding 15 ml of 35% hydrogen peroxide (H_2O_2 , R&M Chemicals) and placing it in a 90°C water bath for at least 4 hours until the sediment was completely dry. After cooling to room temperature, the residual sediment was treated with 50 mL of 1.0 M ammonium acetate ($\text{NH}_4\text{CH}_3\text{COO}$) solution, adjusted to pH 2.0 using hydrochloric acid (HCl). The mixture was then agitated at 100 rpm for 3 hours at room temperature.

In the resistant fraction, the residue is digested according to the procedure outlined for total digestion using the aqua-regia method. All collected supernatants were stored at 4°C before metal analysis.

The residue from each extraction phase was rinsed with 20 mL of distilled water, filtered, and weighed before proceeding to the subsequent extraction fraction. The concentrations of heavy metals in all filtrate samples were then determined using an atomic absorption spectrophotometer (Perkin-Elmer Model Analyst 800).

Quality Control

Acid washing was performed on all glassware and equipment to eliminate contamination. Blank samples were processed concurrently with each experimental batch to verify sample purity. The accuracy of the analytical procedure was validated using Certified Reference Materials (CRM) for marine sediment (PACS-2), with recoveries ranging from 80.48% to 113.85%, as detailed in Table 1. The data obtained from the analysis were converted to and expressed on a µg/g dry weight basis. These results were then compared and adjusted using CRM values to determine the final results.

Table 1
The CRM value and the percentage of recoveries

Metals	Certified Reference Value (ug/g)	Measured Value (ug/g)	Percentage of Recovery (%)
Zn	49.900	43.737	87.65
Pb	11.700	11.397	97.41
Ni	39.500	31.790	80.48
Cd	2.110	1.849	87.65

Environmental Indices

Metal pollution levels in the surface sediment of Kuala Sungai Buloh were evaluated using three environmental indices: the Geoaccumulation Index (I_{geo}), Contamination Factor (CF), and Pollution Load Index (PLI).

a) The Geoaccumulation Index (I_{geo}), developed by Muller (1969), was employed to assess metal contamination in the sediment. This index compares current metal concentrations to pre-industrial baseline levels (Equation 1).

$$I_{geo} = \log_2 (C_n / 1.5B_n) \tag{1}$$

In the equation, C_n represents the measured concentration of element n in the sediment sample, while B_n signifies the geochemical background concentration of element n in average shale, as established by Turekian and Wedepohl in 1961. Table 2 presents the seven distinct categories of I_{geo} , along with the corresponding levels of sediment pollution proposed by Muller (1969).

b) The Contamination Factor (CF) is an index used to evaluate sediment contamination and assess environmental pollution from specific toxic substances. The CF is determined by dividing the sediment concentration of each heavy metal by its corresponding background value, as defined by Turekian and Wedepohl (1961) in Equation 2.

$$CF = \frac{\text{(heavy metal concentration in sediment)}}{\text{(background value of metal)}} \tag{2}$$

Table 2
Classification for the geoaccumulation index (I_{geo})

I_{geo} value	I_{geo} class	Sediment quality
<0	0	Unpolluted
0–1	1	Unpolluted to moderately polluted
1–2	2	Moderately polluted
2–3	3	Moderately polluted to strongly polluted
3–4	4	Strongly polluted
4–5	5	Strongly polluted to extremely polluted
>5	6	Extremely polluted

In the equation, the criteria for assessing CF are defined as follows: $CF < 1$ indicates low contamination, $1 < CF < 3$ indicates moderate contamination, $3 < CF < 6$ indicates considerable contamination, and $CF > 6$ indicates very high contamination. The background concentrations of metals used in this assessment were derived from global average shale values reported by Turekian and Wedepohl (1961).

c) The Pollution Load Index (PLI) comprehensively evaluates heavy metal contamination at potentially polluted locations. The PLI indicates the cumulative toxicity of a sample, incorporating the impacts of various heavy metals. The PLI was determined using Equation 3, proposed by Tomlinson et al. (1980).

$$PLI = (CF_1 \times CF_2 \times CF_3 \dots \times CF_n)^{1/n} \quad [3]$$

In the equation, CF refers to contamination factors, and n is the number of metals. A PLI less than 1 signifies no pollution, while a value greater than 1 indicates pollution.

Data Analysis

Heavy metal concentration data was analysed using IBM SPSS Statistics version 21 and Microsoft Office Excel 2021 (Microsoft Corporation, USA). One-way ANOVA followed by Tukey’s post-hoc test was utilised to determine differences in heavy metal concentrations among sampling points.

RESULTS AND DISCUSSION

Water Quality of Study Areas

The water parameters of Kuala Sungai Buloh are recorded in Table 3. The water temperature ranged from 28.40°C to 30.76°C. Sampling points A to F exhibited consistent temperatures, except for sampling point G, which recorded the lowest temperature. Factors contributing to the variation in temperature values include weather and climate conditions, sampling time, and the locations of the sampling points. In this study, the high temperatures were due to

sunny weather during the sampling activities, and sampling points A, B, C, D, E, and F were in open estuaries. In contrast, sampling point G was in the Sungai Buloh riverine, which was surrounded by palm oil trees. Temperature influences various water parameters, including dissolved oxygen (DO), pH, and nutrient levels. Elevated temperatures reduce oxygen solubility in water while increasing microbial metabolism, resulting in higher oxygen consumption (Chapra et al., 2021). This process leads to increased carbon dioxide (CO₂) release, subsequently lowering pH levels. The resulting low pH caused by elevated CO₂ can impose additional stress on aquatic organisms, impacting their physiological functions and overall ecosystem health (Peytoureau et al., 2023). Furthermore, elevated temperatures enhance microbial enzymatic activity, accelerating nutrient cycling, decomposition rates, and nutrient release (Elena, 2019).

Table 3
The in-situ parameters of water in all sampling points of Sungai Buloh

Sampling point	Parameter			
	Temperature (°C)	Salinity (mg/l)	Dissolve oxygen (mg/l)	pH
A	30.36	28.22	7.07	6.22
B	30.36	26.03	7.39	6.71
C	29.25	26.80	8.77	8.22
D	30.40	41.40	6.59	8.06
E	30.62	41.09	9.41	6.52
F	30.76	39.76	11.64	6.50
G	28.40	0.44	3.40	5.75
Average	30.02	29.11	7.75	6.85

The highest salinity was recorded at sampling points D and E, with values of 41.40 and 41.09 mg/l, respectively, while the lowest value was recorded at sampling point G (0.44 mg/l). Variations in salinity are influenced by river runoff, where fresh water from rivers mixes with seawater, and ocean currents distribute water masses with varying levels of salinity. Varying salinity levels can influence organisms’ distribution and population size within a specific region.

The analysed water samples exhibited dissolved oxygen (DO) levels ranging from 3.40 to 11.64 mg/L. These values comply with the Malaysian Marine Water Quality Standard (MMWQS) Class 1 for sampling points A to F, except for sampling point G, which falls into Class 3. Industrial activities, oil palm plantations, and domestic activities characterise sampling point G. Dissolved oxygen levels are influenced by the photosynthetic production of oxygen by phytoplankton and aquatic plants, which increases during daylight hours. Conversely, biological respiration and bacterial decomposition of organic matter consume oxygen, leading to decreased DO levels. This effect is particularly pronounced in areas with high organic loads, such as sampling point G.

The pH levels ranged from 5.75 at sampling point G to 8.22 at sampling point C. Results falling between 6.5 and 9.0 are within the standard range of the MMWQS. A pH below 6.5 indicates poor water conditions, often due to industrial emissions from chemical manufacturing, paper production, and metal processing upstream of Sungai Buloh. These discharges can introduce acidic substances that directly lower the pH of the receiving water. Significant pH fluctuations can disrupt biodiversity, food webs, and ecosystem dynamics.

Overall, the water quality in the estuary of Sungai Buloh is generally good, except at sampling point G, where discharges from industries, oil palm plantations, and domestic activities contribute to the alteration of water quality. Monitoring and managing water's physicochemical parameters are crucial for protecting aquatic biodiversity and ensuring the sustainability of aquatic resources.

Mean Metal Concentrations of Sediment Cores

Table 4 presents the mean Zn, Pb, Ni, and Cd concentrations at varying depths within the sediment core samples. The mean concentration of metals in sediments that are being studied is generally in order of $[Zn] > [Pb] > [Ni] > [Cd]$. Zn has the highest concentration with a mean of $130.20 \pm 5.02 \mu\text{g/g}$, followed by Pb ($29.24 \pm 1.31 \mu\text{g/g}$), Ni ($13.23 \pm 0.63 \mu\text{g/g}$), and Cd ($0.16 \pm 0.01 \mu\text{g/g}$) ($p < 0.05$). Compared to the average shale values of heavy metals, Zn and Pb exceed the average shale values, clearly indicating the enrichment of these metals in the core. In contrast, the mean values of Ni and Cd are below the average shale values.

The mean concentration of Zn rises towards the top of the sediment core, whereas Pb, Ni, and Cd showed minimal variation throughout the vertical sediment core. Numerous researchers have employed sediment cores to investigate the behaviour of metals, including in Malaysian marinas (Ashraf et al., 2018; Khalid et al., 2019; Vane et al., 2020; Pradit et al., 2022). The concentration of Zn at the bottom of the sediment core is lower than the mean, while the highest Zn concentration was detected at a depth of 19 to 21 cm at a concentration of $140.60 \mu\text{g/g}$. For Pb, the highest concentration detected was $31.43 \mu\text{g/g}$ at a depth of 19 to 21 cm, and the lowest was $27.52 \mu\text{g/g}$ at a depth of 22 to 24 cm. Similarly, for Ni, the highest and lowest concentrations were detected at depths of 19 to 21 cm and 22 to 24 cm, with concentrations of $14.22 \mu\text{g/g}$ and $12.27 \mu\text{g/g}$, respectively. The similar trend of Zn, Pb and Ni suggests that metals were highly distributed within the 15 years from 1825 to 1913 in this area. However, Cd concentrations in the sediment core of Sungai Buloh remained consistent, with $0.15 \mu\text{g/g}$ between depths of 1 to 21 cm and $0.17 \mu\text{g/g}$ between depths of 22 to 36 cm. In contrast, the vertical sediment core study by Lasumin et al. (2022) at Sungai Buloh reported the highest concentrations of Zn, Pb, and Cd as $80.18 \mu\text{g/g}$, $23.24 \mu\text{g/g}$, and $0.19 \mu\text{g/g}$, respectively. The highest concentrations were observed at depths of 9–12 cm for Zn and Pb and 0–3 cm for Cd.

In fact, the metals accumulated in the sediment core show a historical input in previous years in the study area. The difference in metal values is recorded due to metals that are produced naturally or also from a variety of human activities. It should be emphasised that the high Zn concentration may be attributed to the use of fertiliser in the past few years, when agriculture, such as oil palm cultivation, is actively carried out in this area. For instance, elevated levels of heavy metals, including Cu and Zn, have been detected in soil from Felda Jengka 8, Pahang, attributed to the use of fertilisers in oil palm plantations (Manan et al., 2018).

Table 4
The mean concentrations of heavy metals in the sediment core of Sungai Buloh (µg/g)

Depth (cm)	Years	Zn	Pb	Ni	Cd
1–3	2003–2018	131.31	28.23	13.13	0.15
4–6	1988–2003	128.46	27.14	12.50	0.14
7–9	1973–1988	131.99	28.69	13.30	0.15
10–12	1958–1973	133.70	29.25	13.98	0.15
13–15	1943–1958	127.30	28.36	12.32	0.15
16–18	1928–1943	134.83	29.89	13.61	0.15
19–21	1913–1828	140.60	31.43	14.22	0.15
22–24	1898–1913	123.78	27.52	12.27	0.18
25–27	1883–1898	130.88	29.28	13.50	0.17
28–30	1868–1883	131.45	30.04	13.63	0.17
31–33	1853–1868	123.61	30.34	12.97	0.17
34–36	1838–1853	124.50	30.75	13.36	0.16
Mean		130.20	29.24	13.23	0.16
Std		5.02	1.31	0.63	0.01

Vertical Heavy Metal Profiles of Sediment Core

Zinc (Zn)

Figure 2 shows the profiles of Zn in the vertical sediment cores collected from seven sampling points. At sampling point A, the Zn concentration was 109.53 µg/g in surface sediment (1–3 cm depth) and showed small variation between depths of 4–27 cm, with a mean concentration of 126.02 µg/g. A relatively high Zn concentration of 161.87 µg/g was observed in the layer at a 28–30 cm depth. At sampling point B, the Zn concentration decreased in the bottom sediment core at a depth of 22–36 cm, with a higher concentration recorded at 19–21 cm, and the lowest concentration found at a depth of 13 to 15 cm with concentrations of 146.16 and 125.82 µg/g, respectively. This pattern is similar to the Zn profile recorded at sampling point E. At sampling point C,

a high Zn concentration of 131.6 $\mu\text{g/g}$ was recorded in the upper sediment; then, the values decreased until a depth of 13 to 15 cm. Variation in Zn concentration occurred in the middle and lower layers of the sediment core. At sampling point D, the deeper the sediment, the higher the Zn concentration, with the highest concentration of 121.67 $\mu\text{g/g}$ recorded at a depth of 31–36 cm. Sampling point F showed the highest Zn concentration at the sediment surface, 138.55 $\mu\text{g/g}$, with large variations along the vertical core. Unlike the other sampling points, at sampling point G, the Zn concentration decreased from 1–18 cm depth, but at 19–21 cm, it recorded the highest concentration of 208.1 $\mu\text{g/g}$. The pattern of Zn concentrations observed in the sediment core from Sungai Buloh was comparable to findings reported by Baharudin et al. (2021) in their study of the Strait of Malacca, which covered areas in Johor, Selangor, and Penang. The presence of Zn in the Sungai Buloh sediment is primarily attributed to water runoff from palm oil plantations and effluents from nearby manufacturing industries.

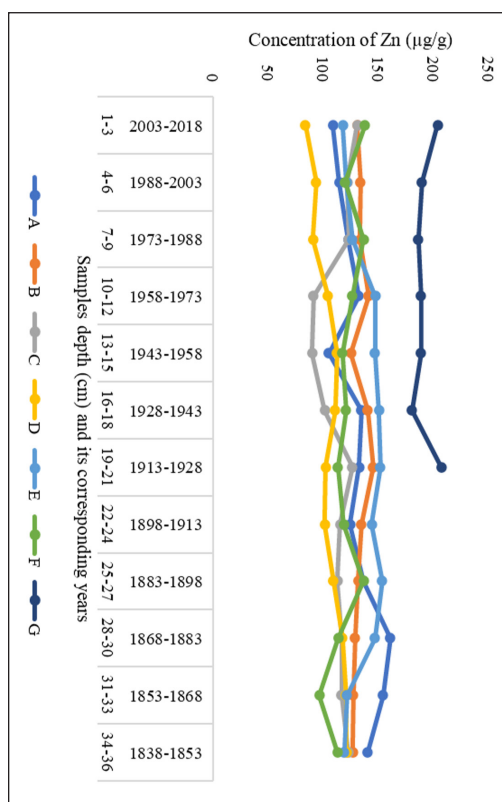


Figure 2. The concentration of Zn in sediment cores from Sungai Buloh

Lead (Pb)

For sampling points A and B, the Pb concentration in the sediment core increased from the 1-12 cm layer (Figure 3). The variation in Pb concentration is small in the middle to bottom layers for both sampling points, with Pb concentrations recorded at 31.89 and 28.68 $\mu\text{g/g}$, respectively, in the final layer. Generally, Pb concentration decreased toward the middle depth of sampling points C, F, and G. Pb increased relatively in the layer 13 to 21 cm before stabilising in the layers 22 to 30 cm and slightly increasing in the lower layer of sampling point C. Sampling point F showed small variation in Pb concentration, but the lowest Pb concentration was documented in the 31–33 cm layer at 21.73 $\mu\text{g/g}$. The Pb concentration at sampling point G was higher compared to other points, with the highest value of 51.71 $\mu\text{g/g}$ in the surface sediment. Sampling points D and E exhibited a similar pattern, where Pb concentration increased with depth, reaching the highest concentrations

of 36.65 and 36.18 $\mu\text{g/g}$, respectively, in a final depth of 34 to 36 cm. The variation of Pb in the sediment core was also observed in the Matang Mangrove Forest Reserve (Mustapha et al., 2022), with Sungai Buloh recording higher Pb levels in the sediment compared to this area. The presence of Pb in the sediment is attributed to boating activities related to fisheries and tourism, where gasoline or diesel is used for boat engines. The large number of boats and potential gasoline leakage can significantly increase Pb levels in the water and sediment (Pazi et al., 2021; Mustapha et al., 2022).

Nickle (Ni)

For sampling points A, D, and E, the Ni concentration followed a similar pattern: an increase in the sediment core from 1 to 18 cm followed by minor variation in the next layer (Figure 4). This Ni pattern is similar to the study by Omorinoye et al. (2019) in the Sadong River in Sarawak,

where the concentration also increased with depth. Among these three points, sampling point E exhibited the highest Ni concentration, reaching 21.39 $\mu\text{g/g}$ at the 25–27 cm depth layer. At sampling point B, the highest Ni concentration was 16.78 $\mu\text{g/g}$, detected in the 1–12 cm layer, after which it decreased, showing only small variations from 13–36 cm in depth. Sampling point C showed large variations in Ni concentration between 1–21 cm. The lowest concentration of 4.31 $\mu\text{g/g}$ was recorded at 13–15 cm, then increased until 19–21 cm, followed by a slight decrease and stable values at 22–30 cm, then increased to 12.10 $\mu\text{g/g}$ at 34 to 36 cm. At sampling point F, both the upper layer from 1 to 9 cm and the bottom layer from 25 to 36 cm exhibited significant variations in Ni concentration, while the middle core (10 to 27 cm) showed small variations. For sampling point G, the Ni concentration slightly decreased with depth, but at the final layer of 19–21 cm, it increased to 21.78 $\mu\text{g/g}$. The concentration of Zn in Sungai Buloh was comparable to that in Sadong River but significantly lower than in the Sungai Buloh in Selangor (Abubakar et al., 2018). Manufacturing activities, including those related to the chemical processes industry, contribute to the presence of Ni in the sediment of Sungai Buloh.

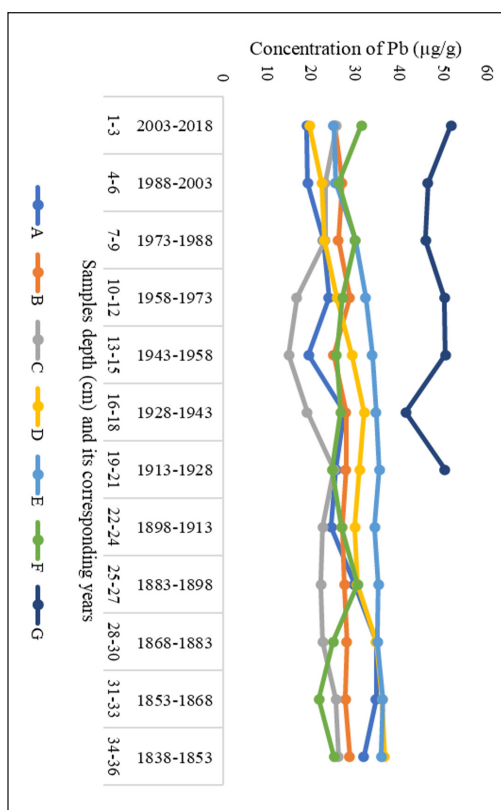


Figure 3. The concentration of Pb in sediment cores from Sungai Buloh

Cadmium (Cd)

At sampling sites A, F, and G, the Cd concentration in the sediment core consistently remained below 0.10 µg/g, with mean values of 0.05 µg/g, 0.09 µg/g, and 0.01 µg/g, respectively (Figure 5). At sampling site A, the Cd concentration increased with depth, whereas at site F, it increased towards the sediment surface. This pattern aligns with findings by Lasumin et al. (2022) in Sungai Buloh, which also reported an increase in Cd concentration towards the surface sediment. At sampling point B, the Cd concentration showed small variations from 1 to 24 cm, with the highest value of 0.26 µg/g recorded at the 19 to 21 cm layer, then decreased towards the bottom layer from 25 to 36 cm. For sampling point C, the Cd concentration decreased from 1 to 12 cm, then increased from 13 to 36 cm, with the highest value of 0.24 µg/g. A constant Cd concentration was observed throughout the sediment core at sampling point D. At sampling point E, variations in Cd concentration were recorded throughout the depth of the sediment core, with the highest

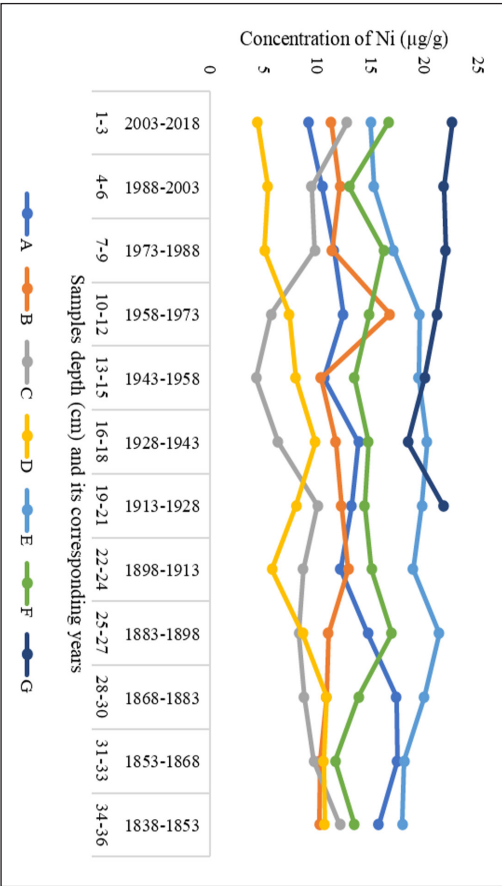


Figure 4. Concentration of Ni in sediment cores from Sungai Buloh

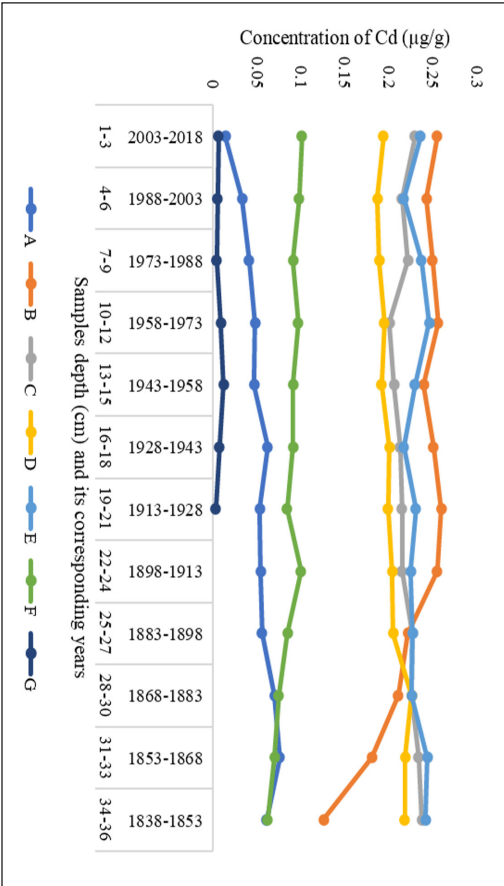


Figure 5. Concentration of Cd in sediment cores from Sungai Buloh

value of 0.25 µg/g at a depth between 10 to 12 cm. The Cd concentration at sampling site G is much lower due to the characteristics of the depositional environment, such as low water pH, which can increase Cd mobility (Zhang et al., 2023). As a result, a significantly lower concentration of Cd was detected at this site. However, the concentration of Cd observed in Sungai Buloh is significantly higher compared to the levels reported in previous studies conducted in Bagan Pasir, Perak; Sungai Buloh, Selangor; and Port Dickson, Negeri Sembilan (Lasumin et al., 2022). Human activities in the town within the study area, such as smelting manufacturing, release effluents into the drainage system, eventually accumulating in Sungai Buloh over time.

The Zn, Pb, and Ni levels were highest on average at sampling point G in the Sungai Buloh sediment cores. Results suggest that heavy metal pollution in the river originated from a combination of upstream contamination and effluents discharged from human activities in the Kuala Sungai Buloh area. This has led to an increased concentration of heavy metals at location G. As a result, heavy metals eventually accumulated in and adhered to the sediment. In contrast to the sampling point in the estuary, runoff carrying heavy metals mixed with seawater was affected by tides, reducing heavy metals' concentration before they finally accumulated in the sediment. In line with the analysed water parameters, the water quality at sampling point G is not particularly good, according to MMWQS. Heavy metals in Malaysian rivers are primarily attributed to anthropogenic and natural occurrences. For example, the anthropogenic activities include industrial waste, agricultural runoff, domestic effluents and landfill materials, as observed in Sungai Merbok in Kedah, Sungai Sembilang in Selangor, and Sepang Besar River in Selangor (Ateshan et al., 2020; Ibrahim et al., 2020; Krishnan et al., 2022).

This study's metal concentrations in sediment cores were compared to previous research in Malaysian marinas. The data revealed significantly higher heavy metal concentrations in the study area compared to sediment cores from coastal Sabah, Kong Kong estuaries in Johor, and the west coast of Peninsular Malaysia (Ashraf et al., 2018; Khalid et al., 2019; Lasumin et al., 2022). However, the mean concentrations of heavy metals from the seven sampling sites were lower than those reported in studies from Kaohsiung Harbor, Taiwan, and Dachan Bay, China (Chen et al., 2016; Yang et al., 2020).

To summarise, heavy metal concentrations exhibited significant spatial variability among the seven sediment cores, possibly due to different hydrodynamic mechanisms, including differences in heavy metal release sources and tidal water, varying sediment core characteristics, and homogeneous or inhomogeneous contaminants which are introduced into rivers and estuaries (Chen et al., 2016). However, Zn and Pb in the vertical sediment cores from sampling points B, D, and E showed a relatively stable pattern. This suggests that chemicals were released from the river and subsequently accumulated near the river mouth with minimal disturbance.

Bioavailability of Heavy Metals in Sediments Samples

Table 5 shows the concentration and distribution of heavy metals in surface sediment. The ranges for Zn, Pb, Ni, and Cd are 126.73 to 199.16, 31.40 to 52.99, 12.00 to 23.93 and 0.003 to 0.070 µg/g, respectively.

In this study, the Zn was mainly residual form, particularly in the surface sediments of sampling points A, B, C, D, and E. The residual proportion ranged from 41.42% to 59.34%. Meanwhile, sampling points F and G were dominated by acid-reducible fractions at 43.39% and 39.64%, respectively. The surface sediments of the study area documented Zn fractionation order of [residual] > [oxidisable-organic] > [acid-reducible] > [exchangeable]. Pb was mainly in the residual form, with a proportion of 41.61 to 63.60 % and an average residual component of 52.50%. The average percentage of Pb proportion of the exchangeable (F1), acid-reducible (F2), and oxidisable-organic fraction (F3) are 1.13, 14.0, and 33.0%, respectively. The fractionation order of Pb was [residual] > [oxidisable-organic] > [acid-reducible] > [exchangeable]. Ni was also mainly in residual form, ranging from 37.43% to 53.05%, averaging 47.06%. The exchangeable fraction has the lowest average of 4.26%. Meanwhile, acid-reducible and oxidisable-organic Ni ranged from 10.13% to 31.69% and 22.66% to 39.79%, respectively. To summarise, the Ni in surface sediments has fractionation in order of [residual] > [oxidisable-organic] > [acid-reducible] > [exchangeable]. Furthermore, Cd was primarily in the residual form, accounting for

Table 5
Concentration of heavy metal for sequential metal extraction (mean ± SD) µg/g and percentage (%)

Sampling point	Zn	Pb	Ni	Cd
A				
F1	1.31±0.23 (0.69)	NA	0.59±0.04 (3.40)	0.004±0.001 (4.48)
F2	48.88±2.26 (25.95)	1.82±0.92 (4.02)	2.00±0.14 (11.47)	0.010±0.002 (11.17)
F3	60.17±0.55 (60.17)	16.84±0.99 (37.15)	6.94±0.11 (39.79)	0.017±0.002 (17.95)
F4	78.04±0.56 (78.04)	26.66±3.02 (58.83)	7.91±0.13 (45.34)	0.061±0.009 (66.40)
Sum total	188.4	45.32	17.45	0.092
Digestion	144.01	31.14	15.5	0.063
Differences	44.39	14.18	1.95	0.029
B				
F1	0.57±0.17 (0.34)	NA	0.65±0.03 (3.44)	0.006±0.001 (7.15)
F2	25.16±0.95 (15.28)	1.09±0.3 (2.66)	1.96±0.07 (10.33)	0.006±0.001 (7.24)
F3	52.87±2.18 (32.1)	16.06±4.44 (39.14)	6.97±0.33 (36.82)	0.010±0.002 (12.97)
F4	86.09±6.10 (52.27)	23.88±5.39 (58.19)	9.36±0.82 (49.41)	0.056±0.006 (72.65)
Sum total	164.69	41.03	18.94	0.077
Digestion	130.75	27.8	11.05	0.199
Differences	33.94	13.23	7.89	0.122

Table 5 (continue)

Sampling point	Zn	Pb	Ni	Cd
C				
F1	0.67±0.09 (0.4)	0.44±0.27 (1.02)	0.74±0.04 (3.84)	0.004±0.002 (5.27)
F2	24.98±0.35 (14.92)	2.27±0.25 (5.22)	1.95±0.06 (10.13)	0.006±0.001 (7.8)
F3	49.76±0.75 (29.72)	18.67±1.61 (43.01)	6.35±0.33 (32.98)	0.011±0.002 (13.57)
F4	92.01±7.71 (54.96)	22.03±2.09 (50.76)	10.22±0.28 (53.05)	0.058±0.009 (73.37)
Sum total	167.41	43.41	19.25	0.079
Digestion	117.49	23.83	9.5	0.228
Differences	49.92	19.58	9.75	0.149
D				
F1	0.39±0.06 (0.25)	0.87 (1.96)	0.71±0.05 (4.26)	0.003±0.001 (3.42)
F2	20.61±0.93 (13.12)	2.22±0.20 (5.02)	1.80±0.15 (10.86)	0.008±0.002 (9.45)
F3	42.87±1.78 (27.29)	18.44±2.16 (41.68)	5.40±0.23 (32.54)	0.011±0.001 (13.2)
F4	93.20±24.93 (59.34)	22.71±4.37 (51.35)	8.68±0.77 (52.34)	0.060±0.007 (73.93)
Sum total	157.08	44.24	16.58	0.081
Digestion	114.65	33.55	9.31	0.214
Differences	42.43	10.69	7.27	0.133
E				
F1	1.75±0.09 (1.18)	NA	0.94±0.08 (6.19)	0.006 (7.5)
F2	31.90±8.80 (21.54)	0.89±0.65 (2.32)	1.84±0.23 (12.1)	0.015±0.003 (17.5)
F3	40.56±12.83 (27.39)	13.11±7.03 (34.09)	4.95±1.81 (32.59)	0.008±0.004 (9.11)
F4	73.89±8.05 (49.89)	24.45±6.68 (63.6)	7.46±1.67 (49.12)	0.055±0.013 (65.89)
Sum total	148.1	38.45	15.18	0.083
Digestion	137.78	35.33	19.28	0.233
Differences	10.32	3.12	4.1	0.15
F				
F1	1.86±0.18 (1.47)	NA	0.70±0.04 (5.8)	0.004±0.001 (7.8)
F2	55.01±11.27 (43.39)	10.35±7.28 (32.97)	2.87±1.13 (23.93)	0.015±0.006 (26.58)
F3	26.45±15.50 (20.86)	7.98±6.43 (25.42)	3.94±1.59 (32.83)	0.003±0.002 (5.07)
F4	43.45±11.19 (34.28)	13.07±4.06 (41.61)	4.49±0.73 (37.43)	0.035±0.010 (60.55)
Sum total	126.78	31.4	12.02	0.057
Digestion	116.36	25.86	14.21	0.078
Differences	10.41	5.54	2.19	0.021
G				
F1	4.31±0.28 (2.17)	0.21 (0.4)	0.70±0.07 (5.8)	NA
F2	78.95±3.95 (39.64)	24.32±1.37 (45.9)	7.58±0.48 (31.69)	0.031±0.003 (30.52)
F3	41.78±6.79 (20.98)	5.73±1.86 (10.82)	5.42±0.59 (22.66)	NA
F4	74.12±1.77 (37.21)	22.72±4.55 (42.88)	10.23±0.49 (42.85)	0.071±0.027 (69.48)
Sum total	199.16	52.99	23.93	0.103
Digestion	191.1	25.86	20.7	0.117
Differences	8.06	27.13	3.23	0.014

an average of 68.90% of the residual component. The proportion of exchangeable, acid-reducible, and oxidisable-organic fractions is 5.09%, 15.75% and 10.27%, respectively. Hence, the fractionation of Cd in surface sediments of the study areas is arranged in order of [residual] > [acid-reducible] > [oxidisable-organic] > [exchangeable].

The residual fraction of heavy metals exhibited the highest concentration among all fractions, suggesting that most heavy metals found in the surface sediment of Sungai Buloh are derived from natural sources (Figure 6). High metal concentrations in the residue fraction may be attributed to proximity to mangrove areas and geological weathering (Doabi et al., 2017; Swati & Hait, 2017). Additionally, metals in this fraction are deemed biologically unavailable because they are bound within the crystal lattice, rendering them inaccessible (El-Azim & El-Moselhy, 2005). Meanwhile, the first exchangeable fraction has the lowest average percentage of metal, followed by the acid-reducible and oxidisable-organic fractions. Together, these three fractions constitute the bioavailable fractions of anthropogenic origin. The high percentage of these fractions indicates significant anthropogenic activities, leading to substantial metal pollution in the water column. The percentage of Zn and Ni were significantly found to be high in these fractions at sampling points A, F, and G. Meanwhile, Pb was detected high at sampling points F and G, such as in Figure 6. This fraction poses the most significant potential risk to humans and aquatic organisms due to its easy availability with minimal changes in the sediment’s physicochemical conditions. The activities that contributed to

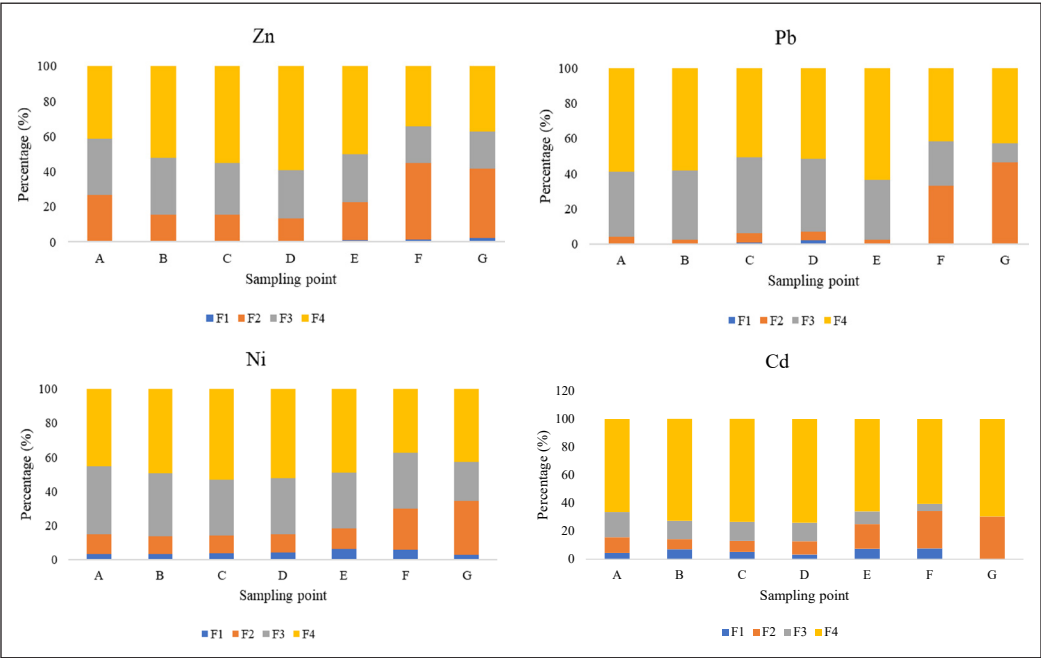


Figure 6. Sequential fractionation of heavy metals in surface sediment samples of Sungai Buloh

these pollutants in the Sungai Buloh area include industrialisation, agricultural activities involving the leaching of fertilisers and pesticides, manufacturing, workshops and other domestic activities.

Environmental Indices

This study uses selected indices such as I_{geo} , CF, and PLI to evaluate the extent of heavy metal contamination in the sediment. Table 6 indicates the I_{geo} of four heavy metals in sediment collected from seven sampling points. The range value of the I_{geo} index of Zn, Pb, Ni and Cd are from -0.23 to 0.45, -0.07 to 0.39, -2.98 to -2.19 and -2.74 to -1.51, respectively. Zn has the highest value of I_{geo} , which is found in sampling point G with the value of 0.45 (I_{geo} Class 1). Meanwhile, I_{geo} for Pb in each site except for sampling point F has values categories in Class 1, indicating that this element presents an ecological risk. In contrast, the I_{geo} values for Ni and Cd at all sites are below 0 (I_{geo} Class 0), indicating that these elements do not pose an ecological risk. Generally, all sampling points are categorised as unpolluted for each metal as the I_{geo} is lower than 1; however, Zn and Pb, which have I_{geo} values 0 to 1, indicate unpolluted to moderately contaminated in selected sampling points that have a chance of causing adverse effects towards the organisms.

Table 6
The I_{geo} index for the sediment from Sungai Buloh

Sampling Point	Zn	Pb	Ni	Cd
A	0.22	0.35	-2.63	-2.54
B	0.05	0.20	-2.77	-1.71
C	0.00	0.16	-2.83	-1.55
D	-0.07	0.37	-2.98	-1.61
E	0.00	0.30	-2.57	-1.51
F	-0.23	-0.07	-2.96	-2.74
G	0.45	0.39	-2.19	-2.03

The results obtained from the Contamination Factor (CF) followed a trend similar to that of I_{geo} . The CF for Zn, Pb, Ni, and Cd are within the ranges of 1.28 to 2.05, 1.43 to 1.97, 0.19 to 0.33, and 0.23 to 0.53, respectively. According to Table 7, Zn and Pb exhibit CF values between 1 and 3, indicating moderate contamination across sampling points A to G. Conversely, Ni and Cd, with CF values below 1 at all sampling points, are classified as low contamination. Sampling point G has the highest PLI value at 0.84, while sampling point F has the lowest at 0.53. PLI values indicated that all sampling points are unpolluted, as the PLI values are less than 1.

The Zn pollution in this area may originate from activities such as metal production, fossil fuel combustion, fertiliser use, and industrial, all of which can elevate Zn levels in

the environment. Pb is widely used as an additive in various applications, including lead pipes and paints, and contributes to pollution and gasoline leaks. Both Zn and Pb are found at moderate levels in the sediment of Sungai Buloh, resulting from a combination of natural occurrences and human activities. In contrast, Ni and Cd exhibit lower contamination levels, primarily due to natural occurrences leading to a low pollution status in Sungai Buloh. However, minimal human activities release Ni, typically used in chemical processing industries. Cd contamination, on the other hand, can be linked to mining and smelting activities, manufacturing processes, fertiliser application, and battery usage.

The findings from the study suggest that ongoing industrial, plantation, and domestic activities in the Sungai Buloh area, which result in the discharge of effluents containing heavy metals into water bodies, appear to be in compliance with the provisions outlined in Section 25 of the Environmental Quality Act 1974 (EQA 1974). This compliance reflects the effectiveness of the existing legal framework in controlling heavy metal pollution. However, the detection of moderate contamination underscores the necessity for continuous environmental monitoring to ensure that pollution levels remain within permissible limits and do not escalate over time.

Table 7
Contamination Factor (CF) and Pollution Load Index (PLI) of sediment from Sungai Buloh

Point	Zn	Pb	Ni	Cd	PLI
A	1.75	1.91	0.24	0.26	0.68
B	1.55	1.72	0.22	0.46	0.72
C	1.50	1.68	0.21	0.51	0.72
D	1.43	1.94	0.19	0.49	0.71
E	1.50	1.84	0.25	0.53	0.78
F	1.28	1.43	0.19	0.23	0.53
G	2.05	1.97	0.33	0.37	0.84

CONCLUSION

The distribution of selected heavy metals of Zn, Pb, Ni, and Cd in Sungai Buloh, Selangor, was assessed using sediment samples. The mean concentrations of these metals in the sediments, determined by aqua regia digestion, are as follows: Zn ($130.406 \pm 25.605 \mu\text{g/g}$) > Pb ($29.221 \pm 7.811 \mu\text{g/g}$) > Ni ($13.083 \pm 4.956 \mu\text{g/g}$) > Cd ($0.166 \pm 0.074 \mu\text{g/g}$). The sediment’s fractionation of these heavy metals was evaluated using a sequential extraction technique. For Zn, Pb, and Ni, the distribution follows the trend: [residual] > [oxidisable-organic] > [acid-reducible] > [exchangeable]. For Cd, the trend is: [residual] > [acid-reducible] > [oxidisable-organic] > [exchangeable]. Environmental indices of the sediment, determined by the I_{geo} index, indicate that Kuala Sungai Buloh, Selangor, is unpolluted to

moderately contaminated at selected sampling points for Zn and Pb. Meanwhile, the CF shows moderate contamination for Zn and Pb and low contamination for Ni and Cd. The PLI indicates no significant heavy metal pollution in the area, as the PLI values are below 1. Manufacturing, industrial, plantation, and domestic activities, mainly natural occurrences, contribute to the presence and occurrence of these heavy metals in the rivers and estuaries of Sungai Buloh; however, they do not cause major pollution in the environment. Further research in Sungai Buloh is recommended, particularly focusing on cockles, as this area is commercially significant for their cultivation. This is essential to ensure the safety of both aquatic life and humans.

ACKNOWLEDGEMENTS

This research was funded by a special Fundamental Research Grant Scheme (FRGS) from the Malaysian Ministry of Education. The grant, reference number KPT.P.(S)400-7/2/29-4(65), supported a matching fund collaboration between the JSPS Asian CORE Program and Universiti Putra Malaysia (UPM).

REFERENCES

- Abollino, O., Malandrino, M., Giacomino, A., & Mentasti, E. (2011). The role of chemometrics in single and sequential extraction assays: A review: Part I. Extraction procedures, uni- and bivariate techniques and multivariate variable reduction techniques for pattern recognition. *Analytica Chimica Acta*, 688(2), 104-121. <https://doi.org/10.1016/j.aca.2010.12.020>
- Abubakar, U. S., Zulkifli, S. Z., & Ismail, A. (2018). Heavy metals bioavailability and pollution indices evaluation in the mangrove surface sediment of Sungai Puloh, Malaysia. *Environmental Earth Sciences*, 77, 1-12. <https://doi.org/10.1007/s12665-018-7399-1>
- Ali, S., Abbas, Z., Rizwan, M., Zaheer, I. E., Yavaş, İ., Ünay, A., Abdel-DAIM, M. M., Jumah, M., Hasanuzzaman, M., & Kalderis, D. (2020). Application of floating aquatic plants in phytoremediation of heavy metals polluted water: A review. *Sustainability*, 12(5), Article 1927. <https://doi.org/10.3390/su12051927>
- Ashraf, A., Saion, E., Gharibshahi, E., Yap, C. K., Kamari, H. M., Elias, M. S., & Rahman, S. A. (2018). Distribution of heavy metals in core marine sediments of coastal east Malaysia by instrumental neutron activation analysis and inductively coupled plasma spectroscopy. *Applied Radiation and Isotopes*, 132, 222-231. <https://doi.org/10.1016/j.apradiso.2017.11.012>
- Ateshan, H. M., Misnan, R., Sinang, S. C., & Koki, I. B. (2020). Evaluation of water pollution and source identification in Merbok River Kedah, Northwest Malaysia. *Malaysian Journal of Fundamental and Applied Sciences*, 16, 458-463.
- Awad, M., Liu, Z., Skalicky, M., Dessoky, E. S., Brestic, M., Mbarki, S., Rastogi, A., & El Sabagh, A. (2021). Fractionation of heavy metals in multi-contaminated soil treated with biochar using the sequential extraction procedure. *Biomolecules*, 11(3), Article 448. <https://doi.org/10.3390/biom11030448>

- Aydın, H., Tepe, Y., & Ustaoglu, F. (2023). A holistic approach to the eco-geochemical risk assessment of trace elements in the estuarine sediments of the Southeastern Black Sea. *Marine Pollution Bulletin*, 189, Article 114732. <https://doi.org/10.1016/j.marpolbul.2023.114732>
- Aziz, K. H. H., Mustafa, F. S., Omer, K. M., Hama, S., Hamarawf, R. F., & Rahman, K. O. (2023). Heavy metal pollution in the aquatic environment: efficient and low-cost removal approaches to eliminate their toxicity: A review. *RSC advances*, 13(26), 17595-17610. <https://doi.org/10.1039/D3RA00723E>
- Badri, M. A., & Aston, S. R. (1983). Observations on heavy metal geochemical associations in polluted and non-polluted estuarine sediments. *Environmental Pollution Series B, Chemical and Physical*, 6(3), 181-193. [https://doi.org/10.1016/0143-148X\(83\)90033-2](https://doi.org/10.1016/0143-148X(83)90033-2)
- Baharudin, W. N. I. M., Ravikumar, L., Maran, V. B., Dass, D. A. A., Rosli, N. A. S., Mustafa, N. K., Dzulkafli, N. F., & Ong, M. C. (2021). Heavy metal pollution in the core sediment of Strait of Malacca. In *International Conference on Mediterranean Geosciences Union* (pp. 41-45). Springer. https://doi.org/10.1007/978-3-031-42917-0_10
- Bhuyan, M. S., Haider, S. M. B., Meraj, G., Bakar, M. A., Islam, M. T., Kunda, M., Siddique, M.A.B., Ali, M.M., Mustary, S., Mojumder, I. A., & Bhat, M. A. (2023). Assessment of heavy metal contamination in beach sediments of eastern St. Martin's Island, Bangladesh: Implications for environmental and human health risks. *Water*, 15(13), Article 2494. <https://doi.org/10.3390/w15132494>
- Buhari, T. R. I. (2020). Pollution status of heavy metals in surface sediments collected from west coast of peninsular Malaysia. *Open Access Library Journal*, 7(10), Article 103482.
- Chapra, S. C., Camacho, L. A., & McBride, G. B. (2021). Impact of global warming on dissolved oxygen and BOD assimilative capacity of the world's rivers: Modeling analysis. *Water*, 13(17), Article 2408. <https://doi.org/10.3390/w13172408>
- Chen, C. F., Ju, Y. R., Chen, C. W., & Dong, C. D. (2016). Vertical profile, contamination assessment, and source apportionment of heavy metals in sediment cores of Kaohsiung Harbor, Taiwan. *Chemosphere*, 165, 67-79. <https://doi.org/10.1016/j.chemosphere.2016.09.019>
- De Morais, C. P., Babos, D. V., Costa, V. C., Neris, J. B., Nicolodelli, G., Mitsuyuki, M. C., Mauad, F. F., Mounier, S., & Milori, D. M. B. P. (2022). Direct determination of Cu, Cr, and Ni in river sediments using double pulse laser-induced breakdown spectroscopy: Ecological risk and pollution level assessment. *Science of the Total Environment*, 837, Article 155699. <https://doi.org/10.1016/j.scitotenv.2022.155699>
- Doabi, S. A., Afyuni, M., & Karami, M. (2017). Multivariate statistical analysis of heavy metals contamination in atmospheric dust of Kermanshah province, western Iran, during the spring and summer 2013. *Journal of Geochemical Exploration*, 180, 61-70. <https://doi.org/10.1016/j.gexplo.2017.06.007>
- Domingues, H., & e Silva, J. M. V. (1990). Copper and zinc in sandy, granitic and schist soils. *Environmental Technology*, 11(5), 463-468. <https://doi.org/10.1080/09593339009384886>
- El-Azim, H. A., & El-Moselhy, K. M. (2005). Determination and partitioning of metals in sediments along the Suez Canal by sequential extraction. *Journal of Marine Systems*, 56(3-4), 363-374. <https://doi.org/10.1016/j.jmarsys.2004.12.001>
- Elena, T. (2019). Impact of climate change on the water quality of the Danube River lower sector. *Revista Riscuri Si Catastrofe*, 25(2), 115-130.

- Frémion, F., Bordas, F., Mourier, B., Lenain, J. F., Kestens, T., & Courtin-Nomade, A. (2016). Influence of dams on sediment continuity: A study case of a natural metallic contamination. *Science of the Total Environment*, 547, 282-294. <https://doi.org/10.1016/j.scitotenv.2016.01.023>
- Golui, D., Datta, S. P., Dwivedi, B. S., Meena, M. C., Trivedi, V. K., Jaggi, S., & Bandyopadhyay, K. K. (2021). Assessing geoavailability of zinc, copper, nickel, lead and cadmium in polluted soils using short sequential extraction scheme. *Soil and Sediment Contamination: An International Journal*, 30(1), 74-91. <https://doi.org/10.1080/15320383.2020.1796924>
- Gu, Y. G. (2021). Risk assessment of eight metals and their mixtures to aquatic biota in sediments with diffusive gradients in thin films (DGT): A case study in Pearl River intertidal zone. *Environmental Sciences Europe*, 33, 1-11. <https://doi.org/10.1186/s12302-021-00564-1>
- Ibrahim, T. N. B. T., Othman, F., & Mahmood, N. Z. (2020). Baseline study of heavy metal pollution in a tropical river in a developing country. *Sains Malaysiana*, 49(4), 729-742. <https://doi.org/10.17576/jsm-2020-4904-02>
- Ismail, A., & Ramli, R. (1997). Trace metals in sediments and molluscs from an estuary receiving pig farms effluent. *Environmental Technology*, 18(5), 509-515. <https://doi.org/10.1080/09593331808616566>
- Khalid, S. A. K., Yusuff, F. M., & Mohd, F. (2019). Spatial and vertical metals distribution in sediment cores from Kongkong Laut Estuary, Masai, Johor. *Pertanika Journal of Science & Technology*, 27(4), 1929-1939.
- Khan, W. R., Zulkifli, S. Z., Kasim, M. R. M., Zimmer, M., Pazi, A. M., Kamrudin, N. A., Rasheed, F., Zafar, Z., Mostapa, R., & Nazre, M. (2020). Risk assessment of heavy metal concentrations in sediments of Matang mangrove forest reserve. *Tropical Conservation Science*, 13, 1-12. <https://doi.org/10.1177/1940082920933122>.
- Krishnan, K., As, N., & My, C. (2022). Ecological risk assessment of heavy metal pollution in mangrove sediments of the Sepang Besar river, West Coast Peninsular Malaysia. *Environment and Ecology Research*, 10(4), 497-507. <https://doi.org/10.13189/eer.2022.100408>
- Lasumin, N., Mohamed, K. N., & Yusuff, F. M. (2022). Vertical distributions of Zn, Cd, Pb and Cu at tropical coastal sediments: In case of West Coast of Peninsular Malaysia. *Oriental Journal of Chemistry*, 38(6), 1514-1524. <http://dx.doi.org/10.13005/ojc/380625>
- Liang, Y., Wang, R., Sheng, G. D., Pan, L., Lian, E., Su, N., Tang, X., Yang, S., & Yin, D. (2023). Geochemical controls on the distribution and bioavailability of heavy metals in sediments from Yangtze River to the East China Sea: Assessed by sequential extraction versus diffusive gradients in thin-films (DGT) technique. *Journal of Hazardous Materials*, 452, Article 131253. <https://doi.org/10.1016/j.jhazmat.2023.131253>
- Liu, H., Chi, L., Shen, J., Arandiyana, H., Wang, Y., & Wang, X. (2023). Principles, applications, and limitations of diffusive gradients in thin films induced fluxes in soils and sediments. *Chemosphere*, 350, Article 141061. <https://doi.org/10.1016/j.chemosphere.2023.141061>
- Manan, W. N. A. A., Sulaiman, F. R., Alias, R., & Laiman, R. (2018). Determination of selected heavy metal concentrations in an oil palm plantation soil. *Journal of Physical Science*, 29, 63-70. <https://doi.org/10.21315/jps2018.29.s3.8>
- Mohamed, C. A. R., Mahmood, Z. W., & Ahmad, Z. (2008). Recent sedimentation of sediments in the coastal waters of Peninsular Malaysia. *International Journal Pollution Research*, 27(1), 27-36.

- Muller, G. (1969). Index of geoaccumulation in sediments of the Rhine River. *GEO Journal*, 2(3), 108-118.
- Mustapha, M. P. A., Khan, W. R., Rosli, N., Nuruddin, A. A., & Gandaseca, S. (2022). Assessment of mangrove sediment quality parameters from different seasons, zones and sediment depths. *Jurnal Manajemen Hutan Tropika*, 28(1), 22-31. <https://doi.org/10.7226/jtfm.28.1.22>
- Naji, A., Ismail, A., & Ismail, A. R. (2010). Chemical speciation and contamination assessment of Zn and Cd by sequential extraction in surface sediment of Klang River, Malaysia. *Microchemical Journal*, 95(2), 285-292. <https://doi.org/10.1016/j.microc.2009.12.015>
- Okerefor, U., Makhatha, M., Mekuto, L., Uche-Okerefor, N., Sebola, T., & Mavumengwana, V. (2020). Toxic metal implications on agricultural soils, plants, animals, aquatic life and human health. *International Journal of Environmental Research and Public Health*, 17(7), Article 2204. <https://doi.org/10.3390/ijerph17072204>
- Omorinoye, O. A., Assim, Z. B., Jusoh, I. B., Iya, N. I. D., & Asare, E. A. (2019) Vertical profile of heavy metal concentration in sediments from Sadong River, Sarawak, Malaysia. *Indian Journal Environmental Protection*, 39(11), 971-978.
- Pavón, A., Riquelme, D., Jaña, V., Iribarren, C., Manzano, C., Lopez-Joven, C., Reyes-Cerpa, S., Navarrete, P., Pavez, L., & García, K. (2022). The high risk of bivalve farming in coastal areas with heavy metal pollution and antibiotic-resistant bacteria: A Chilean perspective. *Frontiers in Cellular and Infection Microbiology*, 12, Article 867446. <https://doi.org/10.3389/fcimb.2022.867446>
- Pazi, A. M. M., Khan, W. R., Nuruddin, A. A., Adam, M. B., & Gandaseca, S. (2021). Development of mangrove sediment quality index in Matang Mangrove Forest Reserve, Malaysia: A synergetic approach. *Forests*, 12(9), Article 1279. <https://doi.org/10.3390/f12091279>
- Peytoureau, A. P., Arribas, A. J. M., Vieira, D. C., & Resgalla, C. (2023). Sensitivity of marine invertebrates to acidification of seawater by an atmosphere enriched with CO₂. *Brazilian Journal of Aquatic Science and Technology*, 27(2), 33-38. <https://doi.org/10.14210/bjast.v27n2.20464>
- Pradit, S., Noppradit, P., Jitkaew, P., Sengloyluan, K., Kobkeatthawin, T., Laerosa, A., & Sirivithayapakorn, S. (2022). Heavy metal contamination and ecological risk assessment in the sediment cores of the wetlands in Southern Thailand. *Journal of Marine Science and Engineering*, 10(12), Article 1921. <https://doi.org/10.3390/jmse10121921>
- Rainbow, P. S. (2018). Heavy metal levels in marine invertebrates. In R. W. Furness (Ed.), *Heavy Metals in the Marine Environment* (pp. 67-79). CRC Press.
- Swati, A., & Hait, S. (2017). Fate and bioavailability of heavy metals during vermicomposting of various organic wastes - A review. *Process Safety and Environmental Protection*, 109, 30-45. <https://doi.org/10.1016/j.psep.2017.03.031>
- Tomlinson, D. L., Wilson, J. G., Harris, C. R., & Jeffrey, D. W. (1980). Problems in the assessment of heavy-metal levels in estuaries and the formation of a pollution index. *Helgoländer Meeresuntersuchungen*, 33, 566-575. <https://doi.org/10.1007/BF02414780>
- Turekian, K. K., & Wedepohl, K. H. (1961). Distribution of the elements in some major units of the earth's crust. *Geological Society of America Bulletin*, 72(2), 175-192. [https://doi.org/10.1130/0016-7606\(1961\)72\[175:DOTEIS\]2.0.CO;2](https://doi.org/10.1130/0016-7606(1961)72[175:DOTEIS]2.0.CO;2)

- Vane, C. H., Turner, G. H., Chenery, S. R., Richardson, M., Cave, M. C., Terrington, R., Gowing, C. J. B., & Moss-Hayes, V. (2020). Trends in heavy metals, polychlorinated biphenyls and toxicity from sediment cores of the inner River Thames estuary, London, UK. *Environmental Science: Processes & Impacts*, 22(2), 364-380. <https://doi.org/10.1039/C9EM00430K>
- Wang, Y., Li, Q., Yun, X., Zhou, J., & Wang, J. (2022). A review on the ecotoxicological effects of heavy metals on aquatic organisms. *Journal of Earth Sciences & Environmental Studies*, 6, 148-161. <https://doi.org/10.25177/JESES.6.2.RA.10797>
- Yang, G., Song, Z., Sun, X., Chen, C., Ke, S., & Zhang, J. (2020). Heavy metals of sediment cores in Dachan Bay and their responses to human activities. *Marine Pollution Bulletin*, 150, Article 110764. <https://doi.org/10.1016/j.marpolbul.2019.110764>
- Ye, Z., Zhou, J., Liao, P., Finckro, Y. Z., Liu, Y., Shu, C., & Liu, P. (2022). Metal (Fe, Cu, and As) transformation and association within secondary minerals in neutralized acid mine drainage characterized using X-ray absorption spectroscopy. *Applied Geochemistry*, 139, Article 105242. <https://doi.org/10.1016/j.apgeochem.2022.105242>
- Yoon, S., Choi, J., Moon, S. J., & Choi, J. H. (2021). Determination and quantification of heavy metals in sediments through laser-induced breakdown spectroscopy and partial least squares regression. *Applied Sciences*, 11(15), Article 7154. <https://doi.org/10.3390/app11157154>
- Yuan, H., Yin, H., Yang, Z., Yu, J., Liu, E., Li, Q., Tai, Z., & Cai, Y. (2020). Diffusion kinetic process of heavy metals in lacustrine sediment assessed under different redox conditions by DGT and DIFS model. *Science of the Total Environment*, 741, Article 140418. <https://doi.org/10.1016/j.scitotenv.2020.140418>
- Zhang, W., Liang, Y., Sun, H., Wang, X., Zhou, Q., & Tang, X. (2023). Initial soil moisture conditions affect the responses of colloid mobilisation and associated cadmium transport in opposite directions. *Journal of Hazardous Materials*, 448, Article 130850. <https://doi.org/10.1016/j.jhazmat.2023.130850>
- Zinia, S. S., Yang, K. H., Lee, E. J., Lim, M. N., Kim, J., & Kim, W. J. (2023). Effects of heavy metal exposure during pregnancy on birth outcomes. *Scientific Reports*, 13(1), Article 18990. <https://doi.org/10.1038/s41598-023-46271-0>
- Zulkifli, S. Z., Ismail, A., Mohamat-Yusuff, F., Arai, T., & Miyazaki, N. (2010). Johor Strait as a hotspot for trace elements contamination in Peninsular Malaysia. *Bulletin of Environmental Contamination and Toxicology*, 84, 568-573. <https://doi.org/10.1007/s00128-010-9998-8>

Comparative Analysis of Ultrasonic Inspection Techniques for Corrosion Monitoring in Petrochemical Plants Using Analytic Hierarchy Process (AHP)

Jan Lean Tai¹, Mohamed Thariq Hameed Sultan^{2,3*} and Farah Syazwani Shahar²

¹Department of Aerospace Engineering, Faculty of Engineering, Universiti Putra Malaysia, 43400 UPM, Serdang, Selangor, Malaysia

²Laboratory of Biocomposite Technology, Institute of Tropical Forest and Forest Product (INTROP), Universiti Putra Malaysia, 43400 UPM, Serdang, Selangor, Malaysia

³Aerospace Malaysia Innovation Centre [944751-A], Prime Minister's Department, MIGHT Partnership Hub, Jalan Impact, 63600 Cyberjaya, Selangor Darul Ehsan, Malaysia

ABSTRACT

Selecting non-destructive inspection methods for corrosion monitoring and detection in petrochemical plants frequently relies on personal preferences rather than a rigorous assessment of the underlying rationale for specific testing techniques. Unchecked corrosion can lead to catastrophic failure; however, many of these inspection techniques are inefficient. Plant owners often struggle to select an inspection technique that is both time-efficient and provides good detectability. This study applied the Analytical Hierarchy Process (AHP) to identify the best ultrasonic testing technique for corrosion monitoring in process plants. Three techniques were evaluated: pulse-echo ultrasonic testing (UT A-Scan), ultrasonic thickness gauging (UTG), and phased-array ultrasonic testing corrosion mapping (PAUT-CM). Four attributes—time efficiency, defect detection, accuracy, and personnel training time—were identified from an initial set of eight attributes through expert surveys to construct the AHP framework. PAUT-CM demonstrated the highest efficiency, detectability, and accuracy, while UTG had the lowest training requirements. The AHP results indicated that PAUT-CM achieved the highest score of 0.4846, reflecting its effectiveness in extensive corrosion mapping scenarios. In contrast, UTG or UT A-Scan may yield higher scores in situations where only a limited number of

spot detections are required. By implementing the systematic approach proposed in this study, engineers can mitigate subjective bias and make informed decisions when selecting the most suitable testing method.

ARTICLE INFO

Article history:

Received: 17 September 2024

Accepted: 16 January 2025

Published: 04 April 2025

DOI: <https://doi.org/10.47836/pjst.33.3.16>

E-mail addresses:

taijanlean2008@hotmail.com (Jan Lean Tai)

thariq@upm.edu.my (Mohamed Thariq Hameed Sultan)

farahsyazwani@upm.edu.my (Farah Syazwani Shahar)

* Corresponding author

Keywords: AHP, non-destructive testing, phased array ultrasonic testing, ultrasonic testing

INTRODUCTION

Petrochemical plants have long encountered deterioration problems (Groysman, 2017), mainly due to the metallic material being the main application for fabrication and the environment being surrounded by corrosive substances such as carbon dioxide (CO_2), which is mainly produced from combustion processes and chemical reactions, and hydrogen sulfide (H_2S), generated during crude oil refining, sour gas processing, and certain wastewater treatment processes (Zhao et al., 2018).

The current industry increasingly utilizes advanced materials, such as glass fiber-reinforced and polyethylene composite pipes, to replace metals and mitigate corrosion issues. However, carbon steel remains the most widely used material due to its favorable mechanical properties and low cost (Ameh et al., 2018). Common failures in industrial settings stem from equipment aging, fatigue, and corrosion, which, if not properly managed, can lead to serious accidents, including fires, explosions, and hazardous substance leaks that pose significant risks to safety and production (Elwerfalli et al., 2016; Shih et al., 2017). Since 2000, one in five major refinery accidents in the European Union have been attributed to corrosion failure. Research by Wood et al. (2013) analyzed 99 corrosion-related accidents over the past 50 years in EU and OECD countries, emphasizing the need for ongoing vigilance regarding critical refinery equipment. Wan and Yang (2021) indicated that 80% of pressure vessel failures in plants are related to corrosion, while Laza (2017) noted that pipelines account for approximately 40% of significant plant losses, largely because many asset integrity management systems overlook piping systems in favor of more prominent components like pressure vessels and heat exchangers.

Corrosion can be classified into two main types: general and localized. General corrosion, or uniform corrosion, occurs when metal loses electrons uniformly, leading to gradual thinning of the material (Fajobi et al., 2019). This type of corrosion typically develops in the presence of chlorides, sulfides, and carbon dioxide on bare metal surfaces. In contrast, localized corrosion, specifically pitting corrosion, is characterized by small diameter but deep pits (Tai, Grzejda, et al., 2023). The detection of localized corrosion is particularly challenging, as it involves a process of pitting nucleation, metastable pit development, and steady-state pitting (Wang et al., 2021). If large pits are ignored, they can lead to leaks once they penetrate the material (Du et al., 2020; Shekari et al., 2017). Various non-destructive testing (NDT) methods, such as ultrasonic inspection, are utilized in petrochemical plants for several reasons. These methods feature portable equipment, making inspections easier to conduct. They provide real-time results, facilitating immediate decision-making and minimizing operational downtime. Additionally, NDT methods are versatile and can be applied to a wide range of materials. Their non-hazardous nature ensures safe inspections without risks to personnel or the environment.

Importantly, these methods are effective in detecting internal flaws, allowing for early identification of potential issues and contributing to the overall safety and reliability of the equipment.

The propagation properties of ultrasonic waves are directly linked to the mechanical properties of materials, such as density and modulus of elasticity (Sampath et al., 2021). Ultrasonic waves are also widely used in on-stream inspections to measure material thickness, aiding in the calculation of corrosion rates and the remaining life of components (Mohan et al., 2019).

Ultrasonic inspection encompasses three primary techniques: Ultrasonic thickness gauging (UTG), Pulse-echo ultrasonic testing (UT A-scan), and Phased array ultrasonic testing corrosion mapping (PAUT-CM). UTG measures the time it takes for ultrasonic waves to travel through a material and reflect back, providing a direct reading of material thickness. However, it is limited to spot measurements, which can be time-consuming for large areas (Ber et al., 2016). The Pulse-Echo method uses a transducer to generate ultrasonic waves and detect echoes, displaying the results as an A-scan, which graphically represents the amplitude of the reflected signals and can also be used to calculate ultrasonic velocity (Bazulin & Sadykov, 2018). PAUT-CM is an advanced technique that integrates ultrasonic testing with corrosion mapping, offering detailed information on the extent and location of corrosion within materials (Jamil & Yahya, 2019). Recent studies have highlighted the efficacy of PAUT-CM in providing comprehensive corrosion assessments, demonstrating its ability to detect and precisely locate corrosion features by utilizing multiple beam angles and depths, thereby significantly enhancing the accuracy and reliability of inspections (Lamarre, 2016; Turcotte et al., 2016).

Although each of these testing techniques has distinct advantages, engineers at petrochemical sites often select a specific technique based on personal preferences, which may lead to practical variations that do not yield the desired outcomes. When asked why a particular testing technique was chosen, it is not always feasible to obtain a satisfactory answer; this may be due solely to personal choices without an in-depth evaluation of the rationale behind the selection.

This study aims to explore the requirements of petrochemical plants in detail and demonstrate the selection procedure for choosing the best testing technique through the Analytic Hierarchy Process (AHP). In comparison to existing studies that have utilized the AHP for NDT, this research demonstrates a novel application specifically centered on ultrasonic testing techniques.

For instance, studies by Omar and Nehdi (2016) and Liu et al. (2022) have highlighted the importance of criteria like capability and cost-effectiveness in NDT methods. However, they did not focus on the comparative efficiency of ultrasonic techniques in the specific context of corrosion monitoring within petrochemical plants.

This approach aims to provide a model for future petrochemical plant owners, enabling them to select a valid and convincing testing technique based on actual conditions rather than purely personal preference.

Time efficiency, defect detection, accuracy, and personnel training time were selected from eight attributes to construct the AHP based on the survey’s higher score. Time efficiency is essential as it minimizes downtime, allowing plants to quickly identify and address corrosion issues, thereby maintaining productivity and reducing financial losses. The capability of defect detection is vital for preventing minor corrosion problems from escalating into major failures, ensuring the integrity of critical equipment and enhancing safety. Accuracy in measurement is crucial for making informed maintenance decisions; inaccurate assessments could lead to misguided repairs or replacements, potentially resulting in catastrophic failures. Lastly, reducing personnel training time is important for ensuring that operators can swiftly adapt to advanced testing techniques, promoting a safer working environment and more reliable inspections.

The AHP provides a structured, objective, and multi-criteria decision-making (MCDM) framework by breaking down complex decisions into manageable components. It enables decision-makers to organize their thoughts by defining a hierarchy of criteria and sub-criteria relevant to the decision at hand. Each criterion is then weighed up based on its importance, allowing for a systematic comparison of different options. AHP quantifies subjective judgments through pairwise comparisons, transforming them into numerical values that facilitate objective analysis. This process culminates in a comprehensive range of alternatives based on their overall scores, helping decision-makers identify the most suitable choice. By integrating both qualitative and quantitative assessments, AHP supports informed decision-making that considers multiple factors, ultimately leading to more robust and justifiable outcomes in selecting testing techniques for corrosion assessment in petrochemical plants.

METHODOLOGY

The methodology is divided into several key steps to determine the most effective ultrasonic testing technique for corrosion monitoring in petrochemical plants using the AHP: Survey design and administration, experimental setup, AHP analysis, and sensitivity analysis (Figure 1).

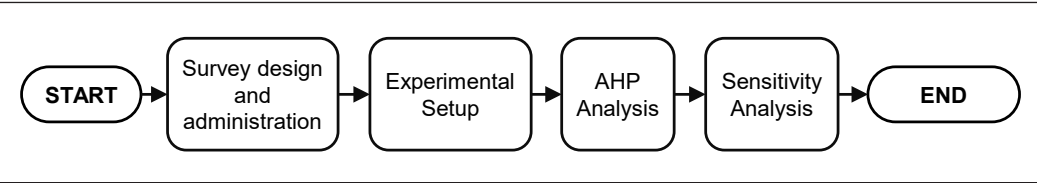


Figure 1. Process flow chart

Survey Design and Administration

The survey aimed to gain insights into the priority needs of petrochemical plants regarding NDT techniques. This information was crucial for selecting the most critical attributes for evaluating various NDT methods. Participants included two engineers from petrochemical plants, one project manager, three project engineers, one quality engineer from plant maintenance contractors, one NDT Level 3 technical manager, and two engineers from NDT companies. The survey involved two management-level candidates and eight engineers; however, they preferred not to disclose their company names.

The questionnaire was designed using the think tank method to ensure comprehensive and consensus-based feedback. This approach involved assembling a small group of experts from relevant sectors, including management-level candidates and engineers, to provide diverse perspectives. These experts participated in face-to-face discussions and video conferences to brainstorm and refine the eight attributes, along with their definitions, that were deemed important and measurable.

The survey evaluated eight attributes: cost-effectiveness, defined as low costs in terms of equipment, resources, and overall implementation; consistency, which ensures the uniform identification of defects over time and among different personnel; competence, indicating that the inspection process is conducted by qualified and certified personnel; detectability, assessing the effectiveness of identifying target defects; accuracy, highlighting the precise identification of defects; efficiency, characterized by minimal preparation and inspection time; safety, focused on minimizing potential risks; and compatibility, ensuring seamless coexistence with other industrial operations. These attributes were selected based on industry standards, expert recommendations, and their potential impact on operational efficiency and safety. Each participant rated the attributes on a scale from 1 to 8, with 8 indicating the most important attribute and 1 the least important.

The survey administration was conducted both face-to-face and via video conference to accommodate scheduling difficulties. The results revealed that “accuracy” received the highest score (73), followed by “detectability” (71), “efficiency” (64), and “competence” (50). In contrast, lower scores were assigned to “safety” (35), “compatibility” (34), “cost-effectiveness” (20), and “consistency” (13). Based on these findings, four key attributes—accuracy, detectability, efficiency, and competence—were selected to construct the hierarchical structure of AHP, as shown in the network diagram in Figure 2.

Experimental Setup

Once the four most important attributes have been identified, the next step is to assign weights to the three testing techniques, with the exception of competence, which will be assessed based on the time required to train personnel using international indicators. The other three attributes will be compared through actual experiments.

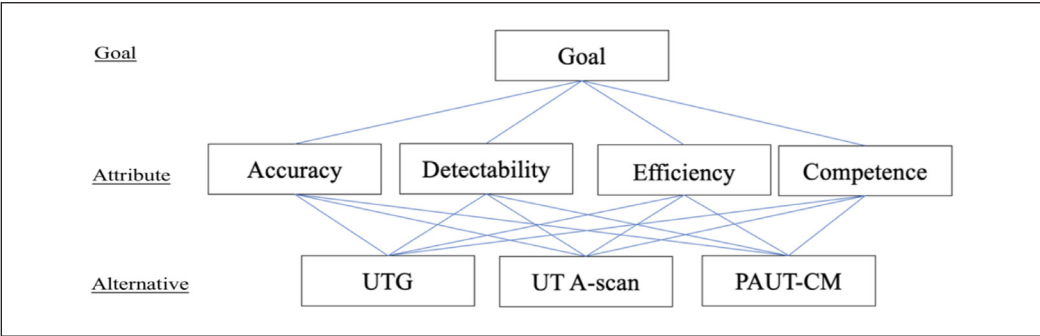


Figure 2. AHP hierarchy structure

A specimen with artificial marks was designed to compare the attribute weights of the three testing techniques (UTG, UT A-scan, and PAUT-CM). As shown in Figure 3, a 300 mm × 280 mm carbon steel plate with an uneven surface represents general corrosion, and some deep abrasion marks represent localized corrosion defects. Three different testing techniques were performed on the same specimen to obtain accuracy, detectability, and efficiency attribute weight results.

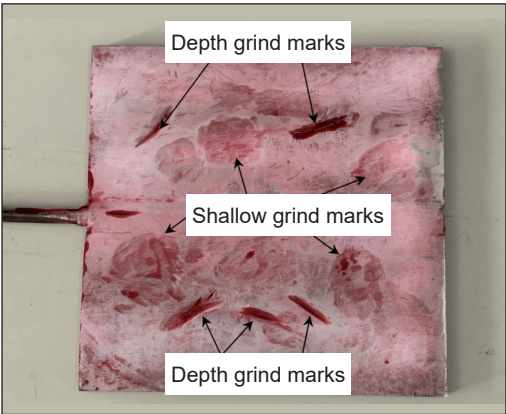


Figure 3. Artifact test specimen

Pulse-echo Ultrasonic Testing

The straight beam probe used for the experiment was a 4 MHz frequency single-crystal probe with a 20 mm diameter (Thanh et al., 2015). The test specimen was marked with a 20 mm × 20 mm grid from A1 to N15 to ensure full coverage during scanning (Figure 4). The 20 mm circle represents the probe diameter, and data was collected from the grid's center point to guarantee complete coverage.

The ultrasonic tests were calibrated using a V1 calibration block, with water used as the contact medium (Tariq et al., 2011). Three sets of readings were taken at each grid point to reduce human error; variations may have resulted from different pressures applied to the probe during the data acquisition (Wall et al., 2009). As illustrated in Figure 5, the A-scan data were referenced to the first backwall echo and verified using the second backwall echo. The total time taken to plot the grid lines and acquire data from 210 test points for a 300 mm × 280 mm test specimen using the UT A-Scan was one hour and twenty minutes, which facilitated the comparison of efficiency attributes.

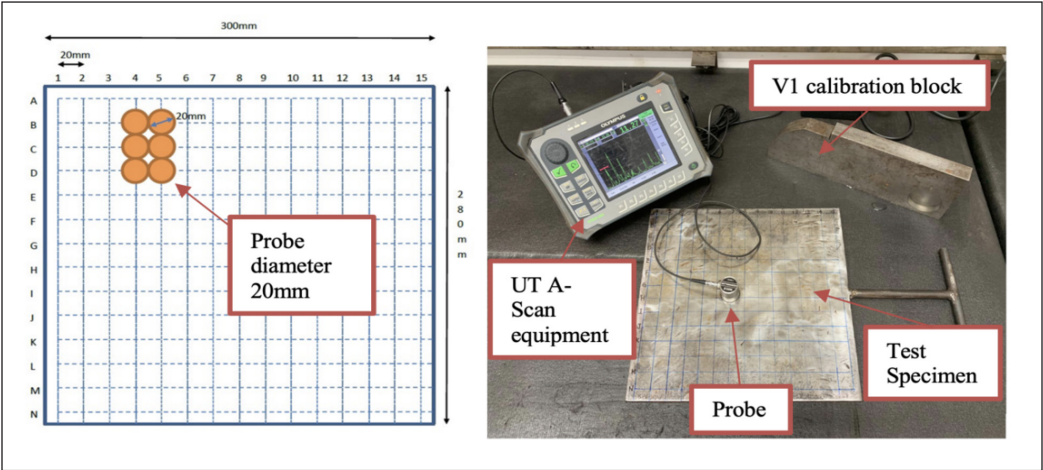


Figure 4. UT A-Scan grid line and setup

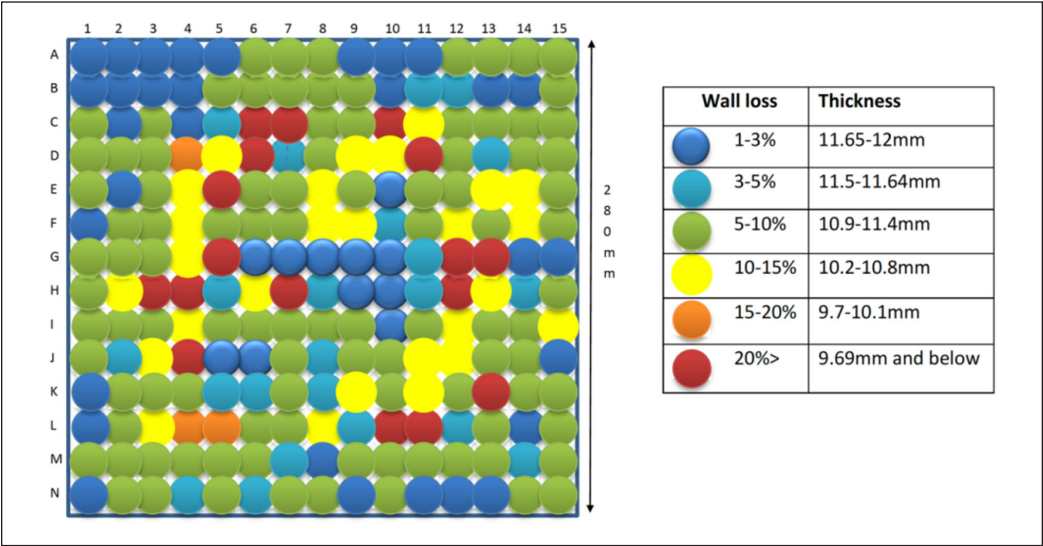


Figure 5. UT A-Scan result presentation

The UT A-Scan results demonstrated the ability to detect a thickness as low as 9.07 mm from a nominal thickness of 12 mm, which is higher than the 20% loss of wall thickness used to assess detectability attributes. To compare accuracy attributes, Figure 5 includes a specified color code to enhance visualization, which the authors added manually.

Ultrasonic Thickness Gauging

UTG is another common testing technique applied in the field to measure material wall loss (Bouchy et al., 2023). A grid was designed for UTG, similar to that used for the UT

A-scan, as shown in Figure 6. The difference was that the UTG probe had a diameter of 10 mm, resulting in a grid design of 10 mm × 10 mm.

Figure 5 illustrates a 5 MHz twin crystal probe with a 10 mm diameter using water as the contact medium. The UTG requires 783 test spots to ensure complete testing coverage of the entire test specimen. The total time taken to plot the grid lines and acquire data from the 783 points is shown in Figure 7, amounting to two hours and forty-five minutes. The authors manually plotted Figure 7 to facilitate attribute comparisons with the other testing techniques.

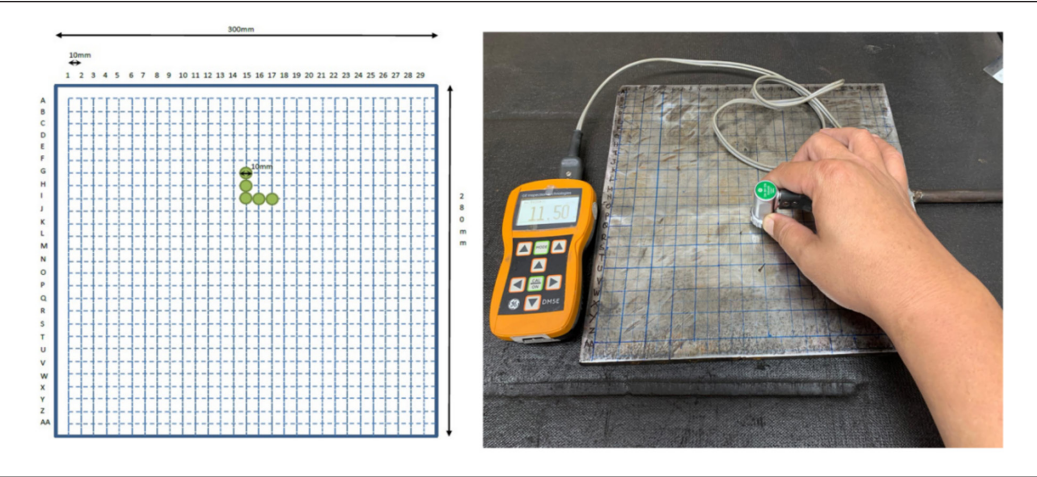


Figure 6. UTG grid line and setup

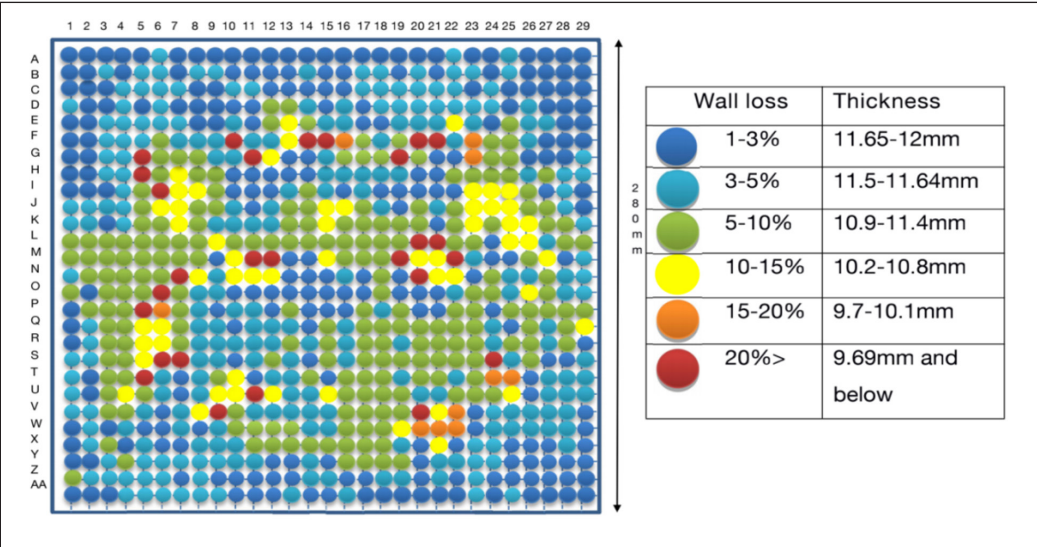


Figure 7. UTG result presentation

Phased Array Corrosion Mapping

PAUT-CM uses a 5L64 A12 probe, an SA12-0L wedge, and water as the contact medium. This technique's advantage is that it can scan a width of 30 mm in a single pass, as shown in Figure 8. Therefore, only 10 scans were required for full coverage, taking a total of 15 minutes.

The PAUT generates a plan view, which significantly reduces manual input by the author and provides a colored visual aid to identify different material depths. It allows extracted thickness readings using the cursor to point to the area of interest (Tai, Sultan, et al., 2023). As illustrated in Figure 9, the dark blue area represents the nominal material thickness of 12 mm, while the dark red indicates the thinnest area at 8.34 mm, showing a clear defect orientation. This feature enhances the accuracy and detectability attributes.

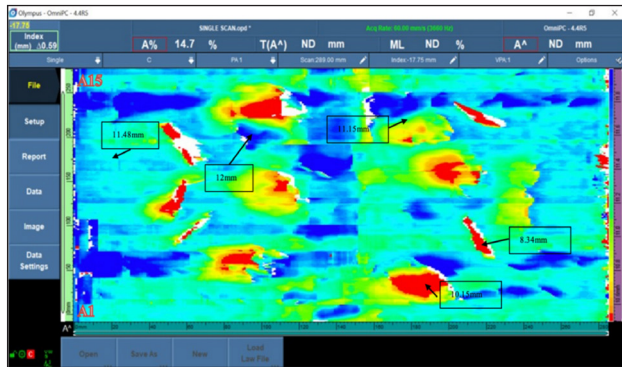
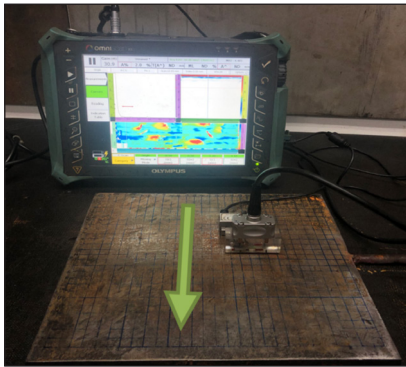


Figure 8. PAUT-CM with 5L64 A12 probe Figure 9. PAUT-CM result presentation

Summary of an Experiment Test

In terms of efficiency, the UT A-Scan required 1 hour and 20 minutes to obtain material thickness data, while the UTG required 2 hours and 45 minutes, and the PAUT-CM only required 15 minutes.

For detectability, Figure 10 illustrates a comparison of the three test techniques with the actual material surface. The labeled numbers 1, 2, and 3 represent examples constructed from the results obtained using different techniques at the same location. This comparison shows that PAUT-CM achieves a high level of detectability, accurately locating defects associated with both general and localized signs of corrosion. In contrast, the UT A-Scan has lower detectability, as it relies on a 20 mm grid size for measurements, leading to inaccurate localization, similar to a low-pixel image that exhibits low resolution. Compared to the UT A-Scan, the UTG has a higher detection and resolution owing to the smaller grid size; however, it requires more time to acquire data because of the increased number of points and additional time needed to manually transfer and record the data. Despite this, its accuracy remains lower than that of PAUT-CM.

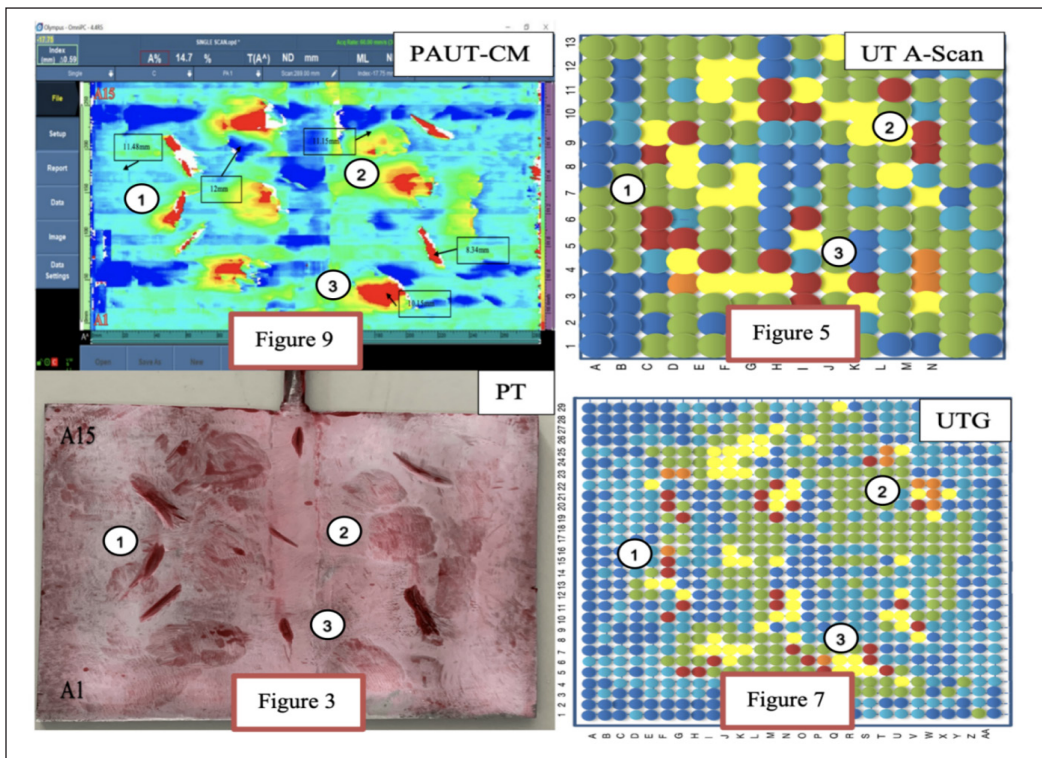


Figure 10. Compare results presentation in three techniques

The third attribute that can be compared to the experiment is accuracy. The PAUT effectively captures all actual damaged surfaces identified by the PT, and the digital cursor allows for measuring uneven surfaces and ground marks, providing depth information. Although the UTG, with its smaller diameter probe and more data points, offers better image quality and detectability than the UT A-Scan, it still showed less sensitivity due to its larger grid with fewer points, resulting in lower accuracy.

AHP Selection Criteria

The experiment assigned weights to the three attributes. In terms of the detectability attribute, PAUT-CM revealed all general and localized defects, matching both shape and location. Each participant was assigned a score of 10. UTG can detect most defects but lacks sufficient detail because the results are obtained via spot measurement; thus, a score of 7 was assigned to the UTG. A score of 4 was assigned to the UT A-Scan due to the board beam of the 20 mm diameter probe, which produced average spot thickness readings.

PAUT-CM scored 10 points for efficiency because of its fast processing capability. In contrast, UT A-Scan and UTG received scores of 5 and 3, respectively, indicating that the UTG required more time to achieve a comparable score. The advantage of 10 points

for PAUT-CM is illustrated in Figure 8, which highlights its excellent accuracy. UTG received 7 points, whereas the UT A-Scan received 3 points, reflecting their noteworthy resolution capabilities.

According to the American Society for Non-destructive Testing’s recommendation practice SNT-TC-1A, personnel qualification and certification in non-destructive testing require 8 hours of training to reach level 2 in UTG, 24 hours UT A-Scan, and a prerequisite to UT level 80 hours plus another 80 hours for PAUT (<https://inspectioneering.com/tag/snt-tc-1a>). Therefore, the highest 10 scores were allocated to UTG, followed by 8 for UT A-Scan and 5 for PAUT-CM, as summarized in Table 1 for the competence attribute.

In summary, PAUT-CM offers superior detectability and efficiency, allowing for precise identification of both general and localized defects while facilitating rapid processing. However, it requires significant personnel training, which may limit its immediate applicability in some contexts. The advantages of UTG include lower training requirements and ease of use, making it accessible for operators with less expertise. Nonetheless, it lacks the detailed information provided by PAUT-CM and may require more time to achieve comparable results. UT A-Scan is beneficial for quick spot checks and simple assessments, making it suitable for specific applications. However, its broad beam limits its ability to detect finer defects and generally offers lower efficiency and resolution compared to the other methods.

The next step was to compare the four attributes and define their importance. Detectability emerged as the most critical attribute, followed by efficiency as the second most important, and accuracy next. The least important factor is competence, primarily because Level 2 technicians can be trained before testing is conducted.

When comparing accuracy to competence, accuracy is deemed more important, as it is typically determined after the inspection site has worked with the tested data. This makes it more critical than one’s competence. Table 2 shows the Saaty matrix for the attributes, including the final comparison between competence and its lesser importance (Saaty, 2004).

Table 1
Summary of attribute weight

Attribute	UT A-Scan	UTG	PAUT-CM
Detectability	4	7	10
Accuracy	3	7	10
Efficiency	5	3	10
Competence	8	10	5

Table 2
The Saaty matrix for attributes

	Detectability	Accuracy	Efficiency	Competence
Detectability (A1)	1	5/1	2/1	7/1
Accuracy (A2)		1	1/3	2/1
Efficiency (A3)			1	5/1
Competence (A4)				1

RESULTS AND DISCUSSION

In the detailed AHP matrix calculation, the scale identifies and interprets rating values 1-9 by pairwise comparison of similar element pairs at each level with criteria at the next level. Next, priority calculations were performed on the four attributes to produce the feature vectors listed in Table 3.

Table 3
The priorities calculation

C	A1	A2	A3	A4	A1	A2	A3	A4	Sum of rows (A)	A/n (w)
A1	1.00	5.00	2.00	7.00	(1/1.84) = 0.5435	(5/9.5) = 0.5263	(2/3.53) = 0.5666	(7/15) = 0.4667	2.103	0.5258
A2	0.20	1.00	0.33	2.00	(0.2/1.84) = 0.1087	(1/9.5) = 0.1053	(0.33/3.53) = 0.0935	(2/15) = 0.1333	0.4408	0.1102
A3	0.50	3.00	1.00	5.00	(0.5/1.84) = 0.2717	(3/9.5) = 0.3158	(1/3.53) = 0.2833	(5/15) = 0.333	1.2041	0.301
A4	0.14	0.50	0.20	1.00	(0.14/1.84) = 0.0761	(0.5/9.5) = 0.0526	(0.2/3.53) = 0.0567	(1/15) = 0.0667	0.252	0.063
	1.84	9.50	3.53	15.00	1	1	1	1		
The sum of individual columns (S)					Standardized matrix The sum of each column = 1				Eigenvector	Priority vector

The priority vectors obtained from the normalized feature vectors were assigned the following weights: detectability (w1) 0.5258, accuracy (w2) 0.1102, efficiency (w3) 0.301, and competence (w4) 0.063

The consistency ratio (CR) was calculated to assess the consistency of the pairwise comparison matrix. The CR is obtained by dividing the consistency index (CI) value by the random consistency index (RI). CI is derived by comparing the principal eigenvalue of the pairwise comparison matrix (denoted as λmax) with the matrix size (denoted as n). The formula for calculating CI is (λmax – n)/(n-1). The RI values can be found in Table 4 and are recommended by Saaty (2004). If CR exceeds 10%, the evaluation may exhibit high randomness or inconsistency. Conversely, if the CR is less than or equal to 10%, the consistency of the assessment is considered acceptable.

The value of λmax represents the maximum eigenvalue of the analysis. Indicating the main factor or criterion that influences selection. The calculations for the maximum eigenvalues are presented in Table 5.

Table 4
Random consistency index

Matrix dimension	1	2	3	4	5	6	7	8	9	10
Random consistency (RI)	0.00	0.00	0.58	0.90	1.12	1.24	1.32	1.41	1.45	1.49

A consistency index of 0.0066 was obtained using this algorithm. Using the RI values listed in Table 4, a CR of 0.007 was obtained. Since the CR is less than 10%, this indicates acceptable consistency in the assessment.

The attribute weights were normalized across the inspection techniques and are listed in Table 1. The calculation of the weighting values and the normalized attribute weights, as indicated in Table 6, presents the calculated normalized attribute weights. These weights are used further to determine the higher score testing technique, as shown in Table 7. According to AHP analysis, the best option was PAUT-CM = 0.4864.

The final step was to conduct a sensitivity analysis to assess the stability and robustness of the optimal solution in the event of changes in the model parameters (Balakrishnan et al., 2022). The first scenario involved altering the weighting method: What if all the weights were equal? The results in Table 8 indicate that the PAUT-CM scores were higher at 0.4373.

The second scenario examines what happens if the efficiency weight of the UTG increases while the efficiency weight of the UT A-Scan remains unchanged and the PAUT-CM efficiency weight decreases due to the higher weight achieved by PAUT-CM. Table 9 lists the equal-importance techniques for the UTG and PAUT-CM. In this scenario, the

Table 5
Maximum eigenvalues calculation

Eigenvector (w)	w1(0.5258)	w2(0.1102)	w3(0.301)	w4(0.063)
The sum of individual columns (S)	1.84	9.50	3.53	15
Maximum eigenvalue (λ_{max})	$(1.84 \times 0.5258) + (9.50 \times 0.1102) + (3.53 \times 0.301) + (15 \times 0.063) = 4.02$			

Table 6
Normalize attributes weight

	Competence	Norm	Efficiency	Norm	Accuracy	Norm	Detectability	Norm
UT A-Scan	8	0.3478	5	0.2778	3	0.15	4	0.1905
UTG	10	0.4348	3	0.1667	7	0.35	7	0.3333
PAUT-CM	5	0.2174	10	0.5555	10	0.5	10	0.4762
	23	1	18	1	20	1	21	1

Table 7
The higher scores in testing technique

	Detectability	Accuracy	Efficiency	Competence	Evaluation Results
Weighting Values	0.5258	0.1102	0.301	0.063	-
UT A-Scan	0.1905	0.15	0.2778	0.3478	0.2222
UTG	0.3333	0.35	0.1667	0.4348	0.2914
PAUT-CM	0.4762	0.5	0.5555	0.2174	0.4864
	1	1	1	1	1

weight of efficiency for UTG has increased from 0.1667 to 0.4904, whereas the weight for PAUT-CM is reduced from 0.5555 to 0.2318.

The third scenario considers what happens if the detectability weight of UTG increases while the detectability weight of the UT A-Scan remains unchanged and the PAUT-CM detectability weight decreases since the detectability weighting values comprise half of the overall weight. Table 10 lists the equal-importance techniques for the UTG and PAUT-CM. In this scenario, the detectability weight for UTG is increased from 0.3333 to 0.5187, whereas the weight for PAUT-CM is reduced from 0.4762 to 0.2908.

The PAUT-CM technique scored the highest, primarily because efficiency, detectability, and accuracy were ranked at the top among the three inspection techniques. Although competence had the least attribute of weight, it was the least important factor contributing to the overall result.

Table 8
Sensitivity checks with equal weighting values

	Detectability	Accuracy	Efficiency	Competence	Evaluation Results
Weighting Values	0.25	0.25	0.25	0.25	-
UT A-Scan	0.1905	0.15	0.2778	0.3478	0.2415
UTG	0.3333	0.35	0.1667	0.4348	0.3212
PAUT-CM	0.4762	0.5	0.5555	0.2174	0.4373
	1	1	1	1	1

Table 9
Sensitivity checks with adjusted efficiency parameter weight

	Detectability	Accuracy	Efficiency	Competence	Evaluation Results
Weighting Values	0.5258	0.1102	0.301	0.063	-
UT A-Scan	0.1905	0.15	0.2778	0.3478	0.2222
UTG	0.3333	0.35	0.4904	0.4348	0.3889
PAUT-CM	0.4762	0.5	0.2318	0.2174	0.3889
	1	1	1	1	1

Table 10
Sensitivity checks with adjusted detectability parameter weight

	Detectability	Accuracy	Efficiency	Competence	Evaluation Results
Weighting Values	0.5258	0.1102	0.301	0.063	-
UT A-Scan	0.1905	0.15	0.2778	0.3478	0.2222
UTG	0.5187	0.35	0.4904	0.4348	0.3889
PAUT-CM	0.2908	0.5	0.2318	0.2174	0.3889
	1	1	1	1	1

A special feature of the AHP method is that the final result also changes when attribute weights change. In this case, PAUT-CM was chosen mainly because a longer detection time and relatively large area were required.

Our findings indicate that the PAUT-CM technique outperforms traditional methods like UTG and UT A-Scan in terms of detectability and efficiency. Specifically, PAUT-CM achieved a time efficiency improvement of approximately 80% over UTG, significantly reducing operational downtime during inspections.

Moreover, the AHP analysis revealed that PAUT-CM provided better detectability and allowed for rapid identification of both general and localized corrosion defects, confirming its superiority compared to methods previously analyzed in the literature. This systematic approach enhances decision-making and addresses the critical need for effective corrosion monitoring strategies in the petrochemical industry.

However, if the job requirements and circumstances have changed, and the new case involves checking only a few points for thickness measurements while requiring new technicians to be trained, then UTG or UT A-Scan may score higher. This is because the order of importance in the new scenario has shifted. PAUT-CM requires 20 times more training time than UTG, and since only point readings need to be checked, the advantage of PAUT-CM in terms of fast-checking times diminishes. Point readings can be reported without accuracy issues, making the other techniques more suitable for such a case.

This study establishes a foundational framework that offers novel insights for petrochemical engineers. Engineers can select an appropriate technique by considering practical requirements and available resources, such as the quantity and volume of materials to be tested, scheduling constraints, and the necessity for training personnel. Moreover, this systematic approach can be extended to other testing methods employed within petrochemical plants.

CONCLUSION

This study presents a systematic selection method aimed at determining the most appropriate ultrasonic detection technique based on predetermined parameters, by experimentally testing three ultrasonic inspection techniques to provide reliable data and evidence for the advantages and limitations of each technique.

The key outcomes of this study are as follows:

1. **PAUT-CM Superiority:** The PAUT-CM technique emerged as the most effective method, scoring the highest in detectability, accuracy, and efficiency. PAUT-CM's ability to provide detailed corrosion assessments and fast-processing capability make it a superior choice for comprehensive inspections.
2. **Efficiency and Accuracy:** PAUT-CM significantly outperformed UTG and UT A-scan in terms of efficiency, requiring only 15 minutes for full coverage compared

to 2 hours and 45 minutes for UTG and 1 hour and 20 minutes for UT A-scan. Additionally, PAUT-CM demonstrated superior accuracy in detecting general and localized corrosion defects.

3. Training Requirements: While PAUT-CM requires more extensive personnel training, its advantages in detectability and efficiency justify the investment. UTG and UT A-scan, though requiring less training, lack the detailed information and speed provided by PAUT-CM.
4. AHP Analysis: The AHP analysis confirmed PAUT-CM as the optimal choice, with a final score of 0.4864, followed by UTG at 0.2914 and UT A-scan at 0.2222. Sensitivity analysis further validated the robustness of these results.
5. Practical Implications: This study offers a foundational framework for petrochemical engineers to select appropriate testing techniques based on practical requirements and available resources. The systematic approach can be extended to other testing methods employed within petrochemical plants, promoting informed decision-making and enhancing overall safety and reliability.

By adopting the systematic approach proposed in this study, engineers can overcome subjective bias and make informed choices when selecting an appropriate testing method. This enhances the overall decision-making process, promotes reliability, and increases the effectiveness of field inspections. It is hoped that this research will introduce the concept of AHP to a broader engineering audience, empowering them to make more informed and reliable decisions in the future.

ACKNOWLEDGMENT

The authors are grateful for the financial support given by The Ministry of Higher Education Malaysia (MOHE) under the Higher Institution Centre of Excellence (HICOE2.0/5210004) at the Institute of Tropical Forestry and Forest Products. The authors would also like to express their gratitude to the Department of Aerospace Engineering, Faculty of Engineering, Universiti Putra Malaysia, and the Laboratory of Biocomposite Technology, Institute of Tropical Forestry and Forest Product (INTROP), Universiti Putra Malaysia (HICOE) for their close collaboration in this study.

REFERENCES

- Ameh, E. S., Ikpeseni, S. C., & Lawal, L. S. (2018). A review of field corrosion control and monitoring techniques of the upstream oil and gas pipelines. *Nigerian Journal of Technological Development*, 14(2), Article 67. <https://doi.org/10.4314/njtd.v14i2.5>
- Balakrishnan, T. S., Sultan, M. T. H., Naveen, J., Shahar, F. S., Najeed, M. I., Shah, A. U. M., Khan, T., & Sebaey, T. A. (2022). Selection of natural fibre for pultruded hybrid synthetic/natural fibre reinforced polymer composites using analytical hierarchy process for structural applications. *Polymers*, 14(15), Article 3178. <https://doi.org/10.3390/polym14153178>

- Bazulin, E. G., & Sadykov, M. S. (2018). Determining the speed of longitudinal waves in an isotropic homogeneous welded joint using echo signals measured by two antenna arrays. *Russian Journal of Nondestructive Testing*, 54(5), 303–315. <https://doi.org/10.1134/S1061830918050029>
- Ber, L. L., Benoist, G., & Dainelli, P. (2016, June 13-17). Corrosion detection and measurement improvement using advanced ultrasonic tools. In *19th World Conference on Non-Destructive Testing* (pp. 1–8). Munich, Germany.
- Bouchy, S., Zednik, R. J., & Belanger, P. (2023). Ultrasonic transducers for in-service inspection and continuous monitoring in high-temperature environments. *Sensors*, 23(7), 1–13. <https://doi.org/10.3390/s23073520>
- Du, L., Wang, Q., Li, X., & Yan, H. (2020). Cause analysis and suggestion on corrosion leakage of pipe in atmospheric and vacuum pressure unit. In *IOP Conference Series: Materials Science and Engineering* (Vol. 711, No. 1, p. 012015). IOP Publishing. <https://doi.org/10.1088/1757-899X/711/1/012015>
- Elwerfalli, A., Khan, M. K., & Munive, J. E. (2016). A new methodology for improving TAM scheduling of oil and gas plants. *Lecture Notes in Engineering and Computer Science*, 2224, 807–812.
- Fajobi, M. A., Loto, R. T., & Oluwole, O. O. (2019). “Crude distillation overhead system”: Corrosion and control. *Journal of Physics: Conference Series*, 1378(4), Article 042090. <https://doi.org/10.1088/1742-6596/1378/4/042090>
- Groysman, A. (2017). Corrosion problems and solutions in oil, gas, refining and petrochemical industry. *Koroze a Ochrana Materialu*, 61(3), 100–117. <https://doi.org/10.1515/kom-2017-0013>
- Jamil, J., & Yahya, S. Y. S. (2019). Corrosion assessment using advanced ultrasonic measurement technique. In *IOP Conference Series: Materials Science and Engineering* (Vol. 554, No. 1, p. 012004). IOP Publishing. <https://doi.org/10.1088/1757-899X/554/1/012004>
- Lamarre, A. (2016, June 13-17). High-resolution corrosion monitoring for reliable assessment of infrastructure. In *19th World Conference on Non-Destructive Testing* (pp. 1–7). Munich, Germany.
- Laza, K. (2017). The piping integrity management challenge. *Inspection Engineering Journal*, 23, 1-11.
- Liu, D., Gong, C., Tang, Y., Jian, Y., Cao, K., & Chen, H. (2022). Evaluation of corrosion damage in sulfate-attacked concrete by CT, ultrasonic pulse velocity testing and AHP methods. *Sensors*, 22(8), Article 3037. <https://doi.org/10.3390/s22083037>
- Mohan, B. C., Jeyasekhar, M. C., Duhan, K., Land, I., Belait, K., & Manager, C. (2019, December 4-5). Oil and gas assets condition monitoring by high sensitive PAUT hydroform corrosion monitoring technique for integrity assessment. In *Proceedings of the Singapore International NDT Conference & Exhibition* (pp. 1-8). Singapore.
- Omar, T., & Nehdi, M. (2016, June 1-4). Resilient infrastructure evaluation of NDT techniques for concrete bridge decks using fuzzy analytical hierarchy process. In *2016 Annual Conference of the Canadian Society for Civil Engineering* (pp. 1-10). London, UK.
- Saaty, T. L. (2004). Decision making - The analytic hierarchy and network processes (AHP/ANP). *Journal of Systems Science and Systems Engineering*, 13(1), 1–35. <https://doi.org/10.1007/s11518-006-0151-5>

- Sampath, S., Dhayalan, R., Kumar, A., Kishore, N. N., & Sohn, H. (2021). Evaluation of material degradation using phased array ultrasonic technique with full matrix capture. *Engineering Failure Analysis*, 120, Article 105118. <https://doi.org/10.1016/j.engfailanal.2020.105118>
- Shekari, E., Khan, F., & Ahmed, S. (2017). Economic risk analysis of pitting corrosion in process facilities. *International Journal of Pressure Vessels and Piping*, 157, 51–62. <https://doi.org/10.1016/j.ijpvp.2017.08.005>
- Shih, J. Y., Hsiao, S. Y., & Chang, T. P. (2017). Life cycle guideline of petrochemical plant underground piping system. In *MATEC Web of Conferences* (Vol. 119, p. 01004). EDP Sciences. <https://doi.org/10.1051/mateconf/201711901004>
- Tai, J. L., Grzejda, R., Sultan, M. T. H., Łukaszewicz, A., Shahar, F. S., Tarasiuk, W., & Rychlik, A. (2023). Experimental investigation on the corrosion detectability of A36 low carbon steel by the method of phased array corrosion mapping. *Materials*, 16(15), Article 5297. <https://doi.org/10.3390/ma16155297>
- Tai, J. L., Sultan, M. T. H., Tarasiuk, W., Napiórkowski, J., Łukaszewicz, A., & Shahar, F. S. (2023). Ultrasonic velocity and attenuation of low-carbon steel at high temperatures. *Materials*, 16(14), Article 5123. <https://doi.org/10.3390/ma16145123>
- Tariq, F., Naz, N., Baloch, R. A., & Faisal. (2011). Characterization of material properties of 2xxx series Al-alloys by non destructive testing techniques. *Journal of Nondestructive Evaluation*, 31(1), 17–33. <https://doi.org/10.1007/s10921-011-0117-5>
- Thanh, P. V., Nhung, P. T. T., Thuy, L. T. M., & Nhai, N. H. (2015). Effect of temperature on ultrasonic velocities, attenuations, reflection and transmission coefficients between motor oil and carbon steel estimated by Pulse-echo technique of ultrasonic testing method. *VNU Journal of Science: Mathematics - Physics*, 31(4), 39–48.
- Turcotte, J., Rioux, P., & Lavoie, J. (2016, June 13-17). Comparison corrosion mapping solutions using phased array, conventional UT and 3D scanners. In *19th World Conference on Non-Destructive Testing 2016* (pp. 1–10). Munich, Germany.
- Wall, M., Burch, S., & Lilley, J. (2009). Human factors in POD modelling and use of trial data. *Insight: Non-Destructive Testing and Condition Monitoring*, 51(10), 553–561. <https://doi.org/10.1784/insi.2009.51.10.553>
- Wan, Z., & Yang, J. (2021). Research on corrosion management technology of petroleum pipeline and pressure vessel. In *IOP Conference Series: Earth and Environmental Science* (Vol. 692, No. 4, p. 042057). IOP Publishing. <https://doi.org/10.1088/1755-1315/692/4/042057>
- Wang, F., Shan, Q., Zhang, F., Lu, F., Li, J., Yu, T., & Qu, C. (2021). Pitting corrosion behavior of metal materials and research methods. In *IOP Conference Series: Earth and Environmental Science* (Vol. 651, No. 3, p. 032039). IOP Publishing. <https://doi.org/10.1088/1755-1315/651/3/032039>
- Wood, M. H., Arellano, A. V., & Wijk, L. V. (2013). *Corrosion-related accidents in petroleum refineries: Lessons learned from accidents in EU and OECD countries*. European Union. <https://doi.org/10.2788/37909>
- Zhao, W., Zhang, T., Wang, Y., Qiao, J., & Wang, Z. (2018). Corrosion failure mechanism of associated gas transmission pipeline. *Materials*, 11(10), Article 1935. <https://doi.org/10.3390/ma11101935>

APPENDIX

Questionnaire for Survey on NDT Techniques

This survey aimed to gather insights into the priorities and needs of petrochemical plants regarding non-destructive testing (NDT) techniques for corrosion monitoring. This survey aimed to identify the most important attributes associated with various ultrasonic testing techniques. The findings from this survey will inform the Analytic Hierarchy Process (AHP) used in this study, ensuring that the selected ultrasonic testing techniques align with the industry’s most pressing needs and preferences. The results will ultimately contribute to the development of a systematic approach for selecting the most suitable corrosion monitoring methods, minimizing subjective bias and enhancing operational efficiency.

Section 1: Participant Information

- Name
- Position
- Company (optional)
- Years of Experience

Section 2: Attribute Evaluation

Please rate the following attributes on a scale from 1 to 8, where 1 indicates the least important and 8 indicates the most important for corrosion monitoring.

Attribute	Description	Rating (1-8)
Cost-effectiveness	The overall costs are associated with the equipment, resources, and implementation of the testing technique.	
Consistency	The ability to uniformly identify defects over time and across different personnel.	
Competence	Qualification and certification levels are required for personnel conducting the inspection.	
Detectability	The effectiveness of the testing technique in identifying target defects.	
Accuracy	The precision in identifying defects and providing reliable data.	
Efficiency	The time required for preparation and inspection is relative to the area being tested.	
Safety	The potential risks involved in the inspection process.	
Compatibility	The ability of the testing method to integrate seamlessly with other industrial operations.	

Section 3: Additional Comments

1. What attributes do you consider most critical for NDT techniques in petrochemical plants?
2. Do you have any other suggestions or comments regarding NDT techniques?

Review Article

Effectiveness of Using Augmented Reality-Based Picture Exchange Communication System (PECS) in Improving Communication Skills of Autistic Students in Indonesian Language Subjects: Bibliometric Analysis

Munir¹, Dwi Novia Al Husaeni^{1*}, Eka Fitrajaya Rahman¹ and Rasim²

¹Computer and Science Education, Universitas Pendidikan Indonesia, Bandung 40154, Indonesia

²Computer Science, Universitas Pendidikan Indonesia, Bandung 40154, Indonesia

ABSTRACT

This research aims to evaluate the effectiveness of employing an augmented reality-based Picture Exchange Communication System (PECS) to enhance the communication skills of autistic students in Indonesian language subjects. A systematic literature review collected and analyzed various studies integrating PECS with augmented reality technology in educational settings. The study comprised three stages: determining keywords, searching for article data, and determining inclusion criteria. The findings from this review indicate that augmented reality-based PECS significantly enhances verbal and nonverbal communication abilities among autistic students. Key advantages of this approach include increased interactivity, enhanced visualization, and heightened student motivation. However, challenges such as requiring specialized equipment and sufficient teacher training were identified. Additionally, the review revealed fluctuations in the number of publications on PECS use across different years. This research aims to contribute to communication training for autistic children, particularly in the context of learning the Indonesian language. This study aims to inform educational practices and stimulate further research in this area by highlighting the benefits and challenges of AR-based PECS integration.

Keywords: Augmented Reality, autism spectrum disorder (ASD), communication, Indonesian, picture exchange communication system (PECS)

ARTICLE INFO

Article history:

Received: 19 September 2024

Accepted: 23 January 2025

Published: 04 April 2025

DOI: <https://doi.org/10.47836/pjst.33.3.17>

E-mail addresses:

munir@upi.edu (Munir)

dwinoviaalhusaeni14@upi.edu (Dwi Novia Al Husaeni)

ekafitrajaya@upi.edu (Eka Fitrajaya Rahman)

rasim@upi.edu (Rasim)

* Corresponding author

INTRODUCTION

Autism Spectrum Disorder (ASD) is a group of neurobiological developmental disorders that present significant challenges in social interaction, communication, and repetitive

behaviors (Parisi et al., 2015). Symptoms of ASD generally appear before a child is three years old (Johnson, 2008). ASD is characterized by varying degrees of difficulty in social interaction and communication. Other characteristics include atypical patterns of activity and behavior, such as difficulty transitioning from one activity to another, a strong focus on details, and unusual reactions to sensory experiences (Kaufmann et al., 2004; Wetherby, 2006).

Children with ASD often experience difficulties understanding and using language, a key aspect of everyday communication skills (Wetherby, 2006; Tager-Flusberg et al., 2005). In Indonesia, as awareness of ASD increases, innovative therapeutic approaches are being introduced to improve the communication skills of these children in formal educational contexts, including Indonesian language learning.

The Picture Exchange Communication System (PECS) is a widely used alternative communication method for children with ASD. PECS utilizes pictures to help children express desires, ask for help, or communicate their needs (Frost, 2002). The PECS method is often combined with augmented reality (AR) technology. For example, Taryadi and Kurniawan (2018) researched using an augmented reality-based multimedia PECS method as a learning alternative to training communication skills in autistic children.

Augmented reality (AR) technology offers new potential in education, especially for children with special needs such as ASD. AR allows integration between the real world and virtual elements, providing a more immersive and engaging learning experience (Billinghurst et al., 2015). In the context of PECS, the use of AR can enhance the interest and involvement of children with ASD in the language learning process.

Previous studies have shown that using AR technology in the education of children with ASD can facilitate learning, improve social skills, and reduce anxiety (Ramdoss et al., 2011). However, little research has focused on the integration of PECS with AR, especially in the context of teaching Indonesian language subjects. Therefore, in-depth research on the effectiveness of using AR-based PECS to improve Indonesian language communication skills in students with ASD is both relevant and important to carry out.

This research aims to explore the extent to which AR-based PECS can improve the verbal and nonverbal communication skills of autistic students in the context of Indonesian language teaching. By utilizing this approach, it is hoped that empirical evidence will be found to support the use of AR technology as an effective tool for increasing the participation and academic achievement of students with ASD in learning the Indonesian language.

STUDY LITERATURE

Review of Picture Exchange Communication System (PECS)

The PECS is an alternative communication method that enables individuals with limited or no communication skills to communicate using pictures (Bondy & Frost, 1994). PECS

involves several phases designed to teach users to recognize, select, and exchange images corresponding to specific situations or needs.

The PECS process starts with an initial phase where individuals learn to exchange images for desired objects. For instance, a child who desires a drink receives a drink card and gives it to an adult to get the drink. Through repetition, children grasp that exchanging pictures elicits desired responses. Subsequent phases in PECS focus on advancing communication skills, including basic sentence structure and comprehension of verbal language (Bondy & Frost, 2001).

Howlin et al. (2007) investigated the effectiveness of PECS in enhancing communication skills among children with autism. The study involved 84 autistic children aged 4 to 10 years, divided into two groups: one received a PECS intervention, while the other received a non-PECS communication intervention as a control. Results indicated significant improvements in communication initiation and use of picture symbols among children in the PECS group compared to the control group. For instance, Danny, a participant who previously relied on non-verbal behavior, successfully used PECS to request food and toys within three months of intensive training. This research underscores PECS as an effective tool for enhancing communication skills in children with autism.

Review of Augmented Reality (AR)

AR technology integrates digital elements interactively and in real-time with the real world (Dargan et al., 2023). AR technology enables users to perceive and interact with virtual objects overlaid in their real-world environment using devices such as smartphones, tablets, or specialized AR glasses (Azuma, 1997). It captures real-world images through a device's camera and augments them with digital information or objects through software processing (Billinghurst et al., 2015).

For instance, educational applications utilizing AR can project 3D models of human body organs when a smartphone camera is aimed at relevant images or text in textbooks (Figure 1). Users can interact with these models, rotate them, and access additional information by tapping on specific parts (Billinghurst & Duenser, 2012). Another application of AR is technical training, where technicians can view step-by-step guides overlaid on the equipment they are repairing, aiding in easier and more efficient instruction-following (Tang et al., 2003).

Review on Autism Spectrum Disorder (ASD)

ASD comprises a range of neurobiological developmental disorders that present significant challenges in social interaction, communication, and consistent behavior (Parisi et al., 2015). Individuals with ASD commonly experience difficulties in various areas, including language comprehension, appropriate social interactions, and cognitive flexibility. The

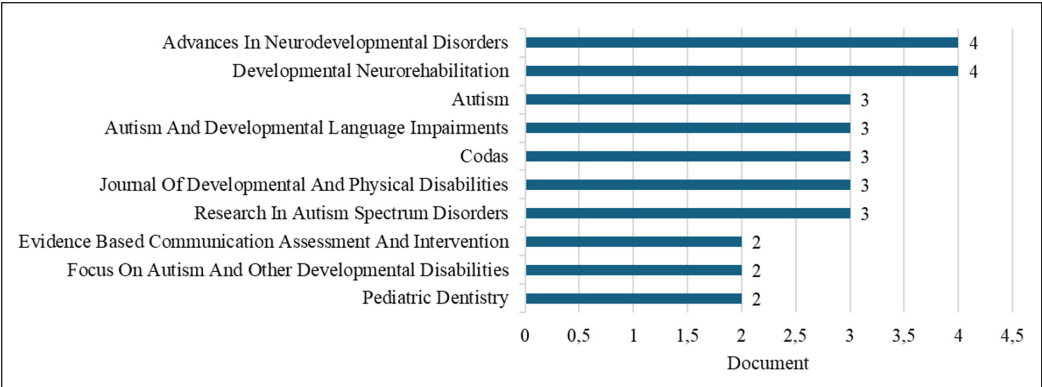


Figure 1. Top 10 publications: Article counts

disorder can manifest across a spectrum of symptoms and severity levels, from mild to severe. Symptoms typically emerge early in life, often before age 3, although diagnosis can occur at any age (Johnson, 2008). Diagnostic criteria for ASD encompass restricted and repetitive behavioral patterns, difficulties in social interaction, and challenges in using and understanding verbal and nonverbal language.

ASD affects approximately 1 in 160 children worldwide, with prevalence showing an upward trend in recent decades (Baio et al., 2020). While the exact causes of ASD remain unclear, research suggests that genetic and environmental factors contribute to its development (Geschwind, 2009). Diagnosis typically involves behavioral observation and standardized diagnostic criteria such as the Diagnostic and Statistical Manual of Mental Disorders (DSM-5) or the International Classification of Diseases (ICD-11), necessitating a comprehensive evaluation by a multidisciplinary team of medical doctors and psychologists.

The management of ASD typically involves an interdisciplinary approach encompassing behavioral therapy, speech therapy, specialized educational interventions, and robust family support (Matson & Kozlowski, 2011). While ASD is a lifelong condition, early intervention and targeted interventions can markedly enhance the quality of life for individuals affected by facilitating their adaptability and independence in diverse social and educational settings (Matson & Kozlowski, 2011).

Review of Indonesia Language Learning

Learning Indonesian in Indonesia is an integral part of the national curriculum, aiming to develop students’ literacy and communication skills (Pakpahan et al., 2023). Indonesian is taught as a main subject and as a language of instruction in various scientific disciplines. One of the challenges in learning Indonesian is the diversity of students’ mother tongue backgrounds, considering that Indonesia consists of various ethnicities and regional languages. Therefore, the approach must be inclusive and able to bridge this linguistics.

Examples of successful implementation can be seen in literacy programs in elementary schools, which combine conventional learning methods with digital technology. For example, interactive reading applications attract students' interest in practicing reading and writing more often. Apart from that, teachers also often use collaborative learning strategies, such as group discussions, which encourage students to think critically and creatively when using Indonesian.

Conditions for learning Indonesian are also influenced by the availability of resources, such as textbooks, learning media, and teacher training (Indriyani et al., 2023). In urban areas, access to these resources is relatively better compared to rural areas. Therefore, the government continues to strive to improve the distribution of educational resources so that equal distribution of learning quality can be achieved throughout Indonesia.

Overall, Indonesian language learning in Indonesia continues to develop, supported by innovation in teaching methods and educational technology. Although there are still challenges, especially related to the diversity of regional languages and limited resources in some regions, ongoing efforts to improve the quality of education are expected to produce a more literate and communicative generation in Indonesia.

METHOD

This research used a literature review as a method. We examine the effectiveness of using an augmented reality-based PECS to improve the communication skills of autistic students in Indonesian language subjects. This research consists of three stages, as shown in Figure 2.

The results of this review aim to provide a comprehensive understanding of the potential benefits and challenges associated with integrating AR-based PECS in educational settings for autistic students.

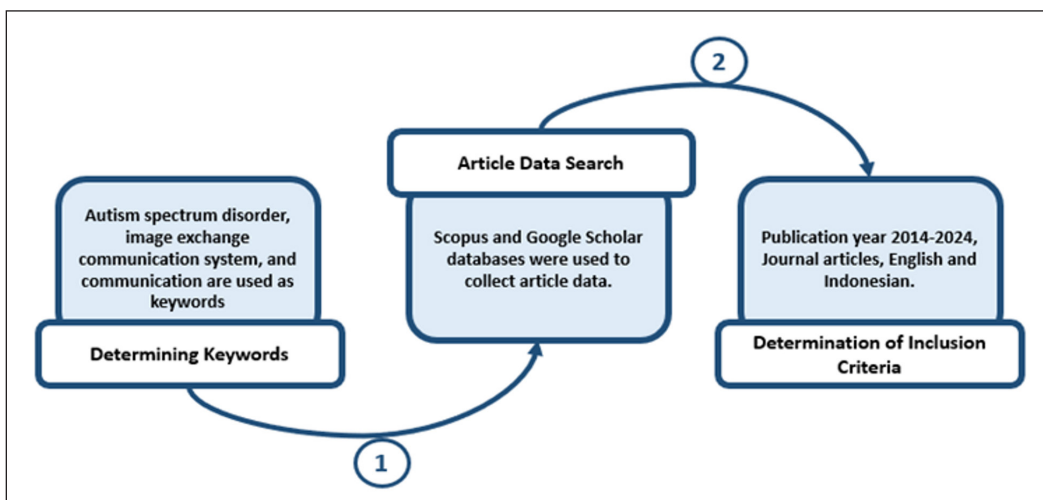


Figure 2. Research stages

Determining Keywords

The first step taken in this research is to determine the keywords that will be used to collect article data. The keywords used in this research are:

1. For Scopus:

- `TITLE-ABS-KEY (“autism spectrum disorder”) AND TITLE-ABS-KEY (“Picture Exchange Communication System”) AND TITLE-ABS-KEY (“communication”) AND PUBYEAR > 2013 AND PUBYEAR < 2025 AND (LIMIT-TO (LANGUAGE, “English”)) AND (LIMIT-TO (SRCTYPE, “j”))

These keywords were chosen to filter relevant and specific articles, particularly those about the use of PECS and its impact on communication in autistic students.

2. For Google Scholar:

- “Autism spectrum disorder” AND “picture exchange communication system” AND “communication” AND “education”

Searches using these keywords were designed to achieve broader coverage of relevant sources, including those not covered in the Scopus database.

The selection of keywords is based on terminology that is often used in related research and is directly relevant to this research topic. In addition, the determination of these keywords took into account the focus of the research, namely the integration of PECS technology with technological approaches such as AR in educational settings for students with ASD.

Article Data Search

The second step after determining the keywords is searching for article data. Scopus and Google Scholar databases were chosen for this purpose. Scopus-indexed articles are collected directly from [Scopus] (<https://www.scopus.com>), while Google Scholar-indexed articles are gathered with the help of the Publish or Perish application and from [Google Scholar] (<https://scholar.google.com>). This process ensures a comprehensive and diverse collection of research articles relevant to the study's focus on AR-based PECS and its impact on communication skills in autistic students.

Determination of Inclusion Criteria

The final stage involves determining inclusion and exclusion criteria to ensure the articles used are appropriate to the research focus. The criteria set are as follows:

1. Inclusion Criteria:

- (a) Only journal articles were considered relevant documents for this research.
- (b) Articles published between 2014 and 2024.
- (c) Articles in English and Indonesian.
- (d) Articles sourced from Google Scholar (<https://scholar.google.com>) and Scopus (<https://www.scopus.com>) databases.

- (e) Articles that explicitly discuss communication skills, children with autism, communication training methods, education, and augmented reality technology.
- 2. Exclusion Criteria:
 - (a) Articles that were not in English or Indonesian were excluded.
 - (b) Articles with incomplete identity data, such as year of publication or citation information.
 - (c) Articles in books, proceedings, technical reports, or other documents that are not scientific journal articles.

The data collection process was carried out on July 5, 2024. Based on the search results:

- (a) A total of 82 articles were found in the Scopus database.
- (b) A total of 98 articles were found in the Google Scholar database.

The article selection process was carried out systematically to ensure that only articles that met the inclusion criteria were used in the analysis. Articles that did not meet the exclusion criteria were excluded from further processing, hereby ensuring the rigor and relevance of the literature review results.

RESULTS AND DISCUSSION

Summary of Findings from Previous Studies

The findings from previous research regarding the use of Augmented Reality-based PECS are presented in Table 1.

Based on Table 1, the use of PECS proves highly beneficial for enhancing communication skills in autistic children (Taryadi et al., 2019; Taryadi & Kurniawan, 2018; Lutfianti et al., 2023; Travis & Geiger, 2010; Pérez-Fuster et al., 2022; Wang et al., 2022; Zhang et al., 2023). These studies demonstrate that PECS helps autistic children express their needs, wants, and feelings effectively. Moreover, findings suggest that PECS can mitigate negative behaviors stemming from communication frustrations.

In addition to improving communication skills, the PECS method can also enhance learning skills in autistic children (Khowaja et al., 2020). This method facilitates communication and increases their engagement in teaching and learning activities. PECS offers a clear structure that is easily understood by autistic children, enabling them to follow instructions and tasks better. Thus, PECS plays a crucial role in promoting more inclusive and effective learning environments for children with special needs.

The integration of PECS with AR has received a highly positive response and can capture student interest. Augmented reality is recognized as a highly effective technology in understanding educational and treatment methods (Hossaeini & Foutohi-Ghazvini, 2016). Using AR with PECS provides a more interactive and immersive learning experience,

Table 1
Research regarding the use of Augmented Reality-based PECS

Research and Year (Ref.)	Journal	Results
Taryadi et al. (2019)	Journal of Telematics and Informatics	The research results demonstrate that the proposed application aligns with the aesthetic design principles of the MDA framework, making it highly acceptable to autistic children and providing a positive impact. Additionally, it creates a more enjoyable learning environment for both autistic children and teachers.
Taryadi and Kurniawan (2018)	Journal of Physics: Conference Series	The study results indicated that the average level of communication skills before treatment was 47%. During the treatment phase, this average increased to 65%. Following the intervention, it increased further to an average of 76%.
Hossaeini and Foutohi-Ghazvini (2016)	Journal of Modern Rehabilitation	The research results demonstrate significant differences in children's performance before and after implementing the play learning method. Furthermore, the study highlights augmented reality as a highly effective technology in enhancing educational and treatment methods.
Lutfianti et al. (2023)	Educational Insights	The research results show that Augmented Alternative Communication (AAC) through PECS media can improve the communication skills of autistic children.
Travis and Geiger (2010)	Child Language Teaching and Therapy	The results from this study indicated highly effective treatment outcomes for requests, while outcomes for comments and length of verbal utterances varied. Both participants demonstrated a significant increase in intentional communicative acts (ICA), notably in demand (function) and the development of communication forms.
Pérez-Fuster et al. (2022)	Children	The results of this study suggest that autistic children can improve their RJA (Responding to Joint Attention) skills with targeted and engaging interventions based on accessible augmented reality technology tools.
Wang et al. (2022)	Applied Sciences	The results showed that our help request module interface was effective in assisting children with ASD at various levels. The proposed AR sentence intervention helps them create their scenarios, organize communication with their peers, and request help.
Zhang et al. (2023)	International Journal of Disability, Development and Education	The results showed that the three participants who acquired the target request skill were able to generalize its use to similar unexpected situations (different classrooms with different teachers), and they also met this criterion during the maintenance sessions. This study contributes to the evidence supporting the use of the PECS-TS for visually impaired (VI) and intellectually disabled (ID) students.
Khowaja et al. (2020)	IEEE Access	The research results demonstrate that A) is beneficial for children with ASD in learning various skills.
Hou et al. (2024)	International Journal of Developmental Disabilities	The results of this study demonstrated a significant increase in verbal and nonverbal communication behaviors following a two-month PECS intervention. A larger proportion of children in the robot-based intervention group showed significantly improved social communication skills, both verbal and nonverbal, compared to those in the human-based intervention group.

Table 1 (continue)

Research and Year (Ref.)	Journal	Results
Munir et al. (2024)	Data and Metadata	The results of this research highlight that studies on the communication skills of autistic children remain a significant research trend, showing increased interest from researchers between 2015 and 2022. Additionally, this research suggests that the characteristics of project-based learning can enhance autistic children's communication skills, particularly when augmented with AR.
Munir et al. (2018)	International Journal of Emerging Technologies in Learning (Online)	The results of the research indicate that learning with the MESE application improves students' reading and memorization skills, although some sessions showed a decline or stability.
Khoirunnisa et al. (2023)	Computers	The results of this research indicate that developing a prototype tailored to the characteristics of autistic children is crucial for ensuring that the information conveyed is readily accepted.
Khoirunnisa et al. (2024)	Journal of Special Education Technology	The research results indicate that using a personalized learning model based on AR can enhance student learning outcomes in reading words and syllables. However, there was no significant improvement in learning outcomes for letter recognition.

which enhances student motivation and engagement. Through AR, children can experience vivid and contextual visualizations, making it easier to understand and retain information. Research indicates that this technology serves as a valuable tool in supporting inclusive and adaptive education for children with autism.

Publication Trends (2015–2024)

Figure 3 illustrates the research development using the PECS based on the Scopus database, while Figure 4 depicts the development based on the Google Scholar database. Analysis of Figures 3 and 4 reveals that research on PECS shows similar trends, characterized by fluctuations in annual publication numbers (peaks and dips). The primary difference lies in the total number of documents found. Figure 3 indicates that the highest peak in publications occurred in 2022, with 12 documents and the lowest peak was in 2016–2017, with three documents each. Conversely, Figure 4 shows the highest peak in 2017 with 14 documents and the lowest peak in 2015–2016 with five documents each.

These results reflect heightened awareness and interest in developing effective intervention methods for children with autism. Increased studies in specific years, such as 2022, can be attributed to greater support from academic institutions and governments for research in education and therapy for children with special needs. Conversely, fluctuations in publication numbers may result from variability in research funding, shifts in educational policies, and advancements in technology supporting PECS applications.

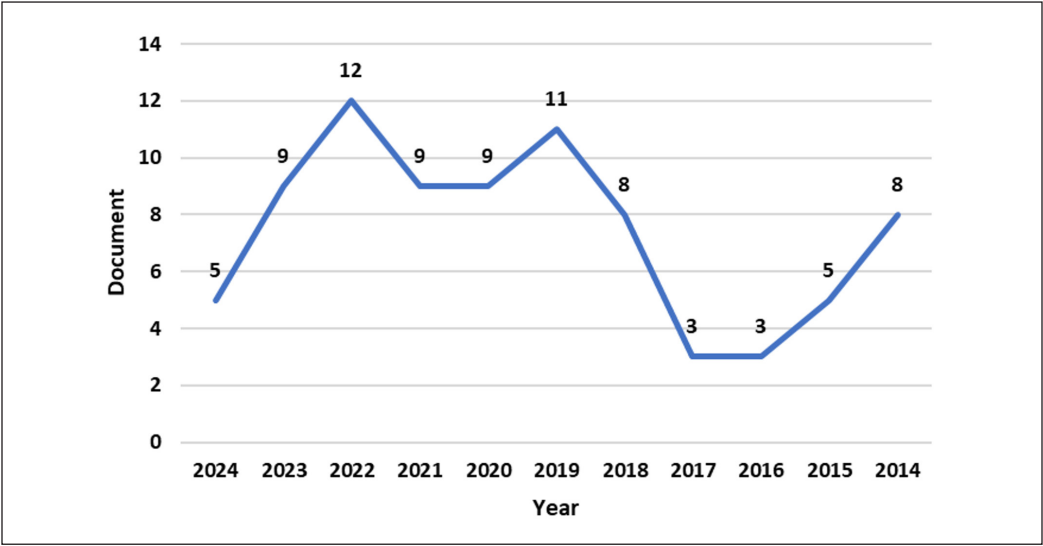


Figure 3. Development of the number of publications per year (Scopus)

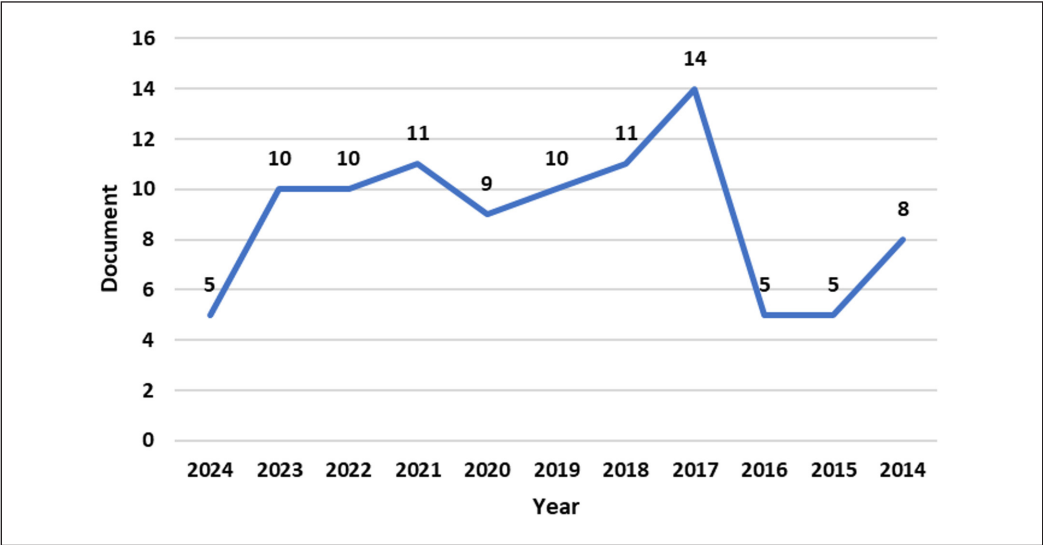


Figure 4. Development of the number of publications per year (Google Scholar)

In years with a few publications, such as 2016–2017, researchers may have been in the early stages of integrating new technologies like augmented reality with PECS. As technology advances over time, more research can be conducted, potentially leading to increased publications in subsequent years. These fluctuations indicate that while there is sustained interest in PECS, external factors such as funding and technological developments significantly influence research productivity (Khowaja et al., 2020).

Influential Publication Sources

Figure 1 shows that *Advances in Neurodevelopmental Disorders*, *Developmental Neurorehabilitation*, and *Autism* are the three main sources that contribute most to this research area, with 4 and 3 articles contributing, respectively. The existence of these journals as main references shows the high relevance and quality of the publications produced. *Advances in Neurodevelopmental Disorders* and *Developmental Neurorehabilitation*, for example, frequently publish in-depth research on intervention and rehabilitation for children with developmental disorders, which provides an important basis for other researchers in developing new methodologies and approaches.

In addition, the autism journal is known as one of the leading journals that specifically focuses on the autism spectrum, offering a variety of research ranging from diagnosis and intervention to educational policy. The dominance of these three journals reflects the tendency of the research community to rely on reliable sources that have high credibility in the field of neurodevelopmental disorders and autism. This also indicates that the research in these journals has a significant impact and is widely recognized by researchers and practitioners in the field, which ultimately contributes to improving the quality and effectiveness of interventions and understanding of developmental disorders in children.

Productive Regions

Figure 5 displays the top 10 countries/regions based on the number of articles published. From this data, the United States contributed the most publications compared to other countries (N=34). Followed by India (N=10) and England (N=8). Of the total publications, the United States accounted for 34%. The dominance of the United States in these publications can be interpreted as an indication of high investment in research and

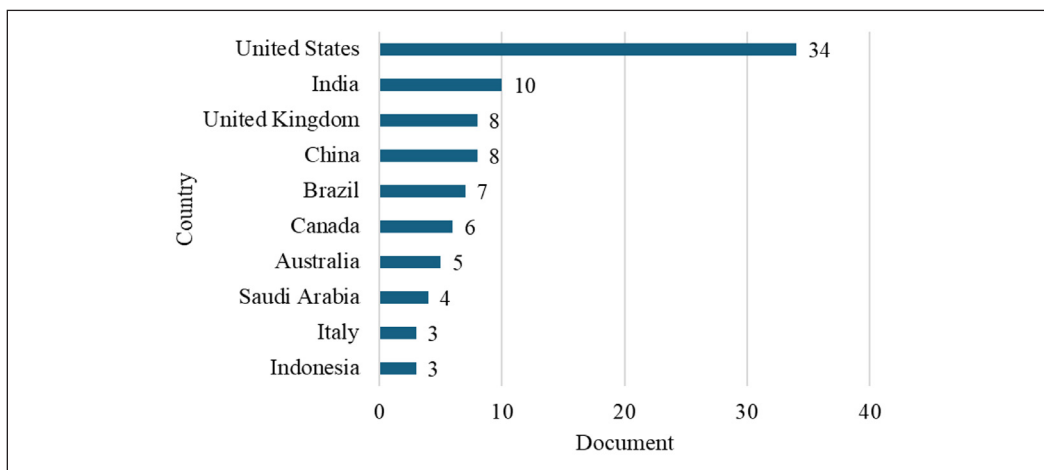


Figure 5. Top 10 countries: Article counts

development, as well as efforts by governments and educational institutions to improve the quality and quantity of research.

The dominance of the United States in the number of publications shows the country’s commitment to supporting scientific research through various initiatives, such as large funding for research projects, partnerships between universities and industry, and the existence of a strong research network. On the other hand, the positions of India and the UK as the second and third largest contributors to publications indicate that these countries are also starting to pay greater attention to scientific research. The significant difference in the number of publications between the United States and other countries reflects gaps in available research resources and infrastructure. However, with increasing globalization and international collaboration, this gap is hoped to decrease so that research can develop more evenly worldwide.

Research Subject Area

Figure 6 presents subject areas frequently used in research. From these data, the medical field is the topic most frequently researched, with a percentage of 28% (N=48) of the total articles. This shows the high interest and need for research in the field of medicine, which is likely driven by efforts to find better and innovative health solutions. The field of psychology followed second with 18% (N=32), reflecting the importance of understanding behavior and mental health in modern society. Social sciences came in third with 14% (N=24), indicating the important role of social studies in addressing various societal issues.

Additionally, health professions (N=18, 10%) and neuroscience (N=15, 10%) also made significant contributions, highlighting the relevance of interdisciplinary research in

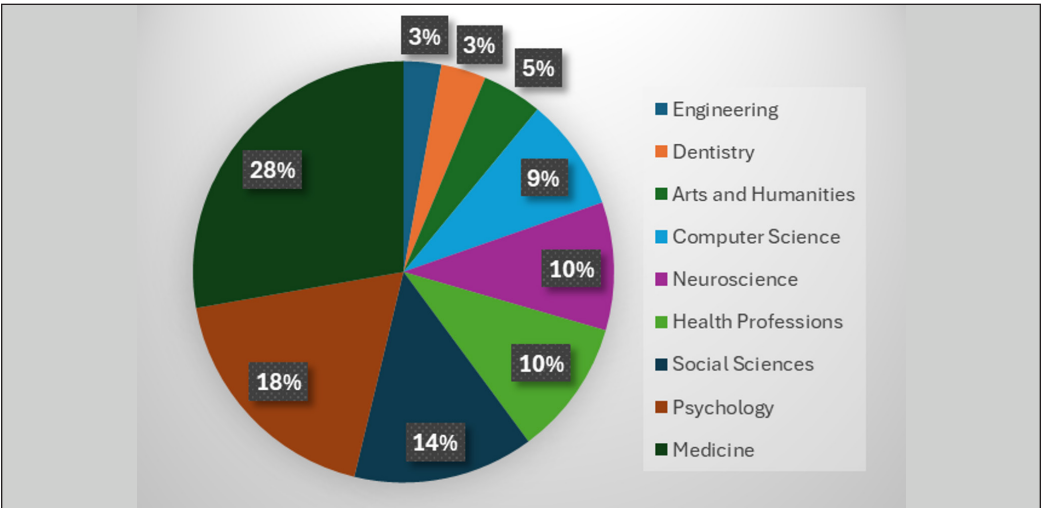


Figure 6. Frequently investigated subject areas and research trends

the health field. Computer science (N=15, 9%) reflects technological developments and their applications in various aspects of life, including medical and social. Meanwhile, the fields of arts and humanities (N=8, 5%), dentistry (N=6, 3%), and engineering (N=5, 3%) show that although their contributions are relatively small, there is still significant attention to these fields. This data indicates the diversity and broad spectrum of research conducted, as well as the importance of collaboration between scientific disciplines to solve complex problems in society.

Autism Spectrum Disorder (ASD) Communication Skills

Communication skills in individuals with ASD commonly face substantial challenges. Studies demonstrate a broad spectrum of communication abilities among those with ASD, ranging from limited language skills to proficient use of complex language in specific contexts (Tager-Flusberg, 2006). Factors including the severity of ASD, level of intelligence, and co-occurrence of other developmental disorders can influence the range of communication skills and individual exhibits (Tager-Flusberg, 2006).

Management of communication skills in individuals with ASD involves an interdisciplinary approach that includes speech therapy, behavioral therapy, and special educational strategies designed to systematically support the development of communication skills (Koegel et al., 2001; Kasari & Smith, 2013). A structured and consistent approach can help individuals with ASD to improve their ability to communicate with their surroundings, as well as facilitate better social and academic integration.

As explained, ASD is a neurobiological condition that can impact various facets of an individual's communication skills. Individuals with ASD frequently encounter difficulties in comprehending and utilizing both verbal and nonverbal language. Verbal communication in individuals with ASD often involves limitations in complex language use and may include echolalia and the repetition of words or phrases. They may struggle with constructing structured sentences or comprehending language in diverse social contexts (Tager-Flusberg, 2007).

In addition to verbal communication, nonverbal communication skills are crucial in ASD. This encompasses the ability to utilize facial expressions, eye contact, hand gestures, or body positioning to convey meaning and engage with others (Mundy et al., 1990). Children with ASD often struggle with interpreting emotional expressions from others or expressing their feelings nonverbally.

Effectiveness of AR-based PECS in Communication with Autistic Children

The PECS is an alternative communication method that utilizes pictures to aid children with ASD in communication (Bondy & Frost, 2001). PECS has demonstrated effectiveness in enhancing both verbal and nonverbal communication skills among children with ASD,

enabling them to express their needs, desires, and emotions more effectively (Bondy & Frost, 2001; Howlin et al., 2007).

AR, as an adjunct to PECS, has emerged as an innovative approach to supporting communication in children with autism. AR enhances learning experiences by blending virtual and real-world elements, which can enhance visual and interactive appeal, particularly for children with ASD (Billinghurst et al., 2015). Recent studies highlight that integrating PECS with AR can increase motivation among autistic children to engage in communication and interaction while also aiding in a better understanding of language context (Taryadi et al., 2019; Taryadi & Kurniawan, 2018; Lutfianti et al., 2023; Travis & Geiger, 2010; Hou et al., 2024).

Although still relatively new, the integration of AR with PECS shows promise as a method to enhance communication effectiveness and learning outcomes in autistic children. This technology supports their social interactions and provides enhanced visual stimuli for understanding language and abstract concepts (Ramdoss et al., 2011). Therefore, the combination of PECS with AR holds significant potential to enhance the quality of life for autistic children by improving their communication abilities across various contexts.

Using AR-based PECS with students with ASD can have a long-term positive impact on their communication skills. With AR technology, students can more easily access symbols and images that represent their needs or desires, making conveying messages easier. This can accelerate the development of their non-verbal communication skills, which are very important in everyday interactions. Through the use of AR, students can be invited to practice communicating in various situations, both at home, school and in public environments, so that they can more easily adapt their skills to different contexts. In addition, AR-based PECS also supports the development of social skills in autistic students. By facilitating more effective communication, students can more actively participate in social interactions with classmates, teachers, and family. However, although AR-based PECS can provide many benefits, there are also potential limitations, such as dependence on technological devices or difficulty transitioning from the use of technology-based symbols to direct interaction with others. Therefore, ongoing supervision and support are very necessary so that this positive impact can be achieved optimally.

As explained, the use of AR-based PECS for children with ASD is considered effective. However, the effectiveness of using AR-based PECS is highly dependent on individual differences among autistic students, such as age, severity of autism, sensory preferences, and social and cognitive abilities. The following is a further explanation regarding the effectiveness of using AR-based PECS for children with ASD:

1. Younger children tend to be more interested in the visual and interactive elements provided by AR, thereby increasing their engagement with AR-based PECS (Bremner, 2023). In contrast, older children, who may be more familiar with the use of technology, can adapt more quickly and use the more complex features of

- AR to improve their communication. Therefore, adjusting the design based on age is essential to maximize the effectiveness of AR-based PECS.
2. Students with milder levels of autism severity may be better able to use AR independently, allowing them to utilize AR-based PECS in a more independent context. Meanwhile, students at higher levels of severity may require additional support in interacting with this technology, either through hands-on guidance or simpler visual elements. This shows the importance of being able to adjust the level of difficulty or interactivity in AR applications according to the severity of the student's condition (Khowaja et al., 2020).
 3. Every autistic student has different sensory preferences (Gentil-Gutiérrez et al., 2021). Some may be more sensitive to visual or sound elements, while others may be more comfortable with simpler elements or more focused on movement. The design of AR-based PECS must be flexible enough to accommodate these varying preferences, allowing students to customize their experience to be more comfortable and effective in communicating.
 4. Children with better social and cognitive skills tend to master the use of AR more quickly to improve their communication. However, students with difficulties in social or cognitive aspects may require a more personalized approach and longer adaptation time. Therefore, ongoing evaluation and adjustments in design are essential to ensure that AR-based PECS can be implemented effectively according to students' social-cognitive needs.

The Role of Augmented Reality (AR) in Education

AR plays a significant role in education by providing a highly interactive and immersive learning approach. AR technology facilitates the integration of virtual elements, such as images, videos, and 3D animations, into the real world through devices like smartphones or tablets. Its application in education enhances learning experiences, making them more engaging and boosting student motivation and participation.

In educating children with autism, AR can be applied with the AR-based PECS system, which helps children communicate using images. This system allows children to exchange virtual images for desired objects or actions. This AR-based implementation of PECS can be applied at various levels of education, from early childhood education (PAUD) to elementary school, especially in subjects that involve communication, such as Indonesian, Mathematics and Science. AR-based PECS can also be used in both formal settings, such as schools, and non-formal settings, such as therapy centers or home learning, allowing for flexibility in teaching approaches (Bai et al., 2014).

One of the advantages of AR is its capability to present educational content visually and contextually, which aids in students' comprehension of complex concepts. AR can

be utilized for virtual simulations and experiments that might be impractical or unsafe to conduct in real-world settings, thereby offering safe and comprehensive learning opportunities (Radu, 2014).

Research indicates that integrating AR in education can enhance student learning outcomes. In their meta-analysis, Küçük et al. (2016) demonstrated that AR increases learning motivation and provides a more enjoyable and effective learning experience. Therefore, AR represents a technology with significant potential for integration into educational curricula across various levels.

In the education of autistic children, AR plays a crucial role in enhancing student engagement and motivation. AR facilitates the creation of interactive and immersive learning environments where students can interact with virtual objects in real-world contexts. This technology aids autistic children in comprehending abstract concepts more easily through clearer and more realistic visualizations (Chen et al., 2015). Moreover, the use of AR in the education of children with autism can alleviate anxiety and enhance attention, addressing common challenges associated with autism spectrum disorders (Escobedo et al., 2014).

Other studies indicate that AR can be utilized to bolster academic skills like reading, writing, and arithmetic through applications tailored to the specific needs of children with autism (Bai et al., 2014). Therefore, integrating AR into the education of children with autism serves as a visual aid and a versatile medium to support various aspects of children’s development. Figure 7 exemplifies the application of AR as a learning medium for autistic children, as researched by Julianingsih and Huda (2022).

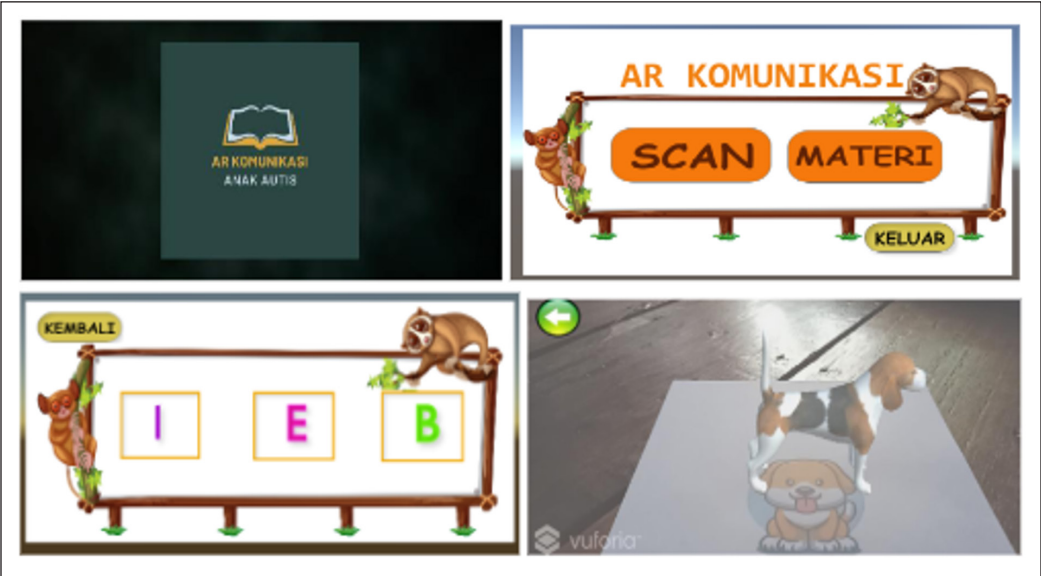


Figure 7. An example of using AR is educating autistic children (Julianingsih & Huda, 2022)

The Importance of AR Research in the Education of Children with Autism in Indonesia

In Indonesia, the use of AR technology to enhance the learning experience of children with ASD has become a rapidly growing research area globally. These studies show that AR is useful not only for improving the academic skills of children with autism but also for reducing anxiety and increasing their attention in educational contexts.

Indonesia, as a country with an increasing number of children with autism (Riany et al., 2016), has great potential to develop and integrate AR technology into the education of children with autism. Research related to the use of AR in Indonesia, such as that conducted by Saripudin et al. (2022) and Julianingsih and Huda (2022), provides an overview of the application of this technology in a local context. Therefore, a recent review of the application of AR for children with autism in Indonesia is very relevant, considering the need to understand the challenges and opportunities in this country, which has different cultural and educational characteristics compared to other countries.

By focusing on AR technology, Indonesia can gain deeper insight into its effectiveness in addressing the specific needs of children with autism and contribute to global research that has developed in various countries. Further research in Indonesia could enrich knowledge about the application of AR in developing countries and provide guidance for wider implementation in the future.

Advantages and Challenges of Using the PECS in Learning

One of the primary advantages of PECS is its effectiveness in enhancing the communication skills of children with autism. Using pictures, PECS enables children to express their wants and needs clearly and clearly, thereby reducing frustration and negative behaviors associated with communication difficulties (Bondy & Frost, 2001). Research demonstrates that PECS can improve verbal and nonverbal communication abilities and enhance social skills in children with autism (Charlop-Christy et al., 2002). Furthermore, PECS is highly adaptable to individual needs, allowing for personalized and effective interventions (Preston & Carter, 2009).

However, implementing AR-based PECS may require a greater investment, especially in the procurement of technological devices such as tablets or smartphones and the development of appropriate applications. In regions with limited resources, this can pose a significant challenge due to budget constraints for providing the necessary equipment and training. Moreover, the ongoing maintenance and updates of the software can add to operational costs in the long term.

In addition to these financial challenges, implementing PECS presents several other obstacles. One of the primary hurdles is the need for intensive training for teachers and parents to ensure the effective use of PECS. Logistical challenges also arise when providing

PECS materials, particularly in schools with limited resources. Furthermore, research indicates that children may require a significant amount of time to master the effective use of PECS, emphasizing the importance of patience and consistency throughout the process (Alsayedhassan et al., 2016).

Although our current research focuses on AR-based PECS for autistic children, it would also be important to explore its application to children who are blind or have other sensory disabilities. In this case, modifications and adjustments are required, such as adding devices to accommodate visual impairments. Therefore, we plan to investigate these modifications further in our future research to ensure that AR-based PECS can be effectively applied to a wider range of sensory disabilities.

The Impact of Using the AR-Based PECS on Indonesian Language Subjects

The impact of implementing a PECS based on AR in Indonesian language subjects can significantly enhance the communication skills and engagement of autistic students. AR-based PECS introduces interactive and dynamic visual aids that capture students' interest, thereby making learning more enjoyable and effective. This technology enables students to comprehend language concepts more readily by providing realistic and contextual visual representations. Research supports that AR in education can bolster learning motivation, improve material comprehension, and enhance information retention (Billinghurst et al., 2015).

The study by Fletcher-Watson et al. (2016) demonstrated that AR-based technology aids in developing communication and social skills among students with ASD. When integrated with PECS, AR enhances student engagement by enabling interaction with vibrant images and captivating animations. AR also promotes collaborative learning environments, facilitating peer communication and teamwork in project-based activities utilizing this technology.

In Indonesian language subjects, integrating AR-based PECS can significantly enhance students' understanding of sentence structure, vocabulary, and grammar through interactive and engaging methods. This approach can positively impact verbal and nonverbal communication skills, fostering increased participation in classroom activities and enhancing overall academic achievement.

However, although many studies demonstrate the effectiveness of AR-based technology in improving the communication and learning skills of students with ASD, some studies also note the existence of challenges that need to be overcome (Chen et al., 2018). These challenges include the risk of overstimulation in students with high sensory sensitivity, the need for special training for teachers to operate AR-based devices, and limited access to this technology in some schools. In addition, the application of AR-based PECS in Indonesian language learning requires adaptations that take into account local language

and cultural characteristics. This adjustment includes selecting visual content relevant to students’ daily lives, as well as developing interactive materials that support grammar mastery and contextual understanding. By overcoming these obstacles, AR-based PECS has the potential to be an inclusive and effective learning tool in supporting the unique needs of students with autism.

Comparison of AR, VR, MR, and XR Technologies in Education for Students with Autism

In this research, we focus on the application of AR in improving the communication skills of students with autism and realize the existence of related technologies such as Virtual Reality (VR), Mixed Reality (MR), and Extended Reality (XR). While these technologies have advantages and disadvantages, understanding their differences in educational contexts, particularly for students with autism, is critical. Therefore, we will add a discussion regarding the comparison of these four technologies through a study of relevant literature.

Table 2 compares AR, VR, MR, and XR technologies based on the results of the literature review.

Table 2
Comparison of AR, VR, MR, and XR technologies

Technology	Description	Advantages	Disadvantages	Applications in the Education of Students with Autism
AR	Technology that combines virtual elements with the real world.	Interaction with the real environment. Can be used with mobile devices (smartphone /tablet).	Depends on the quality of the hardware. Can be less immersive than VR.	Helping students with autism interact with objects or symbols visually, such as in the use of the Picture Exchange Communication System (PECS).
VR	Technology creates a completely virtual environment with which users can interact.	Immersive, can provide a more immersive experience. Suitable for simulating social situations and practicing social skills.	Requires special devices such as VR headsets. May cause disorientation or fatigue in some users.	Can be used for social skills practice or simulating real -ife situations for students with autism.
MR	A combination of AR and VR allows interaction with visual objects recorded in the real world.	Provides richer interactions with the real and virtual world. Can be used in more dynamic learning situations.	Requires more sophisticated and expensive hardware. Still in the development stage for educational applications.	Can help students with autism practice social or communication skills in more realistic and interactive situations.

Table 2 (continue)

Technology	Description	Advantages	Disadvantages	Applications in the Education of Students with Autism
XR	An umbrella term that includes AR, VR, and MR creates a wider world of experiences.	Flexibility to cover a wide range of immersive experiences. Can be adapted to various contexts and learning objectives.	Still in the exploration stage for wider educational applications. Requires complex hardware and software.	Enables the development of more diverse and adaptive educational applications for students with autism, depending on the context of use.

CONCLUSION

This research examines the effectiveness of employing an AR-based PECS to enhance the communication skills of autistic students in Indonesian language subjects. According to the Scopus database, most publications occurred in 2022 (12 documents), with the lowest peaks observed in 2017 and 2016 (three documents each). Similarly, the Google Scholar database data indicated the highest peak in 2017 (14 documents), with the lowest peaks in 2016 and 2015 (five documents each).

In addition, the research results highlight that integrating PECS with augmented reality technology significantly enhances the communication skills of autistic students. The analyzed studies indicate that AR enhances the learning experience by providing engaging and interactive visual stimuli, thereby accelerating language comprehension and usage. This integration also supports more effective communication and participation in Indonesian language learning among autistic students. Despite challenges such as the need for adequate equipment and teaching training, the observed benefits underscore substantial potential for further research and broader implementation within the education system.

Although AR-based PECS may improve the communication skills of students with autism, it should be noted that in conducting research involving students with ASD, ethical considerations are essential, especially related to obtaining information acquisition and safeguarding the well-being of participants during the research. Before research is carried out, basic things that must be considered include obtaining consent from caregivers, transparency and openness, attention to student welfare, both physical, emotional and psychological, and maintaining the confidentiality of student data.

ACKNOWLEDGEMENT

We would like to appreciate and thank Universitas Pendidikan Indonesia for support throughout this research, and special school’s teachers and students for lending their precious time aiding in the success of the research.

REFERENCES

- Alsayedhassan, B., Banda, D. R., & Griffin-Shirley, N. (2016). A review of picture exchange communication interventions implemented by parents and practitioners. *Child and Family Behavior Therapy*, 38(3), 191-208. <https://doi.org/10.1080/07317107.2016.1203135>
- Azuma, R. T. (1997). A survey of augmented reality. *Presence: Teleoperators and Virtual Environments*, 6(4), 355-385. <https://doi.org/10.1162/pres.1997.6.4.355>
- Bai, Z., Blackwell, A. F., & Coulouris, G. (2014). Using augmented reality to elicit pretend play for children with autism. *IEEE Transactions on Visualization and Computer Graphics*, 21(5), 598-610. <https://doi.org/10.1109/TVCG.2014.2385092>
- Baio, J., Wiggins, L., Christensen, D. L., Maenner, M. J., Daniels, J., Warren, Z., Kurzius-Spencer, M., Zahorodny, W., Rosenberg, C. R., White, T., & Durkin, M. S. (2020). Prevalence of autism spectrum disorder among children aged 8 years-autism and developmental disabilities monitoring network, 11 sites, United States, 2016. *Morbidity and Mortality Weekly Report*, 69(16), 503-503.
- Billinghurst, M., & Duenser, A. (2012). Augmented reality in the classroom. *Computer*, 45(7), 56-63. <https://doi.org/10.1109/MC.2012.111>
- Billinghurst, M., Clark, A., & Lee, G. (2015). A survey of augmented reality. *Foundations and Trends® in Human-Computer Interaction*, 8(2-3), 73-272. <http://dx.doi.org/10.1561/11000000049>
- Bondy, A. S., & Frost, L. A. (1994). The picture exchange communication system. *Focus on Autistic Behavior*, 9(3), 1-19.
- Bondy, A., & Frost, L. (2001). The picture exchange communication system. *Behavior Modification*, 25(5), 725-744. <https://doi.org/10.1177/0145445501255004>
- Bremner, L. (2023). *Augmented Reality facial expression tracking interface to improve Theory of Mind in children with ASD, based on design principles created through a user centred design process* (Doctoral dissertation). University of Huddersfield, England. https://pure.hud.ac.uk/ws/portalfiles/portal/70873988/Louisa_Bremner.pdf
- Charlop-Christy, M. H., Carpenter, M., Le, L., LeBlanc, L. A., & Kellet, K. (2002). Using the picture exchange communication system (PECS) with children with autism: Assessment of PECS acquisition, speech, social-communicative behavior, and problem behavior. *Journal of Applied Behavior Analysis*, 35(3), 213-231. <https://doi.org/10.1901/jaba.2002.35-213>
- Chen, C. H., Lee, I. J., & Lin, L. Y. (2015). Augmented reality-based self-facial modeling to promote the emotional expression and social skills of adolescents with autism spectrum disorders. *Research in Developmental Disabilities*, 36, 396-403. <https://doi.org/10.1016/j.ridd.2014.10.015>
- Chen, Y., Fanchiang, H. D., & Howard, A. (2018). Effectiveness of virtual reality in children with cerebral palsy: A systematic review and meta-analysis of randomized controlled trials. *Physical therapy*, 98(1), 63-77. <https://doi.org/10.1093/ptj/pzx107>
- Dargan, S., Bansal, S., Kumar, M., Mittal, A., & Kumar, K. (2023). Augmented reality: A comprehensive review. *Archives of Computational Methods in Engineering*, 30(2), 1057-1080. <https://doi.org/10.1007/s11831-022-09831-7>

- Escobedo, L., Tentori, M., Quintana, E., Favela, J., & Garcia-Rosas, D. (2014). Using augmented reality to help children with autism stay focused. *IEEE Pervasive Computing*, 13(1), 38-46. <https://doi.org/10.1109/MPRV.2014.19>
- Fletcher-Watson, S., Pain, H., Hammond, S., Humphry, A., & McConachie, H. (2016). Designing for young children with autism spectrum disorder: A case study of an iPad app. *International Journal of Child-Computer Interaction*, 7, 1-14. <https://doi.org/10.1016/j.ijcci.2016.03.002>
- Frost, L. (2002). The picture exchange communication system. *Perspectives on Language Learning and Education*, 9(2), 13-16. <https://doi.org/10.1044/llc9.2.13>
- Gentil-Gutiérrez, A., Cuesta-Gómez, J. L., Rodríguez-Fernández, P., & González-Bernal, J. J. (2021). Implication of the sensory environment in children with autism spectrum disorder: Perspectives from school. *International Journal of Environmental Research and Public Health*, 18(14), Article 7670. <https://doi.org/10.3390/ijerph18147670>
- Geschwind, D. H. (2009). Advances in autism. *Annual Review of Medicine*, 60(1), 367-380.
- Hosseini, E., & Foutohi-Ghazvini, F. (2016). Play therapy in augmented reality children with autism. *Journal of Modern Rehabilitation*, 10(3), 110-115.
- Hou, S., Cai, P., Yu, L., Cui, H., Hu, J., & Wei, Z. (2024). Improving the social communication skills of preschoolers with autism spectrum disorder: robot-based intervention on Picture Exchange Communication System use. *International Journal of Developmental Disabilities*, 1-16. <https://doi.org/10.1080/20473869.2024.2345957>
- Howlin, P., Gordon, R. K., Pasco, G., Wade, A., & Charman, T. (2007). The effectiveness of picture exchange communication system (PECS) training for teachers of children with autism: A pragmatic, group randomised controlled trial. *Journal of child Psychology and Psychiatry*, 48(5), 473-481. <https://doi.org/10.1111/j.1469-7610.2006.01707.x>
- Indriyani, V., Kurniawati, E., & Ramadhan, A. (2023). What is the teacher's view of the development of digital teaching materials in Indonesian language learning in middle schools? *Cetta: Jurnal Ilmu Pendidikan*, 6(4), 757-769. <https://doi.org/10.37329/cetta.v6i4.2749>
- Johnson, C. P. (2008). Recognition of autism before age 2 years. *Pediatrics in Review*, 29(3), 86-96.
- Julianingsih, D., & Huda, A. (2022). Rancang bangun media pembelajaran komunikasi anak autis berbasis augmented reality [Design and construction of communication learning media for autistic children based on augmented reality.]. *Jurnal Pendidikan Tambusai*, 6(1), 1192-1201.
- Kasari, C., & Smith, T. (2013). Interventions in schools for children with autism spectrum disorder: Methods and recommendations. *Autism*, 17(3), 254-267. <https://doi.org/10.1177/1362361312470496>
- Kaufmann, W. E., Cortell, R., Kau, A. S., Bukelis, I., Tierney, E., Gray, R. M., Cox, C., Capone, G. T., & Stanard, P. (2004). Autism spectrum disorder in fragile X syndrome: communication, social interaction, and specific behaviors. *American Journal of Medical Genetics Part A*, 129(3), 225-234. <https://doi.org/10.1002/ajmg.a.30229>
- Khoirunnisa, A. N., Munir, & Dewi, L. (2023). Design and prototype development of augmented reality in reading learning for autism. *Computers*, 12(3), Article 55. <https://doi.org/10.3390/computers12030055>

- Khoirunnisa, A. N., Munir, M., Shahbodin, F., & Dewi, L. (2024). Augmented reality based personalized learning in autism spectrum disorder reading skills. *Journal of Special Education Technology*, 39(4), 513-526. <https://doi.org/10.1177/01626434241236738>
- Khowaja, K., Banire, B., Al-Thani, D., Sqalli, M. T., Aqle, A., Shah, A., & Salim, S. S. (2020). Augmented reality for learning of children and adolescents with autism spectrum disorder (ASD): A systematic review. *IEEE Access*, 8, 78779-78807. <https://doi.org/10.1109/ACCESS.2020.2986608>
- Koegel, R. L., Koegel, L. K., & McNERney, E. K. (2001). Pivotal areas in intervention for autism. *Journal of Clinical Child and Adolescent Psychology*, 30(1), 19-32. https://doi.org/10.1207/S15374424JCCP3001_4
- Küçük, S., Kapakin, S., & Göktaş, Y. (2016). Learning anatomy via mobile augmented reality: Effects on achievement and cognitive load. *Anatomical Sciences Education*, 9(5), 411-421. <https://doi.org/10.1002/ase.1603>
- Lutfianti, Z., Ataqi, A.E., Asmiati, N., Putri, E., Puspitasari, R., Widya, L.A., Hikmatullah, H., Saputra, N., Sukmariah, S., Handayani, A., & Jazilatusyifa, J. (2023). The application of augmentative alternative communication (AAC) through picture exchange communication system (PECS) media to improve communication skills of children with autism. *Educational Insights*, 1(2), 97-105. <https://doi.org/10.58557/eduinsights.v1i2.23>
- Matson, J. L., & Kozlowski, A. M. (2011). The increasing prevalence of autism spectrum disorders. *Research in Autism Spectrum Disorders*, 5(1), 418-425. <https://doi.org/10.1016/j.rasd.2010.06.004>
- Mundy, P., Sigman, M., & Kasari, C. (1990). A longitudinal study of joint attention and language development in autistic children. *Journal of Autism and developmental Disorders*, 20(1), 115-128. <https://doi.org/10.1007/BF02206861>
- Munir, M., Al Husaeni, D. F., Rasim, R., Dewi, L., & Khoirunnisa, A. N. (2024). Bibliometric mapping of trends of project-based learning with augmented reality on communication ability of children with special needs (Autism). *Data and Metadata*, 3, 261-261. <https://doi.org/10.56294/dm2024261>
- Munir, M., Setiawan, W., Nugroho, E. P., Kusnendar, J., & Wibawa, A. P. (2018). The effectiveness of multimedia in education for special education (MESE) to improve reading ability and memorizing for children with intellectual disability. *International Journal of Emerging Technologies in Learning (Online)*, 13(8), Article 254. <https://doi.org/10.3991/ijet.v13i08.8291>
- Pakpahan, H. M., Suherni, S., Pujiati, L., & Girsang, R. (2023). The effectiveness of Indonesian education curriculum reform on the quality of processes in learning. *Jurnal Penelitian Pendidikan IPA*, 9(1), 564-569. <https://doi.org/10.29303/jppipa.v9i1.3930>
- Parisi, L., Di Filippo, T., & Roccella, M. (2015). The child with autism spectrum disorders (ASDs): Behavioral and neurobiological aspects. *Acta Medica Mediterranea*, 31(6), 1187-1194.
- Pérez-Fuster, P., Herrera, G., Kossyvaki, L., & Ferrer, A. (2022). Enhancing joint attention skills in children on the autism spectrum through an augmented reality technology-mediated intervention. *Children*, 9(2), Article 258. <https://doi.org/10.3390/children9020258>
- Preston, D., & Carter, M. (2009). A review of the efficacy of the picture exchange communication system intervention. *Journal of Autism and Developmental Disorders*, 39, 1471-1486. <https://doi.org/10.1007/s10803-009-0763-y>

- Radu, I. (2014). Augmented reality in education: A meta-review and cross-media analysis. *Personal and Ubiquitous Computing*, 18, 1533-1543. <https://doi.org/10.1007/s00779-013-0747-y>
- Ramdoss, S., Lang, R., Mulloy, A., Franco, J., O'Reilly, M., Didden, R., & Lancioni, G. (2011). Use of computer-based interventions to teach communication skills to children with autism spectrum disorders: A systematic review. *Journal of Behavioral Education*, 20, 55-76. <https://doi.org/10.1007/s10864-010-9112-7>
- Riany, Y. E., Cuskelly, M., & Meredith, P. (2016). Cultural beliefs about autism in Indonesia. *International Journal of Disability, Development and Education*, 63(6), 623-640.
- Saripudin, D., Ratmaningsih, N., & Anggraini, D. (2022). Smart maps Indonesia based on augmented reality as digital learning resources of social studies. *The New Educational Review*, 67(1), 172-182.
- Tager-Flusberg, H. (2006). Defining language phenotypes in autism. *Clinical Neuroscience Research*, 6(3-4), 219-224. <https://doi.org/10.1016/j.cnr.2006.06.007>
- Tager-Flusberg, H. (2007). Evaluating the theory-of-mind hypothesis of autism. *Current Directions in Psychological Science*, 16(6), 311-315. <https://doi.org/10.1111/j.1467-8721.2007.00527.x>
- Tager-Flusberg, H., Paul, R., & Lord, C. (2005). Language and communication in autism. *Handbook of Autism and Pervasive Developmental Disorders*, 1, 335-364. <https://doi.org/10.1002/9780470939345>
- Tang, A., Owen, C., Biocca, F., & Mou, W. (2003). Comparative effectiveness of augmented reality in object assembly. In *Proceedings of the SIGCHI Conference on Human Factors in Computing Systems* (pp. 73-80). ACM Publishing. <https://doi.org/10.1145/642611.642626>
- Taryadi, T., & Kurniawan, I. (2018). The improvement of autism spectrum disorders on children communication ability with PECS method Multimedia Augmented Reality-Based. *Journal of Physics: Conference Series*, 947, Article 012009.
- Taryadi, T., Kurniawan, I., & Binabar, S. W. (2019). Improved communication skills of children with autism spectrum disorder using augmented reality based on PECS (picture exchange communication system). *Journal of Telematics and Informatics*, 7(4), 185-197.
- Travis, J., & Geiger, M. (2010). The effectiveness of the picture exchange communication system (PECS) for children with autism spectrum disorder (ASD): A South African pilot study. *Child Language Teaching and Therapy*, 26(1), 39-59. <https://doi.org/10.1177/0265659009349971>
- Wang, C. P., Tsai, C. H., & Lee, Y. L. (2022). Requesting help module interface design on key partial video with action and augmented reality for children with autism spectrum disorder. *Applied Sciences*, 12(17), Article 8527. <https://doi.org/10.3390/app12178527>
- Wetherby, A. M. (2006). Understanding and measuring social communication in children with autism spectrum disorders. *Social and Communication Development in Autism Spectrum Disorders: Early Identification, Diagnosis, and Intervention*, 18(3), 3-34.
- Zhang, Y., Zhang, J., Zhang, J., Sutherland, M., & Huang, S. (2023). Teaching requesting skills to children with visual impairment and intellectual disability by using picture exchange communication system combined with tangible symbols. *International Journal of Disability, Development and Education*, 71(7), 1152-1172. <https://doi.org/10.1080/1034912X.2023.2295911>

Optimization and Analysis of Ultrasonic Wedge Bonding Parameters for Enhanced Bonding Performance in 21700 Cylindrical Lithium Battery Modules

Bin Luo, Mohamad Hanif Md Saad, Altaf Hossain Molla and Zambri Harun*

Department of Mechanical and Manufacturing Engineering, Faculty of Engineering and Built Environment, Universiti Kebangsaan Malaysia, 43600 Bangi, Selangor, Malaysia

ABSTRACT

The 21700 cylindrical lithium battery module uses ultrasonic wedge bonding technology to connect the positive terminal and negative terminal of the cell to the busbars. The weak bond of the negative terminal. This paper studied the wire bonding parameter of the negative terminal (Al wire and Fe-base Ni-top can). We aim to analyze the reasons for the poor bonding performance of the central area of the joint. Through stress and strain simulation, the result shows that the stress at the center region is lower than that in the circumference region, and the high-stress region corresponds to the ridges' vein-shaped elliptical rings of the bonding interface (i.e., the effective bonding area). The model was further validated through experimental design. The unbonded area in the center region of the joint can be limitedly reduced by optimizing key parameters, and the influencing parameters in the order of most to least critical are bond power, force, and time. Shear strength and tensile tests were used to evaluate bonding qualities. The regression equations of Al wire deformation and joint width corresponding to key parameters were established. The optimal range of Al wires deformation and joint width is proposed. The minimum value of the deformation was $174\text{ }\mu\text{m}$, and the maximum value was $248\text{ }\mu\text{m}$. The minimum value of the joint width was $560\text{ }\mu\text{m}$, and the maximum value was $1110\text{ }\mu\text{m}$. The optimal bonding parameters obtained by the response optimizer are bond force 1250 gf and bond power 100.

Keywords: Finite element analysis, negative terminal bonding, response surface methodology, shear strength, tensile testing

ARTICLE INFO

Article history:

Received: 23 September 2024

Accepted: 16 January 2025

Published: 04 April 2025

DOI: <https://doi.org/10.47836/pjst.33.3.18>

E-mail addresses:

p114558@siswa.ukm.edu.my (Bin Luo)

hanifsaad@ukm.edu.my (Mohamad Hanif Md Saad)

p114010@siswa.ukm.edu.my (Altaf Hossain Molla)

zambri@ukm.edu.my (Zambri Harun)

* Corresponding author

INTRODUCTION

Wire bonding technology has been continuously developing since the 1960s. Many scholars have researched ultrasonic welding, and it is still a guided document

for ultrasonic bonding. Their theories are briefly summarized as follows: Harman and Albers (1977) studied Al-Al wedge bonding. The results showed that the bonding started at the periphery of the joint, and as the bond time increased, the effective bonding area gradually expanded toward the center and continued to increase until the entire interface. Sometimes, the center was not bonded, which was related to the wedge-shaped shape. Winchell and Berg (1978) studied the effect of bonding parameters on the bonding point formation process. It is concluded that as the ultrasonic power increases, the effective connection area increases; as the bonding time increases, the effective connection part expands to the central unbonded area; the bond point imprint area increases as the bonding force increases. Zhou et al. (2005) studied Au-Au ultrasonic wedge bonding. It was found that the metallurgical bonding started at both ends of the impression, and the center of the impression also achieved a metallurgical connection. The interface underwent shear deformation, micro-slip, and relative sliding. Since increasing pressure will reduce the connection area of the periphery and center, there is no necessary relationship between joint quality and deformation. Chen et al. (2006) conducted experiments on Al-Ni wedge bonding. The research reveals that the Al-Ni interface formed by ultrasonic bonding was the central unbonded and elliptical interface; refer to Figure 1 for the definitions of the central unbonded and elliptical interface. Previous works (Lum et al., 2005; 2006; Mindlin, 1949) studied the 25 μm diameter gold wire with copper substrate wedge bonding. The micro-slip theory concluded that when the ultrasonic power is small, there is only a micro-slip at the periphery of the bonding interface; when the ultrasonic power is enormous, a macro-slip will occur, and the entire interface will form a bond.

Li et al. (2006) studied the Al-1%Si wire bonded onto the Au/Ni/Cu pad. It was found that the wire was softened by ultrasonic vibration; at the same time, pressure was loaded on the wire, and plastic flow was generated in the bonding wire, which promoted the diffusion of Ni into Al. Ultrasonic vibration enhanced the interdiffusion resulting from inner defects

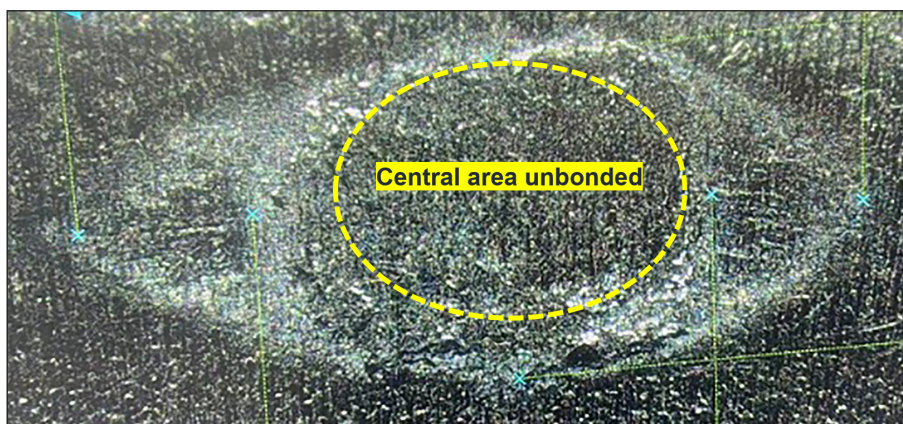


Figure 1. Morphology of the central unbonded area

such as dislocations, vacancies, and voids ascribed to short-circuit diffusion. Li et al. (2007a; 2007b; 2007c) conducted a thermosonic flip chip bonding test between Au bumps and Al and Ag metallization layers, and the results showed that the bonded joint contains several dislocation lines. They believe that a short-circuit diffusion along dislocation lines is the leading cause of interfacial bonding. Therefore, the dynamic effect of ultrasonic vibration is a microscopic joining mechanism that activates many dislocations in the metal lattice. Ji et al. (2005) studied Al-Ni-Cu bonding. It was found that there is an evident diffusion of Ni into Al wire after high-temperature storage at 170°C for 10 days. At age 30 days, the bond interface forms a cloud-like structure, and the primary composition is Al and Ni. At age 40 days, the cloud-like structure transforms into a rectangular island-like structure, and there are many cavities inside the bond wire, which are different from the Kirkendall voids because of the shape and dimension. Ji et al. (2006) It was found that lateral and longitudinal joint marks were observed. The former was perpendicular to the direction of the ultrasonic vibration and distributed at the periphery of the bond interface. However, the latter was parallel to the vibration directions located at the bond center. The features above had an essential influence on bond resistance. The mechanism was ascribed to stress evolution and distribution during the bonding process.

Bieliszczuk et al. (2024a) studied the impact of surface laser cleaning on the properties of the wire-bonded joint in a cylindrical lithium-ion battery pack. The results have shown that laser cleaning with 40% power of the 30 W ATMS4060 laser marker helps to reduce the standard deviation of the shear test results from 16.1% for the uncleaned sample down to 2.6%. Cleaning with 80% of the laser power did not further impact shear test results and almost eliminated oxides from the bonded materials interface. Hamada and Iwamoto (2023) observed the morphology and microstructure of the bond tool with Al adhesion and surface wear. It was found that Al adhered to the area where the vertical load on the bond tool was high during welding. Aluminum oxide and aluminum were present in layers in the adhered wire, indicating that the adhered wires grew due to repeated wire adhesion and destruction processes. Tool wear was related to fretting wear and plastic flow associated with wire deformation.

Researchers also have carried out a lot of research work on the following aspects: measuring the temperature change of the interface during the bonding process (Ho et al., 2004), measuring the vibration amplitude of the bonding tool, measuring the change of the ultrasonic loop signal (Qi et al., 2006), problems with the formation of Kirkendall holes accompanying the growth of intermetallic compound (Chang et al., 2004; Uno & Tatsumi, 2000). The results show that the evolution characteristics of the joint and the interface bonding characteristics are very complex, causing the results to be very divergent, and the microscopic effects of pressure and ultrasound on the bonding material cannot be distinguished. With the support of finite element simulations, fatigue behavior related to the material properties in the bonding wires was investigated (Czerny et al., 2013; Czerny

& Khatibi, 2016). Fatigue lifetime was found to be influenced by wire diameter, junction temperature swing, monitoring current, and aspect ratio of the wedge. The contact and displacement behavior between the wire and the substrate (Schemmel et al., 2018a; Unger et al., 2016;), friction (Long et al., 2020; Schemmel et al., 2018b;), dynamic behavior (Long et al., 2019), and deformation (Li et al., 2019; Tang et al., 2022). However, wire bonding is widely used in the battery industry (Bieliszczuk et al., 2024b; Zwicker et al., 2020). Studies on wedge bonding interface mechanisms and joint quality evaluation of cylindrical batteries are not widely available.

Wire Bonding Process Description

Automotive battery packs for electromobility consist of many interconnected battery cells. The research object of this paper is the 21700 cylindrical lithium battery modules. Here, 21 represents the diameter of the battery, and 70 represents the height of the battery. The cylindrical lithium battery steel shell is called a can (Fe-base Ni-top can), and the connection between the can and the busbar is called the anode bonding (negative terminal). The bonding wire uses aluminum material with a 0.5 mm diameter. The ultrasonic bonder used in this research is the K&S model, ultrasonic frequency 80 kHz. The wedge bonders are driven by constant voltage mode. Bonder “power” parameters correspond to a generator’s drive voltage. For large wires, at a max power of 255 (0–255, where 0 counts as 1), the drive voltage is 300 Vpp. The setting unit is level (approximately 1 level = 1.17 V when converted to unit). For example, power level = 100 for 0.5 mm diameter wire, the calculated drive voltage = $(100/256) \times 300 \text{ Vpp} = 117.18 \text{ Vpp}$.

Ultrasonic wedge bonding technology of Al wire is used to connect the positive terminal and negative terminal of the battery cells to each busbar, respectively, and then each busbar is connected to the flexible printed circuit board (FPCB) to form the required series-parallel relationship. The weak bond of the negative terminal is the primary failure phenomenon (Figure 2). The failure phenomena include the occurrence when the Al wire is separated from the bond interface and a large area unbonded in the central region of the bonding interface. The morphology of the central unbonded area is shown in Figure 1.

MATERIALS AND METHODS

The main approach of this investigation is to conduct interface morphology, perform finite element analysis (FEA), respond surface methodology (RSM) and test

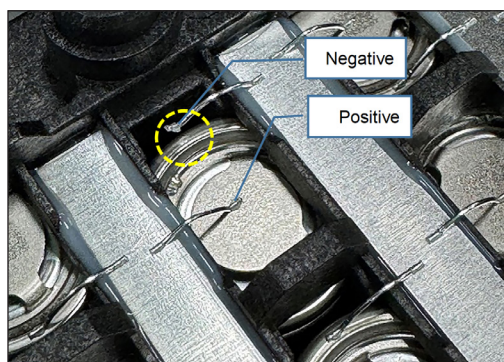


Figure 2. Cylindrical lithium battery module structure negative terminal weak bonded phenomenon

bonding strength on the wedge bonding of the negative terminal (Al wire and Fe-base Ni-plating can shell) in 21700 cylindrical lithium battery modules.

The effect of parameter changes on the central unbonded area of the joint is analyzed using intermetallic layer and vision analysis. The TEM samples were prepared by FIB (focused ion beam), and the bonding characteristics of the ultrasonic wedge-bonded joint interface were observed and analyzed under high-resolution transmission electron microscopy. The ion miller used is the Hitachi ArBlade 5000 model; it achieves ultra-high-speed cross-section grinding. ArBlade 5000 features PLUS II ion gun technology design, and the ion gun emits a high current density ion beam with a cross-section grinding rate of up to 1 mm/h. It uses a wide-area cross-section grinding sample holder with a cross-section grinding width of up to 8 mm. The ion milling system polishes the surface of a sample using the sputtering effect caused by irradiating an argon ion beam on the surface. Unlike mechanical polishing, the ion milling system processes the sample without deforming it or applying mechanical stress. The scanning electron microscope used is Hitachi SU8220, with a cold field electron gun, magnification: 20-1000000X, acceleration voltage: 0.01-30KV, and secondary electron image resolution (0.8nm/15kV). The test sample is based on the 21700-battery assembly process of a company in Nanjing, China, and is commissioned by a Korean institution and equipment for testing.

The finite element analysis (FEA) was used to further analyze the effect of parameter changes on the unbonded area in the center of the joint. The process model was first designed to simulate the deformation of Al wires. Then, the deformation and equivalent plastic strain of the ultrasonic wire bonding process was divided into three physical coupling processes. Firstly, the wire plastically deforms under the force of the tool. Secondly, the tool drives the wire to vibrate at a high frequency in the bonding area. Due to the high-speed friction between the wire and the pad, the oxide layer on the contact surface is fractured. Thirdly, under the effect of ultrasonic power, the wedge part of the wire continuously deforms, and atomic diffusion occurs on the contact interface, forming a stable bonding joint. The ultrasonic bonding process was converted into a numerical calculation process using FEA based on such analysis. The can shell material uses SPCC 0.4 mm thick steel plate as the base material and has a high Young's modulus; hence, a rigid body was used to simulate the mechanical behaviors of bonding. Here, SPCC stands for S-steel, P-plate, C-cold, and C-common. The can shell uses a pre-nickel-plating process. The thickness of the external nickel plating is 3 μm , and the internal nickel plating is 2 μm . The mesh build is essential to the simulation results. Specifically, fine mesh subdivides the areas of Al wires, while the rest of the regions are roughly meshed to accelerate the simulation process. Al wire is defined as a deformable part with an overall meshing size of 0.04 mm, whereas the bond tool and can are modeled as a rigid body with a meshing size of 0.05 mm. For the mesh of the model, a total number of 46167 nodes and 40408 elements. Abaqus software with an explicit solver was applied in this research. The specs of the PC are EX650i 239512-SCC.

The response surface methodology (RSM) was further used in process test verification. The DoE was performed using Minitab software. Shear strength and tensile tests were used to evaluate bonding qualities. A total of 42 normal cell samples with different production dates were randomly selected, and the anode surface was laser-cleaned before testing. There were 10 joints bonded on the anode surface of each cell and 30 joints bonded for each set of parameters, totaling 14 sets of parameters and 420 bonded joints. A digital display tensile tester is used to perform the tensile test. The tensile force is applied to a complete bonding loop, and the tensile force is applied to the highest point of the Al wire bonding loop. A shear strength test is performed using a digital thrust tester until the aluminum wire and the contact are completely separated from the bonding interface.

RESULTS AND DISCUSSION

Bonding Interface Morphology Analysis

Several failed samples were selected for microscopic observations to understand the ultrasonic wedge bonding interface joint characteristics. For the unbonded sample, no. 1 has a noticeable difference in the ratio of the joint and no ridges' vein-shaped elliptical rings (Figure 3a). There are obvious ridges' vein-shaped elliptical rings on the bonding interface of the weakly bonded samples no. 2–4, refer to Figures 3b–3d. The silvery white areas are bonded marks. The morphological characteristics of samples show a common

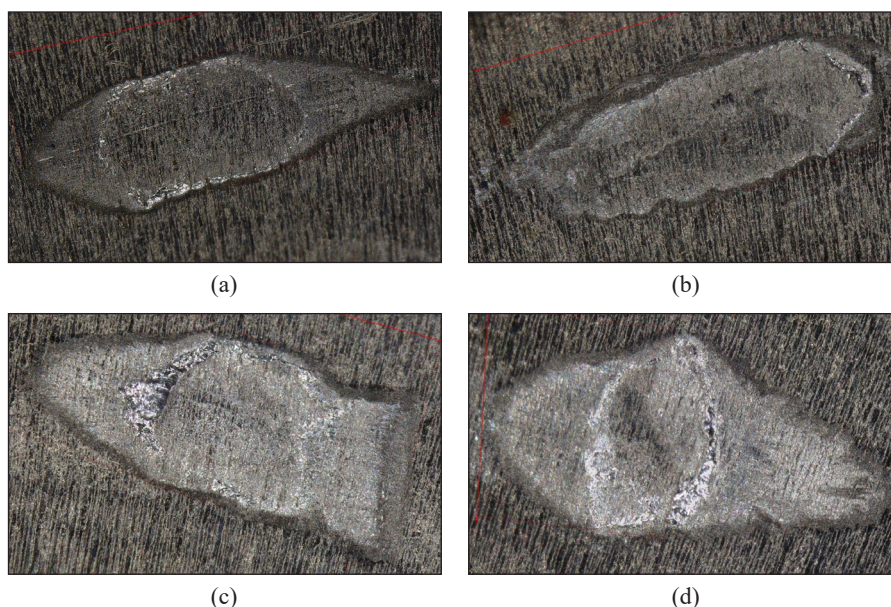


Figure 3. Morphology of weak bonded samples: (a) No. 1 unbonded; bond force 800 gf, bond time 130 ms, bond power 60; (b) No. 2 strength < 300 gf; bond force 1400 gf, bond time 130 ms, bond power 80; No. 3 strength < 800 gf; bond force 800 gf, bond time 130 ms, bond power 100; (d) No. 4 strength < 1500 gf; bond force 800 gf, bond time 130 ms, bond power 130

feature: the shape of the bonding joint is elliptical. Bonding starts from the periphery of the ellipse and gradually spreads to the central area. The effective bonding area is the ridges' vein-shaped elliptical rings, and the central area is not bonded. The aspect ratio and area of the unbonded area also vary significantly.

Figure 4 shows the cross-sectional morphology of another weakly bonded sample. Figure 4a is the normal bonded joint, and Figure 4b is the weak bonded joint. It shows that the distribution of the diffusion layer of Al atoms in the Ni substrate after bonding is significantly different. The diffusion layer of Al atoms at the weak bonding point is very thin and has a small area. The depth and location of the atomic diffusion layer at the bonding

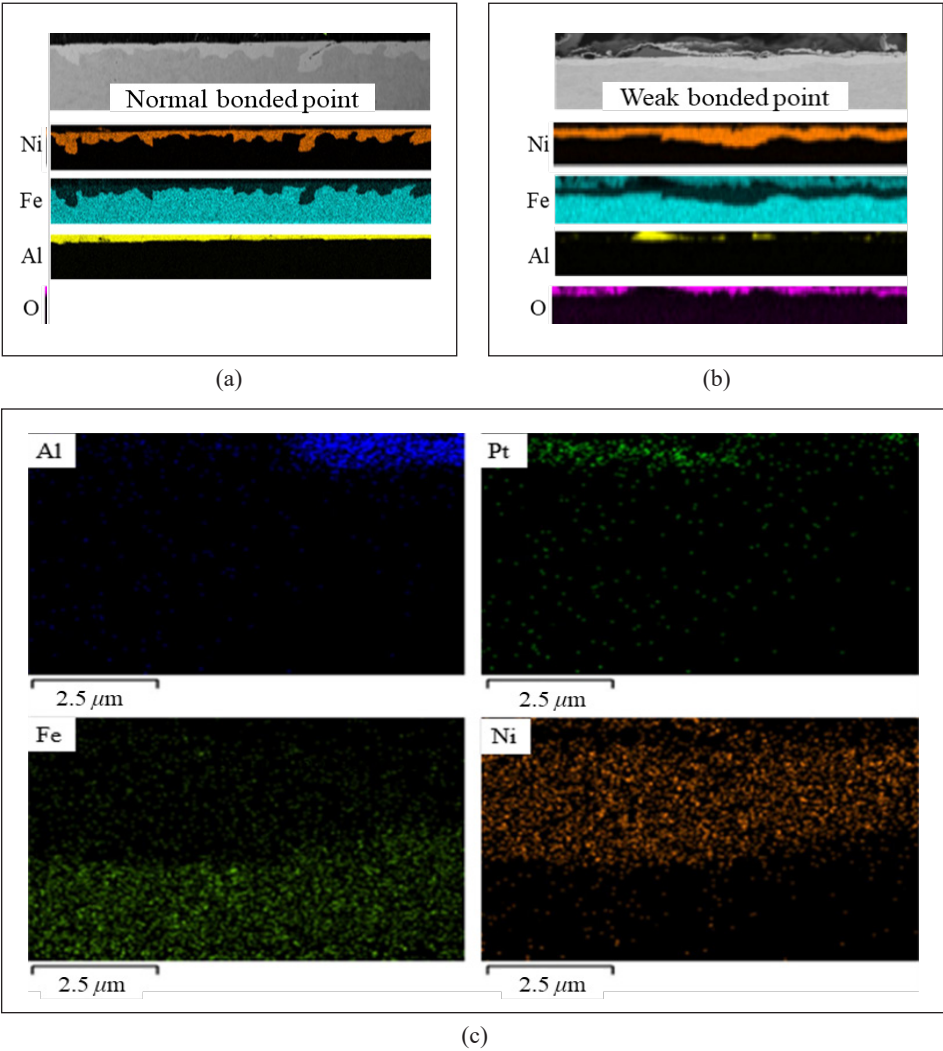


Figure 4. (a) Cross-section of normal bonded joint, (b) cross-section of weak bonded joint, (c) FIB result of weak bonded joint

interface characterize the bonding strength of the joint. The mutual diffusion of Al and Ni atoms produces a solid solution or alloy strengthening in dual material crystals. The bonding interface is a spatial multi-structure (i.e., Al wire-diffusion layer-base material).

At the weak bonding point, in addition to the Al and Ni coatings in a small area at the bonding interface, a large area of Fe and O was detected at the bonding interface. No elements other than Al and Ni were found at the bonding interface at the normal bonded point. Further, a FIB analysis of weakly bonded areas shows the distribution of aluminum, nickel, and iron at the interface in Figure 4c, and no other by-products were observed. However, the presence of the Pt element in the picture may be an element deposited during the FIB sample preparation process. The presence of Fe is suspected to be generated during ion milling.

Through the analysis of the morphological characteristics of the wire bonding interface of cylindrical lithium batteries, the results show that the interface mode of Al-Ni ultrasonic wedge bonding is shaped like a ridged torus, and the center area is unbounded. Ridge wrinkles are high-strength bonding formed by strong physical diffusion under the action of ultrasound. These ridge wrinkles form the bonding strength. So, one can understand the generation of bonding interface strength: the two substances at the bonding interface produce atomic interdiffusion, forming a strong atomic bond. The diffused atoms are solidly dissolved in the Ni matrix, which strengthens the interface microstructure strength, making the bonding interface strength generated by atomic diffusion greater than the strength of the Al wire. Therefore, only Al residues are seen on the separation interface; destruction does not occur in the atomic diffusion layer. It also shows that the interface has a depth range for atomic diffusion. At the same time, the bonding interface inevitably exists as an intermediate phase (compound). The mesophase generated and the impact on bonding quality require further analysis.

Bonding Interface Stress and Plastic Strain Analysis

Bonding parameters are also one of the main reasons for weak bonding. The stress and plastic strain distribution characteristics at the bonding interface in the ultrasonic bonding process and the influence of process parameters on the bonding quality were further analyzed. The major components, such as the bond tool, Al wires and the can, were modeled to focus on wire deformations. A geometric model was established, as shown in Figure 5a. The material of the bond tool was tungsten steel. Figure 5b shows the bond tool's geometry size. Figure 6 shows the stress-strain curve of the component (Al wire) that undergoes large plastic deformation during the simulation. The parameters of Al wire material at room temperature are shown in Table 1.

The ultrasonic vibration system controls the joint quality by adjusting the vibration of the bond tool. The value of ultrasonic power corresponds to sound intensity I . The math between them follows Equation 1.

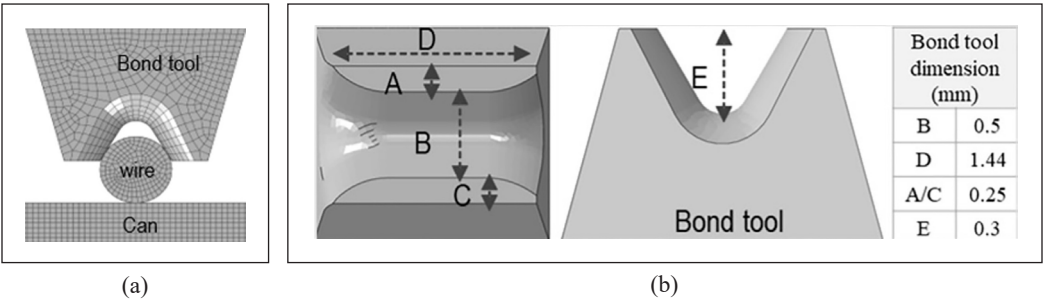


Figure 5. (a) Geometric model of bonding component; (b) Bond tool shape and key size

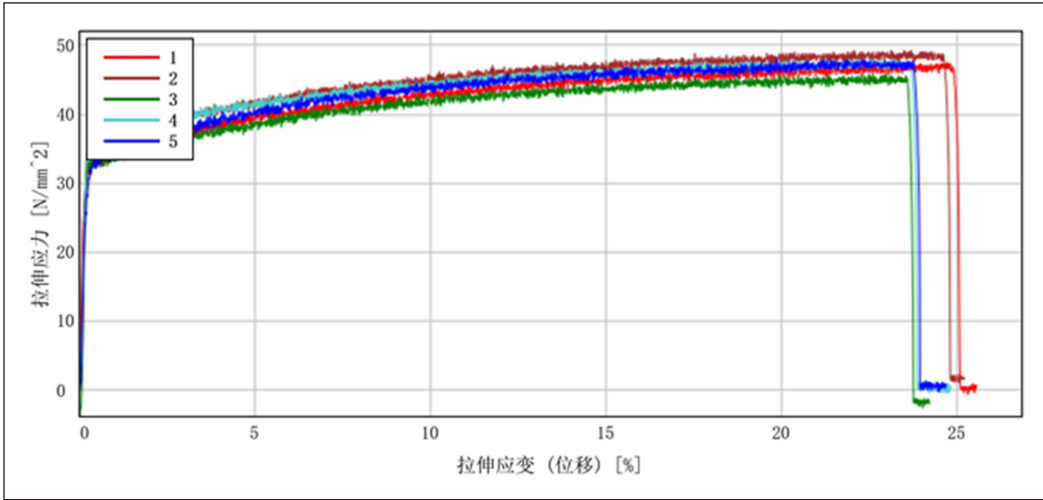


Figure 6. Stress-strain curve of Al wire

Table 1
Material parameters in the simulation model

Item	Material	Young's Modulus	Poisson' Ratio	Yield Stress
Al wire	Aluminum (Al 1050) (Diameter 0.5 mm)	64.2 GPa	0.33	49.5 MPa

$$I = 1/2\rho c\omega^2\xi^2$$
 [1]

Where ρ is the density of the material, c is the velocity of ultrasonic wave propagation, ω is the angular frequency, and ξ is the ultrasonic amplitude (Tang et al., 2022). As the ultrasonic amplitude increases, the ultrasonic energy increases exponentially in a square relationship. Therefore, in the design of the simulation, the adjustment of bond power is equivalent to the control of ultrasonic frequency and ultrasonic vibration amplitude.

The parameters that affect the morphology of bonding joints are bond force, bond power and bond time. In the simulation, the force load and displacement load were regarded as

equivalent factors. Hence, the simulation scheme of bond power is realized by loading the time-varying displacement behavior of the bonding tool. The displacement load was a time-dependent function, and its mathematical expression is shown in Equation 2.

$$X = A \sin (\omega t + \varphi)$$

[2]

Where A is the amplitude, ω is the angular velocity (circular frequency), f is the bonder frequency, $\omega = 2\pi f$. Stress loading $S1$ was implemented on the bond tool, which rose linearly until 30 ms and maximum to 50 N. Then, the curve of displacement load $S2$ is a sinusoidal curve with time, describing the ultrasonic action of the load on the bond tool. The sine function with a frequency of 80 kHz and an amplitude of 10 μm was set. It will be loaded on the bond tool from 0 ms. The operation time was 130 ms, with initiation parameters set in simulation models (Table 2). Substituting the parameters into the formula is $x=10^{-5} \times \sin (1.6\pi \times 105 \times 0.13)$. A total of 9 sets of parameters were simulated (Table 3).

The bond force and ultrasonic amplitude were changed in the simulation to be the variables affecting the bonding results to explore the correlation between ultrasonic bond quality and parameters. In this project, the analysis model focused on the mechanical movement of bond tools and their stress and plastic strain and did not simulate the connection during the vibration. The vibration amplitude parameters in the FEA simulation

Table 2
Initiation parameters setting in simulation models (take an amplitude of 10 μm as an example)

Bond time (ms)	Bond force (N)	Amplitude (μm)
0	35.5 (Touch force)	10 (Vibration start)
5 (start ramp time)	36.3 (Start force)	10
25 (Bond ramp time)	50 (Bond force)	10
100 (Bond hold time)	50	10 (Vibration end)

Table 3
Bonding parameters setting in simulation models

Groups	Bond time (ms)	Bond force (N)	Amplitude (μm)
1	1 \times time (130)	50	10
2	1 \times time (130)	70	10
3	1 \times time (130)	100	10
4	1 \times time (130)	50	10
5	1 \times time (130)	50	20
6	1 \times time (130)	50	30
7	1 \times time (130)	50	10
8	2 \times time (260)	50	10
9	3 \times time (390)	50	10

do not match those in the real world. Hence, this research simulates other cases of higher bond force, which could show real-world situations.

The simulation results of deformation and stress can be used to evaluate the stress and mechanical behaviors of Al wire. Figure 7 shows that region (A) of the bond tool is not contacted with the wire, and region (B) of the bond tool is only contacted with the Al wire. The deformation is generated mainly in the region (D) compared to the region (C). We use letters in parenthesis, i.e., (), to define the different regions.

Refer to Figures 8a–8c for the deformation and stress simulation result. With the increase of ultrasonic amplitude and bond force, the deformation of the Al wire was intensified, and more stress was concentrated in the bottom of the Al wire. In the same group, the bond force has a more significant effect on the deformation

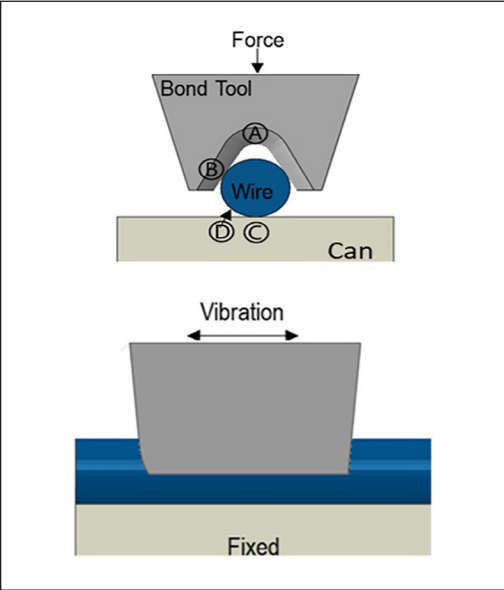
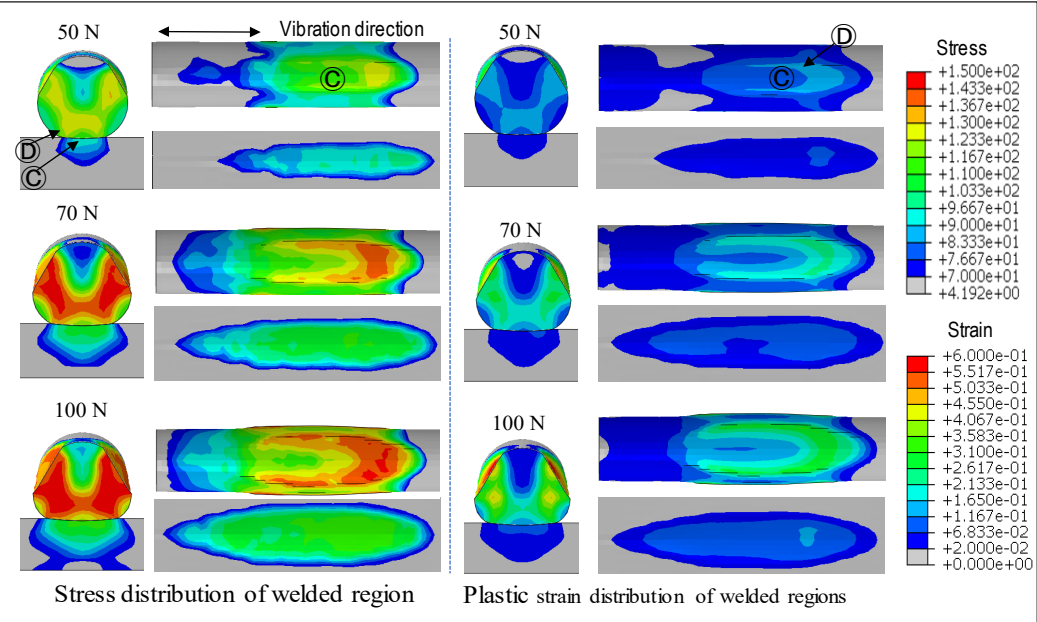
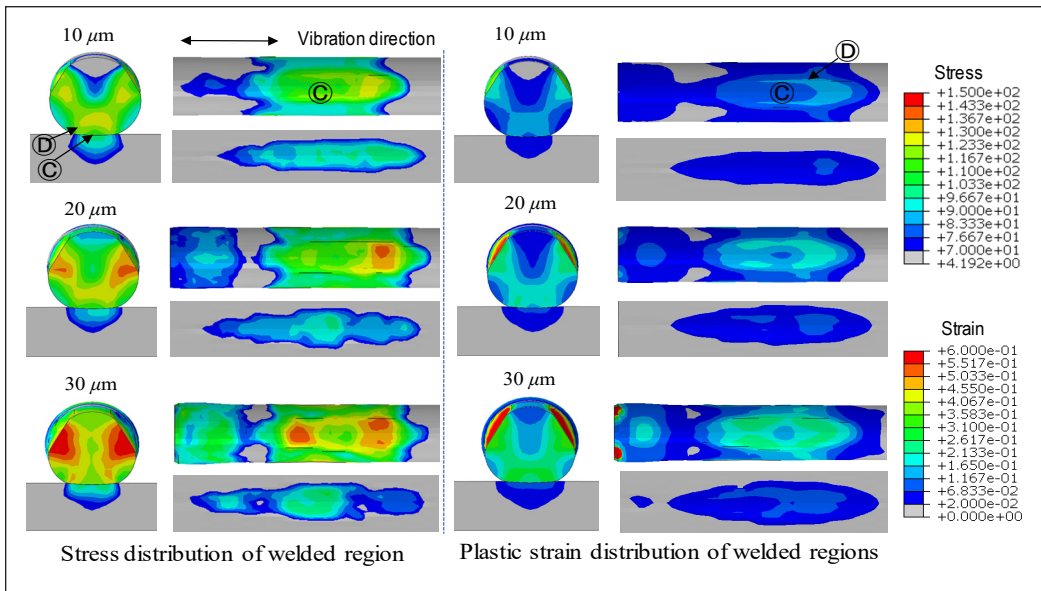


Figure 7. Schematic diagram of stress and strain distribution in different areas of the bonded component

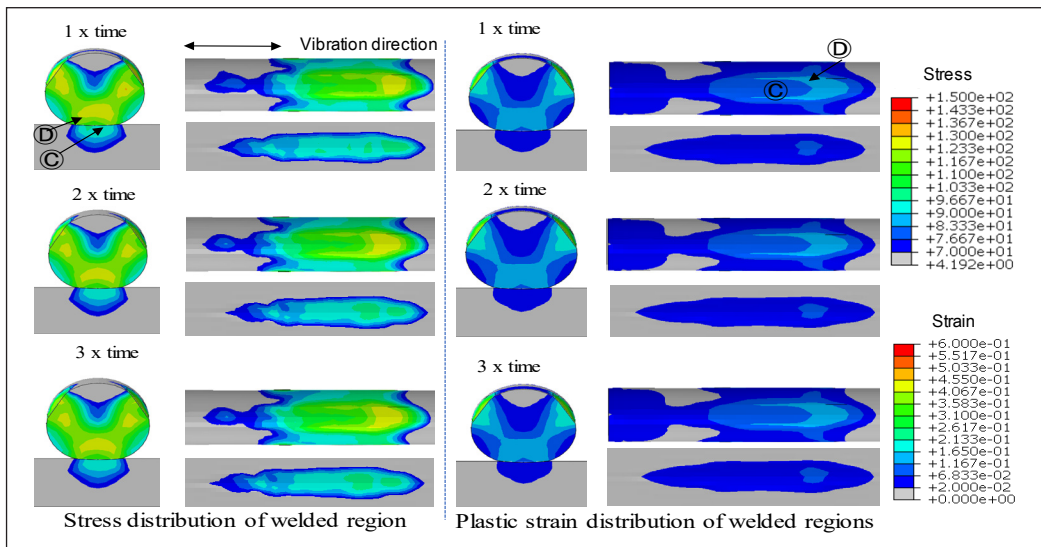


(a)

Figure 8. Simulation result under different parameters: (a) effect by bond force



(b)



(c)

Figure 8 (continue). Simulation result under different parameters: (b) effect by bond power; (c) effect by bond time

of the Al wire than the ultrasonic amplitude. Amplitude has a more significant effect on reducing the unbonded area in the center of the joint than the bond force. The maximum stress region corresponds to the bonding interface's elliptical vital ridge area. The correlation of the three parameters is as follows: First, the effect of bond force on Al wire deformation: High bond force increased the bonding area perpendicular to the wire

direction and increased stress and plastic strain levels on the bonding interface. Despite the increased bond force, region (C) remained at a lower level of stress and plastic strain compared to the surrounding area (D). Second, the effect of ultrasonic amplitudes on Al wire deformation: Due to the increased vibration amplitude of the bonding tool, the increased stress concentration occurred at the fixed end of the wire and near both endpoints. The increased amplitude condition mainly increased stress and plastic strain at the circumference region (D), compared to the stress/plastic strain at the center region (C). Third, the effect of bond time on Al wire deformation: The stress and plastic strain distributions in the bonding area do not continue to change with increasing bond time because 0.135 s is sufficient to balance the forces.

Effect of Parameter Changes on the Central Unbonded Area of the Joint

Phase I testing aims to verify the effect of bonding parameters on the unbonded area in the center of the bond interface. We performed bonding by reducing the parameter level so that we could obtain a complete bonding interface after Al wire peeling. Bond force level settings were 800 gf and 1400 gf, bond power level settings were 80 and 130, bond time settings were 100 and 160 ms, and the center point was set. A total of 27 normal cell samples with different production dates were randomly selected, and the anode surface was laser-cleaned before testing to verify the effects of bonding pressure, bonding power, and bonding time on the bonding interface morphology. There were 10 joints bonded on the anode surface of each cell and 30 joints bonded for each set of parameters, totaling 9 sets of parameters and 270 bonded joints. The results showed that the bonding interface morphology of the 30 joints was similar under the same parameter conditions. The bonding interface morphology under different parameter conditions was significantly different. A typical joint was selected for each set of parameters to observe the interface morphology under a microscope, as shown in Figure 9.

Figures 9a–9c show the interface characteristics of the bonding interface as the ultrasonic power changes. Under low bond force, only the edge of the interface is well connected, and the effective connection area is minimal. The center of the interface is not bonded. As the bonding force increases, the outline of the joint gradually expands inward. The bonding mark gradually expands toward the center, and the effective bonding area increases, but not significantly.

Figures 9d–9f show the characteristics of the bonding interface as the ultrasonic power changes. As the ultrasonic power increases, the bond mark gradually expands inward and develops from an ellipse to a circle, and the aspect ratio decreases. Under lower power, only the edge area of the interface is well connected, and the effective connection area is tiny. When the ultrasonic power increases, the unbonded area in the center area gradually decreases, and the overall effective connection area of the interface increases. Compared

with the increase in bond force, as the ultrasonic power increases, the bond mark expands more obviously to the center region, and the strong ridges' vein-shaped elliptical rings formed are more prominent.

Figures 9g–9i show the characteristics of the bonding interface as the bond time changes. Under lower power, even as the bond time increases, the bond mark gradually expands inward, which is not obvious.

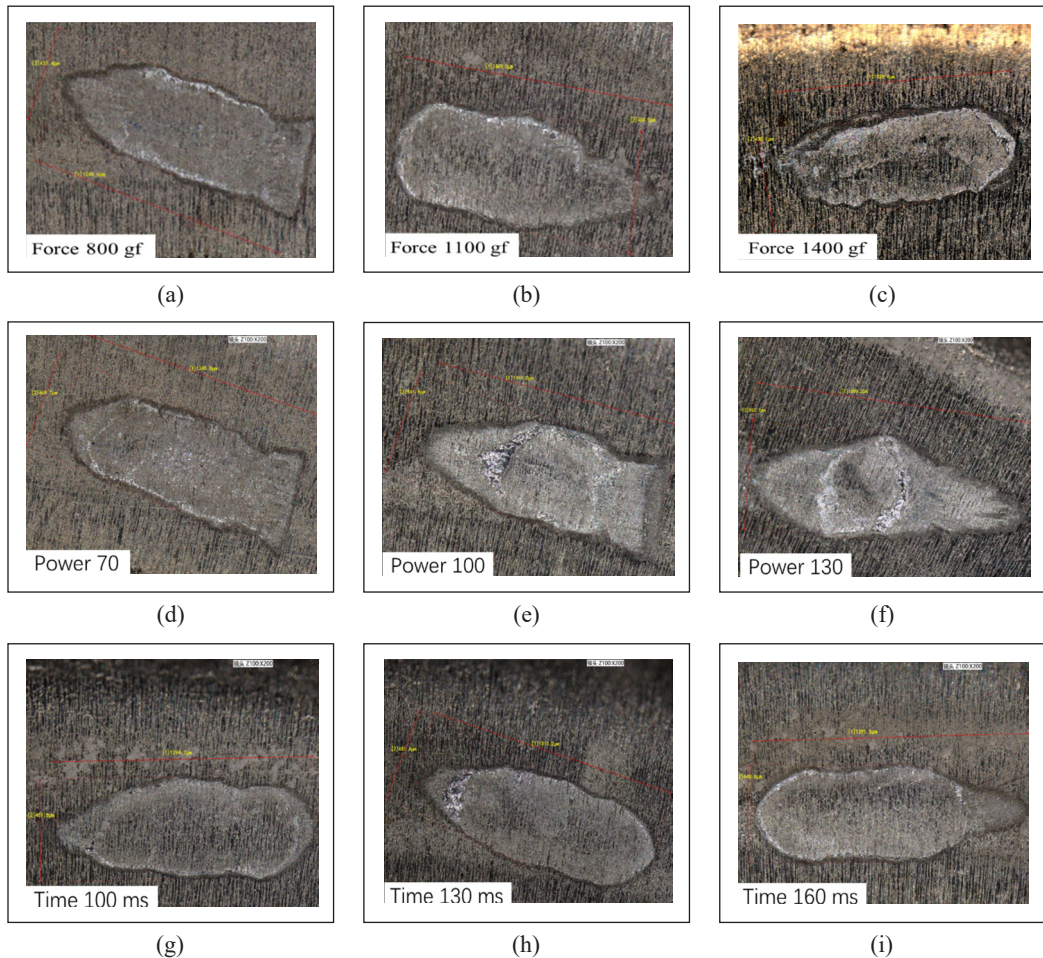


Figure 9. Effect of parameter changes on the central unbonded area of the joint: (a)–(c) Fixed: bond power: 80, bond time: 130 ms, bond force was increased; (d)–(f) Fixed: bond force 800 gf, bond time 130 ms, bond power was increased; (g)–(i) Fixed: bond force: 800 gf, bond power: 80, bond time was increased

Response Surface Methodology (RSM)

The response surface methodology (RSM) was further used in phase II. Shear strength and tensile tests were used to evaluate bonding qualities. The regression equations of aluminum wire deformation and joint width corresponding to key parameters were established.

The optimal range of Al wires deformation and joint width in lithium battery negative ultrasonic bonding is proposed. The response optimizer obtains the optimal values of bonding parameters. However, the shear strength result cannot be used as the only response to determine the parameter range because there are two failure modes in the wire bonding process. One is the contact detachment, and the corresponding minimum parameter range is obtained through shear strength. The second is neck fracture; the necking part between the joint and the Al wire is broken during the tension process, but the bonding interface maintains good connectivity. Therefore, a tensile test is required. If the bonding strength is excellent, the tensile test only shows that the Al wire breaks at the highest point of the bond loop; its fracture strength is the ultimate fracture strength of the Al wire. The data consistency is excellent. Therefore, using the tensile force as the response, the model will not fit. Hence, the maximum parameter value corresponding to the occurrence of necking fracture is obtained by testing the single variable multi-level conditions. After completing the above 2 steps, we can obtain the available parameter range through the parameter values corresponding to joint shedding and the parameter values corresponding to necking fracture.

Considering the influence of factor number and factor level number on DoE experiment number. Bond force level settings were 800 gf and 1700 gf, and bond power level settings were 80 and 130. A total of 42 normal cell samples with different production dates were randomly selected, and the anode surface was laser-cleaned before testing. There were 10 joints bonded on the anode surface of each cell and 30 joints bonded for each set of parameters, totaling 14 sets of parameters and 420 bonded joints. The standard deviation was calculated for 30 values for each set of parameters. Notice that the bond power in a bonder was dimensionless values.

The FEA simulation results confirmed that the stress and plastic strain distributions in the bonding area do not continue to change with increasing bond time because 0.135 s is sufficient to balance the bond force. So, the effect of bond time on bonding quality is no longer considered separately. The bond time is fixed at 0.135 s.

According to the analysis in Table 4, within the range of process parameters in this experiment, when the bond force was 800 gf and bond power was 80, the mean value of shear strength was 2.25 kgf. The minimum shear strength value of the abnormal point is less than 1.5 kgf (Figure 10). Therefore, it does not meet the process capability control requirement of more than 1.5 kgf. It can be concluded that when the bond force is lower than 800 gf and the bond power is lower than 80, the risk of the Al wire falling off from the bonding interface is higher. When the bond force was 1250 gf and bond power was 105, the samples' shear strength performed well, and the shear strength value was centralized. When the bond force was 1700 gf, the corresponding sample bore a large shear strength. However, the shear strength fluctuated greatly. When the bond force was 1700 gf and bond power was 130, the shear strength showed a clear downward trend.

Table 4
Experimental result of shear strength

Std. Order	Run Order	Point Type	Blocks	Bond force (gf)	Bond power	Shear strength (Kgf)	Std. Deviation
1	2	0	2	1250	105	5.172	0.212
2	4	0	2	1250	105	4.932	0.315
3	7	0	2	1250	105	4.684	0.285
4	8	1	1	1700	80	4.157	0.261
5	9	1	1	800	80	2.250	0.229
6	10	0	1	1250	105	4.983	0.293
7	11	1	1	800	130	4.182	0.274
8	12	0	1	1250	105	4.681	0.256
9	13	1	1	1700	130	3.818	0.443
10	14	0	1	1250	105	4.602	0.277
11	1	-1	2	800	105	4.078	0.163
12	3	-1	2	1250	80	3.173	0.161
13	5	-1	2	1250	130	4.575	0.324
14	6	-1	2	1700	105	4.915	0.253

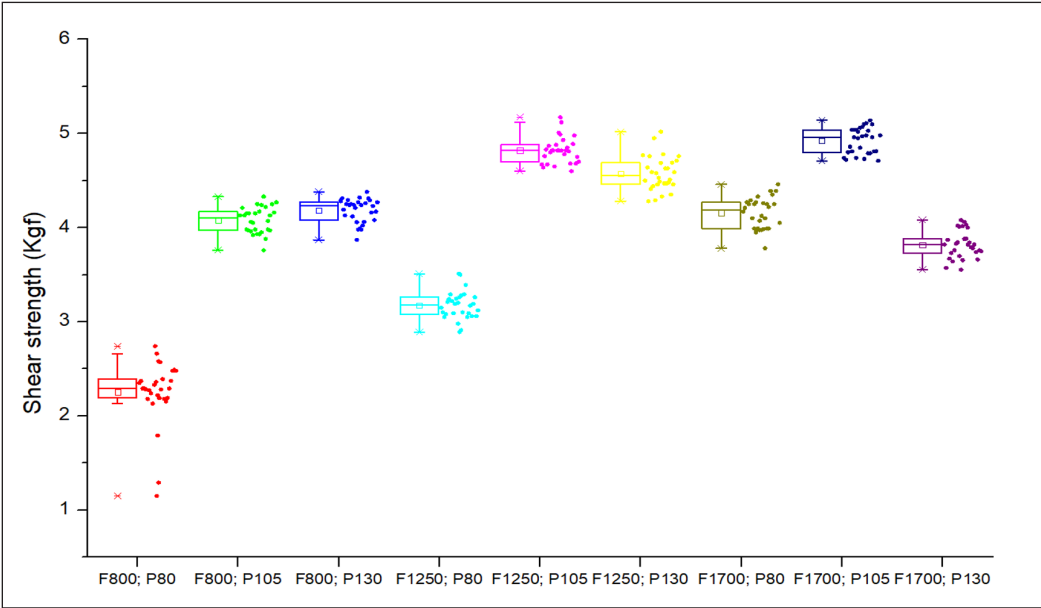


Figure 10. Box plot of shear strength under different parameters

Table 5 and Figure 11 show that bond power had a more significant impact on the width of bonding joint forming than bond force. Table 6 shows that bond force had a more substantial effect on the deformation amount (i.e., Z-axis displacement of the bond tool) of bonding joint forming than bond power. From the standard deviation distribution, the more

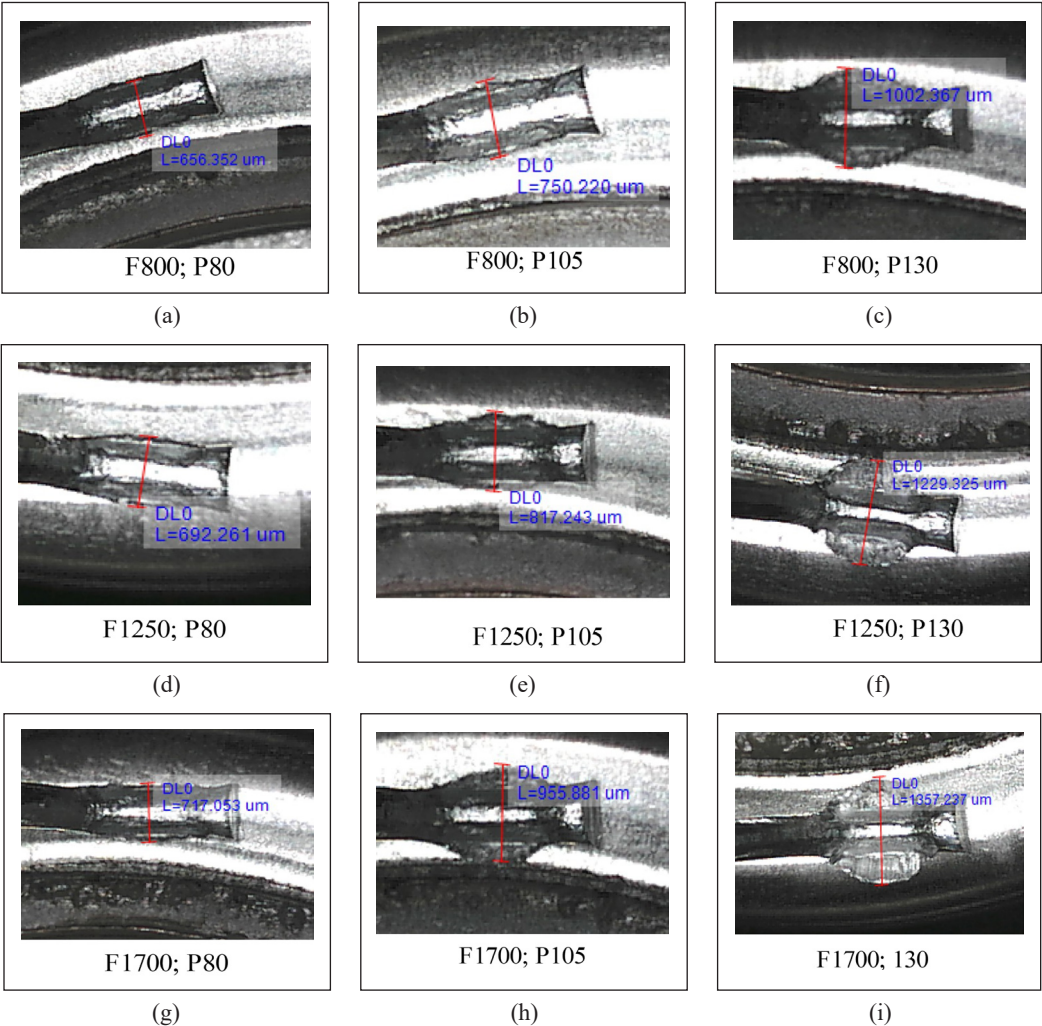


Figure 11. Joint width profile under different parameters: (a)–(c) Fixed: bond force: 800, bond power was increased; (d)–(f) Fixed: bond force 1250 gf, bond power was increased; (g)–(i) Fixed: bond force: 1700 gf, bond power was increased

significant standard deviation means that it was more challenging to control the stability and bonding accuracy of the results.

The failed samples with shear strength lower than 1.5 kgf were analyzed separately, and it was found that the reasons for failure were different. Can surface contamination caused by residual F components in the electrolyte is one of the main reasons? The x-ray photoelectron spectroscopy (XPS) analysis result showed that NiO, NiF₂, and Ni (OH)₂ are confirmed on the can surface. The flatness exceeds the specification of the canned surface (R angle size), which are other factors that influence it. The failure caused by these noise factors should not be confused with the failure caused by unreasonable parameters.

Table 5
Experimental result of joint width

Std. Order	Run Order	Point Type	Blocks	Bond force (gf)	Bond power	Joint width (μm)	Std. Deviation
1	2	0	2	1250	105	809.426	20.14
2	4	0	2	1250	105	824.742	22.11
3	7	0	2	1250	105	797.215	22.31
4	8	1	1	1700	80	727.895	18.34
5	9	1	1	800	80	659.812	15.44
6	10	0	1	1250	105	806.380	21.63
7	11	1	1	800	130	1102.264	29.94
8	12	0	1	1250	105	805.674	20.15
9	13	1	1	1700	130	1445.003	29.26
10	14	0	1	1250	105	793.673	20.13
11	1	-1	2	800	105	778.068	29.048
12	3	-1	2	1250	80	682.397	18.17
13	5	-1	2	1250	130	1273.353	22.46
14	6	-1	2	1700	105	945.726	19.44

Table 6
Experimental result of deformation amount

Std. Order	Run Order	Point Type	Blocks	Bond force (gf)	Bond power	Deformation amount (μm)	Std. Deviation
1	2	0	2	1250	105	206.645	11.18
2	4	0	2	1250	105	202.250	11.25
3	7	0	2	1250	105	208.272	11.95
4	8	1	1	1700	80	216.600	12.04
5	9	1	1	800	80	162.500	10.60
6	10	0	1	1250	105	199.520	10.63
7	11	1	1	800	130	202.500	12.51
8	12	0	1	1250	105	200.400	11.56
9	13	1	1	1700	130	262.700	13.26
10	14	0	1	1250	105	202.520	9.26
11	1	-1	2	800	105	179.485	9.05
12	3	-1	2	1250	80	187.340	12.17
13	5	-1	2	1250	130	227.500	11.65
14	6	-1	2	1700	105	238.500	12.44

Tensile Testing

In this phase, the purpose of the tensile test is to exclude abnormal joints of bonding strength less than Al wire fracture strength; it can also exclude abnormal joints of neck fracture and then obtain the minimum parameter range of the bonded joint neck fracture. In the tensile

test, two main failure modes were neck fracture and Al wire overall or party fall off. The overall and partial detachment of joints indicates that the bonding interface is weakly bonded, and the joints with neck fractures suggest that the aluminum wire at the root of the joint is abnormally deformed. Still, the bonding strength of the bonding interface is good.

The automatic pulling force and over-travel distance must be set to reasonable parameters to enable inspection without damaging the Al wire. Automatic pulling inspection is applied to a single bonding point and only detects bonding points with bonding strength less than 0.60 kgf.

A manual tensile test is suitable for sampling checks. It is on a complete bonding loop, and the pulling force is used at the highest point of the Al wire bond loop. The maximum breaking strength of the Al wire loop at the highest point between two bonding points is about 76 N/mm², which is approximately equal to 1.52 kgf (i.e., 0.1963 mm² × 76 N/mm² = 14.9 N = 1.52 kgf). For this reason, to ensure that the bonding strength is greater than the breaking strength of the Al wire, the tensile strength requirement for bonded joints is greater than 1.5 kgf when performing a tensile test on a complete bond loop.

The tensile test result is shown in Table 7. High bond force and high bond power significantly influenced the neck fracture. The neck fracture occurred when the bond force was 1600 gf and the bond power was 130. However, the bonded joint fall-off occurred at bonder force was 900 gf and bond power less than 90. The fractures occurred at the highest point of the bond loop for the sample group without neck fracture. Due to the consistency of the Al wire in the experiment, the data fluctuates slightly. For the sample group with good bonding strength, the tensile force at the highest point of the bond loop ranges from 1212 gf to 1520 gf. This is consistent with the breaking strength limit of the Al wire in Figure 6.

Table 7
Experimental result of tensile test (unit: gf)

Force	Power						
	80	90	100	110	120	125	130
800	Fall off <1.5 kgf	Fall off <1.5 kgf	1489	1391	1406	1511	1360
900	Fall off <1.5 kgf	1214	1299	1313	1303	1216	1215
1000	1365	1329	1414	1516	1520	1312	1424
1100	1264	1505	1326	1412	1328	1254	1261
1200	1412	1413	1382	1501	1411	1324	1311
1300	1386	1274	1471	1428	1375	1263	1287
1400	1352	1342	1335	1314	1520	1314	1345
1500	1326	1426	1420	1323	1431	1321	1376
1600	1245	1283	1338	1314	1302	1151	Neck fracture
1700	1212	1312	1325	1227	1158	Neck fracture	Neck fracture

Typical Joint Analysis

The morphological characteristics of the joint show that the shape of the bonding joint is elliptical. Bonding starts from the periphery of the ellipse and gradually spreads to the central area. The effective bonding area is the ridges' vein-shaped elliptical rings, and the central area is not bonded. The aspect ratio of the unbonded area of each sample also varies significantly.

Furthermore, under the difference parameter condition, the interface characteristics of the joint vary significantly. Under low bond force, only the edge of the interface is well connected, and the effective connection area is minimal. As the bonding force increases, the outline of the joint gradually expands inward. The bonding mark gradually expands toward the center, and the effective bonding area increases, but not significantly. As the ultrasonic power increases, the bond mark gradually expands inward and develops from an ellipse to a circle, and the aspect ratio decreases. Under lower power, only the edge area of the interface is well connected, and the effective connection area is tiny. When the ultrasonic power increases, the unbonded area in the center area gradually decreases, and the overall effective connection area of the interface increases. Compared with the increase in bond force, as the ultrasonic power increases, the bond mark expands more obviously to the center region, and the strong ridges' vein-shaped elliptical rings formed are more prominent. In contrast, under lower power and low bond force, even as the bond time increases, the bond mark expansion inward is not obvious.

Simulation Prediction and Process Test Verification

The stress and plastic strain simulation results show that the increase in bond force and amplitude generated a large deformation and increased stress/plastic strain level. Despite the rise in the bond force and amplitude, the stress/plastic strain at the center region (C) is lower than that in the circumference region (D). The stress and plastic strain distributions in the bonding area do not continue to change with increasing bonding time because 0.135 s is sufficient to balance the forces. The maximum stress region corresponds to the bonding interface's elliptical vital ridge area. The stress distribution feature offers some explanations of the central region pattern. Due to the increased vibration amplitude of the bonding tool, the increased stress concentration occurred at the fixed end of the Al wire and near both endpoints. The increase in the amplitude has a more significant effect on the diffusion of the elliptical vital ridge toward the central area.

Based on the DoE implemented in phase I, the unbonded area in the center region of joints can be limitedly reduced by optimizing significant parameters. The influencing parameters in the most to least critical order are bond power, bond force, and bond time. Based on the RSM analysis result in phase II, bond power had a more significant impact on the width of joint forming than bond force. The bond force had a more substantial effect on the deformation amount (i.e., Z-axis displacement of the bond tool) of bonding

joint forming than bond power. According to the failure mode in tensile test results, the range of bond force is at least greater than or equal to 900 gf and cannot exceed 1700 gf. The bond power is at least greater than or equal to 90 and cannot exceed 120. The optimal shear strength distribution is in the range of 3.5 kgf to 4.75 kgf after combining the optimal parameter range obtained from the shear strength and tensile tests and the results of the contour plot (Figure 12a). Therefore, the response optimizer sets the shear strength target value to 4.75 kgf. So far, the optimal parameter values are bond force 1250 gf and bond power 100, as shown in Figure 12b. The bonding joint and process parameters regression equation was derived from the deformation data, as shown in Equation 3.

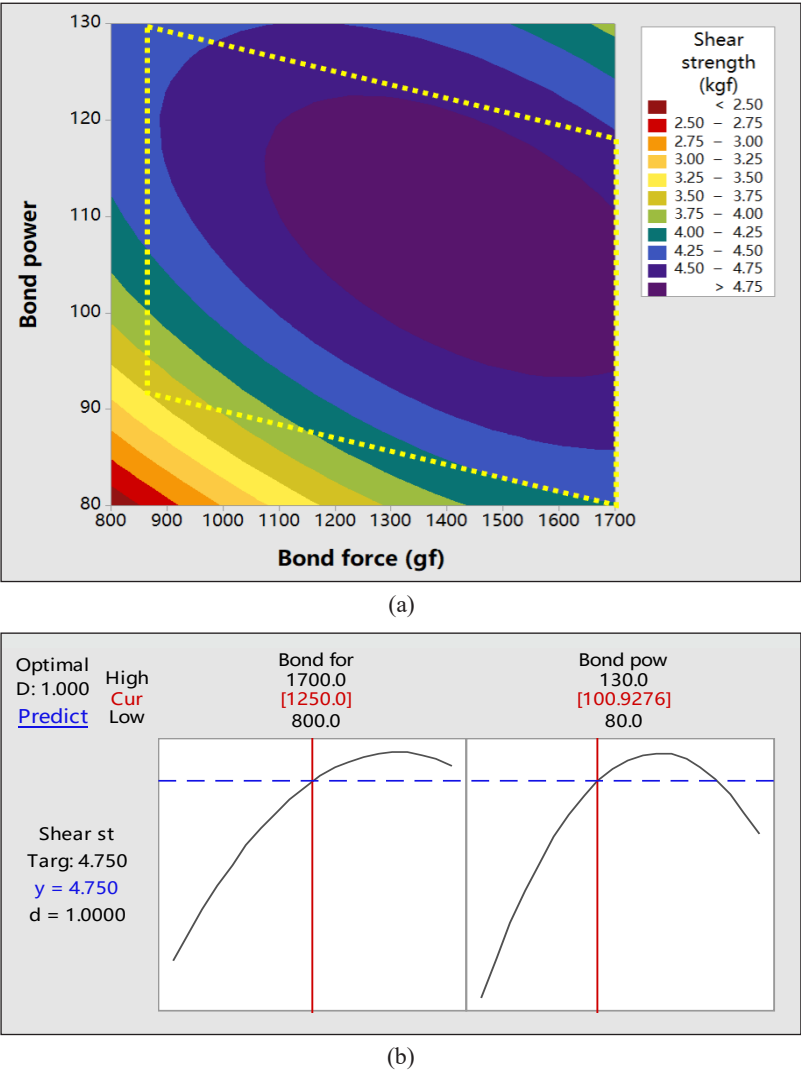


Figure 12. (a) Contour plot of shear strength vs bond power, bond force; (b) The optimal parameters obtained by the response optimizer

$$D_e = 118.3 + 0.0154F_e - 0.063P_e + 0.000022 F_e^2 + 0.0045 P_e^2 - 0.000087 F_eP_e \quad [3]$$

D_e represents the deformation of the bonding joint, F_e represents the actual bond force, and P_e represents the bond power of the bonding machine. The minimum value in this region was $174 \mu\text{m}$, and the maximum value was $248 \mu\text{m}$. The bonding joint and process parameters regression equation was derived from the joint width data, as shown in Equation 4.

$$W_e = 3005 - 0.802 F_e - 48.51 P_e + 0.000153 F_e^2 + 0.2502 P_e^2 + 0.006103 F_eP_e \quad [4]$$

W_e represent the width of the bonding joint. The minimum value of the width was $560 \mu\text{m}$, and the maximum value of the width was $1110 \mu\text{m}$.

In the actual application, the bonding parameters are set to the optimal values of the bond force of 1250 gf and bond power of 100, dramatically reducing the unbonded area in the center region of joints. The morphology of the bonding interface is shown in Figure 13.

The DoE results proved that bond power and force positively affected the bonding joint's reliability in a specific range. However, they will cause an opposite result outside the range, such as a neck fracture or unbonded.

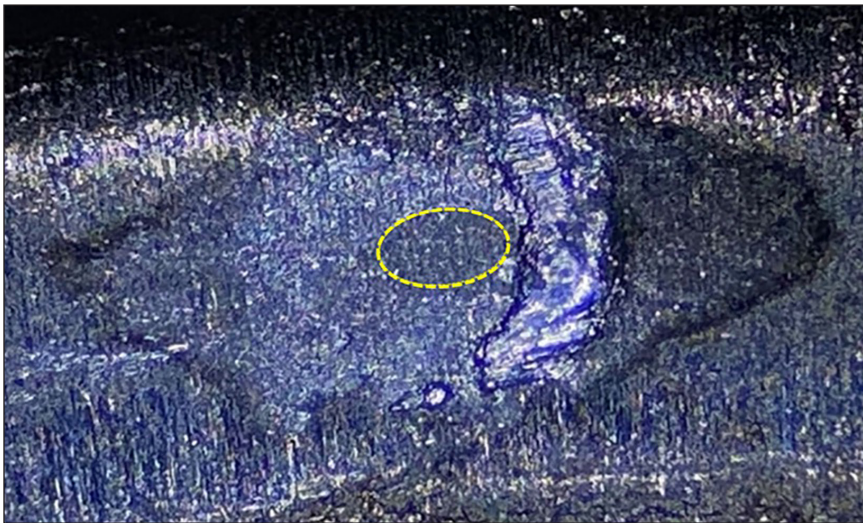


Figure 13. The morphology of the bonding interface under optimal parameter (F: 1250 gf; P: 100)

CONCLUSION

This paper demonstrates that combined experimental and simulation methods can determine the most important wire bonding parameter of the negative terminal (Al wire and Fe-base Ni-top can shell) in 21700 cylindrical lithium battery modules. The effect of parameter changes on the central unbonded area of the joint is analyzed using intermetallic layer and visual analysis. The reasons for the poor bonding performance of the central area of the

joint through stress and strain simulation. The results show that the interface mode of Al-Ni ultrasonic wedge bonding is shaped like a ridged torus, and the center area is unbounded. Ridge wrinkles are high-strength bonding formed by strong physical diffusion under the action of ultrasound. These ridge wrinkles form the bonding strength. Second, the stress at the center region (C) is lower than that in the circumference region (D), and the high-stress region corresponds to the elliptical shape strong ridge area of the bonding interface (i.e., the effective bonding area). Third, optimizing parameters can limit the unbonded area in the center region of joints, and the influencing parameters in the order of most to least significant are bond power, bond force, and bond time. iv. the best shear strength range is 3.5 kgf to 4.75 kgf, and the optimal range of the Al wire deformation amount was 174 μm to 248 μm . The optimal range of joint width was 560 μm to 1110 μm . v. the best parameter range is bond force 900 gf to 1700 gf and bond power 90 to 120. Within this range, no joint fall-off and necking fracture will occur. The simulation and DoE results above provided a new feasible scheme for rapidly finding the optimal process parameters in the bonding process.

ACKNOWLEDGMENT

We would like to thank the company for the detailed experimentation and simulations that were held and the test platform provided. We thank Gilsang Son for providing technical support. We would also like to express our gratitude for UKM grant GUP-2024-058.

REFERENCES

- Bieliszczuk, K., Chmielewski, T. M., & Zręda, J. (2024a). Selected properties of aluminum ultrasonic wire bonded joints with nickel-plated steel substrate for 18650 cylindrical cells. *Journal of Advanced Joining Processes*, 9, Article 100197 <https://doi.org/10.1016/j.jajp.2024.100197>
- Bieliszczuk, K., Chmielewski, T. M., & Zręda, J. (2024b). Influence of cylindrical cells surface cleaning by means of laser ablation on wedge wire bonding process. *Coatings*, 14(4), Article 445.
- Chang, H. S., Hsieh, K. C., Martens, T., & Yang, A. (2004). Wire bond void formation during high-temperature aging. *IEEE Transactions on Components and Packaging Technologies*, 27(1), 155–160. <https://doi.org/10.1109/TCAPT.2004.825752>
- Chen, X., Zhong, Z., & Li, J. (2006). Analysis on characteristics of input power and interface wedge bonding of Al-Ni ultrasonic aluminum wedge bonds. *Material Science and Technology*, 14(4), 416–419.
- Czerny, B., & Khatibi, G. (2016). Interface reliability and lifetime prediction of heavy aluminum wire bonds. *Microelectronics Reliability*, 58, 65–72. <https://doi.org/10.1016/j.microrel.2015.11.028>
- Czerny, B., Khatibi, G., Paul, I., & Thoben, M. (2013). Influence of wirebond shape on its lifetime with application to frame connections. In *2013 14th International Conference on Thermal, Mechanical and Multi-Physics Simulation and Experiments in Microelectronics and Microsystems (EuroSimE)* (pp. 1-5). IEEE Publishing. <https://doi.org/10.1109/EuroSimE.2013.6529909>

- Hamada, K., & Iwamoto, C. (2023). Morphology and microstructure observation of cemented carbide tool with surface wear and Al adhesion for Al wedge wire bonding. *Journal of Light Metal Welding*, 61(10), 492–499. <https://doi.org/10.11283/jlwa.61.492>
- Harman, G. G., & Albers, J. (1977). The ultrasonic welding mechanism as applied to aluminum and gold-wire bonding in microelectronics. *IEEE Transactions on Parts, Hybrids, and Packaging*, 13(4), 406–412. <https://doi.org/10.1109/TPHP.1977.1135225>
- Ho, J., Chen, C., & Wang, C. (2004). Thin film thermal sensor for real time measurement of contact temperature during ultrasonic wire bonding process. *Sensors & Actuators: A. Physical*, 111(2), 188–195. <https://doi.org/10.1016/j.sna.2003.10.018>
- Ji, H., Li, M., & Wang, C. (2006). Interfacial characterization and bonding mechanism of ultrasonic wedge bonding. In *2006 7th International Conference on Electronic Packaging Technology* (pp. 1-5). IEEE Publishing. <https://doi.org/10.1109/ICEPT.2006.359760>
- Ji, H., Li, M., Kung, A. T., Wang, C., & Li, D. (2005). The diffusion of Ni into Al wire at the interface of ultrasonic wire bond during high-temperature storage. In *2005 6th International Conference on Electronic Packaging Technology* (pp. 377-381). IEEE Publishing. <https://doi.org/10.1109/ICEPT.2005.1564652>
- Li, J., Han, L., Duan, J., & Zhong, J. (2007a). Microstructural characteristics of Au/Al bonded interfaces. *Material Characterization*, 58(2), 103-107. <https://doi.org/10.1016/j.matchemphys.2007.06.034>
- Li, J., Han, L., Duan, J., & Zhong, J. (2007b). Interface mechanism of ultrasonic flip chip bonding. *Applied Physics Letters*, 90(24), Article 242902. <https://doi.org/10.1063/1.2747673>
- Li, J., Han, L., Duan, J., & Zhong, J. (2007c). Microstructural characteristics of Au/Al bonded interfaces. *Materials Characterization*, 58(2), 103–107. <https://doi.org/10.1016/j.matchar.2006.03.018>
- Li, L., Xu, S., Liang, Y. K., & Wei, P. (2019). 10 mils Al wire heavy wedge bond wire deformation thickness study. In *2019 20th International Conference on Electronic Packaging Technology (ICEPT)* (pp. 1-4). IEEE Publishing. <https://doi.org/10.1109/ICEPT47577.2019.245791>
- Li, M., Ji, H., Wang, C., Bang, H. S., & Bang, H. S. (2006). Interdiffusion of Al–Ni system enhanced by ultrasonic vibration at ambient temperature. *Ultrasonics*, 45(1–4), 61–65. <https://doi.org/10.1016/j.ultras.2006.06.058>.
- Long, Y., Li, C., Twiefel, J., Wallaschek, J., Schneider, F., & Hermsdorf, J. (2019). Quantification of the energy flows during ultrasonic wire bonding under different process parameters. *International Journal of Precision Engineering and Manufacturing-Green Technology*, 6(3), 449–463. <https://doi.org/10.1007/s40684-019-00061-0>
- Long, Y., Twiefel, J., & Wallaschek, J. (2020). Contact mechanics and friction processes in ultrasonic wire bonding - Basic theories and experimental investigations. *Journal of Sound and Vibration*, 468, Article 115021. <https://doi.org/10.1016/j.jsv.2019.115021>
- Lum, I., Jung, J. P., & Y. Zhou. (2005). Bonding mechanism in ultrasonic gold ball bonds on copper substrate. *Metallurgical & Materials Transactions. Part A*, 36(5), 1279–1286. <https://doi.org/10.1007/s11661-005-0220-2>
- Lum, I., Mayer, M., & Zhou, Y. (2006). Footprint study of ultrasonic wedge-bonding with aluminum wire on copper substrate. *Journal of Electronic Materials*, 35(3), 433–442. <https://doi.org/10.1007/BF02690530>

- Mindlin, R. D. (1949). Compliance of elastic bodies in contact. *Journal of Applied Mechanics*, 16(3), 259–268. <https://doi.org/10.1115/1.4009973>
- Qi, J., Hung, N. C., Li, M., & Liu, D. (2006). Effects of process parameters on bondability in ultrasonic ball bonding. *Scripta Materialia*, 54(2), 293–297. <https://doi.org/10.1016/j.scriptamat.2005.07.042>
- Schemmel, R., Althoff, S., Sextro, W., Unger, A., Hunstig, M., & Brökelmann, M. (2018a). Effects of different working frequencies on the joint formation in copper wire bonding. In *CIPS 2018; 10th International Conference on Integrated Power Electronics Systems* (pp. 1-6). VDE Publishing.
- Schemmel, R., Hemsel, T., & Sextro, W. (2018b, June 11-15). *Numerical and experimental investigations in ultrasonic heavy wire bonding*. [Paper presentation]. Proceedings of the 6th European Conference on Computational Mechanics: Solids, Structures and Coupled Problems, ECCM 2018 and 7th European Conference on Computational Fluid Dynamics, Glasgow, United Kingdom.
- Tang, J., Li, L., Zhang, G., Zhang, J., & Liu, P. (2022). Finite element modeling and analysis of ultrasonic bonding process of thick aluminum wires for power electronic packaging. *Microelectronics Reliability*, 139, Article 114859. <https://doi.org/10.1016/j.microrel.2022.114859>
- Unger, A., Schemmel, R., Meyer, T., Eacock, F., Eichwald, P., Althoff, S., Sextro, W., Brökelmann, M., Hunstig, M., & Guth, K. (2016). Validated simulation of the ultrasonic wire bonding process. In *2016 IEEE CPMT Symposium Japan (ICSJ)* (pp. 251-254). IEEE Publishing. <https://doi.org/10.1109/ICSJ.2016.7801275>
- Uno, T., & Tatsumi, K. (2000). Thermal reliability of gold–aluminum bonds encapsulated in bi-phenyl epoxy resin. *Microelectronics Reliability*, 40(1), 145–153. [https://doi.org/10.1016/S0026-2714\(99\)00087-6](https://doi.org/10.1016/S0026-2714(99)00087-6)
- Winchell, V. H., & Berg, H. M. (1978). Enhancing ultrasonic bond development. *IEEE Transactions on Components, Hybrids, and Manufacturing Technology*, 1(3), 211–219. <https://doi.org/10.1109/TCHMT.1978.1135291>
- Zhou, Y., Li, X., & Noolu, N. J. (2005). A footprint study of bond initiation in gold wire crescent bonding. *IEEE Transactions on Components & Packaging Technologies*, 28(4), 810–816. <https://doi.org/10.1109/TCAPT.2005.848585>
- Zwicker, M. F. R., Moghadam, M., Zhang, W., & Nielsen, C. V. (2020). Automotive battery pack manufacturing – A review of battery to tab joining. *Journal of Advanced Joining Processes*, 1, Article 100017. <https://doi.org/10.1016/j.jajp.2020.100017>

Coastal Bris Wetland Hydrodynamics in Non-monsoon and Monsoon Seasons at Mengabang Telipot Terengganu, Peninsular Malaysia

Syazuani Mohd Shariff^{1,2}, Edlic Sathiamurthy^{1*} and Mohd Sofiyan Sulaiman³

¹*Faculty of Science and Marine Environment, Universiti Malaysia Terengganu, 21030, Kuala Nerus, Terengganu, Malaysia*

²*Faculty of Applied Science, School of Biology, UiTM Cawangan Negeri Sembilan, Kampus Kuala Pilah, 72000, Kuala Pilah, Negeri Sembilan, Malaysia*

³*Faculty of Ocean Engineering Technology and Informatics, Universiti Malaysia Terengganu, 21030, Kuala Nerus, Terengganu, Malaysia*

ABSTRACT

BRIS (beach ridges interspersed with swales) wetlands dominate the coastal plains of the east coast of Peninsular Malaysia. This study examined the impact of rainfall and river levels on groundwater hydrodynamics in a coastal BRIS wetland at Universiti Malaysia Terengganu during the northeast monsoon and non-monsoon seasons (July 2022 to January 2023). Six monitoring wells (WA-WF) were built, with WB, WC and WD positioned on the higher ground, whereas WA, WE and WF were on the lower ground. River levels were observed at three stations (R1–R3), rainfall data were collected using a weather station and tidal data were obtained from an existing station. Measurements at 5-minute intervals identified a strong correlation. Between tidal oscillations and river water level ($r = 0.7\text{--}0.92$, average, 0.81), typical of tidal rivers. However, the influence of tidal oscillation on groundwater level was weak (average $r = 0.22$), suggesting an indirect influence through river dynamics. Groundwater level in lower areas near rivers was more influenced by river water level changes (average $r = 0.54$, monsoon average = 0.76). In contrast, the higher section showed a weak influence in general (average $r = 0.02$, monsoon average = 0.34). During monsoon season, increased upstream flows elevated river levels, enhancing hydraulic connectivity across the wetland. Groundwater fluctuations were limited to

0.5 m below ground, with lower areas frequently saturated or inundated, limiting floodwater retention capacity. Future research could explore the impact of soil texture and porosity to refine understanding of BRIS wetland hydrodynamics.

ARTICLE INFO

Article history:

Received: 12 August 2024

Accepted: 12 February 2025

Published: 23 April 2025

DOI: <https://doi.org/10.47836/pjst.33.3.19>

E-mail addresses:

syazuani@uitm.edu.my; syazuani226@gmail.com (Syazuani Mohd Shariff)

edlic@umt.edu.my (Edlic Sathiamurthy)

sofiyan@umt.edu.my (Mohd Sofiyan Sulaiman)

* Corresponding author

Keywords: Coastal BRIS wetland, hydrodynamics, monsoon season, non-monsoon season

INTRODUCTION

On the east coast of Peninsular Malaysia, the non-monsoon season occurs from May to September, while the monsoon season (northeast monsoon) occurs from November to March annually (Ariffin et al., 2019). During the northeast monsoon, heavy rainfall with an average of 2990 mm occurs, in contrast with the non-monsoon season, with only 740 mm of average rainfall (Ismail et al., 2020; Arrifin et al., 2016). Flooding often occurs when heavy rainfall coincides with high tides (Cai et al., 2022; Pirani & Najafi, 2020; Zhang & Najafi, 2020; Westra et al., 2014). In addition, the average high tide was 2.28 meters, while the average tide height was less than 0.4 meters during the southwest monsoon (Ismail et al., 2020). This indicates the differences in rainfall amount and tidal heights during the two seasons.

The coastal plains of the east coast of Peninsular Malaysia are dominated by beach ridges and swales, i.e. BRIS environment. The soil type is typically sand, silty sand and silty clay. Sandy soil promotes water movement as discharge/recharge, whereas silty-clayey layers aid groundwater accumulation (Mohamad et al., 2002; Roslan, 2010; Koh et al., 2018). Naturally, ridges are occupied by heath forests, while swales are occupied by wetland vegetation (Kamoona et al., 2023; Ikbal et al., 2023; Touchette et al., 2011; Salim et al., 2014).

The tidal activities and river flows affect groundwater in the coastal BRIS area. It depends upon hydraulic properties, the geomorphology of the area, and the topography (Moffett et al., 2012; Ensign, 2013). Hydraulic gradient governs groundwater flow direction, where groundwater flows from high hydraulic head to low hydraulic head areas (Zhang et al., 2022; Gleeson et al., 2011). Ridges have higher elevations and water tables, i.e. higher hydraulic heads. They recharge the swales that are located in lower-elevation areas. Swale groundwater is also replenished by rivers and streams (Curtis et al., 2017). As a result of such hydrologic process, swales become an important water retention area and may have a potential in flood mitigation (Revitt et al., 2017; Gao et al., 2015). Unfortunately, the BRIS study has been more focused on its agriculture potential than ecological services like flood mitigation (Bakar et al., 2023; Zakaria et al., 2023; Ishaq et al., 2019; Toriman et al., 2009; Hossain et al., 2011; Lah et al., 2011).

This study hypothesises a significant difference in groundwater levels between the non-monsoon and monsoon seasons. It suggests that the higher rainfalls during the monsoon season significantly affect groundwater dynamics compared to the non-monsoon season. Additionally, this study suggests that tidal levels affect groundwater dynamics differently across these seasons. Furthermore, the interaction between rainfall amount and tidal levels during the monsoon season substantially affects groundwater dynamics compared to the non-monsoon season.

This study focuses on analysing the behaviour of the groundwater system in response to non-monsoon and monsoon seasons to address the gap in understanding the ecosystem

services in this area. The objective is to determine the impact of rainfalls and tidal levels on the hydrodynamic of groundwater in the BRIS coastal wetland during these distinct seasonal periods.

METHODOLOGY

Study Area

The study area is on the Universiti Malaysia Terengganu (UMT) campus at Mengabang Telipot. It is a coastal BRIS wetland located 15 km north of Kuala Terengganu City (UTM 48N, 287720 m N, 598526 m E) (Figure 1). This coastal area has several beach ridges with low-lying backfill areas in between. The ridges are relict beaches, indicating the coastlines' position changes as the sea level regressed after the Holocene high stand (Sathiamurthy et al., 2021). The estuary of this area is a temporarily open/closed estuary type (Sathiamurthy & Pauzi, 2020). The surrounding rivers could overflow their banks during heavy, prolonged

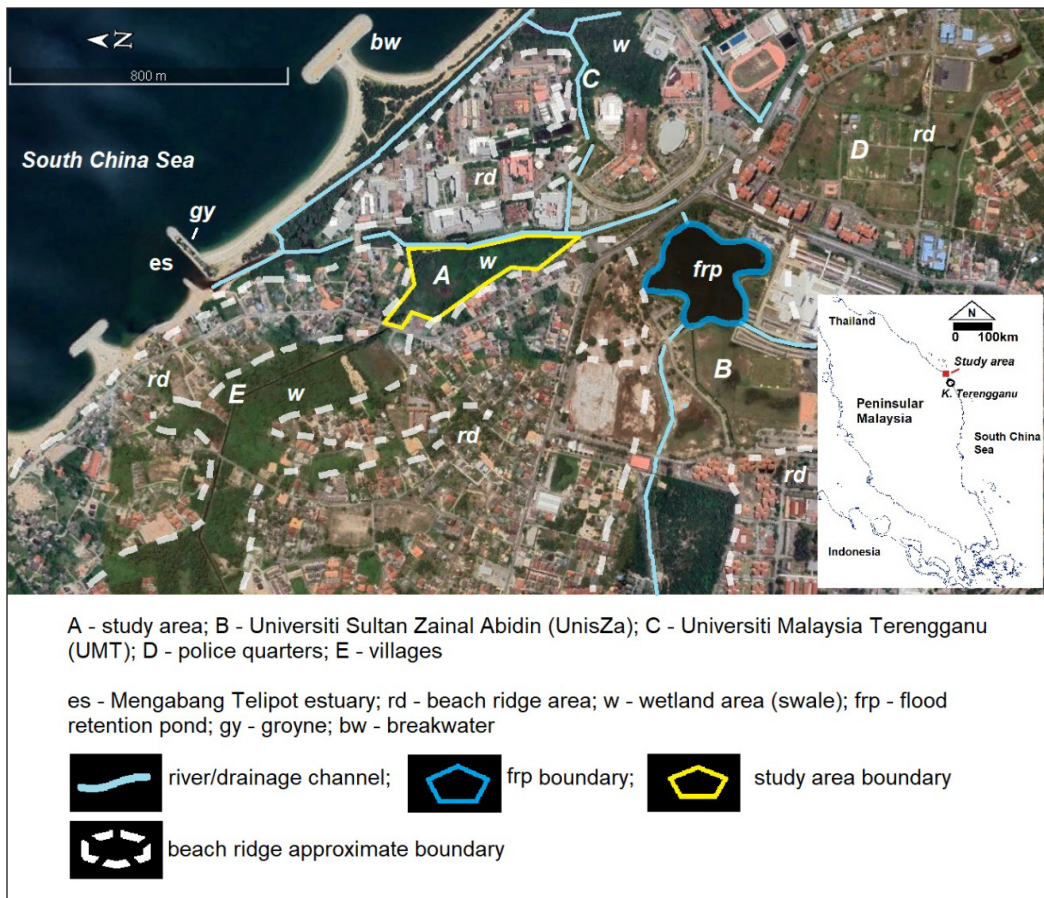


Figure 1. Study area (Source: Google Earth and fieldwork)

monsoonal rainfalls coinciding with high tides or when the estuary is closed. The flood flows would inundate a 5.26-ha wetland located within the UMT campus. Stations were set up to capture the hydrodynamic behaviour of the wetland under study (Figures 2 and 3). The river stations consisted of the outlet near the estuary (R1), the inlet area from the campus of Universiti Sultan Zainal Abidin (UniSZA) and the Kuala Terengganu Golf Resort drainage system (R2), and the Wakaf Tengah River (R3). The wetlands stations, WA, WB, WC, WD, WE and WF were monitoring wells.

River Water Level Measurements

The hydrodynamic behaviour of the wetland corresponding to the rivers was examined by measuring water levels in all stations simultaneously under high temporal resolution, i.e. 5-minute intervals. Every station had a data logger for this purpose (Table 1). Measurements

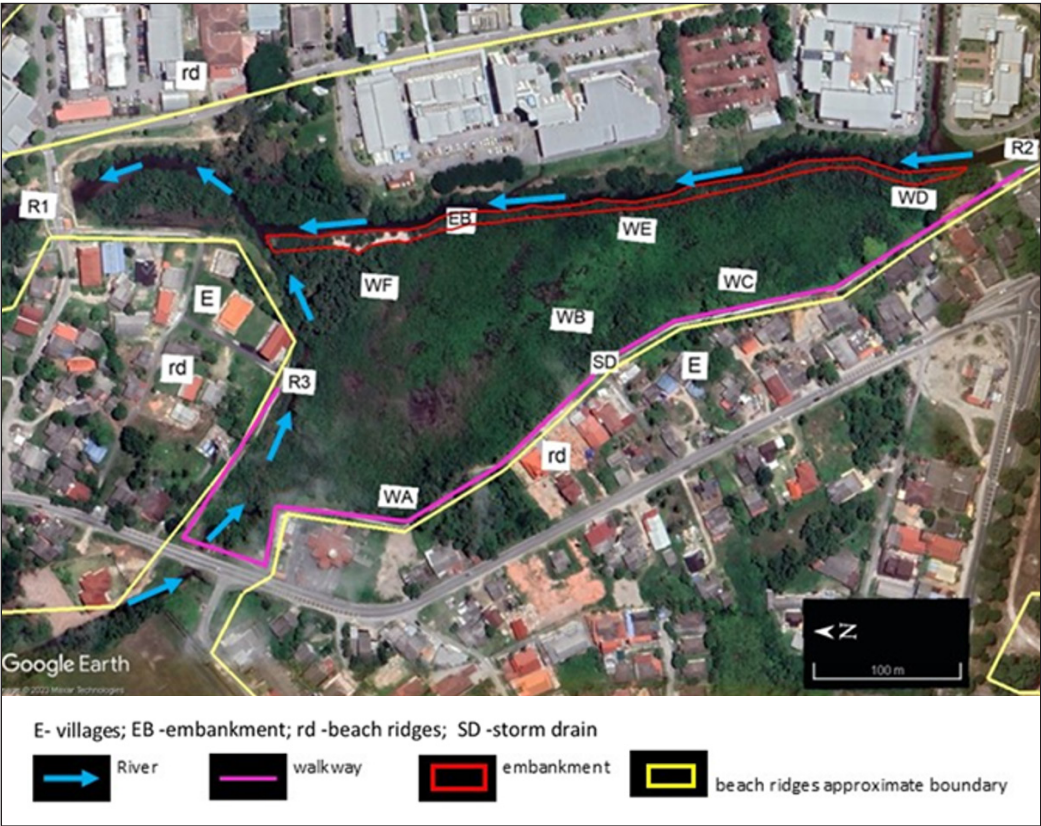


Figure 2. River and wetland station in the study site, Universiti Malaysia Terengganu (Source: Google Earth and fieldwork)

Note. The middle section is inaccessible; no stations were assigned. All stations were scattered across the wetland area, so the sampling work was unaffected as all stations covered the wetland area. R1 is the nearest station to the estuary, about 525 m downstream, whereas R2 is upstream of the same main channel, and R3 is in the main tributary that flows from the west

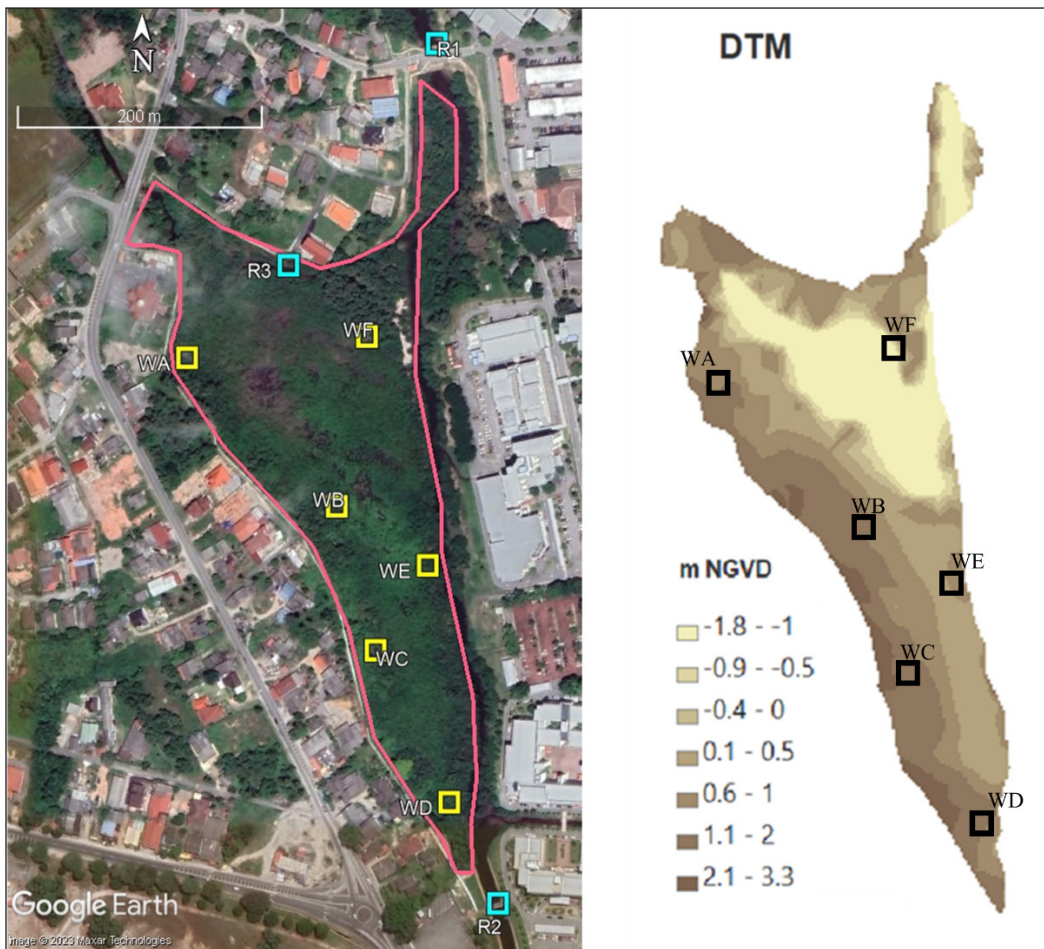


Figure 3. Satellite and digital terrain model (DTM) image of the Universiti Malaysia Terengganu campus study site

Note. The DTM image was analysed using ArcMap software to indicate the ground elevation in this study area. The dark colour shows the high ground level. WB, WC, and WD were high-ground-level wetland stations, while WA, WE, and WF were low-ground-level wetland stations

were done from 10 to 21 July 2022 (non-monsoon season), 22 October to 7 November 2022 (early monsoon season), and 4 December 2022 to 1 January 2023 (middle-monsoon season). It should be noted that the monsoon season here refers to the northeast monsoon, whereas the non-monsoon season refers to the season outside of the northeast monsoon season. These monitoring wells were made from perforated PVC pipes (Figure 4). They reached the marine clay layer in the wetland area at roughly 0.6 m to 2.4 m, with an average depth of 1.9 m.

The marine clay layer is the first confining layer that marks the bottom boundary of the unconfined aquifer. The unconfined layer is only relevant for this study as the focus was surface and upper subsurface hydrodynamics. River stations were equipped with stick gauges and perforated PVC pipes as well. However, the pipes were set up primarily to

Table 1
Basic information on wetland and river stations

The coordinates, the depth and the ground level of the wetland stations			
Station	Coordinates (UTM 48N)	Well Depth (m)	Ground Level (m NGVD)
WA	287600 m N, 598599 m E	3.4	1.31
WB	287724 m N, 598485 m E	3	1.60
WC	287758 m N, 598373 m E	2.6	2.03
WD	287820 m N, 598255 m E	3	1.63
WE	287799 m N, 598440 m E	3.2	1.21
WF	287747 m N, 598618 m E	3	1.09

The coordinates, the bed level and the ground level of the river stations			
Station	Coordinates (UTM 48N)	Bed Level (m NGVD)	Ground Level (m NGVD)
R1	287799 m N, 598849 m E	-0.262	2.744
R2	287861 m N, 598176 m E	0.345	3.312
R3	287681 m N, 598673 m E	-0.139	1.891

Note. WA: Well A, WB: Well B, WC: Well C, WD: Well D, WE: Well E, WD: Well D; R1: River 1, R2: River 2, R3: River 3

gauges and perforated PVC pipes as well. However, the pipes were set up primarily to protect data loggers from debris damage. PVC pipes were chosen because they are inert and stable, lowering the contamination risk. A filter layer made of cloth was used to keep fine soil particles from entering the monitoring wells.

The elevation of each data logger was determined based on the crown elevation of the wells and the elevation points on the stable structures where the river stations were set up. Elevations were determined via ground levelling work based on the National Geodetic Vertical Datum (NGVD) with reference to an existing land survey benchmark. This work was vital to ensure comparable water levels, and hence, their differences and changes through time and space indicate hydrodynamic behaviour.

During the middle monsoon season, on 9 December 2022 at 12:30 pm, monitoring

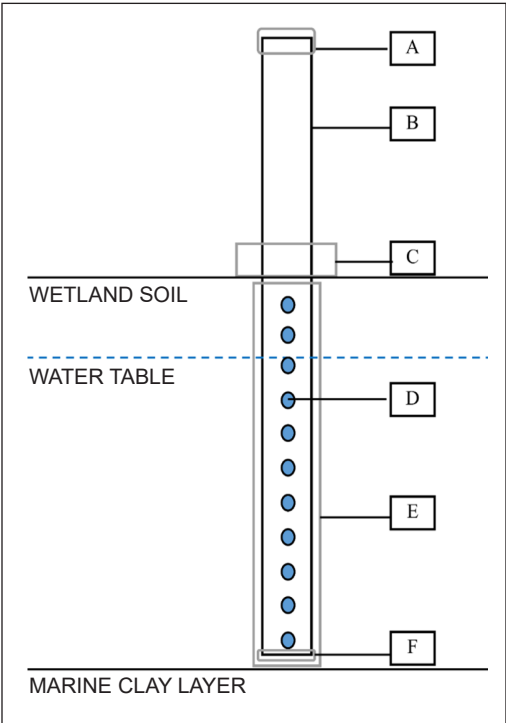


Figure 4. Schematic diagram of wetland monitoring station

Note. A: PVC cap, B: PVC pipe, C: Concrete cement, D: Perforated PVC Pipe, E: Filter layer, F: PVC bottom cap

protect data loggers from debris damage. PVC pipes were chosen because they are inert and stable, lowering the contamination risk. A filter layer made of cloth was used to keep fine soil particles from entering the monitoring wells.

The elevation of each data logger was determined based on the crown elevation of the wells and the elevation points on the stable structures where the river stations were set up. Elevations were determined via ground levelling work based on the National Geodetic Vertical Datum (NGVD) with reference to an existing land survey benchmark. This work was vital to ensure comparable water levels, and hence, their differences and changes through time and space indicate hydrodynamic behaviour.

During the middle monsoon season, on 9 December 2022 at 12:30 pm, monitoring well R2 sustained structural damage due to the rapid water flow through the pipe. As a result, a new station was installed on 11 December 2022 at 3:15 pm. However, the damage has prevented data collection, resulting in an 8.22% absence of recorded data. Nonetheless, the collected data remains suitable for analysis.

Salinity

The salinity in the river and wetland stations was recorded using the same data loggers at 5-minute intervals. Salinity measurements were taken to detect saltwater intrusion. A saltwater intrusion would indicate seawater infiltration into the wetland soil until it reaches the groundwater, which would mean the tidal event influenced the stations. However, the rainfall-runoff process appeared to be the main factor influencing groundwater levels when salinity was low.

Tidal and Rainfall Data

The Department of Survey and Mapping Malaysia provided tidal data, while the Drainage and Irrigation Department provided rainfall data as supplementary data. The data were recorded at 5-minute intervals from 10 to 21 July 2022 (10:50 pm and 11:05 pm, respectively), 22 October (2:00 pm) to 7 November 2022 (8:00 am), and 4 December 2022 (1:25 pm) to 1 January 2023 (10:55 am). Rainfall data primarily came from a portable weather station (RainWise Portlog) set up adjacent to the study area, and rain data were recorded every 5 minutes as well. Hence, the rainfall and tidal data match the water level data. Hence, the cause-and-effect relationship can be examined. They demonstrated how the river and groundwater systems responded to non-monsoon, early monsoon, and mid-monsoon seasons.

Data Analysis

Pearson correlation and X-Y scatter graphs were used to analyse the collected data. Pearson correlation, together with significance tests, was conducted between stations. This was to determine their correlations (corresponding or inverse), strengths, and significance (with

a p-value lower than 0.05). These analyses indicated which stations influence water level changes in other stations. The graphs gave a visual relation between them. For example, a weak positive correlation (r near 0) between two stations would indicate that the rise and fall of water levels of both wells had a very weak influence on each other hydrodynamically. However, if the correlation is strong but the 'p' value is higher than 0.05, it would mean the relation is not significant and could result from randomness, error, or lack of data.

The study area groundwater stations (wells) were divided into high-ground and low-ground stations based on ground elevation (Figure 3). The groundwater levels of these wells were compared because high-ground wells are more likely to be affected by rainfall recharges from the adjacent sand ridge. In contrast, the low-ground wells would be more affected by river water changes caused by tidal intrusions, recessions, and river upstream outflows. Such comparisons also enable the examination of the cause-effect relationship between them. Thus, the factors that affect hydrodynamic behaviour could be determined from these comparisons.

The graph plots helped visually compare the high and low-ground-level wetland stations during the non-monsoon, early-monsoon, and mid-monsoon seasons. The graphs demonstrated the relationship between rainfall intensities, tidal levels, river water levels and groundwater levels in a cause-and-effect manner. They showed the wetland's response patterns or behaviour as the groundwater level fluctuated due to parameter changes.

RESULTS AND DISCUSSION

High Ground-level Wetland Stations During Non-monsoon Season

Groundwater stations (monitoring wells) WB (ground level: 1.60 m NGVD), WC (2.02 m NGVD), and WD (1.63 m NGVD) are located on higher grounds, i.e., close to the middle of the beach ridges (Figure 3). Unlike the other wells and river stations, these WB stations were unaffected by tidal changes during the non-monsoon season, as the salinity range was 0.375 ppt to 0.391 ppt (Figure 3). The WB station has a weak connection with R1 ($r=0.04$, $p=0.02$) and R3 ($r=0.08$, $p<0.001$), as indicated by their almost zero correlation values. On the other hand, the WB station and the R2 station do not have a statistically significant relationship ($r=0.01$, $p=0.64$). This station's water level range was from 1.475 m to 1.658 m NGVD. Nonetheless, when it rained, the water level in WB increased. Water from the nearby village storm drain flowed into the wetland when it rained (Figure 2).

Moreover, it was found that R1 ($r=0.13$, $p<0.001$), R2 ($r=0.09$, $p<0.001$), and R3 ($r=0.15$, $p<0.001$) had a weak positive relation with WC station. That showed WC essentially was not influenced by river water fluctuations. WC was in the upper part of the wetlands and near the middle of the beach ridge. Its water level ranged from 1.967 m to 2.091 m NGVD during the non-monsoon season. The ground level of the WC was higher than other stations, and generally, it had a higher hydraulic head.

There were weak negative relationships between the WD station and R1 ($r = -0.12$, $p < 0.001$), R2 ($r = -0.12$, $p < 0.001$), and R3 ($r = -0.08$, $p < 0.001$). The salinity ranges from 0.122 ppt to 0.136 ppt. It should be noted that in the natural environment, freshwater would show some values for conductivity because of dissolved minerals. Hence, very low values do not necessarily indicate minor seawater intrusions (McCleskey et al., 2011). In addition, although tidal events cause changes in river water levels, it showed a limited susceptibility to these changes, as evidenced by its very low salinity values (Xu et al., 2022). The water level at WD ranges between 1.554 m and 1.638 m NGVD, demonstrating minor fluctuations (less than 10 cm) compared to the large fluctuations in the river (Figure 5). As a result of tidal intrusions and recessions in the river, river water levels showed changes, while groundwater levels at WD displayed a minor drop trend. This indicated that river water level changes had little effect on WD, even though WD was just 15 m away. The natural process of groundwater recharge/discharge relation with the river was most probably impeded by an embankment of compacted clay soil that reduced hydraulic conductivity. Such impeded exchange could harm the ecosystem (Wilopo & Putra, 2021; Aish, 2010; Pang et al., 2009).

During the non-monsoon season, all high-ground level wetland stations were unaffected by the river water fluctuations, as indicated by their weak correlations (average r was only 0.02). The higher groundwater levels prevented river water from reaching this area as it was against the hydraulic gradient. It showed that ground elevation has a significant effect on groundwater flow. In addition, in the case of WD, the embankment impeded the subsurface intrusion of river water into the wetland. This also retarded the recharge/discharge of the groundwater. The total rainfall recorded was 113.2 mm from 10 to 22 July 2022 (10:50 pm and 1:50 am, respectively), indicating no significant groundwater recharge from adjacent ridges. The rainfall amount was classified as type 1 with no runoff occurrence (Othman et al., 2020).

Low Ground-level Wetland Stations During Non-monsoon Season

Changes in river water levels and rain influenced the lower-ground wetland stations. This can be seen in the observations made at WA (ground level: 1:30 m NGVD), WE (1:21 m NGVD) and WF (1:09 m NGVD). The groundwater water level generally ranged from 0.589 m NGVD to 1.431 m NGVD (Figure 6) - the area with lower elevations experienced flooding during spring high tides.

There was a stronger positive relationship between WF with all three river stations, R1 ($r=0.59$, $p<0.001$), as well as R2 ($r=0.66$, $p<0.001$) and R3 ($r=0.61$, $p<0.001$) compared to WA and WE. The moderate correlation coefficients for WA with R1 ($r=0.48$, $p<0.001$), R2 ($r=0.52$, $p<0.001$), and R3 ($r=0.52$, $p<0.001$) river stations indicated a slightly weaker link by comparison. WE station showed a similar moderate relation, indicated by correlation

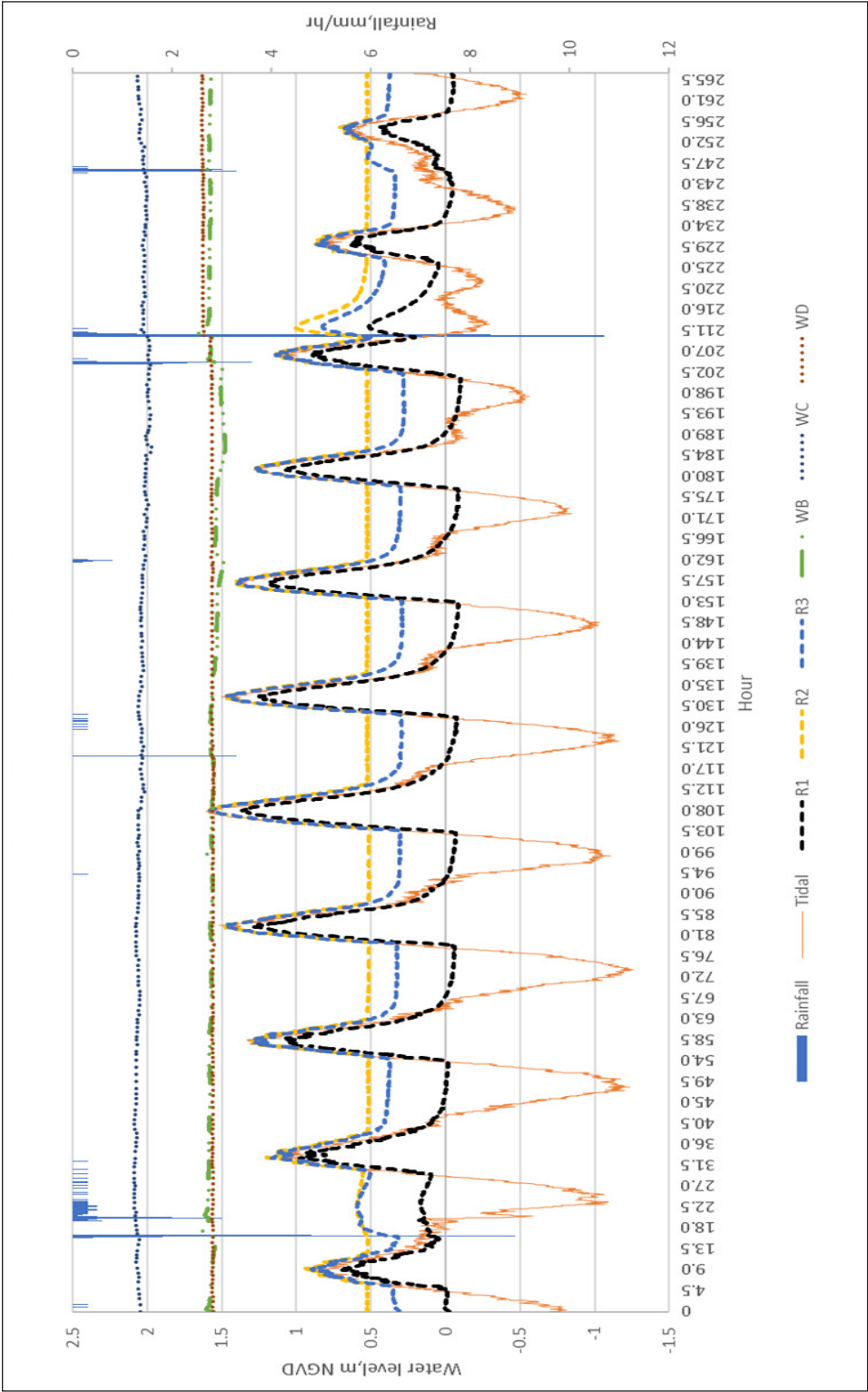


Figure 5. Water levels of high-ground wetland stations (WB, WC, and WD) and river stations (R1, R2 and R3) during non-monsoon season. Notes. The 0 hour starts at 10:50 pm on 10 July 2022, and the 264.3 hour ends at 11:05 pm on 21 July 2022

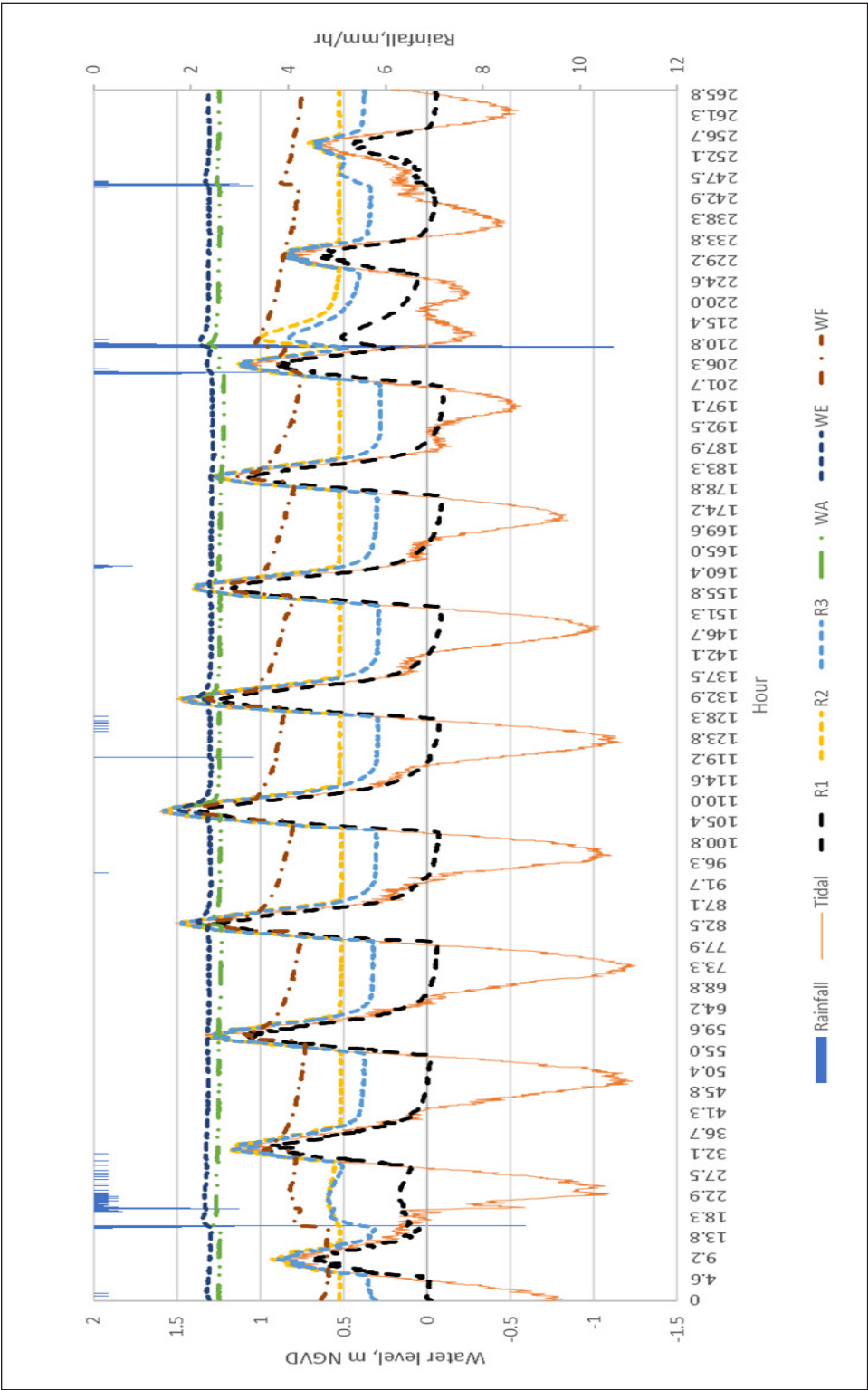


Figure 6. Water levels of low-ground wetland stations (WA, WE, and WF) and river stations (R1, R2 and R3) during non-monsoon season. Notes. The 0-hour starts at 10:50 pm on 10 July 2022. The 264.3 hours period ends at 11:05 pm on 21 July 2022

coefficients of 0.45 ($p < 0.001$), 0.49 ($p < 0.001$), and 0.52 ($p < 0.001$) for R1, R2 and R3. In comparison, these correlation values were significantly higher than those of WB, WC, and WD, indicating that river water fluctuations influenced the lower area of the wetland more.

WE water level ranged from 1.282 m to 1.493 m NGVD and WA, 1.216 m to 1.514 m NGVD in response to the spring tide event in mid-July that reached 1.510 m NGVD. Their water levels showed very little change over time throughout the observation period. In contrast, the WF groundwater level showed fluctuations that corresponded closely to river water level changes, as indicated by its stronger correlations. WF was located on lower ground compared to WE and WA. Unlike WE, it was beside the river, and there was no embankment to impede river overflow. Thus, WF was very susceptible to inundation through direct overflow from the river, and this emphasised the effect of topography and man-made structures like an embankment. The recorded amount of rainfall was just 113.2 mm starting from 10 to 21 July 2022 (10:50 pm and 11:05 pm, respectively), which could not have generated high upstream flows that would have elevated river levels hence high tides were the essential cause of groundwater rise and even inundations (Hsieh et al., 2020). Rainfalls did not have a significant effect.

High Ground-level Stations During Early Monsoon Season

During the monsoon season, changes in river water levels caused slight changes in the water level at three high-ground wetland stations (WB, WC, and WD), just like the non-monsoon season. The average correlation between groundwater and river levels was 0.22. It was stronger than the non-monsoon condition but still a weak one. Figure 7 shows small changes in groundwater water levels during rainfalls, but they were generally insignificant, just like in the non-monsoon conditions.

WB groundwater level rose from 1.578 m to 1.669 m NGVD, showing a bigger change compared to WC and WD. Notably, the salinity range found at this station was in the freshwater category, with a reading of 0.28 ppt. This low salinity was due to the area being closed to a nearby drain that discharged stormwater from the beach ridge and sub-surface flow from the ridge (Figure 2). These were freshwater recharges. The study showed that there was a weak relationship between the station in the wetland and the river stations, with R1 ($r=0.26$, $p < 0.001$), R2 ($r=0.28$, $p < 0.001$), and R3 ($r=0.37$, $p < 0.001$). This discovery suggests that variations in river water levels have a minor influence on the water level of the WB, and the fact that the wells remained fresh indicated no significant saline intrusion into this area.

The correlation coefficients for R1 ($r=0.21$, $p < 0.001$), R2 ($r=0.22$, $p < 0.001$), and R3 ($r=0.25$, $p < 0.001$) with WC showed that the WC station had a weak hydraulic connection to the river station. The high-water levels in WC range from 2.068 m to 2.10 m NGVD compared to the other wells, suggesting that it was a recharge area receiving groundwater

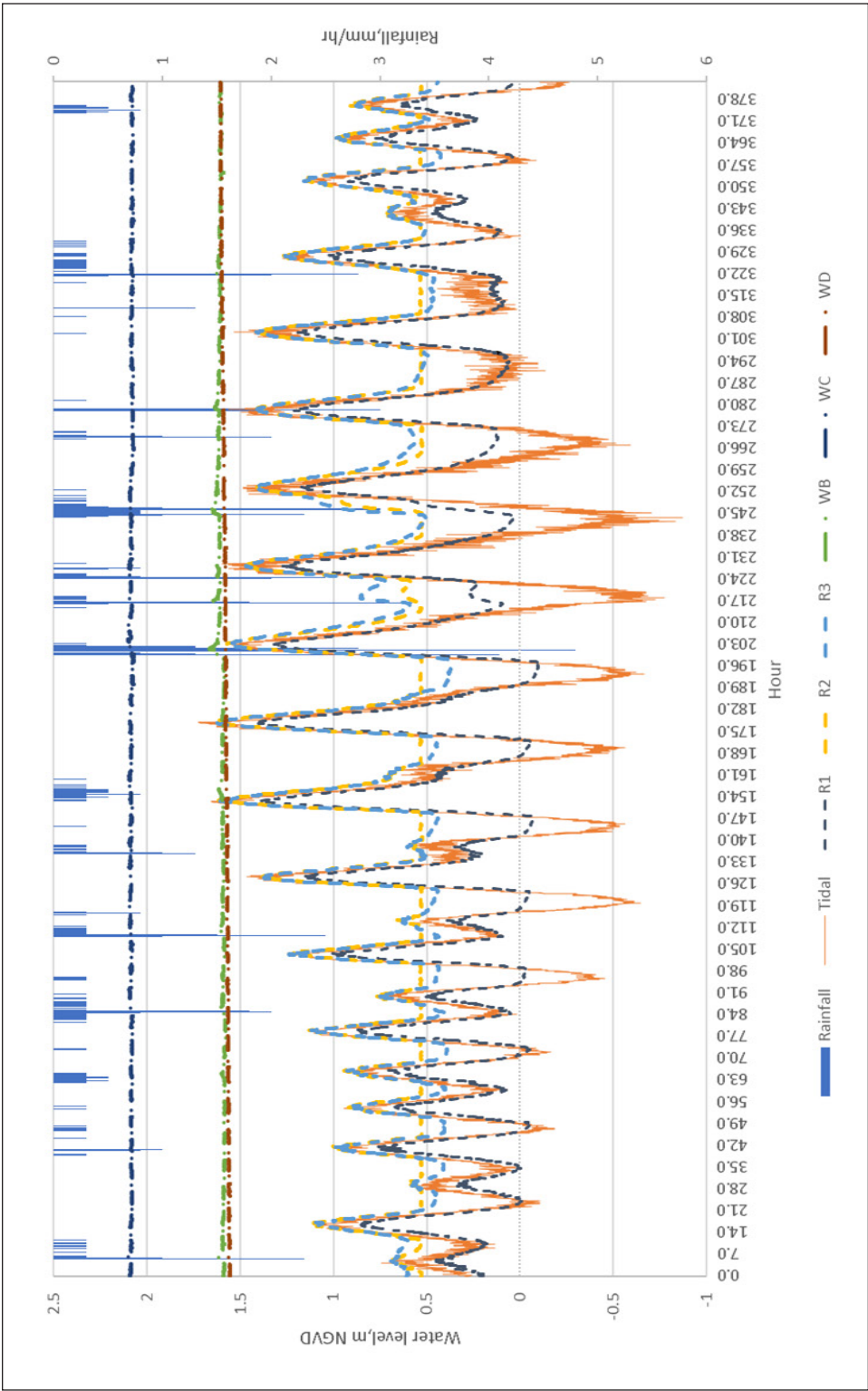


Figure 7. Water levels of high-ground wetland stations (WB, WC, and WD) and river stations (R1, R2 and R3) during the monsoon season. Note. The 0-hour period starts at 2:00 pm on 22 October 2022, and the 378-hour period ends at 8:00 am on 7 November 2022

from the beach ridge. WC was the closest well to the ridge. Ridges are active rainfall recharge areas with high hydraulic conductivity that could transfer sub-surface water downslope since they are made of sand (Sathiamurthy et al., 2021).

The WD station water level ranges from 1.551 m to 1.610 m NGVD, which also results from ridge recharge. The relation of WD to R1, R2, and R3 were positive just like WC but weaker (i.e. $r=0.12$, $p < 0.001$, $r=0.10$, $p < 0.001$, and $r=0.13$, $p < 0.001$, respectively). Also, the salinity of the groundwater ranged between 0.126 ppt to 0.115 ppt, which means it was not affected by the tidal intrusion but received freshwater from rainfalls and ridge sub-surface input (Abdullahi & Garba, 2016).

Early in the monsoon season, the study area received moderate rainfalls of 245.3 mm (22 October 2022, 2:00 pm to 7 November 2022, 1:50 pm). The WD station indicated no influence from the fluctuation of the river water, which means tidal activity had little impact. Meanwhile, WC and WB stations fluctuated after rainfall (total rainfall: 42.4 mm, 30 to 31 October 2022, 9:35 pm and 1:20 am, respectively) (Figure 6). The WB station was exposed to the storm drain, which accumulated rainfall surface runoffs in the wetland station and increased the water level. Meanwhile, the WC received sub-surface water from the ridges.

Low Ground-level Wetland Stations During the Early Monsoon Season

All stations were affected by river water level changes and rainfall events, especially WF. They had an average correlation of 0.54 with river water levels. The water level range of WF was 1.551 m to 1.610 m NGVD and had a strong positive correlation with river stations, i.e. R1 ($r=0.66$, $p < 0.001$), R2 ($r=0.72$, $p < 0.001$), and R3 ($r=0.75$, $p < 0.001$). High tides caused increases in the water levels of R3 and led to an overflow into the WF area when the water level exceeded the ground level (Meng et al., 2022). The water level of R3 needed to reach 1.2 m NGVD for this overflow to occur, as shown in Figure 8.

There was a moderately strong positive link between WA and R1 ($r=0.55$, $p < 0.001$), R2 ($r=0.62$, $p < 0.001$), and R3 ($r=0.61$, $p < 0.001$). Its water levels rose during the spring tide. This observed rise in water levels coincided with increased salinity ranging from 2.759 ppt to 3.368 ppt, indicating saline intrusions. Outside the monsoon season, the water level ranged from 1.216 m to 1.514 m NGVD. Water levels during the early monsoon season ranged from 1.237 m to 1.553 m NGVD, showing small changes. The water table in the area affected by the flooding remained high, causing saturation (Mitsch & Gosselink, 2015).

WE had a stronger positive relation to R1 ($r=0.60$, $p < 0.001$), R2 ($r=0.65$, $p < 0.001$), and R3 ($r=0.66$, $p < 0.001$). Water levels at this station varied from 1.276 m to 1.535 m NGVD, depending on the effect of tidal fluctuations in the river. When the river flow increased, the water level rose. Its salinity rose from 5.543 ppt to 6.461 ppt during spring tides, indicating saline intrusion. Low ground level and a high-water table near WE caused the area to flood often, hence lacking storage for extra flood water. (Jolly et al., 2008).

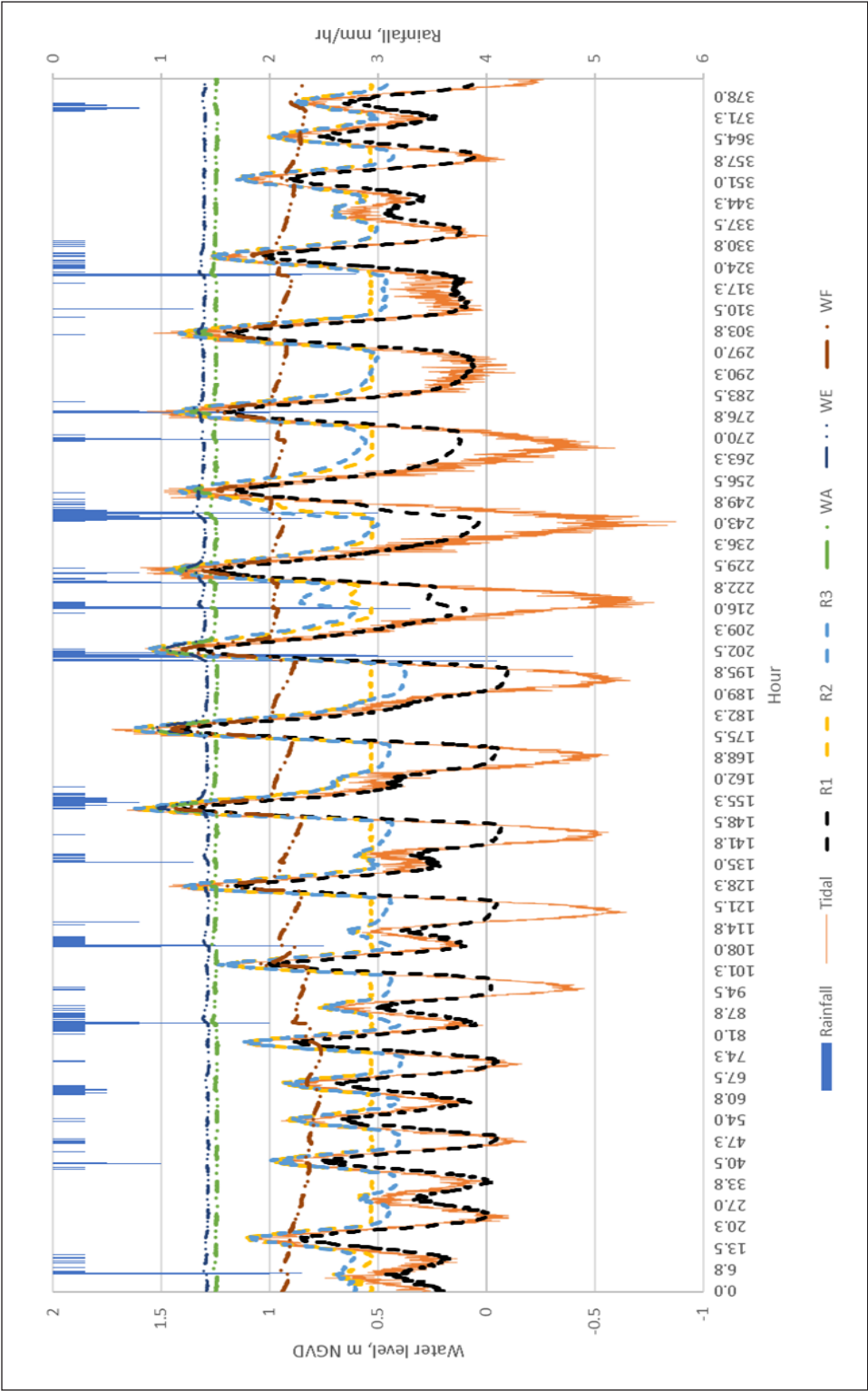


Figure 8. Water levels of low-ground wetland stations (WA, WE, and WF) and river stations (R1, R2 and R3) during the early monsoon season. Note. The 0-hour period starts at 2:00 pm on 22 October 2022, and the 378-hour period ends at 8:00 am on 7 November 2022

Rainfalls amounting to 245.3 mm, 22 October 2022, 2:00 pm to 7 November 2022, 1:50 pm, coinciding with high spring tides elevated river levels affecting all low-ground wetland stations. The river level fluctuation affected the WF station, indicating a corresponding oscillation. In comparison, the WA and WE stations were affected only during spring tides with several inundation episodes.

High Ground-level Wetland Stations During Mid-monsoon Season

A flood event occurred during the mid-monsoon season and reached this wetland section. It was during neap tide; hence, it was not the result of high tidal levels but of river flood flows (Figure 9). Notably, the salinity found at this station was in the freshwater category, with a reading of 0.288 ppt. The higher section of the wetland received river surface overflows. The WB station recorded a water level range of 1.521 m to 2.341 m NGVD (flood event). The WB station showed strong significant correlations with R1 ($r=0.50$, $p<0.001$), R2 ($r=0.66$, $p<0.001$), and R3 ($r=0.63$, $p<0.001$). The R2 station was destroyed during this season due to very strong water flow (refer to Water Level Measurement). As this station was near the storm drain, this area received high stormwater discharge from the beach ridge, and sub-surface flow from the ridge entered the wetland, which was separated from the river overflows.

At the WC station, the water level ranged from 2.041 m to 2.314 m NGVD. This station had a moderately weak positive correlation with R1 ($r=0.30$, $p<0.001$), R2 ($r=0.44$, $p<0.001$), and R3 ($r=0.41$, $p<0.001$), showing that WC had a weak hydraulic connection to the river station. During this season, high rainfall amounts (1056.1 mm) from 4 December 2022 (1:25 pm) to 1 January 2023 (10:55 pm) recharged the beach ridge near the WC station, creating excessive subsurface water from the beach ridges.

The water level in the WD station ranged from 1.639 m to 2.379 m NGVD. This station showed weak correlations with R1 ($r=-0.02$, $p=0.135$), R2 ($r=0.10$, $p=0.001$), and R3 ($r=-0.06$, $p=0.001$). Also, the salinity ranged between 0.07 ppt and 0.10 ppt, which means it was not affected by tidal intrusion despite receiving river flood overflows from R2 and subsurface input.

As recorded during the middle monsoon season, the water level in high-ground-level wetland stations was affected by the water level from the R2 station (Figure 9). The high rainfall amount (668.9 mm) from 4 to 19 December 2022 (1:25 pm and 12:00 pm, respectively) led to the flood event. However, the rainfall amount from 19 to 23 December 2022 was 387.2 mm, which did not increase the groundwater level stations. However, WB and WC station water levels decreased right after the flood event receded, while WD remained with high water levels. WD station was behind an embankment composed of low hydraulic conductivity material (i.e. clay), which slowly discharged water back into the river. This indicated that ground elevation was not solely responsible for retaining water

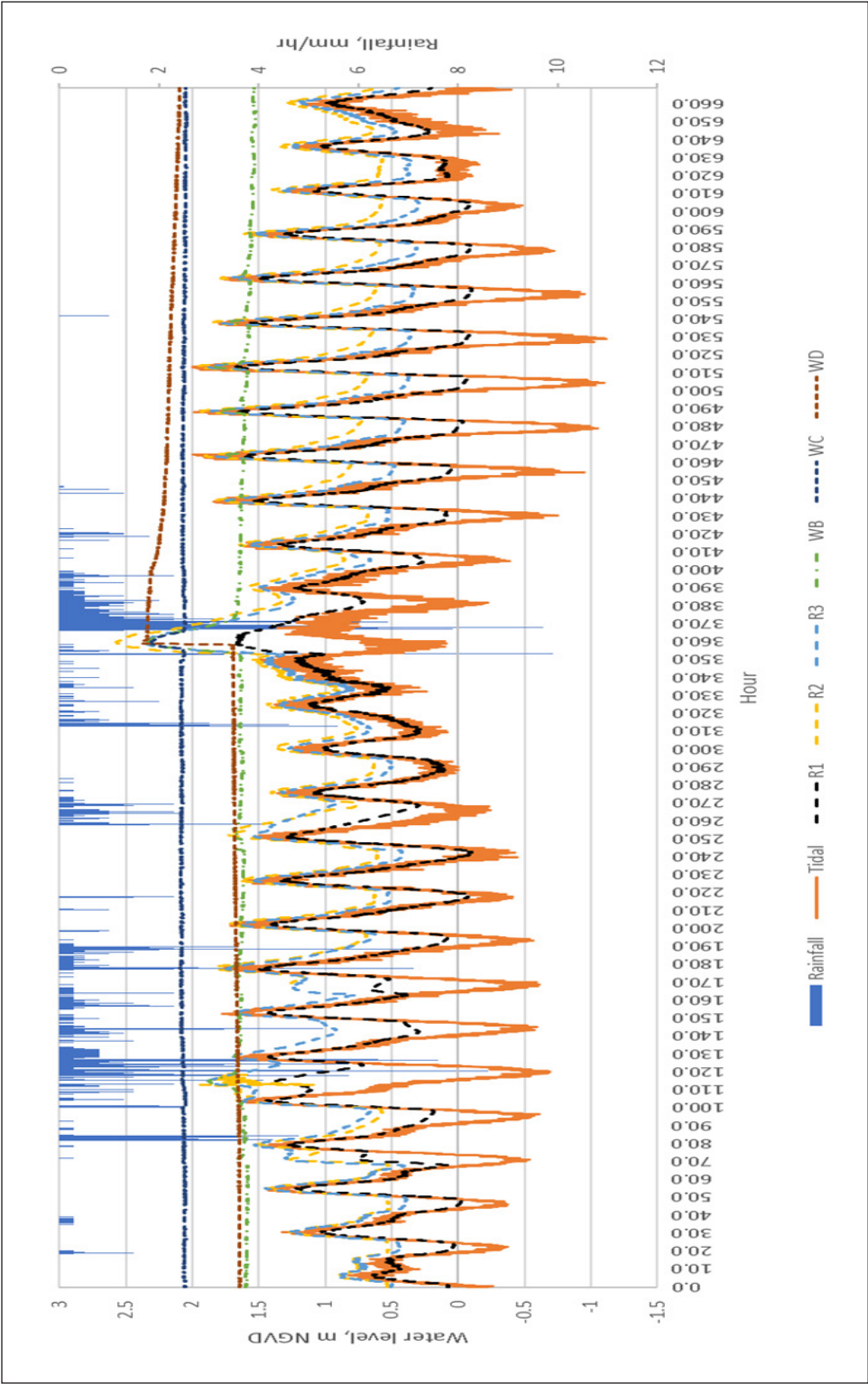


Figure 9. Water levels of high-ground wetland stations (WB, WC, and WD) and river stations (R1, R2 and R3) during the middle monsoon season. Note. The 0-hour starts at 1:25 pm on 4 December 2022, and the 660-hour ends at 1:25 am on 1 January 2023

within the wetland, but the soil texture also influenced it. Moreover, the embankment demonstrated the anthropogenic effect on the natural ecosystem.

Low Ground-level Wetland Stations During the Mid-monsoon Season

Both high tides and rainfall events impacted all stations. The water level of WA ranged from 1.234 m to 2.315 m NGVD during the flood event (Figure 10). WA stations got excess water from R3, as the R3 water level was at 2.360 m NGVD, making the water flow from R3 to WA. There was a strong correlation between this station and R1 ($r = 0.67$, $p < 0.001$), R2 ($r = 0.79$, $p < 0.001$), and R3 ($r = 0.75$, $p < 0.001$). The salinity range at this site varied from 2.924 ppt to 4.113 ppt due to dissolved minerals in the natural environment of freshwater.

The WE station's initial water level measurement was 1.863 m NGVD. However, the water level rose to 2.304 m NGVD during the flood. This station exhibited a positive correlation with R1 ($r = 0.64$, $p < 0.001$), R2 ($r = 0.77$, $p < 0.001$), and R3 ($r = 0.73$, $p < 0.001$). The salinity at this site ranged from 8.126 ppt to 10.186 ppt, indicating some saline intrusions.

The correlation coefficients between WF and R1 ($r = 0.79$, $p < 0.001$), R2 ($r = 0.88$, $p < 0.001$), R3 ($r = 0.85$, $p < 0.001$) were all strong positive. During flood events, the WF water level ranged from 1.737 m to 2.171 m NGVD. The rise in river water levels during the flood increased groundwater levels at low ground-level stations.

During the middle monsoon season, the low ground-level wetland stations were affected by river overflows. The high rainfall amount (668.9 mm) from 4 to 19 December 2022 (1:25 pm and 12:00 pm, respectively) led to the flood event (Figure 10). However, the water levels of WA, WE, and WF stations decreased after the flood, following the decrease in river water levels. This showed that the low ground-level stations discharged excess water quickly and had a short flood retention time. From 19 to 23 December 2022, rainfalls (387.2 mm in total) and a transition from neap to spring tides caused the groundwater level to increase. These low ground-level wetland stations were affected by spring high tides primarily after that, as there was essentially no rainfall event (Figure 10).

There are no previous studies on coastal BRIS wetland hydrodynamics for direct comparison. Nonetheless, an indirect comparison can be made with peatlands. Peatlands are rain-fed, and coastal BRIS wetlands are essentially river-fed, as demonstrated by the results of these studies. Research on peatlands in Kuantan, Pahang, and West Kalimantan, Indonesia, demonstrated a clear seasonal water retention pattern during the northeast monsoon (Wetland International, 2010; Marwanto et al., 2018). In contrast, in this study area, wetland groundwater level changes coincided with changes in river water levels caused by tidal intrusions/recessions and upstream river flow. Hence, coastal BRIS wetlands might not be able to retain water for prolonged periods like peatlands.

Table 2 summarises water level measurements across the non-monsoon, early monsoon, and mid-monsoon seasons for wells on higher and lower wetland grounds. Table 3 shows

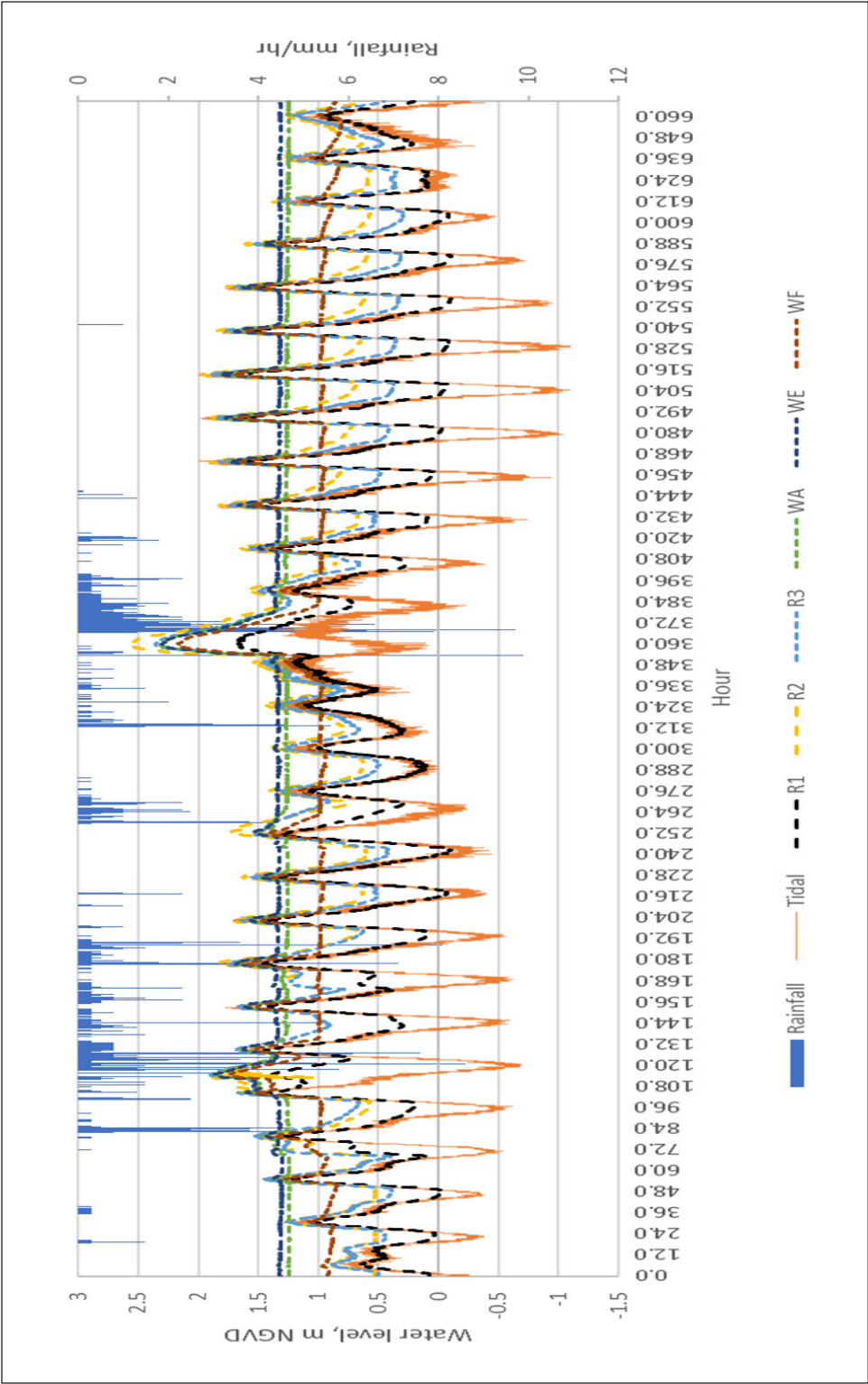


Figure 10. Water levels of low-ground wetland stations (WA, WE, and WF) and river stations (R1, R2 and R3) during the middle monsoon season
Note. The 0-hour starts at 1:25 pm on 4 December 2022, and the 660-hour ends at 1:25 am on 1 January 2023

the correlations between wells, river stations and tidal data. The elevated ground locations were near the ridge line of the beach ridge, whereas the lower ground sites were positioned adjacent to the river. This investigation revealed that the quantity of rainfall significantly influenced high-ground-level stations. These stations received rainfall recharge via sub-surface flow from the ridge area. The ridge consisted of sand sediments; hence, it has a high infiltration rate and hydraulic conductivity, creating higher sub-surface flow compared to surface runoffs. In comparison, river water levels primarily influenced low-ground level stations, which correlated with tidal fluctuations. Table 2 also indicates the percentage change in water level by comparing average levels during the mid-monsoon season with those observed during the non-monsoon season.

These variations indicated the water level retained during the mid-monsoon period at each station. WF stations demonstrated a notably higher percentage change, followed by WD stations. WF station was located at a low ground level adjacent to the river. While the WD station was located at a high ground level, the groundwater level was affected by sub-surface flow from the adjacent ridges. This suggests that water from the ridges moves downwards through the subsurface, recharging the groundwater at the WD station. The river's tidal fluctuation influenced the groundwater level indirectly, as indicated by a weaker correlation between tidal and groundwater levels, with an average of $r = 0.22$. In contrast, tidal and river water levels showed a strong average of $r = 0.81$ (Table 3). River water levels generally rose during high tide and fell during low tide, except for flooding caused by upstream outflows resulting from heavy rainfalls. This phenomenon is

Table 2
Water level ranges, averages and changes during non-monsoon, early monsoon, and middle monsoon seasons at high ground level wetland stations and low ground level wetland stations

Station / Ground level	WC 2.02	WD 1.63	WB 1.60	WA 1.30	WE 1.21	WF 1.09
	High-ground-level wetland stations			Low ground-level wetland stations		
Water level Non-monsoon season	1.967–2.091 (2.042)	1.554–1.638 (1.577)	1.475–1.658 (1.563)	1.216–1.514 (1.251)	1.282–1.493 (1.310)	0.589–1.431 (0.861)
Water level Early monsoon season	2.068–2.10 (2.084)	1.551–1.610 (1.580)	1.578–1.669 (1.602)	1.237–1.553 (1.257)	1.276–1.535 (1.302)	0.761–1.451 (0.937)
Water level Middle monsoon season	2.041–2.314 (2.070)	1.639–2.379 (1.908)	1.521–2.341 (1.628)	1.234–2.315 (1.327)	1.296–2.304 (1.381)	0.804–2.171 (1.072)
Water level changes	0.028	0.331	0.065	0.076	0.071	0.211
Water level changes (%)	1.37	20.98	4.15	6.07	5.41	24.50

Notes. Values in brackets are average water levels. All water levels and ground levels are in meter NGVD. Water level changes in meters were determined by subtracting the average water level during the non-monsoon season from the average of the middle monsoon season.

Table 3
Water level correlation analysis of river station (R1–R3) wetland station (WA–WF) and tide station during three different seasons: (A) the non-monsoon season, (B) early monsoon season and (C) middle monsoon season

A	Tidal	R1	R2	R3	WA	WB	WC	WD	WE	WF
Tidal	NR									
R1	0.86	NR								
R2	0.76	0.96	NR							
R3	0.81	0.99	0.97	NR						
WA	0.32	0.48	0.52	0.52	NR					
WB	-0.06	0.04	<u>0.01</u>	0.09	0.32	NR				
WC	-0.01	0.13	0.09	0.15	0.26	0.58	NR			
WD	-0.01	-0.12	-0.12	-0.08	0.01	0.33	-0.31	NR		
WE	0.27	0.45	0.49	0.52	0.87	0.56	0.39	0.10	NR	
WF	0.44	0.59	0.66	0.61	0.54	-0.11	-0.13	-0.05	0.38	NR
B	Tidal	R1	R2	R3	WA	WB	WC	WD	WE	WF
Tidal	NR									
R1	0.92	NR								
R2	0.85	0.97	NR							
R3	0.83	0.97	0.98	NR						
WA	0.44	0.55	0.62	0.61	NR					
WB	0.10	0.26	0.28	0.37	0.27	NR				
WC	0.15	0.21	0.22	0.25	0.28	0.06	NR			
WD	0.08	0.12	0.10	0.13	<u>0.02</u>	0.63	-0.35	NR		
WE	0.46	0.60	0.65	0.66	0.93	0.45	0.20	0.23	NR	
WF	0.50	0.66	0.72	0.75	0.78	0.51	0.24	0.22	0.81	NR
C	Tidal	R1	R2	R3	WA	WB	WC	WD	WE	WF
Tidal	NR									
R1	0.84	NR								
R2	0.70	0.94	NR							
R3	0.70	0.96	0.97	NR						
WA	0.32	0.67	0.79	0.75	NR					
WB	0.17	0.50	0.67	0.63	0.87	NR				
WC	0.09	0.30	0.45	0.41	0.58	0.81	NR			
WD	<u>-0.02</u>	-0.02	0.14	-0.06	0.12	0.02	-0.11	NR		
WE	0.31	0.64	0.77	0.73	0.99	0.89	0.62	0.11	NR	
WF	0.47	0.79	0.88	0.85	0.95	0.80	0.53	0.06	0.93	NR

Notes. Underscored numbers have a p-value equal to or greater than 0.05, indicating an insignificant correlation. The rest of the results are significant because the p-values are less than 0.05. If the r value is near +0.5, it means a moderate corresponding relationship. If the r value is near -0.5, it means a moderate inverse relationship. If the r value is near +1, it means a strong corresponding relationship. If the r value is near -1, it means a strong inverse relationship. If the positive r value is near 0, it means a weak corresponding relationship. If the negative r value is near 0, it means a weak inverse relationship

understandable as the rivers are connected to the sea as open channels and hence exposed to daily tidal intrusions and recessions. In contrast, wetland groundwater was flowing through the wetland's sediment layer. In comparison, the lower section of the wetland was more influenced by river water level changes than the higher section. During the non-monsoon season, the average correlation between the low-ground wells (WA, WE and WF) with river water levels was 0.54 (r ranged from 0.45 to 0.66). In contrast, the high ground stations (WB, WC and WD) were just 0.02 (r ranged from -0.12 to 0.15) and showed negative correlations. During monsoon season, the lower section was even more influenced, with an average strong r of 0.76. The higher section also experienced greater hydraulic connectivity, as demonstrated by a higher average r of 0.34.

CONCLUSION

Rainfalls and river water levels influenced the behaviour of BRIS coastal wetland groundwater levels during both non-monsoon and northeast monsoon seasons. The study's results indicated that tidal oscillations had a strong correlation with river water level changes, with correlation coefficients (r) ranging from 0.7 to 0.92 and an average of 0.81. This strong relationship is characteristic of tidal rivers, where tidal oscillation significantly modulates river water levels. However, the effect of tidal oscillations on groundwater level changes was found to be relatively weak, with an average correlation coefficient of 0.22. This weak correlation suggests that tidal oscillations partially influence groundwater levels, primarily through their effects on river water levels, which propagate into the subsurface hydrological system. River water levels, although strongly influenced by tidal oscillations, were also found to be dependent on upstream flows, particularly during periods of increased rainfall. This dual dependence highlights the role of upstream discharge in modulating river hydrodynamics and, consequently, their influence on the surrounding wetland.

The lower section of the wetland, as evidenced by data from monitoring wells (WA, WE, and WF), exhibited a stronger response to river water level changes, with an average correlation coefficient of 0.54. During the monsoon season, this influence became even more pronounced, with the average correlation increasing to 0.76. This heightened connectivity during monsoon conditions was likely due to elevated river water levels caused by increased upstream discharge from heavy monsoonal rainfall, which enhanced hydraulic connectivity between the river and the wetland. In contrast, the higher section of the wetland, located nearer to the ridge, showed a much weaker influence from river water levels, with an average correlation coefficient of 0.18. However, even in this elevated region, the influence of river water levels increased during the monsoon season, with the average correlation rising to 0.34. This suggests that during periods of high rainfall and elevated river levels, the hydraulic connectivity between the river and the higher section of the wetland increases, allowing for greater interaction between surface and subsurface water systems. The study

also revealed that fluctuations in river water levels, largely driven by tidal oscillations, are crucial in regulating the wetland's groundwater dynamics, irrespective of the season.

However, the overall groundwater level changes in the wetland were generally limited to approximately 0.5 m below ground level. This limited fluctuation indicates that the wetland system is relatively shallow and constrained in its capacity to store or regulate large volumes of water. Furthermore, low-lying areas adjacent to the rivers were frequently observed to be either saturated or inundated, particularly during high river levels or flood events. This persistent saturation of the wetland soil reduced its ability to act as a prolonged floodwater retention system, further highlighting its limitations as a natural flood mitigation mechanism. Given these findings, the BRIS wetland's effectiveness in retaining flood waters and controlling floods might be significantly constrained by its shallow groundwater table and high degree of soil saturation. These limitations were particularly evident during periods of heavy rainfall and flooding when the capacity for water storage in the vadose zone exceeded. Future research could investigate the impact of soil texture, porosity, and infiltration rates on the hydrodynamic behaviour of BRIS wetlands. Such studies would provide valuable insights into the physical properties of the wetland soil and their influence on water retention capacity, potentially contributing to developing strategies to enhance the flood control functionality of BRIS wetlands.

ACKNOWLEDGMENT

We thank the University Malaysia Terengganu (UMT) for allowing us to conduct this research project on campus. The first author also thanks the UiTM Negeri Sembilan Branch for funding this project.

REFERENCES

- Abdullahi, M. G., & Garba, I. (2016). Effect of rainfall on groundwater level fluctuation in Terengganu, Malaysia. *Journal of Remote Sensing and GIS*, 4(2), 142-146. <http://dx.doi.org/10.4172/2169-0049.1000142>
- Aish, A. (2010). Simulation of groundwater mound resulting from proposed artificial recharge of treated sewage effluent case study - Gaza waste water treatment plant, palestine. *Geologia Croatica*, 63(1), 67-73.
- Ariffin, E. H., Sedrati, M., Akhir, M. F., Norzilah, M. N. M., Yaacob, R., & Husain, M. L. (2019). Short-term observations of beach morphodynamics during seasonal monsoons: Two examples from Kuala Terengganu coast (Malaysia). *Journal of Coastal Conservation*, 23, 985-994. <https://doi.org/10.1007/s11852-019-00703-0>
- Arrifin, E. H., Sedrati, M., Akhir, M. F., Yaacob, R., & Husain, M. L. (2016). Open sandy beach morphology and morphodynamic as response to seasonal monsoon in Kuala Terengganu, Malaysia. *Journal of Coastal Research*, (75), 1032-1036. <https://doi.org/10.2112/SI75-207.1>
- Bakar, A. E., Johari, N. N., Ali, Q. A., & Othman, R. (2023). Bris soil: Natural vegetation and potential cultivated plants. In *Advantages and Disadvantages of Sandy Soils* (pp. 181-207). Nova Science Publishers, Inc.

- Cai, Y., Huang, R., Xu, J., Xing, J. T., & Yi, D. (2022). Dynamic response characteristics of shallow groundwater level to hydro-meteorological factors and well irrigation water withdrawals under different conditions of groundwater buried depth. *Water*, 14(23), Article 3937. <https://doi.org/10.3390/w14233937>
- Curtis, Z. K., Li, S. G., Liao, H. S., & Lusch, D. P. (2017). Data-driven approach for analyzing hydrogeology and groundwater quality across multiple scales. *Groundwater*, 56(3), 377-398. <https://doi.org/10.1111/gwat.12584>
- Ensign, S. H. (2013). The effect of tide on the hydrology and morphology of a freshwater river. *Earth Surface Processes and Landforms*, 38(6), 655-660. <https://doi.org/10.1002/esp.3392>
- Gao, J., Wang, R., Huang, J., & Liu, M. (2015). Application of BMP to urban runoff control using SUSTAIN model: Case study in an industrial area. *Ecological Modelling*, 318, 177-183. <https://doi.org/10.1016/j.ecolmodel.2015.06.018>
- Gleeson, T., Marklund, L., Smith, L., & Manning, A. H. (2011). Classifying the water table at regional to continental scales. *Geophysical Research Letters*, 38(5), 1-6. <https://doi.org/10.1029/2010GL046427>
- Hossain, M., Hanafi, M., Jol, H., & Jamal, T. (2011). Dry matter and nutrient partitioning of kenaf (*Hibiscus cannabinus* L.) varieties grown on sandy bris soil. *Australian Journal of Crop Science*, 5(6), 654-659.
- Hsieh, P., Huang, J., & Wu, M. (2020). Response of groundwater levels in a coastal aquifer to tidal waves and rainfall recharge. *Water*, 12(3), Article 625. <https://doi.org/10.3390/w12030625>
- Ikbāl, I. M., Din, H. H., Tuah, W. H., Jaafar, S. M., Ahmad, N., & Sukri, R. S. (2023). Review: Diversity, structure, and community composition of Bornean heath forest with a focus on Brunei Darussalam. *Biodiversitas*, 24(5), 2814-2829. <https://doi.org/10.13057/biodiv/d240535>
- Ishaq, U. M., Umara, B., Armanto, M. E., & Arshad, A. M. (2019). Assessment and evaluation of bris soil and its implication on maize crop in Merang-Terengganu Region of Malaysia. *Journal of Biology, Agriculture and Healthcare*, 4(5), 69-76.
- Ismail, N. I., Ariffin, E. H., Yaacob, R., Husain, M. L., & Baharim, N. B. (2020). The impact of seasonal monsoons on the morphology of beaches protected by barrier islands in Setiu, Terengganu, Malaysia. *Journal of Sustainability Science and Management*, 15(4), 120-129.
- Jolly, I., McEwan, K., & Holland, K. L. (2008). A review of groundwater-surface water interactions in arid/semi-arid wetlands and the consequences of salinity for wetland ecology. *Ecohydrology*, 1(1), 43-58. <https://doi.org/10.1002/eco.6>
- Kamoonā, S., Ramya, R., Daud, W., Hatta, F., & Othman, R. (2023). Properties of sandy soil and allelochemical compounds of heath forest in rantau abang, terengganu, malaysia: Implication for ecological sustainability and biodiversity conservation. *International Journal of Innovative Research and Scientific Studies*, 6(2), 344-357. <https://doi.org/https://doi.org/10.53894/ijirss.v6i2.1432>
- Koh, M. K., Sathiamurthy, E., & Parham, P. R. (2018). Groundwater processes in a sandbar-regulated estuary, Mengabang Telipot, Peninsular Malaysia. *Bulletin of the Geological Society of Malaysia*, 66, 39-46.
- Lah, M. K. C., Nordin, M. N., ISa, M. M., Khanif, Y. M., & Jahan, S. M. (2011). Composting increases BRIS soil health and sustains rice production. *Science Asia*, 37(4), 291-295. <https://doi.org/10.2306/scienceasia1513-1874.2011.37.291>

- Marwanto, S., Watanabe, T., Iskandar, W., Sabiham, S., & Funakawa, S. (2018). Effects of seasonal rainfall and water table movement on the soil solution composition of tropical peatland. *Soil Science and Plant Nutrition*, 64(3), 386-395. <https://doi.org/10.1080/00380768.2018.1436940>
- McCleskey, R. B., Nordstrom, D. K., & Ryan, J. N. (2011). Eelectrical conductivity method for natural waters. *Applied Geochemistry*, 26, S227-S229. <https://doi.org/10.1016/j.apgeochem.2011.03.110>
- Meng, X., Wang, J., Yang, Y., & Yang, L. (2022). Groundwater Response to tide fluctuation and rainfall in coastal reclamation area. *Lithosphere*, 2022, Article 6294524. <https://doi.org/10.2113/2022/6294524>
- Mitsch, W. J., & Gosselink, J. G. (2015). *Wetland*. John Wiley and Sons.
- Moffett, K. B., Gorelink, S. M., McLaren, R. G., & Sudicky, E. A. (2012). Salt marsh ecohydrological zonation due to heterogeneous. *Water Resources Research*, 48(2). <https://doi.org/10.1029/2011WR010874>
- Mohamad, I. C., Samsudin, A. R., & Rafek, A. G. (2002, May 26-27). Perubahan fasies hidrokimia dalam akuifer aluvium pantai: Kajian kes di kawasan Pekan-Nenasi, Pahang. In *Geological Society of Malaysia Annual Geological Conference* (pp. 23-30). Kelatan, Malaysia.
- Othman, M. A., Ghani, A. A., & Othman, M. S. A. (2020). Distribution of rainfall events in northern region of Peninsular Malaysia. In *IOP Conference Series: Earth and Environmental Science* (Vol. 476, No. 1, p. 012116). IOP Publishing. <https://doi.org/10.1088/1755-1315/476/1/012116>
- Pang, Z., Huang, T., & Chen, Y. (2009). Diminished groundwater recharge and circulation relative to degrading riparian vegetation in the middle Tarim River, Xinjiang Uygur, Western China. *Hydrological Processes*, 24(2), 147-159. <https://doi.org/10.1002/hyp.7438>
- Pirani, F. J., & Najafi, M. R. (2020). Recent trends in individual and multivariate compound flood drivers in Canada's coasts. *Water Resources Research*, 56(8). <https://doi.org/10.1029/2020WR027785>
- Revitt, M., Ellis, B., & Lundy, L. (2017). Assessing the impact of swales on receiving water quality. *Urban Water Journal* 14(8), 839-845. <https://doi.org/10.1080/1573062X.2017.1279187>
- Roslan, I. J. (2010). Occurrence and properties of soils on sandy beach ridges in the Kelantan Terengganu plains, peninsular Malaysia. *Catena*, 83(1), 55-63. <https://doi.org/10.1016/j.catena.2010.07.004>
- Salim, J. M., Nur-Faiezah, A. G., Kehirah, A. S., Nowal, M., & Salam, M. R. (2014). Woody plants on dune landscape of Terengganu, peninsular Malaysia. *Journal of Tropical Forest Science*, 26(2), 267-274.
- Sathiamurthy, E., Min, K. K., Ishak, M. Z., Nagappan, L., & Chuen, Y. J. (2021). Rainfalls and salinity effects on fecal coliform Most Probable Number (MPN) Index distribution in a beach ridge-shore ridge system in Mengabang Telipot, Terengganu, Malaysia. *Bulletin of the Geological Society of Malaysia*, 71, 203-213.
- Sathiamurthy, E., & Pauzi, N. S. (2020). Flow velocity model for a coastal estuarine sandbar using multivariate regression. *Bulletin of the Geological Society of Malaysia*, 69, 89-95.
- Toriman, M. E., Mokhtar, M., Gazim, M. B., & Aziz, N. A. A. (2009). Analysis of the physical characteristics of bris soil in coastal Kuala Kemaman, Terengganu. *Environmental Science, Geography*, 1(1), 1-6.
- Touchette, B. W., Adams, E. C., Laimbeer, P., & Burn, A. G. (2011). Ridges crest versus swale: Contrasting plant-water relations and performance indexes in two understory plant species in a coastal maritime forest. *Journal of Plant Interactions*, 7(3), 271-282. <https://doi.org/10.1080/17429145.2011.603061>

- Westra, S., Fowler, H. J., Evans, J. P., Alexander, L. P., Berg, P., Johnson, F., Kendon, E.J., Kenderik, G., & Roberts, N. M. (2014). Future changes to the intensity and frequency of short-duration extreme rainfall. *Reviews of Geophysics*, 52(3), 522-555. <https://doi.org/10.1002/2014RG000464>
- Wetland International. (2010). *A Quick Scan of Peatlands in Malaysia*. Wetlands International Malaysia.
- Wilopo, W., & Putra, D. P. (2021). Groundwater recharge estimation using groundwater level fluctuation patterns in unconfined aquifer of yogyakarta city, indonesia. *Kuwait Journal of Science*, 48(2). <https://doi.org/10.48129/kjs.v48i2.9397>
- Xu, C., Sun, Y., Shi, B., Wang, X., Li, R., Li, M., Xi, B., & Feng, C. (2022). Study on the processes influencing and importance of ecological water replenishment for groundwater resources: A case study in yongding river. *Water*, 14(5), Article 828. <https://doi.org/10.3390/w14050828>
- Zakaria, N. H., Nordin, M. S., Ibrahim, M. A., Majid, F. A., & Zainuddiin, Z. (2023). Genetic diversity and proteomic analysis of vegetable soybean [*Glycine max* (L.) Merrill] accessions grown in mineral and BRIS soils. *Czech Journal of Genetics and Plant Breeding*, 59(1), 14-22. <https://doi.org/10.17221/38/2022-CJGPB>
- Zhang, X., Jiao, J. J., & Guo, W. (2022). How does topography control topography-driven groundwater flow? *Geophysical Research Letters*, 49(20). <https://doi.org/10.1029/2022GL101005>
- Zhang, Y., & Najafi, M. R. (2020). Probabilistic numerical modeling of compound flooding caused by tropical storm matthew over a data-scarce coastal environment. *Water Resources Research*, 56(10). <https://doi.org/10.1029/2020WR028565>

AI-driven Vision-based Pothole Detection for Improved Road Safety

Muhammad Aizat Rasee¹, Ung Ling Ling^{2*}, Gloria Jennis Tan¹, Tan Chi Wee³, Ron Buking⁴, Norziana Yahya⁵ and Habibah Ismail⁶

¹College of Computing, Informatics and Mathematics, Universiti Teknologi MARA Terengganu Branch, Kuala Terengganu Campus, 21080 Kuala Terengganu, Terengganu, Malaysia

²College of Computing, Informatics and Mathematics, Universiti Teknologi MARA Sabah Branch, Kota Kinabalu Campus, 88997 Kota Kinabalu, Sabah, Malaysia

³Department of Computer Science and Embedded System, Tunku Abdul Rahman University of Management and Technology, 53300 Setapak, Kuala Lumpur, Malaysia

⁴Faculty of Engineering, Universiti Malaysia Sarawak, 94300 Kota Samarahan, Sarawak, Malaysia

⁵College of Computing, Informatics and Mathematics, Universiti Teknologi MARA Perlis Branch, Arau Campus, 02600 Arau, Perlis, Malaysia

⁶Pusat Asasi, Universiti Teknologi MARA Selangor Branch, Dengkil Campus, 43800 Dengkil Selangor, Malaysia

ABSTRACT

Cracked and potholed roads frequently cause deadly accidents, posing serious safety risks and significant maintenance expenses. Vehicles hitting potholes can damage road furniture, increase maintenance costs, and leave road users with significant repair expenditures for their vehicles. Drivers feel insecure and uncomfortable when continually monitoring road conditions to avoid potholes, which detracts from their entire driving experience. This project seeks to create a Pothole Detection System that employs Convolutional Neural Network (CNN) algorithms to explore feature extraction approaches for identifying road potholes. The model was trained with CNN algorithms to identify photos as a pothole or normal, and You Only Look Once (YOLO) to detect and estimate pothole areas. Two datasets were joined to create a cohesive dataset with 681 images from the

first and 4000 images from the second, for 4681 images. These pictures, divided between potholed and typical roads, were cleaned and resized to 256×256 pixels. The dataset was split into two groups: 70% training and 20% testing. Roboflow Annotate was used to annotate images. Following data preparation, the CNN and YOLO algorithms were created independently. The CNN-YOLO model had an accuracy rate of 92.85%. This project increases road safety, infrastructure upkeep, and traffic flow. The

ARTICLE INFO

Article history:

Received: 29 August 2024

Accepted: 12 February 2025

Published: 23 April 2025

DOI: <https://doi.org/10.47836/pjst.33.3.20>

E-mail addresses:

2022801012@isiswa.uitm.edu.my (Muhammad Aizat Rasee)

ungli720@uitm.edu.my (Ung Ling Ling)

gloria@uitm.edu.my (Gloria Jennis Tan)

chiwee@tarc.edu.my (Tan Chi Wee)

acron@unimas.my (Ron Buking)

norzianayahya@uitm.edu.my (Norziana Yahya)

habibahismail@uitm.edu.my (Habibah Ismail)

* Corresponding author

pothole detection technology warns drivers about potential road hazards, decreasing accidents and fatalities. Efficient detection allows for preventive, cost-effective road maintenance, optimises government resource allocation, and enhances the driving experience by lowering car maintenance costs and assuring safer roads.

Keywords: Convolutional Neural Network, pothole detection, preventive maintenance, road safety, vision-based detection, YOLO algorithm

INTRODUCTION

Roads are essential transportation arteries, contributing significantly to any region's economic and social development. They make it easier to move people, commodities, and services, which boosts trade and connection. Well-maintained roads stimulate economic growth by shortening travel times, saving vehicle operating costs, and enhancing access to markets and services. Furthermore, good road infrastructure encourages social contact and provides access to critical services like healthcare and education. Preserving road quality should be prioritised because lousy road conditions can have severe economic and social consequences. According to the Public Works Department (*Jabatan Kerja Raya-JKR*), maintaining good road conditions is critical to preserving the safety and efficiency of transportation networks (Othman, 2023).

Despite the vital role of roads, many places, mainly rural areas, need more maintenance, resulting in road damage such as cracks and potholes. These deteriorated roads offer serious safety issues, frequently leading to accidents and higher vehicle repair costs. According to the Ministry of Public Works, as of November 2023, the MYJalan application had received 4,935 complaints about road concerns, 425 of which were for potholes and 249 concerning other road damage (KKR, 2023). Road maintenance and repair costs are significant and affect government budgets and individual road users. Poor road conditions also impair traffic flow, causing congestion and delays that increase economic losses.

Potholes, which are bowl-shaped depressions in the road surface, are a major issue in Malaysia. They are often formed by minor fractures that grow over time due to water infiltration, traffic stress, and freeze-thaw cycles (Golos, 2024). Poor road management, excessive vehicle traffic, and industrial activity all contribute to the production of potholes in Malaysia. Potholes not only endanger drivers but also raise car maintenance costs. Areas with considerable industrial activity, such as manufacturing and construction zones, are especially vulnerable to severe road damage. The frequency of potholes in areas such as Sabah and Sarawak emphasises the importance of appropriate road repair measures to ensure the safety and efficiency of transportation networks (Manzor, 2021).

The fundamental issue raised in this study is the enormous safety risk created by potholes on Malaysian highways. Poor road conditions were associated with 223 incidents from 2018 to 2020, with 148 fatalities (Noh, 2021). Potholes can cause serious accidents,

particularly for motorcyclists, who are less protected than drivers in other vehicles. The problem is exacerbated during inclement weather and at night when visibility is reduced. Addressing pothole-related issues is critical for improving road safety, lowering accident rates, and limiting economic losses due to car repairs and traffic congestion.

This study aims to create a Pothole Detection System that efficiently identifies road potholes using Convolutional Neural Network (CNN) techniques. The method uses deep learning algorithms to extract information from photographs of road surfaces, allowing for reliable pothole detection. The proposed system's accuracy is also evaluated using a confusion matrix, which ensures the detection process's reliability. The ultimate goal is to deliver a robust system that improves road safety, optimises maintenance operations, and lowers the economic cost of road damage.

This research helps to improve road safety and infrastructure upkeep by tackling the problem of pothole identification using innovative technology techniques. The planned Pothole Detection System alerts drivers to possible road risks and enables timely and cost-effective road repairs. This technique ensures better use of government resources, lowers vehicle maintenance costs and improves the overall driving experience by keeping roads safer and smoother.

BACKGROUND OF STUDY

Pothole Detection System

Potholes, which are bowl-shaped depressions on road surfaces with a minimum dimension of 150mm, pose significant risks to drivers, causing vehicle damage, accidents, and even fatalities (Kaushik & Kalyan, 2022). Climate change, high traffic volume, and inadequate road maintenance are all factors that contribute to pothole formation. Recognising the importance of road safety, there is a rising effort to create effective pothole-detecting systems that use artificial intelligence (AI) technology. Traditional manual pothole detection methods are time-consuming, expensive, and ineffective. For example, taking photographs over several days and having engineers analyse the damage results in longer repair timeframes and higher expenditures. Integrating deep learning (DL) with pavement systems presents a viable option. The pothole detecting system usually includes segmentation, candidate region extraction, and result creation. Images gathered using optical devices on automobiles are processed and matched using predetermined algorithms to detect potholes (Sharma et al., 2023).

Automated pothole detection systems typically involve four steps: data collecting, preprocessing, feature extraction, and pothole classification (Kim et al., 2022). Data acquisition is obtaining raw data, such as photographs or sensor data, to create a dataset. Data preprocessing refines data by employing techniques such as filtering and masking to aid learning or analysis. Feature extraction identifies elements that separate potholes from non-potholes in preprocessed data. In contrast, pothole classification detects potholes

using these features. Various automatic detection methods are used, including vision-based, vibration-based, and 3D reconstruction methods. Vision-based approaches locate potholes using image processing and deep learning. While they are cost-effective, they have limitations in terms of depth measurement. Vibration-based approaches use acceleration sensor data to estimate pothole existence and depth; however, they may be inaccurate in form identification. 3D reconstruction approaches use stereo vision technology to offer accurate pothole volume estimations, but they are more expensive and complicated (Lincy et al., 2023).

Potholes are detected using various methods and technology, including sensors like cameras and accelerometers mounted on vehicles. These methods are classified into four types: vibration-based methods, 3D methods, vision-based methods, and deep learning methods that use 3D point clouds. Vibration-based approaches, often known as “Pothole Patrol,” identify potholes using acceleration data from sensors, needing a vehicle outfitted with many sensors and a central computer. Stereo vision, geometric interactions between cameras, and lidar are used in 3D ways to obtain precise 3D point cloud data, as are multi-sensor combinations such as Kinect and structured light sensors. Vision-based methods, such as 2D image-based systems, rely on single frames and require additional algorithms to detect and count potholes (Kaushik & Kalyan, 2022). Deep learning approaches for 3D point cloud data use advanced algorithms such as Region-based CNN, Range Image-Based Method, Graph-based Network, and PointNet-based Architecture to achieve more precise detection. However, estimating the depth of potholes filled with gravel, sand, pebbles, or water presents hurdles, needing image processing techniques to appropriately classify road conditions (Bhamare et al., 2021). Ultrasonic sensors, LiDAR, accelerometers, and cameras are standard pothole-detecting sensors, each with its own advantages for identifying and monitoring road damage.

Calculation Estimation Module

Potholes pose notable threats to road users, demanding advances in detection and treatment techniques. Recent studies highlighted the importance of AI in improving pothole detection and categorisation accuracy and efficiency. Deep learning techniques, specifically convolutional neural networks (CNNs), rapidly enhance classic pothole detection approaches. For example, Ranyal et al. (2023) created a pothole identification system that uses a modified RetinaNet CNN algorithm with 3D vision to evaluate pothole depth. This technique uses CNNs to recognise and localise potholes in video frames before generating a 3D point cloud with structure-from-motion (SfM) photogrammetry to compute depth. The approach uses the RDD2020 pavement image dataset, which includes photos from Japan, India, and the Czech Republic. It achieves an average depth measurement error of less than 5% while maintaining excellent detection accuracy (98%).

Additional improvements in pothole repair include computer vision technologies for cost prediction. Hossain et al. (2023) used YOLOv4-small and Deep SORT to estimate pothole detection and repair expenses. Their method entails teaching the algorithm to detect potholes and estimate repair costs by drawing bounding boxes around identified anomalies. The average accuracy of area measurement is 66.02%, with potential improvements of up to 97.42% depending on where the pothole is in the frame. The study determines repair costs by multiplying the area of discovered potholes by a repair cost per square foot of USD 12.

Halim et al. (2022) investigated another method for estimating pothole dimensions using YOLO. Their investigation entails taking photographs with a camera placed 80 to 100 cm above the pavement at a 60-degree angle. The photos are processed to determine pothole length and width, which aids in accurate repair cost projections. For optimal detection effectiveness, the YOLO algorithm in this work requires training and test sets, as well as scaled and labelled images.

Arjapure and Kalbande (2021) introduced a method for determining pothole areas using the Mask R-CNN algorithm, combining object identification and mask prediction to identify assigned regions of interest (ROI). Their approach separates photos into two sets: 240 for training and 51 for testing. The pixel size is calculated using the field of view and the image resolution. On the other hand, area calculation takes the number of pixels from the prediction mask and the pixel size into account, as well as any deviation or error calculations. Manual picture annotation is done with the VGG picture Annotator tool, and the Mask R-CNN model provides prediction masks for area measurement. The study accurately calculates the geometric characteristics of potholes in cm². It compares computed areas to actual physical measurements, confirming Mask R-CNN's effectiveness in accurately estimating pothole areas.

Table 1 presents similar works on potholes detection by using other algorithms. And Table 2 depicts the implementation of convolutional neural network algorithm in pothole detection system.

METHODOLOGY

The principles of model design were carefully considered to develop a robust and efficient pothole detection system. Leveraging existing research, a CNN-YOLO8 hybrid approach was chosen due to its proven effectiveness in extracting and recognising complex visual features. CNN was employed for feature extraction because of its ability to analyse hierarchical patterns in images, making it ideal for detecting cracks and potholes with varying textures and shapes. On the other hand, YOLO was integrated for its capability to perform real-time object detection with high accuracy, ensuring the system's practical applicability in real-world scenarios. This architecture addresses the need for a fast and reliable solution to efficiently classify and detect road defects.

Table 1
Similar works on potholes detection by using other algorithms

No.	Title	Problem	Objective	Algorithm	Dataset	Result	References
1.	Detection and Classification of Road Damage Using a Camera with GLCM and SVM	Proposing the challenges of road damage detection and classification	To develop a Road Damage Detection System that can detect various types of road damage, including potholes, cracks, distortions, fatness, and polish aggregates, using Gray Level Co-Occurrence Matrix (GLCM) and Support Vector Machine (SVM) algorithms	Support Vector Machine (SVM)	100 images of road damage and 199 data points	Accuracy: 80% The F1 score for potholes of 0.95, cracks of 0.89, distortion of 0.8, fatness of 0.89, and polished aggregate of 0.95	Sartika et al., 2023
2.	Road Pothole Detection Using Smartphone Sensors	Due to accidents related to potholes in India, many injuries and deaths occur every year	Develop a system that can detect potholes using sensors built into smartphones that can reduce the frequency of accidents related to potholes	Random Forest (RF)	Using the installed CarSense app, which is placed on the car's dashboard in real-time	Accuracy: 91.85% The training-testing split ratio of the dataset is 80:20	Kumar et al., 2023
3.	Detection of potholes for repair works of asphalt flexible pavement optimisation using YOLO	Manually tracing and inspecting road surfaces is a tedious, time-consuming, laborious and dangerous process for road surveyors	Assist road surveyors in detecting potholes using a deep learning approach	You Only Look Once (YOLO)	Apple iPhone 7 smartphone camera is used to capture road images	Accuracy: 80%. None	Halim et al., 2022
4.	Pothole-related Traffic Safety Detection based on Deep Learning	Discussion of road traffic safety is the focus	Develop an intelligent driving system focused on traffic safety based on pothole detection with detection for cars, traffic lanes and traffic signs	Mask Region-Based Convolutional Neural Network	Collect 1000 sample images	Accuracy: None The dataset is annotated using the VGG Image Annotator manual tool	Wang & Ho, 2022

Table 1 (continue)

No.	Title	Problem	Objective	Algorithm	Dataset	Result	References
5.	Deep Learning Model for Pothole Detection and Area Computation	The task of road maintenance and assessment is increasingly challenging	To accurately detect and segment such potholes to predict and calculate their area	Mask Region-Based Convolutional Neural Network	291 images were used, which were collected manually on the local roads of Mumbai city and nearby highways	Accuracy: 90% The dataset is annotated using the VGG Image Annotator manual tool	Arijapure & Kalbande, 2021

Table 2
Implementation of convolutional neural network algorithm in pothole detection system

No.	Title	Problem	Objective	Algorithm	Dataset	Result	References
1.	Convolutional neural network for pothole detection in different road and weather conditions	Pothole identification on roadways can lead to accidents and fatalities. The paper addresses the necessity for an effective and comprehensive pothole-detecting system to improve road safety.	To develop a deep learning algorithm for pothole identification and evaluate the performance of Sigmoid and Softmax activation functions in developing Convolutional Neural Network (CNN) algorithms	Convolutional Neural Network (CNN)	The first dataset includes 500 samples obtained from Maeda et al. (2018) and Nienaber et al. (2015). The second dataset consists of 681 samples obtained from Kumar (n.d.). Finally, the third dataset has 650 samples from Bhutad and Patil (2022)	Accuracy: 96% When identifying pothole photos, the CNN algorithm with the Sigmoid activation function outperforms the CNN method with the Softmax activation function	Gazawy et al., 2023
2.	Pothole Detection Using Deep Learning Classification Method	Potholes on roads are a major cause of road accidents and vehicle damage. Detecting the potholes manually is time-consuming and inaccurate.	To use deep learning techniques and picture datasets to detect potholes on muddy roads and highways Create a web application to test the model and identify road conditions depending on the chosen model	Convolutional Neural Network (CNN)	1000 images are collected from the internet sources (muddy roads) dataset, and another dataset is from the Kaggle (highway roads) dataset	Accuracy: 98% In comparison to the other two models, the VGG19 model achieved the highest accuracy of 97% for highway roads and 98% for muddy roads	Saisree & Kumaran, 2023

Table 2 (continue)

No.	Title	Problem	Objective	Algorithm	Dataset	Result	References
3.	CNN-based Real-time Pothole Detection for Avoidance Road Accident	The pervasive problem of road potholes has a severe influence on both the economy and society.	To enhance traffic safety and infrastructure upkeep by automating the detection of potholes in road images	Convolutional Neural Network (CNN)	Own dataset of road photographs, including images with and without potholes	Accuracy: 95.2% Achieved high accuracy in both pothole detection and segmentation on a large dataset of road images	Chorada et al., 2023
4.	Pothole Detection and Estimation of Repair Cost in Bangladesh Street: AI-based Multiple Case Analysis	A system that can identify potholes, estimate their size and repair cost, and offer a map of their location is needed.	To calculate the pothole repair cost using computer vision technology	Convolutional Neural Network (CNN)	665 RGB images taken from the Roboflow object identification dataset	Accuracy: 97.42% In four of the five instances, the AI-based model (69.57–85.00%) performed better than the human evaluator (43.67–80.67%)	Hossain et al., 2023
5.	A Comprehensive System for Automated Pothole Detection and Vehicle Speed Management using CNN Technology	An automatic system for pothole detection and vehicle speed management is needed because manually detecting potholes while driving at high speeds is difficult.	To use a CNN model to efficiently identify potholes in the road and slow down the car rather than stopping it entirely	Convolutional Neural Network (CNN)	1272 actual road images	Accuracy: 99.56% The system can help reduce accidents, save money on maintenance, and enhance the driving experience	Gangatharan et al., 2023
6.	Pothole detection in bituminous road using CNN with transfer learning	An automated and accurate method is needed to detect potholes and cracks in bituminous roads. The current methods of diagnosing	To create a working system prototype that uses transfer learning to identify potholes in bituminous roads using an already trained AlexNet Convolutional Neural Network (CNN)	Convolutional Neural Network (CNN)	1157 unmanned aerial vehicle (UAV) images designed to segment cracks on highways	Accuracy: 96% The method has potential applications for various intelligent transportation systems (ITS) services, such as	Vinodhini & Sidhaarth, 2024

Table 2 (continue)

No.	Title	Problem	Objective	Algorithm	Dataset	Result	References
		pavement distress are expensive, slow and labour-intensive, leading to increased costs for materials, equipment and labour.				assessing road maintenance needs, alerting drivers and enabling self-driving cars	
7.	Deep Learning Method to Detect the Road Cracks and Potholes for Smart Cities	The challenges of managing road traffic and the high mortality rate due to road traffic accidents (RTAs) in developing countries like Pakistan. Road cracks and potholes are the main causes of RTAs, which require an automated system to detect these road faults for smart city development.	To introduce a Deep Learning Method for detecting road cracks and potholes, which is essential for the development of smart cities	Convolutional Neural Network (CNN)	6000 images captured from various roads in the Lahore district of Punjab, Pakistan. The dataset includes three classes: normal, crack, and pothole, with 2000 images in each class. These images were collected using smart city cameras, smartphones fixed on vehicles, and drone cameras under different weather conditions	Accuracy: 97.47% The study's findings highlight the potential of PCD to significantly improve road safety and maintenance through efficient and automated detection of road damage	Chu et al., 2023
8.	Design and Implementation of Real-time Pothole Detection using Convolutional Neural Network for IoT Smart Environment	The effects of potholes and other bad road conditions on various community activities.	To address the impact of poor road conditions, particularly potholes, on various community activities, automatic pothole detection and display of the results on a website platform will be used	Convolutional Neural Network (CNN)	The images were collected from different online sources and separated into the test and training data sets	Accuracy: n/a The system's stated true positive rate is less than 25%, suggesting it can accurately identify potholes	Pratama et al., 2021

Table 2 (continue)

No.	Title	Problem	Objective	Algorithm	Dataset	Result	References
9.	Detection of Potholes using Convolutional Neural Network Models: A Transfer Learning Approach	Potholes are the primary cause of bad road conditions, and road damage is on the rise in Bangladesh and throughout the world.	To recognise potholes and furnish the Road and Highway Department (RHD) with a Computer Vision based solution	Convolutional Neural Network (CNN)	1490 images of potholes and normal road pictures from various cities and towns around Bangladesh	Accuracy: 98.66% Can help Bangladeshis Road and Highway Department (RHD) maintain road conditions and potentially decrease the number of pothole-related traffic accidents	Pratama et al., 2021

AI-driven Vision-based Pothole Detection Framework

The study employed CNN to improve the recognition of potholes. The development of this project began with the data collection process (Gazawy et al., 2023). The dataset used for this study was sourced from secondary data available on the Kaggle platform (Kumar, 2019). Two datasets were identified as the most suitable for this project. The first dataset comprises 681 image samples, while the second contains 6,000 images, of which only 4,000 were utilised. Figure 1 presents samples of pothole images.

Figure 2 shows the architecture of the project to be developed. The database stores all the images, categorised into potholes and normal roads, before going through the image preprocessing process and pothole segmentation.

These datasets were integrated into a cohesive dataset. They underwent rigorous data cleaning to ensure quality and enhance model performance. This process involved formatting, organising, and discarding some data to address potential class imbalances and achieve a more balanced distribution.

The dataset was categorised into two main groups based on visual characteristics: pothole and normal road images. This categorisation was essential for training the model to accurately differentiate between roads with potholes and those without. Each image was visually inspected to confirm its relevance, with 329 “potholes” and 352 “normal roads.” Labels were assigned systematically:

- Pothole: Images depicting visible potholes.
- Normal: Images showing smooth, undamaged roads.
- A structured labelling framework was implemented to minimise errors and ensure consistency.

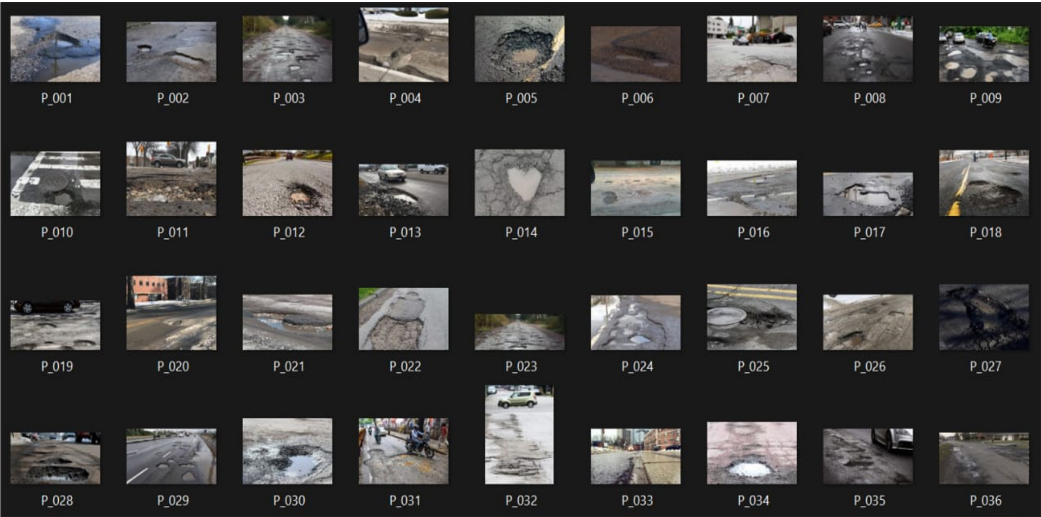


Figure 1. Sample of images

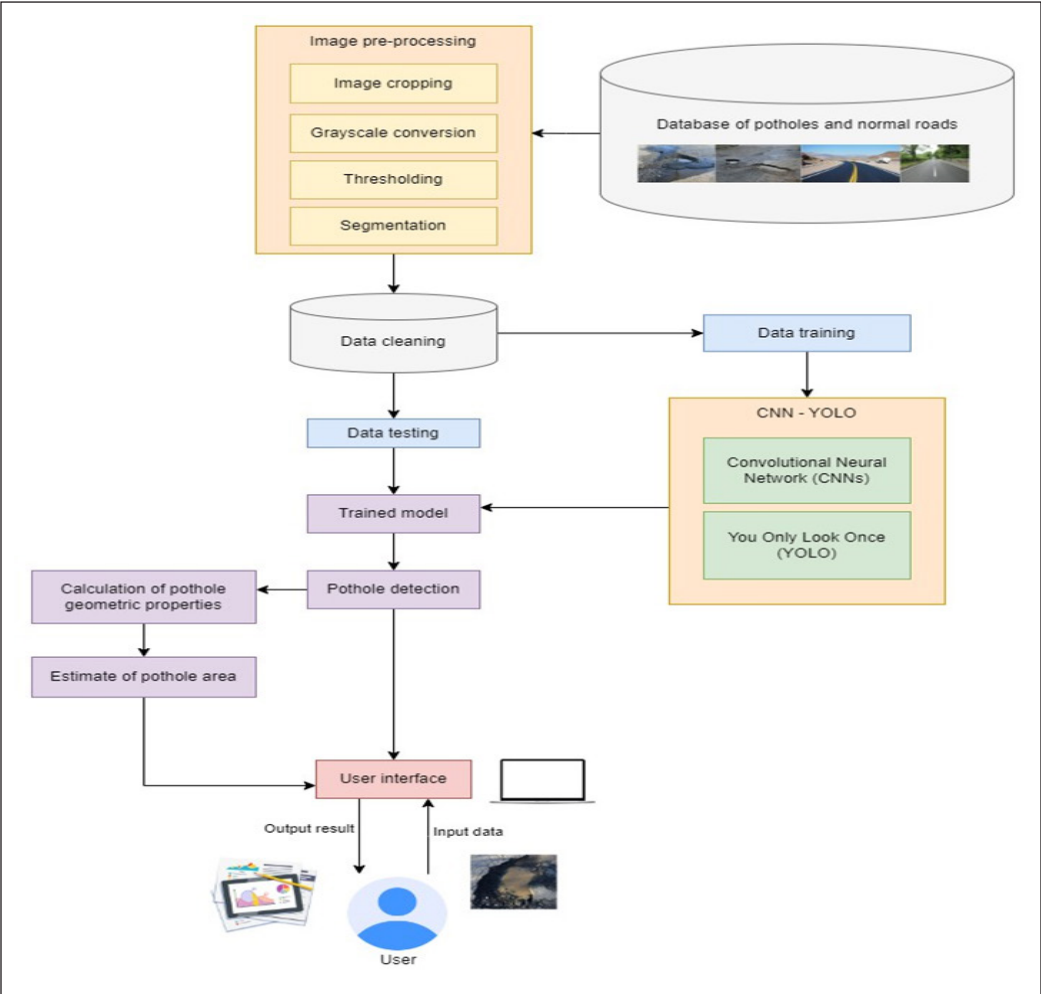


Figure 2. System architecture of pothole detection system

Images were divided into three subsets to prepare the dataset for training:

- Training Set (70%): Used to train the model with diverse image samples.
- Testing Set (20%): Used to evaluate the model’s performance on unseen data.
- Validation Set (10%): Used during training to fine-tune hyperparameters and prevent overfitting.

Before categorisation, images were preprocessed to standardise their dimensions (resized to 250×250 pixels) and normalised to a 0–1 range. Data augmentation techniques, including flipping, rotation, and brightness adjustments, were applied to address class imbalances and improve the model’s ability to recognise potholes under varying conditions. Additionally, duplicate and irrelevant images (e.g., those not containing roads) were removed, and any mislabelled data was corrected through manual verification.

The cleaned and categorised dataset was processed using a sophisticated CNN to analyse road surface features and identify potential potholes. YOLO was integrated for real-time object detection, leveraging a single CNN architecture that scans entire images in one pass. YOLO divides each image into a grid, where each cell predicts bounding boxes and class probabilities. Redundant detections are refined using non-maximum suppression, retaining only the most confident predictions. This integration of CNN and YOLO ensures high precision, rapid processing, and minimising false positives.

The system further enhances detection accuracy, incorporating additional contextual information, such as weather conditions and road surface data, allowing for dynamic adjustments to detection parameters. Detected potholes are mapped and reported in real-time, enabling immediate maintenance actions. As presented in Figure 3, this automated, AI-driven framework streamlines road monitoring and management, reducing labour intensity and improving road safety. By leveraging advanced AI and computer vision technologies, the system provides a robust solution for precise, efficient, and timely pothole detection and management.

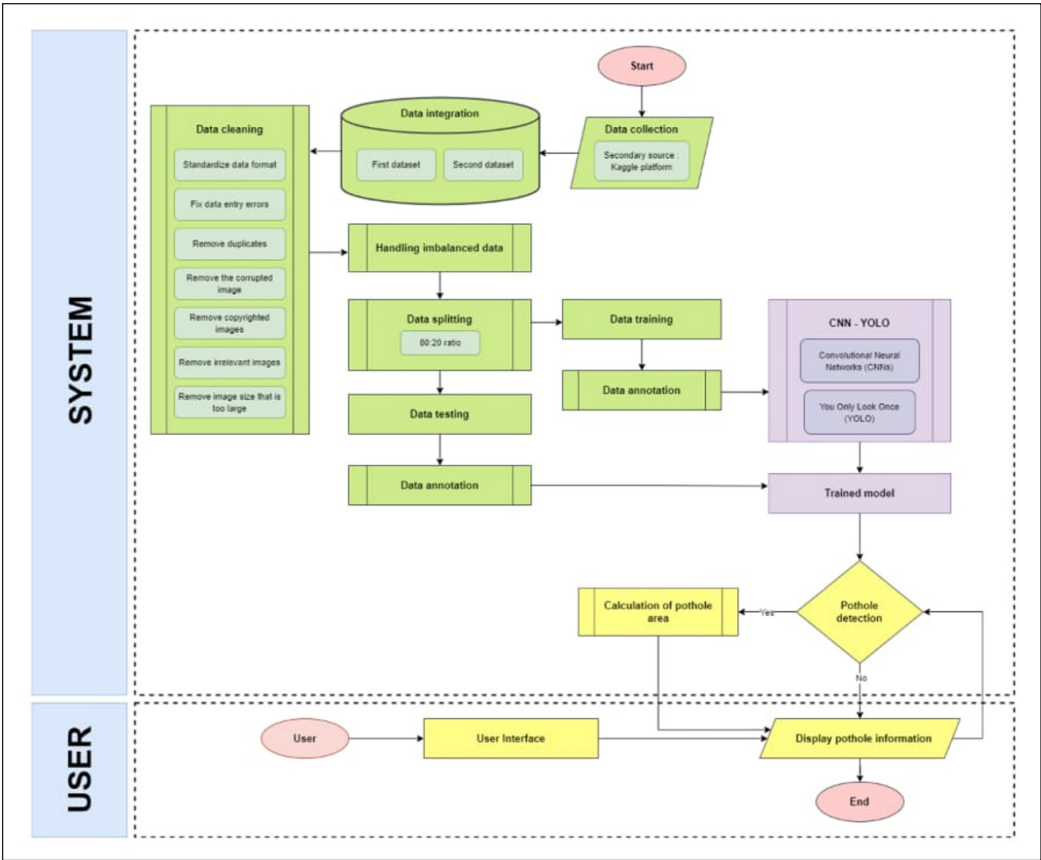


Figure 3. Proposed model framework

CNN-YOLO Model

The CNN model is coded using Python, utilising the Keras library, and follows a sequential architecture, where layers are arranged linearly to progressively extract and refine features from input images. The model processes images of 256x256 pixels with three colour channels (RGB). It comprises four convolutional layers, each with an increasing number of filters (32, 64, 128, and 256) and a 3x3 kernel size. These layers employ the ReLU activation function to introduce non-linearity, which is essential for learning complex patterns. Batch normalisation layers are included after each convolutional layer to normalise activations, thereby speeding up the training process and improving model stability.

MaxPooling2D layers are used to down-sample the data, reducing the spatial dimensions of the feature maps and easing the computational load. Dropout layers are also incorporated to randomly set 10% of the input units to zero during training, which helps prevent overfitting. After the convolutional layers, a GlobalMaxPooling2D layer converts the 2D feature maps into a 1D vector, followed by two dense layers with 256 and 128 units. These dense layers use ReLU activation and a Dropout layer set at 30% to further mitigate overfitting. The model concludes with an output layer featuring a single unit with a sigmoid activation function designed for binary classification.

The Python script, which utilises the Ultralytics library, was employed to train and evaluate the YOLOv8 model. The script trains the YOLOv8 model on a specified dataset, allowing for flexible configuration of parameters such as the number of training epochs, image size, and batch size. After training, the model is evaluated to assess its performance on the validation dataset, providing key metrics such as accuracy, precision, and recall. These metrics offer valuable insights into the model's effectiveness in real-world object detection tasks.

Model Performance Evaluation

Performance evaluation is critical to assessing the effectiveness and efficiency of a system or model in a study and plays a significant role in determining the accuracy of the results. Various evaluation metrics can be employed depending on the study's objectives.

Confusion Matrix

The confusion matrix is a table summarising a classification algorithm's performance on a given dataset. It provides insight into the model's ability to make correct and incorrect predictions, making it particularly useful for binary classification problems. In a binary classification problem, the confusion matrix contains four key entries, as illustrated in Figure 4.

Four main evaluation metrics based on accuracy, precision, recall, and F1 score can be derived from these four entries in the confusion matrix. These metrics comprehensively

evaluate a model’s performance, allowing researchers to gauge its accuracy, precision, recall, and overall effectiveness in classification tasks.

System User Interface Design

A web-based system has been designed and developed for end-users to report road potholes efficiently. This platform enhances user accessibility, enabling them to utilise the system anytime and anywhere with an internet connection. A key feature of the system is the file upload function, which allows users to submit images or videos of potholes for analysis. The system supports only PNG image files and MP4 video formats, with a maximum file size of 300MB and a video length limit of 3 minutes. Once the file is uploaded, users must click the “Generate Information” button to initiate the analysis process. The system then generates a comprehensive report containing critical information, divided into general information, the calculation estimation module, and the performance score, as detailed in Figure 5. After the analysis is complete, users are provided with three options: “New Detection,” “Save This Result,” and “Home Page,” each serving a specific function. For instance, selecting “New Detection” returns the system to the initial page, where users can upload a new file for further analysis. The system’s design was created using Figma software, focusing on ensuring user-friendliness and effective information delivery.

		Actual Values	
		Positive (1)	Negative (0)
Predicted Values	Positive (1)	TP	FP
	Negative (0)	FN	TN

Figure 4. The confusion matrix

RESULTS AND DISCUSSION

Performance Evaluation

The evaluation process systematically assessed the model’s performance and robustness, focusing on key metrics such as accuracy, precision, recall, and F1 scores. Evaluating different data-splitting strategies for the pothole detection model revealed that the 70/20 split provided the highest testing accuracy at 92.85%, as shown in Table 3. This split ensures a balanced approach, allowing the model to train effectively while retaining a substantial portion of data for testing. The comparative results, where a 70/30 split yielded a testing accuracy of 91.01% and a 90/10 split achieved 92.11%, highlight that while more training data can enhance model learning, it may slightly diminish the generalisation capacity when too little data is reserved for testing. The 70/20 ratio emerged as the optimal balance, maximising the training efficiency and the model’s ability to generalise well to unseen data.

Adopting the 70/20 data-splitting strategy in this project underscores its effectiveness in optimising the model’s performance. By providing sufficient training data, the model

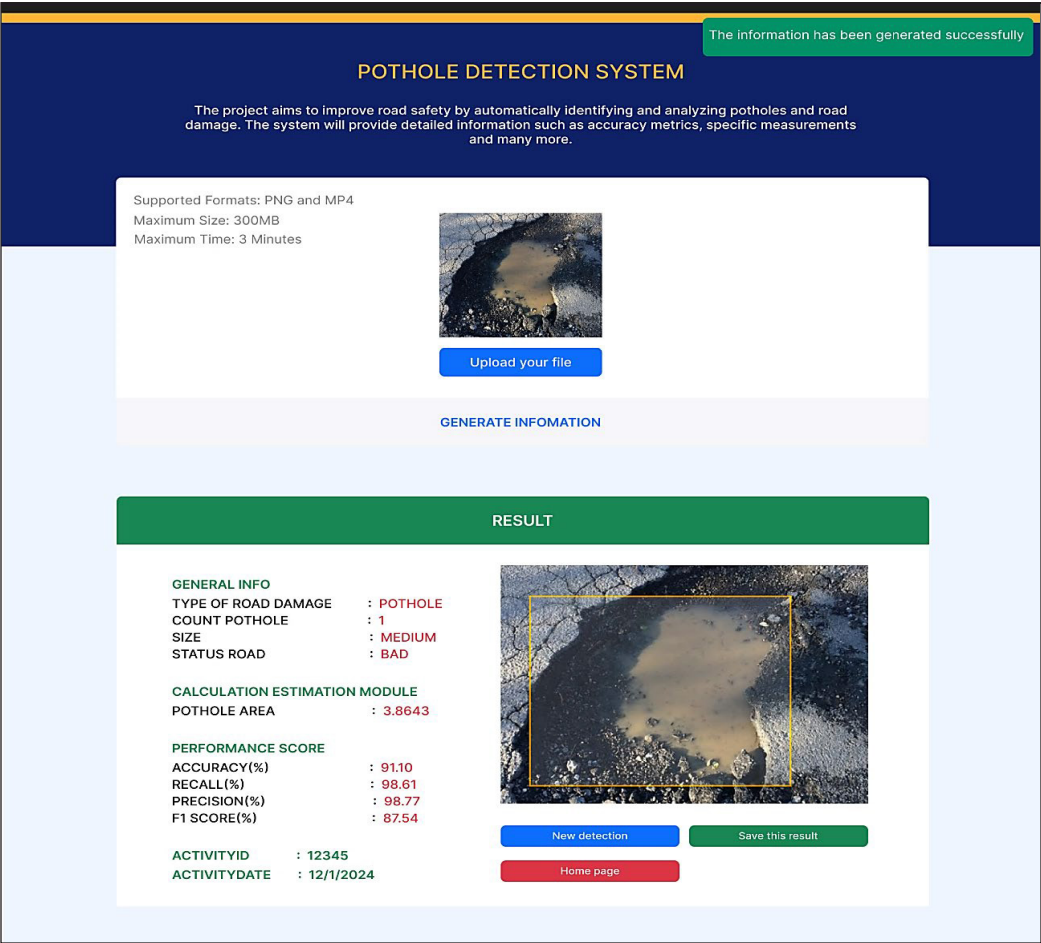


Figure 5. User interface design

Table 3
2-fold cross-validation results

LABEL	MEASURE	BASED ON OUR CODING		BASED ON REFERENCE ARTICLE	
		Epochs 100			
		Batch size 32			
		F1	F2	F1	F2
NORMAL	PRECISION	97.28%	97.49%	86.00%	89.00%
	RECALL	98.50%	97.00%	99.00%	93.00%
	F1 SCORE	97.89%	97.24%	97.00%	91.00%
POTHOLE	PRICISION	98.48%	97.02%	97.00%	89.00%
	RECALL	97.25%	97.50%	86.00%	95.00%
	F1 SCORE	97.86%	97.26%	91.00%	92.00%
TESTING ACCURACY		97.88%	97.25%	90.00%	91.00%

could learn intricate patterns in road images, such as detecting and categorising potholes accurately. Simultaneously, the ample test data allowed for a robust evaluation of the model’s performance across various scenarios, ensuring that the results were not skewed or overfitted. This strategic choice is critical in AI-driven applications, where the balance between training and testing data can significantly impact the model’s reliability and effectiveness in real-world deployments. Ultimately, the findings demonstrate that the 70/20 split enhances data utilisation efficiency and ensures a comprehensive assessment of the model’s generalisation capabilities, laying a strong foundation for future improvements and applications in road safety monitoring.

During the evaluation, several images were identified where the model failed to detect the target objects. These failures predominantly occurred in scenarios with poor lighting conditions, heavy occlusions, or low contrast between the objects and the background. Additionally, small object sizes or distorted perspectives posed significant challenges for the model, as these characteristics reduced the clarity of defining features that the algorithm relies on for recognition. These observations highlight the importance of environmental factors and dataset diversity in ensuring robust model performance.

Furthermore, distinguishing features of the misclassified or undetected images included irregular shapes, water retention, and visual noise, which introduced ambiguity in feature extraction. For example, in some cases, objects with textures or patterns similar to the background were incorrectly classified or entirely ignored. This indicates that the feature maps generated by the model struggled to differentiate these objects due to insufficient contrast in feature saliency. Addressing these issues may require incorporating data augmentation techniques, improving dataset quality, and fine-tuning the model to enhance its sensitivity to complex scenarios. Such improvements are essential for optimising the CNN-YOLOv8 model’s accuracy in real-world applications. Figure 6 present the confusion matrix for 2-fold cross-validation results.

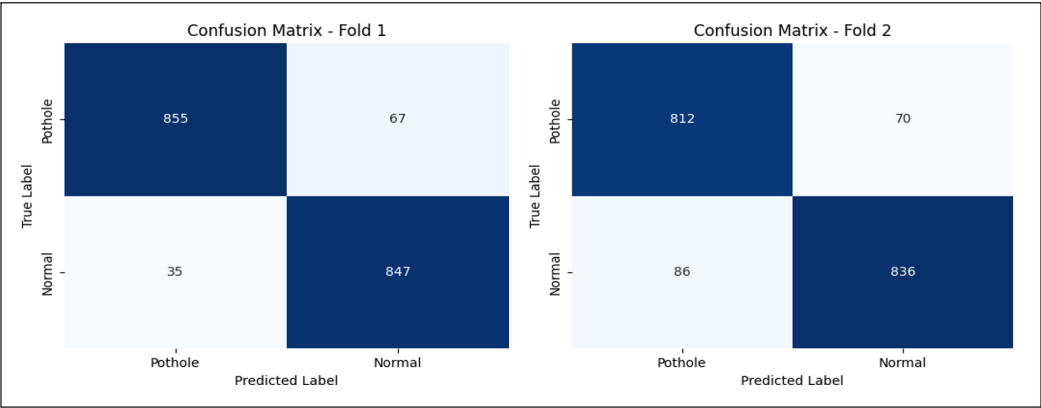


Figure 6. Confusion matrix for 2-fold cross-validation results

Verification of Performance Metrics

A thorough analysis was conducted using confusion matrices derived from 2-fold cross-validation to ensure the accuracy and reliability of the classification model’s performance metrics. This analysis aims to validate the precision, recall, F1-score, and accuracy values, performed using manual calculations based on the confusion matrices. The confusion matrices for each fold provide detailed insights into the true positives, false positives, true negatives, and false negatives for both “Pothole” and “Normal” classes. By meticulously calculating and comparing these performance metrics, the integrity of the reported results is confirmed, and any potential discrepancies are identified. This validation process is crucial for establishing confidence in the model’s ability to accurately classify road conditions and highlight areas for potential improvement. Table 4 presents the confusion matrix for pothole detection for Fold 1, and Table 5 presents the confusion matrix for normal in Fold 1 Predicted: Pothole.

The formula for Precision, Recall and F1-Score for potholes:

$$\begin{aligned} \text{Precision} &= 855 / (855 + 35) = 0.9607 = 96.07\% \\ \text{Recall} &= 855 / (855 + 67) = 0.9273 = 92.73\% \\ \text{F1-Score} &= 2(0.9607 * 0.9273) / (0.9607 + 0.9273) = 0.9437 = 94.37\% \end{aligned}$$

The formula for Precision, Recall and F1-Score for normal:

$$\begin{aligned} \text{Precision} &= 847 / (847 + 67) = 0.9267 = 92.67\% \\ \text{Recall} &= 847 / (847 + 35) = 0.9603 = 96.03\% \\ \text{F1-Score} &= 2(0.9267 * 0.9603) / (0.9267 + 0.9603) = 0.9432 = 94.32\% \end{aligned}$$

Testing Accuracy:

$$\text{Accuracy} = (855 + 847) / (855 + 67 + 35 + 847) = 0.9435 = 94.35\%$$

Table 6 presents the confusion matrix for pothole detection for Fold 2, and Table 5 presents the confusion matrix for normal in Fold 2 Predicted: Pothole.

The formula for Precision, Recall and F1-Score for potholes:

$$\begin{aligned} \text{Precision} &= 812 / (812 + 86) = 0.9042 = 90.42\% \\ \text{Recall} &= 812 / (812 + 70) = 0.9206 = 92.06\% \\ \text{F1-Score} &= 2(0.9042 * 0.9206) / (0.9042 + 0.9206) = 0.9123 = 91.23\% \end{aligned}$$

Table 7 presents the confusion matrix for normal for Fold 1 predicted pothole.

The formula for Precision, Recall and F1-Score for normal:

$$\begin{aligned} \text{Precision} &= 836 / (836 + 70) = 0.9227 = 92.27\% \\ \text{Recall} &= 836 / (836 + 86) = 0.9067 = 90.67\% \\ \text{F1-Score} &= 2(0.9227 * 0.9067) / (0.9227 + 0.9067) = 0.9146 = 91.46\% \end{aligned}$$

Table 4
Table of confusion matrix for pothole in Fold 1
Predicted: Pothole

	Predicted: Pothole	Predicted: Normal
Actual: Pothole	855 (TP)	67 (FN)
Actual: Normal	35 (FP)	847 (TN)

Table 6
Table of confusion matrix for pothole in Fold 2
Predicted: Pothole

	Predicted: Pothole	Predicted: Normal
Actual: Pothole	812 (TP)	70 (FN)
Actual: Normal	86 (FP)	836 (TN)

Table 5
Table of confusion matrix for normal in Fold 1
Predicted: Pothole

	Predicted: Pothole	Predicted: Normal
Actual: Pothole	855 (TN)	67 (FP)
Actual: Normal	35 (FN)	847 (TP)

Table 7
Table of confusion matrix for normal in Fold 1
Predicted: Pothole

	Predicted: Pothole	Predicted: Normal
Actual: Pothole	812 (TN)	70 (FP)
Actual: Normal	86 (FN)	836 (TP)

Testing Accuracy:
 $\text{Accuracy} = (812 + 836) / (812 + 70 + 86 + 836) = 0.9135 = 91.35\%$

Table 8 depicts the Average Metrics Across Folds. The calculation of the pothole area is based on the image’s pixel dimensions. The width and height of the detected pothole are measured in pixels, and the area is computed as the product of these two dimensions. This approach provides a precise estimation of the pothole size, which is critical for assessing the severity of road damage. By including this detailed information, users are better informed about the condition of the road and the specific characteristics of each detected pothole. This added layer of analysis ensures that the model classifies road conditions accurately and provides valuable insights into the extent of the damage, contributing to more effective road maintenance and repair strategies.

Figure 7 shows a detected pothole’s pixel dimensions (width and height). The area is calculated by multiplying the width

Table 8
Average metrics across folds

Average Metrics Across Folds		
	Pothole	Normal
Precision	93.25%	92.47%
Recall	92.40%	93.35%
F1-Score	92.80%	92.89%
Overall Testing Accuracy	92.85%	

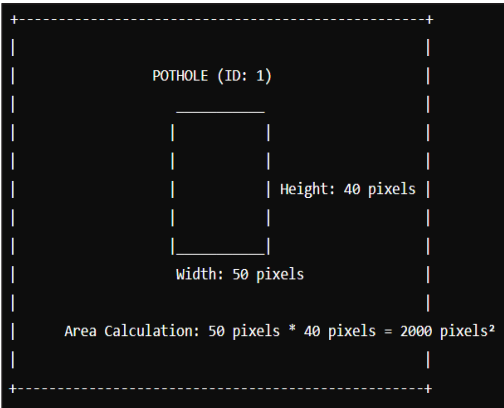


Figure 7. Wireframe image of pothole area calculation

and height. For example, a pothole with a width of 50 pixels and a height of 40 pixels results in an area of 2000 pixels².

Figure 8 depicts the actual scenario as captured and uploaded by the user. The system successfully identifies and highlights the potholes within the image. The program provides specific details for each detected pothole, including the width, height, and area in pixels. Additionally, the detection results offer a comprehensive analysis, including the number of potholes detected, their dimensions, and an overall road condition assessment. This information is crucial for assessing the severity of the road damage and planning necessary maintenance actions.



Figure 8. Detection results for uploaded road image showing pothole area

Web-based System

The web-based system, “Sistem Pintar Pengesanan Jalan Raya (AI),” or “AI Road Safety with Vision-Based Pothole Detection,” is a pioneering technological solution designed to enhance road infrastructure maintenance through the application of AI. The system’s architecture and interface are meticulously crafted to ensure robust functionality, ease of use, and the effective integration of AI for automated road defect detection.

A key feature of this system is its user interface, which is available in Malay. This linguistic choice is essential to making the system more accessible and user-friendly for its primary users in Malaysia, including local authorities and road maintenance crews. Utilising the Malay language reduces the learning curve. It minimises potential misunderstandings, facilitating quicker adoption and more effective training.

The system allows users to upload images or videos or even capture real-time footage using a connected camera to detect road defects like potholes. The AI-driven models, particularly CNN and YOLO, then analyse the media files to identify and label any

detected potholes. Detailed information such as road status, the number of potholes, their dimensions, and risk assessments are provided to the user, enabling precise and efficient maintenance planning.

The system enhances operational efficiency by incorporating Malay and leveraging advanced AI technology. It aligns with local needs and cultural contexts, making it a valuable tool for maintaining Malaysia’s road infrastructure.

System Interface and Architecture

The system has a user-centric interface that ensures easy navigation while maintaining robust technical capabilities. Upon accessing the system, users are greeted with an introductory page as the entry point into the system’s functionalities. This page includes essential elements such as the project title, a login portal for secure access, and a list of contributors involved in the system’s development. Login functionality is critical for managing user sessions and ensuring that data interactions are safe and user-specific, as illustrated in Figure 9.



Figure 9. System introductory page

Core Functionalities and AI Integration

The system’s main interface is divided into two primary sections, each tailored to support the system’s core functionalities: title, media upload/camera activation, and results analysis.

Media Upload and Camera Activation is a system that accommodates a range of input methods, allowing users to upload pre-recorded media files or capture live footage directly through a connected camera. The media upload functionality supports image files in PNG, JPG, and JPEG formats, as well as MP4 video files, with a strict size limit of

10MB per file to optimise processing speed and accuracy. The camera activation feature enables real-time analysis, a critical function for on-the-spot assessments and immediate response scenarios. The system’s flexibility in accepting various media formats and real-time data input underscores its versatility and applicability in diverse operational contexts, as shown in Figure 9. Figure 10 illustrates a sample of an image uploaded by a user. Figure 11 presents user-uploaded pothole images in the system.

The AI models perform detailed analyses and output their findings. Upon processing the uploaded media or live camera feed, the system employs the CNN and YOLO models to detect road defects. If potholes are identified, the system provides a detailed analysis, including the exact location, dimensions, and the calculated area of each detected pothole. This information is presented with high precision, supported by metrics such as the certainty score, which quantifies the confidence of the model’s predictions. The comprehensive nature of the provided data enables maintenance teams to prioritise repairs based on the severity and extent of road damage, optimising resource allocation and enhancing road safety. Figures 12 and 13 present the model detection results when the user uploads a video file and opens the camera. In general, the results displayed are the same for both

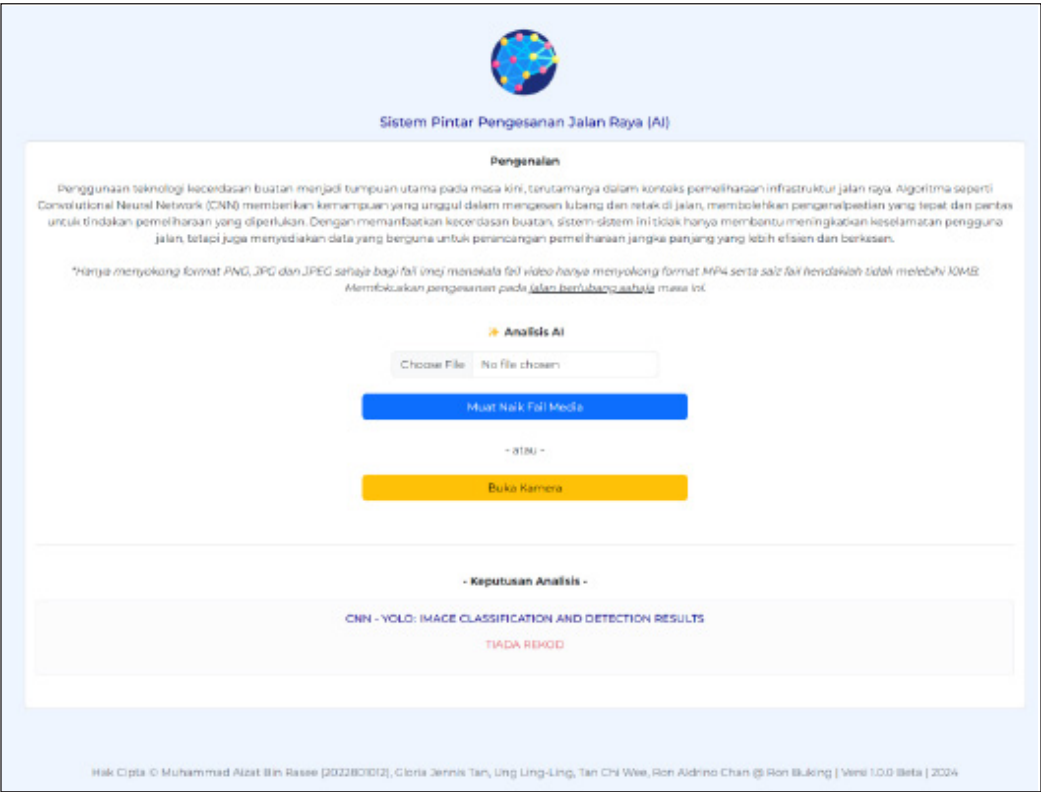


Figure 10. Module for a user to upload a pothole image

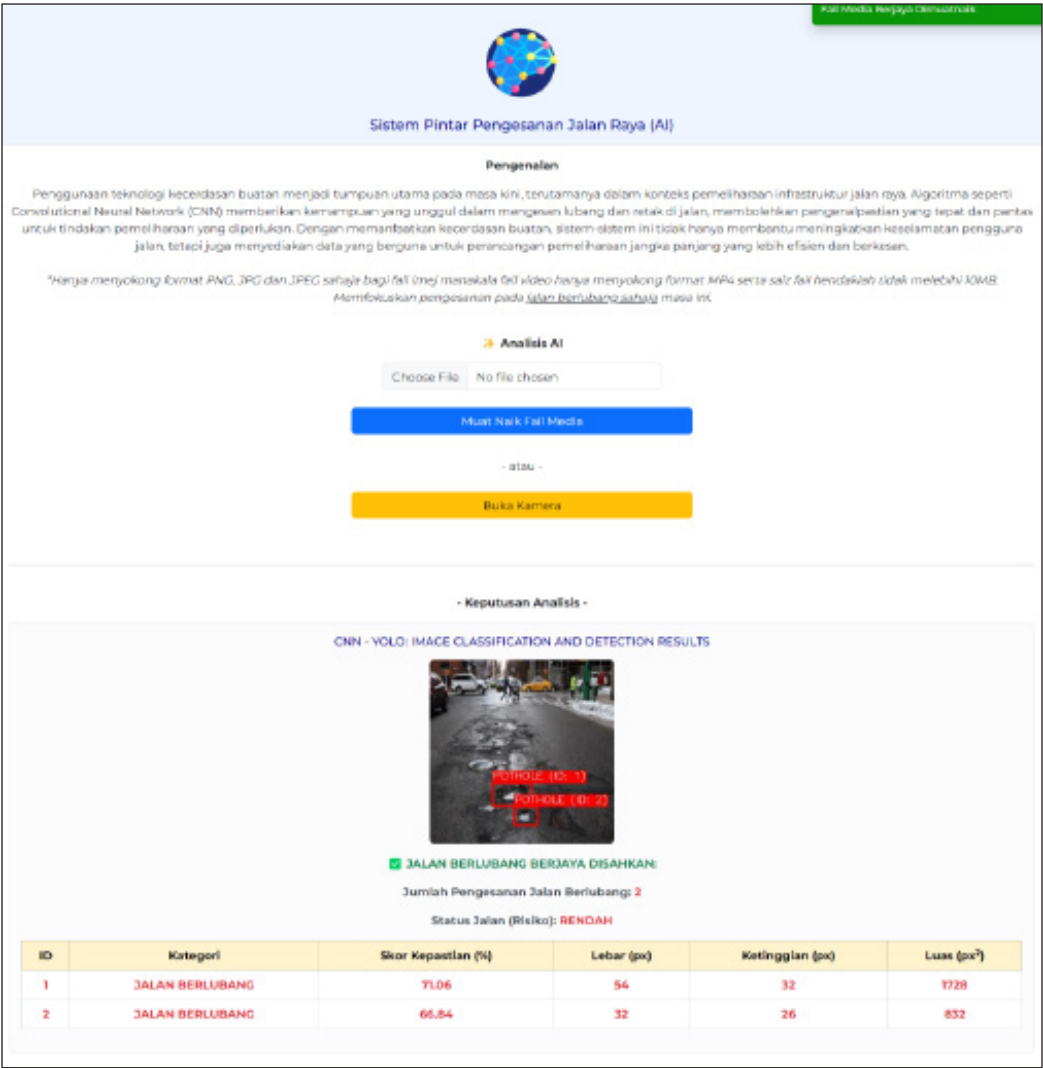


Figure 11. User-uploaded pothole images

methods, where the user will be shown a pothole warning message, the status of the road condition, and the pothole detected is marked and labelled. A green line is in the middle of the video or camera frame. Furthermore, users can also see the certainty score, width, height, and area of each pothole that the model successfully detects. Figures 12 and 13 present the illustrations.

CONCLUSION

This study is a preliminary investigation to demonstrate the feasibility of utilising CNNs and the YOLO algorithm for vision-based pothole detection in road safety applications.

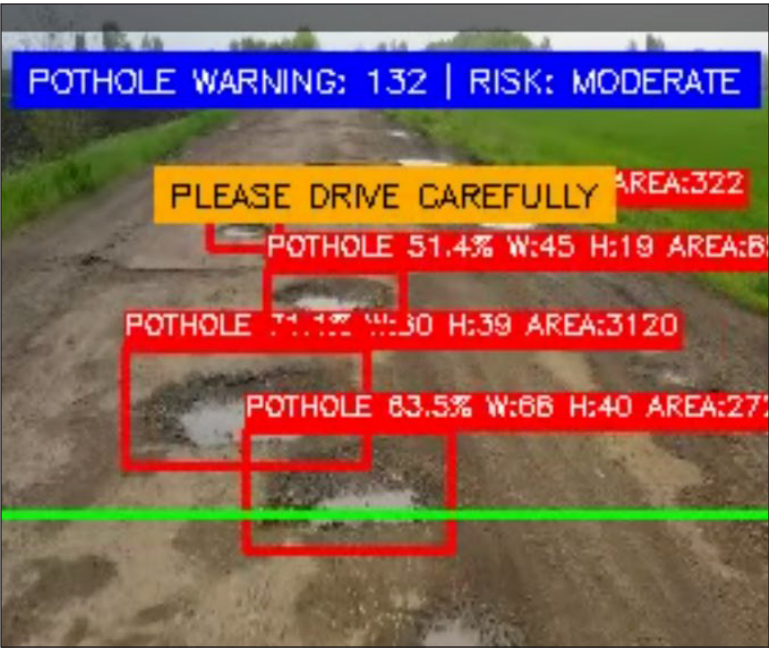


Figure 12. Model detection results on video files uploaded by users

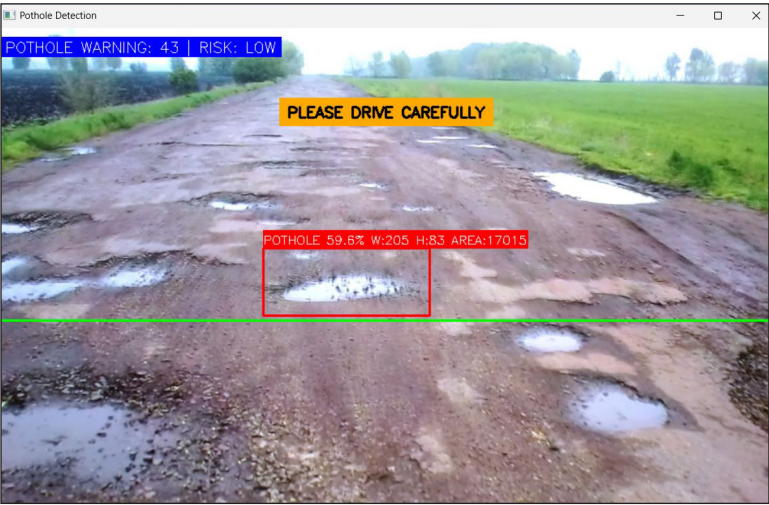


Figure 13. Model detection results when the user opens the camera

Using Kaggle data in this initial stage allows for rapid prototyping and initial model development, providing valuable insights into the potential and challenges of applying these techniques to real-world road surface analysis. While the sources determine the image quality of Kaggle data and may vary, it was deemed sufficient for the objectives of this study. Nevertheless, we acknowledge that image quality from front-facing cameras in real-world

scenarios may introduce additional challenges, such as variations in lighting, resolution, and weather conditions. Future research will address these limitations by collecting and analysing high-quality, real-world road surface images. This will help further refine and validate the proposed methodologies, ensuring the system's robustness and reliability in practical applications.

The “AI Road Safety with Vision-Based Pothole Detection” system addresses a critical issue in road infrastructure maintenance by offering a timely and accurate solution for detecting road defects, particularly potholes. Traditional road inspection methods are often slow, labour-intensive, and prone to human error, leading to delays in maintenance and increased risks for road users. The project proposed an innovative methodology utilising AI, specifically CNN, the YOLO algorithm, to create an automated, real-time system for detecting and analysing potholes. While YOLOv8 is not novel, this study contributes to the field by exploring its integration into vision-based road safety systems, specifically targeting the Malaysian context. The novelty lies in applying and customising YOLOv8 within a framework that includes preprocessing tailored to road surface analysis and data augmentation to handle class imbalances to improve detection accuracy. Furthermore, this research bridges a critical gap by applying and validating YOLOv8 for Malaysia road infrastructure monitoring, a domain where such AI-driven systems remain underexplored.

The system was developed with a strong alignment with Malaysia's Sustainable Development Goals (SDGs), particularly SDG 3 (Good Health and Well-being), SDG 9 (Industry, Innovation, and Infrastructure), and SDG 11 (Sustainable Cities and Communities). With a high testing accuracy of 92.85%, achieved through an optimal 70/20 data-splitting strategy, the system effectively enhances road safety and maintenance practices. By ensuring that road defects are detected and addressed promptly, the system plays a vital role in reducing road accidents and vehicle damage, directly contributing to SDG 3 by promoting safer roads, which is crucial for public health and well-being.

The benefits of this AI-driven solution extend across multiple sectors. The system enhances safety for drivers by minimising the risks associated with poor road conditions, thus contributing to a safer transportation environment. The transportation sector benefits from reduced vehicle damage and maintenance costs, while governments can optimise resource allocation, improving the efficiency of road repair budgets and overall infrastructure quality. Including the Malay language in the system's interface ensures accessibility to a wide range of users in Malaysia, facilitating broader adoption and maximising its impact.

Aligned with Malaysia's SDG 9, which emphasises building resilient infrastructure, promoting inclusive and sustainable industrialisation, and fostering innovation, this project exemplifies the transformative potential of AI in infrastructure management. It improves current road maintenance practices through accurate and efficient detection of road defects. It sets a foundation for further innovation in AI-driven infrastructure management. Future

enhancements could include predictive analytics to anticipate road deterioration, expanding the system's applications to monitor other types of infrastructure, and refining AI models based on real-world deployment data.

In summary, the successful implementation of this system advances road maintenance technology, contributing to safer, more efficient, and sustainable urban development. By aligning with Malaysia's SDGs, particularly SDGs 3, 9, and 11, the project benefits drivers, the transportation sector, governments, and the public by promoting safety, efficiency, and sustainability in infrastructure management, ultimately contributing to society's overall well-being.

ACKNOWLEDGEMENT

We would like to extend our heartfelt gratitude to all the faculty members of KPPIM, with special appreciation to those from the UiTM Terengganu branch, for their unwavering support and invaluable contributions to our work. Your guidance, encouragement, and dedication have been instrumental in shaping our work, and we deeply value your commitment to fostering academic excellence. Thank you for being a vital part of our journey.

REFERENCES

- Arjapure, S., & Kalbande, D. R. (2021). Deep learning model for pothole detection and area computation. In *2021 International Conference on Communication Information and Computing Technology (ICCICT)* (pp. 1-6). IEEE Publishing. <https://doi.org/10.1109/ICCICT50803.2021.9510073>
- Bhamare, L., Mitra, N., Varade, G., & Mehta, H. (2021). Study of types of road abnormalities and techniques used for their detection. In *2021 7th International Conference on Electrical, Electronics and Information Engineering (ICEEIE)* (pp. 472-477). IEEE Publishing. <https://doi.org/10.1109/ICEEIE52663.2021.9616755>
- Chorada, R., Kriplani, H., & Acharya, B. (2023). CNN-based Real-time pothole detection for avoidance road accident. In *2023 7th International Conference on Intelligent Computing and Control Systems (ICICCS)* (pp. 700-707). IEEE Publishing. <https://doi.org/10.1109/ICICCS56967.2023.10142488>
- Chu, H. H., Saeed, M. R., Rashid, J., Mehmood, M. T., Ahmad, I., Iqbal, R. S., & Ali, G. (2023). Deep learning method to detect the road cracks and potholes for smart cities. *Computers, Materials & Continua*, 75(1), 1863-1881. <https://doi.org/10.32604/cmc.2023.035287>
- Gangatharan, N., Reddy, S., Sathvik. I. V. S., & Sabarish, G. (2023). A comprehensive system for automated pothole detection and vehicle speed management using CNN technology. In *2023 8th International Conference on Communication and Electronics Systems (ICCES)* (pp. 749-754). IEEE Publishing. <https://doi.org/10.1109/ICCES57224.2023.10192629>
- Gazawy, Q., Buyrukoğlu, S., & Yılmaz, Y. (2023). Convolutional neural network for pothole detection in different road and weather conditions. *Journal of Computer & Electrical and Electronics Engineering Sciences*, 1(1), 1-4. <https://doi.org/10.51271/JCEES-0001>

- Golos, M. (2024). *What Causes Potholes?* Tensar International Corporation. <https://www.tensar.co.uk/resources/articles/what-causes-potholes>
- Halim, M. H. B. M., Ibrahim, A. B., Osman, M. K., Kader, M. M. M. A., Termizi, M. F. A., & Abu, A. E. M. (2022). Detection of pothole for repair works of asphalt flexible pavement optimization using YOLO. In *AIP Conference Proceedings* (Vol. 2532, No. 1). AIP Publishing. <https://doi.org/10.1063/5.0109961>
- Hossain, M. S., Angan, R. B., & Hasan, M. M. (2023). Pothole detection and estimation of repair cost in Bangladeshi street: AI-based multiple case analysis. In *2023 International Conference on Electrical, Computer and Communication Engineering (ECCE)* (pp. 1-6). IEEE Publishing. <https://doi.org/10.1109/ECCE57851.2023.10101579>
- Kaushik, V., & Kalyan, B. S. (2022). Pothole detection system: A review of different methods used for detection. In *2022 Second International Conference on Computer Science, Engineering and Applications (ICCSEA)* (pp. 1-4). IEEE Publishing. <https://doi.org/10.1109/ICCSEA54677.2022.9936360>
- Kim, Y. M., Kim, Y. G., Son, S. Y., Lim, S. Y., Choi, B. Y., & Choi, D. H. (2022). Review of recent automated pothole-detection methods. *Applied Sciences*, 12(11), Article 5320. <https://doi.org/10.3390/app12115320>
- KKR. (2023). Statistik Jalan Malaysia - Edisi 2023 [*Malaysia Road Statistic - 2023 Edition*]. KKR. <https://www.kkr.gov.my/en/senarai-penerbitan-kkr/buku-statistik-jalan-2023>
- Kumar, A. (2019). *Labelled Image Dataset Containing 300+ Images of Roads Containing Potholes*. kaggle. <https://www.kaggle.com/datasets/atulyakumar98/pothole-detection-dataset>
- Kumar, S., Kumar, N., & Barthwal, A. (2023). Road pothole detection using smartphone sensors. *Journal of Harbin Engineering University*, 44(7), 1341-1346.
- Lincy, A., Dhanarajan, G., Kumar, S. S., & Gobinath, B. (2023). Road pothole detection system. In *ITM Web of Conferences* (Vol. 53, p. 01008). EDP Sciences. <https://doi.org/10.1051/itmconf/20235301008>
- Manzor, Z. (2021, April 6). 206,570 Jalan Berlubang Tahun Lalu [206,570 potholes last year]. *Kosmo Digital*. <https://www.kosmo.com.my/2021/04/06/206570-jalan-berlubang-tahun-lalu/>
- Noh, N. C. (2021, January 6). 223 Kemalangan Akibat Fizikal Jalan Raya [223 accidents due to the physical condition of the road]. *Berita Harian*. <https://www.bharian.com.my/berita/kes/2021/01/773051/223-kemalangan-akibat-fizikal-jalan-raya>
- Othman, M. Z. (2023, May 15). Jalan Umpama di Bulan, 'Korek Tampal' Sampai Bila? [Like walking on the moon, how long will 'lightning and patching' last?] *StraComm USIM*. <https://www.usim.edu.my/news/in-our-words/jalan-umpama-di-bulan-korek-tampal-sampai-bila/>
- Pratama, I. D., Mahmudah, H., & Sudibyo, R. W. (2021). Design and implementation of real-time pothole detection using convolutional neural network for IoT smart environment. In *2021 International Electronics Symposium (IES)* (pp. 675-679). IEEE Publishing. <https://doi.org/10.1109/IES53407.2021.9594038>
- Ranyal, E., Sadhu, A., & Jain, K. (2023). AI assisted pothole detection and depth estimation. In *2023 International Conference on Machine Intelligence for GeoAnalytics and Remote Sensing (MIGARS)* (Vol. 1, pp. 1-4). IEEE Publishing. <https://doi.org/10.1109/MIGARS57353.2023.10064547>
- Saisree, C., & Kumaran, U. (2023). Pothole detection using deep learning classification method. *Procedia Computer Science*, 218, 2143-2152. <https://doi.org/https://doi.org/10.1016/j.procs.2023.01.190>

- Sartika, Zainuddin, Z., & Ilham, A. A. (2023). Detection and classification of road damage using camera with GLCM and SVM. In *2023 IEEE International Conference on Industry 4.0, Artificial Intelligence, and Communications Technology (IAICT)* (pp. 372-376). IEEE Publishing. <https://doi.org/10.1109/IAICT59002.2023.10205539>
- Sharma, M., Saripalli, S. R., Gupta, A. K., Talwar, R., Dadheech, P., & Kanike, U. K. (2023). Real-time pothole detection during rainy weather using dashboard cameras for driverless cars. In *Handbook of Research on Thrust Technologies' Effect on Image Processing* (pp. 384-394). IGI Global. <https://doi.org/10.4018/978-1-6684-8618-4.ch023>
- Vinodhini, K. A., & Sidhaarth, K. R. A. (2024). Pothole detection in bituminous road using CNN with transfer learning. *Measurement: Sensors*, 31, Article 100940. <https://doi.org/https://doi.org/10.1016/j.measen.2023.100940>
- Wang, W., & Ho, Y. (2022). Pothole-related traffic safety detection based on deep learning. In *2022 15th International Conference on Human System Interaction (HSI)* (pp. 1-6). IEEE Publishing. <https://doi.org/10.1109/HSI55341.2022.9869460>

Investigation of Aged-related Metabolites in the Marine Polychaete (*Marphysa moribidii*) Using ¹H NMR Metabolomics and LC-MS/MS Analysis

Nurfarah Aini Mocktar¹, Mohamad Sofi Abu Hassan², Maulidiani Maulidiani¹, Wan Iryani Wan Ismail^{1,3}, Izwandy Idris^{4,5}, Farhanini Yusoff¹ and Noor Aniza Harun^{1,2,6*}

¹Faculty of Science and Marine Environment, Universiti Malaysia Terengganu, Kuala Nerus, 21030 Terengganu, Malaysia

²Higher Institution Centre of Excellence (HICoE), Institute of Tropical Aquaculture and Fisheries, Universiti Malaysia Terengganu, Kuala Nerus, 21030 Terengganu, Malaysia

³Cell Signalling and Biotechnology Research Group (CeSBTech), Faculty of Science and Marine Environment, Universiti Malaysia Terengganu, Kuala Nerus, 21030 Terengganu, Malaysia

⁴South China Sea Repository and Reference Centre, Institute of Oceanography and Environment, Universiti Malaysia Terengganu, Kuala Nerus, 21030 Terengganu, Malaysia

⁵Mangrove Research Unit (MARU), Institute of Oceanography and Environment, Universiti Malaysia Terengganu, Kuala Nerus, 21030 Terengganu, Malaysia

⁶Advanced Nano Materials (ANOMA) Research Interest Group, Faculty of Science and Marine Environment, Universiti Malaysia Terengganu, Kuala Nerus, 21030 Terengganu, Malaysia

ABSTRACT

Marphysa moribidii (marine polychaetes) exhibits distinct age-related characteristics based on body width in the initial seven chaetigers, excluding parapodia or bristles that are classified into three age classes: Class I (body width ranging from 3–5 mm), Class II (6–8 mm), and Class III (9–11 mm). Despite its potential, the exploration of metabolites in marine worms, particularly through metabolomics, remains limited. The aim of this study is to identify the metabolite profile and depict the metabolic pathways of different age classes of *M. moribidii* utilising proton nuclear

magnetic resonance spectroscopy (¹H NMR) metabolomics and liquid chromatography with tandem mass spectrometry (LC-MS/MS) analysis. A total of 35 metabolites were identified using ¹H NMR metabolomics, including amino acids, carbohydrates, fatty acids, glycerol, nitrogenous compounds, organic compounds, and vitamins. LC-MS/MS analysis also discovered 36 metabolites that can be categorised into organic acids, carbohydrates, phenolic compounds, fatty acids, and amino acids. Class II *M. moribidii* emerged to have

ARTICLE INFO

Article history:

Received: 23 September 2024

Accepted: 31 January 2025

Published: 23 April 2025

DOI: <https://doi.org/10.47836/pjst.33.3.21>

E-mail addresses:

farahaini145@yahoo.com (Nurfarah Aini Mocktar)

sofie1495@gmail.com (Mohamad Sofi Abu Hassan)

maulidiani@umt.edu.my (Maulidiani Maulidiani)

waniryani@umt.edu.my (Wan Iryani Wan Ismail)

izwandy.idris@umt.edu.my (Izwandy Idris)

farhanini@umt.edu.my (Farhanini Yusoff)

nooraniza@umt.edu.my (Noor Aniza Harun)

* Corresponding author

the highest concentration of chemicals originating from amino and fatty acids, making it the ideal age for harvesting. Comparing the metabolite profiles across different age groups of *M. moribidii* could provide valuable insights into its physiological processes, metabolic dynamics, and potential bioactive compounds present at various developmental stages.

Keywords: ¹H NMR metabolomics, LC-MS/MS analysis, *Marphysa moribidii*, metabolite profiles, polychaete

INTRODUCTION

Polychaetes are a class of marine worms belonging to the phylum Annelida, which includes over 12,000 known species, such as bloodworms, ragworms, and sea mice (Capa & Hutchings, 2021). Polychaetes are segmented worms characterised by the presence of parapodia, which are paired fleshy protrusions covered in numerous bristles known as chaetae. These leg-like parapodia, adorned with an array of bristles, serve as polychaetes' most prominent and distinguishing features (Glasby & Timm, 2008; Verdonshot, 2015). *Marphysa* is one of the nine genera in the family *Eunicidae*. It comprises around 60 species, which are variously classified based on several characteristics such as the type of subacicular chaetae, shape of the prostomium, location of branchiae initiation, or shape of the pectinate chaetae (Zanol et al., 2016).

Marphysa moribidii is the marine baitworm of the genus *Marphysa* in the family *Eunicidae* that can be found in the mangrove forest on the west coast of Peninsular Malaysia. It is a main baitworm species collected by bait diggers and mostly found in large numbers around the stilt roots of *Rhizophora apiculata* (Idris & Arshad, 2013; Idris & Hutchings, 2014). *M. moribidii* is classified into three age classes depending on their body width. Through this evaluation, the polychaetes can be divided into three different classes: Class I (body width ranging from 3–5 mm), Class II (body width ranging from 6 – 8 mm), and Class III (body width ranging from 9–11 mm) (Rosman et al., 2021).

Research on *M. moribidii* has been performed, and this species has not been utilised as a baitworm. Recent studies have explored the potential of *M. moribidii* in acute wound healing, demonstrating its unique ability to regenerate damaged posterior segments (Rapi et al., 2020). Furthermore, chemical compounds such as alkaloids, phenolics, amino acids, and organic acids have been identified in *M. moribidii* extracts, suggesting their potential contribution to the wound-healing process (Rapi et al., 2020). Additionally, the utilisation of crude extract of *M. moribidii* as a biogenic reducing agent has resulted in significant advancements in the eco-friendly production of silver nanoparticles (Rosman et al., 2020) and gold nanoparticles (Pei et al., 2020; Hassan et al., 2023).

Metabolomic is a broad approach that facilitates identifying and quantifying both endogenous and exogenous metabolites in biological organisms influenced by genetic and environmental factors (Patel et al., 2021). Nevertheless, metabolomics is still not widely

applied in the research of marine worm metabolites despite its enormous potential. To the best of our knowledge, *M. moribidii*'s metabolomic pathways have not yet been reported. The analytical methods that can be utilised to ascertain the structures of a wide variety of metabolite classes are ¹H NMR and LC-MS/MS techniques. Both analytical tools have been extensively used in metabolomics research (Marion, 2013; Emwas et al., 2019; Gathungu et al., 2020; Moco, 2022).

During the wet season, low salinity affects the allelochemicals of *M. moribidii*, influencing its metabolites, including amino acids, organic acids, fatty acids, sterols, and aromatic compounds. *M. moribidii* exhibits stress responses and higher mortality under low salinity. Seasonal variations significantly impact its metabolite profile, as indicated by different FTIR profiles (Wijaya et al., 2024).

Marine polychaetes have shown potential in medical applications, such as antioxidant and wound-healing properties. A positive correlation exists between DPPH activity and total phenolic content (TPC), suggesting that TPC contributes to antioxidant activity. FTIR spectra revealed characteristic signals of polysaccharides, lipids, and carbohydrates. The ATR-FTIR metabolomics approach effectively analysed the chemical profile of polychaete, revealing limited antioxidant activity (Zamzam et al., 2021).

This study extensively explored the metabolite profiles of marine invertebrates *M. moribidii* using the ¹H NMR metabolomics approach and LC-MS/MS analysis. This study aims to identify the metabolite profile and depict the metabolic pathways of *M. moribidii* development at various age classes. Given the success of *M. moribidii* in various applications, including the production of noble metallic nanoparticles and wound treatment, it becomes crucial to investigate the chemical compositions of this marine worm to gain a deeper understanding of its biochemical pathways. The chemical constituents of *M. moribidii* can be explored to identify substances that may have potential applications in agriculture, materials science, food, and other areas. A knowledge of these molecular constituents will yield discernment about the worm's physiology, ecological role, and behaviour, in addition to its metabolic processes and the mechanism that supports its growth, maturation, and ageing.

MATERIALS AND METHODS

Chemicals

LC-MS/MS grade methanol, acetonitrile, formic acid (Merck, Darmstadt, Germany), and de-ionised water were used as the mobile phase in LC-MS/MS analysis. For ¹H NMR analysis, deuterium oxide (D₂O) containing 0.1% 3-(trimethylsilyl) propionic-2,2,3,3-d₄ acid sodium salt (TSP) was employed to selectively obtain signals from the hydrogen atoms in the sample.

***M. moribidii* Sampling**

Individuals of *M. moribidii* were collected from a mangrove strip in Morib, Selangor, within the *Rhizophora apiculata* zonation (2.75827°N 101.4379°E) with the sampling surveys took place in April 2021 when low tide occurred. After gently removing the polychaetes from the mangrove roots, they were transferred into a container containing natural sediment before transportation to the laboratory. To ensure acclimatisation, *M. moribidii* was then placed in an artificial aquarium that mimicked their natural habitat (salinity 30) before proceeding with the experiment.

Identification of *M. moribidii* and Size (Body Width) Classification

Marphysa moribidii classes were assessed and classified according to their body width as recommended by (Occhioni et al., 2009), where it can be divided into three categories: Class I (3–5 mm), Class II (6–8 mm), and Class III (9–11 mm), with measurements taken from the first seven chaetigers of each polychaete (Górska et al., 2019). Notably, these measurements excluded parapodia or bristles.

Preparation of *M. moribidii* Extract

Fresh specimens of *M. moribidii* weighing 15 g from different age classes, namely Class I (body width: 3–5 mm), Class II (body width: 6–8 mm) and Class III (body width: 9–11 mm) were cleaned using artificial seawater and ddH₂O to remove any sediments and dried using tissue paper. The polychaete was dissected and pulverised using a mortar and pestle. The resulting crude extract was mixed with 100 mL of ddH₂O and allowed to incubate at room temperature for 1 hour to facilitate the extraction of bioactive compounds. It was then filtered using the Whatman No.1 filter paper (Rosman et al., 2021). The resulting filtrates were stored at -80°C before undergoing freeze-drying to remove excess water from the polychaete bodies. The dried crude extract obtained from *M. moribidii* was subsequently used for further analysis.

Identification of *M. moribidii* and Size (Body Width) Classification Using Stereo Zoom Microscope

Polychaetes of different age classes were preserved in 70% ethanol for morphological examinations. The specimens were positioned on the stage plate directly beneath the objective lens for viewing. A stereo microscope (Olympus SZ) was utilised, employing natural light that reflected from the specimen for observation.

Sample Preparation for ¹H NMR

About 100 mg of the freeze-dried crude extract from the polychaete samples was placed in a microcentrifuge tube. The sample was then resuspended in 700 µL of 99.9% D₂O

containing 0.1% TSP and sonicated for 30 minutes at room temperature. All samples were vortexed for 10 min at 1300 rpm to ensure a homogeneous mixture. Subsequently, 600 µL of the supernatant solution was transferred to an NMR tube for ¹H NMR analysis.

¹H NMR Spectroscopy Analysis

The ¹H NMR measurements were performed using a Varian INOVA NMR spectrometer (Varian Inc., CA, USA) operating at a frequency of 499.89 MHz and maintained at 25°C. The NMR analysis was conducted for each of the three different age classes with four replicates per class. Each sample was acquired with 64 scans, an acquisition time of 220 s, a pulse width of 3.75 ms, and a relaxation delay of 2.0 s. The spectral width was adjusted to cover the 1.00 and 20.00 ppm range. All spectra were manually phased and baseline corrected.

Data Processing and Multivariate Data Analysis

The Chenomx Processor software (Version 5.1, Alberta, Canada) was utilised to preprocess ¹H NMR spectra, ensuring a consistent configuration across all sample spectra. Each spectrum was manually processed with phasing and baseline corrections, and TSP was selected as the reference peak at δ 0.00. Water-containing regions between δH 4.57 and 4.95 were excluded from all spectra. All ¹H NMR spectra were binned (bin size of 0.04) using Chenomx Profiler software (Version 5.1, Alberta, Canada) to obtain 243 data points, which will be subjected to multivariate data analysis (MVDA) as the x-variables input data. MVDA models such as principal component analysis (PCA) and orthogonal partial least square discriminant analysis (OPLS-DA) were conducted using SIMCA-P 14.1 (Umetrics AB, Umeå, Sweden). Prior to analysis, the data were Pareto scaled to minimise variance distortion. The dataset was initially subjected to PCA to visualise and differentiate groups based on their metabolites, providing an overall overview of the dataset. The NMR spectral data were subjected to OPLS-DA models to further distinguish between classes. The OPLS-DA model was applied to discriminate between two groups (classes) of the polychaetes of different ages. Probable metabolites contributing to the different age classes were identified based on the loading column plot. The OPLS-DA model was validated using CV-ANOVA, with a p-value < 0.05 indicating the model's statistical significance. The supervised model was also validated using permutation tests, with 20 permutations carried out in this study.

Identification of Metabolites Based on ¹H NMR Analysis

The diversity of metabolites associated with these different ages of *M. moribidii* was identified by comparing their chemical shifts in ¹H NMR spectra with the chemical shifts of standard compounds available in the Human Metabolome Database Data Bank (HMDB)

(<http://www.hmdb.ca/metabolites>) and literature. The identification of metabolites was performed using Chenomx Profiler software (Version 5.1, Alberta, Canada). The metabolic pathways were determined using MetaboAnalyst software (<http://www.metaboanalyst.ca/>). MetaboAnalyst is a web-based platform offering a suite of metabolomics data analysis tools, including pathway analysis, PCA and OPLS-DA. It provides a user-friendly interface and integrates various statistical and bioinformatics methods for data preprocessing, normalisation, and visualisation.

LC-MS/MS Data Analysis and Metabolite Identification

The LC-MS/MS analysis was carried out on a Vion IMS LC-QTOF-MS (Waters, USA). The liquid chromatography was separated using an ACQUITY UPLC BEH C18 column (2.1 X 50 mm, 1.7 μ m) with a gradient solvent system of 0.1% formic acid in water and 0.1% formic acid in acetonitrile. The injection volume was 10 μ L, and the flow rate was maintained at 0.4 mL/min for 35 min. The mass spectra were acquired in ESI negative ion mode with the parameters: Capillary voltage 2.50 kV, source temperature 120°C, desolvation temperature 550°C, desolvation gas 800 L/h, and cone gas 50 L/h. The acquired spectra were analysed using the in-house software UNIFI (Version 1.8; Waters Corporation). Metabolite identification was conducted by comparing the retention time and MS/MS data of the sample with the reference compound available in the library. Additionally, the identification of metabolites was verified by comparing them with the literature and consulting available online databases (<http://www.metabolomicsworkbench.org>).

Statistical Analysis

Relative quantification of identified metabolites was performed using the signals of metabolites of interest obtained from the binning dataset. Statistical analysis, including One-way ANOVA and Tukey's honest significant difference (Tukey-HSD) multiple-comparison, was conducted using MetaboAnalyst software (<http://www.metaboanalyst.ca/>). The p-values of <0.05 were considered statistically significant. Supplementary Table 1 in APPENDIX shows the One-way ANOVA and Tukey-HSD Pairwise Test results of the identified metabolites in M1, M2, and M3, along with boxplots comparing the different classes of polychaete samples.

RESULTS AND DISCUSSION

Identification of *M. moribidii* and Size (Body Width) Classification

Body width is commonly used as a standard method to determine the age class of polychaetes, as recommended by Occhioni et al. (2009). The findings indicate that body size variations among populations are stronger than shape. The identification of *M.*

moribidii samples in this study did not involve molecular techniques but relied on morphological comparisons. The detailed morphological features likely focused on external and internal anatomical characteristics, which serve as distinguishing traits among species within the genus *Marphysa* identified by Idris and Hutchings (2014). *M. moribidii* is classified into three age groups based on body width: young (M1) with a body width of 3–5 mm, adult (M2) with 6–8 mm, and old (M3) with 9–11 mm. This classification allows for studying how the metabolite profiles of *M. moribidii* evolve with age, aiding in the identification of metabolic variations. These metabolic changes may reflect physiological, biochemical, or ecological adaptations, providing insights into how the species interacts with its environment (Glasby et al., 2021). The images of *M. moribidii* representing different age classes based on their body width are presented in Figure 1. To facilitate clarity throughout the discussion, the notations M1, M2 and M3 have been assigned to represent each respective class of *M. moribidii* (Table 1).

Table 1
Different age classes of *M. moribidii* based on their body width (mm)

Class	Sample Notation	Width (mm)
I	M1	3 – 5
II	M2	6 – 8
III	M3	9 – 11

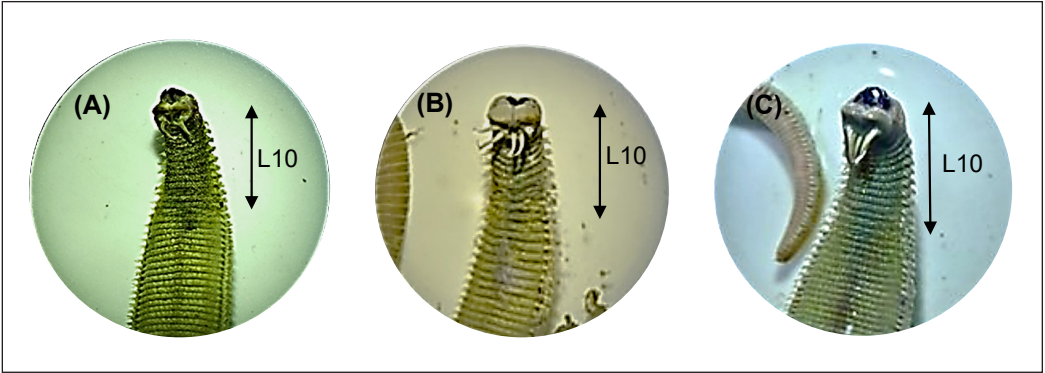


Figure 1. *M. moribidii* images under stereo zoom microscope of (A) Class I (3–5 mm), (B) Class II (6–8mm), and (C) Class III (9–11mm) (Olympus SZ); Scale bar: 100 µm

Metabolite Variations of Different Ages of *M. moribidii* Determined by ¹H NMR Metabolomics

Chemical constituents presented in the polychaete extract were identified using ¹H NMR analysis, a robust technique for compound identification in complex mixtures. The ¹H NMR spectra of the *M. moribidii* extract (Supplementary Figure 1) revealed the presence of various compounds (35 metabolites), including amino acids, organic compounds, nitrogenous compounds, vitamins, carbohydrates, and fatty acids (Table 2). Based on the

^1H NMR signals, the amino acids of phenylalanine, betaine, isoleucine, leucine, glycine, alanine, glutamic acid, methionine, L-aspartic acid, beta-alanine, valine and taurine were discovered. Phenylalanine was identified based on the signals observed at δH 7.41 (m), 7.36 (m), and 7.31 (m). Tentatively, singlets at δH 3.89 and 3.25 were assigned as betaine, and δH 3.55 was assigned to glycine. The characteristic signals for taurine were observed at δH 3.42 (t) and 3.25 (t). Meanwhile, multiple signals for methionine were also identified at δH 3.85 (m), 2.63 (m), 2.19 (m) and a singlet at δH 2.13.

The ^1H NMR spectra exhibited singlets signals for organic compounds at δH 3.65, 2.22, 2.27, 1.91, 3.12, 2.39 and 8.45, corresponding to glycerol, acetone, acetoacetic acid, acetate, malonic acid, succinic acid and formic acid, respectively. Some nitrogenous compounds identified were creatinine, observed at δH 4.05 (s) and 3.04 (s), and creatine at δH 3.92(s) and 3.03(s) along with trimethylamine at δH 2.88 (s). Furthermore, the ^1H NMR spectra revealed characteristic signals of fatty acids, including peaks at δH 5.34 (t), 1.22 (m), and 0.89 (t). Various signals corresponding to carbohydrates, such as sucrose and glucose, were also observed. Two metabolites from the vitamin group were also presented, exhibiting signals at δH 9.11(s), 8.82(m), 8.83(m), 8.07(m), 4.43(s) for trigonelline, and a singlet at δH 4.06, 3.51, and 3.19 for choline.

The experiments involved three distinct age classes of *M. moribidii*, which were subjected to ^1H NMR metabolomics to evaluate their metabolite variations. MVDA via PCA model was employed to reveal underlying patterns within the data in a two-dimensional representation (Figure 2A). The PCA model resulted in five principal components, with PC1 and PC2, considered the most informative for visualising and interpreting the data. The total variation explained by the PC1 and PC2 was 93.6%, which is sufficiently high to effectively describe the dataset. The R^2X cumulative value of 0.991 and Q^2 cumulative value of 0.961 further confirm that the PCA model is reliable and excellent. By examining the PCA loadings plot (Figure 2B), it was possible to identify metabolites associated with the observed clustering. These PCA-selected metabolic features were further validated and supplemented using OPLS-DA modelling. This binary classification approach facilitates discrimination analysis to extract metabolic markers that differentiate sample groups as depicted by the PCA models.

Table 2

Summary of the ^1H NMR metabolites assignment of *M. moribidii*, which categorises the different groups of metabolites and their respective signals

Group	Metabolite	Chemical shift (ppm)
Amino acid	Phenylalanine	7.41 (m), 7.36 (m), 7.31 (m), 4.00 (s, overlap), 3.28 (m, overlap), 3.11 (m, overlap)
	Betaine	3.89 (s), 3.25 (s)
	Isoleucine	1.00 (d), 0.93 (t)

Table 2 (continue)

Group	Metabolite	Chemical shift (ppm)
	Leucine	0.95 (t), 0.94 (t)
	Glycine	3.55 (s)
	Alanine	1.47 (d)
	Glutamic acid	3.75 (s), 2.36 (m), 2.33 (m), 2.12 (m), 2.04 (m)
	Methionine	3.85 (m), 2.63 (m), 2.19 (m), 2.13 (s), 2.11 (m)
	L-Aspartic acid	2.80 (m), 2.67 (m)
	β-Alanine	3.17 (m), 2.54 (t)
	Valine	1.03 (d), 0.98 (d)
	Taurine	3.42 (t), 3.25 (t, overlap)
Organic compound	Acetone	2.22 (s)
	Acetoacetic acid	2.27 (s)
	Acetamide	7.54 (s), 6.78 (s), 1.99 (s)
	Sn-Glycero-3-phosphocholine (GPC)	4.31 (s), 3.94 (m, overlap), 3.91 (m, overlap), 3.87 (m, overlap), 3.67 (m), 3.22 (s)
	Glycerol	3.78 (s), 3.65 (m), 3.55 (m)
	Short-chain keto acids (SCKA)	1.60–1.80 (m), 1.35–1.45 (m), 0.80–0.90 (t)
	Acetate	1.91(s)
	Lactic acid	4.11 (m), 1.34 (d)
	Malonic acid	3.12 (s)
	Succinic acid	2.39 (s)
	2-Oxoglutaric acid	3.00 (t), 2.43 (t)
	Formic acid	8.45 (s)
	Inosinic acid (IMP)	8.56 (s), 8.22 (s, overlap), 6.13 (d, overlap), 4.50 (m, overlap), 4.36 (m, overlap), 4.03 (m, overlap), 4.00 (m, overlap)
	Inosine	8.33 (s), 8.22 (s), 6.08 (m), 4.77 (s), 4.43 (s), 4.27 (s), 3.91 (m, overlap), 3.83 (m, overlap)
	4-Hydroxyphenylacetic acid (4-HPA)	7.15 (m), 6.85 (m), 3.42 (s)
Nitrogenous compound	Creatinine	4.05 (s), 3.04 (s)
	Creatine	3.92 (s), 3.03 (s)
	Trimethylamine (TMA)	2.88 (s)
Carbohydrate	Sucrose	5.40 (d), 4.21 (d), 4.04 (t), 3.88 (overlap), 3.82 (m), 3.80 (m),3.76 (m), 3.69 (s), 3.55 (overlap), 3.47 (t)
	Glucose	5.23 (d), 4.64 (d), 3.89(m), 3.84 (m), 3.76 (m), 3.53 (m), 3.48 (m), 3.39 (m), 3.23 (t, overlap)
Vitamin	Trigonelline	9.11 (s), 8.82 (m), 8.83 (m), 8.07 (m), 4.43 (s)
	Choline	4.06 (s), 3.51 (s), 3.19 (s)
Fatty acid		5.34 (t), 1.22 (m), 0.89 (t, overlap)

s=singlet, d=doublet, t=triplet, and m= multiplet

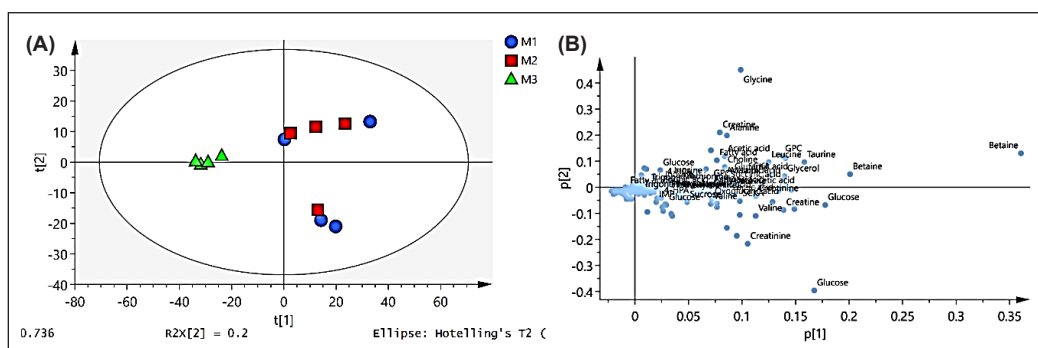


Figure 2. (A) Principal component analysis (PCA) scores plot and (B) loadings plot of ^1H NMR spectral data obtained from M1 (blue), M2 (red), and M3 (green)

This analysis revealed a distinct cluster formation, effectively separating each class of *M. moribidii*. M1 and M2 were in the same cluster within the right quadrant of the PCA scores plot, indicating that they share a similar chemical profile (Figure 2A). As anticipated, the separation between these age classes was primarily attributed to variations in amino acid content and other metabolites overlapping with the glucose region, such as trigonelline, fatty acid, inosinic acid or inosine monophosphate (IMP) and 4-hydroxyphenylacetic acid (4-HPA) (Figure 2B). According to the PCA scores plot, M1 and M2 overlapped, suggesting similar metabolite features between these two groups. The PCA loadings plot indicated that M3 shares the same metabolites as M1, but the metabolites of M3 are presented at lower concentrations, as evidenced by the lower intensity of their chemical shifts compared to the others. The relative quantification of identified metabolites was performed to determine the significant differences between the different classes (Supplementary Table 1). According to the results, the concentrations of M1 and M2 metabolites are not significantly different, while the metabolites of M3 (mostly at low concentrations) are significantly different compared to M1 and M2. In addition, identifying other metabolites in M3 was challenging due to suppressing their signals in the NMR spectra by glucose signals and other metabolites overlapping with the glucose region. Therefore, comparing the two classes via OPLS-DA models was conducted to obtain a clearer metabolite profile of the different classes (M1 versus M2, M2 versus M3, and M1 versus M3).

The OPLS-DA models were conducted to investigate the significant difference between the different age classes of *M. moribidii*. CV-ANOVA and permutation tests were performed to validate the OPLS-DA models (Supplementary Figure 2-4). The model exhibited a distinct cluster formation, effectively separating the M1, M2 and M3. Interestingly, a trend within each age class of *M. moribidii* was observed, as depicted in the loading scatter plot of M1 and M2 (Figure 3A), where no significant cluster was observed in the 2D scores plot. This suggests that there is no significant difference between M1 and M2. When comparing three groups, the data becomes more complex, and the relationships between groups are

harder to interpret, especially if the models struggle to differentiate the classes due to similar metabolites in M1 and M2. Additionally, the p-value (< 0.05) based on the CV-ANOVA test further supports the finding that there is no significant difference between these two classes, as shown in Supplementary Figure 2. Jackknife error used in the OPLS-DA model refers to the estimation of model stability and generalizability by systematically leaving out one data point at a time during the analysis. In the context of an OPLS-DA scores plot, jackknife error helps assess the robustness of the model's ability to discriminate between groups. Some of the jackknife error bars are bigger than others in Figure 3 (A) (M1 versus M2) because certain data points may influence the model's performance more. Larger error bars suggest greater variability in the model's performance.

The OPLS-DA model explains the variation among compositions and their contribution to the discrimination pattern. Figure 3A shows the OPLS-DA scores plot for M1 (blue) versus M2 (red), while Figures 3B and 3C depict scores plots for M1 (blue) versus M3 (green) and M2 (red) versus M3 (green), respectively. Based on the OPLS-DA scores plots, discrimination of different ages of *M. moribidii* was achieved between M1 and M3 (Figure 3B), as well as M2 and M3 (Figure 3C), indicating the significant difference between M3 and other age classes. Based on the OPLS-DA loading column plots, most of the metabolites are shown to be higher in M1 and M2 compared to M3 (Supplementary Figures 3C and 4C). The results suggested that M1 and M2 are the best ages to be cultivated. The findings were also supported by the relative quantification of identified metabolites of M1, M2, and M3, as presented in Supplementary Table 1. Supplementary Figure 5 presents boxplots of metabolites from the three groups of *M. moribidii*.

A previous study found that harvest times influence polychaetes' chemical composition and metabolic variations

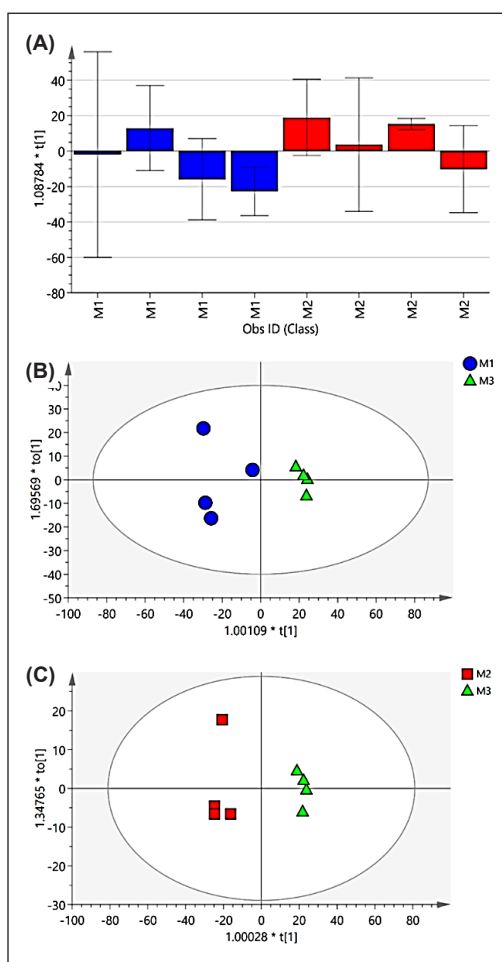


Figure 3. Orthogonal partial least squares discriminant analysis (OPLS-DA) scores plot of (A) M1 (blue) versus M2 (red), (B) M1 (blue) versus M3 (green), and (C) M2 (red) versus M3 (green)

(Wijaya et al., 2024). Metabolites are more abundant during the hot season due to higher temperatures accelerating metabolism and supporting growth and reproduction. In contrast, the rainy season's reduced salinity and variable conditions may stress the polychaetes, lowering metabolic activity and metabolite production.

Metabolite Profile of Three Age Classes of *M. moribidii* Extract Based on LC-MS/MS Analysis

LC-MS/MS analysis was performed to better understand the metabolites present in *M. moribidii* at different ages. Since LC-MS/MS analysis is more sensitive than ^1H NMR analysis, a greater number of secondary metabolites are anticipated to be identified. This study used qualitative metabolite identification based on LCMS/MS analysis. The signal-to-noise (S/N) ratio was an essential factor for the analysis. Signals of metabolites with an S/N ratio below 1 (S/N ratio < 1) were not identified, as they were considered noise rather than meaningful data. This threshold ensures that only reliable and robust signals are included in the interpretation, minimising the risk of false positives due to background noise. Identification of metabolites was performed using the m/z and MS/MS fragmentations of interest compounds and comparing them with the m/z and MS/MS fragmentations of standard compounds available in the database. Nonetheless, a total of 36 compounds were tentatively identified from various age classes of *M. moribidii*, using LC-MS/MS, including organic acids, carbohydrates, phenolic, fatty acids and amino acids, with only one compound extra compared to ^1H NMR metabolomics. The proposed compounds for the three distinct age classes of *M. moribidii* are shown in Table 3, highlighting the differences observed in the presence or absence of these compounds.

Major identified metabolites of *M. moribidii* can be classified into primary and secondary metabolites. Primary metabolites refer to small chemical compounds such as organic acids, carbohydrates, phenolic, fatty acids, and amino acids that are directly involved in the growth, development, and reproduction of living organisms (Salam et al., 2023). These compounds are essential for maintaining normal physiological functions in the body. On the other hand, secondary metabolites are organic acids, carbohydrates, phenolics, fatty acids, and amino acids produced by modifying primary metabolites. These secondary metabolites are typically synthesised during the stationary phase of growth. Unlike primary metabolites, secondary metabolites do not play a direct role in growth, development, or reproduction (Bruce, 2022). Instead, they often serve ecological functions such as defence mechanisms and can exhibit properties such as antibiotics, antimicrobial, antifungal, anticancer, and antiviral (Izzati et al., 2021).

As depicted in Table 3, sucrose was detected in M1, M2 and M3 samples, with a retention time (RT) of 13.65 and a mass-to-charge ratio (m/z) of 341.1069. Sucrose and glucose were also identified in ^1H NMR spectra of *M. moribidii* of different ages. Sucrose,

a simple carbohydrate with low reactivity, plays essential roles in both plants and animals. Sucrose is commonly used in marine worms to store energy. Like many other organisms, marine worms require energy to perform biological processes such as movement, growth, and reproduction (Ulu et al., 2021). Marine worms can consume sucrose directly from their surroundings or by breaking down other organic matter. Once ingested, sucrose can be broken down into monosaccharides (glucose) that are then utilised in cellular respiration to generate ATP (adenosine triphosphate), the primary energy currency of cells (Khowala et al., 2008).

Cyclo (Pro-Val) is a cyclic dipeptide composed of proline and valine. It is found in sponges, molluscs, and some marine bacteria and can perform a variety of functions (Zeng et al., 2023). These organisms produce and utilise Cyclo (Pro-Val) as part of their metabolic processes. These compounds may play a role in osmoregulation, helping marine worms adapt to changes in salinity and other environmental conditions. In some cases, Cyclo (Pro-Val) can provide nitrogen or other nutrients to marine organisms, contributing to their growth and development. Based on its known biological activities, Cyclo (Pro-Val) is anticipated to contribute to various physiological processes that support the health and adaptation of marine worms in their aquatic environment (Bojarska et al., 2021).

L-tyrosine is a natural protein building block presented in M1 and M3 samples while absent in M2. This observation suggests that, rather than being a naturally occurring substance in M2, the source of L-tyrosine may be a nutrient found in sediment that the organism uses as sustenance. Since L-tyrosine is an amino acid that the body can synthesise, it is considered a non-essential amino acid (Lopez & Mohiuddin, 2024).

In contrast, L-phenylalanine is presented only in M2, indicating that the nutrient content in *M. moribidii* extract primarily originates from the soil. According to Aliu et al. (2018), phenylalanine and tyrosine differ primarily because the former is an essential amino acid while the latter is a non-essential amino acid. However, the amino acids of acetylglucosamine, which are well recognised for their structural roles at the cell surface, were only found in M3 at a *m/z* of 266.0891. It is a crucial part of the extracellular matrix found in animal cells, the fungus chitin, and the bacterium peptidoglycan. Furthermore, N-alpha-acetyl-L-lysine, a derivatised alpha amino acid, is identified at *m/z* of 187.1088 in M2 and M3. It is the biologically accessible N-terminal capped form of L-lysine, an alpha amino acid prevalent in proteins.

Interestingly, the only phenolic molecule identified in *M. moribidii* was 2-methoxy-4-acetylphenyl-1-O-β-D-apiofuranosyl-(1''→6')-β-D glucopyranoside and specifically found in M2 sample. It belongs to a group of natural products known as glycosides, commonly occurring as β-D-glucosides, which are presented in various plant pigments such as anthocyanins. Phenolic glycosides have been newly identified in *M. moribidii*, marking the first representative of their presence in this species. Since glycosides are

Table 3
Identification of three different age classes of Marphysa moribidii

No.	RT (min)	m/z	Adduct	Neutral mass (Da)	MS/MS fragment ions	Mass error (ppm)	Tentative compound	Availability		
								M1	M2	M3
1	0.62	367.1060	[M-H] ⁻	368.1132	353, 331	6.8	3-Feruloylquinic acid	x	/	x
2	0.93	180.0667	[M-H] ⁻	181.0739	163, 202	0.2	L-Tyrosine	/	x	/
3	0.94	405.1040	[M+HCOO] ⁻	360.1058	322, 324, 163, 180	0.4	Glucosyringic acid	/	/	/
4	1.23	266.0891	[M+HCOO] ⁻	221.0909	150	3.5	Acetylglucosamine	x	x	/
5	1.73	164.0717	[M-H] ⁻	165.0790	201	0.0	L-Phenylalanine	x	/	x
6	1.83	187.1088	[M-H] ⁻	188.1160	187	-0.3	N-alpha-acetyl-L-lysine	x	/	/
7	3.76	459.1504	[M-H] ⁻	460.1577	258	-0.9	2-Methoxy-4-acetylphenol 1-O- α -L-rhamnopyranosyl-(1" \rightarrow 6')- β -D-glucopyranoside	x	/	x
8	3.76	459.1504	M-H	460.1577	244, 375	-0.9	2-Methoxy-4-acetylphenyl-1-O- β -D-apiofuranosyl-(1" \rightarrow 6')- β -D-glucopyranoside	x	/	x
8	4.18	593.2191	[M-H] ⁻	594.2263	227, 439	-8.2	Pseudolaric acid B O- β -D-glucopyranoside	x	/	x
9	5.43	241.1194	[M+HCOO] ⁻	196.1212	197	0.0	Cyclo(Pro-Val)	/	/	/
10	5.91	255.0882	[M+HCOO] ⁻	210.0900	212	2.9	Ethyl-5-ethoxy-2-hydroxy benzoate	x	/	/
11	13.38	237.1112	[M+HCOO] ⁻	192.1130	197	-8.7	Phenylethyl butanoic acid	/	x	/
12	13.65	341.1069	[M-H] ⁻	342.1142	171	-5.9	Sucrose	/	/	/
13	15.59	417.1560	[M-H] ⁻	418.1633	415, 180	1.2	Pseudolaric acid C2	/	/	/
14	15.85	267.1968	[M-H] ⁻	268.2040	267	0.7	13-Hydroxy-9,11-hexadecadienoic acid	/	x	x
15	15.98	313.2384	[M-H] ⁻	314.2456	201, 313, 96	-0.3	Dibutyl sebacate	/	/	/
16	16.10	361.1634	[M-H] ⁻	362.1707	304, 220	1.2	Thyrotropin Releasing Hormone	/	/	/
17	16.99	311.2231	[M+HCOO] ⁻	266.2249	171, 293, 193	1.0	Methyl 7,10-hexadecadienoic acid	/	/	/
18	17.00	339.2541	[M+HCOO] ⁻	294.2559	315, 319, 321	0.0	9,12-Octadecadienoic acid methyl ester	/	/	/
19	17.00	339.2541	[M+HCOO] ⁻	294.2559	319, 199, 321	0.0	10,13-Ethyl octadecadienoic acid	x	/	/
20	17.28	293.2121	[M-H] ⁻	294.2193	207, 171	-0.5	(E,E)-9-Oxo-octadeca-10,12-dienoic acid	x	/	/

Table 3 (continue)

No.	RT (min)	m/z	Adduct	Neutral mass (Da)	MS/MS fragment ions	Mass error (ppm)	Tentative compound	Availability
21	17.28	379.2102	[M+HCOO] ⁻	334.2120	255, 193	-6.5	Di (2-ethyl butyl) phthalic acid	/ / /
22	17.80	335.2223	[M+HCOO] ⁻	290.2241	295	-1.5	6,9-Octadecadiynoic acid, methyl ester	x / /
23	17.91	253.1807	[M-H] ⁻	254.1879	233	-1.0	9-Hydroxy-10,12-pentadecadienoic acid	x / /
24	17.98	275.2015	[M-H] ⁻	276.2088	275	-0.4	Stearidonic acid	x / /
25	17.99	315.2540	[M-H] ⁻	316.2612	297	-0.4	Dihydroxy stearic acid	/ / /
26	18.21	341.2690	[M+HCOO] ⁻	296.2708	229	-2.0	Methyl oleic acid	x / x
27	18.41	295.2278	[M-H] ⁻	296.2351	277, 195	-0.2	Coronanic acid	x / /
28	18.64	277.2171	[M-H] ⁻	278.2244	195	-0.7	γ-Linoleic acid	x / /
29	19.08	297.2441	[M-H] ⁻	298.2514	343	2.1	Ricinoleic acid	x / /
30	21.81	281.2488	[M-H] ⁻	282.2560	281, 282	0.6	Elaidic acid	x / /
31	21.82	281.2491	[M-H] ⁻	282.2564	281	1.9	(E)-9-Octadecenoic acid	x / x
32	23.46	337.3113	[M-H] ⁻	338.3186	337	0.3	Erucic acid	x / /
33	24.35	383.3529	[M-H] ⁻	384.3602	211, 247, 255	-0.4	α-Hydroxy tetracosanic acid	x / /
34	26.25	744.5538	[M+HCOO] ⁻	745.5611	223	-1.4	Phosphatidyl ethanolamine	x x /
35	328.26	373.2589	[M+HCOO] ⁻	328.2607	353	-1.9	9,12-Dihydroxy-15-nonadecenoic acid	x / x
/ Presence								
X Absence								

classified as secondary metabolites, they can act as chemical defences against predators, and this compound often possesses antimicrobial properties, which help to protect marine invertebrates from infections and diseases in their marine environment (Choudhary et al., 2017).

Fatty acid esters, which are derivatives of carboxylic acid, are also largely found in *M. moribidii* at different ages, as presented in Table 3. Methyl oleic acid and phenylethyl butanoic acid are fatty acid esters found only in M2 samples at m/z of 341.2690 and 237.1112, respectively. Methyl oleic acid results from the condensation of oleic acid with methanol and occurs naturally in various fats and oils of both animal and plant origin. Like other fatty acids, methyl oleic acid can serve as a source of energy when metabolised by the organism, and it is an integral component of cell membranes, providing stability and fluidity (Ali & Szabó, 2023). At the same time, phenylethyl butanoic acid was not classified in the phenyl group and contained a hydrogen atom in its molecular structure. Phenylethyl butanoic acid is an aromatic compound with a butanoic acid side chain and a phenethyl group. Aromatic compounds frequently serve as signalling molecules in intra- and interspecies communication. They can convey information about mating, territorial boundaries, or danger, while some aromatic compounds can influence behaviours such as feeding or social interactions among marine invertebrates (Elgar, 2019).

Stearidonic acid, which is synthesised from alpha-linolenic acid and γ -linoleic acid (LA), was detected at m/z 275.2015 and 277.2171 in both M1 and M2, respectively. LA is an essential nutrient with important physiological functions in various organisms. However, the mechanism of LA synthesis differs among species, as observed in studies involving insects, nematodes, and pulmonates (Malcicka et al., 2018). Ricinoleic acid has been found in M2 and M3 at m/z 297.2441, indicating extensive metabolism in the rumen and tissues, while coronaric acid at m/z 295.2278, is produced by cells and tissues of various mammalian species, including humans, through linoleic acid metabolism. These findings are supported by studies conducted by Alves et al. (2017) and Konkel and Schunck (2011). Furthermore, 9,12-octadecadienoic acid methylester, which has antibacterial properties, was found in all age classes of *M. moribidii* (M1, M2, and M3) at m/z 294.2559 (Rahman et al., 2014). Additionally, according to a study by Gheda and Ismail (2020), methyl 7,10-hexadecanoic at m/z 311.2231, which was also detected in all age classes of *M. moribidii* and classified as a linoleic acid ester, has demonstrated antioxidant, anti-inflammatory, and hypocholesterolemic characteristics.

Additional substances found in M1, M2, and M3 included the peptide thyrotropin-releasing hormone (TRH), a peptide which is mostly generated by brain neurons. Thyroid-stimulating hormone (TSH), which regulates the thyroid axis through neurons in the hypothalamus, is secreted by the anterior pituitary gland in animals in response to stimulation by TRH (Charli et al., 2020). Although TRH was first identified in relation to TSH release,

it has a variety of impacts on different species (Galas et al., 2009). Phthalates are another group of compounds found in all age classes of *M. moribidii*. They are naturally occurring, bioactive substances that plants, bacteria, fungi produce, and other organisms (Huang et al., 2021). On the other hand, only M3 showed signs of phosphatidylethanolamines, which is likely related to *M. moribidii*'s elderly age. Phosphatidylethanolamines, which make up approximately 25% of phospholipids, are essential components in all living cells (Calzada et al., 2016). They are widely distributed in brain tissue, neurons, and the spinal cord in humans and account for 45% of phospholipids. They serve critical roles in several biological pathways, including membrane fusion, cell division, and membrane curvature (Vance & Tasseva, 2013; Imbs et al., 2021).

Compound Distribution in Different Age Classes of *M. moribidii*

The Venn diagram depicts unique compounds that have been discovered in different age classes of *M. moribidii* (designated by M1, M2, and M3), and Figure 4 summarises the distribution of compounds. According to the Venn diagram, all three different age classes of *M. moribidii* share a common set of 41 compounds identified through a combination of LC-MS/MS and NMR metabolite analysis. However, five metabolites appear in both datasets, eliminating these duplicates. The distribution of metabolites was constructed in that way to ensure accuracy and precise analysis by eliminating duplicates and reducing redundancy. After data acquisition, metabolites identified by both LC-MS/MS and NMR are compared for overlap. Duplicate entries are removed when both methods detect the same compound to ensure unique metabolite representation in the final dataset. Redundancy occurs as both techniques can identify the same metabolites, including organic acids, carbohydrates, phenolics, fatty acids and amino acids.

Interestingly, the M1 variety exhibits one unique compound, while the M2 and M3 varieties have seven and two unique compounds, respectively. Relative quantification of identified metabolites based on NMR analysis indicates the metabolite variations in different classes of polychaetes, showing that M3 has fewer metabolites compared to M1 and M2 (Supplementary Table 1). Specifically, only a single, distinctive compound of 13-hydroxy-9,11-octadecadienoic acid was identified in M1. This monohydroxy fatty acid plays a significant role in marine

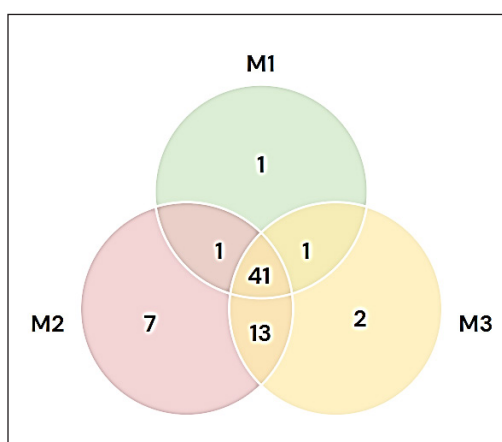


Figure 4. Venn diagram showing compound distribution in different age classes of *M. moribidii*

invertebrates. Previous research has demonstrated the notable antifungal activity of unsaturated hydroxy fatty acids with hydroxylation at the C9–C13 positions in a C18 chain (Guimarães & Venâncio, 2022). Furthermore, hydroxy fatty acids such as 11-HEPE and 15-HEPE have been found in diatoms through investigations on lipoxygenase pathways, suggesting their involvement in a variety of biological activities (Ruocco et al., 2020). According to these findings, 13-hydroxy-9,11-octadecadienoic acid and related compounds may support several various physiological and ecological processes in marine invertebrates, including signalling and defence systems.

Interestingly, M2 is categorised as having the greatest number of unique metabolites found compared to M1 and M3, as it shows seven distinct metabolites. The first metabolite identified in M2 is L-phenylalanine. Limited information is available regarding the specific function of L-phenylalanine in marine invertebrates. However, research indicates that phenylalanine plays important roles in regulating the capacity of intestinal immunity, antioxidants, and apoptosis in fish, including largemouth bass and gilthead seabream. In addition, phenylalanine is essential for synthesising proteins, catecholamines, and melanin (Salamanca et al., 2021; Yi et al., 2023).

The next compound discovered in M2 is 2-methoxy-4-acetylphenol 1-O- α -L-rhamnopyranosyl-(1'' \rightarrow 6')- β -D-glucopyranoside, an aromatic compound classified as phenylpropanoid glycoside. Phenylpropanoid glycosides are known for their wide range of biological activities, including antioxidant, anti-inflammatory, and antimicrobial properties (Skalski et al., 2021). Consequently, this compound holds the potential to contribute to the biological activities associated with marine invertebrates. Another compound identified in M2 is 2-methoxy-4-acetylphenyl-1-O- β -D-apiofuranosyl-(1'' \rightarrow 6')- β -D-glucopyranoside, a complex sugar molecule with recognised activities in marine invertebrates (D'Abrosca et al., 2010). Depending on the specific species and its presence in their tissues or secretions, this compound may serve a variety of functions in marine invertebrates. In general, sugar molecules are essential to many biological functions, including cell signalling, energy storage, and structural support (Rolland et al., 2002).

Additionally, M2 contains pseudolaric acid β -O-beta-D-glucopyranoside, classified as a rifamycin, and has anti-tuberculosis properties. According to Li et al. (2020), pseudolaric acid has been demonstrated to exhibit a variety of biological functions, for instance, serving as an antifungal agent. M2 also contains a fatty acid ester of methyl oleic acid that shares functional similarities with oleic acid, which is recognised for its diverse activities in various roles, including being a carboxylesterase inhibitor and a metabolite in different organisms (Ruiz et al., 2022). Octadecenoic acid is another next-generation metabolite found in M2. Octadecenoic acid content changes according to the species and habitat of the marine invertebrate. It is also found in the phospholipids of *Holothuria mexicana* and is a trace element in *Kamptosoma abyssale*, an abyssal species (Barnathan, 2009).

9,12-dihydroxy-15-nonadecenoic acid, a chemical compound present in various marine invertebrates, is the final distinct metabolite found in M2. Its occurrence in these organisms raises the possibility that it plays a part in their biology and defence systems. Sponge-like marine invertebrates depend on humoral and cellular immunity as part of their innate immune systems (Sperstad et al., 2011). The existence of 9,12-dihydroxy-15-nonadecenoic acid in marine invertebrates suggests a potential contribution to their innate immune system and plays a role in protecting them against various pathogens, even though it is not specifically discussed in the context of these organisms' defence mechanisms.

The old age class of *M. Moribidii* (M3) shows the presence of two distinct chemicals where the first compound identified is acetylglucosamine. According to Riemann and Azam (2002), acetylglucosamine is known as an important constituent of structural polymers found in bacteria, plants, and animals, including various marine invertebrates such as cuttlefish, crab, and lobster, as well as fungi and algae. The subsequent compound identified in M3 is phosphatidylethanolamines (PE), which plays a crucial role in marine invertebrates as a major structural lipid in cell membranes. Furthermore, ethanolamine-containing special glycerophospholipid plasmalogens, which are prevalent in several marine invertebrates, have been associated with benefits for age-associated diseases (Yamashita et al., 2023). Consequently, PE plays a crucial part in the composition and operation of marine invertebrates' cell membranes. In summary, *M. moribidii* has distinct fatty acid, amino acid, and phospholipid components at both the young (M1) and old (M3) ages. Interestingly, *M. moribidii* (M2) has a higher concentration of different substances in its middle age, such as amino acids, fatty acids, fatty acid esters, and phenylpropanoid glycoside.

As far as we know, no research has been conducted on the metabolite profile of various ages of marine worms. Among the most popular model organisms to investigate the molecular mechanisms of ageing are the nematodes of *Caenorhabditis elegans* due to their short lifespan and ease of cultivation in the laboratory (Balashova et al., 2022). Copes et al. (2015) studied global quantification of metabolite and protein levels in young and aged nematodes of *C. elegans* using mass spectrometry, which successfully identified 186 metabolites. The metabolomics data show that as *C. elegans* ages, the levels of free fatty acid and sorbitol content increase, while those of specific purine and pyrimidine metabolites, free hydrophobic amino acids and altered S-adenosyl methionine metabolism decrease, and a shift in cellular redox balance.

Figure 5 summarises the proposed metabolic pathway involved in *M. moribidii*. According to the results, there are four important metabolic pathways in *M. moribidii*: phenylalanine, tyrosine and tryptophan biosynthesis, phenylalanine metabolism, taurine and hypotaurine metabolism, and beta-alanine metabolism. This pathway analysis highlights significant metabolites, particularly emphasising primary metabolites that play essential roles in the metabolism of *M. moribidii*.

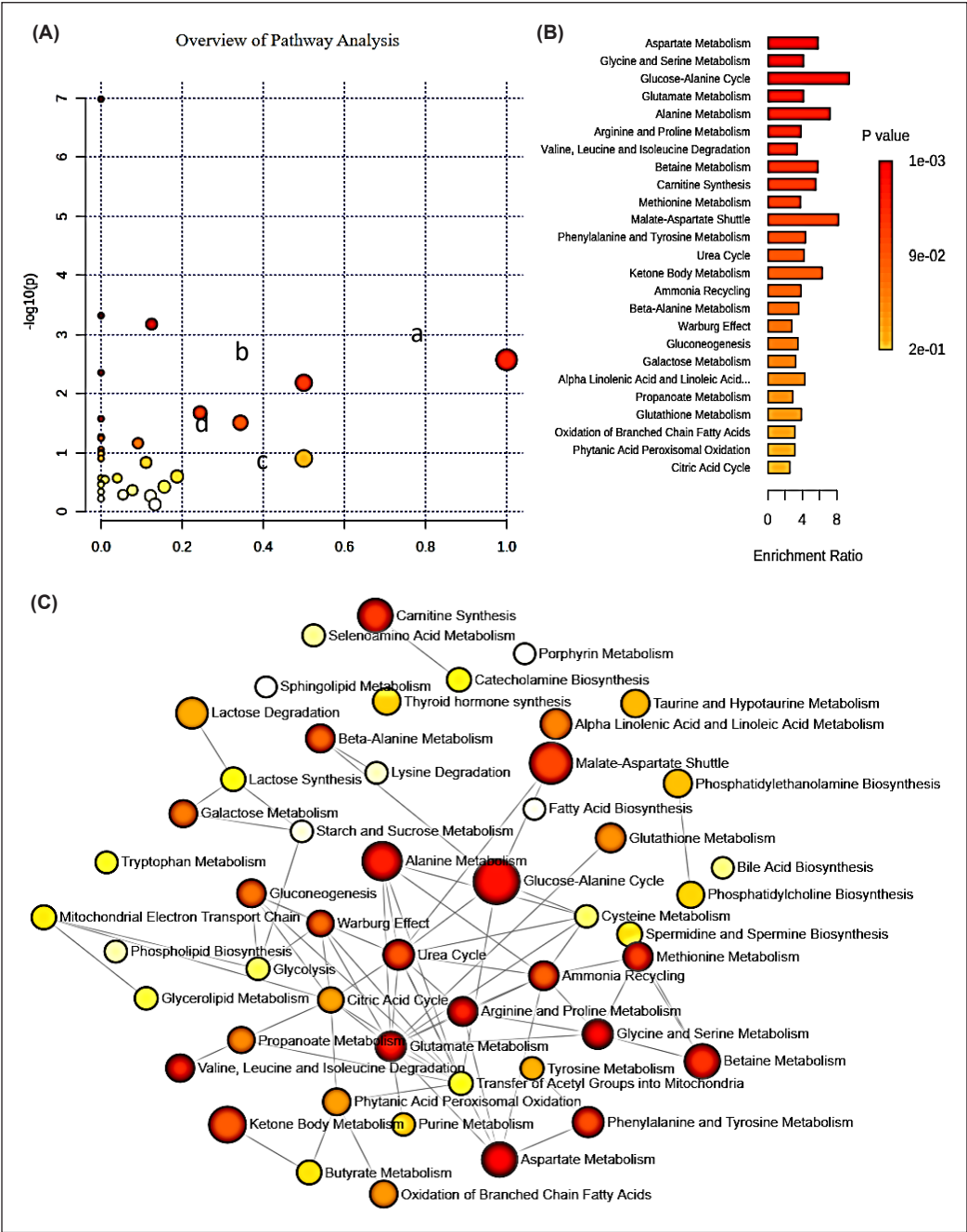


Figure 5. Summary of pathway analysis determined using Metaboanalyst. (A) Pathway impact: (a) Phenylalanine, tyrosine and tryptophan biosynthesis; (b) Phenylalanine metabolism; (c) Taurine and hypotaurine metabolism; (d) beta-Alanine metabolism. (B) Metabolite sets enrichment overview and MetaMapp visualisation of metabolomic data highlighting the differential metabolic regulation. (C) MetaMapp graphs in Cytoscape showed much clearer metabolic modularity and complete content visualisation compared to conventional biochemical mapping approaches

Pathway analysis using MetaboAnalyst typically provides an overview of the key metabolic pathways that are most relevant to *M. moribidii*. This type of analysis integrates metabolite data and maps them to know their metabolic pathways, allowing for a broader understanding of the biochemical processes occurring within the organism. In a MetaMapp graph, nodes represent metabolites like glucose, amino acids, or lipids. At the same time, the edges and the lines connecting the nodes show the relationships or interactions between metabolites. These relationships can include biochemical conversions, where enzymes change one metabolite into another or connect between different metabolic modules. The graph can be adjusted to show how metabolites and pathways are linked, with edges and nodes clearly showing which metabolites are involved in which pathways and how they are grouped together. The metabolic pathways in Figure 5C show the overview of the general metabolite involved in *M. moribidii*.

CONCLUSION

We observed a comprehensive spectrum of metabolite profiles in marine worms, *M. moribidii*, from various age classes using NMR and LC-MS/MS analysis, including organic acids, carbohydrates, phenolics, fatty acids, and amino acids. *M. moribidii*'s middle age (M2) classes have the most identified chemicals (62 metabolites) when compared to the young (M1) and old age (M3) classes. The most noticeable discovery from this study is that M2 has the maximum number of seven distinct metabolites composed of fatty acid, amino acid, phenylpropanoid glycoside, and fatty acid esters compared to the young and old classes of *M. moribidii*. M2 unique metabolites might contribute to a variety of biological activities, including antioxidant, anti-inflammatory, antibacterial, and defence and immunological systems. These data indicate that discrepancies in age classifications of *M. moribidii* result in diverse metabolite profiles, with not all metabolites present in different age classes of *M. moribidii*. Overall, this study improves our understanding of *M. moribidii*, an intriguing annelid species, by emphasising the significance of metabolomics in identifying the numerous metabolic pathways associated with its various age classes. This study's findings shed light on the physiology and ecology of metabolic variability, establishing the groundwork for future research into the genetic and biochemical mechanisms behind the observed changes in *M. moribidii* metabolism.

ACKNOWLEDGEMENT

The author acknowledges the support of the Ministry of Higher Education (MOHE) Malaysia through the Fundamental Research Grant Scheme (FRGS/1/2020/STG02/UMT/02/1). We also thank Universiti Malaysia Terengganu for their generous support.

REFERENCES

- Ali, O., & Szabó, A. (2023). Review of eukaryote cellular membrane lipid composition, with special attention to the fatty acids. *International Journal of Molecular Sciences*, 24(21), Article 15693. <https://doi.org/10.3390/ijms242115693>
- Aliu, E., Kanungo, S., & Arnold, G.L. (2018). Amino acid disorders. *Annals of Translational Medicine*, 6(24), 471–471. <https://doi.org/10.21037/atm.2018.12.12>
- Alves, S. P., Araujo, C. M., Queiroga, R. C., Madruga, M. S., Parente, M. O. M., Medeiros, A. N., & Bessa, R. J. B. (2017). New insights on the metabolism of ricinoleic acid in ruminants. *Journal of Dairy Science*, 100(10), 8018–8032. <https://doi.org/10.3168/jds.2017-13117>
- Balashova, E. E., Maslov, D. L., Trifonova, O. P., Lokhov, P. G., & Archakov, A. I. (2022). Metabolome profiling in aging studies. *Biology*, 11, Article 1570. <https://doi.org/10.3390/biology11111570>
- Barnathan, G. (2009). Non-methylene-interrupted fatty acids from marine invertebrates: Occurrence, characterization and biological properties. *Biochimie*, 91(6), 671–678. <https://doi.org/10.1016/j.biochi.2009.03.020>
- Bojarska, J., Mieczkowski, A., Ziora, Z., Skwarczynski, M., Toth, I., Shalash, A. O., Parang, K., El-Mowafi, S. A., Mohammed, E. H. M., Elnagdy, S., Alkhazindar, M., & Wolf, W. M. (2021). Cyclic dipeptides: The biological and structural landscape with special focus on the anti-cancer proline-based scaffold. *Biomolecules*, 11(10), Article 1515. <https://doi.org/10.3390/biom11101515>
- Bruce, S. O. (2022). Secondary metabolites from natural products. In R. Vijayakumar & S. S. S. Raja (Eds.), *Secondary Metabolites - Trends and Reviews* (pp. 51-70). IntechOpen. <https://doi.org/10.5772/intechopen.102222>
- Calzada, E., Onguka O., & Claypool, S. M. (2016). Phosphatidylethanolamine metabolism in health and disease. *International Review of Cell and Molecular Biology*, 321, 29–88. <https://doi.org/10.1016/bs.ircmb.2015.10.001>
- Capa, M., & Hutchings P. (2021). Annelid diversity: Historical overview and future perspectives. *Diversity*, 13(3), 1–14. <https://doi.org/10.3390/d13030129>
- Charli, J. L., Rodríguez-Rodríguez, A., Hernández-Ortega, K., Cote-Vélez, A., Uribe, R. M., Jaimes-Hoy, L., & Joseph-Bravo, P. (2020). The thyrotropin-releasing hormone-degrading ectoenzyme, a therapeutic target? *Frontiers in Pharmacology*, 11, 1–21. <https://doi.org/10.3389/fphar.2020.00640>
- Choudhary, A., Naughton, L. M., Montánchez, I., Dobson, A. D. W., & Rai, D. K. (2017). Current status and future prospects of marine natural products (MNPs) as antimicrobials. *Marine Drugs*, 15(9), Article 272. <https://doi.org/10.3390/md15090272>
- Copes, N., Edwards, C., Chaput, D., Saifee, M., Barjuca I., Nelson, D., Paraggio, A., Saad, P., Lipps, D., Stevens, S. M., & Bradshaw, P. C. (2015). Metabolome and proteome changes with aging in *Caenorhabditis elegans*. *Experimental Gerontology*, 72, 67–84. <https://doi.org/10.1016/j.exger.2015.09.013>
- D’Abrosca, B., Fiorentino, A., Ricci, A., Scognamiglio, M., Pacifico, S., Piccolella, S., & Monaco, P. (2010). Structural characterization and radical scavenging activity of monomeric and dimeric cinnamoyl glucose

- esters from *Petrorhagia velutina* leaves. *Phytochemistry Letters*, 3(1), 38–44. <https://doi.org/10.1016/j.phytol.2009.11.001>
- Elgar, M. A. (2019). Chemical signaling: Air, water, and on the substrate. *Encyclopedia of Animal Behavior*, 1, 462 – 473. <https://doi.org/10.1016/B978-0-12-809633-8.90718-0>
- Emwas, A. H., Roy, R., McKay, R. T., Tenori, L., Saccenti, E., Gowda G. A. N., Raftery, D., Alahmari, F., Jaremko, L., Jaremko, M., & Wishart, D. S. (2019). NMR spectroscopy for metabolomics research. *Metabolites*, 9(7), Article 123. <https://doi.org/10.3390/metabo9070123>
- Galas, L., Raoult, E., Tonon, M. C., Okada, R., Jenks, B. G., Castaño, J. P., Kikuyama, S., Malagon, M., Roubos, E. W., & Vaudry, H. (2009). TRH acts as a multifunctional hypophysiotropic factor in vertebrates. *General and Comparative Endocrinology*, 164(1), 40–50. <https://doi.org/10.1016/j.ygcen.2009.05.003>
- Gathungu, R. M., Kautz, R., Kristal, B. S., Bird, S. S., & Vouros, P. (2020). The integration of LC-MS and NMR for the analysis of low molecular weight trace analytes in complex matrices. *Mass Spectrometry Reviews*, 39(1-2), 35–54. <https://doi.org/10.1002/mas.21575>
- Gheda, S. F., & Ismail, G. A. (2020). Natural products from some soil cyanobacterial extracts with potent antimicrobial, antioxidant and cytotoxic activities. *Anais da Academia Brasileira de Ciências*, 92(2), 1–18. <https://doi.org/10.1590/0001-3765202020190934>
- Glasby, C. J., & Timm, T. (2008). Global diversity of polychaetes (Polychaeta; Annelida) in freshwater. In E. V. Balian, C. Lévêque, H. Segers, & K. Martens (Eds.), *Freshwater Animal Diversity Assessment* (pp. 107–115). Springer. https://doi.org/10.1007/978-1-4020-8259-7_13
- Glasby, C. J., Erséus, C., & Martin, P. (2021). Annelids in extreme aquatic environments: Diversity, adaptations and evolution. *Diversity*, 13(2), Article 98. <https://doi.org/10.3390/d13020098>
- Górska, B., Gromisz, S., & Włodarska-Kowalczyk, M. (2019). Size assessment in polychaete worms - Application of morphometric correlations for common North Atlantic taxa. *Limnology and Oceanography: Methods*, 17(4), 254–265. <https://doi.org/10.1002/lom3.10310>
- Guimarães, A., & Venâncio, A. (2022). The potential of fatty acids and their derivatives as antifungal agents: A review. *Toxins*, 14(188), 1–21. <https://doi.org/10.3390/toxins14030188>
- Hassan, M. S. A., Elias, N. A., Hassan, M., Rahmah, S., Wan, I. W. I., & Harun, N. A. (2023). Polychaeta-mediated synthesis of gold nanoparticles: A potential antibacterial agent against Acute Hepatopancreatic Necrosis Disease (AHPND)–causing bacteria, *Vibrio parahaemolyticus*. *Heliyon*, 9(2023), Article e21663. <https://doi.org/10.1016/j.heliyon.2023.e21663>
- Huang, L., Zhu, X., Zhou, S., Cheng, Z., Shi, K., Zhang, C., & Shao, H. (2021). Phthalic acid esters: Natural sources and biological activities. *Toxins*, 13(7), Article 495. <https://doi.org/10.3390/toxins13070495>
- Idris, I., & Arshad, A. (2013). Checklist of polychaetous annelids in Malaysia with redescription of two commercially exploited species. *Asian Journal of Animal and Veterinary Advances*, 8(3), 409–436.
- Idris, I., & Hutchings, P. (2014). Description of a new species of *Marphysa* Quatrefages, 1865 (Polychaeta: Eunicidae) from the west coast of Peninsular Malaysia and comparisons with species from *Marphysa* Group A from the Indo-West Pacific and Indian Ocean. *Memoirs of Museum Victoria*, 71, 1447–2554. <https://doi.org/10.24199/j.mmv.2014.71.11>

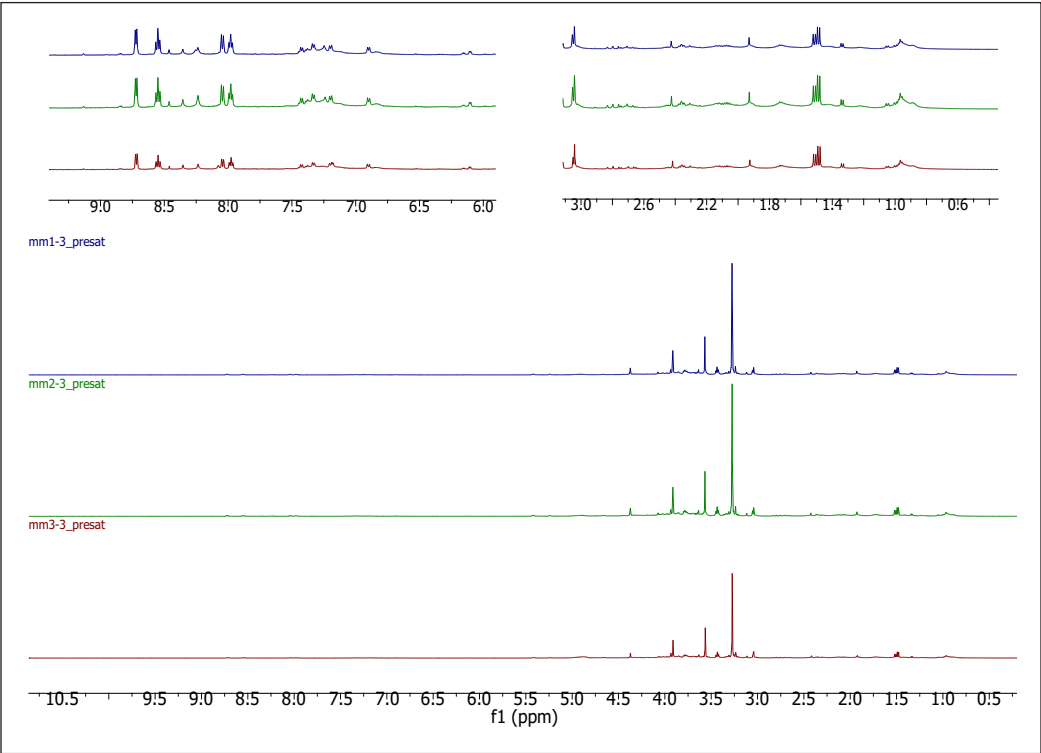
- Imbs, A. B., Ermolenko, E. V., Grigorochuk, V. P., Sikorskaya, T. V., & Velansky, P. V. (2021). Current progress in lipidomics of marine invertebrates. *Marine Drugs*, 19(12), Article 660. <https://doi.org/10.3390/md19120660>
- Izzati, F., Warsito, M. F., Bayu, A., Prasetyoputri, A., Atikana, A., Sukmarini, L., Rahmawati, S. I., & Putra, M. Y., (2021). Chemical diversity and biological activity of secondary metabolites isolated from Indonesian marine invertebrates. *Molecules*, 26(7), Article 1898. <https://doi.org/10.3390/molecules26071898>
- Khowala, S., Verma, D., & Banik, S. P., (2008). Biomolecules: Introduction, structure & function. *Indian Institute of Chemical Biology*, 3–92.
- Konkel, A., & Schunck, W.H. (2011). Role of cytochrome P450 enzymes in the bioactivation of polyunsaturated fatty acids. *Biochimica et Biophysica Acta (BBA) – Proteins and Proteomics*, 1814, 210–222. <https://doi.org/10.1016/j.bbapap.2010.09.009>
- Li, Z., Yin, H., Chen, W., Jiang, C., Hu, J., Xue, Y., Yao, D., Peng, Y., & Hu, X. (2020). Synergistic effect of pseudolaric acid b with fluconazole against resistant isolates and biofilm of candida tropicalis. *Infection and Drug Resistance*, 13, 2733–2743. <https://doi.org/10.2147/IDR.S261299>
- Lopez, M. J., & Mohiuddin, S. S. (2024). *Biochemistry, Essential Amino Acids*. StatPearls Publishing.
- Malcicka, M., Visser, B., & Ellers, J. (2018). An evolutionary perspective on linoleic acid synthesis in animals. *Evolutionary Biology*, 45(1), 15–26. <https://doi.org/10.1007/s11692-017-9436-5>
- Marion, D. (2013). An introduction to biological NMR spectroscopy. *Molecular & Cellular Proteomics*, 12(11), 3006–3025. <https://doi.org/10.1074/mcp.O113.030239>
- Moco, S. (2022). Studying metabolism by NMR-based metabolomics. *Frontiers in Molecular Biosciences*, 9, 1–12. <https://doi.org/10.3389/fmolb.2022.882487>
- Occhioni, G. E., Brasil, A., & Araújo, A. F. (2009). Morphometric study of Phragmatopoma caudata (Polychaeta: Sabellida: Sabellariidae). *Zoologia (Curitiba)*, 26, 739–746.
- Patel, M. K., Pandey, S., Kumar, M., Haque, M. I., Pal, S., & Yadav, N. S. (2021). Plants metabolome study: Emerging tools and techniques. *Plants*, 10(11), 1–24. <https://doi.org/10.3390/plants10112409>
- Pei, A. U. E., Huai, P. C., Masimen, M. A. A., Wan, I. W. I., Idris, I., & Harun, N. A. (2020). Biosynthesis of gold nanoparticles (AuNPs) by marine baitworm *Marphysa moribidii* Idris, Hutchings and Arshad 2014 (Annelida: Polychaeta) and its antibacterial activity. *Advances in Natural Sciences: Nanoscience and Nanotechnology*, 11(1), Article 015001. <https://doi.org/10.1088/2043-6254/ab6291>
- Rahman, M. M., Ahmad, S. H., Mohamed, M. T. M., & Rahman, M. Z. A. (2014). Antimicrobial compounds from leaf extracts of *Jatropha curcas*, *Psidium guajava*, and *Andrographis paniculata*. *The Science World Journal*, 2014, Article 35240. <https://doi.org/10.1155/2014/635240>
- Rapi, H. S., Soh, N. A. C., Azam, N. S. M., Maulidiani, M., Assaw, S., Haron, M. N., Ali A. M., Idris, I., & Ismail, W. I. W. (2020). Effectiveness of aqueous extract of marine baitworm *Marphysa moribidii* Idris, Hutchings and Arshad, 2014 (Annelida, Polychaeta), on acute wound healing using Sprague Dawley rats. *Evidence-Based Complementary and Alternative Medicine*, 2020, Article 408926. <https://doi.org/10.1155/2020/1408926>

- Riemann, L., & Azam, F. (2002). Widespread N-acetyl-D-glucosamine uptake among pelagic marine bacteria and its ecological implications. *Applied and Environmental Microbiology*, 68(11), 5554–5562. <https://doi.org/10.1128/AEM.68.11.5554-5562.2002>
- Rolland, F., Moore, B., & Sheen, J. (2002). Sugar sensing and signalling in plants. *The Plant Cell*, 14(1), 185–205. <https://doi.org/10.1105/tpc.010455.S186>
- Rosman, N. S. R., Harun, N. A., Idris I., & Ismail, W. I. W. (2020). Eco-friendly silver nanoparticles (AgNPs) fabricated by green synthesis using the crude extract of marine polychaete, *Marphysa moribidii*: Biosynthesis, characterisation, and antibacterial applications. *Heliyon*, 6(11), Article e05462. <https://doi.org/10.1016/j.heliyon.2020.e05462>
- Rosman, N. S. R., Masimen, M. A. A., Harun, N. A., Idris, I., & Ismail, W. I. W. (2021). Biogenic silver nanoparticles (AgNPs) from *Marphysa moribidii* extract: Optimization of synthesis parameters. *International Journal of Technology*, 12(3), 635–648. <https://doi.org/10.14716/ijtech.v12i3.4303>
- Ruiz, A. J. C., Boushehri, M. A. S., Phan, T., Carle, S., Garidel P., Buske, J., & Lamprecht, A. (2022). Alternative excipients for protein stabilization in protein therapeutics: Overcoming the limitations of polysorbates. *Pharmaceutics*, 14(12), Article 2575. <https://doi.org/10.3390/pharmaceutics14122575>
- Ruocco, N., Nuzzo, G., d’Ippolito, G., Manzo, E., Sardo, A., Ianora, A., Romano, G., Iuliano, A., Zupo, V., Costantini, M., & Fontana, A. (2020). Lipoxxygenase pathways in diatoms: Occurrence and correlation with grazer toxicity in four benthic species. *Marine Drugs*, 18(1), Article 66. <https://doi.org/10.3390/md18010066>
- Salam, U., Ullah, S., Tang, Z. H., Elateeq, A. A., Khan, Y., Khan, J., Khan, A., & Ali, S. (2023). Plant metabolomics: An overview of the role of primary and secondary metabolites against different environmental stress factors. *Life*, 13(3), 1–25. <https://doi.org/10.3390/life13030706>
- Salamanca, N., Giráldez, I., Morales, E., de La Rosa, I., & Herrera, M. (2021). Phenylalanine and tyrosine as feed additives for reducing stress and enhancing welfare in gilthead seabream and meagre. *Animals*, 11(1), 1–11. <https://doi.org/10.3390/ani11010045>
- Skalski, B., Pawelec, S., Jedrejek, D., Rolnik, A., Pietukhov, R., Piwowarczyk, R., Stochmal, A., & Olas, B. (2021). Antioxidant and anticoagulant effects of phenylpropanoid glycosides isolated from broomrapes (*Orobanchaceae*, *Phelipanche arenaria*, and *P. ramosa*). *Biomedicine & Pharmacotherapy*, 139, Article 111618. <https://doi.org/10.1016/j.biopha.2021.111618>
- Sperstad, S. V., Haug, T., Blencke, H. M., Styrvold, O. B., Li, C., & Stensvåg, K. (2011). Antimicrobial peptides from marine invertebrates: Challenges and perspectives in marine antimicrobial peptide discovery. *Biotechnology Advances*, 29(5), 519–530. <https://doi.org/10.1016/j.biotechadv.2011.05.021>
- Ulu, G., Semerciöz, A. S., & Özilgen, M. (2021). Energy storage and reuse in biological systems: Case studies. *Energy Storage*, 3(5), 1–12. <https://doi.org/10.1002/est2.253>
- Vance, J. E., & Tasseva, G. (2013). Formation and function of phosphatidylserine and phosphatidylethanolamine in mammalian cells. *Biochimica Et Biophysica Acta-Molecular and Cell Biology of Lipids*, 1831(3), 543–554. <https://doi.org/10.1016/j.bbalip.2012.08.016>
- Verdonschot, P. F. (2015). Introduction to Annelida and the class Polychaeta. In J. H. Thorp & D. C. Rogers (Eds.), *Thorp and Covich’s Freshwater Invertebrates: Ecology and General Biology* (pp. 509–528). Academic Press. <https://doi.org/10.1016/B978-0-12-385026-3.00020-6>

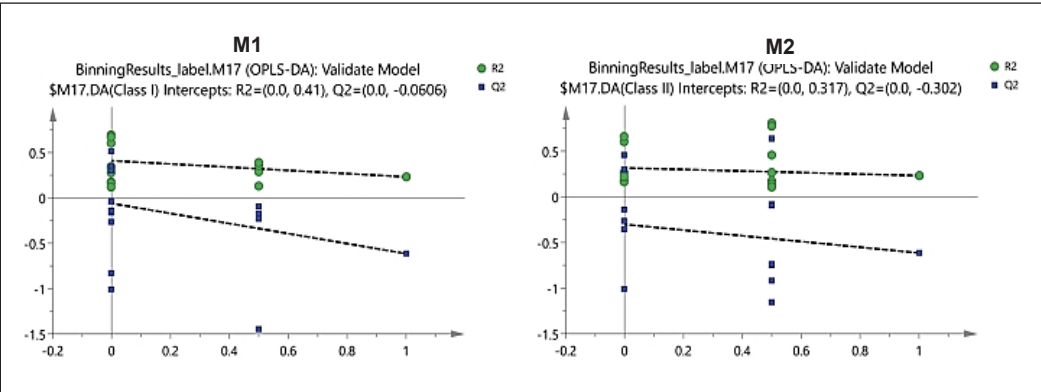
- Wijaya, I. D. M. R., Idris, I., Ismail, W. I. W., Asari, A., Harun, N. A., Rudiyanto, R., Tarman, K., Abas, F., & Maulidiani, M. (2024). Discrimination of marine polychaete species of different harvest times using FTIR metabolomics. *Malaysian Journal of Chemistry*, 26(2), 129-138. <https://doi.org/10.55373/mjchem.v26i2.129>
- Yamashita, S., Miyazawa, T., Higuchi, O., Kinoshita, M., & Miyazawa, T. (2023). Marine plasmalogens: A gift from the sea with benefits for age-associated diseases. *Molecules*, 28(17), Article 6328. <https://doi.org/10.3390/molecules28176328>
- Yi, C., Liang, H., Huang, D., Yu, H., Xue, C., Gu, J., Chen, X., Wang, Y., Ren, M., & Zhang, L. (2023). Phenylalanine plays important roles in regulating the capacity of intestinal immunity, antioxidants and apoptosis in largemouth bass (*Micropterus salmoides*). *Animal*, 13(18), 1–14. <https://doi.org/10.3390/ani13182980>
- Zamzam, N. I., Kamarudin, N. I., Idris, I., Harun, N. A., Ismail, W. I. W., & Abas, F. (2021). Investigation of antioxidant activity and chemical fingerprint of marine polychaete based on ATR-FTIR metabolomics. *Universiti Malaysia Terengganu Journal of Undergraduate Research*, 3(4), 81-88. <https://doi.org/10.46754/umtjur.v3i4.241>
- Zanol, J., da Silva, T., Dos, S. C., & Hutchings, P. (2016). *Marphysa* (Eunicidae, polychaete, Annelida) species of the *Sanguinea* group from Australia, with comments on pseudo-cryptic species. *Invertebrate Biology*, 135, 328–344. <https://doi.org/10.1111/ivb.12146>
- Zeng, M., Tao, J., Xu, S., Bai, X., & Zhang, H. (2023). Marine organisms as a prolific source of bioactive depsipeptides. *Marine Drugs*, 21(2), Article 120. <https://doi.org/10.3390/md21020120>

APPENDIX

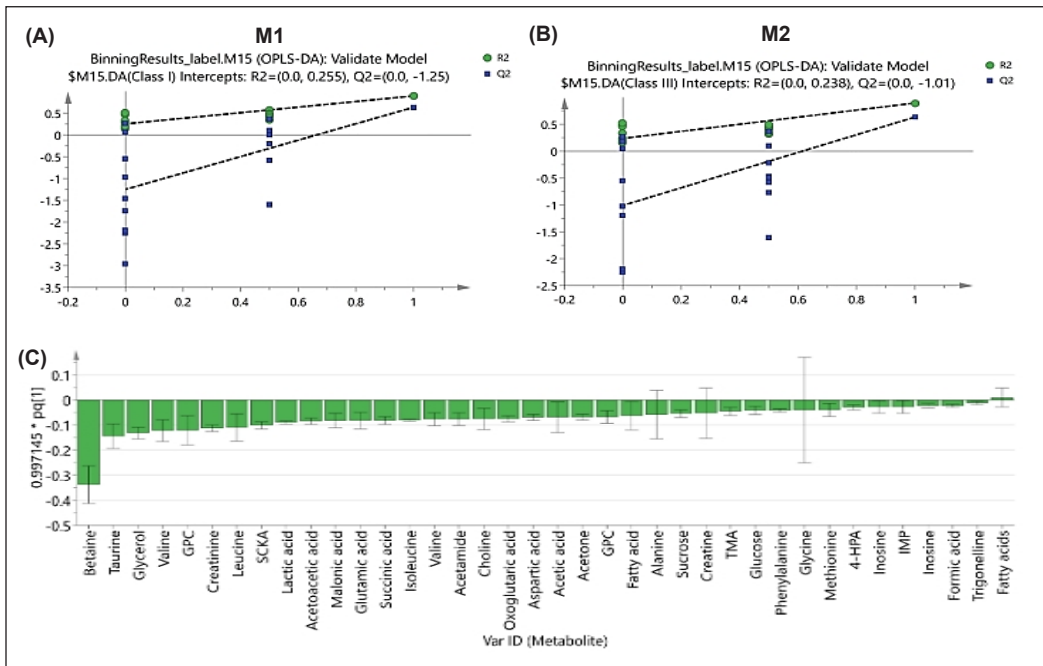
Investigation of Aged-related Metabolites in the Marine Polychaete (*Marphysa moribidii*) Using ¹H NMR Metabolomics and LC-MS/MS Analysis



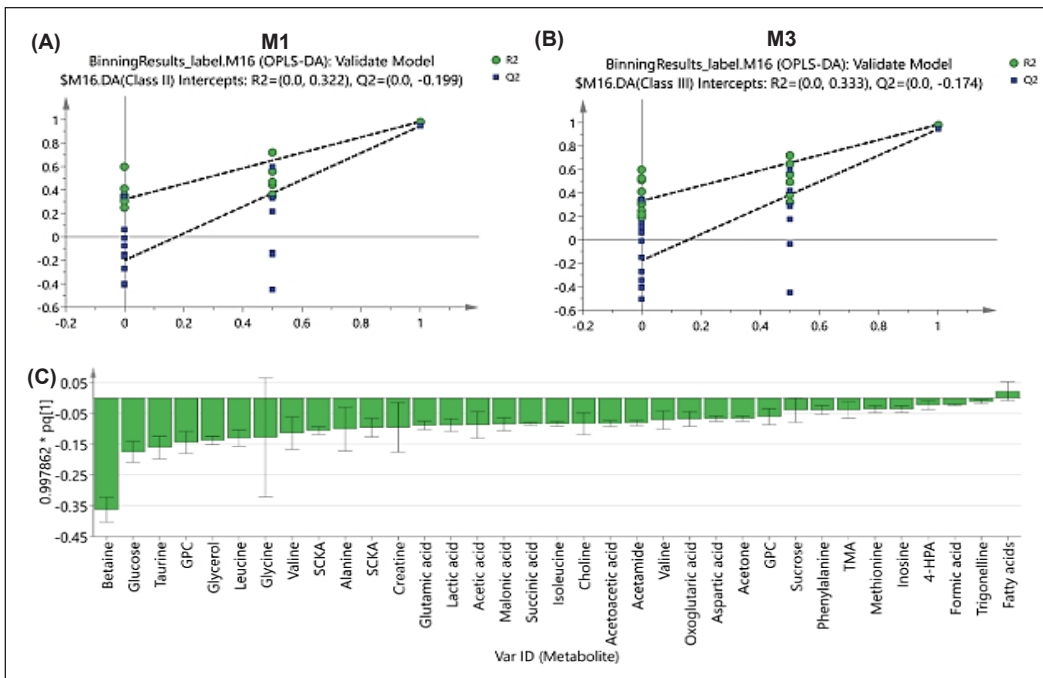
Supplementary Figure 1. Representative ¹H NMR spectra of *M. moribidii* at different ages. Keys: mm1–3 (M1); mm2–3 (M2); and mm3–3 (M3)



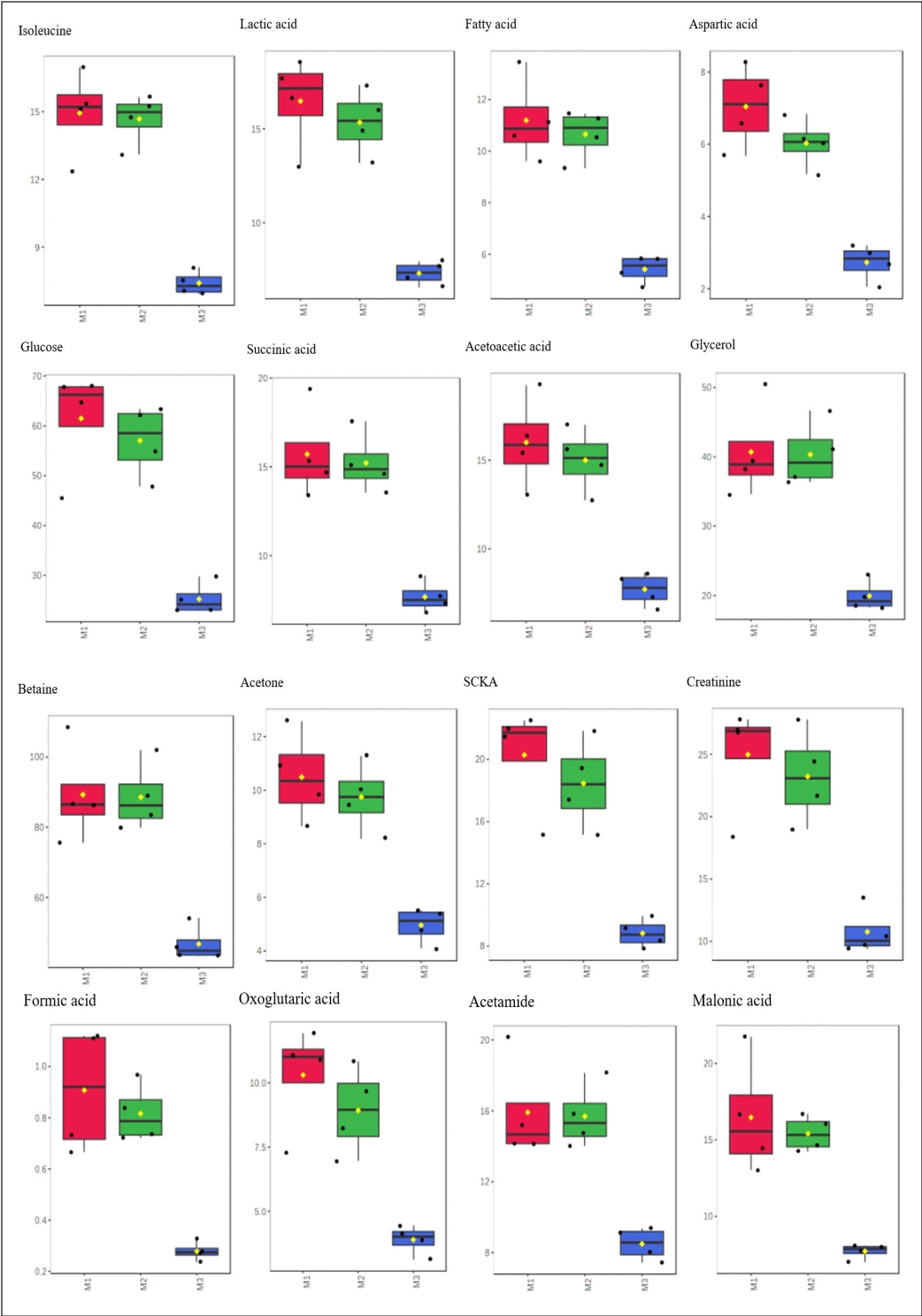
Supplementary Figure 2. Permutation test results of OPLS-DA model M1 versus M2. The permutation tests were carried out with 20 random permutations



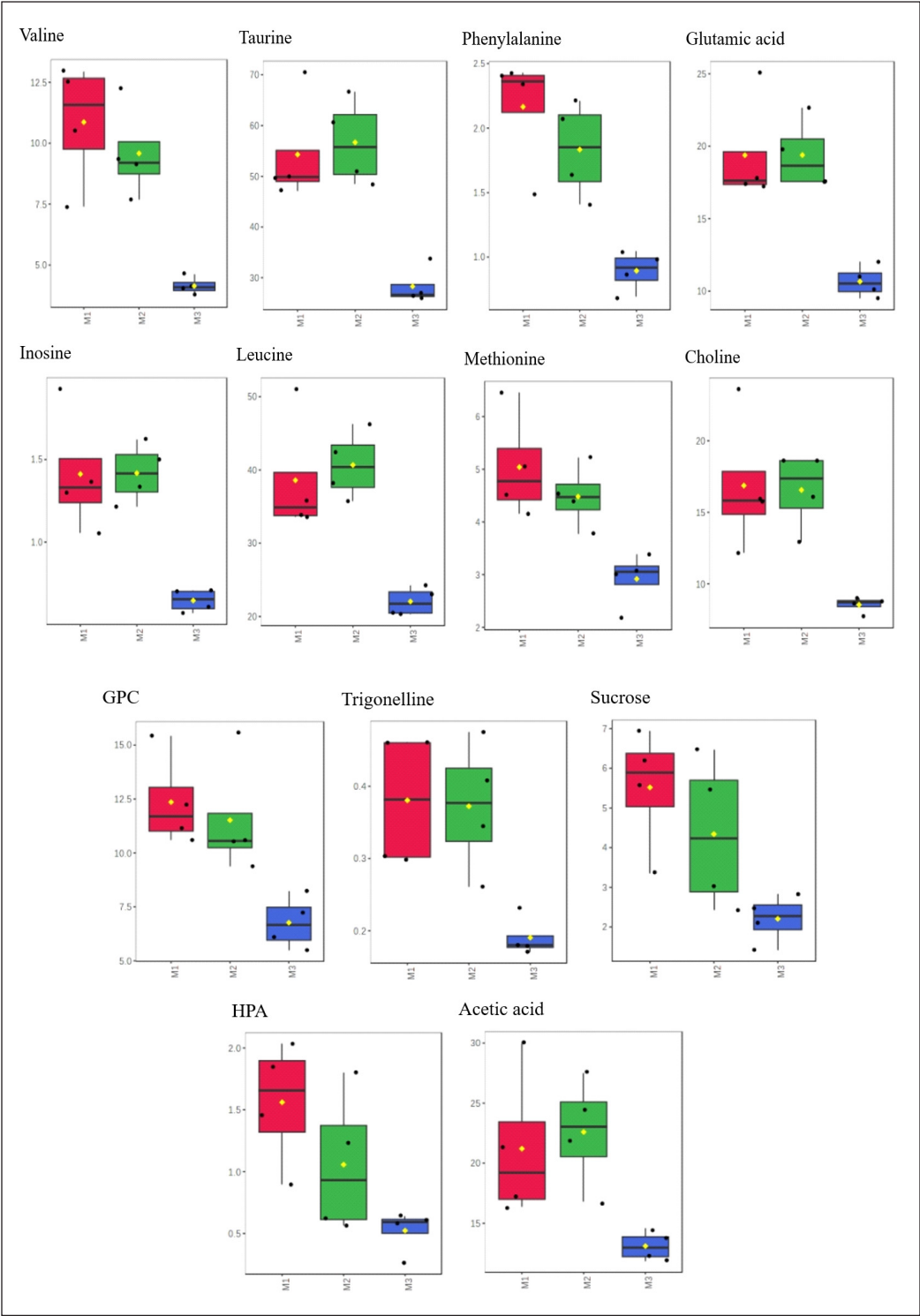
Supplementary Figure 3. OPLS-DA model M1 versus M3 showed the permutation test (20 permutations) results for M1 (A) and M3 (B); and loadings column plot (C)



Supplementary Figure 4. OPLS-DA model M2 versus M3 showed the permutation test (20 permutations) results for M2 (A) and M3 (B); and loadings column plot (C)



Supplementary Figure 5. Boxplots of M1, M2 and M3 metabolites of the *M. moribidii*



Supplementary Figure 5 (continue). Boxplots of M1, M2 and M3 metabolites of the *M. moribidii*

Supplementary Table 1
One-way ANOVA and Tukey-HSD Pairwise Test results of identified metabolites in M1, M2, and M3

No	Metabolite	δH (ppm)	f.value	p.value	FDR	Tukey's HSD
1	Isoleucine	1.02	42.158	2.69E-05	0.0012837	M3-M1; M3-M2
2	Lactic acid	1.34	31.92	8.19E-05	0.0012837	M3-M1; M3-M2
3	Fatty acid	1.22	31.506	8.62E-05	0.0012837	M3-M1; M3-M2
4	Aspartic acid	2.78	30.054	0.00010381	0.0012837	M3-M1; M3-M2
5	Glucose	3.78	26.308	0.00017396	0.0015077	M3-M1; M3-M2
6	Succinic acid	2.42	23.696	0.00025918	0.0015257	M3-M1; M3-M2
7	Acetoacetic acid	2.30	23.577	0.00026417	0.0015257	M3-M1; M3-M2
8	Glycerol	3.62	23.074	0.00028655	0.0015257	M3-M1; M3-M2
9	Betaine	3.26	22.856	0.00029699	0.0015257	M3-M1; M3-M2
10	Acetone	2.22	22.22	0.00033013	0.0015257	M3-M1; M3-M2
11	SCKA	0.90	21.84	0.00035209	0.0015257	M3-M1; M3-M2
12	Creatinine	3.06	19.301	0.00055558	0.001924	M3-M1; M3-M2
13	Formic acid	8.46	18.968	0.000592	0.001924	M3-M1; M3-M2
14	Oxoglutaric acid	2.46	18.348	0.00066784	0.0020428	M3-M1; M3-M2
15	Acetamide	2.02	17.202	0.00084173	0.0023529	M3-M1; M3-M2
16	Malonic acid	3.10	16.863	0.00090352	0.0023529	M3-M1; M3-M2
17	Creatine	3.02	16.856	0.00090497	0.0023529	M3-M1; M3-M2
18	TMA	2.90	15.07	0.0013405	0.0030708	M3-M1; M3-M2
19	Valine	1.06	15.013	0.0013582	0.0030708	M3-M1; M3-M2
20	Taurine	3.42	14.724	0.0014526	0.0030985	M3-M1; M3-M2
21	Phenylalanine	7.42	14.479	0.0015391	0.0030985	M3-M1; M3-M2
22	Glutamic acid	2.34	14.125	0.0016751	0.003226	M3-M1; M3-M2
23	Inosine	8.34	13.627	0.0018923	0.0034441	M3-M1; M3-M2
24	Leucine	0.94	13.099	0.0021616	0.0037467	M3-M1; M3-M2
25	Methionine	2.62	8.7929	0.0076414	0.012417	M3-M1; M3-M2
26	Choline	3.18	8.6828	0.0079327	0.0125	M3-M1; M3-M2
27	GPC	3.22	7.8935	0.010473	0.015739	M3-M1; M3-M2
28	Trigonelline	8.82	7.8621	0.010594	0.015739	M3-M1; M3-M2
29	Sucrose	5.42	5.2582	0.030711	0.041497	M3-M1
30	4-HPA	6.90	5.2095	0.03141	0.041497	M3-M1
31	Acetic acid	1.90	5.1748	0.031921	0.041497	M3-M2

Energy Management Systems Development in Electric Vehicle Charging Stations Based on Multi-Source Inverters with Utilisation of Renewable Energy Sources

Iradiratu Diah Prahmana Karyatanti^{1*}, Belly Yan Dewantara¹, Istiyo Winarno¹, Daeng Rahmatullah² and Nuhman³

¹Department of Electrical Engineering, Faculty of Engineering and Marine Science, Hang Tuah University, Surabaya, 60111, Indonesia

²Department of Electrical Engineering, State University of Surabaya, Surabaya 60111, Indonesia

³Fisheries Science, Faculty of Engineering and Marine Science, Hang Tuah University, Surabaya, 60111, Indonesia

ABSTRACT

The use of electric vehicles (EVs) is growing rapidly and widely, as they produce no gas emissions, reduce pollution, and do not rely on fossil fuels. Solar energy is a reliable and renewable energy source. Problems arise when charging stations cannot meet demand due to unfavourable weather conditions. This research offers a solution using multi-source energy management to ensure the availability of electrical energy sustainably and economically. The multi-source inverter converts from direct current (DC) to alternating current (AC), stabilising the voltage from solar panels, batteries, and the grid. The proposed energy management ensures an uninterrupted power supply, especially when energy absorption from the sun is reduced due to weather. The research contributes to providing and managing energy for electric vehicle charging, prioritising the exploitation of energy from solar panels and batteries. Sourcing electricity from the grid will be the last resort when

the load reaches its peak. With the proposed strategy, the charging station can reduce the use of fossil energy, requiring only 1,795 watt hours (Wh) each week.

ARTICLE INFO

Article history:

Received: 02 October 2024

Accepted: 23 January 2025

Published: 23 April 2025

DOI: <https://doi.org/10.47836/pjst.33.3.22>

E-mail addresses:

iradiratu@hangtuah.ac.id (Iradiratu Diah Prahmana Karyatanti)

bellyyandewantara@hangtuah.ac.id (Belly Yan Dewantara)

istiyo.winarno@hangtuah.ac.id (Istiyo Winarno)

daengrahmatullah@unesa.ac.id (Daeng Rahmatullah)

nuhman@hangtuah.ac.id (Nuhman)

*Corresponding author

Keywords: Charging station, electric energy management system, electric vehicle, solar energy

INTRODUCTION

Electric vehicles (EVs) offer a sustainable transportation solution that can effectively replace traditional fossil fuel-powered

vehicles. This transition is crucial since traditional vehicles are known for emitting harmful air pollutants, carbon dioxide (CO₂) emissions, and greenhouse gases, which resulted in the depletion of petroleum resources. These factors collectively present substantial threats to the environment (Narasipuram & Mopidevi, 2021). Currently, numerous countries are supporting the adoption of EVs to mitigate the rising levels of pollutants. However, various challenges must be addressed to facilitate the widespread implementation of electric vehicles, including the limited development of EV infrastructure, identifying optimal locations for EVs, and managing power usage (Ahmad et al., 2022). One critical approach to increasing the accessibility of electric vehicles is through ongoing research and development in battery technology. Advancements in battery technology will enable electric vehicles to achieve a longer range and improved efficiency. Furthermore, the establishment of charging stations distributed evenly across user activity areas is essential. With accessible charging stations, electric vehicle users will not have to worry about running out of power while on the move. These several key factors have a significant impact on the growth and development of electric vehicles in the automotive industry. With robust support for EV infrastructure, it is anticipated that the adoption of electric vehicles will accelerate in the future. This transition will further aid in decreasing greenhouse gas emissions and fostering a cleaner, more sustainable environment. According to a study conducted by Sanguesa et al. (2021), the presence of a supportive EV infrastructure is essential for facilitating the widespread adoption and utilisation of electric vehicles. Therefore, concrete actions must be continually pursued to enhance electric vehicle infrastructure, from increasing the number of charging stations to improving the battery capacity of electric vehicles.

Users of electric vehicles need to predict energy consumption and optimise battery capacity to avoid running out of power. Efficient route planning can also contribute to energy savings. It is essential to ensure the availability of adequate charging infrastructure, allowing users to recharge their batteries with ease. These strategies allow electric vehicle users to extend battery life and enjoy a more comfortable and efficient driving experience (Zhang et al., 2020). The battery capacity of electric vehicles is affected by the weight of the load being carried. On average, the battery will deplete after covering a maximum distance of 25 km at a speed of 25 km/h, with a load of 58–70 kg and a battery capacity of 80 Ah. Selecting the appropriate battery capacity is crucial for the performance and efficiency of electric vehicles (Lestari & Rangkuti, 2023). Various studies have highlighted the importance of the distribution of charging stations to alleviate electric vehicle drivers' concerns regarding power needs and travel range (Pan et al., 2020). Therefore, the installation of charging stations in public areas must be supported by the availability and continuity of power supply.

In recent times, there has been an increasing focus on utilising renewable energy sources to power charging stations. Solar energy is a renewable and environmentally friendly energy

source. However, its generation is heavily influenced by climatic and weather conditions. The electricity generation from solar power is most effective in regions with sunny climates and during the summer months, while production becomes severely limited in winter or overcast areas. Solar energy can be harnessed only during daylight hours, as it is not accessible at night. Conversely, the demand for energy to power EVs persists until daily activities cease. The energy stored in batteries serves as a solution to ensure the continuity of the energy supply (Kunj & Pal, 2020). To guarantee sustained energy production, the integration of various sources is essential. Efficient power flow management can positively impact energy savings (Baqar et al., 2022).

The utilisation of Renewable Energy Sources (RES) through a hybrid system that combines solar and wind energy has been analysed using HOMER software. The simulation results indicate that solar energy plays a more dominant role compared to wind energy (Ekren et al., 2021). In the context of energy utilisation for electric vehicle charging stations, it is essential to optimise the scheduling of charging and energy absorption to maintain the stability of the electrical system (Ullah et al., 2023). Furthermore, the placement of solar panels significantly impacts energy absorption efficiency (Reddy et al., 2023). Installing solar panels on rooftops presents a viable solution for enhancing energy absorption while also providing shade for the charging stations (Khan et al., 2023). Inverters are required to convert the direct current (DC) into alternating current (AC) and stabilise the voltage by harnessing solar energy as a power source for charging stations (Ebrahimi et al., 2021). Developing inverters capable of integrating multiple energy sources and filtering the output is necessary to produce cleaner energy and ensure a continuous power supply at the charging stations. This article discusses charging stations that utilise energy from various sources, employing multi-source inverters to integrate solar panels, batteries, and the electrical grid. Power flow management from these three sources will be carefully regulated to minimise fossil fuel usage. The primary goal is to maximise energy production from solar panels by implementing battery storage to address any increase in energy consumption. If necessary, the electrical grid will provide energy as a final option. The contributions and innovations presented in this research provide a framework for energy management at charging stations using multi-source inverter technology, expecting to reduce electricity costs and ensure sustainable electricity supply, even during periods of reduced sunlight intensity.

MATERIALS AND METHODS

The recently installed charging station at Hang Tuah University's parking area has been designed to enhance the infrastructure available to electric vehicle users. This charging station was accessible to the public, given its strategic location near public facilities. The station utilises a hybrid power supply system comprised of solar panels, batteries, and the electrical grid to effectively meet the energy demands of electric vehicles. The efficiency

of the solar panels was assessed based on the amount of sunlight converted into electrical energy to the surface area of the solar panels exposed to sunlight, measured in watts. Equation 1 could be employed to calculate the efficiency value of the solar panels exposed to sunlight (Triyanto et al., 2023).

$$\eta_{PV} = \frac{P_{max}}{A_c \times E_{sw.sy}} \quad [1]$$

Where:

P_{max} = Maximum output power (Watt)

A_c = Cell Surface Area (m^2)

$E_{sw.sy}$ = 1000 W/ m^2 , coefficient of incident radiation flux in standard test condition (STC) (W/ m^2)

The requirements for solar panels are determine in two steps: Assess the available area and evaluate the power requirements. Equation 2 can be used to calculate the necessary solar panels.

$$L_{potential} = L_{total} (1 - 0,25) \quad [2]$$

With:

$L_{potential}$ = Potential area of PV installation (m^2)

L_{total} = Total area (m^2)

A value of 0.25 indicates an area that was not utilised for the installation of photovoltaic (PV) systems. Once the potential area has been identified, the subsequent step involves calculating the area designated for PV installation, referred to as the PV Area. The PV Area could be determined using Equation 3.

$$PV_{Area} = L_{potential} \times (1 - 0,2) \quad [3]$$

Where:

PV_{Area} = PV mounting/installation areas (m^2)

$L_{potential}$ = Potential areas for solar PV installation (m^2)

A value of 0.2 indicates an area designated for maintenance or repair pathways within a Solar Power Generation System. Additionally, the size of the solar panel array or the area covered by the photovoltaic installation could be determined to assess the potential power output of the solar power system. Equation 4 was employed to compute the potential power output.

$$P_{wattpeak} = PV_{Area} \times PSI \times \eta_{PV} \text{ [Watt]} \quad [4]$$

Where:

PV_{Area} = Surface Area of the Solar Panel (m^2)

PSI = Peak Solar insolation ($1.000 \text{ W}/m^2$)

η_{PV} = Efficiency of Solar Panels [%]

Subsequently, a calculation was conducted to determine the number of solar panels required for the planning of the Solar Power Plant construction. This calculation aimed to ascertain the quantity of PV modules that could be installed. This information was crucial for understanding the installation capacity of the modules within the proposed solar power plant plan. Equation 5 could be utilised to compute the number of PV modules that could be installed.

$$\Sigma_{Panel \text{ surya}} = \frac{P_{wattpeak}}{P_{mp}} \quad [5]$$

With:

$\Sigma_{Panel \text{ surya}}$ = Number of PV modules (Unit)

$P_{wattpeak}$ = Power generated by PV (Wp)

P_{mp} = Maximum power output of the solar panel (Watt)

A schematic representation of the charging station is illustrated in Figure 1, while the actual implementation of the charging station can be observed in Figure 2. Solar energy was

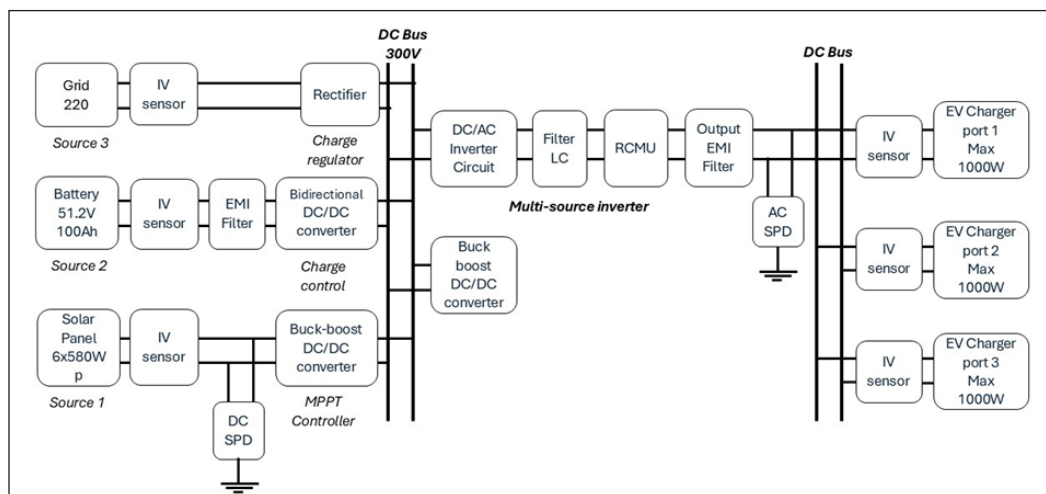


Figure 1. Schematic diagram of multisource inverter-based solar charging station

harnessed through six units of monocrystalline PV panels, each with a capacity of 550 watts peak (WP). The placement of the solar panels followed a rooftop concept. The supporting structure was designed to support the solar panels, protect the panels' enclosure beneath, and provide shade for the electric motor to facilitate the charging process. A multi-source inverter system was employed at this charging station, ensuring a sustainable supply of electrical power. When solar energy absorption peaks, the energy is stored in batteries. The battery capacity needs to be customised to adequately accommodate the daily energy needs of the solar charging system.



Figure 2. Implementation of the solar charging station in the campus area

Depth of Discharge (DOD) was the quantifiable measure of the amount of charge that had been used in relation to the total capacity of a battery. It was expressed as a percentage and indicates the level of discharge the battery has undergone. Instead, the State of Charge (SOC) was a metric that reflects the percentage of battery capacity currently available, indicating the level of energy available for use (Xie et al., 2020). According to existing data, the daily energy requirement for solar charging was 10.78 kWh per day. Consequently, the minimum battery capacity required must be at least equivalent to this daily energy consumption. However, when determining battery capacity, it was crucial to consider the type of battery being used, as each type has a different DOD. In this study, the battery employed was of the lithium variety, which had a DOD of 95%. Therefore, the capacity of the battery that should be selected could be calculated using Equation 6.

$$\text{Battery Capacity} = \frac{\text{Daily energy consumption}}{\text{Depth of Discharge}} \quad [6]$$

Using a DOD of 95%, the required battery capacity was:

$$\text{Battery Capacity} = \frac{10,78 \text{ kWh}}{0,95} = 11,33 \text{ kWh}$$

The required battery capacity should be a minimum of 11.33 kWh, equivalent to 11,400 Wh. However, in this study, the researchers would utilise a battery with a capacity of 5.12 kWh. The selection of a smaller-capacity battery was intended to assess the performance of the multisource inverter in managing charging from various sources, such as solar panels, the electrical grid, and the battery itself.

Based on the load profile data, it has been determined that the maximum power requirement reaches 3 kW. This study utilised a solar panel system comprising six units, each with a capacity of 550 WP, resulting in a total solar panel capacity of 3,300 WP. This configuration will enable an assessment of the efficacy of the solar panels in fulfilling the load power demands, especially during times of peak load. Furthermore, it was acknowledged that solar panels produced fluctuating power output depending on solar radiation, indicating that the load power requirements also vary hourly throughout the day. This research aimed to assess how the inverter manages these fluctuations and identify when the solar panels require additional support from the electrical grid and battery systems.

The multi-source inverter comprised a DC/AC inverter circuit designed to convert direct current (DC) from various sources into alternating current (AC) for use by electrical loads. Distortion in the AC output was mitigated by an LC filter, resulting in a waveform that closely resembles a sinusoidal shape. The Residual Current Monitoring Unit (RCMU) was a key component within the inverter system. The term "residual current" refers to leakage current that flows from the electrical system to the ground, often resulting from ground faults. This leakage current poses a risk of flowing through the human body to the ground, potentially leading to electric shocks, injuries, burns, and an increased risk of overheating and fire hazards. Residual Current Devices (RCD) were employed to detect such leakage currents, automatically disconnecting the circuit from the source when the residual current exceeds a predefined threshold. The RCMU serves a purpose similar to the RCD but cannot disconnect the circuit.

Instead, the RCMU was designed solely to monitor residual current and activate an alarm when necessary. Given that the inverter was equipped with highly precise residual current detection devices, installing leakage protection switches within the system was generally not recommended. Should the need arise, such switches should be installed between the inverter's output and the electrical grid. Additionally, a buck-boost converter was utilised to ensure that the input voltage can be maintained at levels either above or

below the output voltage. Furthermore, an Alternating Current Surge Protective Device (AC-SPD) was incorporated to safeguard the electrical installation from damage or fire caused by voltage surges resulting from lightning strikes or excessive voltage spikes. Consequently, the multi-source inverter is an energy converter from DC to AC. It protects and filters, ensuring the generated energy is cleaner and the output voltage remains stable. The configuration can be observed in Figure 3.

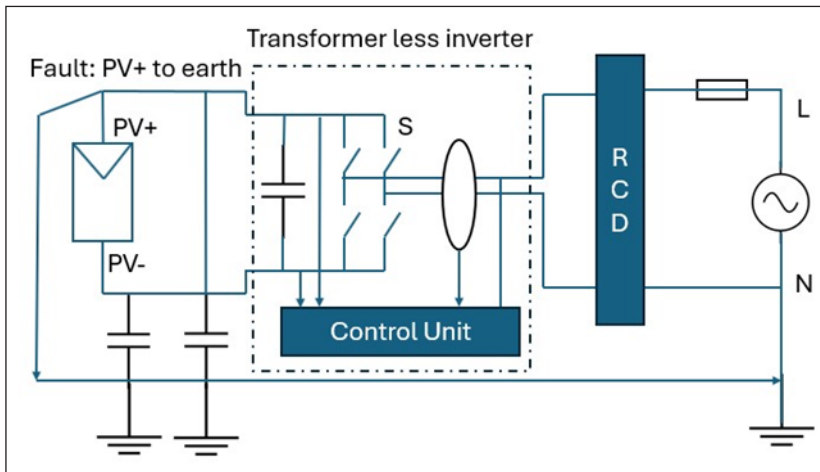


Figure 3. Residual current monitoring unit

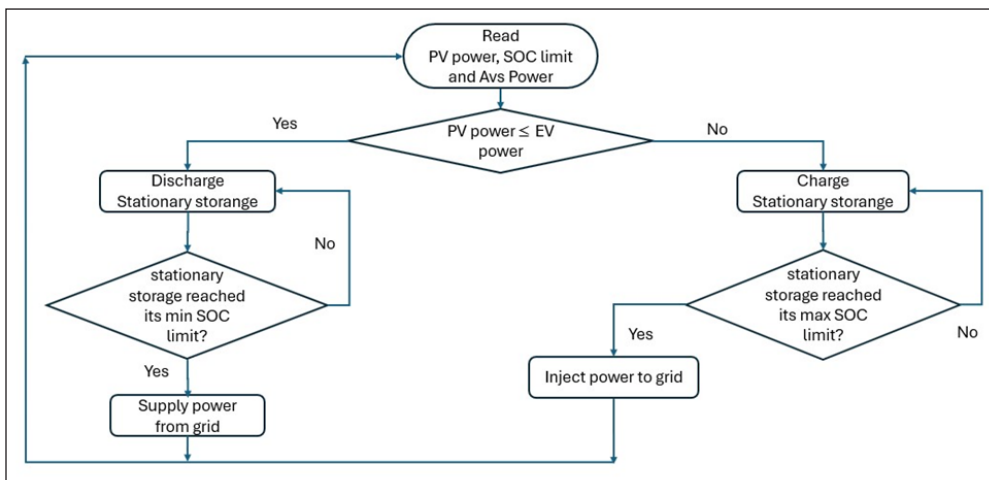


Figure 4. Energy management of solar charging stations

The process algorithm is presented in Figure 4. Energy management regulated by multi-source inverters prioritises the direct use of energy generated from PV panels. When the demand for EVs is lower than the power produced by the PV system, the energy will fully

supply the energy, with any excess energy stored in batteries. Conversely, if the demand from EVs exceeds the power generated by the PV system, the charging station will draw power from the batteries. Throughout this process, as long as the energy discharge does not fall below the minimum SOC threshold, the batteries will undergo an energy discharge. However, should the SOC exceed the maximum limit, the batteries would engage in charging from the electrical grid. Charging will commence when the battery capacity drops below 15%, while the discharge process is capped at 85% of capacity.

RESULTS AND DISCUSSION

Solar Energy Potential at the Charging Station Location

The capacity of solar charging stations was determined based on the potential absorption of solar energy at the specific installation site. This potential was derived from solar irradiation data specific to the location of the charging station, as outlined in Table 1. It was observed that solar irradiation tends to increase in correlation with the sun's position throughout the day. The solar irradiation values in Indonesia demonstrate monthly fluctuations due to seasonal changes. Data for September indicates a peak, with an average daily total irradiation reaching 6.157 Wh/m². On the contrary, January had the lowest recorded values, with an average daily total irradiation of 2.776 Wh/m². This decline in irradiation values was likely attributable to the rainy season, which diminishes the amount of sunlight that can be harnessed. Overall, the annual average solar irradiation stands at 4.208 Wh/m².

Table 1
Solar energy potential as a charging station energy source

Hour	Average Solar Irradiation During the Year (Wh/m2)												Average
	Jan	Feb	Mar	Apr	May	Jun	Jul	Aug	Sep	Oct	Nov	Dec	
0–1	0	0	0	0	0	0	0	0	0	0	0	0	0
1–2	0	0	0	0	0	0	0	0	0	0	0	0	0
2–3	0	0	0	0	0	0	0	0	0	0	0	0	0
3–4	0	0	0	0	0	0	0	0	0	0	0	0	0
4–5	0	0	0	0	0	0	0	0	0	0	0	0	0
5–6	0	0	0	0	0	0	0	0	0	0	0	0	0
6–7	15	6	7	11	12	8	0	14	40	59	60	23	21
7–8	141	126	153	188	211	216	209	264	336	281	218	143	207
8–9	225	242	289	310	358	379	417	460	506	428	323	221	347
9–10	310	328	363	377	433	457	511	573	616	535	377	290	431
10–11	371	368	422	448	504	520	587	657	694	604	447	339	497
11–12	382	402	470	510	565	573	651	720	734	633	471	351	539
12–13	371	392	467	510	580	607	675	740	734	625	434	330	539
13–14	327	364	409	438	539	594	668	725	702	580	353	265	497

Table 1 (continue)

Hour	Average Solar Irradiation During the Year (Wh/m2)												Average
	Jan	Feb	Mar	Apr	May	Jun	Jul	Aug	Sep	Oct	Nov	Dec	
14–15	258	297	306	340	462	535	615	671	637	472	274	198	422
15–16	172	196	205	231	348	429	528	575	530	377	195	122	326
16–17	103	126	138	160	245	322	405	439	394	269	140	78	235
17–18	77	88	94	102	115	179	232	261	223	136	82	54	137
18–19	24	32	14	6	1	3	14	18	11	5	4	6	12
19–20	0	0	0	0	0	0	0	0	0	0	0	0	0
20–21	0	0	0	0	0	0	0	0	0	0	0	0	0
21–22	0	0	0	0	0	0	0	0	0	0	0	0	0
22–23	0	0	0	0	0	0	0	0	0	0	0	0	0
23–24	0	0	0	0	0	0	0	0	0	0	0	0	0
Total	2776	2967	3337	3631	4373	4822	5512	6117	6157	5004	3378	2420	4208

Solar radiation measurement was used to determine how much solar energy can be harnessed. This process also optimises the design of charging station systems, identifies ideal locations, and analyses the performance of these charging stations.

Electric Vehicle (EV) Power Requirements

The electric charging station offered three sockets for charging electric vehicles. Data regarding the energy requirements of electric vehicle (EV) users was essential as a basis for energy management strategies, enabling the prioritisation of renewable energy sources in fulfilment of energy demands. The energy requirements for EVs were measured over 30 days. A dashed line graph illustrated the fluctuations in electricity consumption throughout the usage period from morning until evening, as depicted in Figure 5. The average energy

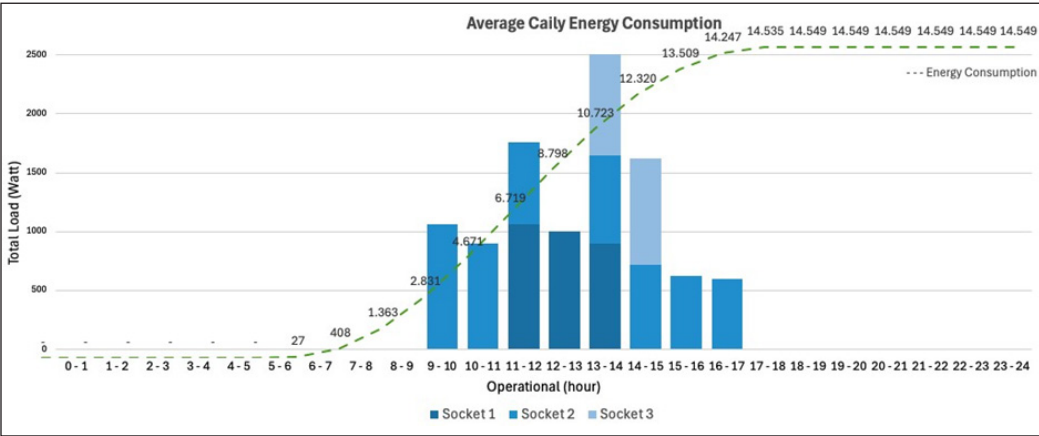


Figure 5. Daily load profile of the charging station

requirement for EVs was recorded at 14,549 Wh. The bar chart analysis reveals that the peak of energy consumption occurs between 1:00 PM and 2:00 PM. This data implies that several charging processes occurred simultaneously during this timeframe.

The study utilised conventional socket charging stations for data collection, allowing for the use of various charging adapters. Monitoring devices recorded charging power for each electric motor ranging from 600 to 1,000 watts. This data was used as a reference for effectively managing energy supply at the charging stations, considering fluctuations in energy consumption and measured charging capacity.

Daily Energy Management of Solar Charging Station

The charging station was equipped with three charging ports, enabling simultaneous use by three electric vehicles (EVs). This study analysed the energy management reports of the charging station over seven days, with a particular focus on energy consumption from photovoltaic (PV) sources. Considering that the charging station was situated in a campus parking area, it was noted that the average users of this station are active during the institution's working hours, specifically between 6:00 AM and 9:00 PM.

On the first day, the utilisation of the charging station is illustrated in Figure 6. The EV charging at socket 1 was entirely fulfilled by the PV energy source, as indicated by the orange colour. However, when the other two sockets were used for EV charging, the power supply from the PV system was insufficient to meet the demand, necessitating additional energy from the battery between 7:00 AM and 8:00 AM. During this period, the battery undergoes a discharge process, decreasing energy levels, as represented by the dashed line. The solar energy absorption in the morning has not reached its full potential. However, as the sun reaches its zenith, the energy generated from the PV system gradually increases, allowing the power needs of the EV to be fully met by the PV source. The excess power generated by the photovoltaic system is transferred to the battery at 1:00 PM.

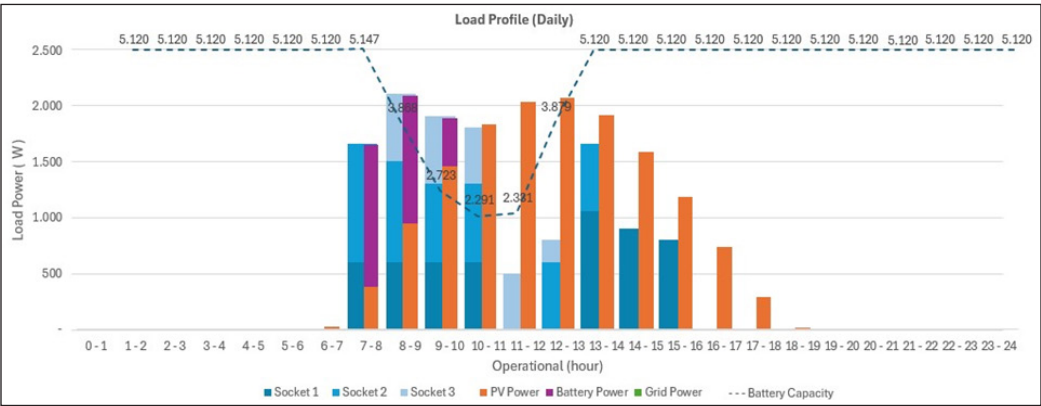
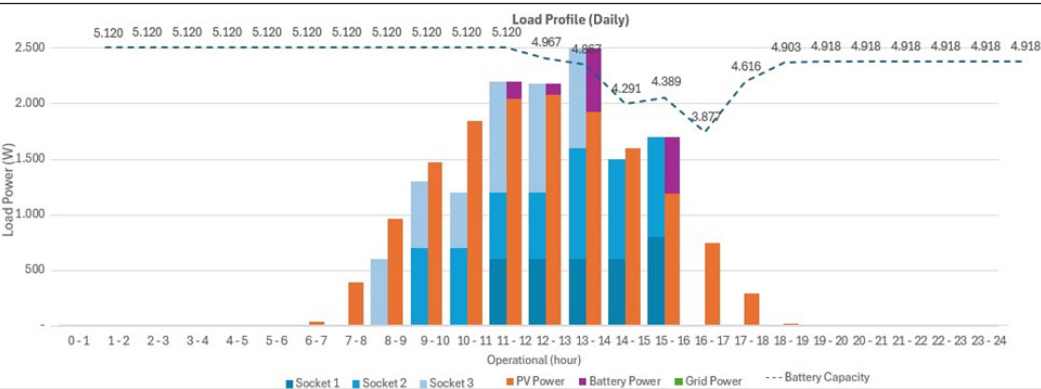


Figure 6. Load profile of day one

During the time range of 8:00 AM to 11:00 AM, the total energy consumption amounted to 2,372 watts, with three EVs utilising the charging stations. The energy requirements for the sockets were 600 watts for socket 1, 1,000 watts for socket 2, and 600 watts for socket 3. At that time, solar energy had not yet reached its full potential, requiring additional support from the battery supply. Once solar energy absorption achieved optimal levels, if the battery's State of Charge (SOC) fell below 15%, the battery would initiate a recharge. During the first day of assessment, the power demand was sufficiently met without drawing from the electrical grid. This enabled the designed charging stations to effectively reduce the reliance on fossil fuels.

For several days following the operation of the EV charging station, the energy requirements could be met through photovoltaic energy and battery storage. Figures 7 to 10 illustrate the effectiveness of this system in maintaining sustainability and energy efficiency at the EV charging station. The photovoltaic system and batteries had consistently delivered a sufficient energy supply for an extended period, allowing the station to function independently without solely depending on grid energy sources.



Gambar 7. Load profile of day two

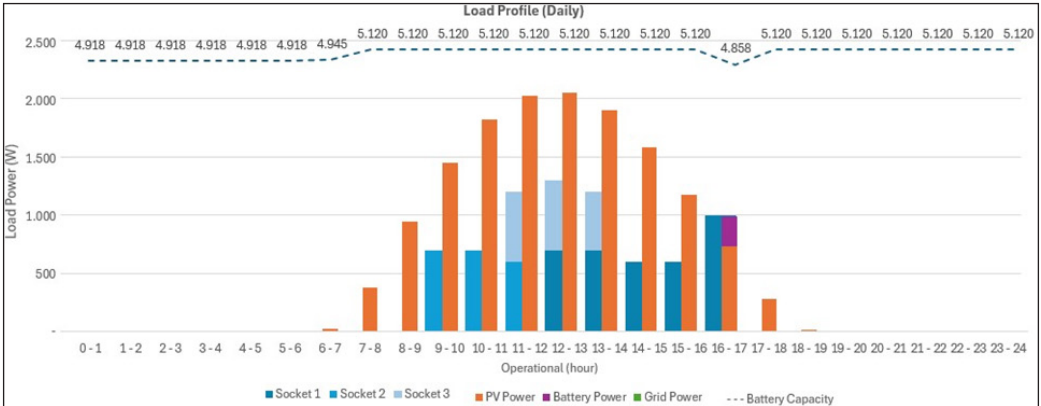


Figure 8. Load profile of day three

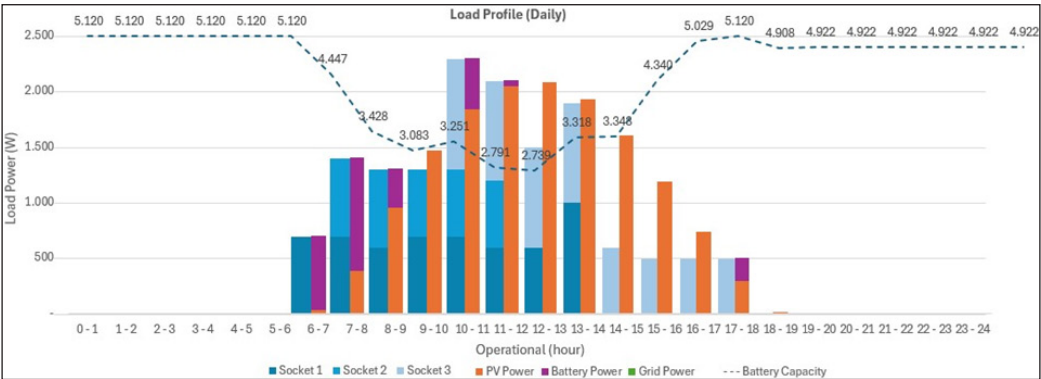


Figure 9. Load profile of day four

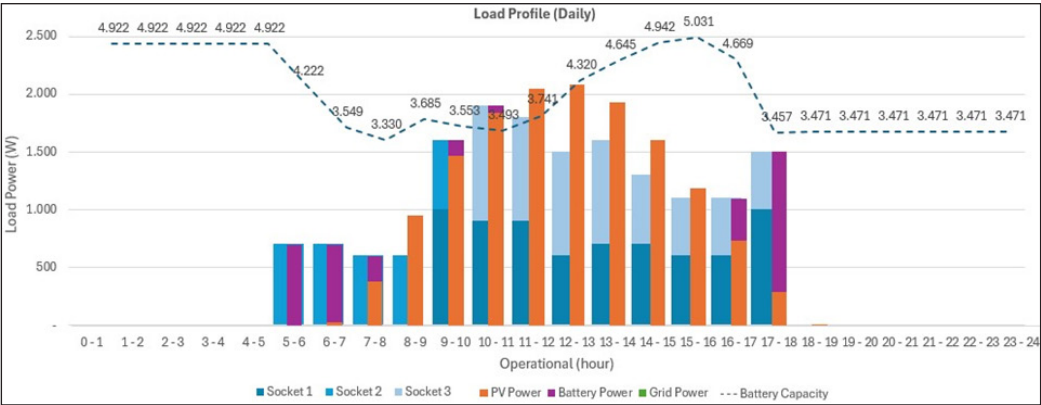


Figure 10. Load profile of day five

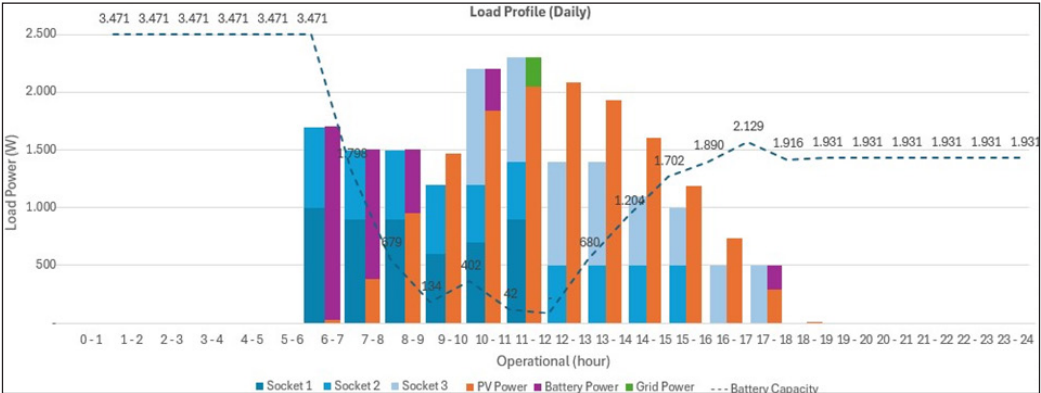


Figure 11. Load profile of day six

In the case observed on the sixth day, as illustrated in Figure 11, it was noted that in the morning, when the solar panels (PV) were not yet generating power, several EVs

were charging, each requiring 600 watts and 1,000 watts, respectively. The vehicles were powered by utilising the energy stored in the batteries. During this procedure, the batteries were discharged. Therefore, this ultimately leads to a decrease in the SOC. Fortunately, the PV systems were able to mitigate the situation by effectively harnessing solar energy.

At 10:00 AM, it was recorded that three EVs were charging, with capacities of 600 watts, 1,000 watts, and 1,000 watts, while the battery conditions were nearing the minimum SOC. As the power generated by the photovoltaic (PV) system and batteries was insufficient to meet the energy demands of the EVs, the power supply was sourced from the electricity grid. The grid provided only 253 watts of the total energy requirement of 18,712 watts. In terms of percentage, the energy contributions were 78% from the PV system, 21% from the batteries, and 1% from the grid on that sixth day.

By the seventh day, the solar panels (photovoltaic) had not fully charged the battery. In the morning, the EVs were observed utilising power from the battery, as shown in Figure 12. When the battery's SOC approached its limit, and the PV system was not providing optimal power, the electrical grid supplied the EVs. As the sun moved, the PV system subsequently took over as the primary energy source for the charging station. Overall, on the seventh day, only 1,795 watts of energy were required from the electrical grid out of a total daily consumption of 17,318. By mean, only 10% of the daily energy requirements for electric vehicles were sourced from the electrical grid. Therefore, it's demonstrating an effective approach to reducing the dependence on fossil fuels.

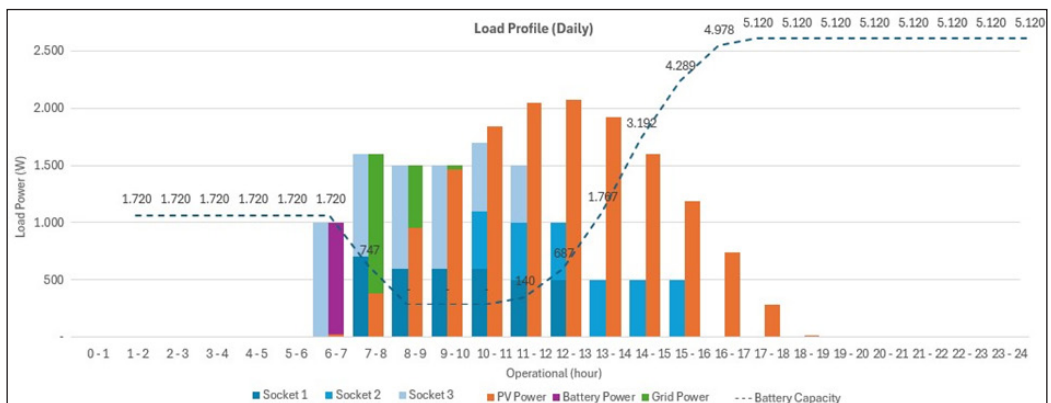


Figure 12. Load profile of day seven

As energy management increasingly relies on power supply from PV systems, the batteries do not engage in charging during the night. The primary focus for battery charging was on utilising PV energy during daylight hours. This approach focuses on harnessing charging stations as renewable energy sources to reduce reliance on fossil fuels and mitigate greenhouse gas emissions. Strategically positioning charging stations throughout

campus enhanced the adoption of photovoltaic energy for battery charging purposes. Future research could explore more complex solutions that would enable EV users to charge their vehicles from day to night. The development of electric vehicle infrastructure necessitates a comprehensive examination from multiple perspectives to ensure that goals are successfully achieved. Research on renewable energy plays a crucial role in contributing to energy sustainability and addressing pollution and environmental degradation issues.

Studies have addressed similar topics to enhance and bolster the advancement of infrastructure for EV utilization, in addition to initiatives aimed at decreasing reliance on fossil fuels. Table 2 presents comparable studies that address the utilisation of renewable energy for charging stations or supporting infrastructure for EV users. Several key highlights were examined from the perspective of developing supporting infrastructure for EVs, encompassing both simulations and implementations. The studies listed in Table 2 focus solely on the energy management of charging stations derived from hybrid sources. The proposed research indicates a significant contribution, suggesting that charging stations with the development of multi-source inverters provide straightforward energy management while simultaneously reducing reliance on fossil fuels. Furthermore, installing charging stations on campus provides complimentary power for members of the academic community who utilize electric vehicles. Such initiatives undoubtedly have a positive impact on reducing operational costs and mitigating greenhouse gas emissions.

Table 2
Similar research

Works	Description	Highlight
Kouka and Krichen (2019)	Simulation	Energy management is being implemented in hybrid sources, with a priority on utilising renewable energy; however, this research is still in the simulation phase.
Cheikh-Mohamad et al. (2023)	Simulation	Electric vehicles (EVs) can utilise 75% of the total energy while charging at a charging station, providing a significant advantage over traditional vehicles. This is attributed to the limitations on the energy consumed by EVs. The Vehicle-to-Grid (V2G) service can be customised to accommodate the user's specific capacity needs.
Chacko and Sachidanandam (2021)	Simulation	A smart energy management system has been developed for a bidirectional converter that can be connected to the grid and installed in electric vehicles. This research focuses on the communication and price negotiation for electric vehicle usage and charging station systems.
Cabrera-Tobar et al. (2022)	Simulation	The current focus of the research is on assessing Energy Management Systems (EMS), with a particular emphasis on reducing emissions and minimising energy costs. At this stage, the research is primarily focused on simulation.
Mohan and Dash (2023).	Simulation	The charging station's resources are derived from hybrid sources. The management of the DC microgrid power is developed using Fuzzy-SSA. This research has been simulated using MATLAB software.

Table 2 (continue)

Works	Description	Highlight
Kumar et al. (2023)	Review	The article reviews EV charging infrastructure, power management, and control techniques. It discusses charging station availability, power efficiency, and technological control methods for optimising energy use. The article aims to provide insights into the current state and future of EV charging.
Cheikh-Mohamad et al. (2022)	Application	The smart grid efficiently manages power balancing by using cutting-edge technology, including batteries, to store excess electricity from solar and traditional sources. This innovative approach optimises renewable energy use and helps us meet fluctuating grid demands, ensuring reliable and sustainable energy for our customers.
Proposed method	Application	The multisource inverter plays a vital role in integrating hybrid sources and filtering, protecting, and prioritising energy from photovoltaic (PV) systems. This involves facilitating direct EV charging services and battery charging capabilities. Energy supplied from the grid is considered the last option when energy demands are not met. The reliance on fossil fuels for EV energy requirements is minimal, accounting for only up to 10% of total energy needs.

CONCLUSION

The establishment of electric vehicle (EV) charging stations powered by multiple energy sources was of significant importance, particularly in facilitating the transition to clean energy and accelerating the adoption of electric vehicles. The implementation of a multi-source inverter, supported by an energy management system, prioritises the use of power generated from photovoltaic (PV) systems. This approach provided a viable solution for the development of EV charging infrastructure. Notable reductions in fossil energy consumption have been observed following the deployment of these charging stations on a university campus. Primarily powered by the PV system, these stations could meet the energy demands of EVs within just two days, contingent on the availability of power from the electrical grid. The peak consumption of grid power occurs on the seventh day. During this period, EVs utilised only 1,795 watts of fossil energy, while the PV system contributed a substantial 17,318 watts. The energy management strategy employed at these stations has effectively reduced fossil energy usage by up to 90%. Furthermore, any excess power generated by the PV system was directed towards charging batteries, which significantly enhances fossil energy savings.

However, a notable limitation arises from the predominant reliance on PV energy, as batteries cannot be charged during nighttime. This situation was not deemed problematic since the charging station was situated within a campus environment, which typically experiences low activity levels at night. Grid power was only harnessed when there was an increase in EV demand, which predominantly occurs during daylight hours. Future research should explore the operation of charging stations during nighttime to address more

complex scenarios similar to those encountered in public area stations. Such investigations will deepen the understanding of energy management across varied operational contexts and aid in the optimisation of renewable energy sources within the broader energy grid. For future research, it is essential to consider the operation of charging stations at night to introduce a more complex scenario akin to charging stations located in public areas.

ACKNOWLEDGEMENT

This research received funding from the Ministry of Education, Culture, Research and Technology (*Kementerian Pendidikan, Kebudayaan, Riset dan Teknologi-Kemdikbud Ristek*) for the year 2024, under contract number: 109/E5/PG/02.00.PL/2024; 036/SP2H/PT/LL7/2024; B/17/HIB-EX/PL/UHT.C7/VI/2024.

REFERENCES

- Ahmad, F., Iqbal, A., Ashraf, I., & Marzband, M. (2022). Optimal location of electric vehicle charging station and its impact on distribution network: A review. *Energy Reports*, 8, 2314-2333. <https://doi.org/10.1016/j.egy.2022.01.180>
- Baqar, A., Camara, M. B., & Dakyo, B. (2022). Energy management in the multi-source systems. *Energies*, 15(8), Article 2713. <https://doi.org/10.3390/en15082713>
- Cabrera-Tobar, A., Blasuttigh, N., Massi Pavan, A., Lughi, V., Petrone, G., & Spagnuolo, G. (2022). Energy scheduling and performance evaluation of an e-vehicle charging station. *Electronics*, 11(23), Article 3948. <https://doi.org/10.3390/electronics11233948>
- Chacko, P. J., & Sachidanandam, M. (2021). An optimized energy management system for vehicle to vehicle power transfer using micro grid charging station integrated Gridable Electric Vehicles. *Sustainable Energy, Grids and Networks*, 26, Article 100474. <https://doi.org/10.1016/j.segan.2021.100474>
- Cheikh-Mohamad, S., Celik, B., Sechilariu, M., & Locment, F. (2023). PV-powered charging station with energy cost optimization via V2G services. *Applied Sciences*, 13(9), Article 5627. <https://doi.org/10.3390/app13095627>
- Cheikh-Mohamad, S., Sechilariu, M., & Locment, F. (2022). Real-time power management including an optimization problem for PV-powered electric vehicle charging stations. *Applied Sciences*, 12(9), Article 4323. <https://doi.org/10.3390/app12094323>
- Ebrahimi, J., Salari, O., Eren, S., Hashtrudi-Zaad, K., Bakhshai, A., & Jain, P. (2021). Efficiency improved multi-source inverter for hybrid energy storage systems in electric vehicle application. *IEEE Transactions on Power Electronics*, 37(2), 1982-1997. <https://doi.org/10.1109/TVT.2019.2915173>
- Ekren, O., Canbaz, C. H., & Güvel, Ç. B. (2021). Sizing of a solar-wind hybrid electric vehicle charging station by using HOMER software. *Journal of Cleaner Production*, 279, Article 123615. <https://doi.org/10.1016/j.jclepro.2020.123615>
- Khan, S., Sudhakar, K., Yusof, M. H. B., Azmi, W. H., & Ali, H. M. (2023). Roof integrated photovoltaic for electric vehicle charging towards net zero residential buildings in Australia. *Energy for Sustainable Development*, 73, 340-354. <https://doi.org/10.1016/j.esd.2023.02.005>

- Kouka, K., & Krichen, L. (2019). Energy management strategy of a photovoltaic electric vehicle charging station. In *2019 19th International Conference on Sciences and Techniques of Automatic Control and Computer Engineering (STA)* (pp. 124-129). IEEE Publishing. <https://doi.org/10.1109/STA.2019.8717285>
- Kumar, M., Panda, K. P., Naayagi, R. T., Thakur, R., & Panda, G. (2023). Comprehensive review of electric vehicle technology and its impacts: Detailed investigation of charging infrastructure, power management, and control techniques. *Applied Sciences*, 13(15), Article 8919. <https://doi.org/10.3390/app13158919>
- Kunj, T., & Pal, K. (2020). Optimal location planning of EV charging station in existing distribution network with stability condition. In *2020 7th International Conference on Signal Processing and Integrated Networks (SPIN)* (pp. 1060-1065). IEEE Publishing. <https://doi.org/10.1109/SPIN48934.2020.9071396>
- Lestari, I., & Rangkuti, C. (2023). Perancangan, pembuatan, dan pengujian pengisi baterai sepeda motor listrik tenaga surya [Design, construction, and testing of solar-powered electric motorcycle battery charger]. *Metrik Serial Humaniora dan Sains*, 4(2), 15-23. <https://doi.org/10.51616/huma.v4i2>
- Mohan, H. M., & Dash, S. K. (2023). Renewable energy-based DC microgrid with hybrid energy management system supporting electric vehicle charging system. *Systems*, 11(6), Article 273. <https://doi.org/10.3390/systems11060273>
- Narasipuram, R. P., & Mopidevi, S. (2021). A technological overview & design considerations for developing electric vehicle charging stations. *Journal of Energy Storage*, 43, Article 103225 <https://doi.org/10.1002/er.5700>
- Pan, L., Yao, E., Yang, Y., & Zhang, R. (2020). A location model for electric vehicle (EV) public charging stations based on drivers' existing activities. *Sustainable Cities and Society*, 59, Article 102192. <https://doi.org/10.1016/j.scs.2020.102192>
- Reddy, G. H., Depuru, S. R., Gope, S., Narayana, B. V., & Bhukya, M. N. (2023). Simultaneous placement of multiple rooftop solar PV integrated electric vehicle charging stations for reliability benefits. *IEEE Access*, 11, 130788-130801. <https://doi.org/10.1109/ACCESS.2023.3335093>
- Sanguesa, J. A., Torres-Sanz, V., Garrido, P., Martinez, F. J., & Marquez-Barja, J. M. (2021). A review on electric vehicles: Technologies and challenges. *Smart Cities*, 4(1), 372-404. <https://doi.org/10.3390/smartcities4010022>
- Triyanto, A., Rozak, O. A., & Aditya, A. (2023). Calculation array solar panel capacity of 50 kWp Pamulang University South Tangerang. *PROtek: Jurnal Ilmiah Teknik Elektro*, 10(3), 193-198. <http://doi.org/10.33387/protk.v10i3.5795>
- Ullah, Z., Wang, S., Wu, G., Hasanien, H. M., Rehman, A. U., Turky, R. A., & Elkadeem, M. R. (2023). Optimal scheduling and techno-economic analysis of electric vehicles by implementing solar-based grid-tied charging station. *Energy*, 267, Article 126560. <https://doi.org/10.1016/j.energy.2022.126560>
- Xie, S., Hu, X., Zhang, Q., Lin, X., Mu, B., & Ji, H. (2020). Aging-aware co-optimization of battery size, depth of discharge, and energy management for plug-in hybrid electric vehicles. *Journal of Power Sources*, 450, Article 227638. <https://doi.org/10.1016/j.jpowsour.2019.227638>
- Zhang, J., Wang, Z., Liu, P., & Zhang, Z. (2020). Energy consumption analysis and prediction of electric vehicles based on real-world driving data. *Applied Energy*, 275, Article 115408. <https://doi.org/10.1016/j.apenergy.2020.115408>

Effect of Heat Treatment on the Properties of Perlis Dolomite Powder

Nur Hasnidah Ahmad Shukeri^{1*}, Syed Nuzul Fadzli Syed Adam¹,
Hasmaliza Mohamad², Heah Cheng Yong¹ and Hamdan Yahya³

¹*Faculty of Mechanical Engineering Technology, Universiti Malaysia Perlis, Kampus Tetap Pauh Putra, 02600 Arau, Perlis, Malaysia*

²*School of Materials and Mineral Resources Engineering, Universiti Sains Malaysia, 14300 Nibong Tebal, Penang, Malaysia*

³*Department of Mineral and Geoscience Perak (JMG), 31400 Ipoh, Perak, Malaysia*

ABSTRACT

Dolomite, $\text{CaMg}(\text{CO}_3)_2$, is a carbonate mineral naturally found in the sedimentary rocks associated with limestone and chalks, which has gained much interest for its potential as a raw material for bioceramic production. Aside from the important natural elements, dolomite is typically composed of organic compounds, carbonates and moisture. Therefore, heat treatment was required for dolomite to decarbonise the carbon content and remove volatiles and impurities, thus improving its purity. However, there were several previous studies on the heat treatment of dolomite minerals, and limited scientific findings have been published specifically for Perlis dolomite. The composition of natural mineral resources always slightly differs with different source locations, which affects some of its properties. Therefore, this study aims to investigate the influence of the heat treatment process on the physical, chemical, and structural properties of Perlis dolomite and evaluate its potential for bioceramic production. The raw and processed dolomite were analysed through XRF, TGA-DSC,

BET, XRD and FTIR. The findings showed that the heat treatment process is crucial for Perlis dolomite to improve its purity, enhance the oxide compounds, especially calcium and magnesium oxide, and activate the dolomite by forming hydroxyl groups. These important findings also proved the high potential of heat-treated Perlis dolomite as a promising precursor for bioceramic production.

ARTICLE INFO

Article history:

Received: 23 October 2024

Accepted: 14 February 2025

Published: 23 April 2025

DOI: <https://doi.org/10.47836/pjst.33.3.23>

E-mail addresses:

hasnidahnur@gmail.com (Hasnidah)

syed.nuzul@unimap.edu.my (Syed Nuzul Fadzli)

hasmaliza@usm.my (Hasmaliza Mohamad)

cyheah@unimap.edu.my (Heah Cheng Yong)

hamdan.yahya@jmg.gov.my (Hamdan Yahya)

*Corresponding author

Keywords: Annealing, bioceramic, heat treatment, material characterisation, Perlis dolomite

INTRODUCTION

Dolomite is one of the natural resources that can be found easily in most of the reservoirs in the northern area of Peninsular Malaysia, which is in Perlis, specifically at most of the quarries in the vicinity of Chuping and Kangar (Azurahaman et al., 2022). Perlis Dolomite is the second most prevalent carbonate after calcite and is usually associated with chalk and limestone. It can be actively exploited to gain large profits for economic importance for the country through various applications in a wide range of industries. In 2017, the Department of Mineral and Geosciences Malaysia (JMG) proclaimed that Chuping, Perlis possess dolomite reserves with weight assumptions of around 200 million metric tonnes, with an approximate cost of nearly RM 1.3 billion (Samad et al., 2019). Up to the present time, Perlis is still available with an abundance of dolomite, which can be proved by the most recent update by the Ministry of Natural Resources, Environment and Climate Change (NRECC) at the beginning of the year 2024. The aim of executing exploration activities upon the dolomite reservoirs will be implemented progressively in the district of Padang Besar, Perlis, as this mineral is valuable to this state and is worth up to RM 19.2 billion. Perlis Dolomite Industries Sdn often managed the local dolomite. Bhd. as the main manufacturer and supplier where the continuous demands from the domestic and international markets were fulfilled.

Ideally, dolomite is a carbonate resource with main constituents of the mineral, which are calcium and magnesium, with a chemical formula of $\text{CaMg}(\text{CO}_3)_2$. Generally, dolomite minerals were formed by the dolomitisation process where the magnesium replacement in calcite (Cai et al., 2021; Zahir et al., 2020; Resio, 2024; Shahraki et al., 2009) over long periods. It is naturally found in the dolomitic rocks called dolostone (Fauzi, Osman, Alrashdi et al., 2022; Cai et al., 2021; Resio, 2023). The Perlis dolomite is mostly known as ‘Batu Reput’ by the locals because of its relatively low hardness and easily crushed into fine powders (Azurahaman et al., 2022; Kamarzamann et al., 2022; Kambakhsh et al., 2024; Mohammed et al., 2013; Osman et al., 2022). Dolomite is practically used for soil conditioning and fertiliser making in agriculture, as well as on road pavement and building materials in construction industries (Hussin et al., 2006; Mohammed et al., 2013). The abundance of dolomite minerals in Perlis should be explored broadly to enhance the material development of the dolomite in other applications, particularly for bone tissue engineering practices in the biomedical industry. This is because the dolomite mineral can be used to acquire its dominant components (CaO and MgO) as precursors in the bioceramic process. Both compounds were believed to play vital roles in bone treatments. Practically, CaO is the crucial component in the bone matrix and assists in bone formation by releasing Ca ions to encourage osteoblast proliferation (Liu et al., 2008; Marzban et al., 2019). Meanwhile, MgO contributes to the growth factor of the bone during the beginning phase of osteogenesis, stimulates bone formation and decreases the implications of osteoporosis,

as well as is associated with bone mineralisation of calcified tissues (Arokiasamy et al., 2022; Liu et al., 2008; Marzban et al., 2019).

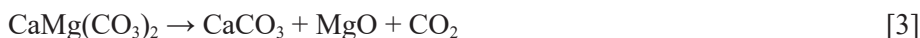
Owing to the unique compositions of dolomite, this mineral has raised researchers' attention to biomedical applications. Moroccan dolomite has been used as the main precursor along with perlite/slag to produce akermanite bioceramic that has great mechanical properties with high formation of apatite layer, indicating its good biocompatibility and bioactivity performances suitable for bone tissue engineering (Arkame et al., 2023; Harrati et al., 2022). Moreover, the addition of calcined dolomite from Qingyang, China, associated with montmorillonite in the hydroxyapatite-based bone adhesive has improved its biocompatibility and degradation performance (Hu, Qu et al., 2024; Hu, Wang et al., 2024). Apart from dolomite from various regions, Perlis dolomite exhibits promising potential for biomedical applications. Hossein Mohammadi et al. performed an investigation by using Perlis dolomite powder along with cockleshell and rice husk ash and successfully produced calcium magnesium silicate (CMS-akermanite) with a relative density of 93.50% and high flexural and tensile strength approximately about 22.16 MPa and 8.21 MPa, respectively which shown potential as bone graft substitutes in the non-load-bearing area (Mohammadi et al., 2020).

Besides, the dolomite has also been used as a mineral filler in the Poly(ethylene-co-vinyl acetate) composite to substitute the non-recyclable silicone elastomer in biomedical applications, and the findings showed that the dolomite has improved the mechanical performances, where the tensile strength and elongation at break of the copolymer matrix were enhanced (Fauzi, Osman, Alosime et al., 2022; Chong et al., 2021). These studies show that dolomite has significant potential as a biomaterial for various biomedical applications. Thus, heat treatment would be required on the dolomite minerals to achieve better structural properties and a high purity grade before further bioceramic production procedures, leading to great performances and responses in biomedical applications.

Heat treatment is an initiative through a controlled process involving thermal reactions to alter the initial properties of the material. The calcination process is one of the heat treatments carried out at a significantly lower temperature than its melting point for certain durations. Besides, the heat treatment process also aims to decarbonise the carbon content and remove any other insignificant compounds from the impurities apart from the materials. Technically, the ideal thermal decompositions of dolomite would be achieved at a temperature range from 700°C to 1000°C. The dolomite mineral could directly decompose completely and produce CaO and MgO at 1000°C (Vaganov et al., 2017). In addition, the decomposition of dolomite can also be divided into two phases where the applied heating temperature contradicts each other.

According to Jablonski (2015), the first decomposition of the dolomite happened at low temperatures (below 700°C), where it forms MgO and CaCO₃ while releasing CO₂

gases. Meanwhile, the second decomposition of the CaCO_3 at higher temperatures above 700°C creates CaO and again releases the excess gases of CO_2 . This statement meets in agreement with Carlos et al., who have stated that the decomposition of dolomite can occur in two different approaches, which are full decomposition (one stage) and half decomposition (two stages) (Rodriguez-Navarro et al., 2012). The dolomite undergoes full decomposition upon the heat applied to the thermal reaction, as in Equation 1. Meanwhile, half of the decompositions are reported in Equations 2 and 3. The exact temperatures of the dolomite decompositions are not stated as they may vary in their scientific data. This is because the thermal mechanism of the dolomite minerals is poorly resolved and obscured (Rodriguez-Navarro et al., 2012; Shahraki et al., 2009) as the findings were varied and inconsistent, occasionally regarding different compositions of impurities in the dolomite carbonate from different quarry sources, followed with different experimental conditions applied during the decomposition process, including contrast atmosphere, heating rate, prevailing pressure of CO_2 , sample mass, size of crystal particle and more else (Jablonski, 2015; Rodriguez-Navarro et al., 2012). Thus, Perlis dolomite powder may require a heat treatment process to subsequently proceed to the sintering process for the preparation of bioceramic samples to avoid samples cracking. This is because the applied sintering temperature may lead to thermal shock on the samples, which is caused by the sudden high temperature and excessive gas burn-off.



According to previous literature, the physical, chemical and structural properties of dolomite are commonly changed by heat treatment and significantly affected by the source location of the dolomite mineral. Even though some research has been carried out on Perlis dolomite recently, the specific knowledge regarding its heat treatment properties, thermal decomposition, and reactions is still relatively limited compared to dolomite minerals in other countries. Therefore, heat treatment studies carried out on the Perlis dolomite are becoming crucial in determining this local natural resource's important properties and characteristics. Furthermore, the scientific discussion which correlates Perlis dolomite and the production of bioceramics is still not well-established, as this local mineral still

focuses on agriculture and construction industries. Thus, the novelty of this study lies in investigating the impact of the heat treatment process (1000°C for 4 hours) on local Perlis dolomite and reveals its suitability and potential as a promising material for bioceramics in biomedical applications. This study aims to characterise the raw Perlis dolomite powder for its physical, chemical, and structural properties and compare it with the heated Perlis dolomite (a post-heating treatment process has been implemented). The testing of samples includes X-Ray Fluorescent (XRF), Thermogravimetric Analysis (TGA) and Differential Scanning Calorimetry (DSC), Brunauer-Emmett-Teller (BET), X-ray diffraction (XRD) and Fourier transform infrared spectroscopy (FTIR).

MATERIALS AND METHODS

Material

The local quarry at Chuping supplied Perlis dolomite, and Perlis was used as it is in this study without sieving or any other mechanical processing. An annealing process was carried out to determine the effect of heat treatment on the properties of this dolomite. The initial dolomite powder with an average particle size distribution of 150 µm was heated in a muffle furnace at 1000 °C for 4 hours with a 10°C/min heating rate. The temperature set for the annealing process was chosen according to the previous researchers' literature study and the author's lab work findings. Then, the annealed powder was ground with a pestle and mortar to obtain uniform fine powder. The purpose of the heat treatment process is to decarbonise the carbon contents and decompose the main compound in this mineral. Other than that, it also aimed to remove moisture and organic impurities from the dolomite composition. The raw and heat-treated dolomite powders were then sieved under 150 µm to obtain uniform fine powders.

Characterisations of Raw and Heated Perlis Dolomite

Chemical compositions of the raw and heated Perlis dolomite were determined by the analysis via X-ray fluorescent (XRF) by Philips PANalytical MiniPAL 4 machine. For sample preparation, 10 g of powders with an average size of about 75 µm were pressed using a hydraulic machine to create pellets. The prepared pellet was loaded into the spectrometer chamber. The X-ray was emitted by operating the machine with the maximum voltage and current at 30 kV and 1 mA, respectively, for 10 minutes of pre-set duration. The data of the detected elements was analysed using MiniPal software. The thermal properties of the materials have also been studied using the Linseis Thermal Balances instrument for Thermogravimetric Analysis (TGA) and Differential Scanning Calorimetry (DSC). The powders with a sample mass of approximately 30 mg were placed in an alumina crucible and inserted into the furnace with heating temperature initiated from room temperature

up to 1200°C with a heating rate of 10°C/min under the flow of nitrogen at the rate of 100 mL/min. Analysette 22 Next Nano (FRITSCH) was used to perform precise Laser Particle Size Analysis (LPSA) to characterise the grain particles' size distribution on the sample powders. It has used the measurement range within 0.01 μm to 3800 μm with the Fraunhofer diffraction theory to calculate the grain size distribution, where the entire grain particles were assumed to have a spherical shape (Houghton et al., 2024).

Next, the surface area of the powders was analysed via Brunauer-Emmett-Teller (BET) analyser by Anton Paar for Nova. The analysis was implemented at room temperature with a thermal delay of 3 minutes. The adsorption of nitrogen gas, N_2 , was set at 77.35 Kelvin, and the samples were degassed in a vacuum condition for 90 minutes at 250 °C with a 10 °C /min heating rate. The phase transformations and the crystallinity between the raw and heated dolomite were identified by X-ray diffraction (XRD) using the Test Instrument Machine Bruker D2 Phaser, German (2010). The powder samples were scanned using $\text{Cu K}\alpha$ radiation at a wavelength of 1.5406 Å, operated under 40 kV voltage and 30 mA current for 10 minutes loading time with the angle diffraction of step-scanning was adjusted within 10° to 80° (2 θ) with step size of 0.02°. The obtained diffractograms were then analysed by X'pert Highscore Plus software to distinguish the formed phases and crystal structures in the powders that have matched peak positions and intensities with the crystallographic database's ICDD Powder Diffraction File (PDF). The Perkin Elmer machine was used to perform the Fourier transform infrared spectroscopy (FTIR) analysis to identify the characteristic bands of the functional groups that transform the dolomite powder following the applied heat treatment. For the testing preparation, each sample of raw and heat-treated dolomite powders was mixed with potassium bromide powder (KBr) with a dolomite to KBr ratio of 3:7 and then pressed into pellet form. The prepared pallet was scanned from 450 cm^{-1} to 4000 cm^{-1} with 4 cm^{-1} resolution, and the transmission percentages of infrared radiation at each wavenumber were recorded.

RESULTS AND DISCUSSION

Chemical Composition Analysis

The chemical compositions of raw and heated dolomite analysed by XRF are shown in Table 1, where the weight composition was expressed in percentage of oxides. It showed that the raw Perlis dolomite was mainly composed of CaO and MgO , with 65.07% and 23.1%, respectively. Na_2O , Ag_2O , and Al_2O_3 were also found to be 1.0% to 8.0%. Other minor compounds are found to be below 1.0%, such as Sc_2O_3 , SiO_2 , SnO_2 and others. It was found that the percentages for all chemical compositions were slightly changed after the heat treatment. CaO has reduced from 65.07% to 54.55% because CaO is more reactive with CO_2 and tends to easily separate from the impurities and volatile substances from the dolomite during heat treatment. Meanwhile, the amount of MgO and Na_2O has increased by

approximately 32% and 50%, respectively, as both compounds are less volatile due to high stability in thermal conditions and are able to maintain stability during the heat treatment. Since the carbonate contents decreased after the heat treatment, the remaining oxides with stable phases, such as MgO and Na₂O, became more concentrated. They appeared higher in the XRF measurement regarding the overall mass reduction. The increase of Na₂O contents after the heat treatment is suggested due to the applied thermal treatment that causes sodium ions to become more mobile and cause the sodium migration and diffusion on the material's surface, which leads to this compound being easily identified in the XRF detection. Subsequently, the percentages of the insignificant compounds have mostly decreased after the heat treatment.

In addition, the loss of ignition (LOI) of both samples in a vacuum was consistently about 10%, where these low values were considered an accurate measurement and precise detection of light elements in the samples. In contrast with most of the studies, the LOI of the dolomite was measured under the heat treatment temperature applied (maximum at 1000°C) and has a higher value around 40%–50%, which leads to decomposition of the carbonate contents and volatile substances and causes the increasing LOI (Dursun & Coşkun, 2020; Khashbaatar et al., 2022; Khoshraftar et al., 2023; Resio, 2023; Srinivasan et al., 2020). Yang et al. (2024) have mentioned that the low LOI is attributed to a few thermal decompositions on the resulting products.

This result shows that the heat treatment process has an average effect on the chemical composition of Perlis dolomite. Apart from that, the raw and heated Perlis dolomite is free from hazardous compounds, has zero toxicity and is safe for bioceramic production. Plus, the dominant compounds in the dolomite, which are CaO and MgO, were already common and mostly used as precursors in bioceramic production since they are able to play vital roles in biomedical applications. Comprehensively, the CaO is the main source of calcium in the matrix of human bone, teeth and skull (Fiume et al., 2020). Meanwhile, the MgO promotes bone growth modulation, repairs and regenerates bone tissues, assists in osteoblast proliferation, mineralises calcified tissue, and performs bone metabolism activity (Arokiasamy et al., 2022; Fiume et al., 2020; Nabyouni et al., 2018).

Table 1
Chemical compositions of dolomite by XRF analysis

Compound	CaO	MgO	Na ₂ O	Ag ₂ O	Al ₂ O ₃	Sc ₂ O ₃	SiO ₂	SnO ₂	Fe ₂ O ₃	Others	LOI
Raw Dolomite	65.07	23.10	8.00	1.46	1.30	0.48	0.25	0.24	0.18	0.12	10.35
Heated dolomite	54.55	30.50	12.00	0.29	1.20	0.23	0.10	0.38	0.10	0.17	10.97

Thermal Analysis

The thermal properties of the dolomite powder were carried out from room temperature to 1200°C, as TGA and DSC illustrated in Figure 1. Based on Figure 1(a), TGA curves of raw dolomite show a significant mass loss process with the total mass loss at 50.24% in the range of 423°C to 844°C. It is expected that mass loss will occur during the heat treatment process due to the decomposition of carbonates, water and organic matter. The major mass loss was attributed to the decomposition of carbonate contents from the raw dolomite by releasing CO₂ gases at an increasing temperature. The decomposition of raw dolomite between 500°C and 800°C has created high heat-resistant compounds CaO and MgO (Harrati et al., 2022). This result indicates that the raw Perlis dolomite powder requires a high annealing temperature of up to 850°C to eliminate the volatile or organic substances, similar to the findings by Shahraki et al. (2009). The constant slope of the TGA curve at the temperature above 840°C indicated the absence of any decomposition, which could support the sintering process at high temperatures over 900°C (Hafriz et al., 2018).

Meanwhile, the TGA curve of heated Perlis dolomite still shows multiple stages of mass losses due to residues and impurities being removed from the sample. However, for the heated dolomite powder, an apparent mass loss occurred approximately twofold lower than the value measured for the raw dolomite. The total mass loss was reduced by 24.98%, and no more significant mass loss was observed after 750°C. These results suggest that the heated dolomite has reached partial decomposition to form primary CaO and MgO compounds (during heat treatment) and that longer heating time is needed. The heat treatment process is suspected of readily activating the dolomite powder, lowering the decomposition and phase transformation temperature, and making it more reactive during heating than raw dolomite. Also, improper packing of the heated dolomite would be another factor for the small mass loss that occurs below 400°C, which is affected by the moisture contents.

Meanwhile, the mass loss above 400°C is due to the decomposition of the residue of calcite into pure CaO and organic matter, which agrees with the exothermic reactions on DSC curves. This result also indicates that the heated dolomite has greater thermal stability when applied at high temperatures compared to the raw dolomite. In order to achieve complete decarbonisation, decomposition, and phase transformation of raw dolomite powder, it is suggested that the heat treatment process be set to a longer soaking time of more than 4 hours. Besides, fine-sized particles of the powders normally promote good decomposition due to more exposure to heat on the surface area, which allows the carbonates to break down easily from the mineral. Complete heat treatment is important to avoid any gaseous burn-off during a powder sintering process, which can lead to deterioration of mechanical properties, thus causing cracking and fracture to the sintered bodies of the ceramic sample.

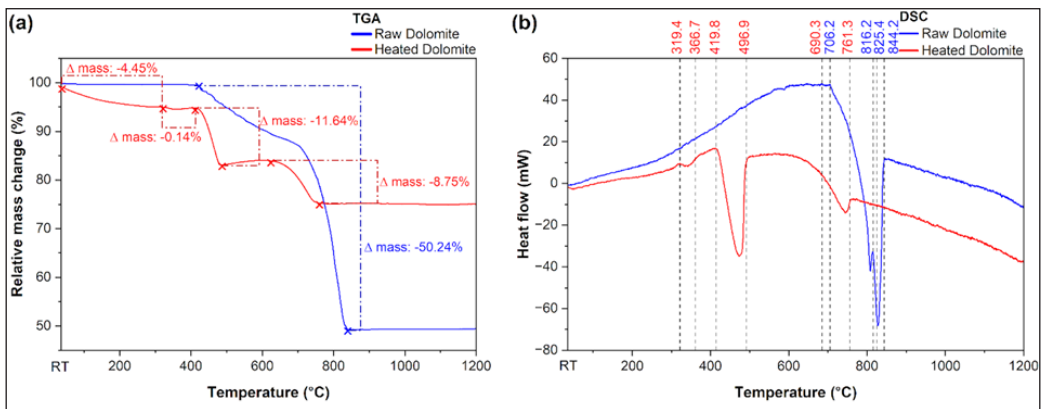


Figure 1. (a) TGA and (b) DSC curves of raw and heated dolomite

Figure 1(b) presents the analysis of DSC curves of the raw and the heated dolomite. The curve of raw dolomite displayed two stages of thermal reactions, which are endothermic and exothermic. The endothermic peak sharply at 706.2°C indicated the thermal decomposition of calcite, CaCO_3 into CaO and CO_2 (C. Li et al., 2024; Zhang et al., 2017). Besides, it also could have occurred due to the thermal decomposition of Ca(OH)_2 resulting from the reaction between CaO and moisture content (Mandrino et al., 2018). The energy absorbed during this reaction reached 173.98 J/g. Then, two exothermic reaction peaks at 816.2°C and 825.4°C with a negative enthalpy of 152.09 J/g were attributed to the crystallisation of MgO and CaO , respectively. Next, the DCS curve of heated dolomite exhibits three obvious exothermic reactions, which agree well with the results discussed on TGA. The first exothermic peak at 319.4°C to 366.7°C was due to the crystallisation of small amounts of calcite from the raw dolomite. Next, both exothermic peaks shifted to an earlier temperature than the raw dolomite curve. The peak at 419.8°C to 496.9°C was due to the crystallisation of MgO and the decomposition of organic matter. Meanwhile, the last exothermic peak was due to the crystallisation of the calcite into pure CaO . This is because the raw dolomite has released more energy during the crystallisation process at high temperatures.

In the end, the heated dolomite powder consisted of a few residues that could crystallise at lower temperatures by involving the discharge of slight energy to create better thermal stability with steady reactions towards heat applied. The significant exothermic reactions by the heated dolomite promote favourable crystallisation with other precursors during a sintering process. This is because the exothermic reaction assists in the cross-linking between the components, forms a better crystalline structure and leads to stronger and solid materials in terms of their mechanical strengths. From these results, it has been shown that thermal treatment through heat treatment on the dolomite mineral is compulsory to provide high thermal stability and a high purity grade of powder. It shows that the applied heat treatment on the raw dolomite is able to decompose most of the organics, impurities,

carbonates, and moisture from the mineral powder. Besides, the heated dolomite's constant slope after 750°C indicates thermal stability, whereas the raw dolomite required higher temperature up to 900°C.

Surface Area Analysis

Figure 2 presents the BET analysis by N₂ adsorption-desorption isotherms on the raw and heated dolomite. This specific surface area analysis is important and beneficial for dolomite powder. Technically, the raw material obtained from the local dolomite quarry is already in fine milled form, and this powder was used as it is. In addition, the processing of bioceramic by solid state sintering is commonly involved in the use of fine powder for the process and the preparation of samples, and it is rarely executed by using bulk or solid rock form. In the case of possible future work using this fine milled dolomite powder for bioceramic sample preparation, the porous characteristics of this mineral need to be clarified. Besides, the surface area, size, and pore volume of raw dolomite powder definitely affect the structural, morphological, and strength of the bioceramic. Hence, performing specific surface area analysis on this dolomite powder is important. The entire isotherm curves were categorised in type IV according to the IUPAC classification, which indicated the presence of mesoporous in the internal structure of the powders (Algoufi et al., 2017) and hysteresis loops commonly caused by H₂ (Chen et al., 2019). The results demonstrated that the heated dolomite has extremely high volume adsorbed during adsorption and desorption conditions compared to the raw dolomite. It shows that the N₂ adsorption of the capacity by the heated dolomite powder was a slackening increase at low pressure and displayed

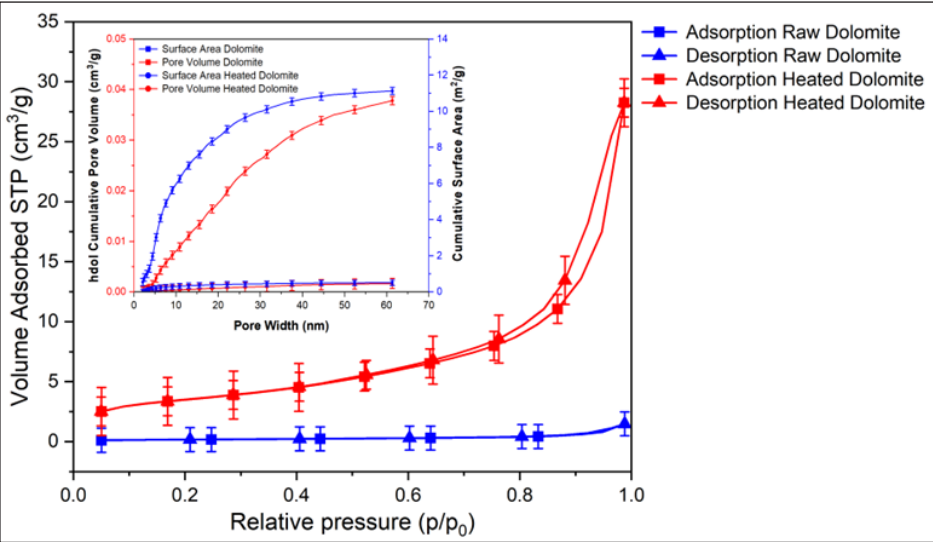


Figure 2. N₂ adsorption-desorption isotherms and pore size distribution of raw and heated dolomite

an expedited increase during $P/P_0 > 0.8$. A study by Chen et al. (2019) has proclaimed that it happened due to the mesoporous formation with size particles around 4 nm based on the pore size distribution curves. Besides, high partial pressures are required in the N_2 adsorption due to the pore constrictions of the powder at the large pore diameter. The results show that the calcined dolomite has high adsorption performance and bioceramic production potential. This is because high adsorption performances are preferable mainly for protein adsorption, drug delivery, and bone growth factors to recover rapidly.

The findings on the specific surface area, pore volume and average pore diameter of Perlis raw dolomite and heated dolomite are summarised in Table 2. It shows that the heat treatment at 1000°C has increased the value of the specific surface area up to 13.3790 m²/g, which is twenty times larger than the raw dolomite, which meets agreement with most studies (Kamarzamann et al., 2022; Hafriz et al., 2018; L. Li et al., 2024). The drastic increase in the surface area found for calcined dolomite is because the heat treatment process on the dolomite powder released CO₂ and removed volatile substances and organic matter, apart from the material, and created porous structures of CaO-MgO particles. The dense and well-packed crystalline structure of the raw dolomite has changed to higher porosity, followed by an increase in surface area after the heat treatment due to the crystal breakdown and loose bonds between the CaO and MgO particles. Subsequently, the size of the particle reduces with the increasing surface area. Besides, the heat treatment process has increased the pore volume and reduced the pore diameter average with values of 0.0438 cm³/g and 14.1556 nm, respectively. It has been assumed that the increase in surface area and pore volume after the heat treatment was attributed to the large formation of CaO and MgO in the powder and the elimination of undesirable impurities, followed by other volatile contaminants (Algoufi et al., 2017; Hafriz et al., 2018). Meanwhile, a slight reduction in average pore diameter was due to the decomposition of carbonate contents and the release of CO₂ gases during the heat treatment process (Hafriz et al., 2018). The higher value in the specific surface area, pore size and larger pore volume can promote a significant improvement in adsorption performances (Kamarzamann et al., 2022). Besides, the larger specific surface areas also improve bioactivity performances, have excellent mechanical properties, and control degradation as intended to complement human cancellous bone. Thus, it can be supported that calcined dolomite can be used as an alternative material in bioceramic production for bone tissue engineering applications.

Table 2
Pore characteristics of raw and heated dolomite

Samples	BET surface area (m ² /g)	Pore volume (cm ³ /g)	Average pore diameter (nm)
Raw dolomite	0.6010	0.0023	15.3193
Calcined dolomite	13.3790	0.0438	14.1556

Phase Transformation Analysis

Figure 3 displays the phase transformation of raw and heated dolomite. Figure 3(a) shows that the XRD pattern of raw Perlis dolomite was mainly formed by calcium magnesium carbonate, $\text{CaMg}(\text{CO}_3)_2$ phase, with a crystal system of hexagonal structure. The phases of $\text{CaMg}(\text{CO}_3)_2$ (JCPDS file no. 01-081-8227) occurred at the most intensified peak located at 31.148° and nearly entire peaks in the diffractogram of Perlis dolomite, which is similar to previous studies. (Abdullah et al., 2021; Sompech et al., 2016). Furthermore, the minority of the peaks in the diffractogram of raw Perlis dolomite were assigned to the phases of calcium magnesium silicate, $\text{CaMgSi}_2\text{O}_6$ (JCPDS file no. 04-008-8060) and sodium aluminium silicate, $\text{NaAlSi}_3\text{O}_8$ (JCPDS file no. 04-021-1621), where the crystal structures of the phases were monoclinic and anorthic, respectively.

Figure 3(b) presents the diffractogram of heated dolomite that demonstrated apparent changes in the XRD patterns because of the phase transformation after the heat treatment. The phases of $\text{CaMg}(\text{CO}_3)_2$ from raw dolomite have decomposed into some single phases individually, where most of the significant peaks were accredited by cubic structures of CaO (JCPDS file no 04-005-4398) and MgO (JCPDS file no 04-016-2776) phases. This result proved that the primary constituents of the heated dolomite were CaO and MgO, which were similar to the findings from Abdullah et al. (2021). The CaO phases were observed at 32.508° , 37.642° and 54.166° while the MgO phases were at 43.184° and 62.564° . Moreover, there were also found in the heated dolomite powder, involving sodium oxide, Na_2O (JCPDS file no 04-005-4449), calcium silicon oxide, Ca_3SiO (JCPDS file no 04-021-0148), aluminium, Al (JCPDS file no 04-014-0129) and silica, SiO_2 (JCPDS file no 04-015-7161). These phases, formed in the heated dolomite, correspond well with the previous results and discussions made for the XRF analysis.

According to the phase analysis, it can be highlighted that the heat treatment at 1000°C is particularly required and sufficient to allow the transformation of dominant carbonate phases of raw dolomite, $\text{CaMg}(\text{CO}_3)_2$ into more significant and more stable CaO and MgO phases in the heated Perlis dolomite powder. This statement can be supported by the findings from Abdullah et al. (2021) where the phases of dolomite showed significant changes at 800°C and 1000°C , while no apparent changes were found at 400°C and 600°C . Therefore, the phase transformation of this Perlis dolomite is found to be equivalent and develops the thermal decomposition and reaction mechanism, as shown previously in Equations 1 to 5. The heat treatment on the raw dolomite powder is able to change the phase transformation of the main compound of the dolomite carbonate matrix into CaO and MgO phases because of the high thermal energy that breaks the bonds between the chemical atoms in the dolomite structures (Ramli et al., 2022). Therefore, the formed phases of CaO and MgO after the heat treatment have arisen and affirm the potential and positive perspective for producing bioceramic-based material, especially for calcium and magnesium-based bioceramics.

These phases have been manifested to be significant and play a crucial part in biomedical applications, especially in the practices of bone engineering tissues (Choudhary et al., 2015; Collin et al., 2021; Zadehnajar et al., 2021).

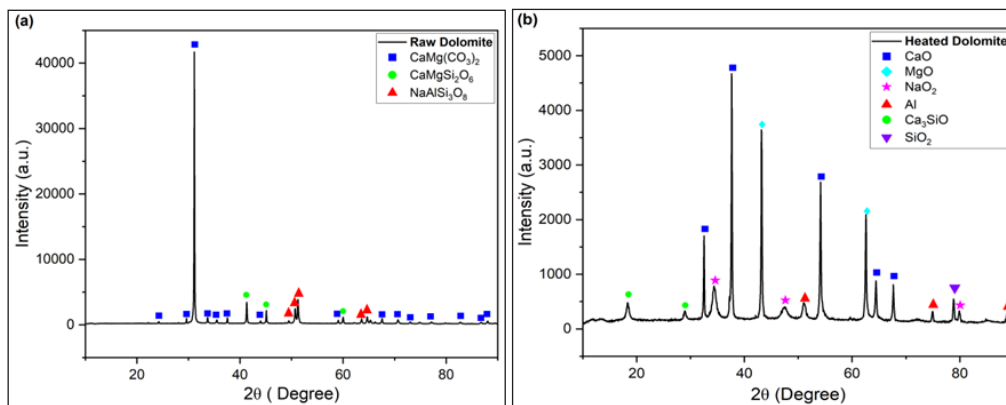


Figure 3. Diffractogram of (a) raw dolomite and (b) heated dolomite

Functional Group Analysis

Figure 4 illustrates the infrared spectral band of raw and heated Perlis dolomite. For raw dolomite, an outstanding and wide asymmetric stretching band at 1421 cm^{-1} , narrow bending bands around 875 cm^{-1} and 726 cm^{-1} have proved the existence of complex carbonate mineral group proportional with the ν_3 , ν_2 and ν_4 vibration modes of $(\text{CO}_3)^{2-}$ groups (Harrati et al., 2022; Shahraki et al., 2009) which incorporates with CaO and MgO compounds as its prime absorption components in the dolomite (Abdullah et al., 2021). The intense bands at 668 cm^{-1} and 3642 cm^{-1} were attributed to the appearance of CaOH bonds in the raw dolomite powder. Meanwhile, the weak bands at 875 cm^{-1} , 1005 cm^{-1} and 1080 cm^{-1} indicated the Si-O vibration bond, which affirmed the statement of silicate occurrence as the small impurities in the raw dolomite as found in the chemical composition analysis (Mohammed et al., 2013). Moreover, the band at 2895 cm^{-1} represented organic matter (C-H bond), while the bands at 3400 cm^{-1} and 3875 cm^{-1} were distinguished as stretching bonds of O-H caused by the moisture contents in the carbonates of dolomite (Buyang et al., 2023; Harrati et al., 2022; Kurtulbaş et al., 2020).

According to the FTIR spectrum analysis of heated dolomite, the heat treatment does not cause any apparent changes compared to the raw dolomite, but there were a few transmission bands that have decreased or disappeared (Resio, 2023; Yuliya et al., 2023), and there was also the formation of new peaks observed. The complex bonds of raw dolomite at 1421 cm^{-1} turn into a sharp band after the heat treatment introduces the decomposition of dolomite, $\text{CaMg}(\text{CO}_3)_2$, into CaO and MgO formation in the heated

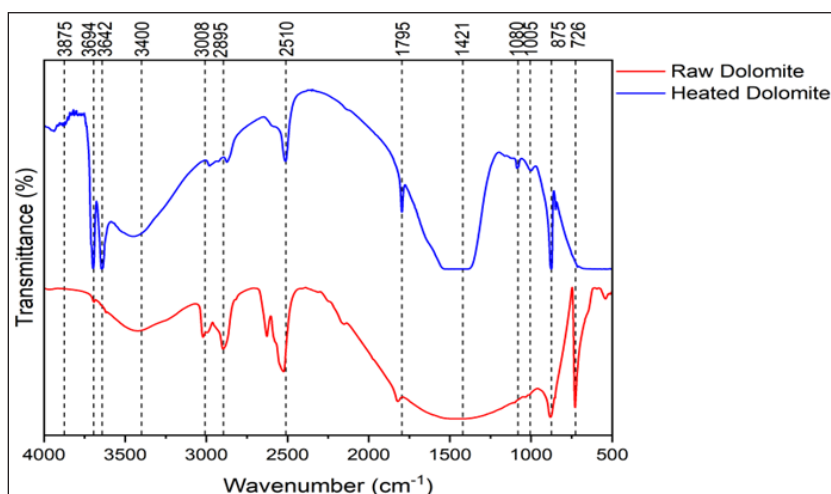


Figure 4. FTIR spectrum of raw and heated dolomite

dolomite powder. This is because the broad band of raw dolomite with overlaying vibrational modes has decomposed into simpler oxide bonds caused by the applied thermal decomposition. Besides, the bond segregation between the main absorbing functional groups of the carbonates from raw dolomite (CO_3)²⁻ has caused the low concentration of carbonate ions subsequently confronted by the concentration of CaO and MgO, which lessens the carbonate intensities and causes the formation of the new peak exhibiting the oxide compounds in the heated dolomite powder. The strong and intense bands at 3642 cm^{-1} and 3694 cm^{-1} existed after the heat treatment, particularly due to $\text{Ca}(\text{OH})_2$ formation from the hydroxyl bonds (Abdullah et al., 2021; Shahraki et al., 2009).

This spectral band transformation introduces the decomposition of the carbonate group of dolomite into the oxide compounds of CaO and MgO. The weak bands at the range of 875-1080 cm^{-1} have merged together to create a strong band indicating the presence of silica, Si-O bond as an impurities substance in the dolomite in the form of silicates vibration mode (Abdullah et al., 2021). The reduced intensity of the bands at 2895 cm^{-1} and 2510 cm^{-1} in the heated dolomite was assigned as the residue of the C-H stretching bonds from organic matter and O-H stretching bonds from the hydroxyl groups, respectively. The insignificant presence of H-bonds can be decomposed completely with high temperatures during the sintering process during bioceramic production. It has been clarified by Shahraki et al. that there is a tendency for the formation of bioceramic, which is wollastonite, due to the decomposition between calcite and quartz in the dolomite mineral after heat treated at 950°C, where its bands centred at 1005 cm^{-1} and 1080 cm^{-1} (Shahraki et al., 2009).

This result shows that the raw dolomite assigned to the changes occurred on the functional groups of Perlis dolomite after the heat treatment. The heat treatment has segregated the functional group of dolomite matrix bonds by decomposing the carbonate

groups and creating CaO and MgO bonds individually. In addition, it also showed the existence of hydroxyl groups in the heated dolomite, as they were important in enhancing the absorption performance, especially for bioceramic production purposes. Hydrogen bonds have significant roles in interacting with biological tissues, providing biocompatibility reactions and accelerating cell proliferation and tissue growth in bone tissue engineering applications. Thus, Perlis dolomite with applied heat treatment has very good potential as the main precursor and is suitable for use in the production of bioceramics.

CONCLUSION

The investigation of the effect of the heat treatment process on the Perlis dolomite was completed, and the objective was successfully achieved. It can be summarised that the heat treatment process done on the raw dolomite at 1000°C for 4 hours had a significant impact and made significant changes to the physical, chemical and structural properties of Perlis dolomite. However, this process is partially decarbonised, and the dolomite phase has been decomposed into multiple oxide phases. The heat treatment process is proposed to be extended to more than 4 hours to complete the reaction. The heat-treated dolomite was very suitable and has potential as a main precursor for bioceramic production. The dolomite was predominated by CaO and MgO, vital in bone tissue engineering applications. The heat treatment at 1000°C for 4 hours, as carried out in this study, is necessary and has shown significant positive impacts on the Perlis dolomite powder. The utilisation of dolomite in bioceramic production should be explored widely to maximise its potential.

ACKNOWLEDGEMENTS

A gratitude was expressed to the Faculty of Mechanical Engineering & Technology, Faculty of Chemical Engineering & Technology of Universiti Malaysia Perlis (UniMAP) and School of Materials and Mineral Resources Engineering, Universiti Sains Malaysia (USM) for providing the facilities of labs, machines and testing equipment.

REFERENCES

- Abdullah, S. F. A., Saleh, S. S. M., Mohammad, N. F., Idris, M. S., & Saliu, H. R. (2021). Effect of thermal treatment on natural dolomite. *Journal of Physics: Conference Series*, 2080(1), Article 012009. <https://doi.org/10.1088/1742-6596/2080/1/012009>
- Algoufi, Y. T., Kabir, G., & Hameed, B. H. (2017). Synthesis of glycerol carbonate from biodiesel by-product glycerol over calcined dolomite. *Journal of the Taiwan Institute of Chemical Engineers*, 70, 179-187. <https://doi.org/10.1016/j.jtice.2016.10.039>
- Arkame, Y., Harrati, A., Jannaoui, M., Et-Tayea, Y., Yamari, I., Sdiri, A., & Sadik, C. (2023). Effects of slag addition and sintering temperature on the technological properties of dolomite based porous ceramics. *Open Ceramics*, 13, Article 100333. <https://doi.org/10.1016/j.oceram.2023.100333>

- Arokiasamy, P., Abdullah, M. M. A. B., Rahim, S. Z. A., Luhar, S., Sandu, A. V., Jamil, N. H., & Nabiałek, M. (2022). Synthesis methods of hydroxyapatite from natural sources: A review. *Ceramics International*, 48(11), 14959–14979. <https://doi.org/10.1016/j.ceramint.2022.03.064>
- Azurahanim, C., Albert, E. L., Een, L. G., Zarin, M. A., & Yusoff, M. Z. M. (2022). Effect of thermal treatment on physical properties of Malaysian dolomitic limestone. *International Journal of Electroactive Materials*, 10(2022), 18-23.
- Buyang, Y., Suprpto, S., Nugraha, R. E., Holilah, H., Bahruji, H., Hantoro, R., Jalil, A. A., Oetami, T. P., & Prasetyoko, D. (2023). Catalytic pyrolysis of Reutealis trisperma oil using raw dolomite for bio-oil production. *Journal of Analytical and Applied Pyrolysis*, 169, Article 105852. <https://doi.org/10.1016/j.jaap.2022.105852>
- Cai, W. K., Liu, J. H., Zhou, C. H., Keeling, J., & Glasmacher, U. A. (2021). Structure, genesis and resources efficiency of dolomite: New insights and remaining enigmas. *Chemical Geology*, 573, Article 120191. <https://doi.org/10.1016/j.chemgeo.2021.120191>
- Chen, T., Li, H., Wang, H., Zou, X., Liu, H., Chen, D., & Zhou, Y. (2019). Removal of Pb(II) from aqueous solutions by periclase/calcite nanocomposites. *Water, Air, and Soil Pollution*, 230(12), Article 299. <https://doi.org/10.1007/s11270-019-4354-z>
- Chong, L. K., Osman, A. F., Fauzi, A. A. A., Alrashdi, A. A., & Halim, K. A. A. (2021). The mechanical and thermal properties of poly (Ethylene-co-vinyl acetate) (pecova) composites with pristine dolomite and organophilic microcrystalline dolomite (OMCD). *Polymers*, 13(18), Article 3034. <https://doi.org/10.3390/polym13183034>
- Choudhary, R., Koppala, S., & Swamiappan, S. (2015). Bioactivity studies of calcium magnesium silicate prepared from eggshell waste by sol-gel combustion synthesis. *Journal of Asian Ceramic Societies*, 3(2), 173–177. <https://doi.org/10.1016/j.jascer.2015.01.002>
- Collin, M. S., Venkatraman, S. K., Sriramulu, M., Shanmugam, S., Drweesh, E. A., Elnagar, M. M., Mosa, E. S., & Sasikumar, S. (2021). Solution combustion synthesis of functional diopside, akermanite, and merwinite bioceramics: Excellent biomineralization, mechanical strength, and antibacterial ability. *Materials Today Communications*, 27, Article 102365. <https://doi.org/10.1016/j.mtcomm.2021.102365>
- Dursun, F., & Coşkun, A. (2020). A preliminary study on material properties of the Zerzevan Castle, Turkey. In *IOP Conference Series: Materials Science and Engineering* (Vol. 949, No. 1, p. 012038). IOP Publishing. <https://doi.org/10.1088/1757-899X/949/1/012038>
- Fauzi, A. A. A., Osman, A. F., Alosime, E. M., Ibrahim, I., Halim, K. A. A., & Ismail, H. (2022). Strategies towards producing non-polar dolomite nanoparticles as nanofiller for copolymer nanocomposite. *International Journal of Molecular Sciences*, 23(20), Article 12620. <https://doi.org/10.3390/ijms232012620>
- Fauzi, A. A. A., Osman, A. F., Alrashdi, A. A., Mustafa, Z., & Halim, K. A. A. (2022). On the use of dolomite as a mineral filler and co-filler in the field of polymer composites: A review. *Polymers*, 14(14), Article 2843. <https://doi.org/10.3390/polym14142843>
- Fiume, E., Tulyaganov, D., Ubertalli, G., Verné, E., & Baino, F. (2020). Dolomite-foamed bioactive silicate scaffolds for bone tissue repair. *Materials*, 13(3), Article 628. <https://doi.org/10.3390/ma13030628>

- Hafriz, R. S. R. M., Salmiaton, A., Yunus, R., & Taufiq-Yap, Y. H. (2018). Green Biofuel production via catalytic pyrolysis of waste cooking oil using Malaysian dolomite catalyst. *Bulletin of Chemical Reaction Engineering & Catalysis*, 13(3), 489–501. <https://doi.org/10.9767/bcrec.13.3.1956.489-501>
- Harrati, A., Arkame, Y., Manni, A., Aqdim, S., Zmemla, R., Chari, A., El Bouari, A., El Amrani El Hassani, I. E., Sdiri, A., Hassani, F. O., & Sadik, C. (2022). Akermanite-based ceramics from Moroccan dolomite and perlite: Characterization and in vitro bioactivity assessment. *Open Ceramics*, 10, Article 100276. <https://doi.org/10.1016/j.oceram.2022.100276>
- Houghton, J. E., Behnsen, J., Duller, R. A., Nichols, T. E., & Worden, R. H. (2024). Particle size analysis: A comparison of laboratory-based techniques and their application to geoscience. *Sedimentary Geology*, 464, Article 106607. <https://doi.org/10.1016/j.sedgeo.2024.106607>
- Hu, M. N., Qu, X. J., Chen, X. L., He, D., Wang, G. Y., Liu, J. H., Roy, T., Kurniawan, A., & Zhou, C. H. (2024). Fabrication of a novel bone adhesive (crosslinked phytic acid-gelatin coordinated with magnesium phosphate and calcined dolomite, and montmorillonite) for enhancing adhesion strength and biocompatibility. *Journal of Inclusion Phenomena and Macrocyclic Chemistry*, 104(5–6), 317–334. <https://doi.org/10.1007/S10847-024-01234-4>
- Hu, M. N., Wang, G. Y., Liu, C. L., Roy, T., & Zhou, C. H. (2024). Mg^{2+} - Ca^{2+} chelating citric acid crosslinked gelatin, a bone adhesive composed of hydroxyapatite and calcined dolomite: Physicochemical characteristics and in-vitro biological activity. *International Journal of Adhesion and Adhesives*, 135, Article 10816. <https://doi.org/10.1016/j.ijadhadh.2024.103816>
- Hussin, K., Shamsul, J., Ruzaidi, C. M., Sobri, M. I., Nazry, M. S., & Nizar, K. (2006). The development of artificial marble from dolomite (Batu Reput) in Perlis. In *KUKUM Engineering Research Seminar 2006* (pp. 617–621). ResearchGate. <https://doi.org/10.13140/2.1.1044.8325>
- Jablonski, M. O. M. (2015). Thermal behavior of natural dolomite. *Journal of Thermal Analysis and Calorimetry*, 119, 2239–2248. <https://doi.org/10.1007/s10973-014-4301-6>
- Kamarzamann, F. F., Abdullah, M. M. A. B., Abd Rahim, S. Z., Kadir, A. A., Jamil, N. H., Ibrahim, W. M. W., & Sandu, A. V. (2022). Hydroxyapatite / Dolomite alkaline activated material reaction in the formation of low temperature sintered ceramic as adsorbent materials. *Construction and Building Materials*, 349, Article 128603. <https://doi.org/10.1016/j.conbuildmat.2022.128603>
- Kambakhsh, H., Haqbin, M., Inanch, S., Qarizada, K., & Qarizada, D. (2024). Unveiling the geological significance and industrial application of limestone: A comprehensive review. *The Journal of The Institution of Engineers Malaysia*, 85(1). <https://doi.org/10.54552/v85i1.238>
- Khashbaatar, Z., Akama, S., Kano, N., & Kim, H. J. (2022). Development of a new dolomite-based adsorbent with phosphorus and the adsorption characteristics of arsenic (III) in an aqueous solution. *Water*, 14(7), Article 1102. <https://doi.org/10.3390/w14071102>
- Khoshraftar, Z., Masoumi, H., & Ghaemi, A. (2023). An insight into the potential of dolomite powder as a sorbent in the elimination of heavy metals: A review. *Case Studies in Chemical and Environmental Engineering*, 7, Article 100276. <https://doi.org/10.1016/j.cscee.2022.100276>
- Kurtulbaş, E., Yıldırım, E., Emik, S., & Şahin, S. (2020). A detailed study on the sorption characteristics of humic acid onto calcined dolomite. *Journal of Molecular Structure*, 1219, Article 128606. <https://doi.org/10.1016/j.molstruc.2020.128606>

- Li, C., Jia, D., Yang, X., Zhao, S., Li, C., Liu, G., Wang, Y., Ding, X. xin, Qin, S., & Song, W. (2024). Effects of dosage and reactivity of modified dolomite dust waste on mechanical properties and shrink-resist of mortar. *Developments in the Built Environment*, 17, Article 100308. <https://doi.org/10.1016/j.dibe.2023.100308>
- Li, L., Otake, Y., & Shimizu, T. (2024). Biomass volatile gasification using dolomite and dolomite-Ni/Al₂O₃ combinations. *International Journal of Biomass & Renewables*, 13(1), 9–15.
- Liu, Q., Cen, L., Yin, S., Chen, L., Liu, G., Chang, J., & Cui, L. (2008). A comparative study of proliferation and osteogenic differentiation of adipose-derived stem cells on akermanite and β-TCP ceramics. *Biomaterials*, 29(36), 4792–4799. <https://doi.org/10.1016/j.biomaterials.2008.08.039>
- Mandrino, D., Paulin, I., Kržmanc, M. M., & Škapin, S. D. (2018). Physical and chemical treatments influence on the thermal decomposition of a dolomite used as a foaming agent. *Journal of Thermal Analysis and Calorimetry*, 131, 1125–1134. <https://doi.org/10.1007/s10973-017-6699-0>
- Marzban, K., Rabiee, S. M., Zabihi, E., & Bagherifard, S. (2019). Nanostructured akermanite glass-ceramic coating on Ti6Al4V for orthopedic applications. *Journal of Applied Biomaterials & Functional Materials*, 17(2), 228080001879381. <https://doi.org/10.1177/2280800018793819>
- Mohammadi, H., Hei, B. Z., Ismail, Y. M. B., Shariff, K. A., & Noor, A. F. M. (2020). Green synthesis of calcium magnesium silicate (CMS-Akermanite) using natural biowastes by solid-state sintering route. *Malaysian Journal of Microscopy*, 16(2), 66–76.
- Mohammed, M. A. A., Salmiaton, A., Azlina, W. A. K. G. W., Amran, M. S. M., & Taufiq-Yap, Y. H. (2013). Preparation and characterization of Malaysian dolomites as a tar cracking catalyst in biomass gasification process. *Journal of Energy*, 2013, Article 791582. <https://doi.org/10.1155/2013/791582>
- Nabiyouni, M., Brückner, T., Zhou, H., Gbureck, U., & Bhaduri, S. B. (2018). Magnesium-based bioceramics in orthopedic applications. *Acta Biomaterialia*, 66, 23-43. <https://doi.org/10.1016/j.actbio.2017.11.033>
- Osman, A. F., Fauzi, A. A. A., Amin, M. B., Halim, K. A. A., & Ul-Hamid, A. (2022). Size reduction of dolomite into nano-size range through milling and tip-sonication processes. *Materials Science Forum*, 1075, 3–8. <https://doi.org/10.4028/p-3zkle9>
- Ramli, M., Maisarah, M. R., Saidi, N., Murniana, & Idris, N. (2022). Aceh local dolomite modified by alkali metals as a low-cost solid inorganic catalyst for biodiesel synthesis. *IOP Conference Series: Earth and Environmental Science*, 1034(1), Article 012027. <https://doi.org/10.1088/1755-1315/1034/1/012027>
- Resio, L. C. (2023). Characterization of Argentine dolostones with potential application in the manufacture of refractory materials. *Open Ceramics*, 15, Article 100374. <https://doi.org/10.1016/j.oceram.2023.100374>
- Resio, L. C. (2024). Dolomite thermal behaviour: A short review. *Physics and Chemistry of Minerals*, 51, Article 19. <https://doi.org/10.1007/s00269-024-01272-x>
- Rodriguez-Navarro, C., Kudlacz, K., & Ruiz-Agudo, E. (2012). The mechanism of thermal decomposition of dolomite: New insights from 2D-XRD and TEM analyses. *American Mineralogist*, 97(1). <https://doi.org/10.2138/am.2011.3813>
- Samad, H. A., Rashid, R. A., Selamat, M., Sultan, J., & Shah, A. (2019). Poly art mabrle: from waste to a commercial product. In *9th Mineral Symposium 2019* (pp. 1-6). ResearchGate.

- Shahraki, B. K., Mehrabi, B., & Dabiri, R. (2009). Thermal behavior of Zefreh dolomite mine (Central Iran). *Journal of Mining and Metallurgy, Section B: Metallurgy*, 45(1), 35–44. <https://doi.org/10.2298/JMMB0901035S>
- Sompech, S., Dasri, T., & Thaomola, S. (2016). Preparation and characterization of amorphous silica and calcium oxide from agricultural wastes. *Oriental Journal of Chemistry*, 32(4), Article 18. <https://doi.org/10.13005/ojc/320418>
- Srinivasan, S., Dodson, D., Charles, M. B. J., Wallen, S. L., Albarelli, G., Kaushik, A., Hickman, N., Chaudhary, G. R., Stefanakos, E., & Dhau, J. (2020). Energy storage in earth-abundant dolomite minerals. *Applied Sciences*, 10(19), Article 6679. <https://doi.org/10.3390/APP10196679>
- Vaganov, V., Kireev, A., Aydeev, S., Šahmenko, G., & Šinka, M. (2017). Prospects for effective use of dolomite in concrete compositions. *Construction Science*, 19(1), 27-32.
- Yang, L., Li, X., Pan, M., Fu, J., Wang, A., Kong, Y., & Ma, C. (2024). Light-weight high strength porous thermal insulation materials based on dolomite-granite waste. *Ceramics International*, 50, 55498–55507. <https://doi.org/10.1016/j.ceramint.2024.10.410>
- Yuliya, B., Ruslan, I., Evgenij, K., Ilgam, K., & Laysan, K. (2023). Low-temperature calcination composite binder from dolomite and its application to facing board materials. *Case Studies in Construction Materials*, 19, Article e02338. <https://doi.org/10.1016/j.cscm.2023.e02338>
- Zadehnajar, P., Mirmusavi, M. H., Bakhtiari, S. S. E., Bakhsheshi-Rad, H. R., Karbasi, S., Ramakrishna, S., & Berto, F. (2021). Recent advances on akermanite calcium-silicate ceramic for biomedical applications. *International Journal of Applied Ceramic Technology*, 18(6), 1901-1920. <https://doi.org/10.1111/ijac.13814>
- Zahir, N. A. M., Beg, M. A., & Kadir, A. A. (2020). Hydrothermal dolomitization on devonian to carboniferous carbonates in Kinta Valley, Perak, Malaysia: A petrographic study. *Indonesian Journal on Geoscience*, 7(1), 25–39. <https://doi.org/10.17014/ijog.7.1.25-39>
- Zhang, Y., Sun, Q., & Geng, J. (2017). Microstructural characterization of limestone exposed to heat with XRD, SEM and TG-DSC. *Materials Characterization*, 134, 285-295. <https://doi.org/10.1016/j.matchar.2017.11.007>

Enhanced White Blood Cell and Platelet Segmentation: A Particle Swarm Optimization-based Chromaticity approach

Aiswarya Senthilvel*, Krishnaveni Marimuthu and Subashini Parthasarathy

Centre for Machine Learning and Intelligence, Department of Computer Science, Avinashilingam Institute for Home Science and Higher Education for Women, Coimbatore, India

ABSTRACT

Microscopic image examination is essential for medical diagnostics to identify anomalies using cell counts based on morphology. Sick Cell Disease (SCD) is an inherited blood condition characterized by defective hemoglobin, leading to severe anemia and complications. Detecting sickle cells in blood smears is essential, but the presence of White blood cells (WBCs) and platelets often leads to miscounting as they are classified incorrectly as red blood cells (RBCs). This study proposed an approach for segmenting WBCs and platelets by resembling the human color recognition process to differentiate the regions for accurate identification. First, the RGB color space is converted to RG chromaticity to locate WBCs and platelets with high pixel chromatic variance. Parametric segmentation is applied to the RG chromaticity images to identify the appropriate chromaticity channel for segmentation based on probability distribution values. The optimal threshold values have been determined using Particle Swarm Optimization (PSO) by dynamically narrowing the search space using values obtained through manual experimentation ranging from 0.001 to 1. This systematic process effectively identifies and segments platelets and WBCs, ensuring that overlapping platelets and WBCs are accurately segmented. Compared to state-of-the-art techniques, the proposed approach achieved an accuracy of 96.32 %, 96.97% for sensitivity, 96.96 % for precision and 97.46% for F- score in the pixel-wise segmentation of WBCs and platelets.

Keywords: Chromaticity, parametric segmentation, particle swarm optimization, platelets, sickle cell disease, white blood cells

ARTICLE INFO

Article history:

Received: 18 November 2024

Accepted: 03 March 2025

Published: 23 April 2025

DOI: <https://doi.org/10.47836/pjst.33.3.24>

E-mail addresses:

21phesf007@avinuty.ac.in (Aiswarya Senthilvel)

krishnaveni_cs@avinuty.ac.in (Krishnaveni Marimuthu)

subashini_cs@avinuty.ac.in (Subashini Parthasarathy)

*Corresponding author

INTRODUCTION

Sickle cell disease (SCD) is an inherited blood disorder characterized by abnormal hemoglobin. This arises when the two aberrant genes are inherited from both parents, leading to the synthesis of

hemoglobin S, which is mainly in charge of the development of irregular red blood cells (RBCs). These abnormal RBCs have difficulty carrying oxygen and get stuck in blood arteries, which can result in many problems, including organ damage, infections, and pain. Because of the significant frequency and serious health effects of hemoglobinopathies worldwide, SCD detection and diagnosis are essential (Alzubaidi, Fadhel, Al-Shamma et al., 2020). SCD national incidence rate was stable between 2000 and 2021; however, the number of newborns with SCD has risen by 13.7% globally due to population growth in the Caribbean, western, and central sub-Saharan Africa. In 2021, the number of patients with SCD increased by 41.4% worldwide. India accounts for 14.5% of infants born with SCD, approximately 42,000 per year, ranking second after sub-Saharan Africa. The quality of life of an individual with SCD can be improved through early diagnosis for disease management. Hematologists examine blood samples under a microscope for diagnosis; this is a time-consuming approach that is subject to errors caused by humans (WHO, 2011). Manual blood smear analysis becomes more difficult due to a difference in cell sizes, shapes, boundaries, and placements, which also challenges screening for the disease. Recent advances in Artificial Intelligence and Machine Learning (ML) have increased recognition and accuracy for diagnosis. Automated equipment assists pathologists and medical professionals in accurately identifying anemia (Acharya & Prakasha, 2019).

Conventional Methods for SCD Identification

SCD has been classified and segmented using different image processing and machine learning techniques (Das et al., 2019). The Circular Hough Transform (CHT) has been used to differentiate between sickle cells and normal RBCs. A fuzzy inference system (FIS) was used together with CHT to differentiate cells and extract the red component. Cell identification and counting have been determined using morphological descriptors, form factors, and gradient-based watershed transformations. Parvathy et al. (2016) analyzed compactness and shape using Otsu's technique and watershed segmentation. Sharma et al. (2016) used marker-controlled watershed transformations to distinguish erythrocytes and K-nearest neighbors (KNN) for classification, whereas Acharya and Kumar (2017) used the K-Medoids approach for erythrocytes segmentation and classification. Neural networks were used by Elsalamony (2017) to classify anemia and Chy and Rahaman (2018) trained a Support Vector Machine (SVM) with several indicators for SCD classification. Many classification methods, such as SVM, Extreme Learning Machine (ELM), and KNN classifiers have been used to distinguish and categorize sickle cells and normal cells (Chy & Rahaman, 2019). Existing approaches concentrate on normal and sickle cell categorization and do not consider the presence of WBCs and platelets in blood smear images. WBCs can be misclassified as RBCs, whereas clustered platelets are often confused with sickle cells. Therefore, enhanced WBC and platelet extraction techniques are necessary to provide an accurate diagnosis.

Deep Learning Methods for SCD Segmentation

Deep learning (DL) methods, such as Recurrent Neural Networks (RNNs) and Deep CNNs, are efficient in medical image data classification (Ker et al., 2017). Convolutional Neural Networks (CNNs) have achieved 86.34% and 87.50% accuracy in RBCs classification (Alzubaidi, Al-Shamma et al., 2020; Xu et al., 2017). DL models require large training datasets to obtain optimal results. Khalaf et al. (2017) used three RNN architectures, whereas Zhang et al. (2018) used a U-Net technique for RBC segmentation. The pre-trained InceptionV3 model extracted 2048 deep features for sickle cell identification (Alagu et al., 2023). An enhanced wrapper-based feature selection approach employing multi-objective binary grey wolf optimization (MO-BGWO), KNN, and SVM was utilized to classify features. The SVM classifier achieved 96% accuracy, which increases system performance. Deep learning techniques depend on well-chosen models and are affected by cell size, color, and form differences. Recent developments in deep learning have shown its potential to address these issues by accurately differentiating normal and sickle-shaped cells based on their features. However, these techniques have difficulty counting sickle and healthy erythrocytes because the present studies do not focus on removing platelets and WBCs from sickle blood smear images, which is essential for cell counting. Deep learning needs the annotation images for the segmentation model, but the dataset does not contain the annotation images. Therefore, the WBCs and platelets for automatic segmentation need to be annotated using a DL-based model for the enhanced process.

Conventional Methods for WBC and Platelets Segmentation

In medical image processing, identifying WBCs is an important area of study. Several researchers have investigated and developed methodologies that leverage deep-learning models and image-processing algorithms to improve WBC detection and classification (Alzubaidi, Fadhel, Oleiwi et al., 2020). WBC segmentation has been studied using several approaches, each with its merits and cons. Certain methods concentrate on segmenting the nucleus or cell (Tosta et al., 2015); however, other methods consider segmenting the nucleus and cytoplasm (Sarrafzadeh & Dehnavi, 2015). Threshold-based segmentation remains one of the easiest and most popular approaches, whether alone or in combination with other strategies. Makem and Tiedeu (2020) employed HSV and CMYK color space color components fused for WBC nuclei identification using adaptive fusion based on principal component analysis. (HSV and CMYK color space color components fused for WBC nuclei detection using adaptive fusion based on principal component analysis. Garcia-Lamont et al. (2021) proposed a method for segmenting WBC nuclei using high chromatic variation in hue components and classifying the cells using unsupervised neural networks. WBC is segmented based on human color discrimination through principal component analysis in HSV, RGB, and L*a*b* spaces which contain chromatic variation by hue extraction without complex mathematical computations (García-Lamont et al., 2022).

Clustering-based segmentation is used to extract WBCs from microscopic images. Tavakoli et al. (2021) proposed a method for segmenting nuclei that combines a balanced color technique with Otsu's thresholding algorithm. The convex hull of the nucleus was then used to detect the cytoplasm, and the SVM was used for classification. Kaur et al. (2016) developed an automated platelet counting method that employs the CHT on microscopic blood images. Their approach was based on platelet size and shape properties, resulting in a 96% accuracy. Cruz et al. (2017) proposed an image analysis framework for segmenting and counting the complete blood count (CBC). Their approach achieved more than 90% accuracy by combining HSV thresholding, linked component identification, and statistical analysis of microscopic blood images. Traditional approaches fail to achieve adequate results due to their variable lighting conditions. State-of-the-art approaches predominantly concentrate on segmenting WBCs and platelets separately rather than combining them in the same study. Traditional processes have limitations and highlight the requirement for improved methodologies to address such challenges with superior precision. Therefore, an individual approach for segmenting WBCs and platelets from blood smear images is essential for improving the precision and effectiveness of medical image analysis.

Deep Learning-based Methods for WBC and Platelets Segmentation

Deep learning (DL) based segmentation can be classified into instance and semantic segments. Instance segmentation detects individual cells, whereas semantic segmentation uses an identical mask for each region of interest (ROI) in a single image to differentiate objects based on pixel-level categorization. The most commonly used network for classifying and segmenting images is CNN. It uses a deep CNN with multiple variables trained on a larger dataset to obtain effective outcomes with deep learning models. Deep learning models are difficult to train on medical datasets because of limited data size; therefore, pretrained models are often used to overcome this limitation. Khouani et al. (2020) utilized various CNN architectures for segmenting WBC, including VGG-16, VGG-19, ResNet-50, ResNet-101, and Inception-v3. ResNet-50, optimized with the Adam optimizer, achieved the highest test accuracy of 95.73%. CNN and pre-trained CNN models are utilized to classify and segment WBCs and platelets process (Anand et al., 2024; Ozcan et al., 2024; Saidani et al., 2024). Ground-truth annotations are essential for the accurate and complete evaluation of deep-learning-based segmentation techniques. Thus, the assessment is based on how precisely and effectively the model identifies regions of interest in medical images. However, the SCD dataset does not contain annotations for WBCs and platelets, making deep learning for segmentation inadequate for this application. This study introduces a method for obtaining accurate ground-truth annotations of WBCs and platelets, which enables effective analysis to assist the segmentation process.

Optimization-based Approaches for Medical Image Segmentation

Optimization-based techniques have gained significant attention for enhancing medical-image segmentation (Wang et al., 2021; Farshi et al., 2020). These methods aim to optimize and fine-tune the segmentation algorithms (Shang et al., 2020). Optimization techniques increase the accuracy and efficiency of segmentation algorithms (Shi et al., 2023; Khosla & Verma, 2023). Existing studies examine classical optimization, metaheuristics, and machine learning-based techniques (Narayana et al., 2022; de Albuquerque et al., 2020; Shehab et al., 2020) with a focus on parameter modifications to minimize segmentation issues and enhance overall performance. PSO is a swarm intelligence-inspired optimization approach widely used in image analysis (Zhang & Lim, 2020; Mandave & Patil, 2023). PSO is effective at addressing complicated, multidimensional problems (Eisham et al., 2023) and is used for feature selection (Kavitha & Chellamuthu, 2019), image registration (Sarvamangala & Kulkarni, 2019), segmentation (Kate & Shukla, 2020; Chakraborty et al., 2019), classification (Singh et al., 2025) and object tracking (Öztürk et al., 2020). PSO effectively examines search regions while reducing local optima, making it a great selection for image analysis. PSO enhances medical image segmentation by determining optimal image segments based on global and local features (Vijh et al., 2020; Shehanaz et al., 2021). The versatility and ability of PSO to solve issues make it an excellent tool for image-processing researchers (Nayak et al., 2023; Dhal et al., 2019). The study proposed by de Albuquerque et al. (2020) expanded the significance of PSO to medical image segmentation by employing its ability to navigate complicated search areas. PSO is well suited for dealing with medical imaging difficulties such as noise, uneven lighting, and complex structures (Guo et al., 2023).

The proposed study uses PSO to improve the accuracy of medical image segmentation, primarily for WBCs and platelets in blood smear images. The study improves segmentation by combining PSO and color space approaches. The contributions of this study are as follows:

- Identification of a suitable color space for WBCs and platelets segmentation in peripheral smear images
- WBCs and platelets were methodically detected using the RG chromaticity approach, with target regions distinguished using parametric segmentation
- Determine the best chromaticity channels for WBC and platelet identification by conducting a comparative examination of the channels
- Particle Swarm Optimization (PSO) was used to construct probability distribution values and optimize the search space for segmentation
- Accuracy of 96.32% on the erythrocyteIDB dataset, demonstrating the efficient results for segmentation

MATERIAL AND METHOD

The proposed approach segmented the platelets and WBCs by combining PSO with image chromaticity. It determined a significant color space, identified regions similar to those of WBCs and platelets, selected the optimal chromaticity channel for segmentation, and applied PSO-based threshold optimization. Figure 1 shows the entire process of segmenting WBCs and platelets.

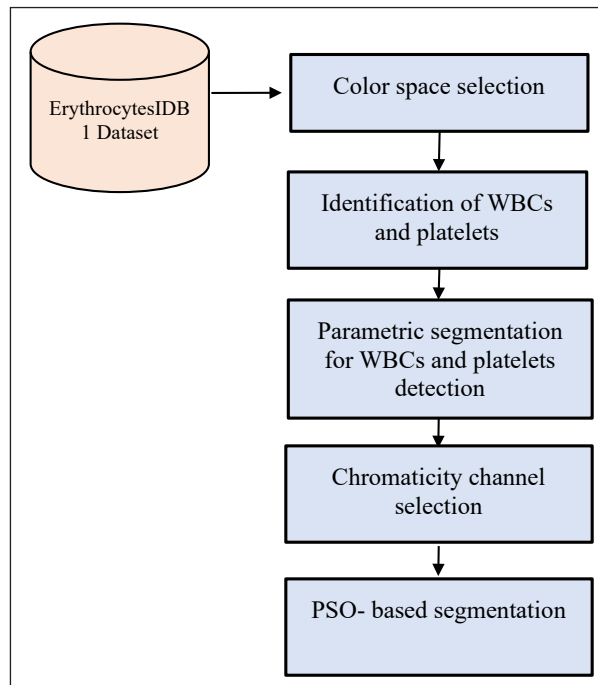


Figure 1. Overview of the Proposed PSO-based segmentation approach for WBCs and platelets segmentation

Identification of Suitable Color Space for WBC and Platelets Detection

This study employed the ErythrocytesIDB1 dataset for a comprehensive analysis. The color space of an image is primarily selected for the segmentation of WBC and platelets. This has different chromatic properties from RBCs. However, selecting the appropriate color space is essential to reduce the influence of the color space for WBC and platelet identification. Blood smear images have color variations because of the staining, lighting conditions, and external characteristics (Fitri et al., 2017). The images were reduced to $256 * 256$ to standardize the image analysis and the color range was normalized using the min-max method (Juliet et al., 2015; Patro et al., 2015). Noise in the images was eliminated using a nonlocal mean (NLM) filter which was selected for its ability to reduce Gaussian noise (Buades et al., 2005). Based on the literature, RGB, HSV, and Lab color spaces were

employed to identify and segment WBCs and platelets. Hue saturation value (HSV) and Lab color spaces are often used for image analysis; however, RGB (red, green, and blue) is still widely used in digital images because of its correspondence with human perception. Figure 2 shows an image of the different color spaces affecting blood cells.

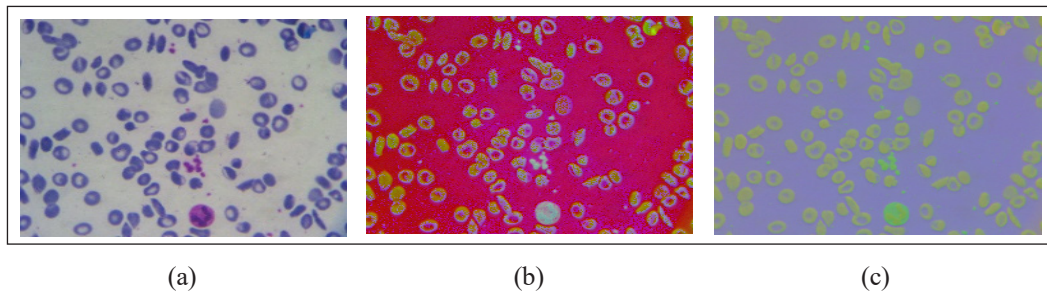


Figure 2. Image representation in different color spaces. (a) RGB color space image; (b) HSV color space image; (c) Lab color space image

WBCs and platelets differ in staining characteristics from RBCs, and it was used to differentiate between them. WBCs typically have a pink to purple color because of their nuclei while platelets are smaller with purple color due to the cytoplasmic granules (Imron & Fitri, 2019). Purple staining in the smear images differentiates WBCs and platelets in RGB color space 2(a), enabling accurate identification across numerous areas. WBCs and platelets are difficult to identify in HSV color space 2(b) because the color regions are not easily distinguished from the human eye. This limitation affects the identification of sickle cells because it affects RBC texture. Similarly, identification is difficult in Lab color space 2(c) because of the distortion of the background hues. The proposed technique uses the RGB color space to identify platelets and WBCs in smear images by maintaining the shapes and textures of the RBCs.

Identification of WBCs and Palettes from Blood Smear Images

Ground truth annotations are required for segmentation tasks to accurately identify regions. However, labeled data are unavailable in this study; therefore, WBC and platelet areas need to be identified prior to segmentation. The RGB color space was selected for such purposes because it is well suited for discriminating between those regions; however, there are limitations in the representation of luminance and brightness, which affects the analysis. This limitation was addressed by converting the RGB color space into a chromaticity format. These chromatic characteristics were separated from the intensity, mimicking human analysis. This is because chromaticity is independent of intensity, as demonstrated by the CIE 1931 xy chromaticity diagram (Sharma, 2017) that converts colors into 2D chromatic coordinates. Luminance-normalized images were determined by normalizing the RGB value to provide (x, y) coordinates on the chromaticity diagram,

representing decreasing brightness. The red (r) and green (g) channels are normalized for RG chromaticity conversion using Equations 1, 2, and 3.

$$r = \frac{R}{(R + G + B)} \quad [1]$$

$$g = \frac{G}{(R + G + B)} \quad [2]$$

$$R + G + B = 1 \quad [3]$$

The normalized red chromaticity component r removes the impact of brightness, whereas the normalized green chromaticity component g provides color as a relative proportion rather than an absolute intensity. Equation 3 sums R , G , and B as the overall intensity, reducing by removing illumination variations, enabling r and g to accurately express chromaticity and minimize dimensionality while maintaining the critical aspects of color (r and g). RG chromaticity separates chromaticity information, which improves color analysis and visual perception, allowing for the better identification of WBCs and platelets. Figure 3 shows the chromaticity distribution of an image, where the source image and chromaticity diagram of the source images are displayed in 3(a) and 3(b), and

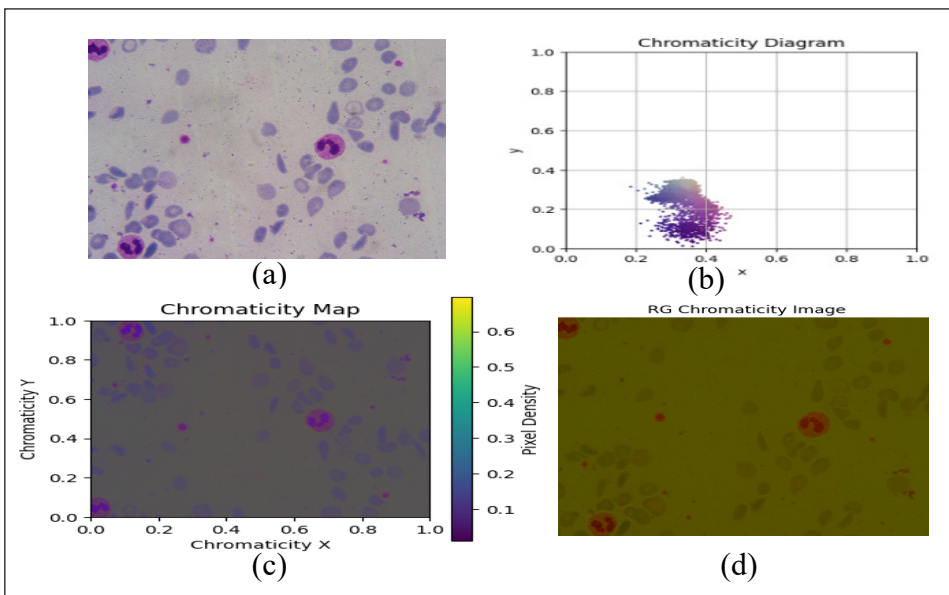


Figure 3. Chromaticity distribution and mapping of an image: (a) WBC and platelets highlighted in pink to purple color in RGB color space; (b) Chromaticity of RGB color space; (c) Chromaticity map of RGB color space; (d) RG chromaticity map

the chromaticity map and RG chromaticity image are shown in 3(c) and 3(d), respectively. Algorithm 1 entails finding the target regions based on the RG Chromaticity pixel density distribution. The RG chromaticity diagram provides significant chromatic variation in WBCs and platelets, which enables accurate differentiation.

Parametric Segmentation Approach for WBC and Platelets Segmentation

This study identified and segmented WBCs and platelets from blood smear images using a parametric segmentation technique (Zhou & Liao, 2022). Because intensity-based thresholding approaches are extensively used for segmentation, the proposed methodology is based on chromatic characteristics. Therefore, standard threshold values are not particularly beneficial. The PS approach divides target areas into a binary mask by utilizing the optimal distribution value. Determining an appropriate threshold value is difficult since different distribution values could provide a binary mask separating foreground and background areas. The PS approach uses a Gaussian distribution to detect WBCs and platelets from RG chromaticity images by concentrating on the region of interest where pixels show a significant degree of chromatic variation.

Algorithm 1: Identification of WBCs and platelets using RG chromaticity

```
Input: rgb_image
(height, width, channels) = image_shape(rgb_image)
r_chromaticity [height, width]
g_chromaticity [height, width]
Chromaticity_map [height, width]
for y from 0 to height 1
  For x from 0 to width -1, as follows:
    (R, G, B) = rgb_values (rgb_image, y, x)
    sum = R + G + B
    r = R/sum
    g =G/sum
    r_chromaticity [y, x] = r
    g_chromaticity [y, x] = g
    rg_value = r + g
    chromaticity_map [y, x] =rg value
return
Output: chromaticity_map
```

The statistical parameters mean (μ) and standard deviation (σ) were used to calculate the pixel chromatic variance values to identify the target region. This indicates the average and variance of pixels scattered in a Gaussian distribution. These statistical characteristics, which include μ and σ , are explained by Equations 4, 5, and 6. The Gaussian distribution applied for segmentation is illustrated in Equation 7, which also explains how the correlations between the R and G chromaticity channels at each pixel determine which

colors combine. The equation is applied to the RG, R, and G chromaticity channels to identify which chromaticity channels are associated with WBCs and platelets.

$$\mu = \frac{1}{N} \sum_{c=1}^N p_c \quad [4]$$

$$\sigma^2 = \frac{1}{N} \sum_{c=1}^N (p_c - \mu)^2 \quad [5]$$

$$\sigma = \sqrt{\sigma^2} \quad [6]$$

The mean pixel intensity μ and the variation around the mean define the variance σ^2 and standard deviation σ of the target patches. The variance σ^2 pixel intensities indicate the distribution of values within the target region. Each pixel-intensity p_c inside the patches includes all pixels in image N.

$$P(c) = \frac{1}{\sigma\sqrt{2\pi}} \exp\left(-\frac{(c - \mu)^2}{2\sigma^2}\right) \quad [7]$$

The Gaussian distribution indicating the probability of the intensity $P(c)$ corresponds to the WBCs and platelet color ranges. The Gaussian function's variable c indicates the intensity of a pixel at specific positions within the image. Probabilistic distribution values for RG chromaticity, as well as individual R and G chromaticity channels, were calculated to determine which chromaticity channel was most suitable for the segmentation process. Determining a significant chromaticity channel for WBC and platelet segmentation is difficult because of the variance in illumination and staining of the image. These differences make it difficult and time-consuming to accurately determine the optimal threshold value for segmentation. Furthermore, the high pixel levels of WBCs, platelets, and size made it difficult to manually determine the binary masking values. An extensive manual evaluation selected distribution values ranging from 0.001 to 1. It accurately recognizes WBCs and platelets while providing no false positives by not detecting RBCs. However, the variations in lighting and illumination connected to the images make it difficult to determine an optimal threshold for every image. Therefore, optimization is required to identify the optimal thresholds for the various images. Algorithm 2 provides a complex approach that determines the best chromaticity channel and enables improved WBC and platelet segmentation, subject to imaging scenarios.

Algorithm 2: Identification of Optimal chromaticity channel for segmentation using Parametric segmentation approach

Input: RG chromaticity image

1. Compute μ , σ^2 and σ using Equations 4, 5 and 6

2. Create a probability map using Equation 7

3. Apply a threshold to identify target region:

Threshold = probability map > Threshold

for each channel (RG, R, G):

Calculate μ , σ^2 , σ and probability map

Apply a threshold to identify areas with the desired color range

End

Output: Best chromaticity channel for segmentation**PSO-based WBCs and Platelets Segmentation**

The optimal threshold was determined using the Particle Swarm Optimization (PSO) (Kennedy & Eberhart, 1995). It adequately searches the parameter space using a swarm of particles implemented with values from manual segmentation and thresholds ranging from 0.001 to 1. The threshold values are iteratively modified by analyzing the search space and optimizing their distribution by altering the position and velocity. The position of each particle shows the threshold values and the aim is to determine a set of ideal threshold values that increases the segmentation accuracy. With a population size of 100, each particle represents a candidate solution determined by its personal best position, $pbest$; the global best position, $gbest$; and a stochastic component indicated by two equally distributed factors, φ_1 and φ_2 . Equation 8 demonstrates the updates in position and velocity. In this equation, $v_i(t)$ indicates the velocity of particle i at time t and $x_i(t)$ is the location of the particle. The inertia weight ω (0.729) determines the prior velocity's contribution to the current update, whereas C_1 and C_2 (1.4944) are cognitive and social factors, respectively, directing the particle to its own best and global best places. The random values φ_1 and φ_2 provide variations in the search process, making it more uncertain and allowing a more comprehensive exploration of the solution space. The position update in Equation 9 directs the particle to a new location based on its velocity. The location denotes a potential threshold value, and the velocity controls how much it is altered throughout each iteration.

$$v_i(t+1) = \omega v_i(t) + C_1 \varphi_1 (pbest(t) - x_i(t)) + C_2 \varphi_2 (gbest(t) - x_i(t)) \quad [8]$$

$$x_i(t+1) = x_i(t) + v_i(t+1) \quad [9]$$

The optimization approach was designed to differentiate between the fitness landscape's global optimum and the local extrema. The peak fitness function z in Equation 10 measures

the accurate segmentation of a particle. The function has three exponential elements that address the essential factors that affect the search space. It examines particle locations by calculating a value that indicates the spatial alignment to optimize the threshold value.

$$z = 3 \cdot (1 - x)^2 \exp(-x^2 - y + 12 - 10 \left(\frac{x}{5} - x^3 - y^5\right) \exp(-x^2 - y^2) - \frac{1}{3} \exp(-(x + 1)^2 - y^2) \tag{10}$$

The first exponential term uses decay and polynomial functions to identify regions of interest and calculate the threshold value. The second term improves the complexity by considering the interactions between the x and y coordinates, which helps refine the search in more complex areas. The third term addresses the boundary effects in the search space, which increases the reliability of the fitness measure. The output of the peak fitness function accurately identifies the swarm to the optimal areas and modifies the threshold values for improved segmentation performance. Algorithm 3 outlines the process of determining the optimal threshold value using PSO. Finally, by averaging the threshold values across iterations, the particle swarm converges to the optimal feasible set of segmentation accuracy. The optimal threshold values were 0.87, 0.68, 0.91, and 0.74, increasing the segmentation performance by accurately distinguishing white blood cells, platelets, and RBCs.

Algorithm 3: PSO-based threshold value selection process
Initialize particles: For each particle i: Initialize position x_i and velocity v_i in the search space [0.001, 1] Evaluate fitness value $f(x_i)$ using eq (10) Set $pbest = x_i$, $pbestFitness = f(x_i)$ If $f(x_i)$ is better than global best: Set $gbest = x_i$, $gbestFitness = f(x_i)$ Set $\omega = 0.729$, $\varphi_1 = 1.4944$, $\varphi_2 = 1.4944$ For each particle i: Calculate fitness value $f(x_i)$ using Equation 10 If $f(x_i)$ is better than particle's personal best: Update personal best: Set $pbest = x_i$, $pbestFitness = f(x_i)$ If $f(x_i)$ is better than global best: Update global best: Set $gbest = x_i$, $gbestFitness = f(x_i)$ For each particle i: random numbers $r1$ and $r2$ distributed in [0, 1] Update velocity: Update position: Use the final $gbest$ as the optimized value Output: Optimal value for detection

RESULTS AND DISCUSSION

The identified and segmented WBCs and platelets were analyzed qualitatively and quantitatively. The analysis employed several quantitative analytic measures, including accuracy, precision, sensitivity, specificity, and F-score.

Dataset Description

Segmentation analysis was performed using sickle cell smear images from the ErythrocytesIDB1 standard database. The blood samples were taken from SCD patients and are available at <https://erythrocytesidb.uib.es/>. The dataset contains labeled samples characterized by cell morphology as circular, elongated, and other cells. The dataset contained 196 full-field images of platelets, WBCs, and RBCs. In particular, seven images were removed from the database due to imperfections, variation in staining and blurring, whereas 189 images were employed in this study.

Identification of WBC and Platelets Using Chromaticity Feature

RGB color space determines the WBC and platelet regions from blood smear images by converting them into RG chromaticity. Each pixel in the RG chromaticity image is examined to identify the most desirable chromaticity channel for the WBCs and platelet regions. The chromaticity distribution in Figure 4 helps to determine the WBCs and platelets for segmentation. Figure 4(a) displays the source image in the RGB color space, while Figure 4(b) shows RG chromaticity density as a Hexbin map. This map is divided into hexagonal bins, and colors indicate the number of pixels. In contrast, the X and Y axes indicate the spatial distributions of red and green chromaticity channels. Higher color density impacts higher color intensity or darkness, whereas lower color sparsity controls higher color illumination or brighter color. This visualization helps recognize color distribution patterns and identify prominent image color regions.

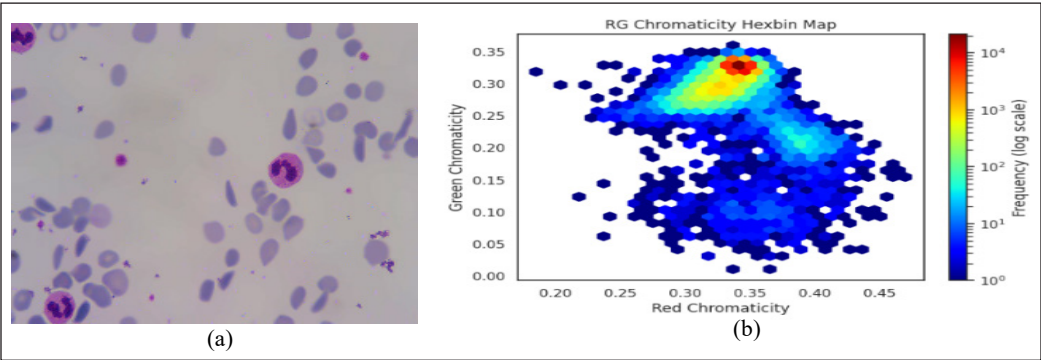


Figure 4. Pixel distribution of RG chromaticity image. (a) Original image; (b) Hexbin representation of RG chromaticity distribution in the smear image

Figure 5 illustrates the density of the pixel distribution in the R and G chromaticity channels for determining WBCs and platelet regions. Figure 5(a) shows the R chromaticity channel with lower pixel density values than the G chromaticity channel in Figure 5(b). The G chromaticity channel exhibited a broader range of pixel density values, extending at both high and low densities. In contrast, the maximum pixel distribution was observed in the G chromaticity channel. The heat map, as shown in Figure 6, provides a graphic representation of the association between red and green components for analyzing each channel of RG chromaticity.

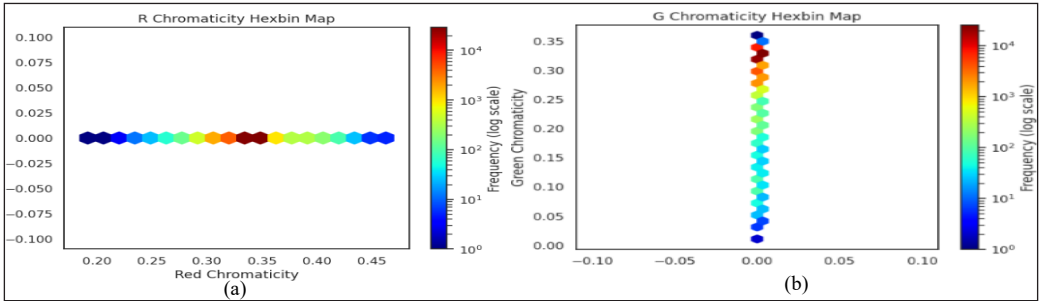


Figure 5. Distribution of chromaticity pixels in the R and G Channels. (a) pixel distribution of R chromaticity channel; (b) pixel distribution of G chromaticity channel

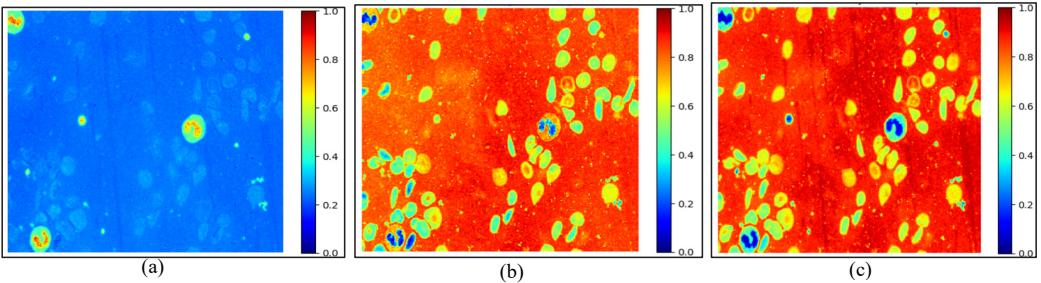


Figure 6. Visualization of RG Chromaticity Heatmap for Target Region Extraction. (a) pixel distribution of RG chromaticity (b) pixel distribution of R chromaticity (c) pixel distribution of G chromaticity

Figure 6(a) shows the RG chromaticity heatmap, while Figures 6(b) and 6(c) display the R and G chromaticity channels, respectively. This examination identified the R and G chromaticity channels as prominent features for identifying WBCs and platelets. These specific areas were retrieved and utilized throughout the segmentation process to identify the target region from the image.

Identification of Optimal Chromaticity Channel for Segmentation

As a result, the WBC and platelets were identified using RG chromaticity, which were considered ground truth images. RG chromaticity and its separate color channels, R and G,

were applied to the parametric segmentation method to identify accurate color channels for segmentation. Figure 7 displays the results, where 7(a) displays the target region retrieved by the chromaticity map. At the same time, 7(b) shows the detection of the regions using RG chromaticity, 7(c) displays the R chromaticity channel that detects WBCs, platelets, and RBC cells, and 7(d) shows the G chromaticity channel, which accurately recognizes the WBCs and platelet regions. The findings demonstrate that RG chromaticity is inefficient for detecting the target regions. In contrast, the R chromaticity channel is limited to the nuclei of WBCs and platelets and detects the RBCs with a bright color.

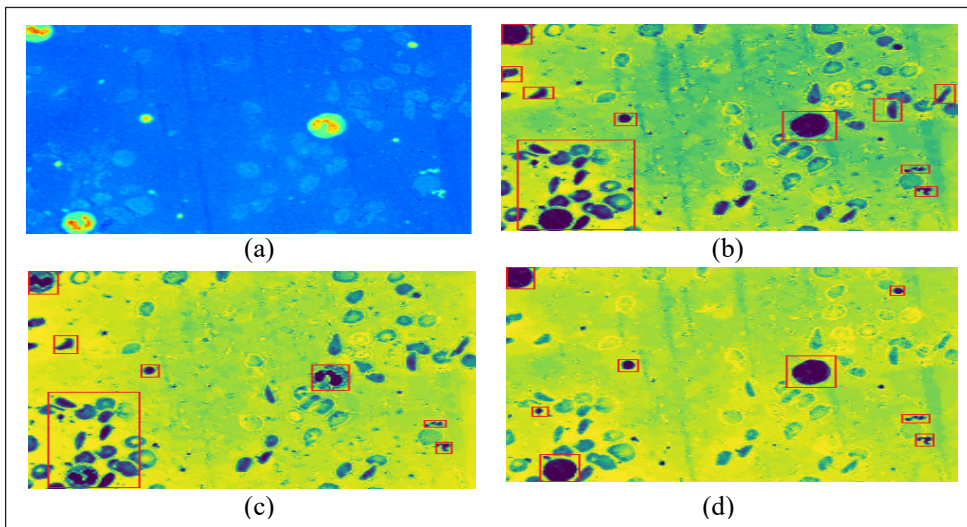


Figure 7. Detection of WBCs and Platelets using RG Chromaticity and separate R and G chromaticity. (a) RG chromaticity map; (b) Parametric segmentation in RG chromaticity; (c) Parametric segmentation in R chromaticity channel; (d) Parametric segmentation in G chromaticity channel

However, the G chromaticity channel highlights WBCs and platelets in the smear image, effectively suppressing other cells by minimizing the impact of illumination and lighting conditions. Based on the examination findings, the G-chromaticity channel was more effective for segmentation.

Identification of Optimal Threshold Value Using PSO

Identifying appropriate threshold values for segmenting WBCs and platelets across various staining images is difficult. Manual segmentation is applied in RG chromaticity and separate R and G channels to determine the appropriate chromaticity channel for WBCs and platelet segmentation. For manual segmentation, the distribution value ranges were selected from 0.001 to 1 and were randomly applied to identify the appropriate channel and visual representation, as shown in Figure 8.

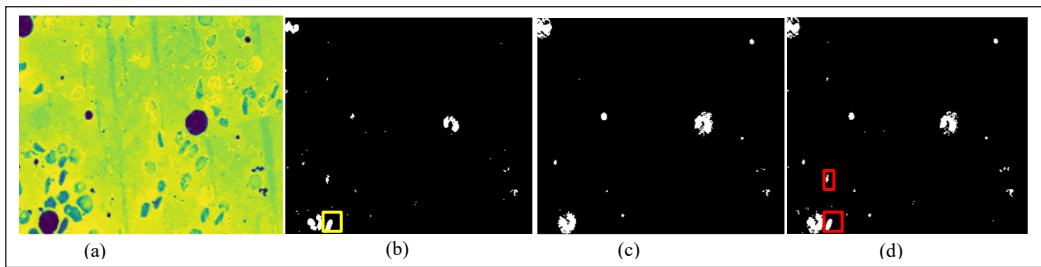


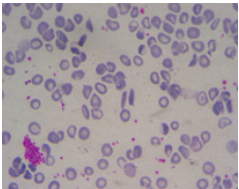


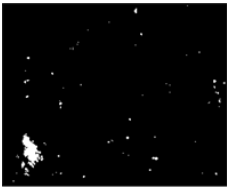
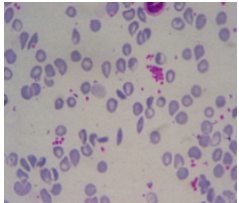

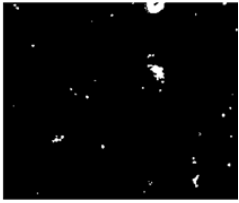
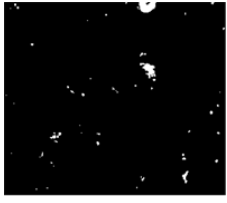
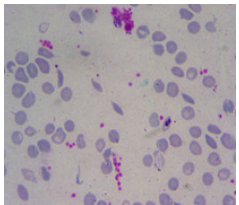


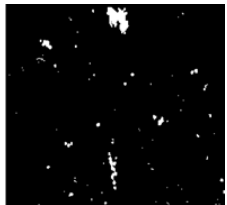
Figure 8. Target region (WBCs and Platelets) binary masked by RG chromaticity and R and G separate channels. (a) Parametric segmentation of WBC and platelets using G chromaticity channel; (b) Target regions detection using R chromaticity channel; (c) Target regions detection using G chromaticity channel; (d) Target regions detection using RG chromaticity channel

Figure 8 displays the experimental results for determining the RG chromaticity channel for WBCs and platelet segmentation using a manual threshold of 0.01. Figure 8(a) shows the targeted region of the G chromaticity image, whereas the regions segmented by the R, G, and RG chromaticity channels are presented in 8(b), 8(c), and 8(d). The findings show that the R chromaticity channel is highly sensitive to the WBCs nucleus and platelet cells, as shown by the yellow box in 8(b). However, it also identifies the color of RBCs while distinguishing each cell. The G chromaticity channel segments the nucleus and cytoplasm of WBCs and platelets while excluding RBCs alone, as shown in 8(c). The RG chromaticity in 8(d) shows the detection of WBCs and platelets and the presence of certain RBCs enclosed within the highlighted red box. These findings demonstrate that the G chromaticity channel can detect WBCs and platelets in the images. However, the manual method is time-consuming and labor-intensive for finding the appropriate threshold value for segmentation. The experimental results of manual segmentation using RG, R, and G chromaticity are shown in Table 1. The manual threshold value of 0.01 is applied for the segmentation process, which fails the segmentation. This limitation is solved using the PSO algorithm by determining the optimal threshold values of 0.68, 0.74, 0.87 and 0.91.

Accurate detection of WBCs and platelets in smear images was achieved using search space optimization, using the range from 0.001 to 1 probability distribution as a search space in the optimization process with the peak's fitness function. From the optimized search space, the threshold values of 0.68, 0.74, 0.87 and 0.91 were achieved for different staining and illuminated images. The segmentation method successfully segmented the target regions using manual and optimized techniques with the G chromaticity channel. Figure 9 shows the segmentation results with a manual and optimal threshold value of 0.01 and 0.87, respectively.

Figure 9(a) shows the source images, and 9(b) shows the target region identified by the G chromaticity channel. Segmentation of platelets and WBCs using manual and optimized threshold values is shown in 9(c) and 9(d), respectively. The segmentation results in Figure

Table 1
Segmentation of WBC and platelets using RG chromaticity, R and G chromaticity channels with 0.01 threshold value

Source Image	R Chromaticity Channel	G Chromaticity Channel	RG Chromaticity Channel
			
			
			

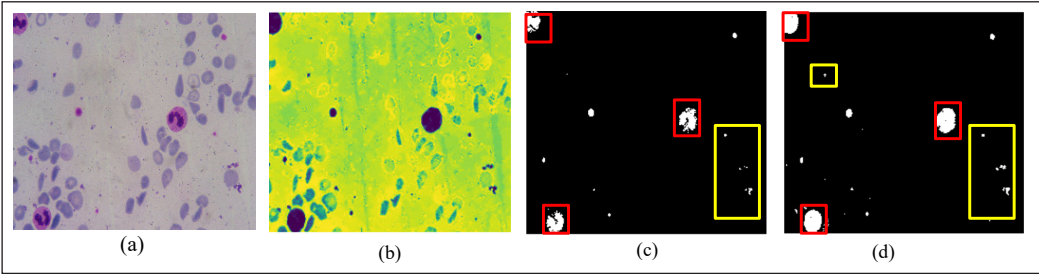


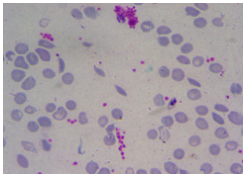
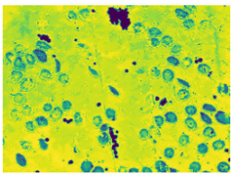
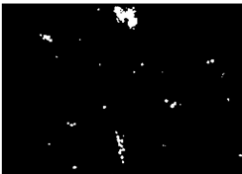
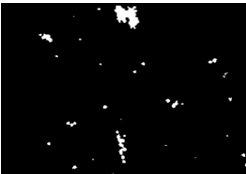
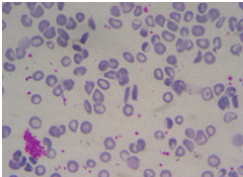
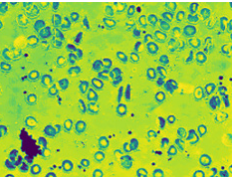


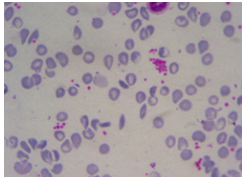
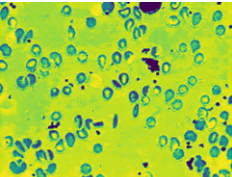


Figure 9. WBC and platelet detection are done using manual and optimal thresholds. (a) Blood smear source image; (b) Parametric segmentation of WBC and platelets using G chromaticity channel; (c) Target region detection using a manual threshold value of 0.01 in G chromaticity channel; (d) Target region detection using an optimized threshold value of 0.87 in G chromaticity channel

9(c) demonstrate that the manual threshold-based technique recognizes only the nuclei of WBCs. In contrast, the cytoplasmic regions are inadequately segmented, as highlighted by the red box. As shown in the yellow box, platelet segmentation was also ineffective for smaller platelets with unclear boundary regions. Figure 9(d) depicts the implementation of an enhanced threshold for segmentation utilizing a Particle Swarm Optimization-based

approach, resulting in significant improvements in results. The red box indicates that both the nucleus and the cytoplasm were detected. The yellow box depicts the optimal threshold value of 0.87, improving the segmentation of small and large platelets over manual thresholding.

The results indicated the significance of selecting accurate threshold values by emphasizing the limitations of manual methods for WBCs and platelet segmentation. The optimization process improved the accuracy and effectiveness of the WBCs and platelet detection approach by segmenting the nucleus and cytoplasm of WBCs and large and small pixels of platelets without including RBCs for the segmentation. It emphasized the significance of the optimized threshold values. The experimental segmentation results using the manual and optimal threshold value are demonstrated in Table 2. The table shows the source images and target regions acquired from the G chromaticity space using manual and optimal threshold values for the segmentation results. Manual segmentation employed 0.01, 0.05, and 0.01 thresholds for each image. In comparison, a PSO-based technique provided optimal thresholds of 0.87 for the first and third images and 0.74 for the second image. Threshold modifications are caused by a variation in lighting conditions between the first and third images, including the second image, which affects the selection of optimal threshold values.

Table 2
Comparison of G chromaticity segmentation using manual and optimal threshold values

Source Image	G chromaticity space	Segmentation using Manual threshold values	Segmentation using Optimal threshold values from PSO
			
			
			

Manual segmentation effectively detects the region of interest and excludes RBCs; however, it has limitations in segmenting small pixel-sized sections and identifying cell borders and edges. The PSO-based technique is superior because it employs optimal threshold values for efficiently segmenting large and small pixel-sized regions without losing their edges, resulting in increased segmentation precision. The segmentation results demonstrate that the PSO approach effectively selects threshold values. This method enables precise segmentation of WBCs and platelets by employing ideal threshold values of 0.68, 0.74, 0.87, and 0.91 for distinct images under diverse lighting and staining conditions.

Quantitative Analysis

In quantitative analysis, pixel-wise binary segmentation is examined by comparing segmented images with their ground truth, which is identified by chromaticity variance and distinctive features of WBCs and platelets in microscopic images (Imron et al., 2019). The quantitative measures used for analysis included accuracy (Acc), specificity (Spe), sensitivity (Sen), precision (Pre), and F-score. Here, specificity determines how accurately a background is segmented where RBCs are considered the background; precision measures how accurately the images are segmented by ensuring that background (RBCs) pixels are not incorrectly classified as WBC or platelets. The sensitivity indicates the accuracy of the segmented images by ensuring that WBC and platelet pixels have been correctly recognized and not mistakenly classified as background (RBCs). The computations for these findings are based on Equations 11 to 15. The pixel-wise categorization of True Positives (TP), False Negatives (FN), False Positives (FP), and True Negatives (TN) is summarized in Table 3.

$$Acc = \frac{TP + TN}{TP + TN + FP + FN} \quad [11]$$

$$Spe = \frac{TN}{TN + FP} \quad [12]$$

$$Sen = \frac{TP}{TP + FN} \quad [13]$$

$$Pre = \frac{TP}{TP + FP} \quad [14]$$

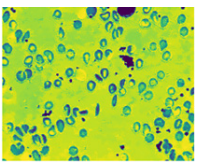
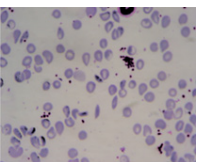
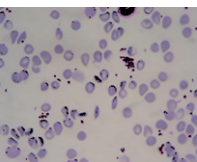
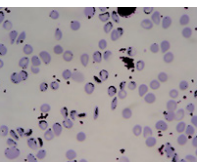
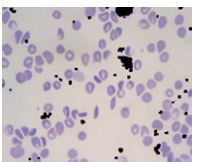
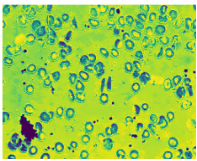
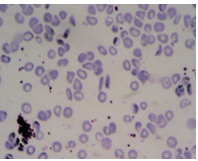
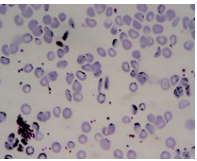
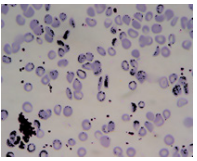
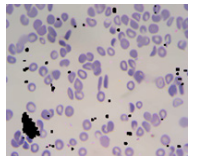
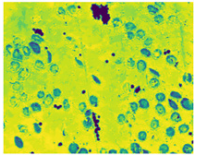
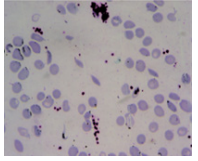
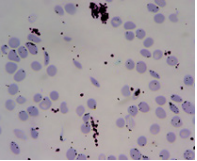
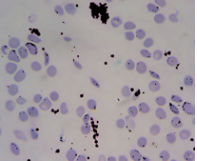
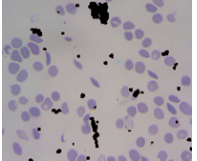
$$F = \frac{2TP}{2TP + FP + FN} \quad [15]$$

Table 3
Classification of WBC and platelets pixel segmentation

Metrics	Ground truth	Segmented as
TP	WBCs and Platelets	WBCs and Platelets
FP	Background (RBCs)	WBCs and Platelets
TN	Background (RBCs)	Background (RBCs)
FN	WBCs and Platelets	Background (RBCs)

Table 4 presents the state-of-the-art techniques for segmenting WBC and platelets. This comparative study focused on chromatic-feature-based approaches. The PCA-based adaptive fusion of HSV and CMYK (Makem & Tiedeu, 2020) correctly recognizes the nucleus area of WBCs but fails to distinguish the cytoplasm and small platelet pixels. PCA fusion with chromatic features from RGB, HSV, and L*a*b* color space (Garcia-Lamont et al., 2021) accurately detects WBCs and platelets; however, this technique is ineffective for locating the cytoplasm in WBCs. Furthermore, this approach fails to detect the edges of WBCs and platelets, whereas it detects bright pixels of RBCs.

Table 4
Qualitative evaluation comparison of segmented images with state-of-the-art techniques

G chromaticity channel	The PCA fusion with chromatic feature	The PCA adaptive fusion method	Chromatic variance	Proposed method
				
				
				

The chromatic variance approach accurately detected the nuclei and cytoplasm of WBCs and platelets (García-Lamont et al., 2022). However, it has limitations when utilized for sickle cell imaging because it identifies unwanted RBCs with bright regions. Table 5 presents the quantitative analysis findings from the state-of-the-art techniques. The results

Table 5
Quantitative evaluation comparison of segmented images with state-of-the-art techniques

Method	Accuracy (%)	Precision (%)	Sensitivity (%)	Specificity (%)	F- Score (%)
The PCA fusion with chromaticity method (Makem & Tiedeu, 2020)	77.30	80.56	80.20	72.58	81.41
The PCA-based adaptive fusion (Garcia-Lamont et al., 2021)	85.53	87.34	88.69	78.95	88.78
Chromatic variance (García-Lamont et al., 2022)	82.28	86.73	85.00	77.59	85.86
Proposed approach with manual method	92.79	95.89	93.94	83.33	95.88
Proposed approach with an optimized method	96.32	96.96	96.97	94.59	97.46

demonstrate that the proposed PSO approach has achieved an accuracy of 96.32%. These results show that the proposed method accurately identifies and segments overlapped WBC and platelets from smear images and has significantly improved performance. The analysis demonstrates that the proposed approach is highly efficient for recognizing and detecting WBCs and platelets while excluding RBCs from the segmentation, which resulted in efficiencies of the optimal threshold value. The experimental findings indicate that the proposed method efficiently identifies and segments the WBCs and platelets while excluding RBCs for the segmentation process. The proposed segmentation approach recognizes WBCs and platelets by examining chromaticity components using the advantages of significant pixel variance for accurate identification and differentiation. This method uses RG chromaticity and a parametric approach to determine the probability distribution for accurate segmentation. Variations in staining and lighting conditions can cause a challenge to blood cell segmentation, as shown by the erythrocytesIDB1 dataset. The first 130 images have different staining and lighting conditions than the final 59 images. Even with these variations, the proposed approach effectively responds to changes, and the segmentation accuracy is higher compared to previous studies, as seen in Table 5. Existing research has concentrated on segmenting WBCs into cropped images, which is not suitable for whole-blood-smear images for cell segmentation. State-of-the-art techniques often fail to segment WBCs and platelets because of color illumination and variation problems. WBCs and

platelets are difficult to segment because of size differences and overlapping regions. Most existing approaches fail to segment platelets because they are small and often appear to be small elements in the image. This size differential and platelet overlapping significantly limit the implementation of a single technique for both WBCs and platelets.

Existing chromaticity-based cell segmentation methods have demonstrated various levels of accuracy. PCA fusion based on chromatic attributes from HSV and CMYK color spaces achieved an accuracy of 77.30% because color values varied among the images, impairing RBC region detection. The PCA-based adaptive fusion approach, which utilizes RGB, HSV, and $L^*a^*b^*$ color spaces, obtained an accuracy of 85.53%. This approach accurately recognizes the nucleus but fails to detect very small platelets without separating the hue components from the color space. The chromatic variance approach, which employed the RGB color space, attained an 82.28% accuracy because of its inefficiency in segmenting WBC cytoplasm. The primary limitation of these approaches is their inability to achieve accurate segmentation across datasets with differences in lighting conditions and staining variances. However, the proposed method overcomes this challenge by utilizing RG chromaticity and a Particle Swarm Optimization-based approach to determine the optimal threshold for segmentation with 96.32% accuracy. Despite its limitations, the proposed approach efficiently addresses these challenges and provides precise segmentation.

Furthermore, the proposed method achieved higher accuracy and sensitivity compared to existing methods, because the color component was included as a significant feature and an optimized technique for threshold-value identification. Compared to the traditional manual threshold process, the proposed method improves specificity by systematically optimizing the threshold, resulting in an accurate segmentation of the WBC nucleus and cytoplasm, as well as various-sized pixels of platelets. Based on an artificial intelligence perspective, the proposed approach is bioinspired and reflects how humans observe colors. Recent experiments on CNNs for WBC segmentation were effective; however, they usually required longer processing, but the suggested technique has the lowest computational cost. Moreover, implementing CNNs requires ground truth images for efficient segmentation training. However, the dataset used in this study did not contain ground truth annotations. The proposed method uses RG chromaticity images with parametric segmentation that involves mathematical operations to find the appropriate chromaticity channel for segmentation with a low computational time. The optimal distribution value for segmentation involves the search space optimization with a low computational cost. Therefore, overlapping WBCs and platelets were identified and segmented using the proposed method and are highly computationally competitive. This study has limitations because it focuses on image processing and optimization methodologies rather than implementing CNN-based deep learning models. These models commonly require ground truth annotations during the segmentation phase; however, this dataset fails to provide such annotations. This drawback

can be overcome by employing the segmented images generated by this method as ground truth annotations, allowing the integration of CNN-based segmentation algorithms to achieve more precision and accuracy.

CONCLUSION

Early diagnosis of SCD is essential for effective treatment, with accurate erythrocyte counts being important in both diagnosis and tracking the progression of the disease. Current cell counting methods misidentified WBCs and platelets as RBCs, resulting in inaccurate cell detection and false diagnosis. The proposed method uses high chromatic variance to find WBCs and platelets in blood smear images. This is performed by applying parametric segmentation to RG chromaticity and its separate channels to identify the WBCs and platelets pixels that display the highest contrast to the average color of the other blood smear components. The proposed method uses PSO-based optimization in the search space to identify the best threshold values for accurate segmentation. Moreover, chromaticity has been considered as a feature rather than separating color components through experimentation, which often occurs in state-of-the-art methods. In this experiment, the performance of the segmentation method was examined by comparing the WBCs and platelets using chromatic images as the ground truth. Previous methodologies segmented WBCs and platelets from separate experiments instead of within a single study. In comparison, the proposed method achieved a precision and sensitivity of 96.96% and 96.97%, respectively, with a higher accuracy of 96.32%. In future work, CNNs will be used for automatic WBC and platelet segmentation. The segmented regions will be eliminated to increase the RBC counts for abnormality detection. This automation has the ability to enhance treatments and reduce the emphasis on manual interventions, thereby improving medical diagnosis accuracy and efficiency. This method can identify leukemia by determining the most effective chromaticity channel for improved WBC segmentation for disease identification.

ACKNOWLEDGEMENT

This work is supported by the Centre for Machine Learning and Intelligence (CMLI), which is ISO Certified (ISO/IEC 20000-1:2018) and funded by the Department of Science and Technology (DST-CURIE).

REFERENCES

Acharya, V., & Kumar, P. (2017). Identification and red blood cell classification using computer aided system to diagnose blood disorders. In *2017 International Conference on Advances in Computing, Communications and Informatics (ICACCI)* (pp. 2098-2104). IEEE Publishing. <https://doi.org/10.1109/icaccci.2017.8126155>

- Acharya, V., & Prakasha, K. (2019). Computer aided technique to separate the red blood cells, categorize them and diagnose sickle cell anemia. *Journal of Engineering Science & Technology Review*, 12(2), 67-80. <https://doi.org/10.25103/jestr.122.10>
- Alagu, S., Ganesan, K., & Bagan, K. B. (2023). A novel deep learning approach for sickle cell anemia detection in human RBCs using an improved wrapper-based feature selection technique in microscopic blood smear images. *Biomedical Engineering/Biomedizinische Technik*, 68(2), 175-185. <https://doi.org/10.1515/bmt-2021-0127>
- Alzubaidi, L., Al-Shamma, O., Fadhel, M. A., Farhan, L., & Zhang, J. (2020). Classification of red blood cells in sickle cell anemia using deep convolutional neural network. In *Intelligent Systems Design and Applications: 18th International Conference on Intelligent Systems Design and Applications (ISDA 2018)* (pp. 550-559). Springer. https://doi.org/10.1007/978-3-030-16657-1_51
- Alzubaidi, L., Fadhel, M. A., Al-Shamma, O., & Zhang, J. (2020). Robust and efficient approach to diagnose sickle cell anemia in blood. In *Intelligent Systems Design and Applications: 18th International Conference on Intelligent Systems Design and Applications (ISDA 2018)* (pp. 560-570). Springer. https://doi.org/10.1007/978-3-030-16657-1_52
- Alzubaidi, L., Fadhel, M. A., Oleiwi, S. R., Al-Shamma, O., & Zhang, J. (2020). DFU_QUTNet: Diabetic foot ulcer classification using novel deep convolutional neural network. *Multimedia Tools and Applications*, 79(21), 15655-15677. <https://doi.org/10.1007/s11042-019-07820-w>
- Anand, V., Gupta, S., Koundal, D., Alghamdi, W. Y., & Alsharbi, B. M. (2024). Deep learning-based image annotation for leukocyte segmentation and classification of blood cell morphology. *BMC Medical Imaging*, 24(1), Article 83. <https://doi.org/10.1186/s12880-024-01254-z>
- Buades, A., Coll, B., & Morel, J. M. (2005). A non-local algorithm for image denoising. In *2005 IEEE Computer Society Conference on Computer Vision and Pattern Recognition (CVPR'05)* (Vol. 2, pp. 60-65). IEEE Publishing. <https://doi.org/10.1109/cvpr.2005.38>
- Chakraborty, R., Sushil, R., & Garg, M. L. (2019). An improved PSO-based multilevel image segmentation technique using minimum cross-entropy thresholding. *Arabian Journal for Science and Engineering*, 44, 3005-3020. <https://doi.org/10.1007/s13369-018-3400-2>
- Chy, T. S., & Rahaman, M. A. (2018). Automatic sickle cell anemia detection using image processing technique. In *2018 International Conference on Advancement in Electrical and Electronic Engineering (ICAEEE)* (pp. 1-4). IEEE Publishing. <https://doi.org/10.1109/icaee.2018.8642984>
- Chy, T. S., & Rahaman, M. A. (2019). A comparative analysis by KNN, SVM & ELM classification to detect sickle cell anemia. In *2019 International Conference on Robotics, Electrical and Signal Processing Techniques (ICREST)* (pp. 455-459). IEEE Publishing. <https://doi.org/10.1109/icrest.2019.8644410>
- Cruz, D., Jennifer, C., Castor, L. C., Mendoza, C. M. T., Jay, B. A., Jane, L. S. C., & Brian, P. T. B. (2017). Determination of blood components (WBCs, RBCs, and Platelets) count in microscopic images using image processing and analysis. In *2017 IEEE 9th International Conference on Humanoid, Nanotechnology, Information Technology, Communication and Control, Environment and Management (HNICEM)* (pp. 1-7). IEEE Publishing. <https://doi.org/10.1109/hnicem.2017.8269515>

- Das, P. K., Meher, S., Panda, R., & Abraham, A. (2019). A review of automated methods for the detection of sickle cell disease. *IEEE Reviews in Biomedical Engineering*, 13, 309-324. <https://doi.org/10.1109/RBME.2019.2917780>
- de Albuquerque, V. H. C., Gupta, D., De Falco, I., Sannino, G., & Bouguila, N. (2020). Special issue on bio-inspired optimization techniques for biomedical data analysis: Methods and applications. *Applied Soft Computing*, 95, Article 106672.
- Dhal, K. G., Ray, S., Das, A., & Das, S. (2019). A survey on nature-inspired optimization algorithms and their application in image enhancement domain. *Archives of Computational Methods in Engineering*, 26(5), 1607-1638. <http://dx.doi.org/10.1007/s11831-018-9289-9>
- Eisham, Z. K., Haque, M. M., Rahman, M. S., Nishat, M. M., Faisal, F., & Islam, M. R. (2023). Chimp optimization algorithm in multilevel image thresholding and image clustering. *Evolving Systems*, 14(4), 605-648. <https://doi.org/10.1007/s12530-022-09443-3>
- Elsalamony, H. A. (2017). Anaemia cells detection based on shape signature using neural networks. *Measurement*, 104, 50-59. <https://doi.org/10.1016/j.measurement.2017.03.012>
- Farshi, T. R., Drake, J. H., & Özcan, E. (2020). A multimodal particle swarm optimization-based approach for image segmentation. *Expert Systems with Applications*, 149, Article 113233. <https://doi.org/10.1016/j.eswa.2020.113233>
- Fitri, Z. E., Purnama, I. K. E., Pramunanto, E., & Pumomo, M. H. (2017). A comparison of platelets classification from digitalization microscopic peripheral blood smear. In *2017 International Seminar on Intelligent Technology and Its Applications (ISITIA)* (pp. 356-361). IEEE Publishing. <https://doi.org/10.1109/isitia.2017.8124109>
- Garcia-Lamont, F., Alvarado, M., & Cervantes, J. (2021). Systematic segmentation method based on PCA of image hue features for white blood cell counting. *Plos One*, 16(12), Article e0261857. <https://doi.org/10.1371/journal.pone.0261857>
- García-Lamont, F., Alvarado, M., López-Chau, A., & Cervantes, J. (2022). Efficient nucleus segmentation of white blood cells mimicking the human perception of color. *Color Research & Application*, 47(3), 657-675. <https://doi.org/10.1002/col.22752>
- Guo, J., Ma, J., García-Fernández, Á. F., Zhang, Y., & Liang, H. (2023). A survey on image enhancement for Low-light images. *Heliyon*, 9(4), Article e14558. <https://doi.org/10.1016/j.heliyon.2023.e14558>
- Imron, A. M. N., & Fitri, Z. E. (2019). A classification of platelets in peripheral blood smear image as an early detection of myeloproliferative syndrome using gray level co-occurrence matrix. In *Journal of Physics: Conference Series (Vol. 1201, No. 1, p. 012049)*. IOP Publishing. <https://doi.org/10.1088/1742-6596/1201/1/012049>
- Juliet, S., Rajsingh, E. B., & Ezra, K. (2015). Projection-based medical image compression for telemedicine applications. *Journal of Digital Imaging*, 28, 146-159. <https://doi.org/10.1007/s10278-014-9731-y>
- Kate, V., & Shukla, P. (2020). Image segmentation of breast cancer histopathology images using PSO-based clustering technique. In *Social Networking and Computational Intelligence: Proceedings of SCI-2018* (pp. 207-216). Springer. http://dx.doi.org/10.1007/978-981-15-2071-6_17

- Kaur, P., Sharma, V., & Garg, N. (2016). Platelet count using image processing. In *2016 3rd International Conference on Computing for Sustainable Global Development (INDIACom)* (pp. 2574-2577). IEEE Publishing.
- Kavitha, A. R., & Chellamuthu, C. (2019). Brain tumour detection using self-adaptive learning PSO-based feature selection algorithm in MRI images. *International Journal of Business Intelligence and Data Mining*, 15(1), 71-97. <http://dx.doi.org/10.1504/IJBIDM.2019.100469>
- Kennedy, J., & Eberhart, R. (1995). Particle swarm optimization. In *Proceedings of ICNN'95-International Conference on Neural Networks (Vol. 4, pp. 1942-1948)*. IEEE Publishing. <https://doi.org/10.1109/ICNN.1995.488968>
- Ker, J., Wang, L., Rao, J., & Lim, T. (2017). Deep learning applications in medical image analysis. *IEEE Access*, 6, 9375-9389. <https://doi.org/10.1109/access.2017.2788044>
- Khalaf, M., Hussain, A. J., Keight, R., Al-Jumeily, D., Keenan, R., Chalmers, C., Fergus, P., Salih, W., Abd, D. H., & Idowu, I. O. (2017). Recurrent neural network architectures for analysing biomedical data sets. In *2017 10th International Conference on Developments in eSystems Engineering (DeSE)* (pp. 232-237). IEEE Publishing. <https://doi.org/10.1109/dese.2017.12>
- Khosla, T., & Verma, O. P. (2023). Optimal threshold selection for segmentation of Chest X-Ray images using opposition-based swarm-inspired algorithm for diagnosis of pneumonia. *Multimedia Tools and Applications*, 83(9), 27089-27119. <http://dx.doi.org/10.1007/s11042-023-16494-4>
- Khouani, A., El Habib Daho, M., Mahmoudi, S. A., Chikh, M. A., & Benzineb, B. (2020). Automated recognition of white blood cells using deep learning. *Biomedical Engineering Letters*, 10, 359-367. <https://doi.org/10.1007/s13534-020-00168-3>
- Makem, M., & Tiedeu, A. (2020). An efficient algorithm for detection of white blood cell nuclei using adaptive three-stage PCA-based fusion. *Informatics in Medicine Unlocked*, 20, Article 100416. <https://doi.org/10.1016/j.imu.2020.100416>
- Mandave, D. D., & Patil, L. V. (2023). Bio-inspired computing algorithms in dementia diagnosis - A application-oriented review. *Results in Control and Optimization*, 12, Article 100276. <https://doi.org/10.1016/j.rico.2023.100276>
- Narayana, V. L., Patibandla, R. S. M. L., Pavani, V., & Radhika, P. (2022). Optimized nature-inspired computing algorithms for lung disorder detection. In *Nature-Inspired Intelligent Computing Techniques in Bioinformatics* (pp. 103-118). Springer.
- Nayak, J., Swapnarekha, H., Naik, B., Dhiman, G., & Vimal, S. (2023). 25 years of particle swarm optimization: Flourishing voyage of two decades. *Archives of Computational Methods in Engineering*, 30(3), 1663-1725. <http://dx.doi.org/10.1007/s11831-022-09849-x>
- Ozcan, S. N., Uyar, T., & Karayegen, G. (2024). Comprehensive data analysis of white blood cells with classification and segmentation by using deep learning approaches. *Cytometry Part A*, 105(7), 501-520. <https://doi.org/10.1002/cyto.a.24839>
- Öztürk, Ş., Ahmad, R., & Akhtar, N. (2020). Variants of artificial bee colony algorithm and its applications in medical image processing. *Applied Soft Computing*, 97, Article 106799. <https://doi.org/10.1016/j.asoc.2020.106799>

- Parvathy, H., Hariharan, S., & Aruna, S. (2016). A real-time system for the analysis of sickle cell anemia blood smear images using image processing. *International Journal of Innovative Research in Science, Engineering and Technology*, 5(4), 6200-6207.
- Patro, S. (2015). *Normalization: A preprocessing stage*. *ArXiv Preprint*. <https://doi.org/10.17148/iarjset.2015.2305>
- Saidani, O., Umer, M., Alturki, N., Alshardan, A., Kiran, M., Alsubai, S., Kim, T. H., & Ashraf, I. (2024). White blood cells classification using multi-fold pre-processing and optimized CNN model. *Scientific Reports*, 14(1), Article 3570. <https://doi.org/10.1038/s41598-024-52880-0>
- Sarrafzadeh, O., & Dehnavi, A. M. (2015). Nucleus and cytoplasm segmentation in microscopic images using K-means clustering and region growing. *Advanced Biomedical Research*, 4(1), Article 174. <https://doi.org/10.4103/2277-9175.163998>
- Sarvamangala, D. R., & Kulkarni, R. V. (2019). A comparative study of bio-inspired algorithms for medical image registration. In J. K. Mandal, P. Dutta & S. Mukhopadhyay (Eds.), *Advances in Intelligent Computing* (pp. 27-44). Springer. https://doi.org/10.1007/978-981-10-8974-9_2
- Shang, H., Zhao, S., Du, H., Zhang, J., Xing, W., & Shen, H. (2020). A new solution model for cardiac medical image segmentation. *Journal of Thoracic Disease*, 12(12), 7298–7312. <https://doi.org/10.21037/jtd-20-3339>
- Sharma, G. (2017). Color fundamentals for digital imaging. In *Digital Color Imaging Handbook* (pp. 1-114). CRC press.
- Sharma, V., Rathore, A., & Vyas, G. (2016). Detection of sickle cell anaemia and thalassaemia causing abnormalities in thin smear of human blood sample using image processing. In *2016 International Conference on Inventive Computation Technologies (ICICT)* (Vol. 3, pp. 1-5). IEEE Publishing. <https://doi.org/10.1109/inventive.2016.7830136>
- Shehab, M., Abualigah, L., Al Hamad, H., Alabool, H., Alshinwan, M., & Khasawneh, A. M. (2020). Moth-flame optimization algorithm: Variants and applications. *Neural Computing and Applications*, 32(14), 9859-9884. <https://doi.org/10.1007/s00521-019-04570-6>
- Shehanaz, S., Daniel, E., Guntur, S. R., & Satrasupalli, S. (2021). Optimum weighted multimodal medical image fusion using particle swarm optimization. *Optik*, 231, Article 166413. <http://dx.doi.org/10.1016/j.ijleo.2021.166413>
- Shi, M., Chen, C., Liu, L., Kuang, F., Zhao, D., & Chen, X. (2023). A grade-based search adaptive random slime mould optimizer for lupus nephritis image segmentation. *Computers in Biology and Medicine*, 160, Article 106950. <https://doi.org/10.1016/j.compbiomed.2023.106950>
- Singh, J., Kumar, V., Sinduja, K., Ekvitayavetchanukul, P., Agnihotri, A. K., & Imran, H. (2025). Enhancing heart disease diagnosis through particle swarm optimization and ensemble deep learning models. In *Nature-Inspired Optimization Algorithms for Cyber-Physical Systems* (pp. 313-330). IGI Global Scientific Publishing. <http://dx.doi.org/10.4018/979-8-3693-6834-3.ch010>
- Tavakoli, S., Ghaffari, A., Kouzehkanan, Z. M., & Hosseini, R. (2021). New segmentation and feature extraction algorithm for classification of white blood cells in peripheral smear images. *Scientific Reports*, 11(1), Article 19428. <https://doi.org/10.1038/s41598-021-98599-0>

- Tosta, T. A. A., De Abreu, A. F., Travencolo, B. A. N., do Nascimento, M. Z., & Neves, L. A. (2015). Unsupervised segmentation of leukocytes images using thresholding neighborhood valley-emphasis. In *2015 IEEE 28th International Symposium on Computer-Based Medical Systems* (pp. 93-94). IEEE Publishing. <https://doi.org/10.1109/cbms.2015.27>
- Vijh, S., Sharma, S., & Gaurav, P. (2020). Brain tumor segmentation using OTSU embedded adaptive particle swarm optimization method and convolutional neural network. In *Data Visualization and Knowledge Engineering: Spotting Data Points with Artificial Intelligence* (pp. 171-194). Springer International Publishing. http://dx.doi.org/10.1007/978-3-030-25797-2_8
- Wang, S., Cao, G., Wang, Y., Liao, S., Wang, Q., Shi, J., Li, C., & Shen, D. (2021). Review and prospect: Artificial intelligence in advanced medical imaging. *Frontiers in Radiology, 1*, Article 781868. <https://doi.org/10.3389/fradi.2021.781868>
- WHO. (2011). *Sickle Cell Disease and other Haemoglobin Disorders* [Fact Sheet No 308]. World Health Organization. <https://aho.org/fact-sheets/sickle-cell-disease-and-other-haemoglobin-disorders-fact-sheet/>
- Xu, M., Papageorgiou, D. P., Abidi, S. Z., Dao, M., Zhao, H., & Karniadakis, G. E. (2017). A deep convolutional neural network for classification of red blood cells in sickle cell anemia. *PLoS Computational Biology, 13*(10), Article e1005746. <https://doi.org/10.1371/journal.pcbi.1005746>
- Zhang, L., & Lim, C. P. (2020). Intelligent optic disc segmentation using improved particle swarm optimization and evolving ensemble models. *Applied Soft Computing, 92*, Article 106328. <https://doi.org/10.1016/j.asoc.2020.106328>
- Zhang, M., Li, X., Xu, M., & Li, Q. (2018). RBC semantic segmentation for sickle cell disease based on deformable U-Net. In *Medical Image Computing and Computer Assisted Intervention–MICCAI 2018: 21st International Conference* (pp. 695-702). Springer. https://doi.org/10.1007/978-3-030-00937-3_79
- Zhou, Z., & Liao, G. (2022). A novel approach to form normal distribution of medical image segmentation based on multiple doctors' annotations. In *Proceedings of SPIE--the International Society for Optical Engineering* (Vol. 12032). NIH Public Access. <https://doi.org/10.1117/12.2611973>

Review Article

Weaving a Greener Tomorrow: A Mini Review of Bamboo Fiber, Textiles and Hand-woven Techniques for Sustainable Innovation

Marzie Hatef Jalil

*Faculty of Applied and Creative Arts, University Malaysia Sarawak, 94300, Kota Samarahan, Malaysia
Institute of Creative and Technology, University Malaysia Sarawak, 94300, Kota Samarahan, Malaysia
Institute of Sustainable and Renewable Energy, University Malaysia Sarawak, 94300, Kota Samarahan, Malaysia*

ABSTRACT

Bamboo, known for its rapid growth and renewability, offers an eco-friendly alternative to traditional fibers, targeting the environmental effects of the textile and clothing industries. This review paper examines art-crafted weaving techniques, highlighting the incorporation of bamboo into traditional and modern designs to enhance the sustainability of bamboo-woven products. The paper thoroughly analyzes bamboo fiber extraction and hand-crafted techniques to produce sustainable, technical, and functional items such as sportswear and medical textiles. It also addresses the challenges linked to utilizing bamboo in textiles. Special emphasis is given to integrating bamboo into traditional weaving methods as a sustainable approach to enhance its uniqueness and preserve cultural heritage. By exploring sustainable practices and artistic innovation, this paper underscores the significance of connecting traditional craftsmanship with contemporary weaving design principles to fill research and practice gaps. In light of the ecological challenges posed by fast fashion, this study promotes sustainable practices by incorporating renewable materials and prioritizing brilliant material selection. Ultimately, this review emphasizes the vital role of design in fostering sustainability and provides a roadmap for preserving weaving traditions.

Keywords: Bamboo fiber, bamboo weaving, design for sustainability, eco-friendly materials, renewable fiber technologies, sustainable textiles, traditional weaving

ARTICLE INFO

Article history:

Received: 02 January 2025

Accepted: 03 March 2025

Published: 23 April 2025

DOI: <https://doi.org/10.47836/pjst.33.3.25>

E-mail address:

hjmarzie@unimas.my

INTRODUCTION

The detrimental environmental impact of the textile and clothing industry underscores the urgent need to adopt sustainable practices.

The fast fashion industry's reliance on non-renewable resources causes significant environmental harm, with millions of fabrics ending up in landfills daily. The global textile and clothing market, valued at USD 1,837 billion in 2023, is projected to grow by 7.4% from 2024 to 2030. Synthetic fibers, a cornerstone of modern textiles, significantly contribute to pollution due to their production processes and resistance to biodegradation. In this context, incorporating renewable materials like bamboo is beneficial and essential for fostering environmental sustainability.

Bamboo, recognized as the fastest-growing woody plant in the world, even surpasses the most rapidly growing trees, with some species capable of growing up to one meter per day. Its remarkable properties, including strength, flexibility, and UV protection, make bamboo culm fibers highly suitable for various applications, such as textile and yarn production. Products made from bamboo range from clothing to hygiene items (e.g., sanitary napkins, masks, bandages) and home furnishings. These unique qualities position bamboo as an intriguing and viable alternative to conventional fibers in the textile industry (Akinlabi et al., 2017; Kozłowski & Mackiewicz-Talarczyk, 2020).

In recent years, global trade and technological advancements have transformed industries, increasing awareness of the essential need to preserve and revitalize traditional crafts like weaving. Handloom and crafted woven products are a vital cultural bridge between heritage preservation and sustainable innovation. As timber from forests becomes scarce, industries seek cost-effective, fast-growing, and readily available alternatives such as bamboo, which has structural and physical properties comparable to wood. Beyond its functionality, bamboo textiles can be transformed into luxury items by incorporating design principles, resulting in intricate aesthetics and improved usability.

Government initiatives, such as expanding bamboo plantations and innovations in bamboo fiber processing, have spurred the growth of bamboo crafts and textiles. While bamboo has been studied for furniture, paper production, and the textile industry, its applications in handcrafted woven design and high-fashion products remain limited. To bridge this gap, integrating bamboo into either craft or handloom weaving practices in clothing and fashion design presents a promising opportunity to preserve the heritage of weaving techniques while allowing designers to create eco-friendly and innovative products. This paper aims to explore the prospects and existing practices in this field.

MATERIAL AND METHODS

This review examines bamboo's role as a sustainable material, from its origin and extraction to handicraft design and handloom weaving, while emphasizing its minimal environmental impact. It synthesizes existing literature on bamboo's unique properties, weaving techniques, and material applications to provide a comprehensive overview. A significant gap exists in extensive research that combines bamboo fiber processing with sustainable,

art-crafted techniques. This gap in the literature highlights the need for further study. This paper investigates how bamboo catalyzes innovation in sustainable textiles while preserving traditional weaving heritage techniques. Bridging traditional craftsmanship with modern design principles offers designers a roadmap for integrating bamboo into future sustainable applications. A systematic literature review was conducted to achieve this, focusing on studies published over the past two decades. Keywords such as “bamboo textiles,” “design innovation,” “bamboo characteristics,” “bamboo weaving,” and “sustainable textile” guided the search across databases like Scopus, Google Scholar, and ScienceDirect. This review provides a detailed analysis of bamboo textiles from sustainability, material science, and design innovation perspectives, offering insights for future research and development.

RESULT AND DISCUSSION

Comparative Analysis of Bamboo Fiber and Other Natural Fibers

Bamboo is an exceptionally fast-growing plant, maturing in 3 to 5 years compared to 20 years for most types of wood. It can grow up to two inches per hour, reaching 60 feet within three months (Neha & Aravendan, 2023). According to Neha and Aravendan (2023), its primary components include cellulose (41%–73%), hemicellulose (61%–73%), and lignin (21%–28%), with its high lignin content providing bamboo with remarkable strength and mechanical properties. Cellulose, the dominant component in bamboo, is a sustainable biomaterial that is non-toxic, biodegradable, and renewable (Amjad, 2024). It imparts rigidity and tensile strength due to its composition of carbon, hydrogen, and oxygen (Neha & Aravendan, 2023). Furthermore, hemicellulose, the amorphous portion of bamboo fibers, contributes to their acidic nature, moisture retention, and bonding with lignin through ester bonds-variations in hemicellulose and lignin content influence bamboo’s mechanical and chemical properties (Hu et al., 2019). For instance, nodes contain higher levels of moisture and hemicellulose but lower levels of lignin and cellulose, leading to reduced density and mechanical properties (Jalil, 2022). Bamboo’s mechanical properties vary depending on species, growth conditions, and structural characteristics (Chen et al., 2017). Research has demonstrated that removing hemicellulose decreases bamboo’s tensile modulus, while removing lignin has no significant effect (Chen et al., 2017). Fiber fineness impacts fiber length and density, with coarser fibers providing better durability and tensile strength (Rocky & Thompson, 2018). Additionally, bamboo’s durability relies on its tensile strength, flexural strength, and moisture absorption. Smaller bamboo culms are less stable under humidity than larger, thicker-walled ones (Liese & Tang, 2015).

As a natural resource, bamboo requires significantly less water for cultivation compared to water-intensive crops like cotton (Gericke & Van der Pol, 2010). Restrepo et al. (2016) highlighted bamboo's potential to reduce environmental harm in manufacturing processes. Many bamboo species thrive without pesticides or fertilizers, which minimizes the

environmental impacts of chemical use in agriculture. This underscores bamboo's potential as an eco-friendly alternative to conventional materials like wood-polymer composites, offering a significantly lower carbon footprint (Rocky & Thompson, 2018). Shinohara et al. (2019) also underscored bamboo's capability to prevent erosion and improve soil quality, emphasizing its long-term conservation value. Despite its numerous benefits, many current extraction techniques are not environmentally sustainable. The extraction processes impact the removal of lignin, which affects fiber stiffness and discoloration, as well as non-cellulosic components that influence properties like strength, density, moisture absorption, and flexibility (Kozłowski & Mackiewicz-Talarczyk, 2020). Additionally, chemical treatments lighten the yellowish-brown fibers caused by lignin and enhance bamboo's UV absorption and antibacterial properties, making it suitable for textiles (Neha & Aravendan, 2023). The following section will address strategies for improving the sustainability of bamboo fiber processing.

Previous research compared bamboo viscose fibers with other textiles, highlighting their superior tensile extensibility and comfort. For instance, Mishra et al. (2012) showed that bamboo viscose fabrics exhibited greater tensile extensibility than cotton and blends of cotton and bamboo viscose. Compared to cotton, bamboo viscose's reduced shear rigidity and bending stiffness contribute to its enhanced comfort and hand feel (Mishra et al., 2012). Additional studies indicate that natural bamboo yarns possess improved tearing strength, excellent dye absorption, and better wrinkle resistance than cotton, making bamboo an appealing choice for sustainable textile applications (Kushwaha et al., 2023; Singh & Dessalegn, 2021). Bamboo's minimal water requirements make it a sustainable option, especially in water-scarce regions, as it uses significantly less water than cotton, sometimes as little as 500 liters per kilogram of biomass without additional irrigation (Nayak & Mishra, 2016). Nassar et al. (2020) examined the thermal comfort properties of single jersey fabrics made from 100% bamboo, cotton-bamboo-polyester microfiber, bamboo-polyester microfiber, and cotton-polyester microfiber blends. The 100% bamboo fabric exhibited the highest thermal conductivity of the tested fabrics, while the cotton-polyester fabric had the lowest (Nassar et al., 2020).

Additionally, bamboo fabric demonstrated better thermal conductivity than bamboo-polyester microfiber fabric (Tausif et al., 2015). Tausif et al. (2015) found that the yarn arrangement within the fabric also plays a crucial role in determining fabric thickness, and the low weight of bamboo samples suggests that bamboo fibers could serve as a competitive alternative to cotton and microfiber polyester, particularly in sportswear applications such as sports headscarves. Figure 1 outlines the key properties of bamboo as a material resource. The methods used for fiber extraction have a significant impact on the characteristics of the final product, with viscose-like chemical processes providing predictability in fiber structure and properties thanks to cost-effective equipment, low energy requirements, and

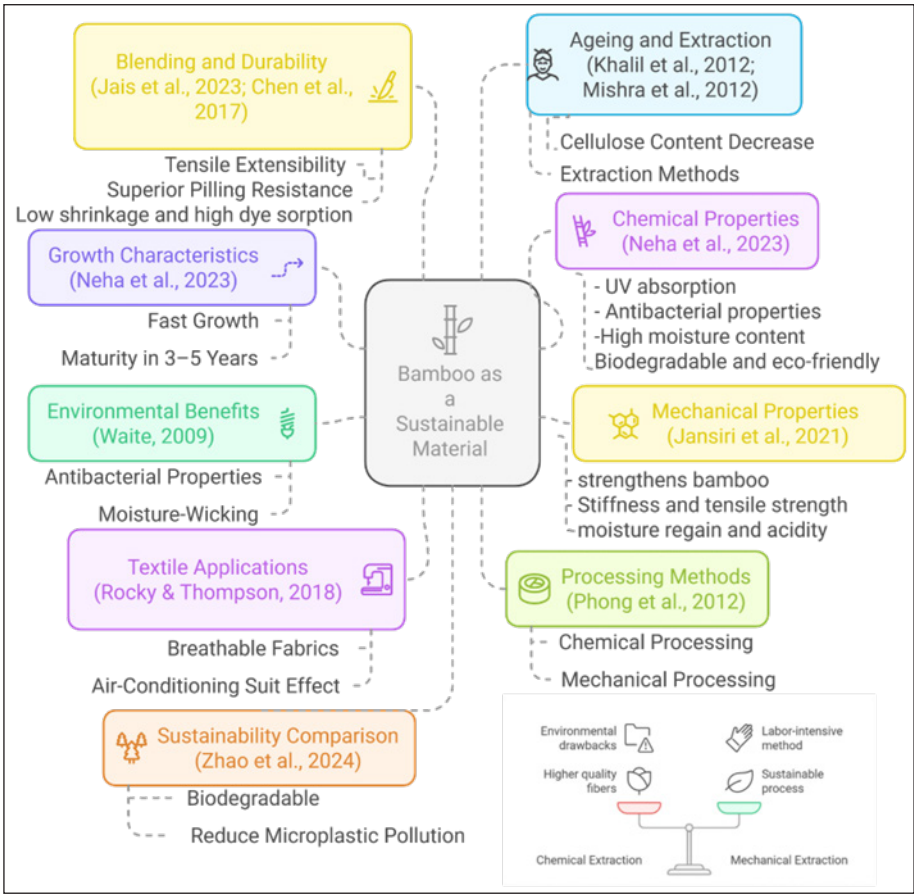


Figure 1. Key characteristics and properties of bamboo as a renewable and sustainable material resource

control over fiber attributes compared to mechanical or steam-explosion methods (Phong et al., 2012).

Bamboo Fiber Extraction Methods and Their Impact on Textile Properties

Bamboo fiber can be obtained through three primary methods: mechanical, chemical, and hybrid extraction techniques (Hu et al., 2019). Mechanical and chemical methods yield bundles of natural bamboo fibers, while chemical processes, such as the viscose method, produce regenerated bamboo cellulose, commonly known as bamboo viscose (Hu et al., 2019). The fiber extraction process begins by splitting bamboo culms into strips, followed by either mechanical or chemical processing based on the intended use (Phong et al., 2012). Mechanical processing produces coarse and rigid fabrics, whereas viscose-extracted fibers create soft, drape-friendly textiles (Singh & Dessalegn, 2021). Mechanical extraction involves soaking bamboo strips in water or boiling them, beating, scraping, and combing

to produce spinnable fibers (Hu et al., 2019). These fibers undergo further treatment with alkali solutions to improve their properties (Nayak & Mishra, 2016). The variations in strength and durability between these methods arise from molecular changes introduced during chemical treatments, which modify the fiber's structural alignment and level of polymerization. Chemical extraction entails treating bamboo slices with caustic chemicals like sodium hydroxide or sodium silicate to produce fine fibers suitable for textiles (Hu et al., 2019). Enzymatic and microbial treatments have also been investigated for degumming; however, these methods are time-consuming and may not suffice for industrial needs (Zhao et al., 2024). Asmarea et al. (2022) noted that the combined extraction methods, which included alkali and a newly developed composite enzyme in both concentrated and solution forms, produced finer bamboo fibers from three different bamboo species by breaking down and removing non-cellulosic components of the bamboo strips.

Sustainable manufacturing practices aim to reduce environmental harm, minimize waste generation, and lessen reliance on non-renewable resources, enhancing overall environmental performance (Jalil, 2022). Mechanical extraction is more sustainable because it avoids chemicals and preserves bamboo's natural properties (Hu et al., 2019). However, this method is labor-intensive, water-intensive, and costly, resulting in coarser fibers. In contrast, less sustainable chemical methods produce finer fibers with superior softness and drape. These distinctions significantly affect the behavior of yarns and fabrics derived from each method (Gericke & Van der Pol, 2010; Khalil et al., 2012). However, chemical bamboo extraction is more cost-effective and generates fine, soft fiber since it eliminates lignin. Despite this advantage, it is less sustainable and requires closed-loop systems to manage environmental damage. Given that the complex structure of bamboo contains high levels of lignin, which obstructs prompt fiber extraction (Phong et al., 2012), it is challenging to achieve absolute benefits from extracting fibers using any one technology (Singh & Dessalegn, 2021).

Previous researchers combining pretreatment or post-treatment of bamboo strips with some alkali solutions, such as softeners and mechanical processes, achieved highly effective and improved thermal properties (Rocky & Thompson, 2018; Singh & Dessalegn, 2021). Some researchers have utilized a combined extraction method that employs low alkali consumption and multiple enzymes to transform spinnable fibers while maintaining their antibacterial properties and minimizing environmental impact (Jalil, 2022). The type of extraction influences fiber characteristics, spinning qualities, and ecological sustainability, benefiting sustainable textile applications. Although enzymatic treatment is the most sustainable, the microbial culture is not economically viable (Rocky & Thompson, 2018). Both extraction methods begin with splitting the strips, followed by either mechanical, chemical, or enzymatic treatment (Zhao et al., 2024). Mechanical treatments demonstrate the highest tensile strength, making them ideal for the construction sector due to their compatibility with high-strength materials (Rocky & Thompson, 2018). In contrast,

chemical or combined treatments result in lower tensile strength as the fiber becomes weaker, finer, and suitable for yarn processing (Neha & Aravendan, 2023).

Several wash cycles are necessary to eliminate the residual chemicals in wastewater, which are not deemed fully sustainable, as Hu et al. (2019) noted, to prevent issues with bamboo crystallinity. However, the primary focus of sustainability in textile products pertains to the use of harsh chemicals and process efficiency. Mechanically extracted bamboo fibers outperform flax and jute in their resistance to pilling and abrasion. Furthermore, they exhibit lower shrinkage, improved color clarity, and a soft luster without mercerization. As illustrated in Figure 2, combined treatments are more sustainable, offer faster processing times, consume less energy, and yield better results. This process produces fine, soft fibers that are beneficial for textile applications. Tausif et al. (2015) discovered that bamboo fibers possess properties comparable to viscose rayon, cotton, and modal fibers but with slightly more extraordinary wet tenacity. Bamboo’s versatility allows it to blend well with other fibers, such as cotton, hemp, and lyocell, resulting in fabrics with varied characteristics (Jais et al., 2023). As shown in Figure 1, maintaining a balance between fiber quality and sustainability is crucial in bamboo fiber production.

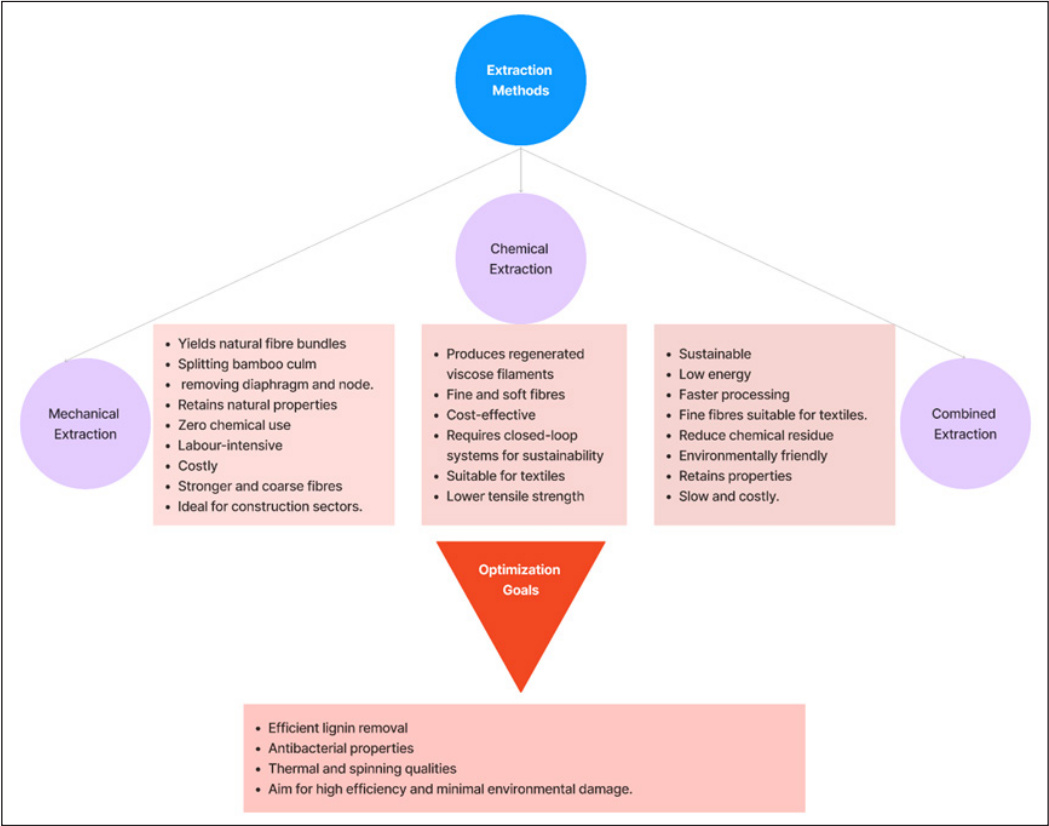


Figure 2. Extraction of bamboo methods and their characteristics

Bamboo Textile Properties

Bamboo fiber is widely used in the textile industry because of its unique properties, with applications in yarns, woven, knitted, and nonwoven fabrics. Bamboo yarn, made from continuous filaments, is the foundation for textile construction (Waite, 2009). Knitted bamboo fabric, created by interlocking loops, is flexible and breathable, making it ideal for comfortable garments (Mishra et al., 2012). In contrast, woven bamboo fabric, produced by interlacing two sets of yarn at right angles, offers durability suitable for garments and upholstery, although its production is not environmentally sustainable (Mishra et al., 2012). Nonwoven bamboo fabric, made directly from fibers without weaving or knitting, is used in items such as filters, wipes, and medical textiles, showcasing bamboo's versatility (Gericke & Van der Pol, 2010; Prakash et al., 2021; Zhao et al., 2024). Integrating bamboo into sustainable textiles and crafts addresses global demands for eco-friendly solutions (Jalil, 2022).

Khalil et al. (2012) noted that its use in functional clothing, sanitary products, biocomposites, and geotextiles illustrates its potential across various industries. Gao et al. (2024) pointed out that innovation in weaving techniques and material combinations can help overcome challenges, ensuring bamboo remains relevant in contemporary design. Products derived from bamboo are often marketed as “green” or “biodegradable,” regardless of their production methods (Hardin et al., 2009). Structurally, bamboo is an anisotropic natural composite material primarily made of vascular bundles embedded in a parenchymatous matrix (Liese & Tang, 2015). Research by Ozkan (2021) examined the engineering potential of bamboo for sustainable textile development, focusing on its unique properties, benefits, and limitations. Previous research highlights the tensile strength of bamboo and its blended fabrics, which enhances the tensile performance of textiles (Chen et al., 2017). Bamboo viscose offers superior hand value to cotton due to its smoother texture and lower bending rigidity (Kaur et al., 2016). These properties position it as a critical resource for sustainable textiles combined with bamboo's rapid renewability and environmental benefits (Waite, 2009). In contrast to modern textiles, which predominantly use non-renewable materials, bamboo fibers are sustainable and have multiple advantages (Hu et al., 2019). Bamboo textiles are lightweight, breathable, moisture-wicking, and anti-static, with antibacterial properties that make them highly marketable (Tausif et al., 2015).

A study conducted by the China Textile Industrial Testing Centre and the Japan Textile Inspection Association found that 100% bamboo fabric achieved a 99.8% antibacterial kill rate (Waite, 2009). Bamboo textiles have inherent antimicrobial properties (Chaowana et al., 2021). Waite (2009) noted that bamboo fibers are soft, lightweight, and low-density, with a loose structure that enhances air permeability and comfort, especially in hot climates. Chonsakorn et al. (2024) indicated that a 70:30 bamboo-to-polyester fiber ratio is optimal for fabric production, providing enhanced strength, antibacterial activity, and suitability for

medical and hygiene applications. This innovation aligns with sustainable textile practices by utilizing waste materials and reducing environmental impact (Chonsakorn et al., 2024). By leveraging these properties, bamboo textiles offer a promising path toward sustainable fashion and ecological responsibility.

Chonsakorn et al. (2024) developed a method for producing nonwoven fabrics by integrating bamboo and polyester fibers, utilizing mechanical bonding techniques such as needle punching. The resulting fabrics exhibited durability, a lightweight structure, and antibacterial efficacy, making them suitable for medical lifestyle products (Chonsakorn et al., 2024). Chonsakorn et al. (2024) emphasized the potential of bamboo waste as a renewable resource for sustainable textile applications, providing significant advantages in tackling environmental and public health challenges (Chonsakorn et al., 2024; Santos et al., 2021). This approach facilitates the creation of antibacterial nonwoven fabric, positioning it as a practical solution for elderly care in community settings (Chonsakorn et al., 2024). Nassar et al. (2020) demonstrated that the arrangement of yarns within the fabric influenced fabric thickness.

Furthermore, most functional bamboo textiles and fabrics feature moisture-wicking properties and UV protection, making them ideal for activewear, intimate apparel, and summer clothing (Amjad, 2024). Their natural antibacterial, hypoallergenic, and UV-blocking qualities further enhance their suitability for baby clothing, pregnant women, undergarments, and socks. Additionally, their smooth texture and draping qualities make them popular choices for home decor and accessories, including scarves, hats, and gloves (Kaur et al., 2016; Rocky & Thompson, 2018). Bamboo fibers and nonwoven bamboo fabrics are also used in sanitary products, such as bandages, masks, and surgical attire, due to their sterilizing and bacteriostatic characteristics (Rocky & Thompson, 2018). Products like hygienic towels and absorbent pads benefit from bamboo's natural antimicrobial attributes, eliminating artificial agents and reducing allergy risks (Lipp-Symonowicz et al., 2011; Tausif et al., 2015).

In addition to textiles, biotechnology has proven effective as a leading approach for advancing a sustainable and environmentally friendly wet-processing sector in textiles and producing eco-friendly value-added products. Therefore, bamboo fibers enhance biocomposites, providing eco-friendly, cost-effective, and biodegradable alternatives to traditional materials (Saha & Mandal, 2020; Santos et al., 2021). Ensuring wearing comfort is crucial since textiles remain in contact with the human body day and night. Ozkan (2021) noted that bamboo fibers have a naturally channeled structure with micro-holes that enable rapid moisture absorption and evaporation. This porous quality contributes to the fiber's capacity to absorb significant water, offering strength and low elasticity. Ozkan (2021) concluded that textiles made from natural bamboo fibers deliver superior wearing comfort due to their breathable structure.

Bamboo Craft Techniques

Gao et al. (2024) noted that the bamboo weaving craft in China, which achieved sophistication during the Song Dynasty (960–1279 AD), has been a hallmark of artistic and technological evolution. This traditional craft, using bamboo silk or splints in intricate weaving techniques, remains culturally significant and sustainable. Moreover, Yu (2023) noted that hand spinning, a unique and ancient technique for producing yarn and weaving, aligns with sustainable goals, as it does not require electric machinery and entails minimal energy consumption. Gao et al. (2024) found that modern and internationalized features in bamboo weaving patterns arise through specific coding styles. Geometric elements like circles, squares, and hexagons symbolize modernity. In contrast, patterns that incorporate traditional characters and motifs or plant-inspired designs evoke ethnic and traditional aesthetics, as noted by Luo et al. (2020). Additionally, central symmetry in patterns is generally linked with conventional designs, whereas asymmetry signifies modern aesthetics (Gao et al., 2024).

According to Kumalasari et al. (2021), the techniques for bamboo craft weaving are generally consistent. The weaving of bamboo products is based on various techniques, with their uniqueness and applications illustrated in Figure 3. Bamboo weaving includes diverse methods, each possessing distinct characteristics and applications. Standard techniques include twilling, coiling, plaiting, and checking, along with herringbone and hexagonal methods, which are widely used for modern three-dimensional designs (Gao et al., 2024; Kumalasari et al., 2021) to create items such as baskets, vases, and straw shoes (Yu, 2023; Kumalasari et al., 2021). Twilling involves the diagonal weaving of bamboo strips to form patterns with adjustable angles, making it very popular in basketry. Historical evidence from the Jomon era shows that bamboo twilling in basket-making is particularly strong and sustainable compared to other types (Gao et al., 2024; Yu, 2023). Kumalasari et al. (2021) noted that coiled and twined baskets employ spiral structures formed by warps and wefts while plaiting and checking techniques enable the creation of diagonal-patterned products. These methods demonstrate the versatility of bamboo weaving in crafting intricate designs (Gao et al., 2024; Kumalasari et al., 2021).

Specific techniques such as parallel weaving, which involves laying thin bamboo strips over molds, allow for greater control over product shapes (Gao & Gu, 2020). Dai bamboo weaving methods-picking, folding, pressing, curving, and coiling-are the foundation for innovative techniques like broken warp weaving, flora weaving, and float carving weaving in conjunction with traditional methods (Zheng & Zhu, 2021). These handcrafted designs incorporate cultural and artistic elements, including geometric and floral patterns, reflecting creativity and cultural expression in bamboo craftsmanship, as Zhang (2019) and Gao and Gu (2020) noted. Modern bamboo weaving combines flat and curved techniques. Flat weaving, categorized into horizontal, vertical, and oblique patterns, presents a consistent

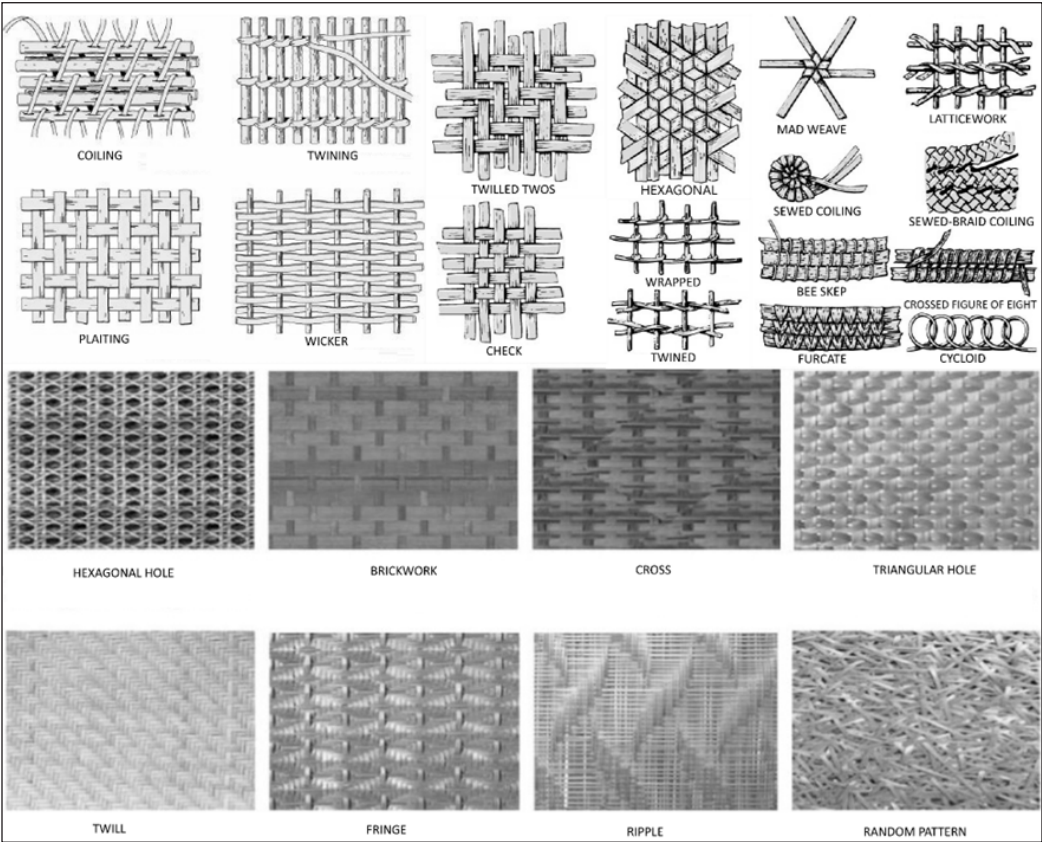


Figure 3. Bamboo art-crafted patterns in craft and woven products

and organized appearance (Gao et al., 2024). Curved weaving offers dynamic and intimate aesthetics and is frequently used in furniture design for elements such as chair backs and cabinet doors (Gao et al., 2024; Kumalasari et al., 2021) 3. Geometrical rules underlying the traditional patterns can be analyzed using digital tools to establish a systematic design framework (Gao et al., 2024; Kumalasari et al., 2021).

Bamboo Handloom Weaving Techniques

Some bamboo products come in different textures and pattern surfaces, crosses, hexagonal holes, firings, and twill map weaving, as shown in Figure 3. Gao et al. (2024) stated that bamboo handloom weaving products, an essential craft in textile decoration, create textures, patterns, and structural modeling. Handloom weaving involves warp and weft yarns, with fabric strength influenced by geometry, thread density, fiber type, and weave design (Yu, 2023). Bamboo yarn is used in warp and weft directions, producing durable fabrics, although the weft’s higher density results in stiffer textures (Gao et al., 2024; Kumalasari et al., 2021). Kumalasari et al. (2021) stated that handcrafted bamboo textiles

are traditionally made using handlooms, a sustainable alternative to industrial weaving, which often involves chemically processed bamboo fibers. Promoting handloom techniques can enhance sustainability by incorporating fibers from various extraction methods (Gao et al., 2024; Kumalasari et al., 2021). Modular textile weaving techniques further expand design possibilities, enabling the assembly of multiple pieces into diverse forms (Yu & Pashkevych, 2023; Yu, 2023).

Additionally, Zhang et al. (2020) stated that combining bamboo with materials like leather or fabric enhances the designs' tactile and visual appeal and can help make products look luxurious and more sustainable. As shown in Figures 4(a), KanaLili 2025 and Figure 4(b), Central Saint Martin's Spring/Summer 2018 Ready-To-Wear, the handcrafted dress showcases the delicate art of bamboo weaving. Central Saint Martin's designers experimented with bamboo strips of varying widths and colors, pressing and weaving them to create a dynamic textile with structural power for the spring-summer 2018 Ready-To-Wear (RTW) collection. The intricate patterning is enhanced with subtle lighting, creating a soft, shimmering effect that captures the eye. Moreover, Balmain applied various weaving techniques to achieve a three-dimensional effect, emphasizing structural lines and layering in the style [Figure 4(c)]. Balmain's square-conjoint pattern of cross-woven leather with bamboo strips also introduced rhythmic, organic designs that adapt to human movement.

Moreover, Dolce & Gabbana explored bamboo weaving's rigidity and flexibility, shaping garments extending freely from the body or contouring to enhance form in the RTW collection of Spring 2013, as shown in Figure 4(d). These innovative approaches highlight combining traditional craftsmanship with contemporary fashion (Yu et al., 2023). Handloom bamboo products exemplify low-carbon, green, and eco-sustainable design, adhering to

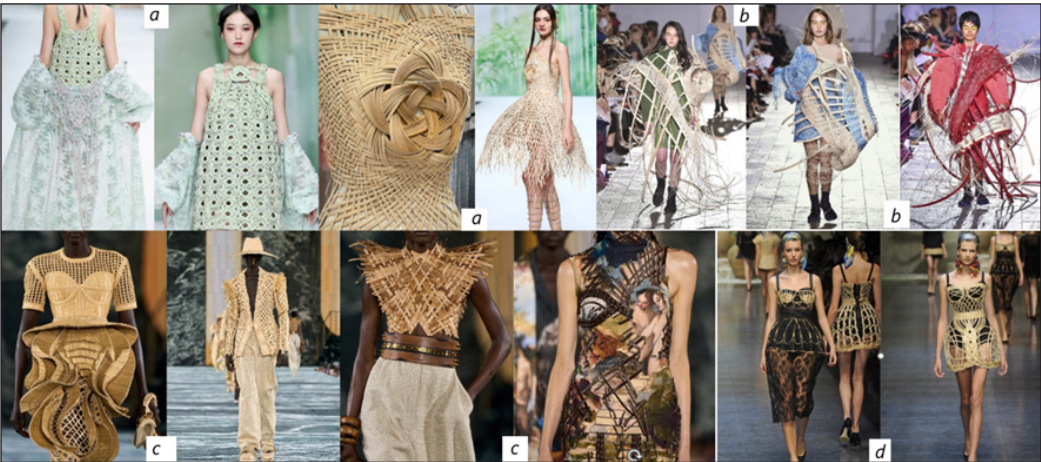


Figure 4. (a) KanaLili 2025, (b) Central Saint Martin's RTW Spring/Summer 2018, (c) Balmain RTW Spring 2023 Collection, (d) Dolce & Gabbana RTW Spring 2013

material efficiency, reduced consumption, and recycling, achieving zero pollution since it is produced based on customization purposes. This aligns with the United Nations Sustainable Development Goal (SDG) 12 (Responsible Consumption and Production) (Gao et al., 2024). Moreover, handloom weaving, a sustainable manual process that avoids reliance on electric machinery and fossil fuels, supports SDG 13 (Climate Action). Despite being labor-intensive, it minimizes textile waste and produces durable, long-lasting fabrics (Yu et al., 2023). Yu et al. (2023) stated that initiatives like the Dirty Fashion Campaign 2017 proposed a closed-loop system for viscose production, illustrating the growing demand for sustainable bamboo-based textiles, which could lead to innovations in fabric technology and broader adoption within the fashion industry. This approach is highly recommended for bamboo textiles and crafted products.

Innovative Techniques and Sustainability Solutions to Weaving a Greener Tomorrow

Traditional art-crafted techniques are employed to craft the textile's base structure, especially the weaving techniques, while bamboo strips are cut, smoothed, and prepared for integration (Luo et al., 2020). Gao and Gu (2020) stated that the innovative approaches expand creative possibilities for artisans, enriching the cultural heritage of traditional weaving while promoting sustainability. The study underscores the crucial need for collaboration between designers and artisans to regenerate sustainable traditional bamboo crafts and integrate them into contemporary design. Due to quality and innovation, Yu (2023) introduced supplemental weft, inlay, and lattice or overlay techniques to make bamboo products more sustainable. In the supplemental weft technique, bamboo strips complement the primary threads, enhancing the fabric's texture and visual appeal. However, inlay involves inserting bamboo strips directly into the fabric structure to create intricate embellishments and designs (Yu, 2023). The lattice or overlay technique weaves bamboo strips over the fabric surface, adding texture and depth through weaving and knotting techniques. Yu (2023) stated that the evolving relationship between bamboo craft and design exemplifies a promising strategy for product development, blending tradition with innovation to create timeless artistry.

Other studies have explored integrating traditional decorative patterns with bamboo weaving for innovative product designs, particularly in textiles and clothing (Yu & Pashkevych, 2023; Yu, 2023). Techniques include combining bamboo weaving with other materials and applying cutting-edge technology to enhance efficiency and precision (Yu & Pashkevych, 2023; Yu, 2023). For instance, attaching bamboo weaving to fabric surfaces using modern production technology and weaving bamboo segments into three-dimensional forms represents innovative approaches (Yu & Pashkevych, 2023). This integration has yielded vibrant patterns and luxurious forms, showcasing bamboo's versatility in crafting modern, sustainable living items. Gao and Gu (2020) stated that bamboo weaving

techniques offer diverse applications, with traditional methods excelling in sustainability and traditional preservation, while modern approaches enhance efficiency and aesthetic versatility. Geometric elements, vibrant colors, and innovative techniques like hexagonal weaves reflect contemporary preferences while maintaining traditional craftsmanship (Yu & Pashkevych, 2023).

Traditional techniques like handloom weaving minimize waste but can be time-consuming and less adaptable to contemporary trends, as Gao and Gu (2020) noted. Techniques such as modular textile weaving and three-dimensional bamboo weaving enable intricate, innovative designs, as Yu (2023) and Yu and Pashkevych (2023) pointed out. Moreover, integrating advanced manufacturing technologies, such as 3D printing, can support personalized designs, standardized production, and mass customization, aligning the bamboo weaving industry with the principles of Industry 4.0 for greater sustainability (Zhang, 2019). Kumalasari et al. (2021) also indicated that artisan cooperatives producing bamboo-woven fabrics could target high-end fashion designers, sustainable clothing brands, and eco-conscious consumers, expanding beyond local markets into international fair trade as part of one of the successful projects in the real world. Despite challenges like production scalability and material rigidity, merging traditional and modern weaving techniques and technology presents opportunities for sustainable and innovative design solutions. The dual benefit of cultural preservation and environmental sustainability highlights the importance of bamboo weaving in contemporary design and production (Yu, 2023).

Additionally, Gao et al. (2024) emphasized the appeal of dynamic arrangements and vibrant patterns in attracting younger generations who appreciate the integration of tradition and modernity. However, production scalability and material rigidity warrant further exploration to maximize bamboo's potential in sustainable fashion and textiles (Zhang, 2019). Zhang (2019) stated that ongoing innovation in weaving methods, such as integrating bamboo with other materials and developing new weaving technologies, is vital for addressing these challenges. Furthermore, Gericke and Van der Pol (2010) mentioned that raising consumer awareness about bamboo products' environmental and cultural value can enhance their marketability and promote sustainable practices. The future of bamboo weaving lies in its ability to adapt to evolving consumer preferences and environmental needs.

It is credible that bamboo is a sustainable material; therefore, addressing concerns about false claims, labeling accuracy, and certifications for bamboo products is becoming increasingly significant. Labeling bamboo clothing presents major challenges that could impact consumer confidence and the broader sustainability goal in the textile industry. Research emphasizes that trust in sustainable fashion (Jalil, 2020) relies on garments' biodegradability and antimicrobial properties at the time of purchase. Standardized certification shapes consumer preferences in distinguishing between greenwashed

alternatives and genuinely sustainable bamboo textiles (Ajmad, 2024). Amjad (2024) noted that several certifications ensure environmental and ethical integrity for bamboo products. The OEKO-TEX Standard 100 guarantees that bamboo textiles are free from harmful substances, while the Global Organic Textile Standard (GOTS) adheres to strict environmental and social criteria. When evaluated through the triple bottom line of sustainability, the textile industry has a poor record of addressing social and ecological issues (Waite, 2009).

Okafor et al. (2021) highlighted the scarcity of textile recycling facilities in many countries, emphasizing the necessity for sustainable fabric waste management through innovative design and production to support a circular economy. Jalil (2020) stressed that achieving sustainability necessitates substantial product design and changes in consumer behavior. While recycling efforts aim to minimize virgin material usage, they often result in "downcycling." A free-market approach might be more effective in managing post-consumer textiles (Okafor et al., 2021). Jalil (2020) also pointed out that waste separation at the source and efficient collection systems cannot transform waste into a valuable resource. Programs such as the Blue Box Recycling Initiative (Okafor et al., 2021), which rewards participants with redeemable points, offer a viable textile recovery, reuse, and reprocessing model. Sustainable textile design, which aims to reduce energy consumption, minimize waste, and create efficient products, has found a promising partner in bamboo (Jalil, 2022).

Integrating bamboo into sustainable textile practices offers a unique opportunity to blend sustainability with textile heritage (Yu & Pashkevych, 2023), providing ecological and economic advantages. This review takes the opportunity to include the circular economy of bamboo, from cultivation to production, usage, and disposal. Bamboo clothes made from organic bamboo, not mixed products, can all be composted (Jalil, 2022). It includes investigating closed-loop technologies that allow for the recycling and reusing of bamboo fibers, reducing waste, and lowering environmental effects (Jalil, 2020). Furthermore, customer behavior is important in boosting demand for genuinely sustainable bamboo goods since conscious purchase decisions can encourage firms to adopt more ethical and transparent methods (Gao et al., 2024). Moreover, artisans can leverage bamboo's renewable properties in textile production to create high-demand sustainable products, opening new markets and enhancing livelihoods while preserving traditional craftsmanship (Gao, 2024). This biodegradable material, with unique properties such as antibacterial capabilities, UV protection, breathability, and moisture absorption, provides a compelling alternative for sustainable textile applications (Tausif et al., 2015).

Chen et al. (2017) investigated the possibility of combining mechanical pretreatment with low-alkaline chemical treatments to produce high-quality bamboo fibers. Further modifications, such as combing and carding, enhance the fibers' usability for textile production, as suggested by Hu et al., 2019. Producing bamboo fabric using hand-spinning

and handloom techniques supports sustainability by reducing energy consumption, waste, and water usage (Gao et al., 2024; Luo et al., 2021). Twill weave is identified as the optimal method for bamboo textile weaving, providing a uniform structure that balances flexibility and durability for various applications (Yu & Pashkevych, 2023). By starting with basic twill patterns, it is possible to develop aesthetically pleasing and advanced designs comparable to those created using other techniques (Hu et al., 2019). Innovations enable businesses to retain a proper competitive position in the market (Zheng & Zhu, 2021). Zheng and Zhu (2021) stated that using bamboo as an ecological material allows for implementing eco-innovations and participation in the closed-loop economy. In many sectors of the economy, the innovative use of bamboo provides a competitive edge while benefiting the environment. Chen et al. (2017) stated that a perfect bamboo product for the circular economy should be durable, replace abiotic materials, and be 100% bio-based, reusable, biodegradable, or energy-efficient when discarded.

Yu et al. (2023) stated innovative approaches to lightweight, portable, and multifunctional bamboo ideas through modular design, composite material innovations, and optimized joint structures. Bamboo weaving patterns, known for their symmetry and rhythmic structure, can be creatively reinterpreted through scattered compositions and free weaving techniques (Yu & Pashkevych, 2023). These innovations break away from traditional rigid designs, offering new possibilities for artistic expression and design flexibility, as demonstrated in various scholarly studies (Yu et al., 2023). De Vos (2010) explored laminated bamboo as a composite material. Luo et al. (2020) examined the evolution of bamboo weaving, emphasizing the integration of modern elements for sustainable development. Despite these studies, limited research exists on applying Interactive Genetic Algorithm (IGA) technology to bamboo weaving design. Pathways to sustainable bamboo textiles are represented in Figure 5.

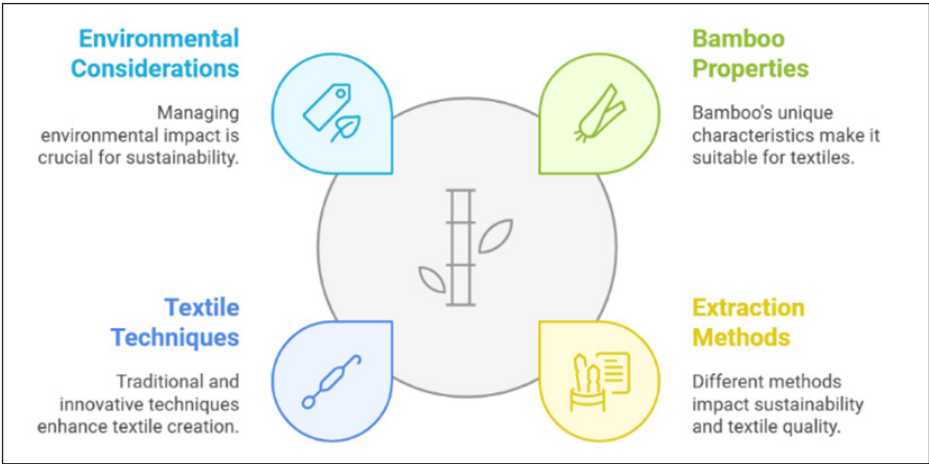


Figure 5. Pathways to sustainable bamboo textiles

CONCLUSION

Bamboo, known for its antibacterial properties and UV protection, offers significant potential for various textile and clothing applications. Despite the environmental benefits of bamboo, some ecological concerns need to be addressed to ensure its sustainable use. This paper reviewed bamboo's potential for sustainable handloom and craft weaving development. However, it acknowledges limitations, particularly regarding the environmental implications of alkaline treatments that reduce lignin content. While these treatments are cost-effective and energy-efficient, they produce chemical-laden wastewater, necessitating proper management through neutralization or closed-loop production systems. Public demand for organic textiles may encourage the adoption of less chemically intensive bamboo farming and production methods. Several areas could be explored to enhance the conclusion with actionable recommendations and future research directions. Further investigation into natural bamboo fiber production, yarn processing, handloom production, and wastewater treatment is vital for establishing fully sustainable bamboo products. Improving mechanical extraction techniques for bamboo fibers is crucial to enhancing efficiency while maintaining eco-friendly processing. Addressing these challenges through innovative solutions could establish bamboo as a cornerstone of sustainable fashion and clothing design. Research could focus on developing scalable, cost-effective, and energy-efficient mechanical methods to lessen reliance on chemical treatments. Incorporating bamboo materials into traditional patterns and weaving techniques represents a blend of tradition and innovation, contributing to cultural preservation and creative expression. Therefore, collaboration between designers and artisans is essential for revitalizing sustainable traditional bamboo crafts and integrating them into contemporary design. The evolving relationship between bamboo craft and design presents a promising strategy for product development, seamlessly combining tradition with innovation to create timeless artistry. Finally, future studies could evaluate the life cycle impact of bamboo textiles, addressing concerns about their long-term environmental benefits and potential ecological drawbacks.

ACKNOWLEDGMENTS

This research is supported by Universiti Malaysia Sarawak, the P. Ramlee Chair Research Grant No. UNI/F03/PRC/86591/2025

REFERENCES

- Akinlabi, E. T., Anane-Fenin, K., & Akwada, D. R. (2017). Applications of bamboo. In *Bamboo: The Multipurpose Plant* (pp. 365–381). Springer. https://doi.org/10.1007/978-3-319-56808-9_5
- Amjad, A. I. (2024). Bamboo fiber: A sustainable solution for textile manufacturing. *Advances in Bamboo Science*, 7, 71–88. <https://doi.org/10.1016/j.bamboo.2024.100088>

- Asmarea, F. W., Liua, X., Qiaod, G., Lia, R., Wua, D., & Kc, M. B. (2022). Physical and mechanical properties of coarse bamboo fibers extracted by different techniques. *Journal of Fiber Bioengineering & Informatics*, 15(4), 287-302. <https://doi.org/10.3993/jfbim00399>.
- Chaowana, K., Wisadsatorn, S., & Chaowana, P. (2021). Bamboo as a sustainable building material - culm characteristics and properties. *Sustainability*, 13(13), 287-294. <https://doi.org/10.3390/su13137376>
- Chen, H., Yu, Y., Zhong, T., Wu, Y., Li, Y., Wu, Z., & Fei, B. (2017). Effect of alkali treatment on microstructure and mechanical properties of individual bamboo fibers. *Cellulose*, 24(1), 333–347. <https://doi.org/10.1007/s10570-016-1116-6>
- Chonsakorn, S., Chombhuphan, R., Rattanaporn, K., Srivorradatphisan, S., Ruangnarong, C., & Khojitmate, S. (2024). A novel non-woven fabric from bamboo fiber in medical lifestyle products. *Heliyon*, 10(9), Article e29893. <https://doi.org/10.1016/j.heliyon.2024.e29893>
- De Vos, V. (2010). *Bamboo for Exterior Joinery* [Doctoral dissertation]. Larenstein University, The Netherlands. https://static1.squarespace.com/static/54cfdd11e4b0416d14b162e6/t/6591c07edca5070e8db3892e/1704050840987/bamboo_for_exterior_joinery-by_valentijn_de_vos.pdf
- Gao, J., & Gu, Y. (2020). Innovative design ideas for bamboo furniture are based on Jiangnan culture. *Research in the Art of Design*, 81, Article 92.
- Gao, M., Cao, X., & Qian, L. (2024). Cultural echoes in modern design: Assessing young consumers' perceptions of traditional bamboo weaving patterns. *Complexity*, 2024(1), Article 5524490. <https://doi.org/10.1155/2024/5524490>
- Gericke, A., & Van der Pol, J. (2010). A comparative study of regenerated bamboo, cotton, and viscose rayon fabrics. Part 1: Selected comfort properties. *Journal of Consumer Science*, 39, 10–188. <https://doi.org/10.4314/jfec.v38i1.61642>
- Hardin, I. R., Wilson, S. S., Dhandapani, R., & Dhende, V. (2009). An assessment of the validity of claims for “Bamboo” fibers. *AATCC Review*, 9(10), 33–36.
- Hu, M., Wang, C., Lu, C., Anuar, N. I. S., Yousfani, S. H. S., Jing, M., Chen, Z., Zakaria, S., & Zuo, H. (2019). Investigation on the classified extraction of bamboo fiber and its properties. *Journal of Natural Fibers*, 17(12), 1798-1808. <https://doi.org/10.1080/15440478.2019.1599311>
- Jais, F. N. M., Mokeramin, M., Roslan, M. N., Halip, J. A., & Jusoh, W. A. W. (2023). Bamboo fiber for textile applications. In P. M. Tahir, S. H. Lee, S. S. O. Al-Edrus, & M. K. A. Uyup (Eds.), *Multifaceted Bamboo: Engineered Products and Other Applications* (pp. 275-290). Springer. https://doi.org/10.1007/978-981-19-9327-5_14
- Jalil, M. H. (2022). Eco-fashion design - A review. *International Journal of Sustainable Design*, 4(3-4), 205–233. <https://doi.org/10.1504/IJSDES.2022.128515>
- Jansiri, S., Deenu, A., Puangsin, B., Sungkaew, S., & Kamthai, S. (2021). Characterization of sweet bamboo craft pulp filled in poly (lactic acid)/polybutylene succinate blend composite. *Polymer Composites*, 42(10), 5090–5100. <https://doi.org/10.1002/pc.26207>
- Kaur, P. J., Kardam, V., Naik, S. N., Satya, S., & Pant, K. K. (2016). Characterization of commercially important Asian bamboo species. *European Journal of Wood and Wood Products*, 74, 137–139. <https://doi.org/10.1007/s00107-015-0977-y>

- Khalil, H. A., Bhat, I., Jawaid, M., Zaidon, A., Hermawan, D., & Hadi, Y. (2012). Bamboo fiber reinforced biocomposites: A review. *Materials and Design*, 42(1), 353–368. <https://doi.org/10.1016/j.matdes.2012.06.015>
- Kozłowski, R. M., & Mackiewicz-Talarczyk, M. (2020). Introduction to natural textile fibers. In R. M. Kozłowski & M. Mackiewicz-Talarczyk (Eds.), *Handbook of Natural Fibers* (pp. 1–13). Woodhead Publishing. <https://doi.org/10.1016/B978-0-12-818398-4.00001-3>
- Kumalasari, R., Habsari, S. K., & Wibowo, P. A. W. (2021). Resistance of bamboo woven craftswomen to natural exploitation. *Kafaah: Journal of Gender Studies*, 11(2), 215–227. <http://dx.doi.org/10.15548/jk.v11i2.438>
- Kushwaha, A., Chaudhary, K., & Prakash, C. (2023). A study on the mechanical properties of pineapple, bamboo, and cotton woven fabrics. *Biomass Conversion and Biorefinery*, 13, 1–12. <https://doi.org/10.1007/s13399-023-03841-6>
- Liese, W., & Tang, T. K. H. (2015). Properties of the bamboo culm. In W. Liese & M. Kohl (Eds.), *Tropical Forestry, Bamboo: The Plant and Its Uses* (pp. 227–256). Springer International Publishing. https://doi.org/10.1007/978-3-319-14133-6_8
- Lipp-Symonowicz, B., Sztajnowski, S., & Wojciechowska, D. (2011). New commercial fibers called “bamboo fibers” - Their structure and properties. *Fibers & Textiles in Eastern Europe*, 1(84), 18–23.
- Luo, B., Ahmed, S., & Long, C. (2020). Bamboos are used for weaving and acquiring relevant traditional knowledge in Sansui, Southwest China. *Journal of ethnobiology and ethnomedicine*, 16, 1–9. <https://doi.org/10.1186/s13002-020-00418-9>
- Mishra, R., Behera, B. K., & Pal, B. P. (2012). Novelty bamboo fabric. *Journal of the Textile Institute*, 103(3), 320–329. <https://doi.org/10.1080/00405000.2011.576467>
- Nassar, K. M., Mohsen, N., & Taleb, E. A. (2020). Improving the thermal comfort of bamboo and bamboo blended fabrics for sports head scarves. *International Design Journal*, 10(4), 131–137. <https://doi.org/10.21608/idj.2020.38068.1006>
- Nayak, L., & Mishra, S. P. (2016). The prospect of bamboo as a renewable textile fiber: Historical overview, labeling, controversies, and regulation. *Fashion and Textiles*, 3(1), 1–12. <https://doi.org/10.1186/s40691-015-0054-5>
- Neha, P., & Aravendan, M. (2023). A review on sustainable product design, marketing strategies and conscious consumption of bamboo lifestyle products. *Intelligent Information Management*, 15(3), 67–99. <https://doi.org/10.4236/iim.2023.153005>
- Okafor, C. C., Madu, C. N., Ajaero, C. C., Ibekwe, J. C., Nzekwe, C. A., Okafor, C., & Nzekwe, C. (2021). Sustainable management of textile and clothing. *Clean Technologies and Recycling*, 1(1), 70–87. <https://doi.org/10.3934/ctr.2021004>
- Ozkan, G. (2021). Investigate the effects of physical parameters of fabrics woven with 100% bamboo fiber yarn on wearing comfort properties. *International Journal of Engineering Science and Application*, 5(4), 106–111.
- Phong, N. T., Fujii, T., Chuong, B., & Okubo, K. (2012). Study how to extract bamboo fibers from raw bamboo and wastewater treatment effectively. *Journal of Materials Science Research*, 1(1), 144–155. <https://doi.org/10.5539/jmsr.v1n1p144>

- Prakash, C., Rajwin, A. J., Periyasamy, S., & Gunasekaran, G. (2021). Effect of bamboo and neem charcoal microparticles application on woven fabrics' antibacterial and UV protection properties. *Journal of the Textile Institute*, 112(7), 1171–1180. <https://doi.org/10.1080/00405000.2020.1805193>
- Restrepo, A., Becerra, R., & Tibaquirá, J. E. (2016). Energetic and carbon footprint analysis in the manufacturing process of bamboo boards in Colombia. *Journal of Cleaner Production*, 126, 563–571. <https://doi.org/10.1016/j.jclepro.2016.02.144>
- Rocky, B. P., & Thompson, A. J. (2018). Production of natural bamboo fibers: Experimental approaches to different processes and analyses. *Journal of the Textile Institute*, 109(10), 1381–1391. <https://doi.org/10.1080/00405000.2018.1482639>
- Saha, D. C., & Mandal, J. N. (2020). Performance of reclaimed asphalt pavement reinforced with bamboo geogrid and bamboo geocell. *International Journal of Pavement Engineering*, 21(5), 571–582. <https://doi.org/10.1080/10298436.2018.1502432>
- Santos, A. S., Ferreira, P. J. T., & Maloney, T. (2021). Bio-based materials for nonwovens. *Cellulose*, 28(14), 8939–8969. <https://doi.org/10.1007/s10570-021-04125-w>
- Shinohara, Y., Misumi, Y., Kubota, T., & Nanko, K. (2019). Characteristics of soil erosion in a moso-bamboo forest of western Japan: Comparison with a broadleaved and coniferous forest. *Catena*, 172, 451–460. <https://doi.org/10.1016/j.catena.2018.09.011>
- Singh, B., & Dessalegn, M. Y. (2021). Effect analysis of extraction processes of bamboo fiber. *Natural Volatiles and Essential Oils Journal*, 8(5), 4226–4246.
- Tausif, M., Ahmad, F., Hussain, U., Basit, A., & Hussain, T. (2015). A comparative study of mechanical and comfort properties of bamboo viscose as an eco-friendly alternative to conventional cotton fiber in polyester blended knitted fabrics. *Journal of Cleaner Production*, 89(1), 110–115. <https://doi.org/10.1016/j.jclepro.2014.11.011>
- Waite, M. (2009). Sustainable textiles: The role of bamboo and a comparison of bamboo textile properties. *Journal of Textiles and Apparel Technology and Management*, 6(2), 1–21.
- Yu, L. (2023). Digital sustainability of intangible cultural heritage: The example of the “Wu Leno” weaving technique in Suzhou, China. *Sustainability*, 15(12), Article 9803. <https://doi.org/10.3390/su15129803>
- Yu, Z., & Pashkevych, K. (2023). Innovative application of traditional bamboo weaving in modern furniture design. *Art and Design*, (3), 79-91. <https://doi.org/10.30857/2617-0272.2023.3.7>
- Zhang, J. (2019). Innovative application of traditional patterns in modern furniture design. In *2019 1st Asia International Symposium on Arts, Literature, Language and Culture (AISALLC 2019)* (pp. 404-408). Francis Academic Press, <https://doi.org/10.25236/aisallc.2019.083>
- Zhang, M., Chen, S., Jiang, H., Peng, C., Zhang, J., & Zhou, G. (2020). The impact of intensive management on net ecosystem productivity and net primary productivity of a Lei bamboo forest. *Ecological Modelling*, 435, 109–248. <https://doi.org/10.1016/j.ecolmodel.2020.109248>
- Zhao, W., Zou, Y., Zhang, W., Chen, H., Zhang, J., Wu, A., & Zhao, Y. (2024). Optimization of process parameters for bamboo fiber extraction by steam explosion. *Journal of Natural Fibers*, 21(1), 230–249. <https://doi.org/10.1080/15440478.2023.2301369>

Zheng, Y., & Zhu, J. (2021). The application of bamboo weaving in modern furniture. *BioResources*, 16(3), 5024-5035. <https://doi.org/10.15376/biores.16.3.5024-5035>

**REFEREES FOR THE PERTANIKA
JOURNAL OF SCIENCE & TECHNOLOGY**

Vol. 33 (3) APR. 2025

The Editorial Board of the Pertanika Journal of Science and Technology wishes to thank the following:

A. Lenin Fred <i>MarEphraem, India</i>	Faizah Che Ros <i>UTM, Malaysia</i>	Kamalrul Azlan Azizan <i>UKM, Malaysia</i>
Adriano Michael Bernardin <i>UNESC, Brazil</i>	Francisco Cruz-Sosa <i>UAM-I, Mexico</i>	Kaveh Moghadasi <i>University of Adelaide, Australia</i>
Ali-Reza Moznebi <i>University of Alberta, Canada</i>	Girish G N <i>IIIT Dharwad, India</i>	Khairunnisa Amreen <i>BITS, India</i>
Ardik Wijayanto <i>PENS, Indonesia</i>	Goh You Keng <i>AARSB, Malaysia</i>	Khor Chu Yee <i>UNIMAP, Malaysia</i>
Arpah Abu <i>UM, Malaysia</i>	H. M. Zakir Hossain <i>JUST, Bangladesh</i>	Kim On Chin <i>UMS, Malaysia</i>
Balasubramanian Malaikozhundan <i>GRI, India</i>	Hedzlin Zainuddin <i>UiTM, Malaysia</i>	Klaus Schwarzer <i>Kiel University, Germany</i>
Cai Yiyu <i>NTU, Singapore</i>	Hermin Pancasakti Kusumaningrum <i>Undip, Indonesia</i>	Lalitha Pottail <i>Avinashilingam University, India</i>
Chaw Jun Kit <i>UKM, Malaysia</i>	I Wayan Sukadana <i>UNDIKNAS, Indonesia</i>	Lilly Suriani Affendey <i>UPM, Malaysia</i>
Arpah Abu <i>UM, Malaysia</i>	Innocent J Macha <i>UDSM, Tanzania</i>	Manjunath K Vanahalli <i>IIIT Dharwad, India</i>
Balasubramanian Malaikozhundan <i>GRI, India</i>	Intan Sorfina Zainal Abidin <i>USM, Malaysia</i>	Maziah Mohamad <i>UTM, Malaysia</i>
Cai Yiyu <i>NTU, Singapore</i>	Izwan Bharudin <i>UKM, Malaysia</i>	Mireia Baeza <i>UAB, Spain</i>
Chaw Jun Kit <i>UKM, Malaysia</i>	Jan Bogacki <i>PW, Poland</i>	Mohamed E. Zayed <i>KFUPM, Saudi Arabia</i>
Dhaou Said <i>University of Sherbrooke, Canada</i>	Javad Seyedmohammadi <i>AREEO, Iran</i>	Mohammad Muqtada Ali Khan <i>UMK, Malaysia</i>
	Kalidasan Balasubramanian <i>Sunway University, Malaysia</i>	Mohd Heikal Husin <i>USM, Malaysia</i>

Mohd Na'im Abdullah <i>UPM, Malaysia</i>	Raja Rina Raja Ikram <i>UTeM, Malaysia</i>	Wan Yusmawati Wan Yusoff <i>UPNM, Malaysia</i>
Mohd Shahrul Nizam Mohd Danuri <i>UM, Malaysia</i>	Saeed Nosratabadi <i>MATE, Hungary</i>	Widi Aribowo <i>UNESA, Indonesia</i>
Muhammad Imran Najeeb <i>UNITEN, Malaysia</i>	Sangappa Ramachandra Biradar <i>SDMCET, India</i>	Xiaoguo Song <i>HIT, China</i>
Nazlina Shaari <i>UPM, Malaysia</i>	Sattar Mohammadi Esfarjani <i>IAU, Iran)</i>	Yong Mao Huang <i>Xihua University, China</i>
Nengchao Lyu <i>WHUT, China</i>	Satyam Panchal <i>University of Waterloo, Canada</i>	Zanariah Hashim <i>UTM, Malaysia</i>
Nikolaos Pellas <i>UOWM, Greece</i>	Shailesh Tiwari <i>ABESEC, India</i>	Zeeshan Ahmad Arfeen <i>IUB, Pakistan</i>
Noé Cheung <i>Unicamp, Brazil</i>	Siti Rabiattull Aisha Idris <i>UMPSA, Malaysia</i>	Zulkarnain Ahmad Noorden <i>UTM, Malaysia</i>
Nor Hanuni Ramli <i>UMP, Malaysia</i>	Suleyman Adak <i>MAU, Turkey</i>	Zulkarnain Jalil <i>USK, Indonesia</i>
Norlaila Mohd Zanuri <i>USM, Malaysia</i>	Syed Abdul Rahman Al-Haddad b. Syed Mohamed <i>UPM, Malaysia</i>	
Peifen Zhu <i>University of Missouri, United States</i>	Tomasz M. Chmielewski <i>PW, Poland</i>	

AARSB	– Applied Agricultural Resources Sdn. Bhd.	UiTM	– Universiti Teknologi MARA Malaysia
ABESEC	– ABES Engineering College	UKM	– Universiti Kebangsaan Malaysia
AREEO	– Agricultural Research, Education and Extension Organization	UM	– Universiti Malaya
BITS	– Birla Institute of Technology and Science	UMK	– University Malaysia Kelantan
GRI	– Gandhigram Rural Institute	UMP	– Universiti Malaysia Pahang
HIT	– Harbin Institute of Technology	UMPSA	– Universiti Malaysia Pahang Al-Sultan Abdullah
IAU	– Islamic Azad University	UMS	– Universiti Malaysia Sabah
IIIT Dharwad	– Indian Institute of Information Technology (IIIT), Dharwad	UNDIKNAS	– Universitas Pendidikan Nasional
IUB	– The Islamia University of Bahawalpur	Undip	– Diponegoro University
JUST	– Jashore University of Science and Technology	UNESA	– Universitas Negeri Surabaya
KFUPM	– King Fahd University of Petroleum & Minerals	UNESC	– University of the Extreme South of Santa Catarina
MarEphraem	– Mar Ephraem College of Engineering and Technology	Unicamp	– State University of Campinas
MATE	– Hungarian University of Agriculture and Life Sciences	UNIMAP	– Universiti Malaysia Perlis
MAU	– Mardin Artuklu University	UNITEN	– Universiti Tenaga Nasional
NTU	– Nanyang Technological University	UOWM	– University of Western Macedonia
PENS	– Politeknik Elektronika Negeri Surabaya	UPM	– Universiti Putra Malaysia
PW	– Politechnika Warszawska	UPNM	– Universiti Pertahanan Nasional Malaysia
SDMCET	– Shri Dharmasthala Manjunatheshwara College of Engineering and Technology	USK	– Universitas Syiah Kuala
UAB	– Universitat Autònoma de Barcelona	USM	– Universiti Sains Malaysia
UAM-I	– Universidad Autónoma Metropolitana-Iztapalapa	UTeM	– Universiti Teknikal Malaysia Melaka
UDSM	– University of Dar es Salaam	UTM	– Universiti Teknologi Malaysia
		WHUT	– Wuhan University of Technology

While every effort has been made to include a complete list of referees for the period stated above, however if any name(s) have been omitted unintentionally or spelt incorrectly, please notify the Chief Executive Editor, *Pertanika* Journals at executive_editor.pertanika@upm.edu.my

Any inclusion or exclusion of name(s) on this page does not commit the *Pertanika* Editorial Office, nor the UPM Press or the university to provide any liability for whatsoever reason.

Effect of Heat Treatment on the Properties of Perlis Dolomite Powder <i>Nur Hasnidah Ahmad Shukeri, Syed Nuzul Fadzli Syed Adam, Hasmaliza Mohamad, Heah Cheng Yong and Hamdan Yahya</i>	1613
Enhanced White Blood Cell and Platelet Segmentation: A Particle Swarm Optimization-based Chromaticity approach <i>Aiswarya Senthilvel, Krishnaveni Marimuthu and Subashini Parthasarathy</i>	1633
<i>Review Article</i>	
Weaving a Greener Tomorrow: A Mini Review of Bamboo Fiber, Textiles and Hand-woven Techniques for Sustainable Innovation <i>Marzie Hatef Jalil</i>	1661

Assessment of the Bioavailability of Zinc (Zn), Lead (Pb), Nickel (Ni), and Cadmium (Cd) in the Sediments of the Sungai Buloh Estuaries, Selangor <i>Aqilah Mukhtar, Mohd Nazri M Yunus, Nur Amiera Kamarudin, Syaizwan Zahmir Zulkifli and Ahmad Ismail</i>	1413
Comparative Analysis of Ultrasonic Inspection Techniques for Corrosion Monitoring in Petrochemical Plants Using Analytic Hierarchy Process (AHP) <i>Jan Lean Tai, Mohamed Thariq Hameed Sultan and Farah Syazwani Shahar</i>	1439
<i>Review Article</i>	
Effectiveness of Using Augmented Reality-based Picture Exchange Communication System (PECS) in Improving Communication Skills of Autistic Students in Indonesian Language Subjects: Bibliometric Analysis <i>Munir, Dwi Novia Al Husaeni, Eka Fitrajaya Rahman and Rasim</i>	1459
Optimization and Analysis of Ultrasonic Wedge Bonding Parameters for Enhanced Bonding Performance in 21700 Cylindrical Lithium Battery Modules <i>Bin Luo, Mohamad Hanif Md Saad, Altaf Hossain Molla and Zambri Harun</i>	1483
Coastal Bris Wetland Hydrodynamics in Non-Monsoon and Monsoon Seasons at Mengabang Telipot Terengganu, Peninsular Malaysia <i>Syazuani Mohd Shariff, Edlic Sathiamurthy and Mohd Sofiyan Sulaiman</i>	1509
AI-driven Vision-based Pothole Detection for Improved Road Safety <i>Muhammad Aizat Rasee, Ung Ling Ling, Gloria Jennis Tan, Tan Chi Wee, Ron Buking, Norziana Yahya and Habibah Ismail</i>	1535
Investigation of Aged-related Metabolites in the Marine Polychaete (<i>Marphysa moribidii</i>) using ¹ H NMR Metabolomics and LC-MS/MS Analysis <i>Nurfarah Aini Mocktar, Mohamad Sofi Abu Hassan, Maulidiani Maulidiani, Wan Iryani Wan Ismail, Izwandy Idris, Farhanini Yusoff and Noor Aniza Harun</i>	1563
Energy Management Systems Development in Electric Vehicle Charging Stations Based on Multi-Source Inverters with Utilisation of Renewable Energy Sources <i>Iradiratu Diah Prahmana Karyatanti, Belly Yan Dewantara, Istiyo Winarno, Daeng Rahmatullah and Nuhman</i>	1595

<i>Review Article</i>	
Thematic Trends on Data Quality Studies in Big Data Analytics: A Review <i>Nazliah Chikon, Shuzlina Abdul-Rahman and Syaripah Ruzaini Syed Aris</i>	1231
Numerical Study on the Effects of Wire bonding Looping Formation on Light-emitting Diode Encapsulation Process <i>Ahmad Amin Azmi Jaludin, Mohd Syakirin Rusdi, Mohd Sharizal Abdul Aziz and Mohammad Hafifi Hafiz Ishak</i>	1257
Development of a Two-board Potentiostat for Square Wave Anodic Stripping Voltammetry: Prospects for Heavy Metal Monitoring <i>Siti Nur Hanisah Umar, Elmi Abu Bakar, Mohammad Nishat Akhtar, Noorfazreena Mohammad Kamaruddin and Naoki Uchiyama</i>	1273
Design of a Two-layer SIW Power Divider with Slot Aperture Y-junction for Enhanced Narrowband Isolation <i>Gan Siang Tan, Siti Zuraidah Ibrahim, Mohd Nazri A Karim, Ping Jack Soh, Khuzairi Masrakin and Sugchai Tantivivat</i>	1301
Phyto Constituents of <i>Ananas comosus</i> Leaf Extract Enhancing the Copper Nanoparticles Synthesis <i>Nur Diyana Zulpahmi, Wan Zuraida Wan Mohd Zain, Fazlena Hamzah, Nurul Wahida Ramli, Nur 'Amira Hamid, Irmaizatussyehdany Buniyamin, Wan Atikah Wan Hamidon and Siti Aisha Na'illa Che Musa</i>	1321
Role of Brassinosteroid on Growth, Metabolic Contents and Wax Ester Fermentation in <i>Euglena</i> sp. <i>Deviko Mardiansah, Tia Erfianti, Khusnul Qonita Maghfiroh, Dedy Kurnianto, Ria Amelia, Brilian Ryan Sadewo and Eko Agus Suyono</i>	1341
Comparative Evaluation of Python-based Heart Rate Variability Analysis Tools for Neonatal Sepsis Detection in Neonatal Intensive Care Units <i>Roshan David Jathanna, Dinesh Acharya Udupi, Faiza Iqbal, Krishnamoorthi Makkithaya and Leslie Edward Simon Lewis</i>	1367
<i>Review Article</i>	
Comprehensive Review on Sustainable Dam Infrastructure: Issues and Challenges, Factors Causing Dam Failure and Future Direction in a Globally Changing Climate <i>Nur Azwa Muhamad Bashar, Mohd Remy Rozainy Mohd Arif Zainol, Mohd Sharizal Abdul Aziz, Ahmad Zhafran Ahmad Mazlan, Mohd Hafiz Zawawi and Teh Sabariah Abd Manan</i>	1387

Pertanika Journal of Science & Technology

Vol. 33 (3) Apr. 2025

Content

Foreword	i
<i>Luqman Chuah Abdullah</i>	
A Clustering-based Hybrid Approach for Analyzing High-grade Gliomas Using Radiomic Features	1105
<i>Sairam Vuppala Adithya, Navaneeth Bhaskar and Priyanka Tupe-Waghmare</i>	
A Transfer Function Modelling Using System Identification for Air-cooling Photovoltaic System	1119
<i>Rozita Mustafa, Mohd Amran Mohd Radzi, Azura Che Soh and Hashim Hizam</i>	
Growth Monitoring of Healthy and BSR-infected Oil Palm Seedlings Using Ground-based LiDAR	1137
<i>Nur Azuan Husin, Ray Clement Ridu, Normahnani Md Noh and Siti Khairunniza Bejo</i>	
<i>Review Article</i>	
Thermal and Mechanical Stability of Bismuth Doped Sn-Ag-Cu Lead-free Solder: A Comprehensive Review	1159
<i>Ong Jun Lin, Azmah Hanim Mohamed Ariff, Nuraini Abdul Aziz and Azizan As'arry</i>	
<i>Review Article</i>	
A Review on Experimental, Numerical, and Machine Learning-based Solar Energy Harvesting for Road Pavements Application	1185
<i>Muhammad Imran Najeeb, Nurul Aqilah Razeman, Zarina Itam, Salmia Beddu, Nazirul Mubin Zahari, Mohd Zakwan Ramli, Mohd Hafiz Zawawi, Nur Liyana Mohd Kamal, Agusril Syamsir and Daud Mohamad</i>	
Examining the Impact of Battery Properties and Energy Storage Connectivity for Electric Vehicle Charging Performance	1209
<i>Muhammad Izzul Mawardi, Nik Hakimi Nik Ali, Muhamad Nabil Hidayat, Ezmin Abdullah, Muhammad Umair, Ahmad Sukri Ahmad and Muzakkir Mohammad Zainol</i>	



Pertanika Editorial Office, Journal Division,
Putra Science Park,
1st Floor, IDEA Tower II,
UPM-MTDC Center,
Universiti Putra Malaysia,
43400 UPM Serdang,
Selangor Darul Ehsan
Malaysia

<http://www.pertanika.upm.edu.my>
Email: executive_editor.pertanika@upm.edu.my
Tel. No.: +603- 9769 1622

PENERBIT
UPM
UNIVERSITI PUTRA MALAYSIA
P R E S S

<http://penerbit.upm.edu.my>
Email: penerbit@upm.edu.my
Tel. No.: +603- 9769 8855

